Nanoscale Materials in Water Purification

Nanoscale Materials in Water Purification

Edited by

Sabu Thomas

Daniel Pasquini

Shao-Yuan Leu

Deepu A. Gopakumar

Elsevier
Radarweg 29, PO Box 211, 1000 AE Amsterdam, Netherlands
The Boulevard, Langford Lane, Kidlington, Oxford OX5 1GB, United Kingdom
50 Hampshire Street, 5th Floor, Cambridge, MA 02139, United States

Notices
Knowledge and best practice in this field are constantly changing. As new research and experience broaden our understanding, changes in research methods, professional practices, or medical treatment may become necessary.

Practitioners and researchers must always rely on their own experience and knowledge in evaluating and using any information, methods, compounds, or experiments described herein. In using such information or methods they should be mindful of their own safety and the safety of others, including parties for whom they have a professional responsibility.

To the fullest extent of the law, neither the Publisher nor the authors, contributors, or editors, assume any liability for any injury and/or damage to persons or property as a matter of products liability, negligence or otherwise, or from any use or operation of any methods, products, instructions, or ideas contained in the material herein.

Library of Congress Cataloging-in-Publication Data
A catalog record for this book is available from the Library of Congress

British Library Cataloguing-in-Publication Data
A catalogue record for this book is available from the British Library

ISBN: 978-0-12-813926-4

Publisher: Matthew Deans
Acquisition Editor: Simon Holt
Editorial Project Manager: Lawrence Lindsay
Production Project Manager: Sruthi Satheesh
Cover Designer: Greg Harris

Typeset by SPi Global, India

Contributors

Shao-Yuan (Ben) Leu
Department of Civil and Environmental Engineering ZS923, The Hong Kong Polytechnic University Hung Hom, Kowloon, Hong Kong

E.C. Abdullah
Malaysia-Japan International Institute of Technology (MJIIT), Universiti Teknologi Malaysia, Kuala Lumpur, Malaysia

M. Ahmed
Department of Chemical Engineering, Khalifa University of Science and Technology, Abu Dhabi, United Arab Emirates

Tejraj M. Aminabhavi
Sonia College of Pharmacy, Dharwad, India

Michael Arkas
Institute of Nanoscience and Nanotechnology NCSR "Demokritos", Athens, Greece

Vishnu Arumughan
Chemistry and Chemical Engineering, Chalmers University of Technology, Gothenburg, Sweden

Yana Bagbi
Special Centre for Nanoscience, Jawaharlal Nehru University, New Delhi; Department of Physics, North Eastern Regional Institute of Science and Technology, Nirjuli, India

Humair Ahmed Baloch
School of Engineering, RMIT University, Melbourne, VIC, Australia

Soumen Basu
School of Chemistry and Biochemistry, Thapar Institute of Engineering & Technology, Patiala, India

Jorge Bedia
Chemical Engineering Section, Universidad Autonoma de Madrid, Madrid, Spain

Carolina Belver
Chemical Engineering Section, Universidad Autonoma de Madrid, Madrid, Spain

Amit Bhatnagar
Department of Environmental and Biological Sciences, University of Eastern Finland, Kuopio, Finland

Irene Bonadies
Institute of Polymers, Composites and Biomaterials, National Research Council of Italy, Pozzuoli, Italy

Priyakshree Borthakur
Materials Sciences and Technology Division, CSIR-North East Institute of Science and Technology; Academy of Scientific and Innovative Research, CSIR-NEIST Campus, Jorhat, India

Purna K. Boruah
Materials Sciences and Technology Division, CSIR-North East Institute of Science and Technology; Academy of Scientific and Innovative Research, CSIR-NEIST Campus, Jorhat, India

Ailish Breen
Nanotechnology and Bio-Engineering Research Group, Department of Environmental Science, School of Science; Centre for Precision Engineering, Materials and Manufacturing Research (PEM), Institute of Technology Sligo, Sligo, Ireland

Mohit Chaudhary
Department of Polymer and Process Engineering, Indian Institute of Technology Roorkee, Roorkee, India

Shiao-Shing Chen
Institute of Environmental Engineering and Management, National Taipei University of Technology, Taipei, Taiwan

Feitai Chen
National Demonstration Center for Experimental Chemistry Education, Jishou University, Jishou, China

Rikarani R. Choudhury
Laboratory for Advanced Research in Polymeric Materials (SARP-LARPM), Central Institute of Plastics Engineering & Technology (CIPET), Bhubaneswar, India

María-José Corbatón-Báguena
Research Institute for Industrial, Radiophysical and Environmental Safety (ISIRYM), Universitat Politècnica de València, Valencia, Spain

Manash R. Das
Materials Sciences and Technology Division, CSIR-North East Institute of Science and Technology; Academy of Scientific and Innovative Research, CSIR-NEIST Campus, Jorhat, India

Mohammad Hossein Davood Abadi Farahani
Department of Chemical & Biomolecular Engineering, National University of Singapore, Singapore, Singapore

Luís Carlos de Morais
Chemistry Department, Federal University of Triangulo Mineiro-UFTM, ICENE Institute, Uberaba, Brazil

Ehsan Dhaneshvar
Department of Environmental and Biological Sciences, University of Eastern Finland, Kuopio, Finland

Ankita Dhillon
Department of Chemistry, Banasthali University, Rajasthan, India

Maya Endo
Institute for Catalysis, Hokkaido University, Sapporo, Japan

Priyanka Ganguly
Nanotechnology and Bio-Engineering Research Group, Department of Environmental Science, School of Science; Centre for Precision Engineering, Materials and Manufacturing Research (PEM), Institute of Technology Sligo, Sligo, Ireland

Jorge García-Ivars
Research Institute for Industrial, Radiophysical and Environmental Safety (ISIRYM), Universitat Politècnica de València, Valencia, Spain

A. Giwa
Department of Chemical Engineering, Khalifa University of Science and Technology, Abu Dhabi, United Arab Emirates

Jaydevsinh M. Gohil
Advanced Polymer Design and Development Research Laboratory (SARP-APDDRL), Central Institute of Plastics Engineering & Technology (CIPET), Bengaluru; Laboratory for Advanced Research in Polymeric Materials (SARP-LARPM), Central Institute of Plastics Engineering & Technology (CIPET), Bhubaneswar, India

Almudena Gómez-Avilés
Chemical Engineering Section, Universidad Autonoma de Madrid, Madrid, Spain

Deepu A. Gopakumar
School of Industrial Technology, Universiti Sains Malaysia (USM), Gelugor, Penang, Malaysia

Andrews Nirmala Grace
Centre for Nanotechnology Research, VIT University, Vellore, India

G.J. Griffin
School of Engineering, RMIT University, Melbourne, VIC, Australia

U.S. Hareesh
Materials Science and Technology Division, National Institute for Interdisciplinary Science and Technology (CSIR-NIIST), Thiruvananthapuram; Academy of Scientific and Innovative Research (AcSIR), New Delhi, India

S.W. Hasan
Department of Chemical Engineering, Khalifa University of Science and Technology, Abu Dhabi, United Arab Emirates

Rongan He
Hunan Province Key Laboratory of Applied Environmental Photocatalysis, Changsha University, Changsha, China

María-Isabel Iborra-Clar
Research Institute for Industrial, Radiophysical and Environmental Safety (ISIRYM); Department of Chemical and Nuclear Engineering, Universitat Politècnica de València, Valencia, Spain

Tahir Jamil
Department of Polymer Engineering and Technology, University of the Punjab, Lahore, Pakistan

Marcin Janczarek
Institute for Catalysis, Hokkaido University, Sapporo, Japan; Department of Chemical Technology, Gdansk University of Technology, Gdansk, Poland

Abdul Khalil H.P.S.
School of Industrial Technology, Universiti Sains Malaysia (USM), Gelugor, Penang, Malaysia

Alireza Khataee
Department of Applied Chemistry, Faculty of Chemistry, University of Tabriz, Tabriz, Iran

Costas Kiparissides
Chemical Process & Energy Resources Institute-Centre for Research and Technology Hellas, Thessaloniki, Greece

I. Kitsou
School of Mining Engineering and Metallurgy, National Technical University of Athens, Athens, Greece

Olympia Kotrotsiou
Chemical Process & Energy Resources Institute-Centre for Research and Technology Hellas, Thessaloniki, Greece

Ewa Kowalska
Institute for Catalysis; Graduate School of Environmental Science, Hokkaido University, Sapporo, Japan

Dinesh Kumar
School of Chemical Sciences, Central University of Gujarat, Gandhinagar, India

Jieun Lee
School of Chemical and Biomolecular Engineering, The University of Sydney, Sydney, NSW, Australia

Youji Li
National Demonstration Center for Experimental Chemistry Education, Jishou University, Jishou, China

Jagannathan Madhavan
Solar Energy Lab, Department of Chemistry, Thiruvalluvar University, Vellore, India

Abhijit Maiti
Department of Polymer and Process Engineering, Indian Institute of Technology Roorkee, Roorkee, India

Arumugam Malathi
Solar Energy Lab, Department of Chemistry, Thiruvalluvar University, Vellore, India

Carlos Martinez-Boubeta
Freelancer in Bilbao, Bilbao, Spain

Shaukat A. Mazari
Department of Chemical Engineering, Dawood University of Engineering and Technology, Karachi, Pakistan

Saurabh Mishra
Department of Polymer and Process Engineering, Indian Institute of Technology Roorkee, Roorkee, India

Amit Mishra
School of Chemistry and Biochemistry, Thapar Institute of Engineering & Technology, Patiala, India

N.M. Mubarak
Department of Chemical Engineering, School of Engineering and Science, Curtin University, Miri, Malaysia

Nguyen Cong Nguyen
Institute of Environmental Engineering and Management, National Taipei University of Technology, Taipei, Taiwan; Faculty of Environment and Natural Resources, University of Da Lat, Da Lat, Vietnam

Hau Thi Nguyen
Institute of Environmental Engineering and Management, National Taipei University of Technology, Taipei, Taiwan; Faculty of Environment and Natural Resources, University of Da Lat, Da Lat, Vietnam

Sabzoi Nizamuddin
School of Engineering, RMIT University, Melbourne, VIC, Australia

Avinash R. Pai
International and Inter University Centre for Nanoscience and Nanotechnology, Mahatma Gandhi University, Kottayam, India

K. Panagiotaki
Institute of Nanoscience and Nanotechnology NCSR "Demokritos", Athens, Greece

Arvind Pandey
Department of Physics, North Eastern Regional Institute of Science and Technology, Nirjuli, India

Suyana Panneri
Materials Science and Technology Division, National Institute for Interdisciplinary Science and Technology (CSIR-NIIST), Thiruvananthapuram; Academy of Scientific and Innovative Research (AcSIR), New Delhi, India

Daniel Pasquini
Chemistry Institute, Federal University of Uberlandia-UFU, Uberlandia, Brazil

Manuel Peñas-Garzón
Chemical Engineering Section, Universidad Autonoma de Madrid, Madrid, Spain

F. Petrakli
School of Mining Engineering and Metallurgy, National Technical University of Athens, Athens, Greece

Suresh C. Pillai
Nanotechnology and Bio-Engineering Research Group, Department of Environmental Science, School of Science; Centre for Precision Engineering, Materials and Manufacturing Research (PEM), Institute of Technology Sligo, Sligo, Ireland

Saikat Sinha Ray
Institute of Environmental Engineering and Management, National Taipei University of Technology, Taipei, Taiwan

Kakarla Raghava Reddy
School of Chemical and Biomolecular Engineering, The University of Sydney, Sydney, NSW, Australia

Juan J. Rodriguez
Chemical Engineering Section, Universidad Autonoma de Madrid, Madrid, Spain

Aneela Sabir
Department of Polymer Engineering and Technology, University of the Punjab, Lahore, Pakistan

Mahdie Safarpour
Department of Chemistry, Faculty of Basic Science, Azarbaijan Shahid Madani University, Tabriz, Iran

Chella Santhosh
Department of Environmental and Biological Sciences, University of Eastern Finland, Kuopio, Finland

Sapna
Department of Chemistry, Banasthali University, Rajasthan, India

Muhammad Shafiq
Department of Polymer Engineering and Technology, University of the Punjab, Lahore, Pakistan

Rekha Sharma
Department of Chemistry, Banasthali University, Rajasthan, India

Nagaraj P. Shetti
Electrochemistry and Materials Group, Department of Chemistry, K. L. E. Institute of Technology, Hubballi, India

M.T.H Siddiqui
School of Engineering, RMIT University, Melbourne, VIC, Australia

Konstantinos Simeonidis
Department of Chemical Engineering, Aristotle University of Thessaloniki, Thessaloniki, Greece

Pratima R. Solanki
Special Centre for Nanoscience, Jawaharlal Nehru University, New Delhi, India

M.P. Srinivasan
School of Engineering, RMIT University, Melbourne, VIC, Australia

Ningmei Tang
National Demonstration Center for Experimental Chemistry Education, Jishou University, Jishou, China

Akshat Tanksale
Department of Chemical Engineering, Monash University, Clayton, VIC, Australia

Sabu Thomas
International and Inter University Centre for Nanoscience and Nanotechnology, Mahatma Gandhi University, Kottayam, India

Vahid Vatanpour
Faculty of Chemistry, Kharazmi University, Tehran, Iran

Ch. Venkata Reddy
School of Mechanical Engineering, Yeungnam University, Gyeongsan, South Korea

Kunlei Wang
Institute for Catalysis; Graduate School of Environmental Science, Hokkaido University, Sapporo, Japan

Yingchun Wang
National Demonstration Center for Experimental Chemistry Education, Jishou University, Jishou, China

Maria Wasim
Department of Polymer Engineering and Technology, University of the Punjab, Lahore, Pakistan

Zhishun Wei
Institute for Catalysis, Hokkaido University, Sapporo, Japan; School of Materials and Chemical Engineering, Hubei University of Technology, Wuhan, China

Wen Zhang
Jiangsu Key Laboratory of Chemical Pollution Control and Resources Reuse, School of Environmental and Biological Engineering, Nanjing University of Science & Technology, Nanjing, China

Xuan Zhang
Jiangsu Key Laboratory of Chemical Pollution Control and Resources Reuse, School of Environmental and Biological Engineering, Nanjing University of Science & Technology, Nanjing, China

Junfeng Zheng
Jiangsu Key Laboratory of Chemical Pollution Control and Resources Reuse, School of Environmental and Biological Engineering, Nanjing University of Science & Technology, Nanjing, China

CHAPTER

1 NANOMATERIALS—STATE OF ART, NEW CHALLENGES, AND OPPORTUNITIES

Deepu A. Gopakumar*, Avinash R. Pai†, Daniel Pasquini‡, Shao-Yuan (Ben)Leu§, Abdul Khalil H.P.S.*, Sabu Thomas†

School of Industrial Technology, Universiti Sains Malaysia (USM), Gelugor, Penang, Malaysia International and Inter University Centre for Nanoscience and Nanotechnology, Mahatma Gandhi University, Kottayam, India† Chemistry Institute, Federal University of Uberlandia-UFU, Uberlandia, Brazil‡ Department of Civil and Environmental Engineering ZS923, The Hong Kong Polytechnic University Hung Hom, Kowloon, Hong Kong§*

1 INTRODUCTION

Nanotechnology is considered an interdisciplinary branch of science integrating engineering aspects with biology, chemistry, and physics [1]. It descends from the present trend of miniaturization in devices and technology (as described by Moore's Law) and combining all other branches of science. Nanotechnology, however, has its drawbacks, and there is a strong need for developing new approaches in manufacturing (bottom-up approaches), which have to be developed to accomplish anticipated milestones. Nanotechnology is generally considered a tool of science that "steps across the limit" of miniaturization, where the materials exhibit different behavior as compared to macroscopic scale. More specifically, when the dimensions of a solid material approach nanoscale, its physical and chemical properties can become very different from those of the same material at the macrolevel. This is the main highlight of nanotechnology, which can be described as a research area in which this limit of new properties is reached, and strategies are developed to exploit the regime of size-controlled properties.

In the past few decades, the term nanotechnology has been extensively discussed and has almost become synonymous for things that are innovative and highly promising. On the other hand, the area of nanoscience is a subject of considerable debate regarding the open question of toxic and health hazards of nanoparticles and other nano-objects [2, 3]. In this argument, a definition of nanotechnology and its underlying sectors, applications, and markets is important for the purpose of risk assessment and risk communication. Many researchers refer to the length scale (nano) of this new science, but not all focus on the novel functionalities and properties of materials at the nanodimension. In general, the most accepted definition refers to the size and varying properties of materials in the size range between 10 and 100 nm, but this gives rise to many uncertainties and discrepancies which need to be resolved.

Nanoscale Materials in Water Purification. https://doi.org/10.1016/B978-0-12-813926-4.00001-X

2 NANOMATERIALS FOR WATER FILTRATION

Conventional water treatment techniques like sedimentation, flocculation, coagulation, and activated carbon are not able to eliminate organic pollutants from water effectively. In this context, membrane techniques play a vital role for water purification [4, 5]. Among the membrane techniques, microfiltration (MF), ultrafiltration (UF), and nanofiltration (NF) have gained considerable interest due to their ease of operation [6, 7]. Because membrane processes are considered important components of advanced water purification and desalination technologies, there is a need for a continuous search for new advanced materials for water purification technologies. In this context, nanomaterials (e.g., carbon nanotubes, nanoparticles, and dendrimers) are contributing to the development of more efficient and cost-effective water filtration processes. Fig. 1 highlights four classes of nanoscale materials that are being evaluated as functional materials for water purification: (1) metal-containing nanoparticles, (2) carbonaceous nanomaterials, (3) zeolites, and (4), dendrimers. These have a broad range of physicochemical properties that make them particularly attractive as separation and reactive media for water purification.

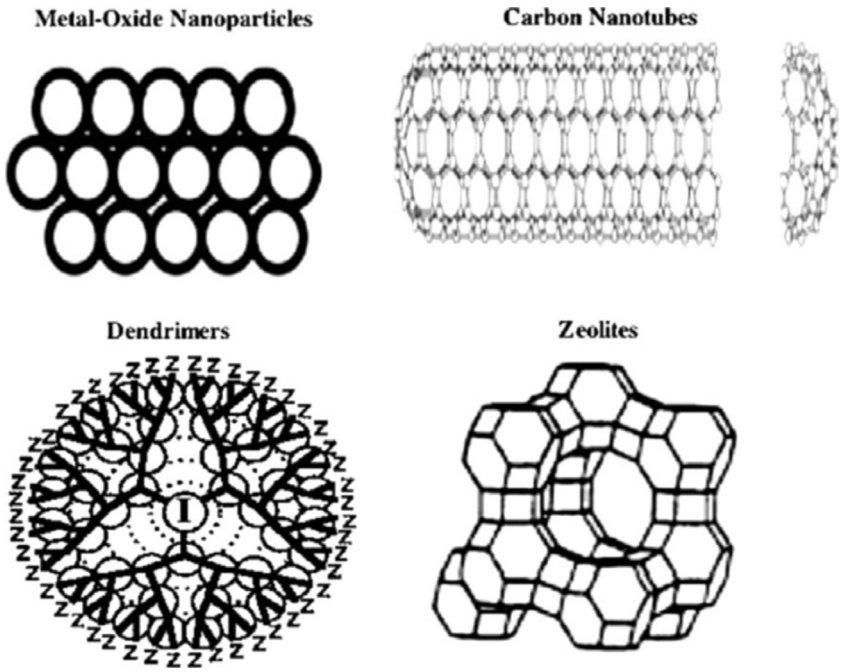

FIG. 1

Selected nanomaterials currently being evaluated as functional materials for water purification.

Reproduced with permission from N. Savage, M.S. Diallo, Nanomaterials and water purification: opportunities and challenges, J. Nanopart. Res. 7 (2005) 331–342, Springer Nature.

2.1 CLASSIFICATION OF NANOMATERIALS FOR WATER PURIFICATION

Nanomaterials can be classified into 0D (fullerenes), 1D (graphene nanoribbons and carbon nanotubes), 2D (graphene sheets), and 3D (nanoparticles) hybrid architectures based on their special confinement in a three-dimensional space. They can exist in single, fused, and hybridized forms with spherical, tubular, and irregular shapes as shown in Fig. 2A–G. Common types of nanomaterials include nanotubes, nanowires, nanofibers, quantum dots, and fullerenes. These hybrid 3D networks of nanomaterials possess several advantages such as highly accessible surface area, minimal aggregation or re-stacking, enhanced thermal and electrical transport, and robust mechanical properties as compared to their nanoscale 1D or 2D building blocks.

OD nanomaterials—fullerenes

The existence of carbon clusters was proposed and came into existence in 1959. It actually took decades to expound the structure and elucidate the properties of fullerenes [8]. The nature and chemical reactivity of fullerenes was first reported by Kroto et al., which attracted researchers' attention to this new, interesting class of carbon allotrope [9]. In 1990, Kratschmer et al. made another breakthrough for synthetic chemists by formulating a process for synthesizing macroscopic amounts of C60 [10]. Much attention has been received by C60 structures in recent times, as many other carbon allotropes may have developing potential applications [11, 12]. The name buckminsterfullerene was coined as an honorific for Buckminster Fuller, an American architect and constructor of the geodesic dome. In the family of fullerenes, C60 (buckminsterfullerene) and C70 (falmarene) have been extensively studied by researchers because of their outstanding properties and cage structure. Following the availability of

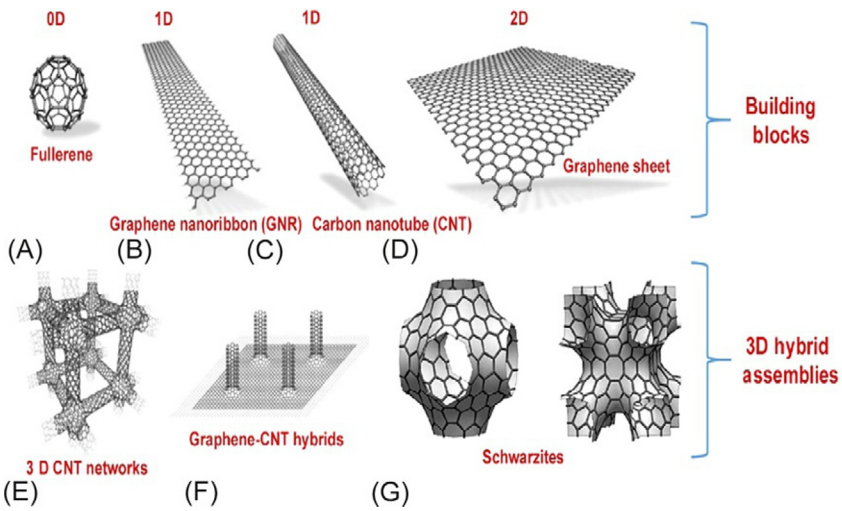

FIG. 2

(A) 0D nanomaterials, (B, C) 1D nanomaterials, (D) 2D nanomaterials, and (E–G) 3D hybrid assemblies of CNT and graphene.

Reproduced with permission from A. Dasgupta, L.P. Rajukumar, C. Rotella, Y. Lei, M. Terrones, Covalent three-dimensional networks of graphene and carbon nanotubes: synthesis and environmental applications, Nano Today (2017) 116–135, Elsevier Ltd.

macroscopic amounts of fullerenes, a variety of chemical modifications, such as, for example, arylation, halogenation, hydroxylation, alkoxylation, and osmylation, have been performed on C60 and its analogues [13]. Progressively, fullerenes have gained much interest from polymer chemists as building blocks for the construction of novel materials with fascinating properties.

Initial attempts to synthesize fullerene were made by irradiating graphite with a laser beam, thereby producing long-chain carbon molecules formed in the interstellar space and producing a remarkably stable cluster consisting of 60 carbon atoms. This experiment led to an outburst of interest in the chemistry of C60. After 5 years, a method for producing large quantities of C60 was developed by vaporizing graphite rods in a helium atmosphere by a resistive heating technique [10]. This method made a significant breakthrough in fullerene science by conducting further modification in the molecule for potential applications in diverse areas of technology. Many different methods have been proposed with the aim of synthesizing C60. Unfortunately, only a few of them have been successful. For instance, one particularly attractive strategy is the assembly of two identical hemispherical hydrocarbons [14]. However, methods for fusing such molecules do not currently exist. The major challenge in the synthesis of fullerenes is the introduction of curvatures or pyramidalizations in the carbon network. Fig. 3 shows an array of applications which have been developed with the advancement of fullerene science.

Fullerenes are molecules with 60 atoms and have received much attention because of their wide application [15]. Due to their insolubility in water, solvent exchange and ultrasonification have been applied to disperse fullerenes as nanoparticles [16]. C60 nanoparticles have a broad spectrum antimicrobial activity, although the mode of action is debatable [17]. The toxicity of C60 is also under investigation. The use of C60 as antifouling agents for ceramic membranes was determined by evaluating the effect on the attachment and respiratory activity of *E. coli* K12. A decrease in bacterial numbers and increase in inactive *E. coli* cells confirmed the bactericidal effect of C60. The increase in membrane hydrophobicity might also play a role in its antimicrobial activity [18].

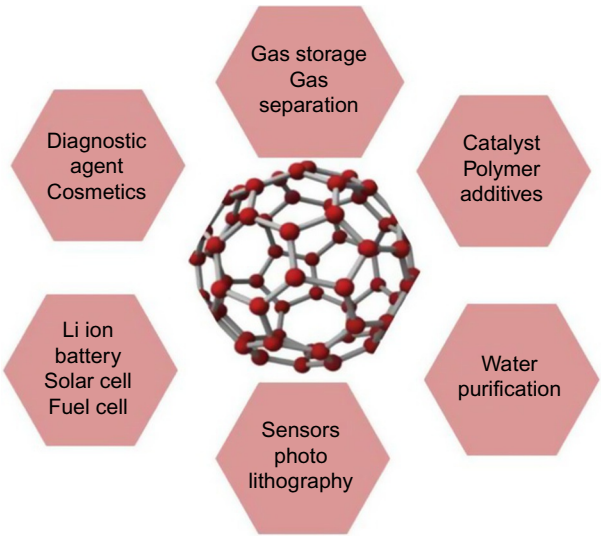

FIG. 3

A schematic representation of potential applications of fullerenes.

1D nanomaterial—carbon nanotubes

Carbon nanotubes (CNTs), also known as bucky tubes, are made of cylindrical carbon moieties with superior physical and chemical properties that make them possibly useful in a wide variety of applications, from sensors to water purification membranes. These include applications in nano-electronics, opto-electronic devices, and other engineered applications. CNTs exhibit extraordinary mechanical strength as well as distinctive electrical and thermal properties. CNTs are considered a sub class of the fullerene family, which was discovered by Kroto et al. in 1985 [19]. Bucky balls are commonly known as spherical fullerenes, whereas CNTs are cylindrical, with at least one end typically capped with a hemisphere that has the bucky ball structure. The name CNT derives from the size, as the diameter of a nanotube is on the order of a few nanometers. The synthesis of multiwalled carbon nanotubes (MWNTs) was first reported by Iijima and his colleagues in 1991 using a simple arc-evaporation method [20]. However, in the early 1950s, predictions were made about the existence of CNTs by Radushkevich and Lukyanovich, who reported the discovery of "worm-like" carbon formations [21]. The formation of long filaments of needle-like carbon crystals with a diameter of about 50 nm was achieved during their study of the soot formed by the decomposition of carbon monoxide (CO) on iron particles at 600°C. The discovery of carbonaceous nanotubes was left unnoticed due to lack of attention to the nanotechnology sector at that time, like a number of other areas before and after [22]. Fig. 4 shows 1D and 3D nanostructured materials derived from 2D graphene sheets.

Carbon nanotubes can be synthesized by various physicochemical methods such as the arc discharge method, chemical vapor deposition, vapor phase growth, and the flame synthesis method. In 1991, Iijima and colleagues reported the existence of a novel tubular-shaped carbonaceous species, which are now known as CNTs [20]. A simple arc-discharge evaporation technique similar to the method used for the production of fullerene was used to prepare CNTs. Long, continuous, needle-like carbon (4–30 nm diameter) and lengths up to 1 mm were grown on the negative end (cathode) of a carbon electrode by means of the direct current (DC) arc-discharge evaporation of carbon in an argon-filled vessel at a pressure of 100 Torr. A method for large-scale synthesis of MWNTs was reported by Ebbesen, and Ajayan reported using the same technique [23]. The arc-discharge assembly consists of two vertical thin electrodes placed at the center of a chamber. The lower electrode (cathode) has a narrow dip to hold a small piece of iron during the evaporation phase. The arc discharge can be generated by running a DC current of 200 A at 20 V between the two electrodes. The ratio of three compositions, that is, argon, iron, and methane, is very crucial for the synthesis of single-walled CNTs. Some of the potential applications of CNTs in diverse technological sectors are given in Fig. 5.

CNTs are composed of cylindrical graphite sheets (allotropic form of carbon) rolled up in a tube-like structure with the appearance of latticework fence [24]. Single-walled carbon nanotubes (SWCNTs) have cylindrical shape consisting of a single shell of graphene. On the other hand, multiwalled carbon nanotubes (MWCNTs) are composed of multiple layers of graphene sheets. Both SWCNTs and MWCNTs have been used for direct water desalination [25–27] or indirectly to remove troublemaking compounds that complicate the desalination processes [28]. CNTs are fascinating in advanced membrane technologies for water desalination because they provide a low-energy solution for water treatment. CNT membranes provide near-frictionless water flow through themselves with the retention of a broad spectrum of water pollutants. The inner hollow cavity of CNTs provides a great possibility for desalinating water. The high aspect ratios, smooth hydrophobic walls, and inner pore diameter of CNTs allow ultra-efficient transport of water molecules. Some prototypes of CNT-based membranes are shown in Fig. 6.

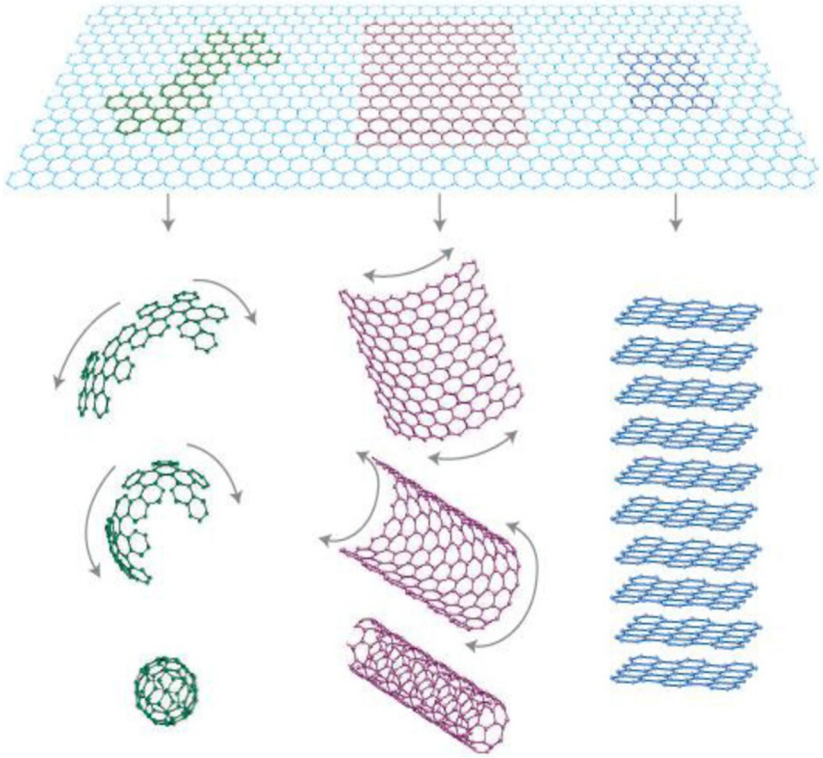

FIG. 4

A graphical representation of various forms of 0D (fullerenes), 1D (carbon nanotubes), and 3D (graphene sheets stacked to graphite) architectures derived from 2D graphene.

Reproduced with permission from A.K. Geim, K.S. Novoselov, The rise of graphene, Nat. Mater. 6(3) (2007) 183–191, Springer Nature.

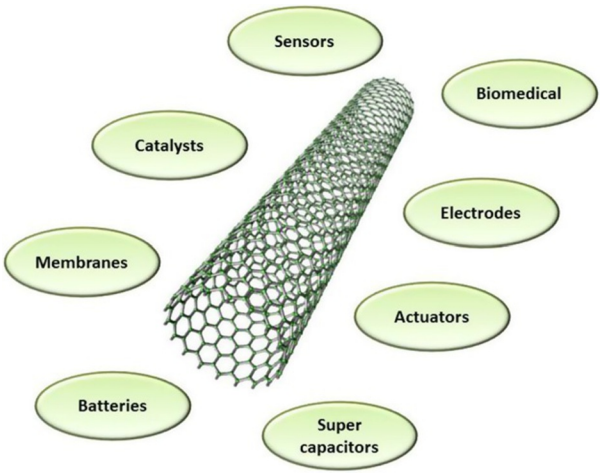

FIG. 5

Few potential applications of carbon nanotubes in diverse technological sectors.

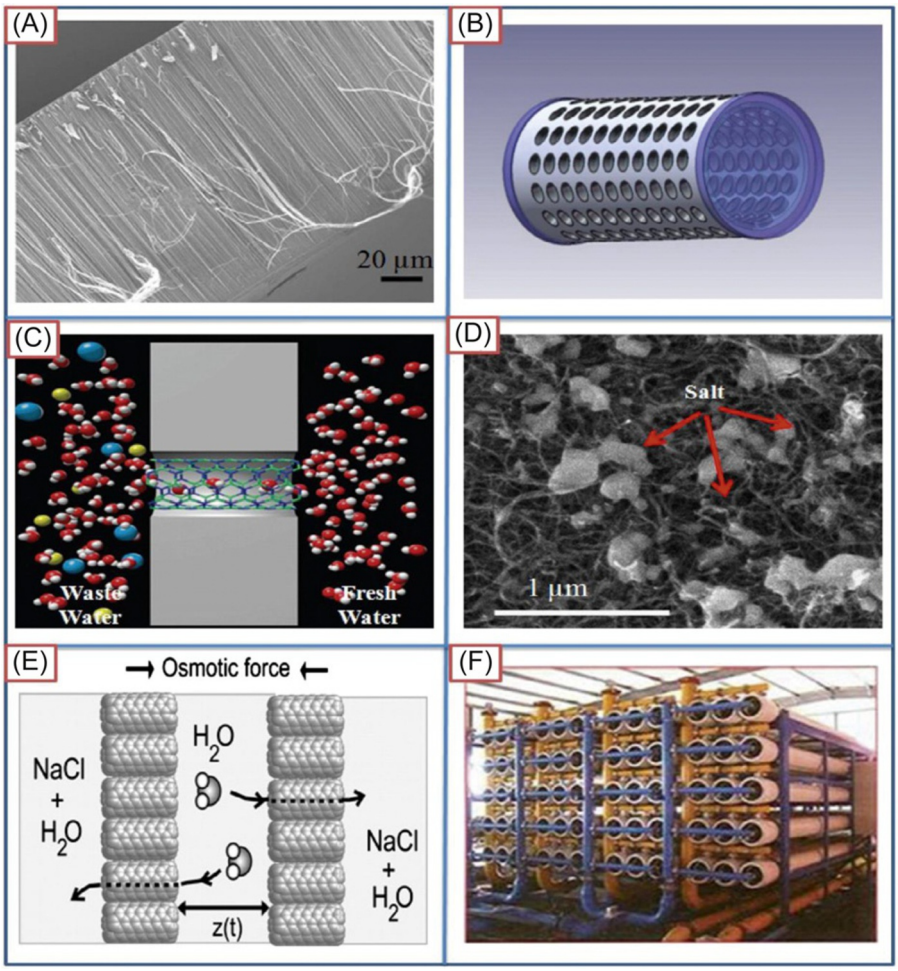

FIG. 6

Structures of some CNT membranes. Shown are (A) a cross-sectional scanning electron microscope (SEM) image of a pristine CNT membrane. (B) A CNT-based water filter with cylindrical geometry. (C) Movement of water molecules through a CNT channel. (D) A SEM image of scattered NaCl nanocrystals on CNT membrane surface. (E) Movement of pure water molecules through a CNT membrane in osmotically imbalanced compartments, and (F), Engineered CNT membranes in an industrial setup.

Reproduced with permission from R. Das, M.E. Ali, S.B.A. Hamid, S. Ramakrishna, Z.Z. Chowdhury, Carbon nanotube membranes for water purification: a bright future in water desalination, Desalination (2014) 97–109, Elsevier Ltd.

2D nanomaterial—graphene

Graphene is basically a flat monolayer of carbon atoms closely packed into a two-dimensional (2D) honeycomb lattice, and is a basic building block for graphitic materials of all other dimensionalities. One can make any kind of nanostructure from this fascinating material by wrapping it up into 0D

fullerenes, rolling it into 1D nanotubes, or stacking it into 3D graphite. Theoretically, graphene and its various configurations have been studied for 60 years, and graphene is widely used for elucidating the properties of different carbonaceous materials [29]. Forty years later, it was realized that graphene also provides an excellent condensed-matter analogue of (2+1)-dimensional quantum electrodynamics, which thrust graphene into a thriving theoretical toy model [30]. On the other hand, although known as an integral part of 3D materials, graphene was presumed not to exist in the free state, being described as an "academic" material, and was believed to be unstable with respect to the formation of curved structures such as soot, fullerenes, and nanotubes. Suddenly, the vintage model turned into reality, when freestanding graphene was unexpectedly found 3 years ago, and especially when follow-up experiments confirmed that its charge carriers were indeed massless Dirac fermions [31].

Graphene sheets can be synthesized on a small scale by chemical vapor deposition (CVD) [32], epitaxial growth [33], and mechanical exfoliation (the Scotch tape method) [34]. Large-scale industrial production of graphene is primarily accomplished by oxidation of graphite and the subsequent reduction of graphene oxide (GO). The synthesis of GO was first reported by Brodie in 1859. Currently, three representative synthesis methods and their variations have been developed, attributable to Brodie [35], Staudenmaier [36], and Hummers [37]. In these three methods, the layers in graphite are thoroughly oxidized by oxidative treatment in fuming acids, as follows: $KClO_3$ in HNO_3 (Brodie), $KClO_3$ in HNO_3/H_2SO_4 (Staudenmaier), and $KMnO_4$ in H_2SO_4 (Hummers). Consequently, the graphene sheets become functionalized with hydroxyl and epoxide groups on their basal plane, while the edges are decorated with carbonyl and carboxyl groups [38].

Han et al. reported graphene nanofiltration membranes (uGNMs) ($\approx$22–53 nm thick) on microporous substrates presented for efficient water purification using chemically converted graphene (CCG) as shown in Fig. 7. The prepared uGNMs exhibited well-packed layer structure formed by CCG sheets, which was confirmed by microscopic techniques. The performance of the uGNMs for water treatment was evaluated on a dead-end filtration device, and the pure water flux of uGNMs was high ($21.8\,L\,m^{-2}\,h^{-1}\,bar^{-1}$). The uGNMs showed high retention (>99%) for organic dyes and moderate retention ($\approx$20%–60%) for ion salts. The rejection mechanism of this kind of negatively charged membranes was intensively studied, and the results revealed that the physical sieving and electrostatic interaction dominated the rejection process. Finally they concluded that the integration of high performance, low cost, and simple solution-based fabrication process promises uGNMs' great potential application in practical water purification [39].

Nanocellulose

With the increase in water quality regulations and decrease in available fresh water supplies, scientists across the world focus on renewable raw materials and environmentally friendly, cost-effective materials for water purification. Among these, nanocellulose has gained considerable interest because of its excellent properties. Many laboratory operations are dependent upon the filtration processes that are performed with cellulose-based filter papers. Nanocellulose's inherent fibrous nature and remarkable mechanical properties, including its low cost and biocompatibility, make nanocellulose a huge potential component in water filtration membranes [40]. Nanocelluloses are very promising adsorbents for removing heavy metals, viruses, dyes, etc., due to their high surface-area-to-volume ratio, low cost, high natural abundance, and inherent environmental inertness [41]. Moreover, the surface of nanocellulose has easily functionalizable OH groups, and this facilitates the incorporation of chemical moieties

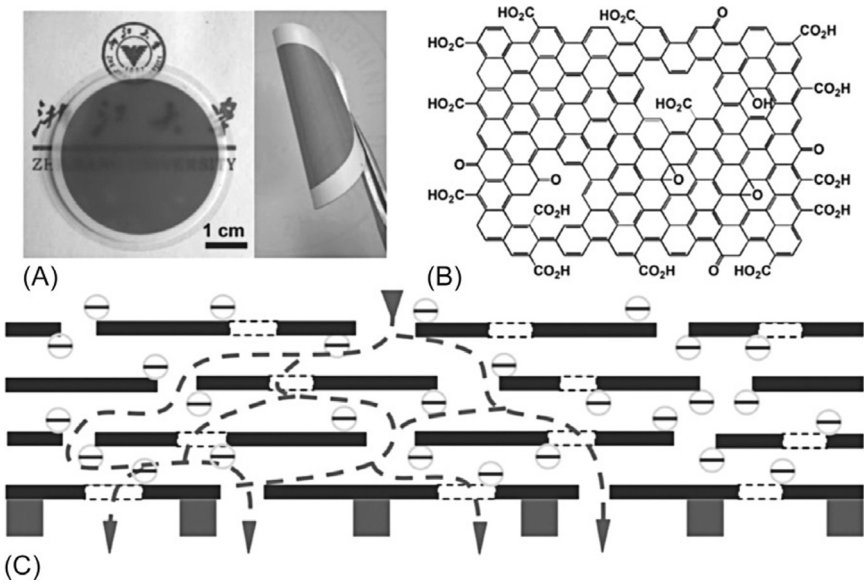

FIG. 7

(A) Digital photo of an uGNM coated on an AAO disk (left) and a twisted uGNM coated on a PVDF membrane (right). (B) Schematic representation of a brGO: graphene sheet with a certain quantity of holes and most of the oxidized groups located on the edges, and the periphery of the holes on it. Note that the real graphene sheets extend further than depicted. (C) Schematic view for possible permeation route: water molecules go through the nanochannels of the uGNMs and the holes on the graphene sheets and at last reach the pores of supporting membranes. The blank squares present the holes on the graphene sheets *(black line)*. The edges of the brGO and the periphery of the holes are negatively charged.

Reproduced with permission from Y. Han, Z. Xu, C. Gao, Ultrathin graphene nanofiltration membrane for water purification ultrathin graphene nanofi ltration membrane for water purifi cation, Adv. Funct. Mater. (2013), John Wiley and Sons.

that may increase the binding efficiency of pollutants to the nanocellulosic materials [40]. Cellulose nanofibers (CNF) are one type of cellulose nanomaterials. CNFs are a promising substitute adsorbent due to their high surface-areato-volume ratio, low cost, high natural abundance, and inherent environmental inertness. Furthermore, CNFs readily functionalized surface facilitates the incorporation of chemical moieties that may enhance the binding efficiency of pollutants to the CNF. Mainly, nanocelluloses are classified into (1) cellulose nanofibers (CNFs) and (2) cellulose nanocrystals (CNCs). The CNCs have nanodimension in both length and diameter, whereas CNFs have length in microdimension and diameter in the nanodimension is shown in Fig. 8. Isolation of nanocellulose from renewable source is becoming an important area for the researchers all over the world. A lot of procedures have been reported for the extraction of CNFs from the plant's cell wall. There are several mechanical treatments which have been used to extract CNFs from various sources. These processes mainly include high-pressure homogenization, grinding, cryocrushing. and high-intensity ultrasonic treatments which lead to the transverse cleavage of cellulose fibers.

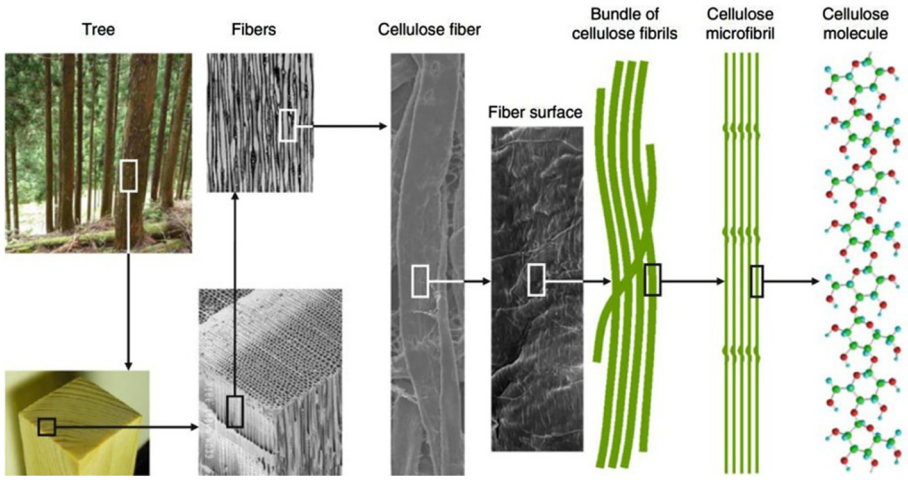

FIG. 8

Hierarchical structure of wood cellulose, forming cellulose nanofibers and nanocrystals.

Reproduced with permission from A. Isogai, Wood nanocelluloses: fundamentals and applications as new bio-based nanomaterials, J. Wood Sci. (2013) 449–459, Springer.

Nanochitin

Chitin is the second most abundant natural polymer after cellulose. Chitin occurs in the structural components of arthropod exoskeletons or in the cell walls of fungi and yeast [42]. Chitin and cellulose are almost similar polysaccharide compounds; cellulose contains a hydroxyl group, whereas chitin contains an acetamide group. Chitin is a high molecular weight polymer, specifically β (1-4)-(*N*-acetyl-D-glucoamine), as shown in Fig. 9. The high crystallinity and mechanical strength of nanochitin make it a suitable candidate for reinforcement in polymer nanocomposites. Chitin is natural, nontoxic, nonallergic, antimicrobial, and biodegradable, and it is insoluble in water. There are several reports in the literature about the extraction of nanochitin from different sources. Acid hydrolysis is a well-known procedure for extracting nanochitin from seafood wastes. Chitin, the second most abundant polysaccharide, is synthesized by an enormous number of living organisms, including fungi and insects. These biopolymers have found many applications in different areas such as packaging material, membranes for removal of metal ions, and dyes and pigments in wastewater engineering. Chitin has been reported to be useful in heavy metal chelating of industrial wastewater. Chitin is inexpensive, nontoxic, and can bind to the common water pollutants (Fig. 10). This binding consists of mercury, copper, iron, nickel, chromium, lead, zinc, cadmium, silver, and cobalt.

The results showed that the strongest binding takes place with mercury and the weakest with cobalt [43].

Noble metal nanoparticles

Noble metal nanoparticle-based chemistry has immense advantages in the area of drinking water purification. The noble metal nanoparticles have multipronged use in drinking water purification (removal of organic compounds, heavy metals, and microorganisms). While the chemistry of noble

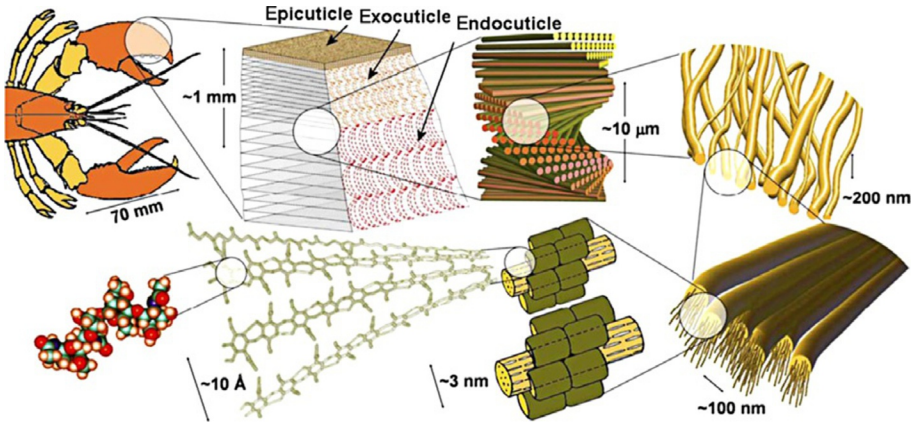

FIG. 9

Schematic representations of hierarchical structure of cuticles and existence of chitin in them.

Reproduced with permission from M. Barikani, E. Oliaei, H. Seddiqi, H. Honarkar, Preparation and application of chitin and its derivatives: a review, Iran. Polym. J. Eng. Ed. (2014) 307–326, Springer Nature.

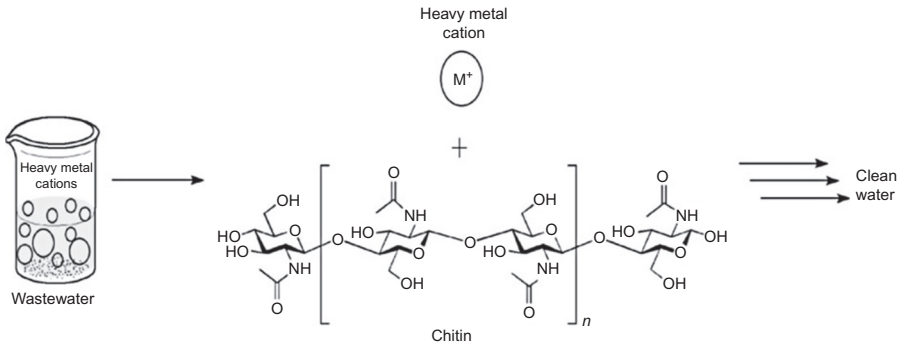

FIG. 10

Biosorption of heavy metals by chitin.

Reproduced with permission from G. Camci-Unal, N.L.B. Pohl, Quantitative determination of heavy metal contaminant complexation by the carbohydrate polymer chitin, J. Chem. Eng. Data 55(3) (2010) 1117–1121, American Chemical Society.

metal nanoparticles is unique in the removal of many contaminants, their high energy surface results in the system attempting to minimize the surface energy through protection or chemical transformation or agglomeration. Therefore, nanoparticles are likely to adsorb a number of other species onto their surface. The same properties of nanomaterials (increased surface area, chemical reactivity, etc.) which confer the unique ability to degrade toxic species present in the environment may also render them toxic to humans. Among all the recently developed nano-adsorbents for drinking water purification, the chemistry of noble metal nanoparticles is truly unique. The chemistry of silver nanoparticles has been utilized to remove a number of toxic contaminants found in drinking water including

pesticides, heavy metals, and microorganisms. Gold nanoparticles have been effectively used to detect ultra-low concentrations of pesticides in water via changes in the signature properties of a functional group attached to the gold nanoparticle surfaces in the presence of organic molecules like pesticides. Gold nanoparticle surfaces can be modified with the OPH enzyme, and fluorophore molecules are positioned at the OPH active sites. The addition of organophosphorus compounds, leading to the release of a fluorophore molecule, is measured through changes in the fluorescence intensity [44]. The AChE (bound on gold nanoparticle surfaces)-mediated hydrolysis reaction of acetylthiocholine has also been utilized as a pesticide sensor through measurement of electrochemical current, which depends on the extent of formation of thiocholine in the presence of pesticides [45].

Metal-basednano-adsorbents

In recent years, the synthesis and utilization of iron oxide metal nanoparticles with novel properties and functions have been widely studied due to their size in nano-range, high surface-area-to-volume ratios, and super paramagnetism [46–48]. Additionally, iron oxide metal nanoparticles with low toxicity, chemical inertness, and biocompatibility show a tremendous potential in combination with biotechnology [49–51]. The stability of iron oxide colloid suspensions could be greatly augmented by surface modification with suitable functional groups, such as phosphonic acids, carboxylic acid, and amines, as shown in Fig. 11 [52, 53].

Mak and Chen [54] investigated the adsorption of methylene blue (MB) from an aqueous solution by polyacrylic acid-bound, iron oxide, magnetic nanoparticle. They demonstrated that the novel magnetic nano-adsorbent was quite efficient for the adsorption/desorption of MB. They showed that the

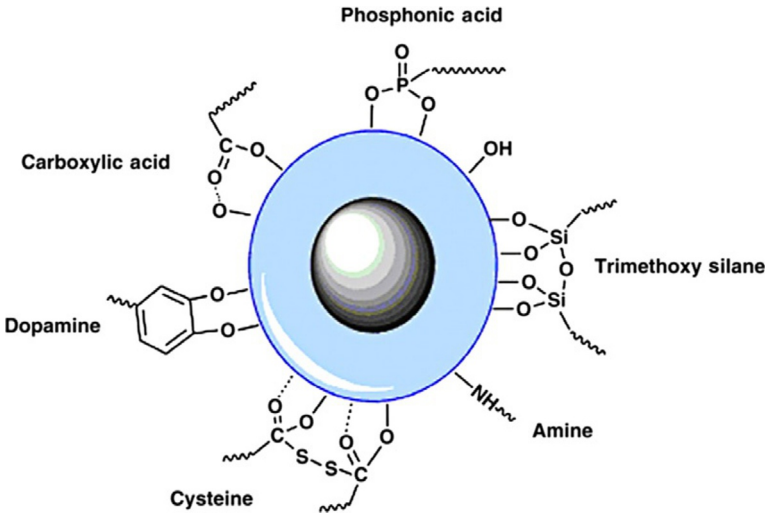

FIG. 11

Common chemical moieties for the anchoring of polymers and functional groups at the surface of iron oxide magnetic nanoparticles.

Reproduced with permission from P. Xu, G.M. Zeng, D.L. Huang, C.L. Feng, S. Hu, M.H. Zhao, C. Lai, Z. Wei, C. Huang, G.X. Xie, et al., Use of iron oxide nanomaterials in wastewater treatment: a review, Sci. Total Environ. (2012) 1–10, Elsevier Ltd.

adsorption capacity increased with the increase in solution pH (2–10), and the adsorption process was endothermic in nature. By using the methanol solution of acetic acid, they demonstrated that the adsorbed MB could be desorbed. Moreover, they concluded that the both adsorption and desorption of MB were quite fast and could be completed within 2 min due to the absence of internal diffusion resistance [54].

Gupta et al. [55] investigated the chromium removal by combining magnetic properties of iron oxide with adsorption properties of carbon nanotubes. The adsorption features of multiwall carbon nanotubes (MWCNTs) with the magnetic properties of iron oxides have been combined in a composite to produce a magnetic adsorbent as shown in Fig. 12. They performed adsorption capability of the composites in batch and fixed-bed modes. They observed that the composites have demonstrated an adsorption capability superior to that of activated carbon. The results also showed that the adsorptions of Cr (III) on the composites are strongly dependent on the pH as shown in Fig. 13. They concluded that the combination of magnetic iron oxide nanoparticles with high surface area carbon nanotubes can be used as adsorbent for contaminants in water and can be subsequently controlled and removed from the medium by a simple magnetic process [55].

Titanium dioxide is an attractive photocatalyst for water treatment as it is resistant to corrosion and nontoxic when ingested [56]. The basic mechanism of TiO_2 photoactivation and reactive oxygen species (ROS) generation is well known [57].

Liga et al. [58] prepared the photocatalytic silver-doped titanium dioxide nanoparticles (nAg/TiO_2) and investigated their capability to inactivate bacteriophage MS2 in aqueous media. They deposited nanosized Ag onto commercial TiO_2 nanopowders using a photochemical reduction method. The MS2 inactivation kinetics of nAg/TiO_2 were compared to the base TiO_2 material and silver ions leached from the catalyst. They found that the inactivation rate of MS2 was enhanced by more than five-fold, depending on the base TiO_2 material, and the inactivation efficiency increased with increasing silver content. The increased production of hydroxyl free radicals was found to be responsible for the enhanced viral inactivation [58].

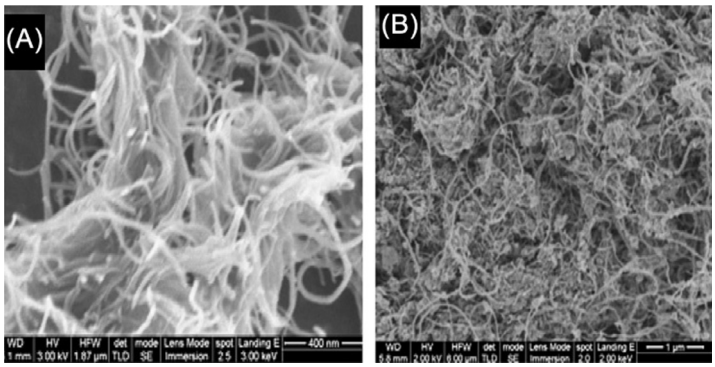

FIG. 12

e SEM images of (A) oxidized MWCNTs (B) MWCNTs/nano-iron oxide.

Reproduced with permission from V.K. Gupta, S. Agarwal, T.A. Saleh, Chromium removal by combining the magnetic properties of Iron oxide with adsorption properties of carbon nanotubes, Water Res. 45(6) (2011) 2207–2212, Elsevier Ltd.

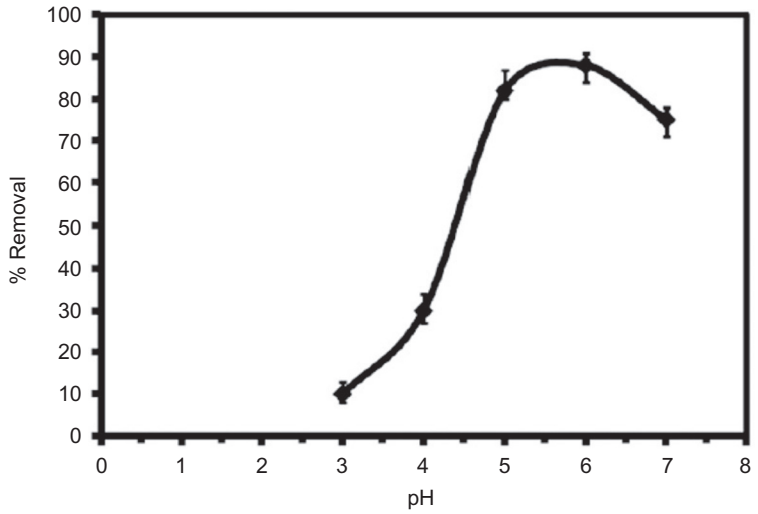

FIG. 13

The effect of pH on the amount of Cr (III) adsorbed on the MWCNT/nano-iron oxide.

Reproduced with permission from V.K. Gupta, S. Agarwal, T.A. Saleh, Chromium removal by combining the magnetic properties of Iron oxide with adsorption properties of carbon nanotubes, Water Res. 45(6) (2011) 2207–2212, Elsevier Ltd.

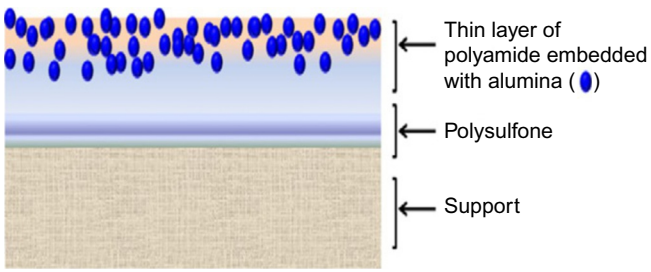

FIG. 14

Schematic representation of polysulfone the polyamide membrane embedded with alumina nanoparticles.

Reproduced with permission from T.A. Saleh, V.K. Gupta, Synthesis and characterization of alumina nano-particles polyamide membrane with enhanced flux rejection performance, Sep. Purif. Technol. 89 (2012) 245–251, Elsevier Ltd.

Aluminum oxide (Al_2O_3) is one of the most stable inorganic materials, and thus it is used as ultrafiltration membranes [59]. In addition, it is inexpensive, nontoxic, highly abrasive, and resistant. Remarkably, the use of alumina nanoparticles in membranes has been extensively studied and reported.

Saleh and Gupta [60] fabricated polyamide (PA) nanocomposite membrane containing alumina nanoparticles synthesized via in situ interfacial polymerization as shown in Fig. 14. In the first part of the work, aluminum oxide (Al_2O_3) nanoparticles with an average size of 14 nm were synthesized by an aqueous sol-gel method using precursors of aluminum nitrate and citric acid mixed solution. In the second part, the Al_2O_3 were used to prepare a nanoparticle-entrapped PA membrane via

interfacial polymerization. SEM analysis demonstrated that nanoparticles were dispersed in the membrane and embedded in polyamide chains. They found that the existence of nanoparticles in the membrane improved the permeate flux and maintained the salt rejection. It also resulted in enhanced hydrophilicity of the membranes, as proven by the decreased water contact angle [60].

Nanodendrimers

Dendrimers are highly branched macromolecules with controlled composition and architecture and monodispersity. They consist of a central core, repeating units, and terminal functional groups [61, 62]. The nature of the internal repeating units determines the microenvironment of the interior and consequently its solubilization properties, while the external groups determine the chemical behavior of dendrimers in the external medium [62, 63].

Reverse osmosis-assisted membranes have pore sizes in the range of 0.1–1 nm, and thus, they are very effective at retaining dissolved inorganic and organic solutes with molar mass below 1000 Da [64]. On other hand, nanofiltration membranes are very promising candidates for removing hardness and organic solutes with molar mass between 1000 and 3000 Da [64]. However, these reverse-osmosis membranes require high pressures to operate. On the other hand, UF membranes require lower pressure (200–700 kPa). Unfortunately, they are not very effective at removing dissolved organic and inorganic solute with molar mass below 3000 Da. Advances and recent developments in macromolecular chemistry, such as the invention of dendritic polymers, are providing unprecedented opportunities to develop effective UF processes for purification of water contaminated by toxic metal ions, radionuclides, organic and inorganic solutes, bacteria, and viruses. Dendritic polymers, which include random hyperbranched polymers, dendrigraft polymers, dendrons, and dendrimers, are relatively monodispersed and highly branched macromolecules with controlled composition and architecture consisting of three components: a core, interior branch cells, and terminal branch cell [63].

Arkas et al. [65] synthesized organosilicon dendrimeric and hyperbranched networks and impregnated these networks into porous ceramic filters, which proved to be promising devices for water purification. They prepared triethoxysilyl-functionalized poly (propylene imine) (DAB32) dendrimers and poly (ethylene imine) (PEI5) hyperbranched polymers in chloroform, which were subsequently allowed to impregnate porous ceramic filters. They showed that the demonstrated filters could encapsulate toxic polycyclic aromatic compounds dissolved in water. They showed that the concentration of polycyclic aromatic compounds in water was lowered to the level of few ppb via continuous filtration of contaminated water at different flow rates. Moreover, the filters were effectively regenerated by treatment with acetonitrile. Finally, they concluded that this demonstrated dendrimer-based ceramic filter had huge potential in water purification, especially for the removal of water-soluble toxic pollutants [65].

3 NANOSTRUCTURED MEMBRANES

Advanced technologies for water purification are an essential part of meeting the current and future needs for water. Innovations in the development of novel technologies to desalinate water are among the most exciting and promising. Additionally, nanotechnology-derived products that reduce the concentrations of toxic compounds to subppb levels can assist in the attainment of water quality standards and health advisories. Nanotechnology for water and wastewater treatment is gaining momentum

globally. The unique properties of nanomaterials and their convergence with current treatment technologies present great opportunities to revolutionize water and wastewater treatment. Advances in nanoscale science and engineering are providing unprecedented opportunities to develop more cost-effective and environmentally acceptable water purification processes. However, the application of nanotechnology to water purification is currently faced with the issue of how to design nanomaterials that are capable of collecting and preconcentrating a large number of contaminants per unit volume. Specifically, it is not clear how to interface nanoparticles with contaminants because direct addition of nanoparticles into drinking water may require extra separation steps to recover the expensive nanomaterials. Traditional membrane filters cannot be used for eliminating smaller particles like viruses, etc., from water as the size of these particles is in the range below 50 nm. In order to rectify these issues, nanostructured membranes have been extensively used and investigated in order to remove submicron particles below 100 nm.

Krieg et al. [66] have demonstrated the fabrication and use of a supramolecular ultrafiltration membrane. The demonstrated membrane can be used in both filtration and size-selective chromatography regimes, which is shown in the Fig. 15, and allowed the filtration of nanoparticles with a cutoff of 5 nm. A thicker layer of the supramolecular material was capable of chromatographic size separation in the sub-5-nm range, which was particularly useful for quantum dots. Moreover, they showed that the supramolecular structure retains its adaptivity, allowing for facile recycling of the membrane material, as well as the retrieval of retained nanoparticles. They proved that the simple fabrication of the membrane,

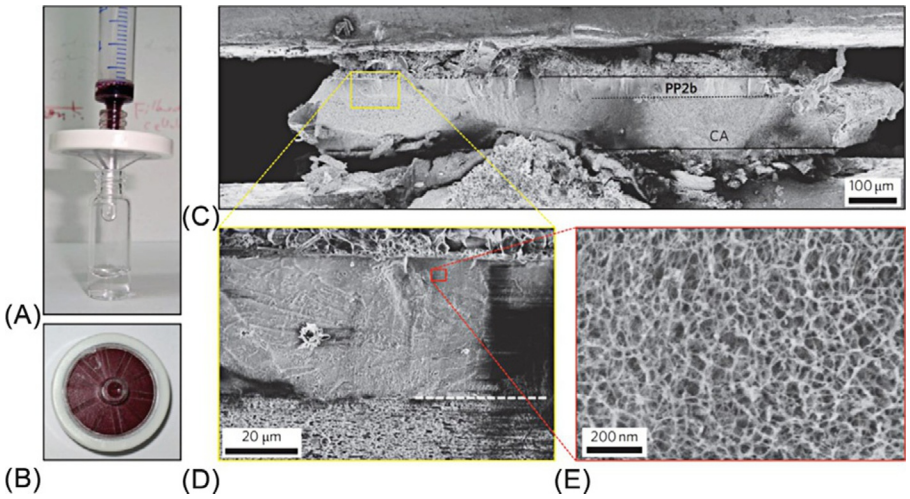

FIG. 15

Supramolecular filtration membrane. (A) Photograph showing the preparation of the membrane by filtration of a supramolecular solution of PP2b (5 × 1024 M) in water over a CA filter (pore size, 0.45 mm). (B) Photograph of the supramolecular membrane deposited on top of the CA support in a commercial syringe filter. (C) Cryo-SEM image of the cross-section of a 1 × 1 mm piece of the supramolecular membrane (0.65 mg PP2b cm22) on the CA support. (D) Magnified image showing the sharp border between the coarse CA and the smooth PP2b layer (dashed line). (E) High-magnification image of the supramolecular PP2b layer.

Reproduced with permission from E. Krieg, H. Weissman, E. Shirman, E. Shimoni, B. Rybtchinski, A recyclable supramolecular membrane for size-selective separation of nanoparticles, Nat. Nanotechnol. 6(3) (2011) 141–146, Springer Nature.

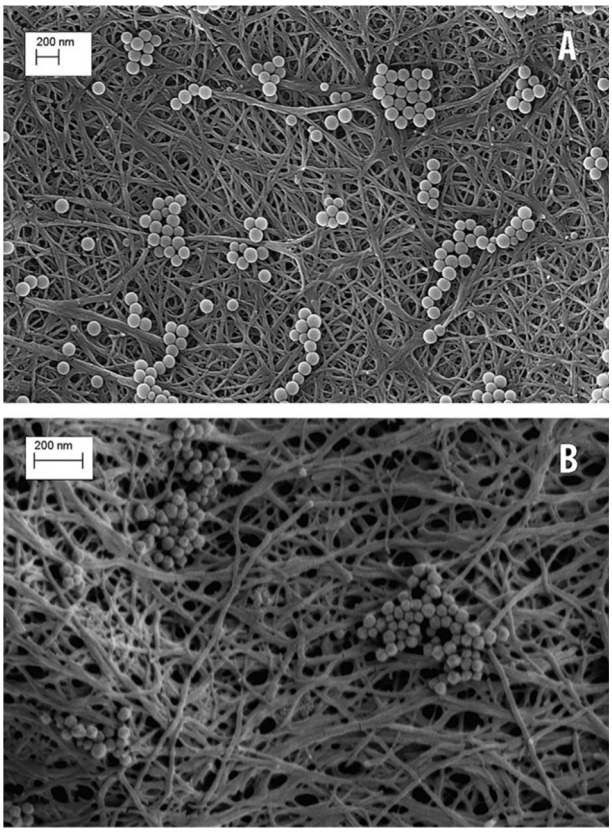

FIG. 16

SEM images of 100 nm latex beads (A) and 50 nm gold nanoparticles (B) retained on the nanocellulose filter paper.

Reproduced with permission from M. Asper, T. Hanrieder, A. Quellmalz, A. Mihranyan, Removal of xenotropic murine leukemia virus by nanocellulose based filter paper, Biologicals 43(6) (2015) 452–456, Elsevier Ltd.

as well as its performance, versatility, and recyclability, represent a significant advantage over conventional membranes with similar rejection properties and performances [66].

Asper et al. [67] demonstrated nanocellulose-based filter paper to remove xenotropic leukemia virus by size exclusion. The filter paper was composed of 100% naturally derived cellulose. The filter paper was fabricated using cellulose nanofibers derived from *Cladophora* algae. They obtained good retention value (LRV $>$ 5.25) against the virus. They also showed that 100 nm latex beads and 50 nm gold nanoparticles can be filtered through the demonstrated nanocellulose based filters as shown in Fig. 16. They concluded that the demonstrated nanocellulose-based filter paper could be useful for the removal of endogenous rodent retroviruses and retrovirus-like particles during the production of recombinant proteins [67].

Quellmalz and Mihranyan [68] fabricated citric acid, crosslinked, nanocellulose-based papers for size-exclusion nanofiltration. They crosslinked the cellulose nanopapers with the citric acid in order to

FIG. 17

A photograph of crosslinked nanocellulose paper filter (diameter 26 mm) covered with a precipitate of Au nanoparticles following the filtration.

Reproduced with permission from A. Quellmalz, A. Mihranyan, Citric acid cross-linkednanocellulose-based paper for size-exclusion nanofiltration, ACS Biomat. Sci. Eng. 1(4) (2015) 271–276, American Chemical Society.

increase the wet strength of the paper. Their particle retention studies revealed that the fabricated paper was capable of removing tracer particles as small as 20 nm, as shown in Fig. 17. They concluded that citric acid crosslinking of nanocellulose was beneficial for developing paper-based sterile (virus) removal industrial filters [68].

4 NANOFIBER MEMBRANES

Currently, adsorption is considered to be an effective method for water purification, and many polymeric and inorganic materials have been developed as adsorbents [69]. In particular, membrane adsorption processes are probably the most attractive method in wastewater decontamination [70]. The adsorption process can be limited by diffusion into the pores of common adsorbents. However, in the membrane adsorption process, convection mass transport through membrane pores may overcome this problem and allow very rapid adsorption and separation processes.

Liang et al. [71] demonstrated a simple filtration process to decontaminate water by employing a freestanding fibrous membrane fabricated from highly uniform carbonaceous nanofibers (CNFs). They demonstrated a process which combines the excellent adsorption behavior of CNFs and the advantages of membrane filtration over conventional adsorption techniques. Their membrane filtration experiments proved that the CNF membranes could remove methylene blue (MB) efficiently at a very high flux of 1580 L $m^{-2}h^{-1}$, which is 10–100 times higher than that of commercial nano- or ultrafiltration membranes with similar rejection properties. In addition, they showed that the CNF membranes are easily regenerated and remain unaltered in adsorption performance over six successive cycles of dye adsorption, desorption, and washing. The concluded that the demonstrated membrane has potential applications in water purification [71].

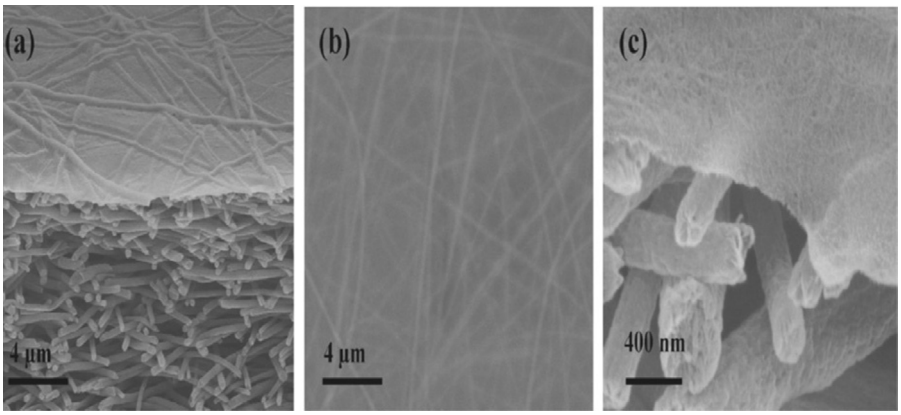

FIG. 18

SEM images of (A) cross-sectioned view of a TFNC membrane with cellulose nanofiber barrier layer. (B) Top view of a TFNC membrane and (C) magnified cellulose nanofiber barrier layer of TFNC membrane.

Reproduced with permission from H. Ma, C. Burger, B.S. Hsiao, B. Chu, Ultrafine polysaccharide nanofibrous membranes for water purification, Biomacromolecules 12(4) (2011) 970–976, American Chemical Society.

Ma et al. [72] fabricated a new class of thin-film nanofibrous composite (TFNC) membranes for water purification by using ultrafine polysaccharide nanofibers (i.e., cellulose and chitin) with 5–10 nm diameters. In this case, ultrafine polysaccharide nanofibers were employed as barrier layers in the polyacrylonitrile (PAN) electrospun membrane as shown in Fig. 18. They compared the demonstrated membrane with two commercial UF membranes (PAN10 and PAN400), and they observed that the demonstrated showed tenfold higher permeation flux with above 99.5% rejection ratio when compared to the commercial membranes. The demonstrated membrane also showed high virus adsorption capacity, as verified by MS2 bacteriophage testing. This high virus adsorption capacity was due to the negatively charged surface of cellulose nanofibers which were coated onto the PAN electrospun membrane. Finally, they concluded that the impressive high-flux performance of the demonstrated membrane indicates that such ultrafine polysaccharide nanofiber-based TFNC membranes can surpass conventional membrane systems in many different water applications [72].

5 CHALLENGES AND LIMITATIONS OF NANOTECHNOLOGY IN WATER TREATMENT

Nanotechnology is actively tracked to both enhance the performance of existing technologies and develop new methodologies. Nanomaterial properties desirable for water and wastewater applications include high surface area for adsorption, high activity for (photo) catalysis, antimicrobial properties for disinfection and biofouling control, superparamagnetism for particle separation, and other unique optical and electronic properties that find use in novel treatment processes and sensors for water quality monitoring. However, there are still some limitations for nanotechnology in water purification. Among them, the dispersion and retention of nanomaterials and the sustainability of antimicrobial activity are major drawbacks. Although nanoparticles provide very high specific surface area, a primary reason for

their high reactivity, aggregation in water, negates this benefit. Nanoparticles such as TiO_2 aggregate severely when added to water. If nanomaterials are applied in the form of slurry, an efficient separation process downstream such as membrane filtration is needed to retain and recycle the nanomaterials. Immobilization of nanomaterials on the reactor surfaces or membrane filters eliminates the need for separation. Nanoparticles may also escape from the treatment system and enter the product water. In addition, because all nanoparticles must be retained in the treatment system, no disinfectant residual is provided. Therefore, they must be used in conjunction with a secondary disinfectant that provides residual through the distribution system. Retention of nanomaterials is critical not only because of the cost associated with loss of nanomaterials, but also, and more importantly, because of the potential impacts of nanomaterials on human health and ecosystems. In the past few years, there has been increase in the number of nanotoxicity studies, which have enabled better understanding of the effect of the nanomaterials on human health and environmental implication.

Another major challenge is the retain ability of nanomaterials. Effective and reliable techniques are needed to anchor the nanoparticles to reactor surfaces or the selective layers of filtration membranes, or to separate and retain suspended nanoparticles in order to reduce costs associated with premature material loss and to prevent potential human health and environmental impacts. This is comprised of developing better surface coating techniques, perhaps through nanoparticle surface functionalization, minimizing membrane fouling by the nanomaterial suspension, and impregnating nanoparticles into filter packing materials, etc. Another strategy is to make use of nanomaterials with different properties allowing them to be mounted on the nanomagnetite core to create a multifunctional nanocomposite material that could be retained and recycled via magnetic separation. Future research needs to address the scalability of nanomaterial production as well as the nanomaterial-based water treatment systems. Low-cost nanomaterials should be explored for potential applications in water treatment. For example, iron-coated sands and microscale iron powder have been reported to adsorb viruses via electrostatic attraction and cause viruses to disintegrate or become noninfective [73].

6 SUMMARY AND CONCLUSION

Hygienic water is vital to human health and is a critical feedstock in various industries including electronics, pharmaceuticals, and food. The entire world is facing tough global challenges in providing clean water due to extended droughts, enhancement in population, more stringent health-based-regulations, and competing demands from variety of users. Nanomaterials play a significant role in developing new materials with high efficiency at low cost for water pollution. Nanomaterials have a number of key physicochemical properties that make them particularly attractive as separation media for water purification. On a mass basis, they have much larger surface areas than bulk particles. Nanomaterials can also be functionalized with various chemical groups to increase their affinity toward a given compound. They can also serve as high capacity/selectivity and recyclable ligands for toxic metal ions, radionuclides, and organic and inorganic solutes/anions in aqueous solutions. Nanomaterials also provide unprecedented opportunities to develop more efficient water-purification catalysts and redox active media due their large surface areas and their size and shape-dependent optical, electronic, and catalytic properties.

Nanotechnology for water and wastewater treatment is gaining momentum globally. Most of the nanotechnologies that have been reported in the literature are still in the laboratory research stage; some

have succeeded in setting pilot plants. The versatile properties of nanomaterials and their conjunction with advanced treatment techniques present great openings for modernizing water and wastewater treatment. Among the nanomaterials, three categories show the most promising candidates in large-scale application in the coming future due to their commercial availability, cost, and compatibility with the existing infrastructure. They are nanoadsorbents, nanotechnology enabled membranes, and nano-photocatalysts. All three categories have commercial products, although they have not been applied in large-scale water or wastewater treatment. The challenges faced by water/wastewater treatment nano-technologies are important, but many of these challenges are perhaps only temporary, including technical hurdles, high cost, and potential environmental and human risk. In order to fix these issues, effective collaboration between academia, industry, government is very crucial. We have confidence that progressing nanotechnology through sensible direction, while avoiding unintentional consequences, can continuously deliver efficient solutions to the challenges that we are facing globally in wastewater treatment.

REFERENCES

[1] J.M. Lehn, Toward self-organization and complex matter, Science 295 (5564) (2002) 2400–2403.
[2] K. Donaldson, V. Stone, C.L. Tran, W. Kreyling, P.J.A. Borm, Nanotoxicology, Occup. Environ. Med. (2004) 727–728.
[3] G. Oberdörster, E. Oberdörster, J. Oberdörster, Nanotoxicology: an emerging discipline evolving from studies of ultrafine particles, Environ. Health Perspect. 113 (2005) 823–839.
[4] J. Theron, J.A. Walker, T.E. Cloete, Nanotechnology and water treatment: applications and emerging opportunities, Crit. Rev. Microbiol. 34 (1) (2008) 43–69.
[5] X. Qu, P.J.J. Alvarez, Q. Li, Applications of nanotechnology in water and wastewater treatment, Water Res. 47 (12) (2013) 3931–3946.
[6] N. Ngwenya, E.J. Ncube, J. Parsons, Recent advances in drinking water disinfection: successes and challenges, Rev. Environ. Contam. Toxicol. 222 (2013) 111–170.
[7] B. Van Der Bruggen, C. Vandecasteele, Removal of pollutants from surface water and groundwater by nanofiltration: overview of possible applications in the drinking water industry, Environ. Pollut. 122 (3) (2003) 435–445.
[8] E. Drnenburg, H. Hintenberger, Das Auftreten Vielatomiger Kohlenstoffmoleküle Im Hochfrequenzfunken Zwischen Graphitelektroden. Zeitschrift fur Naturforschung—Section A, J. Phys. Sci. 14 (8) (1959) 765–767.
[9] H.W. Kroto, J.R. Heath, S.C. O'Brien, R.F. Curl, R.E. Smalley, C 60: buckminsterfullerene, Nature 318 (1985) 162.
[10] W. Krätschmer, L.D. Lamb, K. Fostiropoulos, D.R. Huffman, Solid C60: a new form of carbon, Nature 347 (6291) (1990) 354–358.
[11] M.S. Dresselhaus, G. Dresselhaus, P.C. Eklund, Fullerenes, J. Mater. Res. 8 (1993) 2054–2097.
[12] A.D. Darwish, Fullerenes, Annu. Rep. Prog. Chem., Sect. A: Inorg. Chem 104 (2008) 360–378.
[13] F. Giacalone, N. Martin, Fullerene polymers: synthesis and properties, Chem. Rev. 106 (12) (2006) 5136–5190.
[14] L.T. Scott, Methods for the chemical synthesis of fullerenes, Angew. Chem. Int. Ed 43 (38) (2004) 4994–5007.
[15] Y. Ju-Nam, J.R. Lead, Manufactured nanoparticles: an overview of their chemistry, interactions and potential environmental implications, Sci. Total Environ. 400 (1–3) (2008) 396–414.
[16] S. Deguchi, R.G. Alargova, K. Tsujii, Stable dispersions of fullerenes, C60 and C70, in water, Prep. Charact. Langmuir 17 (19) (2001) 6013–6017.

[17] D.Y. Lyon, D.A. Brown, P.J.J. Alvarez, Implications and potential applications of bactericidal fullerene water suspensions: effect of Nc60 concentration, exposure conditions and shelf life, Water Sci. Technol. 57 (10) (2008) 1533–1538.
[18] S.R. Chae, S. Wang, Z.D. Hendren, M.R. Wiesner, Y. Watanabe, C.K. Gunsch, Effects of fullerene nanoparticles on *Escherichia coli* K12 respiratory activity in aqueous suspension and potential use for membrane biofouling control, J. Membr. Sci. 329 (1–2) (2009) 68–74.
[19] H.W. Kroto, J.R. Heath, S.C. O'Brien, R.F. Curl, R.E. Smalley, C60: buckminsterfullerene, Nature 318 (6042) (1985) 162–163.
[20] S. Iijima, Helical microtubules of graphitic carbon, Nature 354 (6348) (1991) 56–58.
[21] L. Radushkevich, O Strukture Ugleroda, Obrazujucegosja Pri Termiceskom Razlozenii Okisi Ugleroda Na Zeleznom Kontakte, Zhurnal Fizicheskoi Khimii 26 (1) (1952) 88–95.
[22] A.K.-T. Lau, D. Hui, The revolutionary creation of new advanced materials—carbon nanotube composites, Compos. Part B 33 (4) (2002) 263–277.
[23] T.W. Ebbesen, P.M. Ajayan, Large-scale synthesis of carbon nanotubes, Nature 358 (6383) (1992) 220–222.
[24] E.T. Thostenson, Z. Ren, T.-W. Chou, Advances in the science and technology of carbon nanotubes and their composites: a review, Compos. Sci. Technol. 61 (13) (2001) 1899–1912.
[25] K. Dai, L. Shi, J. Fang, D. Zhang, B. Yu, NaCl adsorption in multi-walled carbon nanotubes, Mater. Lett. 59 (16) (2005) 1989–1992.
[26] H. Li, L. Zou, Ion-exchange membrane capacitive deionization: a new strategy for brackish water desalination, Desalination 275 (1–3) (2011) 62–66.
[27] A.T. Nasrabadi, M. Foroutan, Ion-separation and water-purification using single-walled carbon nanotube electrodes, Desalination 277 (1–3) (2011) 236–243.
[28] L. Joseph, J. Heo, Y.G. Park, J.R.V. Flora, Y. Yoon, Adsorption of bisphenol a and 17α-Ethinyl estradiol on single walled carbon nanotubes from seawater and brackish water, Desalination 281 (1) (2011) 68–74.
[29] P.R. Wallace, The band theory of graphite, Phys. Rev. 71 (9) (1947) 622–634.
[30] G.W. Semenoff, Condensed-matter simulation of a three-dimensional anomaly, Phys. Rev. Lett. 53 (26) (1984) 2449–2452.
[31] Y.B. Zhang, Y.W. Tan, H.L. Stormer, P. Kim, Experimental observation of the quantum hall effect and Berry's phase in graphene, Nature 438 (7065) (2005) 201–204.
[32] X. Li, W. Cai, J. An, S. Kim, J. Nah, D. Yang, R. Piner, A. Velamakanni, I. Jung, E. Tutuc, et al., Large-area synthesis of high-quality and uniform graphene films on copper foils, Science 324 (5932) (2009) 1312–1314.
[33] P.W. Sutter, J.I. Flege, E.A. Sutter, Epitaxial graphene on ruthenium, Nat. Mater. 7 (5) (2008) 406–411.
[34] K.S. Novoselov, A.K. Geim, S.V. Morozov, D. Jiang, Y. Zhang, S.V. Dubonos, I.V. Grigorieva, A. A. Firsov, Electric field effect in atomically thin carbon films, Science 306 (5696) (2004) 666–669.
[35] B.C. Brodie, On the atomic weight of graphite, Philos. Trans. R. Soc. Lond. 149 (1859) 249–259.
[36] L. Staudenmaier, Verfahren Zur Darstellung Der Graphits??Ure, Ber. Dtsch. Chem. Ges. 31 (2) (1898) 1481–1487.
[37] W.S. Hummers, R.E. Offeman, Preparation of graphitic oxide, J. Am. Chem. Soc. 80 (6) (1958) 1339.
[38] W. Gao, The chemistry of graphene oxide, in: Graphene Oxide: Reduction Recipes, Spectroscopy, and Applications, Springer, 2015, pp. 61–95.
[39] Y. Han, Z. Xu, C. Gao, Ultrathin graphene nanofiltration membrane for water purification ultrathin graphene nanofi ltration membrane for water purifi cation, Adv. Funct. Mater. 23 (29) (2013) 3693–3700.
[40] A.W. Carpenter, C.F. De Lannoy, M.R. Wiesner, Cellulose nanomaterials in water treatment technologies, Environ. Sci. Technol. 49 (9) (2015) 5277–5287.
[41] D.A. Gopakumar, S. Thomas, Y. Grohens, Nanocelluloses as innovative polymers for membrane applications, in: Multifunctional Polymeric Nanocomposites Based on Cellulosic Reinforcements, Elsevier, 2016, pp. 253–275.

[42] M. Barikani, E. Oliaei, H. Seddiqi, H. Honarkar, Preparation and application of chitin and its derivatives: a review, Iran. Polym. J. Eng. Ed. 23 (4) (2014) 307–326.
[43] G. Camci-Unal, N.L.B. Pohl, Quantitative determination of heavy metal contaminant complexation by the carbohydrate polymer chitin, J. Chem. Eng. Data 55 (3) (2010) 1117–1121.
[44] A.L. Simonian, B.D. Disioudi, J.R. Wild, An enzyme based biosensor for the direct determination of diisopropyl fluorophosphate, Anal. Chim. Acta 389 (1–3) (1999) 189–196.
[45] T. Pradeep, Anshup. Noble metal nanoparticles for water purification: a critical review, Thin Solid Films 517 (24) (2009) 6441–6478.
[46] J.P. Liu, E. Fullerton, O. Gutfleisch, D.J. Sellmyer (Eds.), Nanoscale Magnetic Materials and Applications, Springer Science+ Business Media, LLC, 2009.
[47] A. Afkhami, M. Saber-Tehrani, H. Bagheri, Modified Maghemite nanoparticles as an efficient adsorbent for removing some cationic dyes from aqueous solution, Desalination 263 (1–3) (2010) 240–248.
[48] B. Pan, H. Qiu, B. Pan, G. Nie, L. Xiao, L. Lv, W. Zhang, Q. Zhang, S. Zheng, Highly efficient removal of heavy metals by polymer-supported nanosized hydrated Fe(III) oxides: behavior and XPS study, Water Res. 44 (3) (2010) 815–824.
[49] S.H. Huang, M.H. Liao, D.H. Chen, Direct binding and characterization of lipase onto magnetic nanoparticles, Biotechnol. Prog. 19 (3) (2003) 1095–1100.
[50] M. Roco, C. Nanotechnology, Convergence with modern biology and medicine, Curr. Opin. Biotechnol. 14 (3) (2003) 337–346.
[51] A.K. Gupta, M. Gupta, Synthesis and surface engineering of iron oxide nanoparticles for biomedical applications, Biomaterials 26 (18) (2005) 3995–4021.
[52] C. Boyer, M.R. Whittaker, V. Bulmus, J. Liu, T.P. Davis, The design and utility of polymer-stabilizediron-oxide nanoparticles for nanomedicine applications, NPG Asia Materials 2 (1) (2010) 23–30.
[53] F. Assa, H. Jafarizadeh-Malmiri, H. Ajamein, N. Anarjan, H. Vaghari, Z. Sayyar, A. Berenjian, A biotechnological perspective on the application of iron oxide nanoparticles, Nano Res. 9 (8) (2016) 2203–2225.
[54] S.-Y. Mak, D.-H. Chen, Fast adsorption of methylene blue on polyacrylic acid-bound Iron oxide magnetic nanoparticles, Dyes Pigments 61 (1) (2004) 93–98.
[55] V.K. Gupta, S. Agarwal, T.A. Saleh, Chromium removal by combining the magnetic properties of Iron oxide with adsorption properties of carbon nanotubes, Water Res. 45 (6) (2011) 2207–2212.
[56] K. Hashimoto, H. Irie, A. Fujishima, A historical overview and future prospects, AAPPS Bull. 17 (6) (2007) 12–28.
[57] M.R. Hoffmann, S.T. Martin, W. Choi, D.W. Bahnemann, Environmental applications of semiconductor photocatalysis, Chem. Rev. 95 (1) (1995) 69–96.
[58] M.V. Liga, E.L. Bryant, V.L. Colvin, Q. Li, Virus inactivation by silver doped titanium dioxide nanoparticles for drinking water treatment, Water Res. 45 (2) (2011) 535–544.
[59] B. Wang, M. Lee, K. Li, YSZ-reinforced alumina multi-channel capillary membranes for micro-filtration, Membranes 6 (1) (2015) 5.
[60] T.A. Saleh, V.K. Gupta, Synthesis and characterization of alumina nano-particles polyamide membrane with enhanced flux rejection performance, Sep. Purif. Technol. 89 (2012) 245–251.
[61] A.W. Bosman, H.M. Janssen, E.W. Meijer, About dendrimers: structure, physical properties, and applications, Chem. Rev. 99 (7) (1999) 1665–1688.
[62] M. Malkoch, E. Malmström, A.M. Nyström, Dendrimers: properties and applications, in: Polymer Science: A Comprehensive Reference, 10 Volume Set, vol. 6, 2012, pp. 113–176.
[63] D.A. Tomalia, J.M.J. Fréchet, Discovery of dendrimers and dendritic polymers: a brief historical perspective, J. Polym. Sci. A Polym. Chem. 40 (16) (2002) 2719–2728.
[64] M. Cheryan, Ultrafiltration and Microfiltration Handbook, CRC Press, 1998.

[65] M. Arkas, D. Tsiourvas, C.M. Paleos, Organosilicon dendritic networks in porous ceramics for water purification, Chem. Mater. 17 (13) (2005) 3439–3444.
[66] E. Krieg, H. Weissman, E. Shirman, E. Shimoni, B. Rybtchinski, A recyclable supramolecular membrane for size-selective separation of nanoparticles, Nat. Nanotechnol. 6 (3) (2011) 141–146.
[67] M. Asper, T. Hanrieder, A. Quellmalz, A. Mihranyan, Removal of xenotropic murine leukemia virus by nanocellulose based filter paper, Biologicals 43 (6) (2015) 452–456.
[68] A. Quellmalz, A. Mihranyan, Citric acid cross-linkednanocellulose-based paper for size-exclusion nanofiltration, ACS Biomat. Sci. Eng. 1 (4) (2015) 271–276.
[69] J.C. Crittenden, R. Rhodes Trussell, D.W. Hand, K.J. Howe, G. Tchobanoglous, MWH's Water Treatment: Principles and Design, John Wiley & Sons, 2012.
[70] P. Vandezande, L.E.M. Gevers, I.F.J. Vankelecom, Solvent resistant nanofiltration: separating on a molecular level, Chem. Soc. Rev. 37 (2) (2008) 365–405.
[71] H. Liang, X. Cao, W. Zhang, H. Lin, F. Zhou, L. Chen, Robust and highly efficient free-standing carbonaceous nanofiber membranes for water Purifi cation, Adv. Funct. Mater. 21 (2011) 3851–3858.
[72] H. Ma, C. Burger, B.S. Hsiao, B. Chu, Ultrafine polysaccharide nanofibrous membranes for water purification, Biomacromolecules 12 (4) (2011) 970–976.
[73] J.N. Ryan, R.W. Harvey, D. Metge, M. Elimelech, T. Navigato, A.P. Pieper, Field and laboratory investigations of inactivation of viruses (PRD1 and MS2) attached to Iron oxide-coated quartz sand, Environ. Sci. Technol. 36 (11) (2002) 2403–2413.

FURTHER READING

[74] N. Savage, M.S. Diallo, Nanomaterials and water purification: opportunities and challenges, In J. Nanopart. Res. 7 (2005) 331–342.
[75] A. Dasgupta, L.P. Rajukumar, C. Rotella, Y. Lei, M. Terrones, Covalent three-dimensional networks of graphene and carbon nanotubes: synthesis and environmental applications, Nano Today 12 (2017) 116–135.
[76] A.K. Geim, K.S. Novoselov, The rise of graphene, Nat. Mater. 6 (3) (2007) 183–191.
[77] R. Das, M.E. Ali, S.B.A. Hamid, S. Ramakrishna, Z.Z. Chowdhury, Carbon nanotube membranes for water purification: a bright future in water desalination, Desalination 336 (2014) 97–109.
[78] A. Isogai, Wood nanocelluloses: fundamentals and applications as new bio-based nanomaterials, J. Wood Sci. 59 (6) (2013) 449–459.
[79] P. Xu, G.M. Zeng, D.L. Huang, C.L. Feng, S. Hu, M.H. Zhao, C. Lai, Z. Wei, C. Huang, G.X. Xie, et al., Use of iron oxide nanomaterials in wastewater treatment: a review, Sci. Total Environ. 424 (2012) 1–10.

CHAPTER

2

INTRODUCTION TO NANOSTRUCTURED AND NANO-ENHANCED POLYMERIC MEMBRANES: PREPARATION, FUNCTION, AND APPLICATION FOR WATER PURIFICATION

Jaydevsinh M. Gohil[*,†], **Rikarani R. Choudhury**[†]

*Advanced Polymer Design and Development Research Laboratory (SARP-APDDRL), Central Institute of Plastics Engineering & Technology (CIPET), Bengaluru, India** *Laboratory for Advanced Research in Polymeric Materials (SARP-LARPM), Central Institute of Plastics Engineering & Technology (CIPET), Bhubaneswar, India*[†]

1 INTRODUCTION

The terms "water treatment" and "water purification" are extensively used for any unit operations and processes that involve methods and processing steps for the removal of detrimental contaminants such as particulates, bacteria, minerals, organic pollutants, chemicals, pharmaceuticals, dissolved salts, etc., found in water. These contaminants may be physical, chemical, biological, or radiological in nature. There are three established water purification technologies: physical separation (settling, thermal distillation, filtration, and membrane separation), chemical processes (disinfection, coagulation, ion exchange), and biological processes (slow sand filtration). Among all these techniques, membrane processes alone contribute about 53% toward production of clean water, wastewater treatment/purification, and water recycling. Membrane technology is the science and engineering of separation, recognition, conversion, and recovery processes. The current boom in technological revolution in developing and developed nations, as well as increasing awareness of human beings regarding sustainable development, inspires industrialists, researchers, and entrepreneurs to adopt more economical, efficient, and environmentally benign methods for water purification. In this context, membranes and membrane processes such as microfiltration (MF), ultrafiltration (UF), nanofiltration (NF), and reverse osmosis (RO) have been used in many types of separation methods related to water treatment processes and for the recovery of some important chemical ingredients, solvents, and byproducts from polluted water streams, thereby helping to minimize environmental pollution by maximizing product output. In addition, thin film composite membranes (TFCMs) are dominantly being

Nanoscale Materials in Water Purification. https://doi.org/10.1016/B978-0-12-813926-4.00038-0

employed at the commercial scale for the removal of salt ions from brackish water and seawater, the creation of potable water, and wastewater treatment [1]. Specifically, membrane technologies are also employed in the biotechnology, bioprocessing, and petrochemicals industries for process intensification through improving chemical and any other manufacturing and processing unit operation by decreasing equipment size, energy consumption, and/or waste generation. Membrane systems excel because they are precisely tailored to the specific requirements of these separation processes.

Membranes with nanosized pores, usually known as nanoporous membranes (NPMs) or nanostructured membranes (NSMs), and nano-enhanced membranes (NEMs) have been used to remove suspended solids, bacteria, macromolecules, viruses, colloids, organic compounds, and salt and mineral ions from water streams [2]. Thus, membrane technologies cover the entire spectrum of water clarification, disinfection, and desalination. Water clarification is pretreatment to remove turbidity-causing suspended solids and particulate matter from industrial effluents, municipal wastewater, and municipal potable water. Water disinfection refers to the process of removal, deactivation, and/or killing of pathogenic microorganisms in potable water. Additionally, the membrane process is capable of eliminating organic contaminants from water, contaminants that otherwise serve as a food source for microbial agents. Desalination is the practice of separating dissolved salts and minerals from water by means of thermal distillation, chemical treatment, or membrane processing.

This chapter introduces the state-of-the-art in pressure-driven NSMs and NEMs such as MF, UF, NF, and RO used in water clarification, disinfection and desalination. The introduction briefly describes membranes and membrane processes, and membrane materials and types. Subsequent sections elaborate conventional polymeric membrane preparation and advanced membrane preparation using nanoscale materials, and the applications and functional attributes of NEMs.

2 PRESSURE-DRIVEN MEMBRANES AND MEMBRANE PROCESSES

2.1 DEFINITION OF MEMBRANE

Conventionally, a membrane is described as a selective barrier-layer that permits some molecules, ions, or particles to pass through but constrains others. By nature, membranes can be biological or synthetic. Therefore, a precise and complete definition of the membrane covering all its functional features is quite challenging. In the most general sense, a biological membrane is a complex, multifunctional, and dynamically structured multicomponent system acting as an enclosing or separating barrier within or around the cell. A synthetic membrane is an interphase, which separates two phases and impedes the transport of diverse components in a definite fashion. Also, according to the International Union of Pure and Applied Chemistry (IUPAC), a membrane is a structure possessing lateral dimensions much greater than its thickness, through which mass transfer may occur under a variety of driving forces [3].

2.2 MEMBRANE PROCESSES

Water treatment through a membrane involves the removal of unwanted contaminants from water under the influence of pressure, osmotic pressure (concentration), or potential (electrical) driving forces. Fundamentally, as shown in Fig. 1, pressure-driven water treatment membranes can be classified as MF, UF, NF, and RO membranes. The classification spectrum for these water and wastewater treatment membranes relies on their pore size rating and applied pressure. The nanostructured polymer-based

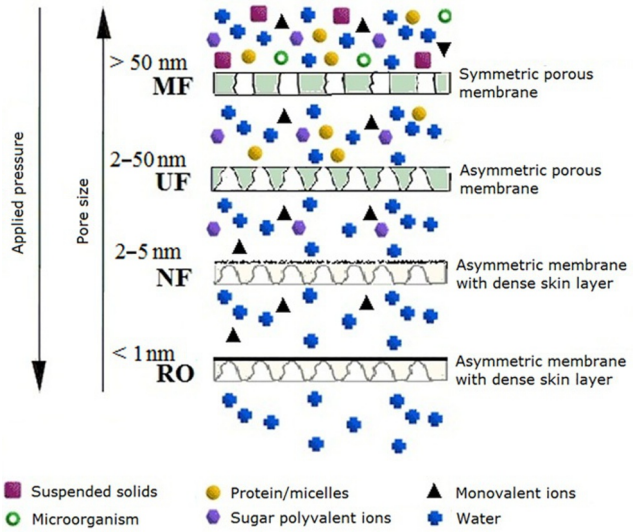

FIG. 1

Pressure-driven membranes processes for water treatment.

membrane is a porous membrane having nanoscale pores (1–100 nm) or a membrane prepared using nanomaterials/nanoparticles (NMs/NPs), or both [4]. These NSMs and membrane processes are well-defined by IUPAC as [3, 5]:

MF membrane: Pressure-driven membrane-based separation procedure; particles and dissolved macromolecules larger than 100 nm are excluded. Permeate transport across MF membranes is best described as occurring by convective flow through pores by a pore-flow/sieving mechanism. Separation of particles and dissolved components takes place by a sieving mechanism, based on a size exclusion principle. MF membranes possess symmetric or asymmetric porous structure.

UF membrane: A separation process in which a solution containing a solute of molecular size notably greater than that of the solvent molecule is removed from the solvent by the application of a hydraulic pressure, forcing only the solvent to flow through a suitable membrane, usually having a pore size in the range of 2–50 nm. In UF, the pressure gradient governs mass transport through the convective flux within membrane pores. Therefore, permeation through these types of membranes is inversely propositional to membrane thickness and directly propositional to pore size and applied pressure.

NF membrane: Pressure-driven membrane-based separation procedure wherein particles and dissolved macromolecules smaller than 2 nm are rejected. The extended Nernst-Planck equation has been extensively employed to explain permeates transport across NF-type membranes. Operating pressure of the NF membrane is in between that of the UF and RO processes, and sometimes, it is also referred to as a loose RO membrane.

RO membrane: Liquid-phase pressure-driven separation method in which an applied trans- membrane pressure instigates selective movement of a solvent against its osmotic pressure difference. Solution diffusion phenomena have been extensively used to describe permeates transport across the RO membranes.

In other words, MF membranes are macroporous, with a pore diameter > 50 nm, UF membranes are mesoporous, with pore diameter ranging from 2 to 50 nm, and NF membranes are considered microporous, with pore size in the range of 2 nm or less.

2.3 CONVENTIONAL MEMBRANES: MATERIALS AND TYPES

Apart from membrane processes, and based on the origin of membranes and their structure (morphology), materials of construction, preparation techniques, potential applications, and configuration, membranes can be categorized as shown in Fig. 2. A variety of materials and techniques are applied to form membranes of varied physicochemical, structural features, which subsequently determine the membrane's selectivity and applications. Essentially, morphological (structural) features can be tailored by appropriate techniques of membrane preparation; hence, based on membrane structure, they can be principally classified as symmetric and asymmetric membranes [5].

Symmetric membranes have uniform pore size or structural morphology throughout the cross-section of membrane, and are widely used in dialysis, MF, and UF applications. An asymmetric or anisotropic membrane possesses gradient in pore morphology, and usually, a top dense layer, or

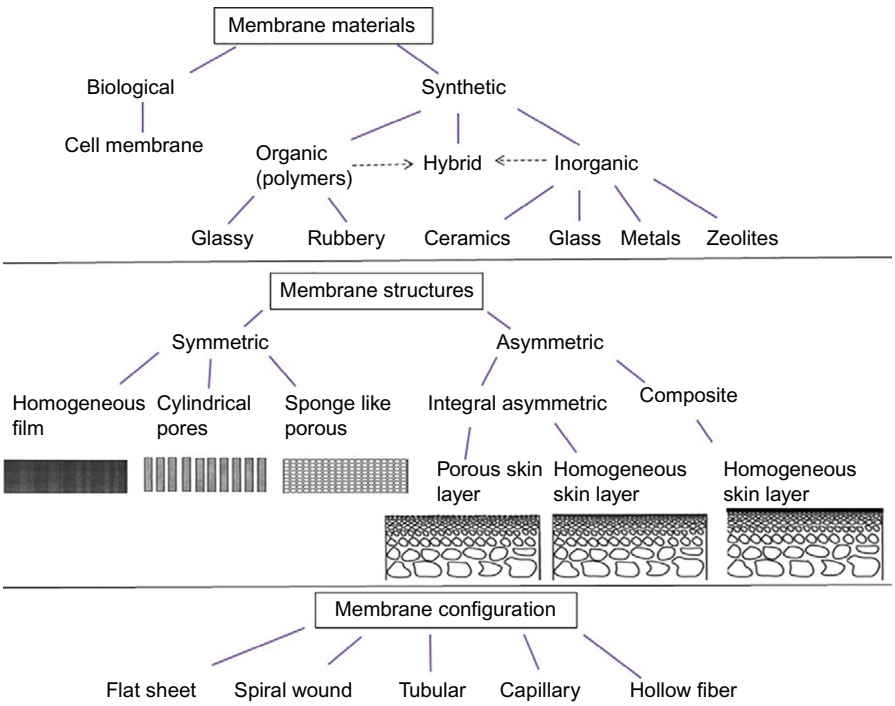

FIG. 2

Classification of membranes based on materials of construction, structural attributes, and configuration.

Modified from H. Strathmann, L. Giorno, E. Drioli, Basic aspects in polymeric membrane preparation, in: E. Drioli, L. Giorno (Eds.) Comprehencive Membrane Science and Engineering, Elsevier, Oxford, 2010, pp. 91–112.

"skin" layer, of 0.1–5 μm thickness is supported onto an underlying porous, 50–200 μm thick layer. These barriers and supporting layers may be produced from the same material or from different materials; functionally, a less-porous top or dense layer acts as a discriminating barrier, while the underlying macroporous layer provides mechanical support. If the dense top layer is produced from same materials, then it is known as an integrally asymmetric membrane, and if the top dense layer consists of another material, it is called a composite membrane. These membranes are employed in RO, NF, UF, and MF, as well as in gas separation applications.

2.4 NM-BASED POLYMERIC MEMBRANES

Conventional nanostructured polymeric membranes (NSMs) (where the term "nano" refers to the internal morphology (structure) of the membrane) have already dominated the market in water purification by the UF, NF, and RO processes due to their already established large-scale production viability and optimized operation procedures. Recently, nanotechnology has opened the way to producing nano-enhanced or nano-engineered membranes (NEMs), where term "nano" signifies NM-based membranes. Typical different types of NMs that have been studied for water purification application and/or membrane preparation are shown in Fig. 3. NEMs are prepared to fine tune the selectivity, permeability, morphology, and physicochemical characteristics of membranes to provide the following functional aspects:

- Improved antifouling and antimicrobial properties
- Enhanced water permeability through making the membrane more hydrophilic

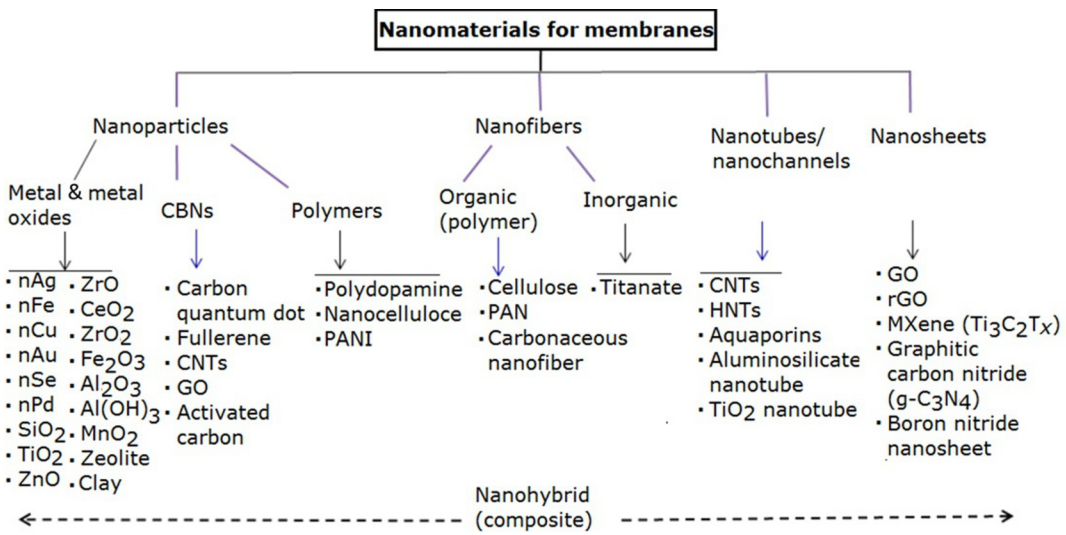

FIG. 3

List of the different types of NMs that have been reported in the literature for preparation of NEMs. (Each category of NMs forms corresponding to NEMs is shown in Fig. 4.) *CBNs,* carbon-based NMs; *CNT,* carbon nanotube; *HNT,* halloysite nanotube; *GO,* graphene oxide; *PAN,* polyacrylonitrile; *PANI,* polyaniline.

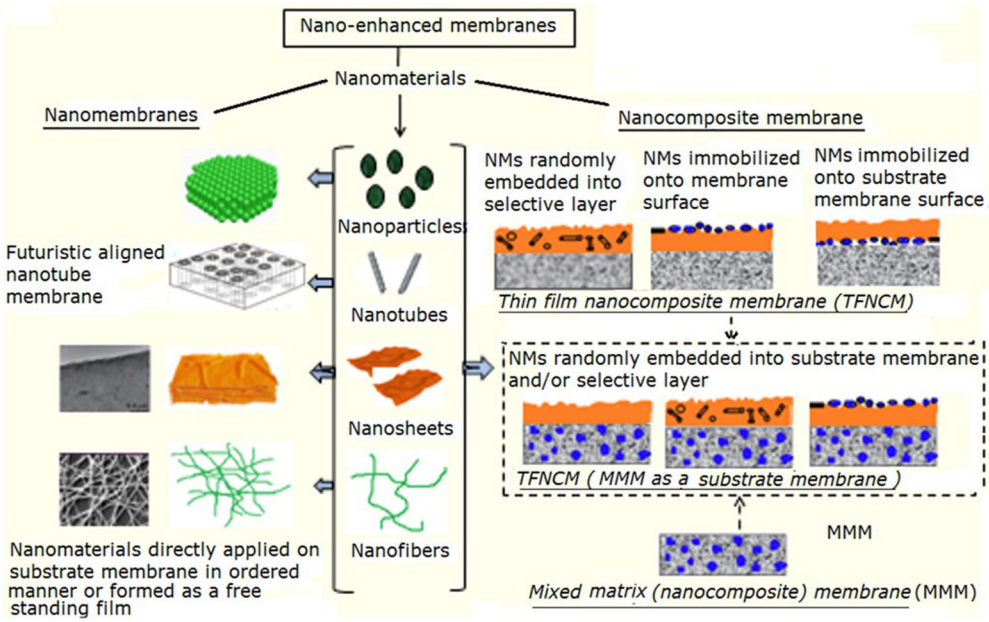

FIG. 4

Types of NEMs.

- Increased selectivity through modifying membrane morphology and surface properties
- Improved chlorine resistance
- Induced catalytic properties
- Broadened application of membranes for various separation processes
- Increased thermal and mechanical stability

NEMs can be categorized as nanomembranes that contain a bare layer of NMs supported onto a porous substrate membrane or prepared as a freestanding, ordered NM film; and nanocomposite membranes (NCM), in which NMs are incorporated along with a polymer binder (Fig. 4). Further, NCMs are subclassified into thin film nanocomposite membranes (TFNCMs), in which engineered nanoparticles are immobilized/entrapped within the top active layer of membrane, surface-coated TFNCMs, in which NMs are coated onto the top surface of a NCM, substrate-coated TFNCMs, in which NMs are located onto a support membrane of TFNCM, and mixed-matrix membranes (MMM), in which NMs are blended/incorporated/entrapped within the matrix of the membrane. Thin film nanocomposite membranes can be prepared using an MMM or a conventional nanostructured UF/MF membrane as a support.

3 NANOSTRUCTURED POLYMERIC MEMBRANE PREPARATION

The structural pore morphology of membranes can be controlled during their preparation. Primarily, membrane preparation techniques are adopted based on materials of construction, end application, and expected geometries of the membrane. Sometimes, postmodification treatments are also performed to

tailor the physicochemical feature of the barrier layer and the pore morphology. Largely, organic polymers are commercially preferred due to their flexibility, permeability, and processability to form diverse structures. For many separation tasks, to obtain higher thermal stability and chemically robust structure, inorganic materials (i.e., ceramics, zeolite, metal powder) are the second most popular choice for membrane production. Additionally, hybrid NMs, blends of organic and inorganic materials, and metal organic framework (MOF) materials have been used to induce synergistic properties into nanostructured polymeric membranes (NSMs). Lately, researchers have been intensely focused on the fabrication of next-generation antifouling and nanochannel-based membranes via bio-inspired and biomimetics pathways.

3.1 PHASE INVERSION TECHNIQUES

Phase inversion (PI), or phase separation (PS), is the first breakthrough technique for anisotropic or isotropic RO membrane preparation, and has become widely accepted at both the industrial and laboratory scales for MF and UF application [6, 7]. The PI process converts polymer melt/dope from a liquid phase to solid phase in a controlled fashion. There are four primary methods applied in PI for membrane preparation.

Nonsolvent induced phase separation (NIPS): Loeb and Saurirajan first invented the NIPS method for asymmetric cellulose acetate (CA)-based RO membrane preparation; it is also called the L-S technique. Precisely, in NIPS, polymers such as CA, polysulfone (PSF), poly(vinylidene fluoride) (PVDF), or polyamide (PA) are solubilized in a suitable solvent, and a 20–200 μm thick film of polymer solution is cast upon a plate or fabric support and subsequently submerged into a nonsolvent water bath, in which coagulation of polymer solution results in the solid polymer-rich and liquid solvent-rich phases, forming symmetric or asymmetric membranes. Membranes with varying chemicomechanical properties and pore sizes (0.1 to >20 μm) can be prepared (by NIPS) through variation of polymer, polymer dope concentration, additives (i.e., pore former) concentration in polymer solution, and temperature of the coagulant bath and polymer dope. A wide range of polymers that can be solubilized in an appropriate solvent and precipitated in a nonsolvent can be employed for flat sheet, capillary, or hollow fiber (HF) membranes preparation. The phase separation mechanism includes liquid-liquid demixing (crystallization), gelation, and vitrification (i.e., the transformation of polymer to the glassy state), depending upon the membrane preparation parameters and type of polymer used [8].

Thermally induced phase separation (TIPS): Polymers that are not readily soluble in solvent at ambient temperature cannot be used to prepare membranes by NIPS, but membranes can be fabricated from them using TIPS; in TIPS, a polymer such as polypropylene (PP) or polyethylene (PE) is dissolved in a suitable amine at elevated temperature and cast into a film at elevated temperature. The polymer solution is then cooled to a point at which precipitation of the polymer induces controlled thermal gelation. After complete precipitation, the solvent is extracted, evaporated, or freeze dried. The pore size of the symmetric membrane relies upon thermodynamic parameters such as temperature and concentration of polymer dope, solvent system, and cooling rate of solution.

Solvent evaporation induced phase separation (EIPS): In this method, a homogeneous polymer (i.e., polyvinyl chloride, polyvinyl acetate, polystyrene, etc.) solution is prepared from two or more volatile solvents of different boiling points and dissolution capacities, and subsequently spread in the form of a thin film [9]. Meticulous evaporation of a more volatile solvent from the cast polymer solution film induces polymer precipitation/demixing to form the membrane.

Vapor-induced phase separation (VIPS): In this technique, a spread polymer solution is exposed to vapor of a nonsolvent (usually water vapor); absorption of nonsolvent vapor onto cast dope solution precipitates the polymer to the solid phase membrane.

3.2 TRACK ETCHING

Track etching is an industrial process for the production of isoporous polymer membranes. Usually, polycarbonate (PC) or polyethylene naphthalate film having a thickness in the 6 μm to 35 μm range is exposed to accelerated heavy ions (charged particles) in a controlled manner [10, 11]. The charged particles pass across the film and leave behind a degraded (damaged) trajectory. The density of these trajectories in the film depends on the time of exposure in the reactor. A longer time in the reactor forms more tracks and causes larger pore density in the final membrane. Consequently, the membrane is treated with a caustic etchant such as sodium hydroxide solution to wash the damaged zone out from the trajectories to generate porosity. This way, the etching treatment widens the tracks into full-fledged pores, the size of which can be regulated precisely through time of exposure, and the concentration and temperature of etchant solution.

3.3 MICROLITHOGRAPHY AND NANOLITHOGRAPHY

Photolithogarphy: Lithography is used to make a precise pattern in the thin film or the bulk substrate through microfabrication. Photolithography uses a light source (UV, optical) to transfer a pattern from a photomask to a light-sensitive photoresist coated onto the substrate [12]. Photoresist is a light-sensitive material which is layered onto a host substrate by spin coating. A pattern mask is then applied to the surface to block light; therefore, only unmasked regions of the photoresist are exposed to light. After exposure to the light source, a chemical called a developer is applied to the surface to remove the unmasked or masked region, depending upon the type of photoresist used. Typically, when a positive photoresist is used, the exposed region is degraded by light, and the chemical treatment dissolves the region that is exposed to light and generates a coating pattern similar to a pattern mask. In the case of a negative photoresist, the light-exposed region of the photoresist is polymerized or cross-linked by light, and subsequent chemical treatment removes the region that is not exposed to light, producing the coating pattern (i.e., negative of the pattern mask) where the mask is not placed. Likewise, electron-beam lithography (EBL) and ion-beam lithography (IBL) employ beam of electrons and charged particles [13], respectively, to scan across a target polymer film, and the exposed polymer area is removed with a positive-tone photoresist to generate porosity in the polymeric membranes. Lithography is used for uniform pore size "membrane sieves" with very thin cross-section (1–10 μm) and uniform pore size ranging from several micrometers to 100 nm.

3.4 SINTERING

Sintering is the method of making a porous membrane from high melting point organic and inorganic powdered materials by application of heat and pressure without liquification of materials [14]. A powder or suspension made from particles of a particular size is converted into a film or an appropriate shape by pressing, tape casting, slip casting, or an extrusion technique and then sintered by

heating the materials just below their melting point. Organic polymers like polytetrafluoroethylene (PTFE), etc., and inorganic materials like ceramics, metal powders, and graphite, are used for the preparation of low porosity (10%–40%) symmetric membranes having wide pore size distribution ranging from 0.2 μm to 20 μm. The size of membrane pores and pore size distribution depend upon the particle size and particle size distribution of the powder, while the choice of materials determines the thermochemical stability and mechanical properties of sintered structures. Membranes of different configurations, such as disks, cartridges, or bore tubes, are constructed for the purification of colloidal solutions and suspensions.

3.5 STRETCHING

Stretching is a versatile technique to induce porosity in partially crystalline polymer film [15] and melt spun hollow fiber precursors [16] by mechanical rupture. Melt of polymers such as PE, PTFE, polyoxymethylene (POM), or PVDF is extruded in the form of a film/hollow fiber at rapid drawdown. This process arranges the crystallites in the film along the direction of drawing. Following annealing and cooling further to generate pores, the film is mechanically ruptured by cold stretching the film perpendicular to the direction of drawing at a faster strain rate; sometimes, the film is also subjected to hot stretching at a slower strain rate to increase its pore size. With precise control of the annealing, as well as cold and hot stretching process parameters (strain rate, temperature, crystallinity, etc.), it is possible to form an asymmetric membrane film with 0.2–20 μm uniform pores.

3.6 TEMPLATE LEACHING

This process is useful for preparation of symmetric microporous membranes from PE, PP, and PTFE, as well as from glass, metal alloys, or ceramics, which are not soluble in common solvent at room temperature. For polymeric membrane fabrication, after preparing the fine dispersion or the blend of the leachable component and the polymer matrix, the homogeneous mixture is extruded as a thin film [17]. The dense extruded film is then immersed into a suitable solvent to remove the leachable constituent from the extruded thin film to generate microporous structure in membrane. Low-molecular-weight liquid paraffin, polystyrene (PS), poly(vinyl alcohol) (PVA), or poly(ethylene glycol) (PEG) can be used as a leachable constituent [18].

3.7 SELF-ASSEMBLY NONSOLVENT-INDUCED PHASE SEPARATION

This strategy is adopted for pore formation in block copolymer membranes. Block copolymers are well known for holding a variety of intricate morphologies in solution/melt, which can be tuned to nanoscale [13]. Self-assembly is defined as the process of self-arrangement of constituents into definite patterns or structures without the aid of any external forces. Immiscibility among the different blocks of the copolymers induces microphase separation, which creates ordered structure. Two types of protocol are in place to create nanoscale isopores in block copolymer membranes: (i) film solution casting and selective block removal tactic, and (ii) self-assembly and NIPS (SNIP).

Fig. 5 shows the schematic representation of a laboratory-scale casting machine for block polymer (polystyrene-*block*-poly(vinylpyridine) membrane preparation by SNIP along with a micrograph of a membrane [19]. In SNIP process, a self-assembled block copolymer is first dissolved into an

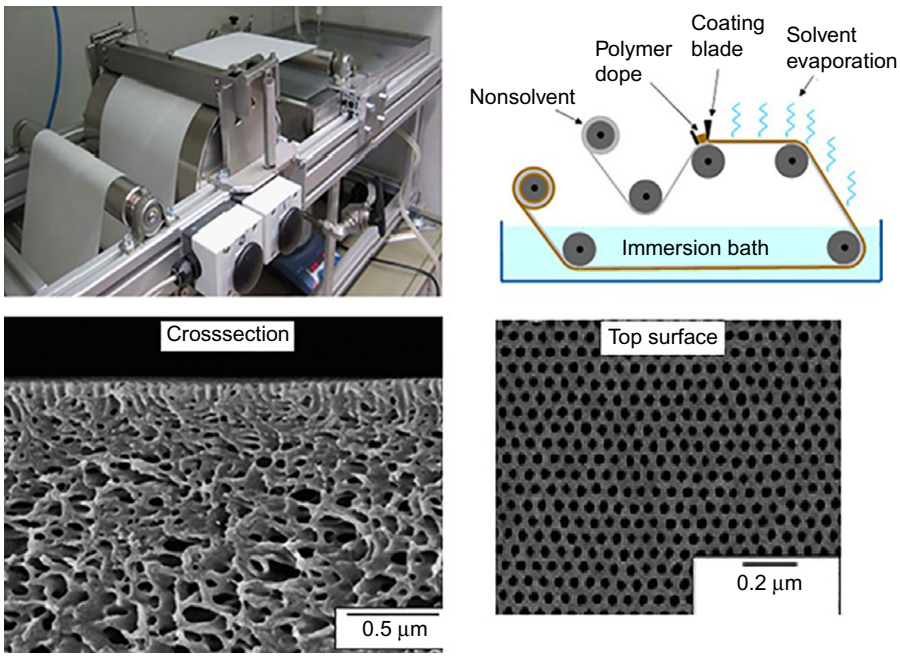

FIG. 5

Schematic of laboratory-scale casting machine for block polymer membrane preparation by SNIP and micrograph of polystyrene-*block*-poly(vinylpyridine)-based membrane.

Reproduced with permission from S. Rangou, K. Buhr, V. Filiz, J.I. Clodt, B. Lademann, J. Hahn, A. Jung, V. Abetz, Self-organized isoporous membranes with tailored pore sizes, J. Membr. Sci. 451 (2014) 266–275, Copyright [2014] Elsevier.

appropriate solvent to obtain a homogeneous solution of a semidiluted concentration range (i.e., 15 to 30 weight %). Next, the solution is spread onto a porous support membrane (usually nonwoven fabric) by solution casting in the form of a thin film. After that, solvent from the cast film is allowed to evaporate at a controlled rate for a predetermined time. During the evaporation stage, the domain of solution-air interface is enriched with the block polymer, and this leads to formation of self-assembled orderly nanostructure along the top active layer of the film. It should be noted that the self-assembled nanopatterns are dynamic and move toward equilibrium morphology; instantaneous development of self-assembled nanostructures at any point during solvent evaporation depends on the composition of polymer dope, solvent vaporization rate, and the properties of block copolymer. Following solvent evaporation, cast films are immersed into nonsolvent bath, where the assembled nanostructures are first precipitated on top of the film, while the underlying polymer layer undergoes PI. In practice, membranes formed by SNIPS consist of three layers: (i) a top surface layer (<100 nm), (ii) an ordered self-assembled middle layer (about 400 nm), and (iii), a disordered bottom layer (>20 µm). NIPS in block polymer membrane formation can be described as a phase separation mechanism including nucleation and growth (NG) and spinodal decomposition (SD). In most cases, this microphase separation phenomenon (i.e., binodal and SD) is thermodynamically predicted using the Gibbs free energy of block copolymer mixing. Details of various block polymer membranes' fabrication, the

effect of thermodynamic and kinetic parameters on micro- and macrophase separation, and types of block polymers that have been studied for isoporous membrane preparation are well presented in recent reviews [20, 21].

3.8 INTERFACIAL POLYMERIZATION FOR TFCM PREPARATION

Interfacial polymerization (IP) reaction is the most accepted route for the preparation of TFC RO and NF membranes in industry. As shown in the figure generally, a support UF or MF membrane (usually PSF, polyethersulfone (PES), etc.) is first soaked with an aqueous solution of diamine or polyamine. Apparently, in the second step, a support membrane is superficially dried and put into contact with an acid chloride solution prepared in water-immiscible solvent (organic medium). These two reactive monomers react at the organic/aqueous interface to form a PA barrier layer [22]. Fortunately, because of the self-inhibiting nature and limited supply of the reactants through the already formed layer, the IP creates an extremely thin selective layer of 100–300 nm thickness. The selectivity and permeability of the PA composite membranes depend on the final thickness of barrier layer, morphology, surface charge, and surface roughness. These membrane characteristics can be varied through selection of amine and acid chloride monomers, concentration of aqueous and organic solution, types of additives and their compositions in solutions, organic solvent, and choice of substrate membrane. Additionally, for industrial membrane production by the continuous process, some parameters such as speed of coating, reaction time, and humidity significantly affect the consistency of the composite membranes.

3.9 SPINNING

Spinning is a method of preparing capillary or hollow fiber membranes (HFM) from ceramics and polymers. Broadly, the term "capillary" is used for tubes having a diameter in the range of 0.5 and 5 mm. Tubes having an inner diameter <0.5 mm are usually known as hollow fibers. Extrusion is the common process for making the tube profiles, while spinning is used for the preparation of hollow fibers. Polymers such as CA, PVDF, PES, etc., involve four steps in hollow fiber membrane formation that includes solution (or melt) formation, extrusion, coagulation, and rinsing/treatment of fibers. The spinneret or extrusion nozzle used to produce hollow fiber/capillary membrane consists of one or more small cylindrical tubes in one or more cylindrical orifices. Membranes can be prepared by (i) melt spinning, in which a usually thermoplastic polymer is melted and extruded through a spinneret into air and then cooled, (ii) dry spinning, in which a polymer dope is extruded through a spinneret into air, (iii) dry-jet wet spinning, in which a polymer dope solution is extruded into air and subsequently coagulated (usually in water), and (iv) wet spinning, in which a polymer dope solution is directly extruded into a coagulant (usually water) bath. A spinneret has an annulus die through which a polymer fluid is extruded, and the bore fluid (nonsolvent) is extruded along the polymer solution through a bore, forming the lumen of the hollow fiber/capillary membranes. As the polymer exits the spinneret, it solidifies into a membrane via a coagulation (wet-spinning) process [23]. The flow of the polymer and bore fluid through the spinneret is driven by inert gas at constant pressure, a metering pump, or by the extrusion process (melt spinning). Inner diameter, wall thickness, and the morphology of hollow fibers can be tuned by adjusting the dimension of the spinneret, compositions and temperature of the polymer dope, bore fluid and coagulant bath, length of air gap, and the speed at which produced fiber is collected by a motorized spool.

4 POLYMERIC NEMs PREPARATION

Nano-enhanced or nano-engineered membranes (NEMs) are usually prepared by incorporation of nanoscale materials into a polymer matrix. Conventional membrane preparation techniques discussed in the above section are the basic principles for the preparation of NSMs based on polymers (where term "nano" refers internal morphology of membrane). In this regard, some strategies have been used to design and fabricate NEMs by modification of traditional techniques. Additionally, regardless of earlier categorization of the membrane preparation techniques, the subsequent sections describe the preparation of NEMs by incorporation of NMs.

4.1 NANOMEMBRANE PREPARATION BY SELF-ASSEMBLY AND FILTRATION-MEDIATED PROCESS

Nanomembranes act as a molecular sieve that permits water/ions separation, having high selectivity and flow rate. NMs, either in the form of freestanding ultrathin film, or a monolayer (or stacked layer) supported onto a microporous substrate in composite form acts as a nanomembrane. Nanoparticles (NPs) such as gold [24] and polystyrene [25] have been reported for the preparation of ultrathin nanoporous film by drying-mediated self-assembly (Fig. 6A) and nanostrand-mediated filtration processes (Fig. 6B). In the drying-mediated self-assembly process, nanoparticles containing solution usually spread onto the top of the water droplet, and after evaporation of the solvent, it forms a nanoparticle monolayer that completely covers the water droplet. A monolayer of gold can also be transferred onto a polycarbonate filter for precise separation of nanosized objects like other nanoparticles or dye molecules. In the filtration-mediated process, a thin nanostrand layer about 100–150 nm is formed onto polycarbonate membrane by filtration, then nanoparticles are filtered to obtain the required number of monolayers. Finally, the nanostrands layer is removed by treatment with dilute HCl solution to obtain a uniform freestanding membrane. Alternatively, the monolayer can be collected and stacked onto a substrate membrane.

Nanomembranes based on nanosheets (GO, rGO, etc.) and nanofibers (TiO_2 nanowire, polymeric nanofibrils, etc.) can be formed into a freestanding film using spray coating, dip coating, or the layer-by-layer method. Vacuum-assisted filtration is most accepted in the laboratory for preparation of ultrathin nanomembranes (Fig. 6C), in which nanosheets arrange into a lamellar form onto a nanoporous support membrane. The nanofilm of nanosheets/nanofibers can be carefully removed from the support layer to obtain a freestanding film. Sometimes, such nanofilms are stacked to obtain multilayer nanofilm membranes.

4.2 NEMs PREPARATION BY BLENDING AND PI

Phase inversion is a versatile technique for preparing flat sheet/hollow fiber UF/MF MMMs by entrapment of NMs within a membrane matrix. In this process, NMs (e.g., SiO_2, zeolite, MWNTs, TiO_2, SiO_2, etc.) can be blended and dispersed in a polymer dope solution (PSF, PES, etc.) (Fig. 7) or can be formed in situ within the casting dope in the presence of solvent [28]. However, agglomeration of NMs often takes place at higher loading of NMs in dope solution. Sometimes, an in situ chemical reduction technique is used in which NPs are formed within membranes during solidification of a dope solution by phase inversion; here, a reducing agent present in a coagulation bath induces in situ chemical reduction

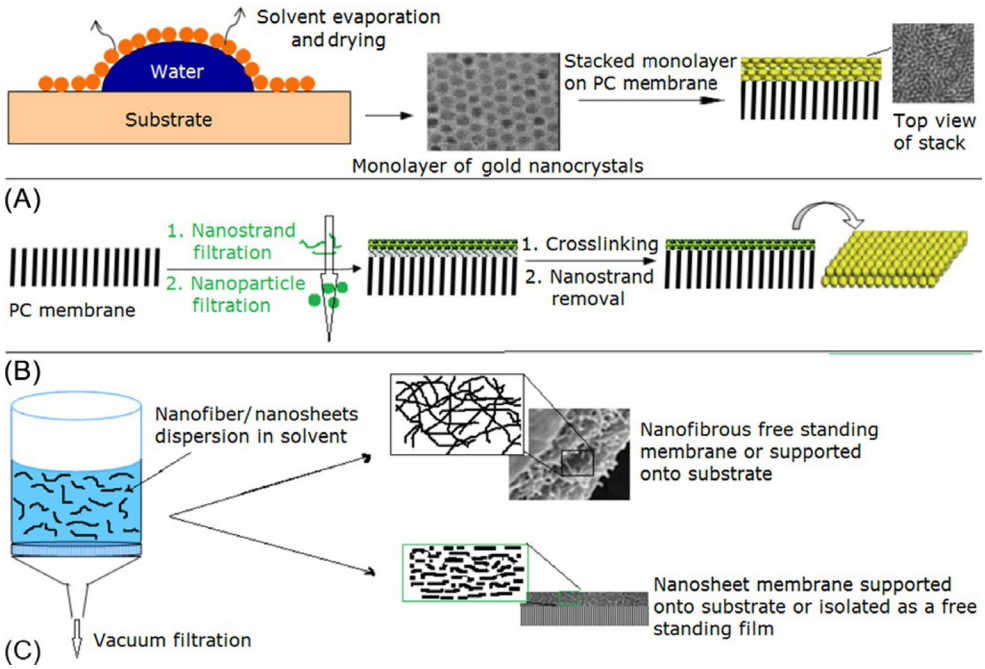

FIG. 6

(A) Drying-mediated self-assembly of gold nanocrystals, freestanding membranes having about 100 times higher filtration coefficient than typical polymer-based nanofiltration membrane [24]., (B) Polystyrene nanoparticles based freestanding nanomembranes formed by a nanostrand-assisted filtration process, membrane separates small proteins and nanoparticles with sharp cut off properties [25], and (C), Vacuum-assisted filtration silk nanofibril membrane assembly (having 64% dye rejection and pure water fluxes 1000 times higher than commercial ultrathin membrane) [26], and rGO nanosheet membranes assembly (shows selectivity for separation of dye molecules) [27].

to generate NPs within a membrane matrix. Further, to minimize agglomeration of NMs during the phase-inversion process, chemically modified NMs and/or a dispersing agent are used to obtain better dispersion of NMs in the polymer dope solution. The resulting membranes have entrapped NPs within their inner structure, rather than accumulated on the surface. Further, it is seen that introduction of block copolymer into polymer dope solution improves the dispersion stability and TiO_2 NPs, and during membrane preparation by NIPS, TiO_2 is enriched at the polymer/nonsolvent interface and forms a self-assembled structure around the membrane pores [29]. The presence of NMs in a membrane influences pore size and pore size distribution of the membrane, and the performance of membranes depends upon the size of NPs and % loading of NPs, and their interaction with the polymer matrix. Usually, bulk addition of NMs within the threshold limit increases the pore size and pore size distribution of asymmetric membranes, resulting in higher permeability and lower compaction of the membrane under pressure. Further, depending upon the type of NMs used, membranes exhibit more

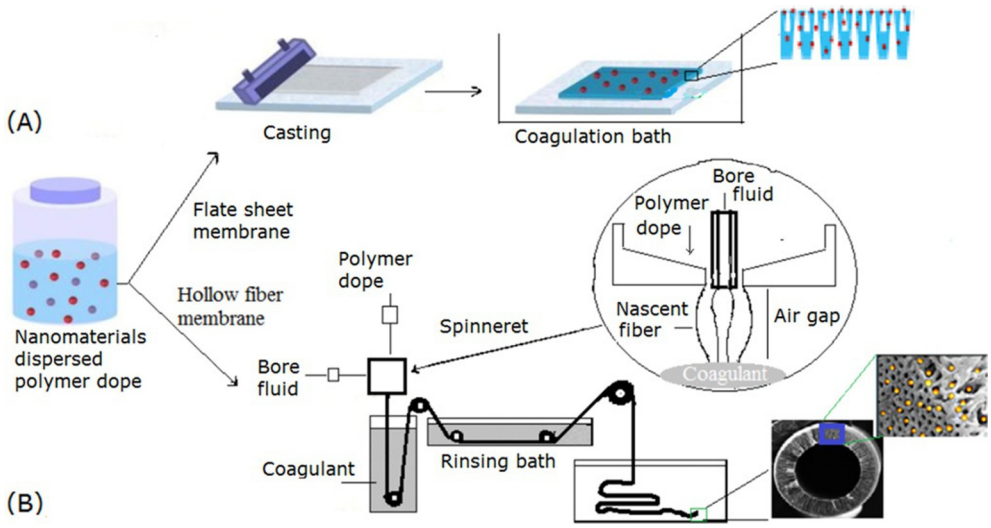

FIG. 7

Schematic of (A) flat sheet, and (B) hollow fiber MMM preparation by blending and phase inversion technique.

hydrophilic characteristics, photocatalytic activities, and antifouling and antimicrobial properties. However, the membrane is not fully benefited by the presence of NPs due to shielding of NPs by the embedded polymer matrix.

The NMs embedded into the polymer matrix by PI are believed to advantageously sustain the porous structure and thickness of membranes without collapse under compaction by high pressure. Further, TFNCMs prepared using MMM as a support show minimum physical compaction, which helps in maintaining the membrane water permeability and minimizing concentration polarization in the case of forward osmosis membranes.

4.3 NEM PREPARATION BY THE SOL-GEL PROCESS

Sol-gel nanocoating is used to incorporate the SiO_2, TiO_2, ZrO_2, $Al(OH)_2$ metal/metal oxide-based nanoparticle network within membranes' pores and surfaces. Sol-gel involves hydrolysis of precursors to form a corresponding hydroxide M-OH, and polycondensation to form a network (M-O-M). Table 1 lists some precursors commonly used for incorporation of NPs into a polymer matrix by the sol-gel process [30]. There are two approaches that have been explored for the incorporation of NPs into a polymer matrix by the sol-gel process (Fig. 8). In in situ formation on the preformed membrane, a porous or TFC membrane is, for instance, immersed into tetraethyl orthosilicate (TEOS)/C_2H_5OH or $TiCl_4/C_2H_5OH$ solution for some time [31]. The dried membrane is then soaked in hydrochloric acid solution at an appropriate temperature and pH to allow the sol-gel process within the membrane's pores and surface. In the case of simultaneous formation with polymeric membrane, the TEOS is dispersed in polymer dope solution, and the membrane is prepared by the phase inversion process; here, the sol-gel process takes place during the coagulation of membrane [32]. Finally, the membrane is thoroughly

Table 1 Common Precursor Used for NP Generation by the Sol-Gel Process for Membrane Formation [30]

NMs	Precursor	Oxygen-Supplying Agents in Sol-Gel Process
TiO_2	$Ti(OCH_2CH_2CH_2CH_3)_4$	Tetrabutyl
	$Ti[OCH(CH_3)_2]_4$	Isopropoxide
	$(NH_4)_2TiF_6$	Aqueous solution of H_3BO_3
	$[CH_3CH(O-)CO_2NH_4]_2$ $Ti(OH)_2$	−OH
SiO_2	$Si(OCH_3)_4$	Methoxyl group
	$Si(OC_2H_5)_4$	Ethoxyl group
ZrO2	$Zr(SO_4)_2$	Aqueous solution containing precursor and HCl
	$ZrOCl_2$	Dichlorine monoxide group
$Al(OH)_3$	$AlCl_3$	−OH provided by anion exchange resin
	$Al_2(SO_4)_3$	Aqueous solution of precursor
β-FeOOH	$FeCl_3$	Aqueous solution containing precursor and HCl

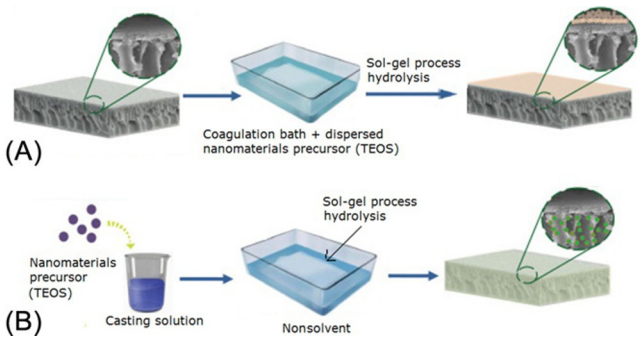

FIG. 8

Sol-gel process for (A) in situ formation of NPs on preformed membrane's pores or surface, and (B) in situ NP formation after casting dope solution during the immersion precipitation (i.e., PI) process.

Reproduced with permission from X. Li, A. Sotto, J. Li, B. Van der Bruggen, Progress and perspectives for synthesis of sustainable antifouling composite membranes containing in situ generated nanoparticles, J. Membr. Sci. 524 (2017) 502–528, Copyright [2017] Elsevier.

rinsed with de-ionized water. NMs can be physically or chemically anchored to the membrane surface or entrapped inside the membrane matrix, depending on the functional groups present in the membrane matrix.

4.4 NEM PREPARATION BY IN SITU CHEMICAL REDUCTION OF NPs

After/before in situ chemical reduction approach (Fig. 9) facilitates in situ reduction and localized immobilization of NPs onto the exterior membrane surface and within the membrane matrix [30]. The in situ chemical reduction method minimizes the agglomeration of nanomaterials. In after

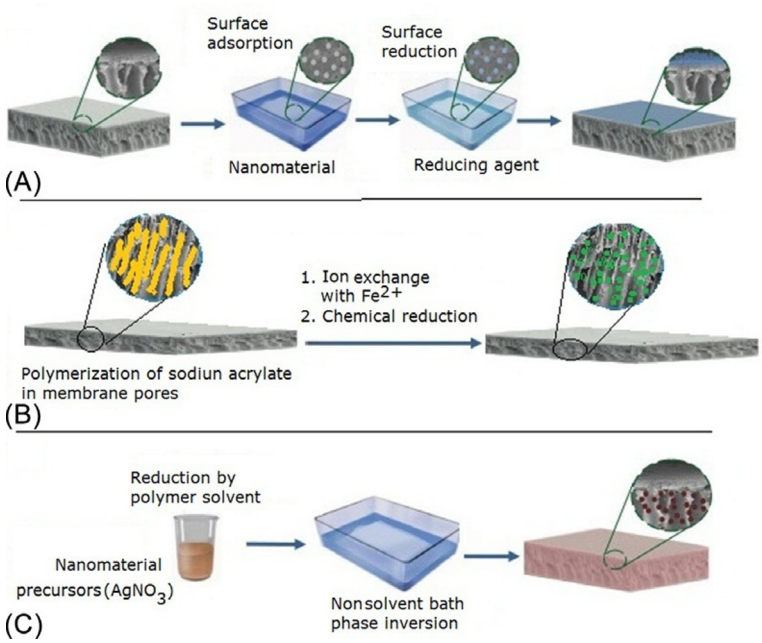

FIG. 9

(A) After in situ chemical reduction for incorporation of NPs into membrane pores/ and surface. (B) ion exchange in situ chemical reduction for incorporation of NPs into membrane pores. (C) before in situ chemical reduction approach for preparation of MMMs having well-dispersed NPs.

in situ chemical reduction, a precursor (e.g., $AgNO_3$, $CuSO_4$, etc.) is applied onto the membrane surface or within the membrane's pores through adsorption, dipping, self-assembly, or LBL techniques, and subsequently, in the second step, a reducing agent (formaldehyde, sodium borohydride, UV irradiation, etc.,) is applied for the reduction of metallic ions to metal NPs. Ion exchange in situ reduction is another attractive method for immobilizing NPs inside a membrane's pores. After a membrane's impregnation with sodium salt of ionic polymers, the sodium ions are replaced by ion exchange with appropriate metal ions, then, the membranes are treated with a reducing agent to form NPs. In before in situ chemical reduction, a nanoparticle precursor is dispersed in a polymer dope solution where a polymer solvent induces chemical reduction to generate nanoparticles within a solution, which is then used to prepare a membrane by the usual phase inversion process. Table 2 lists some common reducing agents and metal ion precursors for the in situ reduction process employed for incorporation metal NPs into a membrane matrix.

4.5 NEM PREPARATION BY SURFACE OR PORE WALL MODIFICATION

Alternatively, adsorption, self-assembly and LBL assembly, chemical grafting, and coating/deposition are versatile strategies widely accepted for the surface modification of various water filtration membranes (i.e., UF, NF, and RO) for preparation of surface-located NCMs for improving performance and

Table 2 Metal Ion Precursors and Reducing Agents Used for NEMs Preparation by in situ Reduction

NMs	Precursor	Reductant
Ag	$AgNO_3$	Dimethyl formamide (solvent), *N*-methyl pyrrolidone (solvent), formaldehyde, $NaBH_4$, dopamine, vitamin C
Fe	$FeCl_3$	$NaBH_4$
Cu	$CuSO_4$	
Pd	$PdCl_2$	
Au	$HAuCl_4$	Dopamine
Pd	$PdCl_2$	$NaBH_4$

antifouling properties (Fig. 10). In chemical bonding (Fig. 10A), nanoparticles (e.g., Ag) are covalently anchored to the surface of a PA TFC membrane using cysteamine as a bridging agent [33]. Immobilization of NPs by self-assembly (Fig. 10B) is achieved by immersing a membrane (or active surface) in a dilute colloidal solution of NMs, which has strong affinity with a polymeric membrane surface [34]. TiO_2 NPs can be self-assembled onto a membrane surface having —COOH, —SO_3H, and sulfone groups by coordination and H-bonding. In some cases, membranes are modified by chemical treatment, grafting, or coating to introduce functionality necessary for NP self-assembly. Additionally, dopamine is a versatile bridging agent (also called bioinspired glue) that is widely used to bind almost all types of NMs onto any type of membrane surface and/or within a membrane's pores. In case of adsorption/deposition technique, membrane is contacted with colloidal solution of nanoparticles followed by

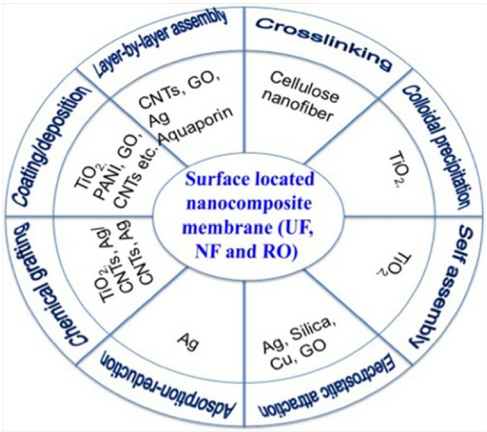

FIG. 10

Technique for immobilization (A) of Ag nanoparticles onto TFC polyamide membrane by cysteamine-mediated covalent bonding. (B) TiO_2 NPs immobilization onto a PA membrane surface by self-assembly and (C), NPs from colloidal solution onto membrane surface via physical adsorption (mediated by dip coating, LBL, and spray coating technique) and solvent drying.

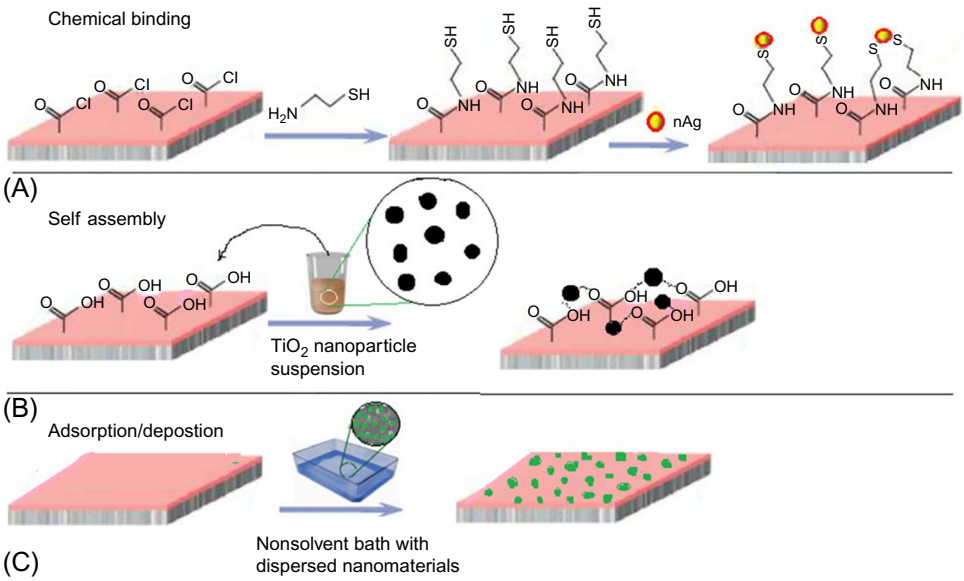

FIG. 11

Techniques for surface-located NCMs preparation.

solvent drying (Fig. 10C). The techniques for the preparation of surface-located nanocomposite membranes have minimum effects upon the inherent structures of the membranes, and hence, have good potential for commercial membrane modification; details of such methods have been elaborated in a recent review [35]. (See Fig. 11.)

4.6 NEM PREPARATION BY IP

This technique of composite membrane preparation is similar to those described in the previous section; analogous IP can be used for the fabrication of thin film nanocomposite membranes (TFNM) [22, 36]. Bare UF substrate membrane or UF membrane previously coated with NMs is used as a support for TFNCM preparation (Fig. 12). More frequently, NPs are dispersed in a solution of organic or aqueous phase monomers, and during IP, NPs are immobilized into a thin selective layer. Sometimes, the "generating afterward" approach is used to make TFNCM, in which IP is carried out in the presence of metal ions (salt) to form a thin selective layer, then this layer is treated with reducing agent to form NPs within a selective layer. This is similar approach as shown in Fig. 9A.

NMs are also immobilized on the surface layer via self-assembly by immersing a thin film composite membrane (TFCM) in dilute-colloidal solution of NPs. Alternatively, in some cases, TFCM is modified with polydopamine and then soaked in a metal ion precursor (e.g., $AgNO_3$) solution, in which reducing catechol groups reduce metal ions to metallic nanoparticles within a selective layer [37].

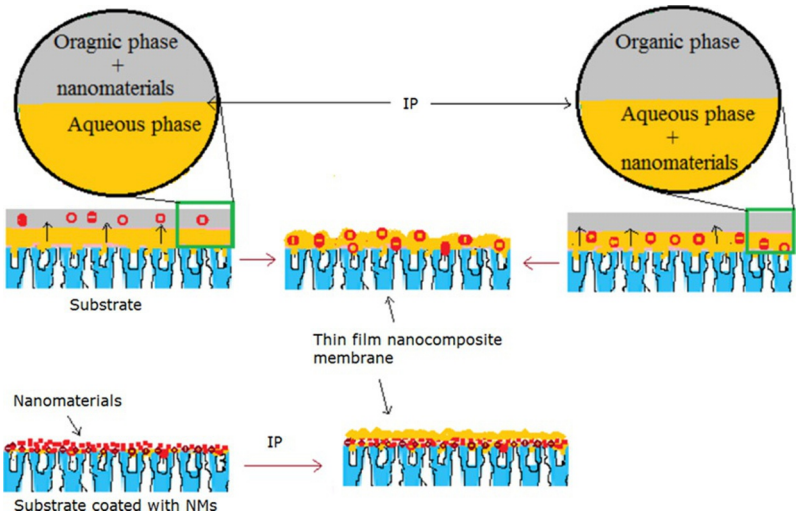

FIG. 12

Outline of interfacial polymerization for preparation of thin film composite membranes where NPs are incorporated into a selective layer.

4.7 NEMs PREPARATION BY ELECTROSPINNING

Electrospinning is a process of nanofiber and nanofibrous membrane production [38]. As seen from Fig. 13, electrospinning is comprised of a high-voltage source, a spinneret (a capillary tube attached with a small diameter needle containing polymer solution or melt), and a metallic collector. A high-voltage source is linked to the spinneret and the collector, which act as electrodes. A liquid droplet at the surface of the spinneret is electrified; when electrostatic repulsion forces (due to the opposite electrode) overcome the surface tension of liquid, the droplet is stretched. If the cohesive forces of the polymer solution or melt are high, at certain threshold voltage, a charged jet is ejected from the tip of spinneret to initiate the electrospinning process [39]. This solution jet experiences bending, elongation, and thinning processes as it is ejected from the tip owing to mutual repulsive forces of the electric charges in the jets. Simultaneously, as the solvent evaporates from the jet, a charged polymer nanofiber is formed as an interconnected web on the collector. Electrospun nanofibers membranes (ENMs) have high porosity, interconnected open pore structure, and desired membrane thickness due to control over the diameter, microstructure, and alignment of fibers. Further, electrospinning of a polymer containing nanofiller, and a biological agent forms nanocomposite/hybrid nanofibrous membranes which exhibit higher filtration efficiency for a wide range of environmental applications than corresponding polymer-based nanofibrous membranes [40].

5 MEMBRANE PARAMETERS AND PRINCIPLES

Principles of membrane filtration: Mass transfer phenomena in the membrane is described by thermodynamic parameters (i.e., driving forces) of the components in the membrane and the kinetic parameters (i.e., friction coefficient) that must be overcome while transporting through the

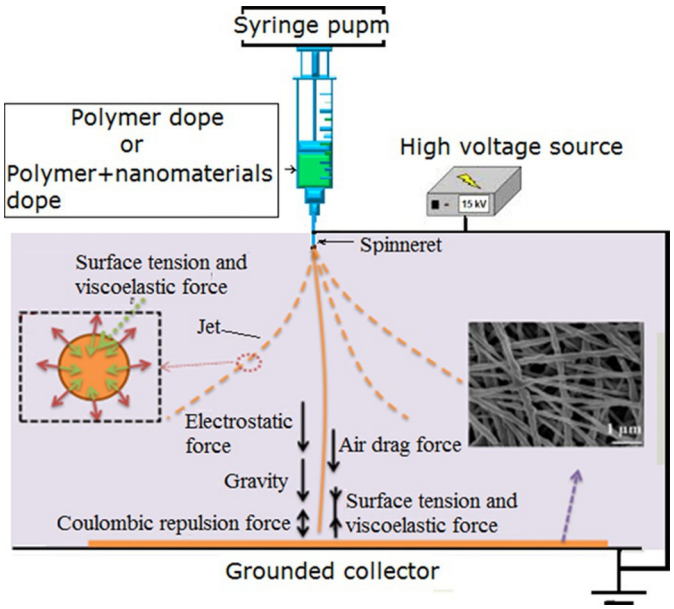

FIG. 13

Schematic of electrospun nanofiber-based NEM preparation.

membrane matrix. Driving forces that act on the components of the system can be expressed by the electrochemical potential gradient and a hydrostatic pressure gradient that triggers a bulk volume flow. Friction coefficient of the component is generally expressed by a hydrodynamic permeability coefficient or diffusion coefficient or in electrolyte solution by electric resistance. Thus, based on driving forces, mass transport through a membrane can occur by three fundamental processes, convection, diffusion, and migration, which are best described by the corresponding phenomenological equations of the Hagen-Poiseuille law, Fick's law, and Ohm's law, respectively [5].

A flux of mass caused by hydrostatic pressure gradient (dP/dx) is described by the Hagen-Poiseuille law:

$$J_v = -L_p \frac{dP}{dx} \tag{1}$$

A flux of individual components caused by concentration gradient (dC/dx) is described by Fick's law:

$$J_i = -D_p \frac{dC}{dx} \tag{2}$$

and a flux of electrical charges caused by an electrical potential gradient ($d\varphi/dx$) is described by Ohm's law:

$$J_e = \kappa \frac{d\varphi}{dx} \tag{3}$$

where J is the flux, L_p hydrodynamic permeability, P is the pressure, D the diffusion coefficient, C the concentration, κ the electrical conductivity, φ the electrical potential, and the subscripts v, i, and e denote volume, individual component, and electrical charges, respectively.

Convective flow is transport of the solute with solvent molecules caused by mechanical force such as a hydrostatic pressure difference across the membrane interfaces (i.e., feed and permeates side). Convection prevails in a porous medium rather than dense membranes. *Diffusive flux* of the molecular components is because of the gradient in chemical potentials, which develops from the gradient in concentration or pressure. Diffusion governs in the homogeneously dense RO and ion-exchange membranes, in which electroneutrality of an aqueous solution is sustained due to transport of the ions such as cations and anions in the same direction with the equivalent magnitude. *Migration* is the movement of ions/molecules because of an electrical potential gradient, induced due to establishment of voltage difference across two electrodes. Charged species (i.e., cations and anions) are either attracted or repelled near the interface by electrostatic forces.

Mass transport through MF and UF: MF and UF membranes are considered isoporous symmetric and asymmetric structure of average pore size in between 0.1–0 μm and 2–50 nm, respectively; hence, mass transport largely governs by pressure gradient by the pore flow model (or convective flow) through the pores. Therefore, the permeability of a component i (J_i) in a porous membrane can be expressed in terms of pore size, membrane structure, and magnitude and character of the pressure gradient (dP/dx), according to Darcy's law:

$$J_i = KC_i \frac{dP}{dx} \tag{4}$$

where, C_i is the concentration of component i in the medium, and K is a coefficient related to the nature of medium.

Specifically, for any isoporous ideal MF/UF membrane in which the pores are presumed to be parallel cylindrical pores of similar radius and length and perpendicular to the membrane surface, the hydrodynamic permeability can be determined in relation to the membrane pore size (i.e., the pore radius, r), the membrane porosity (ε), the tortuosity factor (τ), and the solution viscosity (η) according to the Hagen-Poiseuille law:

$$J_v = \frac{\varepsilon r^2}{8\eta\tau} \frac{\Delta P}{\Delta x} \tag{5}$$

where ΔP and Δx are the pressure difference across the membrane, and thickness of the membrane, respectively.

Classical solution diffusion transport through RO membrane: An RO membrane is considered a dense membrane with asymmetric structure. Mathematical description of diffusion in membranes based on thermodynamic parameters, wherein the driving forces of pressure, temperature, concentration, and electrical potential are interrelated, and the overall driving force producing movement of permeate is the gradient in its chemical potential [41];

$$J_i = -L_i \frac{d\mu_i}{dx} \tag{6}$$

where J_i and (d_{μ_i}/dx) are the flux ($\mathrm{g\,cm^{-2}\,s^{-1}}$) and the chemical potential gradient of component i, respectively, and L_i is the coefficient of proportionality which relates to chemical potential driving

force to permeant. Confining the methodology to driving forces caused by concentration and pressure gradients, the chemical potential is written as;

$$d_{\mu_i} = -RTd\ \ln(\gamma_i n_i) + v_i dp \tag{7}$$

where n_i, γ_i, and v_i are the mole fraction ($\mathrm{mol\,mol^{-1}}$), activity coefficient ($\mathrm{mol\,mol^{-1}}$), and molar volume of component I, respectively, and p is the pressure.

For incompressible liquid or solid membrane phases, volume does not change with pressure, and the chemical potential of pure component i (μ_i^{o}) at a reference pressure p_i^o given by integrating Eq. 7 with respect to concentration and pressure.

$$\mu_i = \mu_i^0 + RT\ \ln(\gamma_i n_i) + v_i\left(p - p_i^0\right) \tag{8}$$

For compressible gases, the molar volume changes with pressure. Using the ideal gas laws in integrating Eq. (7) gives:

$$\mu_i = \mu_i^0 + RT\ \ln(\gamma_i n_i) + RT\ \ln\frac{p}{p_i^0} \tag{9}$$

reference pressure, $p_i{}^0$, is defined as the saturation vapor pressure of i, $p_i{}^{\mathrm{sat}}$ therefore

$$\mu_{(i)} = \mu_i^0 + RT\ \ln(\gamma_i n_i) + v_i\left(p - p_{(i_{\mathrm{sat}})}\right) \text{ for in compressible phase} \tag{10}$$

$$\mu_{(i)} = \mu_i^0 + RT\ \ln(\gamma_i n_i) + RT\ \ln\frac{p}{p_{(i_{\mathrm{sat}})}} \text{ for compressible phase} \tag{11}$$

The pressure inside the membrane is constant at the high-pressure value (p_o), and the gradient in chemical potential within the membrane is expressed as a smooth gradient in solvent activity ($\gamma_i n_i$). Assuming γ_i is constant, Eq. (7) can be expressed by linking Eqs. 6 and 7.

$$J_i = -\frac{RTL_i}{n_i}\cdot\frac{dn_i}{dx} \tag{12}$$

Introducing the term concentration ci ($\mathrm{g\,cm^{-3}}$) $m_i\rho n_i$ in Eq. (12) become.

$$J_i = -\frac{RTL_i}{c_i}\cdot\frac{dc_i}{dx} \approx \text{Fick's law} \tag{13}$$

where, m_i and ρ is the molecular weight ($\mathrm{g\,mol^{-1}}$) and the molar density ($\mathrm{mol\,cm^{-3}}$) of i respectively. A formula (13) is the same form as Fick's law, in which the term RTL_i/c_i represents the diffusion coefficient (D_i), thus,

$$J_i = -D_{pi}\frac{dc_i}{dx} \tag{14}$$

Integrating over the thickness of the membrane (l) then gives

$$J_i = \frac{D_i\left(c_{i_{i(m)}} - c_{i_{l(m)}}\right)}{l} \tag{15}$$

The fluids on either side of a membrane may be at different pressures and concentrations, and within a perfect solution-diffusion membrane, there is no pressure gradient—only a concentration gradient. Flow through this type of membrane is expressed by Fick's law.

Mass transport through NF: NF membrane is considered an asymmetric structure of pore diameter <2 nm, that is, in between that of UF and RO membranes. The surface of an NF membrane contains ionizable groups such as carboxylic acid, sulfonic acid, or amine, which, when in contact with the aqueous solution, is charged due to dissociation of functional groups. Hence, based on the properties of a real membrane, the flux for each component (i) through the NF membrane is determined by the Extended Nernst-Plank equation (ENP) in terms of diffusion, electromigration, and convection [42],

$$J_i = -D_{i,\text{pore}}\frac{dC_{i,\text{pore}}}{dx} - \frac{z_i C_{i,\text{pore}} D_{i,\text{pore}}}{RT} F\frac{d\varphi}{dz} + K_{i,c} C_{i,\text{pore}} J_w \tag{16}$$

where J_i the flux of solute i (mol m^{-2} s^{-1}), $D_{i,\text{pore}}$ the intrapore diffusion coefficient of ion i (m^2 s^{-1}), $C_{i,\text{pore}}$ is the concentration of ion i in the membrane (mol m^{-3}), x is the membrane thickness (m), Z_i the valence of ion i, R the gas constant (j mol^{-1} K^{-1}), T the absolute temperature (K), F the Faraday's constant (C, mol^{-1}), φ the electric potential in the axial direction inside membrane (V), $K_{i,c}$ the hindrance factor for convection of ion i inside the membrane pores, and J_w the permeate volume flux (m s^{-1}). Due to very small pore size in NF membranes and the hindered nature of convection, the terms of the ENP are modified by hindrance factors $K_{i,c}$ (for the convective term) and the $K_{i,d}$ (for the bulk diffusivity) to give hindered diffusivity in the pore ($D_{i,\text{pore}} = K_{i,\text{d}} D_{i,\infty}$). Both these factors are functions of the ratio of the solute radius to pore radius, λ_i, where the effective solute radius is estimated from the Stokes-Einstein correlation, and the effective pore radius is generally calculated from neutral solute rejection.

6 FUNCTIONAL/PERFORMANCE ATTRIBUTES OF NEMs

Nanoscale materials have high surface area and exhibit different optical, magnetic, and electrical properties compared to macroscale materials. Incorporation of NMs form membranes of distinct chemical, physical, and biological properties having refined filtration mechanisms.

6.1 ADSORPTION

Some NEMs based on nanostructured metal oxides, graphene, CNT, porous boron nitride, zeolite, and electrospun nanofibers provides duel functions such as membrane filtration and adsorption of heavy metal ions, nitrate, and phosphate [43]. These NMs offers high porosity and active sites for contaminant adsorption. NM-incorporated, electrospun, nanofiber-based membranes show interesting properties for the removal of various trace amounts of pollutants from water by adsorption and filtration, due to their high surface area and porosity. From aqueous solution, adsorbent is captured by chemical binding (due to the presence of functional groups in NMs), physical adsorption (due to van der Waals forces, porosity, and high surface area of NMs), or electrostatic attraction (negatively charged nanoparticles attract positively charged metal ions).

6.2 PHOTOCATALYSIS

TiO_2 NP-based NEMs show unique photocatalytic activities such as photodegradation and photo-induced superhydrophilicity, which make the membrane surface antimicrobial, fouling resistant, and self-cleaning. Under UV light, valence electrons of the photocatalyst are excited and migrate

to the conduction band of TiO_2 and generate a pair of electrons and positively charged holes which show strong reducing and oxidizing activities, respectively [44]. Subsequently, these electrons and holes react with water and oxygen to generate highly reactive oxygen species (ROS) (·OH and O_2^-) and hydrogen peroxide, which decompose organic micropollutants and inactivate the bacteria and viruses present in the water. Similarly, NPs such as ZnO, ZnS, Zn—CeO_2, Si—Ti, and CdS-TiO_2– based NEMs are reported for the photocatalytic degradation of organic pollutants present in water [45]. All these photocatalysts are self-regenerated after photocatalytic action, and thus, cannot be exhausted.

6.3 ANTIMICROBIAL ACTIVITY

Silver NPs are the most widely used antimicrobial agents for NEM due to their high biocidal properties. Silver interacts with phosphorus and sulfur, which presents in cysteine and other biochemical compounds in the form of thiol groups (S—H) [45]. It shows its biocidal effect by forming a S—Ag or disulfide bond which damages bacterial proteins, denatures DNA, and interrupts the electron transport chain. Antimicrobial membranes provide water disinfection and show a high flux recovery ratio. Other NPs like Cu, CNT, graphene, etc., have been reported for the modification of commercial membranes that show high biocidal efficiency and application duration [35].

6.4 CHLORINE RESISTANCE

Zeolite and silica are promising NMs for making functional NF and RO membranes. The presence of GO, CNT, SiO_2, and zeolite NPs on the barrier layer of TFNCM have proven to improve chlorine-resistance properties. The presence of electron-rich MWCNTs acts as a protective layer for PA against the attack of free chlorine. In the case of GO-based membranes, the enhanced chlorine resistance is predominantly due to formation of a hydrogen bond between GO and PA, which inhibits chlorine's interaction with active N—H links in PA. Zeolite-type membranes are another chemically robust and favorable component for desalination. The stability of the MFY-type zeolite membranes against chlorine cleaning has been explored by Zhu et al. [46] Their study showed that zeolite membranes do not show any significant changes in their water flux or salt rejection even after 7 days' exposure to hypochlorite cleaning solution (1000 ppm) for 168,000 ppm h, signifying their high chlorine-stability. After 7 days' of hypochlorite cleaning, membrane retained its high rejection (without any loss of ion rejection) for Mg^{2+} (90%) and Ca^{2+} (82%), and good rejections for Na^{1+} (70%) and K^{1+} (78%) at an applied pressure of 3 MPa. Table 3 shows RO performance of various TFNCMs before and after chlorine treatment (CT).

7 APPLICATIONS OF MF, UF, NF, AND RO PROCESSES FOR PURIFICATION

7.1 WATER CLARIFICATION BY MF AND UF

Separation by MF predominantly takes place by pore flow (i.e., sieving) due to a relatively large pore size (100 to 1000 nm) that usually eliminates suspended solids or particles, bacteria, and sometimes, large organic colloids. Separation through UF membranes also occurs by sieving, yet they have a wider separation range compared to MF due to their relatively small pore size (10–100 nm) that even rejects

Table 3 Chlorine-Resistance Properties of Some Reverse Osmosis TFNCM

Pristine and Corresponding NEM	Chlorination Conditions	Desalination Conditions	NaCl Rejection (%)		Flux ($Lm^{-2}h^{-1}$)		Ref
			Before CT	After CT	Before CT	After CT	
PA (MPD/TMC) GO-PA(MPD/TMC) TFNC	2000 ppm NaOCl, 24 h, 48,000 ppm h	2000 ppm NaCl, 1.55 MPA	99.3 99.2	91.1 99.2	9.18 18.2	32.5 16.6	[47]
PA (MPD/TMC) rGO-TiO2-PA (MPD/TMC) NCM	2000 ppm, 2 h, pH 4	2000 ppm NaCl, 1.5 MPa	95.4 99.4	65.4 96.4	– 51.3	– –	[48]
PA (MPD/TMC) MWCNT-PA(MPD/TMC) NCM	200 ppm, 24 h	35,000 ppm NaCl, 5 MPa	97 90	80 91	27.1 70.8	66.6 83.3	[49]
PA (PIP/BHTTM/TMC) GO-ODA-PA (PIP/BHTTM/TMC)	3000 ppm NaOCl, 3 h, pH 8	3000 ppm Na_2SO_4, 0.6 MPa	95 96	45 92	31 50	72 62	[50]
PA (MPD-TMC) GO-TA-PA (MPD/TMC)	35,000 ppm h	2000 ppm NaCl and 500 ppm NaOCl, 1.55 MPa	97.5 97	26 90	37.5 41.2	71 51	[51]
PA-(APES+MPD/TMC) TFC Zeolite-PA-(APES+MPD/TMC) TFN	32,000 ppm NaCl, 55 MPa	300 ppm NaOCl, 1 h	94.3 98.8	75.6 86.1	32.5 37.8	45.7 40.3	[52]

APES, *aminated polyether sulfone;* BHTTM, *2,2′-bis(1-hydroxyl-1-trifluoromethyl-2,2,2-triflutoethyl)-4,4′-methylenedianiline;* MPD, m-*phenylene diamine;* PIP, *piperazine;* TA, *tannic acid;* TMC, *trimesoyl chloride*.

viruses and colloids. The classical clarification or coagulation technique that is employed for industrial wastewater has been also applied for water reclamation, sludge thickening, industrial effluent, and potable water production, whereas, water clarification through MF and UF membranes is usually used for the pretreatment of ground and surface water to enhance the product rate and life of NF and RO membranes. Advantageously, MF is capable of removing particulate matter, turbidity, bacteria, and large molecular weight organic matters at high levels and can produce better quality water/effluent than conventional clarification. Clarification membranes also significantly reduce the silt density index below 3 (100%).

Normally, MF and UF membranes are combined with an activated sludge process referred to as membrane bioreactor (MBR) for wastewater treatment in various industries. In MBR, the membrane

module is immersed into the bioreactor, and a vacuum is applied to the permeate side to obtain treated water; hence, the solids are retained in the bioreactor at the feed side. This configuration lowers energy intake as well as membrane fouling compared to a conventional pretreatment process. Typical polymeric membranes based on PVDF, PE, PAN, or PES in a flat sheet or HF configuration are used for MBR applications. Thus, MBR replaces the two-stage conventional activated sludge process (biotreatment and clarification) with a single integrated process which reduces footprint, lessens sludge production, and completely separates suspended solids from the effluent. Overall, the application potential of MF and UF are described as:

- Ultrapure water for the semiconductor industry
- Potable water production
- Clarification of water
- Wastewater treatment
- Pathogen removal
- Pretreatment of NF and RO

7.1.1 Water disinfection by UF and MF

Waterborne diseases are frequently caused by the presence of some detrimental microorganism, including algae, fungi, planktons, viruses, bacteria, and amoebas in water sources. Disinfection kills or inactivates (>99.9%) disease-causing organisms (bacteria, cysts, viruses, etc.) present in a potable water supply to protect health. There are two conventional water disinfection techniques, chemical and physical, that include chlorination and irradiation, respectively; both these techniques have their own merits and demerits. However, the desire to attain sterilization by conventional methods without producing disinfection byproducts (DBP), as well as to satisfy the increasing need for distributed and point-of-use water treatment and recycling mechanisms, has instigated the development of new technologies based on antimicrobial NMs and membranes. Numerous NMs (natural and engineered) show strong antimicrobial activity through photocatalytic reaction that produces ROSs which damage cell components and viruses (e.g., TiO_2, ZnO, and fullerol), compromising the bacterial cell envelope (e.g., peptides, chitosan, carboxyfullerene, carbon nanotubes, ZnO and silver nanoparticles [nAg]), interruption of energy transduction (e.g., nAg and fullerene nanoparticles [nC_{60}]), and inhibition of enzyme activity and DNA synthesis (e.g., chitosan) [53]. Various aspects of water purification using NMs are described in detail in the other sections of this book.

In the past, numerous studies have pointed toward the use of membrane processes that can efficiently be employed for potable water disinfection [54, 55]. Overall, membrane filtration processes include: MF, which removes the most bacteria and protozoa cysts, but its virus removal efficiency is inadequate; UF, which permits complete elimination of bacteria, viruses, and protozoa; and NF, which is capable of rejecting dyes, volatile organic compounds (VOC), pesticides, sulfates, phosphates, and microcystins, which are created by many cyanobacteria species. Compared to usual treatment processes, membrane technologies have the potential to produce better quality water, reduce disinfectant requirement, need less space due to their compact design, require simpler operating mechanism and less maintenance, and generate less sludge [56]. Thus, in addition to water clarification, MF- and UF-based membrane filters are used for water disinfection and sterilization. Sterilizing membrane filters are able to retain organisms in both the laboratory and industry, producing sterile filtrate. Membrane- and NM-based water disinfection technologies have been advantageously combined in

NEMs. NEMs are promising for achieving high water disinfection through the killing/inhibiting of microorganisms and physical capture through the sieving mechanism. In this regard, most of the NEMs prepared for RO, NF, UF, and MF application are intended to produce antifouling properties by imparting antimicrobial/hydrophilic properties to membranes. Using RO and NF membranes' molecular-level separation can be possible, thereby producing water free from any toxic microorganisms, while the extent of disinfection achieved by UF and MF membrane depends on the feed water composition and amount of retention and/or inactivation of microbial cells. Thus, pore size and surface charge of MF and UF membranes are important factors in the retention and inhibition of microorganisms.

The NanoCeram (Argonide Corporation, Sanford, FL, United States) cartridge filter is made by embedding 2-nm alumina nanofibers of surface area 300–600 $m^2\ g^{-1}$ with glass and cellulose nonwoven fabric. NanoCeram is electropositive in nature and exhibits a higher flux rate than UF with high adsorption efficiency for the dirt, bacteria, viruses, and proteins by electrostatic attraction. NanoCeram can be used for pretreatment in ultrapure water production, microbiological sampling, or in a water purification device.

Researchers from Durban University of Technology and Stellenbosch University, South Africa, have developed a membrane-based water disinfection unit using a polyester woven-fabric MF membrane. A gravity filter made of flat-sheet modules captured 95%–99% of effluent *Escherichia coli* in addition to suspended matter to produce potable water having turbidity <1 NTU. Adopting an approach similar to that of a gravity filtration module, the first water disinfection filter was prepared by immobilizing nAg by an in situ reduction method on the nonwoven fabric MF membrane [57]. The *E. coli* removal efficiency of the pristine filter was 84%–91%, and *E. coli* rejection improved by increasing the content of *E. coli* in the feed water (2500–77,000 CFU/100 mL), as the higher content led to more *E. coli* deposition on the filter surface, increasing the rejection efficiency. The nAg-coated membrane filter attained 100% *E. coli* retention. Liu et al. achieved 100% *E. coli* inactivation when dead-end filtration was performed using a Ag/TiO_2-based nanofiber membrane [58]. Nanostructured membranes prepared by phase inversion using interpenetrating polymeric networks consisting of polyamic acid (PAA), glutaraldehyde-derivatized PAA, and chitosan-modified polyamic acid had an average pore size of 5–35 nm and demonstrated 100% disinfection against *E. coli*, *Citrobacter freundii*, and *Staphylococcus epidermidis* [59].

Gunawan et al. [25] applied a water disinfection barrier of Ag/MWNTs (in which Ag NPs were uniformly distributed onto a MWCNTs surface) onto a chemically modified PAN HF membrane. Compared to a native PAN membrane, the Ag/MWNTs modified membrane inhibited the attachment of *E. coli* and completely damaged all the bacteria cells attached to the membrane's surface. A multifunctional composite membrane was prepared by depositing Ag/AgBr/TiO_2-nanofiber (composite materials) onto the CA membrane (0.45 μm pore size) to produce hierarchically micro −/nanostructured barrier layer [60]. Synergistically, the inherent antibacterial activity of Ag and the visible light absorption properties of AgBr were found to be useful contemporaries for water filtration and disinfection in the presence of sunlight. A TiO_2 nanowire UF membrane was prepared by an alkaline hydrothermal synthesis and hot-press process, in which a bottom hierarchical layer of TiO_2 nanowires of 20 nm diameter acted as a support, while a top layer TiO_2 nanowires of 10 nm diameter served as a barrier layer [61]. This membrane separated the *E. coli* from the water, and inactivated *E. coli* under UV irradiation. NMs such as rGO intercalated CNT were successfully layered onto a porous ceramic MF via a vacuum-assisted filtration method for preparation of NF membrane [62]. An rGO-CNT hybrid NF membrane showed water permeability of 20–30 $Lm^{-2}\ h^{-1}\ bar^{-1}$ and about 99% removal of

nanoparticle, dyes, BSA, sugars, and humic acid. Earlier, Yang et al. prepared a composite membrane using conventional MF as a support onto which a barrier layer of polystyrene-*block*-poly(methyl methacrylate) was deposited, and subsequently a PMMA block was selectively removed by irradiating the film with ultraviolet and rinsing with acetic acid to generate nanopores of about 17 nm [63]. This membrane maintained high selectivity (100%) for the filtration of human rhinovirus type 14 (of 30 nm diameter), which is a major pathogen responsible for the common cold in humans.

Researchers from Stony Brook University, United States [64], demonstrated preparation of a nanofibrous composite membrane in which the top active layer was made by infusion of surface-modified cellulose nanofibers of about 200 nm length and 5–10 nm in diameter onto an electrospun nanofibrous polyacrylonitrile (PAN) scaffold of average diameter of 200 nm; the resulting active layer was deposited onto polyethylene terephthalate) nonwoven. The resulting composite membrane exhibited water permeability of 85 $Lm^{-2}\ h^{-1}\ bar^{-1}$ and removed 99.99% of MS2 bacteriophage virus and *E. coli* from water. Such high capturing capability of these nanofibrous membranes was attributed to high nanoscale porosity and the electrostatic attraction of negatively charged viruses. Further, Cruz et al. [65] found that when NOM is not present in water, viruses (*Salmonella Typhimurium*) and bacteria (bacteriophage PP7) are rejected by the UF membrane due to electrostatic repulsion and size exclusion principle, respectively, whereas, the viral removal efficiency was affected by ion concentration, ionic strength, and pH. However, chlorine used for water disinfection usually reacts with NOM present in water to produce low molecular weight (50–100 Da) DBPs, for example, trihalomethanes, haloacetic acids, bromine, and nitrosodimethylamine, which displays toxic effects on human health, causing cancer, and mutagenic and reproductive effects on humans [66]. Due to the smaller size of DBPs, only RO membranes are capable of removing 99% of them; sometimes, and RO system can be coupled with UV/ozone, activated carbon adsorption, or NF to make DBP removal more effective.

7.2 REMOVAL OF DISSOLVED POLLUTANTS AND SALT IONS BY NF AND RO

One of the significant applications of RO and NF membrane technology is removal of dissolved salt ions from sea and brackish water to make it potable. Most of the commercial and laboratory-made NF membranes available in the flat sheet and hollow fiber configurations are TFCM prepared by IP using polypiperazineamide and polyethyleneimine chemistry and membranes. Typically, an NF membrane removes >95% of divalent ions (i.e., anion or cation) of the same charge as that of the membrane surface, and rejects about 20% to 80% monovalent ions, while the rejection of neutral solutes depends on molecular weight of the compound. Generally, 80% to 99% of organic pollutants of molecular mass > 200 Da are rejected, depending upon the MWCO of the NF membrane being used. Usually, NF is also applied for hardness ion removal in potable water recycling as an alternative to RO or as a pretreatment step before the RO process.

RO membranes, preferentially, a hydrophilic dense selective layer, has an affinity for solvent molecules (water) and predominantly hinder the passage of salt ions. Commercial TFC RO membranes used for desalination of seawater and brackish water with rejection efficiency of 99.5%–99.8% for sodium chloride, and 99.7%–99.9% for divalent and multivalent ions (SO_4^{-2}, PO_4^{-2}) are based on aromatic polyamide chemistry. Due to the angstrom-scale pores, RO membranes completely reject pathogens from water. RO membranes are able to reject high molecular weight organic pollutants and are able to reduce biological oxygen demand and chemical oxygen demands up to 96%–98%.

8 CHALLENGES AND FUTURE PERSPECTIVES

Nanoscale materials have wide potential for water treatment through NEMs. The key issues facing NEMs which need to be addressed are NMs' cost effectiveness, the production scalability of NEMs, stability of NEMs, and toxicity of NMs.

- Industrial production of NMs of precise size and functionality requires state-of-the-art production facilities and reagent-grade chemicals that ultimately increase the cost of NMs, so, water purification using NEMs is considerably high in cost.
- Conventional industrial membrane production processes are unsuitable as such for large-scale NEM preparation because they require optimization of the membrane fabrication parameters and equipment design.
- Limited stability of NEMs for long-term water purification is a key concern, as NMs may leach into water, not only decreasing the membrane's functional efficiency over time, but also polluting the water stream with NMs, posing serious health risk to aquatic life and water consumers due to NMs' toxic nature.
- It will require comprehensive study of the properties of NMs, polymers, solvents, and binding agents, and membrane fabrication techniques to devise a correct membrane structure for end use.

Nanotechnology would enable development of next-generation membrane technology for removal of specific micropollutants from water through integration with futuristic water treatment approaches such as solar desalination, microbial desalination, forward osmosis, and nano-enabled MBR. Development of MOF-based NMs would have leapfrogging potential for next-generation antifouling membranes of a mechonochemically robust structure. There is an urgent need for the preparation of high selectivity and high water permeability membranes based on bioinspired nanoscale materials and bioderived NMs in order for sustainable membranes processes to gain wide social acceptability.

9 CONCLUSIONS

In this chapter, we have summarized and discussed pressure-driven membranes processes, nanostructured and nano-enhanced membrane preparation techniques, their functions, and their application for water purification. Scale-up of NEM preparation at pilot and laboratory is the key challenge in obtaining consistent membranes. Electrospinning is a versatile technique for the preparation of multifunctional nanofibrous membranes with high selectivity and water permeability. Nano-enhanced membranes have huge potential for water purification by removing suspended particles, microorganisms, heavy metal ions, salt ions, organic compounds, and other emerging micropollutants.

ACKNOWLEDGMENT

One of the authors (R. Choudhury) acknowledges support from the Science and Engineering Research Board (SERB) under Project No. ECR/2017/000028.

REFERENCES

[1] R. Singh, Water and membrane treatment, in: Membrane Technology and Engineering for Water Purification, Butterworth-Heinemann, Oxford, 2015, pp. 81–178 (Chapter 2).

[2] C. Ursino, R. Castro-Muñoz, E. Drioli, L. Gzara, M.H. Albeirutty, A. Figoli, Progress of nanocomposite membranes for water treatment, Membranes 8 (2018) 18.

[3] W.J. Koros, Y.H. Ma, T. Shimidzu, Terminology for membranes and membrane processes (IUPAC Recommendations 1996), in: Pure and Applied Chemistry, 1996, p. 1479.

[4] W. Salim, W.S.W. Ho, Recent developments on nanostructured polymer-based membranes, Curr. Opin. Chem. Eng. 8 (2015) 76–82.

[5] H. Strathmann, Membrane and membrane separation processes, 1. principles, in: Ullmann's Encyclopedia of Industrial Chemistry, Wiley-VCH, Weinheim, 2011, pp. 413–456.

[6] S. Remanan, M. Sharma, S. Bose, N.C. Das, Recent advances in preparation of porous polymeric membranes by unique techniques and mitigation of fouling through surface modification, ChemistrySelect 3 (2018) 609–633.

[7] M. Sadrzadeh, S. Bhattacharjee, Rational design of phase inversion membranes by tailoring thermodynamics and kinetics of casting solution using polymer additives, J. Membr. Sci. 441 (2013) 31–44.

[8] M. Mulder, Membrane preparation | phase inversion membranes A2—Wilson, Ian D, in: Encyclopedia of Separation Science, Academic Press, Oxford, 2000, pp. 3331–3346.

[9] Q.T. Nguyen, O.T. Alaoui, H. Yang, C. Mbareck, Dry-cast process for synthetic microporous membranes: physico-chemical analyses through morphological studies, J. Membr. Sci. 358 (2010) 13–25.

[10] B. Sartowska, W. Starosta, P. Apel, O.L. Orelovitch, I. Blonskaya, Polymeric Track Etched Membranes—Application for Advanced Porous Structures Formation, 2013.

[11] W. Starosta, D. Wawszczak, B. Sartowska, M. Buczkowski, Investigations of heavy ion tracks in polyethylene naphthalate films, Radiat. Meas. 31 (1999) 149–152.

[12] D.A. Bernards, T.A. Desai, Nanoscale porosity in polymer films: fabrication and therapeutic applications, Soft Matter 6 (2010) 1621–1631.

[13] C. Acikgoz, M.A. Hempenius, J. Huskens, G.J. Vancso, Polymers in conventional and alternative lithography for fabrication of nanostructures, Eur. Polym. J. 47 (2011) 2033–2052.

[14] H. Strathmann, L. Giorno, E. Piacentini, E. Drioli, 1.4 basic aspects in polymeric membrane preparation, in: Comprehensive Membrane Science and Engineering, second ed., Elsevier, Oxford, 2017, pp. 65–84.

[15] H. Strathmann, Membranes and membrane separation processes, 3. membrane preparation and membrane module constructions, in: Ullmann's Encyclopedia of Industrial Chemistry, Wiley-VCH, Weinheim, 2011, pp. 483–512.

[16] J. Kim, S.S. Kim, M. Park, M. Jang, Effect of precursor properties on the preparation of polyethylene hollow fiber membranes by stretching, J. Membr. Sci. 318 (2008) 201–209.

[17] S.-n. Jintawat, R. Rujiravanit, P. Supaphol, S. Tokura, Porous polyethylene membranes by template-leaching technique: preparation and characterization, Polym. Test. 23 (2004) 91–99.

[18] R.W. Baker, Membranes and modules, in: Membrane Technology and Applications, John Wiley & Sons, Ltd, Hoboken, 2012, pp. 97–178.

[19] S. Rangou, K. Buhr, V. Filiz, J.I. Clodt, B. Lademann, J. Hahn, A. Jung, V. Abetz, Self-organized isoporous membranes with tailored pore sizes, J. Membr. Sci. 451 (2014) 266–275.

[20] S.P. Nunes, Block copolymer membranes for aqueous solution applications, Macromolecules 49 (2016) 2905–2916.

[21] Y. Zhang, N.E. Almodovar-Arbelo, J.L. Weidman, D.S. Corti, B.W. Boudouris, W.A. Phillip, Fit-for-purpose block polymer membranes molecularly engineered for water treatment, npj Clean Water 1 (2018) 2.

[22] Y. Song, J.-B. Fan, S. Wang, Recent progress in interfacial polymerization, Mater. Chem. Front. 1 (2017) 1028–1040.

[23] C.Y. Feng, K.C. Khulbe, T. Matsuura, A.F. Ismail, Recent progresses in polymeric hollow fiber membrane preparation, charcterization and applications, Sep. Purif. Technol. 111 (2013) 43–71.
[24] J. He, X.-M. Lin, H. Chan, L. Vukovic, P. Kral, H.M. Jaeger, Diffusion and filtration properties of self-assembled Gold nanocrystal membrane, Nano Lett. 11 (2011) 2430–2435.
[25] P. Gunawan, C. Guan, X. Song, Q. Zhang, S.S.J. Leong, C. Tang, Y. Chen, M.B. Chan-Park, M. W. Chang, K. Wang, R. Xu, Hollow fiber membrane decorated with Ag/MWNTs: toward effective water disinfection and biofouling control, ACS Nano 5 (2011) 10033–10040.
[26] S. Ling, K. Jin, D.L. Kaplan, M.J. Buehler, Ultrathin free-standing bombyx mori silk nanofibril membranes, Nano Lett. 16 (2016) 3795–3800.
[27] B. Liang, P. Zhang, J. Wang, J. Qu, L. Wang, X. Wang, C. Guan, K. Pan, Membranes with selective laminar nanochannels of modified reduced graphene oxide for water purification, Carbon 103 (2016) 94–100.
[28] M. Zahid, A. Rashid, S. Akram, Z.A. Rehana, W. Razzaq, A comprehensive review on polymeric nano-composite membranes for water treatment, J. Membr. Sci. Technol. 8 (2018) 179.
[29] X. Li, J. Li, X. Fang, K. Bakzhan, L. Wang, B. Van der Bruggen, A synergetic analysis method for antifouling behavior investigation on PES ultrafiltration membrane with self-assembled TiO2 nanoparticles, J. Colloid Interface Sci. 469 (2016) 164–176.
[30] S. Al Aani, C.J. Wright, M.A. Atieh, N. Hilal, Engineering nanocomposite membranes: Addressing current challenges and future opportunities, Desalination 401 (2017) 1–15.
[31] Y. Berbar, M. Amara, A. Ammi-said, S. Yuan, B. Van der Bruggen, New method for silica embedding on a PES membrane surface via in situ sol gel process and immobilization in a polyamide thin film composite, J. Environ. Chem. Eng. 5 (2017) 3604–3615.
[32] L.-Y. Yu, Z.-L. Xu, H.-M. Shen, H. Yang, Preparation and characterization of PVDF–SiO2 composite hollow fiber UF membrane by sol–gel method, J. Membr. Sci. 337 (2009) 257–265.
[33] J. Yin, Y. Yang, Z. Hu, B. Debg, Attachment of silver nanoparticles (AgNPs) onto thin-film composite (TFC) membranes through covalent bonding to reduce membrane fouling, J. Membr. Sci. 441 (2013) 73–82.
[34] J.H. Li, Y.Y. Xu, L.P. Zhu, J.H. Wang, C.H. Du, Fabrication and characterization of a novel TiO2 nanoparticle self-assembly membrane with improved fouling resistance, J. Membr. Sci. 326 (2009) 659–666.
[35] R.R. Choudhury, J.M. Gohil, S. Mohanty, S.K. Nayak, Antifouling, fouling release and antimicrobial materials for surface modification of reverse osmosis and nanofiltration membranes, J. Mater. Chem. A 6 (2018) 313–333.
[36] W.J. Lau, S. Gray, T. Matsuura, D. Emadzadeh, J.P. Chen, A.F. Ismail, A review on polyamide thin film nanocomposite (TFN) membranes: history, applications, challenges and approaches, Water Res. 80 (2015) 306–324.
[37] Z. Yang, Y. Wu, J. Wang, B. Cao, C.Y. Tang, In situ reduction of silver by polydopamine: a novel antimicrobial modification of thin-film composite polyamide membrane, Environ. Sci. Technol. 50 (2016) 9543–9550.
[38] F.E. Ahmed, B.S. Lalia, R. Hashaikeh, A review on electrospinning for membrane fabrication: challenges and applications, Desalination 365 (2015) 15–30.
[39] Y. Liao, C.-H. Loh, M. Tian, R. Wang, A.G. Fane, Progress in electrospun polymeric nanofibrous membranes for water treatment: fabrication, modification and applications, Prog. Polym. Sci. 77 (2018) 69–94.
[40] S. Homaeigohar, M. Elbahri, Nanocomposite electrospun nanofiber membranes for environmental application, Materials 7 (2014) 1017–1045.
[41] R.W. Baker, Membrane transport theory, in: R.W. Baker (Ed.), Membrane Technology and Applications, John Wiley & Sons, Ltd, Chichester, 2004, pp. 15–84.
[42] A. Szymczyk, C. Labbez, P. Fievet, A. Vidonne, A. Foissy, J. Pagetti, Contribution of convection, diffusion and migration to electrolyte transport through nanofiltration membranes, Adv. Colloid Interf. Sci. 103 (2003) 77–94.
[43] K.C. Khulbe, T. Matsuura, Removal of heavy metala and pollutants by membrane adsorption techniques, Appl Water Sci 8 (2018) 19.

[44] A. Rahimpour, S. Madaeni, A. Taheri, Y. Mansourpanah, Coupling TiO2 nanoparti- cles with UV irradiation for modification of polyethersulfone ultrafiltration memrabranes, J. Membr. Sci. 313 (2008) 158–168.
[45] S. Kumar, W. Ahlawat, G. Bhanjana, S. Heydarifard, M.M. Nazhad, N. Dilbaghi, Nanotechnology-based water treatment strategies, J. Nanosci. Nanotechnol. 14 (2014) 1838–1858.
[46] B. Zhu, D.T. Myat, J.-W. Shin, Y.-H. Na, I.-S. Moon, G. Connor, S. Maeda, G. Morris, S. Gray, M. Duke, Application of robust MFI-type zeolite membrane for desalination of saline wastewater, J. Membr. Sci. 475 (2015) 167–174.
[47] H.-R. Chae, J. Lee, C.-H. Lee, I.-C. Kim, P.-K. Park, Graphene oxide-embedded thin-film composite reverse osmosis membrane with high flux, anti-biofouling, and chlorine resistance, J. Membr. Sci. 483 (2015) 128–135.
[48] M. Safarpour, A. Khataee, V. Vatanpour, Thin film nanocomposite reverse osmosis membrane modified by reduced graphene oxide/TiO2 with improved desalination performance, J. Membr. Sci. 489 (2015) 43–54.
[49] S. Inukai, R. Cruz-Silva, J. Ortiz-Medina, A. Morelos-Gomez, K. Takeuchi, T. Hayashi, A. Tanioka, T. Araki, S. Tejima, T. Noguchi, M. Terrones, M. Endo, High-performance multi-functional reverse osmosis membranes obtained by carbon nanotube·polyamide nanocomposite, Sci. Rep. 5 (2015) 13562.
[50] S.-M. Xue, C.-H. Ji, Z.-L. Xu, Y.-J. Tang, R.-H. Li, Chlorine resistant TFN nanofiltration membrane incorporated with octadecylamine-grafted GO and fluorine-containing monomer, J. Membr. Sci. 545 (2018) 185–195.
[51] H.J. Kim, Y.-S. Choi, M.-Y. Lim, K.H. Jung, D.-G. Kim, J.-J. Kim, H. Kang, J.-C. Lee, Reverse osmosis nanocomposite membranes containing graphene oxides coated by tannic acid with chlorine-tolerant and antimicrobial properties, J. Membr. Sci. 514 (2016) 25–34.
[52] S.G. Kim, D.H. Hyeon, J.H. Chun, B.-H. Chun, S.H. Kim, Nanocomposite poly(arylene ether sulfone) reverse osmosis membrane containing functional zeolite nanoparticles for seawater desalination, J. Membr. Sci. 443 (2013) 10–18.
[53] J. Zhu, J. Hou, Y. Zhang, M. Tian, T. He, J. Liu, V. Chen, Polymeric antimicrobial membranes enabled by nanomaterials for water treatment, J. Membr. Sci. 550 (2018) 173–197.
[54] S.S. Madaeni, The application of membrane technology for water disinfection, Water Res. 33 (1999) 301–308.
[55] M. Bodzek, K. Konieczny, A. Kwiecinska, Application of membrane processes in drinking water treatment–state of art, Desalin. Water Treat. 35 (2011) 164–184.
[56] M.C. Collivignarelli, A. Abbà, I. Benigna, S. Sorlini, V. Torretta, Overview of the main disinfection processes for wastewater and drinking water treatment plants, Sustainability 9 (2018) 86.
[57] C.A. Mecha, V.L. Pillay, Development and evaluation of woven fabric microfiltration membranes impregnated with silver nanoparticles for potable water treatment, J. Membr. Sci. 458 (2014) 149–156.
[58] L. Liu, Z. Liu, H. Bai, D.D. Sun, Concurrent filtration and solar photocatalytic disinfection/degradation using high-performance Ag/TiO2 nanofiber membrane, Water Res. 46 (2012) 1101–1112.
[59] I. Yazgan, N. Du, R. Congdon, V. Okello, O.A. Sadik, Biofunctionalized poly (amic) acid membranes for absolute disinfection of drinking water, J. Membr. Sci. 472 (2014) 261–271.
[60] C. Tang, H. Bai, L. Liu, X. Zan, W. Yan, A green approach assembled multifunctional Ag/AgBr/TNF membrane for clean water production & disinfection of bacteria through utilizing visible light, Appl. Catal. B Environ. 196 (2016) 57–67.
[61] X.W. Zhang, T. Zhang, J. Ng, D.D. Sun, High-performance multifunctional TiO2 nanowire ultrafiltration membrane with a hierarchical layer structure for water treatment, Adv. Funct. Mater. 19 (2009) 3731–3736.
[62] X.F. Chen, M.H. Qiu, H. Ding, K.Y. Fu, Y.Q. Fan, A reduced graphene oxide nanofiltration membrane intercalated by well-dispersed carbon nanotubes for drinking water purification, Nanoscale 8 (2016) 5696–5705.
[63] S.Y. Yang, J. Park, J. Yoon, M. Ree, S.K. Jang, J.K. Kim, Virus filtration membranes prepared from nanoporous block copolymers with good dimensional stability under high pressures and excellent solvent resistance, Adv. Funct. Mater. 18 (2008) 1371–1377.

[64] A. Sato, R. Wang, H.Y. Ma, B.S. Hsiao, B. Chu, Novel nanofibrous scaffolds for water filtration with bacteria and virus removal capability, J. Electron Microsc. 60 (2011) 201–209.
[65] M.C. Cruz, L.C. Romero, M.S. Vicente, V.B. Rajal, Statistical approaches to understanding the impact of matrix composition on the disinfection of water by ultrafiltration, Chem. Eng. J. 316 (2017) 305–314.
[66] M.A. Zazouli, L.R. Kalankesh, Removal of precursors and disinfection byproducts (DBPs) by membrane filtration from water; a review, J. Environ. Health Sci. Eng. 15 (2017) 25.

FOR FURTHER INFORMATION

[67] S. Al Aani, C.J. Wright, M.A. Atieh, N. Hilal, Engineering nanocomposite membranes: addressing current challenges and future opportunities, Desalination 401 (2017) 1–15.
[68] R.W. Baker, Membrane transport theory, in: R.W. Baker (Ed.), Membrane Technology and Applications, John Wiley & Sons, Ltd, Chichester, 2004, pp. 15–84.
[69] R.R. Choudhury, J.M. Gohil, S. Mohanty, S.K. Nayak, Antifouling, fouling release and antimicrobial materials for surface modification of reverse osmosis and nanofiltration membranes, J. Mater. Chem. A 6 (2018) 313–333.
[70] E. Drioli, L. Giorno, Comprehensive Membrane Science and Engineering: Basic Aspects in Polymeric Membrane Preparation, first ed., Elsevier, Oxford, 2010.
[71] X. Li, A. Sotto, J. Li, B. Van der Bruggen, Progress and perspectives for synthesis of sustainable antifouling composite membranes containing in situ generated nanoparticles, J. Membr. Sci. 524 (2017) 502–528.
[72] R. Sanjay, S. Maya, B. Suryasarathi, D.N. Ch, Recent advances in preparation of porous polymeric membranes by unique techniques and mitigation of fouling through surface modification, ChemistrySelect 3 (2018) 609–633.
[73] A. Szymczyk, C. Labbez, P. Fievet, A. Vidonne, A. Foissy, J. Pagetti, Contribution of convection, diffusion and migration to electrolyte transport through nanofiltration membranes, Adv. Colloid Interf. Sci. 103 (2003) 77–94.
[74] J. Yin, B. Deng, Polymer-matrix nanocomposite membranes for water treatment, J. Membr. Sci. 479 (2015) 256–275.
[75] Y. Ying, W. Ying, Q. Li, D. Meng, G. Ren, R. Yan, X. Peng, Recent advances of nanomaterial-based membrane for water purification, Appl. Mater. Today 7 (2017) 144–158.
[76] H. Strathmann, L. Giorno, E. Drioli, Basic aspects in polymeric membrane preparation, in: E. Drioli, L. Giorno (Eds.), Comprehencive Membrane Science and Engineering, Elsevier, Oxford, 2010, pp. 91–112.

CHAPTER

NANOCELLULOSE-BASED MEMBRANES FOR WATER PURIFICATION

3

Deepu A. Gopakumar*, Vishnu Arumughan†, Daniel Pasquini‡, Shao-Yuan (Ben) Leu§, Abdul Khalil H.P.S.*, Sabu Thomas¶

School of Industrial Technology, Universiti Sains Malaysia (USM), Gelugor, Penang, Malaysia Chemistry and Chemical Engineering, Chalmers University of Technology, Gothenburg, Sweden† Chemistry Institute, Federal University of Uberlandia-UFU, Uberlandia, Brazil‡ Department of Civil and Environmental Engineering, The Hong Kong Polytechnic University, Kowloon, Hong Kong§ International and Inter University Centre for Nanoscience and Nanotechnology, Mahatma Gandhi University, Kottayam, India¶*

1 INTRODUCTION

Excessive human pressures on the planet are causing a range of environmental impacts. Water pollution is a heinous problem that is capable enough of leading the world into a great crisis. Water is known as the universal solvent. It is water's chemical composition and physical attributes that make it such an excellent solvent. Water molecules have a polar arrangement of the oxygen and hydrogen atoms, one side (hydrogen) having a positive electrical charge and the other side (oxygen) having a negative charge. This enables most pollutants to easily dissolve in it and to contaminate it. Several people are dying because of consuming polluted water. The major contaminants in water can be listed in three categories, namely, physical contaminants, chemical contaminants, and biological contaminants. Physical contaminants primarily affect the physical appearance or other physical properties of water. Examples of physical contaminants are sediment or organic material suspended in the water of lakes, rivers, and streams from soil erosion. Chemical contaminants are elements or compounds. These contaminants may be naturally occurring or man-made. They include heavy metal ions, chemical wastes from different industries, organic dyes, and so on. But biological contaminants are pathogens, such as bacteria and viruses, among others. *E. coli* is the major biological contaminant that can generate an adverse effect on human health.

Different strategies are used for removing various pollutants from water, including sedimentation, distillation, filtration, reverse osmosis, adsorption, electronic purification, and treatment with UV radiations, among others [1]. Filtration is an easy, efficient, and economically feasible method for cleaning water. Polymers can be used for many applications of water filtration membranes because of their property of forming membranes with a porous structure. But the major disadvantages of synthetic polymer-based membranes are problems regarding disposal and unsustainable manufacturing. High mechanical strength and selectivity without any compromise in water permeability are desired

Nanoscale Materials in Water Purification. https://doi.org/10.1016/B978-0-12-813926-4.00004-5

for next-generation filters. Cellulose nanomaterials' inherent fibrillar morphology and exceptional mechanical properties, together with its low cost, biocompatibility, and, moreover, high adsorbing property, make them ideal candidates for next-generation water filters [2]. Today, the scientific community all over the world is putting a lot of effort into utilizing cellulose in more advanced applications compared with traditional commodities, such as paper. Nanocellulose membranes and filters have been shown to remove heavy metals, microbes, dyes, and pesticides; moreover, organic contaminants, such as oils and cyclohexanes, can also be removed by using nanocellulose with hydrophobic functionalities, such as silyl groups [3].

This chapter focuses on nanocellulose-based membranes and filters for water purification. The isolation and properties of different kinds of nanocellulosic materials and the major adsorption mechanisms are described briefly, followed by a detailed discussion about the different kinds of chemical modifications of cellulose and their role in the removal of contaminants from water.

2 DIFFERENT TYPES OF CELLULOSIC NANOMATERIALS AND THEIR ISOLATION

The term *nanocellulose* actually represents a class of materials that contain nanocellulose fibers (CNFs), nanocellulose crystals (CNCs), and bacterial nanocellulose (BNC) [4]. The major difference between conventional nanocellulosic materials and BNC is that BNC is produced by using a bottom-up strategy, that is, bacterial cultivation in an aqueous culture media containing glucose, phosphate, and oxygen. It has a ribbonlike shape (<100 nm wide) and a high crystallinity index.

In essence, CNFs are separated microfibrils from the plant cell wall. Their preparation involves breaking down the complex fiber matrix by chemical and mechanical treatments. If true individualization results, the width of CNFs depends on the botanical source and its corresponds to the width of the microfibril in the original plant. Wood-based CNFs have a diameter of 10 nm to 30 nm. CNFs have both a crystalline and an amorphous region. Each microfibril consists of a crystalline domain intermixed with disordered amorphous regions, as shown in Fig.1 [5, 6].

When subjected to acid hydrolysis, cellulose microfibrils undergo a transverse cleavage along the amorphous regions as they have a lower density because of their random orientation; this makes the amorphous regions susceptible to attack by acids, and using centrifugation and sonication results in a rodlike material with a relatively low aspect ratio referred to as cellulose whiskers. Other synonyms for cellulose whiskers include *nanowhiskers*, *nanorods*, and *rodlike cellulose crystals* [7]. Whiskers are fully stretched cellulose chain segments that are arranged in a perfect crystalline arrangement, as shown in Fig. 2. The dimensions of the nanocrystals obtained after hydrolysis mainly depend on the percentage of crystallinity of starting material or on the percentage of the amorphous region in the starting material. The individual crystallites (nanofibrils) have been calculated to have a tensile strength of 10 Gpa and modulus of 150 Gpa. The properties of nanocrystals are affected by hydrolysis conditions and the acid used. CNCs have widths of 10–25 nm and lengths of 100–500 nm. By changing the acid, the surface functionality of the crystals can also be tailored. For instance, if H_2SO_4 is used, CNCs with sulfate groups are obtained; if HCl is used, CNCs with —OH functionality are created.

Strong hydrogen bonding between the individual cellulose crystals promotes reaggregation, which leads to another cellulose structure called microcrystalline cellulose (MCC).

CNCs are lightweight, strong, durable, tough, and highly stable. They also have high wear and abrasion stability [8]. Indeed, compared to cellulose fibers, CNCs have, in addition to their nanoscale

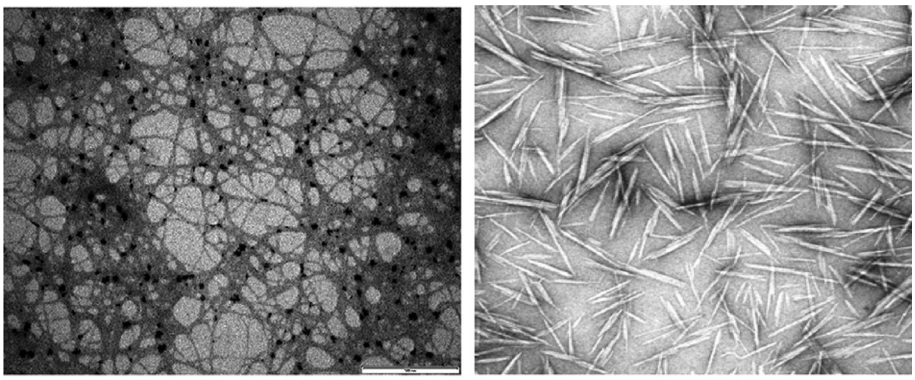

FIG. 1

TEM images of CNFs (A) and CNCs (B).

Reproduced with the permission from R. Masoodi, R.F. El-Hajjar, K.M. Pillai, R. Sabo, Mechanical characterization of cellulose nanofiber and bio-based epoxy composite, Mater. Des. 36 (2012) 570–576, Elsevier Ltd.

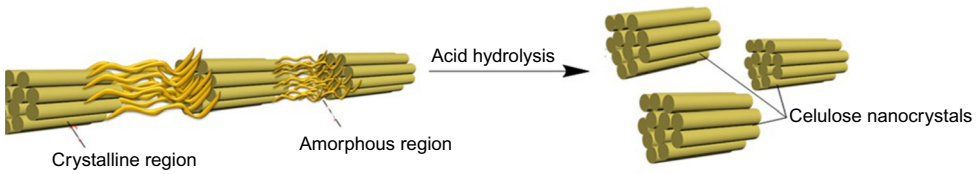

FIG.2

Acid hydrolysis of cellulose for the production of CNCs.

dimensions, many other advantages such as good stability, high surface area, and interesting mechanical and optical properties. Because of the aforementioned properties, cellulose nanomaterials can be considered as a sustainable replacement for carbon nanotubes [2]. Table 1 shows a comparison of the physical properties and life-cycle assessments of carbon nanotubes and cellulose nanomaterials [2].

From Table 1, it is very clear that cost of production is low for cellulose nanomaterials when compared to carbon nanotubes (CNTs). Although the cost of nanocellulose is still not viable for use in some industrial-scale applications, because of its biodegradability and biocompatibility nanocellulose will be of less concern in the contexts of long-term environmental exposure, bioaccumulation, and trophic transfer. Even though nanocellulose and CNTs have some comparable material properties, the complete replacement of CNTs with nanocellulose is not possible, especially in electronic applications. But in terms of versatility and easiness for functionalization, cellulose nanomaterials are far better than CNTs, which is very important in the context of water purification. Because functionalizing cellulose is needed to increase the efficiency and specificity for better removal of different kind of contaminants, previous investigations have demonstrated how functionalities, such as carboxyl groups, phosphate groups, sulfate groups, and so on, can be introduced to cellulose for the selective uptake of contaminants from water [9]. Apart from an active sorbent, cellulose can also be used as a supporting matrix for other active components, such as photocatalytic TiO_2.

Table 1 Comparison of Cellulose Nanomaterials and Carbon Nanotubes

	Cellulose Nanomaterials		Carbon Nanotubes	
	CNCs	**CNFs**	**SWCNTs**	**MWCNTs**
Physical properties				
Diameter	5–70 nm	5–100 nm	0.4–2 nm	2–100 nm
Length	100–250 nm	Several microns	Microns-millimeters	Microns-centimeters
Size distribution	Polydisperse	Polydisperse	Mono- or polydisperse depending on preparation	Mono- or polydisperse depending on preparation
Tensile strength	2–6 GPa	2–4 GPa	13–52 GPa	11–63 GPa
Young's modulus	50–143 GPa	15–150 GPa	0.32–1.47 TPa	0.27–0.95 TPa
Conductivity	None		$\sigma = 10^2$–10^8 S/m	
Optical properties	Transparent and iridescent films	Transparent films	None	
Life-cycle assessment				
Manufacturing (energy requirement)	500–2300 kWh/t		278,000–250,200,000 kWh/t	
Source	Wood, cotton, hemp, flax, wheat straw, ramie, sugar beet, potato tuber, tunicin, algae, certain bacteria (*Gluconacetobacter xylinus*)		Fossil fuels	
Cost	\$1/g (dry) \$5/g (slurry)	\$2/g (dry) \$3/g (slurry)	\$80–\$280/g	\$8–\$15/g
Major use/ application	Paper, packaging, plastic film, cement, automotive components, food products, drug delivery, biomedical implants, wound dressings		Microelectronics, solar cells	Strength enhancers, coatings/ films, biosensors, medical devices, drug delivery
Ecotoxicity	Low toxicity Some proinflammatory cytokines	Low toxicity Some pulmonary inflammation	Oxidative stress and inflammation; inhalation and dermal exposure considered largest risk	
Disposal	Biodegradable by organisms with cellulase enzymes		Persistent, nondegradable	

Reproduced with permission from A.W. Carpenter, C.F. De Lannoy, M.R. Wiesner, Cellulose nanomaterials in water treatment technologies, Environ. Sci. Technol. 49 (2015) (9) 5277–5287, American Chemical Society.

3 NANOCELLULOSE AS AN ACTIVE SORBENT FOR WATER CONTAMINANTS

Nanocellulose surface has an enormous number of hydroxyl groups that enable diverse chemical modifications on its surface. So nanocellulose is an excellent, sustainable material that can be tailor-made for removing specific contaminants from water. It is possible to remove various contaminants in water, such as bacteria, virus, dyes, heavy metals, and so on, via electrostatic attraction by the incorporation of various chemical functionalities.

3.1 ADSORPTION AND REMOVAL OF HEAVY METAL CONTAMINANTS

Heavy metals organic pollutants, such as dyes and pesticides, are major contaminants in water [10]. To remove these pollutants, various strategies such as chemical precipitation adsorption and membrane separation are used [1], of which adsorption is the most effective and efficient for removing the pollutants. Adsorption is an important surface phenomenon in which chemical species bind to a solid substrate called sorbent. The process of adsorption is controlled by the sorbent sorbate interactions and can be modeled by using different isotherms, such as Langmuir isotherms and Freundlich isotherms [11]. Isotherms are a relation between the surface concentration of adsorbate and the adsorbent bulk concentration or pressure. The adsorption behavior of cellulose substrates are usually modeled using Langmuir adsorption isotherms [12]. In this model, adsorption is assumed to be a monolayer, and the adsorbent surface has homogeneous site energies. It can be represented by the following Eq. (1).

$$q_e = \frac{Q_{max}\, bC_e}{1 + bC_e}, \tag{1}$$

where C_e (mg/L) is the concentration of the species to be adsorbed, for example, heavy metal ions or organic pollutants such as dyes in the solution; q_e (mg/g) is the number of species adsorbed on the substrate at equilibrium conditions, where the rate adsorption of adsorption becomes equal to rate of desorption; Q_{max} is the maximum amount of adsorbate species can be adsorbed on unit weight of adsorbate; and b is the Langmuir constant, which is related to adsorption energy of the system. Both Q_{max} and b can be determined from experimental data by plotting a linearized form of the Langmuir equation. Q_{max} and b are very important parameters that can be used to compare the performances of different adsorbents for various specific adsorbates. The major limitation of the Langmuir isotherm is that it can be applied only in low-pressure conditions.

Freundlich isotherms are another important type of empirical model. This model takes into account the multilayer adsorption and heterogeneous site energies. Eq. (2) represents the mathematical formula of Freundlich isotherm:

$$q_e = K_F C_e^{\frac{1}{n}} \tag{2}$$

where K_F and n are Freundlich constants related to the adsorption capacity and intensity, respectively. Langmuir and Freundlich isotherms can be coupled to explain the adsorption processes, particularly when there is competition between the adsorbates.

Cellulose nanomaterials are a promising alternative adsorbent because of their high aspect ratio, low cost, high natural abundance, inherent environmental inertness, and easy functionalization [13]. As mentioned before, heavy metals are the major contaminant that make water undrinkable. They can exist in different forms, such as cationic and anionic species. The efficient removal of heavy

metal species requires identifying dominant contaminant species and modifying the surface chemistry of cellulose accordingly [14]. The adsorption of cationic heavy metal ion species, such as Cu(II), Ag (I) from aqueous solution, can be achieved by introducing negatively charged moieties on the surface of the cellulose by different methods [15]. One such method is TEMPO oxidation, in which C6 carbon in the cellulose is selectively oxidized to the carboxylate group. TOCNF can efficiently remove heavy metal ions such as La(II), Pb(II), and Cu(II) [16]. Sehaqui et al. have done a systematic investigation of the adsorption of Cu(II) on TOCNF as a function of pH and carboxylic group content. They could observe a linear increase in adsorption of Cu(II) with carboxyl content on the cellulose surface in the 3–7 pH range [16]. Interestingly, a study by Zoheb Karim et al. demonstrated in situ TEMPO functionalization of cellulose-based bilayer membranes and its adsorption behavior toward different metal ions such as Fe(II), Fe(III), Ag(I), and Cu(II). Zeta-potential studies revealed that after in situ modification of cellulose membrane, the negative charge on the surface significantly increased, as shown in Table 2 [17].

After in situ functionalization of CNC_{BE} layer of membrane, the researchers could observe a significant increase in the adsorption of metal ions.

In a recently published study, Chuantao et al. explored the adsorption behavior of Cu(II) on TOCNF by using different atomic force microscopy modes, especially PeakForce scanning electron microscopy mode, which provides simultaneous high-resolution mapping of morphology and quantitative mechanical properties at the nanoscale. From the observations, they arrived at a conclusion that Cu(II) was first adsorbed by the carboxylate groups grafted on cellulose chains in an aqueous medium, followed by the copper nanolayer/nanocluster-formation process, while drying in the air [18]. Xiaolin Yu and coworkers demonstrated that esterification of —OH group on cellulose nanocrystals with succinic anhydride increased the binding ability toward Cd(II) and Pb(II). They also prepared a sodic nanosorbent by treating the carboxylated CNC (SCNC) with a saturated solution of $NaHCO_3$.

Both SCNC and NaSCNC exhibited high rates of adsorption for Cd(II) and Pb(II), as shown in Fig.3. They could also observe that the adsorption process is highly pH-dependent. Mechanism studies revealed that adsorption on SCNC follows a complexation mechanism, whereas in the case of NaSCNC, the principal adsorption mechanism was an ion-exchange process [19].

Table 2 Zeta-Potential Study of In Situ TEMPO Functionalized and Unfunctionalized Membranes

Types	Compositions	Nomenclatures	Surface zeta potential (mV)
Supports	Sludge	S	–
	Sludge-CNF_{SL}	S-CNF_{SL}	–
Unoxidized membranes	Sludge/CNC_{BE}	S/CNC_{BE}	−40.1 (1.5)
	Sludge-CNF_{SL}/CNC_{BE}	S-CNF_{SL}/CNC_{BE}	−47.9 (0.7)
In situ TEMPO oxidized membranes	Sludge/TEMPO-CNC_{BE}	S/TEMPO-CNC_{BE}	−57.0 (1.4)
	Sludge-CNF_{SL}/ TEMPO-CNC_{BE}	S-CNF_{SL}/ TEMPO-CNC_{BE}	−65.5 (2.4)

Reproduced with the permission from Z. Karim, M. Hakalahti, T. Tammelin, A.P. Mathew, In situ TEMPO surface functionalization of nanocellulose membranes for enhanced adsorption of metal ions from aqueous medium, RSC Adv. 7 (2017) (9) 5232–5241, Elsevier Ltd.

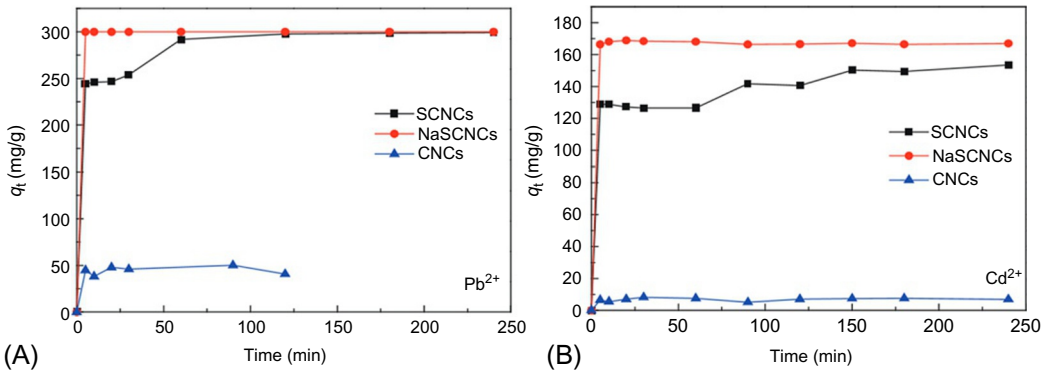

FIG. 3

Effect of contact time on adsorption of (A) Pb(II) and (B) Cd(II).

Reproduced with permission from X. Yu, S. Tong, M. Ge, L. Wu, J. Zuo, C. Cao, W. Song, Adsorption of heavy metal ions from aqueous solution by carboxylated cellulose nanocrystals, J. Environ. Sci. 25 (2013) (5) 933–943, Elsevier Ltd.

Table 3 Uptake Capacity for Different Heavy Metal Ions on PCNC and PCNF at pH 4

Substrate	Uptake Capacity for Ag(I) (mg/g)	Uptake Capacity for Cu (II) (mg/g)	Uptake Capacity for Fe(III) (mg/g)
PCNC	136	117	115
PCNF	120	114	73

Reproduced with permission from P. Liu, P.F. Borrell, M. Božič, V. Kokol, K. Oksman, A.P. Mathew, Nanocelluloses and their phosphorylated derivatives for selective adsorption of Ag^{+}, Cu^{2+} and Fe^{3+} from industrial effluents, J. Hazard. Mater. 2015, 294, 177–185 Elsevier Ltd.

Liu et al. reported that the enzymatic phosphorylation of cellulose nanocrystals and nanofibers and their effective surface area and surface functionality have pivotal roles in the efficiency of the adsorption process for Ag(I), Cu(II), and Fe(III), as shown in Table 3. Fig. 4 shows the enormous increase in adsorption capacity of nanosized cellulose fibers and functionalized cellulose [9].

Pillai et al. [20] reported the synthesis of xanthated cellulose with a high uptake capacity of 154 mg/g for Cd(II) at pH 6. Arsenates and chromates are anionic heavy metal ionic species that are commonly seen in contaminated water. Long-term exposure to these heavy metal ions can cause severe health issues, such as cancer. Adsorption of these anionic species could be achieved by the incorporation of positive charged species on cellulose surface by using chemical modifications. Singh et al. investigated adsorption chromate ions using aminated cellulose nanocrystals. They could observe 98% removal of chromate ions [21].

Another strategy for enhancing the adsorption of heavy metal is grafting a polymer chain that contains ionic or chelating functionalities onto the cellulose surface. Navarro et al. reported the efficiency of a polyethyleneimine-grafted cellulose carrier for removing mercury ions [22]. Per the investigation of Zhang and coworkers, poly(acrylic acid)-grafted bamboo cellulose nanofibers exhibited very good adsorption for Cu(II) ions from water, as shown in Fig. 5 [23].

An overall view of adsorption behavior of cellulose with different functionalities is presented in Table 4.

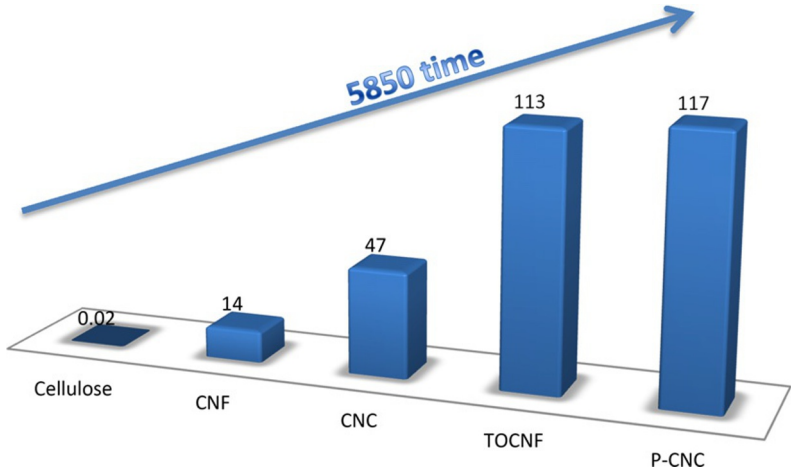

FIG. 4

Comparison of uptake capacity (expressed in mg/g) for Cu(II) on cellulose, CNC, CNF, TOCNF, and P-CNC.

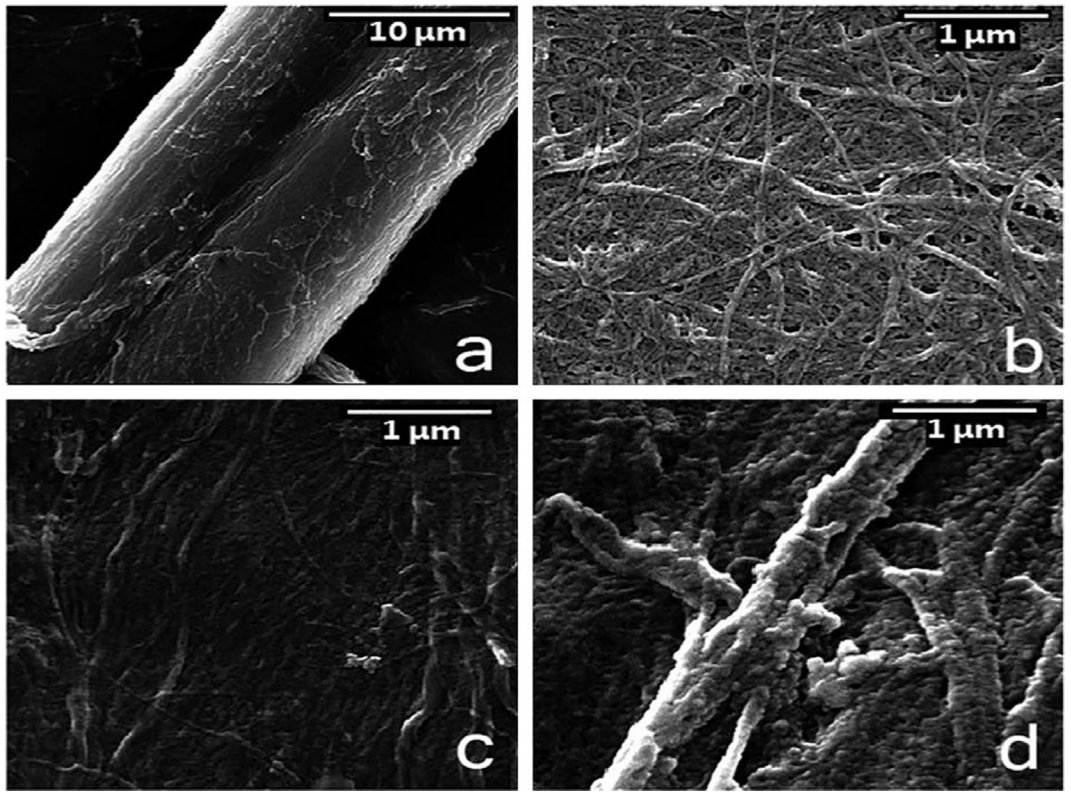

FIG. 5

Scanning electron microscope (SEM) images of bamboo cellulose fibers before and after mechanical nonfibrillation and surface modified bamboo cellulose nanofibers. (A) Bamboo pulp fibers. (B) BCN. (C) BCN-g-PAA. (D) BCN-g-PAA/SH.

Reproduced with permission from X. Zhang, J. Zhao, L. Cheng, C. Lu, Y. Wang, X. He, W. Zhang, Acrylic acid grafted and acrylic acid/sodium humate grafted bamboo cellulose nanofibers for Cu 2+ adsorption. RSC Adv. 4 (2014) (98) 55195–55201, Royal Society of Chemistry.

Table 4 Overview of Adsorption Capacities of Different Functionalized Cellulose

Type of Functionalization and Route	Contaminant	pH	Uptake Capacity (mg/g)	References
Unfunctionalized cellulose obtained by mechanical grinding	Cd(II) Ni(II) Pb(II)	5.5	11 11 10	[24]
CNC-SO^{3-} obtained by sulfuric acid hydrolysis	Ag(I)	6.5	34	[25]
CNC-PO_4^{2-} (phosphorylation of CNC)	Ag(I) Cu(II) Fe(III)	4	136 117 115	[9]
CNC-COOH (succinic anhydride)	Pb(II) Cd(II)	5.5	458 335	[19]
CNC-COOH (sodium periodate/chlorite)	Cu(III)	4	185	[26]
CNF-COOH (TEMPO)	Cu(II) Ni(II) Cr(III) Zn(II) UO_2^{2+}	6.2–6.5	112 49 58 67 167	[16, 27]
CNF-$(PO(OH)_2)$	VO_3^-	2	194	[28]
CNC-NH_2 (reaction with potassium persulfate and ethylenediamine)	Cr(VI)		3	[21]
CNC-NH_2 (grafting of PEG-NH_2)	Hg(II)			[29]
CNC-$CONH_2$	Hg(II)			[30]
TEMPO CNF-PEI	Cu(II)	5	52.3	[31, 32]
CNC-PLA	Cu(II) Ni(II) Cd(II) Pb(II)	4.9 5.9 5.7 4.5		[33–35]

3.2 REMOVAL AND ADSORPTION OF TOXIC TEXTILE DYES

Organic pollutants are a serious issue today. They include a wide range of compounds, such as textile dyes, pesticides, and oils, among others. Each class of these pollutants behaves differently, and it makes the removal process tedious. Many industries, especially the textile, paper, and plastics industries, consume a large number of dyes for coloring their products. Most of these dyes are water soluble, and they can contaminate water easily. This dye contamination can lead to serious environmental and health issues. However, dye-polluted water is very difficult to treat because of the recalcitrant nature of dyes and their resistance to light, heat, and oxidizing agents [36]. These organic dyes possess a complex aromatic structure and can exhibit cationic, anionic, and nonionic natures.

Batmaz and coworkers [37] explored the possibility of carboxylated cellulose nanocrystals as a sorbent for cationic dyes. In this study, they incorporated a carboxylic group by TEMPO oxidation of the cellulose. They could observe that the adsorbance performance of the carboxylated CNC is comparable to activated carbons. Fig. 6 clearly illustrates the efficiency of both CNC and carboxylated CNC over other nonconventional adsorbents.

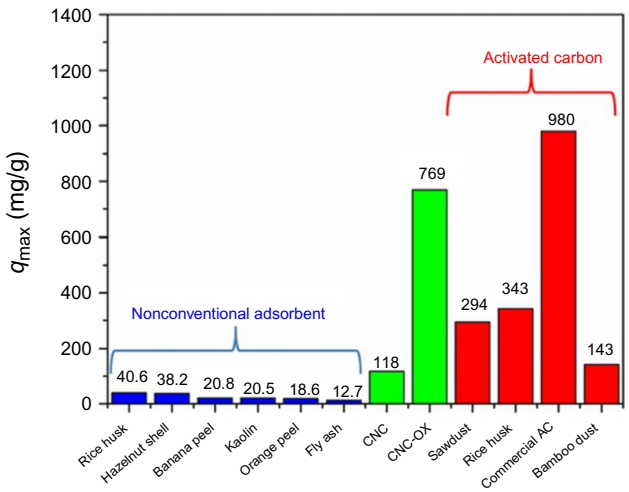

FIG. 6

Comparison of q_{max} of various adsorbents.

Reproduced with permission from R. Batmaz, N. Mohammed, M. Zaman, G. Minhas, R.M. Berry, K.C. Tam, Cellulose nanocrystals as promising adsorbents for the removal of cationic dyes, Cellul. 21 (2014) (3) 1655–1665, Springer Nature.

In a recent report, Yong Yu et al. introduced a new approach for a single-step extraction of cellulose nanocrystals and demonstrated its efficiency in removing cationic dye. They could extract carboxylated CNCs with a typical rodlike structure using a novel $C_6H_8O_7$/HCl hydrolysis of the microcrystalline cellulose. They also demonstrated the efficiency of this extracted CNC (92.3% at 20 mg/mL adsorbent in initial dye concentration of 200 mg/L) was better than that of carboxylated CNCs prepared by TEMPO oxidation, as shown in Fig. 7 [38].

Manna et al. [39] reported a novel method of functionalizing lignocellulosic fibers using a neem oil-phenolic resin emulsion. The treated lignocellulosic fibers exhibited rapid adsorption of methylene blue over a wide range of pH conditions. In this study, they claim that the rapid methylene blue adsorption is due to the coupled effect of electrostatic interactions, van der Waals forces, and hydrogen bonding interactions between the cationic methylene blue and the treated fiber [39].

Anionic dyes can be removed by using positively charged cellulosic materials. Jin et al. demonstrated the efficiency of cationized CNCs in anionic dye removal. The cationic CNCs were prepared by successive sodium periodate oxidation and reaction with ethylenediamine. As in the case of heavy metal ion adsorption process, here the adsorption is also highly pH-dependent. Aminated cellulosic materials generally show a maximum uptake at higher pHs. As the pH decreases, the adsorption efficiency will also decrease. This is attributed to the pH-dependent dissociation of the functional groups [40].

Pei et al. reported surface quarternization of cellulose nanofibers for making nanopapers with high anionic-dye removal abilities, as shown in Fig. 8. Divalent anionic dyes, Congo red, and acid green 25 were utilized for dye-adsorption studies. They could observe a linear relationship between the dye adsorption and the trimethylammonium content from 0.59 to 1.32 mmol/g. Further increases in the trimethylammonium content could not generate a significant increase in dye adsorption [41].

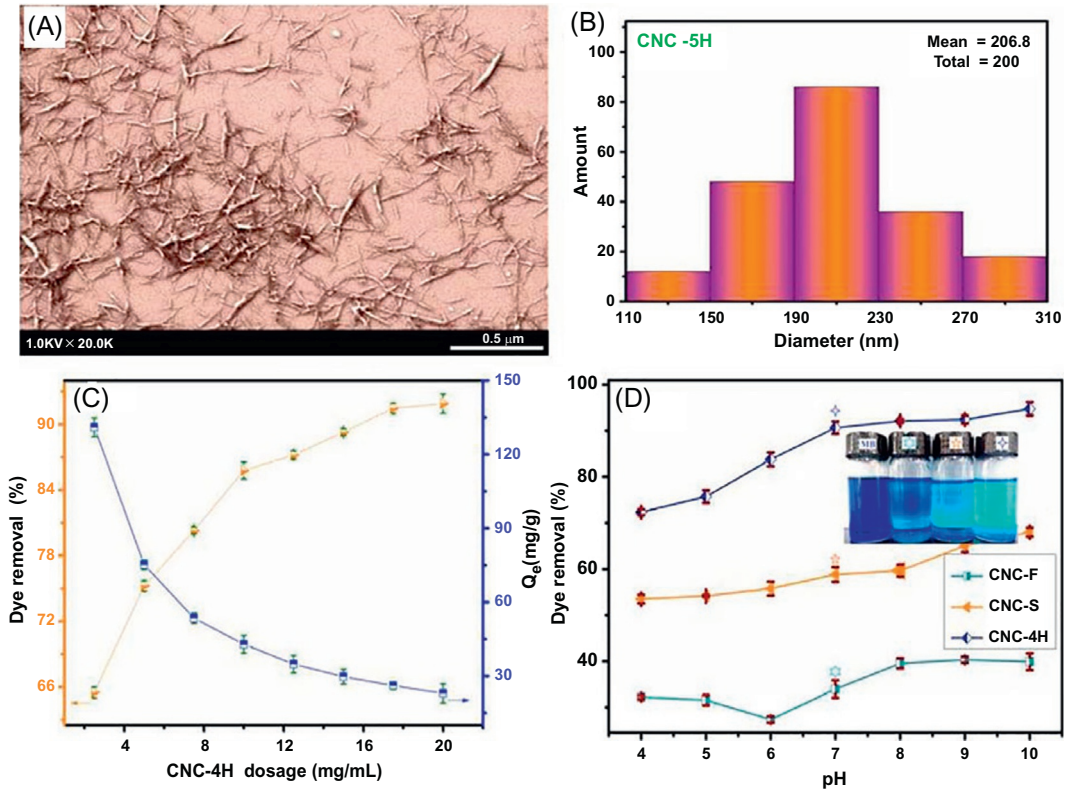

FIG. 7

FESEM images of (A) CNCs 4H and (B) the corresponding particle size distribution of CNCs-4H measured from FESEM images. (C) Effect of CNC-4H dosage on dye removal % and q_e, and (D) effect of pH on dye removal for three kinds of CNCs (inset photos of dye before and after adsorption with CNCs at pH = 7).

Reproduced with permission from H.Y. Yu, D.Z. Zhang, F.F. Lu, J. Yao, New approach for single-step extraction of carboxylated cellulose nanocrystals for their use as adsorbents and flocculants, ACS Sustain. Chem. Eng. 4 (2016) (5) 2632–2643, American Chemical Society.

Recently, Gopakumar et al. removed toxic crystal violet dyes from water by using a cellulose nanofiber-based PVDF membrane via Meldrum's acid modification of CNFs. They introduced a facile method for producing a unique green adsorbent material from the CNFs via a nonsolvent-assisted procedure using Meldrum's acid as an esterification agent for enhancing the adsorption toward positively charged crystal violet dyes. They showed that, with the 10 mg/L of crystal violet (CV) aqueous solution, the CV adsorption of PVDF electrospun membrane, and an unmodified CNF-based PVDF membrane was about 1.368 and 2.948 mg/g of the membrane, respectively, whereas it was 3.984 mg/g of the membrane by Meldrum's acid CNF-based PVDF membrane, as shown in Fig. 9. They found that the enhanced absorption capacity of Meldrum's acid-modified membrane is due to the electrostatic interaction between the protonated crystal violet and Meldrum's acid-modified CNFs, as shown in Fig. 10 [42].

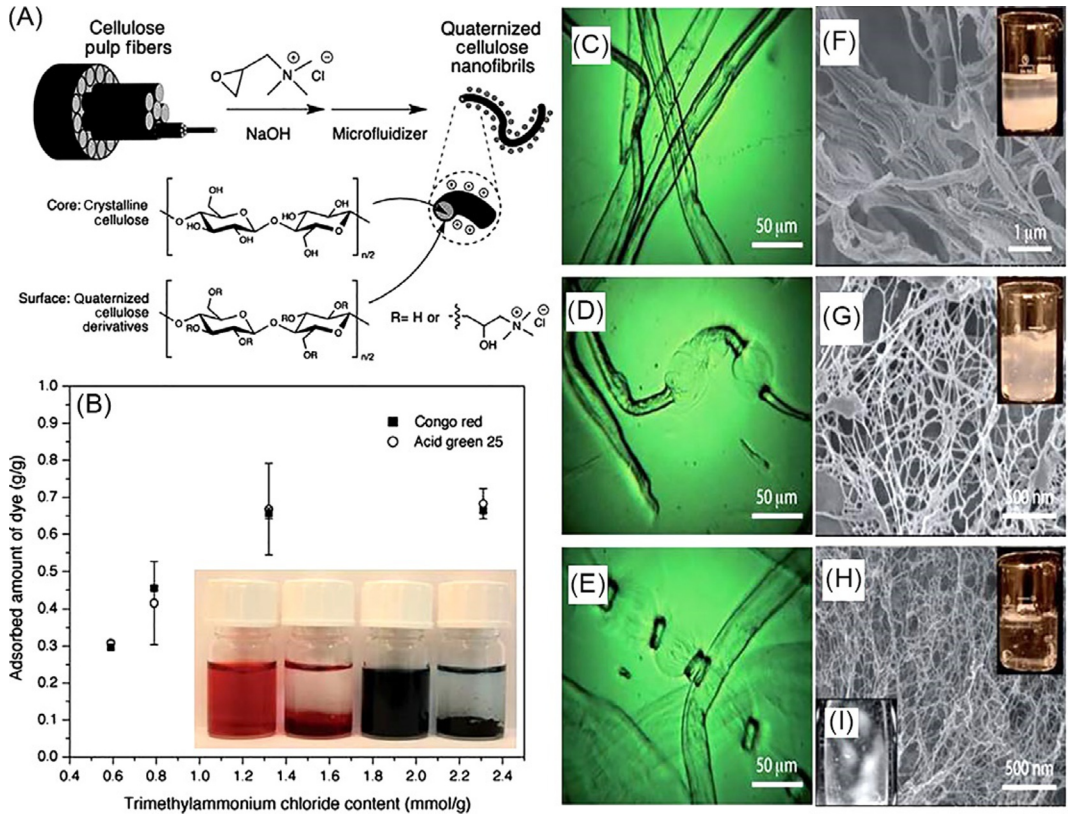

FIG. 8

(A) Schematic illustration of the preparation of surface quaternized cellulose nanofibrils from pulp fibers, (B) adsorbed amount of congored and acid green 25 on Q-NFC nanofibrils as a function of the trim ethyl ammonium chloride content, phase contrast micrographs of (C) the pulp fibers and swollen states of the quaternized fibers having a trimethyl amonium chloride content of (D) 0.5 mmol g^{-1} and (E) 0.79 mmol g^{-1} obtained after chemical reaction with subsequent magnet stirring in water suspension. FESEM images of (F) the pulp fibers, and (G and H) Q-NFC nanofibrils obtained after further mechanical disintegeration of (D and E) by using a microfluidizer, respectively. The insets in (F), (G) and (H) were corresponding fibril dispersions in water (0.2 wt%), (I) water suspensions of 0.1 wt% nanofibrils observed between crosspolarizers.

Reproduced with permission from A. Pei, N. Butchosa, L.A. Berglund, Q. Zhou, Surface quaternized cellulose nanofibrils with high water absorbency and adsorption capacity for anionic dyes, Soft Matter 9 (2013) (6) 2047, Royal Society of Chemistry.

Ma et al. [43] reported the removal of CV dyes by using nanofibrous microfiltration membrane based on cellulose nanowhiskers via adsorption. They used TEMPO oxidation on the cellulose nanowhiskers surface. The cellulose nanowhiskers-based nanofibrous microfiltration membrane was prepared by impregnating cellulose nanowhiskers into the polyacrylonitrile (PAN) electrospun scaffold, resulting in a cross-linked nanofibrous mesh with very high surface-to-volume ratio. They found that the maximum adsorption capacity of the cellulose nanowhisker-based microfiltration

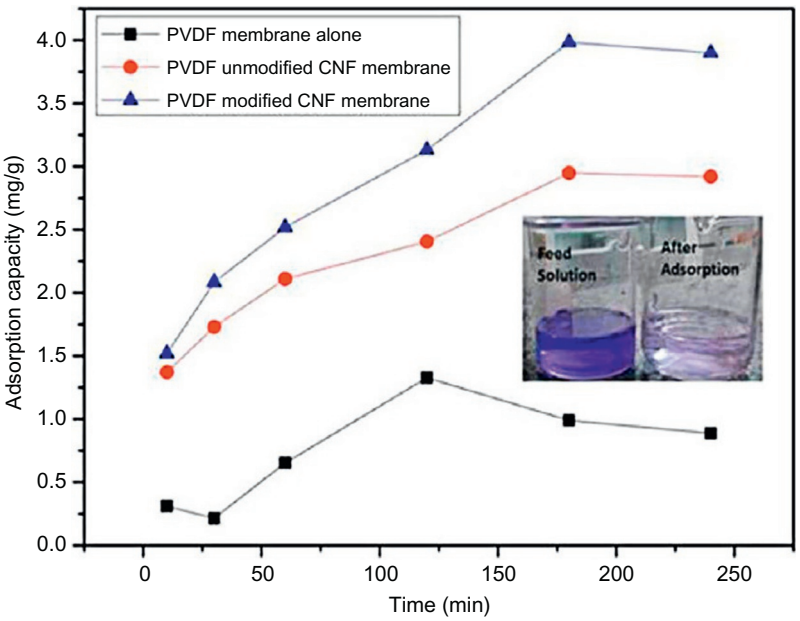

FIG. 9

Adsorption capacity of PVDF membrane alone, PVDF/unmodified CNF membrane, and PVDF/modified CNF membranes against time.

Reproduced with permission from D.A. Gopakumar, D. Pasquini, M.A. Henrique, L.C. de Morais, Y. Grohens, S. Thomas, Meldrum's acid modified cellulose nanofiber-based polyvinylidene fluoride microfiltration membrane for dye water treatment and nanoparticle removal, ACS Sustain Chem. Eng. 5 (2017) (2), 2026–2033, American Chemical Society.

membrane for CV dye was 16 times higher than that of GS0-22 (a commercially available membrane). This was because of the strong electrostatic attraction between protonated CV molecules and the highly negative carboxylate group on the cellulose nanowhiskers' surface [43].

3.3 OIL REMOVAL FROM WATER

Oil contaminants in water are a serious threat to aquatic ecosystems. Industrial effluents discharged into water bodies and accidents that occur during the production and transportation of petroleum products are the key reasons for oil contamination in water.

Absorption of oil from water is the ideal strategy for solving this problem. Compared to conventional methods, such as skimming, centrifugation, and flotation, it is effective and economically viable. Today, the scientific community in all over the world is focusing on developing sustainable sorbent materials for oil spill remediation. Hydrophobicity and oleophilicity are the essential requirements for an oil sorbent material. Different strategies have been used to make cellulose hydrophobic for enhancing oil sorption capacities.

H. Sai et al. reported the surface hydrophobization of cellulose nanofibers by using trimethyl silylation reaction and the successive fabrication of oleophilic aerogel, as shown in Fig. 11.

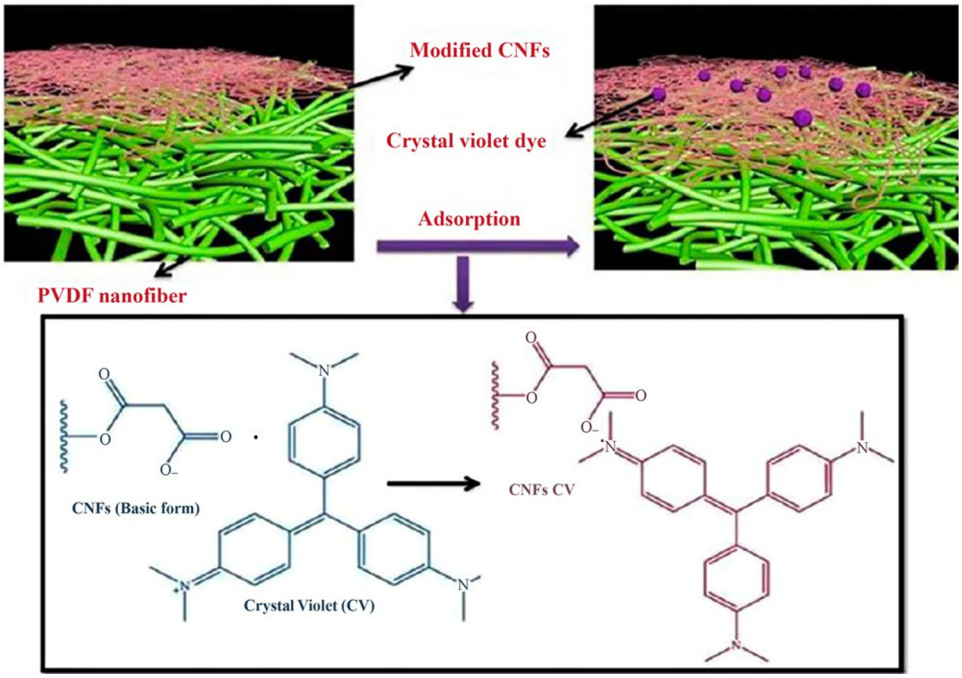

FIG. 10

Schematic representation of crystal violet removal by Meldrum's acid-modified CNF-based PVDF nanofibrous MF membrane and its mechanism.

Reproduced with permission from D.A. Gopakumar, D. Pasquini, M.A. Henrique, L.C. de Morais, Y. Grohens, S. Thomas, Meldrum's acid modified cellulose nanofiber-based polyvinylidene fluoride microfiltration membrane for dye water treatment and nanoparticle removal, ACS Sustain Chem. Eng. 5 (2017) (2), 2026–2033, American Chemical Society.

Silane-modified aerogels exhibited ultralow density and high porosity. They studied the absorption of different kind of organic solvents and oils from water mixture, and they reported maximum sorption capacity of 180 g/g, as shown in Fig. 12. Their study also revealed that the absorption capacity of various kind of oil sorbents depends on the density of the liquid [44].

S. Zhou et al. also reported a silylation for making porous hydrophobic aerogels. They showed that polysiloxane-modified cellulose aerogels have a maximum oil adsorption capacity of 159 g/g, and even after 30 cycles it showed an absorption capacity of 92 g/g, which demonstrated the efficiency and reusability of novel hydrophobic cellulose aerogels [45]. R. Lin and coworkers introduced a novel cold-plasma method for hydrophobizing cellulose. In this method, a trimethyl chlorosilane is used as the cold plasma. Newly developed cellulose aerogels exhibited maximum absorption capacity of 35 g/g for peanut oil and showed excellent reusability of >15 cycles [46]. Another investigation by Zang et al. explored the possibility of plasma treating cellulose aerogels to impart hydrophobicity and oleophilicity to their surfaces. The major importance of this work is that they did not incorporate any additional material or use any chemical modifications to impart hydrophobicity. They could

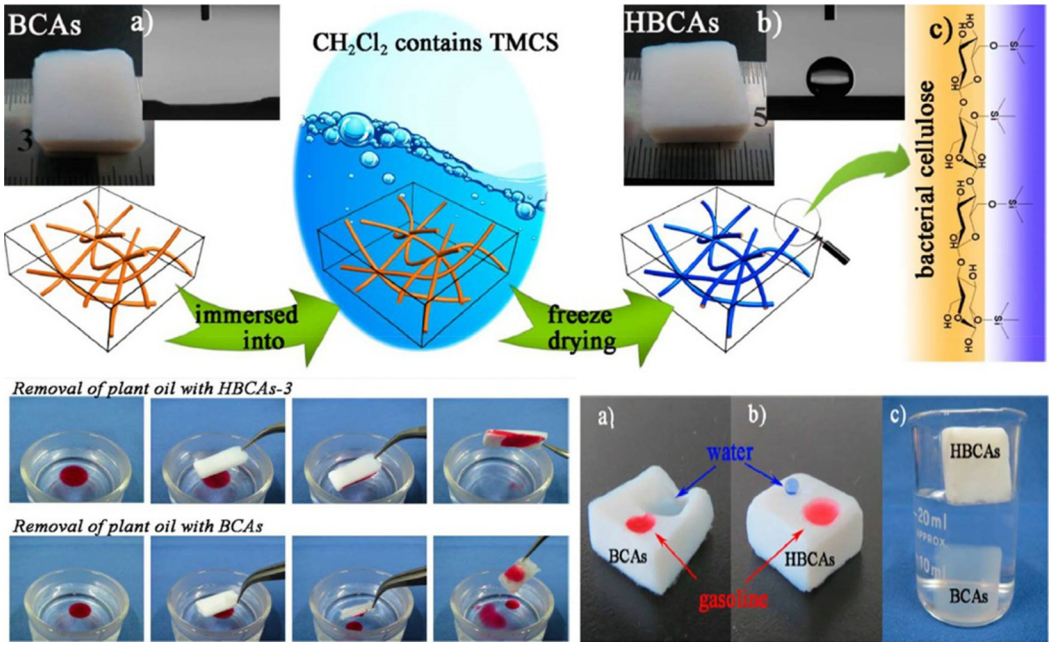

FIG. 11

Schematic illustration of the trimethylsilylation of BCAs. (A) The image and contact angle test of BCA. (B) The image and contact angle test of HBCA. (C) The schematic chemical structure of modified bacterial cellulose.

Reproduced with permission from H. Sai, R. Fu, L. Xing, J. Xiang, Z. Li, F. Li, T. Zhang, Surface modification of bacterial cellulose aerogels' web-like skeleton for oil/water separation, ACS Appl. Mater. Interfaces 7 (2015) (13) 7373–7381, American Chemical Society.

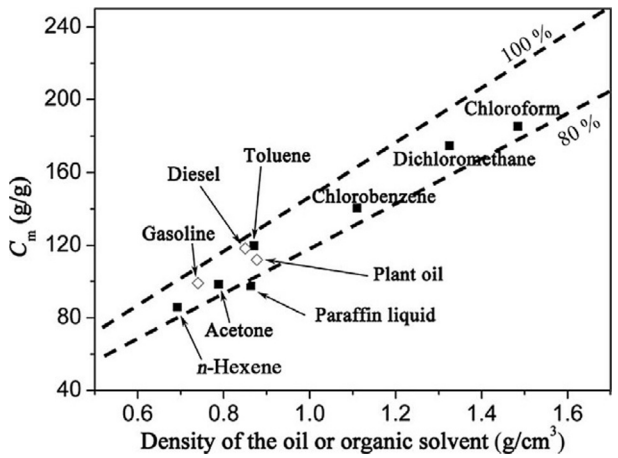

FIG. 12

Plot of the mass-based absorption capacity for different organic solvents and oils as a function of the density of the liquid. The upper dashed line represents the theoretical volume-based absorption capacity (v/v) corresponding to the case where the aerogel is nominally completely filled with the oils or organic liquids, and the lower one dashed line represents the case where it is 80% filled.

Reproduced with permission from H. Sai, R. Fu, L. Xing, J. Xiang, Z. Li, F. Li, T. Zhang, Surface modification of bacterial cellulose aerogels' web-like skeleton for oil/water separation, ACS Appl. Mater. Interfaces 7 (2015) (13) 7373–7381, American Chemical Society.

generate micro/nanostructures on the surface of cellulose fibers by plasma treatment, which, in turn, reduced the surface energy of the material [47].

The fabrication of ultralight cellulose-based carbon aerogels for oil removal has been reported by Meng et al. They synthesized a spongelike carbon aerogel from microfibril cellulose, as shown in Fig. 13, with high porosity (99%), ultralow density (0.01 g/cm^3), and hydrophobic properties with a static contact angle of 149 degrees. They concluded that carbon aerogels' ability to absorb oil was enhanced by their highly porous three-dimensional network structure with interconnected cellulose nanofibrils [48].

In a recent study Prathap et al. [49] developed an organogeletor-cellulose composite material for efficient oil removal. In this study they prepared a sugar-derived organogelater 1,2:5,6-di-*O*-cyclohexylidene-mannitol, which was then impregnated with porous biogenic cellulose matrix. The organogelator can effectively mask the surface-exposed —OH groups via hydrogen bonding interactions that impart a hydrophobic nature to the composite, as shown in Fig. 14.

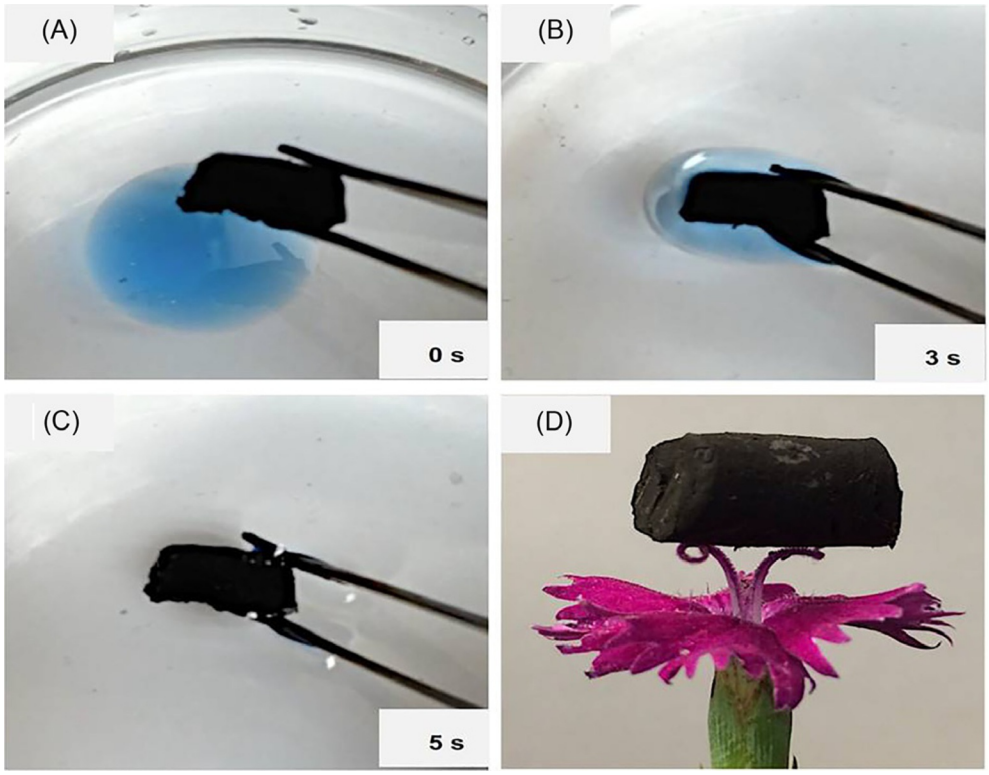

FIG. 13

(A)–(C) Removal of engine oil from the water surface using nanocellulose carbon aerogel. (D) Ultralight carbon aerogel sitting on a flower.

Reproduced with permission from Y. Meng, T.M. Young, P. Liu, C.I. Contescu, B. Huang, S. Wang, Ultralight carbon aerogel from nanocellulose as a highly selective oil absorption material, Cellulose 22 (2015) (1) 435–447, Springer Nature.

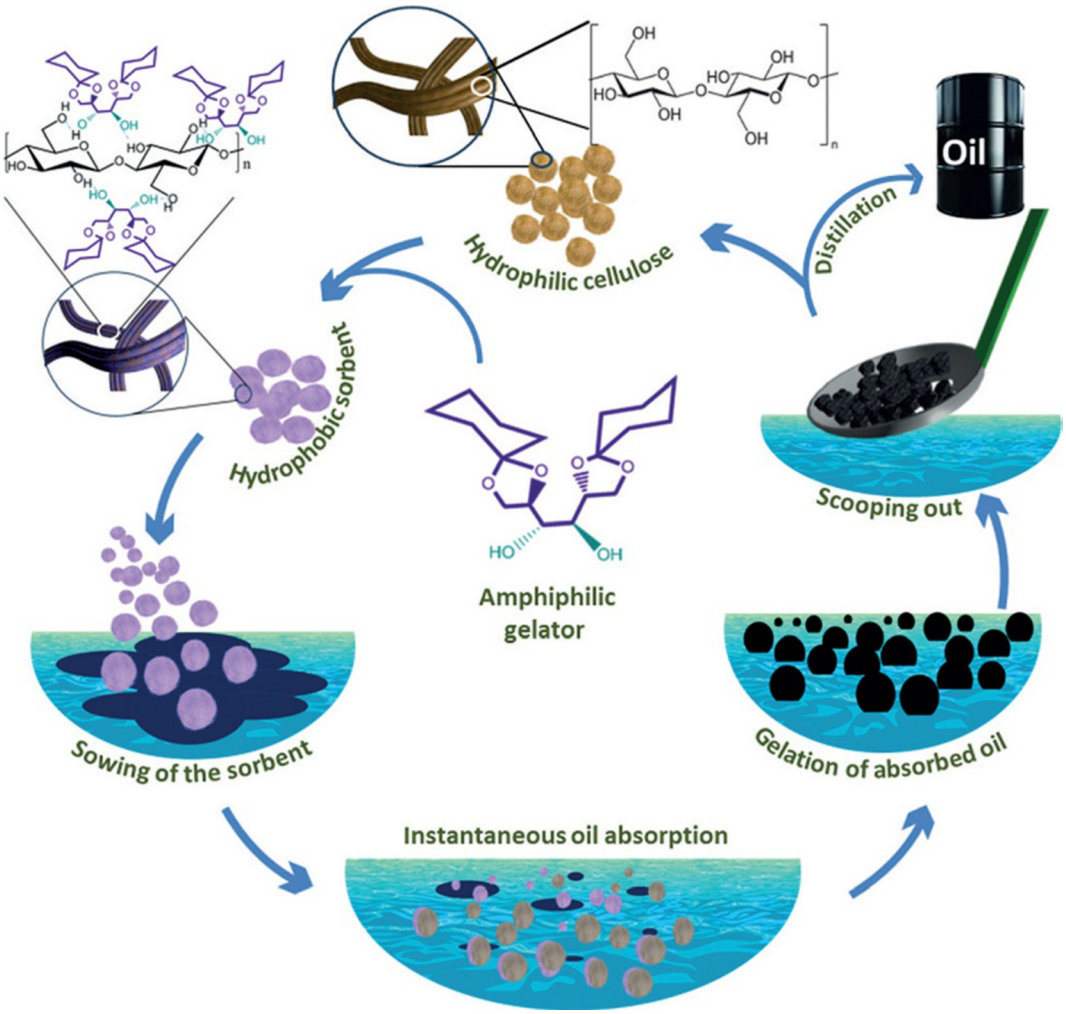

FIG. 14

Scheme of proposal for the eco-friendly marine oil spill recovery.

Reproduced with permission from A. Prathap, K.M. Sureshan, Organogelator–cellulose composite for practical and eco-friendly marine oil-spill recovery, Angew. Chem. Int. Ed. 56 (2017) (32) 9405–9409, John Wiley and Sons.

Because of its highly hydrophobic surface and porous nature, the composite showed excellent oil absorption properties. In terms of reusability and recyclability, this newly developed material is also very good. Once the oil is adsorbed, the gelator molecules go to the oil phase. The evenly distributed organic gelator molecules then undergo self-assembly through hydrogen-bond congealing, making the oil phase a rigid solid that can be removed easily [49].

Korhonen et al. [50] demonstrated such a material, based on functionalized cellulose nanofibrils, where cellulose is natural, renewable, and the most abundant polymer. They prepared highly porous

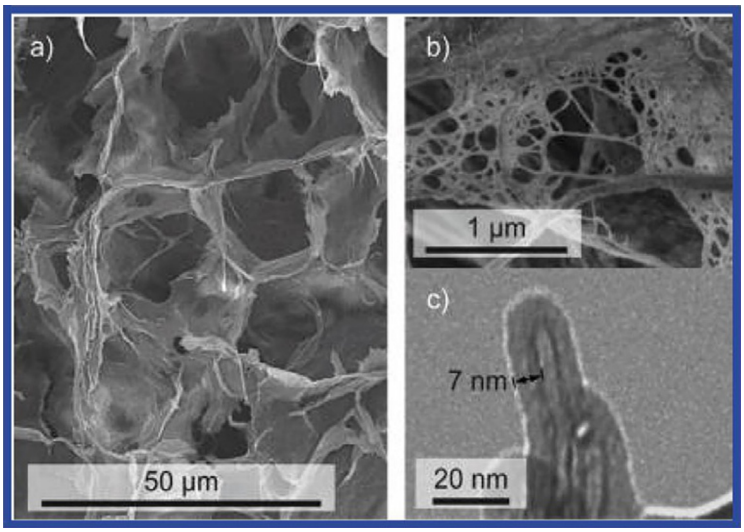

FIG. 15

Microscopic structure of native nanocellulose aerogels. SEM micrographs of (A) freeze-dried nanocellulose aerogels with fibrils packed into sheets, which are connected to form an open, porous aerogel structure, and (B) a magnification of a sheet, which is composed of fibrils making the structure also nanoporous (C) TEM micrograph of a nanocellulose fibril with a uniform 7 nm TiO_2 coating.

Reproduced with permission from J.T. Korhonen, M. Kettunen, R.H.A. Ras, O. Ikkala, Hydrophobic nanocellulose aerogels as floating, sustainable, reusable, and recyclable oil absorbents, ACS Appl. Mater. Interfaces 3 (2011) (6) 1813–1816, American Chemical Society.

nanocellulose aerogels, shown in Fig. 15, via vacuum freeze-drying from microfibrillated cellulose hydrogels. They showed that the native cellulose nanofibrils of the aerogel could be functionalized with a hydrophobic titanium dioxide oleophilic coating to selectively absorb oils from water. Because of the low density and the ability to absorb nonpolar liquids and oils up to nearly all of its initial volume, the surface-modified aerogels allow for the collection of organic contaminants from the water surface, as shown in Fig. 16. They showed that the absorption was close to the overall volume of the aerogel (80%–90% vol/vol) and that the mass-based adsorption capacity varies from 20 to 40 (wt/wt) depending on the density of the liquid. They concluded that the nano-cellulose-based aerogels are good, promising candidates as oil absorbents for sustainable future applications [50].

Other work has been done by Jin et al., and they demonstrated the superhydrophobic and superoleophobic nanocellulose aerogels, consisting of fibrillar networks and aggregates with structures at different length scales, support considerable load on a water surface and on oils. They showed that the load-carrying capacity of the aerogels might be a few orders of magnitude larger than the weight of the aerogel itself. They suggested that this would open a new platform for carriers or for coatings that have large load-bearing capabilities on various organic and aqueous liquids, including oil-polluted water [51]. Interesting work has also been done by Meng et al.; they reported a spongelike nanocellulose-based carbon aerogels for oil absorption. They prepared carbon aerogel material via heat treatment of cellulose microfibril aerogel. They showed that this particular aerogel was useful as a highly porous oil absorbent (99% of porosity) with ultra-light density (0.01 g/cm^3), hydrophobic properties (144 degree

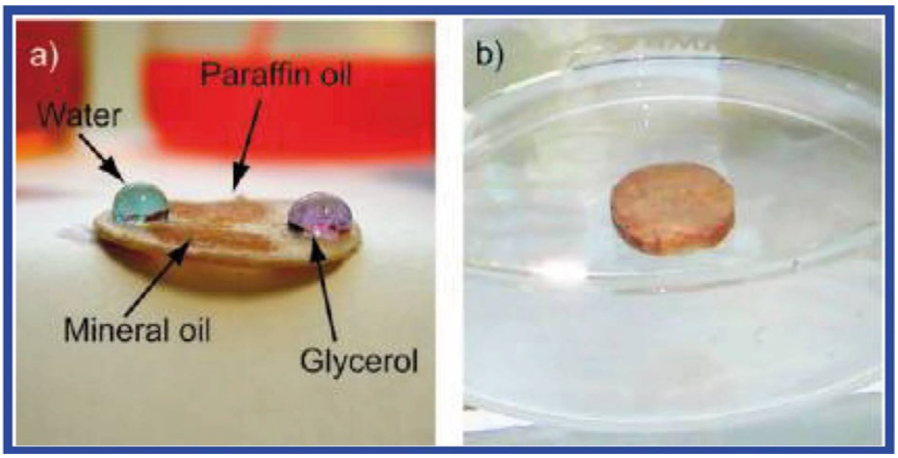

FIG. 16

(A) TiO_2-coated aerogels are hydrophobic and oleophilic: the water and glycerol stay as droplets (colored with reactive *blue dye* for clarity), whereas paraffin oil and mineral oil are readily absorbed. (B) Coated aerogel floating on water.

Reproduced with permission from J.T. Korhonen, M. Kettunen, R.H.A. Ras, O. Ikkala, Hydrophobic nanocellulose aerogels as floating, sustainable, reusable, and recyclable oil absorbents, ACS Appl. Mater. Interfaces 3 (2011) (6) 1813–1816, American Chemical Society.

static contact angle), fast absorption rate, and multiple reusability. Their investigations revealed that carbon aerogel that was heat-treated at 700°C had a higher oil absorption capacity of various types of oils. This was because of the three-dimensional network structure formed by the entanglement of carbonized cellulose fibrils and the large surface energy of carbonized fibers. They concluded that the unique properties of carbon aerogel from nanocellulose, along with the advantages of using a natural renewable, low cost, and sustainable material, recommend carbon aerogel for a wide range of oil-spill cleanup applications [48]. Feng et al. reported the advanced fabrication and oil absorption properties of superhydrophilic recycled cellulose aerogels. They coated the recycled cellulose aerogels with methyl/trimethoxy silane via chemical vapor deposition yielded, a very stable superhydrophobicity for over 5 months and excellent oil absorption capacities up to 95 g/g with the 0.25 wt% cellulose aerogel. It was shown that the initial cellulose fiber concentration significantly affects the oil absorption capability of the developed cellulose aerogels. They concluded that the demonstrated superhydrophobic recycled cellulose aerogels could be one of the very promising sorbents for oil-spill cleaning [52]. Zhang et al. fabricated a highly efficient cellulose-based aerogel with high mechanical strength via a novel method. The prepared aerogel possessed a perfect three-dimensional skeleton and interconnected pores similar to a honeycomb that exhibited excellent oil/water selectivity. In addition, the demonstrated aerogels exhibited stable superhydrophobic and superoleophilic properties, even toward a strong mechanical abrasion. Moreover, they demonstrated that cellulose aerogels can be reused up to 30 cycles [53]. Wang et al. reported an ultra-weight, elastic, cost-effective, highly recyclable superabsorbent from microfibrillated cellulose fibers for oil-spill cleanup. They demonstrated a simple method for producing a low-cost highly recyclable superabsorbent from renewable cellulose fibers via a simple and environmentally friendly microfibillation treatment and freeze-drying. The demonstrated hydrophobic superabsorbent could selectively absorb oil from an oil-water mixture and showed

an ultra-high absorption capacity of 88–228 g/g, which was comparable to those of other novel carbon-based superabsorbents. More important, the superabsorbent showed excellent flexibility and could be repeatedly squeezed (>30 times) without structure failure [54].

3.4 NANOCELLULOSE-BASED MEMBRANES FOR BACTERIA AND VIRUS REMOVAL VIA SIZE EXCLUSION

It has been reported that >4 million people die of illnesses contracted through microorganisms via water contamination [55]. Microorganisms, such as pathogenic bacteria and pathogenic viruses, have been adversely affecting humans' health. The effective removal of these highly dangerous pathogens is a very important issue to study to provide safe water. In this context, nanocellulose derived from biomass has gained considerable interest as an efficient material for fabricating microfiltration membranes among the researchers because of its excellent mechanical and unique properties [56]. Only a few studies have reported on the nanocellulose-based membranes for water purification.

Wang et al. demonstrated a novel class of microfiltration membrane based on a two-layered nanoscale PAN/microscale polyethylene terephthalate (PET) fibrous scaffold containing infused ultrafine cellulose nanofibers (diameter about 5 nm). They did an amine functionalization on the cellulose nanofibers to enhance the adsorption toward the negatively charged MS2 virus. They showed that the membrane could simultaneously remove bacteria and viruses from the water. They found that the demonstrated membrane was capable of completely removing *E. coli* by size exclusion and Log reduction value (LRV) of 4 for MS2 virus removal, which is shown in Table 5. This result was expected because the bacterial cell size (2 μm × 1 μm) was much larger than the maximum pore size of the demonstrated membrane. They found that the cellulose nanofibers with PVAm grafting have an LRV of 4 against MS2 viruses because the electrostatic interaction between the positively charged cellulose nanofiber surface and the negatively charged MS2 virus becomes favorable for the adsorption to take place. They concluded that the electrostatic interactions were found to be an essential factor for virus removal in the tested membrane instead of size exclusion, as in the case for bacteria removal [57].

Another work was done by Ma et al. [43], they prepared a multilayered nanofibrous microfiltration (MF) membrane system with high flux, a low pressure drop, and a high retention capability against both bacteria and bacteriophages (a virus model). The membrane was developed by impregnating ultra-fine cellulose nanowhiskers (with a diameter of about 5 nm) into an electrospun PAN nanofibrous scaffold

Table 5 Retention of MS2 of Composite Membranes

PET/PAN Layer Thickness (μm)	Max. Pore Size (μm)	Mean Flow Pore Size (μm)	Cellulose Nanofiber Loading (mg/cm^2)	LRV for *E. coli* Bacteria	LRV for MS2 Virus
100 + 40	0.78 ± 0.03	0.66 ± 0.01	0	6	0
100 + 40	0.73 ± 0.01	0.38 ± 0.01	0.2 ± 0.05[a]	6	0
100 + 40	0.78 ± 0.01	0.32 ± 0.01	0.2 ± 0.05[b]	6	>4

[a] *Cellulose nanofibers with PVAm grafting.*
[b] *Cellulose nanofibers without PVAm grafting.*
Reproduced with the permission from R. Wang, S. Guan, A. Sato, X. Wang, Z. Wang, R. Yang, B.S. Hsiao, B. Chu, Nanofibrous microfiltration membranes capable of removing bacteria, viruses and heavy metal ions, J. Membr. Sci. 446 (2013) 376–382, Elsevier Ltd.

(with a fiber diameter of about 150 nm) supported by a poly (ethylene terephthalate) (PET) nonwoven substrate (with a fiber diameter of about 20 μm). The cellulose nanowhiskers were anchored on the PAN nanofiber surface, forming a cross-linked nanostructured mesh (shown in SEM in Fig. 17) with very high surface-to-volume ratio and a negatively charged surface. They showed that the membrane had full retention capability against bacteria, for example, *E. coli* and *B. diminuta* (LRV larger than 6), and decent retention against bacteriophage MS2 (LRV larger than 2), which is shown in Table 6**.** They compared the performance of demonstrated membrane with a commercial membrane (GS0.22) prepared from mixtures of nitro cellulose and acetyl cellulose ester [43].

Asper et al. demonstrated that nanocellulose-based filter paper removed xenotropic leukemia virus by size exclusion. The filter paper was composed of 100% naturally derived cellulose. The filter paper was fabricated using cellulose nanofibers derived from *Cladophora* algae. They obtained good retention value (LRV $>$ 5.25) against the virus. They also showed that 100-nm latex beads and 50-nm gold nanoparticles can be filtered through the demonstrated nanocellulose-based filters, as shown in Fig. 18.

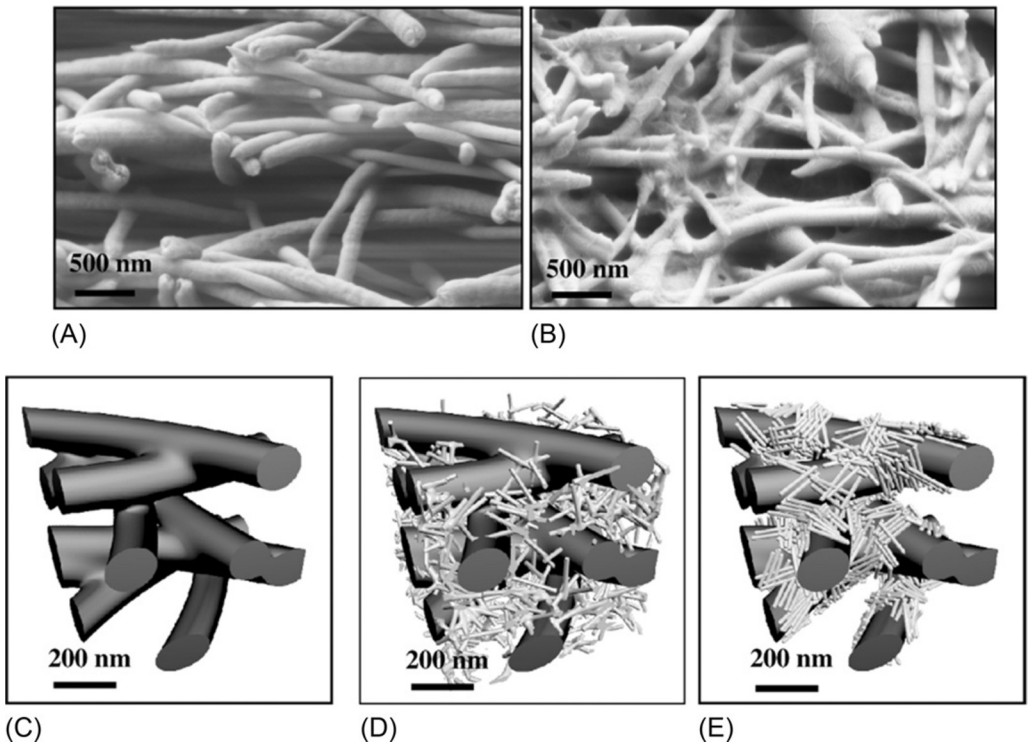

FIG. 17

(A) SEM images of cross-sectional views of PAN Electrospun nanofibrous scaffold and (B) cellulose nanowhisker-modified PAN electrospun nanofibrous scaffold. Schematic representations of electrospun nanofibrous scaffolds: (C) Scaffold before nanowhisker infusion; (D) infused nanowhiskers forming a loose cross-linked mesh; and (E) nanowhiskers collapsed onto the scaffold, forming bundles.

Reprinted with permission from H. Ma, C. Burger, B.S. Hsiao, B. Chu, Nanofibrous microfiltration membrane based on cellulose nanowhiskers, Biomacromolecules 13 (2012) (1) 180–186, American Chemical Society.

Table 6 Permeate Flux, Pressure Drop and LRV Against *E. coli*, *B. diminuta*, and MS2 of Electrospun PAN Nanofibrous Membrane, Cellulose Nanowhisker-Based Nanofibrous MF Membrane and GS0.22

Samples	Permeate Flux (L/m^2h)	Pressure drop (KPa)	*E. coli* (LRV)	*B. diminuta* (LRV)	MS2 (LRV)
PAN electrospun nano scaffolds	192	1.1	6	4	0
Cellulose nanowhisker nanofibrous membrane	192	3.0	6	6	2
GS0.22	192	7.6	6		1

Reproduced with permission from H. Ma, C. Burger, B.S. Hsiao, B. Chu, Nanofibrous microfiltration membrane based on cellulose nanowhiskers, Biomacromolecules 13 (2012) (1) 180–186, American Chemical Society.

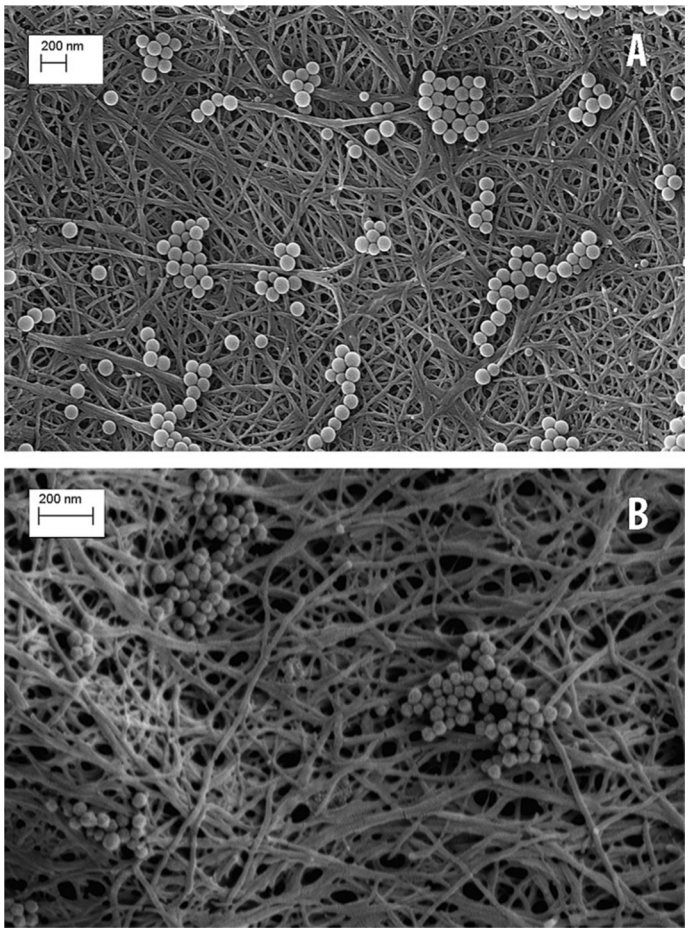

FIG. 18

SEM images of 100-nm latex beads (A) and 50-nm gold nanoparticles (B). Retained on the nanocellulose filter paper.

Reproduced with permission from M. Asper, T. Hanrieder, A. Quellmalz, A. Mihranyan, Removal of xenotropic murine leukemia virus by nanocellulose based filter paper, Biologicals 43 (2015) (6) 452–456, American Chemical Society.

FIG. 19

A photograph of cross-linked nanocellulose paper filter (diameter 26 mm) covered with a precipitate of Au nanoparticles following the filtration.

Reproduced with permission from A. Quellmalz, A. Mihranyan, Citric acid cross-linked nanocellulose-based paper for size-exclusion nanofiltration. ACS Biomater Sci. Eng. 1 (2015) (4) 271–276, American Chemical Society.

They concluded that the demonstrated nanocellulose-based filter paper could be useful for removing endogenous rodent retroviruses and retrovirus-like particles during the production of recombinant proteins [58].

Quellmalz et al. fabricated citric-acid cross-linked nanocellulose-based papers for the size-exclusion nanofiltration. They cross-linked the cellulose nanopapers with the citric acid to increase the wet strength of the paper. Their particle retention studies revealed that the fabricated paper was capable of removing tracer particles as small as 20 nm, as shown in Fig. 19. They concluded that the citric-acid cross-linking of nanocellulose was beneficial for developing paper-based sterile (virus) removal industrial filters [59].

Gustafsson et al. investigated how the pore-size distribution of the nanocellulose-based virus-retentive filter could be tailored. They prepared filter paper using cellulose nanofibers from *Cladophora* green algae via hot-press drying at varying drying temperatures. They showed that by controlling the rate of evaporation during hot-press drying, the pore-size distribution can be precisely tailored in the region between 10 and 25 nm [60].

4 CONCLUSION

Recently, advances in nanoscience and nanotechnology suggest that many of the current problems, including water quality, could be greatly diminished by using nanomaterials because of their good

adsorption efficiency, high surface area, and greater active sites for the interaction with various waterborne pollutants. However, these technologies pose significant challenges in terms of the limited availability of nanomaterials, their cost-effectiveness, and environmental concerns. In this context, nanocellulose is a valuable filtration material because it is affordable, sustainable, hydrophilic, inert, and stable at a broad range of pH/ionic strength. Nanocellulose has a high capacity and potential for reusability, importantly placing it among organic nanoscale materials with a possible use for remediating various toxic pollutants, such as bacteria, viruses, heavy metals, and dyes, among others, from water bodies. Cellulose nanomaterials' inherent fibrous nature and remarkable mechanical properties, coupled with their low cost, biocompatibility, and sustainable source, suggest a great potential as a component in water filtration membranes. Moreover, in this chapter work regarding oil-spill cleanup by using nanocellulose aerogels because of its high oil sorption capacity, excellent oil/water selectivity, and high buoyancy has been discussed. We also discussed nanocellulose-based membranes for water treatment using the electrospinning technique. The literature mentioned in this chapter provides new insight into fabricating low-cost and highly efficient nanocellulose structures, which will offer important opportunities in water purification applications.

REFERENCES

[1] V.K. Gupta, I. Ali, T.A. Saleh, A. Nayak, S. Agarwal, Chemical treatment technologies for waste-water recycling—an overview, RSC Adv. 2 (16) (2012) 6380.
[2] A.W. Carpenter, C.F. De Lannoy, M.R. Wiesner, Cellulose nanomaterials in water treatment technologies, Environ. Sci. Technol. 49 (9) (2015) 5277–5287.
[3] H. Voisin, L. Bergström, P. Liu, A. Mathew, Nanocellulose-based materials for water purification, Nanomaterials 7 (3) (2017) 57.
[4] N. Mahfoudhi, S. Boufi, Nanocellulose as a novel nanostructured adsorbent for environmental remediation: a review, Cellul. (2017) 1171–1197.
[5] R. Masoodi, R.F. El-Hajjar, K.M. Pillai, R. Sabo, Mechanical characterization of cellulose nanofiber and bio-based epoxy composite, Mater. Des. 36 (2012) 570–576.
[6] I. Usov, G. Nyström, J. Adamcik, S. Handschin, C. Schütz, A. Fall, L. Bergström, R. Mezzenga, Understanding nanocellulose chirality and structure-properties relationship at the single fibril level, Nat. Commun. 6 (2015).
[7] C.J. Chirayil, L. Mathew, S. Thomas, Review of recent research in nano cellulose preparation from different lignocellulosic fibers, Rev. Adv. Mater. Sci. (2014) 20–28.
[8] X. Liu, H. Chang, Y. Li, W.T.S. Huck, Z. Zheng, Polyelectrolyte-bridged metal/cotton hierarchical structures for highly durable conductive yarns, ACS Appl. Mater. Interfaces 2 (2) (2010) 529–535.
[9] P. Liu, P.F. Borrell, M. Božič, V. Kokol, K. Oksman, A.P. Mathew, Nanocelluloses and their phosphorylated derivatives for selective adsorption of $Ag^{+,}$ Cu^{2+} and Fe^{3+} from industrial effluents, J. Hazard. Mater. 294 (2015) 177–185.
[10] S. Vasudevan, M.A. Oturan, Electrochemistry: as cause and cure in water pollution-an overview, Environ. Chem. Lett. (2014) 97–108.
[11] M.S. Onyango, Y. Kojima, O. Aoyi, E.C. Bernardo, H. Matsuda, Adsorption equilibrium modeling and solution chemistry dependence of fluoride removal from water by trivalent-cation-exchanged zeolite F-9, J. Colloid Interface Sci. 279 (2) (2004) 341–350.
[12] Y. Al-Degs, M.A.M. Khraisheh, S.J. Allen, M.N. Ahmad, Effect of carbon surface chemistry on the removal of reactive dyes from textile effluent, Water Res. 34 (3) (2000) 927–935.

[13] Y. Zhou, S. Fu, L. Zhang, H. Zhan, M.V. Levit, Use of carboxylated cellulose nanofibrils-filled magnetic chitosan hydrogel beads as adsorbents for Pb(II), Carbohydr. Polym. 101 (1) (2014) 75–82.
[14] S. Hokkanen, E. Repo, S. Lou, M. Sillanpää, Removal of arsenic(V) by magnetic nanoparticle activated microfibrillated cellulose, Chem. Eng. J. 260 (2015) 886–894.
[15] L. Wojnárovits, C.M. Földváry, E. Takács, Radiation-induced grafting of cellulose for adsorption of hazardous water pollutants: a review, Radiat. Phys. Chem. (2010) 848–862.
[16] H. Sehaqui, U.P. de Larraya, P. Liu, N. Pfenninger, A.P. Mathew, T. Zimmermann, P. Tingaut, Enhancing adsorption of heavy metal ions onto biobased nanofibers from waste pulp residues for application in wastewater treatment, Cellul. 21 (4) (2014) 2831–2844.
[17] Z. Karim, M. Hakalahti, T. Tammelin, A.P. Mathew, In situ TEMPO surface functionalization of nanocellulose membranes for enhanced adsorption of metal ions from aqueous medium, RSC Adv. 7 (9) (2017) 5232–5241.
[18] C. Zhu, A. Soldatov, A.P. Mathew, Advanced microscopy and spectroscopy reveal the adsorption and clustering of cu(<scp>ii</scp>) onto TEMPO-oxidized cellulose Nanofibers, Nanoscale 9 (22) (2017) 7419–7428.
[19] X. Yu, S. Tong, M. Ge, L. Wu, J. Zuo, C. Cao, W. Song, Adsorption of heavy metal ions from aqueous solution by carboxylated cellulose nanocrystals, J. Environ. Sci. 25 (5) (2013) 933–943.
[20] S.S. Pillai, B. Deepa, E. Abraham, N. Girija, P. Geetha, L. Jacob, M. Koshy, Biosorption of Cd(II) from aqueous solution using xanthated nano banana cellulose: equilibrium and kinetic studies, Ecotoxicol. Environ. Saf. 98 (2013) 352–360.
[21] K. Singh, J.K. Arora, T.J.M. Sinha, S. Srivastava, Functionalization of Nanocrystalline cellulose for decontamination of Cr(III) and Cr(VI) from aqueous system: computational modeling approach, Clean Techn. Environ. Policy 16 (6) (2014) 1179–1191.
[22] R.R. Navarro, K. Sumi, N. Fujii, M. Matsumura, Mercury removal from wastewater using porous cellulose carrier modified with polyethyleneimine, Water Res. 30 (10) (1996) 2488–2494.
[23] X. Zhang, J. Zhao, L. Cheng, C. Lu, Y. Wang, X. He, W. Zhang, Acrylic acid grafted and acrylic acid/sodium humate grafted bamboo cellulose nanofibers for Cu^{2+} adsorption, RSC Adv. 4 (98) (2014) 55195–55201.
[24] A. Kardam, K.R. Raj, S. Srivastava, M.M. Srivastava, Nanocellulose fibers for biosorption of cadmium, nickel, and lead ions from aqueous solution, Clean Techn. Environ. Policy 16 (2) (2014) 385–393.
[25] P. Liu, H. Sehaqui, P. Tingaut, A. Wichser, K. Oksman, A.P. Mathew, Cellulose and chitin nanomaterials for capturing silver ions (ag+) from water via surface adsorption, Cellul. 21 (1) (2014) 449–461.
[26] A. Sheikhi, S. Safari, H. Yang, T.G.M. van de Ven, Copper removal using electrosterically stabilized nanocrystalline cellulose, ACS Appl. Mater. Interfaces 7 (21) (2015) 11301–11308.
[27] H. Ma, B.S. Hsiao, B. Chu, Ultrafine cellulose nanofibers as efficient adsorbents for removal of UO22+in water, ACS Macro Lett. 1 (1) (2012) 213–216.
[28] J.A. Sirviö, T. Hasa, T. Leiviskä, H. Liimatainen, O. Hormi, Bisphosphonate nanocellulose in the removal of vanadium(V) from water, Cellul. 23 (1) (2016) 689–697.
[29] J. Araki, M. Wada, S. Kuga, Steric stabilization of a cellulose microcrystal suspension by poly(ethylene glycol) grafting, Langmuir 17 (1) (2001) 21–27.
[30] N. Biçak, D.C. Sherrington, B.F. Senkal, Graft copolymer of acrylamide onto cellulose as mercury selective sorbent, React. Funct. Polym. 41 (1) (1999) 69–76.
[31] N. Zhang, G.L. Zang, C. Shi, H.Q. Yu, G.P. Sheng, A novel adsorbent TEMPO-mediated oxidized cellulose nanofibrils modified with PEI: preparation, characterization, and application for Cu(II) removal, J. Hazard. Mater. 316 (2016) 11–18.
[32] R.R. Navarro, K. Sumi, M. Matsumura, Improved metal affinity of chelating adsorbents through graft polymerization, Water Res. 33 (9) (1999) 2037–2044.

[33] A.L. Goffin, Y. Habibi, J.M. Raquez, P. Dubois, Polyester-grafted cellulose nanowhiskers: a new approach for tuning the microstructure of immiscible polyester blends, ACS Appl. Mater. Interfaces 4 (7) (2012) 3364–3371.
[34] A.L. Goffin, J.M. Raquez, E. Duquesne, G. Siqueira, Y. Habibi, A. Dufresne, P. Dubois, From interfacial ring-opening polymerization to melt processing of cellulose nanowhisker-filled polylactide-based nanocomposites, Biomacromolecules 12 (7) (2011) 2456–2465.
[35] B. Braun, J.R. Dorgan, L.O. Hollingsworth, Supra-molecular ecobionanocomposites based on polylactide and cellulosic nanowhiskers: synthesis and properties, Biomacromolecules 13 (7) (2012) 2013–2019.
[36] G. Crini, Non-conventional low-cost adsorbents for dye removal: a review, Bioresour. Technol. (2006) 1061–1085.
[37] R. Batmaz, N. Mohammed, M. Zaman, G. Minhas, R.M. Berry, K.C. Tam, Cellulose nanocrystals as promising adsorbents for the removal of cationic dyes, Cellul. 21 (3) (2014) 1655–1665.
[38] H.Y. Yu, D.Z. Zhang, F.F. Lu, J. Yao, New approach for single-step extraction of carboxylated cellulose nanocrystals for their use as adsorbents and flocculants, ACS Sustain. Chem. Eng. 4 (5) (2016) 2632–2643.
[39] S. Manna, D. Roy, P. Saha, D. Gopakumar, S. Thomas, Rapid methylene blue adsorption using modified lignocellulosic materials, Process. Saf. Environ. Prot. 107 (2017) 346–356.
[40] L. Jin, Q. Sun, Q. Xu, Y. Xu, Adsorptive removal of anionic dyes from aqueous solutions using microgel based on nanocellulose and polyvinylamine, Bioresour. Technol. 197 (2015) 348–355.
[41] A. Pei, N. Butchosa, L.A. Berglund, Q. Zhou, Surface quaternized cellulose nanofibrils with high water absorbency and adsorption capacity for anionic dyes, Soft Matter 9 (6) (2013) 2047.
[42] D.A. Gopakumar, D. Pasquini, M.A. Henrique, L.C. de Morais, Y. Grohens, S. Thomas, Meldrum's acid modified cellulose nanofiber-based polyvinylidene fluoride microfiltration membrane for dye water treatment and nanoparticle removal, ACS Sustain Chem. Eng. 5 (2) (2017) 2026–2033.
[43] H. Ma, C. Burger, B.S. Hsiao, B. Chu, Nanofibrous microfiltration membrane based on cellulose nanowhiskers, Biomacromolecules 13 (1) (2012) 180–186.
[44] H. Sai, R. Fu, L. Xing, J. Xiang, Z. Li, F. Li, T. Zhang, Surface modification of bacterial cellulose aerogels' web-like skeleton for oil/water separation, ACS Appl. Mater. Interfaces 7 (13) (2015) 7373–7381.
[45] S. Zhou, P. Liu, M. Wang, H. Zhao, J. Yang, F. Xu, Sustainable, reusable, and superhydrophobic aerogels from microfibrillated cellulose for highly effective oil/water separation, ACS Sustain. Chem. Eng. 4 (12) (2016) 6409–6416.
[46] R. Lin, A. Li, T. Zheng, L. Lu, Y. Cao, Hydrophobic and flexible cellulose aerogel as an efficient, green and reusable oil sorbent, RSC Adv. 5 (100) (2015) 82027–82033.
[47] W. Zhang, N. Liu, Y. Cao, X. Lin, Y. Liu, L. Feng, Superwetting porous materials for wastewater treatment: from immiscible oil/water mixture to emulsion separation, Adv. Mater. Interfaces (2017).
[48] Y. Meng, T.M. Young, P. Liu, C.I. Contescu, B. Huang, S. Wang, Ultralight carbon aerogel from nanocellulose as a highly selective oil absorption material, Cellulose 22 (1) (2015) 435–447.
[49] A. Prathap, K.M. Sureshan, Organogelator–cellulose composite for practical and eco-friendly marine oil-spill recovery, Angew. Chem. Int. Ed. 56 (32) (2017) 9405–9409.
[50] J.T. Korhonen, M. Kettunen, R.H.A. Ras, O. Ikkala, Hydrophobic nanocellulose aerogels as floating, sustainable, reusable, and recyclable oil absorbents, ACS Appl. Mater. Interfaces 3 (6) (2011) 1813–1816.
[51] H. Jin, M. Kettunen, A. Laiho, H. Pynnönen, J. Paltakari, A. Marmur, O. Ikkala, R.H.A. Ras, Superhydrophobic and superoleophobic nanocellulose aerogel membranes as bioinspired cargo carriers on water and oil, Langmuir 27 (5) (2011) 1930–1934.
[52] J. Feng, S.T. Nguyen, Z. Fan, H.M. Duong, Advanced fabrication and oil absorption properties of superhydrophobic recycled cellulose aerogels, Chem. Eng. J. 270 (2015) 168–175.
[53] H. Zhang, Y. Li, Y. Xu, Z. Lu, L. Chen, L. Huang, M. Fan, Versatile fabrication of a superhydrophobic and ultralight cellulose-based aerogel for oil spillage clean-up, Phys. Chem. Chem. Phys. 18 (40) (2016) 28297–28306.

[54] S. Wang, X. Peng, L. Zhong, J. Tan, S. Jing, X. Cao, W. Chen, C. Liu, R. Sun, An ultralight, elastic, cost-effective, and highly recyclable superabsorbent from microfibrillated cellulose fibers for oil spillage cleanup, J. Mater. Chem. A 3 (16) (2015) 8772–8781.
[55] N.J. Ashbolt, Microbial contamination of drinking water and disease outcomes in developing regions, Toxicol 198 (2004) 229–238.
[56] D.A. Gopakumar, S. Manna, D. Pasquini, S. Thomas, Y. Grohens, 19–Nanocellulose: extraction and application as a sustainable material for wastewater purification, in: New Polymer Nanocomposites for Environmental Remediation, Elsevier, 2018, pp. 469–486.
[57] R. Wang, S. Guan, A. Sato, X. Wang, Z. Wang, R. Yang, B.S. Hsiao, B. Chu, Nanofibrous microfiltration membranes capable of removing bacteria, viruses and heavy metal ions, J. Membr. Sci. 446 (2013) 376–382.
[58] M. Asper, T. Hanrieder, A. Quellmalz, A. Mihranyan, Removal of xenotropic murine leukemia virus by nanocellulose based filter paper, Biologicals 43 (6) (2015) 452–456.
[59] A. Quellmalz, A. Mihranyan, Citric acid cross-linked nanocellulose-based paper for size-exclusion nanofiltration, ACS Biomater Sci. Eng. 1 (4) (2015) 271–276.
[60] S. Gustafsson, A. Mihranyan, Strategies for tailoring the pore-size distribution of virus retention filter papers, ACS Appl. Mater. Interfaces 8 (22) (2016) 13759–13767.

CHAPTER

4 POLYMER/CARBON NANOTUBES MIXED MATRIX MEMBRANES FOR WATER PURIFICATION

Mohammad Hossein Davood Abadi Farahani*, Vahid Vatanpour†

*Department of Chemical & Biomolecular Engineering, National University of Singapore, Singapore, Singapore**

Faculty of Chemistry, Kharazmi University, Tehran, Iran†

1 INTRODUCTION

In the past few decades, global warming and climate changes have altered the natural systems in our environment, such as an increase in sea levels due to ice melting, an increase in surface water evaporation, and freshwater and soil submergence. These phenomena are concertedly converting the fresh water to salty water, are even making the seawater saltier, and are quickly diminishing the existing resources of fresh water. Water covers >70% of the earth's surface, but only 2% of that is fresh water, and even worse, 90% of the fresh water is frozen in glaciers [1]. The difficulty of remarkably controlling or diminishing of the climate changes, global warming, the salination of fresh water, and other types of the water pollutions; the deficiency of a cost-efficient technology for water purification has worsened the tension of having drinkable and clean water for the world's fast-growing population. Because of the importance of this issue and its threat to economic growth, sustainability, global health, and social development, a cost-effective technology for water purification is greatly needed. The failure of our endeavor for producing clean water might subsequently jeopardize human life and the ecosystem at the global scale.

Accordingly, several water purification technologies have been developed, introduced, and applied at both lab and industrial scales to actualize the obvious need for clean water. These technologies are generally categorized into three levels, such as primary (filtration, coagulation, flocculation, sedimentation, screening, and centrifugation), secondary (anaerobic and aerobic treatments), and tertiary (crystallization, solvent extraction, precipitation, distillation, evaporation, oxidation, ion exchange, adsorption, electrolysis, electrodialysis, and membrane technologies such as microfiltration (MF), ultrafiltration (UF), nanofiltration (NF), reverse osmosis (RO), forward osmosis (FO), membrane distillation (MD), and membrane bioreactor (MBR)) [2–4]. However, each technology has its own limitations, and most of them are not able to treat water pollutants effectively. Because some of these methods are operationally and energy intensive and, thus, are not cost-effective, they cannot be properly used at a commercial scale. Also, some methods, such as adsorption techniques, can be simply applied but cannot be used for the desalination of salty water [5]. In this regard, special attention has been paid to membrane technologies because of their numerous inherent advantages.

Nanoscale Materials in Water Purification. https://doi.org/10.1016/B978-0-12-813926-4.00009-4

Membrane separation processes as a widely accepted technology offer an environmentally friendly and an advanced process with low energy consumption for sustainably making fresh water. Membranes can be perfectly replaced with conventional energy-consuming separation processes, such as evaporation and distillation, because of their high chemical usage, energy, and handling costs. Therefore, membranes have a great core competency over other water purification methods [6]. Water purification membranes allow water to pass through them but reject solutes or particles in the dirty water. Among the aforementioned membrane technologies, pressure-driven processes (MF, UF, NF, and RO) are mostly employed by the industry for water treatment applications [7]. About 20% of the desalination plants in the world have utilized RO membranes to convert both brackish and seawater to the pure water [8, 9].

However, pressure-driven membrane technologies need energy because of the input of high pressure. The power consumption costs of an RO plant constitute more than half of the total cost. For instance, 3.4 kWh electricity is needed to desalinate 1 m^3 of seawater [10]. Other issues regarding membrane processes are fouling and pore blocking, which can significantly reduce the membrane modules' lifetime and can affect operational costs [11]. Accordingly, water flux enhancement without scarifying the solute rejection and fouling-resistance improvement are the determinative parameters, which can significantly affect both energy consumption and membrane lifetime [12].

To tailor membranes with improved flux and rejection and with enhanced antifouling characteristics, one must modify the membranes' surface chemistry. Most of the polymeric membranes possess hydrophobic surface characteristics, and thus, it can easily induce the deposition of the macromolecules on the surface of the membrane [13]. A well-established method for effectively improving the membranes' surface hydrophilicity and subsequently minimizing the membrane fouling is using charged membranes [14, 15]. Blending a hydrophilic polymer, such as polyethylene glycol, with a hydrophobic polymer is commonly known as an easy and useful technique for improving membranes fouling resistance [16]. Radiation-induced grafting, chemical grafting, and surface graft polymerization methods have been extensively developed for membranes' surface hydrophilicity enhancement [14, 17]. Furthermore, utilizing the advantages of composite membranes (organic-inorganic) to modify the drawbacks of the organic membranes has gained a great deal of attention. By doing so, using both physicochemical stability of inorganic materials and processability of the polymers for membrane fabrication is possible [18]. In particular, nanocomposite membranes composed of nanosized inorganic material and polymers are worth studying because of their improved characteristics, such as higher hydrophilicity, enhanced permselectivity, and better fouling resistance [19].

Many reports have demonstrated a huge potential for carbon nanotubes (CNTs) as a nanomaterial for improving the polymeric membranes' separation properties. This is due to the fact that CNTs have several unique properties, such as low mass density, high flexibility, effective π-π stacking interaction with aromatic compounds, very low frictional coefficients on their internal surface, a large length-to-diameter ratio, and the existence of substantial nanochannels [20, 21]. In particular, the frictionless water molecule transport through CNTs' hollow structure make CNTs an appropriate choice for high-flux membrane development. Furthermore, an energy barrier might be formed at the CNTs' channel entries because of their suitable pore diameter, which could reject ions and facilitate water passage through the nanotubes [22]. In addition, CNTs' pores could be modified to reach the desired selectivity and rejections [23]. Thus, CNTs' embedded membranes can be applied for size-controlled separation in multipollutant solutions.

In the following sections, the application of CNT-embedded nanocomposite membranes in water purification, CNT synthesis and functionalization, the mechanism of water transport through CNTs, the fabrication of CNT-embedded MMMs, controlling parameters in CNT-embedded membranes, and more details on the status of the CNT-based membranes in the water purification market, as well as their current challenges, are comprehensively discussed.

2 CARBON NANOTUBE APPLICATIONS IN WATER PURIFICATION

The discharge of industrial, agricultural, or domestic wastewater composed of a wide range of contaminants has globally become a major concern because of its effect on the water quality. The contaminants found in wastewater include heavy metal ions [24–27], 1,2-dichlorobenzene [28, 29], and dioxin [30] and are highly carcinogenic, toxic, and nondegradable, which result in accumulative poisoning, nervous system damage, and cancer. A highly efficient sorbent, such as CNT, can effectively remove these contaminants because of its controlled pore-size distribution and high surface's active site-to-volume ratio compared to conventional powder or granular activated carbon, both of which have inherent limitations such as the sorption activation energy and low surface active sites. Based on the literature, the adsorption capacity of CNTs highly depends on both the nature of the sorbate and CNTs' surface functional groups. For example, a higher surface acidity (lactonic, carboxylic, and phenolic groups) may facilitate the adsorption of polar compounds [27]. On the other hand, a higher adsorption capacity for nonpolar compounds such as polycyclic aromatic hydrocarbons was found in the case of using the unfunctionalized CNTs [31]. The CNTs' sorption behaviors mainly rely on the physical interaction for nonpolar compounds and chemical interaction for polar compounds, both of which are fitted with Freundlich or Langmuir isotherms [25, 28, 31, 32].

Besides serving as both inorganic- and organic-contaminant sorbent, CNTs have recently been utilized as nanofilters to remove or decrease particles in wastewater treatment process [33]. The functionalization of the CNTs with the attachment of different groups at the pore entrances can result in variation in the specific selectivity of the CNT filters [34]. In spite of CNTs' hydrophobic characteristic, they are extraordinary water transporters. This ability has been confirmed by molecular dynamics simulations that prove that CNTs' interchannel hydrophobicity results in weak interaction with water molecules, thus providing a frictionless and fast water flow [35]. Additionally, research has revealed the CNT nanofilters' capability for pathogenic microorganism removal because of its retaining microorganisms on the CNT surface based on a depth filtration mechanism [36, 37]. A CNT membrane filter composed of bundles of single-walled CNTs (SWCNTs) and poly(vinylidene fluoride) (PVDF) has shown a highly efficient performance in a complete capturing and removing *E. coli* bacteria at low pressure [38].

Apart from CNTs' applications as nanofilters and sorbents, they have shown strong antimicrobial properties in water purification. These characteristics allow the CNTs to be replaced with chemical disinfectants for controlling microbial pathogens [39, 40]. Using CNTs in water disinfection purification avoids the creation of harmful disinfection by-products, such as haloacetic acids, aldehydes, and trihalomethanes, because they are rather inert in water and are not strong oxidants. For improving CNTs' dispersibility in water, using polymers or surfactants, such as polyvinylpyrrolidone, Triton-X, or sodium dodecyl benzenesulfonate, is suggested [41]. Kang et al. [40] have proved that direct contact

of SWCNTs with *E. coli* cells results in severe membrane cell damage and subsequent cell inactivation, which confirms CNTs' strong antimicrobial properties.

One of the most significant uses of CNTs in water purification is incorporating them into the polymeric membranes to enhance the membranes' properties, such as increasing flux, selectivity, antifouling properties, and mechanical strength [9]. The so-called mixed matrix membranes (MMMs), interestingly, use both the ease of processing and low cost of organic polymeric membranes and the functional characteristics and mechanical strength of the inorganic materials at the same time. It has been discussed that CNTs exhibit antimicrobial activity; therefore, using them in MMMs presents an opportunity for enhanced antifouling or disinfection membranes. An MMM composed of multiwalled CNTs(MWCNTs)/polysulfone (PSf) has been cast by Choi et al. by using nonsolvent-induced phase separation (NIPS) [42]. This work has been chosen as an example of what would happen by adding CNTs into the polymeric matrix, and most of the research on CNT/polymer MMMs for water purification have reported almost the same observations. In the previously mentioned MWCNT/PSf MMMs, the CNTs were acid-pretreated to avoid aggregation and to assist in their dispersion in the solvent. The results showed an improved surface hydrophilicity for MMMs because of the presence of carboxylic acid functional group on the CNTs' surface. The membranes' pore size increases by adding CNTs up to 1.5 wt%, and then it decreases, becoming smaller than that of pristine PSf at 4 wt%. An enhanced rejection and water permeance were observed for the CNTs' concentration of 2 wt%, probably owing to the improved hydrophilicity and antifouling properties. At higher concentration of CNTs, namely, 4 wt%, the rejection increases, but the flux begins to drop. These could be related to the pore blockage at high concentrations of CNTs and to having structural defects at low CNT loadings. However, better performance was obtained by Vatanpour et al. [20] when amine-functionalized CNTs have been used to fabricate polyethersulfone (PES) NF MMMs. A flux improvement of 75%, an enhanced hydrophilicity, a much better selectivity due to the decreased molecular weight cutoff (MWCO), a lower tendency to BSA adsorption, and a 46% flux recovery ratio enhancement as compared to bare a PES membrane were achieved by incorporating only 0.045 wt% amine-functionalized CNTs into the PES.

In essence, using CNTs in water purification processes is significantly important because of their extraordinary properties, which offer a broad range of applications such as sorbent, disinfectant, nanofilter, and inorganic filler in MMMs.

3 SYNTHESIS AND FUNCTIONALIZATION OF CARBON NANOTUBES

3.1 SYNTHESIS METHODS OF CARBON NANOTUBES

The main techniques applied for the synthesis of both SWCNTs and MWCNTs in significant amounts—laser ablation, arc discharge, chemical vapor deposition (CVD) from hydrocarbons, and gas-phase catalytic growth from carbon monoxide (CO) [43]—are illustrated in Fig. 1.

The most widely used and novel methods are laser ablation and arc discharge, but they are used to produce only rather small quantities of CNTs. Also, the resultant products usually include substantial amounts of impurities such as amorphous carbon, catalyst particles, and nontubular fullerenes [43]. Therefore, purification is needed to isolate the valuable product (CNTs) from undesirable by-products (impurities) before exploring CNTs' properties for their potential applications.

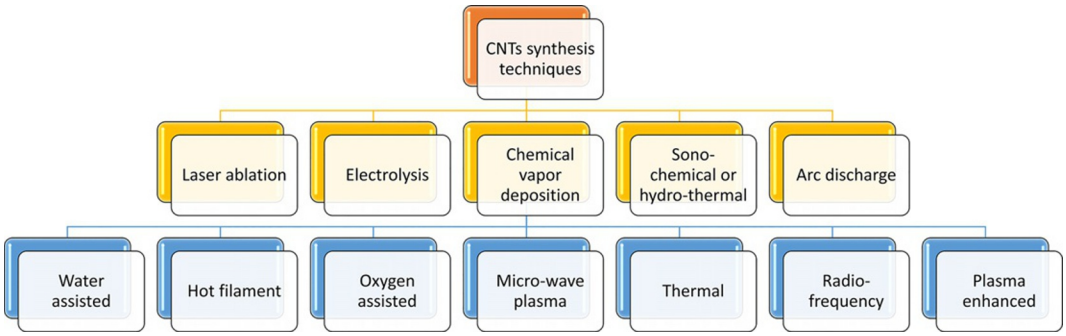

FIG. 1

Currently used techniques to synthesize carbon nanotubes (CNTs).

Reproduced with permission from J. Prasek, J. Drbohlavova, J. Chomoucka, J. Hubalek, O. Jasek, V. Adam, et al., Methods for carbon nanotubes synthesis—review. J. Mater. Chem. 21 (2011) (40) 15872–15884, Royal Society of Chemistry.

The previously mentioned limitations were the motivation for developing gas-phase synthesis methods, for example, low-temperature CVD technique (<800°C), in which carbon-containing gas decomposition synthesizes CNTs. The continuous production of large amounts of CNTs is facilitated by these gas-phase methods, in which a flowing gas can continually replenish the feed source. Furthermore, the synthesized CNTs by CVD techniques generally possess a quite high purity, and thus, it requires fewer subsequent purification steps [44]. For instance, a modified gas-phase CVD technique can be applied to synthesize SWCNTs with >90% (w/w) purity using $Fe(CO)_5$ and CO, which is known as the high-pressure carbon monoxide disproportionation (HiPCO) process [45]. The CNTs produced by the HiPCO techniques has numerous advantages, including the ease of equipment operation, the comparatively low cost, the high purity of the product, and the capability for large-scale production as compared to the conventional methods.

3.2 FUNCTIONALIZATION OF CARBON NANOTUBES

Although the excellent characteristics of the CNTs make them outstanding candidates for numerous applications, the limited processability because of the lack of dispersibility in most common solvents has prevented the development of CNTs for special purposes [20, 46]. By using ultrasonic energy, CNTs' dispersion in some solvents is still doable; however, in most cases, it can be interrupted because of the immediate precipitation. To overcome this problem and facilitate the sustainable dispersion of the CNTs in most solvents, one must utilize the functionalization of the CNTs by using both the covalent attachment of polar functional groups (—OH, —COOH, —COH, and $—NH_2$) to the CNTs' surface and the noncovalent adsorption of different functionalized molecules on the CNTs' surface [47]. The functionalization of the CNTs using polar groups could be easily done by using standard techniques of synthetic chemistry. The resultant functionalized CNTs (F-CNTs) have the potential for a range of further reactions including esterification, alkylation, silanation, and thiolation [47–49]. Moreover, the chemical functionalization of CNTs enables them to participate in strong interfacial bonds with most of the polymers, which are in favor of the fabrication of the CNTs' incorporated nanocomposites with an enhanced mechanical strength. However, the main drawback of the

covalent functionalization is the change of hybridization of the carbon atoms from sp^2 to sp^3 because of the reaction. The result is lower electrical conductivity because of the loss of π-conjugation, and thus, the solubility of the CNTs decreases [46]. However, the noncovalent functionalization of the CNTs uses the adsorption of the polymeric molecules or surfactant. Accordingly, it is an interesting alternative technique to improve both the processability and the dispersibility of the CNTs in the solvent without scarifying their physical properties. For example, using sodium dodecyl sulfate (SDS) as a commercial surfactant with ionic, hydrophilic head groups stabilizes the CNTs' dispersion, owing to the electrostatic repulsion mechanism [50]. This observation could be related to the amphiphilic nature of the CNTs [51].

3.3 USING F-CNTs FOR MMM FABRICATION

As mentioned earlier, a homogeneous and well-dispersed nanocomposite containing a polymer and F-CNTs could be obtained after creating some active functional groups such as hydroxyl, amine, and carboxyl acid on the CNT's surfaces [52]. MMMs containing F-CNTs possess a substantial areal density of graphitic cores with entrances that can be tailored by various molecules of required hydrophilicity, chemical functionality, or length [53]. The most commonly and conventionally used technique for CNTs' functionalization is their surface modification with the aid of strong acids [54]. The acid-treated CNTs contain carboxyl and hydroxyl groups at the defect sites and open ends, which substantially increases their dispersion in a polymeric dope solution containing polymers and polar organic solvents such as *N*, *N*-dimethylformamide (DMF), *n*-methyl-2-pyrrolidone (NMP), and dimethylsulfoxide (DMSO). For example, the nanofiltration membranes were prepared by acid-oxidized MWCNTs being embedded in PES [55]. The hydrophilicity of the membrane was improved by mixing MWCNTs because of the migration of functionalized MWCNTs to the membrane surface through the phase-inversion process. SEM images showed that very large macrovoids appeared in the sublayer because of the addition of low quantities of acidified MWCNT, leading to an increase of pure water flux.

As mentioned earlier, the F-CNTs are also able to interact with polymers and affect both the crystallinity and the mobility of the polymer chains [56]. However, the functionalization reaction conditions should be adequately controlled to diminish possible defects or damage to the CNTs' structure, which can result from the harsh reaction conditions. Therefore, a proper control on reaction during chemical treatment of CNTs is required for generating enough functional groups onto the CNTs.

In addition to the higher F-CNTs/polymer compatibility, functional groups of the CNTs' pore surfaces can also result in improved selective separations by using a forced chemical interaction between the functional molecules and permeates [57].

4 WATER TRANSPORT MECHANISM THROUGH CNTs' HOLLOW TUBES

The structurally stable and perfect nanochannels with different sizes are provided by CNTs' tubular structure, and thus, this property introduces numerous potential applications for the CNT channels [58]. In particular, the fluid or gas transport phenomena through the CNT channels have attracted researchers' attention for drug delivery, biomimetic selective transport of ions, and, especially, membrane separation applications. This attraction is because of the extraordinary improvement of pressure-driven water flow through CNTs as compared to other porous material. For instance, experimentally

obtained pressure-driven flow velocities in MWCNT membrane pores (inner diameter of 7 nm) were 4 to 5 times higher than the predicted velocities from Newtonian flow using the Hagen – Poiseuille equation [59]. Moreover, the measured water flow surpassed values calculated by continuum hydrodynamics models by more than three orders of magnitude in double-walled CNT pores (inner diameter of 1.6 nm) [60]. As the channel pore size increases, especially when this size approaches the size of the molecule, the importance of the interaction between the pore walls and the transported molecules increases. Additionally, this interaction can forcefully affect the thermodynamic state of the molecules in the existing limited system, resulting in possible different transport characteristics in the CNTs' nanoporous media as compared to the common transport in bulk media [61]. A fundamental mechanism of molecular transport through a porous media is diffusion. Self-diffusivity and transport diffusivity are two different pure-fluid diffusivities and are two of the most important topics in transport phenomena. The former is related to the diffusion of a single tagged molecule through a fluid while the latter is the macroscopic mass transport of molecules in a system when the concentration gradient is the driving force [62]. Performing both experimental and theoretical studies on the transport system within and through an individual nanotube is highly challenging because it is not easy to follow and detect the transport behavior of transported molecules inside the nanochannels and to have a self-supporting nanomaterial that possesses a uniform pore size, with a pore size distribution of 1–100 nm [53]. To overcome this difficulty, one may use computational calculation methods, such as molecular dynamic simulation, to study the fluid transport through nanotubes and its behavior at a microscopic level [63].

Because CNTs are known as a promising inorganic material for membrane technology, the fluid transport through them is quite attractive to explore. Evidently, recent scientific publications have proved the high fluid fluxes due to the molecular ordering phenomena inside the nanopores and the atomic-scale smoothness of the CNT walls [64]. To fully understand CNTs' effect in MMMs, knowledge of fluid flow for the cylindrical channel of the nanopores would be useful. Despite several similarities between transport phenomena in cylindrical and slitlike pores (microscopic zeolite channel), the fluid behavior in CNTs' narrow pores is more detailed and complicated [65].

The shape of the pore and the curvature of the surface are dominant factors that strongly affect the fluid transport phenomena in nanopores. Because water in different media shows different properties and the transport mechanism is forced in many systems, density distribution and transport phenomena of water molecules under narrow and limited nanotube channels are important matters. A reduction in the CNTs' diameter in the order of several nanometers can lead to a different observation from that of bulk [66]. Based on this observation, a smaller CNT diameter results in a lower flow rate. This is because of the increase in the mean distance between a carbon atom and a water molecule that leads to the weaker water-CNT interaction. The significant impacts of helicity, pore size, and molecule-wall interaction of CNTs on molecular motion and dynamic behaviors of water are limited in various nanotubes, which, in turn, control the transport properties in CNTs [61]. Based on the literature, the exceptionally fast diffusion for water molecules is facilitated by the intrinsic smoothness of the interior CNTs [67–69]. In other words, the weak carbon-water interaction that is due to the smooth and frictionless CNT surfaces facilitates the substantially high flow velocity. However, the complexity of the flow rate might be increased by different parameters, such as water orientation, interatomic distances, and channel structure. In sum, the excellent, fast water transport through CNTs as compared to other materials, such as polymeric membranes with rough walls, has ensured their fascinating and bright future in water purification membranes.

5 FABRICATION OF CNT-EMBEDDED MEMBRANES FOR WATER PURIFICATION

During past few decades, membrane separation processes, in general, and membranes for water purification, in particular, have attracted significant attention as a promising environmentally friendly, cost-effective, and energy-efficient paradigm for separation process [15, 70, 71]. The membranes that can be used for water purification are MF, UF, NF, RO, FO, MD, and MBR. A key parameter, which results in the replacement of the conventional separation technologies with the existing membrane separation processes, is simultaneously decreasing the production costs and enhancing the performance of the membranes. A limit in the trade-off between permeability and selectivity seemingly occurs for the polymeric membranes, and thus, a new class of membrane material, namely, MMMs, was introduced by Zimmerman et al. [72] and is being considered by many researchers [53, 73]. These MMMs can be fabricated by embedding inorganic nanoparticles into the polymer matrix to use the benefits of the inorganic media and processability and economic advantages of polymers to enhance both selectivity and permeability. One of the most promising inorganic nanoparticles is CNTs, and therefore, in this part, the focus is on CNT-embedded MMMs and vertically aligned CNT (VA-CNT) membranes [74, 75]. The former can be fabricated by directly adding CNTs into the polymeric dope; however, the latter can be synthesized by arranging perpendicular CNTs with supportive filler contents, usually epoxy or silicon nitride, between tubes and was introduced by Hinds et al. [76]. Table 1 shows the differences of polymeric membranes and MMMs.

Choi et al. [42] have found that MWCNT-embedded polysulfone membranes show enhanced flux and rejection as compared with a pristine polysulfone membrane because of the hydrophilicity enhancement in the presence of MWCNTs. Similarly, MWCNT/polysulfone UF membranes showed improved flux, lower protein adsorption, but poorer rejection as compared with the pristine polysulfone membrane [77]. Vatanpour et al. [20] demonstrated that NF MMMs composed of amine-functionalized MWCNT embedded in PES have higher water flux, enhanced hydrophilicity, enhanced salt rejection controlled by the Donnan exclusion mechanism, and better antifouling resistance because of the improved hydrophilicity and surface roughness. As it is discussed previously, the enhanced water flux is attributed to frictionless CNT channels. Baek et al. [78] have demonstrated that aligned CNT membranes exhibited a water flux 3 times higher than that of the commercial UF membrane. Furthermore, they showed an improved biofouling resistance as well as substantially lower levels

Table 1 A Comparison Between Polymeric Membranes and MMMs

Item	Polymeric Membrane	MMMs
Solvent compatibility	Limited	Limited
Thermal and chemical stability	Moderate	High
Mechanical strength	Good	Excellent
Handling	Robust	Robust
Swelling	Frequent	Not frequent
Separation performance	Moderate	High
Fabrication complexity	Low	Moderate
Production cost	Low	Moderate

of bacterial attachment. Shaoyun et al. [79] have prepared vertically aligned VA-MWCNTs embedded in PES with a superefficient pathway for water transport, leading to 3 times higher water flux as compared to MWCNT/PES with randomly oriented MWCNTs. Furthermore, the vertically aligned MWCNTs/PES membranes have shown an excellent antifouling property, in particular a water flux 10 times greater than that of pristine PES membrane operating under same conditions. Interestingly, adding CNTs to the polymer matrix has significantly improved the mechanical strength and durability of the fabricated MMMs [80]. The main conclusions regarding CNT-embedded MMMs are summarized in Table 2.

Table 2 Main Observation in Different CNT/Polymer MMMs for Water Purification

Substrate	Main Observation	References
Polyethersulfone	• Enhanced antifouling resistance and high flux recovery ratio (FRR) • Improved water permeance	[81]
Polyethersulfone	• Increased hydrophilicity • Enhanced antifouling resistance and high FRR • Improved water permeance • Increased salt rejection • Increased surface roughness	[20]
Polyethersulfone	• Increased hydrophilicity • Enhanced antifouling resistance against whey proteins and high FRR	[82]
Polysulfone	• Increased hydrophilicity • Improved water permeance and decreased solute rejection up to 2 wt% CNT loading • Enhanced permeability and diminished rejection at higher CNT loadings	[42]
Polysulfone	• Enhanced hydrophilicity • Increased surface roughness • Improved mechanical stability	[83]
Polysulfone	• Enhanced heavy metal rejection • Increased thermal stability	[84]
Polysulfone	• Improved fouling properties (biofouling)	[85]
Polysulfone	• Improved water flux up to 100% • Enhanced solute rejection • Excellent protein fouling resistance	[86]
Polysulfone	• Increased water flux up to 160%	[87]
Polyvinylidene fluoride	• Increased self-cleaning ability • Enhanced fouling properties • Salt rejection order ($Na_2SO_4 > MgSO_4 > NaCl$)	[88]
Polyvinylidene fluoride	• Size exclusion elimination of *E. coli* cells • High rejection for viruses • High inactivation rate for bacteria within 20 min contact time	[38]
Polyamide/polysulfone	• Improved water permeance • Increased bacterial cytotoxicity (60%/h) • Excellent biofouling resistance	[89]
Polymethylmethacrylate	• Improved water flux (60%) with enhanced selectivity • High Na_2SO_4 rejection (99%)	[90]

6 FACTORS GOVERNING THE QUALITY OF CNT-EMBEDDED MEMBRANES

CNT membranes have emerged as the best possible water purification technique; however, each membrane separation technology has its pros and cons. It has the potential to be commercially viable in future because it has shown excellent performance as compared to commercially available membranes. The CNT-embedded membranes must meet some standards, such as better desalination capability, water permeability, antifouling resistance, robustness, energy savings, scalability, material costs, and compatibility with available industrial settings. The CNT membranes are known for their superior water permeability; better desalination, in some cases; and enhanced antifouling resistance; however, the application of these membranes is still hindered by the complication of handling, the higher membrane fabrication cost, and the technology limitations for continuous and defect-free membrane formation [72, 91, 92]. Another type of membrane, the so-called inorganic membrane, is much more expensive than polymeric membranes. To overcome the performance limitations of organic polymeric materials and to minimize the use of inorganics in the membrane fabrication, which can lead to a cheaper membrane than an inorganic membrane with an enhanced separation performance than that of the polymeric membrane, the competent option is mixed matrix membrane. A slightly higher price for the organic/inorganic MMMs or CNT-based membranes can only be compensated when these membranes could achieve super-high performance compared to the polymeric membranes. In comparison, that the superb properties of the MMMs have significantly surpassed that of the inorganic and polymeric membrane is clear. Thus, MMMs have been extensively investigated, and they showed an excellent potential for today's membrane separation market. The processability of these heterogeneous membranes is as same as polymeric membranes, and it can be used to fabricate both flat-sheet and hollow-fiber configuration as illustrated in Fig. 2 A and B, respectively. Nonetheless, selecting the membrane's configuration is highly dependent on the expected application, and thus, it is important to fabricate MMMs in useful configurations to fully utilize the maximum of the usefulness provided by inorganic materials [93]. Another advantage of MMMs is the robustness of this membrane, which is provided by the polymeric part solving the inherent fragility problem of the inorganic membranes [93–95].

The polymeric layer in the fabricated MMMs is tightly packed with inorganic materials, such as TiO_2, ZnO, CNT, or other porous inorganic materials, to form a dense mixed matrix layer [96–98]. The nanoporous materials are the size and shape selective in nature and consequently provide molecular separation discrimination by permitting smaller molecules to pass at a higher rate than that of larger molecules. To achieve a defect-free MMM, controlling the adhesion between the nanoparticles and the polymer phase is necessary [99]. The very first experiences on MMM fabrication using zeolites and glassy polymers resulted in the formation of voids at the interface between the filler and the polymer, owing to the weak filler-polymer interaction that significantly diminished the separation performance, especially selectivity, of the nanocomposite membrane compared to the pristine membrane [100, 101]. To remove those selectivity diminisher gaps between nanofillers and the polymer, various techniques have been developed [102–105]: [1] surface functionalization of the nanofiller for a better compatibility with polymer, [2] chemically linking the two components together or adding plasticizer to enhance the polymer flexibility, and [3] casting at elevated temperatures and then removing the dense films from the casting surface at solution T_g.

Based on the literature, MMMs may show significantly improved selectivity and permeability that are far beyond the inherent capability of pristine polymeric membrane [106–109]; however, a deep

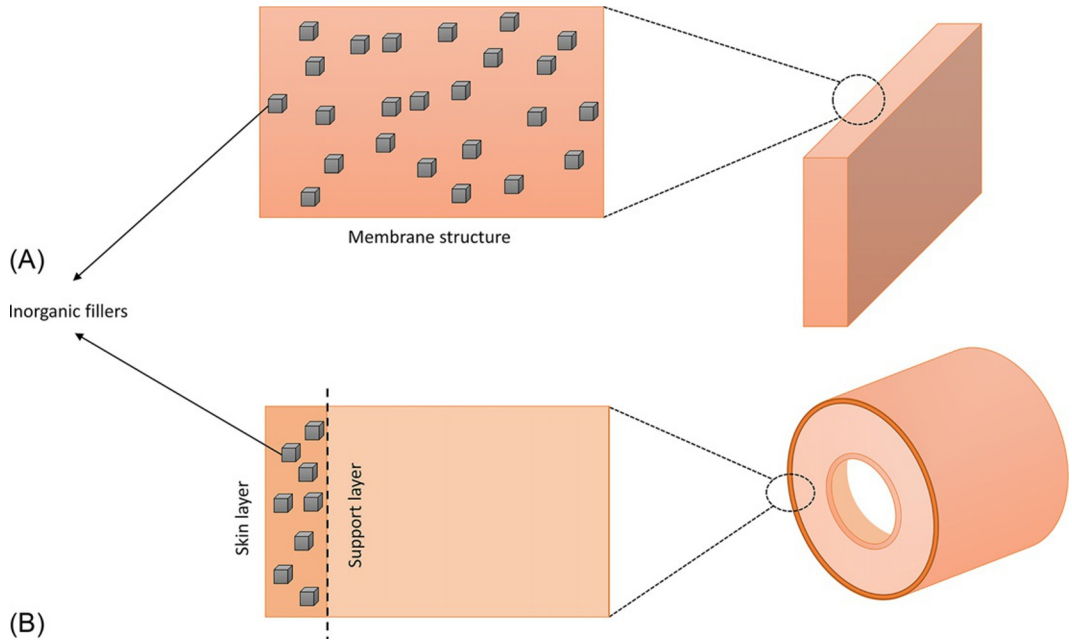

FIG. 2

Schematics of inorganic/polymer MMMs. (A) Asymmetric flat-sheet MMM. (B) Asymmetric hollow fiber with a mixed matrix selective layer.

knowledge of the variation of the permeability for a penetrant with the concentration and type of nanofiller materials is required to make full use of the MMMs' advantages in design and operation [94]. The selected inorganic nanofiller in MMMs plays a crucial role in the membrane selectivity improvement with the absence of defects compared to the insignificant function of the polymer matrix [102].

CNT-based membranes offer another advantage, which is the matching of pore size (pore diameter) of the CNT to that of target molecules. By doing so, a successful improvement in both flux and selectivity can be obtained. Accordingly, the small dispersion of CNTs with an initial pore diameter close to that of target molecule size is beneficial [76]. Controlling the nanotube size can be achieved by varying the size of the catalyst particles during the CNTs' growth, and therefore, it enables the synthesis of the CNTs with nanometer-scale diameter dispersion so that there would be a potential for tuning the porosity of the membranes [110–112]. Accordingly, by using CNTs in the membrane, a perfect control of pore dimension at the nanometer scale will be provided by the CNTs' inner diameter.

Using CNTs to fabricate MMMs for water purification is also originated by the CNTs' enhanced antifouling properties with regard to commercial UF and NF membranes. As it is tabulated in Table 2, using functionalized CNTs can improve the fouling resistance by introducing some hydrophilic functional groups, such as —NH_2, —COOH, and —OH, on the surface of the membrane because of the incorporation of the functionalized CNTs into the MMM. Based on the literature, that CNTs have a potential application in water purification membranes by increasing the overall performance of membranes while minimizing fouling, therefore diminishing operating costs and improving operational

lifetimes, is crystal clear. Moreover, using functionalized CNTs instead of pristine CNTs results in lower CNT aggregation and improved CNT dispersibility into the polymer matrix.

In sum, for a fruitful and practical MMM fabrication for water purification with the incorporation of nanofillers into a polymer, one must pay attention to certain membrane development criteria. These criteria include (1) the properties and compatibility of inorganic nanofiller with the polymer material; (2) the development of a defect-free MMMs that can be associated to the segmental conformance of the polymer at polymer/nanofiller interface and mechanical adhesion; (3) the concentration of nanofiller in the polymer matrix (aggregation of nanoparticles may occur at high concentrations); (4) the choice of nanofiller for any specific application; (5) the choice of nanofiller with antifouling characteristics, such as CNTs with functional groups; and (6) a sufficiently thin selective layer to provide desirable flux [113, 114].

7 COMPARISON OF CNT-EMBEDDED MEMBRANES WITH OTHER COMMERCIALLY AVAILABLE MEMBRANES IN THE WATER PURIFICATION INDUSTRY

Nanotechnology, with unique applications and tremendous versatility, has gained widespread attention for improving the sustainability of water purification technologies, especially membrane-based processes [115, 116]. Membrane science and nanotechnology synergistic combinations lead to promising and sensible approaches to fabricate tunable and novel membranes, that is, nanocomposite membrane or mixed matrix membrane, that possess outstanding features, namely, lower energy consumption, better separation properties, and more environmentally friendly compared to available commercial membranes in the market. Apart from the complexity of the nanocomposite membrane fabrication, which currently is not a challenge thanks to the extensive research that has been done in this area, the main marketplace difficulty regarding these membranes is producing cost-effective nanocomposite membranes. Therefore, cost-effective nanocomposite membranes should provide higher savings for industries because the high efficiency of the membranes must surpass the high cost of membrane module production. Accordingly, using a cheap, earth-abundant, and easily synthesizable inorganic nanofiller in nanocomposite membrane material can definitely control membrane production costs, and thus, these membranes will be ready to be replaced with the currently available commercial membranes. Among the nanomaterials, CNTs, especially MWCNTs, are rather cheap, are easy to synthesize, and are from an earth-abundant element that can be used to improve the separation, chemical stability, mechanical strengths, and antifouling properties of the membranes [117]. Furthermore, a little quantity of functionalized CNTs, for instance, 0.045 wt% of NH_2-MWCNTs in PES, would be enough to extraordinary enhance the flux, retention, hydrophilicity, and antifouling properties of the nanocomposite membrane as compared with pristine membrane [20]. Thus, the fabricated nanocomposite membranes consisting of a low concentration of MWCNTs is much more cost-effective than those using other inorganic materials that need high concentrations of those nanomaterials to improve membrane properties [96, 97].

A benchmark comparison would be useful to evaluate the performance of the CNT-based MMMs. In Table 3, the UF, NF, and RO CNT-based MMMs are compared with the commercially available membranes in the market.

Table 3 Benchmark Study on UF, NF, and RO CNT-Based MMMs and Commercial Membranes

C/L[a]	Membrane	Material	MWCO (Da)	Main Properties	References
C	UH004 (UF)	PESH[b]	4 k	Retention (92%–99%) for Dextran 10	[118]
C	UP005 (UF)	PES[c]	5 k	Retention (91%–98%) for Dextran 10	
C	UP010 (UF)	PES	10 k	Retention (63%–85%) for PVP 17 k	
C	UH050 (UF)	PESH	50 k	Retention (75%–88%) for PVP 30 k	
C	NP010 (NF)	PES	1 k	Retention (35%–75%) for Na_2SO_4	
C	PA20, Hoechst (UF)	PA[d]	20 k	PWF[e] (∼45 LMH) @ 1 bar	[119]
C	PA20H, Hoechst (UF)	Modified PA	20 k	PWF (∼17 LMH) @ 1 bar	
C	FS81, Dow Denmark (UF)	PVDF[f]	20 k	PWF (∼72 LMH) @ 1 bar	
C	Etna20A, Dow Denmark (UF)	Modified PVDF	20 k	PWF (∼58 LMH) @ 1 bar	
C	0.025 CME, Millipore (UF)	Mixed cellulose esters	PS[g] = 0.025 μm	PWP[h] (∼100 LMH. bar^{-1}) @ 2 bar	[120]
C	0.05 CME, Millipore (UF)	Mixed cellulose esters	PS = 0.05 μm	PWP (∼100 LMH. bar^{-1}) @ 2 bar	
C	0.05 PC, Millipore (UF)	Aromatic polycarbonate	PS = 0.05 μm	PWP (∼50 LMH. bar^{-1}) @ 2 bar	
C	30 PVDF, Osmonic (UF)	PVDF	30 k	PWP (∼120 LMH. bar^{-1}) @ 2 bar	
C	50 PVDF, DBD Filtros (UF)	PVDF	50 k	PWP (∼300 LMH. bar^{-1}) @ 2 bar	
C	10 PES, DBD Filtros (UF)	PES	10 k	PWP (∼20 LMH. bar^{-1}) @ 2 bar	
C	NF 90, DOW Filmtec (NF)	Polyamide, TFC[i]	200–300	Water flux (∼32 LMH) @ 4.8 bar Retention (85%–95%) for NaCl	[121]
C	NF 270, DOW Filmtec (NF)	Polypiperazine amide, TFC	200–300	Water flux (∼53 LMH) @ 4.8 bar	

Continued

Table 3 Benchmark Study on UF, NF, and RO CNT-Based MMMs and Commercial Membranes—cont'd

C/L	Membrane	Material	MWCO (Da)	Main Properties	References
				Retention (>97%) for $MgSO_4$	
C	NF 2, Sepro (NF)	Polyamide, TFC	300–400	Water flux (~135 LMH) @ 10.3 bar Retention (98%) for $MgSO_4$	
C	NF PES 10, Microdyn-Nadir (NF)	PES	1 k	Water flux (~200–400 LMH) @ 40 bar Retention (5%–15%) for NaCl	
L	NF MMMs	PES/NH_2-MWCNTs	845	PWF (~23.7 LMH) @ 4 bar Retention (65%–80%) for Na_2SO_4 FRR[j] (>100%)	[20]
L	UF MMMs	PES/F-MWCNTs[k]	NA	PWF (~100 LMH) @ 1 bar Rejection (99.84%) for BSA FRR (~65%–90%)	[81]
L	NF MMMs	PES/F-MWCNTs	PS = 2.26–2.51 nm	PWF (~22–32 LMH) @ 4 bar Rejection (>97%) for whey protein FRR (~53%–95%)	[82]
L	UF MMMs	PSf[l]/F-MWCNTs	PS = 0.05–0.17 μm	PWF (~16–21 m^3/m^2 day) @ 4 bar Rejection (>95%) for PEO[m] 100 k	[42]
L	UF MMMs	PSf/F-MWCNTs	NA	PWF (~30 LMH) @ 2 bar Rejection (93%) for PEO 200 k Improved biofouling properties	[85]
L	Hollow fiber MMMs	PSf/F-MWCNTs	45–55 k	PWF (>70 LMH) @ 2 bar Rejection (~100%) for Humic acid	[86]

Table 3 Benchmark Study on UF, NF, and RO CNT-Based MMMs and Commercial Membranes—cont'd

C/L	Membrane	Material	MWCO (Da)	Main Properties	References
L	NF MMMs	PMMA[n]/ MWCNTs		PWF (~5.4 LMH) @ 10 bar Rejection (99%) for Na_2SO_4	[90]

[a]C: *commercial membrane;* L: *lab fabricated membrane.*
[b]PESH: *hydrophilic polyethersulfone.*
[c]PES: *polyethersulfone.*
[d]PA: *polyaramide.*
[e]PWF: *pure water flux.*
[f]PVDF: *polyvinylidene fluoride.*
[g]PS: *pore size.*
[h]PWP: *pure water permeance.*
[i]TFC: *thin film composite.*
[j]FRR: *flux recovery ratio.*
[k]F-MWCNTs: *functionalized MWCNTs.*
[l]PSf: *polysulfone.*
[m]PEO: *poly (ethylene oxide).*
[n]PMMA: *poly (methyl methacrylate).*

8 CURRENT CHALLENGES FOR CNT-EMBEDDED MEMBRANES

CNT-embedded membranes have a high chance of being ranked first among membrane technologies because of their exceptional advantages only if the challenges regarding the fabrication of these membranes are perfectly resolved. The first difficulty is the complexity of the CNT synthesis method to reach a uniform pore size and pore-size distribution [122] because the existing CVD method is not able to do so. Accordingly, a bottom-up approach could be utilized for synthesizing CNTs with well-controlled pore diameters and structure integrity [123]. However, the demerit of this method is that it is time-consuming and expensive, and thus, this method is not applicable for use in industrial mass production.

The second obstruction is the reduction of pore size and diameter of CNT membranes. Better separation properties that can be obtained by smaller pores is possible only for SWCNTs and double-walled carbon nanotubes (DCNTs) grown on mixed composite matrices or epoxy. The sustainability and large-scale synthesis of both SWCNTs and DWCNTs are commercially limited and not feasible because of their high production cost. Thus, a much cheaper version of CNTs, namely, MWCNTs, with a higher water permeability compared to SWCNTs and DWCNTs, is commonly used to fabricate CNT membranes [124]. MWCNT membranes can be used in place of UF membranes because they have a pore size in the range of 2–50 nm [125]. Based on the literature, CNTs with larger pore diameters showed lower ion retention; however, CNTs with smaller pore diameters reject small ions and produce high-quality potable water [22, 34, 126–128].

The third challenge in VA-CNT membranes might be the growth of CNTs with good alignment. Troubles are encountered when growing CNT membranes on 12 to 13 orders of magnitude of aligned CNTs per sq. cm [85]. Faulty alignment and irregularities in membrane shape lead to an unfavorable

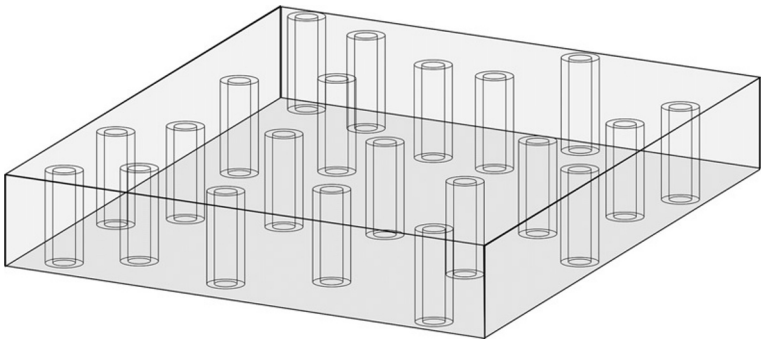

FIG. 3

Schematic of the target CNT-MMM structure in which the pore being the rigid inner-tube diameter of the CNTs.

effect on salt retention and water passage. A proper polymeric filler should be used for filling the intermolecular spaces of the nanotubes to have a higher CNT alignment and a better separation performance. The alignment of CNTs in MMMs composed of CNTs and polymer is also a dominant factor governing both the flux and selectivity improvement. A well-ordered CNT-based MMM should have a structure similar to Fig. 3. It is crucial to develop an effective method for aligning CNTs in the polymer matrix because the mechanical strength, flux, and selectivity of CNT-based MMMs are directly linked to the CNT alignment because the water molecules can only pass through the tubes from head and tail, not through CNT walls. Therefore, the only effective CNTs are those aligned in the polymer matrix. The alignment of the CNTs through conventional composite preparation techniques faces difficulties owing to the high aspect ratio and flexibility of the CNTs [129]. Different techniques have been suggested for fabricating aligned CNT membranes via both chemical and physical approaches [130]. Chen and Tao [131] have demonstrated the alignment and relaxation of polyurethane (TPU) chain within the moisture curing, and swelling steps facilitate the polar solvent, tetrahydrofuran (THF), penetration and are proved to act as a driving force for the fabrication of the well-oriented CNT-based MMMs. The SWCNTs' alignment in TPU during the casting process is shown in Fig. 4.

The fourth issue is the functionalization of the CNT tips with various functional groups. The sensitive atomic structures of the nanotubes network might be changed through some wet chemical modifications, and hence, the destroyed structural properties of CNTs and CNT walls could result in lower solute rejection and water flux [125]. The CNTs' closed tip ends should be unzipped or opened using a proper wet chemical treatment to achieve fast water transport. To open the CNT closed tips, selective oxidizing agent followed by hydrophilic functionalization can be employed. By doing so, the CNT would have an enhanced affinity toward water molecules entering the nanotube and eventually an improved ion selectivity. It has been approved that by entering water molecules into the nanotube pores, the interior hydrophobic wall of the CNTs stimulates the transport of water at super-high flux ($>100\ \mathrm{L\ m^{-2}\ h^{-1}}$) [60, 132]. However, a steric blockage by saturated or attracted ions at the CNT tip ends might be created in the presence of functional groups [133]. In addition, the affinity of the functional groups, which are usually hydrophilic, toward water molecules may lead to a short-term water molecule stoppage close to those groups. Therefore, to properly tune the CNT membrane's water permeability and solute rejection, the functionalization reaction should be carefully optimized because

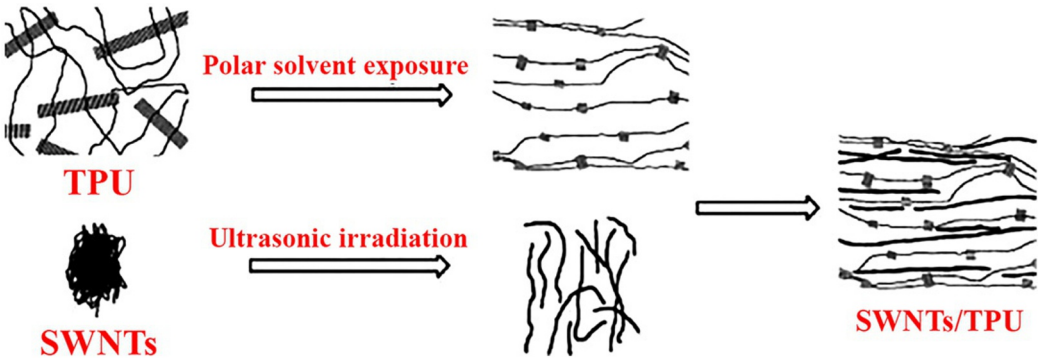

FIG. 4

Schematic illustration of the alignment of SWCNTs in TPU during polar solvent casting process.

Reproduced with permission from A.F. Ismail, P.S. Goh, S.M. Sanip, M. Aziz, Transport and separation properties of carbon nanotube-mixed matrix membrane, Sep. Purif. Technol. 70 (2009) (1) 12–26, Elsevier.

the functional group can be rate limiting. Another issue regarding the CNT membranes is the aggregation of CNTs in the polymer. To prevent aggregation and to make sure that the CNTs are individually and homogeneously dispersed all over the matrix, postprocessing as functionalization is usually needed before incorporating CNTs into a polymer composite.

The fifth problem of the CNT membranes that limits their applications is the high price of SWCNTs because MWCNTs cannot be applied to CNT membrane with subnanometer pore diameter. Few-walled carbon nanotubes are potent for a CNT membrane, which needs pore diameter bigger than 1 nm, but the synthesis of both SWCNTs and FWCNTs is complicated enough. Another way to fabricate a CNT-based membrane is by doping CNTs with polymers, which is a cost-effective and applicable choice. The use of mesoscopic structuring by embedding CNTs in the polymeric membrane has been extensively studied [20, 42, 82, 83, 86, 134]. By doing so, thinner and more stable MMMs with diminished flow resistance would be obtained.

The other minor difficulties relate to the existence of impurities in pristine CNTs, such as contaminated metal catalysts, carbonaceous, amorphous carbon, and ash, that must be removed before use as the membrane material.

9 CONCLUSION

In this chapter, potential proactive to retroactive applications of CNTs in water purification, especially CNT-based membranes, have been covered. Based on the excellent chemical stability, the mechanical strength, the high flexibility, the low mass density, the frictionless water molecule transport, and the ease of functionalization make them a suitable inorganic nanomaterial that can be used as a sorbent, a disinfectant, a nanofilter, and an inorganic filler in MMMs for water purification purposes. The synthesis of the CNTs and the functionalization of the surface of the membrane by attaching different groups has been discussed comprehensively.

The currently available commercial membranes for water purification are mostly based on inorganic or polymeric materials. Both polymeric and inorganic membranes have limitations, for instance, the former has limited performance and lifetime, and the latter is not cost-efficient. The emergence of a novel type of membrane material, namely, MMMs, is going to be developed for the future membrane market. These membranes possess both advantages of the polymeric (processability and cheapness) and inorganic (high performance, excellent chemical and mechanical stability, and enhanced flux) materials. CNTs, as an advantageous choice of inorganic nanofiller, can increase the permeability and rejection of the resultant MMMs because of the smoothness of the CNTs' interior nanochannel.

Using CNTs-based MMMs on an industrial scale for water purification processes can be obtained only if the savings from the improved performance of these membranes surpass the savings from the differences in the price of conventional membranes and MMMs. Many types of research have recently been conducted and confirmed the extraordinary transport of the CNTs in CNT-based MMMs, as the theory has been predicted. Based on these studies, the CNT-based MMMs have shown an enhanced separation performance, including selectivity and permeability. Moreover, the quality of the CNT-based MMMs could be properly controlled and optimized by paying attention to some important parameters, such as controlling the loading of CNTs, polymer-CNT interaction, the dispersibility of the CNTs, the pore size of the CNTs, and other minor parameters. Therefore, further experimental studies are still needed to solve the current shortcomings and to enable the practical applications of CNT-based MMMs in the water purification industry.

REFERENCES

[1] R. Sheikholeslami, Strategies for future research and development in desalination–challenges ahead, Desalination 248 (1–3) (2009) 218–224.
[2] V.K. Gupta, I. Ali, T.A. Saleh, A. Nayak, S. Agarwal, Chemical treatment technologies for waste-water recycling—an overview, RSC Adv. 2 (16) (2012) 6380–6388.
[3] R. Das, M.E. Ali, S.B.A. Hamid, S. Ramakrishna, Z.Z. Chowdhury, Carbon nanotube membranes for water purification: a bright future in water desalination, Desalination 336 (2014) 97–109.
[4] M.H.D.A. Farahani, S.M. Borghei, V. Vatanpour, Recovery of cooling tower blowdown water for reuse: the investigation of different types of pretreatment prior nanofiltration and reverse osmosis, J. Water Process Eng. 10 (2016) 188–199.
[5] H.Y. Yang, Z.J. Han, S.F. Yu, K.L. Pey, K. Ostrikov, R. Karnik, Carbon nanotube membranes with ultrahigh specific adsorption capacity for water desalination and purification, Nat. Commun. 4 (2013) 2220.
[6] M.M. Pendergast, E.M. Hoek, A review of water treatment membrane nanotechnologies, Energ. Environ. Sci. 4 (6) (2011) 1946–1971.
[7] M.M. Khin, A.S. Nair, V.J. Babu, R. Murugan, S. Ramakrishna, A review on nanomaterials for environmental remediation, Energ. Environ. Sci. 5 (8) (2012) 8075–8109.
[8] Association ID, Desalination in 2008: glohal market snapshot, Global Water Intelligence, Oxford, 2008.
[9] P.S. Goh, A.F. Ismail, B.C. Ng, Carbon nanotubes for desalination: performance evaluation and current hurdles, Desalination 308 (2013) 2–14.
[10] R. Semiat, Energy issues in desalination processes, Environ. Sci. Technol. 42 (22) (2008) 8193–8201.
[11] X. Qu, P.J. Alvarez, Q. Li, Applications of nanotechnology in water and wastewater treatment, Water Res. 47 (12) (2013) 3931–3946.
[12] C. Kurth, R. Burk, J. Green (Eds.), Leveraging nanotechnology for seawater reverse osmosis, The IDA World Congress, 2009.

[13] J.-F. Blanco, J. Sublet, Q.T. Nguyen, P. Schaetzel, Formation and morphology studies of different polysulfones-based membranes made by wet phase inversion process, J. Membr. Sci. 283 (1) (2006) 27–37.
[14] Y.-Q. Wang, Y.-L. Su, Q. Sun, X.-L. Ma, Z.-Y. Jiang, Generation of anti-biofouling ultrafiltration membrane surface by blending novel branched amphiphilic polymers with polyethersulfone, J. Membr. Sci. 286 (1) (2006) 228–236.
[15] J. Mulder, Basic Principles of Membrane Technology, Springer Science & Business Media, the Netherlands, 2012.
[16] M.H. Davood Abadi Farahani, H. Rabiee, V. Vatanpour, S.M. Borghei, Fouling reduction of emulsion polyvinylchloride ultrafiltration membranes blended by PEG: the effect of additive concentration and coagulation bath temperature, Desalin. Water Treat. 57 (26) (2016) 11931–11944.
[17] V. Vatanpour, M. Kavian, Synergistic effect of silica nanoparticles in the matrix of a poly (ethylene glycol) diacrylate coating layer for the surface modification of polyamide nanofiltration membranes, J. Appl. Polym. Sci. 133 (33) (2016).
[18] S. Daer, J. Kharraz, A. Giwa, S.W. Hasan, Recent applications of nanomaterials in water desalination: a critical review and future opportunities, Desalination 367 (2015) 37–48.
[19] Y. Yang, H. Zhang, P. Wang, Q. Zheng, J. Li, The influence of nano-sized TiO 2 fillers on the morphologies and properties of PSF UF membrane, J. Membr. Sci. 288 (1) (2007) 231–238.
[20] V. Vatanpour, M. Esmaeili, M.H.D.A. Farahani, Fouling reduction and retention increment of polyethersulfone nanofiltration membranes embedded by amine-functionalized multi-walled carbon nanotubes, J. Membr. Sci. 466 (2014) 70–81.
[21] F. Gojny, M. Wichmann, U. Köpke, B. Fiedler, K. Schulte, Carbon nanotube-reinforced epoxy-composites: enhanced stiffness and fracture toughness at low nanotube content, Compos. Sci. Technol. 64 (15) (2004) 2363–2371.
[22] B. Corry, Designing carbon nanotube membranes for efficient water desalination, J. Phys. Chem. B 112 (5) (2008) 1427–1434.
[23] O. Bakajin, A. Noy, F. Fornasiero, C. Grigoropoulus, J.K. Holt, J.B. In, et al., in: Savage, et al. (Eds.), Nanofluidic carbon nanotube membranes: applications for water purification and desalination, Willian Andrew Inc/Elsevier, New York, 2009, pp. 77–93.
[24] Y.-H. Li, S. Wang, J. Wei, X. Zhang, C. Xu, Z. Luan, et al., Lead adsorption on carbon nanotubes, Chem. Phys. Lett. 357 (3) (2002) 263–266.
[25] C. Lu, H. Chiu, Adsorption of zinc (II) from water with purified carbon nanotubes, Chem. Eng. Sci. 61 (4) (2006) 1138–1145.
[26] C. Lu, H. Chiu, Chemical modification of multiwalled carbon nanotubes for sorption of Zn 2+ from aqueous solution, Chem. Eng. J. 139 (3) (2008) 462–468.
[27] G.P. Rao, C. Lu, F. Su, Sorption of divalent metal ions from aqueous solution by carbon nanotubes: a review, Sep. Purif. Technol. 58 (1) (2007) 224–231.
[28] X. Peng, Y. Li, Z. Luan, Z. Di, H. Wang, B. Tian, et al., Adsorption of 1, 2-dichlorobenzene from water to carbon nanotubes, Chem. Phys. Lett. 376 (1) (2003) 154–158.
[29] H.F. Lin, R. Ravikrishna, K. Valsaraj, Reusable adsorbents for dilute solution separation. 6. Batch and continuous reactors for the adsorption and degradation of 1, 2-dichlorobenzene from dilute wastewater streams using titania as a photocatalysts, Sep. Purif. Technol. 28 (2) (2002) 87–102.
[30] R.Q. Long, R.T. Yang, Carbon nanotubes as superior sorbent for dioxin removal, J. Am. Chem. Soc. 123 (9) (2001) 2058–2059.
[31] K. Yang, L. Zhu, B. Xing, Adsorption of polycyclic aromatic hydrocarbons by carbon nanomaterials, Environ. Sci. Technol. 40 (6) (2006) 1855–1861.
[32] D. Xu, X. Tan, C. Chen, X. Wang, Removal of Pb (II) from aqueous solution by oxidized multiwalled carbon nanotubes, J. Hazard. Mater. 154 (1) (2008) 407–416.

[33] A. Srivastava, O. Srivastava, S. Talapatra, R. Vajtai, P. Ajayan, Carbon nanotube filters, Nat. Mater. 3 (9) (2004) 610–614.
[34] F. Fornasiero, H.G. Park, J.K. Holt, M. Stadermann, C.P. Grigoropoulos, A. Noy, et al., Ion exclusion by sub-2-nm carbon nanotube pores, Proc. Natl. Acad. Sci. 105 (45) (2008) 17250–17255.
[35] A. Noy, H.G. Park, F. Fornasiero, J.K. Holt, C.P. Grigoropoulos, O. Bakajin, Nanofluidics in carbon nanotubes, Nano Today 2 (6) (2007) 22–29.
[36] D.M. Bohonak, A.L. Zydney, Compaction and permeability effects with virus filtration membranes, J. Membr. Sci. 254 (1) (2005) 71–79.
[37] S. Mostafavi, M. Mehrnia, A. Rashidi, Preparation of nanofilter from carbon nanotubes for application in virus removal from water, Desalination 238 (1–3) (2009) 271–280.
[38] A.S. Brady-Estévez, S. Kang, M. Elimelech, A single-walled-carbon-nanotube filter for removal of viral and bacterial pathogens, Small 4 (4) (2008) 481–484.
[39] N. Savage, M.S. Diallo, Nanomaterials and water purification: opportunities and challenges, J. Nanopart. Res. 7 (4) (2005) 331–342.
[40] S. Kang, M. Pinault, L.D. Pfefferle, M. Elimelech, Single-walled carbon nanotubes exhibit strong antimicrobial activity, Langmuir 23 (17) (2007) 8670–8673.
[41] A.J. Blanch, C.E. Lenehan, J.S. Quinton, Optimizing surfactant concentrations for dispersion of single-walled carbon nanotubes in aqueous solution, J. Phys. Chem. B 114 (30) (2010) 9805–9811.
[42] J.-H. Choi, J. Jegal, W.-N. Kim, Fabrication and characterization of multi-walled carbon nanotubes/polymer blend membranes, J. Membr. Sci. 284 (1) (2006) 406–415.
[43] J. Prasek, J. Drbohlavova, J. Chomoucka, J. Hubalek, O. Jasek, V. Adam, et al., Methods for carbon nanotubes synthesis—review, J. Mater. Chem. 21 (40) (2011) 15872–15884.
[44] P. Nikolaev, M.J. Bronikowski, R.K. Bradley, F. Rohmund, D.T. Colbert, K. Smith, et al., Gas-phase catalytic growth of single-walled carbon nanotubes from carbon monoxide, Chem. Phys. Lett. 313 (1) (1999) 91–97.
[45] M.J. Bronikowski, P.A. Willis, D.T. Colbert, K. Smith, R.E. Smalley, Gas-phase production of carbon single-walled nanotubes from carbon monoxide via the HiPco process: a parametric study, J. Vac. Sci. Technol. A 19 (4) (2001) 1800–1805.
[46] M.H.-O. Rashid, S.F. Ralph, Carbon nanotube membranes: synthesis, properties, and future filtration applications, Nanomedicine 7 (5) (2017) 99.
[47] D. Tasis, N. Tagmatarchis, A. Bianco, M. Prato, Chemistry of carbon nanotubes, Chem. Rev. 106 (3) (2006) 1105–1136.
[48] P.C. Ma, J.-K. Kim, B.Z. Tang, Functionalization of carbon nanotubes using a silane coupling agent, Carbon 44 (15) (2006) 3232–3238.
[49] P.-C. Ma, N.A. Siddiqui, G. Marom, J.-K. Kim, Dispersion and functionalization of carbon nanotubes for polymer-based nanocomposites: a review, Compos. A: Appl. Sci. Manuf. 41 (10) (2010) 1345–1367.
[50] M.J. O'connell, S.M. Bachilo, C.B. Huffman, V.C. Moore, M.S. Strano, E.H. Haroz, et al., Band gap fluorescence from individual single-walled carbon nanotubes, Science 297 (5581) (2002) 593–596.
[51] Y. Geng, M.Y. Liu, J. Li, X.M. Shi, J.K. Kim, Effects of surfactant treatment on mechanical and electrical properties of CNT/epoxy nanocomposites, Compos. A: Appl. Sci. Manuf. 39 (12) (2008) 1876–1883.
[52] K.-S. Moon, W. Lin, H. Jiang, H. Ko, L. Zhu, C. Wong (Eds.), Surface treatment of MWCNT array and its polymer composites for TIM application, 58th Conference on Electronic Components and Technology Conference, IEEE, 2008.
[53] A.F. Ismail, P.S. Goh, S.M. Sanip, M. Aziz, Transport and separation properties of carbon nanotube-mixed matrix membrane, Sep. Purif. Technol. 70 (1) (2009) 12–26.
[54] J.H. Choi, J. Jegal, W.N. Kim (Eds.), Modification of performances of various membranes using MWNTs as a modifier, Macromolecular Symposia, Wiley Online Library, 2007.

[55] V. Vatanpour, S.S. Madaeni, R. Moradian, S. Zinadini, B. Astinchap, Fabrication and characterization of novel antifouling nanofiltration membrane prepared from oxidized multiwalled carbon nanotube/polyethersulfone nanocomposite, J. Membr. Sci. 375 (1) (2011) 284–294.
[56] Y.-P. Sun, K. Fu, Y. Lin, W. Huang, Functionalized carbon nanotubes: properties and applications, Acc. Chem. Res. 35 (12) (2002) 1096–1104.
[57] P. Nednoor, N. Chopra, V. Gavalas, L. Bachas, B. Hinds, Reversible biochemical switching of ionic transport through aligned carbon nanotube membranes, Chem. Mater. 17 (14) (2005) 3595–3599.
[58] C. Wei, D. Srivastava, Theory of transport of long polymer molecules through carbon nanotube channels, Phys. Rev. Lett. 91 (23) (2003) 235901.
[59] M. Majumder, N. Chopra, R. Andrews, B.J. Hinds, Nanoscale hydrodynamics: enhanced flow in carbon nanotubes, Nature 438 (7064) (2005) 44.
[60] J.K. Holt, H.G. Park, Y. Wang, M. Stadermann, A.B. Artyukhin, C.P. Grigoropoulos, et al., Fast mass transport through sub-2-nanometer carbon nanotubes, Science 312 (5776) (2006) 1034–1037.
[61] Y. Liu, Q. Wang, L. Zhang, T. Wu, Dynamics and density profile of water in nanotubes as one-dimensional fluid, Langmuir 21 (25) (2005) 12025–12030.
[62] D.M. Ackerman, A.I. Skoulidas, D.S. Sholl, J.J. Karl, Diffusivities of Ar and Ne in carbon nanotubes, Mol. Simul. 29 (10 – 11) (2003) 677–684.
[63] O.G. Jepps, S.K. Bhatia, D.J. Searles, Modeling molecular transport in slit pores, J. Chem. Phys. 120 (11) (2004) 5396–5406.
[64] S. Konduri, H.M. Tong, S. Chempath, S. Nair, Water in single-walled aluminosilicate nanotubes: diffusion and adsorption properties, J. Phys. Chem. C 112 (39) (2008) 15367–15374.
[65] V.P. Sokhan, D. Nicholson, N. Quirke, Fluid flow in nanopores: accurate boundary conditions for carbon nanotubes, J. Chem. Phys. 117 (18) (2002) 8531–8539.
[66] A.L. Yarin, A.G. Yazicioglu, C.M. Megaridis, M.P. Rossi, Y. Gogotsi, Theoretical and experimental investigation of aqueous liquids contained in carbon nanotubes, J. Appl. Phys. 97 (12) (2005) 124309.
[67] A.I. Skoulidas, D.M. Ackerman, J.K. Johnson, D.S. Sholl, Rapid transport of gases in carbon nanotubes, Phys. Rev. Lett. 89 (18) (2002) 185901.
[68] Z. Mao, S.B. Sinnott, A computational study of molecular diffusion and dynamic flow through carbon nanotubes, J. Phys. Chem. B 104 (19) (2000) 4618–4624.
[69] S.K. Bhatia, H. Chen, D.S. Sholl, Comparisons of diffusive and viscous contributions to transport coefficients of light gases in single-walled carbon nanotubes, Mol. Simul. 31 (9) (2005) 643–649.
[70] R.D. Noble, S.A. Stern, Membrane Separations Technology: Principles and Applications, Elsevier, 1995.
[71] R.W. Baker, Membrane technology and applications, John Wiley & Sons, Ltd., 2004, pp. 96–103.
[72] C.M. Zimmerman, A. Singh, W.J. Koros, Tailoring mixed matrix composite membranes for gas separations, J. Membr. Sci. 137 (1–2) (1997) 145–154.
[73] V. Vatanpour, M. Safarpour, A. Khataee, P. Visakh, O. Nazarenko, Mixed matrix membranes for nanofiltration application, Nanostruct. Poly. Membr. 2 (2) (2016) 441. Applications.
[74] S.J. Lue, S. Peng, Polyurethane (PU) membrane preparation with and without hydroxypropyl-β-cyclodextrin and their pervaporation characteristics, J. Membr. Sci. 222 (1) (2003) 203–217.
[75] M.J. O'Connell, P. Boul, L.M. Ericson, C. Huffman, Y. Wang, E. Haroz, et al., Reversible water-solubilization of single-walled carbon nanotubes by polymer wrapping, Chem. Phys. Lett. 342 (3) (2001) 265–271.
[76] B.J. Hinds, N. Chopra, T. Rantell, R. Andrews, V. Gavalas, L.G. Bachas, Aligned multiwalled carbon nanotube membranes, Science 303 (5654) (2004) 62–65.
[77] S. Qiu, L. Wu, X. Pan, L. Zhang, H. Chen, C. Gao, Preparation and properties of functionalized carbon nanotube/PSF blend ultrafiltration membranes, J. Membr. Sci. 342 (1) (2009) 165–172.

[78] Y. Baek, C. Kim, D.K. Seo, T. Kim, J.S. Lee, Y.H. Kim, et al., High performance and antifouling vertically aligned carbon nanotube membrane for water purification, J. Membr. Sci. 460 (2014) 171–177.
[79] S. Li, G. Liao, Z. Liu, Y. Pan, Q. Wu, Y. Weng, et al., Enhanced water flux in vertically aligned carbon nanotube arrays and polyethersulfone composite membranes, J. Mater. Chem. A 2 (31) (2014) 12171–12176.
[80] X. Wang, X. Chen, K. Yoon, D. Fang, B.S. Hsiao, B. Chu, High flux filtration medium based on nanofibrous substrate with hydrophilic nanocomposite coating, Environ. Sci. Technol. 39 (19) (2005) 7684–7691.
[81] L. Liu, M. Son, S. Chakraborty, C. Bhattacharjee, H. Choi, Fabrication of ultra-thin polyelectrolyte/carbon nanotube membrane by spray-assisted layer-by-layer technique: characterization and its anti-protein fouling properties for water treatment, Desalin. Water Treat. 51 (31 – 33) (2013) 6194–6200.
[82] P. Daraei, S.S. Madaeni, N. Ghaemi, M.A. Khadivi, B. Astinchap, R. Moradian, Enhancing antifouling capability of PES membrane via mixing with various types of polymer modified multi-walled carbon nanotube, J. Membr. Sci. 444 (2013) 184–191.
[83] L. Brunet, D.Y. Lyon, K. Zodrow, J.-C. Rouch, B. Caussat, P. Serp, et al., Properties of membranes containing semi-dispersed carbon nanotubes, Environ. Eng. Sci. 25 (4) (2008) 565–576.
[84] P. Shah, C. Murthy, Studies on the porosity control of MWCNT/polysulfone composite membrane and its effect on metal removal, J. Membr. Sci. 437 (2013) 90–98.
[85] S. Kar, M. Subramanian, A. Pal, A. Ghosh, R. Bindal, S. Prabhakar, et al., (Eds.) Preparation, characterisation and performance evaluation of anti-biofouling property of carbon nanotube-polysulfone nanocomposite membranes, AIP Conference Proceedings, AIP, 2013.
[86] J. Yin, G. Zhu, B. Deng, Multi-walled carbon nanotubes (MWNTs)/polysulfone (PSU) mixed matrix hollow fiber membranes for enhanced water treatment, J. Membr. Sci. 437 (2013) 237–248.
[87] M. Amini, M. Jahanshahi, A. Rahimpour, Synthesis of novel thin film nanocomposite (TFN) forward osmosis membranes using functionalized multi-walled carbon nanotubes, J. Membr. Sci. 435 (2013) 233–241.
[88] S. Madaeni, S. Zinadini, V. Vatanpour, Preparation of superhydrophobic nanofiltration membrane by embedding multiwalled carbon nanotube and polydimethylsiloxane in pores of microfiltration membrane, Sep. Purif. Technol. 111 (2013) 98–107.
[89] A. Tiraferri, C.D. Vecitis, M. Elimelech, Covalent binding of single-walled carbon nanotubes to polyamide membranes for antimicrobial surface properties, ACS Appl. Mater. Interfaces 3 (8) (2011) 2869–2877.
[90] J. nan Shen, C. Chao Yu, H. min Ruan, C. jie Gao, B. Van der Bruggen, Preparation and characterization of thin-film nanocomposite membranes embedded with poly (methyl methacrylate) hydrophobic modified multiwalled carbon nanotubes by interfacial polymerization, J. Membr. Sci. 442 (2013) 18–26.
[91] G. Ciobanu, G. Carja, O. Ciobanu, Structure of mixed matrix membranes made with SAPO-5 zeolite in polyurethane matrix, Microporous Mesoporous Mater. 115 (1) (2008) 61–66.
[92] J. Caro, M. Noack, P. Kölsch, R. Schäfer, Zeolite membranes–state of their development and perspective, Microp. Mesop. Mate. 38 (1) (2000) 3–24.
[93] N. Widjojo, T.-S. Chung, S. Kulprathipanja, The fabrication of hollow fiber membranes with double-layer mixed-matrix materials for gas separation, J. Membr. Sci. 325 (1) (2008) 326–335.
[94] R. Pal, Permeation models for mixed matrix membranes, J. Colloid Interface Sci. 317 (1) (2008) 191–198.
[95] S.-L. Wee, C.-T. Tye, S. Bhatia, Membrane separation process—pervaporation through zeolite membrane, Sep. Purif. Technol. 63 (3) (2008) 500–516.
[96] H. Rabiee, M.H.D.A. Farahani, V. Vatanpour, Preparation and characterization of emulsion poly (vinyl chloride)(EPVC)/TiO 2 nanocomposite ultrafiltration membrane, J. Membr. Sci. 472 (2014) 185–193.
[97] H. Rabiee, V. Vatanpour, M.H.D.A. Farahani, H. Zarrabi, Improvement in flux and antifouling properties of PVC ultrafiltration membranes by incorporation of zinc oxide (ZnO) nanoparticles, Sep. Purif. Technol. 156 (2015) 299–310.

[98] P.S. Goh, A.F. Ismail, S.M. Sanip, B.C. Ng, M. Aziz, Recent advances of inorganic fillers in mixed matrix membrane for gas separation, Sep. Purif. Technol. 81 (3) (2011) 243–264.
[99] P. Bernardo, E. Drioli, G. Golemme, Membrane gas separation: a review/state of the art, Ind. Eng. Chem. Res. 48 (10) (2009) 4638–4663.
[100] J.M. Duval, A. Kemperman, B. Folkers, M. Mulder, G. Desgrandchamps, C. Smolders, Preparation of zeolite filled glassy polymer membranes, J. Appl. Polym. Sci. 54 (4) (1994) 409–418.
[101] R. Mahajan, W.J. Koros, Factors controlling successful formation of mixed-matrix gas separation materials, Ind. Eng. Chem. Res. 39 (8) (2000) 2692–2696.
[102] R. Mahajan, R. Burns, M. Schaeffer, W.J. Koros, Challenges in forming successful mixed matrix membranes with rigid polymeric materials, J. Appl. Polym. Sci. 86 (4) (2002) 881–890.
[103] H.H. Yong, H.C. Park, Y.S. Kang, J. Won, W.N. Kim, Zeolite-filled polyimide membrane containing 2, 4, 6-triaminopyrimidine, J. Membr. Sci. 188 (2) (2001) 151–163.
[104] R. Mahajan, W.J. Koros, Mixed matrix membrane materials with glassy polymers. Part 2, Polym. Eng. Sci. 42 (7) (2002) 1432–1441.
[105] R. Mahajan, W.J. Koros, Mixed matrix membrane materials with glassy polymers. Part 1, Polym. Eng. Sci. 42 (7) (2002) 1420–1431.
[106] P.S. Tin, T.-S. Chung, L. Jiang, S. Kulprathipanja, Carbon–zeolite composite membranes for gas separation, Carbon 43 (9) (2005) 2025–2027.
[107] P. Gorgojo, B. Zornoza, S. Uriel, C. Tellez, J. Coronas, Mixed matrix membranes from nanostructured materials for gas separation, Stud. Surf. Sci. Catal. 174 (2008) 653–656.
[108] A.F. Ismail, R. Rahim, W. Rahman, Characterization of polyethersulfone/Matrimid® 5218 miscible blend mixed matrix membranes for O 2/N 2 gas separation, Sep. Purif. Technol. 63 (1) (2008) 200–206.
[109] A.F. Ismail, T.D. Kusworo, A. Mustafa, Enhanced gas permeation performance of polyethersulfone mixed matrix hollow fiber membranes using novel Dynasylan Ameo silane agent, J. Membr. Sci. 319 (1) (2008) 306–312.
[110] H. Ago, T. Komatsu, S. Ohshima, Y. Kuriki, M. Yumura, Dispersion of metal nanoparticles for aligned carbon nanotube arrays, Appl. Phys. Lett. 77 (1) (2000) 79–81.
[111] H. Kanzow, C. Lenski, A. Ding, Single-wall carbon nanotube diameter distributions calculated from experimental parameters, Phys. Rev. B 63 (12) (2001) 125402.
[112] T. Belin, F. Epron, Characterization methods of carbon nanotubes: a review, Mater. Sci. Eng. B 119 (2) (2005) 105–118.
[113] M. Anson, J. Marchese, E. Garis, N. Ochoa, C. Pagliero, ABS copolymer-activated carbon mixed matrix membranes for CO 2/CH 4 separation, J. Membr. Sci. 243 (1) (2004) 19–28.
[114] J. Ahn, W.-J. Chung, I. Pinnau, M.D. Guiver, Polysulfone/silica nanoparticle mixed-matrix membranes for gas separation, J. Membr. Sci. 314 (1) (2008) 123–133.
[115] X. Qu, J. Brame, Q. Li, P.J. Alvarez, Nanotechnology for a safe and sustainable water supply: enabling integrated water treatment and reuse, Acc. Chem. Res. 46 (3) (2012) 834–843.
[116] J. Yin, B. Deng, Polymer-matrix nanocomposite membranes for water treatment, J. Membr. Sci. 479 (2015) 256–275.
[117] G. Mittal, V. Dhand, K.Y. Rhee, S.-J. Park, W.R. Lee, A review on carbon nanotubes and graphene as fillers in reinforced polymer nanocomposites, J. Ind. Eng. Chem. 21 (2015) 11–25.
[118] F.M. Penha, K. Rezzadori, M.C. Proner, G. Zin, L.A. Fogaça, J.C.C. Petrus, et al., Evaluation of permeation of macauba oil and n-hexane mixtures through polymeric commercial membranes subjected to different pre-treatments, J. Food Eng. 155 (2015) 79–86.
[119] J. Lindau, A.-S. Jönsson, Adsorptive fouling of modified and unmodified commercial polymeric ultrafiltration membranes, J. Membr. Sci. 160 (1) (1999) 65–76.

[120] A.M. de Souza, C.C. de Morais, L.A. Gonçalves, L.A. Viotto, Solvent permeability in commercial ultrafiltration polymeric membranes and evaluation of the structural and chemical stability towards hexane, Sep. Purif. Technol. 71 (1) (2010) 13–21.
[121] G. Artuğ, I. Roosmasari, K. Richau, J. Hapke, A comprehensive characterization of commercial nanofiltration membranes, Sep. Sci. Technol. 42 (13) (2007) 2947–2986.
[122] J.M. Schnorr, T.M. Swager, Emerging applications of carbon nanotubes, Chem. Mater. 23 (3) (2010) 646–657.
[123] H. Omachi, T. Nakayama, E. Takahashi, Y. Segawa, K. Itami, Initiation of carbon nanotube growth by well-defined carbon nanorings, Nat. Chem. 5 (7) (2013) 572–576.
[124] F. Du, L. Qu, Z. Xia, L. Feng, L. Dai, Membranes of vertically aligned superlong carbon nanotubes, Langmuir 27 (13) (2011) 8437–8443.
[125] S. Kar, R. Bindal, P. Tewari, Carbon nanotube membranes for desalination and water purification: challenges and opportunities, Nano Today 7 (5) (2012) 385–389.
[126] J. Goldsmith, C.C. Martens, Molecular dynamics simulation of salt rejection in model surface-modified nanopores, J. Phys. Chem. Lett. 1 (2) (2009) 528–535.
[127] T.V. Ratto, J.K Holt, A.W. Szmodis, Membranes with embedded nanotubes for selective permeability, Google Patents (2011).
[128] J. Y-x, L. H-l, M. Wang, L.-y. Wu, Y.-d. Hu, Carbon nanotube: possible candidate for forward osmosis, Sep. Purif. Technol. 75 (1) (2010) 55–60.
[129] J.H. Sung, H.S. Kim, H.-J. Jin, H.J. Choi, I.-J. Chin, Nanofibrous membranes prepared by multiwalled carbon nanotube/poly (methyl methacrylate) composites, Macromolecules 37 (26) (2004) 9899–9902.
[130] R. Cervini, G.P. Simon, M. Ginic-Markovic, J.G. Matisons, C. Huynh, S. Hawkins, Aligned silane-treated MWCNT/liquid crystal polymer films, Nanotechnology 19 (17) (2008) 175602.
[131] W. Chen, X. Tao, Self-organizing alignment of carbon nanotubes in thermoplastic polyurethane, Macromol. Rapid Commun. 26 (22) (2005) 1763–1767.
[132] C.H. Ahn, Y. Baek, C. Lee, S.O. Kim, S. Kim, S. Lee, et al., Carbon nanotube-based membranes: fabrication and application to desalination, J. Ind. Eng. Chem. 18 (5) (2012) 1551–1559.
[133] B. Corry, Water and ion transport through functionalised carbon nanotubes: implications for desalination technology, Energ. Environ. Sci. 4 (3) (2011) 751–759.
[134] F. Ahmed, C.M. Santos, J. Mangadlao, R. Advincula, D.F. Rodrigues, Antimicrobial PVK: SWNT nanocomposite coated membrane for water purification: performance and toxicity testing, Water Res. 47 (12) (2013) 3966–3975.

CHAPTER

DENDRITIC POLYMER—ENHANCED ULTRAFILTRATION

5

Michael Arkas*, K. Panagiotaki*, I. Kitsou†, F. Petrakli†

Institute of Nanoscience and Nanotechnology NCSR "Demokritos", Athens, Greece School of Mining Engineering and Metallurgy, National Technical University of Athens, Athens, Greece†*

1 INTRODUCTION TO DENDRITIC POLYMERS

The dendritic (from the Greek word δενδριτικός, "treelike") architecture naturally occurs in many cases and scales: on the meter scale, in the branches and the roots of the trees; on the centimeter scale, in the flowering heads of broccoli and cauliflower; on the millimeter scale, in the veins of the leaves; and on the micrometer scale, in topologies of the circulatory system of the human anatomy (lungs, kidneys, and liver) and in dendritic cells and the dendrites of the neurons of the brain [1]. Dendritic polymers are a rapidly growing category of artificial compounds with a repetitively branched architecture that governs their molecular and supramolecular structures. Because of this unique architecture and their repertoire of new properties, dendritic polymers are recognized as a fourth major new macromolecular architectural class next to linear, cross-linked, and branched polymers [2–9] They are classified in five main categories:

1. Dendrimers (Fig. 1; [2, 10–13]) possess perfectly symmetrical macromolecular architectures of precisely defined molecular weight. Their shapes are characterized by uniformity and their structural parameters (number of external groups, molecular dimensions) by monodispersity. Most dendrimers are prepared by multistep synthetic procedures via a convergent or divergent method (Fig. 2). Each reaction step practically doubles the molecular weight of the macromolecule, increases the so-called generation by one, and is followed by a very tedious purification process to remove closely related, imperfectly branched by-products.
2. Dendrons (Fig. 3), or dendritic wedges, the branches of the tree, that is, the largest possible and terminal building blocks of dendrimers when the convergent growth is implemented. Their properties and applications resemble those of the dendrimers, and for this reason they are studied and reviewed together [14–16]. Instead of forming dendrimers, they can be grafted to a so-called dendronic surface through their focal point, which, in most cases, is a chemically addressable group. Alternatively, different dendrons can form Janus dendrimers (Fig. 4). These molecules, named for the Roman god for beginnings, transitions, and endings, bear two completely different structures that induce dissimilar properties and, thus, amphiphilicity.
3. Dendronized polymers [17–20], also called dendron-jacketed polymers, are dendrimers with a polymeric core, usually a linear polymer, bearing dendrons (Fig. 5). An unlimited combination of

Nanoscale Materials in Water Purification. https://doi.org/10.1016/B978-0-12-813926-4.00010-0

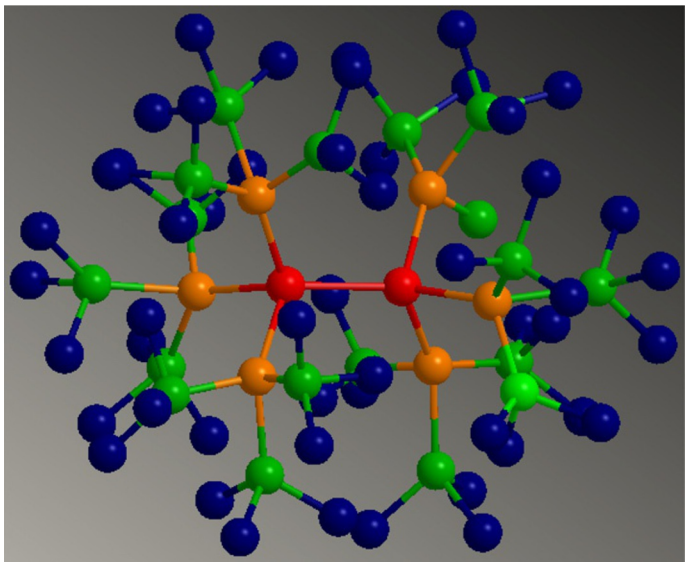

FIG. 1

Schematic representation of a dendrimer. Each sphere represents a monomer. Different colors depict the different generations.

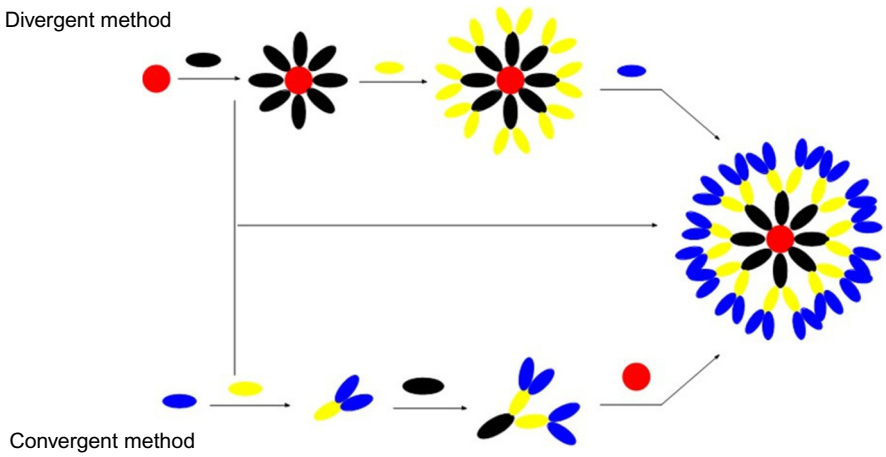

FIG. 2

The two approaches (divergent and convergent method) for the synthesis of dendrimers.

different blocks of polymers with the same or different dendrons results to innovative hybrid dendritic polymers with different topologies, allowing for shape and rigidity control and fascinating functionalities. The control of these hierarchical structures with dimensions on the nanometer scale is receiving ever-increasing interdisciplinary scientific interest.

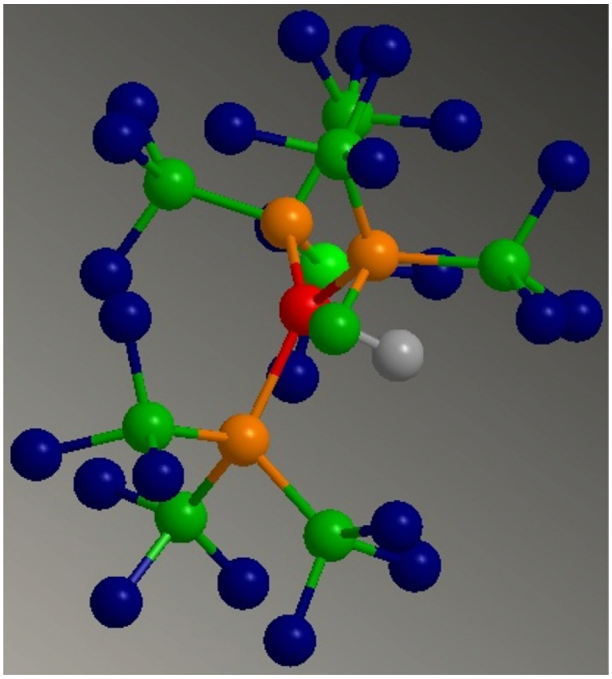

FIG. 3

Schematic representation of a dendron. Each sphere represents a monomer. Different colors depict the different generations whereas the *gray sphere* indicates the focal point.

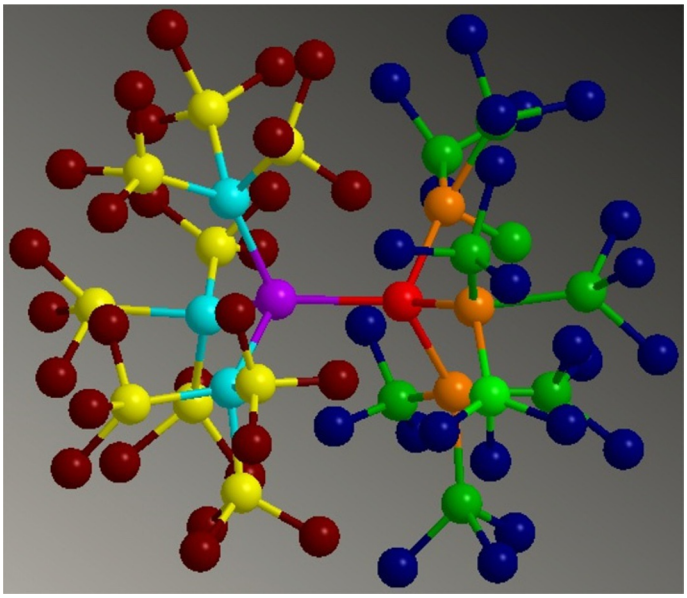

FIG. 4

Schematic representation of a Janus dendrimer. Each sphere represents a monomer. Different colors depict the different generations of the two dendrons.

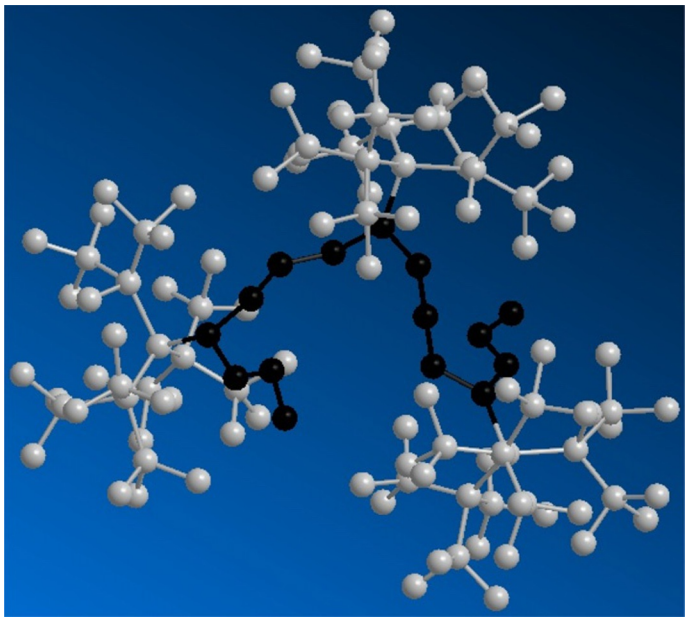

FIG. 5

Schematic representation of a dendronized polymer. Each sphere represents a monomer. Different colors depict the polymeric core (linear polymer) and the grafted dendrons.

4. Hyperbranched polymers (Fig. 6; [21–26]) are irregular, nonsymmetric analogues to dendrimers that can be visualized as trees with some branches overgrown and some not fully developed. They have analogous structural features and similar properties with dendrimers. On the other hand, they are prepared through a one-step polymerization process and present commercially interesting alternatives to large-scale industrial applications in the cases where structural perfection is not needed because they do not require expensive and time-consuming synthesis stages and numerous purification processes of the nonfully substituted unsymmetrical branches [27]. They are polydisperse, with their polydispersity index ranging between 1.3 and 2.5 amorphous because of their randomly branched topology, and are characterized by their high versatility.
5. Dendrigrafts (Fig. 7; [28]) differ from the other highly branched dendritic polymers in the size of their building block, which, in this case, constitutes, by itself, a macromolecule, in most cases, a linear polymer. They are synthesized by two different, divergent methods: the "grafting onto" technique, where the polymer chains are attached to a polymeric substrate, and the "grafting from" scheme, where side chains grow from activated sites of the polymeric substrate. A third "grafting through" convergent approach employs a one-pot reaction of preformed polymeric building blocks with bifunctional monomers possessing vinyl groups and groups capable of either extending a polymeric chain or terminating its growth by coupling. Dendrigrafts are nonsymmetrical, semicontrolled, branched polymer architectures and can be considered a subclass of hyperbranched polymers.

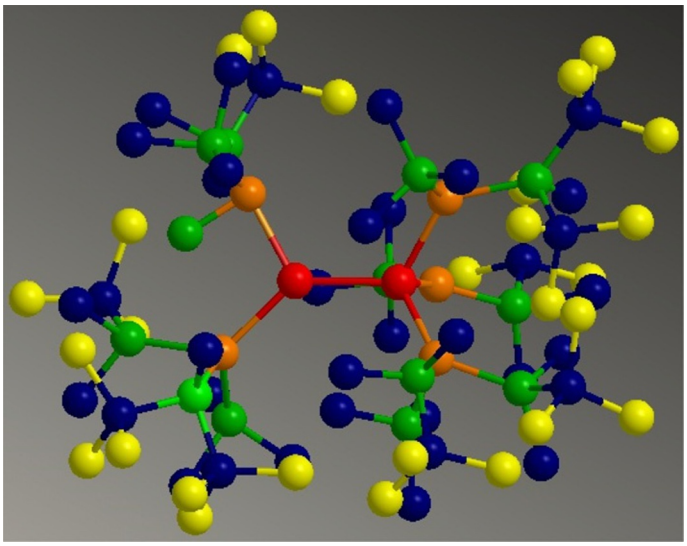

FIG. 6

Schematic representation of a hyperbranched polymer. Each sphere represents a monomer. Different colors depict the different generations.

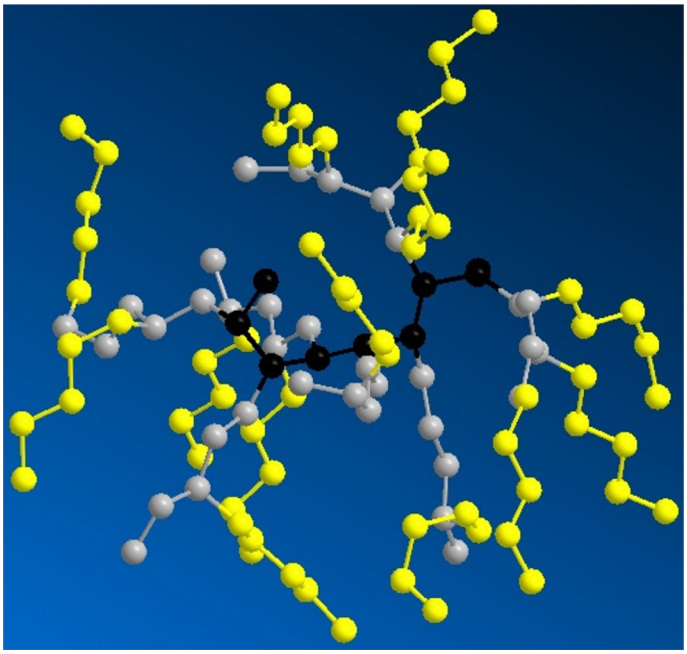

FIG. 7

Schematic representation of a dendrigraft polymer. Each sphere represents a monomer. Different colors depict the polymeric core (linear polymer) and the (linear) polymers forming the different generations.

On the basis of molecular simulations, the three-dimensional shape of the dendritic polymers for the low generations is disklike, whereas higher generations (>3) exhibit roughly globular or ellipsoid conformations. Their physical properties depend strongly on their overall size. Their dimensions fall in the range of 1 nm to 20 nm, with the exception of dendrigrafts, which exhibit sizes 1 or even almost 2 orders of magnitude bigger, up to a few hundred nm. Apart from their characteristic shapes, they differentiate from conventional branched polymers because their unique "branch on branch" structure consists of three easily detectable basic anatomical features: the central point, usually referred to as the "core," from which emanates a dense network of repeating units (the "branches"), and finally end with a large number of terminal end groups:

a. The core, the focal point of the macromolecule, usually serves as the starting construction point from which the polymeric branches emanate. It must have at least two reactive functional groups and sometimes has a characteristic chemical composition that induces a specific function or property different from the surrounding environment.

b. The dense interior branching sequences is composed of the spacer and the branch juncture, with the number of radically concentric layers of branch iterations defining the dendritic polymer generation. This structural feature favors or, rather, dynamically induces the formation of nanocavities characterized by a variety of nano-environments according to their tunable chemical nature. With different sizes and both hydrophilic and hydrophobic domains, these "traps" may either selectively embed specific substances or incorporate a multitude of organic and inorganic molecules.

c. The periphery, composed by an extremely high density of functional groups, produces the so-called multivalency effect. These terminal groups have a notably fractal character and can be fine-tuned to induce the desired chemical properties in terms of reactivity and affinity to various solvents. In this way, the behavior of their solutions and their response to factors such as pH [29] and ionic strength can be predetermined, and the absorption of substances into the dendritic polymer's interior or the diffusion of the embedded materials to the surrounding medium is facilitated or hindered. In addition, these external groups are able to undergo further modifications, affording functional or multifunctional nanostructured carriers with nanoscale porosity that can selectively interact with or bind to specific guest species or substrates.

The unique and tunable properties deriving from these structural characteristics can thus be varied and optimized, justifying the interest these molecules have attracted in the fields of separation and extraction applications, for example, extractive distillation, solvent extraction, absorption, membranes, or preparative chromatography. As a consequence, they are continuously enriched not only by new members but also by novel subclasses.

A number of theoretical and computational approaches [30–32], combined with standard experimental techniques, have been conducted to elucidate the host-guest interactions governing absorption capabilities of dendritic polymers and the supramolecular structures formed. Isothermal titration calorimetry (ITC) is implemented to determine the binding strength of host-guest complexes [33–35]. Other interactions between dendritic polymers and guest molecules are monitored by high-performance liquid chromatography (HPLC) [36] and fluorescence spectroscopy [37–40]. Nuclear magnetic resonance (NMR) was employed to deduce the conformations of dendritic polymers supramolecular structures with the incorporated compounds [41–43] whereas their size is measured by dynamic light scattering (DLS) [40, 44].

One of the most important parameters characterizing the absorption potential of the dendritic polymers is that their loading capacity is affected mainly by the following four factors: (1) the molecular weight-size, (2) the density of the branches, (3) the polarity difference between the core and the periphery and hydrophilicity-hydrophobicity gradients through the whole volume of the host, and (4) the chemical affinity between host and guest molecules.

The branch junctures of the most common dendritic polymers are made of groups, usually nitrogen-based amino or amido groups, capable of serving as electron donors and forming coordination compounds with various metals. The complex formation functionalities of various dendrimers, enhanced by the branched environment of the cavities, make them versatile hosts for chelating metal ions (Figs. 8 and 9). The first example of a dendrimer as a nanochelating agent for the recovery of metal ions dissolved into an aqueous solution was described by Ref. [45, 46]) for the incorporation of Cu^{+2} into polyamidoamine (PAMAM) dendrimer. Polymer-metal interactions have been well interpreted by UV-vis and EPR spectra. A partial list of dendritic polymer complexes with metal ions includes Na^{+}, K^{+}, Cs^{+}, Rb^{+}, Fe^{+}, Fe^{+2}, Gd^{+3}, Cu^{+}, Cu^{+2}, Ag^{+}, Mn^{+2}, Pd^{+2}, Zn^{+2}, Co^{+3}, Rh^{+}, Ru^{+2}, and Pt^{+2} [47, 48]. PAMAM and PPI dendrimers also as deduced by Ottaviani and Diallo by TEM EPR and fluoresce investigations selectively bind to radioactive heavy-atom ions such as the uranyl, UO_2^{2+}, and therefore have the potential to be used for environmental remediation [49, 50].

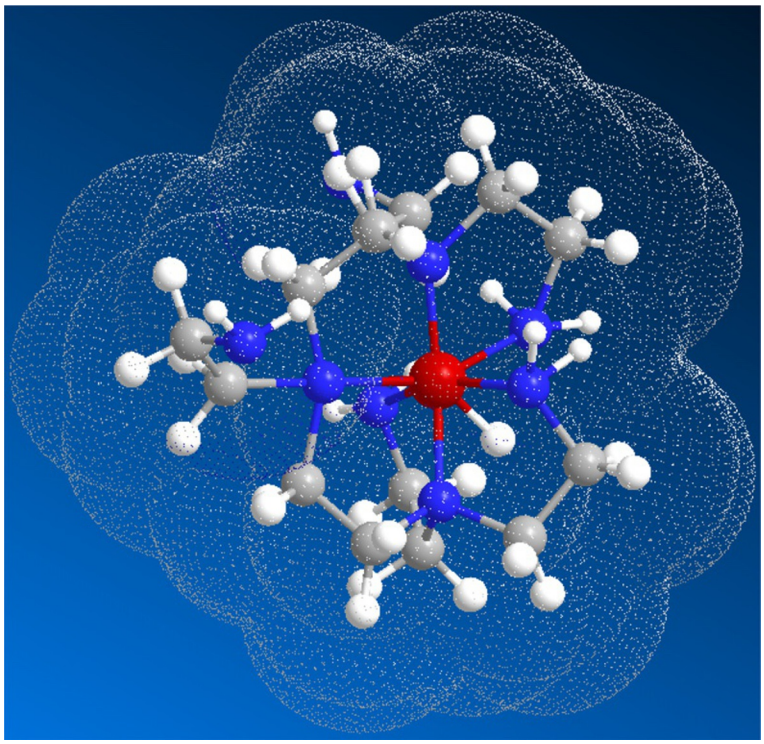

FIG. 8

Complex formation of a metal cation into a dendritic poly(ethylene imine) cavity.

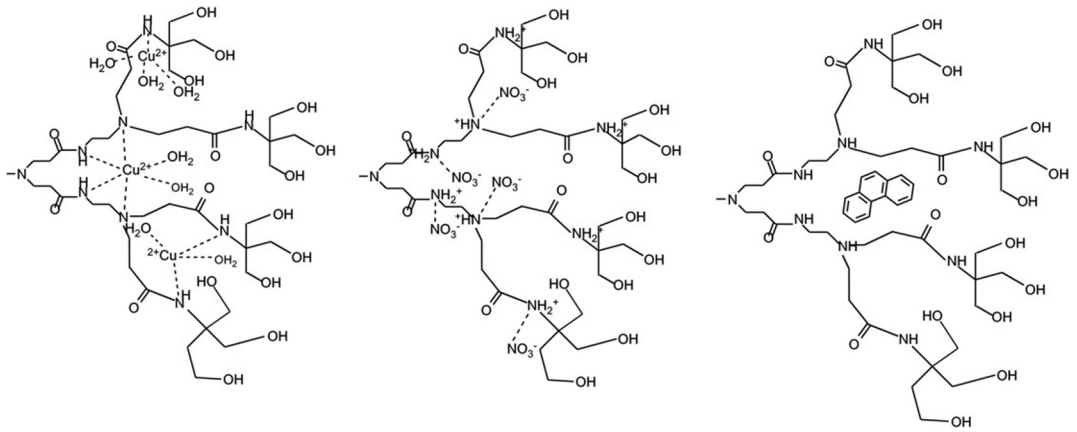

FIG. 9

Some examples of incorporation of polar inorganic ions and apolar polycyclic aromatic hydrocarbons into the adopted cavities of the same dendritic polymer.

Alternatively, by the same chelation procedure and by adding a reducer such as $NaBH_4$, hydrazine, and sodium citrate, the formation of coordination bonds with appropriate reductive groups or by irradiation (UV-light, X-ray, or laser), metal ions incorporated into dendritic polymers undergo nucleation and are transformed to zero-valence metal nanoclusters with possible applications to catalytic systems [51–54].

On the other hand, including anions is more challenging because of their larger size and higher free energy of solvation. Noncoordinating interactions, for example, electrostatic at low pH or hydrogen bonding, permit the removal of anions, such as nitrate, benzoate, arsenate, chromate pertechnate, and perchlorate (Fig. 9) [45, 55–59].

Dendritic architecture is also characterized by the capacity to form both hydrophilic and hydrophobic domains and the potential to encapsulate compounds in the interior regardless of the polarity of the surface. This behavior is reminiscent of conventional micelles. Newkome and his group presented the first example—a dendrimer with a lipophilic interior with saturated long hydrocarbon chains as building blocks and polar tetramethylammonium carboxylate terminal groups at the periphery mimicking the "micellar" behavior—and defined it as a "unimolecular micelle" [60, 61]. A wide variety of lipophilic guest molecules were encapsulated in these dendrimers, including the fluorescence probe naphthalene, the antibiotic chlortetracycline, the polarity indicator phenol blue, and organic dyes such as pinacyanol chloride [62]. Further studies with PAMAM, dendrimer derivatives employing EPR and fluorescence spectroscopy using appropriate probe molecules, by Tomalia and his group [63–66] unequivocally confirmed the unimolecular micellar behavior of the dendritic structures possessing apolar interior cavities and a polar periphery that renders the molecules water-soluble.

Paleos and his group [67–69] also proved that the higher generation of poly(propylene imine) (PPI) dendrimers and their derivatives, despite having hydrophilic amino end groups in their periphery, also possess the capability to encapsulate nonpolar molecules, such as the polycyclic aromatic hydrocarbon (PAH) pyrene, and determined their binding constants as $K_{py/DAB\text{-}32} = 16{,}725 \pm 200\ M^{-1}$ and $K_{py/DAB\text{-}64}$ $33{,}858 \pm 663\ M^{-1}$. This is easily justifiable because the dielectric constant in their interior

is about comparable to that of hexane [70]. The lipophilic environment of the cavities was further established by employing the same fluorescence probe and calculating the ratio of the first to the third principal vibronic peak fluorescence intensity I_1/I_3, which is well correlated with the polarity of pyrene's solubilization site. Furthermore, because the branching points of the dendrimer consisted of tertiary amino groups susceptible to protonation, the incorporation of pyrene was pH-sensitive and reversible in acidic media.

In the same context, with minimal purification manipulations, [71] synthesized second-generation hybrid dendrimers from bisimine and bisamine AB_2 monomers (Fig. 10) without protective groups and calculated comparable pyrene inclusion constants. In another complexation study of structurally related dendrimers, Triano established the positive effect of benzyl ether dendrimeric composition on removing pyrene from water [72].

Instead of binding to the internal cavities, many molecules or ions can also preferentially bind to the external surface of dendrimers. For instance, cationic organic dyes, such as methylene blue, thionine, and thiopyronine, are electrostatically retained on the negatively charged surface of starburst PAMAM dendrimers as established by UV-Vis and fluorescence spectroscopy [73].

Hyperbranched dendritic polymers exhibit analogous encapsulation properties [74]. Refs. [75, 76] performed emission and anisotropy fluoresce experiments to probe the physical properties of the interior regions of the structurally similar PPI dendrimer and its hyperbranched counterpart poly(ethyleneimine) (PEI) and to compare their behavior toward the solvatochromic reporter molecule phenol blue. They showed that the polarity within the nanocavities was the same and was similar to that of *n*-heptane and that although there are some notable differences in the association of the guest molecule with the two dendritic architectures, its incorporation was complete and the polymer-dye complexes were stable. Thus, the absorption properties are not compromised by the polydispersity and the irregularities in the structure of the hyperbranched polymers.

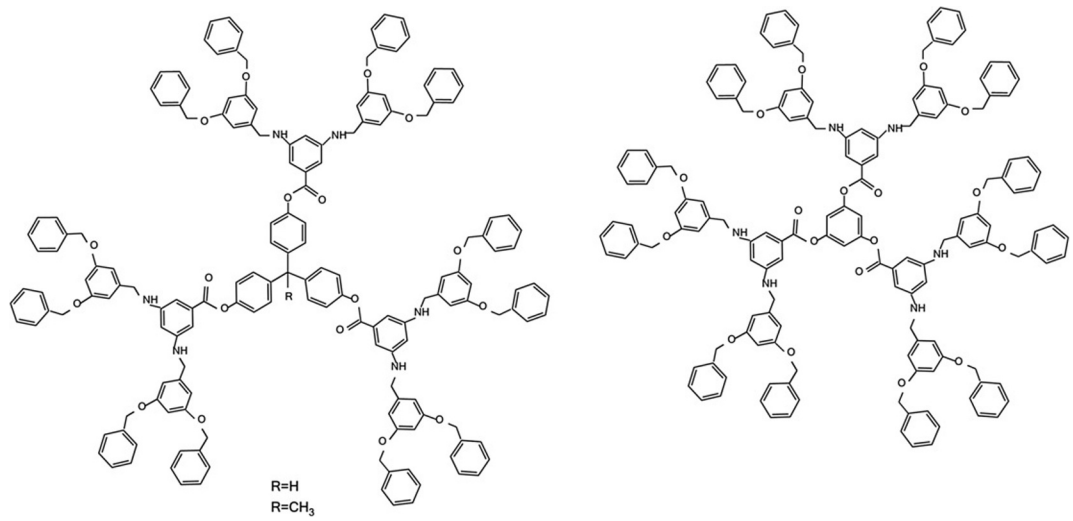

FIG. 10

Bis Benzyl imine dendrimers designed for pyrene absorption.

The first example of an encapsulated metal ion in a hyperbranched polymer was reported by Ref. [77] for palladium ions and amphiphilic hyperbranched polyglycerols. Subsequent reduction afforded stable colloidal solutions of metal-loaded micelles with palladium cluster sizes dependent on the molar mass of the host macromolecule. Wan [78] and Zhu [79] independently correlated the sizes of gold and silver nanoparticles to the molar mass of the hyperbranched host, driving them to the same conclusion.

Unimolecular micellar behavior and analogous properties were also observed in hyperbranched polymers. For example, carboxylated hyperbranched polyphenylene was reported as early as 1990 by Ref. [80], who confirmed the absorption of hydrophobic *p*-toluidine, by ^{1}H NMR spectroscopy. Hyperbranched polymers with nonpolar interior, such as PEI, apart from their affinity for aromatic hydrocarbons, exhibit a higher absorption capacity than do dendrimers for linear hydrocarbons, which is attributed to their less steric hindrance in comparison to symmetrical dendritic analogues [81]. Polar water-soluble organic molecules, such as Congo red, bromophenol blue, and rose Bengal dyes, can also be irreversibly encapsulated in specifically designed, inverse unimolecular micelles, such as amphiphilic hyperbranched polyglycerols bearing an ethylene glycol hydrophilic core and an outer shell functionalized by esterification with hexadecyl aliphatic chains (Fig. 11) [82]. The encapsulation of Congo red was proved to be attributed to the hyperbranched topology because the dye was not absorbed into the hexadecyl linear polyglycerol analogs [83].

Dendritic polymers combining micellar properties with biocompatibility, that is, bearing nontoxic, nonimmunogenic, and preferably biodegradable units, were utilized in biomedical applications for improving pharmaceutical compounds in terms of solubility and bioavailability, paving the way for target-specific drug-delivery systems with controlled release or release via alternative routes [84–88], gene carriers with high transfection efficiency, [89–91], and contrast agents for diagnostic imaging such as magnetic resonance imaging [92–94].

Nowadays, it is therefore well established that dendritic polymers have the properties for spontaneously absorbing a variety of chemical compounds [95, 96] such as hydrophilic and hydrophobic dyes,

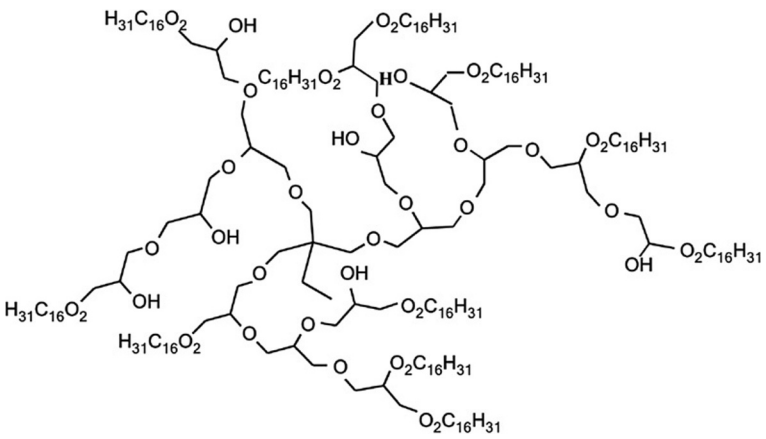

FIG. 11

Hyperbranched polyglycerol bearing long aliphatic chains for the absorption of polar organic dyes.

metal ions and inorganic anions, radionuclides, other lipophilic compounds such antibiotics and fluorescence probes, and even linear aliphatic compounds from water. Because of their unimolecular nature, dendritic micelles are characterized by long-term stability induced by strong chemical bonds, unlike conventional micelles that are formed by weak intermolecular interactions between their monomeric building blocks, and are in a state of dynamic equilibrium with their nonaggregated counterparts [97]. Careful selection of their three structural parts—the central core, the repeating units, and the terminal groups—and appropriate functionalization of the latter determine the nature of the compounds that can be incorporated and the selectivity of the encapsulation process. A differentiation of the properties of the aquatic environment, mainly changes in pH and ionic strength, can protonate or deprotonate the dendritic polymers and drastically change their conformation and polarity, leading to the alteration of the stereochemical parameters of the cavities and the electrostatic forces between the host and guest molecules, triggering the spontaneous desorption and the effective regeneration of the absorbents [67–69].

Because of these properties, dendritic polymers are high-capacity, recyclable functional materials for the removal of toxic pollutants, such as heavy metals; pesticides, radioactive materials, and biological contaminants, such as bacteria; and viruses from the aqueous media. Thanks to their thermal stability, flexibility, low viscosity, high biocompatibility [2, 98–100], and their minimal toxicity [100, 101], they are applied to novel environmental remediation technologies [102–104], mainly water purification [105].

2 PROCESSING DENDRITIC POLYMERS TO IMPROVE THEIR ABSORPTION PROPERTIES

After the selection of the suitable species of these macromolecular compounds for a specific water purification application, fine-tuning of their properties can be attained through appropriate functionalization by simple intermolecular forces or chemical reactions to the terminal reactive groups. The modifications lead to diversified materials with enhanced encapsulation properties, higher affinity, or attachment ability to substrates and selectivity toward intended pollutants. The methods employed for developing efficient dendritic derivatives for pollutant absorption can be divided into five categories.

2.1 DIRECT COMBINATION OF DENDRITIC POLYMER WITH ANOTHER ABSORBING SOLID POROUS SUPPORT

Solid supports deriving from particles of porous organic or inorganic materials such as glass, silica cellulose, or ceramics, can be covered through noncovalent binding by thin films of dendritic macromolecules without compromising their absorption capabilities. These substrates can be impregnated by the polymers by simple techniques such as, for example, simple stirring with optional sonication. Ref. [106] immobilized fourth-generation PAMAM dendrimer on titania. This mixed organic-inorganic absorbent was used for the remediation of synthetic wastewater solutions from metal cations and exhibited selectivity toward Cu^{2+} and Cr^{3+} in comparison to Ni^{2+}.

2.2 MODIFICATION OF THE FUNCTIONAL GROUPS OF THE PERIPHERY TO ADJUST THE POLARITY

For the dendritic polymers to be practically useful for the development of water purification devices, they have to be completely insoluble in water to avoid release in the effluent. The introduction of a lipophilic outer layer should not hinder, although the inclusion of guest molecules and functionalized dendritic polymer-based systems must equal or even outperform nonfunctionalized analogues both in terms of loading capacities and inclusion rates. An easy method proposed for this purpose is the complete substitution of the external amino groups of PPI dendrimers of the fourth and the fifth generation bearing 32 and 64 primary amino groups with long aliphatic chains, respectively, via reaction with *n*-alkyl isocyanates [107]. Inclusion rates for polycyclic aromatic hydrocarbons (PAH) were determined from the time-dependent decrease of fluorescence intensity of contaminated water samples by octyl- and octadecyl-PPI derivatives applied as thin films deposited by slow evaporation on the glass surfaces of round-bottom flasks. A typical example showing the monitoring of the fluorescence of a water sample doped with perylene because of its encapsulation in octylurea DAB-64 dendrimer is shown in Fig. 12. It was deduced that neither encapsulation efficiency nor inclusion rates were compromised by the alkylation of the terminal NH_2 groups and are only slightly affected by the length of the aliphatic chains and the generation of the dendrimers. Because of its larger size, complete absorption of fluoranthene required a longer time compared to the other PAH.

Guest molecules enter alkylated dendrimers because they are practically insoluble in water, and they are, therefore, at a thermodynamically unfavorable condition. In addition, inclusion potential

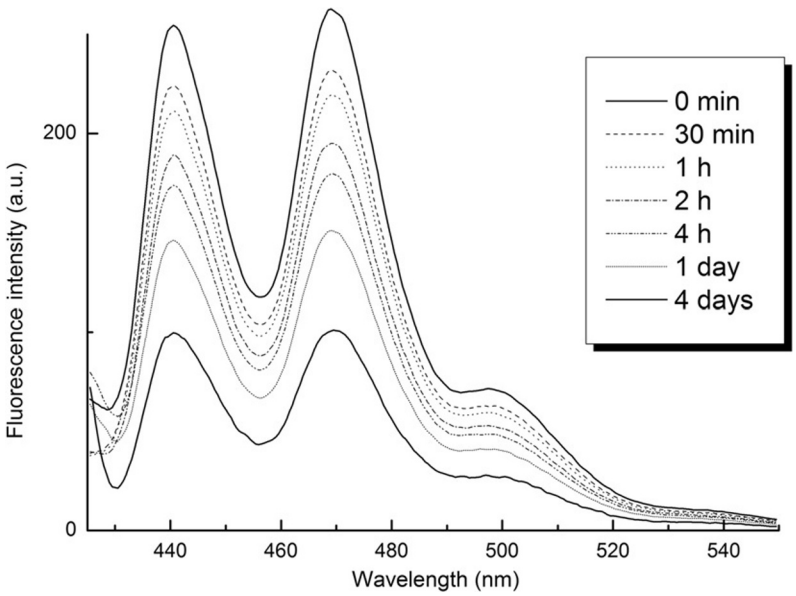

FIG. 12

Time dependence of the fluorescence of a perylene solution added to a glass vial covered by a film of octylurea DAB-64.

is further enhanced by the formation of charge-transfer complexes between polyaromatic hydrocarbons and the tertiary amino branching points [108]. The calculation of inclusion Formation Gibbs free energies (−11 to −8 kcal mol^{-1}) confirmed that PAHs solubilized into the dendritic cavities are, indeed, at a much lower energy state. Inclusion formation constants, calculated for the less water-soluble pyrene and fluoranthene, were of the same order of magnitude as those reported for cyclodextrin polymers 10^9 M^{-1} [109] and many times higher than the respective values for activated carbon (1×10^5 M^{-1}) [110]. Complexation in water of PAH with tertiary nitrogens, although proceeding via nonconventional chemical bonding, is thus practically nonreversible. This is not the case, however, in nonpolar organic solvents, where complete diffusion of PAH is observed permitting the regeneration and reuse of the PAH saturated thin films. The inclusion formation constant of phenanthrene is much smaller because of its higher solubility in water. The loading capacities at saturation calculated for the fourth generation indicate that their maximum inclusion capacities for all PAH were increased depending on the length of the alkyl chains and indicate that functionalization apart from insolubility provided more absorption substrates. This phenomenon was not carried out to the fifth generation, most probably for stereochemical reasons. These observed inclusion characteristics are determined by the dynamic character of branches that also governs the behavior of the aliphatic chains in the exterior. Both are characterized by a flexibility that allows them to modify their conformation and adapt for the accommodation of bulky molecules [111, 112]. This ability to incorporate impurities regardless of size and shape is considered a very important advantage as far as water purification is concerned, widening the environmental remediation applicability to more water pollutants. In another, more recent implementation, instead of a glass vial, Vázquez et al. covered a highly swollen regenerated cellulose (RC/4) membrane by a third-generation thiolated PEI dendrimer (S-DAB) by dip coating. The resulting hybrid material was designed to be used in electrochemical devices for wastewater-metal remediation [113].

The same techniques were applied to a variety of commercially available, low-cost, hyperbranched polymers [114]. Hyperbranched PEI (Mn = 5000) with chemical structure similar to that of PPI dendrimers, polyglycerol (PG) (Mn = 5000), characterized by more polar cavities, and a number of hyperbranched polyesteramides with marginally altered structures, namely, S1200 (Mn = 1200), H1500 (Mn = 1500), PS2550 (Mn = 2500), and SL1520 (Mn = 1500) (Fig. 13), were submitted to alkylation and investigated as potential PAH absorbents from water to study the effect of these variations to the polarity of the absorption sites and the overall encapsulation properties. Alkyl-substituted hyperbranched polymers exhibited slower absorption rates than did symmetric dendrimers, which, in this case, were dependent on the length of the alkyl chains, and slower than the octadecyl compounds, proving that encapsulation is a topochemically affected process. In fact, encapsulation efficiency was greatly affected by the structural diversity of the functionalized hyperbranched derivatives. Faster absorption rates were observed for those having glass transition temperatures far below zero up to room temperature and thus flexible branches (−84°C for PPI64, −25°C for PEI, 20°C for S1200 and SL1520), in comparison to rigid ones, H1500 and PS2550 ($T_g > 40$°C for H1500 and > 70°C for PS2550), that are in a glassy state at room temperature. This flexibility of the dendritic scaffold affords cavities that are adaptable to the volume of bulky molecules, enabling their faster diffusion and entrapment. The chemical affinity of the microenvironment of the encapsulation sites to the guest aromatic molecules is another factor that also has a marked influence on the absorption. The presence of aromatic rings in the interior of PS2550 favored the inclusion of polycyclic aromatic compounds in comparison, for example, to the cyclohexane groups of H1500. The polarity of the absorption sites that was probed by the I_1/I_3 ratio of the first and third principal vibronic band intensities of pyrene also has a

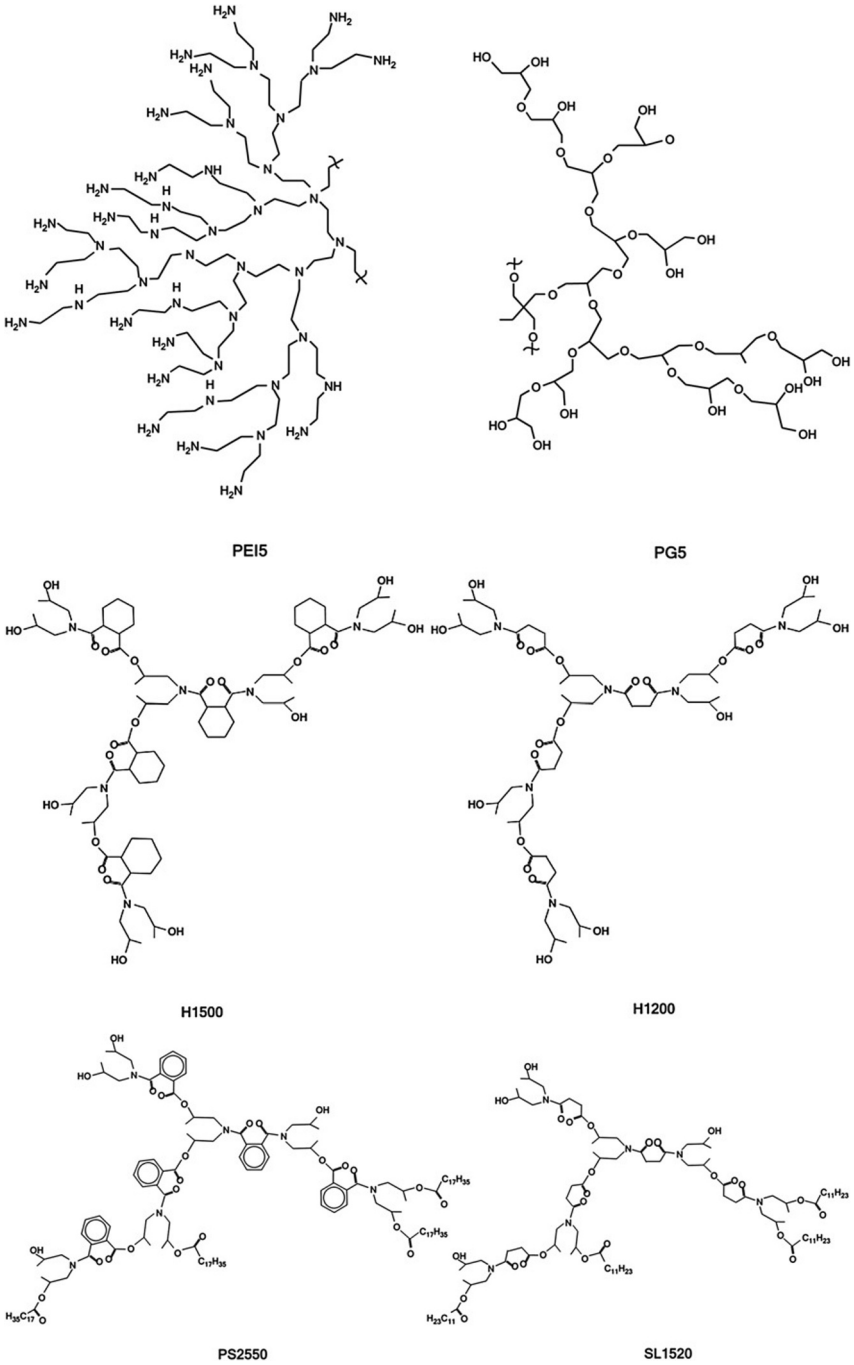

FIG. 13

Hyperbranched polymers selected for the determination of the effect of the polarity of the dendritic cavities to PAH absorption.

drastic effect on encapsulation efficiency. PPI64 and PEI polarities are among the lowest and are roughly the same (I_1/I_3 is 1.41 and 1.37, respectively), which is rather expected if we take into account that they have more or less the same chemical structure, whereas PG exhibits the highest I_1/I_3 ratio (1.61), justifying thus its low inclusion K and ΔG values. Although PEI and all the other hyperbranched compounds have smaller molecular weights and thus sizes than dendrimers, their inclusion formation constants K and loading capacities are comparable and, in some cases, are equal. In addition, for all the dendritic compounds' pollutant inclusion formation constants, Gibbs free energies were in the reverse order of their solubility in water, that is, $K_{pyrene} > K_{fluoranthene} > K_{phenanthrene}$, establishing the validity of the argument that in water, the thermodynamic stabilization obtained by the inclusion of the polycyclic aromatic hydrocarbons inside the dendritic cavities is the main driving force behind the process. In contrast, in acetonitrile spontaneous diffusion of PAH takes place, permitting the painless regeneration of the thin films of the hyperbranched polymers as their dendrimeric counterparts. Conclusively, the overall similar behavior of hyperbranched polymers to that observed for their symmetric dendrimeric cousins and their comparable absorption parameters are very encouraging for the cost-effective application of the former to ultrafiltration devices.

2.3 FUNCTIONALIZATION OF DENDRITIC POLYMERS FOR CROSS-LINKING AND CHEMICAL BINDING

In the previous sections, modified dendritic polymers were incorporated into porous supports through simple intermolecular interactions. The properties of the dendritic nanocomposites cannot be fully exploited by simply impregnating them onto the surface of the solid substrate because their use without a stable attachment to the host matrix may increase the risk of their leaching out into the purified water, making it unsafe for usage. Two strategies have been developed in order to address this problem:

a. Polymerization, for example, by cross-linking of the dendritic material after its impregnation into the pores of the ceramic scaffold. Apart from the profound consequences on the solubility, these reactions will have an equally drastic effect on the dimensions of the compounds, rendering them very bulky and impossible to exit the pores.
b. Direct chemical bonding of the dendritic thin film with the support

Both these goals can be readily achieved by employing a simple modification of the external terminal groups by groups capable of performing these functionalities (polymerization and chemical bond formation). In this way, the films of the absorbing macromolecules are certainly rendered nonleachable, ensuring thus that water contamination cannot take place. For this purpose, alkoxysilylated groups were introduced either on dendrimeric or on hyperbranched polymers by interaction of the amino end groups of a dendrimer (PPI32) and a hyperbranched polymer (PEI) with 3-(triethoxysilyl)propyl isocyanate under extremely mild conditions [115]. This study was inspired by the previous work of Dvornic and his group on silylated polyamidoamine dendrimers termed PAMAMOS [116, 117]. A number of coupling reactions was developed for the attachment of silicon functionalities to three commercially available types of amine-, methyl ester-, and hydroxyl-terminated PAMAM precursors (Fig. 14). Among the wide variety of possibilities, alkoxysilyl groups presented particular interest because they can undergo hydrolysis and subsequent polycondensation, leading to the formation of cross-linked nanostructured networks.

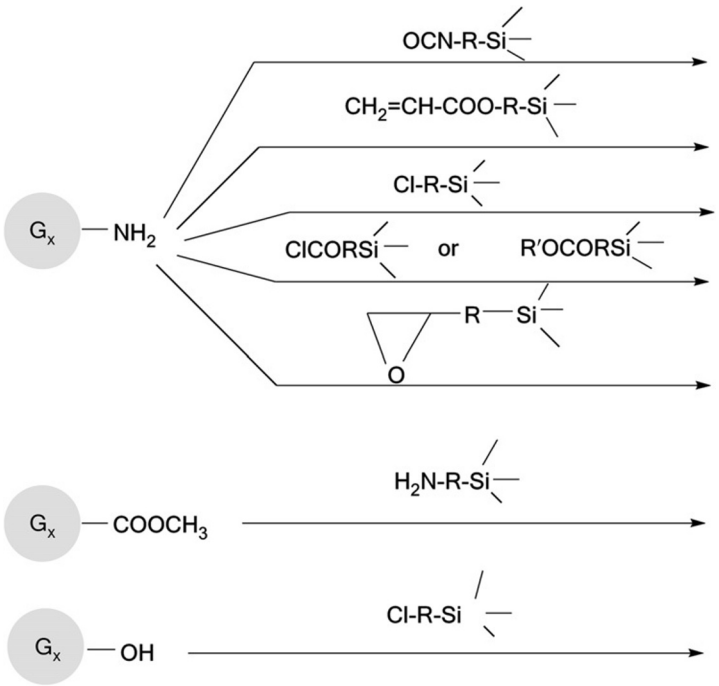

FIG. 14

Main synthetic routes to PAMAMOS dendrimers from three commercially available types of amine-, methyl ester-, and hydroxyl-terminated PAMAM precursors.

The triethoxysilyl derivatives obtained were hydrolyzed to silanols, which subsequently polycondensated either intramolecularly or intermolecularly, affording the cross-linked siloxane networks PPI—Si—O—Si—PPI and PEI—Si—O—Si—PEI. Apart from the aforementioned polymerization, the silanols have the potential to undergo analogous condensation reactions with hydroxyl functionalities present on activated ceramic surfaces, resulting in the formation of covalent bonds of the thin films with the inorganic material. Kinetic experiments performed in round-bottom flasks covered by thin films proved that the encapsulation efficiency of polycyclic aromatic hydrocarbons from water and the corresponding inclusion formation constants of these compounds were comparable to their alkylated counterparts. After 2 h, contact with the PEI—Si—O—Si—PEI film only 8% of pyrene and 30% of phenanthrene remained in solution, whereas within the same period, percentages for PPI—Si—O—Si—PPI were 20% and 52%, respectively. The absorption of more water-soluble aromatic pollutants, such as β-naphthol, was significantly slower, reaching equilibrium only after several days. Inclusion formation constants (10^7 M^{-1} for pyrene, 10^6 M^{-1} for phenanthrene, and 10^5 M^{-1} for β-naphthol) were also almost entirely correlated with the water solubility of the compounds, and the symmetry of dendritic architecture did not enhance them.

Silicon-containing PAMAM-SiO_2 dendrimers similar to those described earlier were prepared starting from the conventional commercially available PAMAM dendrimers of generations 2 and 4

by functionalizing the terminal amino groups of the surface by 3-(trimethoxysilyl) propyl acrylate, mixing them with partly hydrolyzed tetraethyl orthosilicate and then casting the mixture on glass. Complete hydrolysis of methoxy- and ethoxy-silyl groups and sol-gel reaction afforded cross-linked polymers through siloxane bridges with "compartmentalized" and controllable structure analogous to the ratio between PAMAM and TEOS. These hybrid materials have been developed for the extraction of metal ions from aqueous solutions [118]. The absorption capacities observed for the second- and fourth-generation derivative for Cu^{2+} metal ions were 3.69 and 4.80 g per gram of composite absorbent, respectively.

2.4 DIRECT SURFACE MODIFICATION OF INORGANIC OR POLYMER PARTICLES BY DENDRON DEVELOPMENT

Solid adsorbents such as inorganic ceramics and organic polymers are extensively employed for water purification. Ceramic membranes are characterized by large surface areas and well-defined pore sizes and shapes. On the other hand, chitosan, for example, possesses unique flexible structure and excellent absorption properties toward polar substances. An innovative strategy for enhancing adsorption toward toxic water contaminants is the manipulation of their surface properties by the attachment of dendritic macromolecules or the in situ development of dendrons with chemical functionalities inducing selectivity or increased absorption potential. The resulting functionalized solid phase particles are promising adsorbents and can be used as a packing material in filtration columns for water decontamination.

In situ propagation of one to three generations of PAMAM dendrons onto the surface of porous inorganic silica particles using the conventional divergent synthetic route and solid phase synthesis, followed by the functionalization of their terminal groups by long octadecyl aliphatic chains, afforded hybrid materials capable of absorbing organic dyes and surfactants from water (Fig. 15) [119]. More specifically, anionic dyes, such as methyl orange, were completely absorbed by the first generation of octadecyl functionalized PAMAM modified silica (C18G1S), whereas cationic dyes, such as ethidium bromide, were partially absorbed only by unmodified silica particles. Thermodynamically favored electrostatic and host-guest interactions of positively charged dendrons with the anionic dyes were confirmed as the driving forces for their encapsulation in the nanocavities. On the other hand, both anionic, such as sodium dodecylbenzenesulfonate, and cationic, such benzyldimethyltetradecylammonium chloride and 1-dodecylpyridium chloride, surfactants were adsorbed on silica particles, preferably on those bearing low-generation alkyl-functionalized dendrons. The strong hydrophobic interactions between the long alkyl chains of the surfactants and the octadecyl chains of the hybrid organic-inorganic particles were recognized not only as the driving forces for the efficient absorption but also as capable of overcoming the electrostatic repulsions between positively charged host dendrons and the two guest cations. Regeneration was performed by treatment with an alkaline solution.

The divergent strategy was also employed by Niu and his coworkers for modifying the external surface of silica gel by a series of amino- and ester-terminated hyperbranched PAMAM dendrons [120]. These functionalized beads were successfully tested for the retention of Pb^{2+} (Fig. 16), which proved to be strongly dependent on the pH (optimal pH 5) of the solution and on the dendron generation number (optimal generations were 2 and 2.5).

In the same context, Chen and coworkers synthesized new dendron-modified silica particles with hydrocarbonaceous and amine functionalities. Starting by attaching triethoxysilyl propylamine to silica particles, they realized the successive growth of the branched polymer using a divergent synthesis

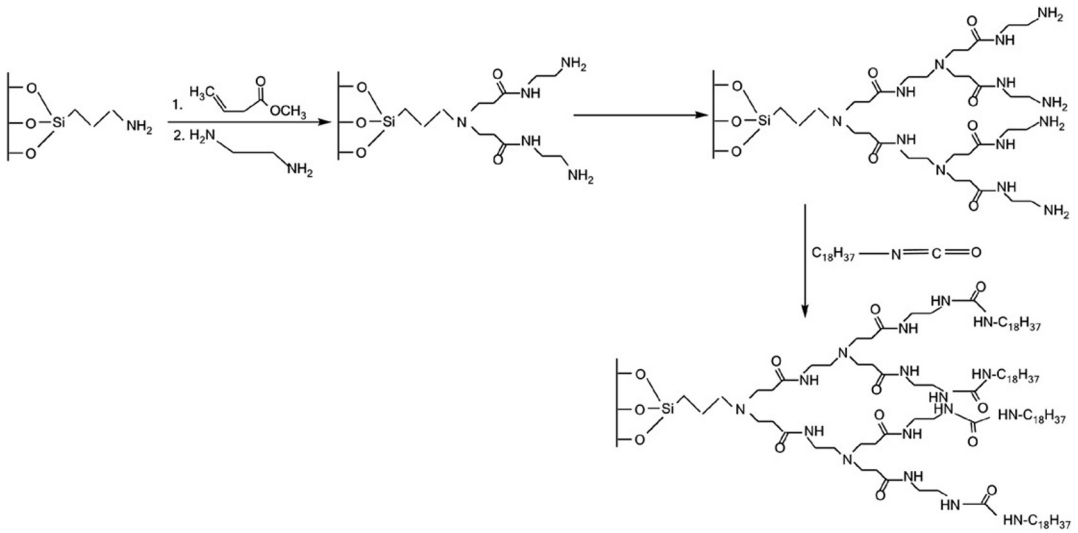

FIG. 15

Development of PAMAM dendrons onto the surface of porous inorganic silica particles and subsequent modification of the terminal amino groups with lipophilic octadecyl chains for the absorption of dyes and surfactants.

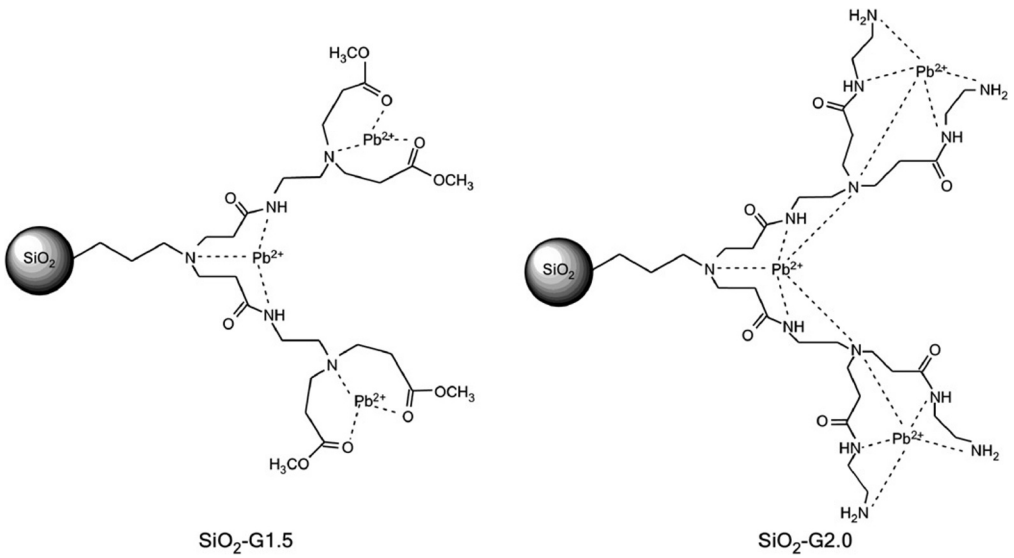

FIG. 16

Proposed structures of Pb(II) complexes with generation 1.5 ester-terminated dendron and generation 2 amino terminated counterpart.

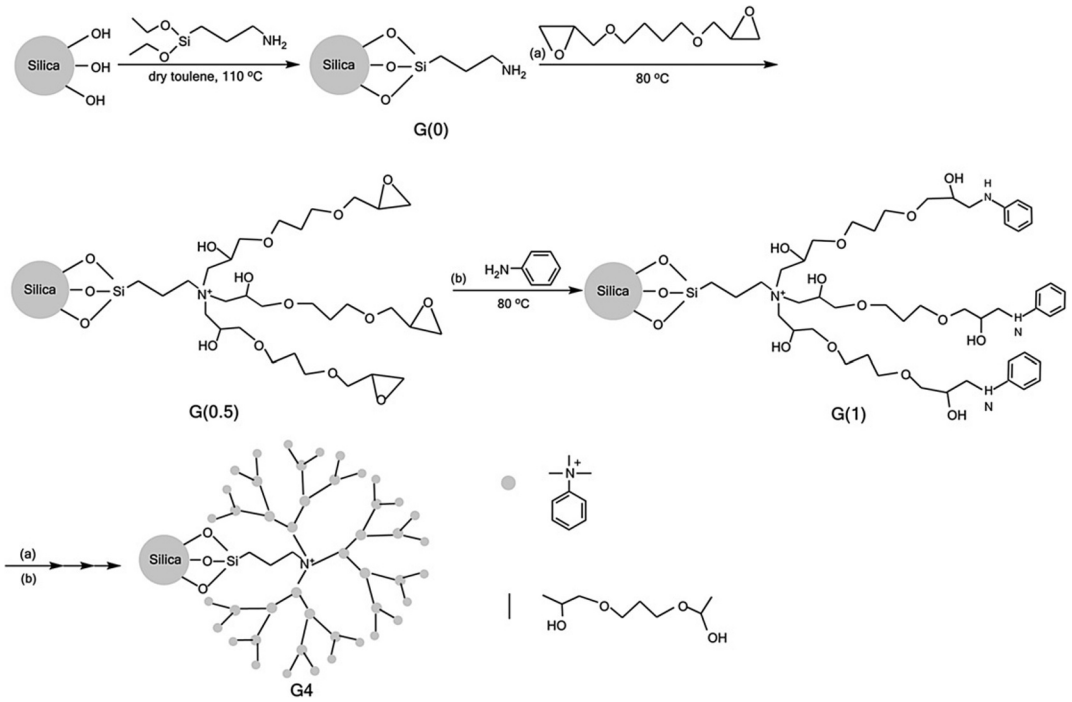

FIG. 17

Dendron development by 1,4-butanediol diglycidyl ether and aniline onto the surface of silica particles.

scheme by consecutive amine-epoxy reactions with 1,4-butanedioldiglycidyl ether and aniline (Fig. 17). The resultant material exhibited multiple retention mechanisms based on hydrophobic, anion-exchange, and hydrophilic interactions. Affinity was observed for polycyclic aromatic hydrocarbons, small polar compounds (such as nucleobases and nucleosides; [121]), and acid drugs, such as ketoprofen, naproxen, and ibuprofen [122].

Jiang et al. [123] functionalized SBA-15 mesoporous silica by PAMAM dendrimers and then further modified the external functional amino groups by EDTA (Fig. 18). The obtained inorganic-organic hybrid materials were capable of selective absorption toward metal cations, such as Pb^{2+}, Zn^{2+}, Cu^{2+}, Ni^{2+}, and Cr^{3+}. The high loading capacities recorded remained after regeneration experiments performed by acid and EDTA aqueous solutions.

By analogous method glycidyoxypropyltrimethoxysilane hyperbranched polyethylene imine was attached to silica microparticles and further functionalization of PEI with hydrophobic hexadecyl groups followed via cetyl glycidyl ether (Fig. 19). An increased absorption performance was observed for sodium dodecyl benzene sulfonate and hexadecylpyridinium chloride surfactants and for anionic dyes, such as methyl orange and Eosin Y [124].

Instead of silica, [125] treated a palygorskite, a clay adsorbent from magnesium aluminum silicate, with the organo-functional groups of PAMAM dendrons to produce high-density amino-terminated sites on its surface for the removal of Pb^{2+} and Reactive Red 3BS from water and observed very high

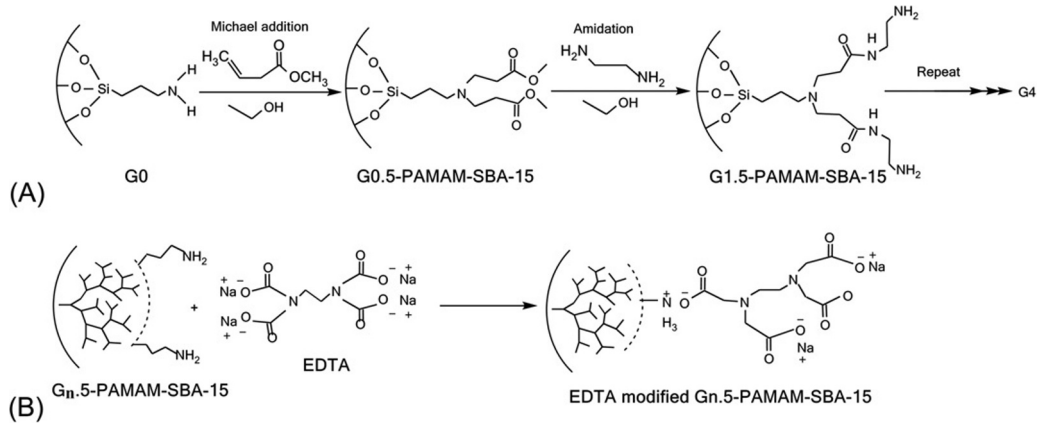

FIG. 18

Mesoporous silica functionalized by PAMAM dendrons (A) and then further modified by EDTA for the selective absorption of metal cations (B).

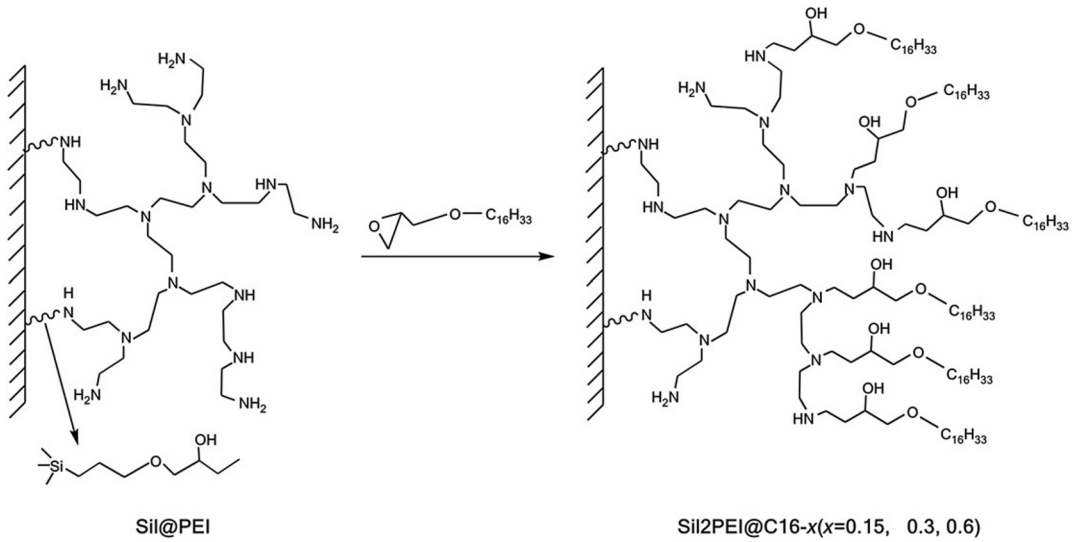

FIG. 19

Attachment of PEI hyperbranched polymers onto inorganic silica microparticles and functionalization with long aliphatic chains for the encapsulation of anionic dyes and surfactants.

adsorption capacities that increased as the number of generations increased. Analogous results were observed when ester- and amino-terminated PAMAM was introduced to chitosan [126]. The mixed materials exhibited better adsorption capabilities for Au^{3+} and Hg^{2+} The same tendency was observed when [127] developed third-generation PAMAM dendrons on a styrene divinylbenzene solid substrate for uranium adsorption. The calculated thermodynamic parameters $\Delta H°$, $\Delta S°$, and $\Delta G°$ proved the

endothermic and spontaneous nature of uranium adsorption into this hybrid substrate. Spontaneous desorption was obtained by decreasing the pH of the solution reaching its peak of 99% at pH 1. The growth of a dendron with amine and halide functionalities on polystyrene copolymer beads was performed by Ref. [128]. The resulting composite material was successfully applied for water disinfection against both Gram-positive and Gram-negative microorganisms.

In another implementation different generations PAMAM dendrons were grafted on poly(styrene-*co*-divinylbenzene) chelating resin and then were functionalized by phosphorus groups. Spontaneous, endothermic adsorption of uranium(VI) from aqueous solution was observed for the first three generations of PAMAM dendrons with maximum capacity (99.89 mg g^{-1}) at pH 5.0 [129].

2.5 BIOMIMETIC PREPARATION OF INORGANIC NANOPARTICLES VIA DENDRITIC MATRICES

Many aquatic organisms such as diatoms and sponges can synthesize an amazing diversity of nanostructured silica frameworks for their protective shells or glass spicules. This "biogenic" silica is formed rapidly under the mild conditions of temperatures, pressures, and pH that occur naturally in seawater. Polycationic peptides called silaffins, such as the R5 peptide, have been isolated from diatom cell walls and have been established as responsible for the formation of this diverse array of nanopatterned silica networks through a process known as biosilicification [130–133]. Based on this principle, Ref. [134] successfully produced silica nanospheres within seconds when they added amine-terminated poly(amidoamine) dendrimers to a solution of silicic acid. In general, it has been observed that poly(cationic) dendritic polymers and, specifically, poly(amidoamine) dendrimers and poly(propylene imine) hyperbranched polymers bearing terminal amino can mimic the behavior of silaffins and catalyze the hydrolysis of organosilicon compounds, leading to the formation of silicon dioxide nanoparticles. They may also act as templates, producing at ambient conditions organic/inorganic hybrid materials where dendritic macromolecules are embedded into silica nanoparticles, and this incorporation was proved by thermogravimetry and FTIR spectroscopy. Indeed, the nanoparticles produced by this environmentally friendly biomimetic method that copies biosilicification when observed employing electron microscopy were found to have spherical shapes similar to their organic matrices, with mean diameters analogous to their generation (Fig. 20).

Although incorporated into the interior of these nanospheres, the dendritic polymers retain their capability to encapsulate impurities; they are, however, firmly attached to the inorganic structure and are therefore practically nonleachable and can readily be applied in water treatment experiments. Hyperbranched PEI/silica hybrid nanoparticles have been synthesized through the biomimetic silicification process in phosphate buffer as potential low-cost adsorbents for two categories of pollutants with completely different characteristics. Under static conditions, the removal of toxic positively charged metal cations (Pb^{2+}, Cd^{2+}, Hg^{2+}) or negatively charged dichromate anions ($Cr_2O_7^{2-}$) and lipophilic polycyclic hydrocarbons (pyrene and phenanthrene) [135]. The nanospheres had isoelectric point of about 8, as determined by zeta-potential measurements, and were essentially nonporous as shown by porosimetry experiments. However, prolonged heat treatment at 700°C completely eliminated the polymer through thermal decomposition and induced pores with radii in the range of 2–5 nm in the respective polymer-free nanospheres and therefore some pollutant sorption capacity. Nevertheless, composite materials exhibited much higher adsorptions for both heavy metals and

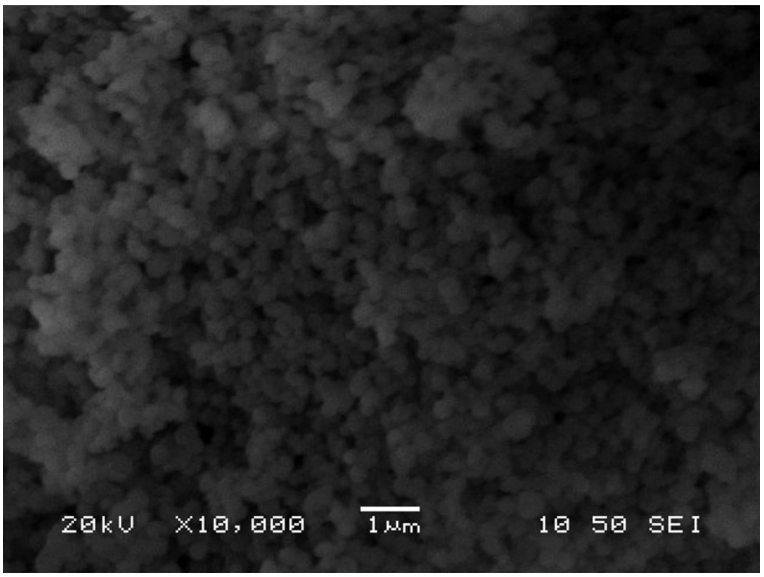

FIG. 20

SEM micrographs PEI-silica nanospheres.

organic aromatic hydrocarbons compared to bare silica nanoparticles. The sorption, for example, of Cr_2O_7 (II) was very fast and efficient, >90% retention reported within 1 h. In contrast negligible absorption to polymer-free counterparts was observed. This was attributed to electrostatic attractions that force the anions to approach the positively charged sorbing substrate bearing protonated amine groups.

For the positively charged metal ions tested—Pb(II), Cd(II), and Hg(II)—electrostatic interactions with the negatively charged silica periphery have been described as the main driving force for their encapsulation because the absorption rate into silica was directly correlated their ionic radii. Polarization tendency of the cations in response to the electric field of the negative charges of the deprotonated silanol groups present onto the silica surface increases as a function their size. It was therefore thermodynamically less likely for bulky Pb^{2+} to remain solvated to water. Although unfavorable from an electrostatic point of view, incorporation into hybrid nanospheres proceeds at a rate comparable, for Pb(II), or faster, for Cd(II) and Hg(II), than silica analogues because the repulsions from the polycationic core are counterbalanced by the strong chelating ability of PEI [136, 137] that lead to the formation of conventional metal – ligand complexes.

Pyrene was readily absorbed into silica down to a level of 40 ppb in static experiments. The sorption of the 10-fold more water-soluble phenanthrene was less thermodynamically favored, and 600 ppb remained in the solution after treatment. Amplification of the encapsulation of both lipophilic aromatic hydrocarbons into the composite PEI-silica to the level of 12 ppb for pyrene and 230 ppb for phenanthrene was observed because of the formation of charge-transfer complexes between the aromatic moiety and the amino groups of the hyperbranched polymer.

3 ROLE OF DENDRITIC POLYMERS IN WATER PURIFICATION BY ULTRAFILTRATION

Water purification via pressure-driven filtration through membranes is becoming the standard technology because conventional alternative processes, such as disinfection, distillation, sedimentation-flocculation, coagulation, and activated carbon water treatment techniques, require chemical additives, need high thermal inputs, or are inadequate for removing many toxic and viral factors to the level of laid-down specifications [138–141]. Membrane devices are flexible, scalable, modular, and relatively easy to operate and maintain. Although reverse osmosis and nanofiltration are effective at removing pollutants with molecular weights below 3000 Da, they have small pore sizes and, thus, require high pressures (100–1000 psi). On the other hand, ultrafiltration analogues require lower pressure to operate (5–60 psi) but lack efficiency for retaining organic and inorganic substances with low molar mass [142]. This restriction can be overcome by employing the dendritic polymers that possess internal nanocavities and much higher density of functional groups [143]. Hybrid materials consisting of porous inorganic scaffolds in conjunction with dendritic macromolecules present synergistic absorption potential because of the encapsulation properties of the macromolecules and the filtration capabilities of the standard porous inorganic solid materials. Apart from the properties of porous inorganic supports (composition, porosity, pore size distribution, and surface area), the efficiency of the developed separation devices is determined by the chemical nature of the periphery and the interior of the dendritic polymers, which, in several combinations, have shown exceptional water purification performance on the lab scale and thus the potential for being the basis for highly effective water purification systems.

Membranes bearing dendritic nanosponges can withstand harsh conditions, such as temperature up to 80°C and pH levels from 2 to 10 [144]. As discussed earlier, in contrast to reverse osmosis and nanofiltration, for water purification procedures, including a guest molecule into the dendritic cavities is a thermodynamically spontaneous process. Additionally, with their small size, globular structure, and lower intrinsic viscosity in comparison to linear polymers with the same molar mass, they have a very low tendency to foul both organic and inorganic types of membranes. Dendritic polymers as, for example, hyperbranched PEI also exhibit 10-fold chelating abilities for metal cations such as Co(II), Ni(II), Cu(II), Zn(II), Cd(II), in comparison to their linear analogues [145]. Generally, the branched structures present a more favorable topochemical environment for absorption than do linear structures, while the effect of the molecular weight on the chelating ability is negligible in both cases. Based on these superior metal ion complexation properties, during the last years hyperbranched PEI has been extensively applied on a variety of organic substrates, such as cation exchange resins [146], cellulose [147, 148], fungal biomass [149], and granules of self-immobilized bacteria [150].

It is concluded, thus, that apart from the comparatively smaller operating pressures, the dendritic macromolecules require less energy consumption in the conventional tangential/cross-flow systems commonly used in ultrafiltration plants. Their recorded loading capacities make them particularly attractive as high-capacity ligands. For most toxic pollutants, there is possibility of washing hybrid systems by an organic or aqueous solution with fine-tuned acidity or polarity. This causes their diffusion and the regeneration of the saturated dendritic films. The recycled filters can be reused without compromising their absorption properties.

Properly functionalized, these nanopolymers can carry out the encapsulation of the pollutants of interest, and then the molecular nanocomposites can be filtered and recovered by ultrafiltration.

Alternatively, they either may be directly integrated into membranes with or without covalent chemical attachment or may provide the basis for nanoparticles for hybrid ultrafiltration devices exhibiting efficient absorption properties, even for the smallest pollutants, for application in environmental remediation [138, 151].

3.1 SIMPLE RECOVERY OF DENDRITIC POLYMER/POLLUTANT COMPLEXES BY CONVENTIONAL ULTRAFILTRATION MEMBRANES

The first example of dendritic polymer application was a dendrimer-enhanced ultrafiltration device (DEUF) proposed by Diallo [56, 152, 153]. PAMAM dendrimers follow the general tendencies of the branched polymers mentioned before. They exhibit much larger binding capacities for metal ions in comparison to their linear polymers bearing terminal amino groups, and because of their globular shape, monodispersity, and larger size, they have much less of a tendency to pass through the pores of ultrafiltration membranes than do linear polymers of similar molar mass.

Water contaminated by copper cations was mixed with a solution of the nanopolymers, and then the resulting complexes were transferred to ultrafiltration units with the appropriate molecular weight cut-off to recover the clean water. The bonded Cu cations were separated from the nanopolymers by changing the acidity of the solution pH to 4.0, leading to the regeneration of the absorbing material. The same group also applied PPI dendrimers with hydrophobic cavities and positively charged internal amino groups for the selective recovery of perchlorate anions ClO_4^- over more hydrophilic anions, such as Cl^-, NO_3^-, SO_4^{2-}, and HCO_3^- [57].

Modifying PAMAM surface groups by benzoylthiourea functional groups provided a new, excellent ion chelating and exchange host with a distinct selectivity for several cations. Using polymer-supported ultrafiltration, Ref. [154] demonstrated the almost quantitative (>90%) retention of Co(II), Ni(II), Pb(II), and Zn(II) at pH 9. The Cu(II) and most all the notably thiophilic Hg(II) cations can be completely absorbed by the PAMAM derivative, even in strong acidic conditions, and therefore can be selectively removed from wastewaters and recovered.

In a first, and to our knowledge the only, example of a dendronized polymers used for retention of contaminants, Tülü and his group attached dendrons to a linear and a branched polymer (Fig. 21). The absorption profiles of these novel metal chelating dendritic molecules, termed "polychelatogens," were determined for a variety of bivalent and trivalent metal cations—Cr(III), Co(II), Ni(II), Cu(II), Zn(II), Cd(II), Pb(II), and Ag(I)—by filtration employing a Teflon membrane; a strong retention was observed because of complex formation. The regeneration of the metal-loaded absorbents was performed by decreasing the pH of the aqueous solutions and specifically applying sulfuric acid in the case of cooper [155].

Simple ultrafiltration "assisted" by dendritic polymers has many potential applications, such as the removal of toxic ions; heavy metal cations (e.g., mercury, lead, arsenate, chromium) and anions (e.g., perchlorate, nitrate, and phosphate), and organic pollutants (e.g., pharmaceuticals and pesticides) from industrial wastewater; the remediation of groundwater contaminated by anions (e.g., perchlorate); or the disinfection from microorganisms, such as bacteria and viruses, and the extraction and recovery of valuable metals (e.g., gold, silver, platinum, uranium) from aqueous solutions generated during in situ recovery mining.

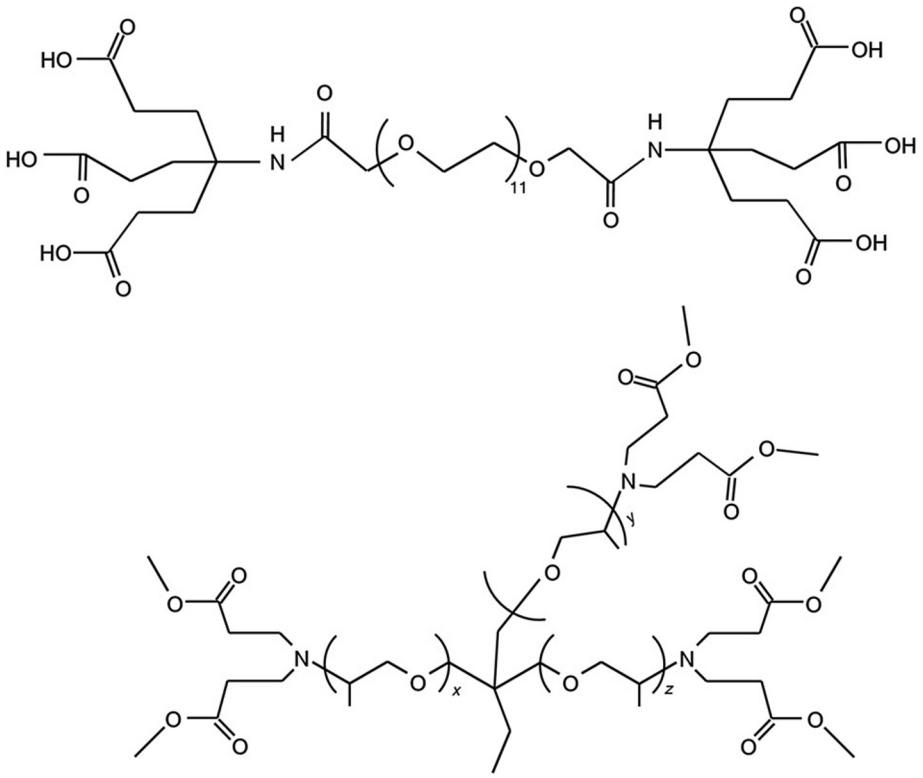

FIG. 21

Linear and branched dendronized polymers employed for the removal of bivalent and trivalent metal ions through filtration.

3.2 ULTRAFILTRATION BY MEMBRANES IMPREGNATED BY DENDRITIC POLYMERS

The encapsulation properties of the previously mentioned PAMAM dendrimers are indeed significant. On the other hand the time necessary to achieve equilibrium is rather long and consuming for their practical application as water pollutant extractors. This drawback can be overcome by combining solid-phase sorbents, that is, porous membranes, conventionally employed in filtration processes with optionally functionalized dendritic polymers. Coating the pores of stable substrates with nanosized dendritic sorbents affords hybrid modules of appropriate mechanical strength and high surface, resulting to increased contact area between contaminated water and the absorbing material. By meeting these prerequisites, which are necessary for an industrial process, hybrid systems are more efficient than the polymers alone and can readily be integrated into existing water filtration systems.

Hybrid organic/inorganic filter modules offer the possibility to affect the pore size and the realization of continuous-flow experiments using lab-scale modules. In a first study [156], a continuous process simulating ultrafiltration in the lab scale was developed. Ceramic multichannel tubes made

from porous titanium dioxide (porosity 37%, median pore diameter 8 μm) were covered with octyl- and octadecyl urea derivatives of the fifth-generation PPI dendrimer and hyperbranched PEI (Mw = 5000) and tested for their ability to remove PAH, polychlorinated biphenyls (PCBs), trihalogen methanes (THMs), methyl tert-butyl ether (MTBE), monoaromatic hydrocarbons (BTX), and pesticides (simazine, atrazine). By employing a single filtration step, considerable retention of representative compounds of organic pollutants having various solubilities in water was observed. Absorption efficiency was correlated to contaminant polarity. When increased percentages of dendritic polymers were employed and sufficient contact time between the absorbents and contaminated water was secured, however, it was possible for hybrid organic/inorganic filter modules to efficiently remove even the most polar pollutants from water. Large impregnation percentages also improve saturation levels. Absorption time can be elongated by lowering the flow rate, by increasing the length or the number of the ceramic filters, and by submitting water to recirculation. Carefully selecting dendritic polymers and fine-tuning their encapsulation properties through chemical reactions, combined with appropriate filtration parameters, can lead to retention levels approaching, in most cases, 100%.

Contact time between contaminated water and the absorbing surface and therefore filtration performance of the composite ceramic filters can be further improved by increasing the polymer impregnation percentage and carefully selecting the pore surface area, pore-size distribution, and mean pore size of the inorganic support. In this context, alumina filters with different structural characteristics were submitted to successive immersions into chloroform solutions of variable concentrations in *n*-octylurea-functionalized hyperbranched PEI [157]. It was concluded that to attain specific or maximum impregnation percentages, the immersions protocol must be experimentally defined and fine-tuned separately for each ceramic membrane depending on the structural parameters of its pore structure. Subsequent continuous filtration lab-scale experiments performed revealed the ideal impregnation percentage for each pollutant and type of hybrid hyperbranched polymer/ceramic filter for better pollutant absorption efficiency. After this optimization, it was possible to produce filtering devices that retain 98% of phenanthrene and 55% of the far more water-soluble β-naphthol, which was less thermodynamically prone to be encapsulated in the hydrophobic interior of the dendritic polymer. It is obvious that this process can be applied for a diversity of pollutants normally found in water and experimental conditions can easily adapted for scaling-up.

Ref. [158] synthesized three generations of amphiphilic aramide dendrimers functionalized by oligoethylene glycol chains (Fig. 22) and integrated them into a commercial polyamide nanofiltration membrane by direct percolation. The accumulation of the polymers into the pores resulted to the formation of a uniform coating of on top of the active layer of the substrate. Membrane performance toward Rhodamine WT dye and Ba^{2+} cations exceeded 85% retention while it was limited to about 30% for As^{3+} [158, 159].

3.3 ULTRAFILTRATION BY HYBRID MEMBRANES BASED ON COVALENT GRAFTING OF DENDRITIC POLYMERS ON INORGANIC OR ORGANIC SUBSTRATES

As mentioned before, triethoxysilyl-functionalization of the fourth-generation PPI and hyperbranched PEI did not compromise their absorption capabilities. Subsequent formation of siloxane bridges through hydrolysis of the ethoxysilyl groups and sol-gel reaction led to their polymerization, rendering the polymer derivatives practically insoluble in water while their adsorption capacity is still retained. If this cross-linking reaction takes place into the pores of ceramic filters, the size of the dendritic polymers

increases dramatically causing their physical immobilization and generating hybrid inorganic modules with practically nonleachable organic films.

Cylindrical ceramic filter modules made by three different materials (TiO_2, Al_2O_3, and SiC) having different porosities and median pore-size diameters were immersed into solutions of triethoxysilylated derivatives of PPI dendrimers and PG and PEI hyperbranched polymers [160]. The percentage of the

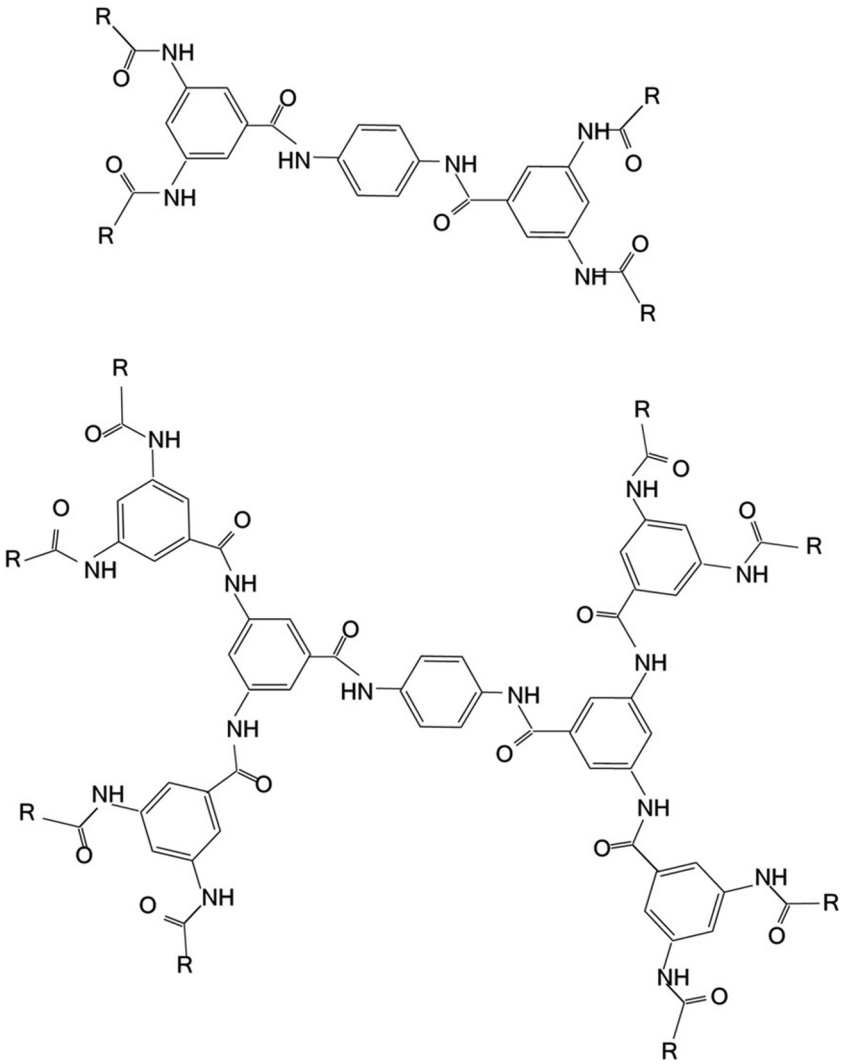

FIG. 22

Amphiphilic aramide dendrimers functionalized by oligoethylene glycol chains designed for the nanofiltration of dyes and metal cations.

Continued

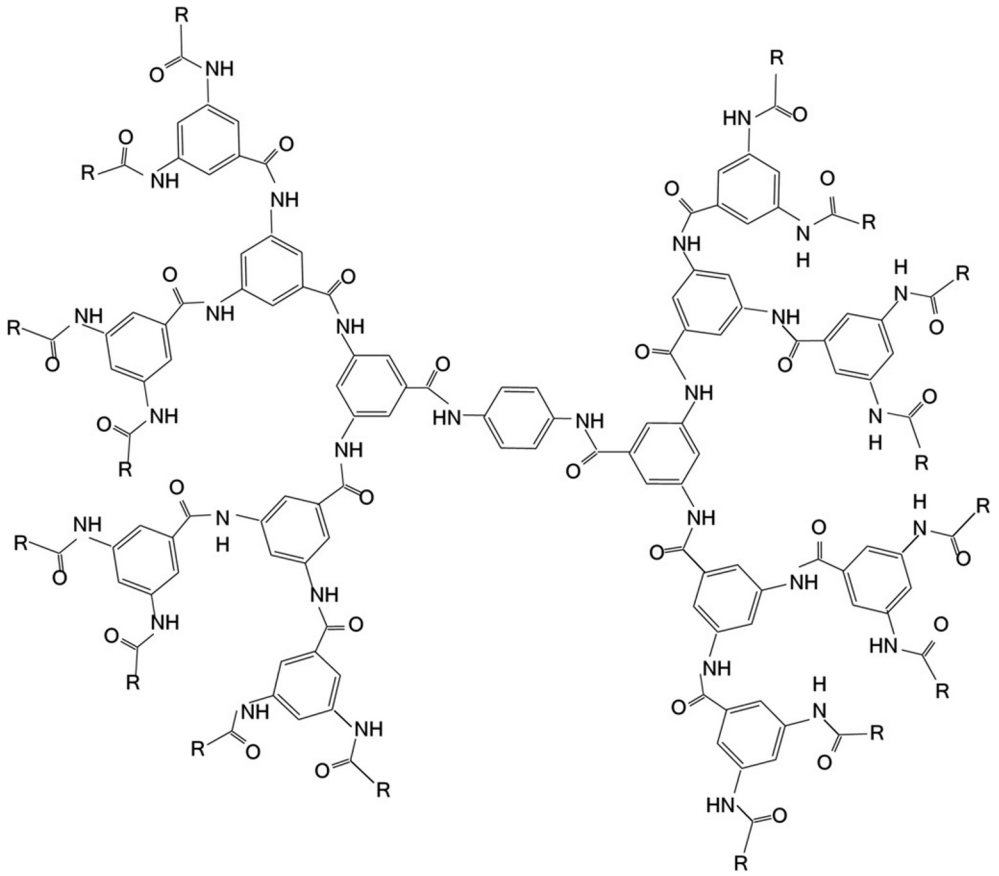

FIG. 22, cont'd

organic absorbing material incorporated into each inorganic substrate was dependent on the concentration and the viscosity of its solution, on the type of polymer, and on the porosity and pore size of the ceramic module.

Resulting composite filters were submitted to continuous filtration experiments in order to test their purification efficiency to a variety of pollutants, including PAH, monocyclic aromatic hydrocarbons, trihalogen methanes, pesticides, and methyl-tert-butyl ether. Superior pollutant retention was observed for all the processed filters compared to the nonimpregnated counterparts where pollutant retention did not exceed in any case 32% and for most pollutants ranged between 10% and 20%. Furthermore, water purification efficiency was improved by an increase in contact time between the contaminated water and the organic coating realized either by increasing impregnation percentages or by reducing water-flow rate and/or using of ceramic substrates with smaller pore size and higher porosity. Careful selection and fine-tuning of the filtration variables led to efficient water purification from anthracene and fluoranthene (up to 99%), benzene, toluene and xylene (up to 93%), and bromodichloromethane and

dibromochloromethane (up to 81%) whereas absorption of atrazine simazine and methyl-tert-butyl was up to about 45%. Regeneration of the filters was successfully performed via acetonitrile and gentle heating.

Apart from the formation of intermolecular and intramolecular Si—O—Si bridges, dendritic silanols can also condensate with hydroxyl groups present on the surfaces of inorganic filters when the latter are submitted to specific activation procedures [115]. From this reaction of the Si—OH groups with the M—OH moieties of the ceramic surface, Si—O—M bridges are formed. For example, titanium dioxide filter modules develop such functionalization when subjected to etching by immersion into 1 N NaOH solution for several hours. A second immersion into the solution of a dendritic triethoxysilyl derivative followed by curing affords as established by infrared spectroscopy, a nanostructured dendrimeric network covalently bound on the ceramic filter.

Continuous filtration experiments employing the resulting composite filters were performed for water-containing pyrene, phenanthrene, and β-naphthol for the assessment of their ability to encapsulate organic pollutants. The absorption of these polycyclic aromatic compounds was largely enhanced by the introduction of the silylated dendritic polymers in comparison to the nonimpregnated titanium dioxide filters. For example, pyrene is almost completely absorbed by 25-mm-long hybrid filters even at high filtration rates (4 and 7 mL min^{-1}), and its retention remains stable with eluted water volume, whereas a dramatical decrease is observed in the unprocessed membranes. Contact time of the contaminated water with the absorbing material is of crucial importance. Thus, an increase of the length of the filter module or, alternatively, the lowering of the water-flow rate improved filtration performance. Therefore, it was possible to remove pyrene and phenanthrene from water up to the level of a few ppb and to absorb >90% of β-naphthol.

Comparison of the symmetric PPI—Si—O—Si—PPI dendrimeric network with the nonsymmetric PEI—Si—O—Si—PEI network revealed that in all cases, the pollutant retention performance of the dendrimeric architecture for polycyclic aromatic hydrocarbons is inferior to that of hyperbranched architectures most notably at high flow rates (4–7 mL min^{-1}). When complete surface functionalization with ethoxysilane groups occurs, the symmetrical nature of PPI allows a high concentration of silanol groups at the external surface of the dendrimer. After hydrolysis and sol-gel reaction, a dense network of intermolecular siloxane bridges is formed. The stereochemistry of the cavities becomes therefore more rigid than the corresponding environment resulting from the silylated hyperbranched polymer polycondensation. This rigidity decreases the capability of the cavities to adopt in order to encapsulate bulky molecules and leads to a reduction of the inclusion rate. On the other hand, the inclusion constant is not affected. It is, thus, concluded that as was the case for the long alkyl chains, the main driving force for the inclusion process is the Gibbs free energy gained by the stabilization of the aromatic compounds inside the nonpolar cavities. The adaptability of the cavities to the stereochemistry of the targeted molecules should not be disregarded because it affects the kinetics of the absorption procedure. After the initial experiments the contaminated filters were also regenerated with acetonitrile at slightly elevated temperatures (<50°C) with no apparent loss in their efficiency.

In another example, Kotte reported a one-pot method for the production of mixed membranes bearing dendrimer nanoparticles formed by in situ PAMAM cross-linking to a matrix polyvinylidene fluoride that can serve as high-capacity sorbents for Cu(II) recovery from aqueous solutions by ultrafiltration [161]. The analogous cross-linking modification strategy was followed for the construction of a graphene oxide framework by ethylenediamine and hyperbranched PEI for effective heavy metal removal via nanofiltration with resulting composite membranes exhibiting comparably high rejections

toward Pb^{2+} (95.7%), Ni^{2+} (96%), Cd^{2+} (90.5%), and Zn^{2+} (97.4%) [162]. Composite nanofiltration membranes have also been fabricated by interfacial polymerization of different generations of hyperbranched polyesters (Fig. 23) impregnated into the pores of polyacrylonitrile. Nanofiltration performance in terms of anionic (Reactive brilliant blue X-BR and Acid red B) and cationic (Cationic red GTL) dyes retention was excellent, reaching to 99% for all dyes for implementation doped by the fourth generation of the dendritic polymer [163].

In a recent pioneering and very interesting work, Malinga and coworkers [164, 165] functionalized hyperbranched PEI by replacing amino groups by *b*-cyclodextrins (Fig. 24) and then chemically attached it to polysulfone (PSf) membranes via interfacial polymerization. The modification of PSf with *b*-CDHPEI resulted in enhanced hydrophilicity and water permeability during filtration experiments while the rejection of the humic acid from the doped membranes was almost double in comparison to the commercially available PSf standard. The authors attributed this result to a combination of size exclusion because of the reduction of the pore size induced by the chemical modification of the membranes and the presence of hydrophilic —OH, —NH groups that can bind water molecules through hydrogen bonding form a thin water film on the membrane that electrostatically repulses the humic acid. This latter property was also responsible for the antifouling properties observed in the implementations with the embedded *b*-CDHPEI complex. A replacement of *b*-cyclodextrin by laccase enzymes afforded membranes capable for the removal of bisphenol A (BPA) from water up to 89.6% [166].

4 CHALLENGES

Dendritic nanopolymers have received great scientific and technological interest in environmental remediation because of their unusual properties that bless them with unique retention behavior. There are, however, many hydrophilic organic contaminants, for example, many herbicides and pesticides that present high water solubility and are not adequately encapsulated into the dendritic cavities. In addition, many toxic metal cations, such as arsenic, do not have the tendency to form complexes. The discovery of new dendritic macromolecules with absorption properties for wider range of pollutants still remains a great challenge. In parallel, the development of absorbents with selectivity for specific compounds for their extraction or the remediation of accidents with environmental impact is also very useful.

Dendritic polymers can be readily integrated into existing ultrafiltration membranes but little reports have been made on the long-term performance of the dendritic nanopolymer composites. The time dependency of their efficiency is an important practical aspect that should be addressed much more in future. Pilot-scale testing is required to successfully integrate these novel nanostructured reactive membranes into existing water treatment plants.

Another requirement to be met in order for dendritic-membrane hybrids to be used in large-scale water remediation plants is to diminish the cost of the manufacturing techniques. This includes mainly expenses for the production of suitable dendritic compounds and their incorporation into the water purification procedure. The development of cheaper composite separation media that can be implemented in complex filtration devices for the decontamination of water from all possible pollutants—(1) polar,

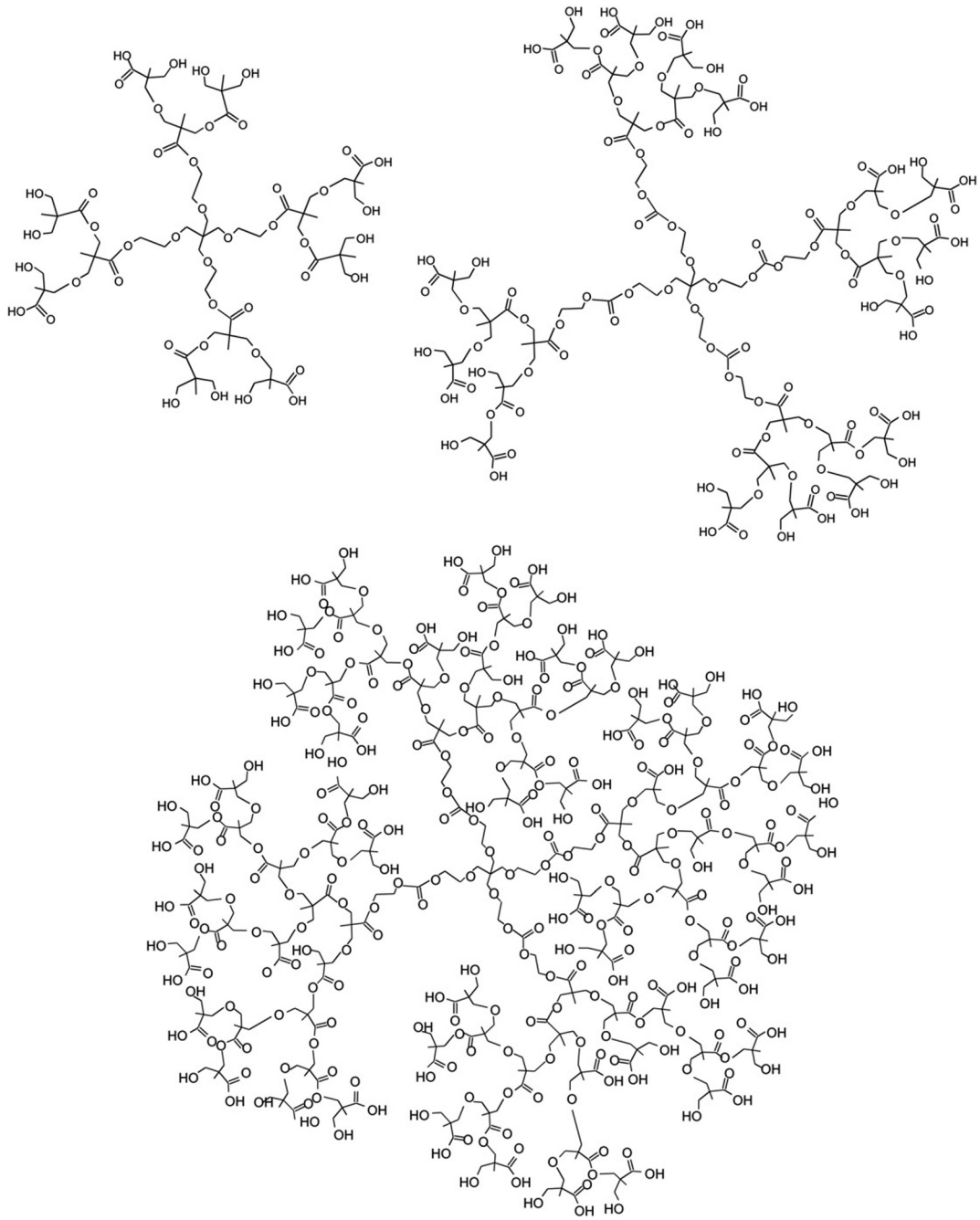

FIG. 23

Chemical structure of the different generation hyperbranched polyester molecules designed for the absorption of anionic and cationic dyes.

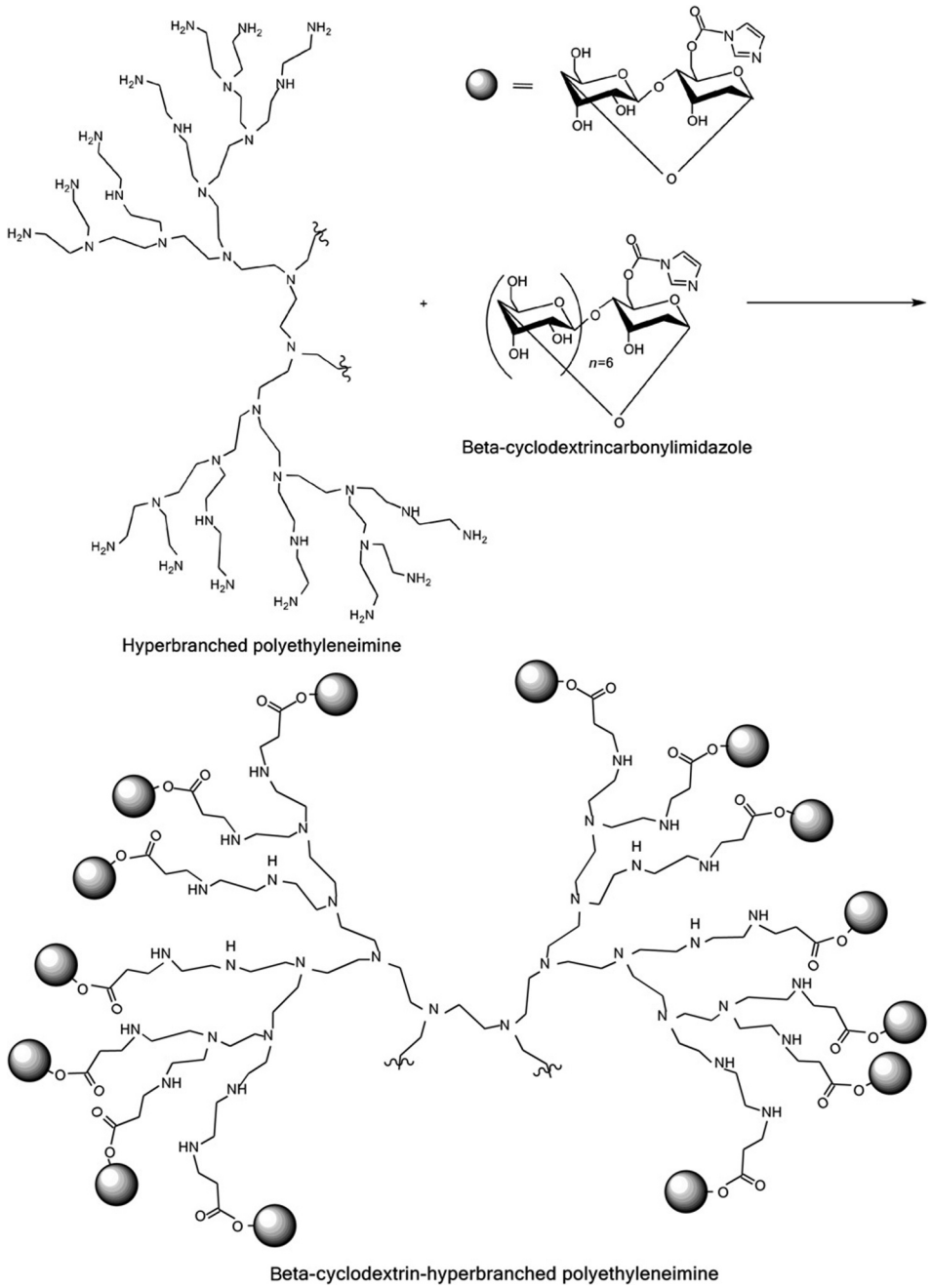

FIG. 24

Modification of hyperbranched PEI by *b*-cyclodextrins.

such as inorganic ions or organic pesticides; (2) lipophilic, such as organic solutes; and (3) biogenic, such as bacteria and other microorganisms—still remains hot research topic.

Another major challenge will be to address the toxicity of the absorbing materials. A number of in vitro and in vivo studies on the critical issues of toxicity, environmental fate, and biodistribution of the dendritic polymers have been carried out [167–169]. Dendritic polymers exhibit marginal toxicity in reference to other types of chemicals used. These studies suggest that the synthesis of nontoxic, environmentally acceptable, and biodegradable dendritic macromolecules is feasible and can be accomplished through a careful selection of the monomeric building blocks and optionally appropriate functionalization of the terminal groups. Therefore, a key aspect for the implementation of these nanomaterials is to meet the environmental regulatory conditions and, hence, by establishing their safety, to gain public acceptance.

5 CONCLUSION

The established ability to encapsulate efficiently a variety of compounds in their interior cavities because of their characteristic highly branched, or "treelike," architecture renders dendritic polymers very promising candidates as nanoscale materials in water purification. Their absorption properties depend on the ability to interact with the targeted pollutants. Structural features, for example, the symmetry and the flexibility of the branches, enhance adaptability and therefore effectiveness. Appropriate selection of the core, repeating units, and terminal end groups, as well as functionalization of the periphery, result in a diversity of nanosized containers with variable inclusion properties that may provide the basis for devices producing water that meets required standards on a case-by-case basis.

Their combination with solid absorbing materials, such as glass and cellulose particles, ceramic or organic membranes affords composite materials with increased surface area and mechanical strength with enhanced pollutant removal capabilities that can be readily incorporated on conventional pure-water production procedures. Various convenient approaches and optimization techniques have been employed toward this objective: (a) the simple covering of the support by a nanolayer of modified non-leachable, water-insoluble polymer; (b) the formation of chemical bonds, for example, by sol-gel reactions; (c) the direct propagation of a dendron on the surface of the solid host; and (d) the biomimetic synthesis of the inorganic substrate at the periphery of a dendritic matrix.

The demonstrated methodologies, where the encapsulation properties of dendritic polymers are not compromised, combined with the defined regeneration protocols, permit the production of effective recyclable filtration/purification systems that can be adopted for an extended range of applications. Although some issues, such as the universality and the cost-effectiveness of the methods, the marginal toxicity of some dendritic polymers, and pilot-scale studies with real water systems still need to be addressed, dendritic polymers exhibit so many important features that are surely very promising functional materials for water purification justifying further research on the field. The dendrimer enhanced ultrafiltration process exploits these unique properties to develop a new generation of low-pressure procedure for treating contaminated water. It is hoped therefore that the experimental work reviewed in this chapter will trigger the interest of other research groups to contribute to this rapidly expanding field.

REFERENCES

[1] R. Laurent, A.-M. Caminade, Dendrimers Inside Materials. Dendrimers: Towards Catalytic, Material and Biomedical Uses, John Wiley & Sons, Ltd, Chichester, 2011, pp. 267–311.

[2] A.W. Bosman, H.M. Janssen, E.W. Meijer, About dendrimers: structure, physical properties, and applications, Chem. Rev. 99 (1999) 1665–1688.

[3] J.M.J. Fréchet, C.J. Hawker, I. Gitsov, J.W. Leon, Dendrimers and hyperbranched polymers: two families of three-dimensional macromolecules with similar but clearly distinct properties, J. Macromol. Sci. Pure Appl. Chem. 33 (1996) 1399–1425.

[4] J.M.J. Fréchet, D.A. Tomalia, Dendrimers and Other Dendritic Polymers, first ed., John Wiley & Sons, Ltd., Chichester, 2001.

[5] C.C. Lee, J.A. MacKay, J.M.J. Fréchet, F.C. Szoka, Designing dendrimers for biological applications, Nat. Biotechnol. 23 (2005) 1517–1526.

[6] G.R. Newkome, C.N. Moorefield, F. Vögtle, Dendrimers and dendrons, in: Concepts, Syntheses, Perspectives, first ed., Wiley-VCH, Weinheim, 2001.

[7] G.R. Newkome, C.D. Shreiner, Poly(amidoamine), polypropyleneimine, and related dendrimers and dendrons possessing different $1 \rightarrow 2$ branching motifs: an overview of the divergent procedures, Polymer 49 (2008) 1–173.

[8] D.A. Tomalia, J.M.J. Fréchet, Discovery of dendrimers and dendritic polymers: a brief historical perspective, J. Polym. Sci. Part A Polym. Chem. 40 (2002) 2719–2728.

[9] F. Vögtle, S. Gestermann, R. Hesse, H. Schwierz, B. Windisch, Functional dendrimers, Prog. Polym. Sci. 25 (2000) 987–1041.

[10] N. Ardoin, D. Astruc, Molecular trees: from syntheses towards applications, Bull. Soc. Chim. Fr. 132 (1995) 875–909.

[11] P.R. Dvornic, D.A. Tomalia, Starburst dendrimers—a conceptual approach to nanoscopic chemistry and architecture, Macromol. Symp. 88 (1994) 123–148.

[12] D.C. Tully, J.M.J. Fréchet, Dendrimers at surfaces and interfaces: chemistry and applications, J. Chem. Commun. 14 (2001) 1229–1239.

[13] F. Zeng, S.C. Zimmerman, Dendrimers in supramolecular chemistry: from molecular recognition to self-assembly, Chem. Rev. 97 (7) (1997) 1681–1712.

[14] D. Astruc, E. Boisselier, C. Ornelas, Dendrimers designed for functions: from physical, photophysical, and supramolecular properties to applications in sensing, catalysis, molecular electronics, photonics, and nanomedicine, Chem. Rev. 110 (4) (2010) 1857–1959.

[15] S.M. Grayson, J.M.J. Fréchet, Convergent dendrons and dendrimers: from synthesis to applications, Chem. Rev. 101 (12) (2001) 3819–3867.

[16] B. Rosen, M. Wilson, C.J. Wilson, D.A. Peterca, M. Imam, M. R. and Percec V., Dendron-mediated self-assembly, disassembly, and self-organization of complex systems, Chem. Rev. 109 (11) (2009) 6275–6540.

[17] Y. Chen, X. Xiong, Tailoring dendronized polymers, Chem. Commun. 46 (28) (2010) 5049–5060.

[18] H. Frauenrath, Dendronized polymers—building a new bridge from molecules to nanoscopic objects, Prog. Polym. Sci. 30 (3–4) (2005) 325–384.

[19] A.D. Schlüter, J.P. Rabe, Dendronized polymers: synthesis, characterization, assembly at interfaces, and manipulation, Angew. Chem. Int. Ed. 39 (5) (2000) 864–883.

[20] A. Zhang, Synthesis, characterization and applications of dendronized polymers, Prog. Chem. 17 (1) (2005) 157–171.

[21] M. Jikei, M.-A. Kakimoto, Hyperbranched polymers: a promising new class of materials, Prog. Polym. Sci. 26 (8) (2001) 1233–1285.

[22] Y.H. Kim, Hyperbranched polymers 10 years after, J. Polym. Sci. A 36 (11) (1998) 1685–1698.

[23] E. Malmström, A. Hult, Hyperbranched polymers: a review J, Macromol. Sci. R. M. C. 37 (3) (1997) 555–579.
[24] A. Sunder, J. Heinemann, H. Frey, Controlling the growth of polymer trees: concepts and perspectives for hyperbranched polymers, Chem. A Eur. J. 6 (14) (2000) 2499–2506.
[25] B.I. Voit, Hyperbranched polymers: a chance and a challenge, C. R. Chim. 6 (8–10) (2003) 821–832.
[26] C.R. Yates, W. Hayes, Synthesis and applications of hyperbranched polymers, Eur. Polym. J. 40 (7) (2004) 1257–1281.
[27] M. Seiler, Hyperbranched polymers: phase behavior and new applications in the field of chemical engineering, Fluid Phase Equilib. 241 (1–2) (2006) 155–174.
[28] S.J. Teertstra, M. Gauthier, Dendrigraft polymers: macromolecular engineering on a mesoscopic scale, Prog. Polym. Sci. 29 (4) (2004) 277–327.
[29] P. Chen, Y. Yang, P. Bhattacharya, P. Wang, P.C. Ke, A tris-dendrimer for hosting diverse chemical species, J. Phys. Chem. C 115 (2011) 12789–12796.
[30] R.S. DeFever, N.K. Geitner, P. Bhattacharya, F. Ding, P.C. Ke, S. Sarupria, PAMAM dendrimers and graphene: materials for removing aromatic contaminants from water, Environ. Sci. Technol. 49 (7) (2015) 4490–4497.
[31] R.S. DeFever, S. Sarupria, Association of small aromatic molecules with PAMAM dendrimers, Phys. Chem. Chem. Phys. 17 (44) (2015) 29548–29557.
[32] S.H. Kim, M.H. Lamm, Multiscale modeling for host-guest chemistry of dendrimers in solution, Polym. Basel. 4 (2012) 463–485.
[33] L.B. Jensen, K. Mortensen, G.M. Pavan, M.R. Kasimova, D.K. Jensen, V. Gadzhyeva, H.M. Nielsen, C. Foged, Molecular characterization of the interaction between siRNA and PAMAM G7 dendrimers by SAXS, ITC, and molecular dynamics simulations, Biomacromolecules 11 (2010) 3571–3577.
[34] C.V. Kelly, M.G. Liroff, L.D. Triplett, P.R. Leroueil, D.G. Mullen, J.M. Wallace, S. Meshinchi, J.R. Baker, B.G. Orr, M.M.B. Holl, Stoichiometry and structure of poly(amidoamine) dendrimer-lipid complexes, ACS Nano 3 (2009) 1886–1896.
[35] W. Yang, Y. Li, Y. Cheng, Q. Wu, L. Wen, T. Xu, Evaluation of phenylbutazone and poly(amidoamine) dendrimers interactions by a combination of solubility, 2D-NOESY NMR, and isothermal titration calorimetry studies, J. Pharm. Sci. 98 (2009) 1075–1085.
[36] X. Shi, X. Bi, T.R. Ganser, S. Hong, L.A. Myc, A. Desai, M.M.B. Holl, J.R. Baker, HPLC analysis of functionalized poly(amidoamine) dendrimers and the interaction between a folate-dendrimer conjugate and folate binding protein, Analyst 131 (2006) 842–848.
[37] E. Froehlich, J.S. Mandeville, C.J. Jennings, R. Sedaghat-Herati, H.A. Tajmir-Riahi, Dendrimers bind human serum albumin, J. Phys. Chem. B 113 (2009) 6986–6993.
[38] M. Lard, S.H. Kim, S. Lin, P. Bhattacharya, P.C. Ke, M.H. Lamm, Fluorescence resonance energy transfer between phenanthrene and PAMAM dendrimers, Phys. Chem. Chem. Phys. 12 (2010) 9285–9291.
[39] J.S. Mandeville, H.A. Tajmir-Riahi, Complexes of dendrimers with bovine serum albumin, Biomacromolecules 11 (2010) 465–472.
[40] M. Orberg, K. Schillen, T. Nylander, Dynamic light scattering and fluorescence study of the interaction between double-stranded DNA and poly(amido amine) dendrimers, Biomacromolecules 8 (2007) 1557–1563.
[41] J. Hu, Y. Cheng, Y. Ma, Q. Wu, T. Xu, Host-guest chemistry and physicochemical properties of the dendrimer-mycophenolic acid complex, J. Phys. Chem. B 113 (2009) 64–74.
[42] J. Hu, Y. Cheng, Q. Wu, L. Zhao, T. Xu, Host-guest chemistry of dendrimer-drug complexes. 2. Effects of molecular properties of guests and surface functionalities of dendrimers, J. Phys. Chem. B 113 (2009) 10650–10659.

[43] M.I. Montanez, F. Najera, E. Perez-Inestrosa, NMR studies and molecular dynamic simulation of synthetic dendritic antigens, Polymer 3 (2011) 1533–1553.
[44] M.J. Jasmine, E. Prasad, Fractal growth of PAMAM dendrimer aggregates and its impact on the intrinsic emission properties, J. Phys. Chem. B 114 (2010) 7735–7742.
[45] M.S. Diallo, L. Balogh, A. Shafagati, J.H. Johnson Jr., W.A. Goddard III, D.A. Tomalia, Poly(amidoamine) dendrimers: a new class of high capacity chelating agents for Cu(II) ions, Environ. Sci. Technol. 33 (1999) 820–824.
[46] M.S. Diallo, S. Christie, P. Swaminathan, L. Balogh, X. Shi, W. Um, C. Papelis, W.A. Goddard III, J.H. Johnson Jr., Dendritic chelating agents. 1. Cu(II) binding to ethylene diamine core poly(amidoamine) dendrimers in aqueous solutions, Langmuir 20 (2004) 2640–2651.
[47] M.C. Feiters, E.W. Meijer, R.J.M. Vogtle, A multi-O_2 complex derived from a copper (I) dendrimer, Chem. A Eur. J. 5 (1999) 65–69.
[48] M.F. Ottaviani, E. Cossu, N.J. Turro, D.A. Tomalia, Characterization of sturburst dendrimers by electron paramagnetic resonance. 2. Positively charged nitroxide radicals of varible chain length used as spin probes, J. Am. Chem. Soc. 117 (1995) 4387–4398.
[49] M.S. Diallo, W. Arasho, J.H. Johnson Jr., W.A. Goddard III, Dendritic chelating agents. 2. U(VI) binding to poly(amidoamine) and poly(propyleneimine) dendrimers in aqueous solutions, Environ. Sci. Technol. 42 (2008) 1572–1579.
[50] M.F. Ottaviani, P. Favuzza, M. Bigazzi, N.J. Turro, S. Jockusch, D.A. Tomalia, A TEM and EPR investigation of the competitive binding of uranyl ions to starburst dendrimers and liposomes: potential use of dendrimers as uranyl ion sponges, Langmuir 16 (2000) 7368–7372.
[51] L. Balogh, D.A. Tomalia, Poly(Amidoamine) dendrimer-templated nanocomposites. 1. Synthesis of zero-valent copper nanoclusters, J. Am. Chem. Soc. 120 (1998) 7355–7356.
[52] Y. Niu, R.M. Crooks, Dendrimer-encapsulated metal nanoparticles and their applications to catalysis, C. R. Chim. 6 (2003) 1049–1059.
[53] M. Zhao, L. Sun, R.M. Crooks, Preparation of cu nanoclusters within dendrimer templates, J. Am. Chem. Soc. 120 (1998) 4877–4878.
[54] M. Zhao, R.M. Crooks, Dendrimer-encapsulated Pt nanoparticles: synthesis, characterization, and applications to catalysis, Adv. Mater. 11 (1999) 217–220.
[55] E.R. Birnbaum, K.C. Rau, N.N. Sauer, Selective anion binding from water using soluble polymers, Sep. Sci. Technol. 38 (2003) 389–404.
[56] M.S. Diallo, S. Christie, P. Swaminathan, J.H. Johnson Jr., W.A. Goddard III, Dendrimer enhanced ultrafiltration. 1. Recovery of Cu(II) from aqueous solutions using PAMAM dendrimers with ethylene diamine core and terminal NH_2 groups, Environ. Sci. Technol. 39 (2005) 1366–1377.
[57] M.S. Diallo, K. Falconer, J.H. Johnson Jr., W.A. Goddard III, Dendritic anion hosts: perchlorate uptake by G5-NH2 poly(propyleneimine) dendrimer in water and model electrolyte solutions, Environ. Sci. Technol. 41 (2007) 6521–6527.
[58] H. Stephan, H. Spies, B. Johannsen, L. Klein, F. Vögtle, Lipophilic urea-functionalized dendrimers as efficient carriers for oxyanions, Chem. Commun. (1999) 1875–1876.
[59] L. Twyman, J. Beezer, A.E. Esfand, R. Hardy M. J. and Mitchell, J. C., The synthesis of water soluble dendrimers, and their application as possible drug delivery systems, Tetrahedron Lett. 40 (1999) 1743–1746.
[60] G.R. Newkome, Z. Yao, G.R. Baker, V.K. Gupta, Micelles. Part 1. Cascade molecules: a new approach to micelles. A [27]-arborol, J. Org. Chem. 50 (1985) 2003–2004.
[61] G.R. Newkome, C.N. Moorefield, G.R. Baker, A.L. Johnson, R.K. Behera, Alkane cascade polymers possessing micellar topology: micellanoic acid derivatives, Angew. Chem. Int. Ed. Engl. 30 (1991) 1176–1178.
[62] G.R. Newkome, C.N. Moorefield, G.R. Baker, M.J. Saunders, S.H. Grossman, Unimolecular micelles, Angew. Chem. Int. Ed. Engl. 30 (1991) 1178–1180.

[63] M.F. Ottaviani, S. Bossmann, N.J. Turro, D.A. Tomalia, Characterization of starburst dendrimers by the EPR technique. 1. Copper complexes in water solution, J. Am. Chem. Soc. 116 (1994) 661–671.
[64] M.F. Ottaviani, C. Turro, N.J. Turro, S.H. Bossmann, D.A. Tomalia, Nitroxide-labeled Ru(II) polypyridyl complexes as EPR probes of organized systems. 3. Characterization of starburst dendrimers and comparison to photophysical measurements, J. Phys. Chem. 100 (1996) 13667–13674.
[65] M.F. Ottaviani, F. Montalti, N.J. Turro, D.A. Tomalia, Characterization of starburst dendrimers by the EPR technique. Copper(II) ions binding full-generation dendrimers, J. Phys. Chem. B 101 (1997) 158–166.
[66] C. Turro, S. Niu, S.H. Bossmann, D.A. Tomalia, N.J. Turro, Binding of *Ru(phen)3^{2+} to starburst dendrimers and its quenching by Co(phen)3^{3+}: generation dependence of the quenching rate constant, J. Phys. Chem. 99 (1995) 5512–5517.
[67] G. Pistolis, A. Malliaris, D. Tsiourvas, C.M. Paleos, Poly(propyleneimine) dendrimers as pH-sensitive controlled-release systems, Chem. A Eur. J. 5 (1999) 1440–1444.
[68] Z. Sideratou, D. Tsiourvas, C.M. Paleos, Quaternized poly(propylene imine) dendrimers as novel pH-sensitive controlled-release systems, Langmuir 16 (2000) 1766–1769.
[69] Z. Sideratou, D. Tsiourvas, C.M. Paleos, Solubilization and release properties of PEGylated diaminobutane poly(propylene imine) dendrimers, J. Colloid Interface Sci. 242 (2001) 272–276.
[70] G. Pistolis, A. Malliaris, Study of poly(propylene imine) dendrimers in water, by exciplex formation, Langmuir 18 (2002) 246–251.
[71] O.N. Monaco, S.C. Tomas, M.K. Kirrane, A.M. Balija, Bis(benzylamine) monomers: one-pot preparation and application in dendrimer scaffolds for removing pyrene from aqueous environments, Beilstein J. Org. Chem 9 (2013) 2320–2327.
[72] R.M. Triano, M.L. Paccagnini, A.M. Balija, Effect of dendrimeric composition on the removal of pyrene from water, Springer Plus 4 (1) (2015) 511.
[73] S. Jockusch, N.J. Turro, D.A. Tomalia, Aggregation of methylene blue adsorbed on starburst dendrimers, Macromolecules 28 (1995) 7416–7418.
[74] M. Irfan, M. Seiler, Encapsulation using hyperbranched polymers: from research and technologies to emerging applications, Ind. Eng. Chem. Res 49 (2010) 1169–1196.
[75] K.K. Kline, S.A. Tucker, Spectroscopic investigations of core-based, randomly hyperbranched polymers and comparison with their dendrimeric counterparts, J. Phys. Chem. A 113 (2009) 12891–12897.
[76] K.K. Kline, S.A. Tucker, Spectroscopic characterization of core-based hyperbranched poly(ethyleneimine) and dendritic poly(propyleneimine) as selective uptake devices, J. Phys. Chem. A 114 (2010) 7338–7344.
[77] S. Mecking, R. Thomann, H. Frey, A. Sunder, Preparation of catalytically active palladium nanoclusters in compartments of amphiphilic hyperbranched polyglycerols, Macromolecules 33 (2000) 3958–3960.
[78] D.C. Wan, Q. Fu, J.L. Huang, Synthesis of amphiphilic Hyperbranched polyglycerol polymers and their application as template for size control of gold, Nano. J. Appl. Polym. Sci. 101 (2006) 509–514.
[79] Z.D. Zhu, L. Kai, Y.C. Wang, Synthesis and applications of hyperbranched polyesters preparation and characterization of crystalline silver nanoparticles, Mater. Chem. Phys. 96 (2006) 447–453.
[80] Y.H. Kim, O.W. Webster, Water-soluble hyperbranched polyphenylene; "a unimolecular micelle"? J. Am. Chem. Soc. 112 (1990) 4592–4593.
[81] N.K. Geitner, P. Bhattacharya, M. Steele, R. Chen, D.A. Ladner, P.C. Ke, Understanding dendritic polymer-hydrocarbon interactions for oil dispersion, RSC Adv. 2 (25) (2012) 9371–9375.
[82] A. Sunder, M. Krämer, R. Hanselmann, R. Mülhaupt, H. Frey, Molecular nanocapsules based on amphiphilic hyperbranched polyglycerols, Angew. Chem. Int. Ed. 38 (1999) 3552–3555.
[83] S.E. Stiriba, H. Kautz, H. Frey, Hyperbranched molecular nanocapsules: comparison of the hyperbranched architecture with the perfect linear analogue, J. Am. Chem. Soc. 124 (2002) 9698–9699.

[84] Y. Cheng, Dendrimer-Based Drug Delivery Systems: From Theory to Practice Hoboken, John Wiley & Sons, Hoboken, NJ, 2012.
[85] A. D'Emanuele, D. Attwood, Dendrimer-drug interactions, Adv. Drug Deliv. Rev. 57 (2005) 2147–2162.
[86] V. Gajbhiye, P. Kumar, V. Tekade, R.K. Jain, N. K., Pharmaceutical and biomedical potential of PEGylated dendrimers, Curr. Pharm. Des. 13 (2007) 415–429.
[87] C.M. Paleos, D. Tsiourvas, Z. Sideratou, Molecular engineering of dendritic polymers and their application as drug and gene delivery systems, Mol. Pharm. 4 (2007) 169–188.
[88] C.M. Paleos, D. Tsiourvas, Z. Sideratou, L.-A. Tziveleka, Multifunctional dendritic drug delivery systems: design, synthesis, controlled and triggered release, Curr. Top. Med. Chem. 8 (2008) 1204–1224.
[89] W. Ke, K. Shao, R. Huang, L. Han, Y. Liu, J. Li, Y. Kuang, L. Ye, J. Lou, C. Jiang, Gene delivery targeted to the brain using an angiopep-conjugated polyethyleneglycol-modified polyamidoamine dendrimer, Biomaterials 30 (2009) 6976–6985.
[90] S.F. Peng, C.J. Su, M.C. Wei, C.Y. Chen, Z.X. Liao, P.W. Lee, H.L. Chen, H.W. Sung, Effects of the nanostructure of dendrimer/DNA complexes on their endocytosis and gene expression, Biomaterials 31 (2010) 5660–5670.
[91] D. Shcharbin, V. Dzmitruk, A. Shakhbazau, N. Goncharova, I. Seviaryn, S. Kosmacheva, M. Potapnev, E. Pedziwiatr-Werbicka, M. Bryszewska, M. Talabaev, A. Chernov, V. Kulchitsky, A.M. Caminade, J.P. Majoral, Fourth generation phosphorus-containing dendrimers: prospective drug and gene delivery carrier, Pharmaceutics 3 (2011) 458–473.
[92] L. Han, J. Li, S. Huang, R. Huang, S. Liu, X. Hu, P. Yi, D. Shan, X. Wang, H. Lei, C. Jiang, Peptide-conjugated polyamidoamine dendrimer as a nanoscale tumor-targeted T1 magnetic resonance imaging contrast agent, Biomaterials 32 (2011) 2989–2998.
[93] Q.T. Nguyen, E.S. Olson, T.A. Aguilera, T. Jiang, M. Scadeng, L.G. Ellies, R.Y. Tsien, Surgery with molecular fluorescence imaging using activatable cell-penetrating peptides decreases residual cancer and improves survival, Proc. Natl. Acad. Sci. U. S. A. 107 (2010) 4317–4322.
[94] E.S. Olson, T. Jiang, T.A. Aguilera, Q.T. Nguyen, L.G. Ellies, M. Scadeng, R.Y. Tsien, Activatable cell penetrating peptides linked to nanoparticles as dual probes for in vivo fluorescence and mr imaging of proteases, Proc. Natl. Acad. Sci. U. S. A. 107 (2010) 4311–4316.
[95] U. Gupta, H.B. Agashe, A. Asthana, N.K. Jain, Dendrimers: novel polymeric nanoarchitectures for solubility enhancement, Biomacromolecules 7 (2006) 649–658.
[96] K. Inoue, Functional dendrimers, hyperbranched and star polymers, Prog. Polym. Sci. 25 (2000) 453–571.
[97] C.M. Paleos, Polymerization in Organized Media, Gordon and Breach Publishers, New York, 1992, pp. 183–214.
[98] K. Freedman, O. Lee, J. Li, Y. Luo, D. Skobeleva, V.B. Ke, P. C., Diffusion of single star-branched dendrimer-like DNA, J. Phys. Chem. B 109 (2005) 9839–9842.
[99] B. Helms, E.W. Meijer, Dendrimers at work, Science 313 (2006) 929–930.
[100] M. Mortimer, K. Kasemets, M. Heinlaan, I. Kurvet, A. Kahru, High throughput kinetic vibrio fischeri bioluminescence inhibition assay for study of toxic effects of nanoparticles, Toxicol. In Vitro 22 (2008) 1412–1417.
[101] P.C. Naha, M. Davoren, A. Casey, H.J. Byrne, An ecotoxicological study of poly(amidoamine) dendrimers-toward quantitative structure activity relationships, Environ. Sci. Technol. 43 (2009) 6864–6869.
[102] P. Bhattacharya, N.K. Geitner, S. Sarupria, P.C. Ke, Exploiting the physicochemical properties of dendritic polymers for environmental and biological applications, Phys. Chem. Chem. Phys. 15 (13) (2013) 4477–4490.
[103] T.A. Felekis, N. Katsaros, Environment and nanotechnology: a promising challenge, J. Environ. Prot. Ecol. 10 (4) (2009) 1146–1154.
[104] M.M. Khin, A.S. Nair, V.J. Babu, R. Murugan, S. Ramakrishna, A review on nanomaterials for environmental remediation, Energ. Environ. Sci. 5 (8) (2012) 8075–8109.

[105] S. Kar, P.K. Tewari, Nanotechnology for domestic water purification in Pacheco-Torgal, in: F. Diamanti, M.V. Nazari, A. Goran-Granqvist, C. Nanotechnology (Eds.), Eco-Efficient Construction: Materials, Processes and Applications., Woodhead Publishing Limited, Sawston, 2013, pp. 364–427 (Chapter 16).
[106] M.A. Barakat, M.H. Ramadan, M.A. Alghamdi, S.S. Algarny, H.T. Woodcock, J.N. Kuhn, Remediation of Cu(II), Ni(II), and Cr(III) ions from simulated wastewater by dendrimer/titania composites, J. Environ. Manage. 117 (2013) 50–57.
[107] M. Arkas, D. Tsiourvas, C.M. Paleos, Functional dendrimeric "nanosponges" for the removal of polycyclic aromatic hydrocarbons from water, Chem. Mater. 15 (2003) 2844–2847.
[108] J.R. Lakowicz, Principles of Fluorescence Spectroscopy, Plenum Press, New York/London, 1983, p. 8.
[109] D.Q. Li, M. Ma, New organic nanoporous polymers and their inclusion complexes, Chem. Mater. 11 (1999) 872–874.
[110] D.Q. Li, M. Ma, Nanoporous polymers: new nanosponge absorbent media, Filtr. Sep 36 (1999) 26–28.
[111] M. Fischer, F. Vogtle, Dendrimers: from design to application—a progress report, Angew. Chem. Int. Ed. 38 (1999) 885–905.
[112] A. Ramzi, R. Scherrenberg, J. Brackman, J. Joosten, K. Mortensen, Intermolecular interactions between dendrimer molecules in solution studied by small-angle neutron scattering, Macromolecules 31 (1998) 1621–1626.
[113] M.I. Vázquez, M. Algarra, J. Benavente, Modification of regenerated cellulose membrane based on thiol dendrimer, Carbohydr. Polym. 131 (2015) 273–279.
[114] M. Arkas, L. Eleades, C.M. Paleos, D. Tsiourvas, Alkylated hyperbranched polymers as molecular nanosponges for the purification of water from polycyclic aromatic hydrocarbons, J. Appl. Polym. Sci. 97 (2005) 2299–2305.
[115] M. Arkas, D. Tsiourvas, C.M. Paleos, Organosilicon dendritic networks in porous ceramics for water purification, Chem. Mater. 17 (2005) 3439–3444.
[116] P.R. Dvornic, PAMAMOS: the first commercial silicon-containing dendrimers and their applications, J. Polym. Sci. Part A Polym. Chem. 44 (2006) 2755–2773.
[117] P.R. Dvornic, M.J. Owen, Radially layered poly(amidoamineorganosilicon) dendrimers, ACS Sym. Ser. 1051 (2010) 135–145.
[118] E. Ruckenstein, W. Yin, SiO_2-poly(amidoamine) dendrimer inorganic/organic hybrids, J. Polym. Sci. Part A Polym. Chem. 38 (2000) 1443–1449.
[119] C.-C. Chu, N. Ueno, T. Imae, Solid-phase synthesis of amphiphilic dendron-surface-modified silica particles and their application toward water purification, Chem. Mater. 20 (2008) 2669–2676.
[120] Y. Niu, R. Qu, C. Sun, C. Wang, H. Chen, C. Ji, Y. Zhang, X. Shao, F. Bu, Adsorption of Pb(II) from aqueous solution by silica-gel supported hyperbranched polyamidoamine dendrimers, J. Hazard. Mater. 244–245 (2013) 276–286.
[121] Y. Li, J. Yang, J. Jin, X. Sun, L. Wang, J. Chen, New reversed-phase/anion-exchange/hydrophilic interaction mixed-mode stationary phase based on dendritic polymer-modified porous silica, J. Chromatogr. A 1337 (2014) 133–139.
[122] Y. Li, J. Yang, C. Huang, L. Wang, J. Wang, J. Chen, Dendrimer-functionalized mesoporous silica as a reversed-phase/anion-exchange mixed-mode sorbent for solid phase extraction of acid drugs in human urine, J. Chromatogr. A 1392 (2015) 28–36.
[123] Y. Jiang, Q. Gao, H. Yu, Y. Chen, F. Deng, Intensively competitive adsorption for heavy metal ions by PAMAM-SBA-15 and EDTA-PAMAM-SBA-15 inorganic–organic hybrid materials, Microporous Mesoporous Mater 103 (2007) 316–324.
[124] F. Chen, D.-C. Wan, M. Jin, H.-T. Pu, Elimination of surfactants and small dyes from water with silica-supported dendritic amphiphiles, Chinese J. Polym. Sci. 34 (1) (2015) 59–68.
[125] S. Zhou, A. Xue, Y. Zhang, M. Li, K. Li, Y. Zhao, W. Xing, Novel polyamidoamine dendrimer-functionalized palygorskite adsorbents with high adsorption capacity for Pb^{2+} and reactive dyes, Appl. Clay Sci. 107 (2015) 220–229.

[126] R. Qu, C. Sun, C. Ji, C. Wang, H. Chen, Y. Niu, C. Liang, Q. Song, Preparation and metal-binding behaviour of chitosan functionalized by ester-and amino-terminated hyperbranched polyamidoamine polymers, Carbohydr. Res. 343 (2008) 267–273.
[127] P. Ilaiyaraja, A. Kumar, S. Deb, K. Sivasubramanian, D. Ponraju, B. Venkatraman, Adsorption of uranium from aqueous solution by PAMAM dendron functionalized styrene divinylbenzene, J. Hazard. Mater. 250–251 (2013) 155–166.
[128] D. Gangadharan, N. Dhandhala, D. Dixit, R. Singh, T. Kiritkumar, M. Popat, P.S. Anand, Investigation of solid supported dendrimers for water disinfection, J. Appl. Polym. Sci. 124 (2) (2012) 1384–1391.
[129] Q. Cao, Y. Liu, C. Wang, J. Cheng, Phosphorus-modified poly(styrene-co-divinylbenzene)-PAMAM chelating resin for the adsorption of uranium(VI) in aqueous, J. Hazard. Mater. 263 (2013) 311–321.
[130] M.R. Knecht, D.W. Wright, Functional analysis of the biomimetic silica precipitating activity of the R5 peptide from cylindrotheca fusiformis, Chem. Commun. 24 (2003) 3038–3039.
[131] N. Kröger, R. Deutzmann, M. Sumper, Polycationic peptides from diatom biosilica that direct silica nanosphere formation, Science 286 (1999) 1129–1132.
[132] N. Kröger, R. Deutzmann, C. Bergsdorf, M. Sumper, Species-specific polyamines from diatoms control silica morphology, Proc. Natl. Acad. Sci. U. S. A. 97 (2000) 14133–14138.
[133] M. Sumper, E. Brunner, Learning from diatoms: nature's tools for the production of nanostructured silica, Adv. Funct. Mater. 16 (2006) 17–26.
[134] M.R. Knecht, D.W. Wright, Amine-terminated dendrimers as biomimetic templates for silica nanosphere formation, Langmuir 20 (2004) 4728–4732.
[135] M. Arkas, D. Tsiourvas, Organic/inorganic hybrid nanospheres based on hyperbranched poly(ethylene imine) encapsulated into silica for the sorption of toxic metal ions and polycyclic aromatic hydrocarbons from water, J. Hazard. Mater. 170 (2009) 35–42.
[136] A. Denizli, S. Senel, G. Alsancak, N. Tüzmen, R. Say, Mercury removal from synthetic solutions using poly (2-hydroxyethylmethacrylate) gel beads modified with poly(ethyleneimine), React. Funct. Polym. 55 (2003) 121–130.
[137] M. Ghoul, M. Bacquet, M. Morcellet, Uptake of heavy metals from synthetic aqueous solutions using modified PEI—silica gels, Water Res. 37 (2003) 729–734.
[138] I. Mohmood, C.B. Lopes, I. Lopes, I. Ahmad, A.C. Duarte, Pereira, E., Nanoscale materials and their use in water contaminants removal-a review, Environ. Sci. Pollut. Res. 20 (2013) 1239–1260.
[139] M.M. Pendergast, E.M.V. Hoek, A review of water treatment membrane nanotechnologies, Energ. Environ. Sci. 4 (6) (2011) 1946–1971.
[140] H. Strathmann, Membrane separation processes: current relevance and future opportunities, AICHE J. 47 (2001) 1077–1087.
[141] J. Theron, J.A. Walker, T.E. Cloete, Nanotechnology and water treatment: applications and emerging opportunities, Crit. Rev. Microbiol. 34 (1) (2008) 43–69.
[142] N. Savage, M.S. Diallo, Nanomaterials and water purification: opportunities and challenges, J. Nanopart. Res. 4 (2005) 331–342.
[143] A. Goyal, K. Johal, E.S. Rath, G., Nanotechnology for water treatment, Curr. Nanosci. 7 (4) (2011) 640–654.
[144] J. Wang, Y. Cheng, T. Xu, Current patents of dendrimers and hyperbranched polymers in membranes, Recent Pat. Chem. Eng. 1 (2008) 41–51.
[145] S. Kobayashi, K. Hiroshi, M. Tokunoh, T. Saegusa, Chelating properties of linear and branched poly(ethylenimines), Macromolecules 20 (1987) 1496–1500.
[146] Y. Chen, B. Pan, H. Li, W. Zhang, L. Lv, J. Wu, Selective removal of cu(II) ions by using cation-exchange resin-supported polyethyleneimine (PEI) nanoclusters, Environ. Sci. Technol. 44 (2010) 3508–3513.

[147] M.U. De La Orden, M.C. Matías, J. Martínez Urreaga, Spectroscopic study of the modification of cellulose with polyethylenimines, J. Appl. Polym. Sci. 92 (2004) 2196–2202.
[148] R. Navarro, R. Sumi, K. Fujii, N. Matsumura, M., Mercury removal from wastewater using porous cellulose carrier modified with polyethyleneimine, Water Res. 30 (1996) 2488–2494.
[149] S. Deng, Y.P. Ting, Polyethylenimine-modified fungal biomass as a high-capacity biosorbent for Cr(VI) anions: sorption capacity and uptake mechanisms, Environ. Sci. Technol. 39 (2005) 8490–8496.
[150] X.-F. Sun, Y. Ma, X.-W. Liu, S.-G. Wang, B.-Y. Gao, X.-M. Li, Sorption and detoxification of chromium(VI) by aerobic granules functionalized with polyethylenimine, Water Res. 44 (2010) 2517–2524.
[151] P.C. Ke, M.H. Lamm, A biophysical perspective of understanding nanoparticles at large, Phys. Chem. Chem. Phys. 13 (2011) 7273–7283.
[152] M.S. Diallo, L. Balogh, S. Christie, P. Swaminathan, X. Shi, W.A. Goddard III, J.H. Johnson Jr., in: B. Karn, T.M. Masciangioli, W.-X. Zhang, V. Colvin, P. Alivisatos (Eds.), Dendritic Nanoscale Chelating Agents: Synthesis, Characterization, and Environmental Applications, American Chemical Society, Washington, DC, 2004, pp. 238–247.
[153] Diallo, M.S., Water treatment by dendrimer enhanced filtration, US Patent Application, US 1006/0021938 A1 (2006).
[154] A. Rether, M. Schuster, Selective separation and recovery of heavy metal ions using water-soluble N-benzoylthiourea modified PAMAM polymers, React. Funct. Polym. 57 (1) (2003) 13–21.
[155] M. Tülü, M. Şenel, Dendritic polychelatogens: synthesis, characterization, and metal ion binding properties, J. Appl. Polym. Sci. 109 (5) (2008) 2808–2814.
[156] M. Arkas, R. Allabashi, D. Tsiourvas, E.-M. Mattausch, R. Perfler, Organic/inorganic hybrid filters based on dendritic and cyclodextrin “nanosponges” for the removal of organic pollutants from water, Environ. Sci. Technol. 40 (2006) 2771–2777.
[157] A. Tsetsekou, M. Arkas, A. Kritikaki, S. Simonetis, D. Tsiourvas, Optimization of hybrid hyperbranched polymer/ceramic filters for the efficient absorption of polyaromatic hydrocarbons from water, J. Membr. Sci. 311 (2008) 128–135.
[158] Y. Gao, A.M.S. De Jubera, B.J. Mariñas, J.S. Moore, Nanofiltration membranes with modified active layer using aromatic polyamide dendrimers, Adv. Funct. Mater. 23 (5) (2013) 598–607.
[159] A.M.S. De Jubera, Y. Gao, J.S. Moore, D.G. Cahill, B.J. Mariñas, Enhancing the performance of nanofiltration membranes by modifying the active layer with aramide dendrimers, Environ. Sci. Technol. 46 (17) (2012) 9592–9599.
[160] R. Allabasi, M. Arkas, G. Hörmann, D. Tsiourvas, Removal of some organic pollutants in water employing ceramic membranes impregnated with cross-linked silylated dendritic and cyclodextrin polymers, Water Res. 41 (2007) 476–486.
[161] M.R. Kotte, A.T. Kuvarega, M. Cho, B.B. Mamba, M.S. Diallo, Mixed matrix PVDF membranes with in situ synthesized PAMAM dendrimer-like particles: a new class of sorbents for Cu(II) recovery from aqueous solutions by ultrafiltration, Environ. Sci. Technol. 49 (16) (2015) 9431–9442.
[162] Y. Zhang, S. Zhang, T.-S. Chung, Nanometric graphene oxide framework membranes with enhanced heavy metal removal via nanofiltration, Environ. Sci. Technol. 49 (16) (2015) 10235–10242.
[163] X. Wei, X. Kong, J. Yang, G. Zhang, J. Chen, J. Wang, Structure influence of hyperbranched polyester on structure and properties of synthesized nanofiltration membranes, J. Membr. Sci. 440 (2013) 67–76.
[164] S.P. Malinga, O.A. Arotiba, R.W.M. Krause, S.F. Mapolie, M.S. Diallo, B.B. Mamba, Nanostructured β-cyclodextrin-hyperbranched polyethyleneimine (β-CD-HPEI) embedded in polysulfone membrane for the removal of humic acid from water, Sep. Sci. Technol. 48 (18) (2013) 2724–2734.

[165] S.P. Malinga, O.A. Arotiba, R.W.M. Krause, S.F. Mapolie, M.S. Diallo, B.B. Mamba, Cyclodextrin-dendrimer functionalized polysulfone membrane for the removal of humic acid in water, J. Appl. Polym. Sci. 130 (6) (2013) 4428–4439.

[166] L.E. Koloti, N.P. Gule, O.A. Arotiba, S.P. Malinga, Laccase-immobilized dendritic nanofibrous membranes as a novel approach towards the removal of bisphenol A, Environ. Technol. (2017) 1–13. in press, https://doi.org/10.1080/09593330.2017.1301570.

[167] S. Hong, A.U. Bielinska, A. Mecke, B. Keszler, J.L. Beals, X. Shi, L. Balogh, B.G. Orr, J.R. Baker Jr., M.M. Banaszak Holl, Interaction of poly(amidoamine) dendrimers with supported lipid bilayers and cells: hole formation and the relation to transport, Bioconjug. Chem. 15 (4) (2004) 774–782.

[168] R. Jevprasesphant, J. Penny, R. Jalal, D. Attwood, N.B. McKeown, A. D' Emanuele, The influence of surface modification on the cytotoxicity of PAMAM dendrimers, Int. J. Pharm. 252 (1–2) (2003) 263–266.

[169] N. Malik, R. Wiwattanapatapee, R. Klopsch, K. Lorenz, H. Frey, J.W. Weener, E.W. Meijer, W. Paulus, R. Duncan, Dendrimers: Relationship between structure and biocompatibility in vitro, and preliminary studies on the biodistribution of ^{125}I-labelled polyamidoamine dendrimers in vivo, J. Control. Release 65 (1–2) (2000) 133–148.

FURTHER READING

[170] M.S. Diallo, Nanotechnology applications for clean water, in: Water Treatment by Dendrimer-Enhanced Filtration: principles and Applications, William Andrew, Norwich, NY, 2008, pp. 144–153 (Chapter 11).

CHAPTER

6 DEVELOPMENT OF MIXED MATRIX MEMBRANES: INCORPORATION OF METAL NANOPARTICLES IN POLYMERIC MEMBRANES

Jorge García-Ivars*, María-José Corbatón-Báguena*, María-Isabel Iborra-Clar*,†

Research Institute for Industrial, Radiophysical and Environmental Safety (ISIRYM), Universitat Politècnica de València, Valencia, Spain Department of Chemical and Nuclear Engineering, Universitat Politècnica de València, Valencia, Spain†*

1 INTRODUCTION

The ever-growing need for high-quality water resources is becoming a serious environmental issue that has motivated researchers to seek new technological innovations to sustainably access to safe water supplies. Among different technologies applied for water reclamation and purification, membrane technology is faster, more efficient, and more economical than conventional separation techniques; it also does not require additives to be used. The sustainability criteria are met by such processes in terms of ease of handling and operation, environmental impact, flexibility, and adaptability, but improvements in affordability, costs, energy consumption, and expertise are needed [1]. Additionally, there are some drawbacks associated with the membrane separation process itself. A high-quality membrane should be designed to have a simple and highly reliable processing based on the water application and on the high-quality standards of the produced permeate and to provide both high and stable flux over filtration time with low transmembrane pressures [2]. However, both membrane flux and selectivity are negatively affected by fouling phenomena (mainly caused by the adsorption [chemical and/or physical] and deposition of foulants such as organic matter, fatty acids, proteins, and macromolecules onto the surface or inside the pores), chemical degradation, and compaction that result in an unpredictable separation performance together with a considerable decline of the membrane efficiency with time and, as direct consequences, a higher energy demand and a severe reduction of their life span, which limit their industrialization [3].

A number of novel strategies for flux enhancement and fouling mitigation have emerged, focusing on the treatment of feed solution (pretreatments with supplementary separation processes, sludge granulation), the improvements in operation units (hydrodynamic optimization), or the modification of base membrane material (incorporation of additives in the structure or only on the surface) [4]. Among them, considerable progress in the development of membrane materials has been made with the advent of

Nanoscale Materials in Water Purification. https://doi.org/10.1016/B978-0-12-813926-4.00011-2

nanotechnology; thus, consequently, the use of inorganic nanomaterials in the manufacturing process of polymeric membranes and their positive effects on membrane performance have been extensively studied in gas separation, pervaporation, and pressure-driven membranes processes (microfiltration, ultrafiltration, nanofiltration, and reverse osmosis) for various applications, including medical purposes, tissue engineering, chemical engineering, drinking-water production, and water and wastewater treatment [2, 5–8]. Over the last decades, metallic nanoscale fillers have been introduced into polymeric matrices to improve the physical and chemical weaknesses of conventional polymeric materials, such as thermal, mechanical, chemical, catalytic, hydrophilic, and antimicrobial properties, and to overcome the undesirable effects of fouling phenomena, chemical degradation, and compaction, thus leading to the preparation of a new class of membranes known as hybrid inorganic-organic nanocomposite or mixed matrix membranes (MMMs).

This chapter gives a short overview of the development of MMMs, with a focus on the different types of nanoparticles that are combined with polymeric materials to prepare superior composite membranes for water applications. This could help us to determine the main properties that nanomaterials can provide to the new composite membrane based on the origin of nanoparticles and the composition of the liquid to be treated. The use of metal/metal oxide nanoparticles for drinking-water production and water purification, which is undoubtedly the most important application, is described in detail. Finally, some further developments are needed to overcome the main shortcomings of these membranes are indicated.

2 MANUFACTURING OF METAL AND METAL OXIDE NANOPARTICLE-BASED MEMBRANES

The development of MMMs has recently attracted considerable academic and industrial interest because metallic nanoparticles have surprising and unique physicochemical properties in comparison to bulk polymer characteristics. Membrane material is frequently accepted as one of the most influential parameters in fouling phenomena, where it is expected that hydrophobic materials will show more severe fouling than hydrophilic ones. Several strategies have therefore been investigated to alleviate fouling, among which the hydrophilic modification of the membrane can be remarked. To this end, the incorporation of hydrophilic inorganic nanomaterials into polymeric membrane structures, which are well implemented in both academia and industry, could be a sustainable and reliable solution to fouling.

Researchers have been continuously studying different techniques to add inorganic nanomaterials to membrane structures. Research publications in recent literature on MMMs for water purification and wastewater treatment are displayed in Fig. 1. The growing development of nanotechnology may bring considerable improvements in membrane preparation, including the effective and controlled combination of polymer with nanosized metal networks rather than the usual heterogeneous mixing between them. However, MMMs preparation techniques should find a compromise between hydrophilicity and mechanical strength, and the added nanoparticles should be located in pore structure and even on membrane surface [3]. Because of the versatility of both organic and inorganic materials, the interaction between both phases can effectively provide a positive influence on the membrane in terms of fouling mitigation, separation, and flux enhancement without compromising mechanical stability. Likewise, the presence of inorganic nanofillers in polymeric membranes can also reduce the loss of selectivity at elevated temperatures, mainly because of the restricted thermal motion of the polymer chain [9, 10].

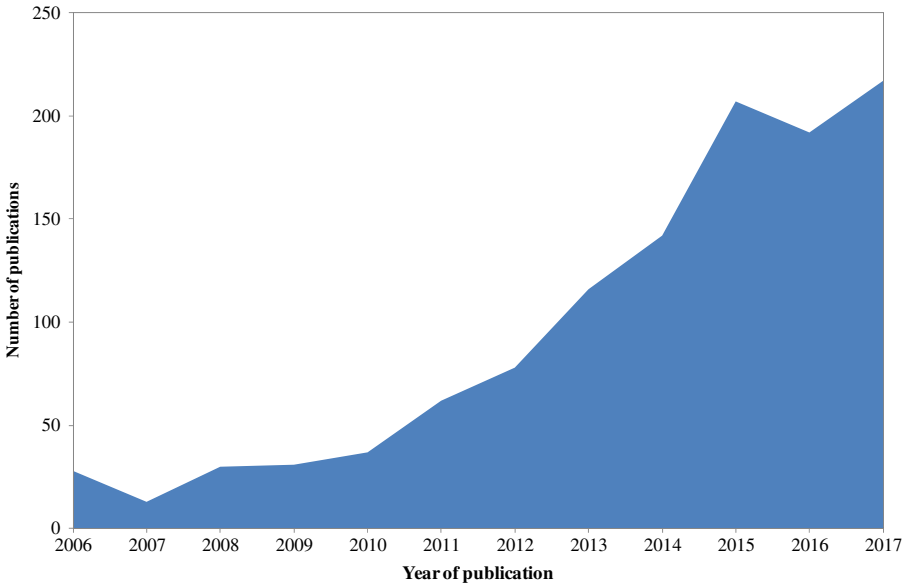

FIG. 1

Number of publications per year on mixed matrix membranes for water purification since 2006. Data extracted from Web of Science on June 29, 2017, by seeking "mixed matrix membrane" and water treatment, "hybrid organic-inorganic membrane" and water treatment, "hybrid inorganic-organic membrane" and water treatment, and, finally, "composite membrane" water treatment.

For this reason, these new MMMs can be flexible and have a very stable nature in comparison to homopolymeric membranes.

One of the most common and versatile methods to prepare polymeric membranes is the phase-inversion method, also known as precipitation phase separation, because membranes with different morphologies, properties, and functions can be obtained. The process is governed by thermodynamic and kinetic interactions of the components that define a ternary system consisting fundamentally of a polymer, solvent and nonsolvent, represented in Fig. 2. In this method, the selected base polymer (or polymers) is dissolved in an appropriate solvent to form a homogeneous single-phase solution (known as polymeric or dope solution), which is transformed in a two-phase system (one rich in polymer and the other poor in polymer) after the separation/solidification process usually induced by the action of a nonsolvent [11]. The phase-inversion method is dominated by the affinity between solvent and nonsolvent, in which a good miscibility between them is related to the formation of porous substructures with open and large channel-like cavities (called macrovoids) and allows water penetration into the casting solution (a phenomenon known as instantaneous demixing). This affinity generates a porous structure. By contrast, slow diffusional rates cause a delayed demixing and, as a result, a slow precipitation that produces a spongelike structure [11, 12]. Common polymers used as base material in the preparation of phase-inversion membranes are cellulose acetate (CA), polyethersulfone (PES), polysulfone (PSf), polyetherimide (PEI), polyamide (PA), polypropylene (PP), polyacrylonitrile (PAN), and polyvinylidene fluoride (PVDF).

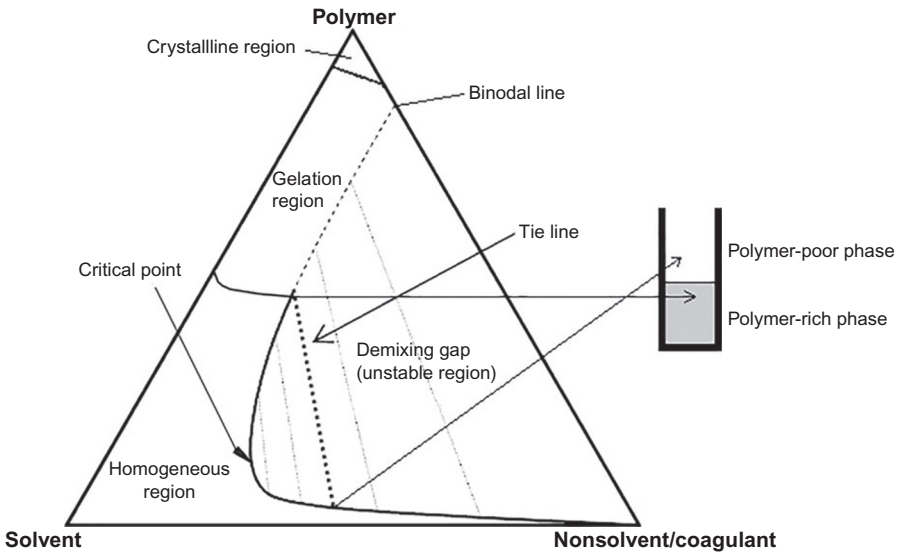

FIG. 2

Schematic phase diagram of the ternary system formed by polymer, solvent and nonsolvent during membrane formation.

The first challenge for manufacturing phase-inversion MMMs is to incorporate the desired amount of nanoparticles into the polymeric solution prior to the synthesis procedure, such as phase separation or immersion precipitation. To this end, the easiest and most preferred way is the physical blending of hydrophilic inorganic nanomaterials with the polymer in the casting solution, thus developing a quasiternary diagram formed by polymer/nanoparticles, solvent and nonsolvent. This diagram can be useful to predict and control morphology and properties of the nascent membrane. Fig. 3 shows a schematic diagram of the phase-inversion method for preparing flat-sheet membranes where hydrophilic metallic nanomaterials can be directly added into the polymeric solution to form the casting solution (option A) or with the solvent forming nanoparticle dispersion previously to introduce the base polymer.

Incorporation of nanomaterials seeks to improve the global hydrophilicity of the previously hydrophobic polymeric membrane. An increasing nanoparticle concentration could enhance the permselective properties (permeability and selectivity) of the membrane prepared by phase-inversion because of the increased affinity for water, but there is a threshold value (an optimal nanoparticle concentration) that limits such an improvement [13, 14]. The presence of metal/metal oxide nanoparticles increases the thermodynamic instability of the casting solution, thus leading to a rapid phase demixing, forming macrovoids and larger fingerlike pores. Because of the higher affinity of metallic nanoparticles for water, the longer the exchange between solvent and nonsolvent, the more developed the processes of polymer-poor phase growth and coalescence are [14]. However, metallic nanoparticles can increase polymer viscosity that results in low diffusion rates of water into the polymer, and hence, this delayed demixing makes macrovoids be partially and totally suppressed [15, 16]. Therefore, the search for the

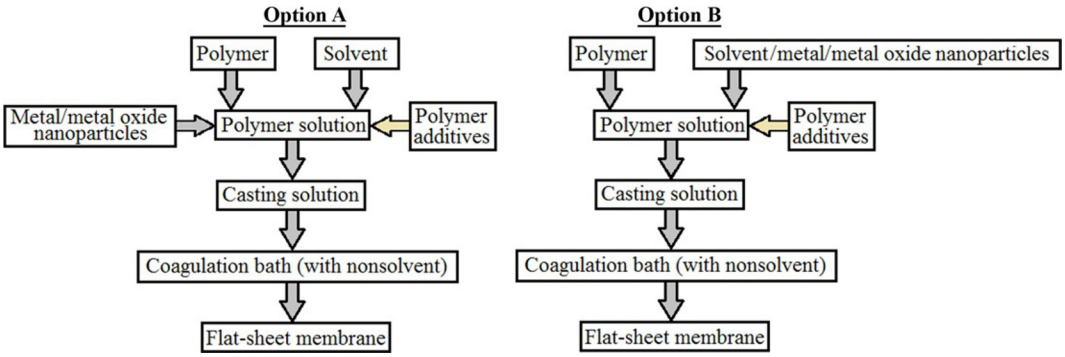

FIG. 3

Schematic diagram of the two main options to incorporate metallic nanoparticles during membrane preparation via phase-inversion method. The addition of polymer additives appears in a different color because of their optional character.

optimal nanoparticle concentration into the polymer solution is of great importance for its application in water purification.

In the same way, in spite of the possible improvement in surface hydrophilicity, the addition of high contents of metallic nanomaterials can have a negative effect on membrane mechanical and thermal stability as well as on the pore size, pore distribution, and internal structure with particle aggregation and agglomeration. These two phenomena might cause macrovoids and cracks by polymer shrink because of inorganic-organic interfacial tension [17].

The presence of well-dispersed nanofillers in the formed MMMs is very difficult to achieve, mainly because of the complexity to form a homogeneously concentrated polymeric solution because of the very beginning of the manufacturing process. A simple incorporation of nanoparticles cannot ensure their homogeneous dispersion in the membrane structure. Particle size is an important property to be considered because it will affect wetting and dispersion. Nanoparticles ($<$100 nm) can be easily suspended and are less likely to settle during the preparation in comparison to macroparticles. Particle shape can affect dispersion as well. Spherical nanomaterials have fewer contact points between particles, which could prevent both agglomeration and aggregation. Compared to polyhedral nanoparticles, the lesser contact area of spherical nanoparticles to wet could be also beneficial for improving dispersion [18]. Therefore, nanomaterials should be homogeneously dispersed prior to membrane formation to achieve their appropriate dispersion in the resulting membrane. A bad nanoparticle dispersion, which is a significant drawback, strongly favors a local increment of the nanoparticle concentration in certain areas of the membrane, which presents irregular properties and an uneven and unpredictable performance during filtration with fouling-resistant areas with high selectivity and other areas with less selectivity. Similarly, the weak attachment of nanoparticles to the polymeric structure also leads to a nanoparticle leakage after its formation, thus indicating that there is a need to find how to strongly attach these nanoparticles to the base polymer during membrane formation. This nanoparticle release from materials containing nanoparticles is an ever-growing concern because of the contamination of the aquatic environment.

Regarding agglomeration/aggregation phenomena, the terms *agglomeration* and *aggregation* can be generally found with similar meaning, but such terms have different definitions. Agglomerations are solid particles that are held together by weak physical interactions (such as Van der Waals forces), which can be broken by simple mechanical forces followed by a combination of steric and electrostatic stabilization to overbalance the surface energy. The occurrence of nanoparticle agglomeration can be related to the high surface energy of nanoparticles, which are naturally prone to agglomeration. This tendency to reach a more thermodynamically stable state negatively affects their capacities and selectivity. Although aggregation can occur in any physical state, it is a much stronger phenomenon than agglomeration, thus being more difficult to break. Hence, the tendency of nanoparticles to be agglomerated is, together with their bad dispersion and weak attachment in the polymeric matrix and their subsequent leakage, the most important drawback to be controlled and solved that drastically affects the successful implementation of MMMs. Metallic nanomaterials therefore tend to be concentrated near the surface structure and in the pore walls, especially those particles or agglomerations with larger sizes. However, phase-inversion method can be considered as a bulk modification mainly because nanofillers are added directly to the polymeric solution, thus modifying the properties of the entire membrane and not only the surface structure.

On the other hand, recent works are focused on the selective modification of membrane surface, which has caught the attention and interest of several researchers to specifically locate the well-chosen metallic nanoparticles on the surface after membrane formation. Surface properties matter because this thin top layer defines the selectivity, performance, and life span of the membrane. On the basis of the theory of metal organic frameworks, the addition of some organic precursors or linkers during surface functionalization with the purpose of promoting better interactions between polymer surface and metal/metal oxide nanoparticles through coating, cross-linking, or embedding could be a sustainable approach to prevent nanoparticle leakage, agglomeration, and aggregation. To this end, hydrophilic functional groups are provided by organic (such as monomers and silane coupling agents) and inorganic additives via chemical modification, redox initiation, cross-linking, and photografting based on plasma treatment, polymerization, γ-ray irradiation, ion beam irradiation, or ultraviolet (UV) irradiation, amongst others [3, 19–22]. These methods provide a thin layer on the surface structure in which strong chemical bonds are created in comparison to direct blending modification combined with phase-inversion method. A very schematic diagram comparing direct blending and UV-induced modification is displayed in Fig. 4, where the (option B) depicts the surface modification method. Some authors have used the photosensitivity of certain types of polymers to generate radical sites under irradiation in the presence of metallic nanoparticles dispersed in aqueous/organic solutions. These in situ-generated radical sites reacted among them and/or with the organic/inorganic compounds in the dispersion, thus allowing the entrapment of such nanoparticles onto the surface structure without affecting the bulk polymer [23, 24]. Polyarylsulfones, such as PSf or PES, are usually selected because of their inherent photosensitivity [24, 25]. Surface modification tends to reduce membrane pore size because of the accumulation of grafted or added material in the radical sites near surface pores [26, 27]. It should be careful with techniques with UV/γ-ray/ion beam irradiation and its operating conditions (such as intensity or irradiation time) because long irradiation times can degrade the polymeric material and interfere in the nanoparticle incorporation on the surface [23].

In the case of water purification, common metallic nanomaterials employed to manufacture MMMs are metal oxides (such as SiO_2, Al_2O_3, ZrO_2, TiO_2, or Fe_3O_4), zerovalent metals (Ag, Pd, or Fe),

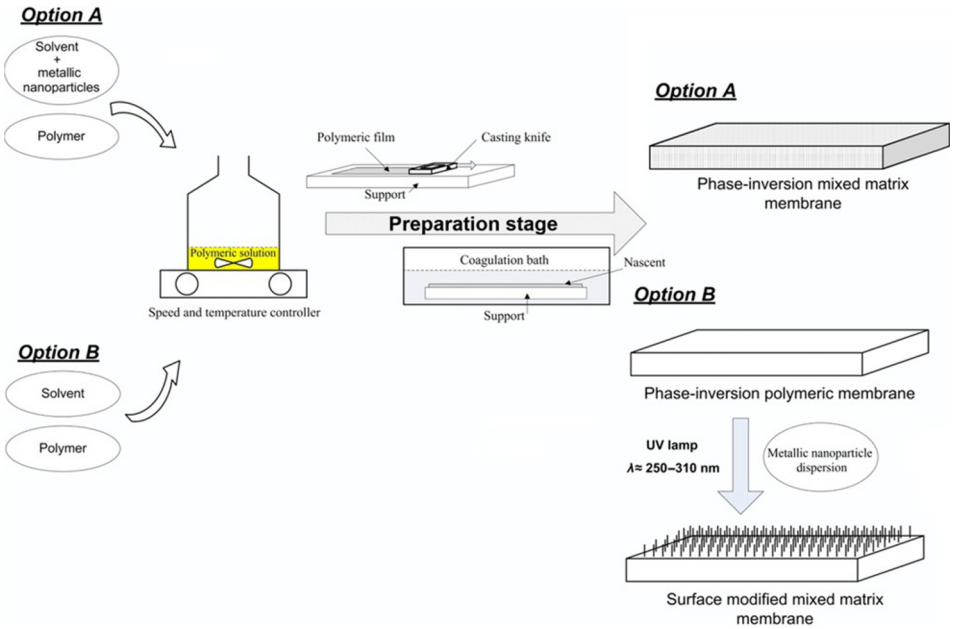

FIG. 4

Schematic diagram of direct blending modification (option A) compared to UV-induced modification (option B).

magnesium-based materials, and transition metal-based materials, which present a positive mutual influence when both inorganic and organic phases meet in a membrane [28]. Some examples of these nanomaterials are discussed further in later sections of the chapter, and their properties are shown in Table 1.

3 MEMBRANES WITH ZEROVALENT METAL NANOPARTICLES FOR WATER TREATMENT

Zerovalent metal nanoparticles have been the focus of numerous investigations in recent years, especially because of their antimicrobial properties. Viruses, bacteria, and other microorganisms are present in nearly all aquatic environments, and they naturally tend to adhere to any surface as a survival mechanism, growing at the expense of nutrients from the water phase [42]. When membranes are used in water separation applications, both the accumulation and the growth of microbial cells lead to develop a biofilm on the surface, which result in a decline in the permeate flux and separation yield (which increase energy consumption and significantly decrease the membrane's life span), as well as the pollution of membrane and the streams of the process (by the cell detachment and dispersal of microorganisms in the aquatic environment). Although pretreatments and physical and chemical cleaning can be effective for controlling biofouling, several polymeric membranes are not able to resist the aggressiveness of chemical cleaning agents. For this reason, biofouling is a critical issue when membranes are

Table 1 Properties and Applications of Selected Metal/Metal Oxide Nanoparticles

Type	Nanomaterials	Properties	Applications	References
Zero-valent metal	Ag	Angiogenesis inhibitor, antimicrobial agent, good conductivity, chemical stability, catalytic activity, good conductivity, optical properties, mechanical properties	Biocide applications, biosensing, paints and household products	[20, 29, 30]
	Fe	Reductive capacity, adsorptive capacity, high surface activity, magnetic properties, mechanical properties	Groundwater remediation, biomedicine, adsorption for water purification	[31–33]
Metal oxide	TiO_2	Stable nature, anticorrosive, high reflective index, chemical stability, thermal stability, strong oxidative potential, deodorizing, optical properties, catalytic activity, mechanical properties	Photocatalysis, gas sensor, skin care products, nanomedicine	[20, 34, 35]
	SiO_2	Oxidative potential, thermal stability, light-diffusing properties, strong surface energy, mechanical properties	Drug delivery, biosensing, biocide applications, tissue engineering	[36–38]
	Al_2O_3	Stable nature, abrasion resistance, very low toxicity, adsorption capacity, resistance to oxidation, chemical inertness, mechanical properties	Biocide, heavy metal removal, catalysis, absorption processes, gas separation	[39–41]

used in place of conventional separation technologies for water purification, and the nanoparticle incorporation with antimicrobial properties may be a potentially innovative solution to control and even to mitigate biofouling and its harmful effects. Some examples of nanosized zerovalent metal particles that are described in the chapter are silver and iron.

3.1 SILVER

Silver nanoscale particles are well known as antimicrobial agents that can significantly accelerate oxidation reactions because of their ability to adsorb molecular oxygen on their surface. Consequently, silver nanoparticles readily interact and react with sulfur and phosphorous groups, most notably with thiol (S—H) groups in proteins, which completely damages bacterial proteins and blocks both

respiration and electron transfer [29]. For this reason, Ag nanoparticles are a very attractive additive to improve antibiofouling membrane properties. However, silver solubility and bioavailability can be altered by the presence of common water constituents, which negatively affect to its toxicity to some target bacteria, such as *E. coli* [43]. Other distinctive properties provided by silver materials are mainly good conductivity, chemical stability, and catalytic activity [44].

Generally, silver nanoparticles have been directly added and dispersed in the casting solution to prepare phase-inversion MMMs by using vigorous stirring or sonication [43–46]. Despite the nanoparticle distribution in the membrane structure, water contact angle measurements demonstrated the improvement in MMM hydrophilicity in comparison to the bare membrane. The improved antimicrobial activity was observed in the prevention of biofilm formation [43, 47]. Although silver-enhanced membranes showed the improvement of some target properties, Ag leakage was detected in the coagulation bath during membrane formation and after soaking tests [46].

Taurozzi et al. synthesized nano-Ag particles in membrane structure by means of two different methods, such as ex situ and in situ reduction of silver. In both methods, no significant difference in cross-section morphologies was observed, thus confirming Ag nanoparticles were physically entrapped in the polymeric matrix without affecting significantly the membrane structure. The difference between both methods came mainly from where nanoparticles were placed along the surface structure. Larger silver nanoparticles and agglomerations/aggregations (50–500 nm) were preferentially located along the internal porous surface with ex situ method, while smaller nanoparticles (smaller than 50 nm) were distributed along the membrane cross section via in situ reduction of ionic silver. Likewise, more density of nanoparticles was observed when ex situ method was employed. However, neither mentioned methods could avoid silver loss during membrane formation and storage [48]. The release of silver nanoparticles in the environment can pose a great threat to human and animal health because of water reuse and silver toxicity [44, 49, 50].

Some works that explored the stable presence of silver-containing membranes reported the incorporation of metal nanoparticles with the aid of organic additives acting as dispersants. Wang and coworkers demonstrated that PVP could be a good dispersant when Ag nanoparticles were prepared by chemical reduction method, even accelerating the reaction between glucose and ionic silver [51]. Basri and coworkers studied the influence of PVP and 2,4,6-triaminopyrimidine (TAP) as appropriate dispersants on the membrane formation of PES material with ionic silver (as $AgNO_3$, 2 wt%) via phase-inversion method. Results confirmed a dispersion enhancement of nano-Ag particles in the membrane structure by adding both PVP and TAP, thus resulting in more silver nanoparticles entrapped in the polymeric matrix and, hence, an improvement in the antibacterial activity. A remarkable loss of silver nanomaterials was observed because of different reasons, such as the decrease in the affinity of silver in both ionic and agglomerated form to water and the poor adhesion to the polymeric matrix [44]. In other work, in situ reduction and immobilization of silver nanoparticles via polydopamine (PDA) deposition were proposed as a method for stabilizing Ag nanoparticles on PSf ultrafiltration membranes. The presence of formed Ag nanoparticles showed a significant improvement in hydrophilicity (from 76 degrees to about 50 degrees in contact angle measurements), which translated into higher permeation flux and better antibiofouling properties. Moreover, an uneven distribution of Ag nanoparticles on the membrane surface was observed at higher silver concentration, which led to the formation of larger agglomerations/aggregations on the surface. However, the silver release (<0.1 mg/L) could not be avoided by this method [30].

Similarly, other researchers combined the photoreaction of silver nanoparticles by UV illumination with the traditional blending of TiO_2 nanomaterials in PVDF-based membranes. Blended TiO_2/PVDF phase-inversion MMMs were immersed into $AgNO_3$ aqueous solutions for several minutes in the dark, being adsorbed the ionic Ag on the nano-TiO_2 particles entrapped in the PVDF structure. Membranes were then irradiated by UV light, and thus, nanoparticles were formed by reducing the silver deposited on the TiO_2/PVDF surface. The appearance of Ag/TiO_2 nanoparticles (40–200 nm) caused an increase in porosity with growing content of surface hydroxyl group (—OH), and therefore, hydrophilicity and solute rejection improved after incorporating Ag nanomaterials [45]. Similar approaches involving in situ UV-induced reduction of silver, self-assembly of TiO_2 nanoparticles, and ultrasonic-induced reduction of silver combined with interfacial polymerization have been recently employed to superficially modify forward osmosis membranes [52, 53].

3.2 IRON

Despite being the most ubiquitous transition metal, zerovalent iron has been somewhat neglected in favor of its own oxides. However, nanoscale zerovalent iron particles (nZVI) have a large reductive and adsorptive capacity to both degrade and remove numerous pollutants, such as organic compounds, heavy metals, pesticides, and inorganic anions, in comparison to iron oxides [31–33, 54]. Zerovalent iron has been extensively used in groundwater remediation because of its high surface activity, its reactivity, and its large specific surface area [33].

Even though they have been recently applied to water treatment processes, nZVI have been seldom implemented on membrane technology. Ma and colleagues investigated the development of zerovalent iron-layered PVDF ultrafiltration membranes. Prior to membrane preparation, the nZVI were synthesized by dropwise addition of $NaBH_4$ solution to $FeCl_3{\cdot}6H_2O$ solution based on the method previously reported by Wang and Zhang [54a], adding ethanol solutions to avoid agglomeration and to favor the adhesion of nanoparticles on PVDF surfaces. Membranes were manufactured by the deposition of a relatively homogeneous layer of nZVI-water slurry onto PVDF surfaces in the presence of a 0.01 M NaCl solution. The size distribution of the formed nZVI varied from 10 to 100 nm, where more than 25% of these particles ranged from 50 to 60 nm. These researchers observed that higher amounts of nZVI on the membrane could increase its antifouling character and rejection efficiency. However, iron nanoparticles have a size closer to the average pore diameter of the membrane, thus blocking membrane pores and hence reducing the pure water flux [55].

[56] had applied the previous method for synthesizing nZVI, which subsequently were introduced on a thin film nanocomposite (TFC) via in situ and ex situ methods. In the in situ method, the active layer of the TFC membrane (formed by a reaction between solutions of 1,3-phenylenediamine, MPD, and 1,3,5-benzenetricarbonyl trichloride, TMC, on a PSf ultrafiltration membrane that was used as a support layer) was immersed into a $FeCl_3$ solution for a certain time to impregnate the surface (which changed its color to brown) and then, this membrane was immersed again in a $NaBH_4$ solution for completing the iron reduction onto the surface (which changed its color from brown to black because of the nZVI formation). For the ex situ method, nZVI were dispersed in an MPD solution, which reacted with a TMC solution onto the ultrafiltration support layer and within its pores to achieve the TFC membrane. The performance of membranes prepared by both methods was improved in terms of rejection and water flux, thus minimizing the biofouling during filtration time because of the behavior of nZVI as an antimicrobial agent. Moreover, the uniformity of pore distribution was higher in membranes

prepared by the in situ method than those prepared by the ex situ method, being the in situ method useful for mitigating both bacteria and biofouling [56].

Several researchers applied the concept of nZVI-based MMMs to achieve the catalytic dechlorination of toxic organics. Wang and coworkers modified PVDF microfiltration membranes by coating with a hydrophilic layer composed of polyvinyl alcohol (PVA), glutaraldehyde (GA), and polyethylene glycol (PEG). After that, nZVI were immobilized in the PVDF material, and then Pd nanoparticles were deposited on nZVI surface. These Pd/Fe/PVDF-based MMMs exhibited rougher surfaces and high reactivities, thus achieving a complete catalytic dechlorination of trichloroacetic acid (TCAA) [57]. The presence of the hydrophilic layer could also facilitate the dispersion of formed Fe/Pd nanoparticles on the surface. In a later work, authors suggested that water pollution caused by the leakage of dissolved nZVI and the formed ferrous chelating by polyacrylic acid (PAA) could be avoided by dissolving oxygen in the storage and being stored in pure ethanol without water [50, 58]. Similar approaches involving in situ reduction of iron and palladium were studied by Xu and Bhattacharyya for polychlorinated biphenyl (PCB) dechlorination [58a, 58b].

4 MEMBRANES WITH METAL OXIDE NANOPARTICLES FOR WATER TREATMENT

Nanostructured metal oxides represent an important class of materials that have been widely employed in manufacturing nanocomposites as well as in optimizing their performance for several applications, such as catalysis and photocatalysis, gas and chemical sensors, ferromagnetism, lithium ion batteries, medical purposes, blood purification, drug delivery, tissue engineering, fuel cells, solar cells, or environmental remediation [5, 59, 60]. Among them, there are many potential applications in water treatment processes. Nanosized metal oxides, such as TiO_2, MnO_2, Fe_3O_4, ZnO, or Al_2O_3, are classified as one of the promising adsorbents for heavy metal removal from water and wastewater effluents mainly because of their large surface area, high activity, and high adsorption capacity [61, 62]. Nowadays, some metal oxide nanomaterials have been applied in ion exchange, electrochemical processes, and membrane filtration. Their embedment in polymeric membranes seeks not only to improve water diffusion into the nascent membrane because of their affinity for water but also to interfere the interaction between polymer and solvent by the hindrance effect of metal oxide nanomaterials [63]. Compared to purely polymeric membranes, they can develop excellent properties, including membrane hydrophilicity, photocatalytic activity, antifouling property, and permselectivity. Following are some examples of TiO_2, SiO_2, and Al_2O_3 nanomaterials applied to MMM preparation in which researchers have incorporated them to treat specific contaminated waters and put forward a possible solution to stabilize such nanoparticles in the polymeric structure.

4.1 TITANIUM OXIDE

Titanium oxide, or titania (TiO_2), has various properties which can considerably draw much attention of several researchers, including its stable nature, high reflective index, low cost, chemical and thermal stability, strong oxidative potential to create OH radicals, deodorizing, high hydrophilicity, fouling resistance, and nontoxic to human life [35, 64, 65]. However, this last statement is being refuted by

other researchers who demonstrated that inhaled TiO_2 nanoparticles could cross the air-blood barrier and be distributed in the bloodstream [59, 66].

Focusing on their application in membrane technology, several researchers have studied the improvement in antifouling and other membrane properties, such as stable permeation flux, better permeability, and solute rejection. Like many of them, Yang and colleagues centered their effort on modifying PSf ultrafiltration phase-inversion membranes with TiO_2 nanoparticles by blending to find out the best TiO_2 concentration to be added to achieve the desired membrane properties to treat emulsified oil wastewater. The presence of TiO_2 nanoparticles (between 1–2 wt% TiO_2 content) was also seen in a higher number of pores in the surface, suppressing the macrovoid formation at higher nanoparticle concentration [67]. Similar observations about increasing porosity and macrovoids suppression were later reported by other researchers [13, 68]. To overcome the nanoparticle agglomeration, authors proposed the surface modification of TiO_2 nanomaterials by means of adding 0.7% sodium dodecyl sulfate (SDS) aqueous solution. Nanoparticle agglomeration was observed since the very beginning when TiO_2 nanomaterials were added and their number increased with higher TiO_2 content than the optimal nanoparticle concentration (2 wt%), thus causing a worsening of membrane performance. These TiO_2 agglomerations produced the formation of large surface pores in their vicinity [67]. Similar results were obtained for blended TiO_2/PVDF/sulfonated PES MMMs [69]. Razmjou and colleagues developed two methods to avoid agglomeration: nanoparticle dispersion in the preparation of phase-inversion ultrafiltration membranes by sonication and grinding and surface chemical modification with silane coupling agents. Both modifications improved the nanoparticle dispersion, but it cannot be completely avoided [68, 70]. Li et al. also demonstrated that low TiO_2 loadings ($\leq$2 wt%) can lead on to a more stable distribution of TiO_2 nanomaterials, which would make them more difficult to be leached out in both filtration and storage [13].

Other researchers investigated the fouling mitigation effect of immobilized titania ultrafiltration membranes in their application as a membrane bioreactor (MBR). Cellulose membranes were coated with TiO_2 nanoparticles (via TiO_2 sol), studying their stability in the nascent structure by ultrasonic washing. After filtration experiments with activated sludge, hydrophilicity and antifouling properties were significantly improved. Additionally, acidic and neutral TiO_2 sol particles were attached to the membrane surface, but this attachment proved to be poor because an important amount of TiO_2 nanomaterials leached out after 3 min of ultrasonic washing [71].

The high photocatalytic activity of TiO_2 nanomaterials and their use as an antibacterial agent have already been largely studied to break down organic pollutants in water. In this case, nanoparticles emit electrons on exposure to UV illumination ($<$387 nm), thus initiating the bond cleavage and rearrangement that result in the formation of hydrophilic groups and hence an increase in both surface roughness and hydrophilicity [72–75]. The wide range of application areas of this technique includes desalination, wastewater treatment, natural organic matter removal, photocatalytic degradation, and oily/water treatments [5, 34].

The combination of properties from polymer and TiO_2 nanoparticles has already been largely studied by several researchers. Rahimpour and his research group compared both methods (blending and UV-surface modification) to introduce TiO_2 nanoparticles in PES phase-inversion ultrafiltration membranes. Blended PES/TiO_2 membranes showed a more porous structure with the presence of large agglomerations, which led to a slight flux enhancement and antifouling properties. However, UV-induced surface modification further improved permselective and antifouling properties of TiO_2/PES membranes. The authors also demonstrated that in the absence of compounds to react to, longer irradiation

times can generate many radicals on the surface and form aggregations and even peroxide groups after UV irradiation at higher energy [14]. Jyothi and coworkers observed titania nanoparticle agglomerations on the surface of UV-modified PSf/TiO_2 composite membranes for its applicability in the removal of toxic Cr (VI). Better hydrophilicity and complete removal efficiencies with 2 wt% TiO_2 content were achieved, especially at acidic pH. Despite the uniform dispersion of nanoparticles by sonication, these authors confirmed the agglomerate formation with increasing nanoparticle concentration, thus blocking pores of the resulting membranes [73]. In a similar way, Hoseini and colleagues studied the photodegradation of chlorophenols by using PES/Co/TiO_2 phase-inversion MMMs. The average size of synthesized Co/TiO_2 nanomaterials (via sol-gel method) was 12–15 nm. Permselective properties and photocatalytic degradation were improved by adding 1 wt% Co/TiO_2 nanoparticles under visible light irradiation. Visual observations demonstrated that pure spherically shaped TiO_2 nanoparticles were more uniformly dispersed with less number of agglomerations whereas Co/TiO_2 nanomaterials showed more agglomerations [76].

As we reported before with aluminum oxide (Al_2O_3) nanomaterials [41, 77], Gebru and Das studied the role of PEG as an organic additive in the introduction of TiO_2 nanomaterials into the casting solution to prepare CA ultrafiltration membranes by phase-inversion method. Modified TiO_2/PES/CA membranes improved their characteristics in terms of morphology, pure water flux, hydraulic resistance, hydrophilicity, thermal stability, and antifouling performance using bovine serum albumin (BSA) solutions, exhibiting their best performance with the following composition: 10.5 wt% CA, 4 wt% PEG and 2 wt% TiO_2. However, the occurrence of nanoparticle agglomeration was found within the polymer surface and structure, negatively changing both hydrophilicity and surface roughness of the modified membranes [64].

4.2 SILICA

Silicon oxide (SiO_2), also known as silica, nanoparticles have drawn the attention because of their capability to form OH bonds and to facile synthesis procedure with low cost and with special properties, such as thermal stability, light-diffusing properties, low toxicity, strong surface energy, or relatively inert material compared to other engineering nanomaterials. For all these properties, these inorganic nanomaterials are excellent additives a priori to manufacture hydrophilic MMMs [36–38].

Some researchers focused the incorporation of properties from nanosized silica in water applications, such as ultrafiltration, nanofiltration, or reverse osmosis by blending modification as occurred with TiO_2. Ng and colleagues investigated their incorporation into PSf/PVA phase-inversion blend membranes in which hydrophilicity, permeability, and salt rejection significantly improved with the presence of SiO_2 nanomaterials. The addition of pore-forming agent PVA molecules prevented the agglomeration of silica nanoparticles and helped improve the nanoparticle stabilization on the membrane surface, but agglomeration could not be avoided completely. These authors also reported that mechanical properties improved with the presence of SiO_2 nanoparticles up to a certain concentration [78]. Similar results were obtained by other researchers who, respectively, prepared CA/SiO_2 and PES/SiO_2 phase-inversion ultrafiltration membranes [79, 80]. However, agglomeration/aggregation phenomena could not be overcome by treating SiO_2 nanomaterials with SDS solutions at acidic conditions for 8 h, previously to be added to the polymeric solution. Ahmad and colleagues studied the effect of adding silica on CA/PEG reverse-osmosis membranes prepared by thermally induced phase separation (TIPS) method. The occurrence of silica in the polymeric structure was demonstrated by morphological

and compositional studies as well as by the improvement in hydrophilicity, permeation properties, and salt rejection. Authors also observed an initial increase in the mechanical stability of MMMs (up to 4% (w/v)) but a subsequent decrease with the further addition of silica nanoparticles. No observations were made about the leakage of nanoparticles during the preparation and filtration processes [37].

Unlike researchers who have used commercial metallic nanoparticles in their works, many authors have preferred generating hydrophilic silica nanoparticles in situ to control their properties. Metal alkoxides have been used to generate in situ SiO_2 nanoparticles for their reaction mechanisms followed by a sol-gel process involving acid hydrolysis and polycondensation with an organic polymer. Some examples of metal alkoxides are tetramethylorthosilicate (TMOS), polydimethyloxysiloxane (PDMS), and tetraethylorthosilicate (TEOS), among which TEOS is the most metal alkoxide employed because of its low cost, safe, easy handling, and controlled reactions during condensation [81, 82]. In situ-generated SiO_2 nanoparticles possess a large amount of OH groups on their surface, which can provide an improvement in the hydrophilic character of the membrane. Ananth and colleagues used TEOS liquid to prepare PES/polyethyleneimine/SiO_2 phase-inversion membranes. Microscopic and spectroscopic measurements demonstrated the presence of SiO_2 nanoparticles in PES structure, revealing an increase in pore size and the formation of thin spongelike microstructures. Similar observations were made with respect to the formation of cross-linking structure of silica nanoparticles with polymeric chains after the sol-gel process and the absence of aggregation or agglomeration in MMMs by other researchers [83]. Likewise, high TEOS concentration caused the emergence of massive agglomeration in the polymeric structure. Lin and coworkers focused their study on the synthesis of ultra-low concentrations of monodisperse SiO_2 nanoparticles (according to the Stöber method [84]) to prepare PES nanofiltration membranes via phase-inversion method for water purification. Such nanofillers not only improved the hydrophilicity, thermal stability, water permeability, and solute rejection of membranes but also enlarged the size and number of macrovoids in the porous sublayer. The suppression of macrovoids was observed at high nanoparticle concentrations, mainly due to the high viscosity of the casting solution and the pore plugging related to the formation of clusters or nanoparticle agglomerations [38].

Niksefat and coworkers synthesized MMMs containing silica nanoparticles via in situ polymerization of MPD and TMC on PSf/PVP support membranes for forward osmosis applications. AFM and contact angle measurements confirmed the increase in surface roughness and hydrophilicity. Silica loadings of 0.05%(w/v) showed the highest improvement in both water flux and salt rejection. Some particle agglomerations were mainly observed at high SiO_2 loading (0.1%(w/v)), but isolated agglomerations were observed at lower SiO_2 loadings. Also, no stabilization tests were performed [36].

Akbari and colleagues synthesized PEG grafted on silica nanoparticles via hydrolysis of TEOS in ethanol. After that, they were added in high-density polyethylene (PE) solutions to form microfiltration MMMs via TIPS method. Morphological and chemical membrane characterization denoted a decrease in nanoparticle size from 70 to 35 nm with increasing PEG concentration. However, no studies about particle stabilization were performed to confirm the persistence of grafted nanoparticles in the membrane structure [85]. Zhu and colleagues studied the preparation of PES ultrafiltration membranes with poly(2-hydroxyethyl methacrylate) (PHEMA)-grafted SiO_2 nanoparticles as the blending additive in the phase-inversion method. As was expected, the presence of SiO_2-enhanced surface hydrophilicity, and consequently, water flux, solute rejection, and antifouling properties remarkably improved. At a PHEMA-*g*-SiO_2 nanoparticle concentration lower than 6 wt%, Zhu and coworkers observed an increase in porosity and thickness because of the dominant role of thermodynamic instability in

membrane formation, while at higher concentrations the opposite effect was observed because of the dynamical delay. After preparing the PES/PHEMA-*g*-SiO_2 MMMs, dispersed grafted nanoparticles were found along the surface structure, only appearing in some isolated agglomerations. Authors attributed the immobilization of PHEMA-*g*-SiO_2 nanoparticles to the inter- and intramolecular entanglement of polymer and PHEMA chains. However, PES/PHEMA/SiO_2 membranes showed an increase in contact angle values during soaking tests with pure water, indicating that there was a loss of PHEMA/SiO_2 nanoparticles after preparation and storage [86].

Mesoporous silica nanoparticles have been also studied for developing MMMs, owing to its high surface areas, narrow pore-size distribution, and adjustable pore sizes [87, 88]. Huang and coworkers prepared PES/mesoporous SiO_2 phase-inversion membranes for ultrafiltration applications with the purpose of improving their antifouling properties. Microscopic observations demonstrated the enlargement of pore size in sublayer and the improvement in pore interconnectivity between sublayer and bottom layer when hydrophilic mesoporous silica was added. Despite obtaining the best results for 2% mesoporous SiO_2, nanoparticle agglomerations were observed since the introduction of inorganic fillers in the membrane structure, becoming more visible with increasing silica particle content [88].

4.3 ALUMINA

Alumina, or Al_2O_3, has been used in a wide range of applications in personal care products as well as industrial processes. This metal oxide is one of the most stable metallic materials with interesting properties such as low cost, chemical and abrasion resistance, and very low toxicity (even in nanoparticle form) [41]. Moreover, nanosized alumina offers excellent performance as a catalyst for several chemical reactions. To improve the efficiency in the removal of organic and inorganic contaminants, nanosized Al_2O_3 particles have been employed as nanofillers in the preparation of MMMs mainly because of their hydrophilicity and good adsorption capacity, especially for heavy metals.

[61] studied the ability of hydrophilic alumina nanoparticles to remove copper from aqueous environments by using PES/PVP/Al_2O_3 phase-inversion membranes. However, the amount of Al_2O_3 loading during membrane formation led to nanoparticle agglomeration and pore blockage, especially with alumina loading higher than 0.1 wt%. Similar observations were obtained by Maximous and colleagues, who focused their work on examining the permselective properties of PES/Al_2O_3 phase-inversion membranes using activated sludge [89, 90]. These authors concluded that there is a strong correlation between the distribution pattern of metal oxide nanomaterials and the performance of Al_2O_3/PES and ZrO_2/PES MMMs [91]. Ghaemi observed a higher copper uptake after increasing nanoparticle content in the membrane, confirming the durability of removal efficiency after four filtration cycles [61].

Other authors have studied the incorporation of alumina nanoparticles on polymeric membrane surfaces by in situ embedment method, presenting an improvement in hydrophilicity, water permeation, and antibiofouling properties [72, 92]. The spontaneous nanoparticle agglomeration was observed when the mean particle size measured was about 302 nm, which was at least 6 times larger than the isolated nanoparticle size (<50 nm). Visual observations indicated a negligible alumina loss by stabilization/soaking tests [72]. Other researchers also studied the modification of PVDF-based phase-inversion membranes but in a different manner. They proposed the formation of a complex Al_2O_3/PVDF solution by adding H_2SO_4 until the solution changed its color from purple-pink to colorless.

This complex solution was more viscous than the bare PVDF solution and was used as a base polymer in the phase-inversion method. Hydrophilicity and fouling resistance were improved after modification. Likewise, not only was good dispersion of nanoparticles achieved, but also nanoparticle agglomerations were seen along the entire membrane, being distributed from surface to bottom layer [93].

In previous studies, our research group analyzed the influence of Al_2O_3 nanoparticles in the membrane structure, introducing low-molecular-weight PEG as both pore-forming and dispersing agent. Membranes were manufactured via phase-inversion method by using separately three different polymers: PES, PSf, and PEI. A remarkable improvement in hydrophilicity was observed with higher Al_2O_3 loading, thus enhancing the antifouling properties of the MMMs in comparison to those observed for control membranes. The incorporation of Al_2O_3 nanoparticles in the presence of PEG resulted in the formation of a hydrophilic finger-like structure with macrovoids, whereas the sole addition of Al_2O_3 in PES matrices led to a hydrophilic structure with a higher amount of nanosized Al_2O_3 particles on the surface and a more porous spongelike substructure. The PEG/Al_2O_3 addition improved the antifouling behavior of the modified membranes. PEG molecules in appropriate amounts therefore acted as an efficient pore interconnector and as a good dispersant for nanoparticle dispersion, thus indicating that higher amounts of PEG than the optimal concentration may intensify the thermodynamic instability of the cast film and form a more open structure. However, the presence of PEG cannot completely avoid the formation of nanoparticle agglomerations during the preparation of phase-inversion membranes, which were observed in the inner membrane structure [41].

To improve the previous modification, UV-induced modification was applied to commercial and self-made PES phase-inversion ultrafiltration membranes. Membranes were irradiated by UV light in presence of different compositions of PEG/Al_2O_3 mixtures, which provided both higher hydrophilicity and selectivity, thus minimizing fouling. The presence of alumina nanoparticles exclusively embedded on the surface (and not in the matrix structure) was confirmed by both microscopic and spectroscopic analyses. However, there was a slightly persistent loss of Al_2O_3 during soaking tests, especially low in PES/PEG/Al_2O_3 membranes, and the addition of grafted PEG could help to entrap nanoparticles in the irradiated structure and thus prevent their leaching out on prolonged use [77, 94]. In a subsequent work, we demonstrated that the pH of the aqueous dispersion that contains metal oxide nanoparticles was a key parameter to successfully incorporate alumina nanoparticles (and, consequently, each type of nanoparticles). At pH 7, where the zero point of charge (pH_{ZPC}) of alumina is, Al_2O_3 nanomaterials had zwitterionic charge and rapidly tended to formed agglomerations because of the fact that maximum electrostatic attraction forces occurred among them. Authors confirmed agglomeration could be hindered at both acidic and alkaline pH values. Permselective and antifouling properties in an agglomeration-free structure were achieved with a more homogeneous nano-Al_2O_3 dispersion, especially at acidic conditions [23].

Finally, although we have focused on some specific examples of metallic nanoparticles, there are other representative works about the development of MMMs in literature, which are displayed in Table 2.

Table 2 Literatures Related to Addition of Metal Oxide Nanoparticles

Type of Filler	Filler	Base Polymer	Preparation Method	Additives	Properties	Application	Reference
Metal oxide	Ag_2O	PES/CA	Reduction of ionic silver + phase inversion + Cu adsorption and growth	Zero-valent Cu	Antibacterial property; photocatalytic activity; hydrophilicity	Ultrafiltration	[49]
	Fe_3O_4	PES	Blending + phase inversion	PANI (polyaniline); SDS/PEG as protective agent	Magnetism; hydrophilicity	Heavy metal removal; salt removal; whey concentration	[95–97]
	Fe_3O_4	PES	Surface functionalization + stöber method + chemical modification + phase inversion	SiO_2-amine + PVP	Magnetism; hydrophilicity	Heavy metal removal	[98]
	Fe_3O_4	PSf	Blending + phase inversion; UV-graft polymerization; interfacial polymerization	PEG; acrylic acid (AA); PA + piperazine/TMC	Hydrophilicity	Ultrafiltration	[19]
	Hydrous MnO_2	PES	Blending + phase inversion	PVP	Hydrophilicity	Pb(II) removal; ultrafiltration	[99]
	Hydrous MnO_2	PC	Coprecipitation method + phase inversion	Glycerol + CA	Adsorption; hydrophilicity	Heavy metal decontamination; ultrafiltration	[100]
	ZnO	PSf	Blending + phase inversion	PVA	Hydrophilicity	Oleic acid rejection	[101]
	ZnO	PES	Blending + phase inversion	–	Hydrophilicity	Dye removal; humic acid removal	[15, 102]
	ZnO	PES	Blending + phase inversion	PVP	Thermal stability; hydrophilicity	BSA rejection; ultrafiltration	[103]
	ZnO	PVDF	Blending + phase inversion	–	Photocatalytic activity; mechanical strength; hydrophilicity	Ultrafiltration	[104]

Continued

Table 2 Literatures Related to Addition of Metal Oxide Nanoparticles—cont'd

Type of Filler	Filler	Base Polymer	Preparation Method	Additives	Properties	Application	Reference
	ZnO	PVDF	Chemical modification + phase inversion	Carboxymethylchitosan	Thermal stability; mechanical strength; hydrophilicity	Nanofiltration	[105]
	ZnO	PVDF	Phase inversion + chemical modification Blending + phase inversion	PVP + cetryltrimethyl ammonium bromide/ sodium dodecyl benzene sulphonic; PVP	Adsorption; hydrophilicity	Heavy metal removal	[106]
	ZrO_2	PES	Blending + phase-inversion	–	Hydrophilicity	Ultrafiltration	[63]
	ZrO_2	CA	Blending + phase-inversion	–	Mechanical strength; hydrophilicity	Ultrafiltration	[107]
	ZrO_2	PES	Blending + phase-inversion	–	Hydrophilicity	Wastewater filtration	[108]
Metal	Se	PES	Blending + phase-inversion	–	Antimicrobial property; hydrophilicity	Protein rejection; activated sludge filtration	[109]
	Cu	PES	Blending + phase-inversion	–	Antimicrobial property; hydrophilicity	Protein rejection; activated sludge filtration	[109]
	Cu	PSf	Blending + phase inversion	–	Mechanical strength; hydrophilicity	Ultrafiltration	[110]
	Pd	PES	Photografting polymerization + surface functionalization (intermatrix synthesis)	AA, 4-hydroxybenzophenone, *N*, *N*-methylenebisacrylamide	Photocatalytic activity	Catalytic reduction of *p*-nitrophenol	[26]
	Mg/Al	PVDF	Coprecipitation + hydrothermal treatment + phase inversion	PVP	Hydrophilicity	Ultrafiltration	[111]
Other metallic nanomaterials	WS_2	PES	Blending + phase inversion	–	Thermal stability; hydrophilicity	Humic acid removal	[15, 112]
	$Mg(OH)_2$	PVDF	Blending + phase inversion	PEG	Antibacterial property; hydrophilicity	Bacterial removal; microfiltration	[4]

5 CONCLUSION AND FURTHER DEVELOPMENTS

Progress in the development of MMMs for water purification has been tremendous in recent years. Generally, the preparation of nanoparticle-enhanced membrane seeks continuous improvements in hydrophilicity, water flux, solute rejection, and antifouling properties. Moreover, the presence of metal/metal oxide nanomaterials can substantially confer and improve some physicochemical properties (pore density, porosity, charge, antimicrobial properties, thermal, and mechanical stability) and even can induce new characteristics to this nanoparticle-enhanced membrane. The potential of incorporating nanosized metallic particles in polymeric membranes makes them able to be applied in the whole filtration spectrum for water purification, from microfiltration to both reverse and forward osmosis.

Previous literature about MMM preparation was mainly focusing on the search of an optimal nanoparticle concentration, in which both permselective and antifouling properties showed their highest values, thus playing down the importance of how these nanoparticles are incorporated and distributed into the membrane. Nanoparticles are unstable in their isolated form and easily tend to form aggregated structures because of their natural tendency toward reaching a more thermodynamically stable state and, as a result, can block membrane pores and leach out from the membrane structure. Therefore, researchers should focus on both avoiding organic biodegradability and guaranteeing nanoparticle stability in the material structure to ensure the durability and reliability of the new nanocomposite material without compromising the main properties of the previous polymeric structure. Recently, many researchers are increasingly aware of the significance of membrane preparation and how to guarantee the homogeneous nanoparticle attachment and dispersion throughout the membrane structure to overcome the main drawbacks during their incorporation, namely, agglomeration/aggregation phenomena and nanoparticle leakage (or leaching-out effect). These major unresolved disadvantages should be carefully analyzed to ensure the homogeneity throughout the resulting MMMs.

Several approaches have been focused on the design of the preparation method and its conditions (including temperature, solvents, nanoparticle concentration, and presence of organic or inorganic additives) to optimize the presence, homogeneous distribution, and stabilization of metallic nanofillers within the host polymeric structure. An improvement in the dispersion of nanomaterials could be achieved by modifying their surfaces, by encapsulating them, or by adding some organic additives that act as binding elements between the dispersed inorganic nanoparticles and polymeric chains via covalent bonds or the use of cross-linkers. This improved dispersion and fixation of nanoparticles may result in a better nanoparticle distribution and could reduce metallic nanomaterials loss during preparation, storage, and operation. Despite the efforts of many experts in membrane technology, uniform and homogeneous nanoparticle dispersion in membrane structures remains an unresolved problem. Future research should be focused on seeking more new approaches or protocols to ideally trap nanoparticles in the selective layer structure of the membrane.

The stabilization of nanofillers within the host polymeric structure strongly depends on the compatibility between nanomaterials and polymers. This compatibility is critical to ensure the persistence of nanomaterials and therefore to enhance the durability and long-term efficiency of MMMs. Their growing implementation in water and wastewater treatment should lead researchers to concentrate on hindering leached nanomaterials to the environment because of their toxicity to both human and animal health. However, very few researchers have considered the toxicity of the nanoparticle loss and its impact on the receiving ecosystem, which would vary the water chemistry. For this reason,

the environmental toxicity of metal/metal oxide nanoparticles should be systematically evaluated. Additionally, the emergence of metal-resistant bacteria is a potential challenge that should be overcome to consolidate the use of MMMs. Some studies also demonstrated that the compatibility of metallic nanomaterials with host polymers is favored at very low nanoparticle concentration at which the agglomeration and aggregation phenomena can be minimized. The existence of this optimal nanoparticle concentration can form more stable and stronger membrane structures.

For all these reasons, the practical application of MMMs for water purification requires appropriate in-depth studies on the actual needs in both laboratory and industrial scales. Very few reports indicate the implementation of MMMs on large-scale processes, monitoring their cost-effectiveness and long-term stability in a full-scale filtration process under practical operating conditions and even considering the water quality of the source and the implications that the implemented MMM could have in the application environment during operation. Finally, the implementation of viable, stable, and long-lasting MMMs can open future applications in which current filtration membranes are trying to carve out a niche, such as the removal of emerging contaminants.

REFERENCES

[1] N.L. Le, S.P. Nunes, Materials and membrane technologies for water and energy sustainability, Sustain. Mater. Technol. 7 (2016) 1–28.
[2] L.Y. Ng, A.W. Mohammad, C.P. Leo, N. Hilal, Polymeric membranes incorporated with metal/metal oxide nanoparticles: a comprehensive review, Desalination 308 (2013) 15–33.
[3] B. Van der Bruggen, Chemical modification of polyethersulfone nanofiltration membranes: a review, J. Appl. Polym. Sci. 114 (2009) 630–642.
[4] C. Dong, G. He, H. Li, R. Zhao, Y. Han, Y. Deng, Antifouling enhancement of poly(vinylidene fluoride) microfiltration membrane by adding $Mg(OH)_2$ nanoparticles, J. Membr. Sci. 387-388 (2012) 40–47.
[5] E. Bet-moushoul, Y. Mansourpanah, K. Farhadi, M. Tabatabaei, TiO_2 nanocomposite based polymeric membranes: a review on performance improvement for various applications in chemical engineering processes, Chem. Eng. J. 283 (2016) 29–46.
[6] I. Gehrke, A. Geiser, A. Somborn-Schulz, Innovations in nanotechnology for water treatment, Nanotechnol. Sci. Appl. 8 (2015) 1–17.
[7] W.J. Lau, S. Gray, T. Matsuura, D. Emadzadeh, J.P. Chen, A.F. Ismail, A review on polyamide thin film nanocomposite (TFN) membranes: history, applications, challenges and approaches, Water Res. 80 (2015) 306–324.
[8] N. Savage, M.S. Diallo, Nanomaterials and water purification: opportunities and challenges, J. Nanopart. Res. 7 (2005) 331–342.
[9] M. Alexandre, P. Dubois, Polymer-layered silicate nanocomposites: preparation, properties and uses of a new class of materials, Mater. Sci. Eng. 28 (2000) 1–63.
[10] S.R. Venna, A. Spore, Z. Tian, A.M. Marti, E.J. Albenze, H.B. Nulwala, N.L. Rosi, D.R. Luebke, D.P. Hopkinson, H.R. Allcock, Polyphosphazene polymer development for mixed matrix membranes using SIFSIX-Cu-2i as performance enhancement filler particles, J. Membr. Sci. 535 (2017) 103–112.
[11] G.R. Guillen, Y. Pan, M. Li, E.M.V. Hoek, Preparation and characterization of membranes formed by nonsolvent induced phase separation: a review, Ind. Eng. Chem. Res. 50 (2011) 3798–3817.
[12] C.A. Smolders, A.J. Reuvers, R.M. Boom, I.M. Wienk, Microstructures in phase-inversion membranes. Part 1. Formation of macrovoids, J. Membr. Sci. 73 (1992) 259–275.

[13] J.F. Li, Z.L. Xu, H. Yang, L.Y. Yu, M. Liu, Effect of TiO_2 nanoparticles on the surface morphology and performance of microporous PES membrane, Appl. Surf. Sci. 255 (2009) 4725–4732.
[14] A. Rahimpour, S.S. Madaeni, A.H. Taheri, Y. Mansourpanah, Coupling TiO_2 nanoparticles with UV irradiation for modification of polyethersulfone ultrafiltration membranes, J. Membr. Sci. 313 (2008) 158–169.
[15] J. García-Ivars, M.I. Iborra-Clar, M.I. Alcaina-Miranda, B. Van der Bruggen, Comparison between hydrophilic and hydrophobic metal nanoparticles on the phase separation phenomena during formation of asymmetric polyethersulphone membranes, J. Membr. Sci. 493 (2015) 709–722.
[16] V. Vatanpour, S.S. Madaeni, L. Rajabi, S. Zinadini, A.A. Derakhshan, Boehmite nanoparticles as a new nanofiller for preparation of antifouling mixed matrix membranes, J. Membr. Sci. 401-402 (2012) 132–143.
[17] C. Liao, J. Zhao, P. Yu, H. Tong, Y. Luo, Synthesis and characterization of low content of different SiO_2 materials composite poly (vinylidene fluoride) ultrafiltration membranes, Desalination 285 (2012) 117–122.
[18] J.P. Ferraris, I.H. Musselman, K.J. Balkus Jr., Chapter 6: mixed matrix membranes based on metal organic frameworks, in: M.G. Buonomenna (Ed.), Advanced Materials for Membrane Preparation, first ed., Bentham Science Publishers Ltd, Oak Park, IL, 2012, pp. 83–93.
[19] M. Homayoonfal, M.R. Mehrnia, M. Shariaty-Niassar, A. Akbari, A.F. Ismail, T. Matsuura, A comparison between blending and surface deposition methods for the preparation of iron oxide/polysulfone nanocomposite membranes, Desalination 354 (2014) 125–142.
[20] S. Kango, S. Kalia, A. Celli, J. Njuguna, Y. Habibi, R. Kumar, Surface modification of inorganic nanoparticles for development of organic-inorganic nanocomposites—a review, Prog. Polym. Sci. 38 (2013) 1232–1261.
[21] K.C. Khulbe, C. Feng, T. Matsuura, The art of surface modification of synthetic polymeric membranes, J. Appl. Polym. Sci. 115 (2) (2010) 855–895.
[22] V. Moghimifar, A. Raisi, A. Aroujalian, Surface modification of polyethersulfone ultrafiltration membranes by corona plasma-assisted coating TiO_2 nanoparticles, J. Membr. Sci. 461 (2014) 69–80.
[23] J. García-Ivars, M.I. Iborra-Clar, M.I. Alcaina-Miranda, J.A. Mendoza-Roca, L. Pastor-Alcañiz, Surface photomodification of flat-sheet PES membranes with improved antifouling properties by varying UV irradiation time and additive solution pH, Chem. Eng. J. 283 (2016) 231–242.
[24] C. Zhao, J. Xue, F. Ran, S. Sun, Modification of polyethersulfone membranes—a review of methods, Prog. Mater. Sci. 58 (2013) 76–150.
[25] M. Nady, M.C.R. Franssen, H. Zuilhof, M.S. Mohy Eldin, R. Boom, K. Schroën, Modification methods for poly(arylsulfone) membranes: a mini-review focusing on surface modification, Desalination 275 (2011) 1–9.
[26] C. Emin, J.C. Remigy, J.F. Lahitte, Influence of UV grafting conditions and gel formation on the loading and stabilization of palladium nanoparticles in photografted polyethersulfone membrane for catalytic reactions, J. Membr. Sci. 455 (2014) 55–63.
[27] A. Rahimpour, UV photo-grafting of hydrophilic monomers onto the surface of nano-porous PES membranes for improving surface properties, Desalination 265 (2011) 93–101.
[28] J. Kim, B. Van der Bruggen, The use of nanoparticles in polymeric and ceramic membrane structures: review of manufacturing procedures and performance improvement for water treatment, Environ. Pollut. 158 (2010) 2335–2349.
[29] R.L. Davies, S.F. Etris, The development and functions of silver in water purification and disease control, Catal Today 36 (1997) 107–114.
[30] L. Huang, S. Zhao, Z. Wang, J. Wu, J. Wang, S. Wang, In situ immobilization of silver nanoparticles for improving permeability, antifouling and anti-bacterial properties of ultrafiltration membrane, J. Membr. Sci. 499 (2016) 269–281.
[31] M.M. Zhang, C. Li, M.M. Benjamin, Y.J. Chang, Fouling and natural organic matter removal in adsorbent/membrane systems for drinking water treatment, Environ. Sci. Technol. 37 (2003) 1663–1669.

[32] A.M. Giasuddin, S.R. Kanel, H. Choi, Adsorption of humic acid onto nanoscale zerovalent iron and its effect on arsenic removal, Environ. Sci. Technol. 41 (2007) 2022–2027.
[33] F.L. Fu, D.D. Dionysiou, H. Liu, The use of zero-valent iron for groundwater remediation and wastewater treatment: a review, J. Hazard. Mater. 267 (2014) 194–205.
[34] R. Molinari, L. Palmisano, E. Drioli, M. Schiavello, Studies on various reactors configurations for coupling photocatalysis and membrane process in water purification, J. Membr. Sci. 206 (2002) 399–415.
[35] U. Diebold, The surface science of titanium dioxide: a review, Surf. Sci. Rep. 48 (2003) 53–229.
[36] N. Niksefat, M. Jahanshahi, A. Rahimpour, The effect of SiO_2 nanoparticles on morphology and performance of thin film composite membranes for forward osmosis application, Desalination 343 (2014) 140–146.
[37] A. Ahmad, S. Waheed, S.M. Kahn, S. e-Gul, M. Shafiq, M. Farooq, K. Sanaullah, T. Jamil, Effect of silica on the properties of cellulose acetate/polyethylene glycol membranes for reverse osmosis, Desalination 355 (2015) 1–10.
[38] J. Lin, W. Ye, K. Zhong, J. Shen, N. Jullok, A. Sotto, B. Van der Bruggen, Enhancement of polyethersulfone (PES) membrane doped by monodisperse stöber silica for water treatment, Chem. Eng. Process. 107 (2016) 194–205.
[39] M.R. Karim, M.A. Rahman, M.A.J. Miah, H. Ahmad, M. Yanagisawa, M. Ito, Synthesis of γ-alumina particles and surface characterization, Open Colloid Sci, J. 4 (2011) 32–36.
[40] M.A. Ahmed, M.F. Abdel-Messih, Structural and nano-composite features of TiO_2-Al_2O_3 powders prepared by sol-gel method, J. Alloys Compd. 509 (2011) 2154–2159.
[41] J. García-Ivars, M.I. Alcaina-Miranda, M.I. Iborra-Clar, J.A. Mendoza-Roca, L. Pastor-Alcañiz, Enhancement in hydrophilicity of different polymer phase-inversion ultrafiltration membranes by introducing PEG/Al_2O_3 nanoparticles, Sep. Purif. Technol. 128 (2014) 45–57.
[42] V. Kochkodan, N. Hilal, A comprehensive review on surface modified polymer membranes for biofouling mitigation, Desalination 366 (2015) 187–207.
[43] K. Zodrow, L. Brunet, S. Mahendra, D. Li, A. Zhang, Q. Li, P.J.J. Alvarez, Polysulfone ultrafiltration membranes impregnated with silver nanoparticles how improved biofouling resistance and virus removal, Water Res. 43 (2009) 715–723.
[44] H. Basri, A.F. Ismail, M. Aziz, K. Nagai, T. Matsuura, M.S. Abdullah, B.C. Ng, Silver-filled polyethersulfone membranes for antibacterial applications—effect of PVP and TAP addition on silver dispersion, Desalination 261 (2010) 264–271.
[45] J.H. Li, B.F. Yan, X.S. Shao, S.S. Wang, H.Y. Tian, Q.Q. Zhang, Influence of Ag/TiO_2 nanoparticle on the surface hydrophilicity and visible-light response activity of polyvinylidene fluoride membrane, Appl. Surf. Sci. 324 (2015) 82–89.
[46] A. Mollahosseini, A. Rahimpour, M. Jahamshahi, M. Peyravi, M. Khavarpour, The effect of silver nanoparticle size on performance and antibacteriality of polysulfone ultrafiltration membrane, Desalination 306 (2012) 41–50.
[47] M. Sile-Yuksel, B. Tas, D.Y. Koseoglu-Imer, I. Koyuncu, Effect of silver nanoparticle (AgNP) location in nanocomposite membrane matrix fabricated with different polymer type on antibacterial mechanism, Desalination 347 (2014) 120–130.
[48] J.S. Taurozzi, H. Arul, V.Z. Bosak, A.F. Burban, T.C. Voice, M.L. Bruening, V.V. Tarabara, Effect of filler incorporation route on the properties of polysulfone-silver nanocomposite membranes of different porosities, J. Membr. Sci. 325 (2008) 58–68.
[49] S. Gul, Z.A. Rehan, S.A. Khan, K. Akhtar, M.A. Khan, M.I. Khan, M.I. Rashid, A.M. Asiri, S.B. Khan, Antibacterial PES-CA-Ag_2O nanocomposite supported Cu nanoparticles membrane towards ultrafiltration, BSA rejection and reduction of nitriophenol, J. Mol. Liq. 230 (2017) 616–624.
[50] X. Wang, J. Yang, M. Zhu, F. Li, Characterization and regeneration of Pd/Fe nanoparticles immobilized in modified PVDF membrane, J. Taiwan Inst. Chem. Eng. 44 (2013) 386–392.

[51] H. Wang, X. Qiao, J. Chen, X. Wang, S. Ding, Mechanisms of PVP in the preparation of silver nanoparticles, Mater. Chem. Phys. 94 (2005) 449–453.
[52] A. Nguyen, L. Zou, C. Priest, Evaluating the antifouling effects of silver nanoparticles regenerated by TiO_2 on forward osmosis membrane, J. Membr. Sci. 454 (2014) 264–271.
[53] A. Zirehpour, A. Rahimpour, M. Ulbricht, Nano-sized metal organic framework to improve the structural properties and desalination performance of thin film composite forward osmosis membrane, J. Membr. Sci. 531 (2017) 59–67.
[54] M. Kobayashi, S. Kurosu, R. Yamaguchi, Y. Kawase, Removal of antibiotic sulfamethoxazole by zero-valent iron under oxic and anoxic conditions: removal mechanisms in acidic, neutral and alkaline solutions, J. Environ. Manage. 200 (2017) 88–96.
[54a] C.B. Wang, W.X. Zhang, Synthesizing nanoscale iron particles for rapid and complete dechlorination of TCE and PCBs, Environ. Sci. Technol. 31 (1997) 2154–2156.
[55] B. Ma, W. Yu, W.A. Jefferson, H. Liu, J. Qu, Modification of ultrafiltration membrane with nanoscale zero-valent iron layers for humic acid fouling reduction, Water Res. 71 (2015) 140–149.
[56] M. Khajouei, M. Jahanshahi, M. Peyravi, H. Hoseinpour, A.R. Rad, Anti-bacterial assay of doped membrane by zero valent Fe nanoparticles via in-situ and ex-situ aspect, Chem. Eng. Res. Des. 117 (2017) 287–300.
[57] X. Wang, C. Chen, H. Liu, J. Ma, Preparation and characterization of PAA/PVDF membrane-immobilized Pd/Fe nanoparticles for dechlorination of trichloroacetic acid, Water Res. 42 (2008) 4656–4664.
[58] J. Wang, D. Thompson, D.Y.H. Pui, Integrative filtration research and sustainable nanotechnology, Particuology 11 (2013) 5–13.
[58a] J. Xu, D. Bhattacharyya, Fe/Pd nanoparticle immobilization in microfiltration membrane pores: synthesis, characterization, and application in the dechlorination of polychlorinated biphenyls, Ind. Eng. Chem. Res. 46 (2007) 2348–2359.
[58b] J. Xu, D. Bhattacharyya, Modeling of Fe/Pd nanoparticle-based functionalized membrane reactor for PCB dechlorination at room temperature, J. Phys. Chem. C 112 (2008) 9133–9144.
[59] H.H. Chang, T.J. Cheng, C.P. Huang, G.S. Wang, Characterization of titanium dioxide nanoparticle removal in simulated drinking water treatment processes, Sci. Total Environ. 601-602 (2017) 886–894.
[60] Z. Yang, D. Coutinho, F. Feng, J.P. Ferraris, K.J. Balkus Jr., Novel inorganic/organic hybrid electrolyte membranes, Prepr. Pap.-Am. Chem. Soc., Div Fuel Chem. 49 (2) (2004) 599–600.
[61] N. Ghaemi, A new approach to copper ion removal from water by polymeric nanocomposite membrane embedded with γ-alumina nanoparticles, Appl. Surf. Sci. 364 (2016) 221–228.
[62] M. Hua, S. Zhang, B. Pan, W. Zhang, L. Lv, Q. Zhang, Heavy metal removal from water/wastewater by nanosized metal oxides: a review, J. Hazard. Mater. 211-212 (2012) 317–331.
[63] J.M. Arsuaga, A. Sotto, G. Del Rosario, A. Martínez, S. Molina, S.B. Teli, J. De Abajo, Influence of the type, size, and distribution of metal oxide particles on the properties of nanocomposite ultrafiltration membranes, J. Membr. Sci. 428 (2013) 131–141.
[64] K.A. Gebru, C. Das, Preparation and characterization of CA-PEG-TiO_2 membranes: effect of PEG and TiO_2 on morphology, flux and fouling performance, J. Membr. Sci. Res. 3 (2017) 90–101.
[65] K.A. Gebru, C. Das, Removal of Pb(II) and Cu(II) ions from wastewater using composite electrospun cellulose acetate/titanium oxide (TiO_2) adsorbent, J. Water Process Eng. 17 (2017) 1–13.
[66] M. Geiser, B. Rothen-Rutishauser, N. Kapp, S. Schurch, W. Kreyling, H. Schulz, M. Semmler, V.I. Hof, J. Heyder, P. Gehr, Ultrafine particles cross cellular membranes by nonphagocytic mechanisms in lungs and in cultured cells, Environ. Health Perspect. 113 (11) (2005) 1555–1560.
[67] Y. Yang, H. Zhang, P. Wang, Q. Zheng, J. Li, The influence of nano-sized TiO_2 fillers on the morphologies and properties of PSF UF membrane, J. Membr. Sci. 288 (2007) 231–238.

[68] A. Razmjou, J. Mansouri, V. Chen, The effects of mechanical and chemical modification of TiO_2 nanoparticles on the surface chemistry, structure and fouling performance of PES ultrafiltration membranes, J. Membr. Sci. 378 (2011) 73–84.
[69] A. Rahimpour, M. Jahanshahi, B. Rajaeian, M. Rahimnejad, TiO_2 entrapped nano-composite PVDF/SPES membranes: preparation, characterization, antifouling and antibacterial properties, Desalination 278 (2011) 343–353.
[70] A. Razmjou, A. Resosudarmo, R.L. Holmes, H. Li, J. Mansouri, V. Chen, The effect of modified TiO_2 nanoparticles on the polyethersulfone ultrafiltration hollow fiber membranes, Desalination 287 (2012) 271–280.
[71] Y.C. Su, C. Huang, J.R. Pan, W.P. Hsieh, M.C. Chu, Fouling mitigation by TiO_2 composite membrane in membrane bioreactors, J. Environ. Eng. 138 (2012) 344–350.
[72] L.X. Dong, H.W. Yang, S.T. Liu, X.M. Wang, Y.F. Xie, Fabrication and anti-biofouling properties of alumina and zeolite nanoparticle embedded ultrafiltration membranes, Desalination 365 (2015) 70–78.
[73] M.S. Jyothi, V. Nayak, M. Padaki, R.G. Balakrishna, A.F. Ismail, The effect of UV irradiation on PSf/TiO_2 mixed matrix membrane for chromium rejection, Desalination 354 (2014) 180–199.
[74] S.H. Kim, S.Y. Kwak, B.H. Sohn, T.H. Park, Design of TiO_2 nanoparticle self-assembled aromatic polyamide thin-film-composition (TFC) membrane as an approach to solve bio-fouling problem, J. Membr. Sci. 211 (2003) 157–165.
[75] H. Yamashita, H. Nakao, M. Takeuchi, Y. Nakatani, M. Anpo, Coating of TiO_2 photocatalysts on superhydrophobic porous Teflon membrane by an ion assisted deposition method and their self-cleaning performance, Nucl. Instrum. Methods Phys. Res. B 206 (2003) 898–901.
[76] S.N. Hoseini, A.K. Pirzaman, M.A. Aroon, A.E. Pirbazari, Photocatalytic degradation of 2,4-dichlorophenol by Co-doped TiO_2 (Co/TiO_2) nanoparticles and Co/TiO_2 containing mixed matrix membranes, J. Water Process Eng. 17 (2017) 124–134.
[77] J. García-Ivars, M.I. Iborra-Clar, M.I. Alcaina-Miranda, J.A. Mendoza-Roca, L. Pastor-Alcañiz, Development of fouling-resistant polyethersulfone ultrafiltration membranes via surface UV photografting with polyethylene glycol/aluminum oxide nanoparticles, Sep. Purif. Technol. 135 (2014) 88–99.
[78] L.Y. Ng, C.P. Leo, A.W. Mohammad, Optimizing the incorporation of silica nanoparticles in polysulfone/poly(vinyl alcohol) membranes with response surface methodology, J. Appl. Polym. Sci. 121 (2011) 1804–1814.
[79] G. Arthanareeswaran, T.K. Sriyamuna Devi, M. Raajenthiren, Effect of silica particles on cellulose acetate blend ultrafiltration membranes: part I, Sep. Purif. Technol. 64 (2008) 38–47.
[80] J.N. Shen, H.M. Ruan, L.G. Wu, C.J. Gao, Preparation and characterization of PES-SiO_2 organic-inorganic composite ultrafiltration membrane for raw water pretreatment, Chem. Eng. J. 168 (2011) 1272–1278.
[81] A. Ananth, G. Arthanareeswaran, H. Wang, The influence of tetraethylorthosilicate and polyethyleneimine on the performance of polyethersulfone membranes, Desalination 287 (2012) 61–70.
[82] W. Chen, Y. Su, L. Zhang, Q. Shi, J. Peng, Z. Jiang, In situ generated silica nanoparticles as pore-forming agent for enhanced permeability of cellulose acetate membranes, J. Membr. Sci. 348 (2010) 75–83.
[83] L.Y. Yu, Z.L. Xu, H.M. Shen, H. Yang, Preparation and characterization of PVDF-SiO_2 composite hollow fiber UF membrane by sol-gel method, J. Membr. Sci. 337 (2009) 257–265.
[84] A.F.Q. Stöber, E. Bohn, Controlled growth of monodisperse silica spheres in the micron size range, J. Colloid Interf. Sci. 26 (1968) 62–69.
[85] A. Akbari, R. Yegani, B. Pourabbas, A. Behboudi, Fabrication and study of fouling characteristics of HDPE/PEG grafted silica nanoparticles composite membrane for filtration of humic acid, Chem. Eng. Res. Des. 109 (2016) 282–296.
[86] L.J. Zhu, L.P. Zhu, J.H. Jiang, Z. Yi, Y.F. Zhao, B.K. Zhu, Y.Y. Xu, Hydrophilic and anti-fouling polyethersulfone ultrafiltration membranes with poly(2-hydroxyethyl methacrylate) grafted silica nanoparticles as additive, J. Membr. Sci. 451 (2014) 157–168.

[87] H.H. Dai, J.T. Yang, J.P. Ma, F. Chen, Z.D. Fei, M.Q. Zhong, A green process for the synthesis of controllable mesoporous silica materials, Microporous Mesoporous Mater. 147 (2012) 281–285.
[88] J. Huang, K. Zhang, K. Wang, Z. Xie, B. Ladewig, H. Wang, Fabrication of polyethersulfone-mesoporous silica nanocomposite ultrafiltration membranes with antifouling properties, J. Membr. Sci. 423-424 (2012) 362–370.
[89] N. Maximous, G. Nakhla, W. Wan, K. Wong, Preparation, characterization and performance of Al_2O_3/PES membrane for wastewater filtration, J. Membr. Sci. 341 (2009) 67–75.
[90] N. Maximous, G. Nakhla, K. Wong, W. Wan, Optimization of Al_2O_3/PES membranes for wastewater filtration, Sep. Purif. Technol. 73 (2010) 291–301.
[91] N. Maximous, G. Nakhla, W. Wan, K. Wong, Effect of the metal oxide particle distributions on modified PES membranes characteristics and performance, J. Membr. Sci. 361 (2010) 213–222.
[92] X.M. Wang, X.Y. Li, K. Shih, In situ embedment and growth of anhydrous and hydrated aluminum oxide particles on polyvinylidene fluoride (PVDF) membranes, J. Membr. Sci. 368 (2011) 134–143.
[93] F. Liu, M.R.M. Abed, K. Li, Preparation and characterization of poly(vinylidene fluoride) (PVDF) based ultrafiltration membranes using nano γ-Al_2O_3, J. Membr. Sci. 366 (2011) 97–103.
[94] J. García-Ivars, M.I. Iborra-Clar, M.I. Alcaina-Miranda, J.A. Mendoza-Roca, L. Pastor-Alcañiz, Treatment of table olive processing wastewaters using novel photomodified ultrafiltration membranes as first step for recovering phenolic compounds, J. Hazard. Mater. 290 (2015) 51–59.
[95] P. Daraei, S.S. Madaeni, N. Ghaemi, E. Salehi, M.A. Khadivi, R. Moradian, B. Astinchap, Novel polyethersulfone nanocomposite membrane prepared by PANI/Fe_3O_4 nanoparticles with enhanced performance for Cu(II) removal from water, J. Membr. Sci. 415-416 (2012) 250–259.
[96] P. Daraei, S.S. Madaeni, N. Ghaemi, M.A. Khadivi, B. Astinchap, R. Moradian, Fouling resistant mixed matrix polyethersulfone membranes blended with magnetic nanoparticles: study of magnetic field induced casting, Sep. Purif. Technol. 109 (2013) 111–121.
[97] J. Alam, L.A. Dass, M. Ghasemi, M. Alhoshan, Synthesis and optimization of PES-Fe_3O_4 mixed matrix nanocomposite membrane: application studies in water purification, Polym, Compos. 34 (11) (2013) 1870–1877.
[98] N. Ghaemi, S.S. Madaeni, P. Daraei, H. Rajabi, S. Zinadini, A. Alizadeh, R. Heydari, M. Beygzadeh, S. Ghouzivand, Polyethersulfone membrane enhanced with iron oxide nanoparticles for copper removal from water: application of new functionalized Fe_3O_4 nanoparticles, Chem. Eng. J. 263 (2015) 101–112.
[99] R.J. Gohari, W.J. Lau, T. Matsuura, E. Halakoo, A.F. Ismail, Adsorptive removal of Pb(II) from aqueous solution by novel PES/HMO ultrafiltration mixed matrix membrane, Sep. Purif. Technol. 120 (2013) 59–68.
[100] M. Delavar, G. Bakeri, M. Hosseini, Fabrication of polycarbonate mixed matrix membranes containing hydrous manganese oxide and alumina nanoparticles for heavy metal decontamination: characterization and comparative study, Chem. Eng. Res. Des. 120 (2017) 240–253.
[101] C.P. Leo, W.P. Cathie Lee, A.L. Ahmad, A.W. Mohammad, Polysulfone membranes blended with ZnO nanoparticles for reducing fouling by oleic acid, Sep. Purif. Technol. 89 (2012) 51–56.
[102] S. Balta, A. Sotto, P. Luis, L. Benea, B. Van der Bruggen, J. Kim, A new outlook on membrane enhancement with nanoparticles: the alternative of ZnO, J. Membr. Sci. 389 (2012) 155–161.
[103] S. Zhao, W. Yan, M. Shi, Z. Wang, J. Wang, S. Wang, Improving permeability and antifouling performance of polyethersulfone ultrafiltration membrane by incorporation of ZnO-DMF dispersion containing nano-ZnO and polyvinylpyrrolidone, J. Membr. Sci. 478 (2015) 105–116.
[104] J. Hong, Y. He, Polyvinylidene fluoride ultrafiltration membrane blended with nano-ZnO particle for photocatalysis self-cleaning, Desalination 332 (2014) 67–75.
[105] K. Ekambaram, M. Doraisamy, Surface modification of PVDF nanofiltration membrane using carboxymethylchitosan-zinc oxide bionanocomposite for the removal of inorganic salts and humic acid, Colloids Surf. A 525 (2017) 49–63.

[106] X. Zhang, Y. Wang, Y. Liu, J. Xu, Y. Han, X. Xu, Preparation, performances of PVDF/ZnO hybrid membranes and their applications in the removal of copper ions, Appl. Surf. Sci. 316 (2014) 333–340.
[107] G. Arthanareeswaran, P. Thanikaivelan, Fabrication of cellulose acetate-zirconia hybrid membranes for ultrafiltration applications: performance, structure and structure analysis, Sep. Purif. Technol. 74 (2010) 230–235.
[108] N. Maximous, G. Nakhla, W. Wan, K. Wong, Performance of a novel ZrO_2/PES membrane for wastewater filtration, J. Membr. Sci. 352 (2010) 222–230.
[109] N. Akar, B. Asar, N. Dizge, I. Koyuncu, Investigation of characterization and biofouling properties of PES membrane containing selenium and copper nanoparticles, J. Membr. Sci. 437 (2013) 216–226.
[110] E.M.V. Hoek, A.K. Ghosh, X. Huang, M. Liong, J.I. Zink, Physical-chemical properties, separation performance, and fouling resistance of mixed-matrix ultrafiltration membranes, Desalination 283 (2011) 80–99.
[111] S. Arefi-Oskoui, A. Khataee, V. Vatanpour, Effect of solvent type on the physicochemical properties and performance of NLDH/PVDF nanocomposite ultrafiltration membranes, Sep. Purif. Technol. 184 (2017) 97–118.
[112] J. Lin, R. Zhang, W. Ye, N. Jullok, A. Sotto, B. Van der Bruggen, Nano-WS_2 embedded PES membrane with improved fouling and permselectivity, J. Colloid Interf. Sci. 396 (2013) 120–128.

FURTHER READING

[113] G.R. Xu, J.N. Wang, C.J. Li, Strategies for improving the performance of the polyamide thin film composite (PA-TFC) reverse osmosis (RO) membranes: surface modifications and nanoparticles incorporations, Desalination 328 (2013) 83–100.
[114] H. Xu, M. Ding, S. Liu, Y. Li, Z. Shen, K. Wang, Preparation and characterization of novel polysulphone hybrid ultrafiltration membranes blended with N-doped GO/TiO_2 nanocomposites, Polymer 117 (2017) 198–207.

CHAPTER

WATER TREATMENT BY MOLECULARLY IMPRINTED MATERIALS

7

Olympia Kotrotsiou, Costas Kiparissides

Chemical Process & Energy Resources Institute-Centre for Research and Technology Hellas, Thessaloniki, Greece

1 INTRODUCTION

In recent years, the release of harmful pollutants to the environment, as a result of the massive exploitation of natural resources and the extensive use of chemicals, has received much attention because of their negative effects to human health. Some of the new emerging organic contaminants, including pharmaceutical active compounds (PhACs), pesticides, and aromatic hydrocarbons, are being faulted for their endocrine-disrupting potency (characterized in literature as endocrine-disrupting compounds, or EDRs). To this point, world-leading drinking-water industries focus their efforts on the development of novel technologies for the removal of various persistent pollutants (i.e., disinfection by-products, pathogens, and synthetic or natural organic compounds) from water sources. Various water treatment methods, including UV radiation, ozonation, activated carbon adsorption, and membrane filtration, have been developed for the removal of toxic compounds from polluted water streams. However, these commonly applied methods are usually nonselective and often lead to secondary pollution effects. For example, the catalytic oxidation/reduction of synthetic organic compounds using metals and metal oxides (i.e., Pd-Cu, titanium oxide) has been recently applied to water treatment. However, these catalytic processes do not specifically target the unwanted pollutants but also other organic compounds in water, resulting in nonspecific side reactions and the production of undesirable by-products that must be removed in a subsequent process step at an additional cost. Thus, the development of catalysts with a high substrate specificity is required in order to eliminate the unwanted side reactions and associated water treatment costs.

It is apparent that the development of novel functional materials for the selective removal of toxic compounds and other contaminants from water sources is of great economic and environmental importance. Thus, current research efforts for "tailor-made" materials, possessing high selectivity and specificity and long-term stability, as well as the development of modern, efficient, environmentally friendly, and cost-effective water purification technologies are very intensive. One category of functional materials that satisfies the above performance criteria, is the molecularly imprinted polymers (MIPs). In this chapter, recent advances in the synthesis and application of MIPs in water treatment separation processes, selective catalytic degradation of pollutants, and

Nanoscale Materials in Water Purification. https://doi.org/10.1016/B978-0-12-813926-4.00012-4

development of novel ultrasensitive sensors for environmental monitoring of pollutants are critically reviewed.

2 THE MOLECULAR IMPRINTING CONCEPT

In molecular imprinting, selected functional monomers and a cross-linker are co-polymerized in the presence of a specific-target molecule, acting as a molecular template, to produce a polymeric material of high specificity. The functional monomers initially form a complex with the template molecule through covalent or noncovalent interactions. Polymerization of the functional monomers with a bifunctional or trifunctional cross-linker results in the template's docking into the polymeric matrix. The template molecules are subsequently removed, revealing specific binding sites that are complementary in size and shape to the template molecule (Fig. 1).

2.1 PRINCIPAL MECHANISMS OF SITE SPECIFICITY IN MIPs

Based on the nature of chemical interactions between the template and functional monomers, two types of chemical bonds (namely, covalent and noncovalent) can be established. In the case of covalent bonding, a stable complex is initially formed between the template molecule and the functional monomer. After polymerization, the covalent bonds that keep the template molecules in the polymer matrix are chemically cleaved (i.e., via hydrolysis of esters, reduction of disulfide bonds, etc.), and the template molecules are washed out, thus revealing the imprinted binding sites. During the adsorption process, for the removal of a target molecule from a liquid stream, the target molecule is specifically adsorbed to the binding site via the action of the same covalent interaction forces. Thus, the key factor to the successful formation of a MIP material with high specificity and selectivity towards a certain target molecule is the selection of the proper functional monomers that effect the covalent interactions between the template molecule and the monomers. Note that

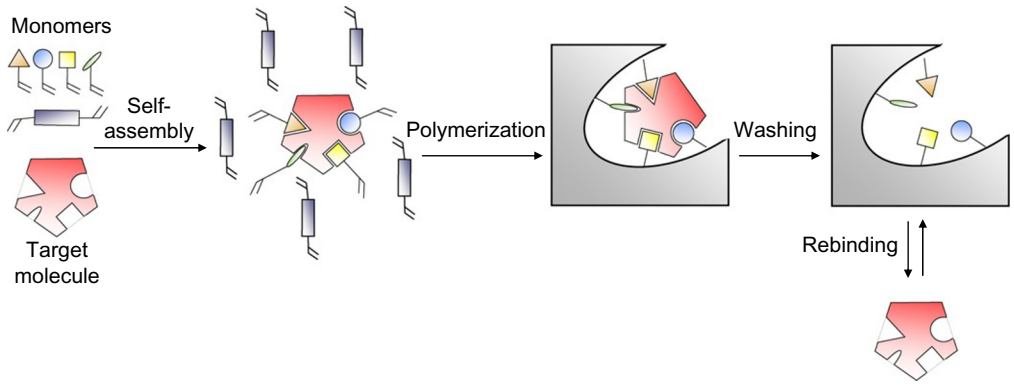

FIG. 1

Schematic representation of the molecular imprinting process.

the covalent bonds need to be stable and reversible, which, in a way, contradict each other. In particular, the established covalent bonds must remain stable during polymerization and, at the same time, can be efficiently broken during the template washing step (i.e., removal of the template molecule under relatively mild conditions) without damaging the generated binding sites. This means that both the association and dissociation of the template molecules with the functional monomers via covalent bonding must be highly selective and fast. The key advantage of the covalent approach is that the functional monomer is totally specific to the template molecule. However, it should be pointed out that there is a limited number of organic compounds (e.g., carboxylic acids, aldehydes, ketones, alcohols [diols], and amines) that satisfy the above criteria for efficient synthesis of MIPs via covalent bonding [1].

An alternative to covalent imprinting method is the so-called metal ion-mediated imprinting mechanism. According to this approach, a metal coordination mechanism between the template molecule and the functional monomer is established as an alternative to covalent bonding mechanism. The main advantages of the metal ion-mediated polymer imprinting method are: (1) presence of strong interactions between the metal ions and the monomer-template ligands that are not affected by the polymerization medium; (2) excess of binding groups is not necessary, which minimizes the formation of nonspecific binding sites; and (3) the potential of replacing the metal ions in a polymeric matrix with other metal ions so that the selectivity and binding kinetics of the MIP material can be altered. Note that combinations of organic molecules and metal ions have been employed in the synthesis of imprinted catalysts with improved selectivity.

In general, the synthesis of MIP materials via noncovalent bonding is easier to achieve and, thus, is applicable to a larger number of candidate templates. According to this MIP approach, noncovalent bonds are commonly formed between the template molecule and functional monomer during polymerization. Note that at the rebinding step, the association of template molecule to the binding site is governed by the same noncovalent interactions. In principle, any type of noncovalent interactions could be effective and employable for molecular imprinting. The interaction forces between the template molecule and functional monomers include: ionic, hydrogen bonding, π-π interactions, and hydrophobic associations. Among the above types of molecular interactions, hydrogen bonding is a very efficient association force that is highly affected by the direction and distance of the monomer functional groups and the template molecule. In the noncovalent synthesis of MIPs, monomers with functional groups (e.g., amino, amide, pyridine, hydroxyl, and carboxyl groups) that are complementary to the functional groups of the template molecule, can be commonly used. The type of the noncovalent interactions (e.g., hydrogen bonding, electrostatic interactions) is controlled by the pK values of the functional monomers and template molecules. This means that when the acid/base character of the interacting molecules is very strong, a proton from the acid is transferred to the base. In this case, the complex formation is controlled by electrostatic interactions. Note that electrostatic interactions do depend on the distance between the opposite charge species and not on the direction of the interactions between the functional groups of monomer and template molecules. On the other hand, when the acidic and basic nature of the selected functional monomers and template molecules is of intermediate strength, the proton resides between the acidic and basic compounds. In this case, the molecular interactions are governed by hydrogen bonding, and thus, efficient imprinting can be achieved [2]. Finally, if the acidic and basic nature of the interacting species is weak, the molecular interactions between the functional monomer and template are also weak. Thus, the specific species are not suitable for synthesis of MIPs.

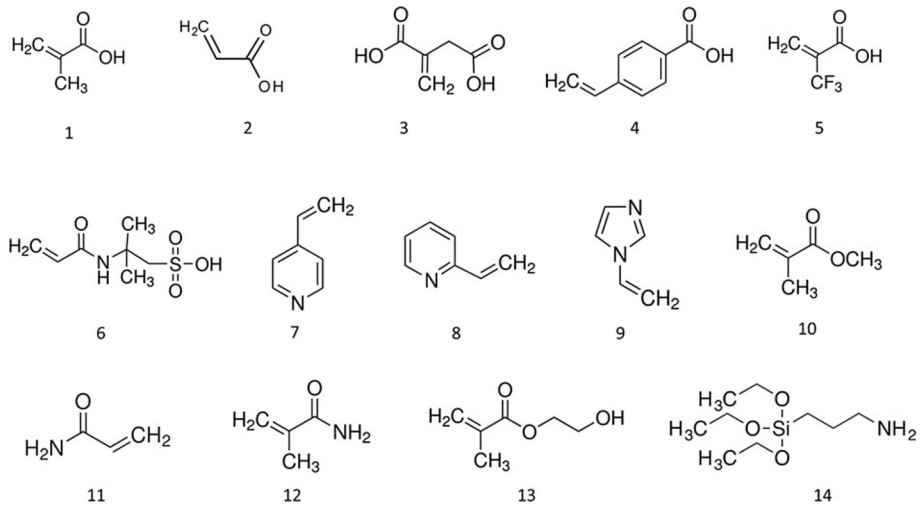

FIG. 2

Functional monomers used in noncovalent molecular imprinting. (1) methacrylic acid (MAA), (2) acrylic acid (AA), (3) itaconic acid (IA), (4) *p*-vinylbenzoic acid, (5) trifluoromethyl acrylic acid (TFMAA), (6) 2-acrylamido-2-methyl-1-propane sulfonic acid, (7) 4-vinylpyridine (4-VP), (8) 2-vinylpyridine (2-VP), (9) 1-vinylimidazole (1-VID), (10) methyl methacrylate (MMA), (11) acrylamide (AAm), (12) methacrylamide (Mam), (13) 2-hydroxyethyl methacrylate (HEMA), and (14) 3-aminopropyltriethoxysilane (APTES).

Many functional monomers are commercially available for noncovalent synthesis of MIPs (Fig. 2). However, custom-synthesized functional monomers have also been reported in the preparation of MIPs. Currently, the most commonly used functional monomer is the methacrylic acid. Other monomers that have been employed in the synthesis of MIPs are: acrylic acid, itaconic acid, p-vinylbenzoic acid, (2-trifluoromethyl) acrylic acid, 2-acrylamido-2-methyl-1-propane sulfonic acid (AMPSA), and 2-(methacryloyloxy)ethyl phosphate. Among the basic monomers, 4-vinylpyridine is the most common one. Other basic monomers, such as vinylimidazole, aminostyrene, and N,N-diethylaminoethyl methacrylate, have been also used in the synthesis of MIPs. Finally, neutral monomers (e.g., 2-hydroxyethyl methacrylate (HEMA), vinyl pyrrolidone, and acrylamide) have been employed in the synthesis of MIPs.

To improve the binding properties of MIPs two or more functional monomers can be combined together. It has been shown that the binding properties of synthesized MIPs in the presence of two or more functional monomers are superior of those obtained with a single functional monomer. Combinations of functional monomers that have been reported in the literature include: 2- (or 4-) vinylpyridine with methacrylic acid, acrylamide with methacrylic acid, acrylamide with acrylic acid, acrylamide with 2-vinylpyridine. In particular, HEMA and methacrylate have been used for the synthesis of hydrophilic MIPs, thus enabling the incorporation of hydrophilic template molecules, for water treatment applications [1].

2.2 SELECTION OF THE CROSS-LINKER AND SOLVENT

Copolymerization of the functional monomer in the presence of a cross-linker results in the formation of a cross-linked polymer matrix around the template molecule. In general, a high cross-linker to functional monomer molar ratio is required to obtain a stable and rigid polymer matrix that can withstand subsequent processing steps related to the removal of the template molecule (via a chemical process) as well as its repetitive use and regeneration as a highly selective adsorption material [3]. Note that the selectivity and binding capacity of MIPs are significantly affected by the type and amount of the cross-linker used in the polymerization recipe. To avoid the formation of copolymer chains with a low degree of incorporation of either the functional monomer or cross-linker, the reactivity of both copolymerizing species must be similar. Thus, by judicious selection of the cross-linker in relation to the functional monomer, a polymer network consisting of random copolymer chains can be obtained. Another important parameter in the selection of a cross-linker regards its hydrophilicity and hydrophobicity in relation to reaction medium. This means that the cross-linker type can also affect its chemical-physical stability and imprinted site's specificity in different reaction and application media. It should be noted that the rebinding properties (i.e., specificity, selectivity and efficiency) of MIPs are highly dependent on the cross-linker to the functional monomer molar ratio (C/M). Thus, low values of the (C/M) molar ratio (e.g., 1–3) lead to the formation of closely located binding sites, largely hindering their rebinding properties due to close site proximity and neighboring molecules interference. On the other hand, large values of the (C/M) ratio (e.g., 7–10) result in a decrease of imprinting efficiency (i.e., the number of formed binding sites decreases) which is particularly true in the case of noncovalent interactions between the cross-linker with the functional monomer [2]. Ethylene glycol dimethacrylate (EGDMA), trimethylolpropane trimethacrylate (TRIM), *p*-divinylbenzene (DVB), and *N*,*N*'-methylene bisacrylamide (MBAA) are the most commonly used cross-linkers in the synthesis of MIPs (Fig. 3).

In particular, for the synthesis of MIPs in organic solvents, EGDMA, TRIM, and DVB have been extensively used. On the other hand, MBAA is often used in the synthesis of MIPs in water. Other types of cross-linkers that have been used are: 1,3-diisopropenyl benzene (DIP), *N*,*O*-bisacryloyl-l-phenylalaninol, tetramethylene dimethacrylate (TDMA), *N*,*N*'-1,4-phenylene diacrylamine, 2,6-bisacryloylamidopyridine, 1,4-diacryloyl piperazine (DAP), 3,5-bisacryloylamido benzoic acid, *N*,*N*'-1,3-phenylene bis(2-methyl 2-propenamide) (PDBMP), *N*,*N*'-ethylene bismethacrylamide, *N*,*N*' hexamethylene bismethacrylamide, pentaerythritol tetraacrylate (PETEA), and pentaerythritol triacrylate (PETRA).

The selected reaction medium plays an important role in the synthesis of MIPs for it acts as a dispersion phase in the production of particulate MIPs by precipitation, suspension and emulsion polymerization. In precipitation (dispersion) polymerization, the selected solvent can also affect the porosity of the precipitated polymer, thus acting as a pore-forming agent as well. Note that the strength of the molecular interactions between the template molecule and the functional monomer and cross-linker are significantly affected by the solvent's polarity which, in turn, can affect the efficiency of the MIP synthesis, especially in noncovalent systems. When the selected dispersion medium plays a dual role (i.e., it acts both as a reaction medium and porogen), it can influence both the strength of noncovalent molecular interactions and the morphology (i.e., porosity) of the precipitated polymer phase. For example, when, in the synthesis of MIPs, chloroform is replaced by acetonitrile (a fairly polar solvent) a more porous polymer matrix is obtained. The most frequently used solvents in the synthesis of MIPs are: acetonitrile, chloroform, toluene, *N*,*N*-dimethylformamide (DMF), methanol, tetrahydrofuran (THF), and

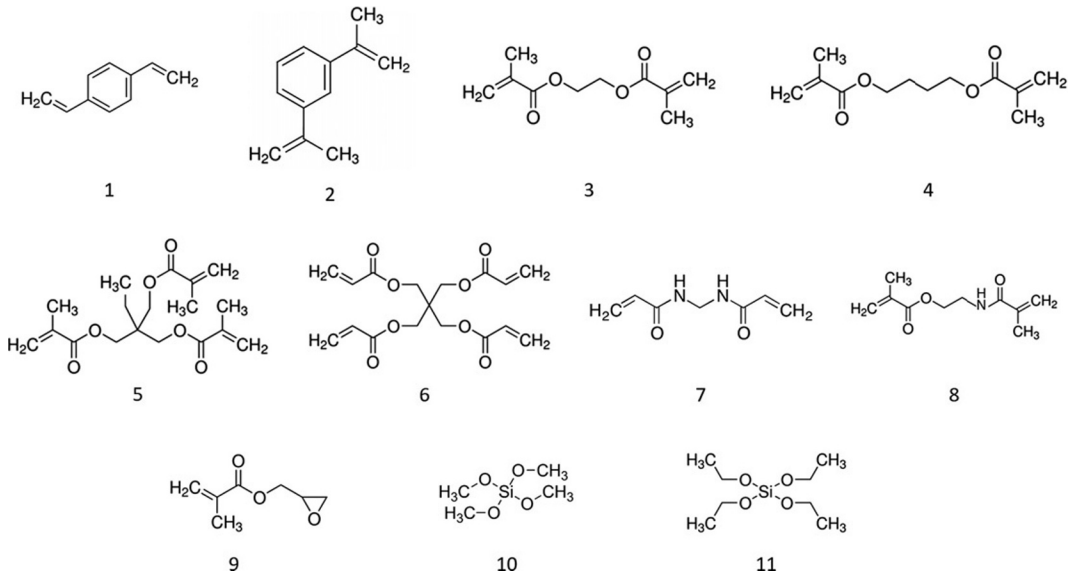

FIG. 3

Chemical structures of common cross-linkers used in noncovalent molecular imprinting. (1) divinylbenzene (DVB), (2) 1,3-diisopropenyl benzene, (3) ethylene glycol dimethacrylate (EGDMA), (4) tetramethylene dimethacrylate, (5) trimethylolpropane trimethacrylate (TRIM), (6) pentaerythritol tetraacrylate, (7) *N,N*′-methylenediacrylamide (MBAA), (8) *N,O*-bismethacryloyl ethanolamine (NOBE), (9) glycidilmethacrylate (GMA), (10) tetramethoxysilane (TMOS), (11) tetraethoxysilane (TEOS).

dichloroethane. In order to increase the imprinting efficiency in the synthesis of MIPs by the noncovalent approach, nonpolar and/or less polar solvents, such as toluene, chloroform, and acetonitrile, are commonly selected. Note that when water is employed as a dispersion/porogen medium, the presence of hydrophobic interactions between the template molecule and the functional monomers (e.g., cyclodextrines) can affect the imprinting efficiency and binding capacity of the MIPs. On the other hand, the presence of water in the MIP synthesis by the metal-ligand complexation approach does not affect the metal-complex interactions, leading to the formation of stable complexes which improves the imprinting efficiency and binding properties of the MIPs. It is worth of noting that molecular dynamic computational tools are now available to aid the optimal selection of required polymerization reagents (i.e., functional monomers, cross-linkers, and solvents) for a given template molecule [3].

With regard to the rebinding process, that is, the use of MIPs as highly selective adsorbents for the removal of a target molecule from a solution, the choice of the solvent is of equal importance to the MIPs synthesis. Thus, the solvent polarity can affect the stability of the noncovalent bonds during the rebinding of target molecules with the specific MIPs' sites. Accordingly, nonpolar solvents are commonly used with MIPs synthesized by the noncovalent approach, leading to an improved rebinding efficiency. It is important to point out that the selected solvent can also affect the degree of polymer swelling and, consequently, the MIPs' morphology. In particular, polymer swelling can change the three-dimensional arrangement of the functional groups at the binding sites and, thus, can dramatically alter the MIPs' binding efficiency.

2.3 POLYMERIZATION MECHANISMS AND METHODS

In general, MIPs can be synthesized by a variety of polymerization mechanisms (i.e., free-radical, anionic, cationic, and condensation) and methods (i.e., bulk, dispersion, precipitation, suspension, emulsion and miniemulsion). The key prerequisite to the selection of a mechanism and method is that the polymerization can proceed to high monomer conversions under the selected conditions (e.g., temperature, reagent concentrations, solvent, etc.) that favor the molecular interactions between the various reagents (i.e., template molecules, cross-linkers, functional monomers, etc.) and, thus, the formation of stable and specific binding sites. Free radical-initiated vinyl polymerization remains the most commonly applied method for the synthesis of molecularly imprinted materials because of the wide availability of a broad range of monomers and cross-linkers or/and the easy synthesis of new ones [2]. Additionally, free-radical polymerization can be carried under relatively mild conditions (e.g., relatively low temperatures). Polymerization can be initiated via the thermal or UV decomposition of a chemical initiator, including 2,2′-azobis(isobutyronitrile) (AIBN), 2,2′-azobis (2,4-dimethylvaleronitrile) (ADVN), 4,4′-azo(4-cyanovaleric acid) (ACID), benzoyl peroxide (BPO), among others.

In free-radical polymerization, control of the molecular weight distribution (MWD) is relatively difficult due to the complex kinetic mechanism, including chain initiation, propagation, transfer and termination reactions as well as the appearance of diffusion-control limitations in the propagation and termination rate constants. As a result, the resulting MWD is often very broad. On the other hand, in living (controlled radical polymerization, CRP), the MWD of the synthesized polymer is narrow due to better control of chain growth and elimination of termination reactions. The most promising CRP techniques are the atom transfer radical polymerization (ATRP) and the reversible addition-fragmentation chain transfer (RAFT) polymerization [3]. Note that ATRP enhances the presence of convertible functional groups on the MIP surface which largely facilitates its subsequent surface modification. However, the main drawback of ATRP is the low tolerance of the functional groups to the presence of metal catalysts and ligands, typically amines or phosphines that are used to increase the solubility of the transition metal salts in solution and tune the reactivity of the metal catalysts. On the other hand, in RAFT polymerization the functional groups are not affected due to the absence of metal catalysts. MIPs synthesized by RAFT polymerization contain convertible end-functional groups, thus enabling their subsequent polymer grafting. According to Ye [4], MIPs prepared by CRP have a more homogeneous polymer structure and improved binding properties.

Several other techniques have been used for the synthesis of MIPs including electro-polymerization and chemical oxidation. In particular, the first method was employed for the synthesis of polypyrrole-based molecularly imprinted conductive films while the latter was applied in the synthesis of MIPs colloids. The synthesis of electropolymerized metal ion-imprinted polypyrrole-based and other conductive MIPs (e.g., poly(o-phenylenediamine), poly(o-aminophenol), poly(o-aminothiophenol), and polyanilines) has been also reported in the open literature [1].

Step-growth (condensation) polymerization of di- or tri-isocyanates with polyhydroxy compounds has been used for the synthesis of molecularly imprinted polyurethanes. A typical application of polyurethane-based MIPs is their use as sensor elements for the detection of solvent vapors, aromatic hydrocarbons, halogenated compounds and engine oil. In another application, carbodiimide-induced condensation polymerization of a mixture of amino acids in the presence of estradiol in aqueous solution resulted in a mixture of peptides possessing high affinity toward estradiol [1].

2.4 SYNTHESIS OF MOLECULARLY IMPRINTED MICRO- AND NANOPARTICLES

Traditionally, MIPs are synthesized by bulk polymerization as porous monoliths. After grinding and sieving of the synthesized monoliths, irregular particles of different sizes (in the range of 5 to 100 μm) are commonly obtained. Although this method allows the easy preparation of particulate MIPs, it only produces moderate amounts (i.e., typical particle yields are less than 50%) of polymer particles of irregular size and shape. As a result of particle irregularity and low functionality, their incorporation into selected organic/inorganic membranes is difficult. Thus, there is a need for the production of well-defined polymer particles (i.e., nano- and microparticles), via alternative polymerization techniques (e.g., precipitation, suspension and miniemulsion).

In precipitation polymerization, the formation of highly cross-linked particles takes place in a solvent excess. The mechanism of particle formation and particle growth in precipitation polymerization is similar to that of dispersion polymerization. The main difference between the two polymerization mechanisms is that the particles formed by precipitation polymerization are stabilized against coagulation by their rigid cross-linked surfaces while the particles in dispersion polymerization are stabilized by the addition of an appropriate stabilizer. In general, the polymer particles formed by precipitation polymerization are free of any stabilizer molecules and, therefore, are devoid of nonspecific binding interactions. Note that polymer particle yield of MIPs produced via precipitation polymerization can be as high as 85%. The solvents used in precipitation polymerization range from nonpolar hydrocarbons to highly polar alcohols or alcohol/water mixtures. Thus, precipitation polymerization can be readily adapted to the synthesis of desirable imprints in polar solvents by covalent, coordination or strong noncovalent (i.e., ionic) approaches. In good solvency conditions for the precipitated polymer, microgels can be formed via precipitation polymerization. On the other hand, when the polymer has a low solubility in the dispersion medium, the method normally produces micrometer- or nanometer-size particles [5].

In suspension polymerization, the organic phase (containing the functional monomer, the cross-linker, the solvent, the template molecules and the chemical initiator) is initially dispersed, with the aid of an agitation system, in the continuous aqueous phase containing the surface-active agents. Subsequently, the temperature in the polymerization vessel is raised to the desired one so that the free-radical copolymerization can be initiated. As the polymerization progresses, the dispersed liquid droplets are gradually transformed into rigid, spherical polymer particles in the size range of 5 to 500 μm. One of the most important issues in suspension polymerization is the control of the droplet/particle size distribution (DSD/PSD). Note that the initial liquid droplet size distribution depends on the type and concentration of the surface-active agents, the quality of agitation and the physical properties (i.e., densities, viscosities and interfacial tension) of the continuous and dispersed phases. Partially hydrolyzed Poly(Vinyl Acetate) (PVA) is commonly used as a stabilizer. The degree of hydrolysis of PVA strongly affects its surface activity at the organic/aqueous interface. In general, the solubility of PVA in the aqueous phase depends on its molecular weight, the sequence length distribution of vinyl alcohol and vinyl acetate monomers in the copolymer chains, the degree of hydrolysis, and temperature. In the inverse suspension polymerization, the aqueous phase, containing the water-soluble functional monomers as well as the template molecules, is dispersed in an organic phase containing the appropriate type of surface-active agents.

Alternatively, perfluorocarbons (PFCs), largely immiscible with most organic compounds, can be used as suspension medium. PFCs are perfluorinated and saturated aliphatic compounds (i.e., perfluoroalkanes, perfluoroalkylamines and perfluoroalkylethers). They usually have a higher density, a lower

boiling point, a lower vaporization temperature, and a lower polarity than the corresponding hydrocarbons. In addition, they have high stability, low miscibility and inertness toward organic compounds which make them an excellent suspension medium. However, in order to obtain a reasonably stable suspension of liquid droplets, containing the functional monomers, cross-linkers, template molecules and initiator, in a PFC suspension medium, the use of suitable fluorinated stabilizers (i.e., surface-active polymers containing fluorinated units) is required. Note that in most cases, the synthesis of new stabilizers suitable for the particular suspension polymerization is required. Moreover, the high cost of PFCs remains an unsolved problem.

In miniemulsion polymerization, stable nanodroplets of the organic phase (containing the functional monomers, the cross-linker, the solvent, the template molecules and the co-surfactant) are dispersed in the continuous-aqueous phase (containing the dissolved surfactant) with the aid of an agitation system. Note that, in the presence of a chemical initiator, polymerization can be initiated in the dispersed nanodroplets which behave like individual batch nanoreactors. At the end of polymerization, the nanodroplets are converted into solid nanoparticles, with an average diameter in the range of 200–1000 nm. In particular, in miniemulsion polymerization the nanodroplet size distribution and, consequently, the final PSD is controlled by the type and concentration of both surfactant and co-surfactant, the ratio of the organic to the aqueous phase, the densities and viscosities of the two phases, the mixing conditions (e.g., agitation intensity, energy dissipation rate and distribution) and polymerization temperature. Note that, in the inverse miniemulsion polymerization, molecularly imprinted nanoparticles can be synthesized using hydrophilic monomers and water-soluble templates that are dispersed in the continuous oil phase. In this case, the required osmotic pressure for the stability of the dispersed droplets is built up by the addition of a so-called lipophobe agent that is insoluble in the continuous oil phase. Candidate lipophobes that have been used in water-in-oil miniemulsions include ionic compounds, salts, and sugars [6]. In Fig. 4, SEM photos of atrazine-imprinted polymer nano- and microparticles prepared by different polymerization methods are depicted.

Core/shell composite MIP particles can be prepared by grafting polymerization on support particles of selected size, shape and porosity. In particular, core/shell particles can be synthesized by grafting a thin MIP layer onto nonporous inorganic or organic supports. “Grafting” techniques are excellently suited for the synthesis of MIP composite materials with a tunable MIP shell (i.e., layer thickness

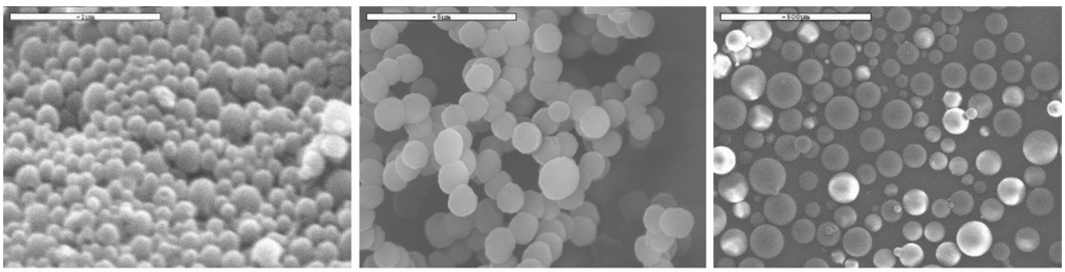

FIG. 4

Atrazine-imprinted polymer nano- and microparticles prepared by (A) miniemulsion, (B) precipitation, and (C) suspension polymerization.

and binding properties). Immobilized dithiocarbamate initiators and chain transfer agents (e.g., RAFT agents) have been employed for grafting polymerization of a MIP layer on nonporous core beads. By controlling the thickness of the grafted MIP layer, nanobeads with surface-accessible binding sites for specific target compounds, displaying negligible bleeding and favorable mass transfer characteristics, can be produced.

2.5 MOLECULARLY IMPRINTED MEMBRANES

Composite membranes are commonly used in advanced molecular separation processes, including reverse osmosis, nanofiltration, pervaporation, and membrane adsorption. Composite MIP membranes are made of an optimally chosen porous organic or inorganic support covalently coated with a highly selective MIP thin layer that provides the surface-accessible recognition sites for specific target molecules [7, 8].

For the synthesis of composite membranes one can follow two approaches (i.e., the sequential and the simultaneous one). In the sequential approach, we take advantage of the support membrane's pore structure (barrier pore size), its layer topology (symmetric vs. asymmetric membrane), and the location of the MIP film. The latter can be formed either on top of the base membrane ("asymmetric" membrane) or inside the base membrane ("symmetric" membrane). Note that based on the MIP film's thickness in the composite membrane, the MIP film can act either as a selective barrier and transport phase or as an affinity adsorption layer [7, 8].

For the synthesis of conventional MIP membranes by the simultaneous method, one can identify two alternative techniques, namely, the "traditional" in situ cross-linking polymerization and the "alternative" polymer solution-phase inversion method. In both cases, the most important imprinting parameter is the MIP membrane thickness that controls the membrane's stability and permeability. Moreover, the "synchronization" of imprinting and film solidification steps are of critical importance in controlling the shape, structure, and functionality of MIP membrane [7, 8].

In the in situ cross-linking polymerization, significant improvements in the mechanical stability and permeability of MIP membranes can be obtained with the addition of linear flexible oligomonomers (e.g., oligourethane acrylate) and high molecular weight linear polymers (e.g., polyethylene glycol, polyurethane, polymethylmethacrylate, polyvinyl alcohol, polystyrene, etc.), respectively. MIP membranes can be also synthesized by the polymer solution film casting and subsequent phase inversion technique (i.e., the main approach used for preparation of technical polymeric membranes). In the "-alternative" membrane synthesis, commonly used materials include cellulose acetate, polyamide, polyacrylonitrile and polysulfone. The formation of porous MIM from a compatible blend of a polymer matrix with a MIP could provide even more alternatives. The use of a "hybrid" approach of in situ polymerization and phase inversion has been also reported for the synthesis of MIM [7, 8]. In hybrid case, the polymerization of the functional monomers is carried out in the presence of the template molecule. Subsequently, the copolymer solution (e.g., P[AN-co-AA] or P[AN-co-MAA]) with the associated template is directly used for film casting and phase inversion leading to the formation of a porous MIP membrane.

Symmetric composite membranes can be prepared using a mixture of monomer and cross-linker (e.g., MAA/EGDMA) that is polymerized inside the porous support (e.g., glass filters or porous polypropylene membranes) to form a thin MIP layer. In this way, symmetric composite membranes with meso- and micro-pores coated by a thin MIP layer can be prepared [7, 8] (Fig. 5A).

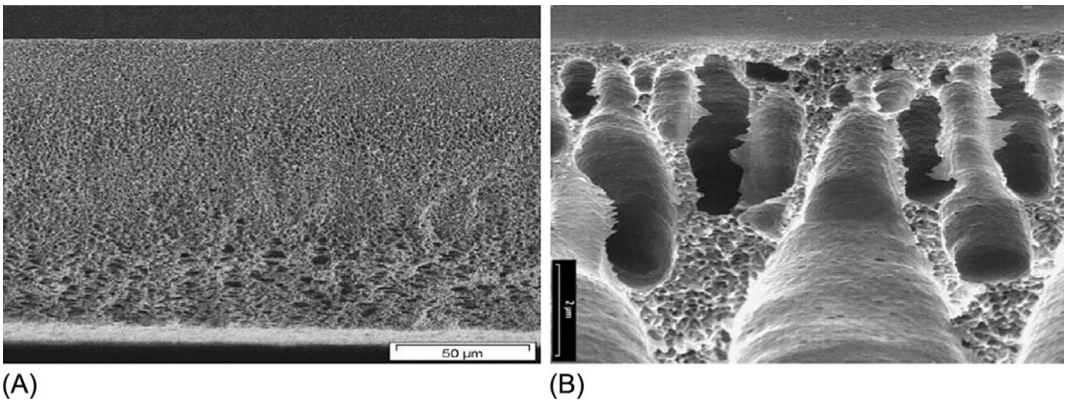

FIG. 5

(A) Symmetric macroporous membrane for microfiltration and adsorption applications and (B) asymmetric membrane for microfiltration and composite membrane applications.

Reproduced with permission from Ulbricht, M. (2004). Membrane separations using molecularly imprinted polymers. J. Chromatogr. B 804, 113.

Asymmetric composite membranes, consisting of a thin MIP film acting as a selective barrier and a base membrane of high permeability, can be also synthesized (Fig. 5B). The porous structure of the base membrane can be selected to control membrane permeability. Accordingly, composite membranes, consisting of a macroporous support covalently grafted to a top thin MIP layer, can be synthesized for high-performance adsorption MIMs. For example, in situ polymerization of the imprinting mixture (e.g., MAA/EGDMA and template molecule) on the top surface of a ceramic membrane (e.g., alumina) can be employed for the synthesis of composite asymmetric membranes. This approach offers several advantages derived from the temperature and morphological stability of ceramic support. Note that ceramic membranes are extremely stable, in the temperature range of 130 to 250°C, and nondeformable which results in a decrease of the degree of shrinking and swelling of MIP layer under separation conditions [7, 8].

Grafting of a MIP layer onto a polymeric support membrane (i.e., porous polypropylene [PP], polyvinylidene fluoride [PVDF], polyacrylonitrile) via free-radical polymerization can be effected via the functionalization of the substrate membrane with a photoinitiator. This is followed by the polymerization of the mixture of functional monomer and cross-linker in the presence of template molecule. In this case, the synthesized thin MIP film is covalently attached to the support membrane's top surface. As a result of MIP incorporation, the produced composite membranes exhibit superior performance and high specificity with respect to target molecules. Moreover, these novel thin-layer MIP-composite asymmetric membranes are characterized by a high permeability similar to that of conventional microfiltration membranes. Alternatively, grafting of a MIP layer to a substrate membrane can be achieved via controlled radical polymerization (CRP).

The use of colloidal crystals as templates for the synthesis of membranes with a well-controlled porous structure has been also described in the literature [9]. According to this approach, polymerization of the functional monomer with the cross-linker takes place in the interconnected nanochannels formed between the colloidal crystals. After the sacrificial removal of the colloids, a well-structured

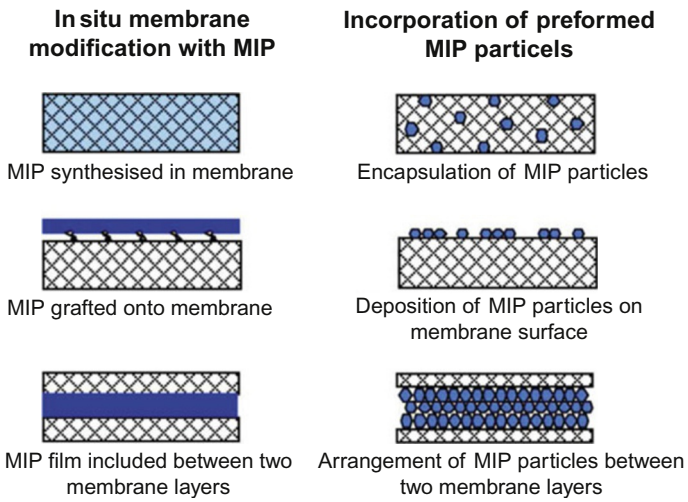

FIG. 6

Summary of composite imprinted membrane preparation methods.

Reproduced with permission from Biffis, A., Dvorakova, G., Cordin, A.F. (2011). Physical forms of MIPs. Topics in Current Chemistry. Berlin/Heidelberg: Springer-Verlag.

porous membrane is obtained. Functionalization of the colloidal crystals' surface with template molecules and subsequent polymerization and removal of the colloidal crystals results in the formation of a porous membrane containing a number of surface-exposed rebinding sites in the membranes pores. Finally, MIP micro- and nanoparticles can be incorporated within, on top, or between support layers for the preparation of composite membranes as illustrated in Fig. 6.

3 MOLECULARLY IMPRINTED MATERIALS FOR WATER TREATMENT

MIPs are a very promising class of functional materials, exhibiting high affinity to target compounds. MIPs additional advantages include: high physical robustness and strength, resistance to elevated temperatures, inertness toward organic solvents, acids or bases. As a result, MIPs can withstand follow-up processing steps related to the removal of the template molecule (via a chemical process) and its repeated use and regeneration as a highly selective adsorption material in wastewater treatment applications. This means that MIPs can be reused several times in water and wastewater separation processes. This MIP property is a key factor in the overall reduction of wastewater treatment costs.

Small and well-shaped molecularly imprinted polymer micro- and nanoparticles exhibit increased binding capacity due to their high specific surface area. Thus, MIP micro- and nanoparticles have been widely used as adsorbing materials for the removal of endogenous estrogens, sulfonates, pharmaceuticals, synthetic dyes, polycyclic aromatic hydrocarbons, cyanotoxins, phenolic compounds, and organophosphate pesticides from polluted water sources. In Table 1, recent applications of MIPs as adsorbing materials for water purification are presented.

Table 1 Molecularly Imprinted Micro- and Nanoparticles Used in Adsorption of Target Compounds From Water Sources

Target Analytes	Materials	Synthesis—Polymerization Method	Medium	Binding Conditions	Maximum Adsorption Capacity	Reference
Pharmaceutically active compounds						
Diclofenac (DFC)	2-VP/EGDMA/ toluene	Precipitation polymerization	Aqueous solutions	10 mg of polymers in 5.0 mL solutions of 300–1000 mg/L DFC	MIP: 324.8 mg/g NIP: 45.2 mg/g	[10]
Ibuprofen (IBP) Naproxen (NPX) Ketoprofen (KEP) Diclofenac (DFC) Clofibric acid (CA)	2-VP/EGDMA/ toluene	Precipitation polymerization	Lake water	2 mg of polymers in 30 mL acidic pharmaceuticals solutions of 10–200 mg/L	MIP: 208.7 mg/g (KEP), 204.6 mg/g (NPX), 241.2 mg/g (CA), 262.3 mg/g (DFC), 189.2 mg/g (IBP) NIP: 53.9 mg/g (KEP), 69.7 mg/g (NPX), 70.2 mg/g (CA), 74.3 mg/g (DFC), 68.1 mg/g (IBP)	[11]
Carbamazepine (CBZ) Clofibric acid (CA)	2-VP/EGDMA/ toluene	Precipitation polymerization	Tap water, lake water, river water	1 mg of polymers in 3.0 mL CBZ and CA solutions of 5–100 mg/L	MIP: 156.7 mg/g (CBZ), 172.9 mg/g (CA) NIP: 72.4 mg/g (CBZ), 74.5 mg/g (CA)	[12]
Tetracyclin (TC)	MAA/ EGDMA/mixture of methanol and acetonitrile	Precipitation polymerization	Aqueous solutions	30 mg of polymers in 3.5 mL TC solution (1–100 mM)	MIP: 8.77 μmol/g NIP: 0.17 μmol/g	[13]

Continued

Table 1 Molecularly Imprinted Micro- and Nanoparticles Used in Adsorption of Target Compounds From Water Sources—cont'd

Target Analytes	Materials	Synthesis—Polymerization Method	Medium	Binding Conditions	Maximum Adsorption Capacity	Reference
Phenolic compounds and phenoxy herbicides						
2,4-Dichlorophenol (2,4-DCP)	Oleic acid/ divinylbenzene/ acetonitrile	Reverse microemulsion polymerization	Aqueous solutions	1 g of polymers in 100 mL of 100 mg/L 2,4-DCP	MIP: 183.8 mg/g NIP: not reported	[14]
2,4-Dichlorophenoxyacetic acid (2,4-D)	4VP/EGDMA/hydrophilic poly (*N*-isopropylacrylamide) (PNIPAAm) and PEG chain-transfer agents (macro-CTAs)	RAFT precipitation polymerization	Aqueous solutions	Polymer concentration 16 mg/mL, 2,4-D 0.08 mM	MIP (grafted with PNIPAAm): 3.94 μmol/g NIP (grafted with PNIPAAm): 2.69 μmol/g MIP (grafted with PEG): 4.33 μmol/g NIP (grafted with PEG); 3.45 μmol/g	[15]
Bisphenol A (BPA) 3, 3′, 5, 5′-Tetrabromobis-phenol A (TBBPA) Phenol and phenol red (PSP)	Diethylenetriaminepentaacetic acid (DTPA)/ teraethyl orthosilicate (TEOS)	Surface molecular imprinting technique with a sol-gel method	Aqueous solutions	0.015 g of polymers in 30 ml of 1–50 μmol/L single, binary or triple solute solution	MIP: 21.04–31.09 μmol/g (BPA) NIP: 7.05–10.01 μmol/g (BPA)	[16, 17]
Bisphenol A (BPA) Bisphenol F (BPF) 4-Nitrophenol (4-NP) 3-Methyl-4-nitrophenol (MeNOPL) 2,4-Dichlorophenol (DCPL) 2,4,5-Trichlorophenol (TCPL) 2,4-Dichlorophenoxyacetic acid (2,4-D) 2,4,5-Trichlorophenoxyacetic acid (2,4,5-T)	4VP/EGDMA/TRIM/ toluene	Precipitation polymerization	Aqueous solutions	10 mg of polymers in 1 mL single solute solutions of 5–200 mg/L	MIP: 3.81 mg/g (BPA), 4.31 mg/g (BPF), 2.18 mg/g (NOPL), 2.87 mg/g (MeNOPL), 3.37 mg/g (DCPL), 4.9 mg/g (TCPL), 4.87 mg/g (2,4-D), 4.15 mg/g (2,4,5-T) NIP: 3.36 mg/g (BPA), 2.76 mg/g (BPF), 1.36 mg/g (NOPL), 1.93 mg/g (MeNOPL), 2.71 mg/g (DCPL), 2.94 mg/g (TCPL), 2.38 mg/g (2,4-D), 2.06 mg/g (2,4,5-T)	[9]
2,4-Dinitrophenol (2,4-DNP)	Acrylamide (AAm)/ glycidilmethacrylate (GMA)/ TRIM/ acetonitrile	Precipitation polymerization	Surface water, wastewater	5 mg of polymers in 5 mL solution of 20–300 mg/L (DNP)	MIP: 138.9 mg/g NIP: 41.5 mg/g	[18]

Polycyclic aromatic hydrocarbons						
Benzo[a]anthracene (B[a]A) Benzo[a]pyrene (B[a]P) Benzo[b]fluoranthene (B[b]F) Chrysene (Chr) Dibenzo[a,h]pyrene (D[a]P) Indeno[1,2,3-c]pyrene (I[2]P)	MAA/TRIM/acetonitrile	Precipitation polymerization	Aqueous solutions	Preweighted polymers (around 10 mg) in 1 mL of mixed compound solution 1.08 mg/mL	MIP: 687 mg/g NIP: 119 mg/g	[19]
Cyanotoxins						
Microcystin-LR (MC-LR) Microcystin-RR (MC-RR) Nodularin (nod)	IA or MAA/EGDMA/ dichloromethane	Bulk polymerization	Surface water	10 mg of polymers in 1 mL of 45 mg/L MC-LR	MIP: 2.76–3.64 mg/g NIP: 0.14–0.17 mg/g	[20]
Dyestuff						
Basic and reactive dyes Red reactive dye Basic red dye	Red reactive dye/AAm /MBA/ water Basic red dye/MAA/EGDMA/ DMF	Bulk polymerization	Aqueous solutions	0.5 g of polymers in 50 mL of dye solutions 10–200 mg/L	MIP: 12 mg/g NIP: 0.55 mg/g	[21]
Direct red 23	Aam/EGDMA/DMSO	Bulk polymerization	Decolorization of textile wastewater	10 mg of polymers in 1 mL of dye solution (10–200 µmol/mL)	MIP (low affinity): 4.915 µmol/g MIP (high affinity): 19.48 µmol/g NIP: not reported	[22]
Estrogens						
α-Estradiol (template) Estriol Estrone Diethylstilbestrol Dihydrofolliculin (β-estradiol)	Aam/TRIM/ACN	Precipitation polymerization	Aqueous solutions	MIPs (∼1 mg/mL) in 0.1 mL of water mixed with 0.9 mL of 0.1 mM estrogenic compound solution	MIP: 380 nmol/mg NIP: 11 nmol/mg	[23]
17β-Estradiol (E2)	MAA/EDGMA/TRIM/ acetone/ acetonitrile	Precipitation polymerization	Aqueous solutions	0.5–20 mg of polymers in 1 mL of 0.1–1.0 mg/L E2	MIP: 15 mg/g NIP: not reported	[24]

Continued

Table 1 Molecularly Imprinted Micro- and Nanoparticles Used in Adsorption of Target Compounds From Water Sources—cont'd

Target Analytes	Materials	Synthesis—Polymerization Method	Medium	Binding Conditions	Maximum Adsorption Capacity	Reference
17β-Estradiol (E2)	Chitosan/epichlorohydrin (ECH)/Aam/*N*,*N*′-methylene bisacrylamide	Graft copolymerization into porous cross-linked chitosan beads	Aqueous solutions	1 g of polymers in 15 mL of 0.03–0.3 mg/mL E2	MIP: 5.01 mg/g NIP: not reported	[25]
Organophosphates						
Chlorpyrifos (CPF) (template) Monocrotophos (MCP)	Styrene/ EDMA/α-MAA	Emulsifier-free polymerization	Aqueous solutions	1 g of polymers in 100 mL of 100 mg/L CPF	MIP: 8.95 mg/g (CP), 1.36 mg/g (MCP) NIP: not reported	[26]
Stimulants-hormones						
Nicotine (NIC) Epinephrine (EPI) Physostigmine (PHY)	IA/EGDMA/ dichloromethane	Bulk polymerization	Aqueous solutions	10 mg of polymers in 10 mL of 1–10 μg/L mix solute solution	MIP: 11.32 mg/g (at equilibrium)	[27]
Surfactants						
Perfluorooctane sulfonate (PFOS)	Chitosan-based MIP prepared by cross-linking with epichlorohydrin (ECH)	Graft copolymerization into porous cross-linked chitosan beads	Aqueous solutions	0.01 g of polymers in 100 mL of 20–550 mg/L PFOS	MIP: 560 mmol/g NIP: 258 mmol/g	[28]

MIPs have been also used for the removal of metal ions, including Cd(II) [29–33], As(V) [34,34a], Ag(II) [35], Pb(II)-IIP [36], Zn(II) [37], Zr(IV) [38], multi-templated Pb-Zn-Hg [39], Hg(II) [40], Li [41], and other heavy metals [42–44] from environmental samples and wastewaters.

Moreover, the incorporation of MIP micro- and nanoparticles in composite membranes has opened new opportunities in the development of continuous separation systems. In a new promising development, a sandwich-type membrane was prepared by placing the MIP nanoparticles between two microfiltration membranes [45, 46].

In another application, nanofiber-based membranes containing MIP nanoparticles were prepared for the effective separation of environmentally hazardous pollutants from water sources. Nanofibers are a new class of materials that can find application in industrial filtration and water purification, due to their unique properties, including their size and high surface area. Composite filtration membranes made of PET nanofibers and embedded MIP nanoparticles have been successfully prepared using an electrospinning method (Fig. 7). Initially, the MIP nanoparticles are suspended in a solvent.

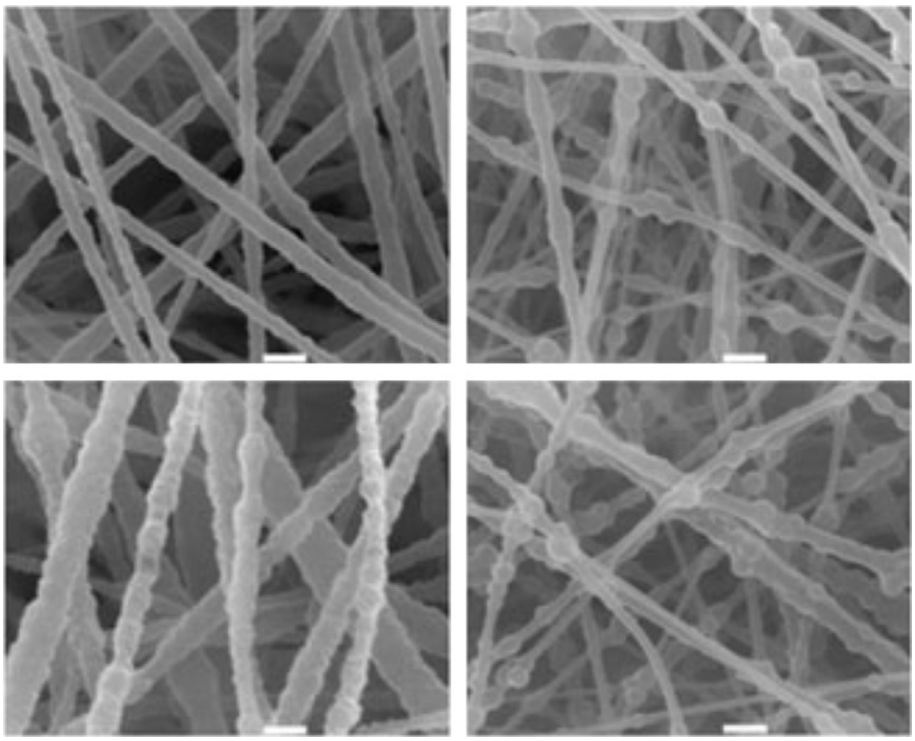

FIG. 7

PET nanofibers prepared by electrospinning loaded with different amounts of MIP nanoparticles.

Reproduced with permission from Yoshimatsu, K., Ye, L., Lindberg, J., Chronakis, I.S. (2008). Selective molecular adsorption using electrospun nanofiber affinity membranes. Biosens. Bioelectron 23, 1208–1215.

Subsequently, the polymer (e.g., PET) is added to the suspension which is then fed to the electrospinning equipment for production of the composite membrane. In one application study, a nanofibers-MIP nanoparticles composite membrane was used for the removal of drug traces from tap water before drug analytical quantification [47].

Cryogels are another novel class of polymeric materials that can be used in water filtration applications. Cryogels have several operational advantages including presence of large pores (i.e., short diffusion path). As a result, they exhibit a low operational pressure drop and short residence times. However, because of the presence of large pores, their adsorption capacity is relatively low. The use of super macroporous cryogels embedded with MIP micro- or/and nanoparticles could largely improve the binding capacity of cryogels [48–50].

In Table 2, relevant applications of molecularly imprinted membranes produced by conventional phase inversion, surface functionalization, MIP grafting, as well as by incorporation of MIP micro- and nanoparticles into a polymer matrix are reviewed.

Molecularly imprinted polymers have been also combined with other nanoparticles including magnetic particles and quantum dots [72–79, 79a]. These advanced composite nanomaterials combine the high selectivity of MIPs with the specific properties of embedded nanoparticles. Thus, the composite

Table 2 Molecularly Imprinted Membranes Applied in Filtration Systems

Target Analytes	Membrane Preparation Method	Medium	Analyte Concentration Range	Reference
Pharmaceutically active compounds				
Theophylline	MIP nanoparticles encapsulated into poly(ethylene terephthalate) nanofibers with the electrospinning method	Organic solutions	Adsorption at mg/mL level	[51]
Propranolol	MIP nanoparticles encapsulated into poly(ethylene terephthalate) nanofibers with the electrospinning method	Tap water	Adsoprtion at ng/mL level	[47]
Levodropopizine	Composite membranes via surface imprinting using PVDF as support membrane	Organic solutions	Filtration at mM level	[52]
Propranolol	MIP composite cryogel synthesized by glutaraldehyde cross-linking reaction of poly(vinyl alcohol) (PVA) in the presence of amino-modified molecularly imprinted core-shell nanoparticles	Aqueous solutions	Adsorption at mM level	[49]
Metoprolol, diclofenac, vancomycin	MIP nanoparticles applied in polyvinylidene fluoride membranes	Aqueous solutions	Adsorption at µg/L level	[53]

Table 2 Molecularly Imprinted Membranes Applied in Filtration Systems—cont'd

Target Analytes	Membrane Preparation Method	Medium	Analyte Concentration Range	Reference
Pesticides				
2,4-Dichlorophenoxyacetic acid	In situ synthesis of MIP thin film on a microporous support	Aqueous solutions	Ion transport at mM-M level	[54]
Desmetryn, atrazine	Sandwich-type composite membranes consisted of a middle packed layer of MIP nanoparticles confined between two microfiltration membranes and MIP thin films via an in situ polymerization method on the top surface of ceramic support membranes	Aqueous solutions	Filtration at μg/L level	[45, 46]
Atrazine, desisopropyl, atraton, carboxin, linuron and chlorpyrifos	Polystyrene-based molecularly imprinted polymer nanofibers synthesized through the electrospinning technique	River water	Adsorption at μg/mL level	[55]
Desethylatrazine (DEA), desisopropylatrazine (DIA), simazine(SIM), cyanazine (CYA), atrazine (ATR), propazine (PPZ) and ter-butylazine (TER)	MIP-coated hollow fiber polypropylene membrane	Tap and river water	Adsorption at μg/l level	[56]
Phenolic compounds				
4-Nonylphenol	MIP composite cryogel synthesized by glutaraldehyde cross-linking reaction of poly(vinyl alcohol) (PVA) in the presence of MIP particles	Aqueous solutions	Filtration at μg/L level	[57]
Bisphenol A	Phase inversion using polysulfone and sulfonated polysulfone	Aqueous solutions	Filtration at mM level	[58]
Bisphenol A	Embedded MIP particles in polyethersulfone hollow-fiber membrane using dry-wet spinning technique	Aqueous solutions	Filtration at μg/L level	[59]
Chlorogenic acid	UV irradiation polymerization method, using 4-vinylpyridine and *N*,*N*-ethylenebisacrylamide with poly(vinylidene fluoride) membrane as a support	Organic solutions	Filtration at mM level	[60]

Continued

Table 2 Molecularly Imprinted Membranes Applied in Filtration Systems—cont'd

Target Analytes	Membrane Preparation Method	Medium	Analyte Concentration Range	Reference
Bisphenol A	Molecularly imprinted supported membranes by supercritical CO_2-assisted phase-inversion method	Aqueous solutions	Filtration at μM-mM level	[61]
Phenol, 4-methylphenol (4MP), 4-propylphenol (4PP), and 2,4-dimethylphenol (2,4 DP)	MIPs fabricated on glass slides with a "sandwich" technique	Aqueous solutions	Adsorption at mg/L level	[62]
Estrogens				
17α-Estradiol	MIP nanoparticles encapsulated into poly(ethylene terephthalate) nanofibers with the electrospinning method	Organic solutions	Adsorption at mg/mL level	[49]
17β-Estradiol	MIPs embedded into various PVA based macroporous gels	Aqueous solutions	Filtration at μg/L level	[63]
17β-Estradiol	MIP particles embedded in poly(hydroxyethyl methacrylate) (PHEMA) cryogel	Aqueous solutions	Filtration at μg/L-mg/L level	[48]
Organophosphates				
Dimethoate	Phase inversion using polyacrylonitrile functionalized with methacrylic acid and acrylamide	Aqueous solutions	Adsorption at 10^{-5} mol/L level	[64]
Inorganic ions				
Bromate	MIP adsorbents using chitosan cross-linked with epichlorohydrin (ECH) incorporated into a cryogel	Aqueous solutions	Adsorption at μg/L level	[46]
Ni(II) ion	Ion imprinted membrane with a porous polyvinylidene fluoride (PVDF) support	Aqueous solutions	Filtration at mg/L level	[65]
Arsenite and arsenate	Cysteine@ZnS:TiO_2 nanoparticle modified molecularly imprinted biofouling-resistant filtration membrane using carboxymethyl cellulose and polyvinyl alcohol	Aqueous solutions	Filtration at μg/L-mg/L level	[66]
Molybdate anion	Surface-grafted imprinted ceramic membrane	Aqueous solutions	Filtration at mM level	[67]

Table 2 Molecularly Imprinted Membranes Applied in Filtration Systems—cont'd

Target Analytes	Membrane Preparation Method	Medium	Analyte Concentration Range	Reference
Other				
Diosgenin (phytosteroid sapogenin)	Phase inversion using acrylonitrile and acrylic acid	Organic solvents for template extraction	Only synthesis protocol available	[68]
4,4′-Methylenedianiline (MDA) (polyurethane precursor)	Phase inversion using acrylonitrile and acrylic acid	Organic solutions	Filtration at mg/L level	[69]
4,4′-Methylenedianiline (MDA) (polyurethane precursor)	Phase inversion applying the dry-wet process using acrylonitrile, acrylic acid, methacrylic acid and itaconic acid as monomers	Organic solutions	Filtration at mg/L level	[70]
4,4′-Methylenedianiline (MDA) (polyurethane precursor)	Phase inversion by dispersing the MIPs in a polyvinylidene fluoride matrix	Organic solutions	Adsorption at mg/L level	[71]

nanomaterials can have high selectivity, high affinity, and rapid kinetics regarding the association/dissociation of the target analyte. MIP composite nanomaterials have received considerable attention because of the highly specific binding properties of the MIPs (Table 3). Several methods have been applied for the synthesis of MIP composite nanomaterials, including free radical polymerization (FRP), reversible addition fragmentation chain transfer (RAFT), atom transfer radical polymerization and the sol-gel methods [103, 104].

Carbon nanotubes (CNTs), multiwalled carbon nanotubes (MCNTs), gold and silver nanoparticles, titanium oxide, and silica-based nanoparticles are typical nanostructured materials that have been used in the synthesis of composite MIPs [92, 93, 95, 103, 105–108]. These nanostructured materials can be combined with MIPs in core-shell structures. These composite nanoparticles offer numerous advantages, including better control of the thickness and morphology of the thin MIP shell that largely facilitate the efficient removal of template molecules. It should be noted that the synthesized composite core-shell nanoparticles are multifunctional, have good dispersibility and fast binding kinetics due to their high specific surface area. These composite nanostructured materials have found application in water treatment [103, 104].

In a recent study, a MIP layer was anchored, via molecular imprinting, onto CNTs. The synthesized nanostructured composite material was then used for adsorption and subsequent determination of trace triclosan (TCS) in water samples [80]. In another case, core-shell MIP composite nanoparticles were synthesized using mesoporous carbon nanoparticles (MCNs) for adsorption of fluoroquinolone antibiotics (FQs) in aqueous solutions. The synthesized composite MIP nanoparticles exhibited a fast adsorption rate and good selectivity to ofloxacin. The composite nanoparticles were reused several times for removal of ofloxacin without any significant loss of their adsorption capacity and specificity [81].

Table 3 Application of MIP-Based Composites in Wastewater Treatment

Target Analytes	Materials	Application/Medium	Reference
Pharmaceutically active compounds			
Triclosan	MIPs/carbon nanotubes	Determination in aqueous samples	[80]
Fluoroquinolone antibiotics	MIPs/carbon nanoparticles	Separation from aqueous samples	[81]
Fluoroquinolone antibiotics	MIPs/Fe_3O_4	Determination in environmental aqueous samples	[82]
Sulfadiazine (SD), sulfamonomethoxine (SMM), sulfamethoxydiazine (SMD), sulfaquinoxaline (SQ)	MIPs/Fe_3O_4	Determination in aqueous samples	[83]
Sulfadiazine (SDZ), sulfadimethoxine (SDM), sulfamethoxazole (SMX), sulfamerazine (SMR)	MIPs/Fe_3O_4/SiO_2	Detection in aqueous samples	[84]
Phenolic compounds			
Bisphenol A (BPA)	MIPs/Fe_3O_4	Determination in environmental aqueous samples	[85]
Bisphenol A (BPA)	MIPs/kaolinite/Fe_3O_4	Separation from aqueous samples	[86]
2,4,6-Trichlorophenol	MIPs/halloysite nanotubes	Determination in environmental aqueous samples	[77]
4-Nitrophenol (4-NP)	MIPs/Fe_3O_4	Selective adsorption/photocatalysis from wastewaters	[87]
Bisphenol A (BPA)	MIPs/Au nanoparticles	Environmental aqueous samples	[88]
Bisphenol A (BPA)	MIPs/Fe_3O_4	Separation from aqueous samples	[89]
4-Nitrophenol	MIPs/Fe_3O_4	Determination in aqueous samples	[76]
Phenol	MIPs/Fe_3O_4/SiO_2	Detection in wastewaters	[90]
Benzoic acid (BA), 4-hydroxybenzoic acid (4-HBA), salicylic acid (SA), protocatechuic acid (PCA), and gallic acid (GA)	MIPs/Fe_3O_4/SiO_2	Determination in aqueous samples	[78]
2,4,6-Trinitrotoluene	MIPs/Fe_3O_4	Determination in aqueous samples	[79a]
Bisphenol A (BPA)	MIPs/Fe_3O_4/SiO_2	Enrichment and determination of synthetic estrogens in aqueous samples	[91]

Table 3 Application of MIP-Based Composites in Wastewater Treatment—cont'd

Target Analytes	Materials	Application/Medium	Reference
Estrogenic compounds			
Estrone (E1)	MIPs/carbon nanotubes	Separation from aqueous samples	[92]
Estrone (E1), 17β-estradiol (E2), estriol (E3), nonylphenol (NP), and bisphenol A (BPA) and also atrazine, sulfamethoxazole, ibuprofen and ofloxacin	MIPs/TiO_2 nanotubes	Separation from secondary effluents	[93]
17β-Estradiol (E2), estriol (E3), bisphenol A (BPA), E2 and ethynylestradiol (EE)	MIPs/Fe_3O_4	Determination in aqueous samples	[94]
Estrone (E1), 17β-estradiol (E2), diethylstilbestrol (DES)	MIPs/Fe_3O_4	Separation from aqueous samples	[89]
Diethylstilbestrol (DES) Hexestrol Dienestrol	MIPs/Fe_3O_4/SiO_2	Enrichment and determination of synthetic estrogens in aqueous samples	[91]
Pesticides			
2,4-Dichlorophenoxy acetic acid (2.4 D)	MIPs/mutiwalled carbon natubes	Determination in environmental aqueous samples	[95]
2,4-Dichlorophenoxy acetic acid (2,4 D)	MIPs/Fe_3O_4	Ultrafast enrichment and separation from aqueous samples	[96]
Atrazine Simazine Propazin Simetryn Prometryne Ametryn Terbutryn	MIPs/PEG/ Fe_3O_4	Extraction from aqueous samples	[97]
Dyestuff			
Water-soluble acid dyes	MIPs/Fe_3O_4	Separation from aqueous samples	[98]
Inorganic/ions			
Cobalt	MIPs/Fe_3O_4/TiO_2/SiO_2	Determination in biological and environmental aqueous samples	[99]
Uranium	MIPs/γ-MPS)/ Fe_3O_4 (γ-methacryloxypropyl trimethoxysilane)	Separation from environmental aqueous samples	[100]
Lead	MIP/Fe_3O_4/SiO_2	Separation from environmental aqueous samples	[101]
Copper	MIP/Fe_3O_4/SiO_2	Separation from environmental aqueous samples	[102]

Magnetic particles (Fe_3O_4) have been extensively used in separation, catalytic, and biological/environmental remediation processes. Fe_3O_4 has a low toxicity and low cost. Thus, Fe_3O_4 particles have been used in the synthesis of composite MIP materials that can selectively adsorb target pollutants from environmental samples. Subsequent recovery of the adsorbed species is efficiently effected via the isolation of the composite particles with the aid of an externally applied magnetic field.

Guo et al. [86] successfully synthesized magnetic MIPs based on Fe_3O_4/kaolinite composites for the selective removal of Bisphenol A from aqueous solutions. Note that kaolinite is a kind of clay that is widely available, has low cost, and it is easily processable. Silica has been used for the encapsulation of Fe_3O_4 microparticles. This prevents the oxidization and aggregation of Fe_3O_4 and also improves the MIP film formation due to the presence of silica surface functional groups [78, 79a, 90, 94] (Fig. 8). Note that the presence of a silica layer around the magnetic Fe_3O_4 nanoparticles largely enables the anchoring of a RAFT agent and the subsequent formation of a MIP shell. These composite MIPs can exhibit not only outstanding magnetic properties but also high adsorption capacity and selectivity toward synthetic estrogens [91].

Composite core-shell MIP materials that are sensitive to both photonic and magnetic stimuli have been prepared using silica functionalized superparamagnetic Fe_3O_4 as core nanoparticles and a MIP shell. For the synthesis of the MIP layer, 4-[(4-methacryloyloxy)phenylazo] benzene sulfonic acid as a water-soluble functional monomer and sulfadiazine as template molecule, were used. The composite MIP material was used as a sensor element for the detection of four sulfonamides in aqueous media [84]. Khoddami and Shemirani [99] described the synthesis of magnetic ion-imprinted particles based on composite magnetic Fe_3O_4/silica nanoparticles functionalized with amino groups for the imprinting of cobalt ions, via a combined surface imprinting and a sol-gel process.

Quantum dots (QDs) have attracted wide interest as sensing elements (e.g., organic and inorganic pollutants) due to their high photostability, photoluminescence efficiency, size-dependent emission

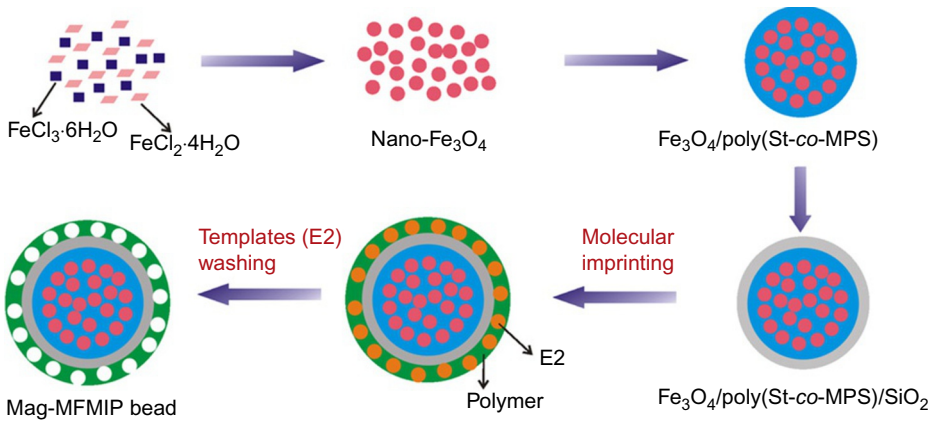

FIG. 8

A schematic diagram showing fabrication procedure of magnetic multifunctional MIP beads.

Reproduced with permission from Lin, Z., He, Q., Wang, L., Wang, X., Dong, Q., Huang, C. (2013). Preparation of magnetic multi-functional molecularly imprinted polymer beads for determining environmental estrogens in water samples. J. Hazard. Mater. 252–253, 57–63.

wavelength, and sharp emission profile [109, 110]. However, QDs are nonselective and induce similar fluorescence responses to structural analogs. In particular, their limited selectivity results in a high level of background fluorescence. This limits their detection sensitivity towards a specific target analyte and is a major drawback to the application of QDs in real samples. It should be pointed out that the binding characteristics of MIPs combined with the fluorescent characteristics of QDs can lead to the development of novel sensors for environmental applications [103, 104].

QDs-MIP composites have been widely used as sensing elements for the recognition and measurement of pollutants by means of chemiluminescence, fluorescence, phosphorescence, and other responses. In an application [111], a MIP layer was successfully formed at the surface of Mn-doped Zns QDs. The QDs-MIP composite sensing element was then used for the detection of phenolic compounds in water by chemiluminescence. In another application [112], composite QDs-MIP nanospheres were synthesized for selective adsorption and quantification of pesticides (e.g., diazinon) by fluorescence. The composite nanospheres exhibited high selectivity and fast binding kinetics in water. Composite MIPs with Mn-doped ZnS QDs have been successfully synthesized and used for detection of chlorophenol compounds in water by the room temperature phosphorescence (RTP) technique. The phosphorescence properties of Mn-doped ZnS QDs, combined with the selective binding properties of MIPs led to a superior opto-sensing element successfully used for selective detection and measurement of target analytes without the need of additional inducers or derivatization [103, 104].

More recently, novel composite MIPs based on CdTe/CdS QDs, magnetic Fe_3O_4, and graphene oxide were synthesized for the selective adsorption of phenolic compounds (e.g., *p-t*-octylphenol, OP). In particular, graphene oxide was used to improve the sensing and adsorption properties of the composite MIP material. The magnetic component (i.e., Fe_3O_4) of composite MIPs enabled their isolation and recovery after adsorption of the phenolic compounds. On the other hand, monitoring of the target compound was effected by the CdTe/CdS QDs. The synthesized composite MIPs exhibited superior selectivity toward the target analyte and, thus, accurate detection of *p-t*-octylphenol in aqueous samples [73].

4 MOLECULAR IMPRINTING FOR CATALYTIC DEGRADATION OF POLLUTANTS

To date, significant efforts have been directed to MIPs application in composite catalytic systems [93, 114–117]. The distinct advantages of MIPs (e.g., tolerance to high temperature and pressure, extreme pH values and organic solvents) have made the development of new MIP-based catalysts a very attractive research and application area. MIP-based catalysts that mimic the activity and specificity of an enzyme have been generally utilized in several reactions and substrates. This means that MIPs can be used as synthetic catalytic antibodies for the development of custom-made catalysts for specific substrates. A great number of studies on the application of MIPs as enzyme-like mimetic catalysts for organic compounds have been published [103]. In particular, MIP catalysts were successfully synthesized for the hydrolysis of ester bonds using p-nitrophenyl phosphate as the transition state analog [118]. In this study, the effects of pH and contact time on the catalytic activity of MIPs were investigated. The results clearly showed that the presence of MIP-based catalysts significantly enhanced the hydrolysis (a 60-fold increase) of the ester bond.

The MIP composite catalysts can be prepared by two approaches. According to the first approach, selected catalytic groups (e.g., metal ions) are incorporated into the active binding sites following a certain orientation that enhances the catalytic efficiency of specific substrates. The second approach is based on the immobilization of metal or metal catalytic complexes in the polymer matrix. Titania (TiO_2), a commonly used photocatalyst, has been extensively studied for environmental applications. However, TiO_2 is a nonselective catalyst, and thus, cannot act as a catalyst for specific pollutants, particularly in complicated environmental samples where other pollutants are present too. In order to improve its selectivity, MIP-coated TiO_2-based photocatalysts have been synthesized for the degradation of specific pollutants (e.g., nitrophenols, among others) [119]. The synthesized MIP-coated TiO_2-based photocatalysts showed great selectivity for the target compounds and improved photodegradation ability as compared to the conventional TiO_2 catalysts [103]. Note that in comparison to commonly proposed approaches (e.g., control of the surface electric charge by adjusting pH [120] and production of a double-region structured TiO_2 catalysts [121, 122]) to enhance the selectivity of a photocatalyst, MIP composite catalysts are more efficient and have a higher selectivity [104]. Thus, several research groups are presently addressing their research efforts to the development of novel MIP composite photocatalysts, see Table 4.

Table 4 MIP-Based Composite Catalysts for the Selective Degradation of Target Pollutants

Template	Materials	Preparation Method	Application	Reference
2-Methyl-1,4-naphthoquinone (2MNQ)	Thiolated β-cyclodextrin (TCD)	Spin-coating an organometallic precursor on silicon wafers	Selective Photocatalysis	[123]
Chlorophenols (2CP or 4CP)	*O*-Phenylenediamine (OPDA) as a precursor and TiO_2 nanoparticles	Coating titania with a thin layer of molecular imprinted polymer by surface modification and in situ polymerization	Selective photocatalysis	[124]
Nitrophenols (2-NP or 4-NP)	*O*-Phenylenediamine (OPDA) and TiO_2 particles	Coating titania with a thin layer of molecular imprinted polymer by surface modification	Enhanced photocatalytic degradation and selective removal	[125]
Salicylic acid (SA)	TiO_2 thin films	Liquid phase deposition	Selective photocatalysis	[126]
Anthracene-9-carboxylic acid (9-AnCOOH)	TiO_2 nanotube arrays modified with molecularly imprinted TiO_2 thin film	Construction of an imprinted film layer onto the surface of a TiO_2 NT array using a sol-gel method	Adsorption and photocatalytic degradation	[127]
Chlorophenols	Molecularly imprinted polymers containing a photosensitizer, rose bengal (RB)	Precipitation polymerization and subsequent incubation in RB	Selective photooxidation	[128]
Methylene blue	Surface modification of TiO_2	Hydration-dehydration process and free radical polymerization using silane-coupling reaction	Selective photodegradation	[129]

Table 4 MIP-Based Composite Catalysts for the Selective Degradation of Target Pollutants—cont'd

Template	Materials	Preparation Method	Application	Reference
4-Nitrophenol (4-NP)	Fe_3O_4/SiO_2 core-shell nanoparticles	Co-precipitation method following surface treatment of magnetic nanoparticles by Stober method and surface imprinting	Selective photocatalysis	[87]
o-, *m*-, or *p*-Nitrobenzyl alcohol (NBA)	Fe(III) catalysts	Polymerization of acrylamide and ethylene dimethacrylate in the presence of the template and a $FeCl_3$ complex	Selective oxidation	[117]
Rhodamine B (RhB)	Polypyrrole/titanium dioxide nanocomposites	Surface molecular imprinting technique	Selective photocatalytic degradation under visible light irradiation	[130]
Estrone	TiO_2 hybridized magnetic Fe_3O_4 nanoparticles	Fe_3O_4 microspheres synthesized by solvothermal method and modified with 3-isocyanatopropyltriethoxysilane (IPTS)	Selective photocatalytic degradation and removal	[108]
p-Nitrophenol	Molecularly imprinted Fe_3O_4/SiO_2 core-shell magnetic composites	Anchoring imprinted polymers on the surface of amino-modified Fe_3O_4/SiO_2 core-shell particles	Preferential catalytic ozonation	[131]
Salicylic acid (SA)	Polycondensation system composed of ammonium hexafluorotitanate and ammonium silicofluoride	Preparation of a thin catalyst layer containing MIPs covered on sheet glasses	Selective photocatalysis	[132]
Rhodamine B (RhB)	Molecular imprinted polymers coated Co-doped TiO_2 nanocomposites (MIP/Co-TiO_2)	Surface molecular imprinting technique	Enhanced photocatalytic activity and selectivity under visible light irradiation	[133]

5 MOLECULAR IMPRINTING FOR THE ANALYSIS OF ENVIRONMENTAL SAMPLES

For the detection of persistent organic compounds in water sources, several analytical methods including High Performance Liquid Chromatography (HPLC), Mass Spectrometry (MS), Gas Chromatography (GC), HPLC/MS, GC/MS, etc. can be employed. However, these methods are nonselective and usually require suitable sample preparation, a complicated and time-consuming analysis step. Despite recent improvements in sensitivity and specificity of new analytical equipment, most analytical

instruments cannot handle directly complex biological, food, and environmental samples. Traditionally, analytical methods involve several sequential steps that include sample collection and preparation, analyte detection, and data analysis. Note that more than 80% of the total analysis time is spent for sample collection and preparation (e.g., analyte extraction, concentration, fractionation and isolation). Moreover, the type of selected sample preparation method greatly influences the accuracy and reliability of the analysis protocol. Off-line and on-line sample methods generally involve a solid-phase extraction (SPE) analysis step. However, the major disadvantage of conventional SPE is the use of packing materials (i.e., C18, size-exclusion, and ion-exchange phases) which have a low selectivity toward the target analyte. This results in the co-extraction of other structural analogs that limits the accuracy of the analytical determination. Hence, additional cleanup of the sample is usually needed before its final chromatographic analysis. To solve this problem the development of SPE packing materials with a high selectivity toward the target analyte is highly desirable. Such selective SPE materials are the immunosorbents (ISs), based on highly selective and reversible analyte-antibody interactions. These biological antibodies are both difficult to obtain and expensive and are characterized by low stability. This has led researchers to the synthesis of antibody mimics for selective extraction of target substances. MIPs is a class of functional materials that can be potentially used as antibody mimics in off-line and on-line chromatographic methods (Table 5). The use of MIPs can minimize the sample loss during preparation, increase the recovery of target analyte, and improve the reproducibility of the results due to the specific adsorption of the target analyte.

6 MIP-BASED SENSOR APPLICATIONS FOR ENVIRONMENTAL MONITORING

Today, billions of euros are annually spent for environmental monitoring and detection of various potentially harmful chemical/biological pollutants in food and water supplies for public safety and health protection. Because the relevant lab analyses are usually cumbersome and time-consuming and rely on very expensive analytical equipment, there is a pressing societal need for the development of inexpensive but highly sensitive microsensors for the detection of harmful analytes in solution and in atmosphere. Although considerable progress has been made in the development of conventional chemical/biological microsensors for environmental monitoring, there is a limited number of successful commercial products due to present limitations in detection sensitivity, selectivity, accuracy, reliability, shelf-life, operational stability, and cost.

Thus, there is a high scientific and technological incentive for the development of novel highly sensitive, robust, and cost-effective sensing devices for the detection of PhACs, EDRs, and biotoxins in water sources. In response to this challenge, molecular imprinting and new sensor fabrication technologies have been successfully applied for the construction of sensing microdevices for water-quality monitoring and detection of highly toxic and dangerous pollutants. The synthesis of highly sensitive MIPs and their effective deposition on novel transducers (e.g., Surface Plasmon Resonance (SPR), Surface Enhanced Raman Scattering (SERS), Quartz Crystal Microbalance (QCM), Electrochemical and Micro-Electro-Mechanical Systems (MEMS), etc.) can lead to the fabrication of a new class of novel microsensors for environmental monitoring applications. Since the sensor's sensitivity is highly dependent on the affinity of MIP element to the target analyte, a high specific surface area is required.

Table 5 Use of MIPs in Analysis of Environmental Samples

Analyte	Template	Functional Monomer/Cross-linker/Porogen	MIP Preparation Technique	Medium	Analytical Technique	LOD and/or LOQ	Linear Range	R (%)	RSD (%)	Reference
Pharmaceutically active compounds										
Amphetamine drugs	N.A.	N.A.	SupelMIP-Amphetamine 25 mg cartridges	Wastewater	SPE-HPLC-MS/MS	0.5–2.7 ng/L	N.A.	91%–114% overall recovery	1.5–4.4	[134]
Carbamazepine	Carbamazepine, Diclofenac	MAA/DVB/ACN/TOL	Precipitation polymerization	Aqueous solutions	HPLC-UV	0.01 and 0.1 mg/L	0.1–1.0 mg/L	>80%	–	[135]
β-Lactam antibiotics	Penicillin G, Amoxicillin, Ampicillin, Nafcillin, Mezlocillin	MAA/EGDMA/MeOH or ACN	Bulk (thermal and photo) polymerization	River water, tap water	SPE-HPLC	12.5–40 ng/L	0.1–20 µg/L	>85%	<15.5	[136]
Antimicrobials-TCS	TCS	APTES/TEOS	Surface imprinting with sol-gel process	River water	HPLC-UV	N.A.	N.A.	92.1%–95.3%	<8.4	[80]
2-Chlorophenol (2-CP)	2-CP derivatized with 4-amino-anti-pyrine (4-AAP)	MAA/ EGDMA/ACN	Bulk polymerization	Aqueous solutions	MISPE-HPLC	0.05 ng/L	10–100 ng/mL	91.3%–99.5%	1.2–5.5	[137]
Diclofenac	Diclofenac	2VP/EGDMA/TOL	Precipitation polymerization	Tap water, river water, wastewater	SPE-HPLC/DAD	5 µg/L (LOD not reported)	N.A.	>95%	N.A.	[138]
Fluoroquinolone related compounds	Ciprofloxacin (CIP)	MAA/EGDMA/MeOH	Bulk polymerization	Wastewater	MISPE-LC–MS/MS	0.5 and 8.1 ng/L	25–1000 ng/L	87%–115%	7.7–13.5	[139]
β-Blockers	Propranolol	MAA/EGDMA/TOL and silica nanoparticles	Pickering emulsion polymerization	Tap water	SPE-HPLC-MS/MS	N.A.	N.A.	64%–92%	N.A.	[140]
Acidic pharmaceuticals	N.A.	N.A.	Affinilute MIP-NSAIDs-Biotage (commercially available)	Aqueous solutions	SPE-HPLC-MS/MS	<0.1 µg/L	0.5–50 µg/L	62%–103%	<19	[141]
Tetracyclines	Oxytetracycline	MAA and 2-hydroxyethyl methacrylate/EGDMA and glycerol dimethacrylate/MeOH	Precipitation polymerization	Aqueous solutions	SPE-HPLC	5 µg/L	5–200 µg/L	N.A.	8.1–18.9	[142]
Diclofenac Mefenamic acid	Diphenylamine	1-Vinylimidazol (1-VI) /divinylbenzene (DVB)/EtOH	Bulk polymerization	Wastewater	Rotating disk sorptive extraction (RDSE)-GC/MS	60 and 223 ng/L	N.A.	100%–112%	5–6	[143]

Continued

Table 5 Use of MIPs in Analysis of Environmental Samples—cont'd

Analyte	Template	Functional Monomer/Cross-linker/Porogen	MIP Preparation Technique	Medium	Analytical Technique	LOD and/or LOQ	Linear Range	R (%)	RSD (%)	Reference
Epinephrine	Epinephrine, bisphenol A, nicotine	VBC/DVB/ACN	Bulk polymerization	Drinking water	SPE-HPLC-UV	0.1 and 1 μg/L	1–10 μg/L	60%–102%	3	[144]
Ibuprofen Naproxen Diclofenac	Multi-template (naproxen, ibuprofen, and diclofenac)	2-Vinyl pyridine (2-VP)/EGDMA/TOL	Bulk polymerization	Wastewater, river water	SPE-HPLC	0.15–1.00 μg/L and 0.49–3.33 μg/L	N.A.	82%–103%	<10	[145, 146]
Ketoprofen	Ketoprofen	2-VP/EGDMA/TOL and ACN	Bulk polymerization	Wastewater, Deionized water(DI)	SPE-HPLC	Wastewater: 0.17–0.23 μg/L DI: 0.09 μg/L	1–10000 μg/L	Wastewater: 68% DI: 114%	<17	[147]
Phenolic compounds										
Phenolic compounds	Bisphenol A	4-VP/EGDMA/TOL/ Dodecanol	In situ polymerization	River water	On-line SPE-HPLC	0.06 and 0.20 μg/L	N.A.	80%–95.2%	<8	[148]
Bisphenol A	4,4′-(Hexa-fluoroisopropylidene)-diphenol (FBPA)	4-VP/TRIM/ACN	Radical cryo-polymerization of aqueous solutions of acrylamide and *N*,*N*′-methylene bisacrylamide in the presence of suspended MIP powders synthesized by bulk polymerization	River water	MISPE-HPLC	10 ng/L	0.1–1 μg/L	75%–125%	3	[149]
Bisphenol A	4,4'-Dihydroxybisphenyl (DDBP) and 3,3',5,5'-tetrabromobisphenylas (TBBPA)	4-VP/GDMA/TOL	Surface imprinting	Tap water, drinking water, rainwater	DMIP-SPE HPLC-UV	15.2 pg/mL	0.076–0.912 ng/mL	92.9%–102%	<11	[150]
Parabens-BuP	BuP	4-VP/EGDMA	Bulk polymerization	Aqueous solutions	HPLC-UV	N.A	–	Up to 97%	<12	[151]
Monobutyl phthalate (mBP)	mBP	4-VP/EGDMA/ Chloroform	Bulk polymerization	Bottle water	MISPE-HPLC	16.5 ng/mL	0.05–10.0 mg/L	68%–81%	<11.1	[152]
Tetrabromobisphenol A (TBBPA)	Diphenolic acid (DPA)	APTES/TEOS/MeOH	Surface imprinting	Tap water, river water, lake water	MISPE-RRLC-DAD	2 ng/mL	8.4–800 ng/mL	85%–97%	3.6	[153]
Bisphenol A	Bisphenol A	4-VP/EGDMA/TOL	Chemical modification of Fe_3O_4/poly(St-*co*-MPS)/SiO_2	Real aqueous solutions	SPE	2.50 and 8.33 pg/mL	5–1000 ng/mL	84.7%–93.8%	<6.4	[154]

4-Nitrophenol	4-Nitrophenol	MAA/EGDMA/ACN	Development of open-tubular MIP-capillaries	Tap water, wastewater, water from contaminated military site	SPE-HPLC	0.33 and 1.1 μg/L	1–10000 μg/L	98%–103%	2.5–4.3	[155]
Musk ambrette (MA), musk xylene (MX), musk moskene (MM), musk tibetene (MT) and musk ketone (MK)	2,4-DNT	PTMS/TEOS	Sol-gel process	Aqueous solutions	GC-MS	MA: 2.6 ng/L MX: 2.7 ng/L MM: 2.2 ng/L MT: 1.8 ng/L MK: 1. 5 ng/L	8–20 ng/mL	Seawater: 77%–87% Wastewater: 69%–87%	<6	[156]
Parabens-BuP	BuP	MAA/EGDMA	Precipitation polymerization	Aqueous solutions	Potentiometry	3.8 μg/L	up to 100 μM	82%–85%	6.3–8.9	[157]
Benzonic acid (BA), 4-hydroxybenzoic acid (4-HBA), salicylic acid (SA), protocatechuic acid (PCA), and gallic acid (GA)	Benzonic acid (BA)/4-hydroxybenzoic acid (4-HBA)	4-VP/EGDMA	Surface imprinting	Aqueous solutions	HPLC-UV	4-HBA: 1.0 μg/L SA: 20.0 μg/L	0.05–5.0 μg/mL	83.2%–103.0%	<4	[78]
Nitrophenol pollutants	2,4-Dinitro-phenol (2,4-DNP)	AAm and glycidyl methacrylate (GMA)/TRIM	Precipitation polymerization	Lake water, river water, wastewater	MIP spin column Extraction-HPLC	0.3–0.5 ng/mL	2–1000 ng/mL	87.3%–92.9%	<7.5	[158]
Benzophenones	2,2′,4,4′-Tetrehydroxybenzophenone	4-VP/EGDMA/ACN	Bulk polymerization	Tap water, river water	MISPE-HPLC-DAD	0.25–0.72 ng/mL	0.2–10 μg/mL	86.9%–103.3%	<9.2	[159]
Phenols	2,4-Dichlorophenol (2,4-DCP)	Methacrylic acid functionalized with β-cyclodextrin/TRIM/DMAC	Bulk polymerization	Tap water, river water	MISPE-GC-FID	0.14–0.75 μg/L	0.01–12 mg/L	97%–115% for tap water and 88%–103% for river water	2.3–3.6	[160]
Bisphenol A	2,2-Bis(4-hydroxyphenyl) butane (BPB), 4,4′-dihydroxydiphenylmethane (BPF), 4-tert-butylphenol (PTBP), tetrabromobisphenol A (TBBA)	Aam/EGDMA/MeOH	MIP stir bar coatings were prepared using fine glass capillary tube as a substrate and a coarse glass capillary tube as a mold	River water, lake water	Barbell-shaped stir bar sorptive extraction-HPLC-DAD	0.003 and 0.009 μg/L	0.01–15 μg/L	63%–99%	<8.4	[133]
Bisphenol A	Bisphenol A	MAA, Aam, 4-VP/EGDMA	Bulk polymerization	River water	SPE-HPLC	25 and 70 μg/L	0.05–10 μg/mL	>85%	<6	[161]
Phthalates	Dibutyl phthalate	MAA/EGDMA/ACN	Precipitation polymerization	Bottled water	SPE-HPLC-ESI-MS	0.16–0.84 and 0.55–2.81 μg/L	–	94%–96%	3.2–8.3	[162]

Continued

Table 5 Use of MIPs in Analysis of Environmental Samples—cont'd

Analyte	Template	Functional Monomer/Cross-linker/Porogen	MIP Preparation Technique	Medium	Analytical Technique	LOD and/or LOQ	Linear Range	R (%)	RSD (%)	Reference
Pesticides										
Methylthiotriazine herbicides	Atrazine, ametryn or irgarol	MAA/TFMAA or 4-VP/EGDMA	MIPs prepared by a multistep swelling and polymerization method and RAM-MIPs prepared by the above method followed by in situ hydrophilic surface modification	River water	Column-switching HPLC system with RAM; MIP as a pretreatment column	25 and 50 pg/mL	50–500 pg/mL	95.1%–101%	0.8–6.3	[163]
Thiabendazole (fungicide, paracitide)	Benzimidazole compounds	MAA/EGDMA and DVB/ACN/TOL	Precipitation polymerization	Tap water, river water	HPLC	0.03 μg/L	–	89%–104%	2.1–6.7	[164]
Ametryn, prometryn, terbutryn, atrazine, aimazine propazine, cyanazine	Ametryn	MAA/EGDMA/ACN	Precipitation polymerization and preparation of fibers using special molds	Tap water	Solid-phase microextraction (SPME) fiber-GC/MS	14–95 ng/mL	50–10000 ng/mL	93.6%–99.8%	4.87–10.6	[165]
Melamine	Cyromazin	MAA/EGDMA/MeOH and water	Bulk polymerization	Tap water, lake water, seawater	SPE-HPLC	0.1 and 0.5 ng/mL	0.5–100.0 ng/mL	>86.3%	<8.8	[166]
Thiabendazole	Thiabendazole	MAA/TRIM and TOL/MeOH	Preparation of MIP-fibres by in situ polymerization in silica capillaries	Aqueous solutions	Solid-phase microextraction (SPME)	4 μg/L	0.01–5.00 mg/L	8%	<10	[167]
Dicofol	-1,1-Bis(4-chlorophenyl)-1,2,2,2-tetrachloroethane (α-chloro-DDT)	MAA/EGDMA/Chloroform	Suspension polymerization	Aqueous solutions	MISPE-GC-ECD	0.1 ng/g	0.4–100 ng/g	95.3%–98.7%	<5.6	[168]
Pyrethroids	Cypermethrin	MAA/EGDMA/ACN/MeCN	Bulk polymerization	Aquaculture seawater	MISPE-GC-ECD	16.6–37.0 ng/L	0.01–0.5 mg/L	86.4%–96.0%	2.4–7.8	[169]
Atrazine	Atrazine	MAA/EGDMA/Chloroform	Bulk polymerization	Tap water, river water, municipal wastewater	Mixed-bed SPE-GC/MS	1.34 and 4.5 μg/L	5–200 μg/L	>85%	1.8–6.3	[170]
Triazines	Atrazine	MAA or HEMA/EGDMA/MeOH or ACN	Reversible addition-fragmentation chain transfer precipitation polymerization (RAFTPP) and grafting of PHEMA	Tap water, river water	SPE-HPLC	3.2–8.6 μg/L	50–1000 μg/L	65.3%–97.6%	<4.8	[171]

Triazines	Trietazine	MAPA/EDMA/EtOH/MeOH	In situ polymerization into the pretreated capillary columns	Aqueous solutions	CEC	N.A.	N.A.	N.A.	N.A.	[172]
Simazine	Simazine	Methyltriethoxysilane as the sol-gel precursor	Polysiloxane nanofibers via self-polycondensation	River water, well water, tap water	SPE-GC/MS	0.005 μg/L	0.02–20 μg/L	94%–97%	4.3–7.6	[173]
Chloroacetamide herbicides	Butachlor	4-VP and alkenyl glycosides glucose (AGG)/*N*,*N*-methylene diacrylamide/ACN	Fe_3O_4 microspheres were used as the magnetic core	Lake water, wastewater	Magnetic molecularly imprinted SPE-HPLC	0.03–0.06 and 0.09–0.15 μg /L	0.1–200 μg /L	82.1%–102.9%	<7	[174]
Estrogens										
β-Estradiol	β-Estradiol	MAA/DVB or TRIM/TOL/ACN	Precipitation polymerization	Surface water	SPE-HPLC/ MS	N.A.	N.A.	81%	N.A.	[175]
Natural and synthetic estrogens	N.A.	Difunctional acrylic cross-linker monomers	Commercially available (AFFINIMIP)	River water, tap water	SPE-UHPLC/MS	4.5–9.8 and 14.9–32.6 ng/L	50–500 ng/L	>82%	<8	[176]
Estrogen	E2	APTES/TEOS/Chloroform	Surface imprinting	Polluted water	MISPE-HPLC	12.0 ng/L	0.05–300 mg/L	82.7%–103.0%	<5	[177]
Dyestuff										
Water-soluble acid dyes	Tratarzine	1-(-Methylacrylate)-3-methylimidazolium bromide/TRIM/MeOH	Precipitation polymerization	Wastewater	SPE-HPLC	0.13–0.51 μg/L	5.0–2000 μg/L	89.1%–101.0%	1.6–3.9	[178]
Crystal violet (CV)	CV	MAA/ EGDMA/MeOH	Bulk polymerization	Seawater	MISPE-HPLC DAD	0.1 ng/mL	0–200 ng/mL	74.27%–92.96%	2.74–4.62	[179]
Tartrazine	Tartrazine	Acrylamide / *N*,*N*′-methylene bisacrylamide	Precipitation polymerization	Aqueous solutions	SPE	N.A.	10^{-5}–7×10^{-5} M	91%	N.A.	[180]
Methylene blue	Methylene blue	4-VP/EGDMA/ACN	Bulk polymerization	Tap water, river water, wastewater	SPE-UV-vis	0.31 μg /L	2–1200 μg /L	>97%	<1.7	[181]
Polycyclic aromatic hydrocarbons										
16 U.S. EPA PAH pollutants	N.A.	N.A.	Magnetic MIPs (mag-MIPs) commercially available by NanoMyP	Tap water, river water, lake water, mineral water	HPLC	1.3–24.3 and 4.3–80.9 ng/L	4.7–44000 ng/L depending on the pollutant	98.8%–100% for the more lipophilic PAHs and 46%–60% for the less lipophilic PAHs	<10	[182]

Another critical issue in the development of a MIP-based microsensor is the required close contact of MIP film to the transducer's surface. To improve the MIP-transducer contact, several methods have been developed, including the in situ polymerization and drop-casting of a polymer solution. InTable 6, typical applications of MIP-based sensors for environmental monitoring are described.

Table 6 MIP-Based Sensors for Environmental Monitoring

Target Analyte	Detection	Time Response	LOD	Medium	Reference
Pharmaceutically active compounds					
Ibuprofen	Electrochemical (differential capacitor)	N.A.	10^{-5} M	Aqueous solutions	[183, 184]
Triclosan	Optical (SPR)	50 min	0.017 ng/mL	Wastewater	[185]
Diclofenac	Optical (SPR)	250 s	1.2 ng/mL	Buffer	[186]
Metoprolol	Optical (SPR)	250 s	15.6 ng/mL	Aqueous solutions	[187]
N-Formylamphetamine	Electrochemical (cyclic voltammetry)	1 min	10 μM	Aqueous solutions	[188]
Phenolic compounds					
Pentachlorophenol	Optical (room-temperature phosphorescence optosensor)	N.A.	86 nM	Buffer solution and river water	[113]
Bisphenol A	Electrochemical (differential capacitor)	N.A.	10^{-5} M	Aqueous solutions	[183, 184]
Bisphenol A	Optical (SPR)	<30 min	40 pg/mL	Drinking water	[189]
4-Nitrophenol	Optical (chemiluminescence)	5 min	15 μM	Tap water	[111]
4-Nonylphenol	Electrochemical (cyclic voltammetry)	500 s	3.20×10^{-7} mol/L	Tab water	[190]
Bisphenol A	Electrochemical (oxidation overpotential and current response)	150 s	8.0×10^{-9} mol/L	Distilled water	[191]
Tetrabromobisphenol A	Optical (fluorescence)	10 min	0.015 μM	Aqueous solutions	[192]
p-Nitrophenol	Electrochemical (electrochemical impedance spectroscopy (EIS) and differential pulse voltammetry (DPV))	N.A.	0.10 μM	Buffer solution	[193]
Bisphenol A	Optical (Raman scattering)	10 min	0.12 mg/L	River water	[88]

Table 6 MIP-Based Sensors for Environmental Monitoring—cont'd

Target Analyte	Detection	Time Response	LOD	Medium	Reference
4-Aminophenol	Photoelectrochemical	40 min	2.3×10^{-8} mol/L	Lake water	[194]
Paranitrophenol (4-NP)	Optical (Fluorescence)	N.A.	9 ng/mL	Tab water and river water	[195]
4-Nitrophenol	Electrochemical (cyclic voltammetry and differential pulse voltammetry)	2 min	5 nM	Tab and lake water	[196]
Bisphenol A	Optical (SPR)	50 min	0.02–0.08 μg/L	Milli Q water, tap water, synthetic wastewater	[197]
1,3,5-Trinitrotoluene (TNT)	Electrochemical (linear sweep voltammetry)	Less than 1 min (after extraction)	0.04 fM	Tap and river water	[198]
Bisphenol A	Optical (fluorescence)	25 min	0.10 μM	Seawater	[199]
Ractopamine	Optical (SPR)	13 min	5 ng/mL	Aqueous solutions (water with ethanol)	[200]
Bisphenol A	Optical (microfluidic paper-based colorimetric sensor)	30 min	6.18 nM	Buffer solution	[201]
Pesticides					
2,4-D	Electrochemical (differential-pulse voltammetry)	>30 min	1 μM	Buffer solution	[202]
2,4-D	Optical (luminescent)	30 min	–	Buffer solution	[203]
Atrazine	Electrochemical (potentiometric sensor)	2 min	0.1 mg/L	Ground water	[204]
Dinitrocresol	Electrochemical (voltammetric microsensor)	–	8×10^{-7} M	Buffer solution	[205]
Desmetryn Terbumeton Terbutrin Metribuzin Atrazine	Electrochemical (differential capacitor)	N.A.	10^{-5} M	Aqueous solutions	[183, 184]

Continued

Table 6 MIP-Based Sensors for Environmental Monitoring—cont'd

Target Analyte	Detection	Time Response	LOD	Medium	Reference
Chlorpyrifos	Electrochemical (constant current potentiometric method)	10 min	1×10^{-13} mol/L	Simulated river water	[206]
λ-Cyhalothrin	Optical (fluorescence)	55 min	1.76 μM	Aqueous solutions	[207]
Atrazine	Acoustic (QCM)	50 min	0.028 nM	Wastewater	[208]
Cyphenothrin	Optical (fluorescence)	10 min	9.0 nmol/L	Aqueous solutions	[209]
Glyphosate herbicide	Electrochemical (linear sweep voltammetry)	20 min	5 fM (0.8 pg/L)	Tap water	[210]
2,4 D	Optical (ratiometric fluorescence sensor)	5 min	0.14 μM	Tap water and lake water	[211]
Diniconazole	Optical (fluorescence)	20 min	6.4 μg/L	River water and wastewater	[212]
Estrogens					
Ethinylestradiol	Electrochemical (cyclic voltammetry/ microfluidic immune-assay)	1 min	0.09 ng/L	River water	[213]
17β-Estradiol	Electrochemical (differential pulse voltammetry)	4 min	1.6×10^{-8} mol/L	Tab water and wastewater	[214]
17β-Estradiol	Electrochemical (linear sweep voltammetry)	20 min	1.09 fM	River water	[215]
Organophosphates					
Methylphosphonic acid (MPA)	Electrochemical (potentiometric sensor)	5 min	5×10^{-8} M	Ground water	[216]
Phosphates	Electrochemical (conductometric analysis of membranes)	6 min	0/16 mg/L	Wastewater	[217, 218]
Haloacetic acids					
Haloacetic acids	Acoustic (QCM)	10 min	20–50 μg/L	Drinking water	[219]
Inorganic ions					
Mercury ion	Electrochemical (linear sweep voltammetry)	4 min	3.06×10^{-9} mol/L	Acetate buffer solution	[220]
Mercury Ion	Electrochemical (square wave stripping voltammetry)	250 s	0.04 ng/mL	River water and wastewater	[221]

Table 6 MIP-Based Sensors for Environmental Monitoring—cont'd

Target Analyte	Detection	Time Response	LOD	Medium	Reference
Cadmium (II) ion	Optical (colorimetric assay by complexation)	6 min	0.4 ng/mL	Lake and river water	[222]
Toxins/Viruses/Bacteria					
Microcystin-LR	Acoustic (piezoelectric sensor)	25 min	0.35 nM	Drinking water	[223]
Bacteriophage MS2 virus	Optical (SPR)	250–500 s	5×106 pfu/mL	Aqueous solutions	[224]
Escherichia coli 0111:B4	Optical (SPR)	250 s	5.6 ng/mL	Buffer solution	[225]
Adenovirus	Optical (SPR)	250 s	8.08×106 pfu/mL	Buffer solution	[226]
Escherichia coli 0111:B4	Optical	200 s	0.44 ng/mL	Buffer solution	[227]

7 TECHNOLOGY MATURITY

A great number of papers on molecular imprinting techniques have been published, hundreds of patent applications have been filed, and several companies are making profits by applying the molecular imprinting technology. Some of the leading companies in MIP technologies are: Biotage, Sphere Medical, Toximet, MipSalus, Imego, Raptol Detection Technologies, PolyIntell, Chrysalis Scientific Technologies, and Semorex. Present commercial applications of MIPs are in the production of SPE packing materials for biomedical, food, and environmental analyses [228, 229]. Other promising applications of MIPs are in the development of new microsensors. Recently, a US company, Raptor, commercialized a MIP-based sensor for the detection of explosives. In another application, an Israeli-US company, Semorex, commercialized a MIP-based device for the removal of toxic compounds (i.e., metal ions) from biological fluids. The use of MIPs as antibody mimics represents another promising commercial application due to their high selectivity and specificity toward particular substrates, stability and reusability. Critical parameters in future commercial exploitation of MIPs are the successful scale-up of MIP production, increase of yield, reduction of production cost and superior functional properties in comparison to existing affinity materials [228, 229].

8 CONCLUSION

Up to the present, huge steps have been made in order to bring the imprinting technology one step closer to water treatment applications. Even though it is quite difficult at the moment to apply directly MIPs in large-scale water purification processes, it is foreseen that due to stringent environmental regulations, new materials, technologies and monitoring devices will be needed in water treatment and

environmental monitoring. MIPs can play an important role in these new market developments. Apart from the water treatment industry, the pharmaceutical and biomedical industries could also benefit by the development of innovative diagnostic, analytical, and separation materials and processes based on imprinting technologies.

ABBREVIATIONS

1-VID 1-vinylimidazole
2,4 DP 2,4-dimethylphenol
2,4,5-T 2,4,5-trichlorophenoxyacetic acid
2,4-D 2,4-dichlorophenoxyacetic acid
2,4-DCP 2,4-dichlorophenol
2,4-DNP 2,4-dinitrophenol
2,4-DNT 2,4-Dinitrotoluene
2-VP 2-vinylpyridine
3-MPTS 3-methylacryloxyprolyl trimethoxysilane
4-HBA 4-hydroxybenzoic acid
4MP 4-methylphenol
4PP 4-propylphenol
4-VP 4-vinylpyridine
AA acrylic acid
AAm acrylamide
ACID 4,4′-azo(4-cyanovaleric acid)
ACN acetonitrile
ADVN 2,2′- azobis (2, 4-dimethylvaleronitrile)
AGG glycosides glucose
AIBN 2,2′- azobis (isobutyronitrile)
AMPSA 2-acryl-amido-2-methyl-1-propanesulfonic acid
AN acrylonitrile
APTES 3-aminopropyltriethoxysilane
APTMS 3-aminopropyltrimethoxysilane
ATR atrazine
ATR-IR attenuated total reflectance fourier transform infrared
ATRP atom transfer radical polymerization
B[a]A benzo[a]anthracene
B[a]P benzo[a]pyrene
B[b]F benzo[b]fluoranthene
BA benzoic acid
BDK dimethylacetal of benzyl
BIPB bis- (1-(tert-butylperoxy)-1-methylethyl)-benzene
BPA bisphenol A
BPB 2,2-bis(4-hydroxyphenyl)butane
BPF 4,4′-dihydroxydiphenylmethane
BPF bisphenol F

BPO	benzoylperoxide
BuP	butyl paraben
CA	clofibric acid
CBZ	carbamazepine
CDB	cumyl dithiobenzoate
Chr	chrysene
CIP	ciprofloxacin
CNTs	carbon nanotubes
CPF	chlorpyrifos
CRP	controlled radical polymerization
CYA	cyanazine
CyD	cyclodextrine
D[a]P	dibenzo[a,h]pyrene
DAP	1,4-diacryloyl piperazine
DCP	dicumyl peroxide
DCPL	2,4-dichlorophenol
DEA	desethylatrazine
DEAEM	diethylamino ethyl methacrylate
DES	diethylstilbestrol
DPV	differential pulse voltammetry
DFC	diclofenac
DIA	desisopropylatrazine
DMAC	dimethylacetamide
DMF	dimethylformamide
DMSO	dimethyl sulfoxide
DTPA	diethylenetriaminepentaacetic acid
DVB	divinylbenzene
E1	estrone
E2	17β-estradiol
E3	estriol
EDMA	ethylene dimethacrylate
EE	ethynylestradiol
EGDMA	ethylene glycol dimethacrylate
EGMRA	ethylene glycol maleic rosinate acrylate
EIS	electrochemical impedance spectroscopy
EPI	epinephrine
EtOH	ethanol
FBPA	4,4′-(hexa-fluoroisopropylidene)-diphenol
FQs	fluoroquinolone antibiotics
FRP	free radical polymerization
GA	gallic acid
GC	gas chromatography
GMA	glycidilmethacrylate
GPTMS	glycidoxypropyltrimethoxysilane

HEMA	2-hydroxyethyl methacrylate
HPLC	high performance liquid chromatography
I[2]P	indeno[1,2,3-c]pyrene
IA	itaconic acid
IBP	ibuprofen
IPTS	3-Isocyanatopropyltriethoxysilane
ISs	immunosorbents
KPS	potassium persulfate
LCRP	living/controlled radical polymerization
MA	Musk Ambrette (6-tert-butyl-3- methyl-2,4-dinitroanisole)
MAA	methacrylic acid
MAPA	methacryloyl phenylalanine
MPS	3-(trimethoxysily) propyl methacrylate
St	Styrene
VBC	vinylbenzyl chloride

REFERENCES

[1] C. Alexander, H.S. Andersson, L.I. Andersson, R.J. Ansell, N. Kirsch, I.A. Nicholls, J. O'Mahony, M.J. Whitcombe, Molecular imprinting science and technology: a survey of the literature for the years up to and including 2003, J. Mol. Recognit. 19 (2006) 10–180.

[2] M. Komiyama, T. Takeuchi, T. Mukawa, H. Asanuma, Molecular Imprinting: From Fundamentals to Applications, WILEY-VCH Verlag GmbH & Co. KGaA, Weinheim, 2003, pp. 9–46.

[3] L. Chen, X. Wang, W. Lu, X. Wu, J. Li, Molecular imprinting: perspectives and applications, Chem. Soc. Rev. 45 (2016) 2137–2211.

[4] L. Ye, Synthetic strategies in molecular imprinting, Adv. Biochem. Eng. Biotechnol. 150 (2015) 1–24.

[5] K. Yoshimatsu, K. Reimhult, A. Krozer, K. Mosbach, K. Sode, L. Ye, Uniform molecularly imprinted microspheres and nanoparticles prepared by precipitation polymerization: the control of particle size suitable for different analytical applications, Anal. Chim. Acta 584 (2007) 112–121.

[6] D. Vaihinger, K. Landfester, I. Krauter, H. Brunner, G.E.M. Tovar, Molecularly imprinted polymer nanospheres as synthetic affinity receptors obtained by miniemulsion polymerization, Macromol. Chem. Phys. 203 (2002) 1965–1973.

[7] A. Biffis, G. Dvorakova, A.F. Cordin, Topics in Current Chemistry. Molecular Imprinting, Springer-Verlag, Berlin/Heidelberg, 2011, pp. 29–82.

[8] M. Ulbricht, Membrane separations using molecularly imprinted polymers, J. Chromatogr. B 804 (2004) 113–125.

[9] U. Beginn, G. Zipp, A. Mourran, P. Walther, M. Möller, Membranes containing oriented supramolecular transport channels, Adv. Mater. 12 (2000) 513–516.

[10] C. Dai, S. Geissen, Y. Zhang, Y. Zhang, X. Zhou, Selective removal of diclofenac from contaminated water using molecularly imprinted polymer microspheres, Environ. Pollut. 159 (2011) 1660–1666.

[11] C. Dai, J. Zhang, Y. Zhang, X. Zhou, Y. Duan, S. Liu, Selective removal of acidic pharmaceuticals from contaminated lake water using multi-templates molecularly imprinted polymer, Chem. Eng. J. 211–212 (2012) 302–309.

[12] C. Dai, J. Zhang, Y. Zhang, X. Zhou, Y. Duan, S. Liu, Removal of carbamazepine and clofibric acid from water using double templates-molecularly imprinted polymers, Environ. Sci. Pollut. Res. 20 (2013) 5492–5501.
[13] M. Sánchez-Polo, I. Velo-Gala, J.J. López-Peñalver, J. Rivera-Utrilla, Molecular imprinted polymer to remove tetracycline from aqueous solutions, Microporous Mesoporous Mater. 203 (2015) 32–40.
[14] Y. Li, X. Li, Y. Li, J. Qi, J. Bian, Y. Yuan, Selective removal of 2,4-dichlorophenol from contaminated water using non-covalent imprinted microspheres, Environ. Pollut. 157 (2009) 1879–1885.
[15] G. Pan, Y. Zhang, Y. Ma, C. Li, H. Zhang, Efficient one-pot synthesis of water-compatible molecularly imprinted polymer microspheres by facile RAFT precipitation polymerization, Angew. Chem. Int. Ed. 50 (2011) 11731–11734.
[16] Y. Ren, W. Ma, J. Ma, Q. Wen, J. Wang, F. Zhao, Synthesis and properties of bisphenol A molecular imprinted particle for selective recognition of BPA from water, J. Colloid Interface Sci. 367 (2012) 355–361.
[17] Y. Ren, J. Yang, W. Ma, J. Ma, J. Feng, X. Liu, The selective binding character of a molecular imprinted particle for bisphenol A from water, Water Res. 50 (2014) 90–100.
[18] T. Jing, J. Wang, M. Liu, Y. Zhou, Y. Zhou, S. Mei, Highly effective removal of 2,4-dinitrophenolic from surface water and wastewater samples using hydrophilic molecularly imprinted polymers, Environ. Sci. Pollut. Res. 21 (2014) 1153–1162.
[19] R.J. Krupadam, M.S. Khan, S.R. Wate, Removal of probable human carcinogenic polycyclic aromatic hydrocarbons from contaminated water using molecularly imprinted polymer, Water Res. 44 (2010) 681–688.
[20] R.J. Krupadam, G.P. Patel, R. Balasubramanian, Removal of cyanotoxins from surface water resources using reusable molecularly imprinted polymer adsorbents, Environ. Sci. Pollut. Res. 19 (2012) 1841–1851.
[21] G.Z. Kyzas, D.N. Bikiaris, N.K. Lazaridis, Selective separation of basic and reactive dyes by molecularly imprinted polymers (MIPs), Chem. Eng. J. 149 (2009) 263–272.
[22] B. Okutucu, S.H. Sanlıer, Decolorization of textile wastewater by dye imprinted polymer, Desalin. Water Treat. 57 (2015) 1–8.
[23] Z. Meng, W. Chen, A. Mulchndani, Removal of estrogenic pollutants from contaminated water using molecularly imprinted polymers, Environ. Sci. Technol. 39 (2005) 8958–8962.
[24] E.P.C. Lai, Z. De Maleki, S. Wu, Characterization of molecularly imprinted and nonimprinted polymer submicron particles specifically tailored for removal of trace 17b-estradiol in water treatment, J. Appl. Polym. Sci. 116 (2010) 1499–1508.
[25] N. Saifuddin, Y.A.A. Nur, S.F. Abdullah, Microwave enhanced synthesis of chitosan-graft-polyacrylamide molecular imprinting polymer for selective removal of 17β-estradiol at trace concentration, Asian J. Biochem. 6 (2011) 38–54.
[26] J. Liu, M. Yang, L.F. Huai, Y.T. Chen, Removal of chlorpyrifos from contaminated water using molecularly imprinted polymeric microspheres, IEEE Xplorer 25 (2010) 978-1-4244-4713-8.
[27] A. Venkatesh, N. Chopra, R.J. Krupadam, Removal of acutely hazardous pharmaceuticals from water using multi-template imprinted polymer adsorbent, Environ. Sci. Pollut. Res. 21 (2014) 6603–6611.
[28] Q. Yu, S. Deng, G. Yu, Selective removal of perfluorooctane sulfonate from aqueous solution using chitosan-based molecularly imprinted polymer adsorbents, Water Res. 42 (2008) 3089–3097.
[29] Z. Li, H. Fan, T. Sun, Application of imprinted functionalized silica gel sorbent for selective removal of Cadmium (II) from industrial waste waters, Adv. Mat. Res. 213 (2011) 441–444.
[30] Y.-K. Lu, X.-P. Yan, An imprinted organic – inorganic hybrid sorbent for selective separation of cadmium from aqueous solution, Anal. Chem. 76 (2004) 453–457.
[31] G. Parameswaran, B. Mathew, Bioremediation of waste water containing hazardous cadmium ion with ion imprinted interpenetrating polymer networks, Hindawi Publ. Corp. Adv. Environ. Chem. (2014) 1–10 Article ID 394841.
[32] V. Yilmaz, H. Yilmaz, Z. Arslan, J. Leszczynski, Novel imprinted polymer for the preconcentration of cadmium with determination by inductively coupled plasma mass spectrometry, Anal. Lett. 50 (2017) 482–499.

[33] F. Zhu, L. Li, J. Xing, Selective adsorption behavior of Cd(II) ion imprinted polymers synthesized by microwave-assisted inverse emulsion polymerization: adsorption performance and mechanism, J. Hazard. Mater. 321 (2017) 103–110.
[34] D. Chen, C. Huang, M. He, B. Hu, Separation and preconcentration of inorganic arsenic species in natural water samples with 3-(2-aminoethylamino) propyltrimethoxysilane modified ordered mesoporous silica micro-column and their determination by inductively coupled plasma optical emission spectrometry, J. Hazard. Mater. 164 (2009) 1146–1151.
[34a] M.S. Jagirani, A. Balouch, A.M.Mahar Abdullah, F.A. Mustafai, K. Rajar, A. Tunio, S. Sabir, M.K. Samoon, Arsenic remediation by synthetic and natural adsorbents, Pak. J. Anal. Environ. Chem. 18 (2017) 18–36.
[35] H. Huo, H. Su, T. Tan, Adsorption of Ag^{+} by a surface molecular-imprinted biosorbent, Chem. Eng. J. 150 (2009) 139–144.
[36] M. Khajeh, Z.S. Heidari, E. Sanchooli, Synthesis, characterization and removal of lead from water samples using lead-ion imprinted polymer, Chem. Eng. J. 166 (2011) 1158–1163.
[37] M. Kim, Y. Jiang, D. Kim, Zn^{2+}-imprinted porous polymer beads: synthesis, structure, and selective adsorption behavior for template ion, React. Funct. Polym. 73 (2013) 821–827.
[38] Y. Ren, P. Liu, X. Liu, J. Feng, Z. Fan, T. Luan, Preparation of zirconium oxy ion-imprinted particle for the selective separation of trace zirconium ion from water, J. Colloid Interface Sci. 431 (2014) 209–215.
[39] M.G.F. Stevens, B.S. Batlokwa, Multi-templated Pb-Zn-Hg ion imprinted polymer for the selective and simultaneous removal of toxic metallic ions from wastewater, Int. J. Chem. 9 (2017) 1–12.
[40] S.R. Thakare, M.R. Pal, S.Z. Jadhao, Simple synthesis of highly selective and fast Hg(II) removal polymer from aqueous solution, Des. Monomers Polym. 18 (2015) 650–660.
[41] X. Luo, W. Zhong, J. Luo, L. Yang, J. Long, B. Guo, S. Luo, Lithium ion-imprinted polymers with hydrophilic PHEMA polymer brushes: the role of grafting density in anti-interference and antiblockage in wastewater, J. Colloid Interface Sci. 492 (2017) 146–156.
[42] J. Aguado, J.M. Arsuaga, A. Arencibia, M. Lindo, V. Gascón, Aqueous heavy metals removal by adsorption on amine-functionalized mesoporous silica, J. Hazard. Mater. 163 (2009) 213–221.
[43] L. Bois, A. Bonhommé, A. Ribes, B. Pais, G. Raffin, F. Tessier, Functionalized silica for heavy metal ions adsorption, Colloids Surf. A Physicochem. Eng. Asp. 221 (2003) 221–230.
[44] H. Yang, Y. Chen, Q. Feng, H. Tian, J. Li, Preparation of ion-imprinted amino-functionalized nano-porous silica for selective removal of heavy metal ions from water environment, J. Nanosci. Nanotechnol. 17 (2017) 6818–6826.
[45] C. Gkementzoglou, O. Kotrotsiou, C. Kiparissides, Synthesis of novel composite membranes based on molecularly imprinted polymers for removal of triazine herbicides from water, Ind. Eng. Chem. Res. 52 (2013) 14001–14010.
[46] C. Gkementzoglou, O. Kotrotsiou, M. Koronaiou, C. Kiparissides, Development of a sandwich-type filtration unit packed with MIP nanoparticles for removal of atrazine from water sources, Chem. Eng. J. 287 (2016) 233–240.
[47] K. Yoshimatsu, L. Ye, J. Lindberg, I.S. Chronakis, Selective molecular adsorption using electrospun nanofiber affinity membranes, Biosens. Bioelectron. 23 (2008) 1208–1215.
[48] S. Hajizadeh, H. Kirsebom, I.Y. Galaev, B. Mattiasson, Evaluation of selective composite cryogel for bromate removal from drinking water, J. Sep. Sci. 33 (2010) 1752–1759.
[49] S. Hajizadeh, C. Xu, H. Kirsebom, L. Ye, B. Mattiasson, Cryogelation of molecularly imprinted nanoparticles: a macroporous structure as affinity chromatography column for removal of β-blockers from complex samples, J. Chromatogr. A 1274 (2013) 6–12.
[50] I. Koç, G. Baydemir, E. Bayram, H. Yavuz, A. Denizli, Selective removal of 17β-estradiol with molecularly imprinted particle-embedded cryogel systems, J. Hazard. Mater. 192 (2011) 1819–1826.
[51] I.S. Chronakis, B. Milosevic, A. Frenot, L. Ye, Generation of molecular recognition sites in electrospun polymer nanofibers via molecular imprinting, Macromolecules 39 (1) (2006) 357–361.

[52] S. Xu, Y. Liu, L. Sun, A. Luo, Preparation and recognition properties of levodropopizine molecularly imprinted composite membranes, Adv. Mat. Res. 399-401 (2012) 355–358.
[53] Z. Altintas, I. Chianella, G. Da Ponte, S. Paulussen, S. Gaeta, I.E. Tothill, Development of functionalized nanostructured polymeric membranes for water purification, Chem. Eng. J. 300 (2016) 358–366.
[54] K.P. Singh, R. Dobhal, R.K. Prajapati, S. Kumar, Sanjesh, and Ansari, M.A., Preparation of isoproturon and 2,4-dichlorophenoxy acetic acid imprinted membranes: ion transport study, Desalin. Water Treat. 24 (1-3) (2010) 176–189.
[55] F. Ruggieri, A.A. D'Archivio, D. Di Camillo, L. Lozzi, M.A. Maggi, R. Mercorio, S. Santucci, Development of molecularly imprinted polymeric nanofibers by electrospinning and applications to pesticide adsorption, J. Sep. Sci. 38 (2015) 1402–1410.
[56] F. Barahona, M. Díaz-Álvarez, E. Turiel, A. Martín-Esteban, Molecularly imprinted polymer-coated hollow fiber membrane forthe microextraction of triazines directly from environmental waters, J. Chromatogr. A 1442 (2016) 12–18.
[57] M. Le Noir, F.M. Plieva, B. Mattiasson, Removal of endocrine-disrupting compounds from water using macroporous molecularly imprinted cryogels in a moving-bed reactor, J. Sep. Sci. 32 (2009) 1471–1479.
[58] M. Bryjak, I. Duraj, Molecularly imprinted membranes for removal of bisphenol A, Solvent Extr. Ion Exch. 29 (2011) 432–439.
[59] L.T. Son, K. Takaomi, Hollow-fiber membrane absorbents embedded molecularly imprinted polymeric spheres for bisphenol A target, J. Membr. Sci. 384 (2011) 117–125.
[60] X.F. Li, S.A. Zhong, L. Chen, A. Whittaker, Computer simulation and preparation of molecularly imprinted polymer membranes with chlorogenic acid as template, Polym. Int. 60 (2011) 592–598.
[61] M. Soares da Silva, R. Viveiros, M.B. Coelho, A. Aguiar-Ricardo, T. Casimiro, Supercritical CO2-assisted preparation of a PMMA composite membrane for bisphenol A recognition in aqueous environment, Chem. Eng. Sci. 68 (2012) 94–100.
[62] A.O. Gryshchenko, C.S. Bottaro, Development of molecularly imprinted polymer in porous film format for binding of phenol and alkylphenols from water, Int. J. Mol. Sci. 15 (2014) 1338–1357.
[63] M. Le Noir, F. Plieva, T. Hey, B. Guieysse, B. Mattiasson, Macroporous molecularly imprinted polymer/cryogel composite systems for the removal of endocrine disrupting trace contaminants, J. Chromatogr. A 1154 (2007) 158–164.
[64] L. Donato, M.C. Greco, E. Drioli, Preparation of molecularly imprinted membranes and evaluation of their performance in the selective recognition of dimethoate, Desalin. Water Treat. 30 (2011) 171–177.
[65] V. Vatanpour, S.S. Madaeni, S. Zinadini, H.R. Rajabi, Development of ion imprinted technique for designing nickel ion selective membrane, J. Membr. Sci. 373 (2011) 36–42.
[66] E. Roy, S. Patra, R. Madhuri, P.K. Sharma, A single solution for arsenite and arsenate removal from drinking water using cysteine@ZnS:TiO_2 nanoparticle modified molecularly imprinted biofouling-resistant filtration membrane, Chem. Eng. J. 304 (2016) 259–270.
[67] J. Zeng, Z. Dong, Z. Zhang, Y. Liu, Preparation of a surface-grafted imprinted ceramic membrane for selective separation of molybdate anion from water solutions, J. Hazard. Mater. 333 (2017) 128–136.
[68] S.-O. Dima, A. Sarbu, T. Dobre, C. Bradu, N. Antohe, A.-L. Radu, T.-V. Nicolescu, A. Lungu, Molecularly imprinted membranes for selective separations, Mater. Plast. 46 (4) (2009) 372–378.
[69] G. De Luca, L. Donato, S.G. Del Blanco, F. Tasselli, E. Drioli, On the cause of controlling affinity to small molecules of imprinted polymeric membranes prepared by non-covalent approach: a computational and experimental investigation, J. Phys. Chem. B 115 (2011) 9345–9351.
[70] S.G. Del Blanco, L. Donato, E. Drioli, Development of molecularly imprinted membranes for selective recognition of primary amines in organic medium, Sep. Purif. Technol. 87 (2012) 40–46.
[71] L. Donato, F. Tasselli, G. De Luca, S. Garcia Del Blanco, E. Drioli, Novel hybrid molecularly imprinted membranes for targeted 4,4'-methylendianiline, Sep. Purif. Technol. 116 (2013) 184–191.

[72] H. Chen, J. Kong, D. Yuan, G. Fu, Synthesis of surface molecularly imprinted nanoparticles for recognition of lysozyme using a metal coordination monomer, Biosens. Bioelectron. 15 (2014) 5–11.
[73] S. Han, X. Li, Y. Wang, S. Chen, Multifunctional imprinted polymers based on CdTe/CdS and magnetic graphene oxide for selective recognition and separation of p-t-octylphenol, Chem. Eng. J. 271 (2015) 87–95.
[74] S. Khan, E.M. Miguela, C.F. de Souza, A.R. da Silvac, R.Q. Aucélio, Thioglycolic acid-CdTe quantum dots sensing and molecularly imprinted polymer based solid phase extraction for the determination of kanamycin in milk, vaccine and stream water samples, Sens. Actuators B 246 (2017) 444–454.
[75] H. Li, W.Z. Xu, N.W. Wang, Synthesis of magnetic molecularly imprinted polymer particles for selective adsorption and separation of dibenzothiophene, Microchim. Acta 179 (1-2) (2012) 123–130.
[76] A. Mehdinia, T.B. Kayyal, A. Jabbari, M.O. Aziz-Zanjani, E. Ziaei, Magnetic molecularly imprinted nanoparticles based on grafting polymerization for selective detection of 4-nitrophenol in aqueous samples, J. Chromatogr. A 1283 (2013) 82–88.
[77] J. Pan, H. Yao, L. Xu, H. Ou, P. Huo, X.X. Li, Y. Yan, Selective recognition of 2, 4, 6-trichlorophenol by molecularly imprinted polymers based on magnetic halloysite nanotubes composites, J. Phys. Chem. C 115 (13) (2011) 5440–5449.
[78] S. Shi, J. Guo, Q. You, X. Chen, Y. Zhang, Selective and simultaneous extraction and determination of hydroxybenzoic acids in aqueous solution by magnetic molecularly imprinted polymers, Chem. Eng. J. 243 (2014) 485–493.
[79] W. Xu, Y. Wang, W. Huang, L. Yu, Y. Yang, H. Liu, W. Yang, Computer-aided design and synthesis of CdTe@SiO_2 core–shell molecularly imprinted polymers as a fluorescent sensor for the selective determination of sulfamethoxazole in milk and lake water, J. Sep. Sci. 40 (2017) 1091–1098.
[79a] A.R. Zarei, R.S. Zafarghandi, Selective determination of 2,4,6-trinitrotoluene in water samples based on magnetic imprinted nanoparticles via grafting polymerization, J. Braz. Chem. Soc. 26 (4) (2015) 741–747.
[80] R. Gao, X. Kong, F. Su, X. He, L. Chen, Y. Zhang, Synthesis and evaluation of molecularly imprinted core-shell carbon nanotubes for the determination of triclosan in environmental water samples, J. Chromatogr. A 1217 (52) (2010) 8095–8102.
[81] F. Tan, D. Sun, J. Gao, Q. Zhao, X. Wang, F. Teng, X. Quan, J. Chen, Preparation of molecularly imprinted polymer nanoparticles for selective removal of fluoroquinolone antibiotics in aqueous solution, J. Hazard. Mater. 244 (2013) 750–757.
[82] L. Chen, X. Zhang, Y. Xu, X. Du, X. Sun, L. Sun, H. Wang, Q. Zhao, A. Yu, H. Zhang, L. Ding, Determination of fluoroquinolone antibiotics in environmental water samples based on magnetic molecularly imprinted polymer extraction followed by liquid chromatography-tandem mass spectrometry, Anal. Chim. Acta 662 (2010) 31–38.
[83] H. Chen, Y. Zhang, B. Gao, Y. Xu, Q. Zhao, J. Hou, J. Yan, G. Li, H. Wang, L. Ding, J. Ding, C. Zhao, Fast determination of sulfonamides and their acetylated metabolites from environmental water based on magnetic molecularly imprinted polymers, Environ. Sci. Pollut. R. 20 (12) (2013) 8567–8578.
[84] F. Chen, Y. Dong, Y. Zhao, Synthesis and characterization of photo-responsive magnetic molecularly imprinted microspheres for the detection of sulfonamides in aqueous solution, J. Sep. Sci. 39 (2016) 4866–4875.
[85] Y. Ji, J. Yin, Z. Xu, C. Zhao, H. Huang, H. Zhang, C. Wang, Preparation of magnetic molecularly imprinted polymer for rapid determination of bisphenol A in environmental water and milk samples, Anal. Bioanal. Chem. 395 (4) (2009) 1125–1133.
[86] W. Guo, W. Hu, J. Pan, H. Zhou, W. Guan, X. Wang, J. Dai, L. Xu, Selective adsorption and separation of BPA from aqueous solution using novel molecularly imprinted polymers based on kaolinite/Fe_3O_4 composites, Chem. Eng. J. 171 (2) (2011) 603–611.
[87] H. Tang, L. Zhu, C. Yu, X. Shen, Selective photocatalysis mediated by magnetic molecularly imprinted polymers, Sep. Purif. Technol. 95 (2012) 165–171.

[88] J.Q. Xue, D.W. Li, L.L. Qu, Y.T. Long, Surface-imprinted core-shell Au nanoparticles for selective detection of bisphenol A based on surface-enhanced raman scattering, Anal. Chim. Acta 777 (2013) 57–62.
[89] X. Xia, E.P.C. Lai, B. Örmeci, Duo-molecularly imprinted polymer coated magnetic particles for class-selective removal of endocrine disrupting compounds from aqueous environment, Environ. Sci. Pollut. Res. 20 (5) (2013) 3331–3339.
[90] K.S. Malihe, W.H. Syed, S.T. Mohammad, M. Ali, A.A. Parviz, Magnetite molecularly imprinted nanoparticles for selective detection of phenol in wastewater samples followed by high performance liquid chromatography, Indian J. Sci. Res. 5 (1) (2014) 362–368.
[91] F. Chen, J. Zhang, M. Wang, J. Kong, Magnetic molecularly imprinted polymers synthesized by surface-initiated reversible addition-fragmentation chain transfer polymerization for the enrichment and determination of synthetic estrogens in aqueous solution, J. Sep. Sci. 38 (2015) 2670–2676.
[92] R. Gao, X. Su, X. He, L. Chen, Y. Zhang, Preparation and characterisation of core-shell CNTs@ MIPs nanocomposites and selective removal of estrone from water samples, Talanta 83 (3) (2011) 757–764.
[93] W. Zhang, Y. Li, Q. Wang, C. Wang, P. Wang, K. Mao, Performance evaluation and application of surface-molecular-imprinted polymer-modified TiO_2 nanotubes for the removal of estrogenic chemicals from secondary effluents, Environ. Sci. Pollut. Res. 20 (3) (2013) 1431–1440.
[94] Z.K. Lin, Q.Y. He, L.T. Wang, et al., Preparation of magnetic multifunctional molecularly imprinted polymer beads for determining environmental estrogens in water samples, J. Hazard. Mater. 252 (2013) 57–63.
[95] W. Yang, F. Jiao, L. Zhou, X. Chen, X. Jiang, Molecularly imprinted polymers coated on multi-walled carbon nanotubes through a simple indirect method for the determination of 2, 4-dichlorophenoxyacetic acid in environmental water, Appl. Surf. Sci. 284 (2013) 692–699.
[96] B. Liu, M. Han, G. Guan, S. Wang, R. Liu, Z. Zhang, Highly-controllable molecular imprinting at superparamagnetic iron oxide nanoparticles for ultrafast enrichment and separation, J. Phys. Chem. C 115 (2011) 17320–17327.
[97] Y. Hu, R. Liu, Y. Zhang, G. Li, Improvement of extraction capability of magnetic molecularly imprinted polymer beads in aqueous media via dual-phase solvent system, Talanta 79 (2009) 576–582.
[98] X. Luo, Y. Zhan, Y. Huang, L. Yang, X. Tu, S. Luo, Removal of water-soluble acid dyes from water environment using a novel magnetic molecularly imprinted polymer, J. Hazard. Mater. 187 (1) (2011) 274–282.
[99] N. Khoddami, F. Shemirani, A new magnetic ion-imprinted polymer as a highly selective sorbent for determination of cobalt in biological and environmental samples, Talanta 146 (2016) 244–252.
[100] N.T. Tavengwa, E. Cukrowska, L. Chimuka, Preparation, characterization and application of $NaHCO_3$ leached bulk U(VI) imprinted polymers endowed with γ-MPS coated magnetite incontaminated water, J. Hazard. Mater. 267 (2014) 221–228.
[101] M. Zhang, Z. Zhang, Y. Liu, X. Yang, L. Luo, J. Chen, S. Yao, Preparation of core–shell magnetic ion-imprinted polymer for selective extraction of Pb(II) from environmental samples, Chem. Eng. J. 178 (2011) 443–450.
[102] X. Luo, S. Luo, Y. Zhan, H. Shu, Y. Huang, X. Tu, Novel Cu (II) magnetic ion imprinted materials prepared by surface imprinted technique combined with a sol-gel process, J. Hazard. Mater. 192 (2011) 949–955.
[103] D.-L. Huang, R.-Z. Wang, Y.-G. Liu, G.-M. Zeng, C. Lai, P. Xu, B.-A. Lu, J.-J. Xu, C. Wang, C. Huang, Application of molecularly imprinted polymers in wastewater treatment: a review, Environ. Sci. Pollut. Res. Int. 22 (2014) 963–977.
[104] X. Shen, L. Zhu, N. Wang, L. Ye, H. Tang, Molecular imprinting for removing highly toxic organic pollutants, Chem. Commun. 48 (2012) 788–798.
[105] C. He, Y. Long, J. Pan, K. Li, F. Liu, A method for coating colloidal particles with molecularly imprinted silica films, J. Mater. Chem. 18 (24) (2008) 2849–2854.
[106] X. Shen, L. Zhu, C. Huang, H. Tang, Z. Yu, F. Deng, Inorganic molecular imprinted titanium dioxide photocatalyst: synthesis, characterization and its application for efficient and selective degradation of phthalate esters, J. Mater. Chem. 19 (2009) 4843–4851.

[107] F. Wei, X. Liu, M. Zhai, Z. Cai, G. Xu, J. Yang, S. Du, Q. Hu, Molecularly imprinted nanosilica solid-phase extraction for bisphenol A in fish samples, Food Anal. Methods 6 (2) (2013) 415–420.
[108] S. Xu, H. Lu, L. Chen, X. Wang, Molecularly imprinted TiO_2 hybridized magnetic Fe_3O_4 nanoparticles for selective photocatalytic degradation and removal of estrone, RSC Adv. 4 (2014) 45266–45274.
[109] H. Liu, D. Liu, G. Fang, F. Liu, C. Liu, Y. Yang, S. Wang, A novel dual-function molecularly imprinted polymer on CdTe/ZnS quantum dots for highly selective and sensitive determination of ractopamine, Anal. Chim. Acta 762 (2013) 76–82.
[110] G.A.F. Van Tilborg, W.J.M. Mulder, P.T.K. Chin, G. Storm, C.P. Reutelingsperger, K. Nicolay, G.J. Strijkers, Annexin A5-conjugated quantum dots with a paramagnetic lipidic coating for the multimodal detection of apoptotic cells, Bioconjug. Chem. 17 (4) (2006) 865–868.
[111] J. Liu, H. Chen, Z. Lin, J.-M. Lin, Preparation of surface imprinting polymer capped Mn-doped ZnS quantum dots and their application for chemiluminescence detection of 4-nitrophenol in tap water, Anal. Chem. 82 (2010) 7380–7386.
[112] Y. Zhao, Y. Ma, H. Li, L. Wang, Composite QDs@MIP nanospheres for specific recognition and direct fluorescent quantification of pesticides in aqueous media, Anal. Chem. 84 (1) (2011) 86–395.
[113] H.-F. Wang, Y. He, T.-R. Ji, X.-P. Yan, Surface molecular imprinting on Mn-doped ZnS quantum dots for room-temperature phosphorescence optosensing of pentachlorophenol in water, Anal. Chem. 81 (2009) 1615–1621.
[114] O. Brüggemann, Catalytically active polymers obtained by molecular imprinting and their application in chemical reaction engineering, Biomol. Eng. 18 (1) (2001) 1–7.
[115] M. Resmini, Molecularly imprinted polymers as biomimetic catalysts, Anal. Bioanal. Chem. 402 (10) (2012) 3021–3026.
[116] D. Sharabi, Y. Paz, Preferential photodegradation of contaminants by molecular imprinting on titanium dioxide, Appl. Catal. Environ. 95 (1) (2010) 169–178.
[117] W. Sun, R. Tan, W. Zheng, D. Yin, Molecularly imprinted polymer containing Fe(III) catalysts for specific substrate recognition, Chin. J. Catal. 34 (2013) 1589–1598.
[118] W. Chen, D.K. Han, K.D. Ahn, Molecularly imprinted polymers having amidine and imidazole functional groups as an enzyme mimetic catalyst for ester hydrolysis, Macromol. Res. 10 (2) (2002) 122–126.
[119] X. Shen, L. Zhu, G. Liu, H. Yu, H. Tang, Enhanced photocatalytic degradation and selective removal of nitrophenols by using surface molecular imprinted titania, Environ. Sci. Technol. 42 (5) (2008) 1687–1692.
[120] D. Robert, A. Piscopo, J.V. Weber, Selective solar photodegradation of organopollutant mixtures in water, Sol. Energy 77 (2004) 553–558.
[121] S. Sampath, H. Uchida, H. Honeyama, Photocatalytic degradation of gaseous pyridine over zeolite-supported titanium dioxide, J. Catal. 149 (1994) 189–194.
[122] H. Uchida, S. Itoh, H. Yoneyama, Photocatalytic decomposition of propyzamide using TiO_2 supported on activated carbon, Chem. Lett. 22 (12) (1993) 1995–1998.
[123] S. Ghosh-Mukerji, H. Haick, M. Schvartzman, Y. Paz, Selective photocatalysis by means of molecular recognition, J. Am. Chem. Soc. 123 (2001) 10776–10777.
[124] X. Shen, L. Zhu, J. Li, H. Tang, Synthesis of molecular imprinted polymer coated photocatalysts with high selectivity, Chem. Commun. 11 (2007) 1163–1165.
[125] X. Shen, L. Zhu, G. Liu, H. Tang, S. Liu, W. Li, Photocatalytic removal of pentachlorophenol by means of an enzyme-like molecular imprinted photocatalyst and inhibition of the generation of highly toxic intermediates, New J. Chem. 33 (2009) 2278–2285.
[126] X. Shen, L. Zhu, H. Yu, H. Tang, S. Liu, W. Li, Selective photocatalysis on molecular imprinted TiO_2 thin films prepared via an improved liquid phase deposition method, New J. Chem. 33 (2009) 1673–1679.
[127] Y. Liu, R. Liu, C. Liu, S. Luo, L. Yang, F. Sui, Y. Teng, R. Yang, Q. Cai, Enhanced photocatalysis on TiO_2 nanotube arrays modified with molecularly imprinted TiO_2 thin film, J. Hazard. Mater. 182 (2010) 912–918.
[128] Y. Shiraishi, T. Suzuki, T. Hirai, Selective photooxidation of chlorophenols with molecularly imprinted polymers containing a photosensitizer, New J. Chem. 34 (2010) 714–717.

[129] Y. Tominaga, T. Kubo, K. Hosoya, Surface modification of TiO_2 for selective photodegradation of toxic compounds, Cat. Com. 12 (2011) 785–789.
[130] M.Q. He, L.L. Bao, K.Y. Sun, D.X. Zhao, W.B. Li, J.X. Xia, H.M. Li, Synthesis of molecularly imprinted polypyrrole/titanium dioxide nanocomposites and its selective photocatalytic degradation of rhodamine B under visible light irradiation, eXPRESS Polym. Lett. 8 (11) (2014) 850–861.
[131] J. Yang, S. Li, Y. Gong, C. He, Q. Zhang, J. Wu, W. Liao, D. Shu, S. Tian, Preferential catalytic ozonation of p-nitrophenol by molecularly imprinted Fe_3O_4/SiO_2 core-shell magnetic composites, Water Sci. Technol. 69 (1) (2014) 170–176.
[132] M. Zhu, S. Wang, S. Li, Titanium catalyst with the molecular imprinting of substrate for selective photocatalysis, J. Chinese Adv. Mater. Soc. 2 (2) (2014) 71–81.
[133] R. Liu, F. Feng, G. Chen, Z. Liu, Z. Xu, Barbell-shaped stir bar sorptive extraction using dummy template molecularly imprinted polymer coatings for analysis of bisphenol A in water, Anal. Bioanal. Chem. 408 (2016) 5329–5335.
[134] I. González-Mariño, J.B. Quintana, I. Rodríguez, R. Rodil, J. González-Penas, R. Cela, Comparison of molecularly imprinted, mixed-mode and hydrophilic balance sorbents performance in the solid-phase extraction of amphetamine drugs from wastewater samples for liquid chromatography-tandem mass spectrometry determination, J. Chromatogr. A 1216 (2009) 8435–8441.
[135] C. Dai, S. Geissen, Y. Zhang, Y. Zhang, X. Zhou, Performance evaluation and application of molecularly imprinted polymer for separation of carbamazepine in aqueous solution, J. Hazard. Mater. 184 (2010) 156–163.
[136] J. Yin, Z. Meng, M. Du, C. Liu, M. Song, H. Wang, Pseudo-template molecularly imprinted polymer for selective screening of trace-lactam antibiotics in river and tap water, J. Chromatogr. A 1217 (2010) 5420–5426.
[137] A.H. El-Sheikh, R.W. Al-Quse, M.I. El-Barghouthi, F.S. Al-Masri, Derivatization of 2-chlorophenol with 4-amino-anti-pyrine: a novel method for improving the selectivity of molecularly imprinted solid phase extraction of 2-chlorophenol from water, Talanta 83 (2010) 667–673.
[138] C. Dai, X. Zhou, Y. Zhang, S. Liu, J. Zhang, Synthesis by precipitation polymerization of molecularly imprinted polymer for the selective extraction of diclofenac from water samples, J. Hazard. Mater. 198 (2011) 175–181.
[139] A. Prieto, S. Schrader, C. Bauer, M. Möder, Synthesis of a molecularly imprinted polymer and its application for microextraction by packed sorbent for the determination of fluoroquinolone related compounds in water, Anal. Chim. Acta 685 (2011) 146–152.
[140] X. Shen, C. Xu, L. Ye, Imprinted polymer beads enabling direct and selective molecular separation in water, Soft Matter 8 (2012) 7169–7176.
[141] N. Gilart, R.-M. Marcé, N. Fontanals, F. Borrull, A rapid determination of acidic pharmaceuticals in environmental waters by molecularly imprinted solid-phase extraction coupled to tandem mass spectrometry without chromatography, Talanta 110 (2013) 196–201.
[142] L.C.C. Abrao, P.P. Maia, E.C. Figueiredo, Determination of tetracyclines by solid-phase extraction with a molecularly imprinted polymer and high-performance liquid chromatography, Anal. Lett. 47 (2014) 2183–2194.
[143] V. Manzo, K. Ulisse, I. Rodríguez, E. Pereira, P. Richter, A molecularly imprinted polymer as the sorptive phase immobilized in a rotating disk extraction device for the determination of diclofenac and mefenamic acid in wastewater, Anal. Chim. Acta 889 (2015) 130–137.
[144] D.G. Gour, R.J. Krupadam, Molecularly imprinted polymer for detection of endocrine disrupting chemical epinephrine in drinking water and biological buffers, Indian J. Chem. 54 (2015) 1051–1056.
[145] L.M. Madikizela, L. Chimuka, Determination of ibuprofen, naproxen and diclofenac in aqueous samples using a multi-template molecularly imprinted polymer as selective adsorbent for solid-phase extraction, J. Pharm. Biomed. Anal. 128 (2016) 210–215.

[146] L.M. Madikizela, L. Chimuka, Occurrence of naproxen, ibuprofen, and diclofenac residues in wastewater and river water of KwaZulu-Natal Province in South Africa, Environ. Monit. Assess. 189 (2017) 348–359.
[147] S.S. Zunngu, L.M. Madikizela, L. Chimuka, P.S. Mdluli, Synthesis and application of a molecularly imprinted polymer in the solid-phase extraction of ketoprofen from wastewater, C. R. Chim. 20 (2017) 585–591.
[148] J. Ou, L. Hu, L. Hu, X. Li, H. Zou, Determination of phenolic compounds in river water with on-line coupling bisphenol A imprinted monolithic precolumn with high performance liquid chromatography, Talanta 69 (2006) 1001–1006.
[149] C. Baggiani, P. Baravalle, C. Giovannoli, L. Anfossi, G. Giraudi, Molecularly imprinted polymer/cryogel composites for solid-phase extraction of bisphenol A from river water and wine, Anal. Bioanal. Chem. 397 (2010) 815–822.
[150] W. Zhao, N. Sheng, R. Zhu, F. Wei, Z. Cai, M. Zhai, S. Du, Q. Hu, Preparation of dummy template imprinted polymers at surface of silica microparticles for the selective extraction of trace bisphenol A from water samples, J. Hazard. Mater. 179 (2010) 223–229.
[151] A. Beltran, R.M. Marcé, P.A.G. Cormack, F. Borrull, Synthetic approaches to parabens molecularly imprinted polymers and their applications to the solid-phase extraction of river water samples, Anal. Chim. Acta 677 (2010) 72–78.
[152] P. Qi, J. Wang, Y. Li, F. Su, J. Jin, J. Chen, Molecularly imprinted solid-phase extraction coupled with HPLC for the selective determination of monobutyl phthalate in bottled water, J. Sep. Sci. 34 (2011) 2712–2718.
[153] Y.M. Yin, Y.P. Chen, X.F. Wang, Y. Liu, H.L. Liu, M.X. Xie, Dummy molecularly imprinted polymers on silica particles for selective solid-phase extraction of tetrabromobisphenol A from water samples, J. Chromatogr. A 1220 (2012) 7–13.
[154] Z. Lin, W. Cheng, Y. Li, Z. Liu, X. Chen, C. Huang, A novel superparamagnetic surface molecularly imprinted nanoparticle adopting dummy template: an efficient solid-phase extraction adsorbent for bisphenol A, Anal. Chim. Acta 720 (2012) 71–76.
[155] M. Zarejousheghani, M. Möder, H. Borsdorf, A new strategy for synthesis of an in-tube molecularly imprintedpolymer-solid phase microextraction device: selective off-line extraction of 4-nitrophenol as an example of priority pollutants from environmental water samples, Anal. Chim. Acta 798 (2013) 48–55.
[156] M. Lopez-Nogueroles, S. Lordel-Madeleine, A. Chisvert, A. Salvador, V. Pichon, Development of a selective solid phase extraction method for nitro musk compounds in environmental waters using a molecularly imprinted sorbent, Talanta 110 (2013) 128–134.
[157] M.Á. Lorenzo, A. Sánchez Arribas, M. Moreno, E. Bermejo, M. Chicharro, A. Zapardiel, Determination of butylparaben by adsorptives tripping voltammetry at glassy carbon electrodes modified with multi-wall carbon nanotubes, Microchem. J. 110 (2013) 510–516.
[158] T. Jing, Y. Zhou, W. Wu, M. Liu, Y. Zhou, S. Mei, Molecularly imprinted spin column extraction coupled with high-performance liquid chromatography for the selective and simple determination of trace nitrophenols in water samples, J. Sep. Sci. 37 (2014) 2940–2946.
[159] H. Sun, Y. Li, C. Huang, J. Peng, J. Yang, X. Sun, S. Zang, J. Chen, X. Zhang, Solid-phase extraction based on a molecularly imprinted polymer for the selective determination of four benzophenones in tap and river water, J. Sep. Sci. 38 (2015) 3412–3420.
[160] H. Surikumaran, S. Mohamad, N.M. Sarih, M. Raoov, β-Cyclodextrin based molecularly imprinted solid phase extraction for class selective extraction of priority phenols in water samples, Sep. Sci. Technol. 50 (2015) 2342–2351.
[161] A. Poliwoda, M. Mościpan, P.P. Wieczorek, Application of molecular imprinted polymers for selective solid phase extraction of bisphenol A, Ecol. Chem. Eng. S. 2 (2016) 651–664.
[162] M.C. Barciela-Alonso, N. Otero-Lavandeira, P. Bermejo-Barrera, Solid phase extraction using molecular imprinted polymers for phthalate determination in water and wine samples by HPLC-ESI-MS, Microchem. J. 132 (2017) 233–237.

[163] H. Sambe, K. Hoshina, J. Haginaka, Molecularly imprinted polymers for triazine herbicides prepared by multi-step swelling and polymerization method and their application to the determination of methylthiotriazine herbicides in river water, J. Chromatogr. A 1152 (2007) 130–137.
[164] C. Cacho, E. Turiel, C. Pirez-Conde, Molecularly imprinted polymers: an analytical tool for the determination of benzimidazole compounds in water samples, Talanta 78 (2009) 1029–1035.
[165] D. Djozan, M. Mahkam, B. Ebrahimi, Preparation and binding study of solid-phase microextraction fiber on the basis of ametryn-imprinted polymer application to the selective extraction of persistent triazine herbicides in tap water, rice, maize and onion, J. Chromatogr. A 1216 (2009) 2211–2219.
[166] L. He, Y. Su, X. Shen, Y. Zheng, H. Guo, Z. Zeng, Solid-phase extraction of melamine from aqueous samples using water-compatible molecularly imprinted polymers, J. Sep. Sci. 32 (2009) 3310–3318.
[167] F. Barahona, E. Turiel, A. Martνn-Esteban, Supported liquid membrane-protected molecularly imprinted fibre for solid-phase microextraction of thiabendazole, Anal. Chim. Acta 694 (2011) 83–89.
[168] H. Wang, H. Yan, M. Qiu, J. Qiao, G. Yang, Determination of dicofol in aquatic products using molecularly imprinted solid-phase extraction coupled with GC-ECD detection, Talanta 85 (2011) 2100–2105.
[169] X. Shi, J. Liu, A. Sun, D. Li, J. Chen, Group-selective enrichment and determination of pyrethroid insecticides in aquaculture seawater via molecularly imprinted solid phase extraction coupled with gas chromatography-electron capture detection, J. Chromatogr. A 1227 (2012) 60–66.
[170] M. Zarejousheghani, P. Fiedler, M. Möder, H. Borsdorf, Selective mixed-bed solid phase extraction of atrazine herbicide from environmental water samples using molecularly imprinted polymer, Talanta 129 (2014) 132–138.
[171] S. Xu, H. Lu, L. Chen, Double water compatible molecularly imprinted polymers applied as solid-phase extraction sorbent for selective preconcentration and determination of triazines in complicated water samples, J. Chromatogr. A 1350 (2014) 23–29.
[172] S. Asir, A. Derazshamshir, F. Yilmaz, A. Denizli, Triazine herbicide imprinted monolithic column for capillary electrochromatography, Electrophoresis 36 (2015) 2888–2895.
[173] M. Saraji, N. Mehrafza, A simple approach for the preparation of simazine molecularly imprinted nanofibers via self-polycondensation for selective solid phase microextraction, Anal. Chim. Acta 936 (2016) 108–115.
[174] W. Ji, R. Sun, W. Duan, X. Wang, T. Wang, Y. Mu, L. Guo, Selective solid phase extraction of chloroacetamide herbicides from environmental water samples by amphiphilic magnetic molecularly imprinted polymers, Talanta 170 (2017) 111–118.
[175] M.D. Celiz, D.S. Aga, L.A. Colón, Evaluation of a molecularly imprinted polymer for the isolation/enrichment of β-estradiol, Microchem. J. 92 (2009) 174–179.
[176] P. Lucci, O. Nuñez, M.T. Galceran, Solid-phase extraction using molecularly imprinted polymer for selective extraction of natural and synthetic estrogens from aqueous samples, J. Chromatogr. A 1218 (2011) 4828–4833.
[177] Z. Jing, X.L. Chao, C. Li, X.Z. Xiang, Q.X. Guang, S.J. Ming, Separation and determination of trace environmental estrogen through molecularly imprinted solid phase extraction coupled to high performance liquid chromatography, J. Environ. Sci. Health, A Toxic/Hazard. Subst. Environ. Eng. 47 (2012) 1889–1896.
[178] X. Luo, Y. Zhan, X. Tu, Y. Huang, S. Luo, L. Yan, Novel molecularly imprinted polymer using 1-(α-methyl acrylate)-3-methylimidazolium bromide as functional monomer for simultaneous extraction and determination of water-soluble acid dyes in wastewater and soft drink by solid phase extraction and high performance liquid chromatography, J. Chromatogr. A 1218 (2011) 1115–1121.
[179] Z. Lian, J. Wang, Determination of crystal violet in seawater and seafood samples through off-line molecularly imprinted SPE followed by HPLC with diode-array detection, J. Sep. Sci. 36 (2013) 980–985.
[180] N. Arabzadeh, A. Khosravi, A. Mohammadi, N.M. Mahmoodi, M. Khorasani, Synthesis, characterization, and application of nanomolecularly imprinted polymer for fast solid-phase extraction of tartrazine from water environment, Desalin. Water Treat. 54 (2014) 1–9.

[181] M. Khajeh, S.A. Moghaddam, M. Bohlooli, M. Ghaffari-Moghaddam, Application of the artificial neural network and imperialist competitive algorithm for optimization of molecularly imprinted solid phase extraction of methylene blue, e-Polymers 16 (2016) 243–253.
[182] M. Villar-Navarro, M.J. Martín-Valero, R.M. Fernández-Torres, M. Callejón-Mochón, M. Á. Bello-López, Easy, fast and environmental friendly method for the simultaneous extraction of the 16 EPA PAHs using magnetic molecular imprinted polymers (mag-MIPs), J. Chromatogr. B 1044-1045 (2017) 63–69.
[183] V. Kochkodan, N. Hilal, V. Melnik, O. Kochkodan, A. Remizovska, The express monitoring of organic pollutants in water with composite imprinted membranes, J. Membr. Sci. 377 (2011) 151–158.
[184] V. Kochkodan, N. Hilal, V. Melnik, O. Kochkodan, O. Vasilenko, Selective recognition of organic pollutants in aqueous solutions with composite imprinted membranes, Adv. Colloid Interface Sci. 159 (2010) 180–188.
[185] N. Atar, T. Eren, M.L. Yola, S. Wang, A sensitive molecular imprinted surface plasmon resonance nanosensor for selective determination of trace triclosan in wastewater, Sens. Actuators B 216 (2015) 638–644.
[186] Z. Altintas, A. Guerreiro, S.A. Piletsky, I.E. Tothill, NanoMIP based optical sensor for pharmaceuticals monitoring, Sens. Actuators B 213 (2015) 305–313.
[187] Z. Altintas, B. France, J.O. Ortiz, I.E. Tothill, Computationally modelled receptors for drug monitoring using anoptical based biomimetic SPR sensor, Sens. Actuators B 224 (2016) 726–737.
[188] K. Graniczkowska, M. Pütz, F.M. Hauser, S. De Saeger, N.V. Beloglazova, Capacitive sensing of N-formylamphetamine based on immobilized molecular imprinted polymers, Biosens. Bioelectron. 92 (2017) 741–747.
[189] K. Hegnerova, J. Homola, Surface plasmon resonance sensor for detection of bisphenol A in drinking water, Sens. Actuators B 151 (2010) 177–179.
[190] J. Huang, X. Zhang, S. Liu, Q. Lin, X. He, X. Xing, W. Lian, D. Tang, Development of molecularly imprinted electrochemical sensor with titanium oxide and gold nanomaterials enhanced technique for determination of 4-nonylphenol, Sens. Actuators B 152 (2011) 292–298.
[191] C. Yu, L. Gou, X. Zhou, N. Bao, H. Gu, Chitosan-Fe_3O_4 nanocomposite based electrochemical sensors for the determination of bisphenol A, Electrochim. Acta 56 (2011) 9056–9063.
[192] Y.-P. Chen, D.-N. Wang, Y.-M. Yin, L.-Y. Wang, X.-F. Wang, M.-X. Xie, Quantum dots capped with dummy molecularly imprinted film as luminescent sensor for the determination of tetrabromobisphenol A in water and soils, J. Agric. Food Chem. 60 (2012) 10472–10479.
[193] G. Xu, L. Yang, M. Zhong, C. Li, X. Lu, X. Kan, Selective recognition and electrochemical detection of p-nitrophenol based on a macroporous imprinted polymer containing gold nanoparticles, Microchim. Acta 180 (2013) 1461–1469.
[194] R. Wang, K. Yan, F. Wang, J. Zhang, A highly sensitive photoelectrochemical sensor for 4-aminophenol based on CdS-graphene nanocomposites and molecularly imprinted polypyrrole, Electrochim. Acta 121 (2014) 102–108.
[195] Y. Zhou, Z. Qu, Y. Zeng, T. Zhou, G. Shi, A novel composite of graphene quantum dots and molecularly imprinted polymer for fluorescent detection of paranitrophenol, Biosens. Bioelectron. 52 (2014) 317–323.
[196] J. Luo, J. Cong, J. Liu, Y. Gao, X. Liu, A facile approach for synthesizing molecularly imprinted graphene for ultrasensitive and selective electrochemical detecting 4-nitrophenol, Anal. Chim. Acta 864 (2015) 74–84.
[197] H. Shaikh, G. Sener, N. Memon, M.I. Bhanger, S.M. Nizamani, R. Uzek, A. Denizli, Molecularly imprinted surface plasmon resonance (SPR) based sensing of bisphenol A for its selective detection in aqueous systems, Anal. Methods 7 (2015) 4661–4670.
[198] Z. Guo, A. Florea, C. Cristea, F. Bessueille, F. Vocanson, F. Goutaland, A. Zhang, R. Săndulescu, F. Lagardea, N. Jaffrezic-Renaulta, 1,3,5-Trinitrotoluene detection by a molecularly imprinted polymer sensor based on electropolymerization of a microporous-metal-organic framework, Sens. Actuators B 207 (2015) 960–966.

[199] X. Wu, Z. Zhang, J. Lib, H. Youa, Y. Li, L. Chen, Molecularly imprinted polymers-coated gold nanoclusters for fluorescent detection of bisphenol A, Sens. Actuators B 211 (2015) 507–514.
[200] T. Yao, X. Gua, T. Li, J. Li, J. Li, Z. Zhao, J. Wang, Y. Qin, Y. She, Enhancement of surface plasmon resonance signals using a MIP/GNPs/rGO nano-hybrid film for the rapid detection of ractopamine, Biosens. Bioelectron. 7 (2016) 596–600.
[201] Q. Kong, Y. Wang, L. Zhang, S. Ge, J. Yu, A novel microfluidic paper-based colorimetric sensor based on molecularly imprinted polymer membranes for highly selective and sensitive detection of bisphenol A, Sens. Actuators B 243 (2017) 130–136.
[202] S. Kroger, A.P.F. Turner, K. Mosbach, K. Haupt, Imprinted polymer-based sensor system for herbicides using differential-pulse voltammetry on screen-printed electrodes, Anal. Chem. 71 (1999) 3698–3702.
[203] M.K.P. Leung, C.-F. Chow, M.H.W. Lam, A sol-gel derived molecular imprinted luminescent PET sensing material for 2,4-dichlorophenoxyacetic acid, J. Mater. Chem. 11 (2001) 2985–2991.
[204] K. Prasad, K.P. Prathish, J.M. Gladis, G.R.K. Naidu, T.P. Rao, Molecularly imprinted polymer (biomimetic) based potentiometric sensor for atrazine, Sens. Actuators B 123 (2007) 65–70.
[205] A. Gomez-Caballero, N. Unceta, M. Aranzazu Goicolea, R.J. Barrio, Evaluation of the selective detection of 4,6-dinitro-o-cresol by a molecularly imprinted polymer based microsensor electrosynthesized in a semi-organic media, Sens. Actuators B 130 (2008) 713–722.
[206] G. Lin, Y. Wang, G. Li, W. Bai, H. Zhang, S. Wang, Construction and application of molecularly imprinted film sensor on determination of chlorpyrifos in water, Adv. Mat. Res. 936 (2014) 843–849.
[207] C. Liu, Z. Song, J. Pan, Y. Yan, Z. Cao, X. Wei, L. Gao, J. Wang, J. Dai, M. Meng, P. Yu, A simple and sensitive surface molecularly imprinted polymers based fluorescence sensor for detection of λ-cyhalothrin, Talanta 125 (2014) 14–23.
[208] V.K. Gupta, M.L. Yola, T. Eren, N. Atar, Selective QCM sensor based on atrazine imprinted polymer: its application to wastewater sample, Sens. Actuators B 218 (2015) 215–221.
[209] X. Ren, L. Chen, Quantum dots coated with molecularly imprinted polymer as fluorescence probe for detection of cyphenothrin, Biosens. Bioelectron. 64 (2015) 182–188.
[210] M.H. Do, A. Florea, C. Farre, A. Bonhomme, F. Bessueille, F. Vocanson, N.-T. Tran-Thi, N. Jaffrezic-Renault, Molecularly imprinted polymer-based electrochemical sensor for the sensitive detection of glyphosate herbicide, Int. J. Environ. Anal. Chem. 95 (15) (2015) 1489–1501.
[211] X. Wang, J. Yu, X. Wu, J. Fu, Q. Kang, D. Shen, J. Li, L. Chen, A molecular imprinting-based turn-on Ratiometric fluorescence sensor for highly selective and sensitive detection of 2,4-dichlorophenoxyacetic acid (2,4-D), Biosens. Bioelectron. 81 (2016) 438–444.
[212] M. Amjadi, R. Jalili, Molecularly imprinted mesoporous silica embedded with carbon dots and semiconductor quantum dots as a ratiometric fluorescent sensor for diniconazole, Biosens. Bioelectron. 96 (2017) 121–126.
[213] N.A. Martnínez, R.J. Schneider, G.A. Messina, J. Raba, Modified paramagnetic beads in a microfluidic system for the determination of ethinylestradiol (EE2) in river water samples, Biosens. Bioelectron. 25 (2010) 1376–1381.
[214] L. Yuan, J. Zhang, P. Zhou, J. Chen, R. Wang, T. Wen, Y. Li, X. Zhou, H. Jiang, Electrochemical sensor based on molecularly imprinted membranes at platinum nanoparticles-modified electrode for determination of 17β-estradiol, Biosens. Bioelectron. 29 (2011) 29–33.
[215] A. Florea, C. Cristea, F. Vocanson, R. Săndulescu, N. Jaffrezic-Renault, Electrochemical sensor for the detection of estradiol based on electropolymerized molecularly imprinted polythioaniline film with signal amplification using gold nanoparticles, Electrochem. Commun. 59 (2015) 36–39.
[216] K.P. Prathish, K. Prasad, T.P. Rao, M.V.S. Suryanarayana, Molecularly imprinted polymer-based potentiometric sensor for degradation product of chemical warfare agents Part I. Methylphosphonic acid, Talanta 71 (2007) 1976–1980.

[217] C. Warwick, A. Guerreiro, A. Gomez-Caballero, E. Wood, J. Kitson, J. Robinson, A. Soares, Conductance based sensing and analysis of soluble phosphates in wastewater, Biosens. Bioelectron. 52 (2014) 173–179.
[218] C. Warwick, A. Guerreiro, E. Wood, J. Kitson, J. Robinson, A. Soares, A molecular imprinted polymer based sensor for measuring phosphate in wastewater samples, Water Sci. Technol. 69 (2014) 48–54.
[219] R. Suedee, W. Intakong, F.L. Dickert, The use of trichloroacetic acid imprinted polymer coated quartz crystal microbalance as a screening method for determination of haloacetic acids in drinking water, Talanta 70 (2006) 194–201.
[220] Z. Liu, S. Huan, J. Jiang, G. Shen, R. Yu, Molecularly imprinted TiO_2 thin film using stable ground-state complex as template as applied to selective electrochemical determination of mercury, Talanta 68 (2006) 1120–1125.
[221] A. Afkhami, T. Madrakian, M. Soltani-Shahrivar, M. Ahmadi, H. Ghaedi, Selective and sensitive electrochemical determination of trace amounts of mercury ion in some real samples using an ion imprinted polymer nano-modifier, J. Electrochem. Soc. 163 (2016) B68–B75.
[222] K. Huang, Y. Chen, F. Zhou, X. Zhao, J. Liu, S. Mei, Y. Zhou, T. Jing, Integrated ion imprinted polymers-paper composites for selective and sensitive detection of Cd(II) ions, J. Hazard. Mater. 333 (2017) 137–143.
[223] I. Chianella, S.A. Piletsky, I.E. Tothill, B. Chen, A.P.F. Turner, MIP-based solid phase extraction cartridges combined with MIP based sensors for the detection of microcystin-LR, Biosens. Bioelectron. 18 (2003) 119–127.
[224] Z. Altintas, M. Gittens, A. Guerreiro, K.-A. Thompson, J. Walker, S. Piletsky, I.E. Tothill, Detection of waterborne viruses using high affinity molecularly imprinted polymers, Anal. Chem. 87 (2015) 6801–6807.
[225] M.J. Abdin, Z. Altintas, I.E. Tothill, In silico designed nanoMIP based optical sensor for endotoxins monitoring, Biosens. Bioelectron. 67 (2015) 177–183.
[226] Z. Altintas, J. Pocock, K.-A. Thompson, I.E. Tothill, Comparative investigations for adenovirus recognition and quantification: plastic or natural antibodies? Biosens. Bioelectron. 74 (2015) 996–1004.
[227] Z. Altintas, M.J. Abdin, A.M. Tothill, K. Karim, I.E. Tothill, Ultrasensitive detection of endotoxins using computationally designed nanoMIPs, Anal. Chim. Acta 935 (2016) 239–248.
[228] C. Alvarez-Lorenzo, A. Concheiro, Handbook of Molecularly Imprinted Polymers, A Smithers Group Company, Shropshire, UK, 2013.
[229] K. Haupt, Preface. Topics in Current Chemistry. Molecular Imprinting, Springer-Verlag, Berlin/Heidelberg, 2011, pp. ix–xi.

CHAPTER

NANOSCALE MATERIALS IN WATER PURIFICATION

8

Irene Bonadies

Institute of Polymers, Composites and Biomaterials, National Research Council of Italy, Pozzuoli, Italy

1 INTRODUCTION

Electrospinning is one of the simplest, user-friendly, and versatile process for making fibers with diameters ranging from micrometers to nanometers. This technology produces nanofibers from polymer solutions, or melts, through the extreme elongation and narrowing of the polymeric jet occurring because of electrostatic repulsion. Over the past decades, electrospinning technology has drawn great attention because of its convenience in obtaining polymer nanofibers mats. The electrospinning technique offers several advantages respect other fiber production techniques: comparatively low cost with relatively high production rate, the possibility of producing nanofibers starting from different materials, and the unique ability to obtain various fibrous assemblies and morphologies such as porous and core-shell fibers by simply changing the equipment setup [1]. Furthermore, one unique feature in electrospinning is the capability of controlling the fiber diameter by varying the processing variable(s), such as solution concentration, applied voltage, fluid flow rate, surface tension, and so on [2].

Nonwoven mats produced in this way are characterized by large specific surface area, high porosity, and small pore size that make them appropriate for many potential applications, including high-efficiency filter media, chemical and biological sensors, solar and fuel cells, or in biomedical applications [3]. The electrospun nonwoven mat can work as a functional layer to modify the surface of a solid substrate, for example, to alter the surface properties of filtering paper [4], or it can also be used as a self-supporting nonwoven mat, especially as a template for tissue engineering [5]. Investigations into the potential of electrospun nanofibers for liquid filtration have mainly focused on their use as membranes where the particle-retaining effect takes place almost entirely at the surface.

The highly interconnected porosity of nonwoven three-dimensional structures and the possibility of fine-tuning the porosity via electrospinning process parameters are intriguing characteristics for fluid filtration devices and strongly affect their filtration performance. In fact, this characteristic pore structure determines the diffusion of gas and liquid through the fibers (flux) and the ability to keep the filter in operation (degree of fouling) and thus the filter effectiveness. Experimental results revealed the typical broad distribution of pore diameters >100 nm; however, the pore diameter can be significantly modified by controlling the overall porosity through the orientation and compactness of the nonwoven structure [6]. The effects of fiber diameter, membrane porosity, and membrane thickness on microfiltration performance were explored in a systematic and well-controlled manner by using

Nanoscale Materials in Water Purification. https://doi.org/10.1016/B978-0-12-813926-4.00013-6

polyacrylonitrile (PAN) as a model polymer. The study revealed that membrane porosity and fiber diameter have significant impacts on the equivalent/apparent pore size, which directly relates to microfiltration performance, while the membrane thickness does not appear to affect the equivalent/apparent pore size [7]. Thanks to the previously mentioned characteristics, pores cannot be entirely blocked by particles that have penetrated the membrane, so it is possible to overcome the intrinsic limitations of membrane manufactured by conventional methods, for example, low flux and high-fouling performance [8, 9]. Consequently, electrospun nanofiber membranes are promising as an innovative microfiltration method and even potentially as ultrafiltration media with high performances [7–10].

In addition, the electrospinning technique provides the possibility of functionalizing nanofibers with chemical or biological functionalities, thus tailoring the properties of membranes according to the application field, as described in the last paragraph [11, 12]. In this way it is possible to realize affinity membranes that operate not only through the sieving mechanism but also via selective separation thanks to the presence of specific ligands on membrane surface able to "capture" molecules.

It is noticeable that the electrospinning process permits realizing high-tailored nanoengineered membranes for a specific cleanup application, thus widening the possible future application fields and accelerating the cleanup process.

2 PROCESSING: FUNDAMENTAL ASPECTS AND PARAMETERS INVESTIGATION

The formal origin of electrospinning can be dated to the last century when in 1934 Anton Formhals patented the experimental apparatus for the practical production of filaments using an electrical field. Later on, a series of patents were issued that focused on improvements and modifications of the electrospinning apparatus. Formhals's spinning equipment consisted of a saw-toothed rotating disc immersed in a solution as a nozzle and a rotating disc as a collector. After that, in the 1964 Geoffrey Ingram Taylor described electrospinning from a theoretical point of view by mathematically modeling the shape of the cone formed by the fluid droplet under the effect of an electric field. In the 1990s academia picked up electrospinning, probably because of a surging interest in nanotechnology, and several research groups, notably the Reneker's group, revived electrospinning by demonstrating the fabrication of ultra-thin fibers from various polymers [13].

Since then, fiber production using electrostatic forces has invoked glare and attention due to its potential to form nanosized fibers. The possibility of obtaining electrospun fibers in the range from the micro- to nanoscale for producing three-dimensional structures characterized by small pore sizes have attracted the attention of researchers in the development of advanced materials for sophisticated applications. Therefore, various groups have conducted simultaneous studies to understand the electrospinning process and to correlate the physical-chemical properties and morphology of nanofibers as a function of process parameters and material characteristics [14–16]. The number of publications and patents about electrospinning has been increasing exponentially every year, and today electrospun nanofibers are widely commercialized.

Both the electrostatic forces and the viscoelastic behavior of the polymer influence the production of electrospun nanofibers. In detail, it is possible to define process parameters such as applied voltage, solution feed rate, nozzle collector distance, spinning environmental conditions (temperature and humidity level), and material properties, such as solution concentration, viscosity, surface tension, conductivity, and solvent vapor pressure.

2.1 ELECTROSPINNING THEORY AND PROCESS

The electrostatic fiber spinning, popularized simply as electrospinning by Doshi and Reneker, is a process to fabricate fibers starting from a polymer solution by using an electrical field as a driving force [17].

At its foundation, the apparatus necessary to obtain fibers by electrostatic force consists of a high-voltage electric source with positive or negative polarity and a metallic nozzle connected to the solution reservoir that, in its turn, is connected to a pump for a constant and controllable feeding rate and a conducting collector, such as an aluminum plate or a mandrel, at a defined distance from the spinneret.

When the high voltage is applied (usually between 0 and 40 kV), free charges are induced into the drop at the tip of the nozzle. The meniscus droplet shape is defined by the balance of hydrostatic pressure, mutual electrostatic repulsion between the surface charges, and the Coulomb force applied by the external electric field [18].

By increasing the voltage, charged ions move toward the electrode of opposite polarity; thus, the drop elongates into a cone named Taylor cone. At a certain critical value, the electrostatic forces overcome the surface tension of the polymer solution, and a liquid jet starts from the tip of the Taylor cone. The jet travels in the air toward the collector; its path is first linear, then chaotic, and then helical because of different instabilities. During its travel, the jet stretches itself, the solvent evaporates and then the polymer is collected in form of dried fibers on the metallic surface (Fig. 1) [19, 20].

The most standard laboratory apparatus for electrospinning consists of circular spin nozzles (usually a metallic needle) and a flat counter electrode. In this configuration, the fibers are collected on the counter electrode in a statistical orientation; consequently, a very open mesh is generated, and the nonwoven mat is fabricated by the layer-by-layer deposition of such planar arrangements [6].

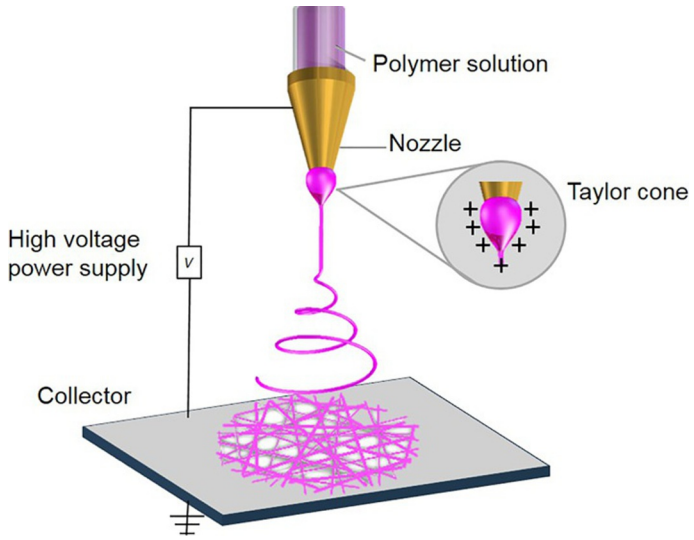

FIG. 1

Basic electrospinning setup apparatus.

Several modifications concerning the nozzle or the collector were developed to spin a wide variety of polymer solution and obtain different three-dimensional structures.

The collector can have different shapes like a flat plate, rotating drum, rotating disc, and more complex configurations to obtain random, aligned, or combined three-dimensional structure or to control the deposited area and density of electrospun fiber [21].

By replacing the classical nozzle with a concentric one, it is possible to perform coaxial electrospinning and to create fibers with core/shell and even a multichannel structure [22]. To perform coaxial electrospinning, different solution reservoirs are required: one feeds the core nozzle, and the other feeds the surrounding concentric annular nozzle. This setup permits to obtain fibers from polymers exhibiting unsuitable rheological behavior to be electrospun by itself. In fact, the presence of easily electrospinnable polymers as core or shell facilitates fiber formation [23]. In addition, by removing the core with a further step, that is, by selective solvent washing or heat treatment, hollow fibers can be realized [23, 24].

2.2 PROCESS PARAMETERS AND FIBER MORPHOLOGY

Several papers report often antithetical results regarding the effect of process parameters, such as applied voltage, on electrospun fiber diameter [25, 26]. To have an overall idea about the electrospinning process, knowing in detail the effect of each process parameter and solution property on the final product is necessary.

Fiber diameter is strongly affected by voltage, nozzle-to-collector distance, solvent evaporation, solution concentration, and conductivity. In fact, high voltage increases the jet stretching, thus reducing the fiber diameter but, at the same time, increases the amount of polymer solution ejected, which has an opposite effect on fiber diameter. The occurrence of each effect depends on the characteristics of solution: a high polymer concentration will result in great viscoelastic force, enabling the charged jet to withstand large electrostatic stretching force [27, 28]. An increase in the applied voltage increases the deposition rate because of the high mass flow ejected from the needle tip [29]. Moreover, high voltages, as well as high feed rates, may lead to the formation of beads as a consequence of an asymmetrical Taylor cone [30].

In the same manner, the nozzle-to-collector distance influences the fiber diameter because it is correlated to the flight time: the longer the flight time, the more stretched are the fibers [31]. On the contrary, decreased nozzle-collector distance produces wet fibers and beaded structures because the solvent has not enough time to evaporate, regardless the concentration of the solution [32–34].

The effects of solvent on the final properties of fibers strongly depend also on environmental parameters such as humidity, temperature, and the composition of the air in the electrospinning chamber. In fact, the elongation and thinning of the charged jet continue until the solvent evaporates and the jet is no longer able to split itself because of the intermolecular forces between macromolecules. The ambient conditions have to encourage solvent evaporation but avoid fast evaporation before the jet lands on the collector, thus inhibiting jet splitting [14]. By controlling the solvent evaporation, it is also possible to obtain porous fibers. Pores may occur on the fiber surface because of the imprints of condensed moisture in the air surrounding the spinneret [35] or because of the phase separation mechanism, as reported in polystyrene fibers at various humidity levels [16].

2.3 SOLUTION PARAMETERS AND FIBER MORPHOLOGY

In conventional fiber spinning, the *spinnability* of a polymer solution or melt means that a continuous filament occurs [36]. In electrospinning, the spinnability of polymer solutions strictly depends on the polymer's molecular weight, the solution's viscosity and conductivity, and the surface tension [37]. The importance of each parameter is evidenced by considering the charged droplet of a low molecular weight conducting liquid at the tip of the nozzle. Several forces exert on the droplet: electrostatic force, drag force, gravity, Coulomb repulsion force, surface tension, and viscoelastic forces [38]. As the jet leaves the needle tip, the polymer solution is stretched, and only the molecular cohesion inside the solution determines the successful formation of electrospun fibers, preventing the breaking up into droplets [20]. Hence, molecular weight plays a pivotal role in the realization of electrospun fibers. In the literature, it is reported that by varying the molecular weight of a synthesized poly(methyl methacrylate) from 12.47 to 365.7 kDa the number of beads and droplets decrease [39].

Similarly, a lower concentration solution promotes droplets or beads-on-a-string morphology because of the influence of surface tension, while higher concentration prohibits fiber formation because of the high viscosity or leads to obtaining fibers with larger average diameters [40]. A study about the effect of concentration on microstructures of electrospun poly(D, L-lactic acid) nanofibers at constant processing conditions and variable concentrations reveal that only highly concentrated solutions (35 wt%) produce more uniform fibers with fewer beads. The shape of the beads changed from spherical to spindlelike when the polymer concentration was increased from 25 wt% to 30 wt% [41]. However, low molecular weights polymers or low concentration solutions can be electrospun by creating effective (i.e., physical) cross-links between molecules [42].

In the same manner, solution conductivity favors the formation of defect-free and thin fibers. In fact, by increasing the solution conductivity, the solution jet can carry more charges, thus influencing the stretching of the electrospun jet. At the same time, the deposition area is also increased [43].

It is possible to tune the solution conductivity by mixing solvents with different dielectric constants or by adding ionic salts to the polymer solution [44, 45]. Mixing solvents or adding a filler, i.e., a surfactant, is also a potential strategy for reducing the surface tension and, as a consequence, the presence of beads [46] (Fig. 2).

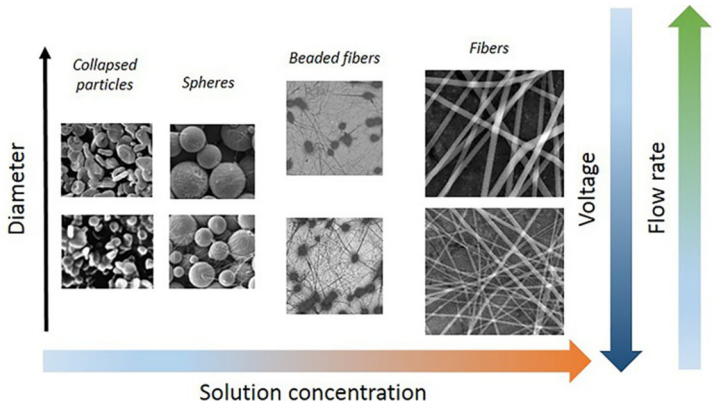

FIG. 2

Effects of processing parameters and material properties on electrospun products.

3 NANOFIBROUS FILTRATION MEMBRANES BASED ON ORGANIC MATERIALS

The high versatility of the electrospinning technique permits the use of various organic materials (e.g., polyethersulfone, cellulose, polyvinylidenefluoride) commonly used for liquid filtration membranes to realize nonwoven nanofibrous membranes.

The fabrication of high-quality polyethersulfone (PES) electrospun nanofibrous membranes is widely reported in the literature. Yoon et al. tested two methods to improve nonwoven integrity and the mechanical strength: the first involves the use of mixed solvents to induce fiber-fiber infusion during electrospinning of PES; the second includes the use of a simple oxidative reaction that can produce highly water wettable (hydrophilic) PES electrospun membranes [47]. In another study, the difficulty in handling the nanofibrous PES web was overcome by using a poly(ethylene terephthalate) (PET) nonwoven mat as a sublayer plus a heat treatment step. This nanofibrous composite membrane showed a high permeability while rejecting microparticles efficiently, thus having the potential to be used in the pretreatment of water, one step before ultra- and nanofiltration membranes [48]. For increasing the solution conductivity and obtaining uniform and homogeneous diameters, the use of sodium dodecyl sulfate (SDS) as a surfactant was investigated. A polysulfone—surfactant solution was electrospun directly on a commercial cellulose filter paper (CFP) membrane acting as the bottom supportive layer. The surface-modified dual-layer polysulfone-SDS/CFP membrane exhibited higher permeate flux, and the salt rejection was >99% compared with the commercial ones [49]. Cao et al. investigated both nanofibrous membranes based on a blend of PES and polyvinylidenefluoride (PVDF) and a novel stellate PVDF/PES microsphere-nanofiber membrane. They obtained good thermal properties compared to the original PVDF and special wetting properties for a range of liquids; additionally, the PES/PVDF membranes showed excellent performance in separation of oil/water mixture [50]. A poly(vinylidene fluoride-*co*-hexafluoropropene) (PVDF-HFP) electrospun (*E*-PH) membrane was fabricated by hybridizing polydimethylsiloxane polymeric microspheres with superhydrophobicity onto the *E*-PH membrane via electrospinning. The resulting hybrid membranes showed quite low fouling tendency in the long-term operation with high dye rejection efficiency because of their surface superhydrophobicity and roughness [51]. Concerning cellulose nanofibers, different studies started with cellulose acetate treated in alkaline solution to remove acetyl groups [52] and used them in combination with commercial ultrafiltration membranes, obtaining a 90% improvement in protein fouling resistance over the control membranes, possibly because the presence of the nanofibers decreased the contact time between the protein and the membranes [53].

The electrospinning technique broadens the range of potential materials also to bio-based ones thanks to the mild working conditions. The use of biopolymers offers the advantage of exploiting their unique properties, such as renewability, biodegradability, abundant availability, and, above all, the peculiar surface chemistry of fibers to achieve improved filtration properties compared to nanofibrous filter media fabricated from synthetic polymers [11]. Chitosan, a polysaccharide derived from chitin with antimicrobial and antibacterial properties, was electrospun in combination with polyethylene oxide (90:10) onto a spun-bonded polypropylene substrate [54] or blended with polycaprolactone [55] to realize bio-based membranes with antimicrobial properties. Also, alginate, a polysaccharide extracted from seaweed, was used in combination with polyethylene oxide and silver nanoparticles [56] or polyethylene oxide and multiwalled carbon nanotubes [57] to create hydrogel composite membranes showing excellent hydrophilic and antifouling properties.

Besides focusing on the most traditional polymers, studies have also been conducted also on electrospinning insoluble cross-linked poly-cyclodextrin. The results demonstrated that nanofibrous mats of electrospun poly-cyclodextrin nanofibers that have flexible and freestanding characteristics could be quite useful for rapid and efficient molecular filtration practices targeting a variety of organic pollutants in wastewater treatment. Besides, poly-cyclodextrin nanofibers kept almost the same performance even after mild washing procedures [58].

With the aim of designing fibrous membranes with more efficient properties, the use of fibers with core/shell, porous, or hollow morphologies has been investigated.

Cellulose acetate (CA) and polyamide acid (PAA) were coaxially electrospun; the PAA core was then imidizated at high temperatures to obtain core/shell CA/polyimide (PI) electrospun fibrous membranes; subsequently, the surface of the fibers was modified with fluorinated polybenzoxazine, in the presence or in absence of silica nanoparticles (SNPs). The newly designed membranes displayed a superhydrophobic character and effective for oil-water mixture separation, solely driven by gravity, with a high flux and a high separation efficiency (>99%) [59]. Analogous abilities were gained for a pH-responsive hydrogel membrane made of core/shell fibers: poly(methylacrylic acid) hydrogel was used as a shell and cellulose acetate as supporting core. Therefore, underwater, the shell can form a hydrate layer on the surface of the membrane and then generate oleophobic behavior while retaining hydrophilicity and permeability. Attractive features, such as high separation efficiency, high flux, excellent antifouling property, and easy recyclability for long-term use, were obtained [60].

A porous structure follows on rapid evaporation of solvent during electrospinning was obtained within polyacrylonitrile (PAN)/ferrous chloride ($FeCl_2$) composite nanofibers. This system proved to be very effective for the absorption and reduction of metal ions thanks to the presence of nanosized pores that deeply increase the overall surface area and offer a convenient pathway for substance exchange between the inner fiber and the surroundings [61].

Symmetric and asymmetric hollow fibers for assembling an ultrafiltration membrane were successfully fabricated by *co*-electrospun different polymers, such as poly(vinylidene fluoride-*co*-hexafluoropropylene), poly(vinylidene fluoride), polysulfone, or poly(etherimide), for the shell and by using poly(vinyl pyrrolidone) as the supporting core, which, afterward, was removed by flowing water through the fibers. Membrane performance analysis revealed relatively high rejection values using poly(acrylic acid-*co*-maleic acid), sodium salt as a contaminant, and considerable flux also for short membranes [62].

4 NANOFIBROUS FILTRATION MEMBRANES BASED ON INORGANIC MATERIALS

Among wastewater purification technologies, wastewater treatments using photocatalytic oxidation based on metal oxides, such as zinc oxide, titanium dioxide, and zirconium dioxide, among others, have an enormous potential for the elimination of organic pollutants. In this frame, electrospun nanofibrous membranes containing metal oxides are very effective for the efficient removal by degrading organic dyes, heavy metals, bacteria, germs, and fungus [63]. Fibrous structures overcome the disadvantage of particles agglomeration in a liquid medium, thus ensuring the high surface-to-volume ratio needed for the mechanism of photocatalysis [64].

Freestanding mats of partially aligned mesoporous ZnO nanofibers with diameters in the range of 50–150 nm were realized by electrospinning a blend of zinc acetate with a carrier polymer, polyacrylonitrile (PAN) in *N*,*N*-dimethylformamide solvent, and subsequent PAN calcination at 650°C. The obtained mat revealed good efficacy in the complete degradation of naphthalene and anthracene dyes in the wastewater treatment thanks to the fast surface reaction and unaltered properties on repeated use [65]. In a similar way, three-dimensional random calcium ferrite, $CaFe_2O_4$, nanofibers were successfully prepared using polyvinylpyrrolidone as a carrier material and different calcination temperatures. Good magnetization with noticeable photocatalytic activity under simulated sunlight was observed, which makes these nanofibers recommendable for use as magnetically separable photocatalysts [66]. TiO_2 nanotubes were prepared in the form of a nonwoven mat by emulsion electrospinning starting from a polyvinylpyrrolidone solution with titanium tetraisopropoxide and oil, followed by calcination in air at 500°C. The highly porous TiO_2 nanotube membranes, characterized by large specific surface areas and excellent ratios of anatase phase to rutile phase, were shown to have excellent catalytic activities [67] (Fig. 3).

By combining electrospinning with a subsequent thermal treatment, it is possible to obtain carbon nanofibers with strong adsorption properties starting from different precursors. Beck et al. fabricated carbon fibrous membranes by electrospinning polyacrylonitrile (PAN) or lignin solutions; nanofibers were stabilized in air with a thermal treatment and then carbonized with argon. Both precursors provided an ideal carbon adsorption medium for high capacity and rapid binding of both larger molecules (methylene blue and tannic acid) as well as smaller molecules (iodine) [68]. Activated carbon

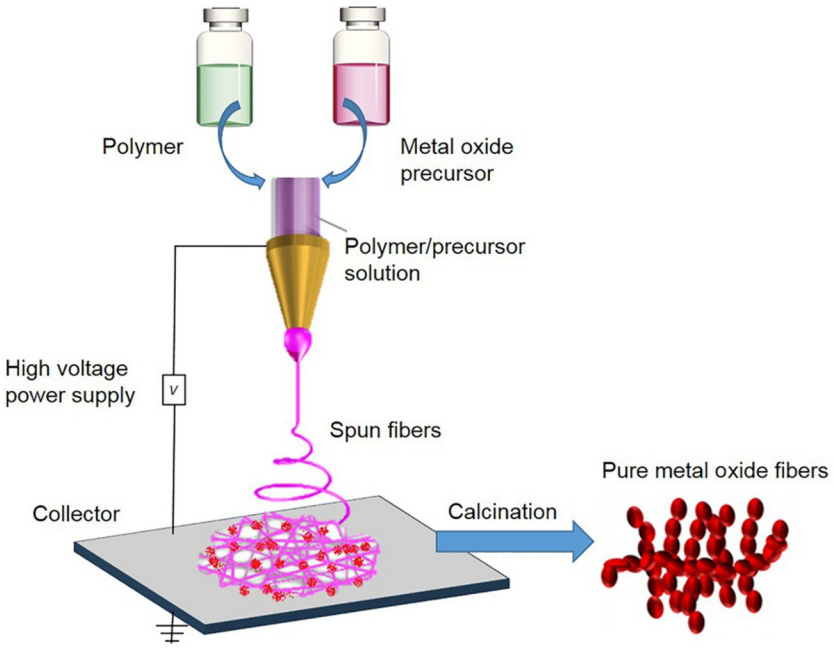

FIG. 3

Electrospinning setup for fabrication of metal oxide nanofibers.

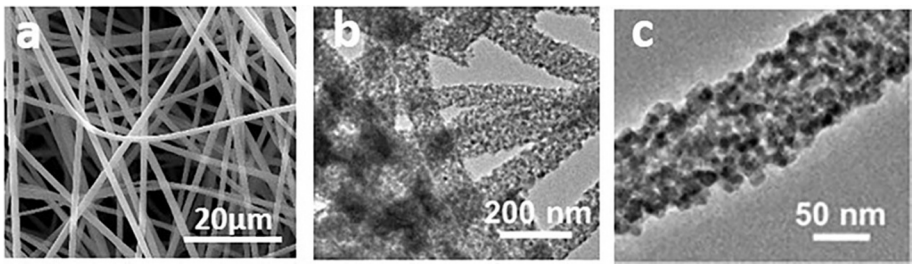

FIG. 4

Morphology of nanofibers decorated with hierarchical nanostructures. Scanning electron microscope images of polyvinylpyrrolidone nanofibers (A). Transmission electron microscope images of decorated nanofibers at (B) low and (C) high resolution [72].

nanofibers with improved characteristics were prepared by electrospinning solution blends of PAN and cellulose acetate at the various blending ratio. The average fiber diameter of samples was about 200 nm, pore characteristics for the adsorption performance were enhanced by increasing the cellulose acetate content (up to 20%) [69].

Otherwise, polymeric nanofibers can be surface-decorated with metal oxide nanoparticles, such as ZnO, by using a two-step approach: first, nanofibers are produced via electrospinning technique; then ZnO-based secondary structures may be assembled directly to the backbones of nanofibers by different methods, such as chemical bath deposition, atomic layer deposition, or hydrothermal process. Both deposition techniques start from plain polymeric nanofibers (i.e., polyl-L-lactide and Nylon 6,6, respectively); by changing the atomic deposition parameters, it is possible to affect the coating morphology to arrive at a compact layer. Thanks to their high surface roughness, the fibers decorated with highly dense ZnO nanoparticles exhibited the highest efficiency for the photocatalytic decomposition of Rhodamine-B dye while keeping good flexibility. Polylactic acid fibers were also used as a substrate for the radial growth of ZnO nanowires for rapid photocatalytic decomposition of organic contaminants in water in a continuous flow mode [70, 71]. Electrospun membranes decorated with SnO_2/ZnO nanostructures as nanorods or nanosheets were fabricated via hydrothermal process starting from a polyvinylpyrrolidone solution containing the metal precursors (Fig. 4) [72].

5 FUNCTIONALIZATION OF ELECTROSPUN NANOFIBROUS MEMBRANES

Recent studies on the functionalization strategies of electrospun nanofibrous membranes have paved the way for achieving the efficient and selective removal of a wide range of molecules from an aqueous solution. A functionalized electrospun membrane not only performs microfiltration by molecular size cutoff, but the functional groups added can also simultaneously capture and remove toxic metal ions, soluble proteins, viruses, or cells from the filtrate. As a consequence, affinity membranes with the potential for application in the removal of any kind of particles or contaminants can easily be fabricated.

Thanks to the flexibility of electrospinning process, electrospun membranes can be designed for targeted liquid filtration application by properly choosing fiber materials, morphology, and further specific moieties. The addition of functional groups may occur directly into the polymer solution before

electrospinning or successively by grafting active species on the fiber surface. It has been reported that surface modification by grafting, interfacial polymerization, nanoparticles coating, and treatment with plasma or chemicals have been found to be suitable methods for altering the surface properties to improve the filtration performance and antifouling properties of nanofibrous membranes [12].

It is reported that the direct incorporation of SiO_2 nanoparticles into Nylon 6 nanofibers renders the electrospun membrane highly hydrophilic (water contact angle: 21 degrees) with both high porosity and mechanical strength. Polyvinyl acetate was then applied as a coating material through casting, and then phrase-inversion techniques were used to decrease the surface roughness and average pore size of the electrospun nanofiber mats. As a consequence, the fabricated membrane showed not only a high water flux but also an almost 99% oil rejection and high antifouling properties [73]. Gopi et al. developed an active functional adsorbent membrane via needleless electrospinning by using chitin nanowhiskers (ChNW) as hydrophilic filler in polyvinylidene fluoride (PVDF) as hydrophobic matrix. Morphological analysis revealed the enriched fiber structure of PVDF/ChNW containing highly dispersed ChNW on the surface. The removal efficiency and adsorption capacity of indigo carmine, one of the main industrial dye, were calculated as 88.9% and 72.6 mg g^{-1}, respectively, which is remarkably increased compared to neat electrospun PVDF [74]. A chitosan/polyvinyl alcohol/zeolite nanofibrous composite membrane was successfully fabricated via the electrospinning process to overcome the limitation of both chitosan and zeolite. The combination of the functional groups of chitosan with the porous frame of zeolite structure ensured mechanical strength and the fast removal of heavy metal ions. The adsorption capacity of the nanofiber was unaltered after five runs, thus ensuring the reusability of membrane [75]. In the literature the incorporation of antimicrobial agents into a polymer solution to obtain membranes with antimicrobial properties is widely reported. For instance, antimicrobial electrospun poly(vinyl alcohol) nanofibers were synthesized by impregnating benzyl triethylammonium chloride (BTEAC), a cationic surface-active agent, as a biocide into the polymer matrix and cross-linked by a heat-methanol treatment. Thanks to the incorporation of BTEAC, the fibers became more hydrophilic and could considerably enhance the removal of *Escherichia coli* and *Staphylococcus aureus* [76].

As concerning the functionalization after electrospinning, a recent study reports phase inversion as a simple approach for the posttreatment of electrospun mats. A surface coating of a poly(vinylidene fluoride-*co*-hexafluoropropylene) nonwoven with polyvinylidene fluoride through phase separation enables control of the membrane pore size by filling the empty domains between the fibers, the mechanical stability, near-complete salt rejection (>99.9%), and fairly high water flux of 30 L m^{-2} h^{-1} [77]. A strong hydrophilic character can be introduced in electrospun membranes with various additional steps. The water contact angle of poly(lactide-*co*-glycolide) electrospun membranes was significantly reduced from 112 to 47 degrees after plasma treatments [78]. The hydrophilicity of polyacrylonitrile (PAN) and polyethersulfone (PES) nanofibrous membranes was improved by an alkaline hydrolysis step and an oxidation treatment using ammonium persulfate, respectively [79–87]. With the aim of improving the adsorption of heavy metal ions in water, the surface of cellulose acetate (CA) electrospun membrane was modified by grafting poly(methacrylic acid) that can provide adsorptive —carboxyl groups on fiber surface. Experimental adsorption results indicated good adsorption selectivity for Hg^{2+} and higher adsorption capacity at high pH value. The membrane can be easily recovered by de-adsorbing the metal ions using saturated (ethylenedinitrilo)tetraacetic acid solution and be reused for the adsorption of metal ions [80]. Similarly, branched polyethylenimine (bPEI)-grafted electrospun polyacrylonitrile (PAN) fibers for Cr(VI) removal were prepared by a facile and rapid refluxing

approach: electrospun PAN fibers were reacted with bPEI in ethylene glycol through refluxing at 140°C for several times. bPEI-EPAN showed a high adsorption capacity toward Cr(VI) because of the electrostatic interaction and reduction mechanism and exhibited a good regeneration and recycling ability even after 10 cycles [81].

By grafting an exact ligand on the fiber surface, it is possible to apply an electrospun membrane as an affinity membrane. For instance, regenerated cellulose nanofibers obtained from cellulose acetate nanofiber were further surface functionalized with a general affinity dye ligand (Cibacron Blue F3GA) via covalent coupling. Under alkaline conditions the nucleophilic reaction between the chloride of dye triazine ring and the hydroxyl groups of the cellulose molecules occurred. The functionalized nanofibrous membrane showed higher water permeability than did a conventional microporous membrane and the ability to capture bovine serum albumin or bilirubin specifically [82]. Amariei et al. prepared an active electrospun membranes showing both antimicrobial action and capacity of retaining low-molecular-weight nonpolar pollutants from aqueous solution by grafting amino-terminated poly(amidoamine) third-generation dendrimers on the surface of polyvinyl alcohol/poly(acrylic acid) (65/35) nanofibers. The results showed toluene removal efficiencies >95% from aqueous solutions and 99.9% reduction of *S. aureus* colonies adhered to the surface [83].

6 THIN FILM NANOFIBROUS COMPOSITE MEMBRANES

Today many efforts are leading to the replacement of traditional filtration membranes with new advanced thin-film nanofibrous composite (TFNC) membranes. TFNC membranes are composed of two or more different layers: a top thin coating layer, a porous mid-layer, and a bottom mechanical support layer as showed in Fig. 5. Different polymers can be electrospun directly onto the support layer that can be constituted, in turn, by nonwoven spun fibers. Thanks to the inherent properties of electrospun nanofibers, such as highly interconnected porosity, tunable pore sizes, and fiber diameters, improved flux and filtration efficiency can be achieved by TFNC membranes [84]. As a consequence, they will play an important role in the replacement of conventional membranes in the near future.

A high-flux three-layer composite membrane was realized by combining a coating layer based on chitosan and chitosan with silver nanoparticles, with electrospun alginate nanofibers as a mid-layer and polyethylene terephthalate (PET) fabric as the supporting substrate. The nanofibers were prepared by electrospinning alginate with the aid of synthetic electrospinnable polyethylene oxide (PEO) and ionically cross-linked with calcium chloride, followed by chemical cross-linking using glutaraldehyde. The alginate mat was then coated with the chitosan solution containing silver nanoparticles. The presence of

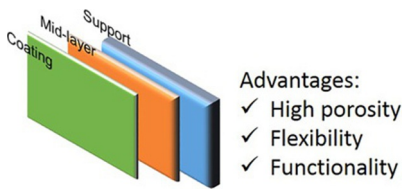

FIG. 5

Schematic representation of a three-layer membrane for ultrafiltration.

silver nanoparticles improved not only the dye rejection, reaching >95% rejection throughout the five filtration cycles test, but also introduced the antibacterial activity in the membrane. The obtained TFNC membranes displayed a higher flux rate and both nanoparticles (>98%) and oil (>93%) rejection than the commercial membranes did [85]. A TFNC membrane with a PAN coating layer, an electrospun nanofibrous PAN mid-layer, and a nonwoven PET substrate was developed and found to be effective in arsenic removal. A comparison of TFNC and commercial ultrafiltration membranes showed the superiority of the former, with a major rise in pure water flux, aqueous solution flux, and rejection efficiency of arsenate [86]. Wen et al. used PAN nanofibers to realize composite membrane where both antibacterial and conductive performance was ensured by silver nanowires and polyaniline (PANI), respectively. Carbon fiber cloth was chosen as the collected electrospinning nanofiber substrate, which improved its strength and thus expanded the application of nanofiber membranes. The characterization results show that PAN/PANI fibers with uniform diameters and without beads were successfully fabricated; moreover, silver nanowires were uniformly distributed in the matrix. The filter was an effective sieve for completely removing both *E. coli* and *S. aureus* in the absence of applied voltage, and the sieved bacteria were completely inactivated by the released silver within 8 h. >99.999% inactivation of the sieved bacteria was achieved within a few seconds by concurrent filtration and electrochemical disinfection under a voltage of 3 V [87].

7 CONCLUSION AND FUTURE TRENDS

In this chapter, a synthetic discussion of more interesting studies focused on the use of nanofibers for the realization of filtration membrane has been provided to demonstrate the great potential and usefulness of them in water purification. During the last decades, several studies have variously proved the relevant contribution of the physicochemical properties and morphological characteristics of fibers at the nanoscale for efficiently removing various contaminants. Research outcomes have shown the importance of high surface area, high porosity, and tunable pore size for realizing effective electrospun fibrous membrane.

Electrospun nanofibers can offer a large versatility in the choice of materials with different properties (i.e., hydrophilicity, biodegradability, electrical conductivity) as a function of the targeting application and the chemical nature of the contaminant, thus realizing both organic and inorganic membranes. Nonwovens can be used efficiently both as a functional layer in the construction of a multilayer membrane and as self-supporting membranes for a specific application as an affinity membrane. They can improve the permeability of liquids and offer the great possibility of adding other functional moieties into the nanofibers for specific chemical foulants, such as dye molecules or bacteria. Last, nanofibers have proved to be a promising substrate on which three-dimensional structures as nanorods and nanosheets can be realized to increase the surface area.

By combining innovative technologies for nanofabrication and conventional ones, a wide range of properties can be achieved, and the main drawbacks in terms of suitable thickness and strength of electrospun nanofibers are overcome. Therefore, electrospun nanofibers result in a very promising tool for fabricating nonconventional membranes highly engineered for the performance requested.

According to these emerging trends, several efforts are oriented toward the selection of functional elements based on organic or inorganic materials with peculiar properties that could further ameliorate the efficiency of filtration devices and drive to a higher expansion of their application areas.

REFERENCES

[1] N. Bhardwaj, S.C. Kundu, Electrospinning: a fascinating fiber fabrication technique, Biotechnol. Adv. 28 (3) (2010) 325–347.

[2] D.H. Reneker, A.L. Yarin, Electrospinning jets and polymer nanofibers, Polymer 49 (10) (2008) 2387–2425.

[3] S. Ramakrishna, K. Fujihara, W.E. Teo, T. Yong, Z. Ma, R. Ramaseshan, Electrospun nanofibers: solving global issues, Mater. Today 9 (3) (2006) 40–50.

[4] J.Y. Feng, J.C. Zhang, D. Yang, Preparation and oil filtration properties of electrospun nanofiber composite material, J. Eng. Fabr. Fiber. 9 (4) (2014) 108–116.

[5] J. Lannutti, D. Reneker, T. Ma, D. Tomasko, D. Farson, Electrospinning for tissue engineering scaffolds, Mater. Sci. Eng. C 27 (3) (2007) 504–509.

[6] A. Greiner, J.H. Wendorff, Electrospinning: a fascinating method for the preparation of ultrathin fibers, Angew. Chem. Int. Ed. 46 (30) (2007) 5670–5703.

[7] Z. Wang, C. Crandall, R. Sahadevan, T.J. Menkhaus, H. Fong, Microfiltration performance of electrospun nanofiber membranes with varied fiber diameters and different membrane porosities and thicknesses, Polymer 114 (2017) 64–72.

[8] R. Balamurugan, S. Sundarrajan, S. Ramakrishna, Recent trends in nanofibrous membranes and their suitability for air and water filtrations, Membranes 1 (3) (2011) 232–248.

[9] K. Yoon, K. Kim, X. Wang, D. Fang, B.S. Hsiao, B. Chu, High flux ultrafiltration membranes based on electrospun nanofibrous PAN scaffolds and chitosan coating, Polymer 47 (2006) 2434–2441.

[10] R. Halaui, A. Moldavsky, Y. Cohen, R. Semiat, E. Zussman, Development of micro-scale hollow fiber ultrafiltration membranes, J. Membr. Sci. 379 (1) (2011) 370–377.

[11] T.C. Mokhena, V. Jacobs, A.S. Luyt, A review on electrospun bio-based polymers for water treatment, Express Polym Lett 9 (10) (2015) 839–880.

[12] S.A.A.N. Nasreen, S. Sundarrajan, S.A.S. Nizar, R. Balamurugan, S. Ramakrishna, Advancement in electrospun nanofibrous membranes modification and their application in water treatment, Membranes 3 (4) (2013) 266–284.

[13] N. Tucker, J. Stanger, M. Staiger, H. Razzaq, K. Hofman, The history of the science and technology of electrospinning from 1600 to 1995, J. Eng. Fiber. Fabr. 7 (2012) 63–73.

[14] S. De Vrieze, T. Van Camp, A. Nelvig, B. Hagström, P. Westbroek, K. De Clerck, The effect of temperature and humidity on electrospinning, J. Mater. Sci. 44 (5) (2009) 1357–1362.

[15] V. Pillay, C. Dott, Y.E. Choonara, C. Tyagi, L. Tomar, P. Kumar, L.C. du Toit, V.M. Ndesendo, A review of the effect of processing variables on the fabrication of electrospun nanofibers for drug delivery applications, J. Nanomater. 2013 (2013) 1–22.

[16] S. Megelski, J.S. Stephens, D.B. Chase, J.F. Rabolt, Micro-and nanostructured surface morphology on electrospun polymer fibers, Macromolecules 35 (22) (2002) 8456–8466.

[17] J. Doshi, D.H. Reneker, Electrospinning process and applications of electrospun fibers, J. Electrostat. 35 (2–3) (1995) 151–160.

[18] A.F. Spivak, Y.A. Dzenis, A condition of the existence of a conductive liquid meniscus in an external eletric field, J. Appl. Mech. 66 (4) (1999) 1026–1028.

[19] D.H. Reneker, I. Chun, Nanometre diameter fibres of polymer, produced by electrospinning, Nanotechnology 7 (1996) 216–223.

[20] K. Garg, G.L. Bowlin, Electrospinning jets and nanofibrous structures, Biomicrofluidics 5 (1) (2011) 013403.

[21] R. Sahay, V. Thavasi, S. Ramakrishna, Design modifications in electrospinning setup for advanced applications, J. Nanomater. 2011 (2011) 1–17.

[22] F. Li, Y. Zhao, Y. Song, in: A. Kumar (Ed.), Core-Shell Nanofibers: Nano Channel and Capsule by Coaxial Electrospinning. Nanofibers, InTech, Croatia, 2010.

[23] I. Bonadies, F. Cimino, C. Carfagna, A. Pezzella, Eumelanin 3D architectures: electrospun PLA fiber templating for mammalian pigment microtube fabrication, Biomacromolecules 16 (5) (2015) 1667–1670.
[24] A. Arinstein, E. Zussman, Postprocesses in tubular electrospun nanofibers, Phys. Rev. E 76 (2007) 056303.
[25] J. Du, S. Shintay, X. Zhang, Diameter control of electrospun polyacrylonitrile/iron acetylacetonate ultrafine nanofibers, J Polym Sci B 46 (15) (2008) 1611–1618.
[26] C. Zhang, X. Yuan, L. Wu, Y. Han, J. Sheng, Study on morphology of electrospun poly (vinyl alcohol) mats, Eur. Polym. J. 41 (3) (2005) 423–432.
[27] D. Fallahi, M. Rafizadeh, N. Mohammadi, B. Vahidi, Effect of applied voltage on surface and volume charge density of the jet in electrospinning of polyacrylonitrile solutions, Polym. Eng. Sci. 50 (7) (2010) 1372–1376.
[28] O.S. Yördem, M. Papila, Y.Z. Menceloğlu, Effects of electrospinning parameters on polyacrylonitrile nanofiber diameter: an investigation by response surface methodology, Mater. Des. 29 (1) (2008) 34–44.
[29] S.R. Coles, D.K. Jacobs, J.O. Meredith, G. Barker, A.J. Clark, K. Kirwan, J. Stranger, N. Tucker, A design of experiments (DoE) approach to material properties optimization of electrospun nanofibers, J. Appl. Polym. Sci. 117 (4) (2010) 2251–2257.
[30] S. Zargham, S. Bazgir, A. Tavakoli, A.S. Rashidi, R. Damerchely, The effect of flow rate on morphology and deposition area of electrospun nylon 6 nanofiber, J. Eng. Fabr. Fiber. 7 (4) (2012) 42–49.
[31] M.M. Demir, I. Yilgor, E. Yilgor, B. Erman, Electrospinning of polyurethanefibers, Polymer 43 (2002) 3303–3309.
[32] M. Chowdhury, G. Stylios, Effect of experimental parameters on the morphology of electrospun nylon 6 fibres, Int. J. Basic Appl. Sci. 10 (6) (2010) 70–78.
[33] S. Koombhongse, W. Liu, D.H. Reneker, Flat polymer ribbons and other shapes by electrospinning, J Polym Sci B 39 (21) (2001) 2598–2606.
[34] C.J. Butchko, L.C. Chen, S. Yu, D.C. Martin, Processing and microstructural characterization of porous biocompatible protein polymer thin films, Polymer 40 (1999) 7397–7407.
[35] M. Srinivasarao, D. Collings, A. Philips, S. Patel, Three-dimensionally ordered array of air bubbles in a polymer film, Science 292 (5514) (2001) 79–83.
[36] A. Ziabicki, Fundamentals of Fibre Formation: The Science of Fibre Spinning and Drawing, Wiley, New York, 1976, p. 488.
[37] B. Ghorani, N. Tucker, Fundamentals of electrospinning as a novel delivery vehicle for bioactive compounds in food nanotechnology, Food Hydrocoll. 51 (2015) 227–240.
[38] B. Ding, C. Li, Y. Miyauchi, O. Kuwaki, S. Shiratori, Formation of novel 2D polymer nanowebs via electrospinning, Nanotechnology 17 (15) (2006) 3685–3691.
[39] P. Gupta, C. Elkins, T.E. Long, G.L. Wilkes, Electrospinning of linear homopolymers of poly(methylmethacrylate): exploring relationships between fiber formation, viscosity, molecular weight and concentration in a good solvent, Polymer 46 (3) (2005) 4799–4810.
[40] Z. Li, C. Wang, Effects of working parameters on electrospinning, in: One-Dimensional Nanostructures, Springer, Berlin/Heidelberg, 2013, pp. 15–28.
[41] X. Zong, K. Kim, D. Fang, S. Ran, B.S. Hsiao, B. Chu, Structure and process relationship of electrospun bioabsorbable nanofiber membranes, Polymer 43 (16) (2002) 4403–4412.
[42] X. Wang, C. Pellerin, C.G. Bazuin, Enhancing the electrospinnability of low molecular weight polymers using small effective cross-linkers, Macromolecules 49 (3) (2016) 891–899.
[43] R. Casasola, N.L. Thomas, A. Trybala, S. Georgiadou, Electrospun poly lactic acid (PLA) fibres: effect of different solvent systems on fibre morphology and diameter, Polymer 55 (18) (2014) 4728–4737.
[44] K.H. Lee, H.Y. Kim, M.S. Khil, Y.M. Ra, D.R. Lee, Characterization of nano-structured poly (ε-caprolactone) nonwoven mats via electrospinning, Polymer 44 (4) (2003) 1287–1294.
[45] S.J. Kim, C.K. Lee, S.I. Kim, Effect of ionic salts on the processing of poly (2-acrylamido-2-methyl-1-propane sulfonic acid) nanofibers, J. Appl. Polym. Sci. 96 (4) (2005) 1388–1393.
[46] K.H. Lee, H.Y. Kim, H.J. Bang, Y.H. Jung, S.G. Lee, The change of bead morphology formed on electrospun polystyrene fibers, Polymer 44 (14) (2003) 4029–4034.

[47] K. Yoon, B.S. Hsiao, B. Chu, Formation of functional polyethersulfone electrospun membrane for water purification by mixed solvent and oxidation processes, Polymer 50 (13) (2009) 2893–2899.
[48] S.S. Homaeigohar, K. Buhr, K. Ebert, Polyethersulfone electrospun nanofibrous composite membrane for liquid filtration, J. Membr. Sci. 365 (1) (2010) 68–77.
[49] S.S. Ray, S.S. Chen, H.T. Hsu, D.T. Cao, H.T. Nguyen, N.C. Nguyen, Uniform hydrophobic electrospun nanofibrous layer composed of polysulfone and sodium dodecyl sulfate for improved desalination performance, Sep. Purif. Technol. 186 (2017) 352–365.
[50] J. Cao, Z. Cheng, L. Kang, M. Chu, D. Wu, M. Li, S. Xie, R. Wen, Novel stellate poly (vinylidene fluoride)/polyethersulfone microsphere-nanofiber electrospun membrane with special wettability for oil/water separation, Mater. Lett. 207 (2017) 190–194.
[51] A.K. An, J. Guo, E.J. Lee, S. Jeong, Y. Zhao, Z. Wang, T. Leiknes, PDMS/PVDF hybrid electrospun membrane with superhydrophobic property and drop impact dynamics for dyeing wastewater treatment using membrane distillation, J. Membr. Sci. 525 (2017) 57–67.
[52] H. Liu, Y.L. Hsieh, Ultrafine fibrous cellulose membranes from electrospinning of cellulose acetate, J Polym Sci B 40 (18) (2002) 2119–2129.
[53] K.M. Dobosz, C.A. Kuo-Leblanc, T.J. Martin, J.D. Schiffman, Ultrafiltration membranes enhanced with electrospun nanofibers exhibit improved flux and fouling resistance, Ind. Eng. Chem. Res. 56 (19) (2017) 5724–5733.
[54] K. Desai, K. Kit, J. Li, P.M. Davidson, S. Zivanovic, H. Meyer, Nanofibrous chitosan non-wovens for filtration applications, Polymer 50 (15) (2009) 3661–3669.
[55] A. Cooper, R. Oldinski, H. Ma, J.D. Bryers, M. Zhang, Chitosan-based nanofibrous membranes for antibacterial filter applications, Carbohydr. Polym. 92 (1) (2013) 254–259.
[56] T.C. Mokhena, A.S. Luyt, Electrospun alginate nanofibres impregnated with silver nanoparticles: preparation, morphology and antibacterial properties, Carbohydr. Polym. 165 (2017) 304–312.
[57] J. Guo, Q. Zhang, Z. Cai, K. Zhao, Preparation and dye filtration property of electrospun polyhydroxybutyrate–calcium alginate/carbon nanotubes composite nanofibrous filtration membrane, Sep. Purif. Technol. 161 (2016) 69–79.
[58] A. Celebioglu, Z.I. Yildiz, T. Uyar, Electrospun crosslinked poly-cyclodextrin nanofibers: highly efficient molecular filtration thru host-guest inclusion complexation, Sci. Rep. 7 (1) (2017) 7369.
[59] W. Ma, Z. Guo, J. Zhao, Q. Yu, F. Wang, J. Han, H. Pan, J. Yao, Q. Zhang, S.K. Smal, S.C. De Smedt, C. Huang, Polyimide/cellulose acetate core/shell electrospun fibrous membranes for oil-water separation, Sep. Purif. Technol. 177 (2017) 71–85.
[60] L. Zang, J. Ma, D. Lv, Q. Liu, W. Jiao, P. Wang, Core-shell fibers constructed pH-responsive nanofibrous hydrogel membrane for efficient oil/water separation, J. Mater. Chem. A 5 (2017) 19398–19405.
[61] Y. Lin, W. Cai, X. Tian, X. Liu, G. Wang, C. Liang, Polyacrylonitrile/ferrous chloride composite porous nanofibers and their strong Cr-removal performance, J. Mater. Chem. 21 (4) (2011) 991–997.
[62] R. Halaui, E. Zussman, R. Khalfin, R. Semiat, Y. Cohen, Polymeric microtubes for water filtration by co-axial electrospinning technique, Polym. Adv. Technol. 28 (5) (2017) 570–582.
[63] M. Anjum, R. Miandad, M. Waqas, F. Gehany, M.A. Barakat, Remediation of wastewater using various nano-materials, Arab. J. Chem. (2016). https://doi.org/10.1016/j.arabjc.2016.10.004.
[64] Y. Ren, S. Wang, R. Liu, J. Dai, X. Liu, J. Yu, A novel route towards well-dispersed short nanofibers and nanoparticles via electrospinning, RSC Adv. 6 (2016) 30139–30147.
[65] P. Singh, K. Mondal, A. Sharma, Reusable electrospun mesoporous ZnO nanofiber mats for photocatalytic degradation of polycyclic aromatic hydrocarbon dyes in wastewater, J. Colloid Interface Sci. 394 (2013) 208–215.
[66] A.M. El-Rafei, A.S. El-Kalliny, T.A. Gad-Allah, Electrospun magnetically separable calcium ferrite nanofibers for photocatalytic water purification, J. Magn. Magn. Mater. 428 (2017) 92–98.
[67] B. Lu, C. Zhu, Z. Zhang, W. Lan, E. Xie, Preparation of highly porous TiO2 nanotubes and their catalytic applications, J. Mater. Chem. 22 (4) (2012) 1375–1379.

[68] R.J. Beck, Y. Zhao, H. Fong, T.J. Menkhaus, Electrospun lignin carbon nanofiber membranes with large pores for highly efficient adsorptive water treatment applications, J. Water Process Eng. 16 (2017) 240–248.
[69] Y.W. Ju, G.Y. Oh, Behavior of toluene adsorption on activated carbon nanofibers prepared by electrospinning of a polyacrylonitrile-cellulose acetate blending solution, Korean J. Chem. Eng. 34 (10) (2017) 2731–2737.
[70] A. Sugunan, V.K. Guduru, A. Uheida, M.S. Toprak, M. Muhammed, Radially oriented ZnO nanowires on flexible poly-l-lactide nanofibers for continuous-flow photocatalytic water purification, J. Am. Ceram. Soc. 93 (11) (2010) 3740–3744.
[71] F. Kayaci, C. Ozgit-Akgun, N. Biyikli, T. Uyar, Surface-decorated ZnO nanoparticles and ZnO nanocoating on electrospun polymeric nanofibers by atomic layer deposition for flexible photocatalytic nanofibrous membranes, RSC Adv. 3 (19) (2013) 6817–6820.
[72] L. Zhu, M. Hong, G.W. Ho, Hierarchical assembly of SnO_2/ZnO nanostructures for enhanced photocatalytic performance, Sci. Rep. 5 (2015) 11609.
[73] M.S. Islam, J.R. McCutcheon, M.S. Rahaman, A high flux polyvinyl acetate-coated electrospun nylon 6/SiO_2 composite microfiltration membrane for the separation of oil-in-water emulsion with improved antifouling performance, J. Membr. Sci. 537 (2017) 297–309.
[74] S. Gopi, P. Balakrishnan, A. Pius, S. Thomas, Chitin nanowhisker (ChNW)-functionalized electrospun PVDF membrane for enhanced removal of indigo carmine, Carbohydr. Polym. 165 (2017) 115–122.
[75] U. Habiba, A.M. Afifi, A. Salleh, B.C. Ang, Chitosan/(polyvinyl alcohol)/zeolite electrospun composite nanofibrous membrane for adsorption of Cr^{6+}, Fe^{3+} and Ni^{2+}, J. Hazard. Mater. 322 (2017) 182–194.
[76] J.A. Park, S.B. Kim, Antimicrobial filtration with electrospun poly (vinyl alcohol) nanofibers containing benzyl triethylammonium chloride: immersion, leaching, toxicity, and filtration tests, Chemosphere 167 (2017) 469–477.
[77] E. Shaulsky, S. Nejati, C. Boo, F. Perreault, C.O. Osuji, M. Elimelech, Post-fabrication modification of electrospun nanofiber mats with polymer coating for membrane distillation applications, J. Membr. Sci. 530 (2017) 158–165.
[78] K.E. Park, K.Y. Lee, S.J. Lee, W.H. Park, Surface characteristics of plasma-treated PLGA nanofibers, Macromol. Symp. 249–250 (2007) 103–108.
[79] H. Liu, Y.L. Hsieh, Preparation of water-absorbing polyacrylonitrile nanofibrous membrane, Macromol. Rapid Commun. 27 (2) (2006) 142–145.
[80] Y. Tian, M. Wu, R. Liu, Y. Li, D. Wang, J. Tan, R. Wu, Y. Huang, Electrospun membrane of cellulose acetate for heavy metal ion adsorption in water treatment, Carbohydr. Polym. 83 (2) (2011) 743–748.
[81] R. Zhao, X. Li, B. Sun, Y. Li, Y. Li, R. Yang, C. Wang, Branched polyethylenimine grafted electrospun polyacrylonitrile fiber membrane: a novel and effective adsorbent for Cr (VI) remediation in wastewater, J. Mater. Chem. A 5 (3) (2017) 1133–1144.
[82] Z. Ma, M. Kotaki, S. Ramakrishna, Electrospun cellulose nanofiber as affinity membrane, J. Membr. Sci. 265 (1) (2005) 115–123.
[83] G. Amariei, J. Santiago-Morales, K. Boltes, P. Letón, I. Iriepa, I. Moraleda, A.R. Fernández-Alba, R. Rosal, Dendrimer-functionalized electrospun nanofibres as dual-action water treatment membranes, Sci. Total Environ. 601 (2017) 732–740.
[84] K. Yoon, B.S. Hsiao, B. Chu, Functional nanofibers for environmental applications, J. Mater. Chem. 18 (44) (2008) 5326–5334.
[85] T.C. Mokhena, A.S. Luyt, Development of multifunctional nano/ultrafiltration membrane based on a chitosan thin film on alginate electrospun nanofibres, J. Clean. Prod. 156 (2017) 470–479.
[86] P. Bahmani, A. Maleki, H. Daraei, M. Khamforoush, R. Rezaee, F. Gharibi, A.G. Tkachev, A. E. Burakov, S. Agarwal, V.K. Gupta, High-flux ultrafiltration membrane based on electrospun polyacrylonitrile nanofibrous scaffolds for arsenate removal from aqueous solutions, J. Colloid Interface Sci. 506 (2017) 564–571.
[87] J. Wen, X. Tan, Y. Hu, Q. Guo, X. Hong, Filtration and electrochemical disinfection performance of PAN/PANI/AgNWs-CC composite nanofiber membrane, Environ. Sci. Technol. 51 (11) (2017) 6395–6403.

CHAPTER

9 ELECTROSPINNING: A VERSATILE FABRICATION TECHNIQUE FOR NANOFIBROUS MEMBRANES FOR USE IN DESALINATION

Saikat Sinha Ray*, Shiao-Shing Chen*, Nguyen Cong Nguyen*,†, Hau Thi Nguyen*,†

*Institute of Environmental Engineering and Management, National Taipei University of Technology, Taipei, Taiwan**

Faculty of Environment and Natural Resources, University of Da Lat, Da Lat, Vietnam†

1 INTRODUCTION

Water scarcity is mainly caused by increasing demand in industrial and agricultural areas. Studies have recently suggested that 1.3 billion people have limited access to safe and hygienic drinking water, 2.6 billion people have little or no sanitation, and every year millions of people die from diseases transmitted through unhygienic water. Thus, novel technology and innovation are required to enable desalination, water reclamation, and wastewater treatment. Recently, nanotechnology combined with nanoengineered materials has offered great potential for advancing desalination and wastewater treatment technologies. In response to these challenges, the electrospinning process for producing nanofibrous membranes has emerged as an efficient technology for fabricating durable and potential membranes for water treatment and advanced desalination [1, 2]. In this chapter, the development of an electrospun nanofibrous membrane through surface chemistry modification is discussed, and potential approaches for producing efficient electrospun nanofibrous membranes are explored. Fig. 1 shows some crucial advantages of the electrospinning technique and its potential for fabricating the desired electrospun nanofibrous membranes.

1.1 HISTORY OF ELECTROSPINNING TECHNIQUE

Studies on the electrospinning process began during the 19th century. Rayleigh (1897) initially demonstrated the process, and it was studied in detail by Zeleny [2a]. During the 1930s, Formhals developed an experimental setup for producing artificial filaments using electric charges, which was finally patented as a viable fiber-spinning technique [3]. Subsequently, Taylor, Saville, Denn, and other researchers demonstrated electrically driven jets and laid the groundwork for the electrospinning research that began in late 1964 [4, 5]. Through extensive nanotechnology research and development (R&D), researchers are examining the electrospinning process from a new perspective. Table 1 shows

Nanoscale Materials in Water Purification. https://doi.org/10.1016/B978-0-12-813926-4.00014-8

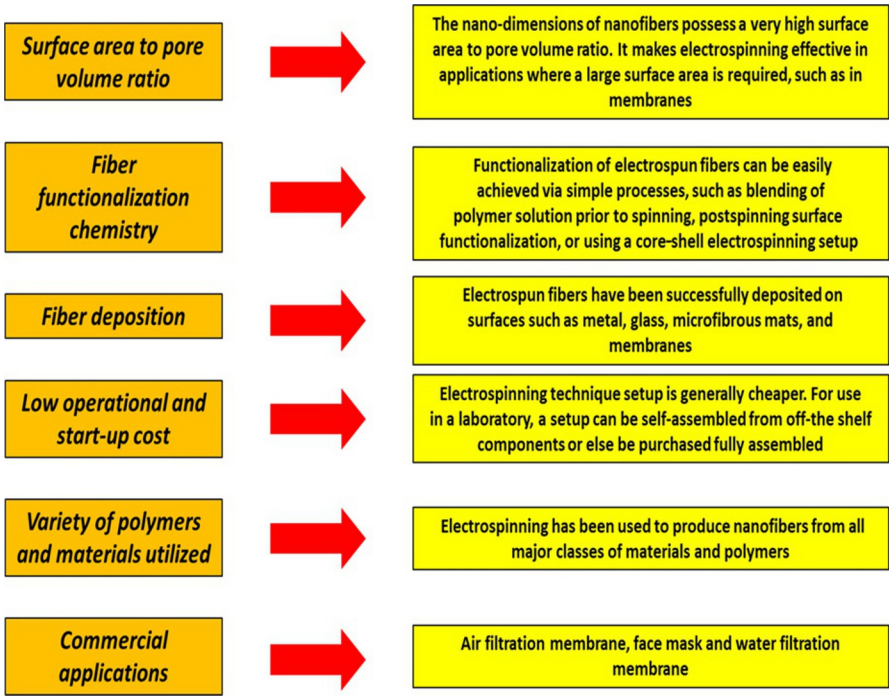

FIG. 1

Unique features of the electrospinning techniques used for fabricating membranes, which enable a high surface area to volume ratio, the use of different polymers and materials, low start-up costs, fiber deposition onto other substrates, fiber functionalization, and commercial applications.

Table 1 Important Milestones in Electrospinning Technology

Year	Progress of Events	References Used
1897	Electrospinning technique was first demonstrated by Raleigh	[6]
1914	Zeleny has studied further on electrospraying technique	[7]
1934	Formhals patented the electrospinning process. (Between 1934 and 1944, patents were published by Formhals)	[3]
1944–2004	About 50 patents were published on electrospinning technique.	[6]
1950–70	Taylor laid the groundwork by his research on electrically driven jets	[5, 8]
1966	Simons patented an apparatus for generation of nonwovens with different patterns using electrical spinning process	[9]
1980s	The electrospinning technique gained more attention because of interest in nanotechnology and an increase in the use of ultrafine nanofibers and fibers in submicron scale	[10]
1981	Larrondo and Manley investigated the electrospinning technique using molten polymeric solution	[11]
1990–2000	A high number of research activities are going on in this field, especially after the advancements of electrospun nanofibers in applications, including composite membrane, tissue engineering, and energy storage.	[12, 13]
2000–10	Research work is also focused on upscaling and on extending the application areas of electrospun nanofibers and nanofibrous membranes	[14, 15]

Research related to electrospinning technology and electrospun nanofibers has gained momentum, especially from early 2000.

some important milestones in the R&D of electrospinning techniques. Apparently, there is a great increase in the R&D of electrospinning techniques. This increase in R&D can be attributed to nanoengineering and nanotechnology gaining more attention, which can easily be determined from the number of publications in this field, especially from 2005 to 2015 [16]. Furthermore, ultrafine nanofibers can be easily produced through electrospinning. The objective in almost all the studies has been to use this technique in a wide range of applications.

1.2 BACKGROUND

Electrospinning is widely used for the electrostatic generation of nanofibers, during which polymeric nanofibers with diameters ranging from 2 nm to a few micrometers are fabricated from various polymeric solutions or polymer melts under high voltage. Compared with conventional technologies, electrospinning is a highly versatile and efficient process.

Electrospinning is the simplest way of fabricating nanofibrous materials, but there are some important parameters that can have a significant impact on the formation and structure of generated nanofibers. These parameters are categorized into (a) solution parameters, (b) process parameters, and (c) ambient parameters. Table 2 summarizes the important parameters, which are discussed in a later section of this chapter.

Electrospun nanofibrous membranes have been used for direct filtration. In addition, electrospun polymeric interconnected webs can be used as porous support layers in thin-film composite (TFC), ultrafiltration (UF), nanofiltration (NF), reverse osmosis (RO), and membrane distillation (MD) membranes. Typically, TFC membranes consist of three layers, including the top ultrathin rejection layer, a middle porous supportive layer, and a bottom nonwoven fabric layer [19]. The application of electrospun nanofibrous materials as a porous supportive layer for TFC membranes has recently gained attention. Between 2010 and 2015, the electrospinning process has attracted worldwide attention owing to its versatility in MD membranes [20, 21]. This chapter mainly focuses on the recent advancements in the field of nanofibrous membranes fabricated by electrospinning for use in MD membranes.

Table 2 Electrospinning Process Parameters

Parameters	Factors to be Considered
Solution parameter	➢ Viscosity ➢ Solution concentration ➢ Molecular weight of the polymer ➢ Solvent properties ➢ Surface tension ➢ Conductivity
Processing parameter	➢ Voltage applied ➢ Distance of the electrode from the collector ➢ Flow rate ➢ Capillary geometry
Ambient parameter	➢ Temperature ➢ Relative humidity

Process advancements achieved by controlling these parameters have led to the fabrication of uniform, nanofibrous membranes [17, 18].

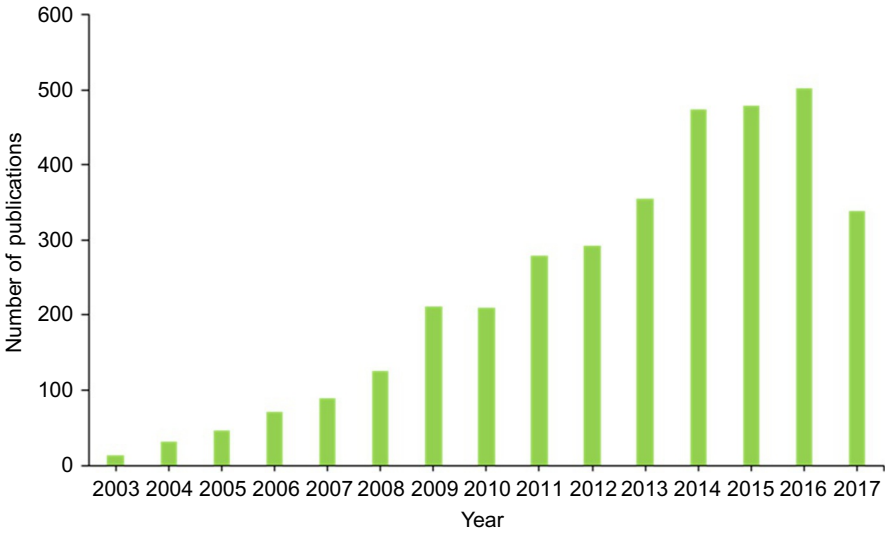

FIG. 2

Comparative study of peer-reviewed publications since 2003. (Analysis of publications was conducted using the Scopus scholar search system with the terms "Electrospinning" and "Membrane" during July 2017.)

The electrospinning process has recently regained considerable attention, probably because, owing to the advancements in nanotechnology. Ultra-fine nanofibers or nanofibrous microstructures with fibers of various diameters can be easily produced using this technique (i.e., electro + spinning) with different polymers [22]. In this chapter, a detailed survey of peer-reviewed publications relating to electrospinning and membranes from the past 15 years is presented (Fig. 2). In addition, the contributions of different countries to research on electrospinning, in terms of published articles, are shown in Fig. 3; interestingly, China leads the table according to the Scopus database. Data from Scopus indicate that electrospinning has attracted considerable attention in recent years. The data suggest that several hundred natural and synthetic polymers that can be dissolved using the appropriate solvent through heating or melting are available. Table 3 provides the polymeric solutions used for fabricating electrospun nanofibrous membranes.

2 FUNDAMENTALS OF ELECTROSPINNING TECHNIQUE

The need for cost- and energy-efficient purification technologies has resulted in increased attention on nanostructure membranes fabricated through electrospinning. Electrospinning is an efficient technique that enables control over the fiber diameter, thickness, arrangement, and microstructure. As shown in Fig. 4, electrospinning techniques typically require three main components: (a) a high voltage supply, (b) a capillary tube with needles, and (c) a metal collecting screen or roller [28, 29]. In this process, high voltage is used to eject an electrically charged jet of polymer solution out of the pipette; just before reaching the metal collector, the polymeric solution jet evaporates and solidifies, and finally it is

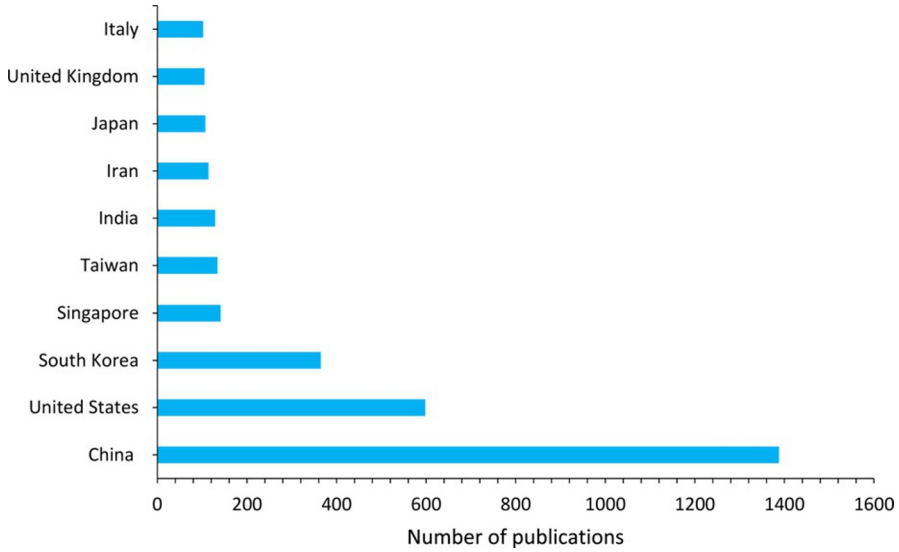

FIG. 3

Graphical representation of the contribution of various countries in the field of electrospinning technique (Data were obtained from the Scopus scholar search system with the terms "Electrospinning" and "Membrane" during July 2017.)

Table 3 Common Polymers and Their Appropriate Solvents

Polymer Name	Solvent
Polymetylmethaacrylate (PMMA)	✓ Chloroform ✓ Acetone ✓ Tetrahydrofuran (THF)
Tetrahydroperfluorooctylacrylate (TAN)	✓ Dimethyl formamide (DMF) Toluene
Polyvinyl alcohol (PVA)	✓ Distilled Water
PVA/cellulose nanocrystals	✓ Distilled Water
Polyvinyl phenol (PVP)	✓ Tetrahydrofuran (THF)
Polyvinylchloride (PVC)	✓ THF ✓ Dimethyl formamide (DMF)
Polyvinylcarbazole	✓ Dichloromethane
PVDF-*co*-hexaflurorpropylene (PVDF-*co*-HFP)	✓ Acetone ✓ DMF
Polyacrylonitrile (PAN)	✓ DMF
Polylactic acid (PLA)	✓ Chloroform ✓ DMF
Polyethylene oxide (PEO)	✓ Distilled water
Poly(vinylidene fluoride) (PVDF)	✓ DMF

This table indicates the polymeric solutions used in electrospinning technology for application in wastewater or desalination technologies [23–25].

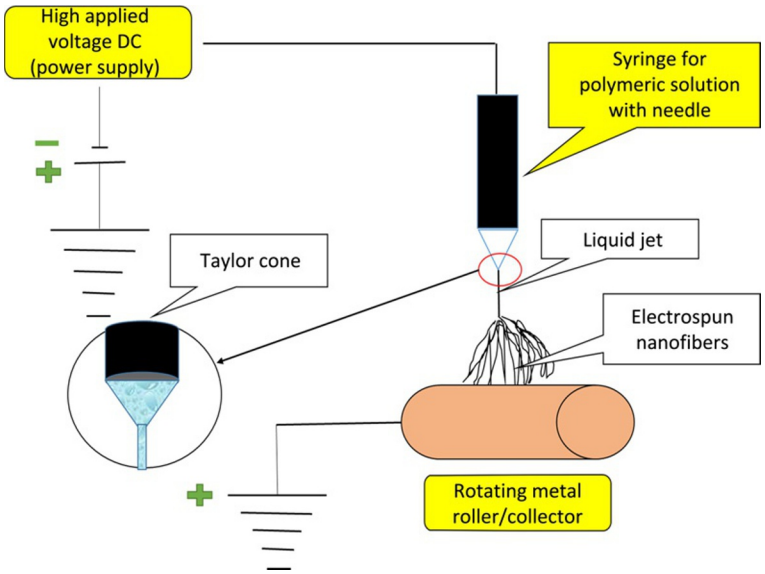

FIG. 4

Schematic of electrospinning process. The setup consists of three components: (1) a high voltage supply, (2) a syringe or capillary tube with needles, and (3) a metal collecting screen and roller [26, 27].

collected as an interconnected web of nanofibers. The electrical field at the tip of the needle typically electrifies the surface of the polymeric droplet located on it. Repulsive forces between the electrical charges present at the surface and their attraction to the oppositely charged electrode yield a force that overcomes the surface tension. Consequently, a charged jet is ejected from the tip of the needle, and because of the repulsion between the electric charges in the jet, it undergoes bending instability, resulting in elongation and thinning. Meanwhile, the evaporation of the solvent results in the formation of charged polymer nanofibers that are collected as an interconnected web on the metal collector. The resulting interconnected web is composed of randomly aligned nanofibers; it resembles a nonwoven nanofibrous membrane [30, 31].

2.1 DIFFERENT ELECTROSPINNING CONFIGURATION

The configuration of the feeding system that ejects the polymeric solution determines the actual composition of the electrospun nanofibers. Tailored products can be obtained as follows:

- Single spinneret: By using a single spinneret, single-component nanofibers can be produced from a homogeneous polymer solution, and multicomponent nanofibers can be electrospun from emulsions and blends.
- Coaxial spinneret: In this technique, two different solutions flow through two coaxial syringes or capillaries, resulting in a core-shell morphological structure.
- Multispinnerets: Membranes made up of different types of nanofibers can be generated by electrospinning different polymeric fluids from different spinnerets [7].

Many researchers have used the single-spinneret configuration for electrospinning. However, a low polymeric-fluid throughput has limited the industrial application of the single spinneret configuration. To increase the fluid throughput, various multijet schemes have been analyzed. Theron et al. developed a model that, under comparable conditions, can be used to steadily electrospin about nine jets from separate nozzles with a pitch of 10 mm positioned on a square of 400 mm^2 [32]. However, Yarin et al. demonstrated a novel approach by employing a ferromagnetic liquid sublayer that generates >2 jets/cm^2. In this case, electrospinning should be initiated with a high applied voltage of approximately 32 kV, and the fiber diameter range is 200 to 800 nm [33]. In addition, Yang et al. [34] showed that electrospinning with needles positioned at different heights is more stable than that with a ring arrangement and that the stable electrospinning voltage for the ring arrangement is considerably higher than that for needles at different heights [34]. In this chapter, advancements in electrospinning technique, such as free-surface electrospinning, rotary electrospinning, and melt electrospinning, are discussed for the mass production of nanofibrous materials. Furthermore, a comprehensive review of the effects of governing parameters on electrospinning techniques and the morphology of nanofibers is presented.

2.1.1 Free-surface electrospinning

Despite promising results, the configuration of free-surface electrospinning multineedle processes is technically inconvenient, owing to the possibility of clogging or blockage. Furthermore, using needles for electrospinning, which is termed capillary spinning, yields a low throughput of nanofibers. Therefore, electrospinning systems that do not use spinnerets have been developed. Typically, this type of electrospinning technique is termed needleless electrospinning or free-surface electrospinning. Many researchers have investigated the free-surface electrospinning technique [33, 35–37]. According to the principle, multiple self-organized electrically driven jets can be obtained from planar and cylindrical surfaces by applying very high voltage electrical fields. Recently, experimental studies have indicated high production rates of nanofibers on an industrial scale through free-surface electrospinning by using viscoelastic polymeric fluids. Furthermore, Thoppey et al. showed a new needle-free electrospinning configuration using an edge-plate geometry [38]. They demonstrated that this technique can be used directly to produce high-quality nanofibrous material from an unconfined polymeric solution without the possibility of blockage or clogging. In addition, they reported that the production rate of the edge-spinning apparatus is 5 times higher than that of a basic needle-based electrospinning system [38].

Therefore, the needle-based electrospinning technique has resulted in the generation of new nanofibrous membranes with a broad array of applications, such as purification, nanocomposites, and membrane fabrication. Conventionally, the production rate of the electrospinning technique for nanofibers with small diameters is rather low. Thus, the use of electrospun nanofibrous materials is limited to low-volume applications. To solve this throughput problem for electrospun nanofibrous materials, several variations of the free-surface electrospinning technique have been proposed.

2.1.2 Melt electrospinning

Melt electrospinning is a technique used to generate nanofibrous microstructures from polymer melts for applications in nanocomposites, textiles, and membrane filters. However, this electrospinning technique has not attracted much attention. The prominent reasons for this are (a) difficulty in controlling the viscosity of polymer melts compared with conventional polymeric solutions, (b) large diameters (at the micron scale) of formed nanofibers, and (c) nonconductive characteristics of polymer melts. In the

initial studies on this topic, Larrondo and St John Manley [39] have mentioned the melt electrospinning technique as part of a three-paper series on electrostatics and polymeric melts. However, because its fiber throughput is higher than that of the solution electrospinning process, interest in melt electrospinning has been prominent only during the past 5–6 years [40].

Zhou et al. studied the melt electrospinning technique in detail. Typically, most of the melt electrospinning processes use polymeric solutions that are difficult to electrospin at room temperature (e.g., polyethylene (PE) and polypropylene (PP)). Hence, temperatures in excess of 150°C are employed. However, the use of high temperatures can result in the degradation of polymers during melt electrospinning [41]. Moreover, melt electrospinning can generate high fiber throughputs without the use of solvents, which reduces the apparatus cost as ventilation equipment are no longer necessary [41].

2.2 CHARACTERIZATION OF ELECTROSPUN NANOFIBROUS MATERIALS

Membrane performance can be directly examined through characterization [42]. Knowledge of membrane material, specifications, structure, and morphology is crucial for various applications [43]. The surface characterization of the membrane is the second stage and follows the adjustment of the electrospinning parameters during the design and development of electrospun nanofibrous membranes [44].

Basic structural characterization techniques are divided into two main classes, covering a wide range of physical methodologies. The first class includes techniques related to membrane permeation analysis, such as liquid and gas flow tests, liquid displacement methods, and solute transport methods. The second class includes all the methods that can measure the surface morphological characteristics of membranes. Table 4 lists all the characterization techniques used for basic structural and morphological analysis.

Table 4 Characterization Techniques for Basic Structural and Morphological Analysis

Class of Methodologies	Methodologies or Techniques
Physical methodology	✓ Liquid and gas flow tests ✓ Liquid displacement method ✓ Solute transport method ✓ Membrane permeability
Morphological methodology	✓ Scanning Electron Microscopy (SEM) ✓ Energy dispersive spectroscopy (EDS) ✓ Transmission Electron Microscopy (TEM) ✓ Field Emission Scanning Electron Microscopy (FE-SEM) ✓ Atomic force microscopy (AFM) ✓ Nuclear magnetic resonance (NMR) ✓ X-ray diffraction (XRD) ✓ Fourier transform infrared spectroscopy (FT-IR) ✓ Confocal microscopy ✓ Raman spectroscopy ✓ Contact angle measuring device

These techniques are broadly divided into two categories: physical methods and morphological analysis methods.

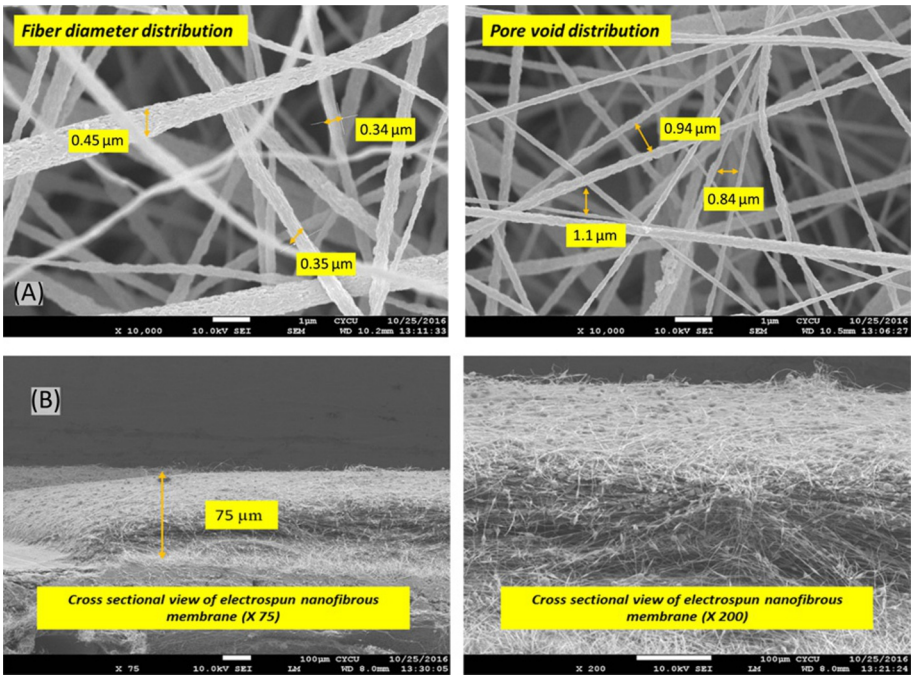

FIG. 5

(A) SEM micrographs of electrospun nanofibrous polysulfone layer indicating the pore void and fiber diameter. (B) The next figure shows the cross-sectional view of the electrospun nanofibrous polysulfone layer. The pore void, fiber diameter, and thickness of the layer can be easily analyzed using the image analysis software ImageJ2x.

The previously mentioned methodologies are used to measure characteristics such as pore size, pore size distribution, fiber diameter, surface roughness, hydrophilicity or hydrophobicity, chemical composition, elemental structure, membrane fouling potential, and morphological structure. Among all the characteristics of electrospun nanofibrous microporous membranes, the most critical for determining the applicability of the membrane in a specific liquid separation process are its pore size, surface morphology, and hydrophilicity or hydrophobicity. Fig. 5 shows the typical morphological structure of an electrospun nanofibrous polysulfone membrane.

3 PROCESS OF ELECTROSPINNING TECHNIQUE

Electrospinning is the most suitable technique for the fabrication of nanofibrous materials. The advantages include its relative ease, high speed, low cost, versatility, and large materials selection. In addition, the technique enables control over pore size, fiber diameter, and arrangement [45, 46]. The operational parameters of electrospinning must be understood because they affect fiber morphologies and microstructure. In general, the key parameters governing electrospinning techniques are

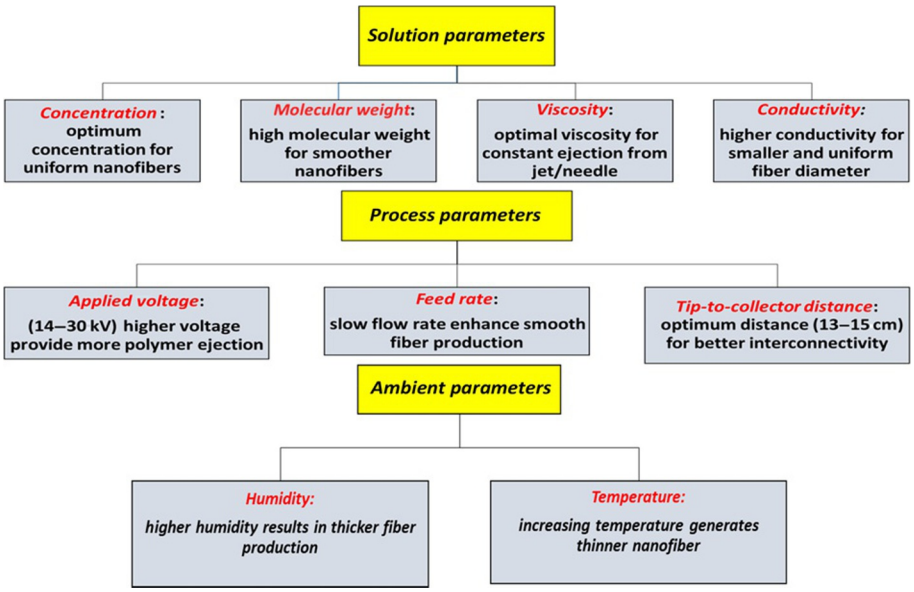

FIG. 6

Electrospinning process parameters. The most crucial parameters governing the electrospinning process are (1) polymer solution parameters, (2) process parameters, and (3) ambient parameters.

(1) polymer solution parameters, (2) process parameters, and (3) ambient parameters. Fig. 6 shows the parameters that may affect electrospinning, along with a brief description of the optimal conditions required for fabricating high-performance electrospun nanofibrous membranes.

3.1 POLYMER SOLUTION PARAMETERS

The preparation of the polymeric solution is the most important part of the production of an electrospun nanofibrous membrane; the factors that influence this step include the concentration and average polymeric weight of the polymer and the type of solvent used for dissolving the polymer pellets. The properties and preparation of polymeric solution are discussed thoroughly in the following sections.

3.1.1 Concentration of polymeric solution

The concentration of the polymeric solution plays a key role in nanofiber formation during the electrospinning process. As the concentration increases from low to high, the following four critical stages must be noted:

(a) At very low polymer concentrations, polymeric micro- (nano)particles are obtained. At this stage, electrospraying takes place instead of electrospinning because of the low viscosity and high surface tension of the polymeric solution.

(b) When the polymer concentration increases slightly, a mixture of bubbles with beads and fibers is obtained.

(c) As the polymer concentration reaches the optimum level, smooth nanofibers are obtained.
(d) When the polymer concentration is very high, helix-shaped microribbons are observed.

Thus, the fiber diameter increases with the polymeric concentration of the solution. In addition, the viscosity of the solution can be also tuned by adjusting the polymeric concentration [47–50].

3.1.2 Molecular weight

The molecular weight of the polymer influences the morphologies and microstructures of electrospun nanofibers. In general, the molecular weight of the polymer reflects the degree of entanglement of the polymeric chains in the solution (i.e., it indicates the solution viscosity). Keeping the solution concentration constant and reducing the polymeric molecular weight results in the formation of beads rather than smooth nanofibers. Thus, using polymers with a high molecular weight produces smooth nanofibers. However, further increasing the molecular weight yields a microribbon structure [51].

3.1.3 Viscosity

The solution viscosity is crucial for determining the microstructure and morphology of the fibers. Many researchers have proved that continuous and smooth nanofibers cannot be produced from solutions with very low viscosity, whereas very high viscosity makes it difficult to eject jets from the solution; thus, there is an optimum viscosity for electrospinning [39]. The viscosity of a solution can be changed by adjusting the polymeric concentration of the solution. Crucially, solution viscosity, polymeric concentration, and molecular weight are related. In fact, for a solution with low viscosity, surface tension is the dominant factor, and thus, beads or beaded nanofibers are obtained. Therefore, continuous nanofibers can be produced from a solution with optimum viscosity.

The polymeric solution used for electrospinning should possess sufficient viscosity to be stretched into nanofibers. Typically, the entanglement number of a polymeric solution can be used to analyze the formation of nanofibers through electrospinning; the entanglement number can be written mathematically as

$$(ne)\text{solution} = \frac{Mw}{(Me)\text{solution}} = \frac{\phi p.Mw}{(Me)},$$

where ne represents the entanglement number, Mw is the molecular weight, Me is the solution entanglement molecular weight, and ϕp is the polymer volume fraction.

Studies have demonstrated that when the entanglement number is higher than 3.5 and a suitable solvent is used, smooth nanofibers are obtained for polystyrene, polylactic acid, and polyethylene oxide. Notably, for $2 < ne < 3.5$, a mixture of beads and nanofibers are formed, and for $ne < 2$, no fibers are obtained [52].

3.1.4 Surface tension

Surface tension is a function of the solvent compositions of the solution, which is another important factor. Many researchers have found that different solvents may contribute different surface tensions. At a fixed concentration, decreasing the surface tension of the polymeric solution can yield smooth nanofibers. Furthermore, recent research has indicated that the surface tension and viscosity of a solution can be adjusted by changing the mass ratio of the solvent mixture [53, 54]. Typically, surface tension can be easily reduced by using various surfactants, but this may introduce impurities into the final electrospun polymeric nanofibrous membrane. Recent research shows that anionic surfactants,

such as sodium dodecyl sulfate, not only reduce the surface tension of the polymeric solution but also introduce additional charge carriers to the solution, thus improving the quality of the nanofibers. This study had the dual function of lowering the bead formation and stretching to produce finer and smoother fibers [26, 27].

3.1.5 Surface charge density and conductivity

The conductivity of a solution is mainly evaluated by the type of polymer and solvent. Natural polymers are polyelectrolytic; that is, they have a low charge density in the solution, resulting in higher surface tension under an electric field and formation of poor-quality nanofibers. Furthermore, the electrical conductivity of the solution can be adjusted by adding ionic salts, such as KH_2PO_4 and NaCl [24, 55], and thus, nanofibers with a uniform fiber diameter can be produced. Furthermore, the electrical conductivity of a solution can be increased by adding an organic acid as the solvent [21].

3.1.6 Solvent volatility

Solvent volatility is another important aspect of a polymeric solution. If a polymer solution is prepared from solvents with very low volatility, wet nanofibers, fused nanofibers, or even negligible nanofiber may be produced. However, a highly volatile solution may result in intermittent spinning because of the solidification of the polymer at the spinneret tip [56, 57]. This layer may grow and choke off the spinning solution until and unless more polymeric solution has been injected to dislodge the solidified skin. Sometimes such electrospinning may produce artifacts on the surface of the membrane [58]. Thus, it can be concluded that using a highly volatile solvent for electrospinning results in flat or ribbonlike nanofibers or fibers with surface pores [59].

3.2 PROCESS PARAMETERS

Process parameters are very crucial for ensuring the conversion of polymeric solutions into smooth and fine fibers via electrospinning.

3.2.1 Applied voltage

When the applied voltage is higher than the threshold voltage, charged jets are ejected from the Taylor cone. However, the effect of the applied voltage on the diameter of electrospun nanofibers is debated. According to Reneker and Chun, applied voltage does not affect the diameter of electrospun polyethylene oxide (PEO) fibers significantly [60]. On the other hand, many researchers have shown that high applied voltages lead to larger fiber diameters. Few researchers have observed that high applied voltages can increase the electrostatic repulsive force on the charged jet, thus reducing the fiber diameter [54]. Furthermore, some research groups have shown that high applied voltages increase the probability of bead formation [61]. Therefore, it can be stated that applied voltage influences the fiber diameter, but the degree of influence varies with the polymeric solution concentration and depends on the distance between the tip and the substrate collector [62, 63].

3.2.2 Feed flow rate

The feed flow rate of the polymeric solution from the syringe or injector is another crucial process parameter. Many researchers recommend a low feed flow rate to allow sufficient time for polarization of the polymeric solution. When the feed flow rate is very high, bead nanofibers with a large fiber

Table 5 Process Parameters and Their Impact on Electrospinning

Parameters or Factors	Impact or Influences	References Used
Jet	The jet initiation is the overall combination of introducing electrical charges to the polymeric solution and subjecting it to a very high voltage	[17]
Voltage	Applied voltage results in stretching of the polymeric solution droplet which may increase with higher applied voltage. On the other hand, the high voltage may also lead to faster acceleration toward the metal plate collector because of the increased voltage, resulting in a shorter flight of time for the jet to stretch prior to deposition. Thus, this condition leads to larger fiber diameter	[66]
Feed rate	At the optimum feed rate, the distribution of fiber diameter will be the narrowest, and thus, any deviation may result in larger fiber diameter	[67]
Temperature	A higher solution temperature may reduce the solution viscosity. Therefore, it is expected that the fiber diameter will be decreased with reduced viscosity	[68]
Nozzle diameter	Typically, an increase in nozzle diameter increases fiber diameter, distribution, and productivity simultaneously. This is because of the higher amount of mass available for the electrospinning process	[58]

This brief information may assist researchers in adjusting and optimizing the conditions required to produce the desired electrospun nanofibrous membrane.

diameter are formed rather than smooth or fine nanofibers with a small diameter owing to the very short drying time prior to reaching the substrate collector and a low stretching force [61].

3.2.3 Distance from syringe tip to substrate collector (H)

It has been observed that the distance (H) between the substrate collector and the tip of the syringe may also affect the morphology and diameter of the fiber [64]. In general, when the distance (H) is very short, the fiber does not have enough time to solidify before reaching the substrate collector, whereas if the distance (H) is too long, beaded nanofibers are formed. Another important physical aspect of the electrospun nanofibers is dryness, and therefore, optimum distance is required. Yuan et al. also observed that a slightly large distance (H) favors the formation of thin fibers [65]. Table 5 lists the important process parameters of electrospinning.

3.3 AMBIENT PARAMETER

Ambient parameters such as humidity and temperature may also affect the fiber diameter and microstructure. According to Mit-uppatham et al., high temperatures favor the formation of thin fibers [56, 57]. Furthermore, low humidity may dry the solvent and accelerate solvent evaporation. On the other hand, high humidity will result in a large fiber diameter. Recently, Casper et al. demonstrated that variations in humidity may affect the surface microstructure and morphology of electrospun nanofibers [69]. This phenomenon can be explained on the basis of rapid precipitation of the polymeric solution when water condenses on the surface of the electrospinning jet; in particular, high humidity prevents the elongation or stretching of the polymeric solution, thus leading to the formation of thick nanofibers. Interestingly, lower humidity may also result in faster solvent vaporization and lead to a larger fiber diameter because of an increase in the solidification rate, whereas for some polymers, higher humidity

Table 6 Summary of Effect of Humidity on Fiber Diameter in Electrospinning Process

Relative Humidity	Impact on Fiber Diameter	Explanation of the Effect
Higher	Increase	Precipitation effect can be observed especially for water-insoluble polymers
Higher	Decrease	Water absorption resulting in reduction of concentration especially for water-soluble polymers
Lower	Increase	Rapid solvent vaporization takes place
Lower	Decrease	Decrease in precipitation effect

The electrospinning process is highly affected by the ambient temperature and relative humidity owing to the effect of solvent vaporization rate and solution sensitivity to humidity, including the ability to produce nanofibers, uniformity in fiber diameter, and smoothness, porosity, and surface morphology of fibers [70–72].

has been shown to reduce fiber diameter [70]. Functionality and performance of the resultant fibers can also be affected by the ambient parameters, depending on the materials and additive used. Table 6 shows the effects of relative humidity on fiber diameter.

4 ELECTROSPINNING METHODOLOGIES

Electrospun nanofibrous membranes are fabricated by incorporating chemical groups or by surface modification. In this section, different types of fabrication and surface modification techniques that may aid future research in water purification and desalination technology are discussed.

4.1 LAYER-BY-LAYER TECHNIQUE

The layer-by-layer technique is based on the adhesion of positively, as well as negatively, charged macromolecules on the surface of the desired material. The advantage of this method is that the functional groups of the layers can be chosen such that either a single property can be improved or multiple properties can be introduced. The high surface area of electrospun nanofibrous membranes has motivated researchers to explore the possibility of constructing highly efficient membranes for water purification and desalination technology. Although layer-by-layer coating is most often carried out by the use of alternately charged organic molecules, positively charged inorganic nanoparticles may also be coated on negatively charged organic molecules (e.g., polyacrylic acid). Coating nanoparticles on the surface of a nanofiber increase its surface roughness, and a final coating of fluoroalkylsilane can be used to fabricate a superhydrophobic material [73]. Owing to its negatively charged surface, cellulose acetate is one of the attractive materials for the layer-by-layer technique. However, to start the process, the surface of the material must be activated by chemical incorporation. Subsequent introduction of alternately charged molecules is used to form the layers. Both charged organic molecules and inorganic chemical groups are used in electrospun nanofibers [21]. Fig. 7 shows the layer-by-layer technique and how it can be used for producing various membranes for water purification and desalination technology.

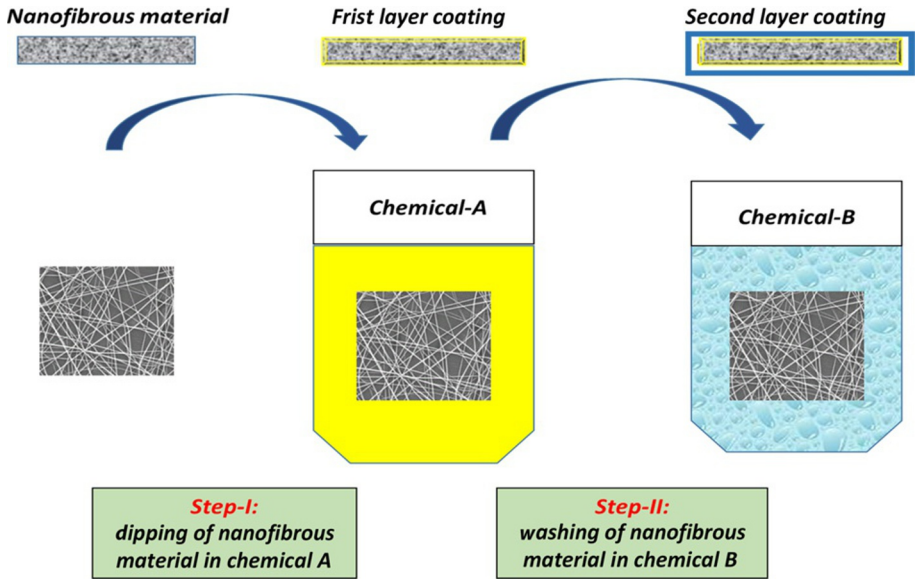

FIG. 7

Layer-by-layer method for functionalization of electrospun nanofibers. This technique can be used to improve a single property or to introduce multiple properties in the desired electrospun nanofibrous material.

4.2 FUNCTIONALIZATION OF ELECTROSPUN NANOFIBERS

Functionalization offers additional features to a single material nanofiber. A material with superior mechanical strength or chemical stability may be incorporated with other desirable properties such as antibacterial effects, biocompatibility, and catalytic or chemical sensing. Introducing additional functional properties to the nanofiber enhances its performance and versatility that can be tailored to specific applications. Table 7 lists various techniques of functionalization with varying degrees of versatility. The functionalization methods may be used together to create multifunctional nanofibers.

4.3 SOLUTION BLENDING METHOD

The solution blending method is one of the most commonly used techniques for introducing an alternative property or function to the base material. This method involves mixing two parts in a solution followed by electrospinning. In many experiments, the blending process is used where the desired material is unable to form nanofibers and, therefore, a companion electrospinnable polymer is used. Basically, colloids, where one part is nonsoluble, such as carbon nanotubes, silica particles, and hydroxyapatite, are suspended in the solution and electrospun to form nanofibers [74]. The other, more commonly incorporated materials are polymers and soluble inorganic salts. Three blending schemes are commonly encountered: the first scheme uses materials that are soluble in a common solvent, the second scheme uses different solvents for both materials, and the third scheme uses insoluble materials, as mentioned earlier. Given the potentiality of solution blending, combinations of the three schemes can be used in nanofiber electrospinning.

Table 7 Functionalization Methods and Their Application Based on Mechanical Properties, Reactivity, and Material Chemistry

Functionalization Method	Location	Improve Mechanical Properties	Reactive/ Functional Groups	Material Chemistry
Blending	Bulk	Yes	Yes	Yes
Plasma treatment	Surface	–	Yes	Yes
Wet chemical treatment	Surface	–	Yes	Yes
Adhesion	Surface	–		Yes
Direct covalent bonding	Surface	–	Yes	Yes
Layer by layer	Surface	–	Yes	Yes
Multicomponent electrospinning (e.g., core-shell)	Core/ surface	Yes	Yes	Yes
Mineralization	Surface	Yes	–	
Sol-gel coating followed by sintering	Surface	–	–	Yes
Inorganic catalytic deposition	Surface	–	–	Yes

Reactive functional groups indicate the presence of carboxyl or amino groups for further bonding of other molecules, whereas material chemistry indicates the possibility of adding secondary group(s) to the principal fiber material.

4.4 WET CHEMICAL TREATMENT

In this technique, the relatively inert polymer nanofiber is treated with a chemical in order to introduce reactive functional groups such as carboxylic (—COOH), amine (—RNH_2), or hydroxyl (—OH) groups, depending on whether the sites on the polymer molecule are susceptible to electrophilic or nucleophilic attack. The nanofibrous material is soaked in an alkaline medium to create a carboxylic or hydroxyl group on the nanofibrous surface. Table 8 lists some chemically treated electrospun fibers and their respective generated activated groups. Moreover, a basic pictorial representation of the wet chemical treatment is shown in Fig. 8, which can be used for the functionalization of electrospun nanofibrous membranes.

5 DESALINATION USING ELECTROSPUN MEMBRANE

Microporous polymeric membranes can be fabricated by various techniques, including phase inversion, film lithography, and stretching [81, 82]. Nevertheless, each method has its advantages and disadvantages [83]. Recently, the electrospinning process has also been explored for the production of microporous polymeric membranes. As compared to the conventional membrane fabrication methods, electrospinning produces membranes with a uniform pore-size distribution, higher interconnectivity of pores, and significantly higher porosity [84]. Thus, electrospun nanofibrous membranes are attracting interest for use in separation and purification processes where these characteristics are highly desirable. Electrospun membranes are used in various separation processes such as pressure-driven separation,

Table 8 Chemically Treated Electrospun Nanofibers

Polymer Used	Chemical Reagent	Activated Group	References Used
Cellulose acetate (CA)	– Hydrolysed in sodium hydroxide and ethanol; – Treated with methacrylate chloride; – Graft polymerization with methyl methacrylate, acrylamide, and *N*-isopropylacrylamide	—OH	[75]
Polyacrylonitrile (PAN)	Sodium hydroxide	—COOH	[76]
Polycaprolactone (PCL)	Potassium hydroxide	—COOH	[77]
Poly(L-lactide-*co*-caprolactone) copolymer (PLCL)	Aminolysis utilizing 1,6-hexanediamine followed by bonding using glutaraldehyde	$—NH_2$	[78]
Polysulfone (PSF)	Formaldehyde solution under acidic conditions	$—CH_2OH$	[79]
Polyimide (PI)	Sodium hydroxide followed by bonding using 1-ethyl-3-(3-dimethylaminopropyl) carbodiimide hydrochloride	—OH, —COOH	[80]

This table has been summarized based on the chemical reagent used and the activated group thus generated.

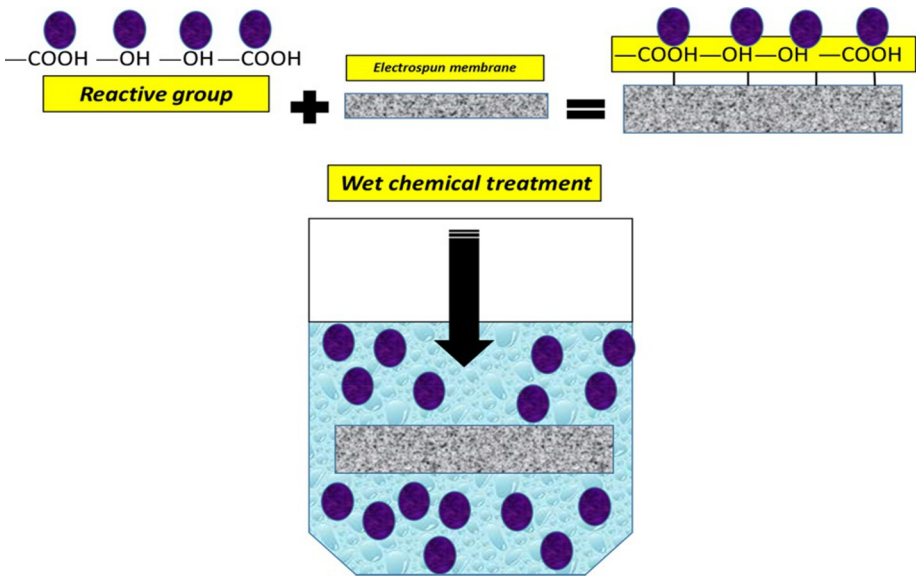

FIG. 8

Schematic diagram of functionalization of electrospun nanofibers by wet chemical treatment. In this process, reactive functional groups are introduced in electrospun nanofibers, such as carboxylic (—COOH), amine ($—RNH_2$), or hydroxyl (—OH) groups.

membrane distillation, pretreatment of feed prior to reverse osmosis (RO) or nanofiltration (NF), and oily wastewater separation. Interestingly, thin-film composite (TFC) membranes, for forward osmosis, and various RO and NF membranes are fabricated by the electrospinning technique. The traditional middle layer is replaced with an electrospun membrane. It is then coated with various layers, and then thin-film nanocomposite (TFNC) membranes are fabricated [85]. In this regard, the permeate flux and oil rejection (for oily wastewater) by TFNC membranes are found to be much higher than those of commercial NF membranes [86]. For enhancing the performance of electrospun membranes as filtration media, they can be used as support layers in the next generation of TFC membranes, including UF, NF, and RO membranes. TFC membranes consist of three fundamental layers, including the top ultrathin selective layer, the middle porous support layer, and the bottom nonwoven fabric layer [19]. Much R&D has been carried out on the preparation and surface modification of electrospun membranes for enhanced desalination and water treatment, especially in the last decade. Therefore, there is a need to review these advancements to pave the way for the next-generation research. Table 9 summarizes all the recent works on the application of electrospun nanofibers in fabricating polymeric membranes.

5.1 MEMBRANE DISTILLATION

Membrane distillation is an efficient separation technology wherein a membrane is used to separate salt water and pure water (as a permeate). There are a few crucial parameters that affect the rate as well as the efficiency of MD. The membrane porosity, pore-size distribution, and tortuosity influence the ease with which vapor passes through the membrane and collected as a permeate. Being hydrophobic, or superhydrophobic in nature, such membranes are used for MD [93].

For membranes to be used in MD, they must be hydrophobic, be porous, have high liquid entry pressure (LEP), and have good chemical/mechanical/thermal stability [93, 94]. Nevertheless, most of the MD membranes are commercially used for microfiltration (MF) and are composed of hydrophobic polymers [95]. Interestingly, electrospun nanofibrous membranes have indicated promising properties for the application of the MD process. The first-ever application of the electrospun nanofibrous membrane in desalination by the MD process was published by Feng et al. [96]. In this research, polyvinylidene fluoride (PVDF)-based electrospun membrane samples were used for desalting 6 wt% NaCl solution by the air-gap membrane distillation (AGMD) process. Salt rejection higher than 98% was achieved in this work.

Su et al. demonstrated the effectiveness of electrospun nanofibrous membranes in salt rejection. The overall results indicate that the salt rejection of PVDF-*co*-HFP (HFP: hexafluoropropylene) and the PVDF electrospun membrane was 99.9% and 99.98%, respectively, whereas the salt rejection of PTFE was calculated as 99.99%. Thus, the salt rejection of PVDF-*co*-HFP is better than that of PVDF electrospun nanofibrous membrane and is almost similar to that of the commercially available PTFE membrane [97].

Liao et al. fabricated dual-layered superhydrophobic membranes composed of PVDF polymers with silica nanoparticles for improved desalination by the MD process. These fabricated membranes have shown significantly high water flux and salt rejection. The researchers concluded that to use these membranes in water industries, modification, as well as optimization, is required for controlling the pore size of the membrane and enhancing the long-term performance of the membranes by optimizing the SiO_2 composition [98].

Table 9 Summary of Recent Research Work on Different Fabricated Electrospun Nanofibrous Membranes for Various Applications

Polymer and Solvent Utilized	Experimental Setup	Applications	References
Polyvinyl alcohol/distilled water	2-Layered membrane with hydrophobic top layer (polypropylene mat) and hydrophilic bottom layer (polyvinyl alcohol electrospun layer)	Membrane distillation (desalination)	[26, 27]
Polysulfone/DMF	2-Layered membrane with electrospun polysulfone hydrophobic membrane as top layer and hydrophilic cellulosic mat as bottom layer	Membrane distillation (desalination)	[26, 27]
Polyethersulfone ($Mw = 7.8 \times 104$ g/mol) and Polysulfone ($Mw = 8.0–8.6 \times 104$ g/mol)/ DMF (anhydrous, 99.8%), NMP (anhydrous, 99.5%), TMC (98%) and MPD (>99%)	TFC fabrication by interfacial polymerization	Forward osmosis	[87]
Polyetherimide/DMF and NMP	TFC fabrication by electrospinning technique	Forward osmosis	[88]
Polyacrylonitrile ($Mw = 150{,}000$ g/mol)/MDP, TMC, and DMF	Engineering the support layer by incorporating the silica nanoparticle (SiO_2: 200 nm particle size, 4 nm pore size)	Reverse osmosis, forward osmosis, and pressure retarded osmosis	[89]
Polyvinylidene fluoride (Mw: 550 kg/mol)/DMF and THF	Fabrication of support layer by electrospinning technique for TFC membrane	Forward osmosis	[90]
Polyvinylidene fluoride-*co*-hexafluoropropylene (PH) ($Mw = 445{,}000$)/acetone and *N*,*N*-dimethylacetamide (DMAc)	Effect of heat treatment on electrospun membrane	Membrane distillation	[91]
Polyvinylidene fluoride-*co*-hexafluoropropylene (pH) and Polyvinyl alcohol (PVA) ($Mw = 85{,}000$ g/mol)—Nylon-6 (N6) ($Mw = 10{,}000$ g/mol)—Polyacrylonitrile (PAN) ($Mw = 150{,}000$ g/mol)/ DMF, LiCl (lithium chloride), and Triton X-100	Dual layer (hydrophobic-hydrophilic) flat sheet membrane	Membrane distillation	[92]

Electrospun nanofibrous polymeric materials can be used as support layers in new-generation of TFC membranes including UF, NF, RO, and FO membranes.

To use an electrospun nanofibrous membrane in the MD process, it must be able to maintain separation between the feed stream and the permeate stream. Thus, a superhydrophobic membrane will be efficient as it is considered to be the best for maintaining water separation. The PVDF electrospun nanofibrous membrane is commonly used for water filtration process. Researchers have evaluated the performance of PVDF-based beaded and smooth nanofibers in MD. Interestingly, beaded nanofibers showed a higher contact angle, whereas the water flux from the smooth nanofibers was much better than that from the beaded nanofibers, owing to the smaller void volume fraction of the beaded nanofibers [20].

5.2 PRESSURE-DRIVEN SEPARATION

Basically, the primary application of a membrane is to separate two distinct phases, preferentially controlling one phase while simultaneously working as a barrier to the other phase (e.g., bacteria and suspended solids; [99, 100]).

Some researchers have reported that electrospun nanofibrous materials can be used as a support layer in advanced TFC membranes [19]. TFC membranes, including those used for UF, NF, RO, and FO, are composed of three fundamental layers, as shown in Fig. 9: a top ultrathin selective layer, a middle porous support layer, and a bottom nonwoven fabric layer.

Kaur et al. studied the performance of an electrospun polymeric web as a support layer in TFC membranes [101]. They fabricated various polyacrylonitrile (PAN)-based microfiltration membranes with various fiber diameters. The fiber diameter changes with the polymer concentration (4%–10% w/v). The interfacial polymerization technique (mixture of piperazine and *p*-phenylene diamine with trimesoyl chloride) was used to coat a thin film onto the surface of the electrospun nanofibrous material.

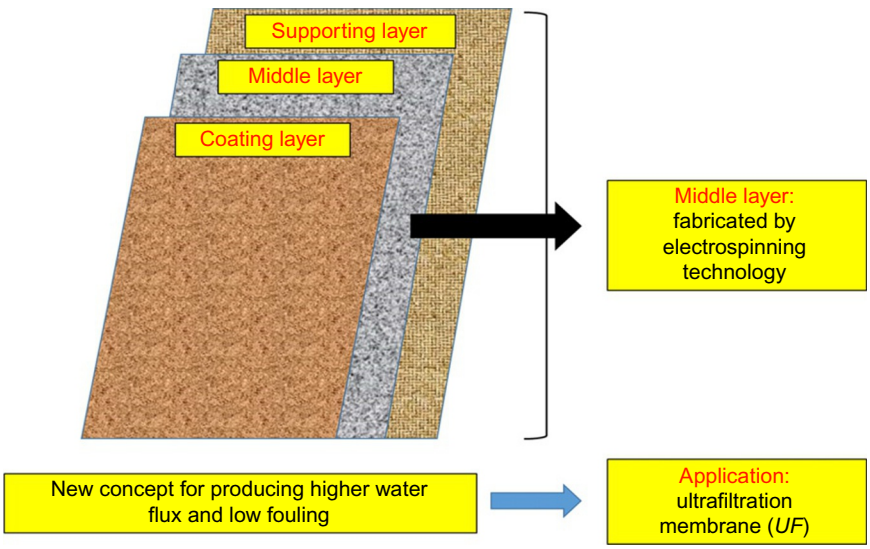

FIG. 9

General fabrication scheme of three-layered, high-flux, and low-fouling UF membrane.

The fabricated membranes were used for the desalination of salt water with a salt concentration of up to 2000 mg/L (including both monovalent and divalent ions). The overall results of the desalting experiments showed that as the fiber diameter decreased (toward the nano range), salt rejection increased but at the expense of permeate water flux. However, when the thickness of the support layer (electrospun nanofibrous layer) and the pore size was decreased, the permeate water flux and salt rejection increased. The optimum concentration of PAN for the electrospun nanofibers was found to be 8 wt%.

6 FUTURE TRENDS AND RESEARCH CHALLENGES

During the early 2000s, the primary concerns in the field of electrospinning were the fabrication of nanofibers from different polymers and their corresponding applications. Researchers have achieved a better understanding of the electrospinning technique process for producing nanofibers of desired morphology and fiber diameter. Despite the significant advantages of electrospun nanofibrous membranes, there are a few limitations that influence the membrane morphology and structure. Therefore, future research should consider these challenges in near future. The drawbacks of electrospun nanofibrous membranes are as follows [21, 22]:

1. Micro-cracking, corner rounding, and temperature-induced problems
2. Fabrication and commercialization of electrospun nanofibrous membranes on a large industrial scale
3. Fabrication of membranes with uniform pore-size distribution
4. Selection of suitable materials and incorporation routes to introduce the desired functionality, during or after the electrospinning process
5. Optimization of the electrospinning process with cost-effective separation and purification technology

The application of this versatile technique is being extended to ceramics, inorganic or organic, and metal composite systems as well. To this end, innovative electrospinning techniques such as coaxial electrospinning, mixing and multiple electrospinning, core-shell electrospinning, and blowing-assisted electrospinning have been developed.

As compared to the traditional or conventional techniques used for generating polymeric and composite membranes, electrospinning technique is found to be more versatile owing to uniform pore size and interconnectivity of pores. Table 10 lists a few applications that can be investigated to ensure the effectiveness of the electrospun nanofibrous membrane.

7 CONCLUSION

Electrospun nanofibrous membranes have attracted much attention from researchers because of its high versatility. Electrospun nanofibrous membranes have become the next-generation filtration media that have promising features and offer good opportunities for advanced filtration techniques in the near future. This versatile technique can be used to fabricate high-performance electrospun nanofibrous membranes with a high surface area, a high surface area-to-pore volume ratio, high pore interconnectivity, and uniform pore distribution. Recently, many researchers have focused on the functionalities of

Table 10 Some Applications That Can Be Further Investigated to Enhance the Potential of Electrospinning Technique

Parameters or Conditions	Future Perspectives
Membrane modules	The electrospun nanofibrous membrane plays an important role in the area of water treatment, but more analysis can be done with respect to ultrafiltration (UF) and nanofiltration (NF) and reverse osmosis (RO). The practical use of electrospun nanofibrous membranes in these modules can further be investigated
Hydrophobic membrane	To make the MD process effective, a higher hydrophobic membrane can be produced
Hydrophilic membrane	Furthermore, hydrophilic membranes can be produced by utilizing an electrospinning technique that can be used in a forward osmosis (FO) system
General characteristics	The general features of an ideal membrane, such as interconnectivity of the pores, uniform pore size, mechanical strength, and stability, should be improved by postthermal treatment as well as chemical treatment
Stability and durability	The longevity and durability must be two of the important fields of research while fabricating membranes by the electrospinning technique

Electrospinning has emerged as an effective technique for fabricating stable and durable membranes. The main focus of this table is to list the possible conditions for future potential applications [21, 30, 102].

electrospun nanofibers to improve their applicability on an industrial scale. For this purpose, nanoparticles have been incorporated into the electrospun nanofibrous membrane to improve its performance. Furthermore, properties such as high porosity, uniform pore size with a narrow pore-size distribution, and a large surface area-to-pore volume ratio make electrospun nanofibrous membranes most desirable as MD membranes to generate a high water vapor flux. Nonwoven nanofibrous membranes are widely used in the removal of small particles by the MF process and in desalination by the MD process. The performance of electrospun nanofibrous membranes can be enhanced by considering features such as pore-size distribution, hydrophilicity or hydrophobicity, mechanical strength, and stability. To increase the permeability and permeate flux, properties such as membrane thickness and pore size should be optimized. The performance of electrospun nanofibrous membranes can further be optimized with a deeper understanding of how operating parameters and solution parameters can control membrane characteristics in different polymeric solution. Unfortunately, upgrading the electrospinning technique to an industrial scale for commercialization remains a challenge. Therefore, more attention has been given to the high durability and stability of the electrospun nanofibrous membranes to eradicate this problem. Currently, electrospinning is one of the crucial, versatile processes that have influenced the R&D on water treatment applications. To improve the morphological and topographical features of electrospun nanofibers, various methodologies, such as molecular bonding, in situ polymerization, and addition of molecular dopants, are used in conjunction with electrospinning. Strategies for surface modification, such as nanoparticle coating, treatment with chemicals or heat, grafting, and interfacial polymerization, have been found to be highly effective in enhancing the filtration performance of electrospun nanofibrous membranes. In addition, electrospun nanofibrous membranes are effective in oily wastewater treatment. Thus, considering features such as tunable selectivity, extraordinary permeability, and energy/cost efficiency, it can be concluded that the new-generation membranes used for environmental applications will be based on cost-effective nanofibrous materials.

ACKNOWLEDGMENT

The authors would like to acknowledge the financial assistance from the Ministry of Science and Technology (MOST), Republic of China (Taiwan) and Institute of Environmental Engineering and Management (IEEM), National Taipei University of Technology under the grant number: 104-2221-E-027-004-MY3.

REFERENCES

[1] F. Mushtaq, M. Guerrero, M.S. Sakar, M. Hoop, A.M. Lindo, J. Sort, X. Chen, B.J. Nelson, E. Pellicer, S. Pané, Magnetically driven bi 2 O 3/BiOCl-based hybrid microrobots for photocatalytic water remediation, J. Mater. Chem. A 3 (47) (2015) 23670–23676.

[2] S. Ramakrishna, M.M.A. Shirazi, Electrospun membranes: next generation membranes for desalination and water/wastewater treatment, Desalination 308 (2013) 198–208.

[2a] J. Zeleny, The electrical discharge from liquid points, and a hydrostatic method of measuring the electric intensity at their surfaces, Phys Rev 3 (2) (1914) 69.

[3] Formhals, A. (1934). Process and apparatus for preparing artificial thr-eads, US Patent, 1975504.

[4] G. Taylor, Disintegration of water drops in an electric field. Proc. Royal Soc. Lond. A 280 (1382) (1964) https://doi.org/10.1098/rspa.1964.0151.

[5] G. Taylor, Electrically driven jets. Proc. Royal Soc. Lond. A 313 (1515) (1969) https://doi.org/10.1098/rspa.1969.0205.

[6] N. Tucker, J. Stanger, M. Staiger, H. Razzaq, K. Hofman, The history of the science and technology of electrospinning from 1600 to 1995, J. Eng. Fiber. Fabr. 7 (2012) 63–73.

[7] G.C. Rutledge, S.V. Fridrikh, Formation of fibers by electrospinning, Adv. Drug Deliv. Rev. 59 (14) (2007) 1384–1391.

[8] M. Bognitzki, W. Czado, T. Frese, A. Schaper, M. Hellwig, M. Steinhart, A. Greiner, J.H. Wendorff, Nanostructured fibers via electrospinning, Adv. Mater. 13 (1) (2001) 70–72.

[9] M. Ngiam, S. Ramakrishna, M. Raghunath, C.K. Chan, Nanofiber patent landscape, Recent Patents on Nanotechnology 1 (2) (2007) 137–144.

[10] G. A. Kinney, Apparatus for preparing a nonwoven web, Google Patents, 1980.

[11] J. Doshi, D.H. Reneker, Electrospinning process and applications of electrospun fibers, J. Electrost. 35 (2–3) (1995) 151–160.

[12] D.H. Reneker, A.L. Yarin, H. Fong, S. Koombhongse, Bending instability of electrically charged liquid jets of polymer solutions in electrospinning, J. Appl. Phys. 87 (9) (2000) 4531–4547.

[13] A. Spivak, Y. Dzenis, D. Reneker, A model of steady state jet in the electrospinning process, Mech. Res. Commun. 27 (1) (2000) 37–42.

[14] T. Lin, H. Wang, H. Wang, X. Wang, The charge effect of cationic surfactants on the elimination of fibre beads in the electrospinning of polystyrene, Nanotechnology 15 (9) (2004) 1375.

[15] N. Bhardwaj, S.C. Kundu, Electrospinning: a fascinating fiber fabrication technique, Biotechnol. Adv. 28 (3) (2010) 325–347.

[16] H. Karakaş, Electrospinning of Nanofibers and There Applications, Istanbul Technical University, Textile Technologies and Design Faculty, Istanbul, 2015.

[17] J. Deitzel, J. Kleinmeyer, D. Harris, N.B. Tan, The effect of processing variables on the morphology of electrospun nanofibers and textiles, Polymer 42 (1) (2001) 261–272.

[18] S. Sukigara, M. Gandhi, J. Ayutsede, M. Micklus, F. Ko, Regeneration of Bombyx mori silk by electrospinning—part 1: processing parameters and geometric properties, Polymer 44 (19) (2003) 5721–5727.

[19] S. Subramanian, R. Seeram, New directions in nanofiltration applications—are nanofibers the right materials as membranes in desalination? Desalination 308 (2013) 198–208.
[20] M. Essalhi, M. Khayet, Self-sustained webs of polyvinylidene fluoride electrospun nanofibers at different electrospinning times: 1. Desalination by direct contact membrane distillation, J. Membr. Sci. 433 (2013) 167–179.
[21] S.S. Ray, S.-S. Chen, C.-W. Li, N.C. Nguyen, H.T. Nguyen, A comprehensive review: electrospinning technique for fabrication and surface modification of membranes for water treatment application, RSC Adv. 6 (88) (2016) 85495–85514.
[22] Z.-M. Huang, Y.-Z. Zhang, M. Kotaki, S. Ramakrishna, A review on polymer nanofibers by electrospinning and their applications in nanocomposites, Compos. Sci. Technol. 63 (15) (2003) 2223–2253.
[23] Y. Dzenis, Y. Wen, Continuous carbon nanofibers for nanofiber composites, MRS Online Proceedings Library Archive, vol. 702, 2001.
[24] X. Zong, K. Kim, D. Fang, S. Ran, B.S. Hsiao, B. Chu, Structure and process relationship of electrospun bioabsorbable nanofiber membranes, Polymer 43 (16) (2002) 4403–4412.
[25] G.-D. Kang, Y.-M. Cao, Application and modification of poly (vinylidene fluoride)(PVDF) membranes–a review, J. Membr. Sci. 463 (2014) 145–165.
[26] S.S. Ray, S.-S. Chen, H.-T. Hsu, D.-T. Cao, H.-T. Nguyen, N.C. Nguyen, Uniform hydrophobic electrospun nanofibrous layer composed of polysulfone and sodium dodecyl sulfate for improved desalination performance, Sep. Purif. Technol. 186 (2017) 352–365.
[27] S.S. Ray, S.-S. Chen, N.C. Nguyen, H.-T. Hsu, H.T. Nguyen, C.-T. Chang, Poly (vinyl alcohol) incorporated with surfactant based electrospun nanofibrous layer onto polypropylene mat for improved desalination by using membrane distillation, Desalination 414 (2017) 18–27.
[28] D. Aussawasathien, C. Teerawattananon, A. Vongachariya, Separation of micron to sub-micron particles from water: electrospun nylon-6 nanofibrous membranes as pre-filters, J. Membr. Sci. 315 (1) (2008) 11–19.
[29] C. Shao, H. Guan, Y. Liu, J. Gong, N. Yu, X. Yang, A novel method for making ZrO_2 nanofibres via an electrospinning technique, J. Cryst. Growth 267 (1) (2004) 380–384.
[30] S. Homaeigohar, M. Elbahri, Nanocomposite electrospun nanofiber membranes for environmental remediation, Materials 7 (2) (2014) 1017–1045.
[31] W. Liu, M. Graham, E.A. Evans, D.H. Reneker, Poly (meta-phenylene isophthalamide) nanofibers: coating and post processing, J. Mater. Res. 17 (12) (2002) 3206–3212.
[32] S. Theron, A. Yarin, E. Zussman, E. Kroll, Multiple jets in electrospinning: experiment and modeling, Polymer 46 (9) (2005) 2889–2899.
[33] S. Theron, E. Zussman, A. Yarin, Experimental investigation of the governing parameters in the electrospinning of polymer solutions, Polymer 45 (6) (2004) 2017–2030.
[34] Y. Yang, Z. Jia, Q. Li, L. Hou, H. Gao, L. Wang, Z. Guan, Multiple jets in electrospinning, Properties and Applications of Dielectric Materials, 2006. 8th International Conference on, IEEE, 2006.
[35] C.J. Angammana, S.H. Jayaram, Fundamentals of electrospinning and processing technologies, Part. Sci. Technol. 34 (1) (2016) 72–82.
[36] J. Kameoka, R. Orth, Y. Yang, D. Czaplewski, R. Mathers, G.W. Coates, H. Craighead, A scanning tip electrospinning source for deposition of oriented nanofibres, Nanotechnology 14 (10) (2003) 1124.
[37] F.L. Zhou, R.H. Gong, I. Porat, Mass production of nanofibre assemblies by electrostatic spinning, Polym. Int. 58 (4) (2009) 331–342.
[38] N.M. Thoppey, J.R. Bochinski, L.I. Clarke, R.E. Gorga, Unconfined fluid electrospun into high quality nanofibers from a plate edge, Polymer 51 (21) (2010) 4928–4936.
[39] L. Larrondo, R. St John Manley, Electrostatic fiber spinning from polymer melts. I. Experimental observations on fiber formation and properties, J. Polym. Sci. B Polym. Phys. 19 (6) (1981) 909–920.
[40] D.W. Hutmacher, P.D. Dalton, Melt electrospinning, Chem. Asian J. 6 (1) (2011) 44–56.

[41] D.D. da Silva Parize, M.M. Foschini, J.E. de Oliveira, A.P. Klamczynski, G.M. Glenn, J.M. Marconcini, L. H.C. Mattoso, Solution blow spinning: parameters optimization and effects on the properties of nanofibers from poly (lactic acid)/dimethyl carbonate solutions, J. Mater. Sci. 51 (9) (2016) 4627–4638.
[42] T. Matsuura, Progress in membrane science and technology for seawater desalination—a review, Desalination 134 (1–3) (2001) 47–54.
[43] D. Rana, T. Matsuura, Surface modifications for antifouling membranes, Chem. Rev. 110 (4) (2010) 2448–2471.
[44] A. Shirazi, M. Mahdi, A. Kargari, S. Ramakrishna, J. Doyle, M. Rajendrian, P. Babu, Electrospun membranes for desalination and water/wastewater treatment: a comprehensive review, J Membr. Sci. Res. 3 (3) (2017) 209–227.
[45] C. Burger, B.S. Hsiao, B. Chu, Nanofibrous materials and their applications, Annu. Rev. Mater. Res. 36 (2006) 333–368.
[46] W.-E. Teo, S. Ramakrishna, Electrospun nanofibers as a platform for multifunctional, hierarchically organized nanocomposite, Compos. Sci. Technol. 69 (11) (2009) 1804–1817.
[47] G. Eda, S. Shivkumar, Bead-to-fiber transition in electrospun polystyrene, J. Appl. Polym. Sci. 106 (1) (2007) 475–487.
[48] H. Fong, I. Chun, D. Reneker, Beaded nanofibers formed during electrospinning, Polymer 40 (16) (1999) 4585–4592.
[49] K. Lee, H. Kim, H. Bang, Y. Jung, S. Lee, The change of bead morphology formed on electrospun polystyrene fibers, Polymer 44 (14) (2003) 4029–4034.
[50] Z. Li, C. Wang, Effects of Working Parameters on Electrospinning. One-Dimensional Nanostructures, Springer, Berlin, Heidelberg, 2013, pp. 15–28, https://doi.org/10.1007/978-3-642-36427-3_2.
[51] A. Koski, K. Yim, S. Shivkumar, Effect of molecular weight on fibrous PVA produced by electrospinning, Mater. Lett. 58 (3) (2004) 493–497.
[52] S.L. Shenoy, W.D. Bates, H.L. Frisch, G.E. Wnek, Role of chain entanglements on fiber formation during electrospinning of polymer solutions: good solvent, non-specific polymer–polymer interaction limit, Polymer 46 (10) (2005) 3372–3384.
[53] A. Haghi, M. Akbari, Trends in electrospinning of natural nanofibers, Physica Status Solidi 204 (6) (2007) 1830–1834.
[54] C. Zhang, X. Yuan, L. Wu, Y. Han, J. Sheng, Study on morphology of electrospun poly (vinyl alcohol) mats, Eur. Polym. J. 41 (3) (2005) 423–432.
[55] C. Huang, S. Chen, C. Lai, D.H. Reneker, H. Qiu, Y. Ye, H. Hou, Electrospun polymer nanofibres with small diameters, Nanotechnology 17 (6) (2006) 1558.
[56] C. Mit-uppatham, M. Nithitanakul, P. Supaphol, Effects of solution concentration, emitting electrode polarity, solvent type, and salt addition on electrospun polyamide-6 fibers: a preliminary report, Macromolecular Symposia, Wiley Online Library, 2004.
[57] C. Mit-uppatham, M. Nithitanakul, P. Supaphol, Ultrafine electrospun polyamide-6 fibers: effect of solution conditions on morphology and average fiber diameter, Macromol. Chem. Phys. 205 (17) (2004) 2327–2338.
[58] P. Heikkilä, A. Harlin, Parameter study of electrospinning of polyamide-6, Eur. Polym. J. 44 (10) (2008) 3067–3079.
[59] S. Koombhongse, W. Liu, D.H. Reneker, Flat polymer ribbons and other shapes by electrospinning, J. Polym. Sci. B Polym. Phys. 39 (21) (2001) 2598–2606.
[60] D.H. Reneker, I. Chun, Nanometre diameter fibres of polymer, produced by electrospinning, Nanotechnology 7 (3) (1996) 216.
[61] C.J. Buchko, L.C. Chen, Y. Shen, D.C. Martin, Processing and microstructural characterization of porous biocompatible protein polymer thin films, Polymer 40 (26) (1999) 7397–7407.

[62] F.-C. Chang, K.-K. Chan, C.-Y. Chang, The effect of processing parameters on formation of lignosulfonate fibers produced using electrospinning technology, Bioresources 11 (2) (2016) 4705–4717.
[63] O. Yördem, M. Papila, Y.Z. Menceloğlu, Effects of electrospinning parameters on polyacrylonitrile nanofiber diameter: an investigation by response surface methodology, Mater. Des. 29 (1) (2008) 34–44.
[64] C.S. Ki, D.H. Baek, K.D. Gang, K.H. Lee, I.C. Um, Y.H. Park, Characterization of gelatin nanofiber prepared from gelatin–formic acid solution, Polymer 46 (14) (2005) 5094–5102.
[65] X. Yuan, Y. Zhang, C. Dong, J. Sheng, Morphology of ultrafine polysulfone fibers prepared by electrospinning, Polym. Int. 53 (11) (2004) 1704–1710.
[66] S. Tan, R. Inai, M. Kotaki, S. Ramakrishna, Systematic parameter study for ultra-fine fiber fabrication via electrospinning process, Polymer 46 (16) (2005) 6128–6134.
[67] M.F. Hossain, R.H. Gong, M. Rigout, Optimization of the process variables for electrospinning of poly (ethylene oxide)-loaded hydroxypropyl-β-cyclodextrin nanofibres, J. Text. Inst. 107 (1) (2016) 1–11.
[68] M. Nangrejo, F. Bragman, Z. Ahmad, E. Stride, M. Edirisinghe, Hot electrospinning of polyurethane fibres, Mater. Lett. 68 (2012) 482–485.
[69] C.L. Casper, J.S. Stephens, N.G. Tassi, D.B. Chase, J.F. Rabolt, Controlling surface morphology of electrospun polystyrene fibers: effect of humidity and molecular weight in the electrospinning process, Macromolecules 37 (2) (2004) 573–578.
[70] A.P. Golin, Humidity effect on the structure of electrospun core-shell PCL-PEG fibers for tissue regeneration applications, Electronic Thesis and Dissertation Repository, 2014. https://ir.lib.uwo.ca/etd/1999.
[71] R.T. Oğulata, H.İ. İçoğlu, Interaction between effects of ambient parameters and those of other important parameters on electrospinning of PEI/NMP solution, J. Text. Inst. 106 (1) (2015) 57–66.
[72] S. Alswid, M. Issa, Study the effect of conditions of the electro spinning cabin (humidity) on electro-spun PolyVinyl alcohol (PVA) Nano-fibers, Al-Nahrain J. Eng. Sci. 20 (3) (2017) 520–525.
[73] T. Ogawa, B. Ding, Y. Sone, S. Shiratori, Super-hydrophobic surfaces of layer-by-layer structured film-coated electrospun nanofibrous membranes, Nanotechnology 18 (16) (2007) 165607.
[74] Y. Zhang, Y. Feng, Z. Huang, S. Ramakrishna, C. Lim, Fabrication of porous electrospun nanofibres, Nanotechnology 17 (3) (2006) 901.
[75] H. Liu, Y.L. Hsieh, Surface methacrylation and graft copolymerization of ultrafine cellulose fibers, J. Polym. Sci. B Polym. Phys. 41 (9) (2003) 953–964.
[76] H. Chiu, J. Lin, T. Cheng, S. Chou, Fabrication of electrospun polyacrylonitrile ion-exchange membranes for application in lysozym, Express Polym Lett 5 (4) (2011).
[77] J. Fang, X. Wang, T. Lin, Functional Applications of Electrospun Nanofibers. Nanofibers-Production, Properties and Functional Applications, InTech, Rijeka, Croatia, 2011.
[78] Y. Zhu, M.F. Leong, W.F. Ong, M.B. Chan-Park, K.S. Chian, Esophageal epithelium regeneration on fibronectin grafted poly (L-lactide-co-caprolactone)(PLLC) nanofiber scaffold, Biomaterials 28 (5) (2007) 861–868.
[79] W.E. Teo, S. Ramakrishna, A review on electrospinning design and nanofibre assemblies, Nanotechnology 17 (14) (2006) R89.
[80] F. Samani, M. Kokabi, M. Soleimani, M.R. Valojerdi, Fabrication and characterization of electrospun fibrous nanocomposite scaffolds based on poly (lactide-co-glycolide)/poly (vinyl alcohol) blends, Polym. Int. 59 (7) (2010) 901–909.
[81] S. Naseri Rad, A. Shirazi, M. Mahdi, A. Kargari, R. Marzban, Application of membrane separation technology in downstream processing of bacillus thuringiensis biopesticide: a review, J. Membr. Sci. Res. 2 (2) (2016) 66–77.
[82] M.T. Ravanchi, T. Kaghazchi, A. Kargari, Application of membrane separation processes in petrochemical industry: a review, Desalination 235 (1) (2009) 199–244.
[83] S.A.A.N. Nasreen, S. Sundarrajan, S.A.S. Nizar, R. Balamurugan, S. Ramakrishna, Advancement in electrospun nanofibrous membranes modification and their application in water treatment, Membranes 3 (4) (2013) 266–284.

[84] M.M. Pendergast, E.M. Hoek, A review of water treatment membrane nanotechnologies, Energy Environ. Sci. 4 (6) (2011) 1946–1971.
[85] X. Wang, X. Chen, K. Yoon, D. Fang, B.S. Hsiao, B. Chu, High flux filtration medium based on nanofibrous substrate with hydrophilic nanocomposite coating, Environ. Sci. Technol. 39 (19) (2005) 7684–7691.
[86] X. Wang, D. Fang, K. Yoon, B.S. Hsiao, B. Chu, High performance ultrafiltration composite membranes based on poly (vinyl alcohol) hydrogel coating on crosslinked nanofibrous poly (vinyl alcohol) scaffold, J. Membr. Sci. 278 (1) (2006) 261–268.
[87] N.-N. Bui, M.L. Lind, E.M. Hoek, J.R. McCutcheon, Electrospun nanofiber supported thin film composite membranes for engineered osmosis, J. Membr. Sci. 385 (2011) 10–19.
[88] M. Tian, Y.-N. Wang, R. Wang, A.G. Fane, Synthesis and characterization of thin film nanocomposite forward osmosis membranes supported by silica nanoparticle incorporated nanofibrous substrate, Desalination 401 (2017) 142–150.
[89] N.-N. Bui, J.R. McCutcheon, Nanoparticle-embedded nanofibers in highly permselective thin-film nanocomposite membranes for forward osmosis, J. Membr. Sci. 518 (2016) 338–346.
[90] L. Huang, J.T. Arena, J.R. McCutcheon, Surface modified PVDF nanofiber supported thin film composite membranes for forward osmosis, J. Membr. Sci. 499 (2016) 352–360.
[91] M. Yao, Y.C. Woo, L.D. Tijing, W.-G. Shim, J.-S. Choi, S.-H. Kim, H.K. Shon, Effect of heat-press conditions on electrospun membranes for desalination by direct contact membrane distillation, Desalination 378 (2016) 80–91.
[92] Y.C. Woo, L.D. Tijing, M.J. Park, M. Yao, J.-S. Choi, S. Lee, S.-H. Kim, K.-J. An, H.K. Shon, Electrospun dual-layer nonwoven membrane for desalination by air gap membrane distillation, Desalination 403 (2017) 187–198.
[93] A. Kargari, M.M.A. Shirazi, Water desalination: Solar-assisted membrane distillation, in: Encyclopedia of Energy Engineering and Technology, CRC Press, Boca Raton, FL, 2014, p. 4.
[94] A.T. Servi, J. Kharraz, D. Klee, K. Notarangelo, B. Eyob, E. Guillen-Burrieza, A. Liu, H.A. Arafat, K.K. Gleason, A systematic study of the impact of hydrophobicity on the wetting of MD membranes, J. Membr. Sci. 520 (2016) 850–859.
[95] M.M.A. Shirazi, A. Kargari, M. Tabatabaei, Evaluation of commercial PTFE membranes in desalination by direct contact membrane distillation, Chem. Eng. Process. Process Intensif. 76 (2014) 16–25.
[96] C. Feng, K. Khulbe, T. Matsuura, R. Gopal, S. Kaur, S. Ramakrishna, M. Khayet, Production of drinking water from saline water by air-gap membrane distillation using polyvinylidene fluoride nanofiber membrane, J. Membr. Sci. 311 (1) (2008) 1–6.
[97] C.-I. Su, J.-H. Shih, M.-S. Huang, C.-M. Wang, W.-C. Shih, Y.-s. Liu, A study of hydrophobic electrospun membrane applied in seawater desalination by membrane distillation, Fiber. Polym. 13 (6) (2012) 698–702.
[98] Y. Liao, C.-H. Loh, R. Wang, A.G. Fane, Electrospun superhydrophobic membranes with unique structures for membrane distillation, ACS Appl. Mater. Interfaces 6 (18) (2014) 16035–16048.
[99] B. Van der Bruggen, C. Vandecasteele, T. Van Gestel, W. Doyen, R. Leysen, A review of pressure-driven membrane processes in wastewater treatment and drinking water production, Environ. Prog. Sustain. Energy 22 (1) (2003) 46–56.
[100] R. Van Reis, A. Zydney, Membrane separations in biotechnology, Curr. Opin. Biotechnol. 12 (2) (2001) 208–211.
[101] S. Kaur, S. Sundarrajan, D. Rana, T. Matsuura, S. Ramakrishna, Influence of electrospun fiber size on the separation efficiency of thin film nanofiltration composite membrane, J. Membr. Sci. 392 (2012) 101–111.
[102] M.T. Hunley, T.E. Long, Electrospinning functional nanoscale fibers: a perspective for the future, Polym. Int. 57 (3) (2008) 385–389.

CHAPTER

10 ELECTROSPUN NANOFIBROUS FILTRATION MEMBRANES FOR HEAVY METALS AND DYE REMOVAL

Yana Bagbi*,†, Arvind Pandey†, Pratima R. Solanki*

Special Centre for Nanoscience, Jawaharlal Nehru University, New Delhi, India Department of Physics, North Eastern Regional Institute of Science and Technology, Nirjuli, India†*

1 INTRODUCTION

Recently, water pollution has been the foremost environmental complication, demanding the vital improvement of novel materials that could provide effective and applied ways for detecting and eliminating deadly agents from water bodies [1, 2]. Furthermore, the contamination of the water surface, including heavy metal ions, such as Cr^{6+}, Cd^{2+}, Pb^{2+}, Hg^{2+}, and Cu^{2+}, among others; dyes; and other pollutants, signifies a latent hazard to human and aquatic life [1–5]. Drinking water that contains heavy metals can cause cancer, kidney diseases, memory problems, high blood pressure, premature birth, brain damage, hearing loss, learning disabilities, and a lower IQ level in children [6–8]. Thus, eliminating these toxic metal ions from water bodies is very essential. Numerous approaches have been used for eliminating the metal ions from the water surface, such as ion. Exchange [9], reverse osmosis [10], chemical precipitation [11], membrane separation [12], and adsorption. Among all these methods, adsorption is generally observed as an outstanding process for wastewater treatment owing to its simplicity, effectiveness, and inexpensiveness [4–6].

Lately, agricultural waste- and bio-organic waste material-constructed adsorbents, such as husk rice, orange waste, and pinewood, have been employed for treating wastewater, owing to their high availability, low cost, and high adsorption effectiveness [13, 14]. Yet, these organic wastes typically include high amounts of chemicals and biological oxygen that are subsequently dumped into water bodies. It can be hazardous to marine life and can produce other ecological complications [13].

Nanostructured materials have recently been considered as the finest adsorbents, offering excellent metal binding sites owing to their outstanding high specific surface area-to-volume ratio [13, 15]. However, there are restrictions for using these materials because of their agglomerate tendencies, difficulties of control in morphology, and leaching problems that reduce the adsorption properties of materials [15, 16]. Some of these nanoparticles have already been recognized as toxic in much of the literature [17]. Many researchers have reported the toxic [12] and inflammatory [13] effects of metal and metal

Nanoscale Materials in Water Purification. https://doi.org/10.1016/B978-0-12-813926-4.00015-X

oxide nanoparticles in living cells. It has also been reported that carbon-based nanotubes are toxic [10] and allure granulomas in animal lungs [11]. The demands for an alternative technique for developing novel material include that it should be nontoxic, eco-friendly, nonagglomerate, and nonleaching, with high specific surface area-to-volume ratio and a high porosity for the effective purification of water, as well as protect the environment. Owing to the excellent characteristics of electrospun nanofibers, such as high porosity, flexibility, light weight, and low cost of membranes, they have appeared as the most favorable, vigorous materials for filtering and trapping metals ions, dyes, and other pollutants from wastewater [8, 9]. Lately, electrospinning technique has developed a widespread technique that is cost-effective and simple, allowing the manufacture of large micro or nanofibers membranes [12–14].

Polymer fibers manufactured through the electrospinning technique have drawn attention because of their extremely high porosity, high specific surface area-to-volume ratios, greater permeability, and slight interfibrous pore sizes that permit many potential applications in various fields [18, 19]. These excellent characteristics of electrospun fibers were effectively used as membranes or sorbents in a wide range of applications in the biotechnology, health care, and environmental fields, including submicroparticle separation, protein purification, air cleaning, and heavy metal ions and dye removal [12–19]. In addition, they show versatile applications for energy storage, defense, and security [19]. Fig. 1 shows the various applications of electrospun nanofibers in different areas. The data on the advanced applications of electrospun nanofibers, based on the published literature, is shown in Fig. 2.

However, the versatile applications of nanofibers as a water-filtering medium, which include the elimination of metal ions and dyes from water sources, are well recognized. Electrospun nanofibers, such as polyacrylonitrile (PAN) via amine assemblies, were reported as successfully eliminating toxic metal ions such as Pb^{2+}, Cu^{2+}, and CrO_4^{2-} from aqueous solution [20, 21]. Similarly, aminated PAN nanofiber mats were inspected for the successful adsorption of metal ions such as Pb^{2+}, Cu^{2+}, Fe^{2+}, and

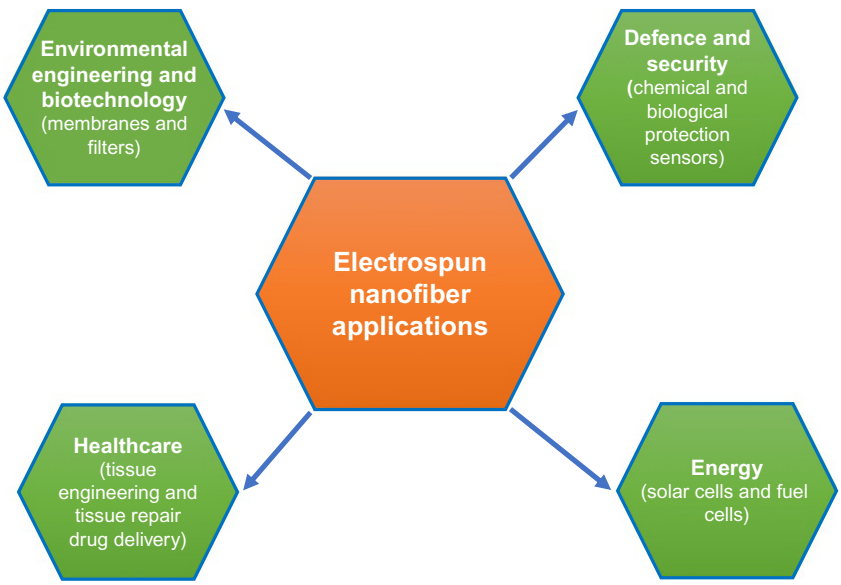

FIG. 1

Latent applications of electrospun fibers in different fields.

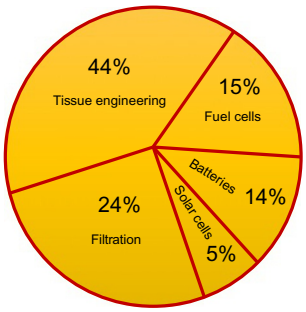

FIG. 2

Statistics data on the advanced applications of electrospun nanofibers reported in the literature (search made through med-link database).

Ag^{+} from water [22, 23]. The effective adsorption of metal ions such as Pb^{2+}, Cd^{2+}, and Cu^{2+} and anionic dyes using polyethyleneimine nanofibers with a sufficient quantity of amino and amino groups have been reported [24, 25]. The excellent adsorption of Cu^{2+} and Pb^{2+} using Chitosan nanofiber mats from water have also been reported [26]. The adsorption of Cu^{2+} was studied using modified ultra-fine hydrolyzed PAN nanofiber mats [27]. A conductive polymer, such as polypyrrole, displays an outstanding capability for eliminating chromium from aqueous solutions [28–31].

To improve the adsorption properties of electrospun nanofibers, many researchers incorporated metal/metal oxide and organic nanoparticles into the nanofibers. PAN/$FeCl_3$-composite membranes are reported to remove 110 mg/g of chromium, including changes Cr^{4+} to Cr^{3+}, which is less harmful [32]. The iron content in PAN nanofibers increases the adsorption of chromium by diffusing into the solution and reacting the chromium ions, dropping the chromium concentration in the solution. Li et al. informed the successful adsorption of 150 mg/g of Cr^{6+} from aqueous solution using composite polyamide 6 and Fe_xO_y membrane [33]. The growth of Fe nanoparticles into polyamide 6 supports in reduction/adsorption of Cr^{6+} to Cr^{3+}.

In this chapter, we provide the overview investigation of processing technique, fundamental aspect, electrospinning parameters, and their potential application of nanofiber membranes for eliminating heavy metal ions and dyes from water bodies. Furthermore, future trends and challenges of electrospun nanofibers are also reported.

2 PROCESSING TECHNIQUE

In recent years, many techniques have been explored for the manufacture of polymer electrospun nanofibers. Yet, their worth is limited because of inadequate production rates, cost, and possible fiber assembly. A few of these techniques include the following:

2.1 DRAWING

This method produces extensive single strands of polymer nanofibers at one time. The dragging method is carried out via solidification, which changes liquid material into electrospun fiber. Solvent evaporation is required in the circumstance of dry spinning, whereas for melt spinning, a cooling step is

essential. However, it has restrictions of using only a viscoelastic material that can experience widespread distortions while creating the fibers.

2.2 TEMPLATE

This progression uses a membrane that has a nanoporous pattern with self-possessed cylindrical pores to produce nanofibers, including solid nanofibers called fibrils and hollow nanofibers called tubules. Nanofibers such as tubules and fibrils can be used for numerous materials; conducting polymers, carbon, semiconductors, and metals/metal oxides can be fabricated. Nevertheless, a disadvantage of this technique is that it cannot produce large numbers of nanofibers at one time.

2.3 THERMAL-INDUCED PHASE SEPARATION

In thermal-induced phase separation, the polymer is distorted into a nanoporous foam. This method is a time-consuming process that splits a homogeneous polymer solution into a multiphase solution through thermodynamic variations. The method is extensively used to produce frameworks for tissue engineering.

2.4 SELF-ASSEMBLY

This method is employed to yield peptide nanofibers and peptide amphiphiles. This process is encouraged via the three-dimensional structures of the naturally folding progression of amino acid remains to obtain proteins. The progression involves numerous driving forces, including hydrophobic interactions, hydrogen bonding, van der Waals forces, and electrostatic forces. It is affected by exterior parameters, such as solution pH and ionic strength. This technique is also time-consuming.

2.5 ELECTROSPINNING

Electrospinning is the most frequently used method to fabricate fibers extending in diameter from the submicron level to the nanometer level by using an electric force to induce the charged filaments of polymer solutions into fibers [18, 19]. This method does not need high temperatures and coagulation chemistry to yield nanofibers from a polymer solution, which results in the predominant production of fibers using bulky and composite molecules [18]. Electrospinning is an old technique of fiber whirling; nevertheless, it is presently the utmost effective, progressive technique for producing large nanofibers. The name "electrospinning" was first coined from "electrostatic spinning," which dates to 1897 [18, 19].

History places the beginning of electrospinning in the 19th century. Rayleigh was the first to observe the electrospray technique in 1897, and later it was detailed deliberately by Zeleny in 1914 [34]. Anton Formhals brought further developments to electrospinning, bringing it to commercialization and obtaining patents for the manufacture of textile yarns between 1934 and 1944 [35, 36]. He set up an experimental process for producing electric charges using artificial filaments for the manufacture of textile yarns. Furthermore, in 1960, Taylor reported the creation of cone-shaped droplet of the polymer at the tip of the needle after applying an electric field to it, which he later called "Taylor cone" [37].

In 1988, Simon reported that electrospinning could possibly be used to manufacture nanoscale and submicron-scale fibrous mats of polystyrene and polycarbonate and precisely proposed in vitro cell substrates be used. He further reported that the changes in the fibers' surface chemistry depend on the electric field polarity during electrospinning [38]. In the 1990s, Reneker and Rutledge confirmed that through electrospinning, various organic polymers could form nanofibers [39, 40]. Subsequently, publications regarding electrospinning have increased greatly.

3 FUNDAMENTAL ASPECT OF ELECTROSPINNING

The processing tools for electrospinning include a high voltage supply, a metal-collecting screen, and a capillary tube with a pipette/small-diameter needle. To obtain an electrospun fiber, a sufficiently high voltage is applied to capillary tube end, which holds the polymer solution. The solution is detained by the surface tension, which ultimately generates a charge on the liquefied surface. As the liquefied surface develops the charge, electrostatic repulsion offsets the surface tension; then finally the droplet is strained. The hemispherical droplet at the tip of the capillary tube stretches to form a conical shape, which is called the Taylor cone.

As soon as the applied electrical field reaches a critical value, the repulsive electric force disables the force of surface tension, which results in an ejection of a charged jet of the solution from the tip of the Taylor cone. As the jet travels through the air, the solvent evaporates. In the case of melt, the discharged jet solidifies while traveling through the air. Finally, the charged polymer fiber is arbitrarily dumped onto a collector, for example, a rotating drum or a metal frame [18–20]. The morphologies and uniform diameters of electrospun fiber can be controlled via parameters such as jet stream movement and polymer concentration. The systematic diagram of basic electrospinning set up to obtain fibers is shown in Fig. 3.

4 ELECTROSPINNING PARAMETERS

Electrospinning parameters are very vital to comprehend because they affect the diameter and morphologies of electrospun fibers. The wanted morphologies and diameter of fibers can easily be attained by governing these parameters. The three main categories that affect electrospun fiber parameters, such as the morphology and diameter, are (a) the intrinsic properties of the solution, (b) the processing conditions, and (c) the ambient parameters [19].

The major task is the formation of fiber diameter uniformity. In electrospun fiber, defects, including beads and pores, are a foremost problem that needs to be sorted out [18]. Fig. 4 shows the scanning electron microscope (SEM) images of uniform (A) and beaded (B) electrospun PAN-SiO_2 nanofibers prepared in our laboratory. The optical images of uniform (A) and beaded (B) electrospun Fe_3O_4-cellulose nanofibers are shown in Fig. 5. Therefore, the intrinsic properties of the polymer solution are among the utmost significant measures in electrospinning. The effects of various electrospinning parameters are summarized in the following.

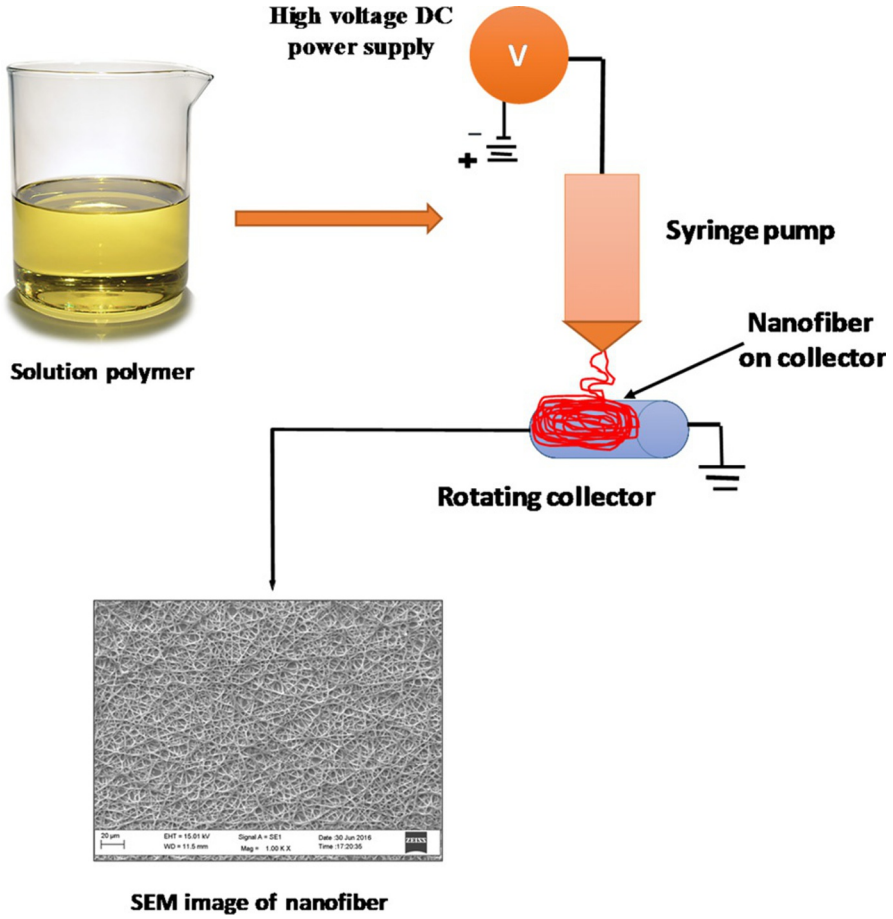

FIG. 3

Schematic diagram of basic electrospinning set up to obtain nanofiber.

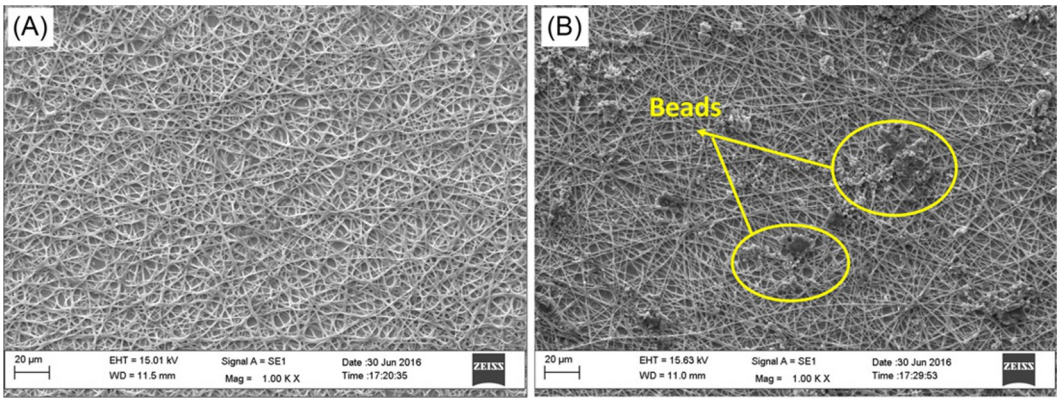

FIG. 4

SEM images of electrospun PAN-SiO_2 nanofiber (A) uniform; (B) beads, prepared in our laboratory.

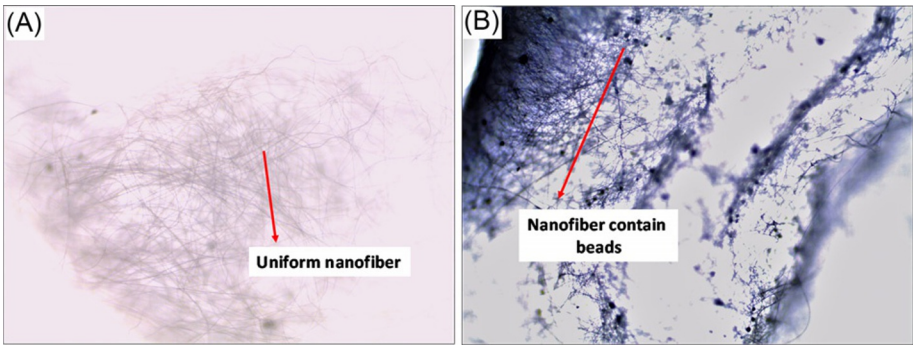

FIG. 5

Optical images of electrospun Fe_3O_4-cellulose anofibers: (A) uniform; (B) beads, prepared in our laboratory.

4.1 THE INTRINSIC PROPERTIES OF THE SOLUTION PARAMETERS

4.1.1 Concentration

The concentration of polymer solution has enormous effects on the formation of electrospun nanofibers. It is well known that the viscosity of the solution is relative to the polymer solution. The higher the viscosity of the solution, the larger the nanofiber diameter. Therefore, a minimum concentration is essential for fiber formation in electrospinning. Furthermore, electrospray arises in its place by electrospinning at very low concentrations. This happens owing to the high surface tensions and low viscosity of the solution [19, 41]. A combination of fibers and beads are obtained when the solution concentrations are low. As the concentration rises, the beads vary from sphere-shaped to spindle-shaped. Last, uniform fibers of enlarged thickness are obtained [42].

Fong et al. reported that the number of beads in the structure will be fewer if the polymer solution concentration is higher [43]. Liu et al. stated that as soon as the concentration of the polymer rises, the number of beads is reduced [44]. It is further specified that with a lower surface tension, more beads will form. Simultaneously, an increase in the polymer concentration leads to a rise in surface tension, resulting in fewer beads.

4.1.2 Molecular weight

Molecular weight has huge effects on the morphology of electrospun nanofiber. It basically affects the surface tension, viscosity, and conductivity of polymer solution. It is reported by many researchers that lower molecular-weight polymer form beads instead of fibers, while smooth fibers are obtained through an increase in the molecular weight. Furthermore, larger-diameter electrospun fibers are obtained at very high molecular weights [44–46].

4.1.3 Solution viscosity

Viscosity is another parameter that affects the formation of fibers during the electrospinning process. If a solution has a very low viscosity, fibers will not form, whereas with a solution with a very high viscosity, there is difficulty discharging the jets from the solution polymer. It is further stated that viscosity is very essential for the morphology of electrospun fibers. Usually, solution viscosity, molecular weight, and the concentration of the polymer are linked to one another. Uniform and larger-diameter

fibers will be obtained with a rise in the solution's concentration or viscosity. However, a low viscosity results in the formation of beaded fibers [42, 44].

4.1.4 Surface tension

Surface tension is another crucial parameter that affects the formation of electrospun fibers. Doshi and Reneker et al. stated that a decrease in surface tension leads to the establishment of electrospun fibers deprived of beads [39, 47]. Yang et al. reported that different solvents contribute to different surface tensions and investigated the morphology of electrospun fiber PVP with DMF, ethanol, and MC as solvents [48]. It is further stated that by keeping the polymer concentration fixed, smooth nanofibers can be obtained by reducing the surface tension, whereas beaded nanofibers can be obtained by an upsurge in surface tension.

4.1.5 Conductivity/surface-charge density

The conductivity of the solution is another important parameter that can affect the morphology of electrospun fiber formation. Basically, the solution conductivity is made resolute by a solvent, a polymer, and the existence of salts. Mostly, the higher the conductivity of a solution polymer, the smaller the diameter of the electrospun nanofibers. It has been further illustrated that the surface-charge density and conductivity of polymer solution rise when salts are added [19, 42, 45]. Numerous polymers, including polyethylene oxide (PEO), polyacrylic acid, collagen-type IPEO, and polyamide 6, among others, need additional salt to increase the conductivity of solution [26].

4.2 PROCESSING PARAMETERS

The processing parameters of applied voltage, flow rate/feed rate, and collector and tip distance play effective roles in the electrospinning process. In addition, processing parameters have large an effect on the morphology and diameter of the nanofibers. The details of these parameters and their effect on fiber diameter and morphology follow.

4.2.1 Applied voltage

Applied voltage is a vital factor in electrospinning for the formation of electrospun fibers. This is because fiber formation occurs only when the applied voltage surpasses the threshold voltage (about $\sim$1 kV/cm, dependent on the gel solution). As previously discussed, a rise in the applied voltage increases the electrostatic force of the polymer solution, which indicates the stretching of the jet, which ultimately leads to a decrease in fiber length. It has been found that changing the applied voltage will change the shape of the initial drop, thereby resulting in a change in the structure and morphology of the fibers [19, 45].

Various arguments have been made about the effect of applied voltage on the electrospinning process. Zhang et al. reported that at higher voltages, there is more polymer ejection, enabling the development of larger-diameter fiber [49]. The researchers reported on the fiber morphology and the diameter of poly(vinyl alcohol) (PVA)/water solution. Reneker et al. stated there is no effect on the fiber diameter of polyethylene oxide when the applied voltage is increased [47]. Other researchers have reported that a rise in the applied voltage results in a decrease of fiber diameter. Furthermore, it was observed that at higher applied voltages, bead formation was obtained on the fibers [45, 50].

4.2.2 Flow rate/feed rate

In the electrospinning technique, the flow rate of the polymer solution is another active parameter that directly affects jet velocity and material transfer. A slower feed rate is proposed to provide enough time for the evaporation of the solvent, whereas a high flow rate results in a beaded fiber structure. As the feed rate of the solution increases, the charge density will decrease. A high charge density may lead to the electrospinning jet undergoing secondary bending instabilities, which contribute to the production of fibers with smaller diameters [19, 43–45]. Thus, with an increase in the feed rate, there is a consistent increase in the diameter of the fibers. It is worth noting that fibers with beads are molded when the feed rate of solution is too high because not enough time is provided for the solvent to evaporate [43, 45].

4.2.3 Collector and tip distance

The distance between the collector and the tip is another parameter that affects controlling the diameters and morphology of nanofibers. It is necessary to select an ideal distance to avoid the polymer solution evaporating before the fiber reaches the collector. Therefore, in the electrospinning technique, a minimum distance is required to ensure enough time for the solvent to evaporate before the fibers reach the collector. Longer distances have yielded thinner fibers [39]. Beads will be produced when the distance was too far or too close [19, 39, 48].

4.2.4 Ambient parameters

The ambient parameters, for example, temperature and humidity, also have enormous effects on the morphology and diameter of electrospun fibers. A rise in temperature produces fibers with reduced diameters, while low humidity could dry the solvent completely. Similarly, a rise in humidity results in small pores forming on the surface of the fiber [44, 45].

5 APPLICATION OF ENMs IN WATER TREATMENT

In the current industrialized era, one of the biggest water pollution problems is the contamination of heavy metals/metalloids in water bodies. Heavy metal-contaminated water results from several industries, such as electroplating, battery construction, tanneries, chemical manufacturing, and metallurgical and mining industries, all of which employ enormous amounts of metal ions [4, 5]. Wastewaters from these industries are directly discharged into freshwater forms, not only hurting the aquatic organisms but also damaging human and animals via their food chain. In many parts of the world, heavy metal concentrations in drinking water are higher than the guidelines reported by the Bureau of Indian Standard and the World Health Organization (WHO). Metals/metalloids ions such as lead, arsenic, fluoride, chromium, zinc, copper, silver, and iron, among others, have nonbiodegradable and high-toxicity properties [4–6]. Thus, eliminating these pollutants from water resources is a foremost priority, and many investigations are concentrating on addressing this issue.

Lately, keen interest has developed regarding nanoscopic materials as effective adsorbents for metal/metalloid ions because of their high surface area-to-unit mass. A lot of research has been carried out on nonadsorbents, including magnetic [2–4], nanocomposites [30, 31], and nanofibrous matrices [19–40] for eliminating heavy metal/metalloids from water bodies. Among these nanomaterials, electrospun nanofibrous matrices have attracted a prodigious consideration because of their numerous benefits, such as high porosity, high specific surface area per unit mass, and high gas permeability, which

results in maximum adsorption capacity [19, 40, 45]. Various polymer, including cellulose [51], Chitosan, Chitosan/polylactide [52], bovine fibrinogen [53], gelatin [54], polyaniline/gelatin [55], and polymer blends such as gelatin/polycaprolactone [56], among others, were used for the preparation of electrospun nanofibers and have been explored for use in water treatment applications. In this section, a few of such pollutants and their removal using nanofibers are discussed.

Kampalanonwat et al. reported successful removal of Ag^{+}, Cu^{2+}, Pb^{2+}, and Fe^{2+} ions via aminated polyacrylonitrile (PAN) (APAN) nanofiber mats [22]. The metal ions' highest adsorption capacities using Langmuir sorption were obtained as 150.6, 155.5, 116.5, and 60.6 mg/g, respectively. The used APAN nanofiber mats were effectively regenerated through hydrochloric acid (HCl) from water. Wang et al. reported the effective elimination of Cr^{6+} ions from water with polyacrylonitrile/polypyrrole (PAN/PPy) nanofibers equipped via in situ polymerization of pyrrole monomer by electrospinning technique [57]. Within 30 and 90 min, the adsorption equilibrium reached, as the concentration of the initial solution was amplified from 100 to 200 mg/L. The pseudo-second-order model was well fitted. Langmuir isotherm model shows the best-fitted result. A thermodynamic study stated that the process of adsorption is spontaneous and endothermic in nature. A successful desorption of 80% was obtained.

Aliabadi et al. examined the adsorption of cadmium (Cd), nickel (Ni), copper (Cu), and lead (Pb) from water using poly ethylene oxide (PEO)/chitosan nanofiber [58]. To inspect the effect of diverse adsorption parameters, experiments were carried out at various temperatures, contact times, and initial concentrations, respectively. The selectivity of adsorption of copper, lead, nickel, and cadmium on the (PEO)/chitosan was $Pb^{2+} < Cd^{2+} < Cu^{2+} < Ni^{2+}$. Isotherm models such as Langmuir, Freundlich, and Dubinin-Radushkevich were used to designate the equilibrium data for the metal ions. Thermodynamic studies revealed that the adsorption of metal ions onto PEO/Chitosan nanofiber membrane was endothermic, spontaneous, and feasible. The successful reusability of the PEO/Chitosan membrane was obtained for next five cycles of sorption-desorption. Haider et al. stated the successful adsorption of metal ions Cu^{2+} and Pb^{2+} using Chitosan electrospun nanofiber mats from aqueous solution. Langmuir isotherms showed the best adsorption data for Cu^{2+} and Pb^{2+} [26]. The obtained Langmuir equilibrium adsorption capacity for Cu^{2+} and Pb^{2+} were 485.44 mg/g (2.85 mmol/g) and 263.15 mg/g (0.79 mmol/g), respectively. This suggests that Chitosan nanofiber mats provide a high adsorption capacity to filter out (or neutralize) toxic metal ions from wastewater.

Alcaraz-Espinoza et al. investigated the high adsorption of Cd^{2+}, Cu^{2+}, Hg^{2+}, Pb^{2+}, and Cr^{2+} from water using polyaniline-polystyrene (PANI-PS) composite electrospun PS mats [8]. The researchers further stated that the composite nanostructured PANI was highly dispersed in the NW PS mat, which showed good electrical properties and surface-wetting characteristics that can be easily precise.

Neghlani et al. reported the high elimination of Cu^{2+} ions from aqueous solution using polyacrylonitrile nanofibers (PAN-nFs) obtained via the electrospinning method [59]. Furthermore, to yield aminated polyacrylonitrile (APAN) nanofibers, the electrospun fibers were improved with diethylenetriamine. The maximum adsorption of Cu^{2+} ions obtained from the Langmuir model was 116.522 mg/g. Sharma et al. investigated successful removal of As^{3+} from water using cerium-loaded Chitosan (CHT)-polyvinyl alcohol (PVA) composite (Ce-CHT/PVA) nanofibers obtained via electrospinning [60]. The result stated that Ce-CHT/PVA composite nanofibers competently remove As^{3+} from water at a limit lower than that prescribed by the WHO and the Environmental Protection Agency. The maximum adsorption capacity obtained from the Langmuir isotherm was 18.0 mg/g. Najafabadi et al. reported maximum removal of Cr^{6+}, Pb^{2+}, and Cu^{2+} from water using a novel Chitosan/Graphene oxide

(GO) nanofibrous material via electrospinning [61]. The maximum monolayer adsorption capacity of Pb^{2+}, Cu^{2+}, and Cr^{6+} metal ions was obtained as 461.3, 423.8, and 310.4 mg/g, respectively. It was further stated that Chitosan/GO nanofibers can be reused without any loss in adsorption capacity.

Tian et al. informed of the successful elimination of Cd^{2+}, Cu^{2+}, and Hg^{2+} from water using a cellulose acetate (CA) nonwoven membrane obtained through surface modification by poly (methacrylic acid) (PMAA) using electrospinning [62]. As the solution pH increased, the capacity of adsorption process increased. The membrane showed the highest adsorption for Hg^{2+}. The successful reusability of the membrane was obtained by using saturated ethylenedinitrilotetra acetic acid.

Saeed et al. stated that they effectively adsorbed Cu^{2+} and Pb^{2+} using polyacrylonitrile (PAN) nanofibers by the electrospinning technique. HM-PAN adsorption capacity increased as the time interval was lengthened, and it remained constant after 24 h at 114 and 217 mg/g for Cu^{2+} and Pb^{2+} ions, respectively [63]. Desorption studies showed more than 90% of recovery of adsorbed metal ions using a 1 M HNO_3 solution.

6 OUTLOOK TRENDS AND CHALLENGES

Although electrospun nanofibers have exhibited great promise for water purification, such as toxic metal ion and dye remediation, there still are numerous challenges. These include the mass manufacture of quality nanofibers, nanofiber-based composites, and the desired functionality to improve the novel chemistry of nanofibers. All these trials are not minor but are insuperable. Innovative approaches in manipulating nanofiber structures, such as porous nanofibers, the modification of nanofiber surfaces, and interfiber adhesion, have been quickly established. In addition, the progression of manufacturing multifunctional nanofibers through several properties, including bi/multicomponent nanofibers and core-shell nanofibers, would be a novel approach for water filtration applications. Nanofiber surface properties can also be measured by using plasma treatment and chemical grafting. All these novel processes and innovative chemistries will increase the parameters in fabricating nanofibers for better filtration membranes, such as their becoming more efficient, having higher flux, and being stronger. Furthermore, electrospun nanofibers can be explored for applications to diverse water filtration/purification because of the intrinsic versatility of electrospinning, including the ease of material selection and the ability to regulate the morphology and functionality of nanofibers.

7 CONCLUSION

Water pollution via heavy metal ions is the foremost problem in the 21st century because of an upsurge in population and a rise in industrial activities. Electronspun fibers have countless advantages in the field of water purification because of their high surface area-to-volume ratio, high porosity, eco-friendliness, high flexibility, light weight, and the low cost of membranes. This chapter has cast a wide-ranging review of the electrospinning skills, electrospinning assemblies, processing technique, the effects of its parameters on nanofiber morphology, and its advanced application for trapping and filtering metals ions from aqueous solutions.

REFERENCES

[1] L. Jarup, Hazards of heavy metal contamination, Br. Med. Bull. 68 (2003) 167–182.

[2] Y. Bagbi, A. Sarswat, D. Mohan, A. Pandey, P.R. Solanki, Lead and chromium adsorption from water using L-cysteine functionalized magnetite (Fe_3O_4) nanoparticles, Sci. Rep. 7 (2017) 7672.

[3] Y. Bagbi, A. Sarswat, D. Mohan, A. Pandey, P.R. Solanki, Lead (Pb^{2+}) adsorption by monodispersed magnetite nanoparticles: surface analysis and effects of solution chemistry, J. Environ. Chem. Eng. 4 (2016) 4237–4247.

[4] Y. Bagbi, A. Sarswat, S. Tiwari, D. Mohan, A. Pandey, P.R. Solanki, Synthesis of L-cysteine stabilized zero-valent iron (nZVI) nanoparticles for lead remediation of water, Environ. Nanotechnol. Monit. Manag. 7 (2017) 34–45.

[5] Y. Bagbi, A. Sarswat, S. Tiwari, D. Mohan, A. Pandey, P.R. Solanki, Nanoscale zero-valent iron for aqueous lead removal, Adv. Mater. Proc. 2 (4) (2017) 235–241.

[6] N. Savage, M. Diallo, Nanomaterials and water purification: opportunities and challenges, J. Nanopart. Res. 7 (2005) 331–342.

[7] R.S. Barhate, S. Ramakrishna, Nanofibrous filtering media: filtration problems and solutions from tiny materials, J. Membr. Sci. 296 (2007) 1–8.

[8] J. Alcaraz-Espinoza, A.E. Chavez-Guajardo, J.C. Medina-Llamas, C.A.S. Andrade, C.P. de Melo, Hierarchical composite polyaniline-(electrospun polystyrene) fibers applied to heavy metal remediation, ACS Appl. Mater. Interfaces 7 (2015) 7231–7240.

[9] Y. Xing, X. Chen, D. Wang, Electrically regenerated ion exchange for removal and recovery of Cr(VI) from wastewater, Environ. Sci. Technol. 41 (2007) 1439–1443.

[10] F.C. Walsh, G.W. Reade, Electrochemical techniques for the treatment of dilute metal-ion solutions, Stud. Environ. Sci. 59 (1994) 3–44.

[11] A. Bodalo-Santoyo, J. Gómez-Carrasco, E. Gomez-Gomez, F. Maximo-Martin, A. Hidalgo-Montesinos, Application of reverse osmosis to reduce pollutants present in industrial wastewater, Desalination 155 (2003) 101–108.

[12] M.E. Ersahin, H. Ozgun, R.K. Dereli, I. Ozturk, K. Roest, J.B. van Lier, A review on dynamic membrane filtration: materials, applications and future perspectives, Bioresour. Technol. 122 (2012) 196–206.

[13] K. Yoon, B.S. Hsiao, B. Chu, Functional nanofibers for environmental applications, J. Mater. Chem. 18 (2008) 5326–5334.

[14] G. Jia, H.F. Wang, L. Yang, X. Wang, R.J. Pei, T. Yan, Y.L. Zhao, X.B. Guo, Cytotoxicity of carbon nanomaterials: single-wall nanotube, multi-wall nanotube, and fullerene, Environ. Sci. Technol. 39 (2005) 1378.

[15] C.W. Lam, J.T. James, R. McCluskey, R.L. Hunter, Pulmonary toxicity of single-wall carbon nanotubes in mice 7 and 90 days after intratracheal instillation, Toxicol. Sci. 77 (2004) 126.

[16] K. Peters, R.E. Unger, C.J. Kirkpatrick, A.M. Gatti, E. Monari, Effects of nano-scaled particles on endothelial cell function in vitro: studies on viability, proliferation and inflammation, J. Mater. Sci. Mater. Med. 15 (2004) 321.

[17] Q. Rahman, M. Lohani, E. Dopp, H. Pemsel, L. Jonas, D.G. Weiss, D. Schiffimann, Evidence that ultrafine titanium dioxide induces micronuclei and apoptosis in Syrian hamster embryo fibroblasts, Environ. Health Perspect. 110 (2002) 797.

[18] Z.M. Huang, Y.Z. Zhang, M. Kotaki, S. Ramakrishna, A review on polymer nanofibers by electrospinning and their applications in nanocpomposites, Compos. Sci. Technol. 0266-3538, 63 (2003) 2223–2253.

[19] J. Venugopal, S. Ramakrishna, Applications of polymer nanofibers in biomedicine and biotechnology, Appl. Biochem. Biotechnol. 0273-2289, 125 (2005) 47–157.

[20] S. Deng, R. Bai, J.P. Chen, Aminatedpolyacrylonitrilefibers for lead and copper removal, Langmuir 19 (2003) 5058–5064.

[21] D.H. Shin, Y.G. Ko, U.S. Choi, W.N. Kim, Design of high efficiency chelate fibers with an amine group to removal heavy metal ions and pH-related FT-IR analysis, Ind. Eng. Chem. Res. 43 (2004) 2060–2066.
[22] P. Kampalanonwat, P. Supaphol, Preparation and adsorption behavior of aminatedelectrospun polyacrylonitrile nanofiber mats for heavy metal ion removal, ACS Appl. Mater. Interfaces 2 (2010) 3619–3627.
[23] P.K. Neghlani, M. Rafizadeh, F.A. Taromi, Preparation of aminatedpolyacrylonitrile nanofiber membranes for the adsorption of metal ions: comparison with microfibers, J. Hazard. Mater. 186 (2011) 182–189.
[24] X. Wang, M. Min, Z. Liu, Y. Yang, Z. Zhou, M. Zhu, Y. Chen, B.S. Hsiao, Poly (ethyleneimine) nanofibrous affinity membrane fabricated *via* one step wet-electrospinning from poly (vinyl alcohol)-doped poly(ethyleneimine) solution system and its application, J. Membr. Sci. 379 (2011) 191–199.
[25] M. Min, L. Shen, G. Hong, M. Zhu, Y. Zhang, X. Wang, Y. Chen, B.S. Hsiao, Micronano structure poly (ether sulfones)/poly(ethyleneimine) nanofibrous affinity membranes for adsorption of anionic dyes and heavy metal ions in aqueous solution, Chem. Eng. J. 197 (2012) 88–100.
[26] S. Haider, S.Y. Park, Preparation of the electrospun chitosan nanofibers and their applications to the adsorption of Cu(II) and Pb(II) ions from an aqueous solution, J. Membr. Sci. 328 (2009) 90–96.
[27] P. Kampalanonwat, P. Supaphol, Preparation of hydrolyzed electrospun polyacrylo nitrile fiber mats as chelating substrates: a case study on copper (II) ions, Ind. Eng. Chem. Res. 50 (2011) 11912–11921.
[28] R. Ansari, N.K. Fahim, Application of polypyrrole coated on wood sawdust for removal of Cr(VI) ion from aqueous solutions, React. Funct. Polym. 67 (2007) 367–374.
[29] T. Yao, T. Cui, J. Wu, Q. Chen, S. Lu, K. Sun, Preparation of hierarchical porous polypyrrole nanoclusters and their application for removal of Cr(VI) ions in aqueous solution, Polym. Chem. 2 (2011) 2893–2899.
[30] M. Bhaumik, A. Maity, V.V. Srinivasu, M.S. Onyango, Enhanced removal of Cr(VI) from aqueous solution using polypyrrole/Fe_3O_4 magnetic nanocomposite, J. Hazard. Mater. 190 (2011) 381–390.
[31] Y. Wang, B. Zou, T. Gao, X. Wu, S. Lou, S. Zhou, Synthesis of orange-like Fe_3O_4/PPy composite microspheres and their excellent Cr(VI) ion removal properties, J. Mater. Chem. 22 (2012) 9034–9040.
[32] Y. Lin, W. Cai, X. Tian, X. Liu, G. Wang, C. Liang, Polyacrylonitrile/ferrous chloride composite porous nanofibers and their strong Cr-removal performance, J. Mater. Chem. 21 (2011) 991–997.
[33] C.J. Li, Y.J. Li, J.N. Wang, J. Cheng, PA6@Fe*x*O*y* nanofibrous membrane preparation and its strong Cr (VI)-removal performance, Chem. Eng. J. 220 (2013) 294–301.
[34] J. Zeleny, The electrical discharge from liquid points, and a hydrostatic method of measuring the electric intensity at their surfaces, Phys. Rev. 3 (2) (1914) 69–91.
[35] A. Formhals et al. Process and apparatus for preparing artificial threads, U.S. Patent 1,975,504, Issue date: October 2, 1934.
[36] A. Formhals et al. Method and apparatus for spinning, U.S. Patent 2,349,950, Issue date: May 30, 1944.
[37] G. Taylor, Disintegration of water drops in an electric field, Proc. R. Soc. A 280 (1382) (1964) 383–397. JSTOR 2415876.
[38] E.M. Simon, NIH phase I final report: fibrous substrate for cell culture (R3RR03544A), Research Gate, 1988. Retrieved 2017-05-22.
[39] J. Doshi, D.H. Reneker, Electrospinning process and applications of electrospunfibers, J. Electrost. 35 (2–3) (1995) 151–160.
[40] S.N. Reznik, A.L. Yarin, A. Theron, E. Zussman, Transient and steady shapes of droplets attached to a surface in a strong electric field, J. Fluid Mech. 516 (2004) 349–377.
[41] C.J. Angammana, S.H. Jayaram, Fundamentals of electrospinning and processing technologies, Part. Sci. Technol. 34 (1) (2016) 72–82.
[42] N. Bhardwaj, S.C. Kundu, Electrospinning: a fascinating fibres fabrication technique, Biotechnol. Adv. 0734-9750, 28 (2010) 325–347.
[43] H. Fong, D.H. Reneker, Elastomeric nanofibers of styrene-butadiene-styrene triblock copolymer, J. Polym. Sci. B Polym. Phys. 1099-0488, 37 (24) (1999) 3488–3493.

[44] Y. Liu, J.H. He, J.Y. Yu, H.M. Zeng, Controlling numbers and sizes of beads in electrospunnanofibers, Polym. Int. 0959-8103, 57 (2008) 632–636.
[45] V. Beachley, X. Wen, Effect of electrospinning parameters on the nanofiber diameter and length, Mater. Sci. Eng. C Mater. Biol. Appl. 0928-4931, 29 (3) (2009) 663–668.
[46] A. Koshi, K. Yim, S. Shiykumar, Effect of molecular weight on fibrous PVA produced by electrospinning, Mater. Lett. 0167-577X, 58 (3–4) (2004) 493–497.
[47] D.H. Reneker, I. Chun, Nanometer diameter fibers of polymer, produced by electrospinning, Nanotechnology 1361-6528, 7 (1996) 216–223.
[48] Q. Yang, Z. Li, Y. Hong, Y. Zhao, S. Qiu, C. Wang, Y. Wei, Influence of solvents on the formation of ultrathin uniform poly (vinyl pyrrolidone) nanofibers with electrospinning, J. Polym. Sci. B Polym. Phys. 1099-0488, 45 (20) (2004) 3721–3726.
[49] C. Zhang, X. Yuan, L. Wu, Y. Han, J. Sheng, Study on morphology of electrospun poly (vinyl alcohol) mats, Eur. Polym. J. 0014-3057, 41 (3) (2005) 423–432.
[50] M.M. Demir, I. Yilgor, E. Yilgor, B. Erman, Electrospinning of polyurethane fibers, Polymer 0032-3861, 43 (11) (2002) 3303–3309.
[51] Z. Ma, M. Kotaki, S. Ramakrishna, Electrospun cellulose nanofiber as affinity membrane, J. Membr. Sci. 265 (2005) 115–123.
[52] M. Peesan, R. Rujiravanit, P. Supaphol, Electrospinning of hexanoyl chitosan/polylactide blends, J. Biomater. Sci. Polym. Ed. 17 (2006) 547–565.
[53] G.E. Wnek, M.E. Carr, D.G. Simpson, G.L. Bowlin, Electrospinning of nanofiber fibrinogen structures, Nano Lett. 3 (2003) 213–216.
[54] Y.Z. Zhang, J. Venugopal, Z.M. Huang, C.T. Lim, S. Ramakrishna, Crosslinking of the electrospun gelatin nanofibers, Polymer 47 (2006) 2911–2917.
[55] M. Li, Y. Guo, Y. Wei, A.G. MacDiarmid, P.I. Lelkes, Electrospinningpolyaniline contained gelatin nanofibers for tissue engineering applications, Biomaterials 27 (2006) 2705–2715.
[56] Y. Zhang, H. Ouyang, C.T. Lim, S. Ramakrishna, Z.M. Huang, Electrospinning of gelatinfibers and gelatin/PCL composite fibrous scaffolds, J. Biomed. Mater. Res. B 72 (2005) 156–165.
[57] J. Wang, K. Pan, Q. He, B. Cao, Polyacrylonitrile/polypyrrole core/shell nanofiber mat for the removal of hexavalent chromium from aqueous solution, J. Hazard. Mater. 244–245 (2013) 121–129.
[58] M. Aliabadi, M. Irani, J. Ismaeili, H. Piri, M.J. Parnian, Electrospun nanofiber membrane of PEO/Chitosan for the adsorption of nickel, cadmium, lead and copper ions from aqueous solution, Chem. Eng. J. 220 (2013) 237–243.
[59] P.K. Neghlani, M. Rafizadeh, F.A. Taromi, Preparation of aminated-polyacrylonitrile nanofiber membranes for the adsorption of metal ions: Comparison with microfibers, J. Hazard. Mater. 186 (2011) 182–189.
[60] R. Sharma, N. Singh, A. Gupta, S. Tiwari, S.K. Tiwari, S.R. Dhakate, Electrospun chitosan–polyvinyl alcohol composite nanofibers loaded with cerium for efficient removal of arsenic from contaminated water, J. Mater. Chem. A 2 (2014) 16669–16677.
[61] H.H. Najafabadi, M. Irani, L.R. Rad, A.H. Haratameh, I. Haririanc, Removal of Cu^{2+}, Pb^{2+} and Cr^{6+} from aqueous solutions using a chitosan/graphene oxide composite nanofibrous adsorbent, RSC Adv. 5 (2015) 16532–16539.
[62] Y. Tiana, M. Wub, R. Liua, Y. Li, D. Wanga, J. Tana, R. Wue, Y. Huanga, Electrospun membrane of cellulose acetate for heavy metal ion adsorption in water treatment, Carbohydr. Polym. 83 (2011) 743–748.
[63] K. Saeed, S.Y. Park, T.J. Oh, Preparation of hydrazine-modified polyacrylonitrile nanofibers for the extraction of metal ions from aqueous media, J. Appl. Polym. Sci. 121 (2011) 869–873.

CHAPTER

11 ELECTROSPINNING: A FIBER FABRICATION TECHNIQUE FOR WATER PURIFICATION

Maria Wasim, Aneela Sabir, Muhammad Shafiq, Tahir Jamil
Department of Polymer Engineering and Technology, University of the Punjab, Lahore, Pakistan

1 INTRODUCTION

To comprehend the electrospinning process, one can depict it as involving the formation of polymeric fibers. It gained worldwide attention during last few decades [1–3]. The traditional method employs tugging a molten form of polymer, withdrawing it through the dye. The lengthened melted polymers will stand as individual fibers on drying. Correspondingly, the electrospinning process can be a technique employed for producing the polymeric fibers from either synthetic or natural polymers in the nanometer to few micrometers range by using an electrical field instead of using an external mechanical force to pull the polymeric jet through the dye, in the case of the conventional method. The electrospinning process takes advantage of the charges that are exerted on the melt to dispense the force required for stretching to the collector, acting as a potential gradient. On applying the critical high voltage, the polymeric jet goes off from the polymer solution source. The polymeric structural entanglements act in the favor of jet, thus avoiding the jet form splitting up. However, the molten polymeric form dries to stand as an individual fiber in both the conventional method and the electrospinning process [4–6]. The model of electrospinning apparatus is shown in Fig. 1. As the mechanism involved in electrospinning is a simple drawing technique, several types of polymers and precursors can be employed to form fibers. The type of material to be used can be determined by the application. However, the polymer can be subjected directly to the electrospinning process, while other classes, such as carbon nanotubes or ceramics, demand a postprocessing step.

This chapter attempts to explain the fiber fabrication technique via the electrospinning process. It embraces some elementary features of the electrospinning process initially by reviewing the different classes of materials that can be employed such as polymers, composites, and ceramics. Then solution properties, such as surface tension, viscosity, and conductivity, and the electrospinning processing factors, including temperature, feed rate, distance between source and conductor, and so on, are discussed, providing some basic information relating to the electrospinning process. In addition, the uses of electrospun membranes for various applications, mainly water purification, are also covered.

Nanoscale Materials in Water Purification. https://doi.org/10.1016/B978-0-12-813926-4.00016-1

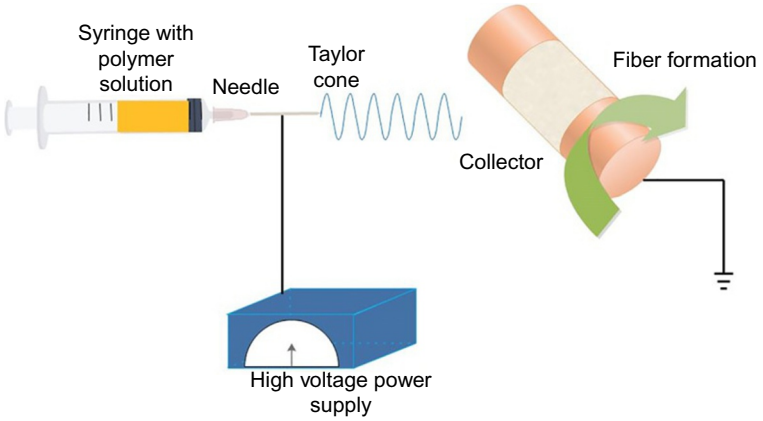

FIG. 1

Model of electrospinning apparatus.

2 CLASSES OF MATERIALS

Owing to the variety of material and applications, the material properties should be considered before implementation. To obtain the expected properties and fiber morphology, the electrospinning technique can be tailored accordingly. Nanofibers can be employed as a sole composite material or may act as a reinforcing filler in a polymer matrix. To form ceramic material into fibers, the material requires a postproduction process [7]. Therefore, having the fundamental knowledge of the different classes of materials prior to the selection of material for the particular practice is a predominant feature.

2.1 POLYMERS

Polymers are a class of materials that are synthesized by repeating units and each particular unit is obtained from the monomer. The quantity of monomers covalently attached is a distinct feature of each polymer and can vary from polymer to polymer type. Each monomer has a specific reactive functional group or a double bond that, under specific conditions, form a covalent bond between monomeric units. This forms the backbone of the polymeric structure. In the early 1930s the theory of molecules being linked to form long chains was suggested by Staudinger; owing to his work on polymers, he attained the Nobel Prize in Chemistry [8].

It is typical for polymeric structures to have weak secondary forces between the monomers, which allows the chain's molecules to glide over each other. The unique properties of polymers attract worldwide attention for various applications. Because the physiochemical characteristics of polymers can be modified by changing the structure simply by varying the synthesis process, this feature makes it a promising material [9].

The increasing demand for polymers is also mainly due to the ease of its fabrication, its low cost, and the medication flexibility nature. Apart from polymers, other classes are also emerging. At the moment, researchers are synthesizing polymers that can be environmentally friendly or be obtained from a natural source [10].

2.1.1 Classification of polymers

The most common way to classify polymers is how it responds to heat. There are two main types of polymers that fall under this classification:

- Thermoset
- Thermoplastic

For thermoset polymers, the polymer is subjected to heat, which leads to the cross-linking between polymeric chains. Later, heating the polymer would only cause the degradation of the structure. Such a polymer has a high upper-limit temperature. Examples of such polymers are epoxy, urea, and phenolic, among others. For thermoplastic polymers, the linear polymeric structure melts when heated and solidifies on cooling. The heating and cooling cycle can be repeated many times without altering the polymer's characteristics. Examples of thermoplastic polymers include poysulphone, poly vinyl, and polystyrene, among others. Although such polymers have a limited temperature range, employing temperatures above the limited range can alter the polymer's structure [11, 12].

2.1.2 Crystallinity

A polymer structure conventionally composed of amorphous and crystalline regions is shown in Fig. 2. The relative proportions of these two regions will govern the characteristics of the polymers. The polymer is assumed to be amorphous when the arrangement of the linear molecules is totally unsystematic. A crystalline polymer has all the linear chains aligned systematically. The universally acknowledged theory of crystalline polymer is the folded chain theory. According to this theory, the polymeric chains are primarily pleated, then loaded on top of one another, and seized together by the tie molecules of the amorphous region to form crystallites.

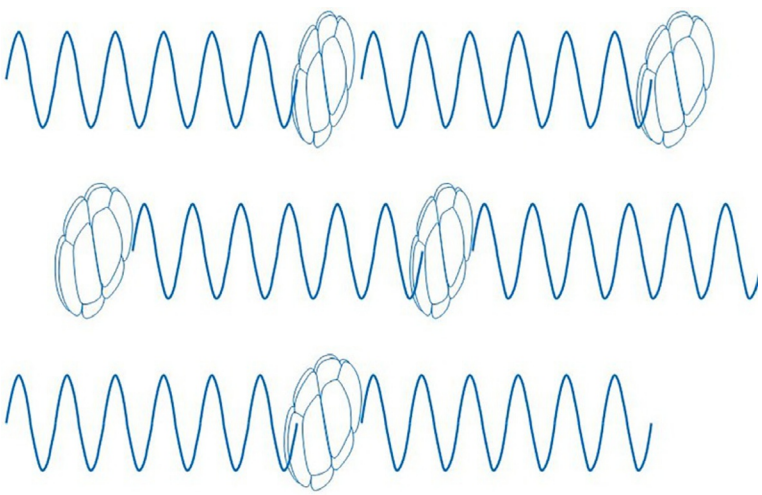

FIG. 2

Model of structure of partially crystalline polymer.

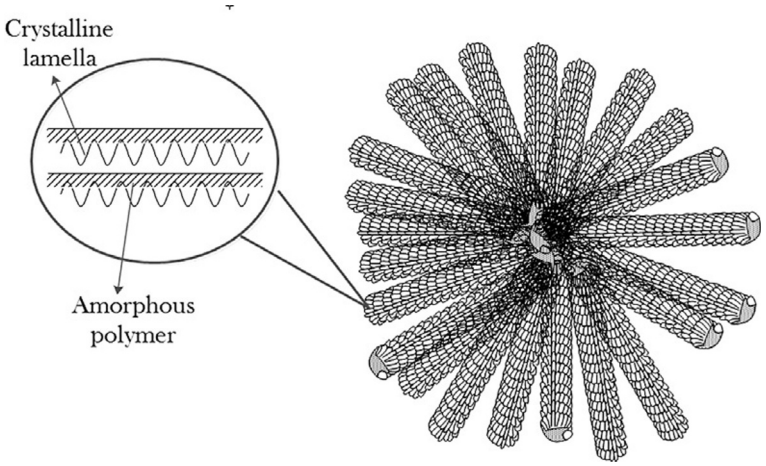

FIG. 3

Structure of spherulites.

Occasionally the chain can be twisted and turned to form ribbon like supramolecular structures termed spherulites, as shown in Fig. 3. A higher crystallinity of polymers leads to an increase in yield strength, hardness, and modulus. When crystalline polymers are subjected to stretching beyond the critical range, the polymeric chains that are aligned in the direction of the applied stress destroy the spherulites' structure, which leads to the necking phenomena. Such polymers have excellent chemical and thermal resistance. Although crystalline polymers are brittle by nature, it can affect their optical properties. A polymer with a higher crystallinity has a high refractive index, thus making them translucent in nature, whereas the amorphous polymer can be entirely transparent [13].

2.1.3 Molecular weight

As the polymeric structure is composed of recurring monomeric units, the molecular weight of the polymer is the sum of the molecular weights of a single monomeric unit. Usually, a polymer with a high molecular weight has an enhanced resistance toward solvent dissolution. The molecular weight determines the viscosity of the solution. A variety of methods can be employed to determine the molecular weight, M_v (viscosity average), M_n (number average), M_w (weight average), and M_z (z average). Here the M_n represents the total weight of monomer molecular weight by the number of molecules present. It is autonomous to the size of the molecule but is highly dependent on the small molecules present in the system. In the case of heterogeneous molecular weight system, it shows the following trend:

$$M_z > M_w > M_n$$

With heterogeneity declines, the numerous molecular weights combine to form a homogenous mixture:

$$M_z = M_w = M_n$$

2.1.4 Glass transition temperature (T_g)

One of the most important characteristics of polymers, the glass transition temperature describes the freedom of movement present within polymeric molecules. Polymers above the T_g are ductile in nature, and molecular chains have the ability to slide over each other because of the sufficient thermal energy. However, polymers above T_g range do not show any movement of the molecules; they are amorphous, making them brittle and thus causing them to have low elastic modulus by several orders of magnitude while above T_g temperature. It is crucial to note that the mechanical performance of a polymer is influenced by the loading rate above the T_g temperature. Because the mobility of molecules is governed by the glass transition temperature, however, the mobility of molecular chains is not immediate. In the case of slow loading rate, the chains have time to move nearer to T_g; however, in the case of fast loading, the decreased time therefore enhances the effective T_g. It can be demonstrated as the temperature below the T_g; the composure time of the molecule is too much for the equilibrium stage to occur. At T_g, the molecular motion in the polymer is temperature-dependent, also termed "cooperatively rearranging." The span of the cooperatively rearranging region is governed by the configurational hindrance attributed to the amorphous nature [14].

A number of aspects can influence the bulk glass transition temperature of polymers. As the polymeric compounds have free volume that permits the free mobility of molecular chains, ultimately decreasing the T_g, the presence of secondary forces, such as hydrogen bonding (intra- or inter H-bonding), can enhance the T_g. As the chain length of molecules increases, so do the entanglements present within the polymeric structure. Several experimental studies have shown that in a polymer membrane, the motion of molecules is higher at the surface than in the rest of the bulk because of significantly reduced T_g at the surface of membrane. However, the bulk present beneath the surface can retard the motion of molecular chain at the surface, causing a high T_g. However, if the membrane thickness is reduced (to approximately 14 nm), the T_g will be the same for both the surface and the bulk [15]. According to studies, a polymeric membrane's T_g is greatly influenced by the mobility of the surface. It has been experimentally illustrated that a nanofiber having a large surface area than the membrane shows a lower T_g than does a casted membrane [16].

2.2 CERAMICS

Distinct to polymers, ceramics need a posttreatment step to be employed in the electrospinning process; their nanofibers can be prepared by using the melt from ceramic precursors. The resulting product should be subjected to a sintering process to achieve ceramic nanofibers [17–19]. Ceramics consist of both metallic and nonmetallic elements and generally occur as compounds of nitrides, sulfides, oxides, and carbides. Although most ceramic materials are crystalline in nature, noncrystalline, such as glass composed of silicon dioxide, also exist. The ceramic structure consists of an ionic or covalent bond, only with no free electron, thus making ceramics outstanding insulators. The strong bonding structure of ceramics allows them to withstand extremely high temperatures and makes them chemical resistant. But such a configuration makes them brittle by nature.

Because of rapid technological progress, ceramics are now being applied to biomaterials because of their unique properties. Ceramic materials, like hydroxyapatite and calcium carbonate-based ceramics, are most important. The use of nanoscale ceramics shows great potential in many applications because of their high surface area-to-volume ratio [20].

2.2.1 Ceramics biomaterials

Ceramics comprising glass have been extensively employed in biomedical fields, including the use of porous glass as a carrier for antibodies, for diagnostic implements, and for restorative dental implants. With their exceptional biocompatibility and corrosion resistivity, they are widely employed in load-bearing prosthetic implants. For the last two decades, alumina has been employed in orthopedic surgery. Lately, zirconia oxide has been used as an articulating ball implant for hip prostheses.

The application of porous ceramic material as an implant reassure bone growth inside the interconnecting pores, with the pore size beyond 100 μm. This type of ceramics is employed for nonload-bearing functions, while the porous ceramic materials have been synthesized from the microstructures of various corals [21]. Additional methods for synthesizing porous ceramic implants for biomedical applications, such as the formation of bacterial threads penetrated with silica nanoparticles to prepare porous the ceramic structure, have also been studied [22].

2.2.2 Structure of crystallite

In most ceramic material the bonding is mostly ionic; the crystallite structure is made up of electrically charged ions. The metal ions are generally positive in nature, termed cation when they lose the electron, while nonmetallic ions are negatively charged, termed anion. In the crystallite structure, the overall charge should be balanced by the number of cations and anions. The equilibrium position of the crystal is governed by anions and cations as the particles have the capability of upholding a specific spatial configuration depending on the interactional forces [23](Fig. 4).

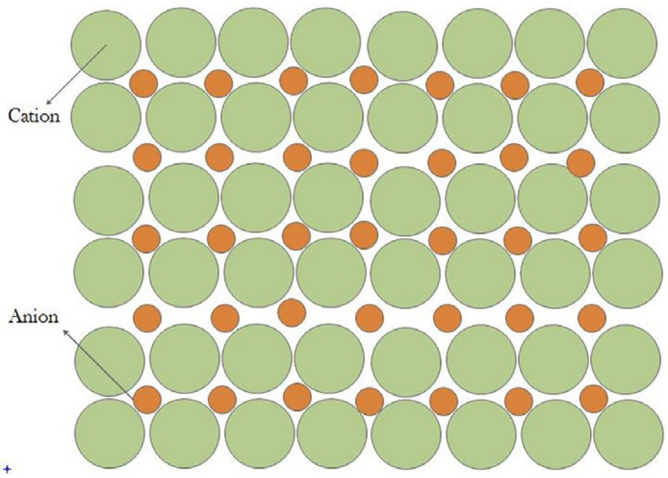

FIG. 4

Illustration of cation and anion in crystallite structure.

2.3 COMPOSITES

The class composite comprises two distinctive phases: the massive phase, termed as the matrix, and the reinforcement phase. The coalescence of durability of the reinforcement phase and the firmness of the matrix provide the composite its ultimate properties that cannot be achieved by using a single material. The material for both phases can be a polymer, a ceramic, or a metal. Commonly, the function of the matrix phase is to bind the reinforcing agents, and collectively they provide the resulting form, surface morphology, and resistivity toward environmental damage. In most cases, the matrix phase is ductile in nature; the reinforcement phase provides strength as composites have low density. The main function of reinforcement is to bear the major applied load, hence providing the composite its strength and toughness. It is possible to synthesize transparent composites using fibrous reinforcement of less than 100 nm [24], even though they are mostly opaque because of light-scattering phenomena. Composites are frequently used for their load-bearing applications, even though other classes of composite materials are employed because of their magnetic, electric, and thermal characteristics.

2.3.1 Classes of reinforcement

There are conventionally two main classes of reinforcement material in composites: particulate reinforcement and fibrous reinforcement. The fibers can be organized in various ways. The most basic fibrous setting in the matrix phase is to align the fiber in a definite direction to build a laminate composite. The fibers can be aligned in unidirectional composite at an angle of 0-, 45-, and 90-degrees directions. Such composites are strong in all directions; within a plane, enclosing fibers, however, are weak in the direction normal to the plane of the composite. Further classes of fiber arrangements are composed of interknitting to form fabric of various shapes and interknitting configuration, weaving, and braiding, as shown in Fig. 5. Determined by the use of composite, various fibrous arrangement can be employed. In an application where high torsional stiffness is required, a braided fibrous arrangement is used. The random distribution of fibers to form nonwoven fabrics can also be used.

To the contrary, the particular reinforcement has a coarsely equal dimension in all directions. Such a composite is termed an aggregate composite. Also, the particles size does not need to be equal in size. As in the case of concrete composition, the volume section of particulates can be greater than the matrix

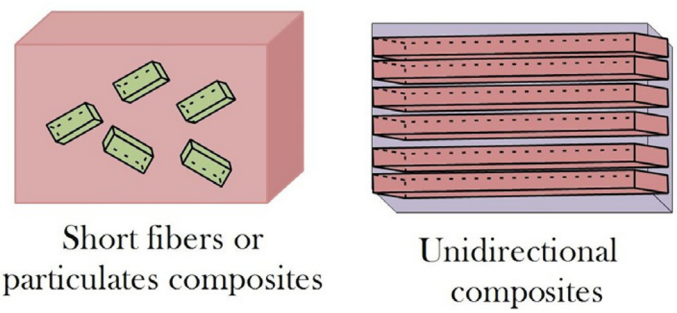

FIG. 5

Types of composite reinforcements.

phase. The presence of asymmetrically shaped particulates gives mechanical strength via mechanical interlocking phenomena. A new class of aggregate composite is termed a particulate composite. In this instance, the volume section of particulates is less than that of the matrix phase. In the case of a traditional composite, the unequal thermal expansion of particulates and the matrix phase will produce a high dislocation density in the matrix phase during the cooling period in the fabrication process. The ended strain toughens the composite, which ultimately increases the mechanical strength of the composite. In the case of nanofiber composite made of nylon, Closite 30B [25] and polyimide, along with single-walled nanotubes [26], were prepared via the electrospinning process.

3 FACTORS AFFECTING THE ELECTROSPINNING PROCESS

3.1 PROPERTIES OF THE SOLUTION

The electrospinning process involves applying charged fluid to form desired properties for a desired application. It involves a high voltage be applied to polymeric solution or melt. When the charge reaches a threshold point, the solution flow develops at the source tip in the form of a Taylor cone. So the jet flows from a high-potential to a low-potential area termed a collector. The morphological structure of fibers can be varied because of the influence of physical and chemical parameters. The polymeric melt was first employed in early 1980 to form fibers through the electrospinning process [27–29]. However, today polymeric solutions are widely employed because of their applications and ease of use. The role of factors governing electrospinning is vital as the polymeric solution plays an important role. The characteristics of the solution greatly influence the electrospinning process and the morphology of fibers. Throughout the electrospinning process, the polymeric solution is dragged from the tip of the needle. The stretching phenomena of melt, or polymer, are largely governed by properties such as electrical property, viscosity, and surface tension. Also, the evaporation rate of the fiber will be affected by solution viscosity as it is dragged. The viscosity is determined by the solubility of the polymer in a solution.

3.1.1 Surface tension

The charge present in the polymeric solution should be critical enough to overpower the surface tension of the polymer solution. The jet of solution moves forward from the tip of the source toward the collector base. The surface tension may cause the stretched jet to break into drops [30, 31]. When forming droplets, the technique is called electrospraying rather than electrospinning [32]. Consequently, understanding the part surface tension plays in a solution is vital because a change in surface tension may cause the bead formation instead of the fiber formation.

The formation of spherical-shaped water droplets when it falls through the air is due to the liquid property, or surface tension. In the case of liquid state, the molecules present within the solution have equal forces exerted on them from equal directions by other molecules around them, whereas the molecules present on the surface only have downward force exerted on them from fluid molecules, which is greater than that exerted by the gas molecules of air, as shown in Fig. 6.

As a consequence, the surface is in tension, and that ultimately effects a contraction at the surface of the fluid that is equalized by the repulsive forces because of the collision of molecules surrounding the fluid. The ultimate effect of all the downward forces acting at the surface becomes the ground reason for the liquid to reduce its surface area. Thus, a water droplet is formed as a spherical shape that has a

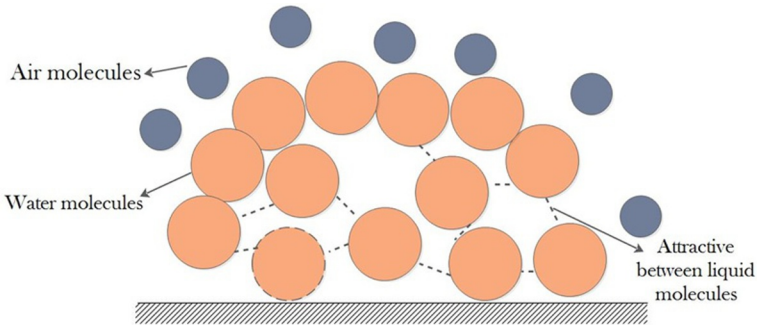

FIG. 6

The forces present between liquid molecules are stronger than forces between air molecules.

minimum surface-to-volume ratio [33]. To suppress the effect of surface tension, ethanol and a surfactant can be added to ensure the formation of smooth fibers. The addition of a surfactant allows the formation of more fibers; it can also be added in the form of filler in a solution [34, 35].

3.1.2 Temperature effect on surface tension

In the case of a pure liquid system, the surface tension of the liquid system tends to drop with a hike in temperature. With an increase in temperature, the equilibrium rate between vapor pressure and surface tension decreases. Once it reaches the critical stage, the boundary between liquid and gas diminishes [36]. The increase in temperature enhances the motion of liquid molecules because of a gain in energy. As a consequence, because of the rapid motion of molecules, they do not settle for any strong bonding to occur, thus causing the decline in surface tension. The different types of mixtures behave differently than pure liquid does. For a methane and nonane mixture, the increase in temperature causes a boost in surface tension, excluding the low pressure. Thus, the composition at low temperature is a dependent factor because of the increased solubility of methane compared to nonane, and it can greatly determine the behavior [37].

3.1.3 Synergistic effect of molecular weight and viscosity

The viscosity of the solution is largely determined and influenced by the molecular weight of the polymer. A larger molecular weight ensures the high viscosity of the polymeric solution when dissolved and vice versa, with low molecular weights indicating low viscosity. For the fiber formation through the electrospinning process, the viscosity should be sufficient as the polymeric jet has to travel from the source to the collector. Throughout its travel, the jet is being stretched, and the polymeric entanglements present in the structure ensure it to happen without breaking the jet. Because of this, monomers cannot be used for electrospinning process [38].

The total length of entanglement present in the polymeric structure is regulated by the molecular weight of the polymer involved, thus controlling the viscosity of the solution. By increasing the polymeric content the viscosity can be increased up to a certain limit. Molecular weight has the same effect: as it increases, the viscosity of the solution is enhanced, which ensures the continuous flow of the jet.

The complexity of the polymeric structure can affect the type of jet formed or whether the jet may break halfway and form droplets or beads. The critical viscosity is mandatory for the electrospinning

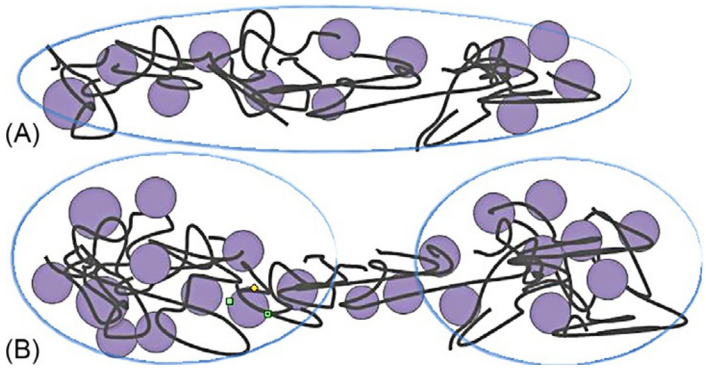

FIG. 7

(A) At high viscosity, the solvent molecules are distributed over the entangled polymer molecules. (B) With a lower viscosity, the solvent molecules tend to congregate under the action of surface tension.

process; a viscosity that is too high or too low can become a problem for pumping the solution through the tip, or it may clot the tip, making it problematic for starting the process, as shown in Fig. 7. [16].

The presence of low-viscous liquid can cause a change in fiber shape. As soon the viscosity increases, the electrospun product changes from beads to spherical to spindle shapes and finally into a fibrous form. A low viscosity solution means a low content of solvent molecules and poor entanglement. In this case, the surface tension becomes a prime factor for bead formation. The increase in viscosity means that when stretched for the electrospinning process, the polymeric content has also increased and spread throughout the solvent molecules [39].

3.1.4 Solution conductivity

During the electrospinning process, an electric field is applied that will stretch the polymeric jet, which is caused by the repulsive forces that exist on the surface's jet. A higher conductivity of the polymeric solution increases the concentration of the charge being stretched. The conductive nature of any solution or fluid can be improved by introducing ionic species. Incorporating a minute amount of salt or polyelectrolyte into the bead-forming electrospun solution will increase its conductivity. The resultant product will be small cylindrical fiber with a diameter smaller than the beads [16].

A rise in ion concentration increases the conductivity of solution at the expense of a decline in the critical voltage of the process and enhances the deposition rate on the collector. Also, using a high conductive solution also decreases the beads' formation during the electrospinning process.

The thickness of fiber forming can also be influenced by the ion size present in the polymer solution. The greater the size of the ions, the thicker the diameter of the fiber, whereas a lesser size yields fibers with a small diameter [40].

3.1.5 Dielectric effect of solvent

The main characteristic of the solvent is dielectric, which has a large impact on the electrospinning process. The larger dielectric ensures a finer fiber formation without any beads in it. Incorporating solvents, such as dimethylformamide (DMF), can improve the morphology of the fibers and the deposition rate on the collector [41].

4 PROCESSING CONDITIONS

The significant factors that can affect the performance of the electrospinning process are the external forces acting on it. They have certain effects on the morphology of fibers and, less important, correspond to other factors.

4.1 TEMPERATURE

A change in temperature can alter the viscosity, as well as the evaporation rate, of the fibers formed. At elevated temperatures, the molecules' motion increases, and as a consequence, this leads to enhanced stretching of the solution [42].

4.2 EXTERNAL VOLTAGE APPLIED

The fiber fabrication technique requires a high voltage to induce a charge on the solution or melt sufficient enough to get over the surface tension by the electrostatic force. Typically a voltage greater than 6 kV is needed to form a Taylor cone or to permit the polymeric jet to travel from tip source to the collector [43]. The extent of voltage necessary to hold a Taylor cone stable can be determined by the rate of feed of the polymeric solution. Voltage applied and the generated electric field can modify the stretching of the solution.

By applying a greater voltage, the stretching of the polymer increases, resulting in the decreased diameter of the fiber that forms, thereby also enhancing the rate of evaporation and ensuring dried fibers. When high voltage is applied to a low-viscous solution, often two Taylor cones are formed, ultimately reducing fiber thickness. Hence, the morphology of fibers can be influenced by the time it takes the jet to reach the collector. The longer it takes causes increased stretching, leading to finer fibers with smaller diameters [44].

4.3 FEED RATE

The volume of the solution for electrospinning can be determined by the rate of feed of the polymeric solution. The definite feed rate should be attuned with the applied voltage to stabilize the Taylor cone. The fiber thickness increases with the increase the voltage applied but up to certain limit. After that, the charge of the solution should also be increased to achieve better results. The drying of fibers will also become difficult if the feed rate is increased because it causes the solvent molecules to attach to the fibers, ultimately forming the web structure [45].

4.4 EFFECT OF THE COLLECTOR PLATE

For the electrospinning process, the electric field should be generated between the source and the collector. To ensure the formation of the electric field, the collector plate should be formed of a conductive material or be covered with conductive material, such as aluminum foil. The use of nonconductive material causes the quick, low fiber formation [46]. The fibers formed on nonconductive collector plates, compared to fibers formed on conductive material, are fibers of low density for packing material because of the repulsive forces collected on the deposited fibers. In this three-dimensional structure of

the same charge, fibers are formed on the plate. If there is a sufficient charge on initial fibers, then a huge honeycomb-like mass structure is formed. It can also happen with conductive material if there is the high feed rate and the diameter of fibers are larger; then the thick mass is deposited on the collector plate, forming pores. The porosity rate is also influenced by the type of collector used during the process. If a paper mesh-type collector is used, then the fibers have low packing density compared to fibers formed on aluminum foil [47].

4.5 DIAMETER OF NEEDLE OF SYRINGE

The diameter of the orifice present in the syringe tip can also somewhat affect the performance of the electrospinning process. The effect of beads being present can be lessened by reducing the diameter of the syringe orifice that forms cylindrical fibers of small diameter. As the diameter decreases, the tension created on the surface of the droplets increases, so high voltage is required in such cases to decrease the accelerating force [48].

4.6 DISTANCE BETWEEN SOURCE AND COLLECTOR PLATE

The distance between the collector plate and that of the syringe greatly affects the power of the generated electric field and the time required for the polymeric jet to travel to the collector plate. For adequate fibers, the distance should be sufficient enough so that when the fibers fall onto the plate, it must dry out, or the solvent should evaporate during its travel; otherwise, the solvent does not evaporate, resulting to the formation of web structure on the plate and the strength of electric field increases with increase in accelerating force [49].

5 WATER PURIFICATION

Currently, the major concern is the access to pure drinking water. The problem is arising more and more with the increased population of the world and decline of freshwater reservoirs throughout the world [50, 51]. It is likely that the half the world's population will be facing water scarcity by 2025, which will cause serious troubles relating to food availability, the ecosystem, and, most important, human health [52].

Besides the scarcity of water, in particular, the availability of fresh, hygienic water is quite low in many regions of the world. Approximately 1.2 billion people do not have access to fresh, hygienic drinking water, and about 2.6 billion people have little or no sanitation. Because of poor sanitation, the death rate is quite high because of unhygienic water that transfers diseases. Each day, 3900 children die because of toxic water. Mostly in the developing countries, the budding number of contaminants that enter the freshwater supply is increasing the health concerns that compel efforts to purify the water. The need of more effective, cheap, and robust processes requires decontaminating the water from the source to the point where it is to be used so that the treatment does not affect the environmental conditions and human health [53, 54]. Mainly, the demand for fresh, clean water in the current century is greater than ever. In particular, the remaining reservoirs require fortification, along with the development of the new reservoirs, to cover the growing demand for water around the world. To achieve this target, a better water treatment is required.

Electrospun nanofibers are widely used for the separation phenomena. Nanofibrous membranes can be employed in traditional filtration processes with a high performance rate, predominantly because of their high porosity rate with adjustable pore size, even though they lack the required mechanical strength and durability. Nonwoven electrospun textiles have a high surface area and a small pore size, in the submicron range, making them favorable for filtration processes. Many scientists have suggested that incorporating an electrospun membrane as a layer within several substrate layers improves the filtration performance without a dominant change in pressure decline [3]. It has been reported that the thickness of the membrane can affect its performance properties; thin fibers provide high flux and excellent separation efficiency, while thicker fibers act as a supporting material [55]. Using electrospun material as an active layer also provides a high flux rate as well as a high separation of divalent ions [56].

In recent years, a range of research has been conducted for the preparation of various materials for the filtration process. The remarkable generated results can progress the class of filtration. Ghaly et al. [57] performed a test filtrating greasy wash water by using aluminum sulfate as a chemical coagulant. The efficiency of the aluminum sulfate was evaluated in terms of optical density, pH, and total solids. The research data showed that the removal of turbidity was 89.6% with effective coagulant dosage of 2 g/L.

Konieczny et al. [58] conducted a filtering experiment employing the coagulation process without the sedimentation process. The two main coagulants employed were aluminum sulfate and iron chloride, and polypropylene and polyether sulfate membranes were used for filtration process. The benefits achieved using this approach were improved water quality along with a decline in fouling intensity. The data illustrated that the overall quality of filtered water yielded iron and aluminum traces of 0.2 mg/dm^3, which is lower than the regulation for drinking water.

Heavy metals, such as copper, chromium, and cadmium, among others, in water are toxic to aquatic life because they can easily accumulate in the body, therefore causing a serious threat to biological life; they should be harshly controlled at the level of few tenths of parts per billion or less [59, 60]. The most conventional processes for eradicating heavy metals from water are the adsorption and filtration processes. Remarkably, electrospun nanofibrous material can be used for both techniques because of their tunable pore size and high surface-to-volume ratio [60]. Silk fibroin and its blending with the wool keratose have shown a remarkable separation efficiency for heavy metals in comparison to wool silver and filter paper [61].

Organic materials, such as humic acid, protein, oil, and so on, are other toxic pollutants, and they need to be eliminated from drinking water. Functionalized electrospun nanofibrous membranes can be used to separate out such organic matter [60]. For example, a nanofibrous membrane of poly(methyl methacrylate) functionalized via phenylcarbamylated and azido phenyl carbamylated β-cyclodextrins demonstrated the removal of phenolphthalein from water [62].

Functionalized electrospun membranes can also be employed for disinfecting, as well as removing, bacteria from water [60]. The addition of silver or its salts, silver-TiO_2, and quaternary ammonium salt consisting cationic polymers can bring excellent antimicrobial properties to the membranes. Owing to nanofibrous membranes' having a high surface-to-volume ratio, they can provide a better efficiency for the removal of such contaminations [59].

Lala et al. [63] fabricated such electrospun membranes using silver-consisting polymer membranes and tested for Gram-negative bacterial groups, including *Escherichia coli* and *Pseudomonas aeruginosa*. The data obtained showed promising results in terms of antimicrobial activity. In a recent study

[64] the performance properties of electrospun polyvinylideine fluoride (PVDF) membrane was compared with commercial ones. To study the filtration phenomena in equal conditions, the pore size of the electrospun nanofibrous membrane was reduced via grafting with methacrylic acid up to the range of its commercial counterpart. The results showed that the water flux of the electrospun membrane was two times higher than that of the commercial one when performing at the same pressure and having the same pore-size distribution. This result confirms these membranes' better efficiency with low energy consumption.

Electrospun fibrous membranes can be employed as ultrafiltration membranes if they have a pore size of less than 0.1 μm. However, such types of membranes with high surface area are susceptible to the fouling process, with, ultimately, a decline in permeation flux during the filtration process, except they can be employed with a thin-film coating [59]. Such an ultrafiltration membrane composed of a microfibrous substrate with a middle barrier layer of electrospun nanofibrous. The electrospun fibrous layer, with its high porosity, provides a higher flux rate than does a conventional membrane. This theory was proved in a recent study [65] that used cross-linked polyvinyl alcohol (PVA) electrospun nanofibrous scaffold having a fiber diameter in the range of 130–300 nm, with 83% porosity used as a mid-layer in a thin-film composite membrane (TFC). The results illustrated the high flux rate (10 times) that of a conventional TFC membrane [65].

6 OTHER APPLICATIONS

Today, scientists are researching numerous applications of fibers and mats synthesized by electrospinning as they can offer various benefits, including high porosity, high surface area-to-volume ratio, and improved physical and chemical characteristics as the factors can easily govern the fibers' strength along with the surface morphology. Also, the electrospinning process is a highly versatile process that can provide fibers in any shape and morphology, and because of they are nanosized, the amount required is also reduced [66, 67]. The electrospun fibers are broadly used in the biomedical field, such as in wound dressing, scaffold formation for tissue engineering, filtration media, vascular graft implants, energy storage, immobilization of enzymes, and in various ongoing research [68–71].

For more than a decade, polymeric nanofibrous mats have been employed for air filtration. To filter the elements, the pore size or channels should be matched with the material to be filtered. Therefore, one can apply very fine fibers into use. The electrospinning process can provide a pore size up to several microns, thus providing the solution for the removal of toxic or desired material. Usually, because of the high surface cohesion resulting from high surface-to-volume ratio, minute particles (order of <0.5 mm) can be trapped in electrospun fibrous membranes, thus enhancing the membranes' performance. Nonwoven mats produced by electrospinning have been successfully employed for the development of an efficient air filter. Such nanofibrous membranes have shown a 100% selectivity rate, having the diameter in the range of 1–5 μm via physical entrapment, as well as through electro-kinetic capture in the air filter membrane [69, 72].

Tissue engineering is a multidisciplinary field that includes engineering principles and that of life science for the production of bio-substitutes required for repairing, preserving, and upgrading tissues. Biomaterials that act as a matrix for cell growth, proliferation, and then the formation of fresh tissues having three-dimensional structures are an emerging research field [73–75]. Compared with other fiber-forming technologies, such as the phase-separation technique and self-assembly, electrospinning

is a simple, cost-effective technique that produces fibers with interconnected pores that have diameters in the nanometer range.

Immobilizing enzymes on an inactive, unsolvable material is currently a progressive area of research for successfully enhancing the performance and functionality of enzymes for a biological processing purpose. Immobilized enzymes provide several benefits rather than soluble ones, such as better control, reusability, and high stability [76–80]. Their performance characteristics are largely determined by the structure and the character of the carrying material or by the modification applied to the material, such as hydrophilicity, rendering, biocompatibility, and so on [81].

Electrospun nanofibers have also been employed in cosmetic industry, with or without the addition of any fillers, such as for a skin care mask used for healing purposes, cleansing, and other therapeutic and medical purposes. The fibrous mask provides benefits, including high surface area, increasing its utilization, and swiftly enhancing the transfer rate of additives to the skin. For healing purposes, the fibrous mat can be applied with causing any pain, providing the three-dimensional topography [82].

Biosensors that conventionally composed of a transducer and a biologically active membrane are widely employed for clinical purposes, environmental use, and for food. Several factors can alter the performance properties of a sensor. Selectivity, response time, sensitivity, aging, and reproducibility are all direct dependent factors. Sensitivity plays an important role in the case of detecting a gas leakage or any other substance as it can be detected in very low concentrations. The accuracy of modern techniques is improving day by day through the use of advanced biomedical sensors [83].

7 FUTURE RECOMMENDATIONS OR PROSPECTS

To avail the applicability of nanofibers, abundant alterations in the electrospinning apparatus are being employed. These changes comprise mixed and multiplex apparatus, blow-assisted, coaxial or core-shell electrospinning, and various others. Among them, the coaxial apparatus utilizes the synthesis of nanofibers by employing two different polymers, of which one forms the core while other uses as shell, or coating, on the core polymer [84]. This equipment can be employed to co-electrospin the polymers that are difficult to be processed individually. This method can revolutionize the electrospinning technique by providing the novel properties and modifications at the nanoscale. This new method allows nanofiber formation with controlled pore structure because of its distinctive properties [85, 86]. In the case of drug delivery, the bust release often observed is due to the large surface-to-volume ratio and high porosity. The coaxial method is widely employed as polymer layer that acts as a diffusion barrier for drug release. Further new technologies can also provide numerous benefits. High molecular-weight polymers are often difficult to electrospin; for this, blow-assisted electrospinning can be employed. Recently, research has been conducted regarding the production of nanowires using nanofibers by adding carbon nanotubes inside the fibrous network that can provide characteristics such as electrical and thermal conductivity [3].

8 CONCLUSION

Electrospinning is a simple yet versatile and cost-effective technique for producing nonwoven nanofibers that have a high surface-to-volume ratio with tunable porosity. Because of these characteristics, it is considered one of the most favorable candidates for numerous applications. The polymeric solution

and processing factors include molecular weight, viscosity, applied voltage, tip-to-collector distance, and conductivity, among others, and these factors can considerably affect the morphological structure of fibers. Modifying these factors can provide desired characteristics. Electrospun nanofibers are widely being used in a number of applications, includes for scaffold formation for tissue engineering, the formation of wound-healing mats, drug delivery, biosensors, the immobilization of enzymes, cosmetics, filtration purposes, and so on. Regardless of numerous benefits and accomplishments of electrospinning process, some acute limitations include small pore size and a lack of proper cellular infiltration inside of the fibers. Several attempts are ongoing for improving the design. In general, the electrospinning process has an outstanding application in the field of biomedical applications.

REFERENCES

[1] Y.C. Ahn, S.K. Park, G.T. Kim, Y.J. Hwang, C.G. Lee, H.S. Shin, J.K. Lee, Development of high efficiency nanofilters made of nanofibers, Curr. Appl. Phys. 6 (6) (2006) 1030–1035, https://doi.org/10.1016/j.cap.2005.07.013.

[2] J. Lannutti, D. Reneker, T. Ma, D. Tomasko, D. Farson, Electrospinning for tissue engineering scaffolds, Mater. Sci. Eng. C 27 (3) (2007) 504–509, https://doi.org/10.1016/j.msec.2006.05.019.

[3] M.T. Hunley, T.E. Long, Electrospinning functional nanoscale fibers: a perspective for the future, Polym. Int. 57 (3) (2008) 385–389.

[4] C. Burger, B.S. Hsiao, B. Chu, Nanofibrous materials and their applications, Annu. Rev. Mater. Res. 36 (2006) 333–368.

[5] A. Frenot, I.S. Chronakis, Polymer nanofibers assembled by electrospinning, Curr. Opin. Colloid Interface Sci. 8 (1) (2003) 64–75, https://doi.org/10.1016/S1359-0294(03)00004-9.

[6] Z.-M. Huang, Y.Z. Zhang, M. Kotaki, S. Ramakrishna, A review on polymer nanofibers by electrospinning and their applications in nanocomposites, Compos. Sci. Technol. 63 (15) (2003) 2223–2253, https://doi.org/10.1016/S0266-3538(03)00178-7.

[7] I.S. Chronakis, Novel nanocomposites and nanoceramics based on polymer nanofibers using electrospinning process—a review, J. Mater. Process. Technol. 167 (2) (2005) 283–293, https://doi.org/10.1016/j.jmatprotec.2005.06.053.

[8] R.O. Ebewele, Polymer Science and Technology, CRC Press, New York, 2000.

[9] J. Gilron, S. Belfer, P. Väisänen, M. Nyström, Effects of surface modification on antifouling and performance properties of reverse osmosis membranes, Desalination 140 (2) (2001) 167–179, https://doi.org/10.1016/S0011-9164(01)00366-6.

[10] M. Elimelech, W.A. Phillip, The future of seawater desalination: energy, technology, and the environment, Science 333 (6403) (2011) 712–717.

[11] M. Biron, Detailed accounts of thermoplastic resins, in: Thermoplastics and Thermoplastic Composites, Elsevier, Oxford, 2007, pp. 217–714 (Chapter 4).

[12] D.N. Saheb, J.P. Jog, Natural fiber polymer composites: a review, Adv. Polym. Technol. 18 (4) (1999) 351–363.

[13] M.M. Farag, Selection of Materials and Manufacturing Processes for Engineering Design, Prentice Hall, New York, 1989.

[14] G. Adam, J.H. Gibbs, On the temperature dependence of cooperative relaxation properties in glass-forming liquids, J. Chem. Phys. 43 (1) (1965) 139–146.

[15] C.J. Ellison, J.M. Torkelson, The distribution of glass-transition temperatures in nanoscopically confined glass formers, Nat. Mater. 2 (2003) 695–700.

[16] X. Zong, K. Kim, D. Fang, S. Ran, B.S. Hsiao, B. Chu, Structure and process relationship of electrospun bioabsorbable nanofiber membranes, Polymer 43 (16) (2002) 4403–4412, https://doi.org/10.1016/S0032-3861(02)00275-6.
[17] H. Dai, J. Gong, H. Kim, D. Lee, A novel method for preparing ultra-fine alumina-borate oxide fibres via an electrospinning technique, Nanotechnology 13 (5) (2002) 674–677.
[18] S. Madhugiri, B. Sun, P.G. Smirniotis, J.P. Ferraris, K.J. Balkus, Electrospun mesoporous titanium dioxide fibers, Microporous Mesoporous Mater. 69 (1) (2004) 77–83, https://doi.org/10.1016/j.micromeso.2003.12.023.
[19] C. Shao, H. Guan, Y. Liu, X. Li, X. Yang, Preparation of Mn_2O_3 and Mn_3O_4 nanofibers via an electrospinning technique, J. Solid State Chem. 177 (7) (2004) 2628–2631, https://doi.org/10.1016/j.jssc.2004.04.003.
[20] L.E. Niklason, Engineering of bone grafts, Nat. Biotechnol. 18 (2000) 929–930.
[21] J. Jamison, Engineering of bone grafts, Nat. Biotechnol. 18 (2000) 914.
[22] S.A. Davis, S.L. Burkett, N.H. Mendelson, S. Mann, Bacterial templating of ordered macrostructures in silica and silica-surfactant mesophases, Nature 385 (1997) 420–423.
[23] R. Pampuch, Constitution and Properties of Ceramic Materials, Elsevier Science Publishing Co., Inc, 1991.
[24] M.M. Bergshoef, G.J. Vancso, Transparent nanocomposites with ultrathin electrospun nylon-4,6 fiber reinforcement, Adv. Mater. 11 (16) (1999) 1362–1365.
[25] H. Fong, W. Liu, C.-S. Wang, R.A. Vaia, Generation of electrospun fibers of nylon 6 and nylon 6-montmorillonite nanocomposite, Polymer 43 (3) (2002) 775–780, https://doi.org/10.1016/S0032-3861(01)00665-6.
[26] C. Park, Z. Ounaies, K.A. Watson, K. Pawlowski, S.E. Lowther, J.W. Connell, E.J. Siochi, J.S. Harrison, T.L. S. Clair, Polymer-single wall carbon nanotube composites for potential spacecraft applications, Paper Presented at the Material Research Society Symposium Proceedings, 2002.
[27] J. Lyons, C. Li, F. Ko, Melt-electrospinning part I: processing and geometric properties, Polymer 45 (22) (2004) 7597–7603.
[28] L. Larrondo, R. St. John Manley, Electrostatic fiber spinning from polymer melts. I. Experimental observations on fiber formation and properties, Polymer Phys. 19 (6) (1981) 909–920, https://doi.org/10.1002/pol.1981.180190601.
[29] L. Larrondo, R. St. John Manley, Electrostatic fiber spinning from polymer melts. III. Electrostatic deformation of a pendant drop of polymer melt, Polymer Phys. 19 (6) (1981) 933–940.
[30] Y. Christanti, L.M. Walker, Surface tension driven jet break up of strain-hardening polymer solutions, J. Non-Newton. Fluid Mech. 100 (1) (2001) 9–26, https://doi.org/10.1016/S0377-0257(01)00135-5.
[31] P. Schümmer, K.H. Tebel, A new elongational rheometer for polymer solutions, J. Non-Newton. Fluid Mech. 12 (3) (1983) 331–347, https://doi.org/10.1016/0377-0257(83)85006-X.
[32] V. Morozov, T. Morozova, N. Kallenbach, Atomic force microscopy of structures produced by electrospraying polymer solutions, Int. J. Mass Spectrom. 178 (3) (1998) 143–159, https://doi.org/10.1016/S1387-3806(98)14083-6.
[33] B.E. Poling, J.M. Prausnitz, O.'.C. John P., The Properties of Gases and Liquids, fourth ed., McGraw-Hill Book Company, Singapore, 1998.
[34] H. Fong, I. Chun, D.H. Reneker, Beaded nanofibers formed during electrospinning, Polymer 40 (16) (1999) 4585–4592, https://doi.org/10.1016/S0032-3861(99)00068-3.
[35] J. Zeng, X. Xu, X. Chen, Q. Liang, X. Bian, L. Yang, X. Jing, Biodegradable electrospun fibers for drug delivery, J. Control. Release 92 (3) (2003) 227–231, https://doi.org/10.1016/S0168-3659(03)00372-9.
[36] A.L. Clark, The critical state of pure fluids, Chem. Rev. 23 (1) (1938) 1–5.
[37] R. James, R.N.M. Deam, Interfacial tension in hydrocarbon systems, J. Chem. Eng. Data 15 (2) (1970) 216–222.
[38] C.J. Buchko, L.C. Chen, Y. Shen, D.C. Martin, Processing and microstructural characterization of porous biocompatibleprotein polymer thin films, Polymer 40 (1999) 7397–7407.

[39] T. Jarusuwannapoom, W. Hongrojjanawiwat, S. Jitjaicham, L. Wannatong, M. Nithitanakul, C. Pattamaprom, P. Supaphol, Effect of solvents on electro-spinnability of polystyrene solutions and morphological appearance of resulting electrospun polystyrene fibers, Eur. Polym. J. 41 (3) (2005) 409–421, https://doi.org/10.1016/j.eurpolymj.2004.10.010.
[40] W.K. Son, J.H. Youk, T.S. Lee, W.H. Park, Electrospinning of ultrafine cellulose acetate fibers: studies of a new solvent system and deacetylation of ultrafine cellulose acetate fibers, J. Polym. Sci. B Polym. Phys. 42 (1) (2004) 5–11.
[41] K.H. Leea, H.Y. Kim, M.S. Khilb, Y.M. Rab, D.R. Lee, Characterization of nano-structured poly(1-caprolactone) nonwoven mats via electrospinning, Polymer 44 (2003) 1287–1294.
[42] M.M. Demir, I. Yilgor, E. Yilgor, B. Erman, Electrospinning of polyurethane fibers, Polymer 43 (11) (2002) 3303–3309, https://doi.org/10.1016/S0032-3861(02)00136-2.
[43] G. Taylor, Disintegration of water drops in an electric field, Proc. R. Soc. Lond. Ser. A Math. Phys. Sci. 280 (1382) (1964) 383–397.
[44] J.M. Deitzel, J. Kleinmeyer, D. Harris, N.C. Beck Tan, The effect of processing variables on the morphology of electrospun nanofibers and textiles, Polymer 42 (1) (2001) 261–272, https://doi.org/10.1016/S0032-3861(00)00250-0.
[45] X. Yuan, Y. Zhang, C. Dong, J. Sheng, Morphology of ultrafine polysulfone fibers prepared by electrospinning, Polym. Int. 53 (11) (2004) 1704–1710.
[46] R. Kessick, J. Fenn, G. Tepper, The use of AC potentials in electrospraying and electrospinning processes, Polymer 45 (9) (2004) 2981–2984, https://doi.org/10.1016/j.polymer.2004.02.056.
[47] H. Liu, Y.-.L. Hsieh, Surface methacrylation and graft copolymerization of ultrafine cellulose fibers, J. Polym. Sci. B Polym. Phys. 41 (9) (2003) 953–964.
[48] X.M. Mo, C.Y. Xu, M. Kotaki, S. Ramakrishna, Electrospun P(LLA-CL) nanofiber: a biomimetic extracellular matrix for smooth muscle cell and endothelial cell proliferation, Biomaterials 25 (10) (2004) 1883–1890, https://doi.org/10.1016/j.biomaterials.2003.08.042.
[49] C.J. Buchko, L.C. Chen, Y. Shen, D.C. Martin, Processing and microstructural characterization of porous biocompatible protein polymer thin films, Polymer 40 (26) (1999) 7397–7407, https://doi.org/10.1016/S0032-3861(98)00866-0.
[50] M.T.M. Pendergast, E.M.V. Hoek, A review of water treatment membrane nanotechnologies, Energy Dyn. Artic. Links Environ. Sci. 4 (2011) 1946–1947, https://doi.org/10.1039/c0ee00541j.
[51] M. Wasim, A. Sabir, M. Shafiq, A. Islam, M. Azam, T. Jamil, Mixed matrix membranes: two step process modified with electrospun (carboxy methylcellulose sodium salt/sepiolite) fibers for nanofiltration, J. Ind. Eng. Chem. 50 (2017) 172–182, https://doi.org/10.1016/j.jiec.2017.02.011.
[52] M. Elbahri, S. Homaeigohar, Nanocomposite electrospun nanofiber membranes for environmental remediation, Materials 7 (4) (2014) 1017–1045, https://doi.org/10.3390/ma7021017.
[53] A.A.M. Lima, S.R. Moore, M.S. Barboza Jr., A.M. Soares, M.A. Schleupner, R.D. Newman, C.L. Sears, J. P. Nataro, D.P. Fedorko, T. Wuhib, J.B. Schorling, R.L. Guerrant, Persistent diarrhea signals a critical period of increased diarrhea burdens and nutritional shortfalls: a prospective cohort study among children in northeastern Brazil, J. Infect. Dis. 181 (5) (2000) 1643–1651.
[54] M. Wasim, A. Sabir, M. Shafiq, A. Islam, T. Jamil, Preparation and characterization of composite membrane via layer by layer assembly for desalination, Appl. Surf. Sci. 396 (2017) 259–268, https://doi.org/10.1016/j.apsusc.2016.10.098.
[55] A.A. Shutov, Composite fluoroplastic fibrous filtration membranes, Tech. Phys. Lett. 31 (12) (2005) 1026–1028.
[56] M. Wasim, S. Sagar, A. Sabir, M. Shafiq, T. Jamil, Decoration of open pore network in polyvinylidene fluoride/MWCNTs with chitosan for the removal of reactive orange 16 dye, Carbohydr. Polymers 174 (2017) 474–483, https://doi.org/10.1016/j.carbpol.2017.06.086.

[57] A.E. Ghaly, A. Snow, B.E. Faber, Effective coagulation technology for treatment of grease filter washwater, Am. J. Environ. Sci. 3 (1) (2007) 19–29.
[58] K. Konieczny, M. Rajca, M. Bodzek, A. Kwiecińska, Water treatment using hybrid method of coagulation and low-pressure membrane filtration, Environ. Prot. Eng. 35 (2009) 5–22.
[59] K. Yoon, B.S. Hsiao, B. Chu, Functional nanofibers for environmental applications, J. Mater. Chem. 18 (44) (2008) 5326–5334.
[60] V. Thavasi, G. Singh, S. Ramakrishna, Electrospun nanofibers in energy and environmental applications, Energy Environ. Sci. 1 (2) (2008) 205–221.
[61] C.S. Ki, E.H. Gang, I.C. Um, Y.H. Park, Nanofibrous membrane of wool keratose/silk fibroin blend for heavy metal ion adsorption, J. Membr. Sci. 302 (1) (2007) 20–26, https://doi.org/10.1016/j.memsci.2007.06.003.
[62] S. Kaur, M. Kotaki, Z. Ma, R. Gopal, S. Ramakrishna, S.C. Ng, Oligosaccharide functionalized nanofibrous membrane, Int. J. Nanosci. 5 (2006) 1–11.
[63] N.L. Lala, R. Ramaseshan, L. Bojun, S. Sundarrajan, R.S. Barhate, Y.-j. Liu, R. Seeram, Fabrication of nanofibers with antimicrobial functionality used as filters: protection against bacterial contaminants, Bitechnol. Eng. 97 (6) (2007) 1357–1365.
[64] S. Kaur, Z. Ma, R. Gopal, G. Singh, S. Ramakrishna, T. Matsuura, Plasma-induced graft copolymerization of poly(methacrylic acid) on electrospun poly(vinylidene fluoride) nanofiber membrane, Langmuir 23 (26) (2007) 13085–13092.
[65] X. Wang, X. Chen, K. Yoon, D. Fang, B.S. Hsiao, B. Chu, High flux filtration medium based on nanofibrous substrate with hydrophilic Nanocomposite coating, Environ. Sci. Technol. 39 (19) (2005) 7684–7691.
[66] J. Doshi, D.H. Reneker, Electrospinning process and applications of electrospun fibers, J. Electrost. 35 (2) (1995) 151–160, https://doi.org/10.1016/0304-3886(95)00041-8.
[67] J.-s. Kim, D.H. Reneker, Mechanical properties of composites using ultrafine electrospun fibers, Polym. Compos. 20 (1) (1999) 124–131.
[68] D.H. Reneker, A.L. Yarin, H. Fong, S. Koombhongse, Bending instability of electrically charged liquid jets of polymer solutions in electrospinning, J. Appl. Phys. 87 (9) (2000).
[69] S. Ramakrishna, K. Fujihara, W.-E. Teo, T. Yong, Z. Ma, R. Ramaseshan, Electrospun nanofibers: solving global issues, Materials Today 9 (3) (2006) 40–50, https://doi.org/10.1016/S1369-7021(06)71389-X.
[70] L.A. Smith, P.X. Ma, Nano-fibrous scaffolds for tissue engineering, Colloids Surf. B Biointerfaces 39 (3) (2004) 125–131, https://doi.org/10.1016/j.colsurfb.2003.12.004.
[71] J.D. Stitzel, P. K, G.E. Wnek, D.G. Simpson, G.L. Bowlin, Arterial smooth muscle cell proliferation on a novel biomimicking, biodegradable vascular graft scaffold, J. Biomater. Appl. 16 (1) (2001) 22–23.
[72] N. Kattamuri, J.H. Shin, B. Kang, C.G. Lee, J.K. Lee, C. Sung, Development and surface characterization of positively charged filters, J. Mater. Sci. 40 (17) (2005) 4531–4539.
[73] R. Langer, J.P. Vacanti, Tissue engineering, Science 260 (5110) (1993) 920–926.
[74] R.M. Nerem, A. Sambanis, Tissue engineering: from biology to biological substitutes, Tissue Eng. 1 (1) (1995) 3–13.
[75] F.J. O'Brien, Biomaterials & scaffolds for tissue engineering, Mater. Today 14 (3) (2011) 88–95, https://doi.org/10.1016/S1369-7021(11)70058-X.
[76] A.V. Bacheva, O.V. Baibak, A.V. Belyaeva, E.S. Oksenoit, T.I. Velichko, E.N. Lysogorskaya, A. K. Gladilin, V.I. Lozinsky, I.Y. Filippova, Activity and stability of native and modified subtilisins in various media, Biochemistry 68 (11) (2003) 1261–1266.
[77] H. Jia, G. Zhu, B. Vugrinovich, W. Kataphinan, D.H. Reneker, P. Wang, Enzyme-carrying polymeric nanofibers prepared via electrospinning for use as unique biocatalysts, Biotechnol. Prog. 18 (5) (2002) 1027–1032.
[78] J. Xie, Y.-L. Hsieh, Ultra-high surface fibrous membranes from electrospinning of natural proteins: casein and lipase enzyme, J. Mater. Sci. 38 (10) (2003) 2125–2133.

[79] S. Onal, A. Telefoncu, Preparation and properties of β-galactosidase chemically attached to activated chitin, Artif. Cells Blood Substit. Immobilization Biotechnol. 31 (3) (2003) 339–355.
[80] Y.M. Yang, J.W. Wang, R.X. Tan, Immobilization of glucose oxidase on chitosan–SiO_2 gel, Enzyme Microb. Technol. 34 (2) (2004) 126–131, https://doi.org/10.1016/j.enzmictec.2003.09.007.
[81] P. Ye, Z.-K. Xu, A.-F. Che, J. Wu, P. Seta, Chitosan-tethered poly(acrylonitrile-co-maleic acid) hollow fiber membrane for lipase immobilization, Biomaterials 26 (32) (2005) 6394–6403, https://doi.org/10.1016/j.biomaterials.2005.04.019.
[82] C.-F. Huang, F.-C. Chang, Comparison of hydrogen bonding interaction between PMMA/PMAA blends and PMMA-co-PMAA copolymers, Polymer 44 (10) (2003) 2965–2974, https://doi.org/10.1016/S0032-3861(03)00188-5.
[83] D.P. Daniel Figeys, Lab-on-a-chip: a revolution in biological and medical sciences—a look at some of the basic concepts and novel components used to construct prototype devices, Anal. Chem. 72 (2000) 330A–335A.
[84] Z. Sun, E. Zussman, A.L. Yarin, J.H. Wendorff, A. Greiner, Compound core–shell polymer nanofibers by co-electrospinning, Adv. Mater. 15 (22) (2003) 1929–1932.
[85] E. Zussman, A. Theron, A.L. Yarin, Formation of nanofiber crossbars in electrospinning, Appl. Phys. Lett. 82 (6) (2003) 973.
[86] J.-H. He, Y.-Q. Wan, J.-Y. Yu, Scaling law in electrospinning: relationship between electric current and solution flow rate, Polymer 46 (8) (2005) 2799–2801, https://doi.org/10.1016/j.polymer.2005.01.065.

CHAPTER

CARBON NANOTUBE-BASED MEMBRANES FOR WATER PURIFICATION

12

Jieun Lee

School of Chemical and Biomolecular Engineering, The University of Sydney, Sydney, NSW, Australia

1 INTRODUCTION

Since researchers introduced new fabrication processes such as interfacial polymerization, multilayer composite casting, and various types of coating techniques, the membrane fabrication process has developed from a lab scale to an industry-scale process [1,2]. However, its energy intensiveness and performance decline due to membrane fouling increases operational costs through consequences such as frequent membrane cleaning, shortening the membrane life cycle and eventually, requiring its frequent replacement.

Attempting to overcome the challenges of conventional polymeric membranes stimulated the incorporation of nanomaterials into polymers [3]. Of nanomaterials, carbon nanotubes (CNTs) have several characteristics favorable to advancing the membrane fabrication process. CNTs are made of graphene sheets rolled into cylinders on a nanometer scale. Due to their hydrophobic channels (which present low friction to water molecules), CNT channels led to a slip length several orders of magnitude higher than that of polymeric UF/NF membranes. Their excellent adsorption capacity, driven by hydrophobicity (π-π interaction between bulk π system on CNTs and organic molecules with C═C bonds), and ease of chemical functionalization is another benefit to removal of organic/heavy metal pollutants in water treatment.

These unique and efficacious properties of CNTs inspired research focused on development of CNT-based membranes for advancing the membrane-production process. CNT membranes can be designed through three types of fabrication on the basis of the CNTs' alignment within the membrane matrix: (i) vertically aligned CNT (VACNTs) membranes via chemical vapor deposition (CVD) and polymer infiltration, (ii) horizontally aligned CNT (HACNTs) membranes via vacuum infiltration, and (iii) CNT mixed-matrix membranes via incorporation of CNTs into polymer matrices prior to phase inversion and/or interfacial polymerization [4]. The VACNT, HACNT, and CNT mixed-matrix membranes exhibited dramatically increased water permeability, high removal efficiency, high flux recovery, and potential for fouling resistance in electrochemical defouling systems. In particular, the CNT mixed-matrix membrane's enhanced performance was achieved by designing multifunctional properties of the CNT material in the polymer matrix based on the specific water treatment concept [5].

Nanoscale Materials in Water Purification. https://doi.org/10.1016/B978-0-12-813926-4.00017-3

Despite their contribution to the development of polymeric membranes, several drawbacks limit these materials' application to the industrial field. VACNT membranes' dramatically high water permeability remains uncertain to large sizes of membrane. Its scale-up for industrial application would be extremely difficult at the current stage. Further, to our knowledge, there has been no report of complete NaCl removal using VACNT membranes that is comparable to the current RO system. In addition, their high adsorption capacity often causes severe fouling issues. Thus, research has focused on developing a defouling system with fouling-resistant, CNT-based membranes using their unique properties, such as electrical conductivity.

This chapter discusses current progress and challenges in CNT-based membranes and assesses their applicability to industry. First, it introduces CNT properties and their potential for water treatment, and systematically summarizes their fabrication and performance evaluation. For in-depth understanding of their high performance, we will discuss CNTs' effects on the physicochemical properties of membranes which govern membrane permeability, removal efficiency, and fouling propensity. Further, it assesses their applicability to industry and compares their performance to commercial membranes, and finally, suggests solutions for current challenges and future study.

2 CARBON NANOTUBES IN WATER TREATMENT

2.1 CNTs MATERIAL

Carbon nanotubes are micrometer-scale graphene sheets rolled into cylinders of nanoscale diameter and capped with spherical fullerene. Delocalized π-electrons in the *z*-axis give CNTs a unique electrical property. CNTs are classified into three groups according to their wall number: single-wall CNTs, double-wall CNTs, and multiwall CNTs. Multiwall CNTs (MWCNTs) are multilayers of rolled graphene sheets, while single wall CNTs (SWCNTs) are a cylinder made of a single graphene sheet. CNTs are tightly aggregated in nature by the van der Waals force between CNTs and the weak interplanar interactions of the graphene sheets (highly polarized π-electron clouds in CNTs). For this reason, the size, shape, and surface area of CNT nanomaterials are governed by their aggregation and solvent chemistry. Thus, overcoming aggregation plays a critical role in the application of carbon-based nanomaterials to the production of membranes for water treatment [6]. CNTs are intrinsically hydrophobic and electrically conductive and have large surface area compared to other carbon materials such as graphite and fullerene, as shown in Table 1.

Table 1 Physical Properties of Carbon Materials [7]

Property	Carbon Materials				
	Graphite	**Diamond**	**Fullerene**	**SWCNTs**	**MWCNTs**
Specific gravity (g/cm^3)	1.9–2.3	3.5	1.7	0.8	1.8
Electrical conductivity (S/cm)	4000^{p}, 3.3^{c}	10^{-2}–10^{-15}	10^{-5}	10^{2}–10^{6}	10^{3}–10^{5}
Electron mobility ($cm^2/(Vs)$)	2.0×10^4	1800	0.5–6	$\sim 10^5$	10^{4}–10^{5}
Thermal conductivity (W/(m K))	198^{p}, 2.2^{c}	900–2320	0.4	6000	2000

p, *in-plane;* c, *c-axis.*

2.2 CNTs AS AN ADSORBENT

CNTs are excellent adsorbents for organic/inorganic contaminants in the environment due to their highly porous hollow structure and high specific area, as compared to traditional adsorbents such as activated carbon [8]. The heavy metal adsorption mechanism of CNTs is chemical interaction with oxygen functional groups on the surface of CNTs [9]. Additionally, CNTs have high adsorption efficiency for organic contaminants such as polycyclic aromatic carbons, dioxin, and benzene, etc.

2.3 RECENT DEVELOPMENT OF CNTs COMPOSITE MEMBRANES

Research has focused on the incorporation of CNTs, with their high adsorption capacity, into polymeric membrane in order to enhance membrane performance by increasing their removal efficiency. However, nanomaterials such as CNTs tend to aggregate due to their strong van der Waals force. There has been progress in CNT composite membranes since the development of various kinds of CNT functionalization for enhanced CNT dispersion into polymer matrices [10,11]. These new functionalization strategies strengthened their high adsorption capacity for organic pollutants and heavy metals within the polymeric matrix. Besides their excellent adsorption capacity, well-dispersed CNTs used as nanofillers enable tuning of polymeric membranes' physicochemical properties, such as pore size, porosity, hydrophilicity, and surface charge, which are key factors for enhancing water permeability and selectivity [12,13]. Progress in CNT composite membranes contributed to their outperforming both pressure-driven membrane processes (such as Microfiltration [MF], Ultrafiltration [UF], Nanofiltration [NF], and Reverse Osmosis [RO]) and Membrane Distillation (MD) by controlling key factors in the fabrication process [14,15].

3 WATER TRANSPORT THROUGH CNT HOLLOW TUBES

CNTs were reported to have 4 to 5 orders of magnitude faster water flux (with 7-nm diameter) than conventional fluid [16]. In the early stages, research on CNTs was focused on theoretical studies of water transport through the CNTs' channels. It is an important step to understand such ultrafast water flux in CNT channels, which is attributed to the CNTs' slippage effect driven by their hydrophobic channels. The atomic-scale smoothness of the CNT wall generates low friction, resulting in single-file water structure within CNT channels. CNTs' large slip length can be explained by their narrow pore diameter, reduced viscosity, and hydrophobicity. Holt et al. examined slip length of CNTs and polymeric membranes using molecular dynamic simulation [6]. The significantly higher slip length in CNT channels (<1400 nm) is due to their relatively smaller pore diameter (1.3–2.0 nm), as compared to their pore length (a 15-nm diameter polycarbonate membrane has only 5.1 nm of slip length). Besides its narrow diameter, the frictionless surface of the CNT wall made fluid velocity inside the CNT channels high [16]. The results demonstrated that flow velocity increased with more hydrophilic fluid, while slip length decreased as solvents became more hydrophobic. This indicates stronger interaction with the CNT walls. Last, due to the hydrophobicity of the CNT walls, the attraction between water molecules inside CNT channels becomes greater than that between hydrophobic solids (CNTs wall) and water molecules.

4 FABRICATION AND FUNCTIONALIZATION OF CNTs MEMBRANES FOR WATER PURIFICATION

4.1 HORIZONTALLY ALIGNED CNTs MEMBRANES (BUCKY PAPER)

HACNT membranes are formed by randomly arranged CNT structures, as shown in Fig. 1A. It is fabricated by (i) CNT functionalization for uniform CNT dispersion, and (ii) vacuum filtration of CNT ethanol dispersion for proper membrane structure. These homogenously dispersed CNTs on the filter (CA membrane, GF/C filter, etc.) are oven-dried to remove solvents and moisture from the films, and to detach the films from the substrate (the whole size of the membrane shown in Fig. 1B, and its thickness by SEM image in Fig. 1C) [19–21].The diameter and thickness of the HACNT membrane is controlled by the scale of vacuum infiltration device. Its pore size and porosity are determined by the arrangement and fabrication procedure. Its size varies from a few nanometers to micrometers. Due to its array structure, HACNT membranes are microporous and display high adsorption capacity. However, their poor mechanical strength compared to CNT composite membranes may hinder HACNT membranes' application to the high-pressure-driven membrane process.

4.2 VERTICALLY ALIGNED CNT MEMBRANES

Vertically aligned CNT (VACNT) membranes facilitate carbon nanotubes as water transport channels. Fig. 2 shows a photo of a VACNT membrane and the structure of a synthesized VACNT's array in microscale. VACNT membranes are fabricated in three steps: First, the VACNT array is synthesized through chemical vapor deposition [24–26]. CNTs' morphology (length, diameter, alignment, etc.) is dependent on temperature, operating pressure, the choice of metallic catalyst, concentration of hydrocarbon, reaction time, and the nature of support (substrate) [25,27]. Ethylene [C_2H_4(g)] reacted with ferrocene [$Fe(C_5H_5)_2$] as a catalyst precursor is decomposed with Fe by heating. CNTs grow on silicon wafers coated with Al in the furnace. Here, Al acts as a template for the CNTs' growth. CNTs' pore diameter can be controlled by either modulating the feed rate of the catalyst precursor and/or selecting a different catalyst (Al, Cu, Pd, Pt, and Ni, etc.) coated on the substrate. Second, the VACNT array on the

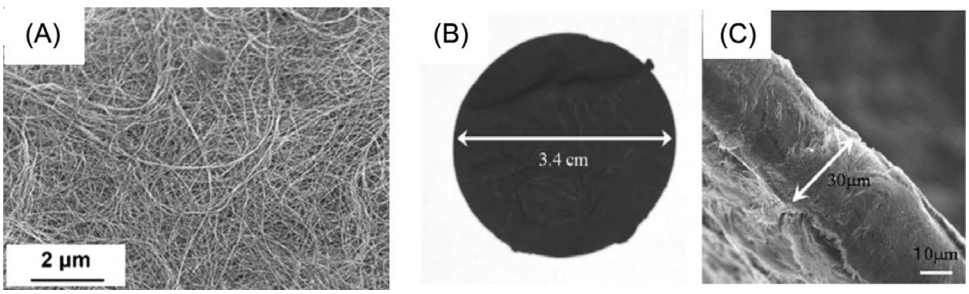

FIG. 1

(A) SEM top-down view of Bucky paper [17], (B) photograph of DWNT-derived Bucky paper, and (C) SEM cross view [18].

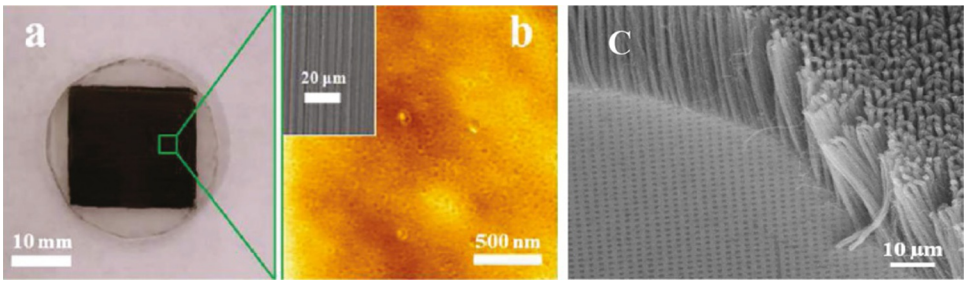

FIG. 2

(A) Photograph of a VACNT membrane [22], (B) SEM top view [22], and (C) SEM images of VACNT array [23].

substrate is infiltrated with low-viscosity fillers such as epoxy [28], polystyrene [29], and/or parlyene [30] in order to keep the membrane's structure without destroying its array. Fig. 3 illustrates the fabrication procedure for VACNT membranes. Gaps between the VACNT's array are filled under vacuum pressure so the water molecule can pass through the CNT channels. After gap infiltration, a Si substrate is removed by NaOH etching. Eventually, the tip of the CNT is opened by mechanical polishing, microtome, ion etching, and/or plasma etching. However, the VACNT membrane requires high pressure to introduce water molecules into the nanochannel due to its hydrophobicity. In Hinds' group, an H_2O plasma-enhanced oxidation process was used to open the tip of the VACNTs' arrays, making the CNT entrance hydrophilic by attaching a carboxylic group on the CNT's tip [29].

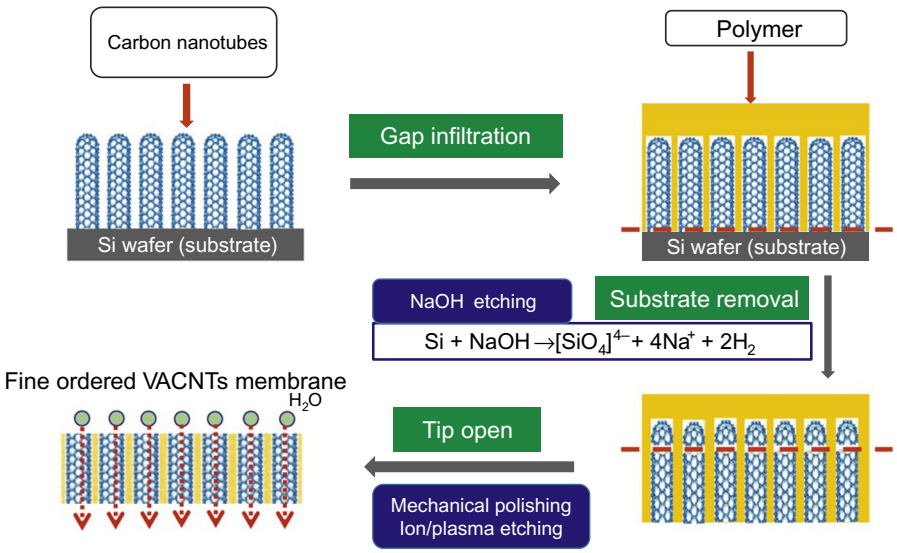

FIG. 3

Fabrication procedure for VACNT membranes [4].

4.3 CNT MIXED-MATRIX MEMBRANES

Rather than facilitating CNTs to membrane structures (such as HACNTs and VACNTs membranes), here, CNTs are incorporated into the polymer matrix. CNT mixed-matrix membranes are intended for enhancing polymeric membranes' separation performance. The incorporation of CNTs as inorganic fillers enables alteration of the physicochemical properties of polymeric membranes, significantly contributing to permeability, rejection efficiency, and fouling [13]. The vertical structure of pores is asymmetrical, as shown in Fig. 4A (nanometer range of pore diameter on top [Fig. 4B] and micrometer range of pores in the sublayer [Fig. 4C]). Fabrication of CNT mixed-matrix membranes for NF/RO filtration is relatively easy, compared to VACNT membranes. The procedure is divided into two steps: (i) preparation of MF/UF membrane as a support layer, and (ii) formation of polyamide layer as a selective layer. Fig. 5 illustrates the whole CNTs/PA composite membrane procedure. In the first step, a UF membrane support layer is prepared by phase inversion. Its pore size, surface porosity, and thickness (which affects the permeate flux of NF/RO membranes) are controlled during the phase inversion step. The second step is the formation of a selective PA thin film layer via interfacial polymerization. The water-soluble monomer, m-phenylene diamine (MPD), and the organic solvent-soluble monomer, trimesolychloride (TMC), react at a water/organic solvent interface, forming a polyamide layer (<1 nm pore size) on top of the porous support layer (PES or PSf UF membrane) [34,35]. Despite its high selectivity to NaCl, PA layer results in low permeate flux. Further, PA is vulnerable to degradation of its amide group by free chlorine, Cl_2. Several research projects focused on the incorporation of modified CNTs into (i) the support layer (Fig. 5A) and (ii) the PA selective layer (Fig. 5B), and (iii) in-between the support and PA selective layer (Fig. 5C) in order to enhance the permeate flux [32,33,36]. More specifically, CNTs are mixed into the aqueous MPD solution (the support layer) or organic TMC/hexane solution (in the PA selective layer) for the purpose of the enhanced permeability, durability, and chemical resistance [37–40]. Additionally, CNTs can be incorporated in between the selective PA thin film layer and PSf support layer. Wu et al. reported that a CNT interlayer can improve PA polymerization efficiency by adsorbing and storing amino monomer solution [41].

4.4 FUNCTIONALIZATION OF CNTs MEMBRANES

As explained in Sections 2 and 3, CNTs convey ultrafast water transport within their channels due to their intrinsic hydrophobicity. However, CNTs with van der Waals force agglomerate in polymer matrices, hindering their wide application to nanocomposite membranes. For the purpose of CNT

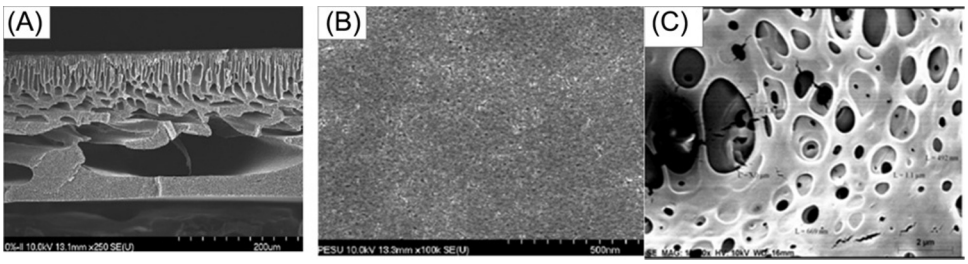

FIG. 4

Morphology of (A) cross-sectional, (B) top view [31], and (C) bottom images of the CNTs composite membrane.

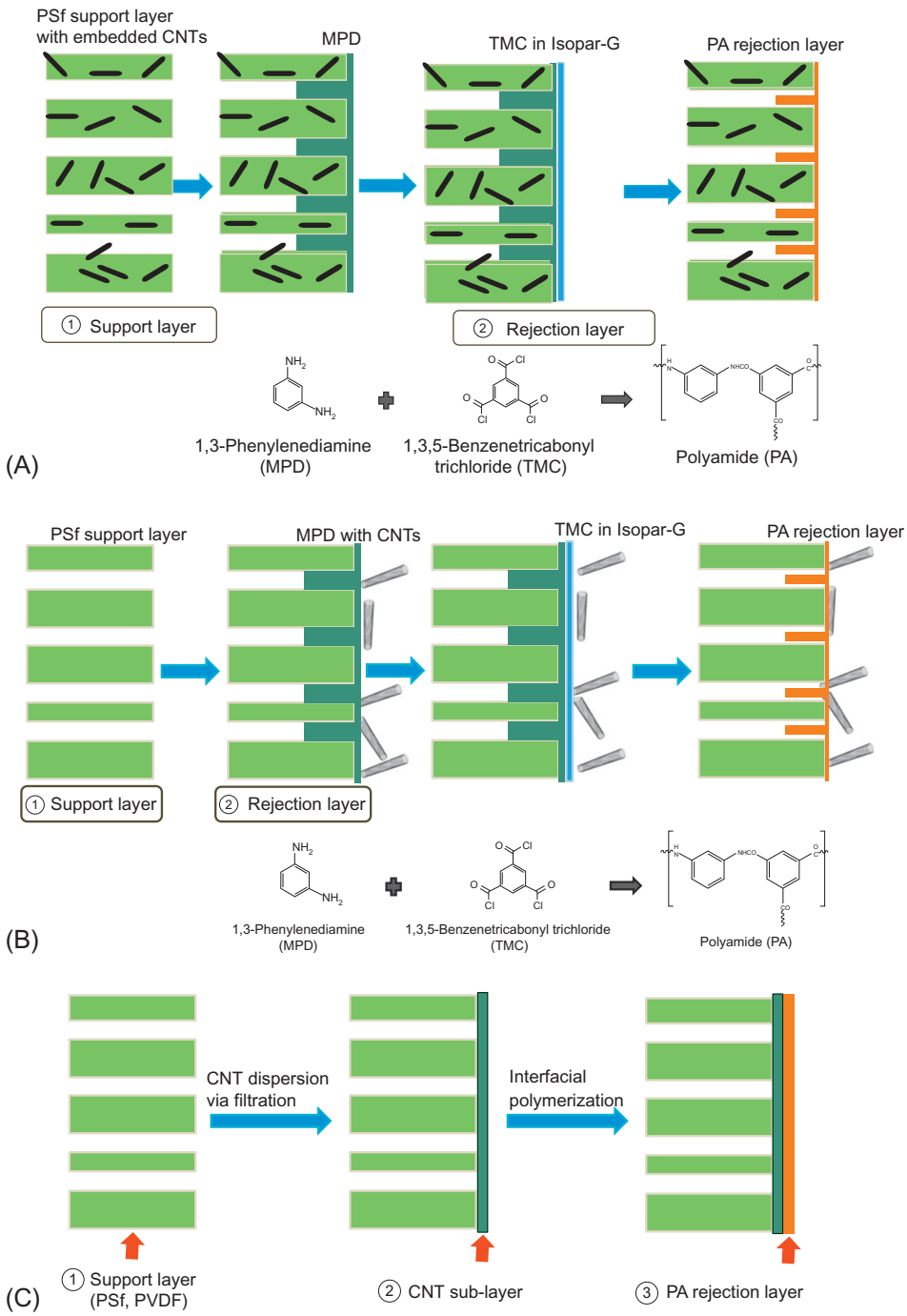

FIG. 5

Schematic CNT composite membranes procedure in (A) CNTs/PES(or PSf) UF membrane via phase inversion, (B) CNTs/PA RO membrane via interfacial polymerization [4], and (C) CNT interlayer between PA thin film and porous support layer [32,33].

dispersion in polymer matrices, various CNT functionalization methods are applied [10]. In addition to CNT dispersion, CNTs can be purified in order to remove amorphous carbon and metal oxide impurities during their synthesis, adding another beneficial side effect: hydrophilic group (OH/COOH) functionalization [42]. Such hydrophilic functional groups enable CNTs to be well-dispersed in polymer matrices due to their affinity for H_2O molecules.

Oxidation by acid treatment. CNTs were reacted with mixed acid (HNO_3/H_2SO_4) at 90–100°C in order to be OH/COOH functionalized via oxidation. Such hydrophilic, modified CNTs contribute to enhanced water permeability and antifouling propensity [43].

Plasma treatment. Plasma treatment attaches OH and COOH groups on CNT surfaces, increasing CNT dispersion and membrane hydrophilicity, further enhancing capacity for adsorption of organic matter and heavy metals. Ar plasma-treated CNTs doped inside hollow-fiber UF membranes exhibited enhanced Zn removal due to the deprotonation of these functional groups on CNTs binding to the cationic metal ions (Zn) [44]. Yang et al. developed the plasma-treated HACNT membrane for water desalination [45]. This membrane exhibited 400 w/w% salt adsorption capacity, which is two orders of magnitude higher than activated-carbon-based systems. Estimating interfacial energy change during salt adsorption demonstrates that the Langmuir adsorption is derived from the high surface energy of plasma-treated CNTs. In particular, 250 g of plasma-treated CNT membranes can treat 100 L of brackish water (10,000 ppm).

Plasma treatment significantly enhances VACNT membranes' water permeability. Due to the intrinsic hydrophobicity of CNTs, VACNT membranes require high operation pressure. Plasma treatment as a post-production treatment opens the CNTs' caps, removing excess polymer filling, leaving OH/COOH groups at the CNT tips. These functional groups induce water molecules into the CNT channels, further increasing water permeability, as illustrated in Fig. 6 [6,29].

Zwitter-ion-functionalized CNTs/PA membranes were developed for water desalination [46]. CNTs were functionalized using zwitter ionic groups which have a positive charge at the tertiary amine group and a negative charge at the carboxylic group. Water flux increased from 6.8 to 28.7 GFD because zwitter ions along the CNT walls and entrance/end create new water transport channels.

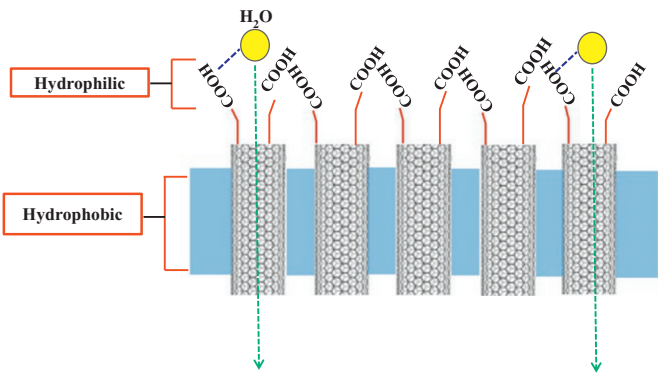

FIG. 6

Schematic of introduction of water molecule to the hydrophilic functionalized CNT channel [4].

Ion rejection increased from 97.6% to 98.6% due to the zwitter ions' enhanced steric hindrance on the CNT gates. In addition, MWCNT-composite UF membranes were modified with quaternary ammonium groups and carboxylate groups introduced onto MWCNTs [47]. MWCNTs were incorporated into the brominated polypropylene oxide (BPPO) matrix using the crosslinking agent triehanolamine (TEOA). These zwitter ionic groups increased water permeability and dispersion of CNTs into the polymer matrix. This enhanced permeability was due to the increase in exchange between solvent-nonsolvent through strong interaction between the hydrophilic casting solution and nonsolvent (water), further leading to the increase in pore size. Good dispersion of CNTs was attributible to the increased hydrophilicity of MWCNTs through zwitter ionic groups.
Amine-functionalized CNTs/PES membranes were modified by two steps: carboxyl functionalization by mixed acid treatment (sulfuric/nitric acid) followed by amine functionalization by reacting with 1,3-phenylenediamine (mPDA) under 70°C [48]. The functionalization of CNTs increased hydrophilicity and decreased surface roughness. This alteration of physicochemical properties contributed to the enhancement in water permeability and total flux loss by total fouling.
Sulfonated CNTs/PA membrane [40]. The purpose of functionalized CNTs with 1,3-propane sultone is to achieve good CNT dispersion in water. Sulfonated CNTs with pendant alkyl sulfonic acid groups were created through nucleophilic ring open reaction. Thes sulfonated CNTs were incorporated into the polyamide selective layer during the interfacial polymerization (IP) process and exhibited 1.6 times increased water permeability compared to the pristine PA membrane. It also demonstrated enhanced BSA fouling alleviation.
ICIC functionalized CNTs/PSf membrane [12]. First, CNTs were COOH/OH functionalized by treating them with sulfuric/nitric acid. Then they reacted with 5-isocyanato-isophthaloyl chloride (ICIC) using a reflux device at 50°C for 48 h under N_2 at atmospheric pressure.
COOH- and PEG-modified CNTs was coated on the PES membrane for NOM fouling alleviation [49]. In the NOM fouling test, COOH- and PEG-modified CNT PES membranes showed enhanced HA flux and total fouling ratio compared to raw CNT membranes due to the decreased surface charge and roughness of the modified membrane.
CNTs/ZnO/TiO_2 membranes were modified by hydrothermal synthesis and acid treatment through ultra-sonication [50]. These functionalized CNT membranes conveyed photocatalytic activity, leading to further enhanced water permeability and potential self-decomposition of contaminants.
Grafting 3-aminopropyltrethoxy-silane (APTES) coupled with dopamine copolymerization [51]. Multi-walled carbon nanotubes (MWCNTs) were functionalized with grafting 3-aminopropyltrethoxy-silane (APTES) in order to make MWCNTs well-dispersed. Next, they were copolymerized with dopamine to improve the adhesion ability of the functionalized MWCNTs to the PVDF membrane. Such modification caused pristine PVDF membranes to be superhydrophilic and superoleophobic underwater. The bio-inspired membrane exhibited high water permeability (900 LMH at 0.9 bar) and high oil/water separation (99%).
Enzyme immobilization on CNT. Biocatalytic CNTs membranes created by enzyme immobilization were applied to the removal of micropollutants [52]. CNTs were laccase immobilized via physical sorption and covalent bonding, contributing to the enhancement of MP removal, compared to CNT membranes without enzyme immobilization. 70% of their original activity after four regeneration cycles was reported.
Conductive polymer-CNTs composite. Synthesis of CNT-conductive polymer nanocomposites exhibited enhanced water permeability and fouling resistance. For example, hydrophilic

polypyrrole (PPY) and polyaniline were coated with CNTs via in-situ oxidative polymerization [53,54]. This nanocomposite made the membrane surface more hydrophilic, and increased pore size and porosity via tuning the membrane structure.

5 FACTORS GOVERNING CNT MEMBRANES' PERFORMANCE

There is a strong correlation between membrane performance (water permeability, rejection efficiency, and membrane fouling propensity) and the physicochemical properties of the membrane. When CNTs are used as nanofillers, their intrinsic properties tend to change the membrane's structure and physicochemical properties during membrane formation via the phase inversion process. CNTs used as nanofillers control pore size, porosity, and membrane structure during the mixing-demixing process in a nonsolvent bath [55]. Further, hydrophilic, functionalized CNTs change membrane structures, making them more dense on the top with a relatively large microstructure sublayer. Pore diameter, porosity, membrane structure, hydrophilicity, surface charge, and surface roughness are important factors affecting water permeability, selectivity of contaminant in feed, and fouling propensity. In addition, CNTs' intrinsic properties such as hydrophobicity, large surface area, and electrical conductivity govern flux and selectivity in water transport and mass transfer, particularly in the VACNT/HACNT membranes and electrochemical defouling systems.

5.1 CNT PROPERTIES

- *Diameter*. VACNT membranes remove salt in NF/RO systems through size exclusion. Thus, CNT diameters play a crucial role in rejecting salt ions. In order to apply VACNT membranes to salt removal (seawater desalination), the ideal internal tube diameter is reported to be <0.59 nm [(7.7) armchair type] above 95% of ion removal [56]. Molecular dynamic simulation reported that the (5, 5) and (6, 6) armchair types of CNTs do not pass through Na^+ and Cl^- ions, indicating that the designed CNT membrane can effectively separate salt from water.
- *Hydrophobicity*. The membrane distillation process happens when water vapor passes through a membrane's channels, driven by vapor pressure difference. Thus, a hydrophobic membrane is required in this system in order to avoid wetting the membrane [57]. In this sense, intrinsically hydrophobic CNT membranes can contribute to 30%–60% of permeability enhancement of membrane distillation (MD) by increasing liquid entry pressure (LEP) and porosity ($>85\%$) [58].
- *Large surface area*. CNTs have a high surface-area-to-volume ratio and they exhibit ease of surface functionalization. Due to the high adsorption capacity and rapid equilibrium rates, CNT adsorbents are superior to traditional sorbents. Their hydrophobicity and capillarity affect adsorption efficiency. By facilitating high adsorption capacity, CNTs have been employed to remove organic and inorganic contaminants, including NOM and heavy metals [59–61]. For example, HACNT membranes remove NOM by an adsorption mechanism: π-π interactions and hydrophobic interaction between bulk π system on CNT surfaces and organic molecules with C═C double bonds or benzene rings [62–64]. Yang et.al, determined that the maximum adsorption capacity of HACNT membranes is 3.34 mg HA/cm^2.g CNTs. Another example is polyhydroxybutyrate-calcium alginate/carboxyl multiwalled, carbon nanotube composite, nanofibrous filtration membranes (PHB-CaAlg/CMWCNTs) [65]. Insertion of MWCNT increased dye adsorption capacity by two-fold, compared to PHB/CAlg

membranes. The adsorption behavior of the composite membrane was surface physical adsorption and was affected by initial concentration and adsorption active sites. The Freundlich model fits to the data more than Langmuir, indicating nonuniform adsorption of the nonmonolayer.

- *Toxicity: Anti-bacterial effect*. Like other nanomaterials, CNTs can inactivate bacteria/viruses by creating reactive oxygen species (ROS). First, CNTs produce free radicals when interacting with viruses. This induces in vitro apoptosis, and peroxidative products deplete cell antioxidants [66]. Such properties were employed in membranes, resulting in an antibacterial effect [67,68].
- *Electrical conductivity*. Inherently electric conductivity of CNTs is employed for fabricating electrically conductive membranes for performance enhancement. In an electrochemical defouling system, electrical potential forces an electron to flow through from the cathode (where nanobubbles are generated) to the anode (where oxidation of organic foulants occurs). Electrically conductive CNT membranes contribute three ways to fouling mitigation: (i) foulant layer removal by electrochemical oxidation, (ii) early developed fouling detection via inserting electrochemical system (electrochemical impedance spectroscopy, EIS) into the filtration set up, and (iii) electrolytic cleaning via generation of nanobubbles [69–71].

  Application of electric fields to the membrane-production process minimizes membrane fouling. CNTs' electrical conductivity can be employed to the electrochemical defouling system to remove foulant layers by oxidizing contaminants. During membrane filtration, contaminants tend to concentrate near the membrane surface and form a concentration boundary layer. This then blocks the transport of fluid across the membrane. Application of an electric field (via DC power) on the membrane surface removes the contaminants from the membrane surface due to the electrophoretic effect. It leads to greater bulk flow through the membrane due to an electro-osmotic effect [72]. Furthermore, adsorbed foulants can be pushed away by the electrophoretic flow of large cations ($Ru\ (Bpy)_3^{2+}$) during defouling process as a membrane cleaning [71].

  To elucidate, electrically conductive CNTs/PA RO membranes were fabricated by interfacial polymerization [73]. Conductive CNTs/PA rejection layer was conveyed to a PES support layer. It exhibited 300 S/cm, which is 20 orders of magnitude greater than PA polymer. Additionally, an applied electrical field of conductive CNTs affected antifouling efficiency by decreasing foulant adsorption. A conductive CNTs/PVDF dual layer membrane was fabricated by covering a CNT filter onto the PVDF casting solution [74]. The conductivity of the dual layer membrane (~105 S/cm) was comparable to that of conductive CNTs paper (~118 S/cm). Under 2 V DC pulsed condition, the transmembrane pressure (TMP) of CNT/PVDF membranes was shown to be lower than the PVDF membrane during three cycles of filtration, indicating that foulant layer was removed from the membrane surface by an applied electrical field.

  Besides having an effect on fouling resistance, the electrochemical property of CNTs can contribute to the removal of trace organic contaminants from industrial/waste water. While conventional treatments such as chemical reduction and NF/RO membranes generate waste sludge and toxic brine, electrochemically conductive CNTs/PVA UF membranes combine electrochemical reduction [Cr(VII) to Cr(III)] with a UF membrane process [removal of $Cr(OH)_3$] [75]. Under the presence of ionic strength, 99% of Cr was removed under the application of 7 V.

  Sandwich-like, three-layer CNT hollow fiber UF membranes fabricated by sequential layer-by-layer coating can switch adsorption and electrochemical oxidation of micropollutants [76]. The adsorption and electrochemical reaction occur between three layers-outer CNT separation layer (cathode), PVDF porous insulator, and inner CNTs support layer (anode). First, outer CNTs adsorb

microcystine-LR (MC-LR) molecules via π-π coupling, hydrogen bond and electrostatic interaction. This is because CNTs have noncovalent interaction between the π system on the CNT's surface and organic molecules with C═C or benzene rings on MC-LR. Furthermore, its structure enables multilayer adsorption to increase its adsorption capacity. In the next step, by applying potential, the adsorbed MC-LR is desorbed from the CNT cathode through the PVDF layer, then decomposed by the inner CNT layer as anode via electrochemical interaction. Elemelech et al. developed conductive carbon nanotube filters for virus removal and inactivation [77]. By applying 2–3 V, LRV increased from 5.8 to 7.4 in the presence of NOM and alginate.

There has been further enhancement of electrochemical reaction in CNT-enhanced membranes for improving selectivity to nanoparticles, heavy metals, pharmaceuticals, endocrine hormones, and foulant degradation [78]. An alternative way of improving electrochemical reaction is an immobilization of metal/nonmetal on CNTs. For example, doping with zero-valent Fe nanoparticles on CNTs via purse voltametric electrodeposition demonstrated an improved removal efficiency (74%→97%) on beta blocker metoprolol (pharmaceutical, present in aquatic environment) at 1 V. This is due to the fact that a Fenton type reaction of the nanostructure of Fe immobilized on CNTs induces oxidative species toward degradation more efficiently [79].

– *Photocatalytic activity*. Hybrid nanomaterials such as CNTs-TiO_2 are employed to complement drawbacks of individual materials. Large bandgap energy (3.2 eV) and rapid recombination of electron holes in TiO_2, low adsorption capacity, and limited response to UV limit a wide application of TiO_2 to photocatalytic degradation of micropollutants in water/wastewater treatment. When CNTs are immobilized with TiO_2, it prevents TiO_2 from rapid recombination of electron via excellent channels of electron transportation. Further, it provides large surface area for adsorption, and expands the light response of TiO_2 to visible light [80]. Such photocatalytically active CNTs-TiO_2 membranes demonstrated high removal efficiency and photocatalytic degradation to acid orange 7 (AO7), methyl orange, ibuprofen, and diethyl phthalate [50,81,82].
– *Thermal conductivity*. CNTs provide Joule heating at the membrane surface. Higher temperature of membrane surface and that of bulk via Joule heating increase the thermal driving force for self-heating membranes [83]. They enhance desalination performance under the highly ionizable environments of saline waters. Thus, if energy efficiency is addressed on a large scale, self-heating, CNT-based membranes would contribute to a wide application of MD for recycling concentrate from desalination plants [84].

5.2 MEMBRANE CHARACTERISTICS AFFECTED BY CNT INCORPORATION

– *Porosity*. Incorporation of CNTs into polymer matrices affects membrane porosity during the mixing-demixing process. Proportion of CNTs increases the viscosity of casting solution, and delays or slows down the mixing-demixing rate. It induces the diffusion rate of organic solvents (NMP, DMF, etc.) and nonsolvents (water), thus, forming denser or porous membrane structures. In several studies, CNT incorporation increased porosity by diffusive tunnels, further contributing to enhanced water permeability [85,86]. Insertion of CNTs into both the support and selective layers of PA thin film composite (TFC) membranes formed nanocorridors and hollows inside the nanochannel between CNTs and PSf polymers due to the incompatibility between CNTs and polymers [87]. This facilitated water transfer through the membrane, resulting in increased water permeability.

- *Pore size*. Insertion of hydrophilic MWCNTs affects the pore size of the membrane [47,88]. This is because during the phase inversion process, hydrophilic MWCNTs increase the exchange rate between solvent and nonsolvent in a coagulation bath. This increased pore diameter increases membrane permeability. By contrast, pore size decreases as MWCNT concentration increases to a certain point. This is mostly due to the increased viscosity and lowered thermodynamic condition of the casting solution. Higher viscosity of casting solution achieved by hydrophilic CNT insertion delays demixing during the phase inversion process, and kinetic hindrance affects the thermodynamic factor, resulting in thermodynamic immiscibility [89].
- *Membrane pore structure*. Insertion of MWCNTs tunes the membrane pore structure to favor water flux. Increased water permeability is attributed to a very dense top skin layer, porous sublayer, and fully developed finger-like macrovoids at the bottom [53,90]. To investigate the effect of the membrane structure as a water channel on water permeability, structure parameter (S value) was obtained from the filtration test. Structure parameter (S) is proportional to the substrate thickness and tortuosity, and inversely proportional to the porosity. This indicates support resistance to diffusion. In this regard, low S means minimized internal concentration polarization (ICP) of the FO membrane, leading to improved water permeability. Insertion of CNTs into the substrate contributed to the reduced S value by enhanced compaction resistance and high porosity [91]. In addition, insertion of a CNT layer changed the surface morphology of the PA TFN membranes in a forward osmosis system [33]. CNTs were formed as a sublayer in between a polyvinylidene fluoride (PVDF) support layer and polyamide (PA) selective layer. Due to its three-dimensional structure, a CNTs/PA/PVDF membrane had changed microstructure underneath a PA active layer. This free-spaced and more effective area in the structure increased water permeability in the active layer in the draw solution mode. Decreased S in the CNT-layered PA/PVDF membrane confirmed that a CNT sublayer alleviates concentration polarization.
- *Hydrophilicity*. Although CNTs are intrinsically hydrophobic, they can be modified by hydrophilic functional groups such as COOH and OH, as explained in Section 4.4. Such functionalization induces hydrophilicity in CNTs, increasing the hydrophilicity of the CNT-based membrane surface. Several studies reported that such hydrophilic, functionalized, CNT mixed-matrix membranes exhibited enhanced permeability and high rejection efficiency, compared to pristine polymer membranes [48,85,92]. Increase in hydrophilicity resulted in BSA fouling resistance (less flux decline than raw CNTs/PA membrane) by decreasing foulant accumulation [43]. CNTs were incorporated into a polyamide (PA) selective layer via diamine aqueous solution of interfacial polymerization.
- *Surface charge of the membrane*. Modified CNTs altered the surface charge of the membrane. For example, insertion of CNTs/PANI complex into a PES matrix changed negatively charged PES membrane into positively charged CNTs/PANI/PES membranes [53]. This significantly increased HA removal efficiency by increasing electrostatic interaction with negatively charged HA. Positively charged, aminated hydrophilic poly(arylene ether sulfone) MWCNTs-COOH UF membranes exhibited antifouling efficiency in positively charged Lys due to an electrostatic repulsion [90]. MWCNTs-NH_2 incorporation into PES and/or PA increased salt rejection in the MWCNTs/PES NF membrane via the Donnan exclusion mechanism [93].
- *Surface roughness*. Surface roughness is related to the water permeability of membranes. Higher surface roughness means more area for membrane transport, resulting in improved permeability [91]. CNT-incorporated PA TFN membranes exhibited higher water permeability than pristine TFC

membranes [87]. This is due to the fact that insertion of CNTs in a PA selective layer increased the surface roughness of the PA layer. In comparison to the positive effect on permeability, surface roughness is inversely correlated to membrane fouling due to the propensity for foulant adsorption on the membrane. Membranes with rough surfaces are more susceptible to membrane fouling than smooth ones [94]. The valley of the rough membrane surface induces foulant accumulation, leading to membrane pore blocking. Well-dispersed nanoparticles such as CNTs in membrane matrices (polymer) lead to smooth membrane surfaces (low roughness).

- *Chlorine tolerance*. Hydroxylated CNT-incorporated PVP/PSf membranes improved chlorine tolerance [95]. Chlorine is found to attack the C═O bond on the pyrrole ring of PVP [96], rendering PVP/PSf membranes vulnerable to chlorine. Therefore, hydrogen bonding between PVP (C═O) or PSf (O═S═O) and carboxylic groups in CNT formed a protective layer from chlorine-reactive sites in PVP.
- *Mechanical strength*. Incorporation of CNTs increases tensile strength of membranes. A research demonstrated that CNT insertion increased 60%–70% of Young's modulus [86].

6 COMPARISON OF CNTs MEMBRANES WITH OTHER COMMERCIALLY AVAILABLE MEMBRANES

Enhancing membranes with CNTs contributes to high water permeability, high removal efficiency, and low operation pressure in the conventional polymeric membranes due to its efficacious properties to water treatment. However, some drawbacks still limit them so that they only outperform the commercially available membranes.

Fabrication procedure. Despite their superior performance, their fabrication procedure needs to be more developed to scale up for further commercialization in water desalination [97]. For example, the CVD method is known for synthesis of VACNT membranes. Although the CVD method brings benefits to VACNT synthesis, this method is time consuming, complicated procedure, and produces too low a total membrane area to scale up, in particular, for large volumes of SWCNTs [98]. This indicates that greatly enhanced performace driven by CNT incorporation at the lab scale might be realized for industrial application if that fabrication in large scale is set up. While development of CNT polymer composite membranes may ease the difficult fabrication of VACNT membranes, such membranes are still limited to controling tunable structure, uniformity of pores, and aspect ratio.

Performance. The peformance of amine-functionalized CNTs/PA NF membranes was compared with commercial PA NF membranes [99]. The prepared CNTs/PA membranes exhibited 3-fold enhanced permeability and less flux decline for 48 h filtration, while its poor NaCl rejection (37%) did not outperform the complete rejection of the commercial PA membrane. However, the CNT composite membrane showed Na_2SO_4 rejection efficiency comparable with that of the commercial one. This high water pemability is due to the fact that insertion of CNTs in NF/RO membrane fabrication process (UF via phase inversion+PA layer via interfacial polymerization) changes physical properties of the NF/RO membrane, such as porosity, structural parameter, and surface roughness, that govern membrane water permeability. Insertion of CNTs forms more water channels between CNTs and polymers (PSf, PA, etc.) due to the incompatiblity between CNTs and

polymers. Such hollows inside the nanochannels facilitates enhanced water transfer through the membranes. Furthermore, for MF/UF membrane fabrication, CNT insertion increases pore size and porosity via delaying/inducing the mixing-demixing process during phase inversion.

Cost effectiveness. CNT-based membranes are reported for limiting the large-scale and long-term operation of the process. The cost of producing freestanding CNT-based membranes with a loading of 2–5 g/m^2 was 75 times higher than that of polymeric membranes [100]. However, due to recent industrial development in CNT synthesis, MWCNTs with 50–80 nm diameter cost \$600–\$700/kg for bulk purchase. This corresponds to \$13–\$15/m^2 at the common surface loading in recent study [101]. Compared with the manufacturing cost of hollow fiber (\$10–\$50/m^2) and flat sheet (\$50–\$100/m^2) membranes, the cost would be feasible to industrial application. In particular, additional operational cost savings will benefit from long lifecycle, low operational pressure, and a simplified process step due to the CNT-enhanced membranes [2].

Energy efficiency. An additional capital cost of CNTs/PVDF membranes is 15%–30% higher than that of commercial PVDF membranes for reducing biofouling. Considering energy savings and energy cost reduction, it will take 1.5 to 5 years to pay back the extra cost [102]. However, recent studies report that electrochemically assisted CNT hollow fiber membranes can save 12%–15% of energy, compared to the conventional MD system, due to it being self-powered (by thermo-electric power generating module from the temperature gradient) [103]. Furthermore, its negatively polarized surface can repel NOM (negatively charged) via electrostatic repulsion, further increasing membrane life. Thus, such advantage will accelerate their commercialization in water desalination if the high cost in their fabrication stage is solved by further development in mass production.

Energy efficiency of the CNT modified membrane is observed in the anion exchange membrane in electron dialysis (ED) [104]. It is notable that the anion exchange membrane is more vulnerable to organic fouling due to its negative charge. Polypropylene membranes mofified with CNTs, sulfonated iron oxide nanoparticles Fe_2O_3-SO_4^{2-} and Poly (2,6-dimethyl-1,4-phenylene oxide) PPO improved fouling resistance by showing a 45%–53% decrease in voltage drop (ΔV) versus time, compared to the commercial polypropylene membrane. Its 59.7%, 57.7%, and 48.5% decreased energy consumption in the first, second, and third cycle indicates that CNT modification may contribute to higher energy efficiency than that of the commercial anion exchange membranes.

7 CURRENT CHALLENGES

Progress in CNT-enhanced membranes led them to outperform relatively low permability and poor rejection efficiency as observed in conventional polymeric membranes. CNT-enhanced membranes exhibited ultra-fast water flux and high selectivity to organic matter due to their high slip lengh (frictionless wall) and chemically functionalizable tips and outer walls. Neverthless, it is questionable that CNT membranes would reproduce their superiority in large-scale and long-term application, and that its high water flux would correspond to savings in operational costs in water treatment [2]. Besides the limits to their practical application, fouling issues driven by high rejection efficiency in CNT-based membranes have yet to be solved completely. For instance, CNT-layered PAN nanofibers fabricated by electrospraying achieved high indigo (dye) rejection efficiency due to the increasing number of sieving steps and adsorption on CNT layers [105]. However, its enhanced dye adsorption capacity resulted in fouling.

As a solution to fouling issues, an electrochemical defouling system employing electrical conductivity of CNTs membrane was developed to oxidize and remove foulants at the surface of the membrane. However, the system encounters high capital cost issues due to its uneconomic power supply, compared to normal membrane filtration, even though it could save operational cost from frequent cleaning and membrane replacement. Nevertheless, development of novel elecrokinetic CNTs materials with high conductivity efficiency would significantly contribute to fouling alleviation, if their material development and operation (DC power application) cost effectivness issues are simultaneously solved. For example, an application of conductive CNTs membranes to an impedence spectroscopy system for detecting fouling at early stages would save operational costs for replacing membranes and CIP if the design of membrane modules and filtration set-up is upgraded to the large scale. Further development in membrane fabrication is required to increase attachment of CNTs on the support layer so as to increase the long-lasting performance.

VACNT membranes. Significantly fast water flux has a lack of repeatibility due to the relatively smaller membrane active area and uncertainty of diameter distribution compared to commercial NF/RO membranes. Furthermore, low ionic selectivty driven by trade-off prevents them from outperforming their competition and being commercialized. Based on their ion rejection mechanisms and size exclusion, one suggestion for improving their selectivity is to synthesize CNTs with 0.59 nm of internal diameter as discussed in Section 5.1. The desirable density for effective ion removal is suggested to be $(6\pm3)\times0^{10}$–2.5×10^{11} [6,29].

HACNT membranes (Bucky papers). HACNT membranes have high permeability due to their high microporosity, high removal efficiency, and inactivation of *E.coli* cells due to their high adsorption capacity and hydrophobicity. However, due to their limited fabrication method, their membrane structure cannot bear high operating pressure, resulting in limited application (low-pressure filtration system, e.g., MF). If we can overcome these membranes' *poor mechanical strength* by developing the fabrication process, they will greatly contribute to MD systems due to their highly microporus structure and hydrophobicity.

CNT composite membranes. Based on their relatively easy fabrication process and potential for scale up, compared to VACNT and HACNT membranes, these composite membranes would likely be highly commercialized. However, CNTs serve the role as nanofillers within polymer matrices, consiquently having drawbacks similar to those of polymeric membranes. Their high water permability and high selectivity are not attributible to the CNTs but to the membranes' physicochemical properties tuned by CNT insertion. Therefore, increasing their concentration and alignment within polymer matrices is imperative for the commercialization of CNT composite membranes for advanced water treatment [106].

8 CONCLUSION

This chapter discusses progress and challenges of CNT-based membranes in water treatment. First, fabrication of three types of CNT-based membranes were introduced systematically. We thoroughly discussed their outperformance caused by CNTs' effect on membrane characteristics that govern membrane flux and selectivity. CNTs' intrinsic properties have contributed dramatically to fast water flux, high removal efficiency (due to their high adsorption capacity), and defouling propensity (driven by

their electrical conductivity). CNTs' role as a nanofiller in polymer matrices result in greatly enhanced water permeability, selectivity enabled by tuning the membrane structure (in particular, increasing pore size and porosity, and creating a dense top layer with fully developed finger-like macrovoids at the bottom), and change in the membranes' surface charge.

Three types of CNT-based membranes have advantages and limits due to their alignment in membrane matrices. VACNT membranes are reported to have ultra-fast water flux due to their frictionless walls, which result in water molecules in hydrophobic channels. However, technical limits on their fabrication, holding their highly oriented vertical structure in polymer matrices, optimal density, and durability of tip functionalization must be resolved in order to obtain repeatible performance and industrial application. HACNT membranes have weak mechanical strength due to the orientation of their membrane structure, despite its high adsorption capacity driven by high surface area. Those VACNT and HACNT membranes would be ideal candidates for MD systems based on their properties—hydrophobicity, high porosity, and membrane structures favoring water vapor transport. In addition, CNT composite membranes contributed to the advancement of polymeric membranes, in particular, by enhancing the membranes' water permeability. While their easy fabrication enables CNT composite membranes to be scaled up for industrial application, we must overcome the tradeoff between permeability selectivity, and fouling. Electrically conductive CNT membranes for electrochemical defouling systems are attractive for dealing with fouling via oxidation and self cleaning (microbubbles). However, their cost effectiveness with regard to material development (high electrical efficiency) and operation (DC power application) is the first consideration for industrial application in defouling systems.

REFERENCES

[1] R.W. Baker, Membrane Technology and Applications, John Wiley & Sons, Ltd, 2005.
[2] K. Goh, H.E. Karahan, L. Wei, T.-H. Bae, A.G. Fane, R. Wang, Y. Chen, Carbon nanomaterials for advancing separation membranes: a strategic perspective, Carbon 109 (2016) 694–710, https://doi.org/10.1016/j.carbon.2016.08.077.
[3] A.G. Fane, R. Wang, M.X. Hu, Synthetic membranes for water purification: status and future, Angew. Chem. Int. Ed. 54 (11) (2015) 3368–3386, https://doi.org/10.1002/anie.201409783.
[4] J. Lee, S. Jeong, Z. Liu, Progress and challenges of carbon nanotube membrane in water treatment, Crit. Rev. Environ. Sci. Technol. 46 (11–12) (2016) 999–1046, https://doi.org/10.1080/10643389.2016.1191894.
[5] R. Li, L. Zhang, P. Wang, Rational design of nanomaterials for water treatment, Nanoscale 7 (41) (2015) 17167–17194, https://doi.org/10.1039/C5NR04870B.
[6] J.K. Holt, H.G. Park, Y. Wang, M. Stadermann, A.B. Artyukhin, C.P. Grigoropoulos, et al., Fast mass transport through sub-2-nanometer carbon nanotubes, Science 312 (5776) (2006) 1034.
[7] P.-C. Ma, N.A. Siddiqui, G. Marom, J.-K. Kim, Dispersion and functionalization of carbon nanotubes for polymer-based nanocomposites: a review, Compos. A: Appl. Sci. Manuf. 41 (10) (2010) 1345–1367, https://doi.org/10.1016/j.compositesa.2010.07.003.
[8] X. Ren, C. Chen, M. Nagatsu, X. Wang, Carbon nanotubes as adsorbents in environmental pollution management: a review, Chem. Eng. J. 170 (2) (2011) 395–410, https://doi.org/10.1016/j.cej.2010.08.045.
[9] C. Lu, H. Chiu, C. Liu, Removal of zinc(II) from aqueous solution by purified carbon nanotubes: kinetics and equilibrium studies, Ind. Eng. Chem. Res. 45 (8) (2006) 2850–2855, https://doi.org/10.1021/ie051206h.
[10] S.W. Kim, T. Kim, Y.S. Kim, H.S. Choi, H.J. Lim, S.J. Yang, C.R. Park, Surface modifications for the effective dispersion of carbon nanotubes in solvents and polymers, Carbon 50 (1) (2012) 3–33, https://doi.org/10.1016/j.carbon.2011.08.011.

[11] Y. Lin, B. Zhou, K.A. Shiral Fernando, P. Liu, L.F. Allard, Y.-P. Sun, Polymeric carbon nanocomposites from carbon nanotubes functionalized with matrix polymer, Macromolecules 36 (19) (2003) 7199–7204, https://doi.org/10.1021/ma0348876.
[12] S. Qiu, L. Wu, X. Pan, L. Zhang, H. Chen, C. Gao, Preparation and properties of functionalized carbon nanotube/PSF blend ultrafiltration membranes, J. Membr. Sci. 342 (1) (2009) 165–172, https://doi.org/10.1016/j.memsci.2009.06.041.
[13] J. Yin, B. Deng, Polymer-matrix nanocomposite membranes for water treatment, J. Membr. Sci. 479 (2015) 256–275, https://doi.org/10.1016/j.memsci.2014.11.019.
[14] P.S. Goh, A.F. Ismail, N. Hilal, Nano-enabled membranes technology: sustainable and revolutionary solutions for membrane desalination? Desalination 380 (2016) 100–104, https://doi.org/10.1016/j.desal.2015.06.002.
[15] S.S. Shenvi, A.M. Isloor, A.F. Ismail, A review on RO membrane technology: developments and challenges, Desalination 368 (2015) 10–26, https://doi.org/10.1016/j.desal.2014.12.042.
[16] M. Majumder, N. Chopra, R. Andrews, B.J. Hinds, Nanoscale hydrodynamics: enhanced flow in carbon nanotubes, Nature 438 (7064) (2005) 44. http://www.nature.com/nature/journal/v438/n7064/suppinfo/438044a_S1.html.
[17] L. Dumée, V. Germain, K. Sears, J. Schütz, N. Finn, M. Duke, et al., Enhanced durability and hydrophobicity of carbon nanotube Bucky paper membranes in membrane distillation, J. Membr. Sci. 376 (1) (2011) 241–246, https://doi.org/10.1016/j.memsci.2011.04.024.
[18] H. Muramatsu, T. Hayashi, Y.A. Kim, D. Shimamoto, Y.J. Kim, K. Tantrakarn, et al., Pore structure and oxidation stability of double-walled carbon nanotube-derived Bucky paper, Chem. Phys. Lett. 414 (4) (2005) 444–448, https://doi.org/10.1016/j.cplett.2005.08.110.
[19] M. Endo, H. Muramatsu, T. Hayashi, Y.A. Kim, M. Terrones, M.S. Dresselhaus, Nanotechnology:/ 'Buckypaper/' from coaxial nanotubes, Nature 433 (7025) (2005) 476. http://www.nature.com/nature/journal/v433/n7025/suppinfo/433476a_S1.html.
[20] L. Hussein, G. Urban, M. Kruger, Fabrication and characterization of buckypaper-based nanostructured electrodes as a novel material for biofuel cell applications, Phys. Chem. Chem. Phys. 13 (13) (2011) 5831–5839, https://doi.org/10.1039/C0CP02254C.
[21] Y.A. Kim, H. Muramatsu, T. Hayashi, M. Endo, M. Terrones, M.S. Dresselhaus, Fabrication of high-purity, double-walled carbon nanotube buckypaper, Chem. Vap. Depos. 12 (6) (2006) 327–330, https://doi.org/10.1002/cvde.200504217.
[22] F. Du, L. Qu, Z. Xia, L. Feng, L. Dai, Membranes of vertically aligned superlong carbon nanotubes, Langmuir 27 (13) (2011) 8437–8443, https://doi.org/10.1021/la200995r.
[23] Y. Dajun, L. Wei, G. Rui, C.P. Wong, D. Suman, The fabrication of vertically aligned and periodically distributed carbon nanotube bundles and periodically porous carbon nanotube films through a combination of laser interference ablation and metal-catalyzed chemical vapor deposition, Nanotechnology 23 (21) (2012) 215303.
[24] A. Barreiro, S. Hampel, M.H. Rümmeli, C. Kramberger, A. Grüneis, K. Biedermann, et al., Thermal decomposition of ferrocene as a method for production of single-walled carbon nanotubes without additional carbon sources, J. Phys. Chem. B 110 (42) (2006) 20973–20977, https://doi.org/10.1021/jp0636571.
[25] J. Prasek, J. Drbohlavova, J. Chomoucka, J. Hubalek, O. Jasek, V. Adam, R. Kizek, Methods for carbon nanotubes synthesis-review, J. Mater. Chem. 21 (40) (2011) 15872–15884, https://doi.org/10.1039/C1JM12254A.
[26] X. Yang, L. Yuan, V.K. Peterson, Y. Yin, A.I. Minett, A.T. Harris, Open-ended aligned carbon nanotube arrays produced using CO2-assisted floating-ferrocene chemical vapor deposition, J. Phys. Chem. C 115 (29) (2011) 14093–14097, https://doi.org/10.1021/jp203469y.
[27] A. Szabó, C. Perri, A. Csató, G. Giordano, D. Vuono, J.B. Nagy, Synthesis methods of carbon nanotubes and related materials, Materials 3 (5) (2010) https://doi.org/10.3390/ma3053092.

[28] Y. Baek, C. Kim, D.K. Seo, T. Kim, J.S. Lee, Y.H. Kim, et al., High performance and antifouling vertically aligned carbon nanotube membrane for water purification, J. Membr. Sci. 460 (2014) 171–177. Suppl C. https://doi.org/10.1016/j.memsci.2014.02.042.
[29] B.J. Hinds, N. Chopra, T. Rantell, R. Andrews, V. Gavalas, L.G. Bachas, Aligned multiwalled carbon nanotube membranes, Science 303 (5654) (2004) 62.
[30] S. Kim, F. Fornasiero, H.G. Park, J.B. In, E. Meshot, G. Giraldo, et al., Fabrication of flexible, aligned carbon nanotube/polymer composite membranes by in-situ polymerization, J. Membr. Sci. 460 (Suppl C) (2014) 91–98, https://doi.org/10.1016/j.memsci.2014.02.016.
[31] E. Celik, H. Park, H. Choi, H. Choi, Carbon nanotube blended polyethersulfone membranes for fouling control in water treatment, Water Res. 45 (1) (2011) 274–282, https://doi.org/10.1016/j.watres.2010.07.060.
[32] X. Song, L. Wang, C.Y. Tang, Z. Wang, C. Gao, Fabrication of carbon nanotubes incorporated double-skinned thin film nanocomposite membranes for enhanced separation performance and antifouling capability in forward osmosis process, Desalination 369 (2015) 1–9, https://doi.org/10.1016/j.desal.2015.04.020.
[33] X. Zhao, J. Li, C. Liu, A novel TFC-type FO membrane with inserted sublayer of carbon nanotube networks exhibiting the improved separation performance, Desalination 413 (2017) 176–183, https://doi.org/10.1016/j.desal.2017.03.021.
[34] M. Paul, S.D. Jons, Chemistry and fabrication of polymeric nanofiltration membranes: a review, Polymer 103 (2016) 417–456, https://doi.org/10.1016/j.polymer.2016.07.085.
[35] N.Y. Yip, A. Tiraferri, W.A. Phillip, J.D. Schiffman, M. Elimelech, High performance thin-film composite forward osmosis membrane, Environ. Sci. Technol. 44 (10) (2010) 3812–3818, https://doi.org/10.1021/es1002555.
[36] L. Dumée, J. Lee, K. Sears, B. Tardy, M. Duke, S. Gray, Fabrication of thin film composite poly(amide)-carbon-nanotube supported membranes for enhanced performance in osmotically driven desalination systems, J. Membr. Sci. 427 (2013) 422–430. Suppl C. https://doi.org/10.1016/j.memsci.2012.09.026.
[37] G.N.B. Baroña, J. Lim, M. Choi, B. Jung, Interfacial polymerization of polyamide-aluminosilicate SWNT nanocomposite membranes for reverse osmosis, Desalination 325 (2013) 138–147, https://doi.org/10.1016/j.desal.2013.06.026.
[38] H.J. Kim, K. Choi, Y. Baek, D.-G. Kim, J. Shim, J. Yoon, J.-C. Lee, High-performance reverse osmosis CNT/polyamide nanocomposite membrane by controlled interfacial interactions, ACS Appl. Mater. Interfaces 6 (4) (2014) 2819–2829, https://doi.org/10.1021/am405398f.
[39] H. Wu, B. Tang, P. Wu, MWNTs/polyester thin film nanocomposite membrane: an approach to overcome the trade-off effect between permeability and selectivity, J. Phys. Chem. C 114 (39) (2010) 16395–16400, https://doi.org/10.1021/jp107280m.
[40] J. Zheng, M. Li, K. Yu, J. Hu, X. Zhang, L. Wang, Sulfonated multiwall carbon nanotubes assisted thin-film nanocomposite membrane with enhanced water flux and anti-fouling property, J. Membr. Sci. 524 (2017) 344–353, https://doi.org/10.1016/j.memsci.2016.11.032.
[41] M.-B. Wu, Y. Lv, H.-C. Yang, L.-F. Liu, X. Zhang, Z.-K. Xu, Thin film composite membranes combining carbon nanotube intermediate layer and microfiltration support for high nanofiltration performances, J. Membr. Sci. 515 (2016) 238–244, https://doi.org/10.1016/j.memsci.2016.05.056.
[42] V. Datsyuk, M. Kalyva, K. Papagelis, J. Parthenios, D. Tasis, A. Siokou, et al., Chemical oxidation of multiwalled carbon nanotubes, Carbon 46 (6) (2008) 833–840, https://doi.org/10.1016/j.carbon.2008.02.012.
[43] J. Farahbakhsh, M. Delnavaz, V. Vatanpour, Investigation of raw and oxidized multiwalled carbon nanotubes in fabrication of reverse osmosis polyamide membranes for improvement in desalination and antifouling properties, Desalination 410 (2017) 1–9, https://doi.org/10.1016/j.desal.2017.01.031.
[44] M. Usman Farid, H.-Y. Luan, Y. Wang, H. Huang, A. Kyoungjin An, R. Jalil Khan, Increased adsorption of aqueous zinc species by Ar/O2 plasma-treated carbon nanotubes immobilized in hollow-fiber ultrafiltration membrane, Chem. Eng. J. 325 (2017) 239–248, https://doi.org/10.1016/j.cej.2017.05.020.

[45] H.Y. Yang, Z.J. Han, S.F. Yu, K.L. Pey, K. Ostrikov, R. Karnik, Carbon nanotube membranes with ultrahigh specific adsorption capacity for water desalination and purification, Nat. Commun. 4 (2013) 2220, https://doi.org/10.1038/ncomms3220. https://www.nature.com/articles/ncomms3220#supplementary-information.
[46] W.-F. Chan, H.-y. Chen, A. Surapathi, M.G. Taylor, X. Shao, E. Marand, J.K. Johnson, Zwitterion functionalized carbon nanotube/polyamide nanocomposite membranes for water desalination, ACS Nano 7 (6) (2013) 5308–5319, https://doi.org/10.1021/nn4011494.
[47] H. Wu, B. Tang, P. Wu, Novel ultrafiltration membranes prepared from a multi-walled carbon nanotubes/polymer composite, J. Membr. Sci. 362 (1) (2010) 374–383, https://doi.org/10.1016/j.memsci.2010.06.064.
[48] A. Rahimpour, M. Jahanshahi, S. Khalili, A. Mollahosseini, A. Zirepour, B. Rajaeian, Novel functionalized carbon nanotubes for improving the surface properties and performance of polyethersulfone (PES) membrane, Desalination 286 (Suppl C) (2012) 99–107, https://doi.org/10.1016/j.desal.2011.10.039.
[49] L. Bai, H. Liang, J. Crittenden, F. Qu, A. Ding, J. Ma, et al., Surface modification of UF membranes with functionalized MWCNTs to control membrane fouling by NOM fractions, J. Membr. Sci. 492 (2015) 400–411. Suppl C. https://doi.org/10.1016/j.memsci.2015.06.006.
[50] H. Bai, X. Zan, L. Zhang, D.D. Sun, Multi-functional CNT/ZnO/TiO2 nanocomposite membrane for concurrent filtration and photocatalytic degradation, Sep. Purif. Technol. 156 (Part 3) (2015) 922–930, https://doi.org/10.1016/j.seppur.2015.10.016.
[51] X. Yang, Y. He, G. Zeng, X. Chen, H. Shi, D. Qing, et al., Bio-inspired method for preparation of multiwall carbon nanotubes decorated superhydrophilic poly(vinylidene fluoride) membrane for oil/water emulsion separation, Chem. Eng. J. 321 (2017) 245–256, https://doi.org/10.1016/j.cej.2017.03.106.
[52] C. Ji, J. Hou, V. Chen, Cross-linked carbon nanotubes-based biocatalytic membranes for micro-pollutants degradation: performance, stability, and regeneration, J. Membr. Sci. 520 (2016) 869–880, https://doi.org/10.1016/j.memsci.2016.08.056.
[53] J. Lee, Y. Ye, A.J. Ward, C. Zhou, V. Chen, A.I. Minett, et al., High flux and high selectivity carbon nanotube composite membranes for natural organic matter removal, Sep. Purif. Technol. 163 (2016) 109–119, https://doi.org/10.1016/j.seppur.2016.02.032.
[54] M.R. Mahdavi, M. Delnavaz, V. Vatanpour, J. Farahbakhsh, Effect of blending polypyrrole coated multiwalled carbon nanotube on desalination performance and antifouling property of thin film nanocomposite nanofiltration membranes, Sep. Purif. Technol. 184 (2017) 119–127, https://doi.org/10.1016/j.seppur.2017.04.037.
[55] M. Mulder, Basic Principles of Membrane Technology, kluwer Academic Publishers, 1996.
[56] B. Corry, Designing carbon nanotube membranes for efficient water desalination, J. Phys. Chem. B 112 (5) (2008) 1427–1434, https://doi.org/10.1021/jp709845u.
[57] M.A.E.-R. Abu-Zeid, Y. Zhang, H. Dong, L. Zhang, H.-L. Chen, L. Hou, A comprehensive review of vacuum membrane distillation technique, Desalination 356 (2015) 1–14. Suppl C. https://doi.org/10.1016/j.desal.2014.10.033.
[58] L.D. Tijing, Y.C. Woo, W.-G. Shim, T. He, J.-S. Choi, S.-H. Kim, H.K. Shon, Superhydrophobic nanofiber membrane containing carbon nanotubes for high-performance direct contact membrane distillation, J. Membr. Sci. 502 (2016) 158–170, https://doi.org/10.1016/j.memsci.2015.12.014.
[59] Y. Cai, G. Jiang, J. Liu, Q. Zhou, Multiwalled carbon nanotubes as a solid-phase extraction adsorbent for the determination of bisphenol a, 4-n-nonylphenol, and 4-tert-octylphenol, Anal. Chem. 75 (10) (2003) 2517–2521, https://doi.org/10.1021/ac0263566.
[60] N.M. Mubarak, J.N. Sahu, E.C. Abdullah, N.S. Jayakumar, Removal of heavy metals from wastewater using carbon nanotubes, Sep. Purif. Rev. 43 (4) (2014) 311–338, https://doi.org/10.1080/15422119.2013.821996.
[61] X. Yang, J. Lee, L. Yuan, S.-R. Chae, V.K. Peterson, A.I. Minett, et al., Removal of natural organic matter in water using functionalised carbon nanotube buckypaper, Carbon 59 (2013) 160–166. Suppl C. https://doi.org/10.1016/j.carbon.2013.03.005.

[62] B. Pan, B. Xing, Adsorption mechanisms of organic chemicals on carbon nanotubes, Environ. Sci. Technol. 42 (24) (2008) 9005–9013, https://doi.org/10.1021/es801777n.
[63] N.B. Saleh, L.D. Pfefferle, M. Elimelech, Aggregation kinetics of multiwalled carbon nanotubes in aquatic systems: measurements and environmental implications, Environ. Sci. Technol. 42 (21) (2008) 7963–7969, https://doi.org/10.1021/es801251c.
[64] X. Wang, S. Tao, B. Xing, Sorption and competition of aromatic compounds and humic acid on multiwalled carbon nanotubes, Environ. Sci. Technol. 43 (16) (2009) 6214–6219, https://doi.org/10.1021/es901062t.
[65] J. Guo, Q. Zhang, Z. Cai, K. Zhao, Preparation and dye filtration property of electrospun polyhydroxybutyrate–calcium alginate/carbon nanotubes composite nanofibrous filtration membrane, Sep. Purif. Technol. 161 (2016) 69–79, https://doi.org/10.1016/j.seppur.2016.01.036.
[66] G. Oberdörster, E. Oberdörster, J. Oberdörster, Nanotoxicology: an emerging discipline evolving from studies of ultrafine particles, Environ. Health Perspect. 113 (7) (2005) 823–839, https://doi.org/10.1289/ehp.7339.
[67] S. Kang, M. Pinault, L.D. Pfefferle, M. Elimelech, Single-walled carbon nanotubes exhibit strong antimicrobial activity, Langmuir 23 (17) (2007) 8670–8673, https://doi.org/10.1021/la701067r.
[68] H.J. Kim, Y. Baek, K. Choi, D.-G. Kim, H. Kang, Y.-S. Choi, et al., The improvement of antibiofouling properties of a reverse osmosis membrane by oxidized CNTs, RSC Adv. 4 (62) (2014) 32802–32810, https://doi.org/10.1039/C4RA06489E.
[69] F. Ahmed, B.S. Lalia, V. Kochkodan, N. Hilal, R. Hashaikeh, Electrically conductive polymeric membranes for fouling prevention and detection: a review, Desalination 391 (2016) 1–15, https://doi.org/10.1016/j.desal.2016.01.030.
[70] B.S. Lalia, F.E. Ahmed, T. Shah, N. Hilal, R. Hashaikeh, Electrically conductive membranes based on carbon nanostructures for self-cleaning of biofouling, Desalination 360 (2015) 8–12, https://doi.org/10.1016/j.desal.2015.01.006.
[71] X. Sun, J. Wu, Z. Chen, X. Su, B.J. Hinds, Fouling characteristics and electrochemical recovery of carbon nanotube membranes, Adv. Funct. Mater. 23 (12) (2013) 1500–1506, https://doi.org/10.1002/adfm.201201265.
[72] S.N. Jagannadh, H.S. Muralidhara, Electrokinetics methods to control membrane fouling, Ind. Eng. Chem. Res. 35 (4) (1996) 1133–1140, https://doi.org/10.1021/ie9503712.
[73] C.-F. de Lannoy, D. Jassby, K. Gloe, A.D. Gordon, M.R. Wiesner, Aquatic biofouling prevention by electrically charged nanocomposite polymer thin film membranes, Environ. Sci. Technol. 47 (6) (2013) 2760–2768, https://doi.org/10.1021/es3045168.
[74] S. Wang, S. Liang, P. Liang, X. Zhang, J. Sun, S. Wu, X. Huang, In-situ combined dual-layer CNT/PVDF membrane for electrically-enhanced fouling resistance, J. Membr. Sci. 491 (2015) 37–44. Suppl C. https://doi.org/10.1016/j.memsci.2015.05.014.
[75] W. Duan, G. Chen, C. Chen, R. Sanghvi, A. Iddya, S. Walker, et al., Electrochemical removal of hexavalent chromium using electrically conducting carbon nanotube/polymer composite ultrafiltration membranes, J. Membr. Sci. 531 (2017) 160–171, https://doi.org/10.1016/j.memsci.2017.02.050.
[76] G. Wei, X. Quan, X. Fan, S. Chen, Y. Zhang, Carbon-nanotube-based sandwich-like hollow fiber membranes for expanded microcystin-LR removal applications, Chem. Eng. J. 319 (2017) 212–218, https://doi.org/10.1016/j.cej.2017.02.125.
[77] M.S. Rahaman, C.D. Vecitis, M. Elimelech, Electrochemical carbon-nanotube filter performance toward virus removal and inactivation in the presence of natural organic matter, Environ. Sci. Technol. 46 (3) (2012) 1556–1564, https://doi.org/10.1021/es203607d.
[78] G. Wei, S. Chen, X. Fan, X. Quan, H. Yu, Carbon nanotube hollow fiber membranes: high-throughput fabrication, structural control and electrochemically improved selectivity, J. Membr. Sci. 493 (2015) 97–105, https://doi.org/10.1016/j.memsci.2015.05.073.

[79] H. Yanez, J. E, Z. Wang, S. Lege, M. Obst, S. Roehler, C.J. Burkhardt, C. Zwiener, Application and characterization of electroactive membranes based on carbon nanotubes and zerovalent iron nanoparticles, Water Res. 108 (2017) 78–85, https://doi.org/10.1016/j.watres.2016.10.055.
[80] H. Dong, G. Zeng, L. Tang, C. Fan, C. Zhang, X. He, Y. He, An overview on limitations of TiO2-based particles for photocatalytic degradation of organic pollutants and the corresponding countermeasures, Water Res. 79 (2015) 128–146. Suppl C. https://doi.org/10.1016/j.watres.2015.04.038.
[81] C.-H. Hung, C. Yuan, H.-W. Li, Photodegradation of diethyl phthalate with PANi/CNT/TiO2 immobilized on glass plate irradiated with visible light and simulated sunlight—effect of synthesized method and pH, J. Hazard. Mater. 322 (Part A) (2017) 243–253, https://doi.org/10.1016/j.jhazmat.2016.01.073.
[82] C. Yuan, C.-H. Hung, H.-W. Li, W.-H. Chang, Photodegradation of ibuprofen by TiO2 co-doping with urea and functionalized CNT irradiated with visible light—effect of doping content and pH, Chemosphere 155 (2016) 471–478, https://doi.org/10.1016/j.chemosphere.2016.04.055.
[83] A.V. Dudchenko, C. Chen, A. Cardenas, J. Rolf, D. Jassby, Frequency-dependent stability of CNT Joule heaters in ionizable media and desalination processes, Nat. Nanotechnol. 12 (6) (2017) 557–563, https://doi.org/10.1038/nnano.2017.102. http://www.nature.com/nnano/journal/v12/n6/abs/nnano.2017.102.html#supplementary-information.
[84] C. Boo, M. Elimelech, Thermal desalination membranes: carbon nanotubes keep up the heat, Nat. Nanotechnol. 12 (6) (2017) 501–503, https://doi.org/10.1038/nnano.2017.114.
[85] E.-S. Kim, G. Hwang, M. Gamal El-Din, Y. Liu, Development of nanosilver and multi-walled carbon nanotubes thin-film nanocomposite membrane for enhanced water treatment, J. Membr. Sci. 394–395 (Suppl C) (2012) 37–48, https://doi.org/10.1016/j.memsci.2011.11.041.
[86] R. Sengur, C.-F. de Lannoy, T. Turken, M. Wiesner, I. Koyuncu, Fabrication and characterization of hydroxylated and carboxylated multiwalled carbon nanotube/polyethersulfone (PES) nanocomposite hollow fiber membranes, Desalination 359 (2015) 123–140, https://doi.org/10.1016/j.desal.2014.12.040.
[87] X. Song, L. Wang, L. Mao, Z. Wang, Nanocomposite membrane with different carbon nanotubes location for nanofiltration and forward osmosis applications, ACS Sustain. Chem. Eng. 4 (6) (2016) 2990–2997, https://doi.org/10.1021/acssuschemeng.5b01575.
[88] J.-H. Choi, J. Jegal, W.-N. Kim, Fabrication and characterization of multi-walled carbon nanotubes/polymer blend membranes, J. Membr. Sci. 284 (1) (2006) 406–415, https://doi.org/10.1016/j.memsci.2006.08.013.
[89] M.-J. Han, S.-T. Nam, Thermodynamic and rheological variation in polysulfone solution by PVP and its effect in the preparation of phase inversion membrane, J. Membr. Sci. 202 (1) (2002) 55–61, https://doi.org/10.1016/S0376-7388(01)00718-9.
[90] M. Kumar, M. Ulbricht, Novel antifouling positively charged hybrid ultrafiltration membranes for protein separation based on blends of carboxylated carbon nanotubes and aminated poly(arylene ether sulfone), J. Membr. Sci. 448 (2013) 62–73, https://doi.org/10.1016/j.memsci.2013.07.055.
[91] M. Tian, Y.-N. Wang, R. Wang, Synthesis and characterization of novel high-performance thin film nanocomposite (TFN) FO membranes with nanofibrous substrate reinforced by functionalized carbon nanotubes, Desalination 370 (2015) 79–86, https://doi.org/10.1016/j.desal.2015.05.016.
[92] L. Wang, X. Song, T. Wang, S. Wang, Z. Wang, C. Gao, Fabrication and characterization of polyethersulfone/carbon nanotubes (PES/CNTs) based mixed matrix membranes (MMMs) for nanofiltration application, Appl. Surf. Sci. 330 (2015) 118–125. Suppl C. https://doi.org/10.1016/j.apsusc.2014.12.183.
[93] V. Vatanpour, M. Esmaeili, M.H.D.A. Farahani, Fouling reduction and retention increment of polyethersulfone nanofiltration membranes embedded by amine-functionalized multi-walled carbon nanotubes, J. Membr. Sci. 466 (2014) 70–81, https://doi.org/10.1016/j.memsci.2014.04.031.
[94] E.M.V. Hoek, S. Bhattacharjee, M. Elimelech, Effect of membrane surface roughness on colloid – membrane DLVO interactions, Langmuir 19 (11) (2003) 4836–4847, https://doi.org/10.1021/la027083c.

[95] P. Xie, C.-F. de Lannoy, J. Ma, Z. Wang, S. Wang, J. Li, M.R. Wiesner, Improved chlorine tolerance of a polyvinyl pyrrolidone-polysulfone membrane enabled by carboxylated carbon nanotubes, Water Res. 104 (2016) 497–506, https://doi.org/10.1016/j.watres.2016.08.029.
[96] I.M. Wienk, E.E.B. Meuleman, Z. Borneman, T. van den Boomgaard, C.A. Smolders, Chemical treatment of membranes of a polymer blend: mechanism of the reaction of hypochlorite with poly(vinyl pyrrolidone), J. Polym. Sci. A Polym. Chem. 33 (1) (1995) 49–54, https://doi.org/10.1002/pola.1995.080330105.
[97] S. Daer, J. Kharraz, A. Giwa, S.W. Hasan, Recent applications of nanomaterials in water desalination: a critical review and future opportunities, Desalination 367 (2015) 37–48, https://doi.org/10.1016/j.desal.2015.03.030.
[98] R. Das, S.B. Abd Hamid, M.E. Ali, A.F. Ismail, M.S.M. Annuar, S. Ramakrishna, Multifunctional carbon nanotubes in water treatment: the present, past and future, Desalination 354 (2014) 160–179, https://doi.org/10.1016/j.desal.2014.09.032.
[99] H. Zarrabi, M.E. Yekavalangi, V. Vatanpour, A. Shockravi, M. Safarpour, Improvement in desalination performance of thin film nanocomposite nanofiltration membrane using amine-functionalized multiwalled carbon nanotube, Desalination 394 (2016) 83–90, https://doi.org/10.1016/j.desal.2016.05.002.
[100] A.I. Schäfer, A.G. Fane, T.D. Waite, Cost factors and chemical pretreatment effects in the membrane filtration of waters containing natural organic matter, Water Res. 35 (6) (2001) 1509–1517, https://doi.org/10.1016/S0043-1354(00)00418-8.
[101] G.S. Ajmani, D. Goodwin, K. Marsh, D.H. Fairbrother, K.J. Schwab, J.G. Jacangelo, H. Huang, Modification of low pressure membranes with carbon nanotube layers for fouling control, Water Res. 46 (17) (2012) 5645–5654, https://doi.org/10.1016/j.watres.2012.07.059.
[102] Q. Zhang, C.D. Vecitis, Conductive CNT-PVDF membrane for capacitive organic fouling reduction, J. Membr. Sci. 459 (2014) 143–156, https://doi.org/10.1016/j.memsci.2014.02.017.
[103] X. Fan, Y. Liu, X. Quan, H. Zhao, S. Chen, G. Yi, L. Du, High desalination permeability, wetting and fouling resistance on superhydrophobic carbon nanotube hollow fiber membrane under self-powered electrochemical assistance, J. Membr. Sci. 514 (2016) 501–509, https://doi.org/10.1016/j.memsci.2016.05.003.
[104] C. Fernandez-Gonzalez, B. Zhang, A. Dominguez-Ramos, R. Ibañez, A. Irabien, Y. Chen, Enhancing fouling resistance of polyethylene anion exchange membranes using carbon nanotubes and iron oxide nanoparticles, Desalination 411 (2017) 19–27, https://doi.org/10.1016/j.desal.2017.02.007.
[105] Z. Xu, X. Li, K. Teng, B. Zhou, M. Ma, M. Shan, et al., High flux and rejection of hierarchical composite membranes based on carbon nanotube network and ultrathin electrospun nanofibrous layer for dye removal, J. Membr. Sci. 535 (2017) 94–102, https://doi.org/10.1016/j.memsci.2017.04.029.
[106] D. Mattia, K.P. Lee, F. Calabrò, Water permeation in carbon nanotube membranes, Curr. Opin. Chem. Eng. 4 (2014) 32–37, https://doi.org/10.1016/j.coche.2014.01.006.

CHAPTER

13 CARBON NANOTUBES FOR ADVANCING SEPARATION MEMBRANES

Junfeng Zheng, Wen Zhang, Xuan Zhang

Jiangsu Key Laboratory of Chemical Pollution Control and Resources Reuse, School of Environmental and Biological Engineering, Nanjing University of Science & Technology, Nanjing, China

1 INTRODUCTION

Membrane-based filtration, with numerous advantages such as small grounding, easy operation, and being environmentally friendly, can remove dangerous impurities without chemical additives and has become the current leading technology for water treatment and desalination [1]. Nevertheless, the dramatically increased energy consumption, particularly accompanied by the elevated feed concentration, has become the main factor limiting its advanced application for achieving the higher water recovery ratio [2, 3]. As such, one of the most promising approaches over the last decades for addressing this issue is the investigation of transformative membrane technologies, in which novel transport mechanisms were fundamentally put forward [1].

The application of carbon nanotubes (CNTs) in desalination and water purification has made great breakthroughs over the past decades [3, 4]. CNT-based membranes use CNTs as membrane pores to achieve higher water flux, selectivity, and lower energy consumption because of their outstanding inherent features [5]. Hollow CNTs with atomic-scale smooth surfaces provide water molecules with frictionless channels, which contribute to excellent water permeability [6]. CNTs with appropriate nanometer-range diameters can also serve as selective barriers that allow water molecules to pass through but reject salt ions [7]. In addition, incorporating functionalized CNTs, such as those with added hydrophilic ($-SO_3^-$), positive ($-NH_3^+$), or negative (-COO^-) groups, can improve the membrane's water permeability and its self-cleaning, antifouling, and antibacterial properties [8]. Because of these advantages, CNT-based membranes have a bright future in water purification.

This chapter presents the basic structures and properties of CNTs in terms of mass transportation. On this basis, the types of CNT-based membranes and state-of-the-art approaches to achieving functionalities related to the applicability and feasibility of CNTs for water purification applications are summarized. Finally, the current hurdles and future outlook of CNT-based membranes are also discussed.

Nanoscale Materials in Water Purification. https://doi.org/10.1016/B978-0-12-813926-4.00018-5

2 CNT CHEMISTRY

2.1 BASIC STRUCTURES AND PROPERTIES

CNTs, which are one-dimensional (1D) materials comprising nanometer-range seamless cylinders obtained by rolling graphite sheets, were first synthesized by Iijima's group [9]. A pair of rolled-up indices (n, m; i.e., unit vectors that can reflect the matched position of a rolled graphene sheet) were used to characterize the structures of CNTs (Fig. 1) [1]. The inner diameter (d) of a CNT can be calculated based on the following Eq. (1) according to the rolled-up indices [6]:

$$d = \left(\frac{a}{\pi}\right)\sqrt{(n^2 + m^2 + mn) - 2r_c} \tag{1}$$

where a (=2.46 Å) is the lattice parameter of graphene and r_c (=1.7 Å) is the van der Waal's radius of a carbon atom.

In the following years, CNTs were investigated by many scientists worldwide, mainly because of their outstanding properties, which include superior mechanical properties, high tensile strength, and thermal conductivity [10–12]. Generally, based on the results of in-depth studies, CNTs have great potential applications in many fields of engineering and science [13–17].

Depending on the number of graphite sheet layers, CNTs are typically categorized into single-walled CNTs (SWCNTs), double-walled CNTs (DWCNTs), and multiwalled CNTs (MWCNTs) [18]. Many approaches for the fabrication of CNTs have been explored, such as the chemical vapor deposition (CVD) method, the laser method, and the arc discharge method [19–21]. Among these methods, CVD is the method most commonly used for producing CNTs because it is a simple process and generates high-quality products, which even makes fabricating individual and densely packed vertically aligned CNTs (VA-CNTs) possible [1]. However, some technical issues relating to controlling the diameter distribution of VA-CNTs within a rather narrow range remain to be resolved; these could be the focus of future research [22, 23].

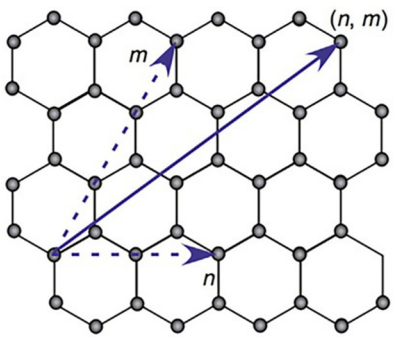

FIG. 1

Schematic of a graphene sheet and CNT roll-up indices (n, m) [1].

2.2 WATER TRANSPORTATION

Although strong, ordered hydrogen bonds exist between water molecules, minimal interactions exist between water molecules and CNT graphite sheets [24, 25]. Therefore, water molecules can uninterruptedly and spontaneously pass through the smooth and hydrophobic inner walls of CNTs [26, 27].

Conventional fluid mechanics (i.e., Fickian motion) does not apply to the movement of water molecules through CNTs [28, 29]. This phenomenon may be ascribed to the single-file mechanism of this movement; indeed, water molecules could be hindered from passing each other through the narrow 1D channels [30]. Thus, a novel theory, "nanofluidics," must be introduced in place of simple fluidics to describe the mass movement of water molecules through nanotube structures [31, 32]. This theory assumes that the fluid passing through the nanochannel has a slip length without friction force [32]. Adopting the slip-flow conditions, Q_{slip} (i.e., the slip length of the water flux in a nanochannel) was calculated using the Hagen-Poiseuille Eq. (2) [28]:

$$Q_{slip} = \frac{\pi(d/2)^4 + 4(d/2)^3 \cdot L_s(d)}{8\mu} \cdot \frac{\Delta P}{L} \tag{2}$$

where d is the nanochannel diameter, ΔP is the pressure difference at both ends of the nano-channel, μ is the water viscosity, L is the length of the nanochannel, and L_S (d) is the slip length, which can be calculated as follows (Eq. 3):

$$L_s(d) = L_{S,\infty} + \frac{C}{d^3} \tag{3}$$

where $L_{S,\infty}$ (30 nm) is the slip length of the graphene surface, C refers to a fitting parameter, and d indicates the diffusion coefficient of the water molecules (0.9423×10^{-9} m^2 s^{-1} for a nanotube with a diameter of 2.1 nm) [29]. This theory can also be applied to gas and oil transport through nanochannel membranes, such as CNT-based membranes [33, 34].

VA-CNT membranes have great potential for use as high-flux membranes in water purification. Holt et al. fabricated sub-2-nm VA-CNT membranes by first applying a catalytic CVD method and then uncapping the nanotubes by laser etching [7]. The water permeability of these small-pore-size CNT-based membranes was several orders of magnitude faster than that of commercial polycarbonate membranes. Subsequently, CNT membranes with larger pore sizes were studied by Majumder's group [5]. The results demonstrated that water molecules passed through an VA-MWCNT membrane with 7-nm-diameter CNTs at high velocities of 9.5–43.9 cm s^{-1} bar^{-1}, which are four to five orders of magnitude faster than those of conventional fluid flow (i.e., 0.00015–0.000157 cm s^{-1} bar^{-1}) [5]. In addition, the types and conformations of CNTs also exert special influences on water permeability. Corry et al. performed molecular dynamics simulations to study the mass transportation behaviors of four "armchair"-type CNTs with rolled-up indices of (5, 5), (6, 6), (7, 7), and (8, 8) [6]. As shown in Fig. 2, a single-file water chain formed in the (5, 5) and (6, 6) tubes, whereas double- and quadruple-file water chains developed in the (7, 7) and (8, 8) tubes, respectively. The simulation results clearly showed that the water conductance of (8, 8) CNTs is approximately quadruple to that of (6, 6) CNTs. Furthermore, although single-file water chains were found in both the (5, 5) and (6, 6) tubes, the permeability of the (5, 5) tube was less than half that of the (6, 6) tube. The reason for this difference is that water chains formed across the narrower pore half of the time [6].

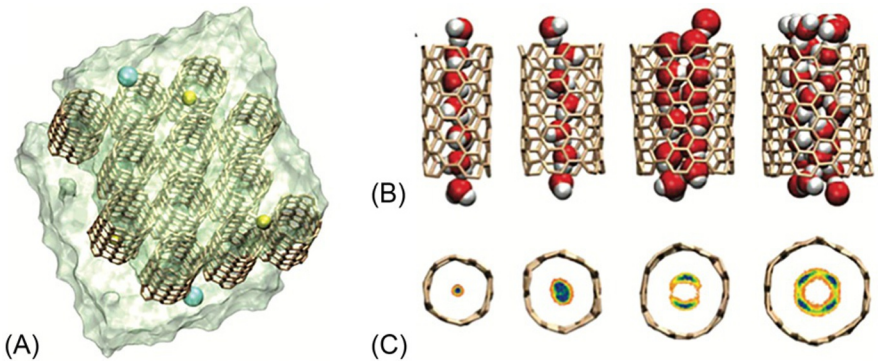

FIG. 2

(A) Simulation system. A CNT-based membrane formed by hexagonally packing 12 CNTs in a periodic cell; snapshots of water and ions in the nanotubes from molecular dynamics simulations. (B) Plane and (C) top views of water in each of the (5, 5), (6, 6), (7, 7), and (8, 8) CNTs [6].

From B. Corry, Designing carbon nanotube membranes for efficient water desalination, J. Phys. Chem. B 112 (5) (2007) 1427.

3 FUNCTIONALIZATION OF CNTs

Despite the excellent properties of CNTs, their generally poor compatibility with organic phases has caused great difficulties in the industrial-scale application of these materials [35]. Furthermore, their poor dispersity in solvents makes their fabrication difficult on the molecular level. Therefore, appropriately modifying CNTs to make them suitable for a variety of application has become a critical issue in recent years. In this section, the main methods of functionalizing CNTs are introduced from a chemical perspective; these methods include covalent and noncovalent functionalization, as shown in Fig. 3.

3.1 COVALENT FUNCTIONALIZATION

3.1.1 Oxidation

The ends and bendings of CNTs are easily broken by oxidation and turned into carboxyl groups, which can react with other chemical reagents. To enhance the effects of acidic etching and increase the density of surface oxygen-containing groups on the sidewalls of MWCNTs, Xing and coworkers reported the sonication-assisted oxidation of CNT materials in a sulfuric/nitric acid mixture. Sonochemical treatment duration-dependent surface structural damage was observed on MWCNTs, which affected their electronic properties [36].

3.1.2 Amidation

After the initial acid oxidation of CNTs, further reactions, such as amidation, can be conducted on the -COOH groups of CNTs, leading to their replacement by various substituents. Liu et al. grafted alkanethiol onto oxygenated SWCNTs containing NH_2-$(CH_2)_{11}$-SH through the formation of amide linkages. Because of the presence of thiol units, such fillers could be subsequently bonded with gold nanoparticles via chelating effects [37].

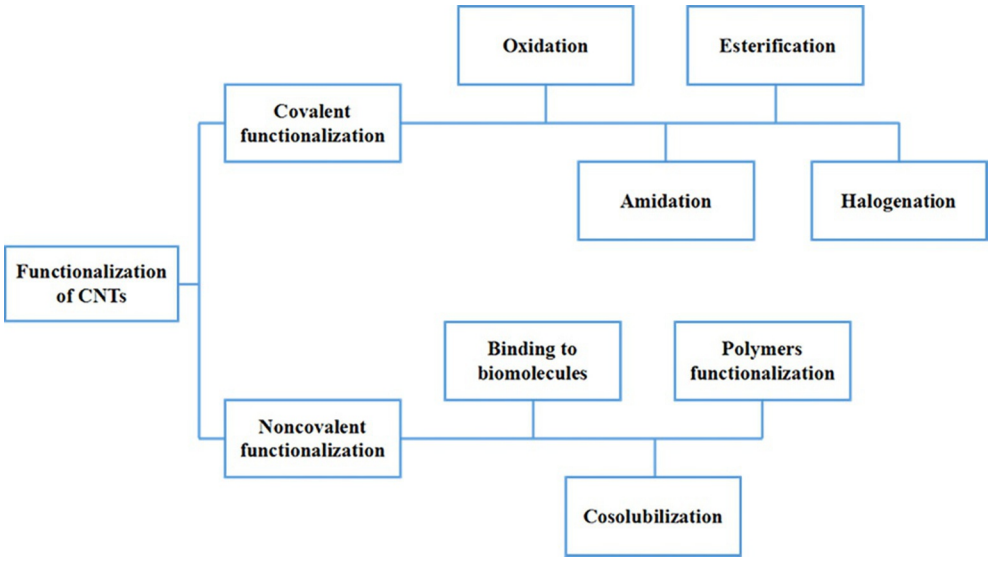

FIG. 3

Functionalization classification of CNTs.

3.1.3 Esterification

In addition to amidation, several organic compounds can be added to CNTs through esterification. Georgakilas and coworkers took advantage of the 1,3-dipolar cycloaddition of azomethine ylides generated by the condensation of an α-amino acid and an aldehyde to enhance the solubility of CNTs in $CHCl_3$, CH_2Cl_2, acetone, methanol, ethanol, and other polar solvents [38]. Furthermore, several biomolecules, polymers, and photosensitive compounds can also be used to functionalize CNTs via the esterification of oxygenated CNTs [39–44].

3.1.4 Halogenation

According to Lee, the fluorination of CNTs can be achieved with a CHF_3 plasma generated by a reactive-ion etching (RIE) reactor; this provides reaction sites for subsequent modification [45]. Stevens et al. used fluorinated CNTs as precursors and terminal amino groups (diamine) as nucleophiles to covalently attach *N*-alkylidene amino groups to the sidewalls of CNTs through the C—N bond [46]. However, the grafting efficiency was low, with degrees of functionalization of 1/8–1/12. In general, this type of C—N functionalization for bonding amino acids, DNA, and polymers could represent an appropriate synthetic method to synthesize nylon-CNT polymeric materials. Recently, the chemical modification of CNTs via an electrolytic method that facilitates the realization of both chlorination and bromination of CNT sidewalls has been reported. Because of the better leaving abilities of Cl and Br compared to F, such halogenated CNTs may exhibit better reactivity under nucleophilic reaction conditions.

Furthermore, some additional covalent modification methods, such as cycloaddition reactions, radical additions, nucleophilic additions, and electrophilic addition, have also been reported [47–50].

3.2 NONCOVALENT FUNCTIONALIZATION

It should be noted that the process of covalent functionalization can damage the graphite lattice structure of CNTs and thus exert a certain negative impact (i.e., the loss of the p-stacking system or the appearance of defects), hindering the development of CNTs for use in practical applications. As a result, a series of noncovalent functionalization methods based on, for example, van der Waals forces, hydrogen bonding, and electrostatic forces have drawn substantial scientific attention, which has expanded their applications significantly [51–56].

3.2.1 Binding to biomolecules

Biological functionalization methods commonly used for CNTs mainly consist of combinations of DNA, protein, and other substances to increase their dispersity in an aqueous solution. Dieckmann et al. specifically designed an amphiphilic α-helical peptide to coat and solubilize CNTs. Through noncovalent interactions with the nanotube surface, the peptide folds into an amphiphilic α-helix in the presence of CNTs and disperses them in aqueous solution [57].

3.2.2 Cosolubilization

Kim and coworkers have developed a convenient and efficient process for dissolving SWCNTs in aqueous dimethyl sulfoxide (DMSO) in the presence of amylose. To achieve immediate and complete solubilization, this process proceeds through two steps: separating SWNT bundles and achieving maximum cooperative interactions between SWNTs and amylose in an optimum mixture of DMSO/H_2O [58].

3.2.3 Polymer functionalization

Cho et al. systematically introduced the design of amphiphilic polymer compatibilizers to manipulate the solubility of CNT composites [59]. The developed multiamphiphilic compatibilizer was used for the noncovalent functionalization of CNTs and resulted in remarkable dispersion stability, solubility, and hybridization with Ag nanoparticles. Morishita and coworkers used N-substituted maleimide to synthesize maleimide polymers (MIPs) that showed strong physical adsorption on various CNT surfaces. As a result of the excellent CNTs dispersants, such polymer-modified CNTs displayed excellent solubility in a wide variety of organic solvents [60].

4 CNT-BASED MEMBRANES

Recently, notable progress in the synthesis and functionalization of CNTs has opened the possibility for these materials to be applied in membranes [61–66, 66a]. At this stage, CNT-based membranes can be classified into three categories according to the position and distribution of the CNTs and the synthetic approach used: (1) CNT filter membranes, (2) CNT/polymer mixed matrix membranes (MMMs), and (3) CNTs as membrane fillers.

In this section, these three types of CNT-based membranes are discussed systematically. In addition, the application and development of CNT materials in membrane separation technology, such as membrane distillation (MD), ultrafiltration (UF), nanofiltration (NF) reverse osmosis (RO), and forward osmosis (FO), and the methods used to synthesize membranes are highlighted. Furthermore, membrane performance (e.g., flux, salt rejection, antifouling property, mechanical strength, and stability) is discussed in detail. The major water treatment processes in which CNT-based membranes are used are summarized in Table 1.

Table 1 Summary of Conventional CNT-Based Membranes

Fabrication Methods	Application	Functionalization	Flux[a] ($L\ m^{-2}\ h^{-1}\ bar^{-1}$)	Highlight	Ref.
Phase inversion (PAN)	UF	MWCNTs-OH	33.5	Rejection to dextrane with a molecular weight of 50 kg mol^{-1} over 90.0% The tensile strength increased over 97% compared to neat ones	[67]
Phase inversion (PVDF)	UF	Oxidized MWCNTs (mixed with GO)	409.7	Minimizing the stacking effect and aggregation of low-dimensional carbon nanomaterials Good antifouling property, the pure water flux recovery achieved 98.3%	[68]
Phase inversion (PSF)	UF	MWCNTs-ICIC (5-isocyanato-isophthaloyl chloride)	175.0	Rejection to PEG-20000 is about 92.0% The membrane fouling resulting from protein adsorption is reduced	[69]
Phase inversion (PES)	UF	Polymer brush grafted CNTs (ATRP)	354.6	Rejection to PEG-20000 is 80.2% High antifouling ability and antibacterial activity Efficient toxin removal ability	[70]
In situ amination crosslinked	UF	MWCNTs-COOH	243.5	Rejection to egg albumin (MW: 45,000 g mol^{-1}) is 94.0% High permeation flux and excellent selectivity	[71]

Continued

Table 1 Summary of Conventional CNT-Based Membranes—cont'd

Fabrication Methods	Application	Functionalization	Flux ($L\ m^{-2}\ h^{-1}\ bar^{-1}$)	Highlight	Ref.
VF	MD	Pristine MWCNTs	–	The water vapor flux is 12 kg m^{-2} h^{-1} NaCl rejection is 99% at salt concentration 35,000 ppm Highly hydrophobic (contact angle of 113 degrees) and porous (90%)	[72]
VF	MD	MWCNTs coated a thin layer of PTFE	–	Higher permeability and salt rejection at salt concentration 35,000 ppm Life span has improved	[73]
Phase inversion (PVDF)	MD	MWCNTs-COOH	–	The water vapor flux is 36.8 kg m^{-2} h^{-1} at 70°C NaCl rejection is greater than 99.9% at salt concentration 10,000 ppm Higher thermal stability	[74]
Phase inversion (PVDF)	MD	Pristine MWCNTs	–	Flux has increased 1.85 times at 80°C with 34,000 mg L^{-1} salt concentration. MMMs facilitate MD process at a 20°C lower temperature than pristine MD process	[75]
Phase inversion (PTEE)	MD	MWCNTs-COOH	–	Permeate flux has enhanced 54% (69 kg m^{-2} h^{-1}) with 4000 mg L^{-1} NaCl at 70°C	[76]
VF	NF	MWCNTs (-COOH, -CONH)	16.5	Good rejection to divalent heavy metal Excellent separation of organic molecules and long-term filtration stability	[77]
VF	NF	MWCNTs (H_2SO_4/HNO_3) mixed with GO	11.3	Rejection to Na_2SO_4 is 83.5% High dye rejection (>99.0% for direct yellow and >96.0% methyl orange) Excellent antifouling performance	[78]

Table 1 Summary of Conventional CNT-Based Membranes—cont'd

Fabrication Methods	Application	Functionalization	Flux ($L\ m^{-2}\ h^{-1}\ bar^{-1}$)	Highlight	Ref.
Phase inversion (PES)	NF	CNTs-COOH	9.7	Rejection order: Na_2SO_4 (87.0%) > $MgSO_4$ > (60.0%) > NaCl (30.0%)	[79]
Phase inversion (PES)	NF	MWCNTs-NH_2	3.9	Rejection order: Na_2SO_4 (65.0%) > $MgSO_4$ > (45.0%) > NaCl (20.0%) Improvement of antifouling ability	[80]
Phase inversion (PVDF)	NF	MWCNTs (H_2SO_4/HNO_3)	1.9	Rejection order: Na_2SO_4 (75.0%) > $MgSO_4$ (42.0%) > NaCl (17.0%) Superior antifouling property	[81]
IP	NF	MWCNTs (H_2SO_4/HNO_3)	3.5	Rejection to Na_2SO_4 is 80.0% Good long-term stability	[82]
IP	NF	PMMA-MWCNTs	7.0	Rejection to Na_2SO_4 is 99.0% Significantly improve selectivity and permeability	[83]
IP	NF	MWCNTs-COOH; MWCNTs-OH; MWCNTs-NH	6.2 6.9 5.3	Rejections to Na_2SO_4 are 96.6%, 97.6%, and 96.8%, respectively All the membranes possessed a good operation stability	[84]
IP	NF	MWCNTs-SO_3H	13.2	High rejection to Na_2SO_4 (96.8%) Excellent antifouling ability	[85]
IP	NF	ZCNTs	14.9	Improvement of selectivity for monovalent/divalent Excellent antibacterial properties	[86]
IP	NF	PDA-MWCNTs	15.3	Well-suited for water softening and heavy metals removal Rejections to $ZnCl_2$, $MgCl_2$, $CuCl_2$, and $CaCl_2$ were all above 90.0%	[87]

Continued

Table 1 Summary of Conventional CNT-Based Membranes—cont'd

Fabrication Methods	Application	Functionalization	Flux ($L\ m^{-2}\ h^{-1}\ bar^{-1}$)	Highlight	Ref.
VF + IP	NF	MWCNTs (H_2SO_4/HNO_3)	17.6	High rejection to Na_2SO_4 (95.0%) Excellent structure stability	[88]
In situ ionic cross-linking	NF	MWCNTs (H_2SO_4/HNO_3)	4.5	Rejection to $MgCl_2$ maintained at around 93.5% Good Na^+/Mg^{2+} selectivity Well suited for water softening	[89]
Gross-linking (PEG400 as pore-forming agent)	NF	MWCNTs-COOH/ calcium alginate	19.6	Rejection for Congo red reached to 99.2% High tensile strength up to 1.8 MPa Good antifouling property	[90]
Deposited CNTs	NF	MWCNTs with surfactants	6.0	Rejection to Na_2SO_4 is 81.0% Superior antibiofouling property	[91]
IP	RO	CNTs-COOH	1.8	Rejection to NaCl remained relatively high (90.0%) Better antifouling and antioxidant properties than TFC membranes	[110]
IP	RO	CNTs-COOH	2.9	Rejection to NaCl is 95.7% Improved stability	[93]
IP	RO	MWCNTs (H_2SO_4/HNO_3)	1.9	Rejection to NaCl is between 96.7% and 97.8% Good antifouling property	[94]
VF + IP	RO	ZCNTs	1.3	Rejection to NaCl is 98.6% Combining with theoretical analysis	[95]
VF + IP	RO	Zwitterion functionalized SWCNTs	1.4	Rejection to NaCl is 98.5% The mechanical stability is improved Increased surface fouling resistance	[96]

Table 1 Summary of Conventional CNT-Based Membranes—cont'd

Fabrication Methods	Application	Functionalization	Flux ($L\ m^{-2}\ h^{-1}\ bar^{-1}$)	Highlight	Ref.
Deposited CNTs + IP	RO	MWCNTs (H_2SO_4/HNO_3)	2.1	Rejection to NaCl is 96.1% Excellent antibiofouling properties	[97]
IP	FO[b]	MWCNTs-NH_2	3.6	Rejection to NaCl is 89.3% higher than TFC membrane (70.0%) (2.0 M and 10.0 mM NaCl solution are used as DS and feed solution)	[98]
VF + IP	FO	CNTs-COOH	1.3	Rejection to NaCl is 91.3% Alleviate the ICP problem in the FO process (2.0 M NaCl and DI water are used as DS and feed solution)	[99]
Phase inversion (CNT/PEI substrates) + IP	FO	MWCNTs (HCl/HNO_3)	2.6	Increased the substrate porosity by 18%, reduced S value by 30%, and improved the substrate tensile modulus by 53% (1.0 M NaCl and DI water are used as DS and feed solution)	[100]
Phase inversion (CNT/PES substrates) + IP	FO	MWCNTs (H_2SO_4/HNO_3)	2.3	Rejection rate of NaCl is 97.0% Open interior pore structure and smoother selective layer resulted in less ICP Improved tensile strength (17.1 mM NaCl and DI water are used as DS and feed solution)	[101]

[a] *The flux is the optimized flux.*
[b] *In the FO process, the flux is pure water permeability coefficient (A).*

4.1 CNT FILTER MEMBRANES

A membrane that consists of only CNTs is called a CNT filter membrane. According to the distribution of CNTs, we divide these types of membranes into VA-CNT and nonaligned CNT (NA-CNT) membranes.

4.1.1 VA-CNT membranes

The VA-CNT membrane, in which the distribution direction of the nanotubes is perpendicular to the membrane surface, was first fabricated by Hinds's research group and contained polystyrene (PS) as a filler between the CNTs [26, 102]. To create this membrane, CNTs were grown for 30 min on a quartz substrate via CVD, and then, 50 wt% of PS and toluene were spin-coated on this surface [26]. After drying under vacuum, the VA-CNT membrane, which had a thickness of 5–10 μm, was obtained by removing the CNT-PS composite from the quartz substrate using hydrofluoric acid (Fig. 4) [26]. The water-flow rates of the VA-CNT membrane were four- to fivefold higher than those of conventional ones, but the obtained membrane pore size was irregular. Additionally, Holt et al. subjected sub-2-nm CNTs (average inner diameter: 1.6 ± 0.4 nm) to a microelectromechanical method to fabricate another type of VA-CNT membrane and obtain improved nanofluidic effects [7]. They incorporated inorganic filler (silicon nitride [Si_3N_4]) into the CNTs' gaps so that water could pass only through the nanochannels of the CNTs. The resulting membrane exhibited a high water flux that was more than threefold

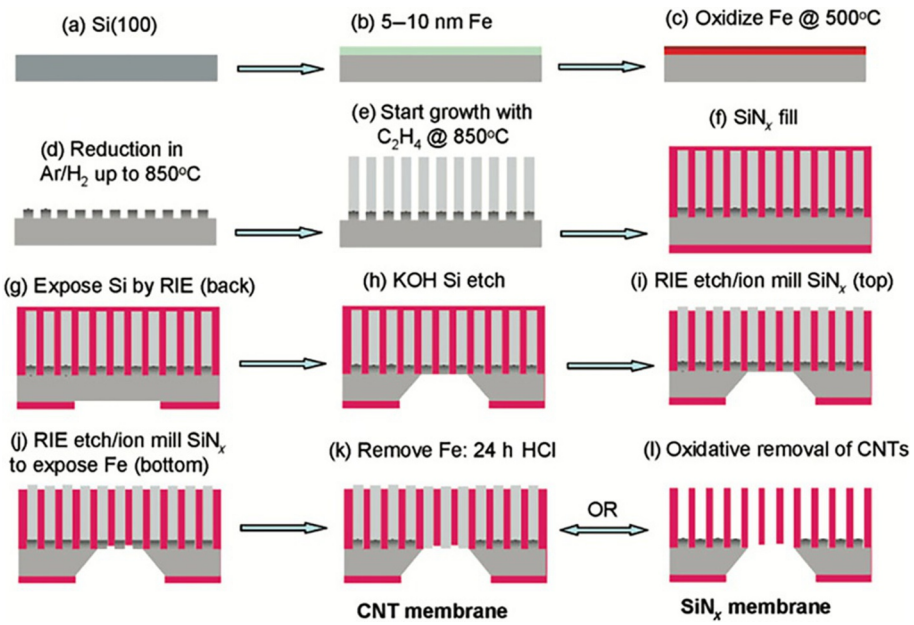

FIG. 4

Schematic of VA-CNT membrane fabrication [102].

From J.K. Holt, A. Noy, T. Huser, A. David Eaglesham, O. Bakajin, Fabrication of a carbon nanotube-embedded silicon nitride membrane for studies of nanometer-scale mass transport, Nano Lett. 4 (2004) 2245–2250.

greater than that of the nonslip membrane. Furthermore, this membrane could transport Ru^{2+} $(bipyr)_3$ species (analyte size = 1.3 nm) but prevented the passage of Au particles (analyte size = 2 ± 0.4 nm), indicating that the pore size was between 1.3 and 2 nm.

Although these VA-CNT membranes have some advantages, such as low energy consumption, high selectivity for multiple variants, and high water fluxes, the fabrication of homogeneous CNT membranes is rather complicated and remains challenging [31]. Currently, the most common method remains applied CVD, which involves multiple steps, as illustrated in Fig. 4.

4.1.2 NA-CNT membranes

Compared with the complex and difficult-to-control method used to synthesize a VA-CNT membrane, NA-CNT membranes can be prepared by a relatively simple vacuum filtration (VF) technique. Dumee et al. fabricated a self-supporting CNT buckypaper membrane with unique structural and surface properties through VF [72]. The obtained membrane was composed of CNTs held together by van der Waals forces alone and thus had many advantages, such as high hydrophobicity, high porosity (90%), and low thermal conductivity (2.7 kW m^{-2} h^{-1}), which is favorable for MD [72]. During the MD process, this novel membrane exhibited a high salt rejection of 99% and an acceptable flux rate of 12 kg m^{-2} h^{-1}. However, despite the outstanding performance of the CNT buckypaper membrane in the MD process, the water flux inevitably decreased with the long-term operation because of the lack of chemical bond interactions. To address this issue, the same research group coated a thin layer of poly(tetrafluoroethylene) (PTFE) on a CNT buckypaper membrane to further improve its hydrophobicity and mechanical stability [73]. Indeed, the higher hydrophobicity of PTFE can improve the water meniscus surface, thereby increasing the surface available for water evaporation and achieving high flux in MD [103–105]. Unsurprisingly, the coating-modified membranes exhibited improved life span, higher water vapor permeability, and high salt rejection (exceeding 99%) when tested with a model seawater containing 35-g L^{-1} NaCl in the feed solution [73].

However, CNTs may leach out from membranes that are held together by van der Waals forces exclusively. Soyekwo et al. grafted cross-linked polyethyleneimine (PEI) onto carboxylated CNTs (CNTs-COOH) and applied a VF technique on a macroporous cellulose acetate substrate to produce an NA-CNT membrane [77]. The cross-linked system significantly enhanced the polymer interactions with the CNT interlayer and, in turn, generated a CNT interlayer with good mechanical strength and maintained an appropriate membrane pore structure under pressure-driven filtration. The cross-linked NA-CNT membrane was then used as an NF membrane after in situ surface Zn^{2+} deposition. The positively charged and hydrophilic group-functionalized nanocomposite membrane displayed outstanding water permeation (16.5 ± 1.3 L m^{-2} h^{-1} bar^{-1}) and good rejection of divalent heavy metal cations because of the Donnan exclusion effect. For this type of membrane, water molecules pass through both the CNT nanochannels and the gaps between the CNTs. Other methods of fabricating CNT membranes, such as combining VF with interfacial polymerization (IP) technology, are discussed in Section 4.3.

4.2 CNT/POLYMER MMMs

One of the most common and promising methods for the application of CNTs in water purification is MMMs, which incorporate CNTs into a polymer matrix via physical blending [106]. Scholars have modified CNTs and incorporated them into membrane matrices to improve the membrane separation

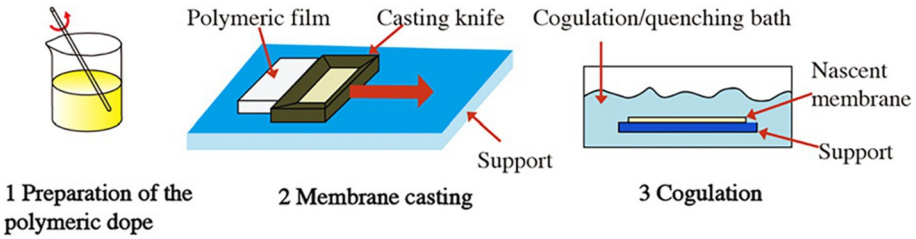

FIG. 5

Conventional flat sheet membrane preparation via phase inversion.

performance, hydrophilic properties, and mechanical properties. The most commonly used method is the phase inversion method; a diagram of the synthesis is shown in Fig. 5 [107].

UF membranes constitute a large portion of CNT-based MMMs. UF, which utilizes pore diameters ranging from 1 to 100 nm, is a low-pressure membrane filtration process [108]. Choi et al. fabricated UF membranes by blending MWCNTs (up to 4 wt%) with polysulfone (PSF) using *N*-methyl-2-pyrrolidone (NMP) as a solvent and water as a coagulant through the phase-inversion method [109]. MWCNT/PSF blend membranes exhibit high (>95%) rejection efficiency against poly(ethyleneoxide) (MW 100,000) and high water flux (14–17 L m^{-2} h^{-1}) under an operating pressure of 4 bar. However, unmodified CNTs in the MMMs may cause some defects because of their poor interfacial compatibility with polymers, and as a result, CNTs may fall off during the filtration process. Tang et al. synthesized a novel UF membrane by incorporating MWCNTs-COOH into a brominated polyphenylene oxide (BPPO) matrix with triethanolamine (TEOA) as a cross-linking agent using the dry-wet phase-inversion approach [71]. The flux of his novel membrane increased to 243.5 L m^{-2} h^{-1} bar^{-1} with MWCNT loading of 5 wt% (the flux of the pristine membrane was 98.5 L m^{-2} h^{-1} bar^{-1}), whereas the rejection of egg albumin remained unchanged. These findings can be attributed to the adsorption and hydrophilicity effects and nanochannels of MWCNTs-COOH [71]. Moreover, Abetz's group blended hydroxyl MWCNTs (MWCNTs-OH) with polyacrylonitrile (PAN) to fabricate a UF membrane [67]. The PAN matrix loaded with 2 wt% CNTs was quite homogeneous; however, a small quantity of aggregates could still be observed in transmission electron microscopy (TEM) images. The water flux of the as-prepared MMMs increased nearly by 63% with 0.5 wt% MWCNTs-OH loading compared to the pristine membrane [67]. This increase was attributed to the increased hydrophilicity of the prepared membrane caused by the hydroxyl groups of the CNTs and existing special nanochannels. Furthermore, the tensile strength of the novel membrane increased by nearly 34% compared to that of the pristine membrane, facilitating the practical application of this membrane at high transmembrane pressures.

Another typical representative of MMMs can be used in the MD process. Gethard et al. incorporated MWCNTs into a polyvinylidene fluoride (PVDF) membrane to improve membrane permeability and selectivity [75]. In this study, the CNTs served as the sorbent and provided an extra pathway for vapor molecule transport. Additionally, the superhydrophobic CNTs prevented liquid from entering the membrane pores because of the surface tension forces. CNT/PVDF MMMs have several advantages compared to conventional MD membranes. First, these membranes exhibit higher flux and greater

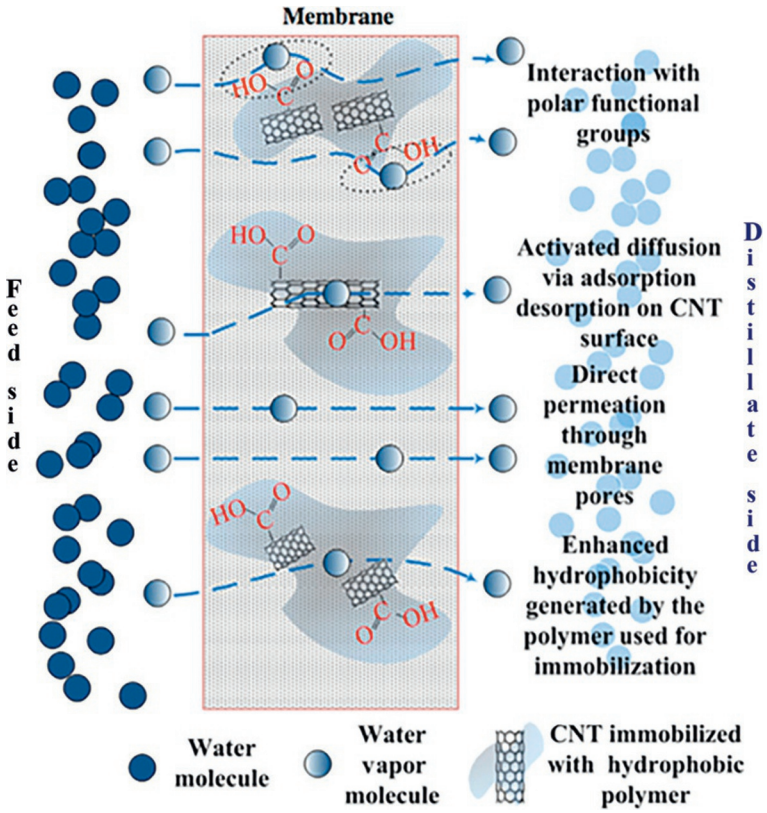

FIG. 6

MD mechanisms in the presence of CNTs-COOH [74].

compatibility with a wide range of saline concentrations up to the equivalent of seawater [75]. Additionally, using this membrane, the MD process can reach the same level of salt reduction as the pristine MD process at a 20°C lower temperature. However, one technical issue remains: the CNTs may cause some defects in the membrane matrix because of their poor dispersity in solution and weak compatibility with organic phases. More recently, Mitra's group fabricated CNTs-COOH-immobilized membranes. CNTs-COOH alter the hydrophilic-hydrophobic interactions between liquid and the membrane surface supply an extra pathway for water permeation [74]. The water flux of the novel membrane was as high as 36.8 kg m^{-2} h^{-1} at 70°C, 1.5 times higher than that of the unmodified membrane; furthermore, the salt reduction exceeded 99.9%. The CNTs serve as nanochannels for vapor molecule transport while rejecting liquid water. Additionally, the polar CNTs-COOH absorb water and thereby improve the overall flux. The transport and separation mechanisms of the MD process in the presence of CNTs-COOH are shown in Fig. 6.

The phase inversion technique can be also used to prepare NF MMMs. Vatanpour et al. embedded amine-functionalized MWCNTs (NH_2-MWCNTs) into polyethersulfone (PES) matrix to increase the

surface hydrophilicity and water permeability [80]. The flux of this membrane increased by 1.7 times as the NH_2-MWCNT dosage increased from 0 to 0.045 wt%. Additionally, because the membrane was more hydrophilic and more negatively charged and exhibited lower roughness, it retained good antifouling properties.

4.3 CNTs AS MEMBRANE FILLERS

In the context of highly effective water treatment, CNTs can be used as aqueous or organic phase additives to fabricate NF, RO, or FO thin-film nanocomposite (TFN) membranes by means of an IP technique [92, 110]. However, two main issues remain and may strongly hinder the application of CNTs in this area. First, pristine CNTs agglomerate easily and thus have poor dispersion in both aqueous and organic solutions. Second, the poor compatibility of CNTs with polymer matrices is attributable to their weak interfacial interactions [84]. Despite the improved water permeability, these challenges will create nonselective defects and large gaps, which may reduce salt rejection and performance stability [87, 111].

Thus, researchers have been seeking solutions to address these two challenges for TFN membranes. Roy et al. functionalized MWCNTs with hydrophilic (-COOH) and hydrophobic (-CONH) groups and successfully synthesized NF membranes using the conventional IP method wherein MWCNTs were dispersed in aqueous and organic phases, respectively [112]. The fluxes of these two novel membranes are one order of magnitude larger than those of the conventional membrane, whereas their solute rejection results were equivalent. The MWCNTs dispersed in the polyamide (PA) matrix provide a low resistance pathway for solvent transport; a schematic of the CNT distribution in PA matrix is shown in Fig. 7. More recently, Zhang's group modified CNTs by grafting alkyl sulfonic acid side chains and incorporated them into an NF membrane to improve the membrane flux and hydrophilicity [85]. The pure water permeability of this membrane increased by 160% when only 0.01 wt% of sulfonated CNTs was incorporated. An's group used poly-dopamine (PDA), which is easily obtained by self-polymerization under alkaline conditions, to initially coat MWCNTs and thereby improve their dispersion in water and interactions with the PA matrix [87]. Subsequently, the water-dispersible PDA-MWCNTs were blended with PEI and incorporated into the PA layer via the IP process. The pure-water permeability of the optimized CNT-based membrane was as high as 15.32 L m^{-2} h^{-1} bar^{-1}, which is more than 1.6 times that of the pristine membrane. Furthermore, the positively charged membrane exhibited high rejection of multivalent cations and, thus, has applications in water softening and heavy metal ion removal [87].

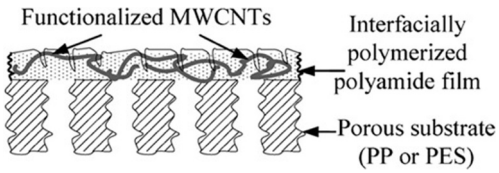

FIG. 7

Schematic of CNTs in a PA matrix [112].

RO membranes, which can reject monovalent ions, such as Na^+ and Cl^-, are widely used in the desalination of seawater or brackish water [113]. Considering the high operation pressure (i.e., the high energy consumption), CNTs have been introduced into RO membranes, and thus, the insufficient flux resulting from the high rejection of monovalent ions must be compensated for. Analogous to NF membranes, many current RO membranes are fabricated by the IP technique with the only difference being the substitution of *m*-phenylenediamine (MPD) for the aqueous solution [114]. Zhao et al. incorporated MWCNTs that had been modified with diisobutyryl peroxide into the PA layer of RO membrane [111]. The water flux of the resulting CNT-based RO membrane increased to 1.75 L m^{-2} h^{-1} bar^{-1} (the flux of the pristine membrane was 0.93 L m^{-2} h^{-1} bar^{-1}) without sacrificing the salt rejection. Meanwhile, the novel TFN membrane possessed better antioxidative and antifouling properties than did the unmodified one. The more negative charges, higher hydrophilicity, and unique nature of the functionalized CNTs are responsible for these membrane performance improvements.

Recently, studies combining IP technology and VF (IP-VF) have been performed to fabricate CNT-based RO membranes. Martin's group incorporated zwitterionic functionalized CNTs (ZCNTs) into a PA thin-film composite (TFC) RO membrane (the synthetic procedure is shown in Fig. 8 [96]). The ZCNTs in the PA layer can offer nanochannels for fast water transport, and the zwitterionic groups located at the ends of the CNTs contribute to the high salt rejection because of strong steric hindrance [96]. On one hand, those membranes, which use CNTs as active layer fillers, commonly have high flux values, likely because of the nanochannels provided by the CNTs. On the other hand, nanomaterials can disrupt part of the cross-link network and thus lead to nanosized defects (Fig. 9), facilitating the transport of water molecules [96]. Furthermore, CNTs have been known to exhibit good antibiofouling

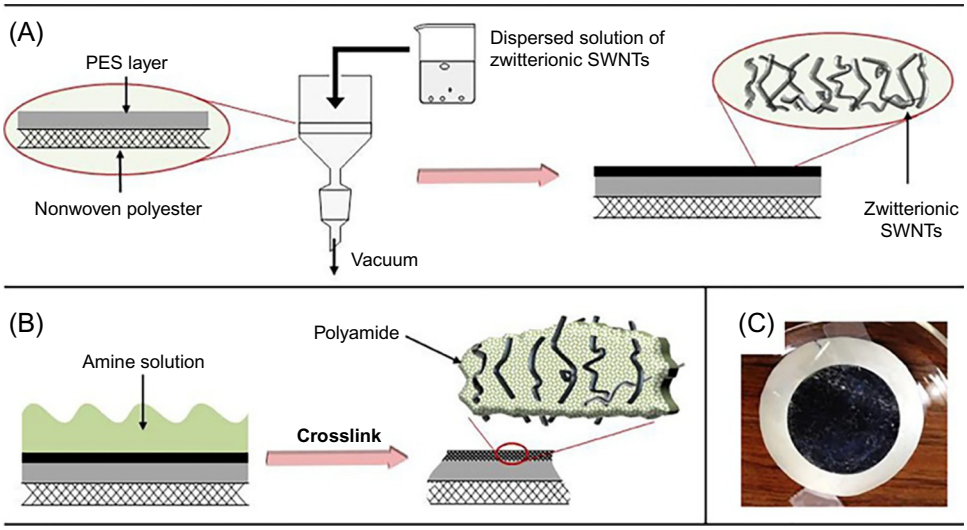

FIG. 8

Cross-sectional schematics of the fabrication of a Z-SWCNT/PA TFN membrane: (A) ZCNTs deposited onto the PES membrane support through vacuum filtration, (B) PA layer formed between the semialigned ZCNTs via IP, and (C) photograph of the top of the ZCNT TFN membrane [96].

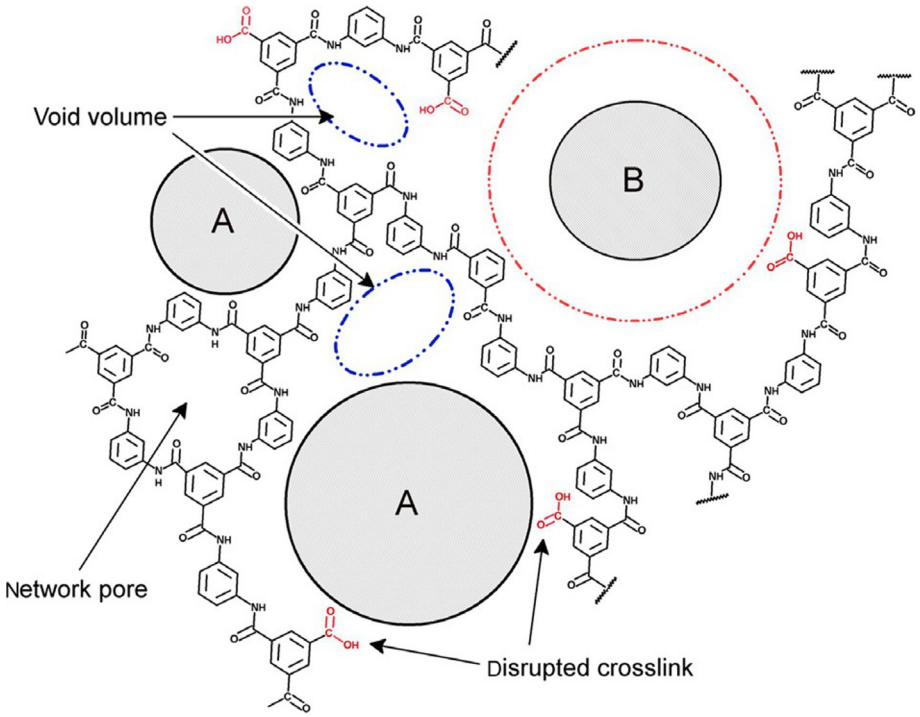

FIG. 9

Schematic illustrating the defects of PA chains in TFN membranes when nanomaterials are present in the PA layer [96].

properties because they can disrupt the metabolic pathways and damage the cell membranes of bacteria [115–117]. Lee's group fabricated a PA-CNT-poly(vinyl alcohol) (PVA) membrane using oxidized CNTs and PVA via an IP-VF method [97]. In their study, CNTs coated with PVA were deposited on the membrane surface; the CNTs provided frictionless channels and imbued the membranes with antibiofouling properties, whereas PVA acted to immobilize the CNTs on the membrane surface [97]. The novel membrane with optimum CNT and PVA contents exhibited encouraging characteristics, including high water flux, high salt rejection, good antibiofouling, and durability; thus, this membrane has promising applications in practical water treatment.

FO, which is a rapidly developing process that is osmotically driven by a concentrated draw solution (DS), possesses several advantages, such as low operating cost, low fouling, and a wide range of feed solutions and has thus attracted substantial attention in a variety of industries [118–120]. Notably, CNT-based membranes can be also applied in the FO field. Rahimpour and coworkers used amine-functionalized MWCNTs as additives in MPD solution to synthesize a novel TFN FO membrane by IP [98]. Those researchers used a 10-mM NaCl solution as the feed solution and a 2-M NaCl solution as the DS. The flux of the optimized TFN membrane reached 95.7 L m^{-2} h^{-1}, which is almost 1.6 times higher than that of the TFC FO membrane. The nanochannels and interfacial gap provided by

CNTs, in addition to the increase in the surface hydrophilicity and roughness, accounted for this membrane's superior flux. However, TFCs with porous substrates usually suffer from severe internal concentration polarization (ICP), which can cause the flux to decline, especially in the FO field [121–123]. Therefore, designing a substrate layer with a low structure parameter S ($S = t\tau/\varepsilon$, where t, τ, and ε are the membrane thickness, tortuosity, and porosity, respectively) to minimize ICP may have great potential in the FO process [101, 124]. Wang et al. fabricated a PES/MWCNT substrate by dispersing MWCNTs-COOH with PES via phase inversion and then prepared the corresponding FO membrane on this substrate by IP using MPD and trimesoyl chloride (TMC) [101]. The FO membrane with this co-system substrate had a higher water-flux value and NaCl rejection than that with the PES substrate alone; this difference can be ascribed to the relatively open interior pore structure, which resulted in less ICP [101].

5 CURRENT HURDLES AND FUTURE OUTLOOK

CNTs have many outstanding advantages in water treatment and desalination applications [125, 126]. However, some critical issues remain to be addressed effectively [127, 128]. The first issue hindering the development of CNTs relates to the synthesis methods. Currently, fabricating CNTs with uniform and size-controlled pores is difficult. The bottom-up organic chemistry approach can synthesize CNTs with the desired pore diameters, but it is time-consuming and expensive and is thus not suitable for industrial production [129]. CNTs with smaller pores tend to exhibit better desalination properties, but MWCNTs with subnanometer pore diameters cannot be synthesized [4]. Furthermore, the synthesis, of few-walled CNTs, SWCNTs, and DWCNTs with small pores is extremely expensive and not straightforward. Because of the imperfect synthesis methods that are currently available, CNT membrane applications cannot be scaled up to the industrial level.

Adding the desired functional groups to CNTs is the second hurdle. CNTs are widely used because of their excellent properties; however, some key characteristics, such as easy aggregation, poor dispersibility in solution, and poor compatibility with organic matrixes, are serious drawbacks. Therefore, functionalizing CNTs is highly necessary. However, the conditions needed to achieve these chemical modifications can be harsh and may destroy the tubular structures of CNTs and thereby reduce their fluxes and rejection abilities. Additionally, it is reported that ions that are attracted to and saturate the CNT tip ends (i.e., the functional groups) may block the nanotubes [130]. Therefore, finding a suitable method for the functionalization of CNTs is important.

Despite their advantages and potentials, the effects of CNTs on the environment and human health cannot be neglected. The emission of CNTs into the environment may represent a safety issue because CNTs can spread quickly in the environment. The toxicities of CNTs, such as lung toxicity and skin irritation, and their potential environmental health risks have been investigated in recent years [131, 132]. Additionally, evidence suggests that CNTs interact strongly with heavy metal ions and organic compounds because of their functional groups and hydrophobic surfaces [133]. Therefore, a sustainable technology for detecting and reducing the impact of CNTs on the environment and human health is urgently needed.

In 2008, Elimelech et al. summarized the development process of CNTs and predicted the future development trends, as shown in Fig. 10 [134]. Currently, these forecasts, including progress toward aligned and functionalized MWCNT membranes with tailored selectivity and antifouling properties,

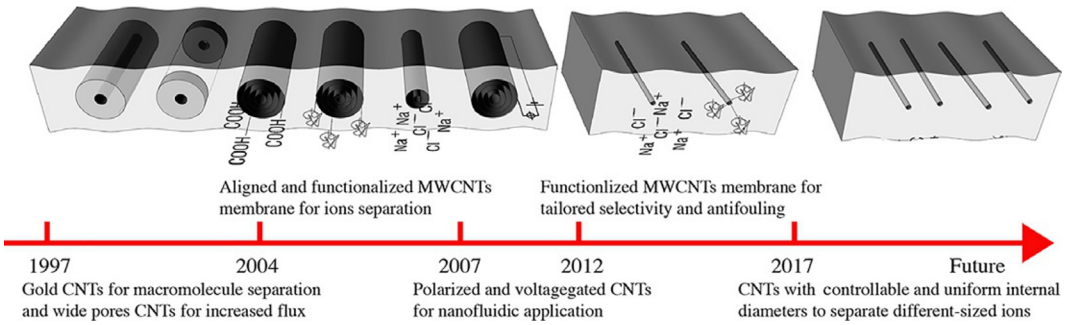

FIG. 10

Research progress and prospects of CNTs [134].

From M.S. Mauter, M. Elimelech, Environmental applications of carbon-based nanomaterials, Environ. Sci. Technol. 42 (2008) 5843–5859.

are becoming the focus of today's research. In future studies, finding straightforward and cost-effective approaches for the synthesis CNTs with controllable and uniform internal diameters to separate different-sized ions will be important. Using mild modification methods to significantly improve CNTs' dispersity in solution and compatibility with organic matrixes is also a trend.

ACKNOWLEDGMENT

This work was financially supported by the Natural Science Foundation of China (21774058, 51778292).

REFERENCES

[1] O. Balcajin, A. Noy, F. Fornasiero, C.P. Grigoropoulos, J.K. Holt, J.B. In, S. Kim, H.G. Park, Nanofluidic carbon nanotube membranes: applications for water purification and desalination, in: Nanotechnology Applications for Clean Water, Elsevier Inc., 2014, pp. 173–188.

[2] W.J. Lau, S. Gray, T. Matsuura, D. Emadzadeh, J. Paul Chen, A.F. Ismail, A review on polyamide thin film nanocomposite (TFN) membranes: history, applications, challenges and approaches, Water Res. 80 (2015) 306–324.

[3] V.K. Upadhyayula, S. Deng, M.C. Mitchell, G.B. Smith, Application of carbon nanotube technology for removal of contaminants in drinking water: a review, Sci. Total Environ. 408 (2009) 1–13.

[4] R. Das, M.E. Ali, S.B.A. Hamid, S. Ramakrishna, Z.Z. Chowdhury, Carbon nanotube membranes for water purification: a bright future in water desalination, Desalination 336 (2014) 97–109.

[5] M. Majumder, N. Chopra, R. Andrews, B.J. Hinds, Nanoscale hydrodynamics: enhanced flow in carbon nanotubes, Nature 438 (2005) 44.

[6] B. Corry, Designing carbon nanotube membranes for efficient water desalination, J. Phys. Chem. B 112 (2008) 1427.

[7] J.K. Holt, H.G. Park, Y. Wang, M. Stadermann, A.B. Artyukhin, C.P. Grigoropoulos, A. Noy, O. Bakajin, Fast mass transport through sub-2-nanometer carbon nanotubes, Science 312 (2006) 1034–1037.
[8] X. Qu, P.J. Alvarez, Q. Li, Applications of nanotechnology in water and wastewater treatment, Water Res. 47 (2013) 3931–3946.
[9] S. Iijima, Helical microtubes of graphite carbon, Nature 354 (1991) 56–58.
[10] M.A.L. Manchado, L. Valentini, J. Biagiotti, J.M. Kenny, Thermal and mechanical properties of single-walled carbon nanotubes-polypropylene composites prepared by melt processing, Carbon 43 (2005) 1499–1505.
[11] F. Vahedi, H.R. Shahverdi, M.M. Shokrieh, M. Esmkhani, Effects of carbon nanotube content on the mechanical and electrical properties of epoxy-based composites, New Carbon Mater. 29 (2014) 419–425.
[12] C.S. Kang, K. Fujisawa, Y.I. Ko, H. Muramatsu, T. Hayashi, M. Endo, H.J. Kim, D. Lim, J.H. Kim, Y.C. Jung, M. Terrones, M.S. Dresselhaus, Y.A. Kim, Linear carbon chains inside multi-walled carbon nanotubes: growth mechanism, thermal stability and electrical properties, Carbon 107 (2016) 217–224.
[13] R. Chavan, U. Desai, P. Mhatre, R. Chinchole, A review: carbon nanotubes, Int. J. Pharm. Sci. Rev. Res. 13 (2012) 124–134.
[14] Q. Liu, W. Ren, B. Liu, Z.G. Chen, F. Li, H. Gong, H.M. Cheng, Synthesis, purification and opening of short cup-stacked carbon nanotubes, J. Nanosci. Nanotechnol. 9 (2009) 4554–4560.
[15] C. Santhosh, V. Velmurugan, G. Jacob, S.K. Jeong, A.N. Grace, A. Bhatnagar, Role of nanomaterials in water treatment applications: a review, Chem. Eng. J. 306 (2016) 1116–1137.
[16] M.F. De Volder, S.H. Tawfick, R.H. Baughman, A.J. Hart, Carbon nanotubes: present and future commercial applications, Science 339 (2013) 535–539.
[17] E. Celik, H. Park, H. Choi, H. Choi, Carbon nanotube blended polyethersulfone membranes for fouling control in water treatment, Water Res. 45 (2011) 274–282.
[18] L.S. Ying, M.A. Bin Mohd Salleh, H.B.M. Yusoff, S.B. Abdul Rashid, J.B.A. Razak, Continuous production of carbon nanotubes-a review, J. Ind. Eng. Chem. 17 (2011) 367–376.
[19] Y. Kobayashi, H. Nakashima, D. Takagi, Y. Homma, CVD growth of single-walled carbon nanotubes using size-controlled nanoparticle catalyst, Thin Solid Films 464–465 (2004) 286–289.
[20] M. Keidar, Factors affecting synthesis of single wall carbon nanotubes in arc discharge, J. Phys. D. Appl. Phys. 40 (2007) 2388–2393.
[21] M. Kusaba, Y. Tsunawaki, Production of single-wall carbon nanotubes by a XeCl excimer laser ablation, Thin Solid Films 506–507 (2006) 255–258.
[22] T. Yamada, T. Namai, K. Hata, D.N. Futaba, K. Mizuno, J. Fan, M. Yudasaka, M. Yumura, S. Iijima, Size-selective growth of double-walled carbon nanotube forests from engineered iron catalysts, Nat. Nanotechnol. 1 (2006) 131–136.
[23] C.L. Cheung, A. Kurtz, H. Park, C.M. Lieber, Diameter-controlled synthesis of carbon nanotubes, J. Phys. Chem. B 106 (2002) 2429–2433.
[24] T.A. Hilder, D. Gordon, S.H. Chung, Salt rejection and water transport through boron nitride nanotubes, Small 5 (2009) 2183.
[25] F. Fornasiero, H.G. Park, J.K. Holt, M. Stadermann, C.P. Grigoropoulos, A. Noy, O. Bakajin, Ion exclusion by sub-2-nm carbon nanotube pores, PNAS 105 (2008) 17250.
[26] B.J. Hinds, N. Chopra, T. Rantell, R. Andrews, V. Gavalas, L.G. Bachas, Aligned multiwalled carbon nanotube membranes, Science 303 (2004) 62–65.
[27] M. Yu, H.H. Funke, J.L. Falconer, R.D. Noble, Gated ion transport through dense carbon nanotube membranes, J. Am. Chem. Soc. 132 (2010) 8285–8290.
[28] J.A. Thomas, A.J. Mcgaughey, Reassessing fast water transport through carbon nanotubes, Nano Lett. 8 (2008) 2788–2793.
[29] A. Striolo, The mechanism of water diffusion in narrow carbon nanotubes, Nano Lett. 6 (2006) 633.
[30] D.G. Levitt, Dynamics of a single-file pore: non-fickian behavior, Phys. Rev. A 8 (1973) 3050–3054.

[31] H.A. Chang, Y. Baek, C. Lee, O.K. Sang, S. Kim, S. Lee, S.H. Kim, S.B. Sang, J. Park, J. Yoon, Carbon nanotube-based membranes: fabrication and application to desalination, Ind. Eng. Chem. Res. 18 (2012) 1551–1559.
[32] J.K. Holt, Carbon nanotubes and nanofluidic transport, Adv. Mater. 21 (2009) 3542–3550.
[33] A.F. Ismail, P.S. Goh, S.M. Sanip, M. Aziz, Transport and separation properties of carbon nanotube-mixed matrix membrane, Sep. Purif. Technol. 70 (2009) 12–26.
[34] C. Lee, S. Baik, Vertically-aligned carbon nano-tube membrane filters with superhydrophobicity and super-oleophilicity, Carbon 48 (2010) 2192–2197.
[35] N. Karousis, N. Tagmatarchis, D. Tasis, Current progress on the chemical modification of carbon nanotubes, Chem. Rev. 110 (2010) 5366–5397.
[36] Y. Xing, L. Li, C.C. Chusuei, R.V. Hull, Sonochemical oxidation of multiwalled carbon nanotubes, Langmuir 21 (9) (2005) 4185–4190.
[37] J. Liu, A.G. Rinzler, H. Dai, J.H. Hafner, R.K. Bradley, P.J. Boul, A. Lu, T. Iverson, K. Shelimov, C.B. Huffman, Fullerene pipes, Science 280 (1998) 1253–1256.
[38] V. Georgakilas, K. Kordatos, M. Prato, D.M. Guldi, M. Holzinger, A. Hirsch, Organic functionalization of carbon nanotubes, J. Am. Chem. Soc. 124 (2002) 760–761.
[39] P. He, M.W. Urban, Controlled phospholipid functionalization of single-walled carbon nanotubes, Biomacromolecules 6 (2005) 2455.
[40] Z. Wu, W. Feng, Y. Feng, Q. Liu, X. Xu, T. Sekino, A. Fujii, M. Ozaki, Preparation and characterization of chitosan-grafted multiwalled carbon nanotubes and their electrochemical properties, Carbon 45 (2007) 1212–1218.
[41] X. Deng, G. Jia, H. Wang, H. Sun, X. Wang, S. Yang, T. Wang, Y. Liu, Translocation and fate of multi-walled carbon nanotubes in vivo, Carbon 45 (2007) 1419–1424.
[42] E.B. Malarkey, R.C. Reyes, B. Zhao, R.C. Haddon, V. Parpura, Water soluble single-walled carbon nanotubes inhibit stimulated endocytosis in neurons, Nano Lett. 8 (2008) 3538.
[43] M. Fagnoni, A. Profumo, D. Merli, D. Dondi, P. Mustarelli, E. Quartarone, Water-miscible liquid multi-walled carbon nanotubes, Adv. Mater. 21 (2009) 1761–1765.
[44] C.H. Andersson, H. Grennberg, Reproducibility and efficiency of carbon nanotube end-group generation and functionalization, Eur. J. Org. Chem. 2009 (2009) 4421–4428.
[45] K.K. Lee, Y. Li, Fluorination of single-walled carbon nanotubes via CHF3 plasma, in: 2012 Conference on Optoelectronic and Microelectronic Materials & Devices, 2012, pp. 175–176.
[46] J.L. Stevens, A.Y. Huang, H. Peng, I.W. Chiang, V.N. Khabashesku, J.L. Margrave, Sidewall amino-functionalization of single-walled carbon nanotubes through fluorination and subsequent reactions with terminal diamines, Nano Lett. 3 (2003) 331–336.
[47] Y. Zhu, A.T. Peng, K. Carpenter, J.A. Maguire, N.S. Hosmane, M. Takagaki, Substituted carborane-appended water-soluble single-wall carbon nanotubes: new approach to boron neutron capture therapy drug delivery, J. Am. Chem. Soc. 127 (2005) 9875–9880.
[48] J.J. Stephenson, J.L. Hudson, A. Samina Azad, J.M. Tour, Individualized single walled carbon nanotubes from bulk material using 96% sulfuric acid as solvent, Chem. Mater. 18 (2) (2010) 374–377.
[49] R. Graupner, J. Abraham, D. Wunderlich, A. Vencelová, P. Lauffer, J. Röhrl, M. Hundhausen, A.L. Ley, A. Hirsch, Nucleophilic-alkylation-reoxidation: a functionalization sequence for single-wall carbon nanotubes, J. Am. Chem. Soc. 128 (2006) 6683–6689.
[50] Y. Xu, X. Wang, R. Tian, S. Li, L. Wan, M. Li, H. You, Q. Li, S. Wang, Microwave-induced electrophilic addition of single-walled carbon nanotubes with alkylhalides, Appl. Surf. Sci. 254 (2008) 2431–2435.
[51] S.R. Vogel, M. Katharina, P. Ulrich, M.M. Kappes, R. Clemens, DNA-carbon nanotube interactions and nanostructuring based on DNA, Phys. Status Solidi 244 (2010) 4026–4029.

[52] Q. Mu, W. Liu, Y. Xing, H. Zhou, Z. Li, Y. Zhang, L. Ji, F. Wang, Z. Si, A.B. Zhang, Protein binding by functionalized multiwalled carbon nanotubes is governed by the surface chemistry of both parties and the nanotube diameter, J. Phys. Chem. C 112 (2016) 3300–3307.
[53] J.G. Yu, K.L. Huang, S.Q. Liu, J.C. Tang, Preparation and characterization of polycarbonate modified multiple-walled carbon nanotubes, Chin. J. Chem. 26 (2008) 560–563.
[54] X.H. Huang, R.P. Johnson, S.I. Song, I. Kim, Noncovalent functionalization of carbon nanotubes by fluorescent polypeptides: supramolecular conjugates with pH-dependent absorbance and fluorescence, J. Nanosci. Nanotechnol. 13 (2013) 7406–7412.
[55] D. Zhang, L. Shi, J. Fang, X. Li, K. Dai, Preparation and modification of carbon nanotubes, Mater. Lett. 59 (2005) 4044–4047.
[56] S. Lefrant, J.P. Buisson, J. Schreiber, O. Chauvet, M. Baibarac, I. Baltog, Raman studies of carbon nanotubes and polymer nanotube composites, Mol. Cryst. Liq. Cryst. 415 (2004) 125–132.
[57] G.R. Dieckmann, A.B. Dalton, P.A. Johnson, J. Razal, J. Chen, G.M. Giordano, E. Muñoz, I.H. Musselman, R.H. Baughman, R.K. Draper, Controlled assembly of carbon nanotubes by designed amphiphilic peptide helices, J. Am. Chem. Soc. 125 (2003) 1770–1777.
[58] O.K. Kim, J. Je, J.W. Baldwin, S. Kooi, P.E. Pehrsson, L.J. Buckley, Solubilization of single-wall carbon nanotubes by supramolecular encapsulation of helical amylose, J. Am. Chem. Soc. 125 (2003) 4426–4427.
[59] K.Y. Cho, S.Y. Yong, H.Y. Seo, Y.H. Park, H.N. Jang, K.Y. Baek, H.G. Yoon, Rational design of multi-amphiphilic polymer compatibilizers: versatile solubility and hybridization of non-covalently functionalized CNT nanocomposites, ACS Appl. Mater. Interfaces 7 (2015) 9841–9850.
[60] T. Morishita, M. Matsushita, Y. Katagiri, K. Fukumori, Noncovalent functionalization of carbon nanotubes with maleimide polymers applicable to high-melting polymer-based composites, Carbon 48 (2010) 2308–2316.
[61] A. Bianco, K. Kostarelos, M. Prato, Applications of carbon nanotubes in drug delivery, Curr. Opin. Chem. Biol. 9 (2005) 674–679.
[62] V.N. Popov, Carbon nanotubes: properties and application, Mater. Sci. Eng. R 43 (2004) 61–102.
[63] A. Bianco, K. Kostarelos, C.D. Partidos, M. Prato, Biomedical applications of functionalised carbon nanotubes, Chem. Commun. (5) (2005) 571.
[64] C. Cuevas, D. Kim, K.P. Katuri, P. Saikaly, S.P. Nunes, C. Cuevas, D. Kim, K.P. Katuri, P. Saikaly, S.P. Nunes, Electrochemically active polymeric hollow fibers based on poly(ether-b-amide)/carbon nanotubes, J. Membr. Sci. 545 (2018) 323–328.
[65] T.H. Lee, Y.L. Min, H.D. Lee, S.R. Ji, H.W. Kim, H.B. Park, Highly porous carbon nanotube/polysulfone nanocomposite supports for high-flux polyamide reverse osmosis membranes, J. Membr. Sci. 539 (2017) 441–450.
[66] I.W. Azelee, P.S. Goh, W.J. Lau, A.F. Ismail, M.R. Dashtarzhandi, K.C. Wong, M.N. Subramaniam, Enhanced desalination of polyamide thin film nanocomposite incorporated with acid treated multiwalled carbon nanotube-titania nanotube hybrid, Desalination 409 (2017) 163–170.
[66a] H. Matsumoto, S. Tsuruoka, Y. Hayashi, K. Abe, K. Hata, S. Zhang, Y. Saito, M. Aiba, T. Tokunaga, T. Iijima, Water transport phenomena through membranes consisting of vertically-aligned double-walled carbon nanotube array, Carbon 120 (2017) 358–365.
[67] S. Majeed, D. Fierro, K. Buhr, J. Wind, B. Du, A. Boschetti-De-Fierro, V. Abetz, Multi-walled carbon nanotubes (MWCNTs) mixed polyacrylonitrile (PAN) ultrafiltration membranes, J. Membr. Sci. 403–404 (2012) 101–109.
[68] J. Zhang, Z. Xu, M. Shan, B. Zhou, Y. Li, B. Li, J. Niu, X. Qian, Synergetic effects of oxidized carbon nanotubes and graphene oxide on fouling control and anti-fouling mechanism of polyvinylidene fluoride ultrafiltration membranes, J. Membr. Sci. 448 (2013) 81–92.

[69] S. Qiu, L. Wu, X. Pan, L. Zhang, H. Chen, C. Gao, Preparation and properties of functionalized carbon nanotube/PSF blend ultrafiltration membranes, J. Membr. Sci. 342 (2009) 165–172.
[70] Y. Yang, C. Nie, Y. Deng, C. Cheng, C. He, L. Ma, C.S. Zhao, Improved antifouling and antimicrobial efficiency for ultrafiltration membrane by functional carbon nanotubes, RSC Adv. 6 (2016) 88265–88276.
[71] H.Q. Wu, B.B. Tang, P.Y. Wu, Novel ultrafiltration membranes prepared from a multi-walled carbon nanotubes/polymer composite, J. Membr. Sci. 362 (2010) 374–383.
[72] L. Dumée, K. Sears, J. Schütz, N. Finn, M. Duke, S. Gray, Characterization and evaluation of carbon nanotube bucky-paper membranes for direct contact membrane distillation, J. Membr. Sci. 351 (2010) 36–43.
[73] L. Dumée, K. Sears, J. Schütz, N. Finn, M. Duke, S. Gray, The impact of hydrophobic coating on the performance of carbon nanotube bucky-paper membranes in membrane distillation, Desalination 283 (2011) 64–67.
[74] S. Roy, M. Bhadra, S. Mitra, Enhanced desalination via functionalized carbon nanotube immobilized membrane in direct contact membrane distillation, Sep. Purif. Technol. 136 (2014) 58–65.
[75] K. Gethard, O. Saekhow, S. Mitra, Water desalination using carbon-nanotube-enhanced membrane distillation, ACS Appl. Mater. Interfaces 3 (2015) 110.
[76] M. Bhadra, S. Roy, S. Mitra, Flux enhancement in direct contact membrane distillation by implementing carbon nanotube immobilized PTFE membrane, Sep. Purif. Technol. 161 (2016) 136–143.
[77] F. Soyekwo, Q. Zhang, R. Gao, Y. Qu, R. Lv, M. Chen, A. Zhu, Q. Liu, Metal in situ surface functionalization of polymer-grafted-carbon nanotube composite membranes for fast efficient nanofiltration, J. Mater. Chem. A 5 (2016).
[78] Y. Han, Y. Jiang, C. Gao, High-flux graphene oxide nanofiltration membrane intercalated by carbon nanotubes, ACS Appl. Mater. Interfaces 7 (2015) 8147–8155.
[79] L. Wang, X. Song, T. Wang, S. Wang, Z. Wang, C. Gao, Fabrication and characterization of polyethersulfone/carbon nanotubes (PES/CNTs) based mixed matrix membranes (MMMs) for nanofiltration application, Appl. Surf. Sci. 330 (2015) 118–125.
[80] V. Vatanpour, M. Esmaeili, M.H.D.A. Farahani, Fouling reduction and retention increment of polyethersulfone nanofiltration membranes embedded by amine-functionalized multi-walled carbon nanotubes, J. Membr. Sci. 466 (2014) 70–81.
[81] V. Vatanpour, S.S. Madaeni, R. Moradian, S. Zinadini, B. Astinchap, Fabrication and characterization of novel antifouling nanofiltration membrane prepared from oxidized multiwalled carbon nanotube/polyethersulfone nanocomposite, J. Membr. Sci. 375 (2011) 284–294.
[82] H. Wu, B. Tang, P. Wu, Optimization, characterization and nanofiltration properties test of MWNTs/polyester thin film nanocomposite membrane, J. Membr. Sci. 428 (2013) 425–433.
[83] J. Shen, C. Yu, H. Ruan, C. Gao, B.V. Bruggen, Preparation and characterization of thin-film nanocomposite membranes embedded with poly(methyl methacrylate) hydrophobic modified multiwalled carbon nanotubes by interfacial polymerization, J. Membr. Sci. 442 (2013) 18–26.
[84] S.M. Xue, Z.L. Xu, Y.J. Tang, C.H. Ji, Polypiperazine-amide nanofiltration membrane modified by different functionalized multiwalled carbon nanotubes (MWCNTs), ACS Appl. Mater. Interfaces 8 (2016) 19135–19144.
[85] J. Zheng, M. Li, K. Yu, J. Hu, X. Zhang, L. Wang, Sulfonated multiwall carbon nanotubes assisted thin-film nanocomposite membrane with enhanced water flux and anti-fouling property, J. Membr. Sci. 524 (2017) 344–353.
[86] J. Zheng, M. Li, Y. Yao, X. Zhang, L. Wang, Zwitterionic carbon nanotube assisted thin-film nanocomposite membranes with excellent efficiency for separation of mono/divalent ions from brackish water, J. Mater. Chem. A 5 (2017) 13730–13739.
[87] F.Y. Zhao, Y.L. Ji, X.D. Weng, Y.F. Mi, C.C. Ye, Q.F. An, C.J. Gao, High-flux positively charged nanocomposite nanofiltration membranes filled with poly(dopamine) modified multiwall carbon nanotubes, ACS Appl. Mater. Interfaces 8 (2016) 6693–6700.

[88] M.B. Wu, Y. Lv, H.C. Yang, L.F. Liu, X. Zhang, Z.K. Xu, Thin film composite membranes combining carbon nanotube intermediate layer and microfiltration support for high nanofiltration performances, J. Membr. Sci. 515 (2016) 238–244.
[89] F.Y. Zhao, Q.F. An, Y.L. Ji, C.J. Gao, A novel type of polyelectrolyte complex/MWCNT hybrid nanofiltration membranes for water softening, J. Membr. Sci. 492 (2015) 412–421.
[90] J. Guo, K. Zhao, X. Zhang, Z. Cai, M. Chen, T. Chen, J. Wei, Preparation and characterization of carboxyl multi-walled carbon nanotubes/calcium alginate composite hydrogel nano-filtration membrane, Mater. Lett. 157 (2015) 112–115.
[91] S.S. Madaeni, S. Zinadini, V. Vatanpour, Preparation of superhydrophobic nanofiltration membrane by embedding multiwalled carbon nanotube and polydimethylsiloxane in pores of microfiltration membrane, Sep. Purif. Technol. 111 (2013) 98–107.
[92] H. Zarrabi, M.E. Yekavalangi, V. Vatanpour, A. Shockravi, M. Safarpour, Improvement in desalination performance of thin film nanocomposite nanofiltration membrane using amine-functionalized multiwalled carbon nanotube, Desalination 394 (2016) 83–90.
[93] H.J. Kim, K. Choi, Y. Baek, D.G. Kim, J. Shim, J. Yoon, J.C. Lee, High-performance reverse osmosis CNT/polyamide nanocomposite membrane by controlled interfacial interactions, ACS Appl. Mater. Interfaces 6 (2014) 2819–2829.
[94] J. Farahbaksh, M. Delnavaz, V. Vatanpour, Investigation of raw and oxidized multiwalled carbon nanotubes in fabrication of reverse osmosis polyamide membranes for improvement in desalination and antifouling properties, Desalination 410 (2017) 1–9.
[95] W.F. Chan, H.Y. Chen, A. Surapathi, M.G. Taylor, X. Shao, E. Marand, J.K. Johnson, Zwitterion functionalized carbon nanotube/polyamide nanocomposite membranes for water desalination, ACS Nano 7 (2013) 5308–5319.
[96] W.F. Chan, E. Marand, S.M. Martin, Novel zwitterion functionalized carbon nanotube nanocomposite membranes for improved RO performance and surface anti-biofouling resistance, J. Membr. Sci. 509 (2016) 125–137.
[97] H.J. Kim, Y. Baek, K. Choi, D.G. Kim, H. Kang, Y.S. Choi, J. Yoon, J.C. Lee, The improvement of anti-biofouling properties of a reverse osmosis membrane by oxidized CNTs, RSC Adv. 4 (2014) 32802–32810.
[98] M. Amini, M. Jahanshahi, A. Rahimpour, Synthesis of novel thin film nanocomposite (TFN) forward osmosis membranes using functionalized multi-walled carbon nanotubes, J. Membr. Sci. 435 (2013) 233–241.
[99] X. Zhao, J. Li, C. Liu, A novel TFC-type FO membrane with inserted sublayer of carbon nanotube networks exhibiting the improved separation performance, Desalination 413 (2017) 176–183.
[100] M. Tian, Y.N. Wang, R. Wang, Synthesis and characterization of novel high-performance thin film nanocomposite (TFN) FO membranes with nanofibrous substrate reinforced by functionalized carbon nanotubes, Desalination 370 (2015) 79–86.
[101] Y. Wang, R. Ou, Q. Ge, H. Wang, T. Xu, Preparation of polyethersulfone/carbon nanotube substrate for high-performance forward osmosis membrane, Desalination 330 (2013) 70–78.
[102] J.K. Holt, A. Noy, T. Huser, A. David Eaglesham, O. Bakajin, Fabrication of a carbon nanotube-embedded silicon nitride membrane for studies of nanometer-scale mass transport, Nano Lett. 4 (2004) 2245–2250.
[103] P.S. Goh, A.F. Ismail, B.C. Ng, Carbon nanotubes for desalination: performance evaluation and current hurdles, Desalination 308 (2013) 2–14.
[104] D.E. Suk, T. Matsuura, P. Hobum, L. Youngmoo, D. Hasson, Development of novel surface modified phase inversion membranes having hydrophobic surface-modifying macromolecule (nSMM) for vacuum membrane distillation, Desalination 261 (2010) 300–312.
[105] Z.D. Hendren, J. Brant, M.R. Wiesner, Surface modification of nanostructured ceramic membranes for direct contact membrane distillation, J. Membr. Sci. 331 (2009) 1–10.

[106] E.M.V. Hoek, M.T.M. Pendergast, A.K. Ghosh, Nanotechnology-based membranes for water purification, in: Nanotechnology Applications for Clean Water, Elsevier Inc., pp. 47–58 (Chapter 9).
[107] A. Figoli, T. Marino, S. Simone, E.D. Nicolo, X.M. Li, S. Tornaghi, E. Drioli, ChemInform abstract: towards non-toxic solvents for membrane preparation: a review, Green Chem. 45 (2015) 4034–4059.
[108] W. Gao, H. Liang, J. Ma, M. Han, Z.L. Chen, Z.S. Han, G.B. Li, Membrane fouling control in ultrafiltration technology for drinking water production: a review, Desalination 272 (2011) 1–8.
[109] J.H. Choi, J. Jegal, W.N. Kim, Fabrication and characterization of multi-walled carbon nanotubes/polymer blend membranes, J. Membr. Sci. 284 (2006) 406–415.
[110] S. Inukai, R. Cruzsilva, J. Ortizmedina, A. Morelosgomez, K. Takeuchi, T. Hayashi, A. Tanioka, T. Araki, S. Tejima, T. Noguchi, High-performance multi-functional reverse osmosis membranes obtained by carbon nanotube·polyamide nanocomposite, Sci. Rep. 5 (2015) 13562.
[111] H. Zhao, S. Qiu, L. Wu, L. Zhang, H. Chen, C. Gao, Improving the performance of polyamide reverse osmosis membrane by incorporation of modified multi-walled carbon nanotubes, J. Membr. Sci. 450 (2014) 249–256.
[112] S. Roy, S.A. Ntim, S. Mitra, K.K. Sirkar, Facile fabrication of superior nanofiltration membranes from interfacially polymerized CNT-polymer composites, J. Membr. Sci. 375 (2011) 81–87.
[113] L.F. Greenlee, D.F. Lawler, B.D. Freeman, B. Marrot, P. Moulin, Reverse osmosis desalination: water sources, technology, and today's challenges, Water Res. 43 (2009) 2317–2348.
[114] J. Hu, Y. Pu, M. Ueda, X. Zhang, L. Wang, Charge-aggregate induced (CAI) reverse osmosis membrane for seawater desalination and boron removal, J. Membr. Sci. 520 (2016) 1–7.
[115] A.S.B. Estevez, S. Kang, M. Elimelech, A single-walled-carbon-nanotube filter for removal of viral and bacterial pathogens, Small 4 (2008) 481–484.
[116] S. Kang, M. Herzberg, D.F. Rodrigues, M. Elimelech, Antibacterial effects of carbon nanotubes: size does matter! Langmuir 24 (2008) 6409–6413.
[117] A. Tiraferri, C.D. Vecitis, M. Elimelech, Covalent binding of single-walled carbon nanotubes to polyamide membranes for antimicrobial surface properties, ACS Appl. Mater. Interfaces 3 (2011) 2869–2877.
[118] T.Y. Cath, A.E. Childress, M. Elimelech, Forward osmosis: principles, applications, and recent developments, J. Membr. Sci. 281 (2006) 70–87.
[119] S. Zou, Y. Gu, D. Xiao, C.Y. Tang, The role of physical and chemical parameters on forward osmosis membrane fouling during algae separation, J. Membr. Sci. 366 (2011) 356–362.
[120] R. Wang, L. Shi, C.Y. Tang, S. Chou, C. Qiu, A.G. Fane, Characterization of novel forward osmosis hollow fiber membranes, J. Membr. Sci. 355 (2010) 158–167.
[121] A. Tiraferri, N.Y. Yip, W.A. Phillip, J.D. Schiffman, M. Elimelech, Relating performance of thin-film composite forward osmosis membranes to support layer formation and structure, J. Membr. Sci. 367 (2011) 340–352.
[122] C.Y. Tang, Q. She, W.C.L. Lay, R. Wang, R. Field, A.G. Fane, Modeling double-skinned FO membranes, Desalination 283 (2011) 178–186.
[123] C.H. Tan, H.Y. Ng, Modified models to predict flux behavior in forward osmosis in consideration of external and internal concentration polarizations, J. Membr. Sci. 324 (2008) 209–219.
[124] S. Zhang, R. Zhang, Y.C. Jean, D.R. Paul, T.S. Chung, Cellulose esters for forward osmosis: characterization of water and salt transport properties and free volume, Polymer 53 (2012) 2664–2672.
[125] S.A. Aani, V. Gómez, C.J. Wright, N. Hilal, Fabrication of antibacterial mixed matrix nanocomposite membranes using hybrid nanostructure of silver coated multi-walled carbon nanotubes, Chem. Eng. J. 326 (2017) 721–736.
[126] L. Ma, X. Dong, M. Chen, Z. Li, C. Wang, F. Yang, Y. Dong, Fabrication and water treatment application of carbon nanotubes (CNTs)-based composite membranes: a review, Membranes 7 (2017) 16.

[127] B. Sarkar, S. Mandal, Y.F. Tsang, P. Kumar, K.H. Kim, Y.S. Ok, Designer carbon nanotubes for contaminant removal in water and wastewater: a critical review, Sci. Total Environ. 612 (2017) 561.
[128] F. Fornasiero, Water vapor transport in carbon nanotube membranes and application in breathable and protective fabrics, Curr. Opin. Chem. Eng. 16 (2017) 1–8.
[129] H. Omachi, T. Nakayama, E. Takahashi, Y. Segawa, K. Itami, Initiation of carbon nanotube growth by well-defined carbon nanorings, Nat. Chem. 5 (2013) 572–576.
[130] B. Corry, Water and ion transport through functionalised carbon nanotubes: implications for desalination technology, Energy Environ. Sci. 4 (2011) 751–759.
[131] G. Tejral, N.R. Panyala, J. Havel, Carbon nanotubes: toxicological impact on human health and environment, J. Appl. Biomed. 7 (2009) 1–13.
[132] C.W. Lam, J.T. James, R. Mccluskey, S. Arepalli, R.L. Hunter, A review of carbon nanotube toxicity and assessment of potential occupational and environmental health risks, Crit. Rev. Toxicol. 36 (2006) 189.
[133] X. Ren, C. Chen, M. Nagatsu, X. Wang, Carbon nanotubes as adsorbents in environmental pollution management: a review, Chem. Eng. J. 170 (2011) 395–410.
[134] M.S. Mauter, M. Elimelech, Environmental applications of carbon-based nanomaterials, Environ. Sci. Technol. 42 (2008) 5843–5859.

CHAPTER

14

CARBON NANOTUBE AND GRAPHENE OXIDE BASED MEMBRANES

Aneela Sabir, Maria Wasim, Muhammad Shafiq, Tahir Jamil
Department of Polymer Engineering and Technology, University of the Punjab, Lahore, Pakistan

GRAPHICAL ABSTRACT

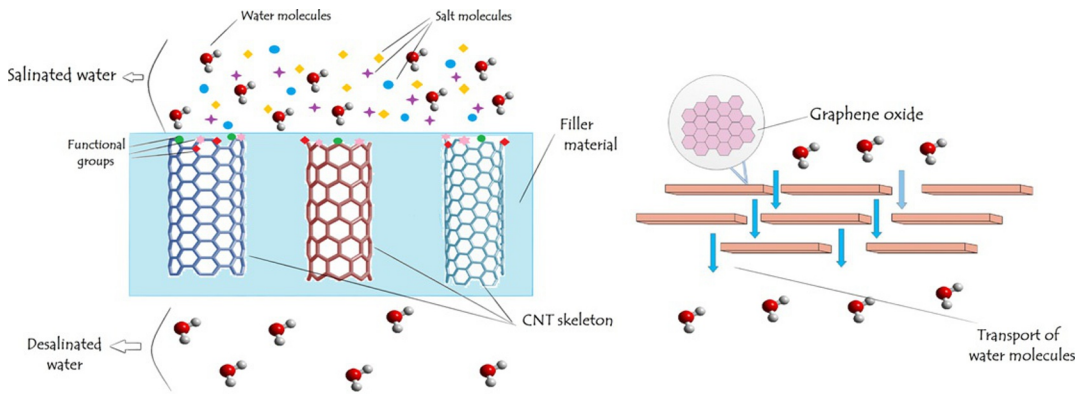

Transport of water molecules through CNT and graphene oxide

1 MEMBRANE

A membrane is regarded as a semipermeable barrier that allows certain species of a specific size to pass through it while blocking others, as illustrated in Fig. 1. The characteristics of membranes are what allow which species are to be filtered. Membrane science is a quickly growing field with real-time applications, including water purification and desalination. Research has been ongoing for developing a precise, cost-effective membrane, although the accuracy, precise ability, and cost-effectiveness can be dependent on the class of membrane used. However, until now, fabricating atomic-scale pores within membranes that allow the perfect retention of ions and molecules depending on their size is a challenging issue [1].

Nanoscale Materials in Water Purification. https://doi.org/10.1016/B978-0-12-813926-4.00019-7

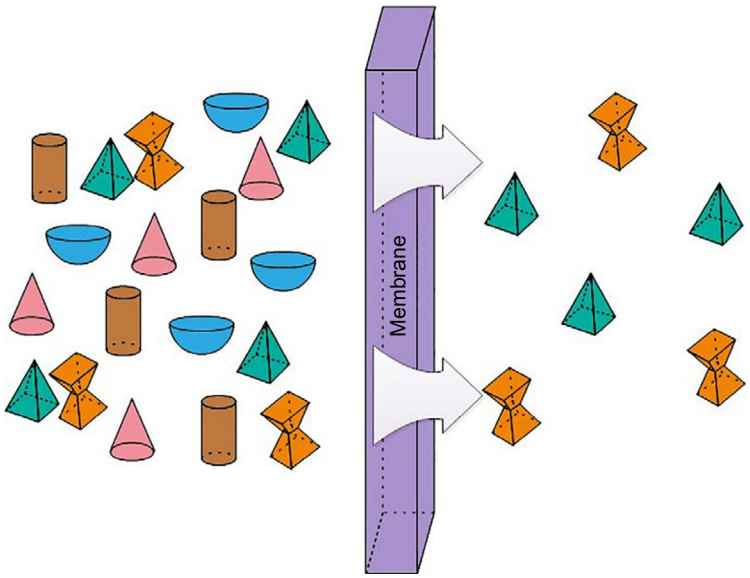

FIG. 1

Schematic illustration of a membrane system.

2 CURRENT MEMBRANES

Conventionally, membranes have been categorized into two types: polymeric [2–5] and inorganic membranes [6–8]. Based on their applicability, choosing which among them is the most ideal membrane type is difficult as they each have their own advantages and disadvantages. For example, polymeric membranes have shown excellent permeability, as well selectivity, but have limited resistance to high temperatures, solvents, and corrosive substances [9], whereas inorganic membranes, mostly composed of metals and ceramics, show superior thermal and mechanical stability, along with high mechanical and structural strength. However, these membranes have shown high selectivity at the expense of poor or limited permeability, which can deter their use for commercial-scale applications. Also, microporous silica-based membranes, which belong to the inorganic membrane class, have been employed for molecular sieving applications. The prime issue is fabricating a size-dependent filtration membrane with the precise control of pore size (in submicron range). However, the use of zeolite membranes, a type of inorganic membrane, has been fixing these issues to some extent.

Zeolite-based membranes have shown stability at high temperatures, as well as a hydrophilic character and organophilic characteristics [10–13]. Zeolite membranes could be employed at the molecular scale but have some limitation, including their ion-exchange capability, solid acidity, adsorption, and the catalytic nature of zeolite. These limitations can act as properties for certain applications but forbid the use of zeolite as a neutral filler in membranes. It has also been shown that zeolite can also catalyze the filtration for a few species [11, 12, 14]. Other factors that can influence the potential applicability of zeolite are the presence of various-sized zeolite pores (within the submicron range) in membranes. To resolve this issue, crystals of zeolite should be grown in such a manner that flow only occurs through zeolitic pores. But this can enhance the processing steps for synthesizing precise molecular sieves of zeolite.

3 CARBON-BASED MEMBRANES

In recent decades, carbon nanotube (CNT) membranes have gained attention for water filtration applications [9, 15, 16]. Research associated with CNT membranes has brought a breakthrough for the understanding of the science related to filtration and its mechanism. However, the use of CNTs is limited because of the complications linked to making their inner hollow cavity in atomic range, which requires a complex synthesis process. On the other hand, a gold nanotube, with an inner diameter of 0.6 nm, has been successfully synthesized [17]. For this purpose, the template-based electrochemical growth technique was employed. Unfortunately, these unique nanotubes have not gained substantial attention because of the complex synthesizing step, along with the issues linked to their reproduction. Graphene, discovered in 2004, has shown outstanding properties in every field it has been tested for. Several studies have shown the properties of pure graphene [18–20].

A pure graphene membrane having zero pores showed a superior permeation flux, mainly because of the tightly packed structure of atoms in the lattice as well as the presence of π-electrons, which repel all the other electrons. Because of its high permeability, graphene can be employed for the synthesis of impermeable capsule shells, gels, and sealed cages. Under normal conditions, using pure graphene films as a molecular sieving agent is still a dare. However, research has been going on to achieve a substantial water flux by using a graphene membrane. Being a two-dimensional (2D) planar structure, graphene has mechanical strength; it requires low pressure to ensure an ultra-fast gas phase and liquid-phase filtration.

3.1 CARBON NANOTUBE IN MEMBRANES TECHNOLOGY

CNTs are composed of cylindrical-shaped graphite sheets (an allotropic form of carbon) curved up in a roll-like structure with the appearance of a latticework railing [21]. Single-walled carbon nanotubes (SWCNTs) have a cylindrical shape consisting of a single shell of graphene, whereas the multiwalled carbon nanotubes (MWCNTs) consist of more than one layer of graphene sheets. Both classes of CNTs are widely employed directly for desalination purposes [22–24] or indirectly for separating foreign substances that can disturb the desalination process [25]. Using CNTs for desalination is a promising technique because it can require low energy consumption. The flow of water through CNT channels is usually frictionless and allows a specific size range of particles to pass through it. The presence of hollow cylindrical tubes in CNTs with high aspect ratio and the hydrophobic inner tubes improve the flux properties, making it favorable to use for desalination.

3.1.1 Water transport through CNT inner hollow cavity

The presence of smooth, hydrophobic inner hollow cavities of CNTs acts in a favor of the natural, continuous flow of water with a very low adsorption rate, as illustrated in Fig. 2. The aligned CNTs in a membrane are of great interest for those fabricating CNT membranes. The pore diameter of the aligned CNTs has a determining effect on the water transport through them. The motion of water molecules through the hollow cavity of CNTs usually follows Fickian motion [26], which demonstrates the types of molecular motion as, first, a disorderly mass flowing through the cavity whereas, second, the motion of water molecules via a one-directional tube is a single-file mechanism. According to this mechanism, the molecules hinder each other when passing through the tube [27]. The water molecules' diffusion through the CNTs' channel is an extremely synchronized movement and can be better elucidated by the ballistic motion of a water chain [26, 28].

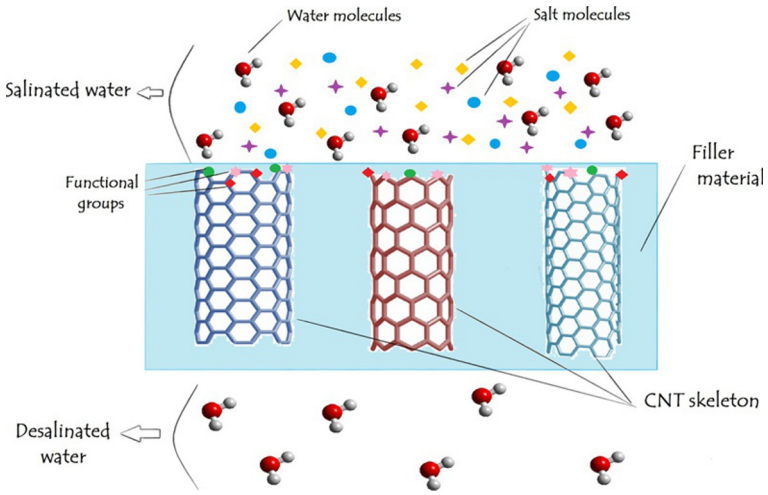

FIG. 2

Transport of water molecules through hollow CNT structure.

Generally, the water molecules do not follow simple fluids mechanics [29]. The term *nanofluidics*, instead of simple fluidics, is used to simulate the water movement through the nanotube structure [28]. The water passing through the nanochannels has a slippery nature [30] in which the water, acting as a nanofluid, slides through the nanochannel with an insignificant change in friction.

3.1.2 Functionalization of CNT

To improve the functionality and performance properties of CNT membrane for water purification, they are often subjected to functionalization as a pretreatment process. The pure CNTs often form an agglomerate that considerably drops the water flux, as well as the selectivity of the foreign materials. In general, CNTs are contaminated with metal catalysts, their impurities, and physical heterogeneities [31]. Moreover, CNTs can be crowned into hemispheres that are more like a fullerene curvature during synthesis or the purification step [32]. These crowned CNTs often have opened tips that could easily be oxidized into the desired functional groups that can be used as traps for attracting selective particles. Additionally, the functionalization can be both positive, like NH_3^+, or negative, like —COO—, and sulfonic acids, and, in some cases, hydrophobic, like the aromatic rings on the surface of CNTs [33, 34]. In this way, CNT membranes could be made selective for specific applications, along with an increased flux of water through cylindrical nanoholes, as shown in Fig. 2. The performance properties of functionalized membranes have been shown to have better permselectivity, thermal and chemical stability, increased mechanical strength, fouling resistivity, and self-cleaning functions [35]. The point-end functionalized CNT membrane can have selective groups at the nanotubes' ends or at the interior core. Both cases have shown enhanced water flux and selectivity of pollutants [36]. The numerous nanoparticles, including Ag, Au, Pt, Cu, TiO_2, polymers, and biomolecules, can also be decked on the CNT's surface to broadened the application for water purification [37].

3.1.3 Atomic structure and morphology of CNTs

CNTs can be imagined as a plane of graphite rolled to form a cylindrical tube, which is distinct from the diamond structure, where a three-dimensional (3D) cubic crystal structure is formed, with each carbon atom having its four nearest neighbors arranged in a tetrahedron. Graphite is designed as a plane sheet of carbon atoms arranged hexagonally. In such cases, the individual carbon atoms have three nearby atoms. Then, the sheet of graphite is rolled to form carbon nanotubes. The characteristics of CNTs are governed by the atomic array (i.e., how the sheet is rolled), the length and the diameter of the nanotube, and the surface morphology.

Nanotube structure

The nanotube's atomic structure is usually portrayed by helicity or the tube chirality. The tube chirality is described by chiral angle θ and chiral vector $\vec{C}\,h$. As illustrated in Fig. 3, we can visualize cutting the sheet of graphite along the red line and then rolling the tube so that the tip of the chiral vector dashes is the tail. This is why it also termed a rolled-up vector, commonly represented as Eq. (1):

$$\vec{C}\,h = n\vec{a}_1 + m\vec{a}_2\,, \tag{1}$$

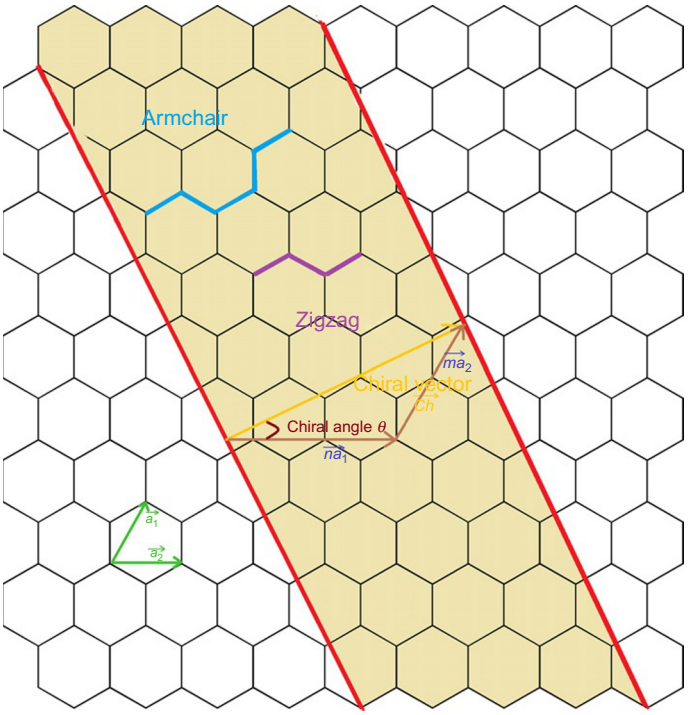

FIG. 3

Schematic display of graphite sheet rolled to form a nanotube.

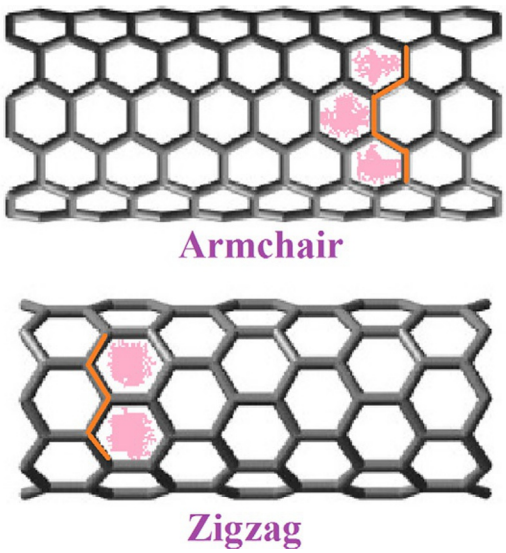

FIG. 4

Representation of armchair and zigzag structure of carbon nanotubes.

where n and m represent the number of steps present along the zigzag carbon bonds and $\vec{a_1}$ and $\vec{a_2}$ are the unit vectors illustrated in Fig. 3. The amount of twist in the nanotube is determined by the chiral angle. The distinction between zigzag and armchair nanotube structures is described in Fig. 4. The chirality of nanotube structure has a substantial effect on material characteristics. Predominantly, the chirality of tube structure has a strong influence on the electric properties of CNTs. The graphite is considered semimetallic in nature, whereas the CNT can be a semiconductor or metallic in nature depending on to tube's chirality [38]. The influence of chirality on mechanical properties has been studied. Yakobson et al. [39, 40] studied the instability of nanotubes beyond linear response. The studies showed that CNTs are noteworthy, robust in sustaining harsh strain with no marks of plasticity or brittleness.

3.1.4 Properties of CNT membranes

Mechanical properties

CNTs are the strongest and hardest materials ever discovered with respect to their tensile strength and elastic modulus, respectively. Such strength arises from the sp^2 covalent bond that forms between the carbon atoms, that is, less in the presence of disordered arrangements and defects in the sidewalls of nanotubes. The young modulus of SWCNTs is determined by the chirality and diameter of the nanotube. An experimental study has shown that in the case of MWCNTs, only the outer shell supports stress when nanotubes are incorporated into the matrix phase, whereas in SWCNTs, a prominent decline in the individual modulus has been observed because of poor intertube cohesion [41]. The tensile strength of CNTs can be 50 times greater than steel. These characteristics collectively give the small mass carbon atoms their remarkable potential in various fields, such as aerospace, as first proposed by Arthur C. Clarke. CNTs also have extraordinary electronic properties. It is noteworthy that CNTs can

be metal or semiconductors depending on their chirality. They have higher conductivities that make their possible use in electronic devices, particularly nanobased ones. Still, such useful device nanotubes require thousands be prepared in a specific arranged pattern. To do this, a controlled synthesis step is needed. CNTs are being employed in numerous fields, including the creation of the flat-panel displays of scanning probe microscopes and sensing devices. The remarkable properties of CNTs will indisputably lead to many uses for it [42–46].

Electrical properties

CNTs have remarkable electrical properties. A single graphite sheet is semimetal, as it has characteristics between metals and semiconductors. When the graphite planar sheet is twisted to form a nanotube, not only do the carbon atom have to line up around the perimeter of the nanotube, but the quantum mechanical wave functions of the electrons should also be matched. According to theoretical studies, the metallic nanotube can have an electrical current density 1000 times greater than most of the metals such as copper [44]. The macroscopic structures of a singular nanotube can be elucidated by several electrical properties, such as capacitance, resistance, and inductance, that are due to intrinsic structure of nanotube and its interaction with other things. The transport of electricity inside the hollow cylindrical nanotube can be affected by defects, scattering phenomena and through lattice vibrations that primarily lead to resistance analogous to bulk material. However, the one-dimensional (1D) character of CNTs, along with their solid covalent bonding, considerably affects these processes. In 1D material, the scattering phenomena by small angles is generally not allowed as there is only frontward and backward motion of carrier occur. Significantly, the 1D character of CNTs cause the new type of quantized resistance linked to its interaction with 3D macroscopic materials, such as metallic electrodes. In addition, with quantized resistance, several new types of interaction resistance, such as Schottky barriers at metal-semiconducting nanotube interfaces, and parasitic resistance are simply due to bad contacts. The intrinsic structures of CNTs lead to capacitance mainly linked to the density of states and its independence from electrostatics. Last, CNTs have inductance that resists any change in the current flowing through the nanotubes. Conventionally, inductance depends on the diameter of the nanotube, its geometrical structure, and the magnetic permeability of the media. CNTs often behave as transmission lines, owing to their inductance in response to the alternating current signal [42, 44].

Thermal properties

It is anticipated that all nanotubes have a high thermal conductivity, particularly along the axis, demonstrating the characteristics termed "ballistic conduction." It is expected that nanotubes will transmit up to 6000 W m^{-1} K^{-1} at ambient temperature in comparison to copper, which only transmits 385 W m^{-1} K^{-1}. The thermal stability of CNTs is up to 2800°C in vacuum and 750°C in air media. In traditional graphite fibers, thermal expansion is strongly anisotropic; in contrast, CNT thermal expansion is mainly isotropic. Such a property can be beneficial for carbon-carbon composites. It is predicted that CNTs with few defects will show low thermal expansion coefficients [46, 47].

Chemical properties

The curved graphene sheet showed a high thermal stability as compared to the planar graphite sheet. The curvature allows the mixing of σ- and π-orbital, leading to hybridization among the orbitals. As the diameter of SWCNTs gets smaller, the degree of hybridization increases as the reactivity of CNTs is directly dependent on the mismatched π-orbital because of the increased curve. For that reason,

a difference must be prepared between the sidewall and the tip-end caps of a nanotube. Also the small-diameter nanotube shows high reactivity. The side walls or tip-end caps can be covalently modified; for example, the solubility of CNTs in numerous solvents can be controlled in such a way, whereas achieving the covalent bond attachment to any molecular species to fully sp^2-bonded carbon atoms on sidewalls of nanotubes is quite difficult. Hence, CNTs can be considered chemically inert in nature [48].

Optical properties

In the case of SWCNTs, the optical properties of nanotubes are connected to their quasi-1D nature. Several studies theoretically conducted have demonstrated that the optical nature of chiral CNTs diminishes as the size of nanotubes increases to a certain limit. Consequently, it is likely that other physical characteristics are also affected by these factors. The applicability of the optical activity of CNTs allows it to be used in optical devices [49].

3.1.5 Application of CNTs in desalination

Having clean, safe water is one of the basic human rights. Unfortunately, that right has been deteriorating with population increases, urbanization, and climate change. These factors not only have stalled development of humans but have also created an imbalance in nature cycle [50, 51].

With the advancement in nanotechnology, many impressive nanomaterials, including carbon nanotubes [52], nano-zinc particles [53], electrospun nanofibers [51], and numerous other nanoparticles, have been employed for purifying water, and in particular, CNTs have shown remarkable achievements in purifying wastewater [16].

The current desalination process mostly depends on polymeric reverse-osmosis membranes for separating out the dissolved salts and fine solids [54]. For this process, high pressure is required, which means that high energy consumption is needed to drive the desalination plant. There also exists a high trade-off between the high selectivity and high permeation flux in the membrane design process.

In the last few decades, theoretically calculated [55] and experimental [56] studies have been demonstrated that water transport through nanotubes is several orders of magnitude higher than that through porous materials of comparable size, owing to the high velocity attributed to the smooth, hydrophobic nature of inner cylindrical walls of CNTs. Ordered hydrogen bonds are formed at the interface of water and CNTs that initiate a vapor phase barrier between the nonpolar CNT wall and water molecular chain, causing the frictionless movement of water molecules inside the hollow cylindrical tube. The aligned CNT structural membranes are responsible for the highest permeation flux. Recently, 2-nm aligned membranes have been developed employing the chemical vapor deposition process, followed by a laser-etching process to uncap the nanotubes [57]. The permeation of water molecules through these membranes are of several orders of magnitude higher than the commercially available polycarbonate membranes despite having a smaller pore size. To fully use the hollow structure of CNTs, a vertically aligned high-density membrane was synthesized by Yu et al. [58]. The CNT arrangement was made using a chemical vapor deposition process, and then CNT was immersed in an organic solvent, such as *n*-hexane; then formed layers were dried at room temperature. The evaporation process decreased the layer size up to 5% of its original size, which led to an increased density and a crowded, vertically arranged CNT structure.

The tip of a CNT membrane can be functionalized by achieving ion exclusion. Gong et al. [59] fabricated the ion-selective, controlled nanopores based on SWCNTs with arranged carbonyl oxygen group atoms inside the nanotube. The varying pattern of carbonyl oxygen atoms determined the

hydration structure of Na^+ and K^+ within the hollow structure, which led to tunable ion selectivity. In their work, Majumder et al. [60] functionalized the tips of the CNT structure via an electrochemical grating process using diazonium salts, and they suggest that the separation efficiency of CNTs can be altered by changing voltage. Fornasiero and coworkers [61] introduced a negatively charged functional group via a plasma treatment process that caused an ion rejection up to 98% through an aligned CNT membrane; also, the ion-exclusion process was dominated by the charge-exclusion process.

However, in a high ion-concentrated environment such as the sea or brackish water, the separation ability of the charge-exclusion process can decrease considerably. Until now, the smallest diameter achieved for CNTs is 0.3 nm [62], which is roughly equal to the radius of hydrated sodium ions, which ranges from 0.178 to 0.358 nm, depending on environmental conditions [63, 64] Consequently, fabricating defect-free CNT membranes that have subnanometer pore size can shine a light on future desalination technologies.

3.1.6 Potentiality of CNT membranes

CNT membranes consist of nanopores that are ideal for rejecting micropollutants and ions mostly in the liquid phase. The presence of hydrophobic inner walls in cylindrical nanotubes allows the flow of water with almost zero friction, negating the need of any external force to push the water molecules through the hollow cylindrical pore. CNT membranes have shown less foulant attachment between of cytotoxic effects that kill or eradicate pathogens, thus ultimately increasing the membranes' lives. The selective synthesis or functionalization of CNTs allows the rejection of selective pollutants from water [34, 37]. Last, CNTs can be modified for reuse with less complexity, high durability, and environmentally friendly, devoid of any complicated chemical alteration.

3.2 GRAPHENE OXIDE

The graphene-based materials have been widely studied for numerous thin-film and membrane application as they have unique 2D structure, are only one atom wide, and have remarkable mechanical strength and excellent flexibility [65–67]. Graphene oxide (GO), a derivative of graphene material, has gained an immense attraction for the development of ultra-thin and high-permselective membranes. Because they have a high area-to-thickness ratio and great number of functional groups, GO fragments can be loaded on each other such that they arrange to form thin film or membrane [66, 68]. Graphene oxide (GO) has become one of the excellent materials for membrane fabrication. In 2012, a study demonstrated that a GO membrane allows unrestricted flow of water through it but hinders everything else in vapor form [69]. However, this study did not rule out the joint propagation of organic molecules present in water passing through the GO membrane. The ease of fabricating the thin GO layers to form the membrane act in favor of their practical use. Generally, graphene does not allow anything to pass through it. However, graphene oxide (GO) has constantly shown superior membrane properties and provides a great potential for commercial use.

3.2.1 Graphene oxide membrane

Graphene-based functional membranes have gained recent attention as outstanding candidates for filtration and separation processes because of to their porous microstructure [70, 71]. Unimpeded permeation flux of water through the submicrometer-thick GO membranes was compared with impermeable membranes for a performance study for liquids, gases, and vapors, such as helium. The high

permeability is attributed both to the capillary-driven force and low friction flow that are present between the 2D channels of pure graphene [69]. As the derivative of graphene, the advancements of GO and reduced graphene forms have moved toward the use or water purification purpose [72–75]. Distinct form the nanosheets of graphene that have nanopores, the selective separation property is mainly due to the presence of numerous nanochannels inside the assembled membranes that compose an interlayer gallery, lengthened paths, and the functional groups present on the surface [70]. Because of the abundance of oxygen-containing functional groups inside the GO nanosheets, it is facile to arrange them into the laminar-structure membrane through spray coating, spin or dip coating, vacuum filtration, or layer-by-layer assembly techniques [66].

3.2.2 Preparation of GO membrane

GO can be generally prepared by an amended Hummers method, where graphite flakes are used as starting material [76, 77]. In the synthesis process, graphite flakes are first subjected to oxidization by employing strong oxidizing agents, such as $NaNO_3$, $KMnO_4$, and concentrated sulfuric acid. The single-layer GO sheets are then exfoliated by long, continuous stirring or are ultrasonicated [78]. Compared with graphene surface, these chemically treated GO flakes have numerous functional groups on their edges and surface, for example, carboxyl and hydroxyl groups [79]. The presence of the hydroxyl groups on the GO flakes allows them to dissolve in water or any other polar solvents, thus reducing the cost of forming graphene-oxide-based materials, such as GO thin films [67, 79, 80].

The initial crystal size of the graphite flakes and the purification stage govern the diameter of GO flakes, which differ from several hundred nanometers to micrometers. Through a self-assembly process, GO flakes are arranged on top of each other, forming a continuous laminar-structure membrane. Between the GO flakes exists a hydrogen bonding responsible for the higher mechanical strength [66]. Although a freestanding thick GO membrane can be synthesized [69], conventionally an ultra-thin membrane is maintained on a porous substrate to enhance the mechanical strength and ease of handling. The porous substrate can be either polymeric or inorganic material, either in the form of a hollow fibrous structure or a flat sheet [72, 81, 82].

There are numerous processes to synthesize GO membranes; the simplest is by vacuum filtration. In this process, the GO suspension is filtered onto a substrate so that the width of the membrane can be skillfully controlled by the volume of GO filtered. Several studies have suggested that the during the filtration step, the driving force can alter the arrangement of GO sheets in the film [83]. Moreover, in addition to pressure-controlled processes, some fabrication methods employ the surface tension of the liquid for the self-assembly technique of GO sheets. Another method is the evaporation method, which involves heating the GO suspension up to 80°C [68]. The rapid evaporation occurs at the liquid-air interface, ultimately causing to GO sheets to self-assemble and thus their arrangement into a thin film or membrane of GO. Other methods include dip coating, drop coating, and spray coating. In these methods, a suspension of GO is dispersed onto supporting material, and after drying, a GO membrane formed [69, 81].

3.2.3 GO membrane filtration mechanism

A study has demonstrated that a GO membrane with submicrometer thickness can absolutely hinder the flow of liquid and gas molecules, only allowing the permeation of water vapors [69]. This might be due to the presence of an empty interspace between the nonoxidized GO sheets that allows the transport of water vapors through low-friction channels. In another study, the coefficient of water diffusion in these

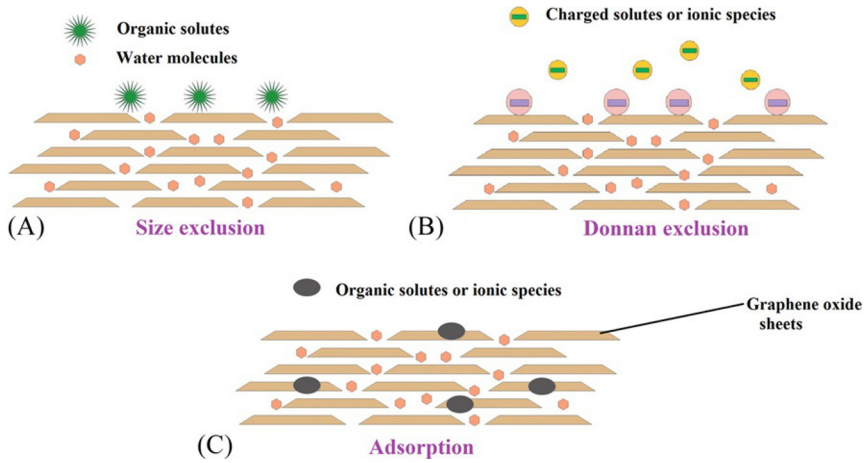

FIG. 5

Schematic display of proposed separation mechanism (A) size exclusion, (B) Donnan exclusion, and (C) adsorption phenomena.

GO nanochannels was illustrated to have 4–5 orders of magnitude, which is generally higher than most of the polymeric membranes. Thus, GO membranes can also be employed for ultra-fast liquid water permeation [84]. From these research findings, a tremendous amount of research on GO membranes for filtration purpose has been done.

Fig. 5 demonstrates all the possible filtration mechanisms of GO membranes in the filtration application. Through the size-exclusion process, the bulky organic molecules could be filtered because of the presence of nanochannels in GO membranes. According to one study, the spacing between GO sheets can be manipulated to increase or decrease the size of nanochannels for the precise separation of ionic species or bulky molecules [85]. Hence, for desalination, water purification, and other pharmaceutical filtration, one can fabricate the specific GO membrane with specific interlayer spacing between GO sheets or by incorporating the nanofiller or nanoparticles with a desired size for desired applications.

Moreover, GO membranes can be subjected to reduction to eliminate the hydrophilic functional groups present on the edges and surface of GO that lead to a decrease in d-spacing. The reduced GO can be prepared either by chemical reduction or thermal annealing in order to remove the oxygen-based functional groups [86]. The simplest and most effective method for reducing GO by eliminating oxygen-containing functional groups, particularly OH groups, is thermal annealing [87]. A rise in temperature assists the thermal deoxygenation of GO. However, in this process, high energy consumption is required, and the degree of oxidation is also difficult to control. On contrary, the chemical reduction of GO required a low temperature range by the addition of reducing agents, such as metal hydrides, hydrazine, and hydroiodic acid [86]. Such reducing agents target different functional groups, thus allowing control over the whole reduction process. The reduced GO provides the channels at the angstrom level without conceding the permeability of water, which is mainly ideal for ionic-level filtration [88]. Also, the prepared GO membranes can be reduced by chemical reduction, providing that the reduced nanochannels have an increased hydrophobic character. Besides the size-exclusion effect,

the material could be separated by Donnan exclusion process [89, 90]. The GO membrane is negatively charged because of the removal of a proton from the carboxyl group present on the edge or tip of the GO sheet. This causes the pure GO membrane to reject the negatively charged organic species or divalent ions [20, 91]. Nevertheless, the charge on GO membrane can be altered [92].

The remarkable rejection can be achieved by the strong adsorption of small ionic species via various interactions with varying regions on GO sheets [93]. This was attributed to the fact that the transition metal cations can form a coordinate interaction with any oxygen-containing functional groups, leading to a complete blockage by GO membrane [94]. In the same way, the permeability of alkaline earth metals and alkali are also predominantly lessened because of the interaction with the sp^2 cluster of GO sheets via cation-π interactions [95].

3.2.4 Microstructures of GO membranes

The microstructure of the GO membrane includes the stacking of GO sheets and the defects present in the membrane that can be influenced by the synthesizing step, which ultimately affects the performance properties of the GO membrane. A study has revealed that a GO membrane fabricated by the drop- or spin-casting method has a denser packed structure and showed a high selectivity for CO_2 [81]. Another study revealed that among GO membranes prepared by three different process—vacuum-assisted filtration, pressure-assisted filtration, and evaporation [96]—the membrane prepared by pressure-assisted filtration process illustrated superior performance properties in butanol dehydration, predominantly because of the arranged laminar structure. The surface roughness and hydrophilicity of GO membranes are the main parameters that can influence the membrane microstructures.

The magnitude of the GO sheets can be influenced the microstructure and thus performance properties of GO membranes in terms of permeability and selectivity [95]. The use of nanosized GO sheets for fabricating membranes showed fewer crumples and folds on the surface when compared to membranes prepared by the use of micron-size GO sheets, even though the interlayer space distance remained constant in both cases. However, XRD results showed a broad peak range in the case of nanosized GO sheets. Moreover, the ions' flow through nanosized GO membrane was also enhanced, mainly because of the less densely packed laminar structure. In a study, GO paper was prepared from large GO sheets showed a more compact structure with ordered microstructures and less structural defects than those fabricated from small GO sheets. Also they showed a superior mechanical strength [97]. The influence of the size of GO sheet used in membranes was studied regarding the evaporation process [98]. The large and bulky micron-sized GO sheet was inclined to move toward the water surface, causing the form of continuous membrane formation after the drying step, while nanosized GO sheets tended to disperse in the water phase, causing a "coffee-ring-stain" type of pattern after drying. This might be due to the increase in surface charge density as a consequence of enhanced edge-to-area ratio.

3.2.5 Modifications, challenges, and prospects

Several alterations have been done to improve the performance properties of GO membranes. Several approaches, including the pore formation of GO sheet and the microstructural path formation, have been tested for forming additional transport channels in pure GO membranes that can ultimately reduce the water transport pathway and hence increase the permeability of water, as shown in Fig. 6 [99, 100]. However, the selectivity of the membrane may be compromised, dropping the filtration property of the

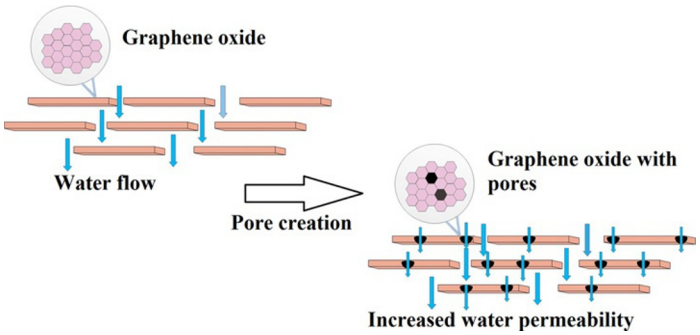

FIG. 6

Water flow through pure graphene oxide and pores generated graphene oxide.

GO membrane. Several studies have been done on cross-linking GO sheets or the decoration of GO sheets with polymeric materials or nanoparticles [91, 101, 102]. The GO-flake interlayer can be modified for selective separation purposes. The increased interaction between the sheets or the flakes of GO ensures the high stability of the membrane. Even though the GO membrane has hydrophilic character, several studies have further improved the hydrophilicity, showing much better results for butanol dehydration [103]. The reduced form of GO has also shown high performance properties in terms of permeability and selectivity in the forward-osmosis and nanofiltration processes [104, 105].

Regardless of the all the remarkable discoveries for the research of GO membranes, some challenges for the commercial application of GO membranes exist. One of the major issues is the stability of GO membranes. Recent research has depicted the implication of ceramic material, as a substrate, releasing various multivalent ions that allow the cross-linking of GO sheets, ultimately improving the stability of membrane in the aqueous phase. On the other hand, polymeric material, when used as a substrate, showed instability in the aqueous phase [106].

Moreover, GO membranes have also shown instability in the air medium as they reduce in size after the drying process. The reduction issue can be solved by storing the membranes in the water phase to avoid excessive drying [72] or by employing the upper sacrificial coating during membrane preparation [107]. Further work is required to solve the stability issue of GO membranes, mainly where the membrane width is just at the submicron level. In addition, there are also some limitations on how to characterize GO membranes in several studies. Their uses beyond fluid filtration can also be explored further.

3.2.6 Comparison of CNTs and graphene oxide-based membranes with other conventional membranes

Conventional RO and NF membranes have shown dense porous structures with good separation properties that can be employed because of their easy fabrication and comparatively low cost. Also, these membranes require that pressure be applied to force the molecules of water to pass through them. On the other hand, MF and UF technologies require less energy consumption but separate out only the suspended solid particles [28, 108], whereas polymer-based membranes have some restrictions, such

as poor resistance toward chemicals and high temperature, membrane fouling, and aging under extreme conditions, mostly in organic solvents [109]. Carbon-based materials, such as CNTs and graphene, or its derivatives GO, have been widely studied because of their easy availability, high mechanical strength, and chemical, as well as thermal, stability [110, 111].

GO can be economically prepared from the pure graphitic flakes via the modified Hummer's method [79]. It consist of single layer of atomic structure having both sp^2 CC and sp^3 CO bonds and numerous oxygen-containing groups, including hydroxyl, carbonyl, and epoxy groups, situated at the basal region and on edges of graphite sheet [111a]. The lateral dimension of GO sheet ranges from nanometers to a few micrometers [111b]. Owing to their high aspect ratio, GO sheets can be arranged on each other to form a thin laminate membrane [66] with excellent separation performance properties for numerous applications, such as gas separation [82], membrane filtration [102], and pervaporation [83]. Additionally, mixed matrix membranes composed of functionalized GO sheets can increase the separation efficiency and overall membrane performance [111c]. Owing to the ultra-fast property of water flow through the carbon nanochannels, GO membranes have great potential in the field of desalination.

The hydrophobic hollow inner cylinders of CNTs allow the frictionless movement of polar water molecules. The presence of nanoscale pore sizes rejects the movement of salts and retains the ions. The choice of membrane type is totally determined by its functionality, energy consumption, robustness, permeability of water, antifouling capability, and selectivity toward contamination. CNT-based membranes have predominantly shown excellent permeation of water molecules, as well as selectivity of salts, thus making them attractive for desalination process [28, 112, 113]. The aligned CNT membranes have been proved to have excellent permeability compared to conventional polymeric RO membranes. Cohen and his coworkers [114] have employed CNT membranes as substitutes for RO membranes to separate salt from wastewater. The altered membranes have shown excellent separation compared to RO membrane [115]; also, they overpower the limitations faced with conventional membranes when employed for water purification techniques. The salt-selectivity capability of CNT-based membranes have shown almost similar performance properties to that of commercial NF membranes [28]. Also, CNT membranes with pore sizes smaller than 2 nm were synthesized [57]; they not only showed an increase in the selectivity of ions but also demonstrated better performance than conventional polycarbonate membranes. Today, research is mainly focus on achieving the pore size smaller than 1 nm that will retain almost all solute particles. By modifying the surface properties of CNTs, it is possible to separate out smaller ionic solutes with high selectivity and greater affinity [61]. Research has been conducted showing that modifying the surface charge of the CNT structure can cause the removal of Na^+. The 100% removal efficiency of $K_3Fe(CN)_6$ has been studied employing carboxyl functional CNT arrays. Such an arrangement forms an electrostatic repulsion at the tips of the CNTs, thus successfully retaining the salt ions. Chan et al. [116] formed the simulation, as well as synthetically formed a CNT membrane with a diameter of 1.5 nm, having two zwitterions at the end of tips, that provide 100% rejection, while 20% rejection was achieved in the case of five carboxyl groups present at the tip end of CNTs. The combined effect may be due to the steric hindrance and electrostatic cloud present at the nanotubes' ends. Ratto and his coworkers [117] have patented their research showing that CNT membranes shown an ion-rejection capability higher than 99%, demonstrating a remarkable achievement in the field of desalination.

3.2.7 Conclusion and future perspective

Pressure-driven membranes are widely used for wastewater purification and in pharmaceutical industry. The exceptional physical and mechanical characteristics shown by carbon-based materials, carbon nanotubes, and graphene oxide, combined with their low density and high area-to-volume ratio, make them suitable candidates for membrane fabrication. The ideal ultra-fast membrane is predicted to have an extremely low thickness to ensure high permeability and mechanical strength for withstanding the applied pressure. Today, there is alarming situation requiring the development of a membrane with the prospect of potential application in environmental research. Such ideal membranes should also exhibit the high selectivity and remarkable permeability. Even though numerous polymeric membranes have been developed for specific purposes, they have shown low permeance. Some shortcomings of using such polymeric membranes for energy, as well as environmental, purposes are their poor temperature resistivity and chemical stability in presence of acid, bases, or organic solvents [118, 119]. All the previously mentioned problems linked to polymeric membranes have led to the development of substitute membranes. Owing to their superior mechanical strength, chemical stability, accessibility of functional groups, and eco-friendly nature, carbon-based materials are being extensively researched for membrane purpose. Primarily, CNTs are considered as a remarkable contender for membrane fabrication mainly because of their 1D hollow cylindrical structure, along with their superior mechanical property. Nevertheless, the commercial application of these vertically aligned CNTs for membrane fabrication is quite challenging. Consequently, using CNTs membranes at the commercial scale remains theoretical [113, 120]. Then, the amorphous carbon structure, such as that of diamonds, has been employed for membrane fabrication because of to their harness and chemically inert behavior [121, 122]. However, their real-life use is also very restricted, owing to their high energy utilization and the size of equipment needed [123]. We consider GO to be the material of interest for membrane use. Recent research on the stability on GO in the aqueous phase has paved the way for its future use [106]. The numerous studies reporting on GO membranes [69, 124], along with GO being used as a layered material [125], will maintain the versatile future of the GO. Definitely, there are some advantages and disadvantages regarding the experimental results and the proposed transport mechanism. Nonetheless, these can be undoubtedly understood in the near future through ongoing continuous efforts. Compared with other membrane materials, GO membranes foremost have a superiority owing to the simplicity of their fabrication method, which provides a uniform pore-size distribution throughout the membrane. Moreover, the GO membrane can be altered according to the needs for real-time application. Also, the thin membrane, with its high permselectivity, is also linked to issues such as reproducibility, durability, and scalability. To the contrary, the multilayer membranes have prospects for real-life applications because their thickness can be controlled, but they also have some restrictions, such as the thermal stability of GO membrane [123].

REFERENCES

[1] R.K. Joshi, S. Alwarappan, M. Yoshimura, V. Sahajwalla, Y. Nishina, Graphene oxide: the new membrane material, Appl. Mater. Today 1 (1) (2015) 1–12, https://doi.org/10.1016/j.apmt.2015.06.002.

[2] D.F. Sanders, Z.P. Smith, R. Guo, L.M. Robeson, J.E. McGrath, D.R. Paul, B.D. Freeman, Energy-efficient polymeric gas separation membranes for a sustainable future: a review, Polymer 54 (18) (2013) 4729–4761, https://doi.org/10.1016/j.polymer.2013.05.075.

[3] P. Shao, R.Y.M. Huang, Polymeric membrane pervaporation, J. Membr. Sci. 287 (2) (2007) 162–179, https://doi.org/10.1016/j.memsci.2006.10.043.
[4] M. Ulbricht, Advanced functional polymer membranes, Polymer 47 (7) (2006) 2217–2262, https://doi.org/10.1016/j.polymer.2006.01.084.
[5] C. Zhao, S. Nie, M. Tang, S. Sun, Polymeric pH-sensitive membranes—a review, Prog. Polym. Sci. 36 (11) (2011) 1499–1520, https://doi.org/10.1016/j.progpolymsci.2011.05.004.
[6] X. Chen, S.Y.E. Yeo, J.Y.I. Woo, Y.E. Zhou, L. Hong, Lanthanum-doped kaolinite for hierarchical bi-modal porous inorganic membrane, J. Eur. Ceram. Soc. 37 (10) (2017) 3443–3451, https://doi.org/10.1016/j.jeurceramsoc.2017.04.009.
[7] L. Cot, A. Ayral, J. Durand, C. Guizard, N. Hovnanian, A. Julbe, A. Larbot, Inorganic membranes and solid state sciences, Solid State Sci. 2 (3) (2000) 313–334, https://doi.org/10.1016/S1293-2558(00)00141-2.
[8] T.L. Ward, T. Dao, Model of hydrogen permeation behavior in palladium membranes, J. Membr. Sci. 153 (2) (1999) 211–231, https://doi.org/10.1016/S0376-7388(98)00256-7.
[9] M. Wasim, A. Sabir, M. Shafiq, A. Islam, T. Jamil, Preparation and characterization of composite membrane via layer by layer assembly for desalination, Appl. Surf. Sci. 396 (2017) 259–268, https://doi.org/10.1016/j.apsusc.2016.10.098.
[10] J. Caro, M. Noack, Zeolite membranes – recent developments and progress, Microporous Mesoporous Mater. 115 (3) (2008) 215–233, https://doi.org/10.1016/j.micromeso.2008.03.008.
[11] L. Li, J. Dong, T.M. Nenoff, R. Lee, Desalination by reverse osmosis using MFI zeolite membranes, J. Membr. Sci. 243 (1) (2004) 401–404, https://doi.org/10.1016/j.memsci.2004.06.045.
[12] L. Li, N. Liu, B. McPherson, R. Lee, Influence of counter ions on the reverse osmosis through MFI zeolite membranes: implications for produced water desalination, Desalination 228 (1) (2008) 217–225, https://doi.org/10.1016/j.desal.2007.10.010.
[13] E.E. McLeary, J.C. Jansen, F. Kapteijn, Zeolite based films, membranes and membrane reactors: progress and prospects, Microporous Mesoporous Mater. 90 (1) (2006) 198–220, https://doi.org/10.1016/j.micromeso.2005.10.050.
[14] M. Severance, B. Wang, K. Ramasubramanian, L. Zhao, U.S. Winston Ho, P.K. Dutta, Rapid crystallization of Faujasitic zeolites, Langmuir 30 (2014) 6929–6937.
[15] W. Falath, A. Sabir, K.I. Jacob, Highly improved reverse osmosis performance of novel PVA/DGEBA cross-linked membranes by incorporation of Pluronic F-127 and MWCNTs for water desalination, Desalination 397 (2016) 53–66, https://doi.org/10.1016/j.desal.2016.06.019.
[16] A. Sabir, M. Shafiq, A. Islam, A. Sarwar, M.R. Dilshad, A. Shafeeq, T. Jamil, Fabrication of tethered carbon nanotubes in cellulose acetate/polyethylene glycol-400 composite membranes for reverse osmosis, Carbohydr. Polym. 132 (2015) 589–597, https://doi.org/10.1016/j.carbpol.2015.06.035.
[17] K.B. Jirage, J.C. Hulteen, C.R. Martin, Nanotuble-based molecular-filtration membranes, Science 278 (1997) 655–658.
[18] M.S.H. Boutilier, C. Sun, S.C. O'Hern, A. Harold, N.G. Hadjiconstantinou, R. Karnik, Implications of permeations through intrinsic defects in graphene on the design of defect-tolerant membranes for gas separation, ACS Nano 8 (1) (2014) 841–849.
[19] S.C. O'Hern, M. Boutilier, J.C. Idrobo, Y. Song, J. Kong, T. Laoui, M. Atieh, R. Karnik, Selective ionic transport through tunable sub-nanometer pores in single-layer graphene membranes, Nano Lett. 14 (3) (2014) 1234–1241.
[20] Y. Han, Z. Xu, C. Gao, Ultrathin graphene nanofiltration membrane for waterpurification, Adv. Funct. Mater. 23 (29) (2013) 3693–3700.
[21] E.T. Thostenson, Z. Ren, T.-W. Chou, Advances in the science and technology of carbon nanotubes and their composites: a review, Compos. Sci. Technol. 61 (13) (2001) 1899–1912, https://doi.org/10.1016/S0266-3538(01)00094-X.

[22] K. Dai, L. Shi, D. Zhang, J. Fang, NaCl adsorption in multi-walled carbon nanotube/active carbon combination electrode, Chem. Eng. Sci. 61 (2) (2006) 428–433, https://doi.org/10.1016/j.ces.2005.07.030.
[23] H. Li, L. Zou, Ion-exchange membrane capacitive deionization: a new strategy for brackish water desalination, Desalination 275 (1) (2011) 62–66, https://doi.org/10.1016/j.desal.2011.02.027.
[24] A.T. Nasrabadi, M. Foroutan, Ion-separation and water-purification using single-walled carbon nanotube electrodes, Desalination 277 (1) (2011) 236–243, https://doi.org/10.1016/j.desal.2011.04.028.
[25] L. Joseph, J. Heo, Y.-G. Park, J.R.V. Flora, Y. Yoon, Adsorption of bisphenol A and 17α-ethinyl estradiol on single walled carbon nanotubes from seawater and brackish water, Desalination 281 (2011) 68–74, https://doi.org/10.1016/j.desal.2011.07.044.
[26] A. Striolo, The mechanism of water diffusion in narrow carbon nanotubes, Nano Lett. 6 (4) (2006) 633–639.
[27] D.G. Lcvitt, Dynamics of a single-file pore: non-Fickian behavior, Phys. Rev. A 8 (6) (1973) 3050–3054.
[28] C.H. Ahn, Y. Baek, C. Lee, S.O. Kim, S. Kim, S. Lee, … J. Yoon, Carbon nanotube-based membranes: fabrication and application to desalination, J. Ind. Eng. Chem. 18 (5) (2012) 1551–1559, https://doi.org/10.1016/j.jiec.2012.04.005.
[29] J.A. Thomas, A.J.H. McGaughey, Reassessing fast water transport through carbon nanotubes, Nano Lett. 8 (9) (2008) 2788–2793.
[30] J.K. Holt, Carbon nanotubes and nanofluidic transport, Adv. Mater. 21 (5) (2009) 3542–3550.
[31] M.S. Mauter, M. Elimelech, Environmental applications of carbon-based nanomaterials, Environ. Sci. Technol. 42 (16) (2008) 5843–5859.
[32] J. Li, H.T. Ng, A. Cassell, W. Fan, H. Chen, Y. Qi, J. Koehne, J. Han, M. Meyyappan, Carbon nanotube nanoelectrode array for ultrasensitive DNA detection, Nano Lett. 3 (5) (2003) 597–602.
[33] P.S. Goh, A.F. Ismail, B.C. Ng, Carbon nanotubes for desalination: performance evaluation and current hurdles, Desalination 308 (2013) 2–14, https://doi.org/10.1016/j.desal.2012.07.040.
[34] S. Kar, R.C. Bindal, P.K. Tewari, Carbon nanotube membranes for desalination and water purification: challenges and opportunities, Nano Today 7 (5) (2012) 385–389, https://doi.org/10.1016/j.nantod.2012.09.002.
[35] X. Qu, P.J.J. Alvarez, Q. Li, Applications of nanotechnology in water and wastewater treatment, Water Res. 47 (12) (2013) 3931–3946, https://doi.org/10.1016/j.watres.2012.09.058.
[36] M. Majumder, B. Corry, Anomalous decline of water transport in covalently modified carbon nanotube membranes, Chem. Commun. 47 (27) (2011) 7683–7685.
[37] E. Van Hooijdonk, C. Bittencourt, R. Snyders, J.F. Colomer, Functionalization of vertically aligned carbon nanotubes, Beilstein Int. J. Nanotechnol. 4 (1) (2013) 129–152.
[38] M.S. Dresselhaus, G. Dresselhaus, P.C. Eklund, Electronic Structure Science of Fullerenes and Carbon Nanotubes, Academic Press, San Diego, 1996, pp. 413–463 (Chapter 12).
[39] B.I. Yakobson, C.J. Brabec, J. Bernholc, Nanomechanics of carbon tubes: instabilities beyond linear range, Phys. Rev. Lett. 76 (14) (1996) 2511–2514.
[40] B.I. Yakobson, G. Samsonidze, G.G. Samsonidze, Atomistic theory of mechanical relaxation in fullerene nanotubes, Carbon 38 (11) (2000) 1675–1680, https://doi.org/10.1016/S0008-6223(00)00093-2.
[41] P.J.F. Harris, Carbon Nanotubes and Related Structures: New Materials for the 21st Century, Cambridge University Press, Cambridge, 1999.
[42] P.R. Bandaru, Electrical properties and applications of carbon nanotube structures, J. Nanosci. Nanotechnol. 7 (2007) 1–29.
[43] M.B. Nardelli, J.L. Fattebert, D. Orlikowski, C. Roland, Q. Zhao, J. Bernholc, Mechanical properties, defects and electronic behavior of carbon nanotubes, Carbon 38 (11) (2000) 1703–1711, https://doi.org/10.1016/S0008-6223(99)00291-2.
[44] H. Dai, A. Javey, E. Pop, D. Mann, Y. Lu, Electrical transport properties and field effect transistors of carbon nanotubes, Nano Lett. (1) (2006) 1.

[45] M. Meo, M. Rossi, Prediction of Young's modulus of single wall carbon nanotubes by molecular-mechanics based finite element modelling, Compos. Sci. Technol. 66 (11) (2006) 1597–1605, https://doi.org/10.1016/j.compscitech.2005.11.015.
[46] E. Pop, D. Mann, J. Cao, Q. Wang, K. Goodson, H. Dai, Negative differential conductance and hot phonons in suspended nanotube molecular wires, Phys. Rev. Lett. (15) (2006) 95.
[47] H. Stahl, J. Appenzeller, R. Martel, P. Avouris, B. Lengeler, Intertube coupling in ropes of single-wall carbon nanotubes, Phys. Rev. Lett. 85 (2000) 5186.
[48] V. Lordi, N. Yao, Molecular mechanics of binding in carbon-nanotube-polymer composites, J. Mater. Res. 15 (12) (2000) 2770–2779.
[49] H. Kataura, Y. Kumazawa, Y. Maniwa, I. Umezu, S. Suzuki, Y. Ohtsuka, Y. Achiba, Optical properties of single-wall carbon nanotubes, Synth. Metals 103 (1) (1999) 2555–2558, https://doi.org/10.1016/S0379-6779(98)00278-1.
[50] A. Sabir, A. Islam, M. Shafiq, A. Shafeeq, M.T.Z. Butt, N.M. Ahmad, … T. Jamil, Novel polymer matrix composite membrane doped with fumed silica particles for reverse osmosis desalination, Desalination 368 (2015) 159–170, https://doi.org/10.1016/j.desal.2014.12.041.
[51] M. Wasim, A. Sabir, M. Shafiq, A. Islam, M. Azam, T. Jamil, Mixed matrix membranes: two step process modified with electrospun (carboxy methylcellulose sodium salt/sepiolite) fibers for nanofiltration, J. Ind. Eng. Chem. 50 (2017) 172–182, https://doi.org/10.1016/j.jiec.2017.02.011.
[52] M. Wasim, S. Sagar, A. Sabir, M. Shafiq, T. Jamil, Decoration of open pore network in polyvinylidene fluoride/MWCNTs with chitosan for the removal of reactive orange 16 dye, Carbohydr. Polym. 174 (2017) 474–483, https://doi.org/10.1016/j.carbpol.2017.06.086.
[53] A. Sabir, W. Falath, K.I. Jacob, M. Shafiq, N. Gull, A. Islam, T. Jamil, Integrally skinned nano-cellular crosslinked asymmetric thin films infused with PEO-PPO-PEO block copolymer/ZnO-NPs for desalination using sea salt, Mater. Chem. Phys. 183 (2016) 595–605, https://doi.org/10.1016/j.matchemphys.2016.09.022.
[54] A. Sabir, W. Falath, K.I. Jacob, M. Shafiq, M.A. Munawar, A. Islam, T. Jamil, Hyperbranched polyethyleneimine induced polycationic membranes for improved fouling resistance and high RO performance, Eur. Polym. J. 85 (2016) 266–278, https://doi.org/10.1016/j.eurpolymj.2016.10.032.
[55] G. Hummer, J.C. Rasaiah, J.P. Noworyta, Water conduction through the hydrophobic channel of a carbon nanotube, Nature 414 (2001) 188–190.
[56] M. Majumder, N. Chopra, R. Andrews, B.J. Hinds, Nanoscale hydrodynamics-enhanced flow in carbon nanotubes, Nature 438 (44) (2005).
[57] J.K. Holt, H.G. Park, Y. Wang, M. Stadermann, A.B. Artyukhin, C.P. Grigoropoulos, A. Noy, O. Bakajin, Fast mass transport through sub-2-nanometer carbon nanotubes, Science 312 (5776) (2006) 1034–1037.
[58] M. Yu, H.H. Funke, J.L. Falconer, R.D. Noble, High density, vertically aligned carbon nanotube membranes, Nano Lett. 9 (1) (2009) 225–229.
[59] X. Gong, J. Li, X. Ke, J. Wang, H. Yang, A controllable molecular sieve for Na + and K + ions, J. Am. Chem. Soc. 132 (6) (2010) 1873–1877.
[60] M. Majumder, X. Zhan, R. Andrews, B.J. Hinds, Voltage gated carbon nanotube membranes, Langmuir 23 (16) (2007) 8624–8631.
[61] F. Fornasiero, H.G. Park, J.K. Holt, M. Stadermann, C.P. Grigoropoulos, A. Noy, O. Bakajin, Ion exclusion by sub-2-nm carbon nanotube pores, Proc. Natl. Acad. Sci. U. S. A. 105 (45) (2008) 17250–17255.
[62] X. Zhao, Y. Liu, S. Inoue, T. Suzuki, R.O. Jones, Y. Ando, Smallest carbon nanotube is 3 angstrom in diameter, Phys. Rev. Lett. (12) (2004) 92.
[63] M. Carrillo-Tripp, M.L. San-Román, J. Hernańdez-Cobos, H. Saint-Martin, I. Ortega-Blake, Ion hydration in nanopores and the molecular basis of selectivity, Biophys. Chem. 124 (3) (2006) 243–250, https://doi.org/10.1016/j.bpc.2006.04.012.

[64] B. Tansel, J. Sager, T. Rector, J. Garland, R.F. Strayer, L. Levine, … J. Bauer, Significance of hydrated radius and hydration shells on ionic permeability during nanofiltration in dead end and cross flow modes, Sep. Purif. Technol. 51 (1) (2006) 40–47, https://doi.org/10.1016/j.seppur.2005.12.020.
[65] J.S. Bunch, S.S. Verbridge, J.S. Alden, A.M. van der Zande, J.M. Parpia, H.G. Craighead, P.L. McEuen, Impermeable atomic membranes from graphene sheets, Nano Lett. 8 (2008) 2458–2462.
[66] D.A. Dikin, S. Stankovich, E.J. Zimney, R.D. Piner, G.H.B. Dommett, G. Evmenenko, S.T. Nguyen, R.S. Ruoff, Preparation and characterization of graphene oxide paper, Nature 448 (2007) 457–460.
[67] Y. Zhu, S. Murali, W. Cai, X. Li, J.W. Suk, J.R. Potts, R.S. Ruoff, Graphene and graphene oxide: synthesis, properties, and applications, Adv. Mater. 22 (2010) 3906–3924.
[68] C. Chen, Q.-H. Yang, Y. Yang, W. Lv, Y. Wen, P.-X. Hou, M. Wang, H.-M. Cheng, Self-assembled free-standing graphite oxide membrane, Adv. Mater. 21 (2009) 3007–3011.
[69] R.R. Nair, H.A. Wu, P.N. Jayaram, I.V. Grigorieva, A.K. Gei, Unimpeded permeation of water through helium leak-tight graphene based membranes, Science 335 (6067) (2012) 442–444.
[70] N. Wei, X. Peng, Z. Xu, Understanding water permeation in graphene oxide membranes, Appl. Mater. Interfaces 6 (2014) 5877–5883.
[71] L. Qiu, X. Zhang, W. Yang, Y. Wang, G.P. Simon, D. Li, Controllable corrugation of chemically converted graphene sheet in water and potential application for nanofiltration, Chem. Commun. 47 (2011) 5810–5812.
[72] N.F.D. Aba, J.Y. Chong, B. Wang, C. Mattevi, K. Li, Graphene oxide membranes on ceramic hollow fibers – microstructural stability and nanofiltration performance, J. Membr. Sci. 484 (2015) 87–94, https://doi.org/10.1016/j.memsci.2015.03.001.
[73] K. Goh, L. Setiawan, L. Wei, R. Si, A.G. Fane, R. Wang, Y. Chen, Graphene oxide as effective selective barriers on a hollow fiber membrane for water treatment process, J. Membr. Sci. 474 (2015) 244–253, https://doi.org/10.1016/j.memsci.2014.09.057.
[74] H.M. Hegab, L. Zou, Graphene oxide-assisted membranes: fabrication and potential applications in desalination and water purification, J. Membr. Sci. 484 (2015) 95–106, https://doi.org/10.1016/j.memsci.2015.03.011.
[75] S. Liu, F. Yao, O. Oderinde, Z. Zhang, G. Fu, Green synthesis of oriented xanthan gum–graphene oxide hybrid aerogels for water purification, Carbohydr. Polym. 174 (2017) 392–399, https://doi.org/10.1016/j.carbpol.2017.06.044.
[76] M. Hirata, T. Gotou, S. Horiuchi, M. Fujiwara, M. Ohba, Thin-film particles of graphite oxide 1, Carbon 42 (14) (2004) 2929–2937, https://doi.org/10.1016/j.carbon.2004.07.003.
[77] W.S. Hummers Jr., R.E. Offeman, Preparation of graphitic oxide, J. Am. Chem. Soc. 80 (1958) 1133–1339.
[78] D. Li, M.B. Müller, S. Gilje, R.B. Kaner, G.G. Wallace, Processable aqueous dispersions of graphene nanosheets, Nat. Nanotechnol. 3 (2008) 101–105.
[79] D.R. Dreyer, S. Park, C.W. Bielawski, R.S. Ruoff, The chemistry of graphene oxide, Chem. Soc. Rev. 39 (2010) 228–240.
[80] S. Park, R.S. Ruoff, Chemical methods for the production of graphenes, Nat. Nanotechnol. 4 (2009) 217–224.
[81] H.W. Kim, H. Yoon, S.-M. Yoon, B.M. Yoo, B.K. Ahn, Y.H. Cho, H.J. Shin, H. Yang, U. Paik, S. Kwon, Selective gas transport through few-layered graphene and graphene oxide membranes, Science 342 (2013) 91–95.
[82] H. Li, Z. Song, X. Zhang, Y. Huang, S. Li, Y. Mao, H.J. Ploehn, Y. Bao, M. Yu, Ultrathin, molecular-sieving graphene oxide membranes for selective hydrogen separation, Science 342 (2013) 95–98.
[83] Y.P. Tang, D.R. Paul, T.S. Chung, Free-standing graphene oxide thin films assembled by a pressurized ultrafiltration method for dehydration of ethanol, J. Membr. Sci. 458 (2014) 199–208.
[84] P. Sun, H. Liu, K. Wang, M. Zhong, D. Wu, H. Zhu, Ultrafast liquid water transport through graphene-based nanochannels measured by isotope labelling, Chem. Commun. 51 (2015) 3251–3254.

[85] B. Mi, Graphene oxide membranes for ionic and molecular sieving, Science 343 (2014) 740–742.
[86] S. Pei, H.-M. Cheng, The reduction of graphene oxide, Carbon 50 (9) (2012) 3210–3228, https://doi.org/10.1016/j.carbon.2011.11.010.
[87] X. Gao, J. Jang, S. Nagase, Hydrazine and thermal reduction of graphene oxide reaction mechanisms product structures and reaction design, J. Phys. Chem. C 114 (2) (2010) 832–842.
[88] B. Lee, K. Li, H.S. Yoon, J. Yoon, Y.b. Mok, Y. Lee, H.H. Lee, Y.H. Kim, Membrane of functionalized reduced graphene oxide nanoplates with angstrom-level channels, Sci. Rep. (2016) 6.
[89] M.-Y. Lim, Y.-S. Choi, J. Kim, K. Kim, H. Shin, J.-J. Kim, … J.-C. Lee, Cross-linked graphene oxide membrane having high ion selectivity and antibacterial activity prepared using tannic acid-functionalized graphene oxide and polyethyleneimine, J. Membr. Sci. 521 (2017) 1–9, https://doi.org/10.1016/j.memsci.2016.08.067.
[90] Q. Nan, P. Li, B. Cao, Fabrication of positively charged nanofiltration membrane via the layer-by-layer assembly of graphene oxide and polyethylenimine for desalination, Appl. Surf. Sci. 387 (2016) 521–528, https://doi.org/10.1016/j.apsusc.2016.06.150.
[91] M. Hu, B. Mi, Enabling graphene oxide nanosheets as water separation membranes, Environ. Sci. Technol. 47 (8) (2013) 3715–3723.
[92] Y. Zhang, S. Zhang, T.-S. Chung, Nanometric graphene oxide framework membranes with enhanced heavy metal removal via nanofiltration, Environ. Sci. Technol. 49 (16) (2015) 10235–10242.
[93] G. Zhao, X. Ren, X. Gao, X. Tan, J. Li, C. Chen, Y. Huang, X. Wang, Removal of Pb(II) ions from aqueous solutions on few-layered graphene oxide nanosheets, Dalton Trans. 40 (2011) 10945–10952.
[94] P. Sun, M. Zhu, K. Wang, M. Zhong, J. Wei, D. Wu, X. Zhiping, H. Zhu, Selective ion penetration of graphene oxide membranes, ACS Nano 7 (2013) 428–437.
[95] P. Sun, F. Zheng, M. Zhu, Z. Song, K. Wang, M. Zhong, D. Wu, R.B. Little, Z. Xu, H. Zhu, Selective trans-membrane transport of alkali and alkaline earth cations through graphene oxide membranes based on cation-p interactions, ACS Nano 8 (2014) 850–859.
[96] C.-H. Tsou, Q.-F. An, S.-C. Lo, M. De Guzman, W.-S. Hung, C.-C. Hu, J.-Y. Lai, Effect of microstructure of graphene oxide fabricated through different self-assembly techniques on 1-butanol dehydration, J. Membr. Sci. 477 (2015) 93–100, https://doi.org/10.1016/j.memsci.2014.12.039.
[97] J. Chen, Y. Li, L. Huang, N. Jia, C. Li, G. Shi, Size fractionation of graphene oxide sheets via filtration through track-etched membranes, Adv. Mater. 27 (24) (2015) 3654–3660.
[98] J. Luo, L.J. Cote, V.C. Tung, A.T.L. Tan, P.E. Goins, J. Wu, J. Huang, Graphene oxide nanocolloids, J. Am. Chem. Soc. 132 (50) (2010) 17667–17669.
[99] H. Huang, Z. Song, N. Wei, L. Shi, Y. Mao, Y. Ying, L. Sun, Z. Xu, X. Peng, Ultrafast viscous water flow through nanostrand-channelled graphene oxide membranes, Nat. Commun. 4 (2013).
[100] Y. Ying, L. Sun, Q. Wang, Z. Fan, X. Peng, In-plane mesoporous graphene oxide nanosheet assembled membranes for molecular separation, RCS Adv. 4 (2014) 21425–21428.
[101] W.-S. Hung, Q.-F. An, M. De Guzman, H.-Y. Lin, S.-H. Huang, W.-R. Liu, J.-Y. Lai, Pressure-assisted self-assembly technique for fabricating composite membranes consisting of highly ordered selective laminate layers of amphiphilic graphene oxide, Carbon 68 (2014) 670–677, https://doi.org/10.1016/j.carbon.2013.11.048.
[102] O.C. Compton, M.J. Palmeri, S.B.T. Nguyen, L.C. Brinson, High-nanofiller-content graphene oxide–polymer nanocomposites via vacuum-assisted self-assembly, Adv. Funct. Mater. 20 (2010) 3322–3329.
[103] K. Huang, G. Liu, J. Shen, Z. Chu, H. Zhou, X. Gu, W. Jin, N. Xu, High efficiency water-transport channels using the synergistic effect of a hydrophilic polymer and graphene oxide laminates, Adv. Funct. Mater. 25 (2015) 5809–5815.
[104] H. Liu, H. Wang, X. Zhang, Facile fabrication of freestanding ultrathin reduced graphene oxide membranes for water purification, Adv. Funct. Mater. 27 (2015) 249–254.
[105] Y. Han, Z. Xu, C. Gao, Ultrathin graphene nanofiltration membrane for water purification, Adv. Funct. Mater. 23 (2013) 3693–3700.

[106] C.-N. Yeh, K. Raidongia, J. Shao, Q.-H. Yang, J. Huang, On the origin of the stability of graphene oxide membranes in water, Nat. Chem. 7 (2015) 166–170.
[107] J.Y. Chong, N.F.D. Aba, B. Wang, C. Mattevi, K. Li, UV-enhanced sacrificial layer stabilised graphene oxide hollow fibre membranes for nanofiltration, Sci. Rep. (2015) 5.
[108] S.P. Sun, K.Y. Wang, N. Peng, T.A. Hatton, T.-S. Chung, Novel polyamide-imide/cellulose acetate dual-layer hollow fiber membranes for nanofiltration, J. Membr. Sci. 363 (1) (2010) 232–242, https://doi.org/10.1016/j.memsci.2010.07.038.
[109] P. Marchetti, M.F. Jimenez Solomon, G. Szekely, A.G. Livingston, Molecular separation with organic solvent nanofiltration: a critical review, Chem. Rev. 114 (21) (2014) 10735–10806.
[110] D. An, L. Yang, T.-J. Wang, B. Liu, Separation performance of graphene oxide membrane in aqueous solution, Ind. Eng. Chem. Res. 55 (17) (2016) 4803–4810.
[111] G. Liu, W. Jin, N. Xu, Graphene-based membrane, Chem. Soc. Rev. 44 (15) (2015) 5016–5030.
[111a] A.K. Geim, Graphene: status and prospects, Science 324 (5934) (2009) 1530–1534.
[111b] J.C. Meyer, A.K. Geim, M.I. Katsnelson, K.S. Novoselov, T.J. Booth, S. Roth, The structure of suspended graphene sheets, Nature 446 (2007) 60–63.
[111c] M. Yang, C. Zhao, S. Zhang, P. Li, D. Hou, Preparation of graphene oxide modified poly(m-phenylene isophthalamide) nanofiltration membrane with improved water flux and antifouling property, Appl. Surface Sci 394 (Suppl C) (2017) 149–159.
[112] B.J. Hinds, N. Chopra, T. Rantell, R. Andrews, V. Gavalas, L.G. Bachas, Aligned multiwalled carbon nanotube membranes, Science 303 (5654) (2004) 62–65.
[113] S. Li, H. Li, X. Wang, Y. Song, Y. Liu, L. Jiang, D. Zhu, Super hydrophobicity of large area honeycomb like aligned carbon nanotubes, J. Phys. Chem. B 106 (36) (2002) 9274–9276.
[114] D. Cohen-Tanugi, J.C. Grossman, Water desalination across nanoporous graphene, Nano Lett. 12 (7) (2012) 3602–3608.
[115] E.A. Müller, Purification of water through nanoporous carbon membranes: a molecular simulation viewpoint, Curr. Opin. Chem. Eng. 2 (2) (2013) 223–228, https://doi.org/10.1016/j.coche.2013.02.004.
[116] W.-F. Chan, H.-Y. Chen, A. Surapathi, M.G. Taylor, X. Shao, E. Marand, J.K. Johnson, Zwitterion functionalized carbon nanotube/polyamide nanocomposite membranes for water desalination, ACS Nano 7 (6) (2013) 5308–5319.
[117] T.V. Ratto, J.K. Holt, A.W. Szmodis, G. patents, 2011.
[118] M. Mulder, Basic Principles of Membrane Technology, second ed, Kluwer Academic Publisher, London, 1996.
[119] B. Van der Bruggen, M. Mänttäri, M. Nyström, Drawbacks of applying nanofiltration and how to avoid them: a review, Sep. Purif. Technol. 63 (2) (2008) 251–263, https://doi.org/10.1016/j.seppur.2008.05.010.
[120] M. Majumder, N. Chopra, B.J. Hinds, Mass transport through carbon nanotube membranes in three different regimes: ionic diffusion and gas and liquid flow, ACS Nano 5 (2011) 3867–3877.
[121] S. Karan, S. Samitsu, X. Peng, K. Kurashima, I. Ichinose, Ultrafast viscous permeation of organic solvents through diamond like carbon nanosheets, Science 335 (2012) 444–447.
[122] D.R. Paul, Creating new types of carbon-based membranes, Science 335 (2012) 413–414.
[123] D. Krishnan, F. Kim, J. Luo, R. Cruz-Silva, L.J. Cote, H.D. Jang, J. Huang, Energetic graphene oxide: challenges and opportunities, Nano Today 7 (2) (2012) 137–152, https://doi.org/10.1016/j.nantod.2012.02.003.
[124] R.K. Joshi, P. Carbone, F.C. Wang, V.G. Kravets, Y. Su, I.V. Grigorieva, H.A. Wu, A.K. Geim, R.R. Nair, Precise and ultrafast molecular sieving through graphene oxide membrane, Sci. Rep. 343 (6172) (2014) 752–754.
[125] K. Raidongia, J. Huang, Nanofluidic ion transport through reconstructed layered materials, J. Am. Chem. Soc. 134 (2012) 16528–16531.

CHAPTER

GRAPHENE-BASED MATERIALS FOR WATER PURIFICATION 15

Mahdie Safarpour*, Alireza Khataee†

Department of Chemistry, Faculty of Basic Science, Azarbaijan Shahid Madani University, Tabriz, Iran Department of Applied Chemistry, Faculty of Chemistry, University of Tabriz, Tabriz, Iran†*

1 INTRODUCTION

The population boom, urbanization, and climate changes have intensified the demand for clean water. It is expected that by the year 2025, several countries will face severe water crises [1] that may pose a substantial threat to global health, economic growth, sustainability, and social progress. Therefore, available water and a cost-effective water purification technology are urgently needed for the near future. Water purification is the process of removing distasteful chemicals, biological contaminants, suspended solids, and gases from water. The goal of purification is production of water suitable for a specific application. The main application of purified water is human consumption (drinking water), but many others are also designed for the requirements of medical, pharmacological, chemical, agricultural and industrial applications. Among various water purification techniques, some important methods have been developed in recent decades such as adsorption, physical and chemical treatments, membrane-based separation, and biological treatment. Although these methods have played vital roles in sustaining human society in the past century, the ever-increasing demand for safe and clean water has raised the necessity of novel technologies for water purification.

The application of nanotechnology in environmental remediation has attracted great attention in recent years. Nanostructured materials represent several advantages for water purification because of their unique physicochemical and surface properties, such as large specific surface area [2]. Graphene is a two-dimensional layer of carbon atoms that are strongly connected in a hexagonal honeycomb matrix at atomic scale. Graphene and graphene-based materials have been considered one of the hottest and most rapidly rising research areas because of their distinctive physical and chemical properties. Recently, graphene-based nanocomposites have shown promise for application in different water purification systems. The present chapter summarizes recent developments in the application of graphene and graphene-based materials in water purification processes including adsorption, photocatalysis, membrane separation, and electrochemistry. The use of graphene-based materials in these methods will be discussed individually with a focus on the properties and performance of these materials. Finally, the challenges and future perspectives will be considered.

Nanoscale Materials in Water Purification. https://doi.org/10.1016/B978-0-12-813926-4.00021-5

2 WATER-PURIFICATION METHODS USING GRAPHENE-BASED MATERIALS

Since Geim and Novoselov achieved the Nobel Prize in physics in 2010 [3], graphene has attracted growing interest in different research areas due to its great surface area, high thermal and electrical conductivity, fracture and breaking strength, good mechanical properties, superior mobility as a charge carrier, proper optical transmittance, specific magnetism, and chemical stability [4]. The length of molecule bonds in the carbon layer of graphene is 0.142 nm. The arrangement of graphene sheets on top of one another makes graphite a three-dimensional material with interplanar gaps of 0.335 nm [5,6]. Functionalization of graphene with oxygen-containing functional groups such as carboxyl, hydroxyl, ether, and epoxy creates graphene oxide (GO), a widely used carbon-based material. Different composites of graphene have also been prepared through incorporation of other materials such as inorganic particles and polymers. Graphene and graphene-based materials have recently gained the attention of scientists as ideal substitutes for carbon nanotubes (CNTs) in environmental remediation processes. Compared to CNTs, the production processes for GO and reduced graphene oxide (RGO) are very simple with no need for complex apparatus or specific catalysts. Graphene material can be synthesized by chemical exfoliation of graphite, resulting in a final product free of catalyst residues, and no further purification is required.

The following sections focus on recent advances in the application of graphene-based materials in different water purification methods, with a major emphasis on the adsorption, photocatalytic oxidation, electrochemical oxidation, and membrane-based techniques.

2.1 ADSORPTION

Adsorption is a traditional, effective process for water and wastewater treatment because of its convenience, ease of operation, and simplicity of design. This process can be utilized for the removal of dissolved contaminants remaining after biological or chemical oxidation treatments [7]. Carbon-based materials such as activated carbon are the most commonly used adsorbent in the adsorption process. Recently, graphene-based composites have been successfully used for the adsorption of different pollutants including heavy metals [8–23], organic dyes [24–26], halomethanes [27], and other pollutants [28] because of their high specific surface area and electron-rich environment. Table 1 summarizes some of the recently published studies on graphene-based adsorbents used for water purification. Graphene-based adsorbents have several advantages over other materials such as CNTs. The single-layer structure of graphene materials provides two basal planes and huge surface area available for contaminant adsorption, while the inner walls of CNTs are not accessible to pollutants. Moreover, as the most widely used compound of graphene, GO has a large number of oxygen-containing functional groups that impart a hydrophilic nature and high negative charge density to GO. These functional groups effectively improve the adsorption of pollutants by GO sheets [31].

Ramesha et al. [30] investigated the adsorption of cationic and anionic dyes on exfoliated graphene oxide (EGO) and reduced graphene oxide (RGO) adsorbents. They showed that a number of functional groups such as carboxyl, epoxy, ketone, and hydroxyl in the basal and edge planes of the GO create large negative charge density in aqueous solution and increase the adsorption of cationic dyes on EGO. The adsorption of anionic dyes is negligible with EGO. In contrast, RGO was much more efficient for the adsorption of anionic dyes because of its high surface area and less-negative charge. Investigation

Table 1 Some of the Recently Published Research on Graphene-Based Adsorbents Used for Water Purification

Graphene-Based Adsorbent	Target Pollutant	Adsorption Capacity at Equilibrium (q_e (mg/g))	Maximum Adsorption Capacity (q_{max} (mg/g))	Performance	Ref.
Graphene-supported Fe-Mg oxide composite	Arsenic	25.5	103.9	The prepared composite exhibited significant fast adsorption of arsenic over a wide range of solution pHs, with exceptional durability and recyclability	[15]
Fe_3O_4/RGO, GO/Cu-ZEA, Fe_3O_4/RGO/Cu-ZEA, Fe_3O_4/GO/Cu-ZEA	Arsenic	50.51	–	Among the prepared composites, Fe_3O_4/RGO/Cu-ZEA composite had the highest efficiency in removing arsenic resulted from the high specific surface area	[13]
Fe_3O_4/RGO	As(V), Ni(II), Pb(II)	As(V): 15.97 Ni(II): 18.88 Pb(II): 15.63	As(V): 58.48 Ni(II): 76.34 Pb(II): 65.79	Fe_3O_4/RGO showed superparamagnetic properties at room temperature and saturation magnetization. The adsorption models of As(V), Ni(II), and Pb(II) on the Fe_3O_4/RGO indicated surface heterogeneity and monolayer adsorption of the adsorbents	[12]
Graphene nano zero-valent iron (G-nZVI)	Trichloronitromethane	–	–	About 99% of initial trichloronitromethane could be adsorbed and removed under 60 mg/L G-nZVI dosage within 120 min	[27]
GO/Fe_3O_4	Methylene blue and Rhodamine B	Methylene blue: 33.333 Rhodamine B: 30.211	–	For cationic dye, dye removal rate reached nearly 100% even after the 6th round. For cationic Rhodamine B, removal rate reached 90% in the 1st round, 80% in the 2nd round, and still above 60% in the 6th round	[25]

Continued

Table 1 Some of the Recently Published Research on Graphene-Based Adsorbents Used for Water Purification—cont'd

Graphene-Based Adsorbent	Target Pollutant	Adsorption Capacity at Equilibrium (q_e (mg/g))	Maximum Adsorption Capacity (q_{max} (mg/g))	Performance	Ref.
$FeMnO_x$/RGO	Arsenic	As(III): 47.05 As(V): 49.01	–	$FeMnO_x$/RGO had larger specific surface area in comparison with bare $FeMnO_x$, and showed higher adsorption capacities for As(III) and As(V)	[23]
Magnetic GO/poly(vinyl alcohol) (mGO/PVA)	Methylene blue and Methyl violet	>150 by mGO/PVA-50%	Methylene blue: 270.94 Methyl violet: 221.23	The mGO/PVA not only exhibited strong superparamagnetic property, but also showed obvious GO content-dependent enhancement in adsorption capacity for organic dyes	[24]
Nanoscale zero-valent iron-RGO	As(III) and As(V)	As(III): 17.498 As(V): 17.150	As(III): 35.83 As(V): 29.04	The adsorption capacity of As(III) and As(V) was 35.83 mg/g and 29.04 mg/g, respectively	[19]
Ce-Fe/RGO	Congo Red	92	179.5	The driving force for the adsorption was electrostatic action between adsorbent materials with positive electricity and Congo Red with negative electricity	[26]
Graphene Oxide-$MnFe_2O_4$	Pb(II), As(III), As(V)	Pb(II): 350 As(III): 65 As(V): 100	Pb(II): 673 As(III): 146 As(V): 207	The exceptional adsorption property was due to the combination of the unique layered nature (allowing maximum surface area) of the hybrid system and the good adsorption capabilities of both GO and $MnFe_2O_4$ nanoparticles	[14]

Table 1 Some of the Recently Published Research on Graphene-Based Adsorbents Used for Water Purification—cont'd

Graphene-Based Adsorbent	Target Pollutant	Adsorption Capacity at Equilibrium (q_e (mg/g))	Maximum Adsorption Capacity (q_{max} (mg/g))	Performance	Ref.
TiO_2-graphene @Fe_3O_4	Microcystin-LR	–	–	The huge surface of graphene dramatically enhanced the adsorbability and the reduced recombination rate of electron-hole pairs increased the photocatalytic activity. The concentration of Microcystin-LR lowered to less than 1 μg/L from 500 μg/L under UV light in 30 min	[28]
Thiol-functionalized magnetite/GO	Hg^{2+}	30.94	289.9	The synthesized adsorbent exhibited a higher adsorption capacity compared to the bare GO and magnetite/GO due to the combined adsorption of thiol groups and magnetite nanocrystals	[8]
Smart magnetic graphene (SMG)	Cr(VI), As(V), Pb(II)	Cr(VI): <6 As(V): <5 Pb(II): <4	Cr(VI): 4.86 As(V): 3.26 Pb(II): 6.00	The SMG possesses increased the adsorption sites with tunable superparamagnetic properties, facilitating the adsorption and magnetic separation of aqueous Cr(VI), As(V), and Pb(II) with ~99% removal efficiencies	[11]
GO-$ZrO(OH)_2$	As(III) and As(V)	As(III): 89.53 As(V): 79.05	As(III): 95.15 As(V): 84.89	The GO-$ZrO(OH)_2$ nanocomposite showed high adsorption capacity in a wide pH range, and the monolayer adsorption amounts were 95.15 and 84.89 mg/g for As(III) and As(V), respectively, which are 3.54 and 4.64 times that of $ZrO(OH)_2$	[17]

Continued

Table 1 Some of the Recently Published Research on Graphene-Based Adsorbents Used for Water Purification—cont'd

Graphene-Based Adsorbent	Target Pollutant	Adsorption Capacity at Equilibrium (q_e (mg/g))	Maximum Adsorption Capacity (q_{max} (mg/g))	Performance	Ref.
RGO-Fe(0)-Fe_3O_4	Cr(VI), Pb(II), Cd(II), Hg(II)	As(III): >40 Cr(VI): >25 Pb(II): >20 Cd(II): >5 Hg(II): >20	As(III): >40 Cr(VI): >30 Pb(II): >20 Cd(II): <5 Hg(II): >20	The porous RGO-Fe(0)-Fe_3O_4 material was highly efficient in adsorbing heavy metal ions and employed for catalytic oxidation reactions	[9]
GO-iron oxides and RGO-iron oxides	Pb(II), 1-naphthol, and 1-naphthylamine	–	GO-iron oxides: 285.7 RGO-iron oxides: 303.03	The GO-iron oxide was a good adsorbent for Pb(II) but not for 1-naphthol and 1-naphthylamine due to oxygen-containing groups on the surface, whereas the RGO-iron oxide was a good adsorbent for 1-naphthol and 1-naphthylamine but not for Pb(II)	[21]
Magnetic graphene oxide (MGO)	Arsenate	>30	>50	The adsorption of As(V) on MGO decreased with ascending pH due to the electrostatic interaction. The adsorption of As(V) on MGO was greatly affected by the nature and concentration of coexisting cations and anions	[18]
GO-TiO_2	Zn^{2+}, Cd^{2+}, Pb^{2+}	–	Zn^{2+}: 88.9 Cd^{2+}: 72.8 Pb^{2+}: 65.6	The various and dense oxygenated groups on the GO surface enhanced its capacity to remove heavy metals	[29]

Table 1 Some of the Recently Published Research on Graphene-Based Adsorbents Used for Water Purification—cont'd

Graphene-Based Adsorbent	Target Pollutant	Adsorption Capacity at Equilibrium (q_e (mg/g))	Maximum Adsorption Capacity (q_{max} (mg/g))	Performance	Ref.
Exfoliated graphene oxide (EGO) and reduced graphene oxide (RGO)	Methylene blue, Methyl violet, hodamine B, Orange G	–	Methylene blue: 17.3 Methyl violet: 2.47 Rhodamine B: 1.24 Orange G: 5.98	The large negative charge density available in aqueous solutions helped in the effective adsorption of cationic dyes on EGO while the adsorption is negligible for anionic dyes. On the other hand, RGO with high surface area and lower negative charge was found to be very good adsorbent for anionic dyes	[30]
Magnetite-graphene-LDH (MGL)	Arsenate	–	73.14	The results showed an enhanced adsorption capacity of arsenate on the MGL as compared to that of pure Mg/Al LDHs due to the high surface area and more active sites for arsenate uptake	[20]
Magnetite/ Graphene Oxide (M/GO)	Cobalt(II)	>10	12.98	The ionic strength-independent and pH-dependent Co(II) sorption on M/GO indicated that the sorption mechanism of Co(II) was inner-sphere surface complexation at low pH values, whereas the removal of Co(II) was done by simultaneous precipitation and inner-sphere surface complexation at high pH values	[16]

Continued

Table 1 Some of the Recently Published Research on Graphene-Based Adsorbents Used for Water Purification—cont'd

Graphene-Based Adsorbent	Target Pollutant	Adsorption Capacity at Equilibrium (q_e (mg/g))	Maximum Adsorption Capacity (q_{max} (mg/g))	Performance	Ref.
Few-layered graphene oxide	Cd(II) and Co(II)	–	Cd(II): 106.3 Co(II): 68.2	Cd(II) and Co(II) sorption on graphene oxide nanosheets was strongly dependent on the pH and weakly dependent on ionic strength of the solution	[22]
Magnetite-RGO	Arsenic	As(V): 4.23 As(III): 7.81	–	The composites showed near complete (over 9.9%) arsenic removal within 1 ppb	[10]

by FT-IR and Raman analysis revealed that the type of interactions between the dyes and adsorbents are electrostatic and/or van der Waals, depending on the system.

Although GO is considered an emerging and promising adsorbent for water purification, but its separation from water after adsorption is a challenge due to its high hydrophilicity and stable dispersion in water. It needs high-speed centrifugation in most cases. This problem can restrict its utilization in large-scale and industrial applications. An effective solution to this problem is magnetization [12]. In this technique, graphene-based adsorbent is combined with magnetic materials such as Fe_3O_4 that can be magnetically separated from the treated solution [8,10,11,14,16,18,20,24,25,28,32]. Yoon and colleagues [32] compared the removal efficiency of As (III) and As (V) using Fe_3O_4 particles decorated onto the GO and RGO sheets. It should be noted that arsenic is one of the most toxic and carcinogenic elements on Earth, and it is widely present in soil, rocks, surface water, and ground water because of natural sources, mine effluents, and anthropogenic activities [32]. The results of Yoon and colleagues showed that the adsorption efficiency of Fe_3O_4-GO composite was more than Fe_3O_4-RGO for both As (III) and As (V). The numerous functional groups on the GO could lead to hosting more Fe_3O_4 particles on the GO sheets. TEM images of the Fe_3O_4-GO and Fe_3O_4-RGO confirmed that the number of black dots of Fe_3O_4 in the Fe_3O_4-GO was much higher than Fe_3O_4-RGO (Fig. 1).

In a study conducted by Cheng et al. [24], a simple one-step technique was applied to fabricate magnetic GO/poly(vinyl alcohol) (PVA) composite gels (mGO/PVA CGs) as adsorbents with convenient separation and proper adsorption capacity for organic dyes. Fig. 2 shows the one-step synthesis route of this adsorbent. In a typical synthesis process, PVA, $FeCl_3$, and $FeCl_2{\cdot}4H_2O$ solutions were added in a flask and stirred for a specified time period to dissolve the iron salt. A predefined amount of GO was added to the above mixture and stirred again. Finally, ammonia solution was added, and black mGO/PVA CG formed immediately. The results showed that the adsorption capacity of the studied organic dyes was increased by increasing GO to PVP ratio from 5 to 50% in the synthesized composite [24].

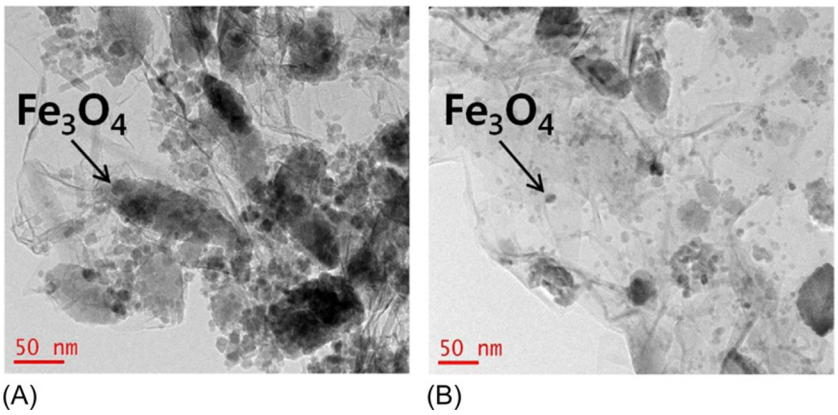

FIG. 1

TEM image of the (A) Fe_3O_4-GO and (B) Fe_3O_4-RGO adsorbents.

Adapted from Y. Yoon, W.K. Park, T.-M. Hwang, D.H. Yoon, W.S. Yang, J.-W. Kang, Comparative evaluation of magnetite–graphene oxide and magnetite-reduced graphene oxide composite for As(III) and As(V) removal, J. Hazard. Mater. 304 (2016) 196–204 with permission from Elsevier.

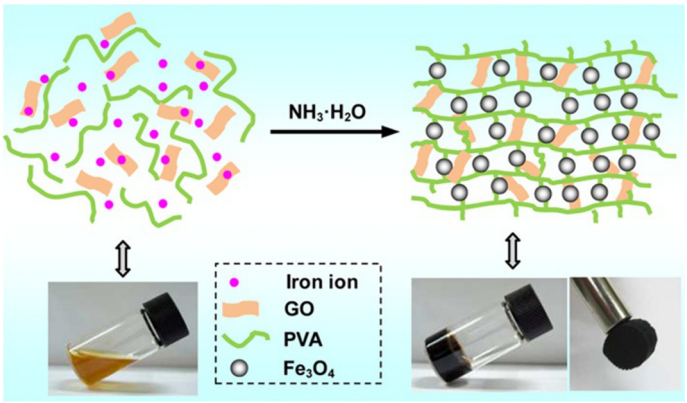

FIG. 2

Schematic illustration of the synthesis route of mGO/PVA CG adsorbent.

Adapted from Z. Cheng, J. Liao, B. He, F. Zhang, F. Zhang, X. Huang, L. Zhou, One-step fabrication of graphene oxide enhanced magnetic composite gel for highly efficient dye adsorption and catalysis, ACS Sustain. Chem. Eng. 3 (2015) 1677–1685 with permission from American Chemical Society.

In another study, Gollavelli and colleagues [11] introduced a one-pot, solvent-free and rapid synthesis of smart magnetic graphene (SMG) by microwave irradiation of GO and ferrocene precursors. Selective adsorption and efficient regeneration are reported as two main advantages of smart adsorbents [33,34]. Fig. 3 shows the schematic microwave-assisted synthesis of SMG. The prepared SMG adsorbent was tested for removal of Cr (VI), As (V), and Pb (II) heavy metals, disinfection, biocompatibility, and recyclability. The results showed that SMG had improved adsorption capacity

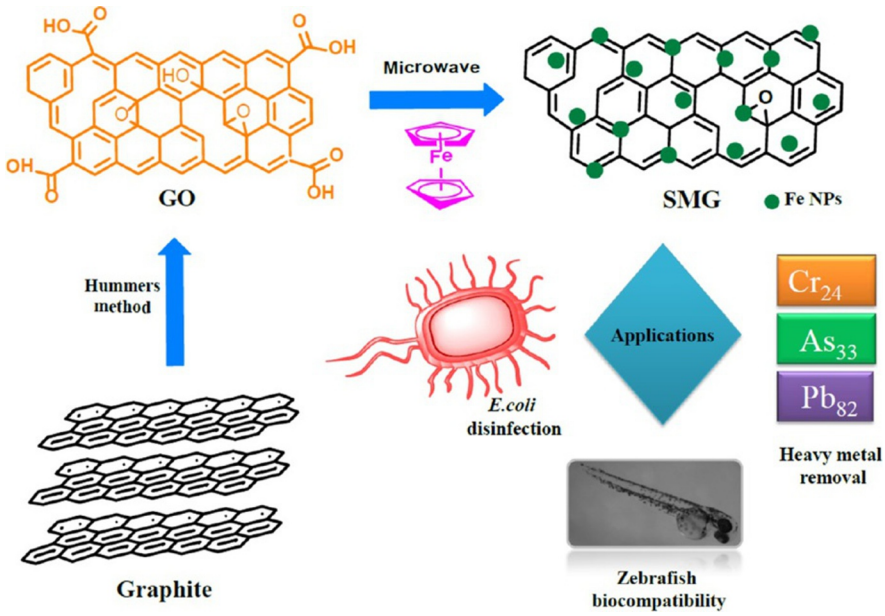

FIG. 3

Schematic synthesis of smart magnetic graphene (SMG) adsorbent for heavy metals removal and disinfection. *Adapted from G. Gollavelli, C.-C. Chang, Y.-C. Ling, Facile synthesis of smart magnetic graphene for safe drinking water: heavy metal removal and disinfection control, ACS Sustain. Chem. Eng. 1 (2013) 462–472 with permission from American Chemical Society.*

over a wide range of pH and proper magnetic property for facile separation from aqueous solution. In addition, SMG acted as a great disinfectant against *E. coli* bacteria while displaying favorably low toxicity toward zebra fish, making it a preferred adsorbent for purification of drinking water.

In another attempt for removal of As (III) and As (V) from aqueous solutions, Wang et al. [19] synthesized nanoscale, zero-valent, iron-reduced graphite oxide (NZVI-RGO) composite and used it as an adsorbent for arsenic. RGO was employed as a support for NZVI to reduce the aggregation of the small particles of NZVI. TEM images of the prepared composite showed that NZVI nanoparticles are well loaded to the GO sheet and dispersed homogeneously, indicating that the RGO acted as a dispersing agent (Fig. 4).

2.2 PHOTOCATALYSIS

Heterogeneous photocatalytic oxidation of pollutants is a growing and promising water purification technology. In a typical photocatalyst, the electrons of the valence band can be excited to the conduction band under sufficient photo energy and will generate electron-hole pairs. The photo-induced electron-hole pairs enable a series of oxidation/reduction reactions to produce further active species that promote the photocatalytic degradation of contaminants [35,36]. A number of metal oxides such as TiO_2, ZnO, SnO_2, and CeO_2 are reported as the most predominant photocatalysts due to their abundance in nature, biocompatibility, great stability under different conditions, and capacity to generate

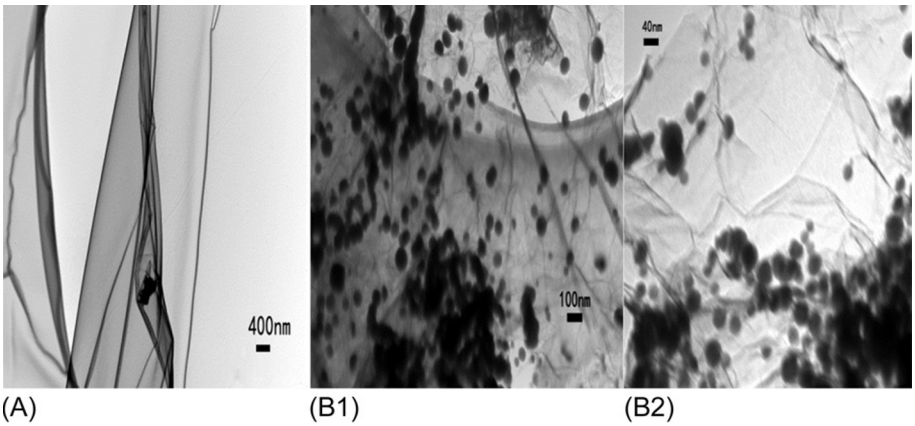

FIG. 4

TEM image of the (A) GO; (B1 and B2) NZVI-RGO.

Adapted from C. Wang, H. Luo, Z. Zhang, Y. Wu, J. Zhang, S. Chen, Removal of As(III) and As(V) from aqueous solutions using nanoscale zero valent iron-reduced graphite oxide modified composites, J. Hazard. Mater. 268 (2014) 124–131 with permission from Elsevier.

charge carriers when exposed to a sufficient amount of light energy [37]. However, the widespread application of these photocatalysts is still restricted by their wide energy band near-UV range and fast recombination of the produced electron-hole pairs. Various approaches have been reported to overcome these drawbacks with a focus on the fabrication of novel photocatalysts with modified structures and properties.

Among several materials that can be selected to prepare novel composite photocatalysts, carbon-based materials are valuable candidates because of their advantages, such as chemical stability in a wide range of pH, tunable structural and chemical characteristics, and striking electronic properties. In this respect, graphene has recently been considered as one of the most promising materials for synthesis of next-generation of photocatalysts, because of the excellent mobility of its charge carriers, large specific surface area, flexible structure, high transparency, and good electrical and thermal conduction [38]. In composite photocatalysts containing classic metal oxides and graphene materials, the superior pollutant degradation performance can be attributed to the synergy effect of the increased specific surface area in the presence of graphene nanosheets, and the formation of ionic interactions between organic contaminants and oxygenated functional groups of the graphene material. Moreover, graphene contributes to the photocatalytic process as an adsorbent, electron acceptor, and photosensitizer to accelerate photodecomposition [39]. Fig. 5 shows the general photocatalytic mechanism of a metal oxide semiconductor such as ZnO in the absence and presence of graphene for removal of a typical contaminant, methyl orange. In the graphene-ZnO composite, the energy level of the graphene is slightly less than the conduction band of ZnO, so, the photo-generated electrons in the conduction band can transfer to graphene. Highly conductive graphene transfers electrons to the organic contaminant, resulting in the reduction of the contaminant and separation of electron-hole pairs [40].

The number of reports in the literature about investigating the photocatalytic performance of the graphene-based composites is rising rapidly. Several review papers have been devoted to detailed

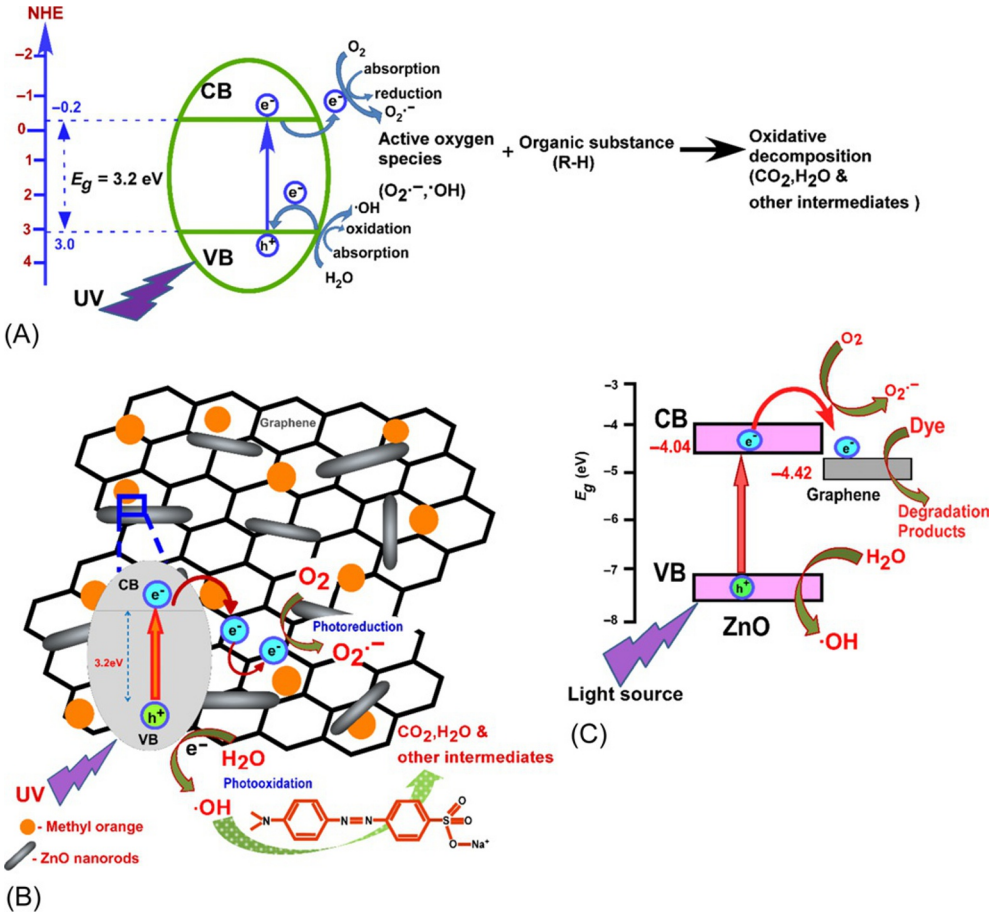

FIG. 5

Schematic representation of photocatalytic mechanism of (A) ZnO photocatalyst and (B) graphene-ZnO photocatalyst, (C) band diagram for graphene-ZnO.

Adapted from R. Beura, P. Thangadurai, Structural, optical and photocatalytic properties of graphene-ZnO nanocomposites for varied compositions, J. Phys. Chem. Solids 102 (2017) 168–177 with permission from Elsevier.

discussion on the introduction, mechanism study, synthesis, and performance evaluation of graphene-based photocatalysts [4,38,41–46]. Herein, we give an overview of some of the most recent studies in this field (Table 2).

Chen and colleagues [47] prepared a TiO_2/chitosan/RGO macroporous composite for photocatalytic removal of methyl orange. Fig. 6 shows the SEM images of the prepared composites with different TiO_2 contents. As shown, by increasing TiO_2 concentration, the width of lamellar pores decreased while the thickness of lamellar increased. The aligned lamellar pore structure can provide an easy pathway for mass transfer and facilitate effective photocatalytic reactions and subsequently increase the decontamination efficiency of pollutants. The introduced composite was reported as a low-cost

Table 2 Some of the Recently Published Studies on the Graphene-Based Composite Photocatalysts Used for Water Purification

Graphene-Based Photocatalyst	Target Pollutant	Light Source	Performance	Ref.
TiO_2/chitosan/RGO	Methyl orange	UV lamp ($\lambda = 365$ nm)	The composites with 1.0 wt % RGO showed a degradation percentage of 97% for methyl orange	[47]
GO-Ag	Cyclohexane	Solar light	By using the GO-Ag photocatalysts the highest cyclohexane conversion of 37.0% with the selectivity of 94.0% to cyclohexanol and cylohexanone was achieved	[48]
Ag loaded TiO_2 nanowire arrays/GO coated carbon fiber	Tetracycline hydrochloride	Visible light	The maximum photocatalytic efficiency of the composite for tetracycline hydrochloride was 95.73%	[49]
Sulfur-doped $SnFe_2O_4$/graphene	Chlorotetracycline	Visible light	The combination of the three components of S, $SnFe_2O_4$, and graphene increased the visible light absorption capability and prevented the recombination of photo-generated electron-hole	[50]
Three-dimensional titanate-graphene oxide (TiGO)	Methyl orange	UV light (mercury lamp)	Ti-GO composite gels showed high photocatalytic activity due to its unique 3D structure and presence of various chemical bonds between titanate and GO	[51]
Cu_2O/RGO/In_2O_3	methylene blue and Cr^{+6} solutions	Simulated solar light	The presence of oxygen vacancies in Cu_2O/RGO/In_2O_3 and the formation of heterojunction between In_2O_3 and Cu_2O decreased the band gap of the hybrid	[52]
Ag_2CO_3/RGO	Rhodamine B	Visible light	The Ag_2CO_3/RGO composite had much higher photocatalytic activity than that of pure Ag_2CO_3 because of the multiple effects of RGO such as reducing the crystal size of Ag_2CO_3, accelerating electron transfer, and increasing light absorption	[53]

Continued

Table 2 Some of the Recently Published Studies on the Graphene-Based Composite Photocatalysts Used for Water Purification—cont'd

Graphene-Based Photocatalyst	Target Pollutant	Light Source	Performance	Ref.
Bi_2S_3/TiO_2/RGO	Methylene blue	Visible light	The synthesized composite showed about threefold increase in the photocatalytic activity over TiO_2 nanoparticles	[54]
TiO_2-RGO	Cr(VI)	Visible light	The photocatalytic activity of the synthesized composites was strongly affected by the concentration of RGO in the composites, and the photocatalyst containing 5 wt% RGO had the highest Cr(VI) removal efficiency	[55]
TiO_2-Fe and TiO_2-RGO	Carbamazepine, ibuprofen, and sulfamethoxazole	UV and visible light	TiO_2-RGO had higher photocatalytic activity for the decomposition of pharmaceuticals under UV irradiation, while TiO_2-Fe was more efficient for visible light oxidation	[56]
TiO_2/RGO/Fe_3O_4	Uranium(VI)	UV light	The electron acceptor action of the RGO in the TiO_2/RGO/Fe_3O_4 composite decreased the Fe_3O_4 dissolution and rendered much higher stability to the ternary composite	[57]
TiO_2 Nanotube/RGO/FTO	Methylene blue	UV lamp ($\lambda = 365$ nm)	The synthesized photocatalyst showed improved photocatalytic reaction rate, three times greater than that of pure TiO_2 nanotube	[58]
ZnS/RGO	Methyl orange	UV lamp	The ZnS/RGO showed higher photocatalytic activity compared to pure ZnS; also, the surface reaction rate of the nanocomposites was six times higher than that of the pure ZnS	[59]
	Rhodamine B, methyl orange, 7 phenol,	Sunlight	The Bi_2WO_6/RGO hybrid with 1 wt% RGO had the	[60]

Table 2 Some of the Recently Published Studies on the Graphene-Based Composite Photocatalysts Used for Water Purification—cont'd

Graphene-Based Photocatalyst	Target Pollutant	Light Source	Performance	Ref.
Self-assembled hollow sphere-shaped Bi_2WO_6/RGO	sulfamonomethoxine and sulfanilamide		optimal photocatalytic activity in aqueous solution. The improvement in the photocatalytic activity when incorporating RGO with Bi_2WO_6 was related to the enhanced light harvesting and improved charge separation of the composites	
RGO/WS_2/Mg-doped ZnO (RGOWMZ)	Rhodamine B	Solar-light	The photocatalytic decomposition rate of Rhodamine B reached 100% within 5 min using RGOWMZ. Also, the RGOWMZ hybrids showed better anti-bacterial activity in dark compared to RGOMZ hybrid	[61]
Graphene-ZnO (GZ)	Methyl orange	UV light and sunlight	Maximum photocatalytic degradation efficiency of methyl orange was 97.1% and 98.6% under UV and sun light, respectively	[40]
ZnO-GO/nanocellulose	Ciprofloxacin	Visible light	The synthesized nanocomposite exhibited enhanced adsorption and photocatalytic performance	[62]
Polyacrylic acid grafted-carboxylic graphene/ titanium nanotube	Enrofloxacin	Sunlight	Above 99.0% removal of antibiotic enrofloxacin was achieved at pH 5.0 within 90 min	[63]
$NiWO_4$-ZnO-NRGO	Methylene blue 4-nitro phenol	Visible light	The photocatalytic activity of the synthesized nanocomposite for removal of methylene blue was 9 times higher than that of $NiWO_4$	[64]
Copper Phthalocyanine (CuPc) functionalized RGO	Rhodamine B	Visible light	The RGO/CuPc composite had much higher photocatalytic activity (87%) than the pristine CuPc nanotube (28%) for dye removal	[65]

Continued

Table 2 Some of the Recently Published Studies on the Graphene-Based Composite Photocatalysts Used for Water Purification—cont'd

Graphene-Based Photocatalyst	Target Pollutant	Light Source	Performance	Ref.
Bi-TiO_2 nanotube/graphene	Methylene blue and Dinoseb (phenolic herbicide)	Visible light	The prepared composite with 2 wt% bismuth displayed the best photocatalytic activity.	[66]
$Ce(MoO_4)_2$ nanocubes/GO	Chloramphenicol	Visible light	The synthesized composite had about 99% degradation efficiency for chloramphenicol after 50 min and it showed a good stability and reusability during five cycles.	[67]
Leaf-templated ZnO nanoparticles combined with graphene quantum dots co-doped with sulfur and nitrogen (S,N:GQD)	Rhodamine B	Visible light	The visible light absorbance of ZnO red-shifted due to the S,N:GQD coupling. Compared with non-templated ZnO, Leaf-templated ZnO composites exhibit higher photocatalytic activity for degradation of organic dye	[68]
RGO-$BiPO_4$	Rhodamine B	UV light	The RGO-$BiPO_4$ nanocomposite showed higher photocatalytic degradation of dye (87.5%) compared to pure $BiPO_4$ (45.7%) within 2 h	[69]
Sn-doped BiOCl/RGO	Rhodamine B	Sunlight	The incorporation of RGO reduced the band-gap energy of BiOCl, and the composite showed much higher photocatalytic activity for degradation of the dye	[70]
RGO-Cu_2O/Bi_2O_3	Tetracycline	Visible light	The optimum composite presented a photocatalytic antibiotic degradation of 75% which was about two and three times higher than that of RGO-Cu_2O and RGO-Bi_2O_3, respectively	[71]
TiO_2-graphene (P25-GR)	Naphthenic acids	UVC lamp ($\lambda = 254$ nm)	The synthesized P25-GR composite showed better photocatalytic activity than pure P25	[72]
Flower-like TiO_2 sphere/RGO	Rhodamine B and trichloroethylene	Simulated solar light	The composite with 1 wt% RGO had the best photocatalytic activity, while composites with RGO contents over 1 wt% had lower photocatalytic activities	[73]

Table 2 Some of the Recently Published Studies on the Graphene-Based Composite Photocatalysts Used for Water Purification—cont'd

Graphene-Based Photocatalyst	Target Pollutant	Light Source	Performance	Ref.
RGO/$CoFe_2O_4$/Ag	Short chain chlorinated paraffins	Visible light	The degradation ratio of 91.9% over RGO/$CoFe_2O_4$/Ag was achieved after 12 h, while only about 21.7% was obtained with commercial P25 TiO_2 under the same experimental conditions	[74]
GO/goethite	Tylosin	Simulated sunlight	The degradation efficiency of antibiotic by synthesized composite was 84% after 120 min	[75]
CuS-RGO	Congo Red	Sunlight	The presence of RGO in the CuS-RGO nanocomposite led to better photocatalytic degradation of diazo dye (98.76%) as compared to CuS nanoparticles and RGO alone	[76]
ZnO-graphene-TiO_2	Rhodamine B texbrite BAC-L and texbrite NFW-L	Visible light	Synthesized composite showed higher photocatalytic activity than other samples (ZnO-graphene-TiO_2 > graphene > TiO_2)	[77]
CuO-CeO_2/GO	Methyl orange	Visible light	The nanocomposite showed better catalytic activity than pure CuO and CuO/GO in the presence of H_2O_2 under visible light irradiation ($\lambda > 400$ nm)	[78]
Ag-modified $LaMnO_3$ nanorod/RGO	Direct green	UV-Vis irradiation	The improved photocatalytic activity resulted from the fast transfer of surface charge and the effective separation of electron-hole pairs induced by the incorporated Ag and RGO	[79]
Graphene-Ag_3PO_4/$LaCO_3OH$	Methylene blue	Visible light	Composite with 20% $LaCO_3OH$ exhibited the highest photocatalytic activity for dye degradation	[80]

Continued

Table 2 Some of the Recently Published Studies on the Graphene-Based Composite Photocatalysts Used for Water Purification—cont'd

Graphene-Based Photocatalyst	Target Pollutant	Light Source	Performance	Ref.
Ag-RGO	Methylene blue	Visible light	The photocatalytic degradation efficiency of methylene blue by Ag-RGO (99.71%) was higher than Ag nanoparticle and GO	[81]
CdS/RGO	Rhodamine B	Visible light	The optimized nanocomposite exhibited 93% photocatalytic degradation efficiency for Rhodamine B	[82]
3D $CeVO_4$/Graphene aerogels	Methylene blue	Visible light	The synthesized composite increased the dye degradation efficiency (98%) compared to that of $CeVO_4$ particles (62%)	[83]
Graphene quantum dots (GQDs) and polymer-modified GQDs	Methylene blue	Visible light	The GQDs presented a strong blue and excitation-independent photoluminescent behavior under excitation wavelengths of 320–420 nm	[84]
GO/$CuInS_2$/ZnO	Rhodamine B	Visible light	The GO with high specific surface area and excellent conductivity played as a good support for $CuInS_2$/ZnO and enhanced degradation efficiency of dye	[85]
CdS-graphene	Methylene blue, Methyl orange, and Rhodamine B	Visible light	The photocatalytic degradation efficiency of Methylene blue was ~16%, ~40%, and ~95% for pure graphene, CdS nanoparticles, and CdS-graphene composite respectively after 5 h	[86]
ZnO/RGO	H_2 evolution	Xenon lamp (λ: 320–1100 nm)	RGO/ZnO nanorods showed the highest photocatalytic H_2 evolution rate which was about 1.1, 1.9, and 2.6 times higher than that of ZnO/RGO particles, ZnO/RGO nanospheres, and ZnO/RGO nanosheets, respectively	[87]

Table 2 Some of the Recently Published Studies on the Graphene-Based Composite Photocatalysts Used for Water Purification—cont'd

Graphene-Based Photocatalyst	Target Pollutant	Light Source	Performance	Ref.
Polythiophene (PTh)-RGO-TiO_2	Methylene blue	Visible light	0.1%w/v of PTh-RGO-TiO_2 showed a H_2 production rate of 214.08 μmol/h with the quantum efficiency of 14.17% at 400 nm and efficient degradation of dye	[88]
RGO@TiO_2 nanorod	Brilliant X-3B	LED lamp ($\lambda = 365$ nm)	The presence of GO led to the formation of a flake-like TiO_2 nanorod-assembled grafted RGO hybrid. The photocatalytic activity of the composite increased first and then decreased with increasing GO loading from 0 to 10 wt%	[89]
$BiFeO_3$/(N-doped) graphene	Congo red	Visible light	Compared with $BiFeO_3$/graphene and pristine $BiFeO_3$, $BiFeO_3$/N-doped graphene exhibited much higher photocatalytic activity	[90]
Nitrogen-doped graphene-BiOBr	Methyl orange	Visible light	The nitrogen-doped graphene-BiOBr had the highest photodegradation performance of methyl orange which was about 50, 4.6, and 3.8 times of P25, BiOBr, and RGO-BiOBr composite efficiencies, respectively	[91]
Electrospun RGO/TiO_2 composite nanofibers	Methyl orange	Visible light	The presence of RGO sheets decreased the band gap energy of TiO_2 to 2.9 eV. The kinetic of dye removal by RGO/TiO_2 was 6 times higher than that by commercial TiO_2	[92]
3D free-standing ZnO/RGO foam	Rhodamine B	Xe lamp (simulate solar light)	The results showed that Rhodamine B was steadily mineralized by the prepared samples, the TOC residual ratio was 20.2% after 150 min illumination, while the concentration change ratio of Rhodamine B was 5.0%	[93]

Continued

Table 2 Some of the Recently Published Studies on the Graphene-Based Composite Photocatalysts Used for Water Purification—cont'd

Graphene-Based Photocatalyst	Target Pollutant	Light Source	Performance	Ref.
N, S co-doped graphene quantum dots-graphene-TiO_2 nanotubes	Methyl orange	Visible light	The N, S-GQDs + 10% RGO + TiO_2NT composite showed the highest apparent rate constant for photodegradation of dye which was 1.8 times and 16.3 times higher than those of 10% RGO + TiO_2NT and pure TiO_2NT, respectively	[94]
ZnO hollow nanospheres/graphene	Methylene blue	Visible light	The synthesized composites had the band gap of 2.61 eV, and enhanced charge carries separation efficiency	[95]
SnO_2@RGO	Methyl orange	Mercury lamp ($\lambda = 365$ nm)	The SnO_2@RGO composite showed increased photocatalytic activity compared to pure SnO_2	[96]
AgBr/ZnO/RGO	Methyl orange	Visible light	The photocatalytic removal of dye by AgBr/ZnO/RGO composite was 12.8 and 2.3 times higher than that of ZnO/RGO and AgBr/ZnO, respectively	[97]
Ag-Ag_2O-ZnO/GO	Acid blue 74	Visible light	The Ag-Ag_2O-ZnO/GO nanocomposite showed a higher photocatalytic activity (90%) compared to Ag-Ag_2O-ZnO (85%) and ZnO (75%), respectively	[98]

photocatalyst with high surface area for water purification applications. Lin et al. [56] reported a comparative study on the photocatalytic removal of pharmaceutical pollutants by TiO_2-Fe and TiO_2-reduced graphene oxide nanocomposites. They coated the nanocomposites on the optical fibers by a polymer-assisted hydrothermal deposition method and evaluated their photocatalytic activity under UV and visible light irradiation. The obtained results showed that the band gap energy of Fe-doped TiO_2 particles was reduced more (2.40 eV) than the band gap of RGO-incorporated TiO_2 (2.85 eV). Therefore, TiO_2-Fe presented more photocatalytic activity under visible light irradiation, while TiO_2-RGO was more efficient under UV irradiation due to the reduced recombination rate of photo-excited electrons-hole pairs.

A three-dimensional titanate-graphene oxide (Ti-GO) composite gel was also prepared by Lin et al. [51] through a one-pot solvothermal technique. They used tetra-butyl titanate as a Ti source and acetic acid as stabilizer and cross-linking agent. Fig. 7 shows the macrographs of the synthesized

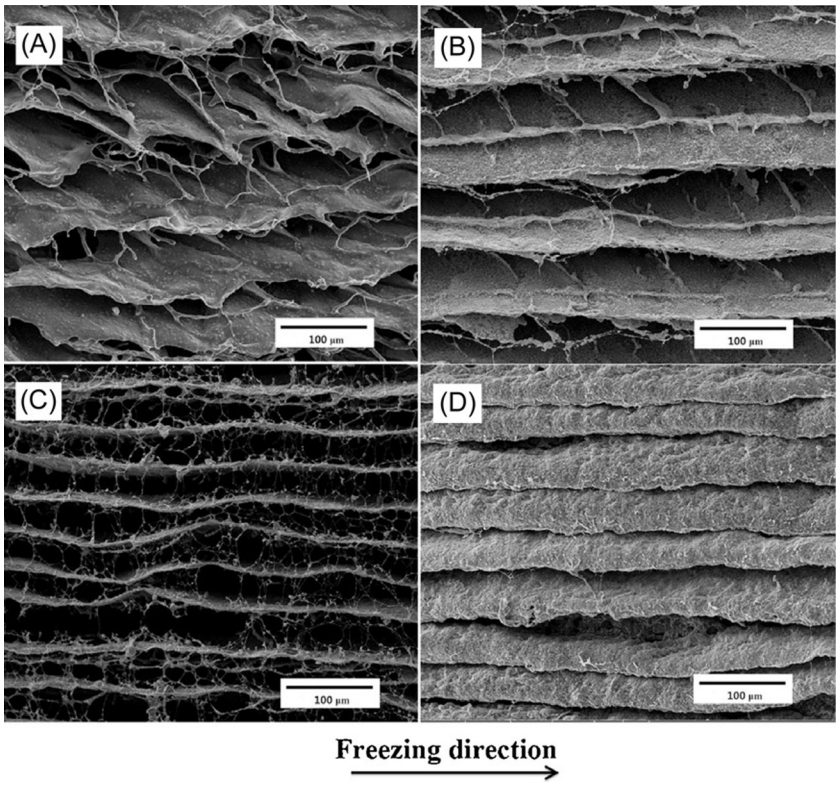

FIG. 6

SEM images of the macroporous TiO_2/chitosan/RGO composites prepared by 1.0 wt% RGO with TiO_2 contents of (A) 45 vol%, (B) 62 vol%, (C) 71 vol%, and (D) 77 vol%.

Adapted from C. Chen, Y. Zhang, J. Zeng, F. Zhang, K. Zhou, C.R. Bowen, D. Zhang, Aligned macroporous TiO2/chitosan/reduced graphene oxide (rGO) composites for photocatalytic applications, Appl. Surf. Sci. 2017, 424, 170–176 with permission from Elsevier.

photocatalyst gels with different GO contents. Keeping in various solutions such as NaOH (pH 12), water (pH 7), HAc (analytically pure), 1 M NaCl and several organic solvents for specific time improved stability of the as-prepared gels. The proper chemical stability of the Ti-GO composites was assigned to the strong numerous non-covalent and electrostatic/hydrogen bonding interactions between the titanate precursor chains and oxygen-containing groups of GO sheets [51]. The Ti-GO composite gel exhibited an improved photocatalytic performance for decolorization of methyl orange solution under UV irradiation.

ZnO has been frequently used as another good conjugate for preparing graphene-based composite photocatalysts [99–107]. Kang et al. [87] studied the effect of different morphologies of ZnO on the photocatalytic activity of ZnO/RGO nanocomposites. They showed that the ZnO morphologies considerably affected the photo-absorption, separation efficiency of the photo-induced charges, and photocatalytic performance of the ZnO/RGO composites. The RGO/ZnO composite containing ZnO nanorods grown vertically on both sides of graphene sheets displayed the highest photocatalytic H_2

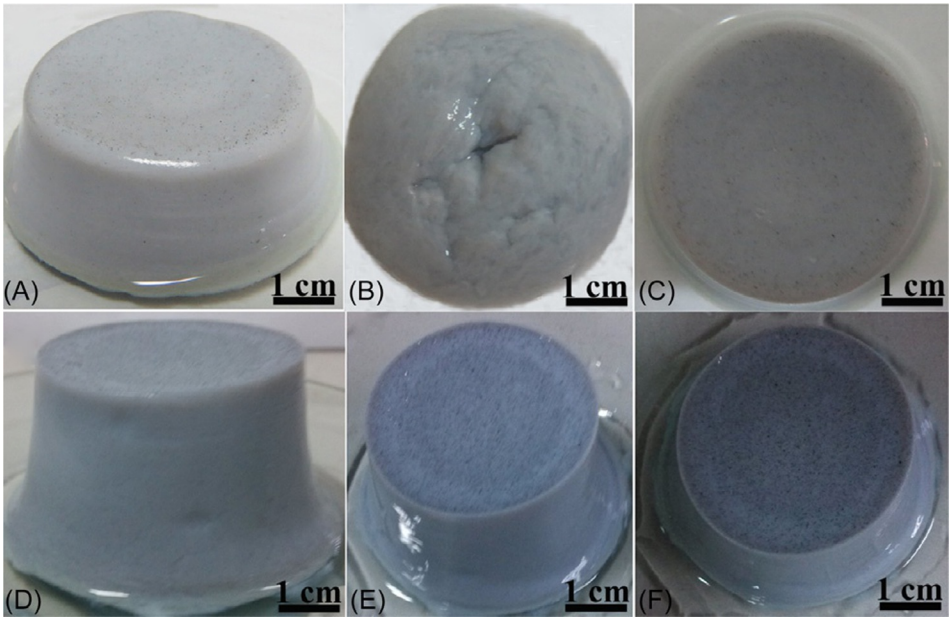

FIG. 7

Macrographs of Ti-GO gel composites with (A–C) 6 mg and (D–F) 18 mg GO content taken at various angles.

Adapted from R. Liu, X. Li, S. Li, G. Zhou, Three-dimensional titanate–Graphene oxide composite gel with enhanced photocatalytic activity synthesized from nanofiber networks, Catal. Today 2017, 297, 264–275 with permission from Elsevier.

production rate due to the higher transfer rate of the photo-generated electron from ZnO to RGO, and decreased recombination of the photo-induced hole-electron pairs. Beura and Thangadurai [40] also investigated the effect of ZnO concentration on the structural, optical and photocatalytic properties of the graphene-ZnO nanocomposites. They observed that the shape of ZnO changes from sphere to rod by increasing ZnO content.

ZnO/GO/nanocellulose composite was used for adsorption and photocatalytic removal of ciprofloxacin antibiotic from aqueous solutions by Anirudhan and Deepa [62]. Cellulose was converted to nanocellulose to enhance adsorption efficiency by increased surface area, number of available functional moieties, and crystalline nature. The band gap of ZnO/GO and ZnO/GO/nanocellulose was 2.4 and 2.8 eV, respectively, indicating the photocatalytic activity of these composites in the visible region. The highest photodegradation efficiency of ciprofloxacin (98.0%) was observed at pH 6.0. Jia et al. [50] introduced a magnetically separable sulfur-doped $SnFe_2O_4$/graphene nanocomposite for photocatalytic degradation of chlorotetracycline under visible light. They separated the used nanocomposite using a magnet and reused the nanocomposite five times, maintaining a photocatalytic efficiency around 70%.

Most recently, Liu and colleagues [52] prepared a novel shape-controlled Cu_2O/RGO/In_2O_3 hybrid with abundant oxygen vacancies for photocatalytic degradation of methylene blue and Cr^{6+} solutions. They investigated the band structure and position of various synthesized photocatalysts by UV–vis diffuse reflection spectroscopy (DRS), Mott-Schottky (M-S) plots, and valence band XPS (VB-XPS) analysis, as presented in Fig. 8. The band gap of the Cu_2O/RGO/In_2O_3 hybrid was decreased due to

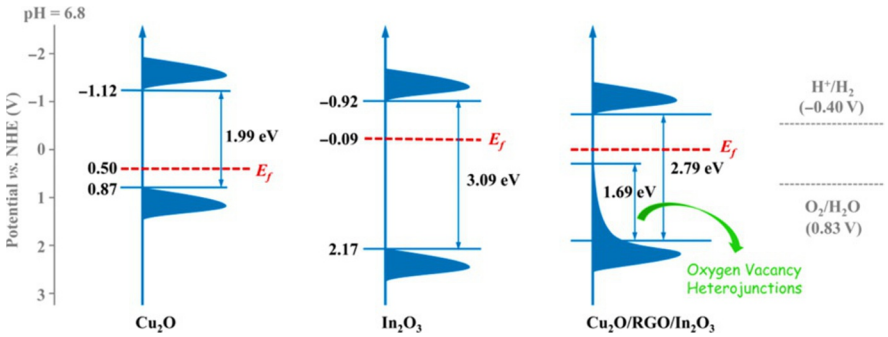

FIG. 8

Proposed band positions of Cu_2O, In_2O_3, and $Cu_2O/RGO/In_2O_3$ photocatalysts.

Adapted from J. Liu, J. Ke, D. Li, H. Sun, P. Liang, X. Duan, W. Tian, M.O. Tadé, S. Liu, S. Wang, Oxygen vacancies in shape controlled Cu2O/reduced graphene oxide/In2O3 hybrid for promoted photocatalytic water oxidation and degradation of environmental pollutants, ACS Appl. Mater. Interfaces 9 (2017) 11678–11688 with permission from American Chemical Society.

the presence of oxygen vacancies and the formation of heterojunction between In_2O_3 and Cu_2O, which induced additional diffusive electronic states above the valence band edge.

2.3 MEMBRANE FILTRATION

In recent years, membrane technology has developed as an efficient and promising technique for water purification. The increasing application of membrane-based technologies is mainly due to their features and applicability to sustainable industrial designs [108]. Membrane water purification is expected to play a growing important role in areas such as drinking water treatment, brackish and seawater desalination, and wastewater treatment and reuse, because of its simplicity and ease of operation, low energy consumption, lack of phase changes or chemical additives, lower space requirements, and easy scale-up, compared to conventional technologies. Now, polymeric membranes are the most widely used membrane type for water purification due to their relatively low cost, clear pore-forming mechanism, and higher flexibility compared to inorganic membrane equivalents [109]. However, there are still some shortcomings, such as high hydrophobicity, low flux, high tendency toward fouling, and low mechanical strength, which restrict industrial applications of the polymeric membranes.

Among various strategies introduced for development of membranes with high hydrophilicity, good permeability, and desired antifouling properties, fabrication of nanocomposite membranes (in which inorganic nanomaterials are used for modification of polymeric membranes) has attracted a great deal of attention. Using nanomaterials in the preparation of membranes not only resulted in excellent fouling resistance, but also could be a possible solution to overcome the trade-off between water permeability and solute selectivity. Nanomaterials can affect the permeability, selectivity, hydrophilicity, conductivity, mechanical strength, thermal stability, and the antiviral and antibacterial properties of the polymeric membranes. In this respect, carbon-based nanomaterials are among the most promising candidates owing to their great physicochemical properties. Graphene and its derivatives (in particular, GO) have been frequently used for preparing nanocomposite membranes due to their abundant functional groups, including epoxide, carboxyl, and hydroxyl, providing functional reactive sites and

hydrophilic properties. Hegab and Zou [5] comprehensively reviewed the fabrication and applications of various GO-assisted membranes for desalination and water purification. A number of the most recent advances in the graphene-assisted membranes used for water purification are overviewed in the following sections (Table 3).

Table 3 Some of the Recently Published Researches on the Graphene-Assisted Membranes Used for Water Purification

Membrane	Membrane Material	Graphene-Based Additive	Performance of Modified Membrane	Ref.
MF	Commercially cellulose nitrate filters	Graphene, poly (*N*-vinylcarbazole)-graphene (PVK-G), GO, and PVK-GO	– Improved antibacterial properties	[110]
UF	PES	GO	– 20% higher pure water flux than pristine PES – Higher humic acid rejection	[111]
UF	PSF	Fe_3O_4/GO	– Three times higher permeate flux than the unmodified membrane – Drop in humic acid rejection from 89% to 84%	[112]
UF	PES	UiO-66@GO	– High flux – Good solute rejection – Excellent antifouling performance	[113]
UF	Commercial cellulose acetate membrane	RGO/graphitic carbon nitride	– Increased flux – Improved separation rate of oil/water emulsion – Improved retention rate of methylene blue – Steady performance after 5 times of recycling under visible-light irradiation.	[114]
UF	Polyphenylene sulfone (PPSU)	GO	– Improved hydrophilicity – Improved thermal stability – Enhanced fouling resistance	[115]
UF	PES	Crumpled graphene oxide (CGO)/TiO_2 CGO/Ag	– High water flux – Excellent separation efficiencies for model organic and biological foulants	[116]
UF	PSF	ZnO-GO	– Enhanced hydrophilicity, high permeability and porosity – Improved humic acid rejection rate – Good antifouling and antibacterial control	[117]

Table 3 Some of the Recently Published Researches on the Graphene-Assisted Membranes Used for Water Purification—cont'd

Membrane	Membrane Material	Graphene-Based Additive	Performance of Modified Membrane	Ref.
UF	PVDF	GO and oxidized multi-walled carbon nanotubes (OMWCNTs)	– Increased hydrophilicity and water permeability – Improved rejection of TDS, phosphorus, hardness, COD, chlorine, turbidity, color, and TSS – Enhanced antifouling properties	[118]
UF	PVDF	GO	– Increased hydrophilicity and water permeability – Proper dye removal	[119]
UF	PVC	GO	– Significant enhancement in hydrophilicity, water flux, and mechanical properties	[120]
UF	PSF	Polyamine functionalized GO (fGO)	– Higher porosity and permeability – Improved structural and mechanical properties – Better anti-fouling potential with high flux recovery with little change in BSA rejection	[121]
FO substrate	PES	RGO modified graphitic carbon nitride	– Increased osmotic water flux – Reduced internal concentration polarization	[122]
FO substrate	PSF	GO	– High water permeability – Enhanced ion selectivity – Reduced internal concentration polarization	[123]
NF	PES	GO nanoplates	– Increased pure water flux – Increased FRR value – Decreased dye rejection	[124]
NF	PES	RGO/TiO_2	– Increased pure water flux – Increased FRR value – Increased dye rejection	[125]
NF	PEI/PAN	GO	– Enhanced solute rejection – Promising long-term operation stability – Excellent solvent resistance for practical application	[126]

Continued

Table 3 Some of the Recently Published Researches on the Graphene-Assisted Membranes Used for Water Purification—cont'd

Membrane	Membrane Material	Graphene-Based Additive	Performance of Modified Membrane	Ref.
NF	PAN	GO	– Significantly increased water flux – High rejection performance for organic dye and Na_2SO_4	[127]
NF	Polyamide/PES	Exfoliated hydrotalcite (EHT)/GO	– Enhanced water flux – Superior water softening performance.	[128]
FO	Commercial polyamide membrane	GO-Ag	– 80% inactivation rate against attached *Pseudomonas aeruginosa* cells – Promising anti-biofouling property without sacrificing the membrane intrinsic transport properties	[129]
FO	Polyamide	GO	– Enhanced hydrophilicity and higher water flux – Higher salt rejection – Smoother surface – Lower fouling propensity	[130]
FO	Commercial polyamide membrane	GO/Ag	– Improved bacterial inactivation – Super-hydrophilic properties	[131,132]
FO	Polyamide/PSF	TiO_2/GO	– Increased surface hydrophilicity and roughness – Higher water flux	[133]
FO	Polyamide	GO	– Increased surface hydrophilicity – Improved antimicrobial activity	[134,135]
RO	Anodic aluminum oxide (AAO)	Chitosan cross-linked graphene oxide/titania	– 30% higher salt rejection rate – Increased water flux	[136]
RO	Polyamide/PSF	GO	– Improved water flux – Improved mechanical stability – Improved chlorine and fouling resistances	[137]
RO	Polyamide/PSF	GO	– Lower membrane surface energy – Enhanced hydrophilicity and water flux – Superior anti-microbial activity	[138]

Table 3 Some of the Recently Published Researches on the Graphene-Assisted Membranes Used for Water Purification—cont'd

Membrane	Membrane Material	Graphene-Based Additive	Performance of Modified Membrane	Ref.
RO	Polyamide/PSF	RGO/TiO_2	– Improved hydrophilicity and water flux – Smoother surface – Improved salt rejection – Improved antifouling property	[139]
RO	Aramid	GO	– Increased surface porosity – Increased permeability	[140]
RO	Commercial polyamide RO membrane	GO	– Increased hydrophilicity and water permeat – Enhanced anti-microbial performance	[141]
RO	Commercial polyamide RO membrane	GO	– Increased water flux – Good chlorine resistance	[142]
NF	Polyamide/PSF	RGO/TiO_2	– Improved hydrophilicity and water flux – Increased salt rejection – Decreased surface roughness – Improved antifouling property	[143]
NF	Polyamide/ polyphenylsulfone (PPSU)	GO	– higher permeate flux than unmodified membrane – Removal of Kinetic Hydrate Inhibitors (KHIs)	[144]
NF	Polyamide/PES	RGO-NH_2	– Improved salt rejection – Increased water flux – Improved antifouling property	[145]
NF	Polyamide/PSF	GO	– Improved hydrophilicity and water flux – negligible decrease in salt rejection – Improved antifouling property	[146]
NF	PES	TiO_2@GO	– Increased permeate flux – Improved antifouling effect	[147]
NF	Polyamide/PSF	Carboxylated graphene oxide (cGO)	– Improved surface hydrophilicity and water permeability – Improved salt rejection – Improved antifouling properties	[148]

Continued

Table 3 Some of the Recently Published Researches on the Graphene-Assisted Membranes Used for Water Purification—cont'd

Membrane	Membrane Material	Graphene-Based Additive	Performance of Modified Membrane	Ref.
NF	PES	Acyl chlorided GO	– Increased water flux – Increased salt rejection	[149]
NF	PSF	GO	– Enhanced selectivity towards polycyclic aromatic hydrocarbons in water – Improved hydrophilicity and water flux – Increased salt rejection	[150]
NF	PSF	GO	– Increased water flux – Increased rejection for different heavy metals	[151]
NF	Poly (m-phenylene isophthalamide) (PMI)	GO	– More negatively charged and greater hydrophilic surface – Increased pure water flux – Slightly higher dye rejection – Better fouling resistance BSA	[152]
Photocatalytic membrane	–	Fe_2O_3/TiO_2/GO	– Improved photocatalytic activity – Enhanced humic acid removal	[153]
Anion exchange membrane	Commercial anion exchange membrane	Sulfonated reduced graphene oxide (S-RGO)	– Increased permselectivity and separation efficiency of monovalent anions	[154]
Membrane adsorbent	zirconium-chitosan (CTS)/GO	GO	– Effective removal of anions such as fluoride, bicarbonate, and sulfate	[155]
Membrane adsorbent	PSF	GO	– High removal efficiency for pharmaceuticals, personal care products, a dye, and a surfactant from water	[156]

In order to fabricate a thin film composite (TFC) nanofiltration membrane with both high water permeability and high salt rejection, Wen and colleagues [149] embedded acyl chloride graphene oxide (GO-COCl) in the polyamide layer of these membranes through interfacial polymerization. Different amounts of the synthesized GO-COCl and ethanol (for better dispersion of GO-COCl) were added into TMC/hexane solution to obtain a homogeneous GO-COCl/TMC organic solution. The water flux of the modified membranes was increased nearly two times and salt rejection of Na_2SO_4 was enhanced from 95.0 to 97.1%, compared with those of the unmodified NF membrane. They assigned the improved performance of the modified membranes to the incorporation of laminated graphene oxide sheets into

the polyamide layer, which reduced the effective thickness of this layer without creating any defects or flaws, thus providing high water permeability and salt rejection rate. However, the surface roughness of the polyamide layer was increased in the presence of GO and ethanol and led to a higher fouling tendency for the nanocomposite membranes.

A remarkable increase in water flux (80%) was observed by He et al. [138] when they modified reverse osmosis (RO) membranes by GO nanosheets. The GO-polyamide membranes also displayed antibacterial activity around 2.6 times higher than that of pure polyamide membrane. They related the antibacterial activity of the modified membranes to both physical and chemical interactions between the GO and the bacteria. In the presence of GO, the cell membranes of bacteria may be damaged physically by the sharp edges of the graphene nanosheets. In addition, GO can disrupt the microbial mechanism of bacteria by chemical effect on the cellular oxidative processes. The improved antifouling property of the GO-containing membranes was also related to the highly negative surface charge and smoother surface of these membranes [130,139,143,145,147].

Rao and colleagues [153] prepared a photocatalytic membrane consisting of interconnecting TiO_2 nanowires, Fe_2O_3 nanoparticles, and GO sheets. The synthesized membrane showed an enhanced performance for humic acid removal under simulated solar irradiation due to the greater adsorption of humic acid by Fe_2O_3 nanoparticles, and improved photocatalytic activity of TiO_2 by the GO sheets. On the other hand, Li et al. [145] utilized the reduced graphene oxide-NH_2 for modification of polyamide nanofiltration membranes with the intent of enhancing water flux and antifouling ability. They functionalized the surface of the GO with a highly reactive amine group to increase the compatibility between graphene and polymer matrix. The better compatibility of the GO-NH_2 and polyamide layer was related to the reaction of the amino group and TMC during the interfacial polymerization process. A number of studies reported improvement in the chlorine resistance of the polyamide membranes incorporated with GO [139,157]. The chemically robust GO sheets embedded in the polyamide layer acted as a barrier layer and protected the polyamide against chlorine attack, as illustrated in Fig. 9. It was also suggested that the intermolecular hydrogen bonding between functional groups of GO and polyamide layer can hinder the substitution of hydrogen with chlorine in the aromatic polyamide layer and enhance the chlorine resistance of the membrane [139,158,159].

Number of researchers have utilized GO nanosheets as a surface coating agent for modification of polymeric membranes. The additional surface coating can increase membrane stability and durability. However, an undesired reduction in the membrane permeability usually occurs because of the known trade-off between membrane flux and durability. This phenomenon was observed by Hu and Mi [160] who deposited GO nanosheets on a polydopamine-coated polysulfone membrane. They dip-coated porous polysulfone support in the dopamine solution to form polydopamine coating on the membrane surface. After drying the coated support, it was alternately soaked in TMC and GO solutions for several times to form a desired number of additional layers of TMC and GO. The water flux of the polydopamine-coated membrane sharply decreased after coating GO nanosheets. In an attempt to overcome this challenge, Choi et al. [157] prepared a dual-action barrier coating layer of GO multilayers on the polyamide surface of RO membrane via layer-by-layer (LbL) deposition of oppositely charged GO nanosheets. The objective was to enhance the resistance to both fouling and chlorine-induced degradation of polyamide layer, while preserving the flux and separation performance of the original membrane. In order to LbL deposition of GO and aminated-GO (AGO) nanosheets onto the polyamide layer, the prepared TFC membrane was alternately dipped in the aqueous suspensions of negatively charged GO and positively charged AGO, respectively. This cycle was repeated several times until the desired

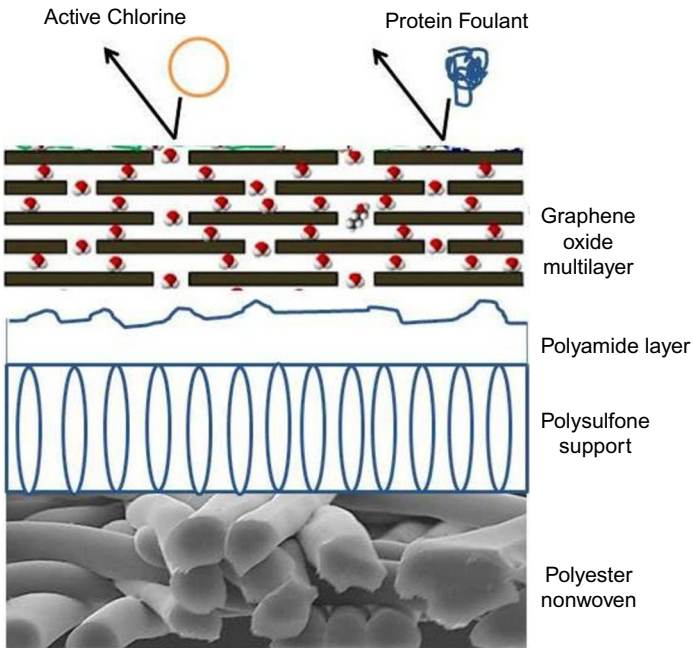

FIG. 9

GO protective layer against foulants and active chlorine in the polyamide membrane.

number of AGO/GO bilayers was obtained. Fig. 10 shows the scheme of LbL deposition of AGO and GO nanosheets on the surface of TFC membrane [157]. Although the antifouling property and chlorine resistance of the modified membranes was increased, the desalination performance including water flux and salt rejection of them were not significantly changed compared with the pristine membrane, indicating no trade-off between membrane coating thickness and permeability. Choi and colleagues attributed this observation to the unique water transport across the stacked GO nanosheets that improved the surface hydrophilicity and permeability of the GO coating and prevented flux loss in the modified membranes [157].

Wang et al. [127] also prepared a GO based nanofiltration membrane on a highly porous polyacrylonitrile nanofibrous (GO@PAN) for water treatment applications. GO nanosheets were assembled on the PAN mat by a vacuum suction method and formed a barrier on the top of PAN nanofibrous with controllable thickness. This GO layer presented "ideal" pathways (hydrophobic nanochannel) for water molecules between the well-stacked GO nanosheets (Fig. 11). Therefore, a significant increased water flux was observed at a low external pressure (1.0 bar). The GO@PAN membrane exhibited nearly 100% rejection performance of Congo red dye and 56.7% rejection for Na_2SO_4 salt.

Hegab et al. [161] also improved the antifouling ability of commercial RO membranes by deposition of GO functionalized chitosan layer on the membrane surface. They observed a significant increase in the surface hydrophilicity of the modified membranes because of the presence of amphiphilic GO and hydrophilic chitosan.

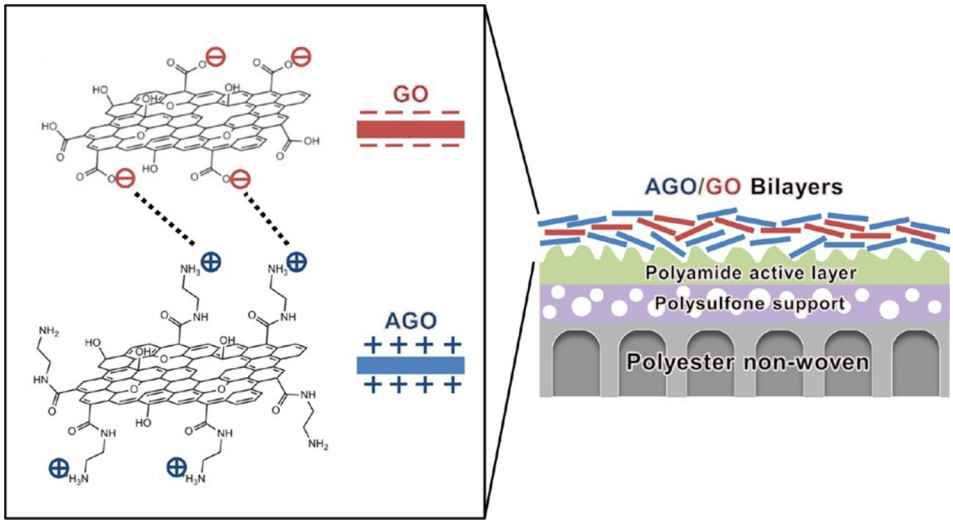

FIG. 10

Schematic illustration of layer-by-layer (LbL) deposition of positively charged GO and negatively aminated-GO nanosheets on a polyamide membrane surface.

Adapted from W. Choi, J. Choi, J. Bang, J.-H. Lee, Layer-by-layer assembly of graphene oxide nanosheets on polyamide membranes for durable reverse-osmosis applications, ACS Appl. Mater. Interfaces 5 (2013) 12510–12519 with permission from American Chemical Society.

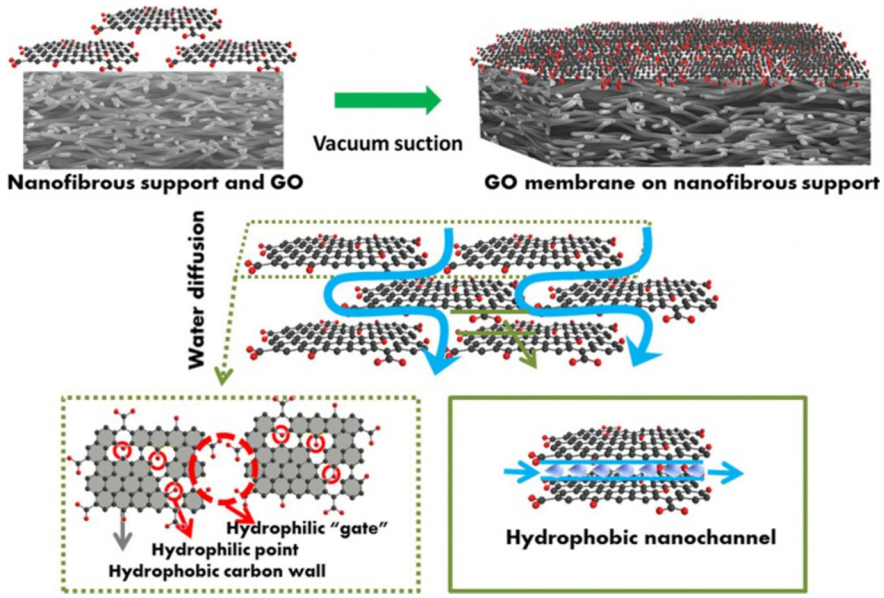

FIG. 11

Conceptual illustration of pathways (hydrophilic "gate" and hydrophobic nanochannel) for water molecule between GO nanosheets.

Adapted from J. Wang, P. Zhang, B. Liang, Y. Liu, T. Xu, L. Wang, B. Cao, K. Pan, Graphene oxide as an effective barrier on a porous nanofibrous membrane for water treatment, ACS Appl. Mater. Interfaces 8 (2016) 6211–6218 with permission from American Chemical Society.

2.4 ELECTROCHEMICAL PURIFICATION

Over the past decades, among different water purification techniques, electrochemical methods have drawn considerable attention because of their merits such as high efficiency, ease of operation, and environmental compatibility [162]. The electrochemical advanced oxidation processes (EAOPs) such as anodic oxidation, electro-Fenton, solar photo-electro-Fenton, and other electro-Fenton like processes were developed as powerful methods for effective removal of pollutants [163]. In the EAOPs, pollutants are destructed at the anode (anodic oxidation) or using the Fenton's reagent partially or completely produced from electrode reactions. Electro-Fenton (EF) is the most common technique used for EAOPs, in which H_2O_2 is generated at the cathode with O_2 or air feeding, while an iron catalyst (Fe^{2+}, Fe^{3+}, or iron oxides) is added to the solution. Fenton reaction between Fe^{2+} and electrogenerated H_2O_2 produces hydroxyl radicals ($^{\bullet}OH$) as a powerful oxidizing agent for removal of contaminants [164]. As expected, the electrode material has prominent effects on the features and efficiency of electrochemical water purification methods. Carbonaceous materials are applied as suitable electrodes because of their high conductivity, stability, non-toxicity, and commercial availability. On the other hand, modification of other electrode materials with carbon-based nanomaterials can improve their electroactive surface area and the rate of oxygen mass transfer, resulting in the increased electro-generated species and process efficiency. According to their previously mentioned properties, graphene-based materials are appropriate candidates for fabrication or modification of electrode materials employed in electrochemical systems. Table 4 represents a number of the most recently published scientific reports on the electrochemical water treatment methods using graphene-based materials.

Table 4 Number of the Recently Published Studies on the Electrochemical Water Purification Using Graphene-Based Materials

Process	Graphene-Based Electrode	Target Pollutant	Performance	Ref.
Anodic oxidation	SnO_2/GO	Inorganic (iodide-, chloride-, sulfite-anions) and organic (ascorbic acid) substances	SnO_2/RGO film electrode showed a high electrocatalytic activity in the anodic oxidation of inorganic and organic substances	[165]
EF	Graphene ink-coated carbon cloth	Phenol	3.08-fold increase was observed in the phenol degradation rate	[166]
EF	Pristine graphene	Phenol	Graphene foam exhibited the highest H_2O_2 electro-generation yield, and phenol degradation rate	[167]
EF	nitrogen-doped graphene @carbon nanotube	Dimethyl phthalate	The degradation rate of dimethyl phthalate was 14 times higher than that of graphite cathode	[165]
EF	RGO/carbon felt	Acid Orange 7	Using modified cathode, dye solution decolorized efficiently within only 5 min and completely mineralized (94.3%) in 8 h	[168]

Table 4 Number of the Recently Published Studies on the Electrochemical Water Purification Using Graphene-Based Materials—cont'd

Process	Graphene-Based Electrode	Target Pollutant	Performance	Ref.
EF	Quinone-functionalized graphene	Bisphenol A	Using modified electrode, significant enhancement in the production of H_2O_2 and degradation efficiency of Bisphenol A was observed	[169]
EF	GO and RGO Coated Graphite	Methylene Blue and Acid Red 14	Electrochemical analysis and experimental results showed better electrochemical properties of RGO-graphite electrode for degradation of organic dyes	[170]
EF	Graphene/carbon nanotube	Methyl blue	99% removal efficiency of dye was achieved after 60 min with the initial pH value of 3 and applied current of 15 mA using modified cathode	[171]
EF	30 wt% graphene-Fe_3O_4	Methylene blue	The fabricated cathode material possessed high EF catalytic activity after prolonged cycling. The decolorization of dye solution was 97% in 24 min	[172]
EF	Activated carbon fibers@reduced graphene oxide@ordered mesoporous carbon	Phthalic acid esters	Using composite electrode, the reduction of O_2 to generate H_2O_2 was increased from 31 mg/L to 85 mg/L, and current efficiency of EF process was improved from 25.0% to 40.0%	[173]
EF	RGO/graphite	Ciprofloxacin	The RGO-graphite composite electrode improved cell efficiency of H_2O_2 production by 16%	[174]
EF	Graphene/graphite-PTFE	Reactive brilliant blue	33.3% TOC decay was observed after 180 min reaction time	[175]
EF	Graphene/glassy carbon	Methylene blue	97% dye removal efficiency was achieved after 160 min reaction time.	[176]
EF-cathodic membrane filtration	Graphene-PPy/polyester filter cloth/fabric	Methylene blue	95% dye removal efficiency obtained within 90 min	[177]

Continued

Table 4 Number of the Recently Published Studies on the Electrochemical Water Purification Using Graphene-Based Materials—cont'd

Process	Graphene-Based Electrode	Target Pollutant	Performance	Ref.
Cathodic electrochemical advance oxidation	RGO/GDE	Bisphenol A	Using modified cathode, 100% Bisphenol A removal and 74.6% TOC removal was observed within 30 min	[178]
Heterogeneous-EF	Graphene @Fe_3O_4/Ni foam	Methylene blue	Methylene blue removal efficiency was 97% within 24 min	[172]
EF	Graphene@PTFE	2,4-Dichlorophenol and Rhodamine B	Rhodamine B and 2,4-Dichlorophenol removal efficiency was 100% and 97.6%, respectively	[179]
EF	Pd@RGO/carbon felt	EDTA-Ni	83.8% removal efficiency was observed for 10 mg/L EDTA-Ni within 100 min treatment	[180]
Heterogeneous-EF	AQ@ERGO/Ni screen	Rhodamine B	Rhodamine B removal efficiency was 100% within 120 min reaction time	[181]
EF	CeO_2/RGO	Ciprofloxacin	90.97% removal efficiency for 50 mg/L ciprofloxacin was obtained within 6.5 h treatment	[182]
	$Ce_{0.75}Zr_{0.25}O_2$/RGO		100% removal efficiency for 50 mg/L ciprofloxacin was obtained within 5 h treatment	[183]
Heterogeneous-EF	quinone@graphene@ Fe_3O_4/carbon cloth	Bisphenol A	100% removal efficiency for 5 mg L^{-1} Bisphenol A was observed after 90 min treatment	[169]

Mousset and colleagues [167] investigated the performance of pristine graphene in the forms of graphene monolayer, graphene multilayer, and graphene foam, as electrode materials for the electro-Fenton treatment of wastewater. They observed that all the studied forms of graphene can sufficiently regenerate Fe^{2+} and produce H_2O_2 resulting in a sustainable formation of $^{\bullet}OH$ through the Fenton reaction and efficient degradation of phenol. Among three investigated forms of graphene, graphene foam presented the highest H_2O_2 electro-generation rate and phenol mineralization efficiency. The superior electrochemical activity of graphene foam was assigned to its high purity, low interfacial charge-transfer resistance, high specific surface area, and 3D porous structure. Akerdi et al. [170] compared the performance of the GO- and RGO-coated graphite cathodes for decolorization of dye solutions in a heterogeneous electro-Fenton process. They deposited the as-synthesized GO and RGO on the surface of the pretreated graphite electrode by electrochemical method in the presence of Cetyl Trimethyl Ammonium Bromide (CTAB).

Graphene sheets can be a suitable surface for attachment of iron oxide particles as the catalyst of the electro-Fenton process. Govindaraj et al. [169] prepared a quinone-functionalized graphene/Fe_3O_4

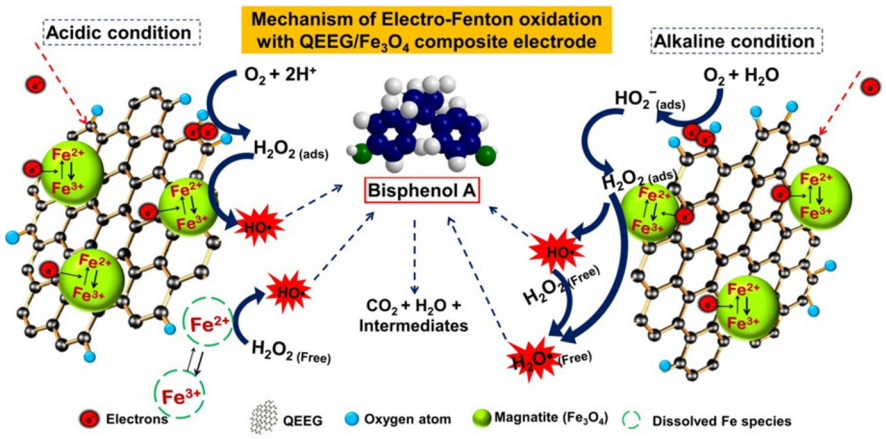

FIG. 12

Schematic representation of the overall mechanisms of electro-Fenton oxidation in the presence of quinone functionalized graphene/Fe_3O_4 electrode.

Adapted from D. Govindaraj, I. M.Nambi, J. Senthilnathan, An innate quinone functionalized electrochemically exfoliated graphene/Fe3O4 composite electrode for the continuous generation of reactive oxygen species, Chem. Eng. J. 316 (2017) 964–977 with permission from Elsevier.

electrode for continuous electro-generation of H_2O_2 and $^{\bullet}OH$ radicals. TEM analysis showed the uniform dispersion of Fe_3O_4 nanoparticles (<10 nm) on the surface of the quinone-functionalized graphene. Using new electrode material with less than 1% of iron leaching, complete removal of Bisphenol A was observed at optimized condition. Fig. 12 shows the schematic representation of the overall mechanisms of electro-Fenton oxidation in the presence of quinone-functionalized graphene/Fe_3O_4 cathode [169].

Capacitive deionization (CDI) is another promising electrochemical technology for water treatment. In the CDI, or electrosorption, process, a direct voltage is applied through the electrodes, and the ionic species are adsorbed on the electrodes [184]. Graphene-based materials have been intensively investigated as CDI electrodes mainly because of their great electrical conductivity and high specific surface area [185–205]. However, graphene has some drawbacks (such as small specific capacitance, high resistance between layers, and hydrophobicity) which reduce the ion adsorption efficiency of the CDI process. Tuan et al. [206] prepared a uniformly dispersed Fe_3O_4/RGO nanocomposite as an effective electrode for CDI. In the Fe_3O_4/RGO electrode, the iron oxide nanoparticles anchored on the graphene sheets, reduced the agglomeration of RGO sheets, and subsequently increased their electrical conductivity, electrochemical activity, and specific capacity. The maximum ion removal of the Fe_3O_4/RGO electrode was 4.3 mg/g, which was three times higher than that of the RGO electrode.

2.5 OTHER METHODS

A quick survey of the literature shows that there is an increasing trend toward developing graphene-based bactericidal materials for various environmental and biomedical applications. The antibacterial activity of graphene and its derivatives, including GO and RGO, was reported by several researchers

[207–213]. It is believed that the cell membrane of the bacteria is damaged by direct contact of the bacteria with the extremely sharp edges of the graphene nanosheets that cause the bacterial inactivation. In addition, it was found that the RGO nanosheets are more toxic to the bacteria than unreduced GO nanosheets. The better antibacterial activity of the reduced nanosheets was attributed to the better charge transfer between the bacteria and the more sharpened edges of the reduced nanosheets, during the contact interaction [214,215]. Deng et al. [216] prepared a graphene sponge decorated with Cu nanoparticles as a novel bactericidal filter for water disinfection. The synthesized composite could inactivate more than 99.9% of viable *E. coli* cells with a 5-min hydraulic retention time, confirming its efficient antibacterial activity. Pourbeyram and colleagues [217] reported that water-dispersive CuO/RGO nanocomposite has much higher antibacterial activity compared to Cu^{+2}/GO and CuO nanoparticles. Vatanpour et al. also improved the antifouling and antibacterial capability of the polyethersulfone membranes by incorporating Ag-GO nanocomposite [212].

A graphene-based composite was utilized in photocatalysis and ozonation combined system for mineralization of Bisphenol A [218]. Liao et al. synthesized the TiO_2-RGO hybrid by the liquid-phase deposition (LPD) method and observed that the recombination of photogenerated charges is significantly reduced by RGO contribution. The TOC removal efficiency was 98.4% using TiO_2-RGO/O_3/UV system in 45 min, which was 1.17 times higher than that of TiO_2/O_3/UV system. Also, the TiO_2-RGO hybrid presented high stability after recycling in five consecutive runs.

3 CHALLENGES OF GRAPHENE-BASED MATERIALS

Despite the rapid growth in the application of graphene-based materials for water and wastewater purification and the achieved valuable improvements at laboratory scale, there are still some challenges that restrict their application at a large scale and industrial cases. One of the main challenges is aggregation of graphene in the aqueous solutions, which reduces the active surface area of the graphene-based material and limits the accessibility of the contaminant and their interaction. Many researchers have tried to overcome this challenge by modifying graphene materials with surface treatment and functional groups. It is well-proven that the presence of hydrophilic functional groups (oxygen containing groups) on the graphene surface can improve its dispersion and decrease its aggregation. The separation of graphene-based materials used in a water purification process is another challenge which often needs membrane filters or high-speed centrifugation. As an alternative and more practical solution for this issue, magnetic graphene-based composites have been proposed with promising performances and easy separation using an external magnetic field.

Similar to other nanomaterials, the practical applications of graphene-based materials are directly dependent upon their cost, processability, and environmental aspects. The facile, green, and cost-effective preparation of graphene, GO, and RGO is still a challenging process. Also, the development of more simple, robust, and efficient methods for synthesis of graphene-based composites are of great importance to produce enormous quantities at economically viable prices. Regarding the environmental implications, the release of the graphene-based materials during a water treatment process, and the effect of their toxicity on living things, human exposure, and ecosystem, should be seriously addressed to minimize the associated health and environmental impact.

4 CONCLUSIONS AND FUTURE PERSPECTIVES

Graphene, an individual, two-dimensional layer of carbon atoms, bonded in a hexagonal honeycomb lattice, has attracted rising attention in recent years because of its unique physicochemical properties. One of the interesting and promising application areas of the graphene-based materials is water and wastewater treatment. In the present chapter, an overview of recent developments in the application of graphene and graphene-based materials in the water purification methods including adsorption, photocatalysis, membrane separation, and electrochemistry was presented with an emphasis on the most recent scientific reports. The graphene-based adsorbents present high pollutant removal efficiency because of the huge surface area available for adsorption. Moreover, the presence of a large number of oxygenated functional groups on the GO sheets imparts a hydrophilic nature and high negative charge density to the GO surface and improves the adsorption of pollutants. The superior photocatalytic activity of the graphene-based composites was mainly assigned to the electron acceptor role of the graphene, which prevents the recombination of the photo-induced electron-hole pairs. In the membrane-based water purification processes, contribution of the graphene-based materials in the membrane matrix displayed positive effects on the hydrophilicity, permeability, antifouling, and antibacterial properties of the membranes.

More scientific and technical efforts and exhaustive studies are still needed to overcome the challenges of graphene-based materials considering their preparation, structural and physical properties, viability, and reproducibility, as well as improvements in their dispersion, compatibility, and stability in different water purification systems. Also, further investigation is required to evaluate the cost-effectiveness of large-scale application of graphene-based materials, and monitoring their long-term durability under practical conditions in water and wastewater purification.

REFERENCES

[1] http://www.un.org/waterforlifedecade/scarcity.shtml.
[2] R. Narayan, Use of nanomaterials in water purification, Mater. Today 13 (2010) 44–46.
[3] A.K. Geim, K.S. Novoselov, The rise of graphene, Nat. Mater. 6 (2007) 183–191.
[4] M.R. Gandhi, S. Vasudevan, A. Shibayama, M. Yamada, Graphene and Graphene-based composites: a rising star in water purification—a comprehensive overview, ChemistrySelect 1 (2016) 4358–4385.
[5] H.M. Hegab, L. Zou, Graphene oxide-assisted membranes: fabrication and potential applications in desalination and water purification, J. Membr. Sci. 484 (2015) 95–106.
[6] H.M. Hegab, A. ElMekawy, T.G. Barclay, A. Michelmore, L. Zou, C.P. Saint, M. Ginic-Markovic, Effective in-situ chemical surface modification of forward osmosis membranes with polydopamine-induced graphene oxide for biofouling mitigation, Desalination 385 (2016) 126–137.
[7] S. De Gisi, G. Lofrano, M. Grassi, M. Notarnicola, Characteristics and adsorption capacities of low-cost sorbents for wastewater treatment: a review, Sustain. Mater. Technol. 9 (2016) 10–40.
[8] J. Bao, Y. Fu, Z. Bao, Thiol-functionalized magnetite/graphene oxide hybrid as a reusable adsorbent for Hg^{2+} removal, Nanoscale Res. Lett. 8 (2013) 486.
[9] P. Bhunia, G. Kim, C. Baik, H. Lee, A strategically designed porous iron-iron oxide matrix on graphene for heavy metal adsorption, Chem. Commun. 48 (2012) 9888–9890.
[10] V. Chandra, J. Park, Y. Chun, J.W. Lee, I.-C. Hwang, K.S. Kim, Water-dispersible magnetite-reduced graphene oxide composites for arsenic removal, ACS Nano 4 (2010) 3979–3986.

[11] G. Gollavelli, C.-C. Chang, Y.-C. Ling, Facile synthesis of smart magnetic graphene for safe drinking water: heavy metal removal and disinfection control, ACS Sustain. Chem. Eng. 1 (2013) 462–472.
[12] N.T.V. Hoan, N.T.A. Thu, H.V. Duc, N.D. Cuong, D.Q. Khieu, V. Vo, Fe3O4/reduced graphene oxide nanocomposite: synthesis and its application for toxic metal ion removal, J. Chem. 2016 (2016) 10.
[13] M. Khatamian, N. Khodakarampoor, M. Saket-Oskoui, Efficient removal of arsenic using graphene-zeolite based composites, J. Colloid Interface Sci. 498 (2017) 433–441.
[14] S. Kumar, R.R. Nair, P.B. Pillai, S.N. Gupta, M.A.R. Iyengar, A.K. Sood, Graphene oxide–$MnFe_2O_4$ magnetic nanohybrids for efficient removal of lead and arsenic from water, ACS Appl. Mater. Interfaces 6 (2014) 17426–17436.
[15] D.D. La, J.M. Patwari, L.A. Jones, F. Antolasic, S.V. Bhosale, Fabrication of a GNP/Fe–Mg binary oxide composite for effective removal of arsenic from aqueous solution, ACS Omega 2 (2017) 218–226.
[16] M. Liu, C. Chen, J. Hu, X. Wu, X. Wang, Synthesis of magnetite/graphene oxide composite and application for cobalt(II) removal, J. Phys. Chem. C 115 (2011) 25234–25240.
[17] X. Luo, C. Wang, L. Wang, F. Deng, S. Luo, X. Tu, C. Au, Nanocomposites of graphene oxide-hydrated zirconium oxide for simultaneous removal of As(III) and As(V) from water, Chem. Eng. J. 220 (2013) 98–106.
[18] G. Sheng, Y. Li, X. Yang, X. Ren, S. Yang, J. Hu, X. Wang, Efficient removal of arsenate by versatile magnetic graphene oxide composites, RSC Adv. 2 (2012) 12400–12407.
[19] C. Wang, H. Luo, Z. Zhang, Y. Wu, J. Zhang, S. Chen, Removal of As(III) and As(V) from aqueous solutions using nanoscale zero valent iron-reduced graphite oxide modified composites, J. Hazard. Mater. 268 (2014) 124–131.
[20] X.-L. Wu, L. Wang, C.-L. Chen, A.-W. Xu, X.-K. Wang, Water-dispersible magnetite-graphene-LDH composites for efficient arsenate removal, J. Mater. Chem. 21 (2011) 17353–17359.
[21] X. Yang, C. Chen, J. Li, G. Zhao, X. Ren, X. Wang, Graphene oxide-iron oxide and reduced graphene oxide-iron oxide hybrid materials for the removal of organic and inorganic pollutants, RSC Adv. 2 (2012) 8821–8826.
[22] G. Zhao, J. Li, X. Ren, C. Chen, X. Wang, Few-layered graphene oxide nanosheets as superior sorbents for heavy metal ion pollution management, Environ. Sci. Technol. 45 (2011) 10454–10462.
[23] J. Zhu, Z. Lou, Y. Liu, R. Fu, S.A. Baig, X. Xu, Adsorption behavior and removal mechanism of arsenic on graphene modified by iron-manganese binary oxide ($FeMnO_x$/RGO) from aqueous solutions, RSC Adv. 5 (2015) 67951–67961.
[24] Z. Cheng, J. Liao, B. He, F. Zhang, F. Zhang, X. Huang, L. Zhou, One-step fabrication of graphene oxide enhanced magnetic composite gel for highly efficient dye adsorption and catalysis, ACS Sustain. Chem. Eng. 3 (2015) 1677–1685.
[25] T. Jiao, Y. Liu, Y. Wu, Q. Zhang, X. Yan, F. Gao, A.J.P. Bauer, J. Liu, T. Zeng, B. Li, Facile and scalable preparation of graphene oxide-based magnetic hybrids for fast and highly efficient removal of organic dyes, Sci. Rep. 5 (2015)12451.
[26] Q. Ling, M. Yang, C. Li, A. Zhang, Preparation of highly dispersed Ce-Fe bimetallic oxides on graphene and their superior adsorption ability for Congo red, RSC Adv. 4 (2014) 4020–4027.
[27] H. Chen, Y. Cao, E. Wei, T. Gong, Q. Xian, Facile synthesis of graphene nano zero-valent iron composites and their efficient removal of trichloronitromethane from drinking water, Chemosphere 146 (2016) 32–39.
[28] Y. Liang, X. He, L. Chen, Y. Zhang, Preparation and characterization of TiO_2-graphene@Fe_3O_4 magnetic composite and its application on the removal of trace microcystin-LR, RSC Adv. 4 (2014) 56883–56891.
[29] Y.-C. Lee, J.-W. Yang, Self-assembled flower-like TiO_2 on exfoliated graphite oxide for heavy metal removal, J. Ind. Eng. Chem. 18 (2012) 1178–1185.
[30] G.K. Ramesha, A. Vijaya Kumara, H.B. Muralidhara, S. Sampath, Graphene and graphene oxide as effective adsorbents toward anionic and cationic dyes, J. Colloid Interface Sci. 361 (2011) 270–277.

[31] C. Santhosh, V. Velmurugan, G. Jacob, S.K. Jeong, A.N. Grace, A. Bhatnagar, Role of nanomaterials in water treatment applications: a review, Chem. Eng. J. 306 (2016) 1116–1137.
[32] Y. Yoon, W.K. Park, T.-M. Hwang, D.H. Yoon, W.S. Yang, J.-W. Kang, Comparative evaluation of magnetite–graphene oxide and magnetite-reduced graphene oxide composite for As(III) and As(V) removal, J. Hazard. Mater. 304 (2016) 196–204.
[33] L. Cheng, Y. Jiang, N. Yan, S.-F. Shan, X.-Q. Liu, L.-B. Sun, Smart adsorbents with photoregulated molecular gates for both selective adsorption and efficient regeneration, ACS Appl. Mater. Interfaces 8 (2016) 23404–23411.
[34] J.-J. Ding, J. Zhu, Y.-X. Li, X.-Q. Liu, L.-B. Sun, Smart adsorbents functionalized with thermoresponsive polymers for selective adsorption and energy-saving regeneration, Ind. Eng. Chem. Res. 56 (2017) 4341–4349.
[35] A. Mills, R.H. Davies, D. Worsley, Water purification by semiconductor photocatalysis, Chem. Soc. Rev. 22 (1993) 417–425.
[36] A.R. Khataee, M.B. Kasiri, Photocatalytic degradation of organic dyes in the presence of nanostructured titanium dioxide: influence of the chemical structure of dyes, J. Mol. Catal. A Chem. 328 (2010) 8–26.
[37] M.M. Khan, S.F. Adil, A. Al-Mayouf, Metal oxides as photocatalysts, J. Saudi Chem. Soc. 19 (2015) 462–464.
[38] S. Morales-Torres, L.M. Pastrana-Martínez, J.L. Figueiredo, J.L. Faria, A.M.T. Silva, Design of graphene-based TiO_2 photocatalysts—a review, Environ. Sci. Pollut. Res. 19 (2012) 3676–3687.
[39] H. Dong, G. Zeng, L. Tang, C. Fan, C. Zhang, X. He, Y. He, An overview on limitations of TiO_2-based particles for photocatalytic degradation of organic pollutants and the corresponding countermeasures, Water Res. 79 (2015) 128–146.
[40] R. Beura, P. Thangadurai, Structural, optical and photocatalytic properties of graphene-ZnO nanocomposites for varied compositions, J. Phys. Chem. Solids 102 (2017) 168–177.
[41] C. Hu, T. Lu, F. Chen, R. Zhang, A brief review of graphene–metal oxide composites synthesis and applications in photocatalysis, J. Chin. Adv. Mater. Soc. 1 (2013) 21–39.
[42] N. Yang, Y. Liu, H. Wen, Z. Tang, H. Zhao, Y. Li, D. Wang, Photocatalytic properties of graphdiyne and graphene modified TiO_2: from theory to experiment, ACS Nano 7 (2013) 1504–1512.
[43] L.-L. Tan, S.-P. Chai, A.R. Mohamed, Synthesis and applications of graphene-based TiO_2 photocatalysts, ChemSusChem 5 (2012) 1868–1882.
[44] B.A. Bhanvase, T.P. Shende, S.H. Sonawane, A review on graphene–TiO_2 and doped graphene–TiO_2 nanocomposite photocatalyst for water and wastewater treatment, Environ. Technol. Rev. 6 (2017) 1–14.
[45] T.-F. Yeh, J. Cihlář, C.-Y. Chang, C. Cheng, H. Teng, Roles of graphene oxide in photocatalytic water splitting, Mater. Today 16 (2013) 78–84.
[46] X. Li, J. Yu, S. Wageh, A.A. Al-Ghamdi, J. Xie, Graphene in photocatalysis: a review, Small 12 (2016) 6640–6696.
[47] C. Chen, Y. Zhang, J. Zeng, F. Zhang, K. Zhou, C.R. Bowen, D. Zhang, Aligned macroporous TiO_2/chitosan/reduced graphene oxide (rGO) composites for photocatalytic applications, Appl. Surf. Sci. 424 (2017) 170–176.
[48] Y. Xiao, J. Liu, Y. Lin, W. Lin, Y. Fang, Novel graphene oxide-silver nanorod composites with enhanced photocatalytic performance under visible light irradiation, J. Alloys Compd. 698 (2017) 170–177.
[49] Y. Wang, J. Li, C. Ding, Y. Sun, Y. Lin, W. Sun, C. Luo, Synthesis of surface plasma photocatalyst Ag loaded TiO_2 nanowire arrays/graphene oxide coated carbon fiber composites and enhancement of the photocatalytic activity for tetracycline hydrochloride degradation, J. Photochem. Photobiol. A Chem. 342 (2017) 94–101.
[50] Y. Jia, C. Wu, B.W. Lee, C. Liu, S. Kang, T. Lee, Y.C. Park, R. Yoo, W. Lee, Magnetically separable sulfur-doped $SnFe_2O_4$/graphene nanohybrids for effective photocatalytic purification of wastewater under visible light, J. Hazard. Mater. 338 (2017) 447–457.

[51] R. Liu, X. Li, S. Li, G. Zhou, Three-dimensional titanate–Graphene oxide composite gel with enhanced photocatalytic activity synthesized from nanofiber networks, Catal. Today 297 (2017) 264–275.
[52] J. Liu, J. Ke, D. Li, H. Sun, P. Liang, X. Duan, W. Tian, M.O. Tadé, S. Liu, S. Wang, Oxygen vacancies in shape controlled Cu_2O/reduced graphene oxide/In_2O_3 hybrid for promoted photocatalytic water oxidation and degradation of environmental pollutants, ACS Appl. Mater. Interfaces 9 (2017) 11678–11688.
[53] W. Wang, Y. Liu, H. Zhang, Y. Qian, Z. Guo, Re-investigation on reduced graphene oxide/Ag_2CO_3 composite photocatalyst: an insight into the double-edged sword role of RGO, Appl. Surf. Sci. 396 (2017) 102–109.
[54] Y. Liu, Y. Shi, X. Liu, H. Li, A facile solvothermal approach of novel Bi_2S_3/TiO_2/RGO composites with excellent visible light degradation activity for methylene blue, Appl. Surf. Sci. 396 (2017) 58–66.
[55] L. Liu, C. Luo, J. Xiong, Z. Yang, Y. Zhang, Y. Cai, H. Gu, Reduced graphene oxide (rGO) decorated TiO_2 microspheres for visible-light photocatalytic reduction of Cr(VI), J. Alloys Compd. 690 (2017) 771–776.
[56] L. Lin, H. Wang, W. Jiang, A.R. Mkaouar, P. Xu, Comparison study on photocatalytic oxidation of pharmaceuticals by TiO_2-Fe and TiO_2-reduced graphene oxide nanocomposites immobilized on optical fibers, J. Hazard. Mater. 333 (2017) 162–168.
[57] Z.-J. Li, Z.-W. Huang, W.-L. Guo, L. Wang, L.-R. Zheng, Z.-F. Chai, W.-Q. Shi, Enhanced photocatalytic removal of uranium(VI) from aqueous solution by magnetic TiO_2/Fe_3O_4 and its graphene composite, Environ. Sci. Technol. 51 (2017) 5666–5674.
[58] X. Niu, J. Yu, L. Wang, C. Fu, J. Wang, L. Wang, H. Zhao, J. Yang, Enhanced photocatalytic performance of TiO_2 nanotube based heterojunction photocatalyst via the coupling of graphene and FTO, Appl. Surf. Sci. 413 (2017) 7–15.
[59] Y. Qin, Z. Sun, W. Zhao, Z. Liu, D. Ni, Z. Ma, Improved photocatalytic properties of ZnS/RGO nanocomposites prepared with GO solution in degrading methyl orange, Nanostruct. Nano-Objects 10 (2017) 176–181.
[60] S. Dong, X. Ding, T. Guo, X. Yue, X. Han, J. Sun, Self-assembled hollow sphere shaped Bi_2WO_6/RGO composites for efficient sunlight-driven photocatalytic degradation of organic pollutants, Chem. Eng. J. 316 (2017) 778–789.
[61] C. Chen, W. Yu, T. Liu, S. Cao, Y. Tsang, Graphene oxide/WS_2/Mg-doped ZnO nanocomposites for solar-light catalytic and anti-bacterial applications, Sol. Energy Mater. Sol. Cells 160 (2017) 43–53.
[62] T.S. Anirudhan, J.R. Deepa, Nano-zinc oxide incorporated graphene oxide/nanocellulose composite for the adsorption and photo catalytic degradation of ciprofloxacin hydrochloride from aqueous solutions, J. Colloid Interface Sci. 490 (2017) 343–356.
[63] T.S. Anirudhan, F. Shainy, J. Christa, Synthesis and characterization of polyacrylic acid- grafted-carboxylic graphene/titanium nanotube composite for the effective removal of enrofloxacin from aqueous solutions: adsorption and photocatalytic degradation studies, J. Hazard. Mater. 324 (Part B) (2017) 117–130.
[64] M.M.J. Sadiq, U.S. Shenoy, D.K. Bhat, $NiWO_4$-ZnO-NRGO ternary nanocomposite as an efficient photocatalyst for degradation of methylene blue and reduction of 4-nitro phenol, J. Phys. Chem. Solids 109 (2017) 124–133.
[65] M. Mukherjee, U.K. Ghorai, M. Samanta, A. Santra, G.P. Das, K.K. Chattopadhyay, Graphene wrapped Copper Phthalocyanine nanotube: enhanced photocatalytic activity for industrial waste water treatment, Appl. Surf. Sci. 418 (Part A) (2017) 156–162.
[66] U. Alam, M. Fleisch, I. Kretschmer, D. Bahnemann, M. Muneer, One-step hydrothermal synthesis of Bi-TiO_2 nanotube/graphene composites: an efficient photocatalyst for spectacular degradation of organic pollutants under visible light irradiation, Appl. Catal. B Environ. 218 (2017) 758–769.
[67] R. Karthik, J. Vinoth Kumar, S.-M. Chen, C. Karuppiah, Y.-H. Cheng, V. Muthuraj, A Study of electrocatalytic and photocatalytic activity of cerium molybdate nanocubes decorated graphene oxide for the sensing and degradation of antibiotic drug chloramphenicol, ACS Appl. Mater. Interfaces 9 (2017) 6547–6559.

[68] A. Cai, X. Wang, Y. Qi, Z. Ma, Hierarchical ZnO/S,N:GQD composites: biotemplated synthesis and enhanced visible-light-driven photocatalytic activity, Appl. Surf. Sci. 391 (Part B) (2017) 484–490.
[69] P. Hu, J. Niu, M. Yu, S.-Y. Lin, Facile solvothermal synthesis of reduced graphene oxide-$BiPO_4$ nanocomposite with enhanced photocatalytic activity, Chin. J. Anal. Chem. 45 (2017) 357–362.
[70] X. Han, S. Dong, J. Sun, K. Wang, W. Zhang, J. Sun, Incorporation of Sn-doped BiOCl with reduced graphene oxide for enhanced natural sunlight photocatalysis, Mater. Lett. 187 (2017) 154–157.
[71] H. Shen, J. Wang, J. Jiang, B. Luo, B. Mao, W. Shi, All-solid-state Z-scheme system of RGO-Cu_2O/Bi_2O_3 for tetracycline degradation under visible-light irradiation, Chem. Eng. J. 313 (2017) 508–517.
[72] J. Liu, L. Wang, J. Tang, J. Ma, Photocatalytic degradation of commercially sourced naphthenic acids by TiO_2-graphene composite nanomaterial, Chemosphere 149 (2016) 328–335.
[73] T.-W. Kim, M. Park, H.Y. Kim, S.-J. Park, Preparation of flower-like TiO_2 sphere/reduced graphene oxide composites for photocatalytic degradation of organic pollutants, J. Solid State Chem. 239 (2016) 91–98.
[74] X. Chen, Q. Zhao, X. Li, D. Wang, Enhanced photocatalytic activity of degrading short chain chlorinated paraffins over reduced graphene oxide/$CoFe_2O_4$/Ag nanocomposite, J. Colloid Interface Sci. 479 (2016) 89–97.
[75] X. Shan, X. Guo, Y. Yin, Y. Miao, H. Dong, Surface modification of graphene oxide by goethite with enhanced tylosin photocatalytic activity under visible light irradiation, Colloids Surf. A Physicochem. Eng. Asp. 520 (2017) 420–427.
[76] P. Borthakur, P.K. Boruah, G. Darabdhara, P. Sengupta, M.R. Das, A.I. Boronin, L.S. Kibis, M.N. Kozlova, V.E. Fedorov, Microwave assisted synthesis of CuS-reduced graphene oxide nanocomposite with efficient photocatalytic activity towards azo dye degradation, J. Environ. Chem. Eng. (4) (2016) 4600–4611.
[77] P. Nuengmatcha, S. Chanthai, R. Mahachai, W.-C. Oh, Visible light-driven photocatalytic degradation of rhodamine B and industrial dyes (texbrite BAC-L and texbrite NFW-L) by ZnO-graphene-TiO_2 composite, J. Environ. Chem. Eng. 4 (2016) 2170–2177.
[78] T. Huang, J. Wu, Z. Zhao, T. Zeng, J. Zhang, A. Xu, X. Zhou, Y. Qi, J. Ren, R. Zhou, H. Tian, Synthesis and photocatalytic performance of CuO-CeO_2/graphene oxide, Mater. Lett. 185 (2016) 503–506.
[79] J. Hu, Y. Liu, J. Men, L. Zhang, H. Huang, Ag modified $LaMnO_3$ nanorods-reduced graphene oxide composite applied in the photocatalytic discoloration of direct green, Solid State Sci. 61 (2016) 239–245.
[80] S.S. Patil, M.G. Mali, A. Roy, M.S. Tamboli, V.G. Deonikar, D.R. Patil, M.V. Kulkarni, S.S. Al-Deyab, S.S. Yoon, S.S. Kolekar, B.B. Kale, Graphene-wrapped Ag_3PO_4/$LaCO_3OH$ heterostructures for water purification under visible light, J. Energy Chem. 25 (2016) 845–853.
[81] K. Hareesh, R.P. Joshi, S.S. Dahiwale, V.N. Bhoraskar, S.D. Dhole, Synthesis of Ag-reduced graphene oxide nanocomposite by gamma radiation assisted method and its photocatalytic activity, Vacuum 124 (2016) 40–45.
[82] X. Fu, Y. Zhang, P. Cao, H. Ma, P. Liu, L. He, J. Peng, J. Li, M. Zhai, Radiation synthesis of CdS/reduced graphene oxide nanocomposites for visible-light-driven photocatalytic degradation of organic contaminant, Radiat. Phys. Chem. 123 (2016) 79–86.
[83] C. Fan, Q. Liu, T. Ma, J. Shen, Y. Yang, H. Tang, Y. Wang, J. Yang, Fabrication of 3D $CeVO_4$/graphene aerogels with efficient visible-light photocatalytic activity, Ceram. Int. 42 (2016) 10487–10492.
[84] J. Fan, D. Li, X. Wang, Effect of modified graphene quantum dots on photocatalytic degradation property, Diam. Relat. Mater. 69 (2016) 81–85.
[85] H. Fakhri, A.R. Mahjoub, A.H. Cheshme Khavar, Improvement of visible light photocatalytic activity over graphene oxide/$CuInS_2$/ZnO nanocomposite synthesized by hydrothermal method, Mater. Sci. Semicond. Process. 41 (2016) 38–44.
[86] M.E. Khan, M.M. Khan, M.H. Cho, CdS-graphene nanocomposite for efficient visible-light-driven photocatalytic and photoelectrochemical applications, J. Colloid Interface Sci. 482 (2016) 221–232.

[87] W. Kang, X. Jimeng, W. Xitao, The effects of ZnO morphology on photocatalytic efficiency of ZnO/RGO nanocomposites, Appl. Surf. Sci. 360 (Part A) (2016) 270–275.
[88] R. Kalyani, K. Gurunathan, PTh-rGO-TiO_2 nanocomposite for photocatalytic hydrogen production and dye degradation, J. Photochem. Photobiol. A Chem. 329 (2016) 105–112.
[89] K. Lv, S. Fang, L. Si, Y. Xia, W. Ho, M. Li, Fabrication of TiO_2 nanorod assembly grafted rGO (rGO@TiO2-NR) hybridized flake-like photocatalyst, Appl. Surf. Sci. 391 (Part B) (2017) 218–227.
[90] P. Li, L. Li, M. Xu, Q. Chen, Y. He, Enhanced photocatalytic property of $BiFeO_3$/N-doped graphene composites and mechanism insight, Appl. Surf. Sci. 396 (2017) 879–887.
[91] X. Li, C. Dong, K.-L. Wu, S.-H. Xia, Y. Hu, M. Ling, K. Liu, X.-L. Lu, Y. Ye, X.-W. Wei, Synthesis of nitrogen-doped graphene–BiOBr nanocomposites with enhanced visible light photocatalytic activity, Mater. Lett. 164 (2016) 502–504.
[92] M. Nasr, S. Balme, C. Eid, R. Habchi, P. Miele, M. Bechelany, Enhanced visible-light photocatalytic performance of electrospun rGO/TiO_2 composite nanofibers, J. Phys. Chem. C 121 (2017) 261–269.
[93] X. Men, H. Chen, K. Chang, X. Fang, C. Wu, W. Qin, S. Yin, Three-dimensional free-standing ZnO/graphene composite foam for photocurrent generation and photocatalytic activity, Appl. Catal. B Environ. 187 (2016) 367–374.
[94] H. Tian, K. Shen, X. Hu, L. Qiao, W. Zheng, N, S co-doped graphene quantum dots-graphene-TiO_2 nanotubes composite with enhanced photocatalytic activity, J. Alloys Compd. 691 (2017) 369–377.
[95] Y. Song, P. Shao, J. Tian, W. Shi, S. Gao, J. Qi, X. Yan, F. Cui, One-step hydrothermal synthesis of ZnO hollow nanospheres uniformly grown on graphene for enhanced photocatalytic performance, Ceram. Int. 42 ((2016) 2074–2078.
[96] H. Shen, X. Zhao, L. Duan, R. Liu, H. Wu, T. Hou, X. Jiang, H. Gao, Influence of interface combination of RGO-photosensitized SnO_2@RGO core-shell structures on their photocatalytic performance, Appl. Surf. Sci. 391 (Part B) (2017) 627–634.
[97] H. Wang, D. Peng, T. Chen, Y. Chang, S. Dong, A novel photocatalyst AgBr/ZnO/RGO with high visible light photocatalytic activity, Ceram. Int. 42 (2016) 4406–4412.
[98] E.H. Umukoro, M.G. Peleyeju, J.C. Ngila, O.A. Arotiba, Photocatalytic degradation of acid blue 74 in water using Ag–Ag_2O–Zno nanostuctures anchored on graphene oxide, Solid State Sci. 51 (2016) 66–73.
[99] A. Tayyebi, M. outokesh, M. Tayebi, A. Shafikhani, S.S. Şengör, ZnO quantum dots-graphene composites: formation mechanism and enhanced photocatalytic activity for degradation of methyl orange dye, J. Alloys Compd. 663 (2016) 738–749.
[100] W. Yu, X.A. Chen, W. Mei, C. Chen, Y. Tsang, Photocatalytic and electrochemical performance of three-dimensional reduced graphene Oxide/WS2/Mg-doped ZnO composites, Appl. Surf. Sci. 400 (2017) 129–138.
[101] M. Ahmad, E. Ahmed, Z.L. Hong, J.F. Xu, N.R. Khalid, A. Elhissi, W. Ahmed, A facile one-step approach to synthesizing ZnO/graphene composites for enhanced degradation of methylene blue under visible light, Appl. Surf. Sci. 274 (2013) 273–281.
[102] S. Ameen, M. Shaheer Akhtar, H.-K. Seo, H. Shik Shin, Advanced ZnO–graphene oxide nanohybrid and its photocatalytic Applications, Mater. Lett. 100 (2013) 261–265.
[103] Y. Bu, Z. Chen, W. Li, B. Hou, Highly efficient photocatalytic performance of graphene–ZnO quasi-shell–core composite material, ACS Appl. Mater. Interfaces 5 (2013) 12361–12368.
[104] R.C. Pawar, D. Cho, C.S. Lee, Fabrication of nanocomposite photocatalysts from zinc oxide nanostructures and reduced graphene oxide, Curr. Appl. Phys. 13 (2013) S50–S57.
[105] S. Vijay Kumar, N.M. Huang, N. Yusoff, H.N. Lim, High performance magnetically separable graphene/zinc oxide nanocomposite, Mater. Lett. 93 (2013) 411–414.
[106] X. Zhou, T. Shi, H. Zhou, Hydrothermal preparation of ZnO-reduced graphene oxide hybrid with high performance in photocatalytic degradation, Appl. Surf. Sci. 258 (2012) 6204–6211.

[107] A. Wei, L. Xiong, L. Sun, Y. Liu, W. Li, W. Lai, X. Liu, L. Wang, W. Huang, X. Dong, One-step electrochemical synthesis of a graphene–ZnO hybrid for improved photocatalytic activity, Mater. Res. Bull. 48 (2013) 2855–2860.
[108] N.H.H. Abu Bakar, W.L. Tan, Natural composite membranes for water remediation: toward a sustainable tomorrow, in: M.I. Ahmad, M. Ismail, S. Riffat (Eds.), Renewable Energy and Sustainable Technologies for Building and Environmental Applications: Options for a Greener Future, Springer International Publishing, Cham, 2016, pp. 25–49.
[109] J. Yin, B. Deng, Polymer-matrix nanocomposite membranes for water treatment, J. Membr. Sci. 479 (2015) 256–275.
[110] Y.L.F. Musico, C.M. Santos, M.L.P. Dalida, D.F. Rodrigues, Surface modification of membrane filters using graphene and graphene oxide-based nanomaterials for bacterial inactivation and removal, ACS Sustain. Chem. Eng. 2 (2014) 1559–1565.
[111] K.H. Chu, Y. Huang, M. Yu, J. Heo, J.R.V. Flora, A. Jang, M. Jang, C. Jung, C.M. Park, D.-H. Kim, Y. Yoon, Evaluation of graphene oxide-coated ultrafiltration membranes for humic acid removal at different pH and conductivity conditions, Sep. Purif. Technol. 181 (2017) 139–147.
[112] P.V. Chai, E. Mahmoudi, Y.H. Teow, A.W. Mohammad, Preparation of novel polysulfone-Fe_3O_4/GO mixed-matrix membrane for humic acid rejection, J. Water Process Eng. 15 (2017) 83–88.
[113] J. Ma, X. Guo, Y. Ying, D. Liu, C. Zhong, Composite ultrafiltration membrane tailored by MOF@GO with highly improved water purification performance, Chem. Eng. J. 313 (2017) 890–898.
[114] F. Li, Z. Yu, H. Shi, Q. Yang, Q. Chen, Y. Pan, G. Zeng, L. Yan, A Mussel-inspired method to fabricate reduced graphene oxide/g-C3N4 composites membranes for catalytic decomposition and oil-in-water emulsion separation, Chem. Eng. J. 322 (2017) 33–45.
[115] S. Xiao, S. Yu, L. Yan, Y. Liu, X. Tan, Preparation and properties of PPSU/GO mixed matrix membrane, Chin. J. Chem. Eng. 25 (2017) 408–414.
[116] Y. Jiang, W.-N. Wang, D. Liu, Y. Nie, W. Li, J. Wu, F. Zhang, P. Biswas, J.D. Fortner, Engineered crumpled graphene oxide nanocomposite membrane assemblies for advanced water treatment processes, Environ. Sci. Technol. 49 (2015) 6846–6854.
[117] Y.T. Chung, E. Mahmoudi, A.W. Mohammad, A. Benamor, D. Johnson, N. Hilal, Development of polysulfone-nanohybrid membranes using ZnO-GO composite for enhanced antifouling and antibacterial control, Desalination 402 (2017) 123–132.
[118] K.C. Ho, Y.H. Teow, W.L. Ang, A.W. Mohammad, Novel GO/OMWCNTs mixed-matrix membrane with enhanced antifouling property for palm oil mill effluent treatment, Sep. Purif. Technol. 177 (2017) 337–349.
[119] Z. Zhu, L. Wang, Y. Xu, Q. Li, J. Jiang, X. Wang, Preparation and characteristics of graphene oxide-blending PVDF nanohybrid membranes and their applications for hazardous dye adsorption and rejection, J. Colloid Interface Sci. 504 (2017) 429–439.
[120] Y. Zhao, J. Lu, X. Liu, Y. Wang, J. Lin, N. Peng, J. Li, F. Zhao, Performance enhancement of polyvinyl chloride ultrafiltration membrane modified with graphene oxide, J. Colloid Interface Sci. 480 (2016) 1–8.
[121] R.S. Zambare, K.B. Dhopte, A.V. Patwardhan, P.R. Nemade, Polyamine functionalized graphene oxide polysulfone mixed matrix membranes with improved hydrophilicity and anti-fouling properties, Desalination 403 (2017) 24–35.
[122] Y. Wang, R. Ou, H. Wang, T. Xu, Graphene oxide modified graphitic carbon nitride as a modifier for thin film composite forward osmosis membrane, J. Membr. Sci. 475 (2015) 281–289.
[123] S. Lim, M.J. Park, S. Phuntsho, L.D. Tijing, G.M. Nisola, W.-G. Shim, W.-J. Chung, H.K. Shon, Dual-layered nanocomposite substrate membrane based on polysulfone/graphene oxide for mitigating internal concentration polarization in forward osmosis, Polymer 110 (2017) 36–48.
[124] S. Zinadini, A.A. Zinatizadeh, M. Rahimi, V. Vatanpour, H. Zangeneh, Preparation of a novel antifouling mixed matrix PES membrane by embedding graphene oxide nanoplates, J. Membr. Sci. 453 (2014) 292–301.

[125] M. Safarpour, V. Vatanpour, A.R. Khataee, Preparation and characterization of graphene oxide/TiO2 blended PES nanofiltration membrane with improved antifouling and separation performance, Desalination 393 (2016) 65–78.
[126] R. Ding, H. Zhang, Y. Li, J. Wang, B. Shi, H. Mao, J. Dang, J. Liu, Graphene oxide-embedded nanocomposite membrane for solvent resistant nanofiltration with enhanced rejection ability, Chem. Eng. Sci. 138 (2015) 227–238.
[127] J. Wang, P. Zhang, B. Liang, Y. Liu, T. Xu, L. Wang, B. Cao, K. Pan, Graphene oxide as an effective barrier on a porous nanofibrous membrane for water treatment, ACS Appl. Mater. Interfaces 8 (2016) 6211–6218.
[128] X. Wang, H. Wang, Y. Wang, J. Gao, J. Liu, Y. Zhang, Hydrotalcite/graphene oxide hybrid nanosheets functionalized nanofiltration membrane for desalination. Desalination (2017). https://doi.org/10.1016/j.desal.2017.05.012. (in press).
[129] A.F. Faria, C. Liu, M. Xie, F. Perreault, L.D. Nghiem, J. Ma, M. Elimelech, Thin-film composite forward osmosis membranes functionalized with graphene oxide–silver nanocomposites for biofouling control, J. Membr. Sci. 525 (2017) 146–156.
[130] L. Shen, S. Xiong, Y. Wang, Graphene oxide incorporated thin-film composite membranes for forward osmosis applications, Chem. Eng. Sci. 143 (2016) 194–205.
[131] A. Soroush, W. Ma, M. Cyr, M.S. Rahaman, B. Asadishad, N. Tufenkji, In situ silver decoration on graphene oxide-treated thin film composite forward osmosis membranes: biocidal properties and regeneration potential, Environ. Sci. Technol. Lett. 3 (2016) 13–18.
[132] A. Soroush, W. Ma, Y. Silvino, M.S. Rahaman, Surface modification of thin film composite forward osmosis membrane by silver-decorated graphene-oxide nanosheets, Environ. Sci. Nano 2 (2015) 395–405.
[133] T. Sirinupong, W. Youravong, D. Tirawat, W.J. Lau, G.S. Lai, A.F. Ismail, Synthesis and characterization of thin film composite membranes made of PSF-TiO_2/GO nanocomposite substrate for forward osmosis applications. Arab. J. Chem. (2017). https://doi.org/10.1016/j.arabjc.2017.05.006. (in press).
[134] F. Perreault, H. Jaramillo, M. Xie, M. Ude, L.D. Nghiem, M. Elimelech, Biofouling mitigation in forward osmosis using graphene oxide functionalized thin-film composite membranes, Environ. Sci. Technol. 50 (2016) 5840–5848.
[135] F. Perreault, M.E. Tousley, M. Elimelech, Thin-film composite polyamide membranes functionalized with biocidal graphene oxide nanosheets, Environ. Sci. Technol. Lett. 1 (2014) 71–76.
[136] D. Hui, S. Penzhan, Z. Yingjiu, Z. Hongwei, Reverse osmosis desalination of chitosan cross-linked graphene oxide/titania hybrid lamellar membranes, Nanotechnology 27 (2016)274002.
[137] M.E.A. Ali, L. Wang, X. Wang, X. Feng, Thin film composite membranes embedded with graphene oxide for water desalination, Desalination 386 (2016) 67–76.
[138] L. He, L.F. Dumée, C. Feng, L. Velleman, R. Reis, F. She, W. Gao, L. Kong, Promoted water transport across graphene oxide–poly(amide) thin film composite membranes and their antibacterial activity, Desalination 365 (2015) 126–135.
[139] M. Safarpour, A.R. Khataee, V. Vatanpour, Thin film nanocomposite reverse osmosis membrane modified by reduced graphene oxide/TiO_2 with improved desalination performance, J. Membr. Sci. 489 (2015) 43–54.
[140] A. Kaveh, A. ArefAzar, Surface modification of graphene oxide and investigation of its effects on surface properties of aramid membranes, Polym.-Plast. Technol. Eng. 54 (2015) 1606–1614.
[141] W. Ma, A. Soroush, T.V.A. Luong, M.S. Rahaman, Cysteamine- and graphene oxide-mediated copper nanoparticle decoration on reverse osmosis membrane for enhanced anti-microbial performance, J. Colloid Interface Sci. 501 (2017) 330–340.
[142] F. Shao, L. Dong, H. Dong, Q. Zhang, M. Zhao, L. Yu, B. Pang, Y. Chen, Graphene oxide modified polyamide reverse osmosis membranes with enhanced chlorine resistance, J. Membr. Sci. 525 (2017) 9–17.
[143] M. Safarpour, V. Vatanpour, A.R. Khataee, M. Esmaeili, Development of a novel high flux and fouling-resistant thin film composite nanofiltration membrane by embedding reduced graphene oxide/TiO_2, Sep. Purif. Technol. 154 (2015) 96–107.

[144] M. Golpour, M. Pakizeh, Development of a new nanofiltration membrane for removal of kinetic hydrate inhibitor from water, Sep. Purif. Technol. 183 (2017) 237–248.
[145] X. Li, C. Zhao, M. Yang, B. Yang, D. Hou, T. Wang, Reduced graphene oxide-NH_2 modified low pressure nanofiltration composite hollow fiber membranes with improved water flux and antifouling capabilities, Appl. Surf. Sci. 419 (2017) 418–428.
[146] S. Bano, A. Mahmood, S.-J. Kim, K.-H. Lee, Graphene oxide modified polyamide nanofiltration membrane with improved flux and antifouling properties, J. Mater. Chem. A 3 (2015) 2065–2071.
[147] J. Wang, Y. Wang, J. Zhu, Y. Zhang, J. Liu, B. Van der Bruggen, Construction of TiO_2@graphene oxide incorporated antifouling nanofiltration membrane with elevated filtration performance, J. Membr. Sci. 533 (2017) 279–288.
[148] H. Li, W. Shi, Q. Du, R. Zhou, H. Zhang, X. Qin, Improved separation and antifouling properties of thin-film composite nanofiltration membrane by the incorporation of cGO, Appl. Surf. Sci. 407 (2017) 260–275.
[149] P. Wen, Y. Chen, X. Hu, B. Cheng, D. Liu, Y. Zhang, S. Nair, Polyamide thin film composite nanofiltration membrane modified with acyl chlorided graphene oxide, J. Membr. Sci. 535 (2017) 208–220.
[150] R.W. Kibechu, D.T. Ndinteh, T.A.M. Msagati, B.B. Mamba, S. Sampath, Effect of incorporating graphene oxide and surface imprinting on polysulfone membranes on flux, hydrophilicity and rejection of salt and polycyclic aromatic hydrocarbons from water, Phys. Chem. Earth Parts A/B/C 100 (2017) 126–134.
[151] M.G. Kochameshki, A. Marjani, M. Mahmoudian, K. Farhadi, Grafting of diallyldimethylammonium chloride on graphene oxide by RAFT polymerization for modification of nanocomposite polysulfone membranes using in water treatment, Chem. Eng. J. 309 (2017) 206–221.
[152] M. Yang, C. Zhao, S. Zhang, P. Li, D. Hou, Preparation of graphene oxide modified poly(m-phenylene isophthalamide) nanofiltration membrane with improved water flux and antifouling property, Appl. Surf. Sci. 394 (2017) 149–159.
[153] G. Rao, Q. Zhang, H. Zhao, J. Chen, Y. Li, Novel titanium dioxide/iron (III) oxide/graphene oxide photocatalyticmembrane for enhanced humic acid removal from water, Chem. Eng. J. 302 (2016) 633–640.
[154] Y. Zhao, K. Tang, H. Ruan, L. Xue, B. Van der Bruggen, C. Gao, J. Shen, Sulfonated reduced graphene oxide modification layers to improve monovalent anions selectivity and controllable resistance of anion exchange membrane, J. Membr. Sci. 536 (2017) 167–175.
[155] J. Zhang, N. Chen, M. Li, C. Feng, Synthesis and environmental application of zirconium–chitosan/graphene oxide membrane, J. Taiwan Inst. Chem. Eng. 77 (2017) 106–112.
[156] M. Zambianchi, M. Durso, A. Liscio, E. Treossi, C. Bettini, M.L. Capobianco, A. Aluigi, A. Kovtun, G. Ruani, F. Corticelli, M. Brucale, V. Palermo, M.L. Navacchia, M. Melucci, Graphene oxide doped polysulfone membrane adsorbers for the removal of organic contaminants from water, Chem. Eng. J. 326 (2017) 130–140.
[157] W. Choi, J. Choi, J. Bang, J.-H. Lee, Layer-by-layer assembly of graphene oxide nanosheets on polyamide membranes for durable reverse-osmosis applications, ACS Appl. Mater. Interfaces 5 (2013) 12510–12519.
[158] Y.-N. Kwon, S. Hong, H. Choi, T. Tak, Surface modification of a polyamide reverse osmosis membrane for chlorine resistance improvement, J. Membr. Sci. 415–416 (2012) 192–198.
[159] S.G. Kim, J.H. Chun, B.-H. Chun, S.H. Kim, Preparation, characterization and performance of poly(aylene ether sulfone)/modified silica nanocomposite reverse osmosis membrane for seawater desalination, Desalination 325 (2013) 76–83.
[160] M. Hu, B. Mi, Enabling graphene oxide nanosheets as water separation membranes, Environ. Sci. Technol. 47 (2013) 3715–3723.
[161] H.M. Hegab, Y. Wimalasiri, M. Ginic-Markovic, L. Zou, Improving the fouling resistance of brackish water membranes via surface modification with graphene oxide functionalized chitosan, Desalination 365 (2015) 99–107.
[162] E. Brillas, C.A. Martínez-Huitle, Decontamination of wastewaters containing synthetic organic dyes by electrochemical methods. An updated review, Appl. Catal. B Environ. 166–167 (2015) 603–643.

[163] A.R. Khataee, M. Safarpour, M. Zarei, S. Aber, Combined heterogeneous and homogeneous photodegradation of a dye using immobilized TiO_2 nanophotocatalyst and modified graphite electrode with carbon nanotubes, J. Mol. Catal. A Chem. 363–364 (2012) 58–68.
[164] E. Brillas, I. Sirés, M.A. Oturan, Electro-Fenton process and related electrochemical technologies based on Fenton's reaction chemistry, Chem. Rev. 109 (2009) 6570–6631.
[165] T. Liu, K. Wang, S. Song, A. Brouzgou, P. Tsiakaras, Y. Wang, New electro-Fenton gas diffusion cathode based on nitrogen-doped graphene@carbon nanotube composite materials, Electrochim. Acta 194 (2016) 228–238.
[166] E. Mousset, Z.T. Ko, M. Syafiq, Z. Wang, O. Lefebvre, Electrocatalytic activity enhancement of a graphene ink-coated carbon cloth cathode for oxidative treatment, Electrochim. Acta 222 (2016) 1628–1641.
[167] E. Mousset, Z. Wang, J. Hammaker, O. Lefebvre, Physico-chemical properties of pristine graphene and its performance as electrode material for electro-Fenton treatment of wastewater, Electrochim. Acta 214 (2016) 217–230.
[168] T.X.H. Le, M. Bechelany, S. Lacour, N. Oturan, M.A. Oturan, M. Cretin, High removal efficiency of dye pollutants by electron-Fenton process using a graphene based cathode, Carbon 94 (2015) 1003–1011.
[169] D. Govindaraj, I.M. Nambi, J. Senthilnathan, An innate quinone functionalized electrochemically exfoliated graphene/Fe3O4 composite electrode for the continuous generation of reactive oxygen species, Chem. Eng. J. 316 (2017) 964–977.
[170] A.G. Akerdi, Z. Es'haghzade, S.H. Bahrami, M. Arami, Comparative study of GO and reduced GO coated graphite electrodes for decolorization of acidic and basic dyes from aqueous solutions through heterogeneous electro-Fenton process, J. Environ. Chem. Eng. 5 (2017) 2313–2324.
[171] W. Chen, X. Yang, J. Huang, Y. Zhu, Y. Zhou, Y. Yao, C. Li, Iron oxide containing graphene/carbon nanotube based carbon aerogel as an efficient E-Fenton cathode for the degradation of methyl blue, Electrochim. Acta 200 (2016) 75–83.
[172] J. Shen, Y. Li, Y. Zhu, Y. Hu, C. Li, Aerosol synthesis of Graphene-Fe_3O_4 hollow hybrid microspheres for heterogeneous Fenton and electro-Fenton reaction, J. Environ. Chem. Eng. 4 (2016) 2469–2476.
[173] W. Ren, D. Tang, X. Lu, J. Sun, M. Li, S. Qiu, D. Fan, Novel multilayer ACF@rGO@OMC cathode composite with enhanced activity for electro-Fenton degradation of phthalic acid esters, Ind. Eng. Chem. Res. 55 (2016) 11085–11096.
[174] V. Rani, R.K. Das, A.K. Golder, Fabrication of reduced graphene oxide-graphite paste electrode for H2O2 formation and its implication for ciprofloxacin degradation, Surf. Interfac. 7 (2017) 99–105.
[175] X. Xu, J. Chen, G. Zhang, Y. Song, F. Yang, Homogeneous electro-Fenton oxidative degradation of reactive brilliant blue Using a graphene doped gas-diffusion cathode, Int. J. Electrochem. Sci. 9 (2014) 569–579.
[176] C.-Y. Chen, C. Tang, H.-F. Wang, C.-M. Chen, X. Zhang, X. Huang, Q. Zhang, Oxygen reduction reaction on graphene in an Electro-Fenton System: in situ generation of H_2O_2 for the oxidation of organic compounds, ChemSusChem 9 (2016) 1194–1199.
[177] F. Zhao, L. Liu, F. Yang, N. Ren, E-Fenton degradation of MB during filtration with Gr/PPy modified membrane cathode, Chem. Eng. J. 230 (2013) 491–498.
[178] H. Dong, H. Su, Z. Chen, H. Yu, H. Yu, Fabrication of electrochemically reduced graphene oxide modified gas diffusion electrode for In-situ electrochemical advanced oxidation process under mild conditions, Electrochim. Acta 222 (2016) 1501–1509.
[179] X. Zhao, S. Liu, Y. Huang, Removing organic contaminants by an electro-Fenton system constructed with graphene cathode, Toxicol. Environ. Chem. 98 (2016) 530–539.
[180] Z. Zhang, J. Zhang, X. Ye, Y. Hu, Y. Chen, Pd/RGO modified carbon felt cathode for electro-Fenton removing of EDTA-Ni, Water Sci. Technol. 74 (2016) 639–646.
[181] G. Zhang, Y. Zhou, F. Yang, FeOOH-catalyzed heterogeneous electro-Fenton system upon anthraquinone@graphene nanohybrid cathode in a divided electrolytic cell: catholyte-regulated catalytic oxidation performance and mechanism, J. Electrochem. Soc. 162 (2015) H357–H365.

[182] Y. Li, J. Han, B. Xie, Y. Li, S. Zhan, Y. Tian, Synergistic degradation of antimicrobial agent ciprofloxacin in water by using 3D CeO_2/RGO composite as cathode in electro-Fenton system, J. Electroanal. Chem. 784 (2017) 6–12.
[183] Y. Li, Y. Li, B. Xie, J. Han, S. Zhan, Y. Tian, Efficient mineralization of ciprofloxacin using a 3D $Ce_xZr_{1-x}O_2$/RGO composite cathode, Environ. Sci. Nano 4 (2017) 425–436.
[184] A. Aghigh, V. Alizadeh, H.Y. Wong, M.S. Islam, N. Amin, M. Zaman, Recent advances in utilization of graphene for filtration and desalination of water: a review, Desalination 365 (2015) 389–397.
[185] Z. Li, B. Song, Z. Wu, Z. Lin, Y. Yao, K.-S. Moon, C.P. Wong, 3D porous graphene with ultrahigh surface area for microscale capacitive deionization, Nano Energy 11 (2015) 711–718.
[186] P.F. Cai, C.J. Su, W.T. Chang, F.C. Chang, C.Y. Peng, I.W. Sun, Y.L. Wei, C.J. Jou, H.P. Wang, Capacitive deionization of seawater effected by nano Ag and Ag@C on graphene, Mar. Pollut. Bull. 85 (2014) 733–737.
[187] X. Xu, Y. Liu, M. Wang, X. Yang, C. Zhu, T. Lu, R. Zhao, L. Pan, Design and fabrication of mesoporous graphene via carbothermal reaction for highly efficient capacitive deionization, Electrochim. Acta 188 (2016) 406–413.
[188] Z. Wang, B. Dou, L. Zheng, G. Zhang, Z. Liu, Z. Hao, Effective desalination by capacitive deionization with functional graphene nanocomposite as novel electrode material, Desalination 299 (2012) 96–102.
[189] Q. Dong, G. Wang, B. Qian, C. Hu, Y. Wang, J. Qiu, Electrospun composites made of reduced graphene oxide and activated carbon nanofibers for capacitive deionization, Electrochim. Acta 137 (2014) 388–394.
[190] X. Xu, L. Pan, Y. Liu, T. Lu, Z. Sun, Enhanced capacitive deionization performance of graphene by nitrogen doping, J. Colloid Interface Sci. 445 (2015) 143–150.
[191] A.S. Yasin, H.O. Mohamed, I.M.A. Mohamed, H.M. Mousa, N.A.M. Barakat, Enhanced desalination performance of capacitive deionization using zirconium oxide nanoparticles-doped graphene oxide as a novel and effective electrode, Sep. Purif. Technol. 171 (2016) 34–43.
[192] X. Liu, T. Chen, W.-C. Qiao, Z. Wang, L. Yu, Fabrication of graphene/activated carbon nanofiber composites for high performance capacitive deionization, J. Taiwan Inst. Chem. Eng. 72 (2017) 213–219.
[193] X. Gu, M. Hu, Z. Du, J. Huang, C. Wang, Fabrication of mesoporous graphene electrodes with enhanced capacitive deionization, Electrochim. Acta 182 (2015) 183–191.
[194] Y. Bai, Z.-H. Huang, X.-L. Yu, F. Kang, Graphene oxide-embedded porous carbon nanofiber webs by electrospinning for capacitive deionization, Colloids Surf. A Physicochem. Eng. Asp. 444 (2014) 153–158.
[195] A.G. El-Deen, N.A.M. Barakat, H.Y. Kim, Graphene wrapped MnO_2-nanostructures as effective and stable electrode materials for capacitive deionization desalination technology, Desalination 344 (2014) 289–298.
[196] A.G. El-Deen, N.A.M. Barakat, K.A. Khalil, M. Motlak, H. Yong Kim, Graphene/SnO_2 nanocomposite as an effective electrode material for saline water desalination using capacitive deionization, Ceram. Int. 40 ((2014) 14627–14634.
[197] T.N. Tuan, S. Chung, J.K. Lee, J. Lee, Improvement of water softening efficiency in capacitive deionization by ultra purification process of reduced graphene oxide, Curr. Appl. Phys. 15 (2015) 1397–1401.
[198] T. Zhang, H. Zhao, X.X. Huang, G. Wen, Li-ion doped graphene/carbon nanofiber porous architectures for electrochemical capacitive desalination, Desalination 379 (2016) 118–125.
[199] H. Song, Y. Wu, S. Zhang, W. Li, B. Wang, C. Wang, J. Gao, A. Li, Mesoporous generation-inspired ultrahigh capacitive deionization performance by sono-assembled activated carbon/inter-connected graphene network architecture, Electrochim. Acta 205 (2016) 161–169.
[200] Y. Zhang, L. Zou, Y. Wimalasiri, J.-Y. Lee, Y. Chun, Reduced graphene oxide/polyaniline conductive anion exchange membranes in capacitive deionisation process, Electrochim. Acta 182 (2015) 383–390.
[201] K. Mohanapriya, G. Ghosh, N. Jha, Solar light reduced graphene as high energy density supercapacitor and capacitive deionization electrode, Electrochim. Acta 209 (2016) 719–729.
[202] Y. Wimalasiri, M. Mossad, L. Zou, Thermodynamics and kinetics of adsorption of ammonium ions by graphene laminate electrodes in capacitive deionization, Desalination 357 (2015) 178–188.

[203] A.G. El-Deen, J.-H. Choi, C.S. Kim, K.A. Khalil, A.A. Almajid, N.A.M. Barakat, TiO_2 nanorod-intercalated reduced graphene oxide as high performance electrode material for membrane capacitive deionization, Desalination 361 (2015) 53–64.
[204] H. Li, L. Zou, L. Pan, Z. Sun, Using graphene nano-flakes as electrodes to remove ferric ions by capacitive deionization, Sep. Purif. Technol. 75 (2010) 8–14.
[205] G. Wang, Q. Dong, T. Wu, F. Zhan, M. Zhou, J. Qiu, Ultrasound-assisted preparation of electrospun carbon fiber/graphene electrodes for capacitive deionization: importance and unique role of electrical conductivity, Carbon 103 (2016) 311–317.
[206] N.T. Trinh, S. Chung, J.K. Lee, J. Lee, Development of high quality Fe_3O_4/rGO composited electrode for low energy water treatment, J. Energy Chem. 25 (2016) 354–360.
[207] Z.M. Marković, D.M. Matijašević, V.B. Pavlović, S.P. Jovanović, I.D. Holclajtner-Antunović, Z. Špitalský, M. Mičušik, M.D. Dramićanin, D.D. Milivojević, M.P. Nikšić, B.M. Todorović Marković, Antibacterial potential of electrochemically exfoliated graphene sheets, J. Colloid Interface Sci. 500 (2017) 30–43.
[208] W. Xu, W. Xie, X. Huang, X. Chen, N. Huang, X. Wang, J. Liu, The graphene oxide and chitosan biopolymer loads TiO_2 for antibacterial and preservative research, Food Chem. 221 (2017) 267–277.
[209] C. Zhao, J. Lv, X. Xu, G. Zhang, Y. Yang, F. Yang, Highly antifouling and antibacterial performance of poly (vinylidene fluoride) ultrafiltration membranes blending with copper oxide and graphene oxide nanofillers for effective wastewater treatment, J. Colloid Interface Sci. 505 (2017) 341–351.
[210] M. Moghayedi, E.K. Goharshadi, K. Ghazvini, H. Ahmadzadeh, R. Ludwig, M. Namayandeh-Jorabchi, Improving antibacterial activity of phosphomolybdic acid using graphene, Mater. Chem. Phys. 188 (2017) 58–67.
[211] R. Rahimi, S. Zargari, A. Yousefi, M. Yaghoubi Berijani, A. Ghaffarinejad, A. Morsali, Visible light photocatalytic disinfection of E. coli with TiO2–graphene nanocomposite sensitized with tetrakis(4-carboxyphenyl)porphyrin, Appl. Surf. Sci. 355 (2015) 1098–1106.
[212] V. Vatanpour, A. Shockravi, H. Zarrabi, Z. Nikjavan, A. Javadi, Fabrication and characterization of antifouling and anti-bacterial Ag-loaded graphene oxide/polyethersulfone mixed matrix membrane, J. Ind. Eng. Chem. 30 (2015) 342–352.
[213] C.-H. Deng, J.-L. Gong, L.-L. Ma, G.-M. Zeng, B. Song, P. Zhang, S.-Y. Huan, Synthesis, characterization and antibacterial performance of visible light-responsive Ag_3PO_4 particles deposited on graphene nanosheets, Process Saf. Environ. Prot. 106 (2017) 246–255.
[214] O. Akhavan, E. Ghaderi, Toxicity of graphene and graphene oxide nanowalls against bacteria, ACS Nano 4 (2010) 5731–5736.
[215] W. Hu, C. Peng, W. Luo, M. Lv, X. Li, D. Li, Q. Huang, C. Fan, Graphene-based antibacterial paper, ACS Nano 4 (2010) 4317–4323.
[216] C.-H. Deng, J.-L. Gong, G.-M. Zeng, P. Zhang, B. Song, X.-G. Zhang, H.-Y. Liu, S.-Y. Huan, Graphene sponge decorated with copper nanoparticles as a novel bactericidal filter for inactivation of Escherichia coli, Chemosphere 184 (2017) 347–357.
[217] S. Pourbeyram, R. Bayrami, H. Dadkhah, Green synthesis and characterization of ultrafine copper oxide reduced graphene oxide (CuO/rGO) nanocomposite, Colloids Surf. A Physicochem. Eng. Asp. 529 (2017) 73–79.
[218] G. Liao, D. Zhu, J. Zheng, J. Yin, B. Lan, L. Li, Efficient mineralization of bisphenol A by photocatalytic ozonation with TiO_2–graphene hybrid, J. Taiwan Inst. Chem. Eng. 67 (2016) 300–305.

CHAPTER

IRON OXIDE NANOMATERIALS FOR WATER PURIFICATION

16

Chella Santhosh*, Arumugam Malathi†, Ehsan Dhaneshvar*, Amit Bhatnagar*, Andrews Nirmala Grace‡, Jagannathan Madhavan†

Department of Environmental and Biological Sciences, University of Eastern Finland, Kuopio, Finland Solar Energy Lab, Department of Chemistry, Thiruvalluvar University, Vellore, India† Centre for Nanotechnology Research, VIT University, Vellore, India‡*

1 INTRODUCTION

In the present scenario, environmental protection and remediation are the biggest challenge in day-to-day life [1,2] because of the scientific advances following industrial development, exhausted water resources, global warming causing anomalous climate change, environmental pollution, and uncontrolled ground water development [3]. Waste water from various industrial sectors (including leather, printing, food, textile, cosmetic, etc.) contains large amounts of organic and inorganic compounds that are very toxic and non-biodegradable, thereby posing a huge threat to the environment [4–8]. Various chemical and physical treatments have been developed for wastewater treatment, which include photocatalytic degradation, adsorption, membrane route, ion exchange, and electrochemical method, respectively [9]. Among these methods, photocatalytic degradation and adsorption has gained significant interest in the elimination of organic and inorganic pollutants because of its low operating cost, eco-friendly approach, and effective method towards elimination of toxic pollutants [10–12]. Hence, it is essential to design highly active catalytic materials to resolve serious problems related to creating a pollutant-free environment. Iron oxide (α-Fe_2O_3) gained immense attention because of its low production cost, eco-friendliness, non-toxicity, high photostability, and high efficiency. Moreover, magnetic iron oxides can be easily separated and removed from solution by applying an external magnetic field, an exceptional benefit [13]. There are different crystal structures of iron oxide, which includes magnetite (Fe_3O_4), hematite (α-Fe_2O_3), β-Fe_2O_3, maghemite (γ-Fe_2O_3), and wustite (FeO). Among these crystalline structures, hematite (α-Fe_2O_3) is the most stable state of iron oxide at ambient conditions [14–16]. The wide applications of α-Fe_2O_3 derive from their superior physical and chemical properties, which can be tailored to various morphologies, particle dimensions, and heterostructures. This chapter deals with the recent advances in α-Fe_2O_3 nanostructured materials for environmental areas of application. Special focus has been placed on their application to photocatalysis and adsorption for the removal of organic and inorganic pollutants. The reaction mechanism of the photocatalysis for the degradation of organic pollutants is also discussed in detail.

Nanoscale Materials in Water Purification. https://doi.org/10.1016/B978-0-12-813926-4.00022-7

2 BASIC PRINCIPLE OF SEMICONDUCTOR PHOTOCATALYSIS

Fig. 1 shows a schematic illustration of photoactivation of semiconductors and the generation of electron-hole pairs. Photocatalysis on semiconductor photocatalyst involves three main steps [2]:

(i) Upon irradiation of light with energies greater than the semiconductor band gap, will lead to the generation of electrons (e^-) in the conduction band (CB) and holes (h^+) in the valence band (VB) pairs in the semiconductor photocatalyst.
(ii) Both the electrons (e^-) and holes (h^+) migrate to the surface of the semiconductor.
(iii) The photogenerated h^+ oxidize the water molecules to produce hydroxyl radical ($^{\bullet}OH$) while the photogenerated e^- reduce the dissolved oxygen to form superoxide radical anion ($^{\bullet}O_2^-$). The formation of hydroxyl radical ($^{\bullet}OH$) and superoxide radical anion ($^{\bullet}O_2^-$) having higher oxidation potential may degrade the organic pollutant into readily biodegradable compounds.

The major reactions that occur in photocatalysis are shown below in the reactions (1)–(4).

$$\text{Photocatalysts} \xrightarrow{h\nu} e^-_{CB} + h^+_{VB} \tag{1}$$

$$\text{Photocatalyst}\,(e^-_{CB}) + O_2 \rightarrow O_2^{\bullet -} \tag{2}$$

$$\text{Photocatalyst}\,(h^+_{VB}) + H_2O \rightarrow H^+ + {}^{\bullet}OH \tag{3}$$

$$\text{Pollutants} + {}^{\bullet}OH + O_2^{\bullet -} \rightarrow \text{Degradation products} \downarrow (CO_2 + H_2O + \text{Mineral acids}) \tag{4}$$

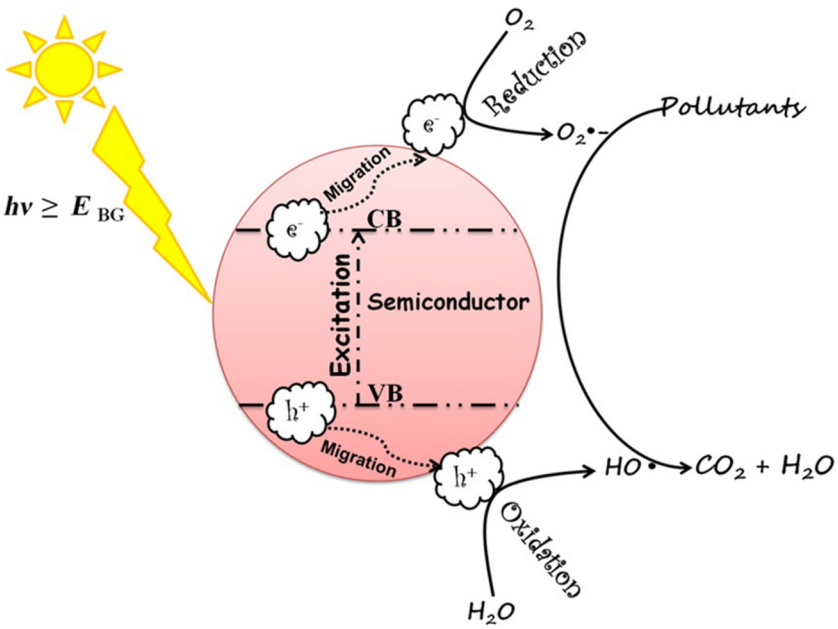

FIG. 1

Schematic illustration of photoactivation of semiconductor and generation of electron-hole pairs.

3 IRON OXIDE (α-Fe_2O_3) AS PHOTOCATALYST FOR POLLUTANT DEGRADATION

With the rising interest in eco-friendly processes, the development of facile and effective methods for environmental remediation is of great importance. The advanced oxidation process (AOPs) with semiconductor photocatalysis has drawn much attention as a green approach to the degradation of organic pollutants without producing secondary byproducts at comparatively lower costs [11,17]. TiO_2, ZnO, ZrO_2, Sb_2O_3, etc., have been utilized as traditional photocatalysts due to their wide band gap, high photocatalytic activity, and chemical stability. However, these materials exploit only 5% of energy from the solar spectrum from 46% of the available energy. Researchers are focused on effectively harvesting energy directly from sunlight, leading to the development of various visible light active photocatalysts [8]. Among the various highly efficient photocatalysts capable of exploiting the solar spectrum that have been developed, iron oxide (α-Fe_2O_3) has drawn great attention due to its absorption of light (around 43%) in the visible light region. Iron oxide (α-Fe_2O_3, hematite) is a n-type semiconductor with a band gap of ~2.1 eV, which makes it a promising candidate for potential application to wastewater treatment under visible light. However, the photocatalytic activity of α-Fe_2O_3 is limited due to the low separation efficiency and fast recombination of photoinduced charge carriers [18–22]. In order to improve the photocatalytic activity of α-Fe_2O_3, various strategies have been made to overcome the drawbacks, which include morphology controlled synthesis, doping with metal or nonmetal elements, and the construction of α-Fe_2O_3 with another semiconductor material to form composite photocatalysts, as recommended by several researchers. Constructing two semiconductors with different energy levels is an ideal system for enhancing the charge separation and reducing the recombination rate of photogenerated electron and hole pairs [23–26]. For instance, Zheng et al. [27] synthesized BiOBr/α-Fe_2O_3 composite by a hydrothermal method and utilized the composite as a visible light active photocatalyst for the degradation of RhB as target organic pollutant under visible light irradiation. As a result, it has been reported that the BiOBr/α-Fe_2O_3 composite exhibited a remarkable photocatalytic activity higher than that of the pristine α-Fe_2O_3 and BiOBr. The enhanced photocatalytic activity was credited to the synergetic effect resulting from the construction of a p-n heterojunction between BiOBr and α-Fe_2O_3. A possible degradation mechanism for the RhB over BiOBr/α-Fe_2O_3 p-n heterojunction under visible light irradiation is shown in Fig. 2.

Zheng et al. [28] synthesized α-Fe_2O_3 nanoplates combined with flower-like BiOCl through a two-step growth and assembly route, and the corresponding synthesis scheme is presented in Fig. 3. As a comparison of photocatalytic activity between pristine α-Fe_2O_3, BiOCl and α-Fe_2O_3/BiOCl composites, the optimized α-Fe_2O_3/BiOCl exhibited highly enhanced (~80%) photodegradation of RhB in 2 h compared with pure α-Fe_2O_3 and BiOCl, due to the effective separation of electrons and holes between α-Fe_2O_3 and BiOCl.

Zhao et al. [29] developed a one dimensional (1D) nanofiber α-Fe_2O_3/Bi_2MoO_6 composite by the electrospinning followed by calcination process. In comparison with pure α-Fe_2O_3 and Bi_2MoO_6, the α-Fe_2O_3/Bi_2MoO_6 composite exhibited superior photodegradation efficiency for MB under visible light. After 4 h of illumination, α-Fe_2O_3/Bi_2MoO_6 composite exhibited about 90.7% photodegradation of MB while pure α-Fe_2O_3 or Bi_2MoO_6 showed less than 65% degradation. Similarly, Zhao et al. [21] designed one dimensional (1D) nanofiber viz. α-Fe_2O_3/Bi_2MoO_6 heterostructures by combining the electrospinning with solvothermal technique and evaluate the visible light driven photocatalyst for

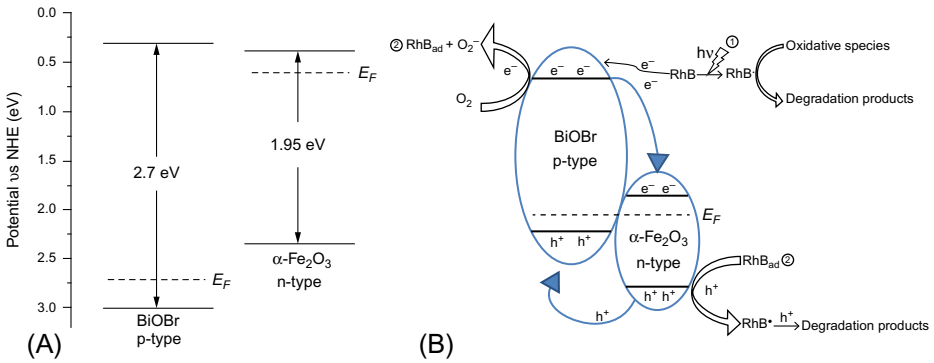

FIG. 2

Schematic diagrams of the energy band position of α-Fe_2O_3 and BiOBr, and supposedly formed heterojunction between α-Fe_2O_3 and BiOBr and the proposed photocatalytic process.

Reprinted with permission from Y. Zheng, C. Li, X. Meng, Z. Zhang, A conjugated composite of -Fe2O3 and BiOBr with enhanced visible-light-induced photocatalytic activity, J. Mol. Catal. A Chem. 421 (2016) 16–28 copyright from Elsevier.

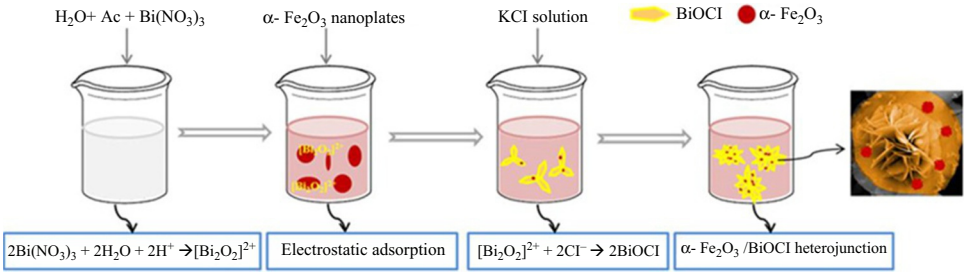

FIG. 3

Schematic illustration of the formation process of α-Fe_2O_3/BiOCl heterojunctions.

Reprinted with permission from Y. Zheng, X. Zhang, J. Zhao, P. Yang, Assembled fabrication of -Fe2O3/BiOCl heterojunctions with enhanced photocatalytic performance, Appl. Surf. Sci. 430 (2018) 585–594 copyright from Elsevier.

the degradation of RhB and MB. The α-Fe_2O_3/Bi_2MoO_6 heterostructures exhibited higher photocatalytic activity than the pure α-Fe_2O_3 and Bi_2MoO_6. The enhanced photocatalytic activity of heterostructures was attributed to the low band gap energy and higher surface area that lead to the enhanced photocatalytic activity. At the same period, Li et al. [30] prepared a flower-like α-Fe_2O_3/Bi_2MoO_6 heterojunction by a simple solvothermal followed by a calcination process. The photocatalytic activity was assessed by the photodegradation of RhB and para-chlorophenol (4-CP) under visible light irradiation. As a result, they reported that the optimized composite was highly efficient for the photodegradation of RhB and 4-CP in the presence of visible light. The improved photocatalytic activity was credited to the synergistic effects of Fe_2O_3 and Bi_2MoO_6 in efficient separation of photogenerated electron-hole pairs, and the hierarchical structures of heterostructure had more reactive sites for the degradation of pollutants.

Yan et al. [18] synthesized an Ag_3PO_4/Fe_2O_3 composite photocatalyst with a n-n heterojunction system by ultrasound assisted precipitation method. TheAg_3PO_4/Fe_2O_3 composite with the n-n heterojunction system exhibited highly efficient degradation of MO under visible light illumination. In comparison with pure $Ag_3PO_4$and Fe_2O_3, the optimized composite demonstrates an excellent photocatalytic activity for the degradation of MO. The enhancement of photocatalytic activity was mainly due to the improved charge separation of photogenerated charge carriers. Zhang et al. [31] synthesized a nanofiber α-$Fe_2O_3/NiTiO_3$ heterojunction by a calcination process and evaluated its photocatalytic performance toward the degradation of RhB as a target organic pollutant under visible light irradiation. Under visible light illumination for 180 min, about 90.4% degradation of RhB was observed over the optimized heterojunction. Under the same conditions, pure α-Fe_2O_3 and $NiTiO_3$ reached only 55.1% and 59.0% degradation of RhB. The enhanced photocatalytic of α-$Fe_2O_3/NiTiO_3$ nanofibers was credited to its greater light-absorptive ability at a longer wavelength region and its slow recombination rate of photogenerated electron-holes.

Du et al. [32] fabricated α-Fe_2O_3/GO composite by the microwave-assisted route. The synthesized α-Fe_2O_3/GO composite was utilized as photocatalyst for the reduction of Cr(VI) to Cr(III) under visible light irradiation. The optimized composite exhibited highly enhanced (95.2%) photo-reduction of Cr(VI) to Cr(III) in 160 min compared with pure α-Fe_2O_3 (25.2%). Mehraj et al. [33] constructed a p-n heterojunction of BiOI 100–500 nm width with Fe_2O_3 by a facile solvothermal method and evaluated the photocatalytic performance towards the degradation of RhB under visible light irradiation. They reported that the optimized Fe_2O_3/BiOI composite exhibited a higher photocatalytic activity than the pure Fe_2O_3 and BiOI. The enhanced photocatalytic activity may be because of the development of p-n heterojunction between Fe_2O_3 and BiOI, which facilitates the transfer and separation of photogenerated electron-hole pairs.

Xiao et al. [34] synthesized α-Fe_2O_3/g-C_3N_4 composite for the photo-reduction of Cr(VI) under visible light illumination. A series of α-Fe_2O_3/g-C_3N_4 composite were developed by hydrothermal process in order to find out the optimum levels of α-Fe_2O_3 doping in g-C_3N_4 photocatalyst. As a result, they reported that doping α-Fe_2O_3 nanoparticles with 0.5wt% α-Fe_2O_3/g-C_3N_4 was found to be optimal and resulted in enhanced photocatalytic performance for the removal of organic pollutants. The α-Fe_2O_3/g-C_3N_4 composite exhibited the highest photocatalytic activity, and 98% Cr(VI) was reduced after 150 min, which is 2.4 times and 1.8 times higher than that of pure g-C_3N_4 and α-Fe_2O_3, respectively. The enhanced photocatalytic activity of α-Fe_2O_3/g-C_3N_4 is ascribed to the efficient charge separation and transfer on the interface between g-C_3N_4 and α-Fe_2O_3. The TEM images of g-C_3N_4 and α-Fe_2O_3/g-C_3N_4 composites are shown in Fig. 4. The pure g-C_3N_4 sample displays a wrinkled two-dimensional nanosheet structure (Fig. 4A). The TEM image of α-Fe_2O_3/g-C_3N_4 composite showed that the α-Fe_2O_3 nanoparticles are well dispersed on the surface of the g-C_3N_4 nanosheets with an average size of 50 nm (Fig. 4B). The HR-TEM image demonstrates that the interplanar spacing is about 0.36 nm (Fig. 4C), corresponding to the (012) plane of α-Fe_2O_3. The result of HR-TEM image showed that an intimate contact between g-C_3N_4 and α-Fe_2O_3 is beneficial to the separation and transfer of photogenerated charge carriers.

Liu et al. [35] fabricated nanowire morphology of $SrTiO_3/Fe_2O_3$ composite by an electrospinning process, and the corresponding synthesis scheme is presented in Fig. 5. The photocatalytic activity of the as-synthesized $SrTiO_3/Fe_2O_3$ composite was evaluated by the degradation of tetracycline (TC) under visible light illumination. For 140 min of illumination, ~82.7% of the TC was removed over the optimized composite, while pure Fe_2O_3 and $SrTiO_3$ showed only 33.3% and 8.5% removal,

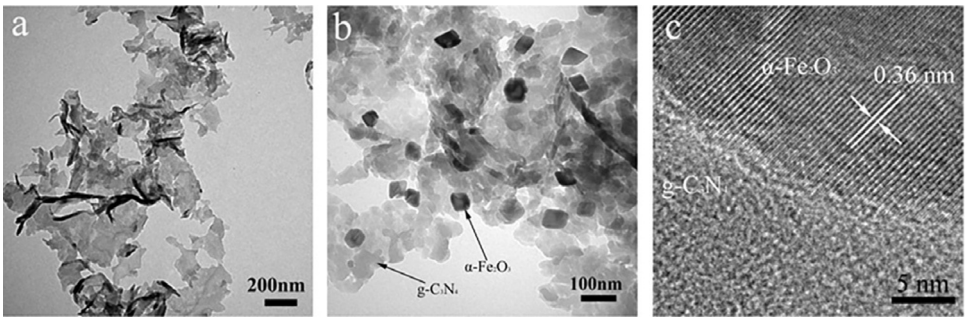

FIG. 4

(A) TEM images of g-C_3N_4, (B) α-Fe_2O_3/g-C_3N_4 composite and (C) HR-TEM image ofα-Fe_2O_3/g-C_3N_4 composite.

Reprinted with permission from D. Xiao, K. Dai, Y. Qu, Y. Yin, H. Chen, Hydrothermal synthesis of -Fe_2O_3/g-C_3N_4 compositeand its efficient photocatalytic reduction of Cr(VI) under visible light, Appl. Surf. Sci. 358 (2015) 181–187 copyright from Elsevier.

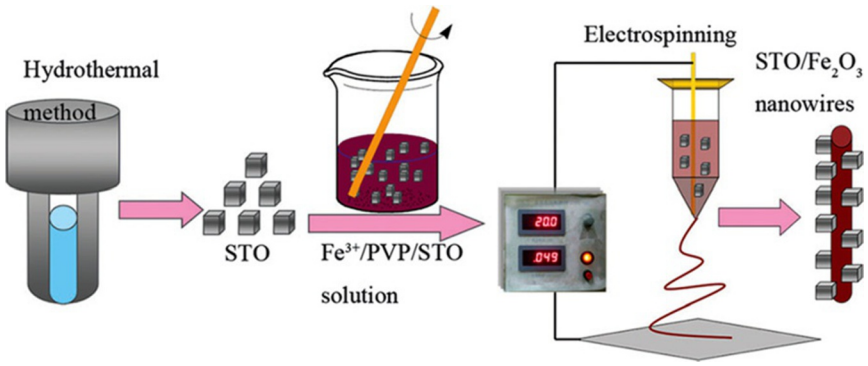

FIG. 5

Schematic representation of the synthesis of $SrTiO_3$/Fe_2O_3 composites.

Reprinted with permission from C. Liu, G. Wu, J. Chen, K. Huang, W. Shi, Fabrication of a visible-light-driven photocatalystand degradation of tetracycline based on the photoinduced interfacial charge transfer of $SrTiO_3$/Fe_2O_3 nanowires, New J. Chem., 40 (2016) 5198–5208 copyright from Royal Society of Chemistry.

respectively. The enhanced photocatalytic activity of the composites might be credited to the enhancement in visible light absorption efficiency and the efficient separation and charge transfer of photogenerated electrons and holes.

Bai et al. [36] prepared Fe_2O_3 nanoparticles on the WO_3 surface by the simple impregnation method and utilized it as a visible light active photocatalyst for the degradation of RhB as a model organic pollutant. The Fe_2O_3@WO_3 composite photocatalyst showed an enhanced photocatalytic activity for the degradation of RhB compared with pure WO_3 and Fe_2O_3. The enhanced photocatalytic activity could be attributed to the formation of n-n heterojunction between Fe_2O_3 and WO_3, which enhanced the charge separation efficiency and expanded the optical absorption properties in the visible region.

Xia et al. [37] fabricated a magnetic Fe_2O_3/SnO_2 composite by the co-precipitation method. This magnetic nanocomposite photocatalyst showed enhanced photocatalytic degradation of organic pollutant under visible light illumination. The photodegradation of acid blue 62 over the composite structure

was 3.6 times higher compared to a standard Degussa P25 photocatalyst. The enhanced photocatalytic activity of Fe_2O_3/SnO_2 nanocomposite was attributed due to the synergistic effect on the specific adsorption property and efficient electron-hole separation at the Fe_2O_3/SnO_2 nanocomposite photocatalyst interfaces and surfaces. Li et al. [38] prepared a composite of ~19 nm sized heterojunction of Ag_2O with Fe_2O_3 by a solvothermal precipitation deposition route. The synthesized Ag_2O/Fe_2O_3 heterojunction exhibited an enhanced photodegradation of RhB under visible light irradiation. As a result, it was reported that the optimized composite showed 85.3% degradation of RhB in 120 min under visible light illumination. This higher photocatalytic activity might be attributed to the formation of p-n heterojunction and facilitating the separation of electron-hole pairs. A possible degradation mechanism for the RhB over Ag_2O/Fe_2O_3 heterojunction under visible light irradiation is shown in Fig. 6.

Cheng et al. [39] used the hydrothermal method for the fabrication of TiO_2/Fe_2O_3 hybrids and utilized them as a visible light driven photocatalyst for the degradation of RhB. A schematic of the hydrothermal process employed for the synthesis of composites is shown in Fig. 7. The photodegradation efficiency of TiO_2/Fe_2O_3 nanocomposite was higher than that of the pristine Fe_2O_3 and TiO_2. The enhanced activity was due to the higher separation efficiency of photogenerated charge carriers and slow recombination rate of photogenerated electron-hole pairs. Zhu et al. [40] constructed 1D nanotube SnO_2/Fe_2O_3 heterojunction by the electrospinning method and evaluated the photocatalytic activity towards the degradation of RhB under visible light illumination. The heterojunction of SnO_2 with Fe_2O_3 enhanced the photocatalytic performance, due to the improved light harvesting of SnO_2/Fe_2O_3 heterojunction compared with pristine SnO_2 and Fe_2O_3 photocatalysts. Xu et al. [41] synthesized Fe_2O_3/Ag_3VO_4 composite by chemical precipitation method and investigated the photocatalytic activity under visible light irradiation for the degradation of RhB. Fe_2O_3/Ag_3VO_4 composite showed an enhanced photocatalytic activity than pure Ag_3VO_4, due to the synergistic effects between Fe_2O_3 and Ag_3VO_4. Guo et al. [42] synthesized α-Fe_2O_3/Bi_2WO_6 composite with a sphere-like hierarchical structure assembled by a one-step hydrothermal route. The photodegradation efficiency of the optimized composite was 2.4 times higher than that of pure Bi_2WO_6 (Table 1).

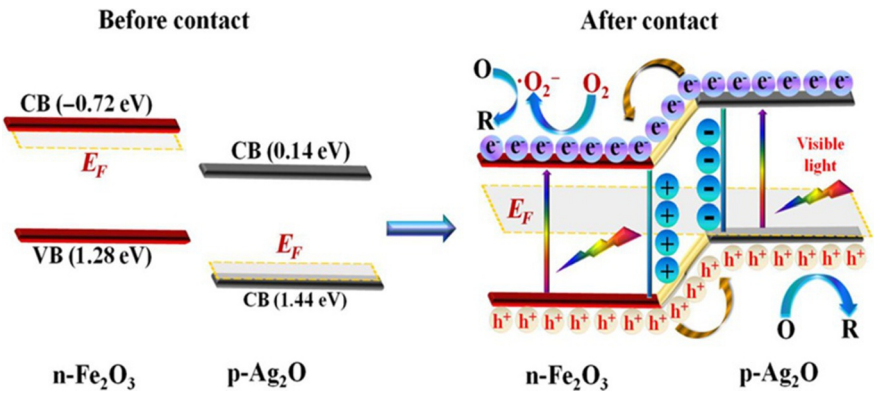

FIG. 6

The possible degradation mechanism for the RhB over Ag_2O/Fe_2O_3 heterojunction under visible light irradiation.

Reprinted with permission from S. Li, S. Hu, K. Xu, W. Jiang, J. Hu, J. Liu, Excellent visible-light photocatalytic activity of p type Ag2O coated n-type Fe2O3 microspheres, Mater. Lett. 188 (2017) 368–371 copyright from Elsevier.

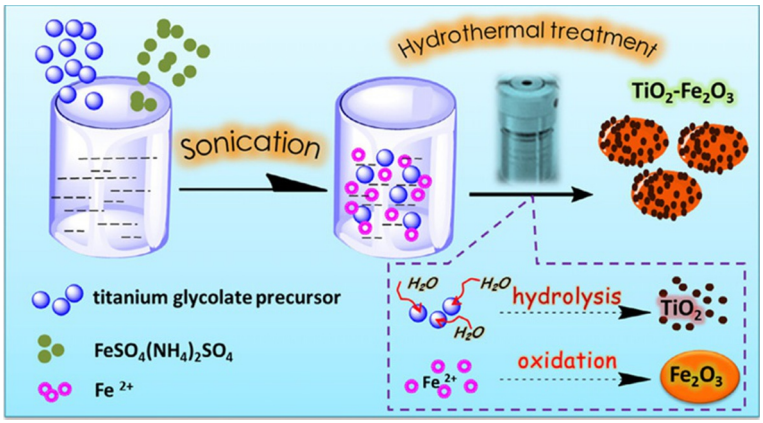

FIG. 7

Schematic representation of the TiO_2-Fe_2O_3 nanocomposties fabricated by the hydrothermal method.

Reprinted with permission from G. Cheng, F. Xu, J. Xiong, Y. Wei, F.J. Stadler, R. Chen, A novel protocol to design TiO2-Fe2O3 hybrids with effective charge separation efficiency for improved photocatalysis, Adv. Powder Technol. 28 (2017) 665–670 copyright from Elsevier.

Table 1 Review of α-Fe_2O_3-Based Composite Photocatalyst for Degradation of Organic Pollutants

Materials and Method of Synthesis	Photocatalytic Activity	Refs.
Material: BiOBr/α-Fe_2O_3 Method: Microwave (200°C for 60 min)	Pollutant: RhB 0.05 g/100 mL of 5 mg/L RhB sol. Light source: 300 W halogen tungsten lamp % deg. of TiO_2/$BiVO_4$: 94% in 330 min	[27]
Material: α-Fe_2O_3/BiOCl Method: No data	Pollutant: RhB 10 mg/25 mL of 10 mg/L RhB sol. Light source: 500 W Xe lamp % deg. of α-Fe_2O_3/BiOCl: 80% in 2 h	[28]
Material: α-Fe_2O_3/Bi_2MoO_6 Method: Electrospinning with calcination (500°C for 2 h)	Pollutant: MB 0.1 g/40 mL of 20 mg/L MB sol. Light source: 500 W Xe lamp % deg. of α-Fe_2O_3/Bi_2MoO_6: 90.7% in 4 h	[29]
Material: α-Fe_2O_3/Bi_2MoO_6 Method: Electrospinning with Solvothermal (180°C for 18 h)	Pollutant: RhB, MB 0.06 g/40 mL of RhB, MB sol. Light source: 500 W Xe lamp % deg. of α-Fe_2O_3/Bi_2MoO_6: 95.3% in 4.5 h (MB) % deg. of α-Fe_2O_3/Bi_2MoO_6: 66.8% in 18 h (RhB)	[21]

Table 1 Review of α-Fe_2O_3-Based Composite Photocatalyst for Degradation of Organic Pollutants—cont'd

Materials and Method of Synthesis	Photocatalytic Activity	Refs.
Material: α-Fe_2O_3/Bi_2MoO_6 Method: Solvothermal (160°C for 20 h) with calcination (400°C for 10 min)	Pollutant: RhB, 4-CP 30 mg/50 mL of 5 mg/L & 1 mg/L RhB & 4-CP sol. Light source: 300 W Xe lamp % deg. of α-Fe_2O_3/Bi_2MoO_6: 100% in 1 h (RhB) % deg. of α-Fe_2O_3/Bi_2MoO_6: 84.7% in 2 h (4-CP)	[30]
Material: Ag_3PO_4/Fe_2O_3 Method: Ultrasound-assisted precipitation	Pollutant: MO 200 mg/125 mL of 25 mg/L MO sol. Light source: 300 W halogen tungsten lamp % deg. of Ag_3PO_4/Fe_2O_3: No data	[18]
Material: α-$Fe_2O_3/NiTiO_3$ Method: Calcination (600°C for 60 min)	Pollutant: RhB 5 mg/50 mL of 3 mg/L RhB sol. Light source: 300 W Xe lamp % deg. of α-$Fe_2O_3/NiTiO_3$: 90.4% in 180 min	[31]
Material: α-Fe_2O_3/GO Method: Microwave (180 s and 500 W)	Pollutant: $K_2Cr_2O_7$ 50 mg/50 mL of 10 mg/L $K_2Cr_2O_7$ sol. Light source: 300 W Xe lamp % deg. of α-Fe_2O_3/GO: 95.2% in 160 min	[32]
Material: $BiOI/Fe_2O_3$ Method: Solvothermal (170°C for 16 h)	Pollutant: RhB 0.18 g/180 mL of RhB sol. Light source: 500 W tungsten halogen lamp % deg. of $BiOI/Fe_2O_3$: 92.4% in 24 min	[33]
Material: α-Fe_2O_3/g-C_3N_4 Method: Hydrothermal (180°C for 12 h)	Pollutant: $K_2Cr_2O_7$ 100 mg/50 mL of 10 mg/L $K_2Cr_2O_7$ sol. Light source: 300 W Xe lamp % deg. of α-Fe_2O_3/g-C_3N_4: 98% in 150 min	[34]
Material: $SrTiO_3/\alpha$-Fe_2O_3 Method: Electrospinning with calcination (500°C for 2 h)	Pollutant: Tetracycline (TC) 0.1 g/100 mL of 10 mg/L TC sol. Light source: 250 W Xe lamp % deg. of $SrTiO_3/\alpha$-Fe_2O_3: 82.7% in 140 min	[35]
Material: Fe_2O_3/WO_3 Method: Impregnation (400°C for 4 h)	Pollutant: RhB 0.1 g/100 mL of 10 ppm RhB sol. Light source: 350 W Xe lamp % deg. of Fe_2O_3/WO_3: 98% in 75 min	[36]
Material: α-Fe_2O_3/SnO_2 Method: Calcination (400°C for 3 h)	Pollutant: acid blue 62 50 mg/L acid blue 62 sol. Light source: 1000 W Xe lamp % deg. of α-$Fe_2O_3/NiTiO_3$: 98.0% in 60 min	[37]
Material: Ag_2O/Fe_2O_3 Method: Solvothermal	Pollutant: RhB 50 mL of 5 mg/L RhB sol. Light source: 300 W Xe lamp % deg. of Ag_2O/Fe_2O_3: 85.3% in 120 min	[38]

Continued

Table 1 Review of α-Fe_2O_3-Based Composite Photocatalyst for Degradation of Organic Pollutants—cont'd

Materials and Method of Synthesis	Photocatalytic Activity	Refs.
Material: TiO_2/Fe_2O_3 Method: Hydrothermal (180°C for 6 h)	Pollutant: RhB 0.05 g/100 mL of 10^{-5} M/L RhB sol. Light source: 500 W tungsten halogen lamp % deg. of TiO_2/Fe_2O_3: No data	[39]
Material: SnO_2/Fe_2O_3 Method: Electrospinning with calcination (700°C for 2 h)	Pollutant: RhB 40 mg/50 mL of 10 mg/L RhB sol. Light source: 250 W Xe lamp % deg. of α-Fe_2O_3/g-C_3N_4: No data	[40]
Material: Fe_2O_3/Ag_3VO_4 Method: Chemical precipitation	Pollutant: RhB 0.05 g/100 mL of 10 mg/L RhB sol. Light source: 300 W Xe lamp % deg. of Fe_2O_3/Ag_3VO_4: 96.1% in 60 min	[41]
Material:Fe_2O_3/Bi_2WO_6 Method: Hydrothermal (160°C for 12 h)	Pollutant: RhB 0.15 g/100 mL of 30 mg/L RhB sol. Light source: 300 W Dy lamp % deg. of Fe_2O_3/Bi_2WO_6: 98% in 120 min	[42]

4 IRON OXIDE (α-Fe_2O_3) AS ADSORBENTS FOR WATER TREATMENT

In the past decades, the exploitation of nanomaterials for environmental remediation has attracted a great interest because of their superior specific surface area which favors excellent adsorption and degradation. The rapid development of industries and agricultural activities has contaminated pure water with untreated dye stuff, heavy metal ions, and organic and inorganic pollutants [43]. Recently, adsorption technologies have attracted much attention for removing heavy metal ions, dyestuffs, and pharmaceutical waste from contaminated water. So far various novel nanomaterials and compounds have been reported as adsorbents, including silica gel, hydrophilic polymers, zeolites, activated carbon, aluminosilicate materials, metal organic frameworks (MOFs), and so on. Among these, nanomaterials are perfect adsorbents and have gained huge attention due to their large surface areas, high pore volume, and ordered pore distributions [44].

Lately, iron oxide (α-Fe_2O_3) nanomaterial has been widely investigated due to their unique optical, magnetic, electrical, and catalytic properties, as well as their potential application in environmental remediation. Iron oxide nanomaterials demonstrate not only excellent photocatalytic activity for the degradation of organic pollutants, but are also efficient adsorbents for organic dyes and heavy metal ions [45]. The magnetic nature of the iron oxide material allows fast magnetic separation after the adsorption process. Therefore, magnetic particles can be a very good option for the adsorption of various dyes and metal ions [46]. For instance, Liu et al. [47] synthesized α-Fe_2O_3 nanoparticles with various morphologies, such as hollow spheres, nanotubes, nanoplates, and nanorings by hydrothermal method and utilized it as an adsorbent for the removal of Cr(VI) from aqueous solution. The SEM micrographs of α-Fe_2O_3 nanoparticles with different morphologies are given in Fig. 8. As a result, they reported that α-Fe_2O_3 with nanoring morphology exhibited higher adsorption efficiency of Cr(VI) from aqueous

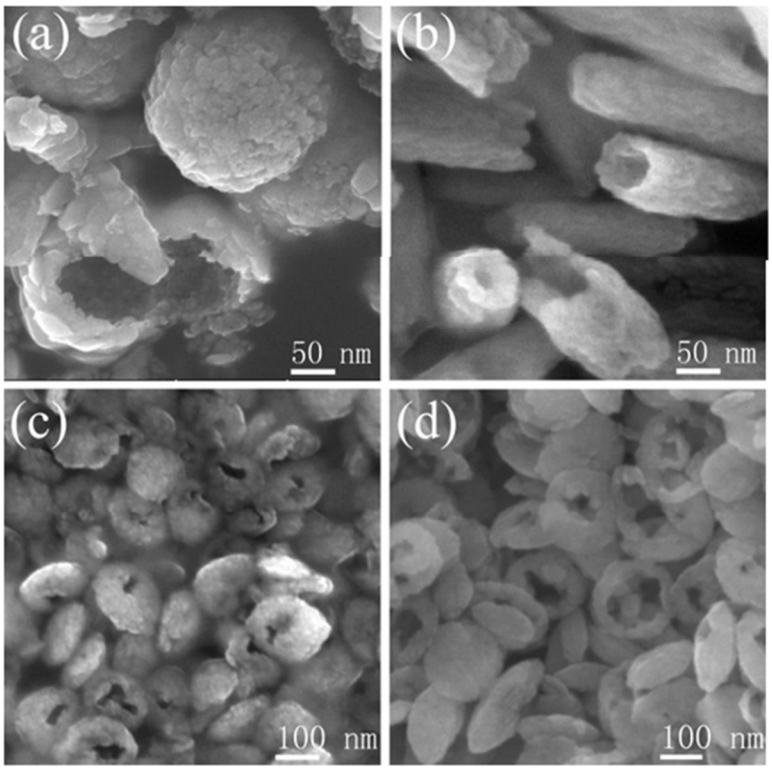

FIG. 8

SEM images of α-Fe_2O_3 particles, (A) hollow spheres, (B) nanotubes, (C) nanoplates, (D) nanorings.

Reprinted with permission from Z. Liu, R. Yu, Y. Dong, W. Li, W. Zhou, Preparation of -Fe_2O_3 hollow spheres, nanotubes, RSC Adv. 6 (2016) 82854–82861 copyright from Royal Society of Chemistry.

solution. The adsorption capacity of Cr(VI) on α-Fe_2O_3 nanoring was found to be 16.9 mg/g at pH 3 to pH 11. Su et al. [48] reported a magnetic α-Fe_2O_3/GO nanocomposite for the removal of As(III) and As(V) from aqueous solutions and investigated adsorption kinetic and Langmuir adsorption isotherms. In comparison with GO and α-Fe_2O_3, the optimized α-Fe_2O_3/GO nanocomposites exhibited higher adsorption efficiency of As(III) and As(V) from aqueous solution. The adsorption capacity of As(III) and As(V) on α-Fe_2O_3/GO nanocomposite was found to be 147 and 113 mg/g at pH 7 and pH 3, respectively.

Verdugo et al. [49] have investigated α-Fe_2O_3/MWCNTs hybrids for the removal of Cu(II) and Cr(VI) from aqueous solutions. From the experimental results, they reported that the α-Fe_2O_3/MWCNTs nanohybrids exhibited a higher adsorption capacity than α-Fe_2O_3. A maximum adsorption capacity for Cu(II) and Cr(VI) was found to be 470 and 60 mg/g at pH 6, 20°C, respectively. Wang et al. [50] fabricated α-Fe_2O_3 nanoparticles with three different morphologies (nanopolyhedra, nanorods, and rice-shaped) by solvothermal process using 2,4,6-tris(pyrazol-1-yl)-1,3,5-triazine (Tptz) as a template and tested the adsorption efficiency of the modified adsorbent for Congo red (CR) elimination.

They reported that the rice-shaped α-Fe_2O_3 nanoparticles showed the highest adsorption capacity (161 mg/g) of all the other morphologies. This might be because of the high specific surface area (110.2 m^2/g), which provides more active sites for the reactant by improving adsorption of pollutant on their surface. Ravindranath et al. [51] synthesized cube-like heterostructures of Fe_2O_3/Al_2O_3 composites by the precipitation method. The cube-like heterostructures of Fe_2O_3/Al_2O_3 composite had a large surface area (208.3 m^2/g), which acted as a good adsorbent for the removal of toxic Hg(II) in aqueous solution. The maximum adsorption capacity for Hg(II) was found to be 216 mg/g at pH 7, correspondingly. Also, they studied the effect of pH value on the adsorption efficiency of Fe_2O_3/Al_2O_3 for Hg(II) removal. The adsorption capacity of Fe_2O_3/Al_2O_3 for Hg(II) increased from pH 2.0 to pH 7.0 and then slightly decreased from pH 7.0 to pH 12.0. Upon increasing the pH values, the negative charge density on the surface of Fe_2O_3/Al_2O_3 increased, leading to greater adsorption of Hg^{2+} through electrostatic interaction. On the other hand, at pH values >7.0, formation of species such as HgO and Hg_2O led to their decreased adsorption onto the surface. Liu et al. [45] evaluated the performance of porous α-Fe_2O_3 nanorods for the adsorption of Cr(VI) and Congo red (CR) dye present in the aqueous solution. The adsorption of Cr(VI) onto porous α-Fe_2O_3 nanorods was highly pH-dependent and a maximum adsorption (29.52 mg/g) by the porous α-Fe_2O_3 nanorods took place at pH 5.0. As a result, they reported that the Cr(VI) ions could be effectively removed in the pH range of 3 to 9 because of the strong coulombic attraction between the positively charged α-Fe_2O_3 nanoparticles and the negatively charged Cr(VI) ions ($HCrO_4^-$ or CrO_4^{2-}). On the other hand, the development of the uncharged H_2CrO_4 species at pH 3 results in the poor Cr(VI) adsorption ability. Nevertheless, with the increase of the pH value to alkaline conditions, large quantities of OH^- ions in the solutions would participate with the Cr(VI) species for adsorption sites on the surface of α-Fe_2O_3 resulting in the decrease of Cr(VI) removal efficiency. A maximum adsorption capacity of Congo red of porous α-Fe_2O_3 nanoparticles was reported as 66.3 mg/g with 98% dye removal taking place with initial dye concentration of 100 mg/L.

Liu et al. [52] evaluated the α-Fe_2O_3/rGO nanohybrids composite for the removal of malachite green (MG) from aqueous solution. The Langmuir isotherm is found to fit well with the experimental isotherm data, with a maximum adsorption capacity of 438.8 mg/g for MG dye. The enhanced adsorption capacity of α-Fe_2O_3/rGO to remove MG from water is credited to the synergetic adsorptive effect between α-Fe_2O_3 and rGO. Jia et al. [53] investigated the adsorption efficiency of iron oxide nanoparticles with three different crystal structures such as α-Fe_2O_3, Fe_3O_4, and γ-Fe_2O_3 for the Congo red (CR) removal from dye waste water. As a result, they reported that the pseudo-second-order and Lagergren-first-order kinetic models are a perfect fit with the experimental results for the adsorption of CR over α-Fe_2O_3 nanoparticles. The maximum adsorption capacities of CR onto magnetic α-Fe_2O_3, Fe_3O_4 and γ-Fe_2O_3 nanoparticles were found to be 47.24, 39.10, and 27.52 mg/g, correspondingly. The higher adsorption capacity of CR onto α-Fe_2O_3 nanoparticles might be credited to the larger number of adsorption sites due to its higher specific surface area. Khosravi et al. [46] synthesized nanosphere morphology of iron oxide nanoparticles by solvothermal method using polyvinyl pyrrolidone (PVP) as a surfactant, and utilized as an effective adsorbent for the removal of anionic dyes such as, Reactive orange (RO) and Reactive yellow (RY) from aqueous solutions. The maximum adsorption of RO and RY over iron oxide was found to be 32.50 and 25.04 mg/g at pH 4.0, respectively. Also, they investigated the effect of solution pH on the adsorption of dye molecules. They reported that the removal percentage for the RO and RY decreases with the increase of pH values. This might be due to the repulsion forces between anionic dyes and negative surface charge (Table 2).

Table 2 Adsorption of Various Pollutants Using α-Fe_2O_3-Based Nanomaterials

Adsorbents	Pollutants	Adsorption Capacity (mg/g)	Refs.
α-Fe_2O_3	Cr(VI)	16.9	[47]
α-Fe_2O_3/GO	As(III), As(V)	147, 113	[48]
α-Fe_2O_3/MWCNTs	Cu(II), Cr(VI)	470, 60	[49]
α-Fe_2O_3	CR	161	[50]
Fe_2O_3/Al_2O_3	Hg(II)	216	[51]
α-Fe_2O_3	Cr(VI), CR	29.52, 66.3	[45]
α-Fe_2O_3/rGO	MG	438.8	[52]
α-Fe_2O_3	CR	47.24	[53]
α-Fe_2O_3	RO, RY	32.50, 25.04	[46]

5 CONCLUSIONS

In this book chapter, we have summarized the recent advances of iron oxide (α-Fe_2O_3) nanomaterials for environmental applications. A special focus has been laid in the fields of adsorption and photocatalysis for the elimination of organic and inorganic pollutants. α-Fe_2O_3 is one of the most commonly used catalysts for the photocatalytic process due to its advantages such as harmless, cost-effectiveness, narrow band gap, and high photostability and recyclability. The photocatalytic activity of pristine α-Fe_2O_3 photocatalyst must be further improved because of the fast recombination of charge carriers as a result of narrow band gap energy. To overcome this obstacle, researchers have gone to great lengths to increase the separation of photogenerated charge carriers. The combination of α-Fe_2O_3 with other semiconductors (composite) can reduce recombination between electrons and holes produced during irradiation of the catalyst to enhance photocatalytic degradation efficiency. On the other hand, α-Fe_2O_3 and its composites are an attractive option due to their efficiency in removing environmental pollutants such as heavy metal ions via the application of an external magnetic field. The cheap and harmless nature of α-Fe_2O_3 nanomaterials makes them even highly appealing as adsorbents. The α-Fe_2O_3 nanomaterials and their composites are good candidates for wastewater treatment and reuse processes.

REFERENCES

[1] W. Zhang, M. Wang, W. Zhao, B. Wang, Magnetic composite photocatalyst $ZnFe_2O_4$/$BiVO_4$: synthesis, characterization, and visible-light photocatalytic activity, Dalton Trans. 42 (2013) 15464–15474.
[2] A. Malathi, J. Madhavana, M. Ashokkumar, P. Arunachalam, A review on $BiVO_4$ photocatalyst: activity enhancement methods for solar photocatalytic applications, Appl. Catal. A Gen. 555 (2018) 47–74.
[3] S.Y. Lee, S.J. Park, TiO_2 photocatalyst for water treatment applications, Ind. Eng. Chem. Res. 19 (2013) 1761–1769.
[4] U.T.D. Thuy, N.Q. Liem, C.M.A. Parlett, G.M. Lalev, K. Wilson, Synthesis of CuS and CuS/ZnS core/shell nanocrystals for photocatalytic degradation of dyes under visible light, Catal. Commun. 44 (2014) 62–67.
[5] M. Saranya, R. Ramachandran, E.J.J. Samuel, S.K. Jeong, A.N. Grace, Enhanced visible-light photocatalytic reduction of organic pollutant and electrochemical properties of CuS catalyst, Powder Technol. 279 (2015) 209–220.

[6] A. Malathi, J. Madhavan, Synthesis and characterization of CuS/CdS photocatalyst with enhanced visible light-photocatalytic activity, J. Nanopart. Res. 48 (2017) 49–61.
[7] K. Vignesh, R. Priyanka, M. Rajarajan, A. Suganthi, Photoreduction of Cr (VI) in water using Bi_2O_3-ZrO_2 nanocomposite under visible light irradiation, Mater. Sci. Eng. B 178 (2013) 149–157.
[8] A. Malathi, P. Arunachalam, J. Madhavana, A.M. Al-Mayouf, M.A. Ghanem, Rod-on-flake α-FeOOH/BiOI nanocomposite: facile synthesis, characterization and enhanced photocatalytic performance, Colloids Surf. A: Physicochem. Eng. Aspects 537 (2018) 435–445.
[9] C. Santhosh, E. Daneshvar, P. Kollu, S. Peraniemi, A.N. Grace, A. Bhatnagar, Magnetic SiO_2@$CoFe_2O_4$ nanoparticles decorated on graphene oxide as efficient adsorbents for the removal of anionic pollutants from water, Chem. Eng. J. 322 (2017) 472–487.
[10] A. Malathi, V. Vasanthakumar, P. Arunachalam, J. Madhavan, M.A. Ghanem, A low cost additive-free facile synthesis of $BiFeWO_6$/$BiVO_4$ nanocomposite with enhanced visible-light induced photocatalytic activity, J. Colloid Interface Sci. 506 (2017) 553–563.
[11] A. Malathi, P. Arunachalam, A.N. Gracec, J. Madhavan, A.M. Al-Mayouf, A robust visible-light driven $BiFeWO_6$/BiOI nanohybrid with efficient photocatalytic and photoelectrochemical performance, Appl. Surf. Sci. 412 (2017) 85–95.
[12] C. Santhosh, V. Velmurugan, G. Jacob, S.K. Jeong, A.N. Grace, A. Bhatnagar, Role of nanomaterials in water treatment applications: a review, Chem. Eng. J. 306 (2016) 1116–1137.
[13] R. Satheesh, K. Vignesh, A. Suganthi, M. Rajarajan, Visible light responsive photocatalytic applications of transition metal (M = Cu, Ni and Co) doped α-Fe_2O_3 nanoparticles, J. Environ. Chem. Eng. 2 (2014) 1956–1968.
[14] S. Shen, S.A. Lindley, X. Chen, J.Z. Zhang, Hematite heterostructures for photoelectrochemical water splitting: rational materials design and charge carrier dynamics, Energy Environ. Sci. 9 (2016) 2744–2775.
[15] M. Mishra, D.M. Chun, α-Fe_2O_3, as a photocatalytic material: a review, Appl. Catal. A 498 (2015) 126–141.
[16] J. Liu, Z. Wu, Q. Tian, W. Wu, X. Xiao, shape-controlled iron oxide nanocrystals: synthesis, magnetic properties and energy conversion applications, CrystEngComm 18 (2016) 6303–6326.
[17] M. Yuan, F. Tian, G.G. Li, H. Zhao, Y. Liu, R. Chen, Fe(III)-modified BiOBr hierarchitectures for improved photocatalytic benzyl alcohol oxidation and organic pollutants degradation, Ind. Eng. Chem. Res. 56 (2017) 5935–5943.
[18] Y. Yan, H. Guan, S. Liu, R. Jiang, Ag_3PO_4/Fe_2O_3 composite photocatalysts with an n-n heterojunction semiconductor structure under visible-light irradiation, Ceram. Int. 40 (2014) 9095–9100.
[19] G. Haiying, J. Tifeng, Z. Qingrui, L. Adan, G. Faming, Preparation, characterization and photocatalytic property of cubic α-Fe_2O_3 nanoparticles, Rare Metal Mater. Eng. 44 (2015) 2688–2691.
[20] K. Zhang, Y. Liu, J. Deng, S. Xie, H. Lin, X. Zhao, J. Yang, Z. Han, H. Dai, Fe_2O_3/3DOM $BiVO_4$: high-performance photocatalysts for the visible light-driven degradation of 4-nitrophenol, Appl. Catal. B 202 (2017) 569–579.
[21] J. Zhao, Q. Lu, Q. Wang, Q. Ma, α-Fe_2O_3 nanoparticles on Bi_2MoO_6 nanofibers: one dimensional heterostructures synergistic system with enhanced photocatalytic activity, Superlattice. Microst. 91 (2016) 148–157.
[22] P. Zhang, X. Yang, Z. Zhao, B. Li, J. Gui, D. Liu, J. Qiu, One-step synthesis of flower like C/Fe_2O_3 nanosheet assembly with superior adsorption capacity and visible light photocatalytic performance for dye removal, Carbon 116 (2017) 59–67.
[23] R.A. Senthil, J. Theerthagiri, A. Selvi, J. Madhavan, Synthesis and characterization of low-cost g-C_3N_4/TiO_2 composite with enhanced photocatalytic performance under visible-light irradiation, Opt. Mater. 64 (2017) 533–539.
[24] J. Theerthagiri, R.A. Senthil, A. Priya, J. Madhavan, R.J.V. Michael, M. Ashokkumar, Photocatalytic and photoelectrochemical studies of visible-light active α-Fe_2O_3-g-C_3N_4 nanocomposites, RSC Adv. 4 (2014) 38222–38229.

[25] T. Jayaraman, S.A. Raja, A. Priya, M. Jagannathan, M. Ashokkumar, Synthesis of a visible-light active V_2O_5-g-C_3N_4 heterojunction as an efficient photocatalytic and photoelectrochemical material, New J. Chem. 39 (2015) 1367–1374.
[26] J. Theerthagiri, R.A. Senthil, A. Malathi, A. Selvi, J. Madhavan, M. Ashokkumar, Synthesis and characterization of a CuS-WO_3 composite photocatalyst for enhanced visible light photocatalytic activity, RSC Adv. 5 (2015) 52718–52725.
[27] Y. Zheng, C. Li, X. Meng, Z. Zhang, A conjugated composite of α-Fe_2O_3 and BiOBr with enhanced visible-light-induced photocatalytic activity, J. Mol. Catal. A Chem. 421 (2016) 16–28.
[28] Y. Zheng, X. Zhang, J. Zhao, P. Yang, Assembled fabrication of α-Fe_2O_3/BiOCl heterojunctions with enhanced photocatalytic performance, Appl. Surf. Sci. 430 (2018) 585–594.
[29] J. Zhao, Q. Lu, M. Wei, C. Wang, Synthesis of one-dimensional α-Fe_2O_3/Bi_2MoO_6 heterostructures by electrospinning process with enhanced photocatalytic activity, J. Alloys Compd. 646 (2015) 417–424.
[30] S. Li, S. Hu, J. Zhang, W. Jiang, J. Liu, Facile synthesis of Fe_2O_3 nanoparticles anchored on Bi_2MoO_6 microflowers with improved visible light photocatalytic activity, J. Colloid Interface Sci. 497 (2017) 93–101.
[31] Y. Zhang, J. Gu, M. Murugananthan, Y. Zhang, Development of novel α-Fe_2O_3/$NiTiO_3$ heterojunction nanofibers material with enhanced visible-light photocatalytic performance, J. Alloys Compd. 630 (2015) 110–116.
[32] Y. Du, Z. Tao, J. Guan, Z. Sun, W. Zeng, P. Wen, K. Ni, J. Ye, S. Yang, P. Du, Y. Zhu, Microwave assisted synthesis of hematite activated graphene compositeswith superior performance for photocatalytic reduction of Cr(VI), RSC Adv. 5 (2015) 81438–81444.
[33] O. Mehraj, B.M. Pirzada, N.A. Mir, M.Z. Khan, S. Sabir, A highly efficient visible-light-driven novel p-n junction Fe_2O_3/BiOI photocatalyst: surface decoration of BiOI nanosheets with Fe_2O_3 nanoparticles, Appl. Surf. Sci. 387 (2016) 642–651.
[34] D. Xiao, K. Dai, Y. Qu, Y. Yin, H. Chen, Hydrothermal synthesis of α-Fe2O3/g-C3N4 compositeand its efficient photocatalytic reduction of Cr(VI) under visible light, Appl. Surf. Sci. 358 (2015) 181–187.
[35] C. Liu, G. Wu, J. Chen, K. Huang, W. Shi, Fabrication of a visible-light-driven photocatalystand degradation of tetracycline based on the photoinduced interfacial charge transfer of $SrTiO_3$/Fe_2O_3 nanowires, New J. Chem. 40 (2016) 5198–5208.
[36] S. Bai, K. Zhang, J. Sun, R. Luo, D. Li, A. Chen, Surface decoration of WO_3 architectures with Fe_2O_3 nanoparticles for visible-light-driven photocatalysis, CrystEngComm 16 (2014) 3289–3295.
[37] H. Xia, H. Zhuang, T. Zhang, D. Xiao, Visible-light-activated nanocomposite photocatalyst of Fe_2O_3/SnO_2, Mater. Lett. 62 (2008) 1126–1128.
[38] S. Li, S. Hu, K. Xu, W. Jiang, J. Hu, J. Liu, Excellent visible-light photocatalytic activity of p type Ag_2O coated n-type Fe_2O_3 microspheres, Mater. Lett. 188 (2017) 368–371.
[39] G. Cheng, F. Xu, J. Xiong, Y. Wei, F.J. Stadler, R. Chen, A novel protocol to design TiO_2-Fe_2O_3 hybrids with effective charge separation efficiency for improved photocatalysis, Adv. Powder Technol. 28 (2017) 665–670.
[40] C. Zhu, Y. Li, Q. Su, B. Lu, J. Pan, J. Zhang, E. Xie, W. Lan, Electrospinning direct preparation of SnO_2/Fe_2O_3 heterojunction nanotubes as an efficient visible-light photocatalyst, J. Alloys Compd. 575 (2013) 333–338.
[41] Y. Xu, L. Jing, X. Chen, H. Ji, H. Xu, H. Li, H. Li, Q. Zhang, Novel visible-light-driven Fe_2O_3/Ag_3VO_4 composite with enhanced photocatalytic activity to organic pollutants degradation, RSC Adv. 6 (2016) 3600–3607.
[42] Y. Guo, G. Zhang, J. Liu, Y. Zhang, Hierarchically structured α-Fe_2O_3/Bi_2WO_6 composite for photocatalytic degradation of organic contaminants under visible light irradiation, RSC Adv. 3 (2013) 2963–2970.
[43] G. Bharath, N. Ponpandian, Hydroxyapatite nanoparticles on dendritic α-Fe_2O_3 hierarchical architectures for heterogeneous photocatalyst and adsorption of Pb(II) ionsfrom industrial wastewater, RSC Adv. 5 (2015) 84685–84693.

[44] F. Cao, D. Li, R. Deng, L. Huang, D. Pan, J. Wang, S. Li, G. Qin, Synthesis of small Fe_2O_3 nanocubes and their enhanced water vapour adsorption-desorption properties, RSC Adv. 5 (2015) 84587–84591.
[45] E. Liu, H. Zhao, H. Li, G. Li, Y. Liu, R. Chen, Hydrothermal synthesis of porous α-Fe_2O_3 nanostructures for highly efficient Cr(VI) removal, New J. Chem. 38 (2014) 2911–2916.
[46] M. Khosravi, S. Azizian, Adsorption of anionic dyes from aqueous solution by iron oxide nanospheres, J. Ind. Eng. Chem. 20 (2014) 2561–2567.
[47] Z. Liu, R. Yu, Y. Dong, W. Li, W. Zhou, Preparation of α-Fe_2O_3 hollow spheres, nanotubes, RSC Adv. 6 (2016) 82854–82861.
[48] H. Su, Z. Ye, N. Hmidi, High-performance iron oxide-graphene oxide nanocomposite adsorbentsfor arsenic removal, Colloids Surf. A: Physicochem. Eng. Aspects 522 (2017) 161–172.
[49] E.M. Verdugo, Y. Xie, J. Baltrusaitis, D.M. Cwiertny, Hematite decorated multi-walled carbon nanotubes (α-Fe_2O_3/MWCNTs) as sorbents for Cu(II) and Cr(VI): comparison of hybrid sorbent performance to its nanomaterial building blocks, RSC Adv. 6 (2016) 99997–100007.
[50] J. Wang, L. Xu, Z. Zhang, P.P. Sun, M. Fang, H.K. Liu, Shape-controlled synthesis of α-Fe_2O_3 nanocrystals for efficient adsorptive removal ofcongo red, RSC Adv. 5 (2015) 49696–49702.
[51] R. Ravindranath, P. Roy, A.P. Periasamy, Y.W. Chen, C.T. Liang, H.T. Chang, Fe_2O_3/Al_2O_3 microboxes for efficient removal of heavy metal ions, New J. Chem. 41 (2017) 7751–7757.
[52] A. Liu, W. Zhou, K. Shen, J. Liu, X. Zhang, One-pot hydrothermal synthesis of hematite-reduced graphene oxide composites for efficient removal of malachite green from aqueous solution, RSC Adv. 5 (2015) 17336–17342.
[53] Z. Jia, J. Liu, Q. Wang, S. Li, Q. Qi, R. Zhu, Synthesis of 3D hierarchical porous iron oxides for adsorption of congo red from dye wastewater, J. Alloys Compd. 622 (2015) 587–595.

CHAPTER

17 IRON OXIDE NANOMATERIALS FOR THE REMOVAL OF HEAVY METALS AND DYES FROM WASTEWATER

Sabzoi Nizamuddin*, M.T.H Siddiqui*, N.M. Mubarak†, Humair Ahmed Baloch*, E.C. Abdullah‡, Shaukat A. Mazari§, G.J. Griffin*, M.P. Srinivasan*, Akshat Tanksale¶

School of Engineering, RMIT University, Melbourne, VIC, Australia Department of Chemical Engineering, School of Engineering and Science, Curtin University, Miri, Malaysia† Malaysia-Japan International Institute of Technology (MJIIT), Universiti Teknologi Malaysia, Kuala Lumpur, Malaysia‡ Department of Chemical Engineering, Dawood University of Engineering and Technology, Karachi, Pakistan§ Department of Chemical Engineering, Monash University, Clayton, VIC, Australia¶*

1 INTRODUCTION

There is no life without water. Because of its use and the necessity of its use, water is of the utmost importance, and a significant portion of the world population is striving for clean, affordable drinking water. This issue has been a very complicated during the last decades. As technology and science have grown in the speed of light, humans have tended to have no time to take care of Mother Nature [1]. Environmental issues such as global warming, dry climates, and earthquakes are a few examples of the worst environmental issues currently occurring in our world [2]. The main reason behind these issues is the growth of the industrialization era. Metal plating facilities, mining operations, and battery production are a few examples of industries involved in the environmental issues [3]. The textile industry is involved in operations such dyeing and washing, which result in the disposal of millions of gallons of exhaust water that contains various types of dyes, including toxic dyes and pigments. Each year the world consumes around 0.7 million tons of more than 10,000 different kinds of pigment and dyes [4]. These dyes are generally anionics that are highly carcinogenic, toxic, and even mutagenic and are capable of causing severe risks to humans and aquatic life when exposed to them [5]. Therefore, disposing of these toxic dyes without proper treatment can cause massive issues that lower the oxygen levels in water, which can lead to health issues. Furthermore, heavy metals are very harmful and sometimes dissolve in water, contaminating it. One should understand the definition of heavy metals before learning the effects caused by it to the environment. Generally, heavy metals are known as the metallic elements that are very hazardous and poisonous at low concentrations while having comparatively high densities [6]. As the term indicates, heavy metals are very poisonous at a very low concentration itself.

Nanoscale Materials in Water Purification. https://doi.org/10.1016/B978-0-12-813926-4.00023-9

The presence of heavy metals, such as zinc, copper, chromium, nickel, and mercury, is very much a concern in any industrial area, but the presence differs depending on the type of industry [7–11]. In addition, various studies have reported that long-term contact with higher quantities of heavy metals present in drinking water and other resources may have harmful effects to human health [12, 13]. The high intake of heavy metals tends to generate numerous issues, such as mild dental fluorosis and crippling skeletal fluorosis, as the amount of heavy metals and exposure duration increases [14]. Furthermore, a few methods are used to remove these pollutants from the wastewater system, such as chemical precipitation, ion exchange, membrane separation, filtration, and adsorption. Among these, the adsorption technique is very cost-efficient and simple. It works simply by adding adsorbents into the wastewater system and the heavy metals are adsorbed onto the adsorbent because of the difference in the electronegative charge [15]. Nanomaterials have an internal structure or surface structure within 1–100 nm, have at least one dimension, are be used to form layered films, are available in bulk, and have filamentary morphological clusters [16]. Combining these, nanomaterials with carbon-based as surface catalysts have unique chemical [17], mechanical [18], electrical [19], energy storage [20, 21] properties, and they are different than their bulk material because of their tiny size and high surface area-to-volume ratio [22]. In the current generation, the amount of new research being done on designing new material technology is drastically increasing, and it has attracted the attention of many well-known researchers around the world. The main idea behind any new research is to design a new material or to improve the properties of the current material by a new method. One method for improving the properties of a material would be by reacting it or coating it with other substances that will manipulate and improve the properties by either a chemical or a physical reaction [17]. Various type of nanomaterials such as carbon-based nanomaterials [23], carbon nanotube [24], graphene [25], and TiO_2-based nanomaterials [26]. Recently iron-based nanomaterials have shown outstanding adsorption capacity for removing heavy metals, dyes, and inorganic and organic compounds. Over the past two decades, the outstanding performance and advantages of using iron oxide nanomaterials have opened possibilities and have led to a new step in the nanotechnology arena [17, 27–29].

The aim of this study, an extremely brief study, is to narrate the use of iron-based nanomaterials for wastewater treatment. Removing heavy metals and organic compounds and the environmental impact of these metals are elaborated. Finally, environmental applications and future challenges for using iron-based nanomaterials for wastewater are discussed.

2 IRON OXIDE NANOMATERIALS IN WATER TREATMENT

Recently, iron-based nanomaterials have shown amazing properties for sorption activities because of their larger specific surface area, high porosity, and strong magnetic response, resulting in an extraordinary sorption capacity [30, 31]. In nature, iron oxide materials exist in different forms, such as maghemite (gamma Fe_2O_3), magnetite (Fe_3O_4), and hematite (alpha-Fe_2O_3; [32]). In addition, iron-based magnetic materials are gaining research focus of various areas such as catalysis, environmental remediation, data storage, and magnetic resonance imaging [33–36]. Nanoparticle sizes of 10–20 nm have been reported as providing optimal performance. Superparamagnetic behavior, a kind of magnetism, has been reported for such particles, which has been noticed in ferromagnetic particles. The time required for magnetizing the ferromagnetic material has been recorded as longer than *Neel relaxation time* (time measured when the magnetization of small particles flip direction because of a change in temperature), which results in a zero magnetization [37, 38]. Behavior similar to the giant paramagnetic

atom and a larger constant magnetic moment have been depicted by the magnetic particles that are responsible for a prompt response to the external magnetic field. A major role of the superparamagnetism of these particles is reported by Lu et al. [39]. The reduction in demand of the magnetic materials, due to the particles' size, may cause instability as micro- and nanometer-size particles are inclined to produce agglomerates, which reduce the energy-related ration of surface area-to-volume nanomaterial. In this way, the active response of iron oxide–based nanoparticles to chemical reactions causes them to lose their magnetism and dispersibility. This adheres to a proper plan for reducing active surfaces by means of coating/grafting with surfactants and polymers. On the other hand, coating these materials with carbon or silica offers improved stability in them. During the coating process, a combination of two different magnetic phases creates a transformation of hysteresis loop within field axis of ferromagnetic (FM) and antiferromagnetic (AFM). According to the *Neel* temperature of the antiferromagnet, the change, caused by strange anisotropy produced with cooling of the system, tends to deliver an additional anisotropy source to tempt the steadiness of magnetic particles. Originally determination of the exchange bias effect was found when cobalt particles experienced an antiferromagnetic CoO layer that results founded basis for extensive research on the coating mechanism of ferromagnetic particles with antiferromagnetic oxides, sulfides particles or nitrides. The appropriate combination of ferromagnetic materials and antiferromagnetic material has the capability to bring highly stabilized morphology for the synthesis of magnetic nanomaterial. In a similar way, magnetic properties can also be controlled by various factors, including material size, morphology, phase purity, and surface defects of the materials. In contrast, it is a still challenging to fabricate magnetic material with a definite structure, higher physiochemical stability, a controlled composition, and a functionalizable surface [39].

The application of iron oxide nanomaterials as effective adsorbents is being considered globally. Furthermore, some magnetite oxides and other ferrites have enhanced their effectiveness, especially inverse-spinel nickel ferrite ($NiFe_2O_4$). The main reason is that its specific tetrahedral and octahedral structure originates with strong momentum in the ferromagnetic state by an antiparallel rotation between Fe^{3+} and Ni^{2+}. Another reason of the high potential for sorption operations using metal ferrites is because of their high porosity, greater surface area, and good magnetic character. The reduction in size of magnetic materials, ranging from micrometer to nanometer, consequently increase its surface energy; however, the overall stability of material decreases. To deal with this issue, scientists have successfully utilized hydrothermal co-precipitation technique, with graphene oxide as the feedstock, to produce high-quality inverse-spinel $NiFe_2O_4$. In this way, economically effective results have been seen using it as a sorbent that allows easier isolation of it from adsorbed heavy metals. Removing heavy metals is directly proportional to the material's magnetic moment. However, greater magnetic moment causes easy separation of the adsorbent with the use of a magnet in an aqueous medium that also contains grease oil and suspended solids. This technique is effective for avoiding high pressure drops and long separation methods, such as filtration. Moreover, the highly effective adsorbent can be reused for continuous operation that reduces the overall cost. Synthesizing iron oxide nanomaterials depends on the properties and mechanisms has been widely studied earlier. Iron-based nanomaterials have attract tremendous attention in recent years because of their high BET surface area, high pore volume, and supermagnetic properties, which lead to a key issue in wastewater treatment [40]. The removal of toxic heavy metals such as Cd(II), Pb(II), and Cu(II) by using different carob forms such as (graphene, expanded carbon, multiwall nanotubes) and paramagnetic particles (Fe_2O_3) for adsorption-based nanoparticles for the removal of heavy metals from wastewater. In their study, Fialova et al. [28] found that graphene and Fe_2O_3 were good candidates for removing heavy metals from the environment and that reduced graphene oxide and Fe_2O_3 magnetic properties (MPs) had a higher adsorption efficiency for all

tested metals than the other two carbon materials. Copper-based oxide nanoparticles can be used for removing Fe^{3+} and Cd(II) from wastewater. Removing these metals depends on the pH level, contact time, and metal concentration. It was observed that both metals were successfully removed via a batch adsorption mechanism. The optimum conditions were an adsorption time of 20 min and an agitation speed of 250 rpm, with the initial concentration varying from 25 to 250 mg/L of Fe^{3+} and Cd(II) achieving a high efficiency of removing of metals from wastewater. Furthermore, it was observed that selectivity order of the adsorbent is $Fe^{3+} > Cd(II)$. Hence, copper-based nanoparticles are effective adsorbents for removing heavy metals from wastewater [41]. In another study, the use of various magnetic nanoparticle the removal efficiency of C(VI) was as follows: $MnFe_2O_4 > MgFe_2O_4 > ZnFe_2O_4 > CuFe_2O_4 > NiFe_2O_4 > CoFe_2O_4$. The efficiency of using these magnetic nanoparticles for removal depends on the pH, the shaking rate, and the magnetic properties of the nanoparticle. It was found that $MnFe_2O_4$-based magnetic particles with an optimum pH of 2 and shaking rate of 100–400 rpm give the highest efficiency for removing 99.5% of Cr(VI) from wastewater [41]. An overview of an iron oxide nanoparticle is shown in Fig. 1.

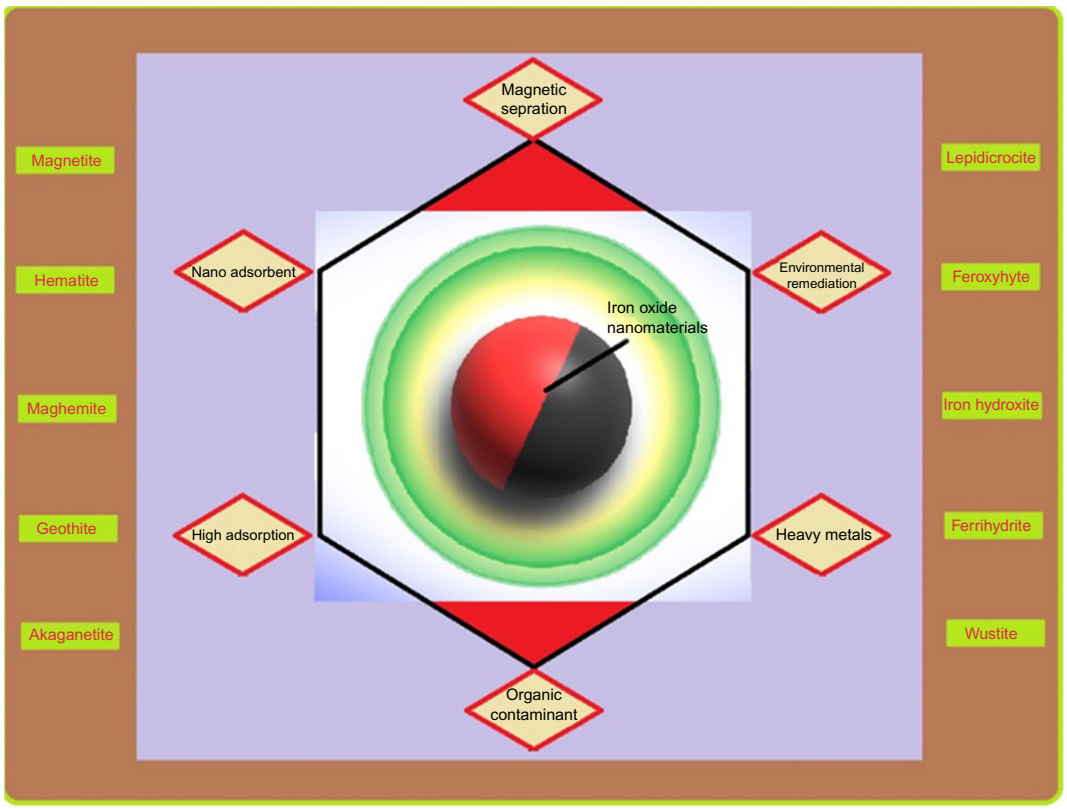

FIG. 1

The overview of iron-based nanoparticle application.

3 IRON OXIDE NANOMATERIALS FOR DYES REMOVAL FROM WASTEWATER

Iron-based nanomaterials are used for removing dyes from wastewater. This is possible because of the interaction between the compounds and the functional groups at the surface of absorbent. The functional groups serve to define the effectiveness, selectivity, capacity, and reusability of an absorbent [42]. Furthermore, in the case of high iron oxide loading at the surface, the higher rate of reduction in NO^{3-} ions to NO^{2-} ions takes place. In addition, iron oxide nanoparticles have an impact as they reduce the Gibb's free energy requirement [32, 43]. Dyes are mostly organic chemicals that are mainly used in the textile and pulp industries. These chemicals are responsible for generating significant amounts of toxic, colored, and carcinogenic wastewater that is a potential threat to sea-living organisms such as fish. This contaminated water is highly toxic for humans and animals. The fact that dyes are nonbiodegradable and have a higher resistant to aerobic digestion are the main reasons [44]. Iron-based oxide nanomaterial displayed diverse sorption properties for excellently removing dyes, organic contaminants, and inorganic pollutants simultaneously. This fact demonstrates the great potential of iron oxide nanomaterials as nanoadsorbents in environmental remediation processes. Organic pollutants are a common contaminant in water bodies. They are mainly composed of carbon along with another element, such as hydrogen and oxygen. Methylene blue ($C_{16}H_{18}N_3SCl$) is considered as a typical heterocyclic aromatic compound [45], and it is used in many areas of biology and chemistry. Furthermore, methylene blue is also applied as a pharmaceutical drug [46, 47]. It generally is an odorless, dark-green powder and forms a blue-colored solution when dissolved in an aqueous medium. In 1887, Paul Ehrlich reported that its exposure can cause supravital or intravital impacts, damaging nerve fibers [48]. The blue color is also developed whenever the dye is exposed to oxygen; also, it is stable when the stained specimen is dissolved in a solution of ammonium molybdate [49, 50]. One common application of it is to inspect the innervation of interior organs, muscles, and skin [51]. Recently, it was utilized as a medication for fungal infections in sea species, such as tropical fish, while a mixture of formaldehyde and malachite green dye, as well as parasitic protozoa *Ichthyophthirius multifiliis*, is comparatively more effective [52]. In this way, freshly laid fish eggs can be prevented from infections caused by bacteria and fungus. Methylene blue is also very useful for treating ammonia, nitrite, and even cyanide poisoning and is therefore commonly used in a "medicated fish bath" [53]. Methylene blue is known as an inhibitor of monoamine oxidase (MAOI). When its dosages exceed 5 mg/kg, it can cause a serious serotonin toxicity known as serotonin syndrome [54–56].

Recently, iron oxide nanomaterials have been used for effective removal of dyes from wastewater. Singh et al. [57] synthesized supermagnetic Fe_3O_4 nanoparticles and coated them with green tea polyphenols (GTP) for dye removal from an aqueous solution. Fe_3O_4 coated with GTP showed a high capacity of adsorption for dye removal with quick adsorption rate. Es'haghzade et al. [58] fabricated magnetic iron oxide nanoparticles and utilized them for azo dye removal. It was reported that the fabricated Fe_3O_4 nanoparticles exhibited an admirable performance for dye removal in a broad range of pH levels. Angamuthu et al. [59] prepared Fe_3O_4@mesoporous carbon shell nanomaterial and applied it to degrading methylene blue dye. It was observed that the synthesized nanomaterial showed excellent catalytic activity toward degradation of methylene blue dye. An ORMOSIL-Fe_3O_4-RGO composite was synthesized at a low temperature and was used for water remediation: the removal of Rhodamine B dye from wastewater. The adsorption capacity of the ORMOSIL-Fe_3O_4-RGO composite was noted to be 1339 mg/g, which is much greater than the adsorption capacity of the Fe_3O_4-RGO composite (342 mg/g) [60]. According to Ebrahiminezhad et al. [61], fabricated iron nanoparticles exhibited a

high potential for dye removal from an aqueous solution. The efficiency of decolorization in removing methyl orange was noted to be 95% at 6 h' process time. Asfaram et al. [62] studied the ultrasound-assisted adsorption of malachite green and brilliant green onto Mn-doped Fe_3O_4 nanoparticles loaded with activated carbon. The parameters, including pH level, adsorbent loading, and time, were optimized for the dyes' removal. The optimized removal of dyes, up to 99% for malachite green and 99.50% for brilliant green, was reported at 7.0 pH, 0.02 g of adsorbent loading, and 3 min of ultrasonication time. In addition to that, the maximum absorbance capacity was found to be 87.566 mg/g and 101.215 mg/g for brilliant green and malachite green, respectively. Nickel-supported iron oxide magnetic nanoparticles were prepared for removal of malachite green from an aqueous solution, and it was observed the formed nanoparticles show a high rate of degrading malachite green [62].

4 IRON OXIDE NANOMATERIALS AS NANOADSORBENTS

Recent developments in nanomaterials have revolutionized different areas, including operations in air purification, pollution removal, and hazardous waste treatment. Among these materials, iron oxide nanomaterials, including distinct phases of iron oxides, such as hydroxides ($Fe(OH)_2$, $Fe(OH)_3$, $Fe_5HO_8{\cdot}4H_2O$, FeO, Fe_3O_4), oxy-hydroxides (five forms of FeOOH), and oxides (four different forms of Fe_2O_3), have been the focus of researchers for sustainable applications for dealing with environmental pollutants and toxicants [63–65]. Because of their ultra-fine sizes and higher surface areas, these iron oxide nanomaterials have shown a tremendous capability for the adsorption of pollutants with high reactivity and high removal efficiencies with fast operation [66]. On the other hand, it is economically feasible to utilize iron oxide nanomaterials in terms of their reusability through simple desorption processes [67]. This property allows these materials to regain their original properties; therefore, they can be reused for further treatment of pollutants for a longer time, making them cost-effective materials. According to Gutierrez et al. [68], the utilization of iron oxide nanoparticles as nanoadsorbents has formulated a new type of magnetic separation scheme for water treatment that has turned the treatment to next level. Recently, it was found that when combined with various composite materials, iron-based nanoparticles' performance is highly enhanced; for example, integrating it with an alumina-based nanocomposite, it leads to the high, efficient adsorption for various heavy metals [69]. A novel nanocomposite was fabricated by encasing iron nanoparticles on the surface of halloysite nanotubes, which showed a highly orderly adsorption of naphthol green B by creating a layer on the surface of the nanocomposite [70]. Similarly, combining nanozerovalent iron oxide with reduced graphene has enabled the efficient removal of the toxic dye Rhodamine B [71]. Recently, it was revealed that adding a special nanocomposite of cyclodextrin iron nanomaterial/reduced graphene after vortexing with high viscous fluids, such as honey, can be directly be detected in gas chromatography–mass spectrometry (GC-MS) because of its having a higher molecular recognition capability as well as adsorption [72]. As nanocomposites, iron nanoparticles with various composites have shown extraordinary characteristics that have multiplied the adsorption capacity many times in numerous experiments. For these reasons, numerous research studies have therefore utilized iron oxide nanomaterials as nanoadsorbents for removing various contaminants from water, including heavy metals, organic and inorganic compounds, and various dyes [4, 40, 73].

4.1 ADVANTAGES OF USING IRON OXIDE NANOMATERIALS FOR THE ADSORPTION PROCESS

According to a research report [74], an adsorbent should possess four main characteristics to be utilized in the remediation of water: (1) an ability to remove higher quantities of a contaminant, (2) high porosity, (3) high reactivity, and (4) a nontoxic nature. Silver nanomaterials offer a higher reactivity and an adsorption efficiency for an aqueous pollutant; however, the material is extremely costly [75]. Therefore, apart from these key properties, cost is considered to be another significant factor that plays an important role in application of the material substituting others materials and technologies. Very few nanomaterials fulfill these criteria. The cost-effectiveness, higher environmental stability, higher adsorption capability, and nontoxic nature of iron oxide nanomaterials make them suitable for water treatment operations [74]. Another distinctive characteristic that favors using iron oxide nanomaterials in the field of adsorption of polluted water is magnetism. This potential property has made the separation process easier. Therefore, after the adsorption iron oxide nanomaterial can be easily separated by the aid of a magnetic field. This characteristic also enables the process to avoid conventional separation techniques, including filtration and centrifuging. In this way, it is a cost-effective solution for separating magnetic media from the aqueous media, as shown in Fig. 2. Furthermore, the magnetic characteristic also enables the improvement of adsorption affinity for removing organic contaminants and heavy metals from water by using iron oxide nanomaterial [77–79]. In this way, the adsorption capacity of the materials can be enhanced by combining them with iron oxide–based nanomaterial. Even porosity is always considered as a main feature for an adsorbent, but the experiments have shown that the use of iron oxide nanomaterials have a tendency to adsorb higher pollutant despite having a low surface area. Recently Petala et al. [80] synthesized iron-based nanocomposite that exhibited

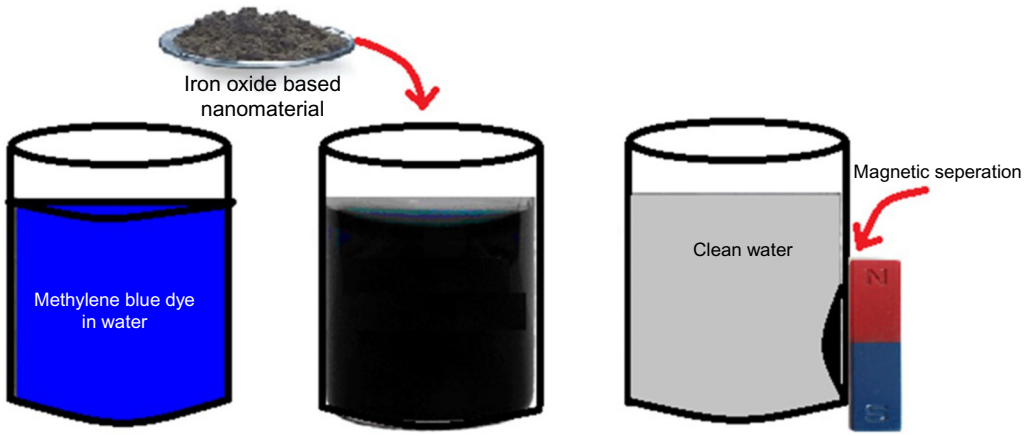

FIG. 2

Separation of Fe_3O_4/C nanocomposite by magnetic field [76].

From Z. Zhang, J. Kong, Novel magnetic Fe_3O_4@C nanoparticles as adsorbents for removal of organic dyes from aqueous solution, J. Hazard. Mater. 193 (2011) 325–329.

an incredible capability for the adsorption of arsenic, with the highest capacity of 363 mg/g even with a lower surface area of 177 m^2/g [80]. Besides this, waste biomass is a good source of carbon, and because it is available in bulk but has no proper application, combining the iron oxide nanomaterial with biochar produced through pyrolysis of waste biomass will be a cost-effective approach that is also proficient for employing waste material in an environmental friendly mode [81, 82]. One study used an empty fruit bunch as a waste biomass, impregnated it with the iron materials, and finally processed it in a microwave reactor to form an iron oxide–based biochar that led to an absolute removal of 99.99% methylene blue dye [35]. Furthermore, through this process, a greater surface area, 890 m^2/g, for the iron-based biochar was achieved.

4.2 MECHANISM OF IRON OXIDE NANOMATERIALS FOR THE ADSORPTION PROCESS

The most common iron nanomaterial nanoparticles are Fe_2O_3 and Fe_3O_4. Because these nanoparticles have different oxidation states, they undergo different removal mechanisms for various pollutants [66]. Numerous studies have attempted to explain the mechanism of iron oxide–based nanomaterials for the adsorption of various contaminants. Yoon et al. [83] investigated the adsorption mechanism of iron oxide nanoparticles for phosphate isolation in an aqueous state [83]. Furthermore, the isolation mechanism for arsenic using an iron oxide–based nanocomposite (magnetic carbon nanocages) was elaborated on in an earlier report [80]. Cao et al. [84] summarized a mechanism process of flowerlike α-Fe_2O_3 nanostructures for removing As(V) and Cr(VI) that started with the electrostatic attraction of α-Fe_2O_3 and As(V)/Cr(VI) ions for surface bonding [84]. These researchers further reported that these heavy metal ions were found in the forms of H_2AsO_4 and $HCrO_4^-/Cr_2O_7^{2-}$ and were attached to the surface of positively charged flowerlike α-Fe_2O_3 cations as a result of adsorption. In addition, techniques including X-ray diffraction (XRD) and X-ray photoelectron spectroscopy (XPS) can be utilized to understand the mechanism of the adsorption process in a better way. According to a research report, the interaction of α-Fe_2O_3 and the anions is formed as a result of a weak bond [85]. The mechanism of ionic attraction is also dependent on pH level. Hu et al. [86] observed that an ionic attraction between α-Fe_2O_3 and Cr(VI) was found at a pH lower than 6.3; however, when the pH was increased no adsorption was experienced because of the domination of electrostatic repulsion in the process [86]. Therefore, the mechanism of adsorption between Fe_2O_3 and Cr(VI) is mainly because of ion exchange and electrostatic attraction activities. On the other hand, the organic contaminants exchange ions (OH^-) with iron oxide or hydroxide by finding inner-sphere complexes [87, 88]. In the case of an iron oxide–based carbon composite, the active sites that play an important role in the adsorption of As(V) are C_xOH_2 surface sites from the carbon medium, $FeOH_2$ sites from the Fe-oxide coating, and Fe_3C sites [80]. The mechanisms of removal of As(V) can be defined by following equations (Eqs. 1–4) in which removal takes place in two steps, including protonation of As and adsorption of As:

Step 1: Protonation of As

$$H_3AsO_3 \leftrightarrow H^+ + H_2AsO_3^- \tag{1}$$

$$H_2AsO_3 \leftrightarrow H^+ + HAsO_3^{2-} \tag{2}$$

Step 2: Adsorption of As

$$\equiv Fe_3C + H_3AsO_3 \leftrightarrow \equiv Fe_3C - [H_3AsO_3] \tag{3}$$

$$\equiv FeOH_2 + H_3AsO_3 \leftrightarrow \equiv FeOH_2 - [H_3AsO_3] \tag{4}$$

4.3 IRON OXIDE NANOMATERIALS AS NANOADSORBENT FOR HEAVY METALS

Heavy metals are a great threat to world in terms of water pollution and environmental contamination and are capable to affecting the health and safety of organisms [89]. Furthermore, these metal ions, including Pb^{2+}, Hg^{2+}, Cu^{2+}, As^{5+}, Zn^{2+}, and Cr^{6+}, have toxic and carcinogenic natures that can adversely affect the health of humans, animals, and plants [90]. These heavy metals are capable of forming complexes, combining with a biological substance that can result breakage of hydrogen bonds in proteins or inhibition of enzymes, and therefore, direct exposure can badly affect the nervous system, the liver, the kidneys, skin, teeth, and bones [91]. Therefore, efficient and environmentally friendly removal techniques are greatly required for the removal of hazardous heavy metals from water. According to Xu et al. [40] the removal technique should be (1) a flexible and efficient method, (2) reusable, (3) eco-friendly, and (4) cost-effective [40]. Among the techniques, adsorption is considered one of the effective, fast, and simple operations for the efficient removal of heavy metals from aqueous solution.

Recently many researchers have focused on iron oxide–based nanomaterials because of their outstanding characteristics and easy isolation methods in adsorption technique. Using iron-based nanomaterials allowed the separation process to be not only simple through the use of a magnetic field but also boosted the overall performance by enhancing the adsorption capacity. Recently, nanocomposite Fe_2O_3/biochar derived from pyrolysis of cottonwood has shown excellent efficiency for removing aqueous As(V) [92]. Furthermore, the highest value of magnetic saturation, 69.2 emu/g, allowed for easier magnetic isolation from an aqueous solution. The higher surface area of nanomaterials has definite importance in terms of ion uptake in the adsorption process [93]. Research has reported the production of nanocomposite Fe_3O_4/phenol-formaldehyde resin that was synthesized by hydrothermal carbonization [94]. The highly ultra-fine size of 3.2 nm of carbon aerogel, which showed a higher surface area of 487 m^2/g, was formed. In addition, it was used for removing arsenic from water, exhibiting a higher adsorption capacity of 216.9 mg/g. The nanosize of Fe_3O_4-based adsorbents was found suitable for the transmission of arsenic ions from an aqueous solution to the electrostatic site on the surface of the nanocomposite. Moreover, by using an iron oxide–based nanocomposite, the surface of the material was stabilized with the help of organic or inorganic modification, which also protects the material from oxidation and therefore offers a special upgrade in the material that can be helpful in improving overall performance in the adsorption of heavy metals [40].

A novel composite was synthesized by using multiwalled carbon nanotube (MWCNT) magnetic nanocomposites combining MnO_2/Fe_3O_4/MWCNT. It was found capable of removing a large quantity of hexavalent chromium. The highest adsorption capacity achieved was 186.9 mg/g in 150 min of process time. The physiochemical properties were improved through the process, and easy magnetic isolation was accomplished after the adsorption. Furthermore, the removal capacity was retained to 85% after completing five cycles using the iron oxide–based nanocomposite material. Considering these facts, iron oxide nanomaterials, as potential nanoadsorbents, can play a significant role in treating wastewater for heavy metals. A summary of the adsorption of heavy metals by iron oxide–based nanomaterial is provided in Table 1.

Table 1 Research Summary of Removal of Heavy Metals by Iron Oxide–Based Nanomaterials in Adsorption

Nanoadsorbent	Heavy Metal	Key Findings	Ref.
Magnetic iron–nickel oxide	Cr(VI)	Highest adsorption capacity achieved was 30 mg/g for Cr(VI)	[95]
Fe_3O_4-humic acid nanoparticles	Hg(II), Pb(II)	10 nm of adsorbent formed aggregate of 140 nm Saturation magnetization value of 79.6 emu/g with 99% removal for both Hg(II) and Pb(II)	[29]
Fe_3O_4-humic acid nanoparticles	Cd(II), Cu(II)	95% removal efficiency for Cd(II) and Cu(II)	[29]
Nanocomposite Fe_2O_3/biochar	As(V)	Saturation magnetization of 69.2 emu/g Higher uptake of As(V) ion	[92]
Iron oxide–based carbon aerogel	As(V)	Highest ion uptake of 216.9 mg/g High specific surface areas of 487 m^2/g	[94]
Polypyrrole/Fe_3O_4 magnetic nanocomposite	Cr(VI)	100% removal was achieved at PH of 2.0 of initial concentration 200 mg/L Fast adsorption process	[96]
Magnetic Chitosan nanocomposites	Pb(II)	94.6% of removal efficiency 80 emu/g of saturation magnetization allowed easy separation	[97]
Fe_3O_4-silica nanocomposite	Pb(II), Hg(II)	The removal efficiency achieved Pb(II) 97.34% and 90% Hg(II)	[98]
Magnetic nanocomposites (MnO_2/Fe_3O_4/MWCNT)	Cr(VI)	Highest adsorption capacity achieved 186.9 mg/g Retained 85% of adsorption capacity after five cycles	[90]
Mesoporous iron oxide carbon encapsulate	As(V)	3 nm uniform particle size was fabricated Maximum adsorption capacity achieved 29.4 mg/g	[99]
Pectin-iron oxide magnetic nanocomposite	Cu(II)	77 ± 5 nm in diameter of nanomaterial Highest adsorption capacity achieved 48.99 mg/g	[100]

4.4 IRON OXIDE NANOMATERIALS FOR ORGANIC CONTAMINANTS

Scholars have recently considered iron oxide nanomaterials for the removal of organic pollutants using adsorption process. Being extremely efficient, of low cost, and fast; having high removal capacities; and having the advantage of easier isolations by external magnetic field has made iron nanomaterials suitable to be utilized as nanoadsorbents for organic contaminants [40]. Furthermore, they are also highly flexible, insensitive to toxic contaminants, and capable of dealing with a wider range of contaminants. The adsorption mechanism for organic pollutants is quite similar to that of heavy metals, as it proceeds with a reaction on the surface and then a diffusion of an organic contaminant on active sites of the functional groups, leaving the aqueous medium completely [101, 102]. In the past, it has been utilized in numerous studies for removing various organic contaminants, including different

hydrocarbons, pesticides, different dyes, and complex organic structures, such as carbon tetrachloride (CCl_4), chloroform ($CHCl_3$), trichloro ethene (C_2HCl_3), trichloro benzene ($C_6H_3Cl_3$), 1,1-dichloro ethene ($C_2H_2Cl_2$), hexachlorobenzene (C_6Cl_6), vinyl chloride (C_2H_3Cl), bromoform ($CHBr_3$), dichlorobromomethane ($CHBrCl_2$), dibromochloromethane ($CHBr_2Cl$), lindane ($C_6H_6Cl_6$), DDT ($C_{14}H_9Cl_5$), orange II ($C_{16}H_{11}N_2NaO_4S$), tropaeolin O ($C_{12}H_9N_2NaO_5S$), *n*-nitro sodium ethylamine ($C_4H_{10}N_2O$), chrysoidin ($C_{12}H_{13}ClN_4$), and TNT ($C_7H_5N_3O_6$) [103, 104].

In one study, an iron oxide/sodium dodecyl sulfate nanocomposite was used for the adsorption of Safranin O dye from the aqueous medium [105]. The nanocomposite exhibited a tremendous capability for adsorbing the organic dye, with removal capacity of 769.23 mg/g. Furthermore, the effects of crystallinity, pH, ionic strength, and adsorption time were also analyzed. Continuous development allowed the researchers to focus on rapid adsorption techniques for fast operations. Recently, Tang et al. [106] used rapid adsorption for 2,4-dichlorophenolxyacetic acid, using a mesoporous iron oxide–carbon composite as a nanoadsorbent [106]. The adsorbent showed amazing potential in removing 97% of organic contaminant within 5 min of treatment. The amazing magnetic separability led the researchers to combine the extraordinary porosity of the activated carbon to produce efficient nanoadsorbents. In this way, iron oxide nanoparticles were impregnated on activated carbon to form a novel magnetic nanomaterial [107]. The 10 nm of nanomaterial synthesized displayed an excellent adsorption capacity for removing organic dyes, including methylene blue and methyl orange. Furthermore, 95% of the adsorption capacity was retained by completing one cycle. On the other hand, researchers are also keen to fabricate a unique composite by combining iron nanoparticles with functional nanomaterials, such as graphene. A novel graphene/iron oxide–hybrid nanocomposite was fabricated by using a modified Hummer's method followed by chemical co-precipitation [108]. The crystalline hybrid material was utilized as a nanoadsorbent for isolating 1-naphthol and 1-naphthylamine solutions. For both organic pollutants, a maximum adsorption capacity of 528 mg/g and 625 mg/g, respectively, was achieved. It was observed that the adsorption of organic aromatic compounds on the graphene/iron oxide–hybrid nanocomposite oxides was due to the π-π interaction. In addition to that, an easier isolation of nanocomposite was attained using a magnetic field.

From the experimental analysis of various studies, iron nanomaterials are found to be effective nanoadsorbents for organic material. However, their use in industrial processes in bulk quantities for removing organic pollutants will decide the future of this potential nanomaterial. A research summary of iron oxide–based nanomaterial for the removal of organic contaminants is provided in Table 2.

5 ENVIRONMENTAL APPLICATIONS OF THE IRON OXIDE–BASED NANOMATERIALS

A prompt pace in industrialization and the resulting products have greatly affected the environment by releasing the hazardous wastes, poisonous fumes and smokes produced from industries into the environment [112]. Therefore, interpreting what effects these hazards can have on both human health and the environment while eliminating them through different routes is important [113]. Among other technologies, nanotechnology has been proposed as suitable for mitigating environmental hazards. However, little work provides information about the potential adverse effects of nanomaterials on occupational health and the environment [114, 115], but current developments in nanotechnology have

Table 2 Research Summary of Removal of Organic Pollutants by Iron Oxide–Based Nanomaterials in Adsorption

Nanoadsorbent	Organic Components	Key Findings	Ref.
Flowerlike iron oxide nanostructures	Orange dye II	A highest removal capacity of 43.5 mg/g was achieved	[109]
Mesoporous carbon iron oxide nanocomposite	2,4-Dichloro phenoxy acetic acid	Rapid adsorption was accomplished removing 97% of contaminant in 5 min Highest adsorption capacity was achieved 310.78 mg/g	[106]
Amine/Fe_3O_4 functionalized with biopolymer resin	Methyl orange, Reactive Brilliant Red K-2BP, and Acid Red 18	Highest adsorption capacity achieved 101.0 mg/g, 222.2 mg/g and 99.4 mg/g, respectively Higher surface area was found for nanocomposite	[4]
Nano sized Fe_3O_4-loaded coffee waste hydrochar	Acid Red 17	The surface area of hydrochar was doubled Decolorization efficiency was reduced from 100% to 74% Ultra sound assisted adsorption	[110]
Magnetic carbon composite	Malachite green	Highest adsorption capacity of 476 mg/g was experienced Saturation magnetization of 38.5 emu/g was attained	[111]
Graphene/iron oxide nanocomposite	1-Naphthol and 1-naphthylamine	588 and 625 mg/g of adsorption capacity Thermodynamic parameters, including ΔH, ΔS, ΔG, were calculated for both the adsorbates	[108]
Iron oxide trapped activated carbon	Methyl orange and methylene blue	10 nm of nanoparticles accomplished Saturation magnetization of 42.2 emu/g was attained 99% of removal efficiency with retaination percent of 95% after first cycle	[107]
Magnetic Fe_3O_4/C nanoparticles	Methylene blue and cresol red	250 nm particle size of the composite helped to achieve 44.38 mg/g and 11.22 mg/g for both dyes, respectively	[76]

led to a rapid proliferation of engineered nanoparticles in the environment [116]. Among other nanomaterials, the iron oxide nanomaterials have recently been given preference for utilization in environmental applications. Iron oxide nanomaterials can be classified into two types, that is, natural, such as products from the weathering of iron-bearing minerals and biominerals, and engineered/derived nanomaterials, such as iron oxides from pigments [117]. Fig. 3 shows the sources of the nanomaterials relevant to their exposure assessment. Nanomaterials—natural, accidental, or engineered—occur in the air, water, or soil, as shown in Table 3. Natural nanoparticles are generally found in a wide range of environments, such as natural water, sediments, weathered minerals and rocks, and volcanic ash [117].

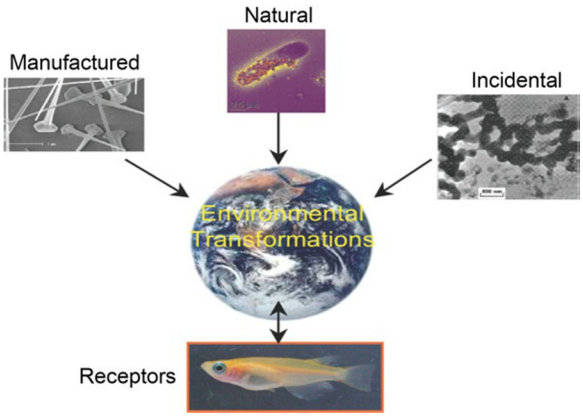

FIG. 3

Sources of nanomaterials relevant to exposure assessment [118].

Table 3 Main Sources of the Nanomaterials in Environment [119]

Source of Exposure	Engineered/Derived	Natural Origin	Incidental Origin
Air	**1.** Nanotechnology production process	**1.** Biological process **2.** Hydrothermal vent systems **3.** Nucleation processes **4.** Physicochemical wearing of rocks **5.** UV degradation from aquatic system **6.** Volcanic eruption	**1.** Combustion processes **2.** Industrial emissions
Soil	**1.** Spillage from nanotechnology	**1.** Biogenic origin **2.** Nanomaterials **3.** Natural organic materials aggregates	**1.** Deposition from atmosphere **2.** Transport or sorption from aquatic system
Water	**1.** Spillage from nanotechnology	**1.** Hydrous iron **2.** Manganese oxide **3.** Metal sulfide nanoclusters	**1.** Deposition from atmosphere

Iron oxide nanomaterials, either natural nanoparticles or engineered nanomaterials, have an impact on element cycling and pollutant fate and transport. Concerns about the environment and human health have led to elucidating what the behavior of the nanoparticles is in the environment and how they participate in environmental processes.

Recently, iron oxide–based nanomaterials are being readily studied for their environmental applications. These materials have potential to provide a solution to some of the environmental cleanup problems in environmental remediation technologies [104]. These materials have supporting physicochemical

characteristics that enhance their utilization for environmental applications, such as decontaminating contaminated soil and groundwater [64]. They are highly reactive because of their small size and can be easily contacted directly onto a site directly because they can be suspended in slurry. It has been reported that nanomaterials tend to aggregate in solution [120], which reduces their reactivity. Therefore, the stability of the nanomaterials is important for their high reactivity and mobility because the more stable the material, the aggregation and the deposition rate will be lower [121–123]. The stability of iron oxide colloid suspensions for applications may be highly improved with the help of surface modification with appropriate functional groups, such as carboxylic and phosphonic acids and amines, as shown in Fig. 4. It is worth noting that the intrinsic properties of iron oxide nanomaterials play an important role in their wide-ranging applications. The intrinsic properties of iron oxide nanomaterials are highly dependent on the synthesis method as well as on the modification media [126, 127].

The method of preparing iron oxide nanoparticles plays an important role for determining the particle shape and size, size distribution, surface chemistry, and, subsequently, the applications [43]. Moreover, the methods also help determine the level/degree and distribution of defects and impurities in the particle [128]. Three broad types of methods are used to synthesize iron oxide–based nanomaterials: chemical, biological, and physical, as shown in Fig. 5. Physical synthesis methods include inert gas condensation, high energy ball milling, severe plastic deformation, and ultrasound shot peening, whereas chemical methods include microemulsion, chemical co-precipitation, chemical vapor condensation, liquid flame spray, liquid-phase reduction, pulse electro-deposition, and gas-phase reduction [64]. The applications of iron oxide nanomaterials, specifically regarding the environment, are highly dependent on their properties, such as their magnetic properties, their specific surface area, and their core-shell structure. The other advantages of iron oxide nanomaterials are their low toxicity, biocompatibility, and chemical inertness [40]. The important characteristics of iron oxide–based nanomaterials are discussed in the following section.

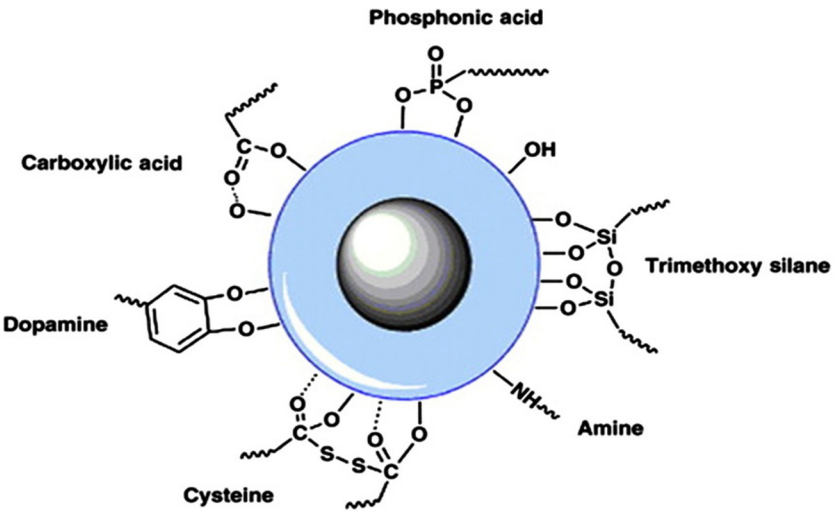

FIG. 4

The functional groups and chemical moieties at the surface of the iron oxide nanomaterials [124, 125].

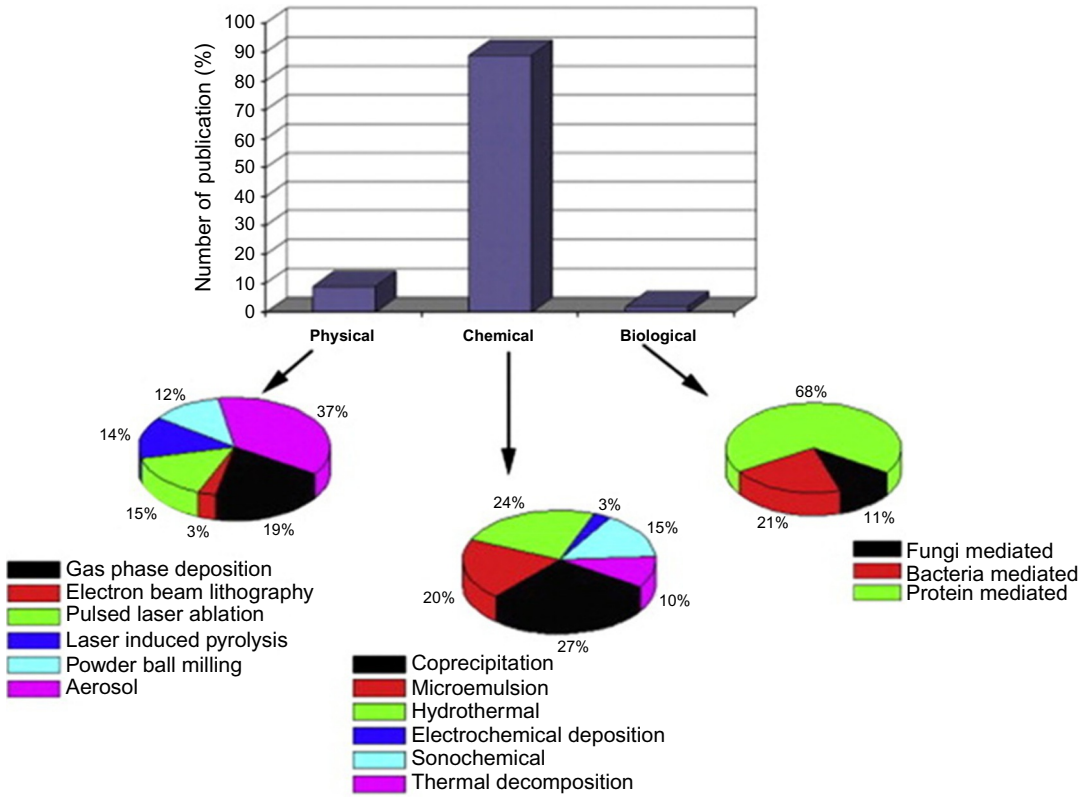

FIG. 5

Production methods of nanomaterials iron oxide nanomaterials [40, 129].

From P. Xu, G.M. Zeng, D.L. Huang; C.L. Feng, S. Hu, M.H. Zhao, C. Lai, Z. Wei, C. Huang, G.X. Xie, Use of iron oxide nanomaterials in wastewater treatment: a review, Sci. Total Environ. 424 (2012) 1–10.

6 IMPORTANT PROPERTIES OF IRON OXIDE NANOMATERIAL FOR ENVIRONMENTAL APPLICATIONS

The iron nanoparticles have a typical core-shell structure. The shell structure of iron nanoparticles is of great importance for their application in environmental remediation [130] because the reactivity of the core-shell nanoparticles is created through the oxidation of Fe^0 core [130, 131]. To protect the iron core from further oxidation, different techniques, such as shell coatings, have been applied [132]. The shell can be composed of different materials, but the native iron oxides are the most attractive for shell formation because of their higher efficiency for suppressing the oxidation of the iron core [133–135]. Lu et al. [136] synthesized Fe-Fe_2O_3 core-shell nano-necklaces and nanowires in the ambient atmosphere using a borohydride reduction method.

The iron oxide nanoparticles have a high specific surface, which is considered one of the important parameters that affects the physical and chemical properties of nanomaterials. It helps enhance the rate

of reaction with some kinds of contaminants, therefore making the iron oxide nanomaterials more effective for reducing such contaminants [64]. Zhang et al. [137] reported that the surface area of the nanoscale metal particles is one to two times higher than that of the commercially available microscale metal particles. Along with high surface area, their high intrinsic reactivity, and their high density of the reactive surface sites, of metal oxide nanomaterials also exhibit their effect on the enhanced reactivity of the iron-based nanoparticles [131].

The magnetic properties of iron oxide nanoparticles are not considered to be supporting properties for their environmental applications; however, these properties are important for utilizing these materials effectively in biomedical, catalysis, magnetic fluids, synthesis of biochemical and organics, industrial water treatment, and magnetic recording applications [43, 64, 138–141]. The dispersion of the magnetic nanoparticles is an important factor for improving the efficiency of the reaction, while high magnetic properties cause the reduction in dispersion [64]. Magnetic nanoparticles start aggregating because of the magnetic dipole–dipole attraction and high surface area, which result in the production of large chains, reactivity loss, and a reduction in nanoparticles transformation in contaminated sites [142].

7 APPLICATIONS IN THE ENVIRONMENT

Because of the higher efficiency of the iron-based nanoparticles than iron-based regular materials in terms of reactivity, the former is preferred for their environmental applications. It has been reported that nano-iron particles have been recognized as a tool for remediating air, groundwater, and soil. Furthermore, these particles are capable of reacting effectively with hazardous environmental contaminants. When a release of nanomaterials occurs into the environment, then their behavior will be highly dependent on several factors: specific properties, that is, chemical composition, shape, size, surface charge, and coating; the state of the particle, that is, either free or matrix incorporated; the chemistry of the surrounding solution, that is, the natural organic matter content, ionic composition, ionic strength, and pH; and the hydrodynamic conditions [143, 144]. The application of iron oxide nanoparticles for reducing polyhalogenated methanes has been reported. Ardejani et al. [44] found from their experimental study that Fe^{II}–Fe^{III} particles are beneficial for their application in remediating carbon tetrachloride–contaminated soil or groundwater.

Heavy metal contamination is a great concern, and their removal, because of their toxic effects on human beings, animals, and plants, is important [40]. It has been suggested that the metallic ions, such as lead, arsenic, and chromium, among others, are also dangerous for the environment. Arsenic is a known carcinogen and causes bladder, lung, and skin cancer [64]. According to the World Health Organization, a maximum concentration of arsenic in drinking water should be 10 ppb, or 0.01 mg/L. Lead and chromium are also great threats to the environment and human health if their amounts in drinking water are higher than the allowed limit. According to US Environmental Protection Agency (EPA), the maximum limit for lead and chromium is 0.015 mg/L and 0.1 mL/L, respectively, in drinking water. Selenium is also considered hazardous for the environment and human health. The maximum level for selenium in drinking water set by EPA is 0.05 mg/L. Long-term exposure to selenium at higher levels than allowed limit causes various health problems, such as the loss of fingernails and hair. Also, it tends to damage the circulatory and nervous systems, the kidneys, and the liver. These metals get into the environment either by processes or by the human activities. Iron oxide

nanomaterials are being widely used as effective adsorbents for heavy metals removal, such as mercury, cadmium, copper, and lead [40].

Using iron oxide nanomaterials for removing metallic ions from drinking water has been reported in the literature, showing their environmental application. Dixit and Hering [145] studied a comparative behavior for adsorption of As(III) and As(V) on the surface of iron oxide nanoparticles. It was reported that both As(III) and As(V) adsorb significantly onto the surface of the iron oxide. Furthermore, it was suggested the adsorption behavior is completely dependent on the oxidation state, the mineralogy of the iron oxide, and the experimental conditions. Nassar [146] investigated the adsorption capacity of iron oxide nanoparticles for lead removal, and it was concluded that the iron oxide nanoparticles show greater efficiency than reported adsorbents for removing lead. It also was recommended that iron oxide nanoparticles are the most economical and effective adsorbents.

It is also reported that iron oxide nanomaterials have a great potential of the reduction of carbon monoxide (CO) because of its small particle size, high surface area, and dual functions for CO oxidation. During CO oxidation, iron oxides react both as catalysts in presence of oxygen and as oxidants in absence of oxygen, intensifying the CO oxidation [64]. Li et al. [147] studied the effect of the iron oxide nanoparticles both as oxidants and as catalysts. In addition, the researchers compared the effect of the nanoscale and nonnanoscale iron oxide. When comparing the effect of nanoscale and nonnanoscale iron oxides, they found that the nanoscale oxides catalyzes the oxidation of almost 100% of the CO to CO_2, whereas the same amount of nonnanoscale iron oxides can catalyze even less than 5% of CO. Moreover, it is also observed that the nanoscale iron oxide oxidized CO significantly, acting both as a catalyst and as a reagent.

8 LIMITATIONS AND CHALLENGES OF IRON NANOMATERIALS IN FUTURE

Recently, iron oxide nanomaterials are being considered as extremely competent nanoadsorbents for removing different types of contaminants because of their high sorption capacities, fast removal capabilities, and easy isolation methods in an aqueous medium. However, the main hurdle in the successful utilization is their production cost. However, researchers are still working to reduce their production cost that will enable its practical use as nanoadsorbents for wastewater treatment. Another issue is the lack of full-scale plant operation outcomes to determine their feasibility. Regarding the production of iron nanomaterial, no project is available for producing iron oxide–based nanomaterials in bulk. Therefore, the fate of these nanomaterials will depend on their commercialization. One more aspect that requires in-depth research is the discharge of iron oxide–based nanomaterials and their impact on aquatic environments. Very limited information is available at present with respect to their disposal in water bodies, which must be analyzed in detail. In this way, risk identification in this area will be greatly helpful in finding out the effects of nanotoxicity on the ecosystem. Furthermore, various new testing methods are also required to understand the effectiveness of these nanomaterials.

The development of iron oxide–based nanocomposite with materials such as silica or carbon have modified physiochemical stabilities, and key magnetic characteristics also have provided amazing advantages in application of these novel materials. One challenge is to find the right source for incorporating them into the development of a nanocomposite that can boost the overall efficiency of adsorption. For example, combining iron oxide nanomaterials with activated carbon is increasing the overall performance of these materials as nanoadsorbents. Researchers have highlighted the

potential efficient application of these nanomaterials in adsorption operations as well as in biomedicine and catalysis. One more advantage of these materials is that, as catalysts, they do not require a carrier. The use of iron oxide nanomaterials combined with polymers for drug delivery in the desired portion of the body is also attracting many experts in the field. Several scholars are working to enhance these nanomaterials' practical output so that they can be utilized as biosensors. In short, iron oxide nanomaterials have shown dramatic growth, and their diverse and multifunctional application can bring about enormous changes in various areas, including environmental remediation.

9 CONCLUSION

Water is the most essential element for living things on this planet, which are humans, animals, and plants. Today, the most popular worldwide issue involves the basic need to provide clean and affordable water. Wastewater is the polluted water that is no longer suitable for use. Wastewater treatment is the process of improving the quality of wastewater and converting it into an effluent that can be either returned to the nature or incorporated to the water cycle with minimum environmental issues or that can be reused. Water pollution caused by heavy metals and dyes continues, and some problems have even been left unattended. The most crucial cause of this pollution is industrial waste, especially water that has been released into the drainage system without first being treated. These activities have been done illegally and have had a huge impact on the environment as well as humans. Therefore, this research has been conducted for one of the solution to overcome this problem in an effective way. For these reasons and many more, the environmental laws on heavy metals and dyes discharge are becoming more and more stringent in various part of the world. To overcome these shortcomings, iron-based nanomaterials are potential adsorbents for current wastewater treatment because iron-based nanomaterials, posttreatment, can separated via magnetic field from the metals and dyes, so there is no need for additional energy or materials to separate purified drinking water from the metal-dye-laden adsorbent. Therefore, iron-based materials play a vital role in their wide-ranging application in various industries for removing metals and dyes from wastewater. Another key advantage of using iron oxide–based nanoparticles includes that they can be simply regenerated with various chemicals, such as hydrogen peroxide, and therefore can be reused. This has made them feasible for commercial utilization in various full-scale units and promising as adsorbents for treating pollutants in wastewater. However, because of the high cost of these materials, more intensive work is needed to address this issue. Iron-based nanomaterials are one of best adsorbents for treating industrial effluent and saving the environment and humankind. Hence, finding a cheaper, more efficient means of purifying contaminated water to meet safety standards is increasingly occupying the attention of governments and environmental scientists around the world.

REFERENCES

[1] D. Grey, D. Garrick, D. Blackmore, J. Kelman, M. Muller, C. Sadoff, Water security in one blue planet: twenty-first century policy challenges for science, Philos. Trans. R. Soc. A Math. Phys. Eng. Sci. 371 (2013).

[2] A.S. Adeleye, J.R. Conway, K. Garner, Y. Huang, Y. Su, A.A. Keller, Engineered nanomaterials for water treatment and remediation: costs, benefits, and applicability, Chem. Eng. J. 286 (2016) 640–662.

[3] M.N. Chong, B. Jin, C.W.K. Chow, C. Saint, Recent developments in photocatalytic water treatment technology: a review, Water Res. 44 (2010) 2997–3027.
[4] W. Song, B. Gao, X. Xu, L. Xing, S. Han, P. Duan, W. Song, R. Jia, Adsorption–desorption behavior of magnetic amine/Fe_3O_4 functionalized biopolymer resin towards anionic dyes from wastewater, Bioresour. Technol. 210 (2016) 123–130.
[5] T. Yao, S. Guo, C. Zeng, C. Wang, L. Zhang, Investigation on efficient adsorption of cationic dyes on porous magnetic polyacrylamide microspheres, J. Hazard. Mater. 292 (2015) 90–97.
[6] M.N. Moore, Do nanoparticles present ecotoxicological risks for the health of the aquatic environment? Environ. Int. 32 (2006) 967–976.
[7] S. Mahdavi, M. Jalali, A. Afkhami, Heavy metals removal from aqueous solutions using TiO_2, MgO, and Al_2O_3 nanoparticles, Chem. Eng. Commun. 200 (2013) 448–470.
[8] N. Mubarak, J. Sahu, E. Abdullah, N. Jayakumar, Removal of heavy metals from wastewater using carbon nanotubes, Sep. Purif. Rev. 43 (2014) 311–338.
[9] Y.C. Sharma, V. Srivastava, V.K. Singh, S.N. Kaul, C.H. Weng, Nano-adsorbents for the removal of metallic pollutants from water and wastewater, Environ. Technol. 30 (2009) 583–609.
[10] R.K. Thines, N.M. Mubarak, S. Nizamuddin, J.N. Sahu, E.C. Abdullah, P. Ganesan, Application potential of carbon nanomaterials in water and wastewater treatment: a review, J. Taiwan Inst. Chem. Eng. 72 (2017) 116–133.
[11] M.A. Tofighy, T. Mohammadi, Adsorption of divalent heavy metal ions from water using carbon nanotube sheets, J. Hazard. Mater. 185 (2011) 140–147.
[12] Y.-H. Li, S. Wang, J. Wei, X. Zhang, C. Xu, Z. Luan, D. Wu, B. Wei, Lead adsorption on carbon nanotubes, Chem. Phys. Lett. 357 (2002) 263–266.
[13] T. Masciangioli, W.-X. Zhang, Peer reviewed: environmental technologies at the nanoscale, Environ. Sci. Technol. 37 (2003) 102A–108A.
[14] J. Calderon, M. Navarro, M. Jimenez-Capdeville, M. Santos-Diaz, A. Golden, I. Rodriguez-Leyva, V. Borja-Aburto, F. Diaz-Barriga, Exposure to arsenic and lead and neuropsychological development in Mexican children, Environ. Res. 85 (2001) 69–76.
[15] J. Ruparelia, S. Duttagupta, A. Chatterjee, S. Mukherji, Potential of carbon nanomaterials for removal of heavy metals from water, Desalination 232 (2008) 145–156.
[16] T.W. Odom, J.-L. Huang, P. Kim, C.M. Lieber, Atomic structure and electronic properties of single-walled carbon nanotubes, Nature 391 (1998) 62–64.
[17] L. Xiao, Z. Wen, S. Ci, J. Chen, Z. He, Carbon/iron-based nanorod catalysts for hydrogen production in microbial electrolysis cells, Nano Energy 1 (2012) 751–756.
[18] B. Baranowski, S. Zaginaichenko, D. Schur, V. Skorokhod, A. Veziroglu, Carbon Nanomaterials in Clean Energy Hydrogen Systems, Springer Science & Business Media, Sudak (Crimea, Ukraine), 2008.
[19] P.J. Weicker, T.M. Henigan, Solid-state battery management using real-time estimation of nano material electrical characteristics, Google Patents, 2016.
[20] M. Lefèvre, E. Proietti, F. Jaouen, J.-P. Dodelet, Iron-based catalysts with improved oxygen reduction activity in polymer electrolyte fuel cells, Science 324 (2009) 71–74.
[21] L. Zhang, H.B. Wu, X.W.D. Lou, Iron-oxide-based advanced anode materials for lithium-ion batteries, Adv. Energy Mater. 4 (2014).
[22] W. Zhou, L. Guo, Iron triad (Fe, Co, Ni) nanomaterials: structural design, functionalization and their applications, Chem. Soc. Rev. 44 (2015) 6697–6707.
[23] V.K. Upadhyayula, S. Deng, M.C. Mitchell, G.B. Smith, Application of carbon nanotube technology for removal of contaminants in drinking water: a review, Sci. Total Environ. 408 (2009) 1–13.
[24] N.M. Mubarak, J.N. Sahu, E.C. Abdullah, N.S. Jayakumar, P. Ganesan, Single stage production of carbon nanotubes using microwave technology, Diam. Relat. Mater. 48 (2014) 52–59.

[25] C. Zhu, S. Dong, Recent progress in graphene-based nanomaterials as advanced electrocatalysts towards oxygen reduction reaction, Nano 5 (2013) 1753–1767.
[26] K. Shankar, J.I. Basham, N.K. Allam, O.K. Varghese, G.K. Mor, X. Feng, M. Paulose, J.A. Seabold, K.-S. Choi, C.A. Grimes, Recent advances in the use of TiO_2 nanotube and nanowire arrays for oxidative photoelectrochemistry, J. Phys. Chem. C 113 (2009) 6327–6359.
[27] D.G. Capco, Y. Chen, Nanomaterial: Impacts on Cell Biology and Medicine, Springer, Netherlands, 2014.
[28] D. Fialova, M. Kremplova, L. Melichar, P. Kopel, D. Hynek, V. Adam, R. Kizek, Interaction of heavy metal ions with carbon and iron based particles, Materials 7 (2014) 2242–2256.
[29] J.-F. Liu, Z.-S. Zhao, G.-B. Jiang, Coating Fe_3O_4 magnetic nanoparticles with humic acid for high efficient removal of heavy metals in water, Environ. Sci. Technol. 42 (2008) 6949–6954.
[30] S.-H. Huang, D.-H. Chen, Rapid removal of heavy metal cations and anions from aqueous solutions by an amino-functionalized magnetic nano-adsorbent, J. Hazard. Mater. 163 (2009) 174–179.
[31] Y. Pang, G. Zeng, L. Tang, Y. Zhang, Y. Liu, X. Lei, Z. Li, J. Zhang, Z. Liu, Y. Xiong, Preparation and application of stability enhanced magnetic nanoparticles for rapid removal of Cr (VI), Chem. Eng. J. 175 (2011) 222–227.
[32] R.M. Cornell, U. Schwertmann, The Iron Oxides: Structure, Properties, Reactions, Occurrences and Uses, John Wiley & Sons, USA, 2003.
[33] S. Gubin, Y.I. Spichkin, G.Y. Yurkov, A. Tishin, Nanomaterial for high-density magnetic data storage, Russ. J. Inorg. Chem. 47 (2002) S32–S67.
[34] A.H. Lu, W. Schmidt, N. Matoussevitch, H. Bönnemann, B. Spliethoff, B. Tesche, E. Bill, W. Kiefer, F. Schüth, Nanoengineering of a magnetically separable hydrogenation catalyst, Angew. Chem. 116 (2004) 4403–4406.
[35] N. Mubarak, A. Kundu, J. Sahu, E. Abdullah, N. Jayakumar, Synthesis of palm oil empty fruit bunch magnetic pyrolytic char impregnating with $FeCl_3$ by microwave heating technique, Biomass Bioenergy 61 (2014) 265–275.
[36] H. Sozeri, U. Kurtan, R. Topkaya, A. Baykal, M.S. Toprak, Polyaniline (PANI)–Co 0.5 Mn 0.5 Fe_2O_4 nanocomposite: synthesis, characterization and magnetic properties evaluation, Ceram. Int. 39 (2013) 5137–5143.
[37] M. Blatt, S. Wiseman, E. Domany, Superparamagnetic clustering of data, Phys. Rev. Lett. 76 (1996) 3251.
[38] C.V. Bowen, X. Zhang, G. Saab, P.J. Gareau, B.K. Rutt, Application of the static dephasing regime theory to superparamagnetic iron-oxide loaded cells, Magn. Reson. Med. 48 (2002) 52–61.
[39] A.H. Lu, E.E.L. Salabas, F. Schüth, Magnetic nanoparticles: synthesis, protection, functionalization, and application, Angew. Chem. Int. Ed. 46 (2007) 1222–1244.
[40] P. Xu, G.M. Zeng, D.L. Huang, C.L. Feng, S. Hu, M.H. Zhao, C. Lai, Z. Wei, C. Huang, G.X. Xie, Use of iron oxide nanomaterials in wastewater treatment: a review, Sci. Total Environ. 424 (2012) 1–10.
[41] J. Hu, I.M. Lo, G. Chen, Comparative study of various magnetic nanoparticles for Cr (VI) removal, Sep. Purif. Technol. 56 (2007) 249–256.
[42] S.K. Giri, N.N. Das, G.C. Pradhan, Synthesis and characterization of magnetite nanoparticles using waste iron ore tailings for adsorptive removal of dyes from aqueous solution, Colloids Surf. A Physicochem. Eng. Asp. 389 (2011) 43–49.
[43] A.S. Teja, P.-Y. Koh, Synthesis, properties, and applications of magnetic iron oxide nanoparticles, Prog. Cryst. Growth Charact. Mater. 55 (2009) 22–45.
[44] F.D. Ardejani, K. Badii, N.Y. Limaee, N. Mahmoodi, M. Arami, S. Shafaei, A. Mirhabibi, Numerical modelling and laboratory studies on the removal of Direct Red 23 and Direct Red 80 dyes from textile effluents using orange peel, a low-cost adsorbent, Dyes Pigments 73 (2007) 178–185.
[45] A. Gürses, S. Karaca, Ç. Doğar, R. Bayrak, M. Açıkyıldız, M. Yalçin, Determination of adsorptive properties of clay/water system: methylene blue sorption, J. Colloid Interface Sci. 269 (2004) 310–314.

[46] B. Hameed, A. Ahmad, Batch adsorption of methylene blue from aqueous solution by garlic peel, an agricultural waste biomass, J. Hazard. Mater. 164 (2009) 870–875.
[47] E. Haque, J.W. Jun, S.H. Jhung, Adsorptive removal of methyl orange and methylene blue from aqueous solution with a metal-organic framework material, iron terephthalate (MOF-235), J. Hazard. Mater. 185 (2011) 507–511.
[48] K. Krafts, E. Hempelmann, A. Skórska-Stania, From methylene blue to chloroquine: a brief review of the development of an antimalarial therapy, Parasitol. Res. 111 (2012) 1–6.
[49] M. Fujii, T. Kusama, Fixation of horseradish peroxidase reaction products with ammonium molybdate, Neurosci. Res. 1 (1984) 153–156.
[50] M.J. Stark, K.N. Smalley, E.C. Rowe, Methylene blue staining of axons in the ventral nerve cord of insects, Stain. Technol. 44 (1969) 97–102.
[51] W.R. Kennedy, Opportunities afforded by the study of unmyelinated nerves in skin and other organs, Muscle Nerve 29 (2004) 756–767.
[52] E. Sudova, J. Machova, Z. Svobodova, T. Vesely, Negative effects of malachite green and possibilities of its replacement in the treatment of fish eggs and fish: a review, Vet. Med. Praha 52 (2007) 527.
[53] A. Belayachi, B. Bestani, A. Bendraoua, N. Benderdouche, L. Duclaux, The influence of surface functionalization of activated carbon on dyes and metal ion removal from aqueous media, Desalin. Water Treat. (2015) 1–13.
[54] C. Aeschlimann, T. Cerny, A. Küpfer, Inhibition of (mono) amine oxidase activity and prevention of ifosfamide encephalopathy by methylene blue, Drug Metab. Dispos. 24 (1996) 1336–1339.
[55] A. Petzer, B.H. Harvey, G. Wegener, J.P. Petzer, Azure B, a metabolite of methylene blue, is a high-potency, reversible inhibitor of monoamine oxidase, Toxicol. Appl. Pharmacol. 258 (2012) 403–409.
[56] R. Ramsay, C. Dunford, P. Gillman, Methylene blue and serotonin toxicity: inhibition of monoamine oxidase A (MAO A) confirms a theoretical prediction, Br. J. Pharmacol. 152 (2007) 946–951.
[57] K. Singh, K. Senapati, K. Sarma, Synthesis of superparamagnetic Fe_3O_4 nanoparticles coated with green tea polyphenols and their use for removal of dye pollutant from aqueous solution, J. Environ. Chem. Eng. 5 (3) (2017) 2214–2221.
[58] Z. Es' Haghzade, E. Pajootan, H. Bahrami, M. Arami, Facile synthesis of Fe_3O_4 nanoparticles via aqueous based electro chemical route for heterogeneous electro-Fenton removal of azo dyes, J. Taiwan Inst. Chem. Eng. 71 (2017) 91–105.
[59] M. Angamuthu, G. Satishkumar, M. Landau, Precisely controlled encapsulation of Fe_3O_4 nanoparticles in mesoporous carbon nanodisk using iron based MOF precursor for effective dye removal, Microporous Mesoporous Mater. (2017).
[60] T.K. Sahu, S. Arora, A. Banik, P.K. Iyer, M. Qureshi, Efficient and rapid removal of environmental malignant arsenic (III) and industrial dyes using re-usable, recoverable ternary iron oxide–ormosil-graphene oxide composite, ACS Sustain. Chem. Eng. 5 (7) (2017) 5912–5921.
[61] A. Ebrahiminezhad, S. Taghizadeh, Y. Ghasemi, A. Berenjian, Green synthesized nanoclusters of ultra-small zero valent iron nanoparticles as a novel dye removing material, Sci. Total Environ. 621 (2017) 1527–1532.
[62] A. Asfaram, M. Ghaedi, S. Hajati, A. Goudarzi, E.A. Dil, Screening and optimization of highly effective ultrasound-assisted simultaneous adsorption of cationic dyes onto Mn-doped Fe_3O_4-nanoparticle-loaded activated carbon, Ultrason. Sonochem. 34 (2017) 1–12.
[63] B.I. Kharisov, H.R. Dias, O.V. Kharissova, V.M. Jiménez-Pérez, B.O. Pérez, B.M. Flores, Iron-containing nanomaterials: synthesis, properties, and environmental applications, RSC Adv. 2 (2012) 9325–9358.
[64] L. Li, M. Fan, R.C. Brown, J. van Leeuwen, J. Wang, W. Wang, Y. Song, P. Zhang, Synthesis, properties, and environmental applications of nanoscale iron-based materials: a review, Crit. Rev. Environ. Sci. Technol. 36 (2006) 405–431.

[65] Y. Shen, J. Tang, Z. Nie, Y. Wang, Y. Ren, L. Zuo, Tailoring size and structural distortion of Fe_3O_4 nanoparticles for the purification of contaminated water, Bioresour. Technol. 100 (2009) 4139–4146.
[66] S.C. Tang, I.M. Lo, Magnetic nanoparticles: essential factors for sustainable environmental applications, Water Res. 47 (2013) 2613–2632.
[67] Y.-M. Hao, C. Man, Z.-B. Hu, Effective removal of Cu (II) ions from aqueous solution by amino-functionalized magnetic nanoparticles, J. Hazard. Mater. 184 (2010) 392–399.
[68] A.M. Gutierrez, T.D. Dziubla, J.Z. Hilt, Recent advances on iron oxide magnetic nanoparticles as sorbents of organic pollutants in water and wastewater treatment, Rev. Environ. Health 32 (2017) 111–117.
[69] A.K. Gupta, P.S. Ghosal, B.K. Dubey, Hybrid nanoadsorbents for drinking water treatment: a critical review, in: Hybrid Nanomaterials: Advances in Energy, Environment, and Polymer Nanocomposites, 2017, p. 199. Wiley, USA.
[70] R. Riahi-Madvaar, M.A. Taher, H. Fazelirad, Synthesis and characterization of magnetic halloysite-iron oxide nanocomposite and its application for naphthol green B removal, Appl. Clay Sci. 137 (2017) 101–106.
[71] X. Shi, W. Ruan, J. Hu, M. Fan, R. Cao, X. Wei, Optimizing the removal of rhodamine B in aqueous solutions by reduced graphene oxide-supported nanoscale zerovalent iron (nZVI/rGO) using an artificial neural network-genetic algorithm (ANN-GA), Nano 7 (2017) 134.
[72] S. Mahpishanian, H. Sereshti, One-step green synthesis of β-cyclodextrin/iron oxide-reduced graphene oxide nanocomposite with high supramolecular recognition capability: application for vortex-assisted magnetic solid phase extraction of organochlorine pesticides residue from honey samples, J. Chromatogr. A 1485 (2017) 32–43.
[73] S. Thakur, N. Karak, One-step approach to prepare magnetic iron oxide/reduced graphene oxide nanohybrid for efficient organic and inorganic pollutants removal, Mater. Chem. Phys. 144 (2014) 425–432.
[74] R. Crane, T. Scott, Nanoscale zero-valent iron: future prospects for an emerging water treatment technology, J. Hazard. Mater. 211 (2012) 112–125.
[75] A. Panáček, L. Kvítek, R. Prucek, M. Kolář, R. Večeřová, N. Pizúrová, V.K. Sharma, T.J. Nevěčná, R. Zbořil, Silver colloid nanoparticles: synthesis, characterization, and their antibacterial activity, J. Phys. Chem. B 110 (2006) 16248–16253.
[76] Z. Zhang, J. Kong, Novel magnetic Fe_3O_4@ C nanoparticles as adsorbents for removal of organic dyes from aqueous solution, J. Hazard. Mater. 193 (2011) 325–329.
[77] S.-F. Lim, Y.-M. Zheng, J.P. Chen, Organic arsenic adsorption onto a magnetic sorbent, Langmuir 25 (2009) 4973–4978.
[78] H.A. Wiatrowski, S. Das, R. Kukkadapu, E.S. Ilton, T. Barkay, N. Yee, Reduction of Hg (II) to Hg (0) by magnetite, Environ. Sci. Technol. 43 (2009) 5307–5313.
[79] L. Zeng, X. Li, J. Liu, Adsorptive removal of phosphate from aqueous solutions using iron oxide tailings, Water Res. 38 (2004) 1318–1326.
[80] E. Petala, Y. Georgiou, V. Kostas, K. Dimos, M.A. Karakassides, Y. Deligiannakis, C. Aparicio, J. Tuček, R. Zboril, Magnetic carbon nanocages: an advanced architecture with surface-and morphology-enhanced removal capacity for arsenites, ACS Sustain. Chem. Eng. 5 (7) (2017) 5782–5792.
[81] K. Thines, E. Abdullah, N. Mubarak, M. Ruthiraan, Synthesis of magnetic biochar from agricultural waste biomass to enhancing route for waste water and polymer application: a review, Renew. Sust. Energ. Rev. 67 (2017) 257–276.
[82] M. Tripathi, N. Mubarak, J. Sahu, P. Ganesan, Overview on synthesis of magnetic bio char from discarded agricultural biomass, in: Handbook of Composites from Renewable Materials, Structure and Chemistry, vol. 1, 2016, p. 435 Wiley, USA.
[83] S.-Y. Yoon, C.-G. Lee, J.-A. Park, J.-H. Kim, S.-B. Kim, S.-H. Lee, J.-W. Choi, Kinetic, equilibrium and thermodynamic studies for phosphate adsorption to magnetic iron oxide nanoparticles, Chem. Eng. J. 236 (2014) 341–347.

[84] C.-Y. Cao, J. Qu, W.-S. Yan, J.-F. Zhu, Z.-Y. Wu, W.-G. Song, Low-cost synthesis of flowerlike α-Fe_2O_3 nanostructures for heavy metal ion removal: adsorption property and mechanism, Langmuir 28 (2012) 4573–4579.
[85] M. Ding, B. De Jong, S. Roosendaal, A. Vredenberg, XPS studies on the electronic structure of bonding between solid and solutes: adsorption of arsenate, chromate, phosphate, Pb^{2+}, and Zn^{2+} ions on amorphous black ferric oxyhydroxide, Geochim. Cosmochim. Acta 64 (2000) 1209–1219.
[86] J. Hu, G. Chen, I.M. Lo, Selective removal of heavy metals from industrial wastewater using maghemite nanoparticle: performance and mechanisms, J. Environ. Eng. 132 (2006) 709–715.
[87] B. Pan, J. Wu, B. Pan, L. Lv, W. Zhang, L. Xiao, X. Wang, X. Tao, S. Zheng, Development of polymer-based nanosized hydrated ferric oxides (HFOs) for enhanced phosphate removal from waste effluents, Water Res. 43 (2009) 4421–4429.
[88] Z. Ren, L. Shao, G. Zhang, Adsorption of phosphate from aqueous solution using an iron–zirconium binary oxide sorbent, Water Air Soil Pollut. 223 (2012) 4221–4231.
[89] L. Zhou, C. Gao, W. Xu, Magnetic dendritic materials for highly efficient adsorption of dyes and drugs, ACS Appl. Mater. Interfaces 2 (2010) 1483–1491.
[90] C. Luo, Z. Tian, B. Yang, L. Zhang, S. Yan, Manganese dioxide/iron oxide/acid oxidized multi-walled carbon nanotube magnetic nanocomposite for enhanced hexavalent chromium removal, Chem. Eng. J. 234 (2013) 256–265.
[91] H. Bagheri, A. Afkhami, M. Saber-Tehrani, H. Khoshsafar, Preparation and characterization of magnetic nanocomposite of Schiff base/silica/magnetite as a preconcentration phase for the trace determination of heavy metal ions in water, food and biological samples using atomic absorption spectrometry, Talanta 97 (2012) 87–95.
[92] M. Zhang, B. Gao, S. Varnoosfaderani, A. Hebard, Y. Yao, M. Inyang, Preparation and characterization of a novel magnetic biochar for arsenic removal, Bioresour. Technol. 130 (2013) 457–462.
[93] M. Baalousha, Aggregation and disaggregation of iron oxide nanoparticles: Influence of particle concentration, pH and natural organic matter, Sci. Total Environ. 407 (2009) 2093–2101.
[94] Y.-F. Lin, J.-L. Chen, Magnetic mesoporous Fe/carbon aerogel structures with enhanced arsenic removal efficiency, J. Colloid Interface Sci. 420 (2014) 74–79.
[95] L. Wei, G. Yang, R. Wang, W. Ma, Selective adsorption and separation of chromium (VI) on the magnetic iron–nickel oxide from waste nickel liquid, J. Hazard. Mater. 164 (2009) 1159–1163.
[96] M. Bhaumik, A. Maity, V. Srinivasu, M.S. Onyango, Enhanced removal of Cr (VI) from aqueous solution using polypyrrole/Fe_3O_4 magnetic nanocomposite, J. Hazard. Mater. 190 (2011) 381–390.
[97] X. Liu, Q. Hu, Z. Fang, X. Zhang, B. Zhang, Magnetic chitosan nanocomposites: a useful recyclable tool for heavy metal ion removal, Langmuir 25 (2008) 3–8.
[98] R.D. Ambashta, M. Sillanpää, Water purification using magnetic assistance: a review, J. Hazard. Mater. 180 (2010) 38–49.
[99] Z. Wu, W. Li, P.A. Webley, D. Zhao, General and controllable synthesis of novel mesoporous magnetic iron oxide@ carbon encapsulates for efficient arsenic removal, Adv. Mater. 24 (2012) 485–491.
[100] J.-L. Gong, X.-Y. Wang, G.-M. Zeng, L. Chen, J.-H. Deng, X.-R. Zhang, Q.-Y. Niu, Copper (II) removal by pectin–iron oxide magnetic nanocomposite adsorbent, Chem. Eng. J. 185 (2012) 100–107.
[101] J. Hu, D. Shao, C. Chen, G. Sheng, X. Ren, X. Wang, Removal of 1-naphthylamine from aqueous solution by multiwall carbon nanotubes/iron oxides/cyclodextrin composite, J. Hazard. Mater. 185 (2011) 463–471.
[102] X. Zhao, J. Wang, F. Wu, T. Wang, Y. Cai, Y. Shi, G. Jiang, Removal of fluoride from aqueous media by Fe_3O_4@ Al $(OH)_3$ magnetic nanoparticles, J. Hazard. Mater. 173 (2010) 102–109.
[103] X.-Q. Li, D.W. Elliott, W.-X. Zhang, Zero-valent iron nanoparticles for abatement of environmental pollutants: materials and engineering aspects, Crit. Rev. Solid State Mater. Sci. 31 (2006) 111–122.

[104] W.-X. Zhang, Nanoscale iron particles for environmental remediation: an overview, J. Nanopart. Res. 5 (2003) 323–332.
[105] S. Shariati, M. Faraji, Y. Yamini, A.A. Rajabi, Fe_3O_4 magnetic nanoparticles modified with sodium dodecyl sulfate for removal of safranin O dye from aqueous solutions, Desalination 270 (2011) 160–165.
[106] L. Tang, S. Zhang, G.-M. Zeng, Y. Zhang, G.-D. Yang, J. Chen, J.-J. Wang, J.-J. Wang, Y.-Y. Zhou, Y.-C. Deng, Rapid adsorption of 2,4-dichlorophenoxyacetic acid by iron oxide nanoparticles-doped carboxylic ordered mesoporous carbon, J. Colloid Interface Sci. 445 (2015) 1–8.
[107] X. Luo, L. Zhang, High effective adsorption of organic dyes on magnetic cellulose beads entrapping activated carbon, J. Hazard. Mater. 171 (2009) 340–347.
[108] X. Yang, C. Chen, J. Li, G. Zhao, X. Ren, X. Wang, Graphene oxide-iron oxide and reduced graphene oxide-iron oxide hybrid materials for the removal of organic and inorganic pollutants, RSC Adv. 2 (2012) 8821–8826.
[109] L.S. Zhong, J.S. Hu, H.P. Liang, A.M. Cao, W.G. Song, L.J. Wan, Self-assembled 3D flowerlike iron oxide nanostructures and their application in water treatment, Adv. Mater. 18 (2006) 2426–2431.
[110] A. Khataee, B. Kayan, D. Kalderis, A. Karimi, S. Akay, M. Konsolakis, Ultrasound-assisted removal of Acid Red 17 using nanosized Fe_3O_4-loaded coffee waste hydrochar, Ultrason. Sonochem. 35 (2017) 72–80.
[111] X. Zhu, Y. Liu, C. Zhou, S. Zhang, J. Chen, Novel and high-performance magnetic carbon composite prepared from waste hydrochar for dye removal, ACS Sustain. Chem. Eng. 2 (2014) 969–977.
[112] M.M. Khin, A.S. Nair, V.J. Babu, R. Murugan, S. Ramakrishna, A review on nanomaterials for environmental remediation, Energy Environ. Sci. 5 (2012) 8075–8109.
[113] A.R. Petosa, D.P. Jaisi, I.R. Quevedo, M. Elimelech, N. Tufenkji, Aggregation and deposition of engineered nanomaterials in aquatic environments: role of physicochemical interactions, Environ. Sci. Technol. 44 (2010) 6532–6549.
[114] A.D. Maynard, E.D. Kuempel, Airborne nanostructured particles and occupational health, J. Nanopart. Res. 7 (2005) 587–614.
[115] M. Methner, L. Hodson, A. Dames, C. Geraci, Nanoparticle emission assessment technique (NEAT) for the identification and measurement of potential inhalation exposure to engineered nanomaterials—Part B: results from 12 field studies, J. Occup. Environ. Hyg. 7 (2010) 163–176.
[116] E. Navarro, A. Baun, R. Behra, N.B. Hartmann, J. Filser, A.-J. Miao, A. Quigg, P.H. Santschi, L. Sigg, Environmental behavior and ecotoxicity of engineered nanoparticles to algae, plants, and fungi, Ecotoxicology 17 (2008) 372–386.
[117] A.M. Vindedahl, J.H. Strehlau, W.A. Arnold, R.L. Penn, Organic matter and iron oxide nanoparticles: aggregation, interactions, and reactivity, Environ. Sci. Nano 3 (2016) 494–505.
[118] M.R. Wiesner, G.V. Lowry, K.L. Jones, J. Hochella, F. Michael, R.T. Di Giulio, E. Casman, E.S. Bernhardt, Decreasing Uncertainties in Assessing Environmental Exposure, Risk, and Ecological Implications of Nanomaterials, ACS Publications, American Chemical Society, 2009.
[119] M. Farré, J. Sanchís, D. Barceló, Analysis and assessment of the occurrence, the fate and the behavior of nanomaterials in the environment, TrAC Trends Anal. Chem. 30 (2011) 517–527.
[120] C.-L. Lin, C.-F. Lee, W.-Y. Chiu, Preparation and properties of poly (acrylic acid) oligomer stabilized superparamagnetic ferrofluid, J. Colloid Interface Sci. 291 (2005) 411–420.
[121] S.R. Kanel, D. Nepal, B. Manning, H. Choi, Transport of surface-modified iron nanoparticle in porous media and application to arsenic (III) remediation, J. Nanopart. Res. 9 (2007) 725–735.
[122] B. Schrick, B.W. Hydutsky, J.L. Blough, T.E. Mallouk, Delivery vehicles for zerovalent metal nanoparticles in soil and groundwater, Chem. Mater. 16 (2004) 2187–2193.
[123] A. Tiraferri, K.L. Chen, R. Sethi, M. Elimelech, Reduced aggregation and sedimentation of zero-valent iron nanoparticles in the presence of guar gum, J. Colloid Interface Sci. 324 (2008) 71–79.

[124] C. Boyer, M.R. Whittaker, V. Bulmus, J. Liu, T.P. Davis, The design and utility of polymer-stabilized iron-oxide nanoparticles for nanomedicine applications, NPG Asia Mater. 2 (2010) 23–30.
[125] A. Dias, A. Hussain, A. Marcos, A. Roque, A biotechnological perspective on the application of iron oxide magnetic colloids modified with polysaccharides, Biotechnol. Adv. 29 (2011) 142–155.
[126] P.I. Girginova, A.L. Daniel-da-Silva, C.B. Lopes, P. Figueira, M. Otero, V.S. Amaral, E. Pereira, T. Trindade, Silica coated magnetite particles for magnetic removal of Hg^{2+} from water, J. Colloid Interface Sci. 345 (2010) 234–240.
[127] L. Machala, R. Zboril, A. Gedanken, Amorphous iron (III) oxide a review, J. Phys. Chem. B 111 (2007) 4003–4018.
[128] P. Tartaj, S. Veintemillas-Verdaguer, C.J. Serna, The preparation of magnetic nanoparticles for applications in biomedicine, J. Phys. D. Appl. Phys. 36 (2003) R182.
[129] M. Mahmoudi, S. Sant, B. Wang, S. Laurent, T. Sen, Superparamagnetic iron oxide nanoparticles (SPIONs): development, surface modification and applications in chemotherapy, Adv. Drug Deliv. Rev. 63 (2011) 24–46.
[130] Y. Liu, S.A. Majetich, R.D. Tilton, D.S. Sholl, G.V. Lowry, TCE dechlorination rates, pathways, and efficiency of nanoscale iron particles with different properties, Environ. Sci. Technol. 39 (2005) 1338–1345.
[131] J.T. Nurmi, P.G. Tratnyek, V. Sarathy, D.R. Baer, J.E. Amonette, K. Pecher, C. Wang, J.C. Linehan, D.W. Matson, R.L. Penn, Characterization and properties of metallic iron nanoparticles: spectroscopy, electrochemistry, and kinetics, Environ. Sci. Technol. 39 (2005) 1221–1230.
[132] J. Guo, R. Wang, W.W. Tjiu, J. Pan, T. Liu, Synthesis of Fe nanoparticles@graphene composites for environmental applications, J. Hazard. Mater. 225 (2012) 63–73.
[133] E. Carpenter, S. Calvin, R. Stroud, V. Harris, Passivated iron as core-shell nanoparticles, Chem. Mater. 15 (2003) 3245–3246.
[134] M. Fan, P. Yuan, J. Zhu, T. Chen, A. Yuan, H. He, K. Chen, D. Liu, Core–shell structured iron nanoparticles well dispersed on montmorillonite, J. Magn. Magn. Mater. 321 (2009) 3515–3519.
[135] C.M. Wang, D.R. Baer, L.E. Thomas, J.E. Amonette, J. Antony, Y. Qiang, G. Duscher, Void formation during early stages of passivation: initial oxidation of iron nanoparticles at room temperature, J. Appl. Phys. 98 (2005)094308.
[136] L. Lu, Z. Ai, J. Li, Z. Zheng, Q. Li, L. Zhang, Synthesis and characterization of $Fe-Fe_2O_3$ core − shell nanowires and nanonecklaces, Cryst. Growth Des. 7 (2007) 459–464.
[137] W.-X. Zhang, C.-B. Wang, H.-L. Lien, Treatment of chlorinated organic contaminants with nanoscale bimetallic particles, Catal. Today 40 (1998) 387–395.
[138] I. Avital, D. Inderbitzin, T. Aoki, D.B. Tyan, A.H. Cohen, C. Ferraresso, J. Rozga, W.S. Arnaout, A.A. Demetriou, Isolation, characterization, and transplantation of bone marrow-derived hepatocyte stem cells, Biochem. Biophys. Res. Commun. 288 (2001) 156–164.
[139] L. Cumbal, J. Greenleaf, D. Leun, A.K. Sengupta, Polymer supported inorganic nanoparticles: characterization and environmental applications, React. Funct. Polym. 54 (2003) 167–180.
[140] H. Lee, E. Lee, D.K. Kim, N.K. Jang, Y.Y. Jeong, S. Jon, Antibiofouling polymer-coated superparamagnetic iron oxide nanoparticles as potential magnetic resonance contrast agents for in vivo cancer imaging, J. Am. Chem. Soc. 128 (2006) 7383–7389.
[141] S. Signoretti, L. Del Bianco, L. Pasquini, G. Matteucci, C. Beeli, E. Bonetti, Electron holography of gas-phase condensed Fe nanoparticles, J. Magn. Magn. Mater. 262 (2003) 142–145.
[142] Z. Liu, H. Wang, Q. Lu, G. Du, L. Peng, Y. Du, S. Zhang, K. Yao, Synthesis and characterization of ultrafine well-dispersed magnetic nanoparticles, J. Magn. Magn. Mater. 283 (2004) 258–262.
[143] S.J. Klaine, P.J. Alvarez, G.E. Batley, T.F. Fernandes, R.D. Handy, D.Y. Lyon, S. Mahendra, M.J. Mclaughlin, J.R. Lead, Nanomaterials in the environment: behavior, fate, bioavailability, and effects, Environ. Toxicol. Chem. 27 (2008) 1825–1851.

[144] M. Wiesner, J.-Y. Bottero, Environmental Nanotechnology, McGraw-Hill Professional Publishing, 2007.
[145] S. Dixit, J.G. Hering, Comparison of arsenic (V) and arsenic (III) sorption onto iron oxide minerals: implications for arsenic mobility, Environ. Sci. Technol. 37 (2003) 4182–4189.
[146] N.N. Nassar, Rapid removal and recovery of Pb (II) from wastewater by magnetic nanoadsorbents, J. Hazard. Mater. 184 (2010) 538–546.
[147] P. Li, D.E. Miser, S. Rabiei, R.T. Yadav, M.R. Hajaligol, The removal of carbon monoxide by iron oxide nanoparticles, Appl. Catal. B Environ. 43 (2003) 151–162.

CHAPTER

18 MAGNETIC METAL/METAL OXIDE NANOPARTICLES AND NANOCOMPOSITE MATERIALS FOR WATER PURIFICATION

Purna K. Boruah[*,†], **Priyakshree Borthakur**[*,†], **Manash R. Das**[*,†]

*Materials Sciences and Technology Division, CSIR-North East Institute of Science and Technology, Jorhat, India**

Academy of Scientific and Innovative Research, CSIR-NEIST Campus, Jorhat, India[†]

1 INTRODUCTION

Clean water is the most important element for all living organisms to survive. Today, water pollution has become a serious worldwide problem because a significant amount of water has been polluted because of global industrialization and the incredible increase in the world population [1]. Organic pollutants such as dye molecules are released into the aquatic ecosystem from a number of industries, such as the textile, food, cosmetics, pharmaceuticals, paper, and fabric industries, among others. Similarly, phenolic compounds present in wastewater are considered a toxic threat because of their toxic and carcinogenic nature, which is released from textiles, pharmaceuticals, oil refineries, plastics, and coal conversion plants, as well as the food and paper industries, among others [1, 2]. Pesticides, which are generally used in the agriculture sector to protect plants from damage by weed, pests, and so forth, are another class of water pollutant. On the other hand, inorganic heavy metals ions such as Cr, As, Cd, Pb, and Hg ions, which are carcinogenic and toxic, are also widely applied in various industries including steel production, dye production, electroplating, leather tanning, and industry, among others [3, 4]. Moreover, even a low concentration of pathogenic bacteria exists in drinking water, causing serious human health problem [5]. The contamination of the aquatic ecosystem from these organic, inorganic, and biological pollutants are responsible for causing serious human diseases, such as cancer, lung diseases, cholera, dysentery, diarrhea, hepatitis A, typhoid, muscle weakness, salivation, lead poisoning, arsenicosis, and fluorosis, among others [6, 7]. The dyes present in water bodies are also interrupting the incoming sun rays, resulting in a decrease the photosynthetic activity of aquatic plants [8]. Therefore, removing water contaminants before surface discharge is extremely important. Many techniques have been adopted for the water-contaminant removal [9–11]. Among them, the adsorption and photocatalytic degradation/reduction are considered the most suitable methods for removing these water contaminants because of their simplicity, eco-friendly nature, and capability of producing high-quality water [12].

Nanoscale Materials in Water Purification. https://doi.org/10.1016/B978-0-12-813926-4.00024-0

Nanomaterials are widely used as adsorbents as well as catalysts for removing water contaminants. The properties of the nanomaterials are absolutely different from their bulk equals because of their large surface area-to-volume ratio, which has novel optical, thermal, electrical, and magnetic properties. In this regard, nanomaterials are extensively used in numerous fields such as medicine, materials manufacturing, energies, electronics, environmental remediation, and so forth. However, designing environmentally benign nanomaterials that have specific properties like low preparation cost, specific selectivity, high stability, efficient recovery, and excellent recyclability by tailoring their size and shape is one of the urgently needed challenges for practical applications [13–23]. In the last decades, the most extensively applied nanomaterials in the wastewater treatment process are zerovalent metal nanoparticles (NPs; such as Ag, Fe, and Zn), carbon nanotubes (CNTs), and metal oxide NPs (TiO_2, ZnO, and iron oxides) [24]. Because of their small sizes and large surface area-to-volume ratios, nanomaterials have strong adsorption as well as excellent photocatalytic capacities. However, without using any supporting materials, the zerovalent metal NPs and metal oxide NPs undergo agglomeration during the adsorption and photocatalytic degradation process and thus reducing their catalytic activities. In this regard, several nanocomposite materials like TiO_2-graphene-Pd, α-Fe_2O_3 nanorod/RGO, graphdiyne-ZnO, activated carbon/TiO_2, SiO_2/Au/TiO_2, among others, have been developed for water purification [9, 25–29] because these nanomaterials are conventionally recovered from the aqueous suspension by filtration or centrifugation after performing the reaction. However, these methods are inconvenient and inefficient for separating nanosized materials, which hampers the sustainability and economics of the nanomaterials strategy. Nanomaterials with magnetic properties are providing excellent tools for removing water pollutants, which are magnetically separable from the reaction [30–35]. Because of these concerns, the Fe-, Co-, and Ni-based magnetic materials are widely studied in different areas, such as the biological and medical fields, including enzyme immobilization, protein immobilization, radiopharmaceuticals, diagnostics, DNA and RNA purification, immunoassays, magnetic cell separation, transport of anticancer drugs, water purification, and so on [36–38]. During the last decades, varieties of magnetic Fe-, Co-, and Ni-based nanomaterials, such as Fe_3O_4/reduced graphene oxide, $ZnFe_2O_4$-graphene, γ-Fe_2O_3/carbon hybrids, Fe_3O_4@SiO_2, $CuFe_2O_4$, $MnFe_2O_4$@Mn-Co, $CoFe_2O_4$, Ni/C, Ni/Mo_2C, and $NiFe_2O_4$, among others, have been developed for water purification [39–46].

This chapter gives a comprehensive overview of the reported synthesis of magnetic NPs and nanocomposite materials and their application in the removal of water contaminants. The resulting NPs and nanocomposite materials have been characterized by different analytical techniques, such as powder X-ray diffractometry (PXRD), high-resolution transmission electron microscopy (HRTEM), field emission scanning electron microscopy (FESEM), Raman spectroscopy, X-ray photoelectron spectroscopy (XPS), vibrating sample magnetometer (VSM), and so on, which are discussed in detail.

2 MAGNETIC SEPARATION FOR WATER PURIFICATION

The nanomaterials are usually recovered by filtration or centrifugation from the aqueous suspension. These are inconvenient, inefficient, and time-consuming methods for separating the nanosized materials, which hamper the sustainability and economics of the nanomaterials strategy. Magnetic nanomaterials are strongly attracted by a magnet or can be magnetized themselves [47, 48], which can easily separate by simply applying an external MF.

2.1 MAGNETIC NANOMATERIALS AND ITS FUNDAMENTAL FEATURE

Magnetic nanomaterials are broadly divided into four main types on the basis of their magnetic behavior: ferromagnetic, paramagnetic, superparamagnetic, and diamagnetic [49]. If the applied magnetic field (AMF) is not present, then the magnetic dipole does not exist for diamagnetic nanomaterials. In the presence of AMF, a magnetic dipole is generated in the materials that is oriented opposite to the AMF. Therefore, diamagnetic materials are repelled by an AMF. The magnetic dipoles are existing for paramagnetic materials. However, these dipoles are aligned only on application of the AMF. The magnetic dipoles are oriented in random directions for paramagnetic behavior at room temperature because of the unpaired electrons, which results in a low susceptibility in a magnetic field (MF). Otherwise, in the ferromagnetic materials, existing net dipole moment in the absence of an AMF, even in the absence of an AMF, their domain structure remains magnetized. However, they undergo a significant change when the size decreases to less than the domain size. The magnetization of the superparamagnetic NPs is zero in the absence of the AMF, but they provide a robust response to an AMF. The magnetic moment of the entire NPs brings into line in the AMF direction for the superparamagnetic materials; they tend to have a higher magnetic susceptibility than paramagnetic materials have. Thus, superparamagnetic nanomaterials are easily separated using an external magnet [50].

The magnetic behavior of the magnetic NPs can be clearly described by the magnetic hysteresis loop, which demonstrates the magnetic moment (M) with respect to the AMF strength (H). The magnetic moment is zero in the absence of AMF, as shown in Fig. 1A. The magnetization of the particle determines the field direction in the presence of an AMF because of the magnetic interaction of the particles with the field. All the particles are associated with the field direction when the field is sufficiently strong; then particles are assumed to be saturated. This respective magnetic moment is designated as saturation magnetization (M_s). Reducing the AMF strength leads to decreases in the magnetic moment of the NPs. Ferromagnetic NPs have a considerable magnetic moment when the external AMF is zero, which is called remnant magnetic moment (M_r). The external AMF must be

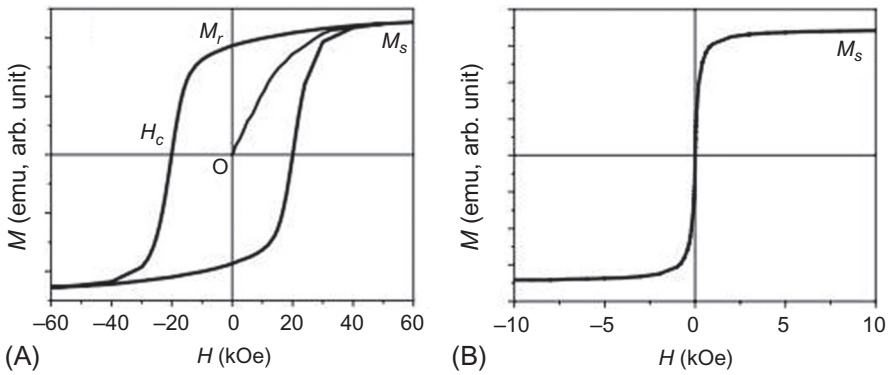

FIG. 1

Schematic representation of the hysteresis loops of a group of magnetic NPs that are (A) ferromagnetic and (B) superparamagnetic.

Reproduced with permission from S. Sun, Recent advances in chemical synthesis, self-assembly, and applications of FePt nanoparticles, Adv. Mater. 18 (2006) 393–403, Copyright© 2006, Wiley publication.

reversed and increases the value up of the total magnetic moment to zero for particle demagnetize, which is called the coercivity (H_c). The magnetization of each NPs undergoes a fluctuation when the NPs are superparamagnetic (Ms). Furthermore, when the AMF is removed, the overall magnetic moment is randomized to zero; then there has no remnant magnetic moment (Fig. 1B) [51].

3 TYPES OF MAGNETIC NANOMATERIALS

3.1 IRON-BASED MAGNETIC NANOMATERIALS

Among the iron-based magnetic nanomaterials, iron and its oxides are extensively used in the environmental remediation applications. Iron is a ferromagnetic material; at room temperature it has a high magnetic susceptibility. It can be easily magnetized in presence of a weak MF. Moreover, Fe_2O_3 and Fe_3O_4 NPs show superparamagnetic behavior, and they can be magnetized in the presence of a low, intense AMF [38, 52, 53]. Iron-based magnetic materials are very cheap and can be easily synthesized.

Zerovalent iron (ZVI) NPs have several advantages because of the larger specific surface area-to-volume ratio compared to the bulk counterpart, which facilitates greater reaction rates and avoids the by-product generation from the particular reaction [54]. ZVI NPs are widely used in the environmental remediation applications because of their less toxic effect on the human and other living organisms' health. They offer excellent magnetic properties and show superparamagnetic behavior with 218 emu/g saturation magnetization values [55]. ZVI NPs are generally synthesized by chemical reduction method, where iron salts are used as a precursor and strong reducing agents are utilized to reduce this precursor [56, 57].

Elliott and Zhang synthesized ZVI NPs by mixing equal amount of $NaBH_4$ (0.5 M) and $FeCl_3$ (0.09 M) solutions; the chemical reaction involved during this synthesis method is [58].

$$Fe^{3+} + 3BH_4^- + 9H_2O \rightarrow 4Fe^0 \downarrow + 3H_2BO_3^- + 12H^+ + 6H_2$$

Recently, Kozma et al. synthesized ZVI NPs by adopting an environmentally benign method using Virginia creeper leaf extract and a less toxic reducing agent [59]. In this report, they presented a comparative evaluation of green and semigreen synthesis methods. ZVI NPs were synthesized by a totally green approach based on green tea and Virginia creeper plant extracts and a semigreen method based on sodium dithionite and sodium borohydride as less toxic and low-cost reducing agents. For the green synthesis of ZVI NPs, they washed the dry leaves thoroughly with deionized water to remove surface dust and dried them at room temperature to obtain constant weight at ambient conditions. The leaf extract was prepared by 5 g of dry leaves placed in 100 mL of deionized water and heated at 80°C for 80 min. The extract was vacuum-filtered and stored at 4°C for further use. The prepared leaf extract was mixed with 0.1 M $FeCl_3 \cdot 6H_2O$ solution with 1:1 volume ratio stirred for 24 h at room temperature. In the semigreen synthesis method, ferric chloride, ferrous chloride, and ferrous sulfate were used as precursor salts; first, NaOH was added to this iron-salt solution and stirred for 10 min. Then $Na_2S_2O_4$ or $NaBH_4$ was added to this solution and stirred until the solution became completely black. When the $Na_2S_2O_4$ used as a reducing agent, the reaction mixture was completely black within 5 min; however, 40 min was required when $NaBH_4$ was used as a reducing agent. They used Virginia creeper, green tea, and coffee leaf extracts in the green synthesis method, and the synthesized ZVI NPs were labeled

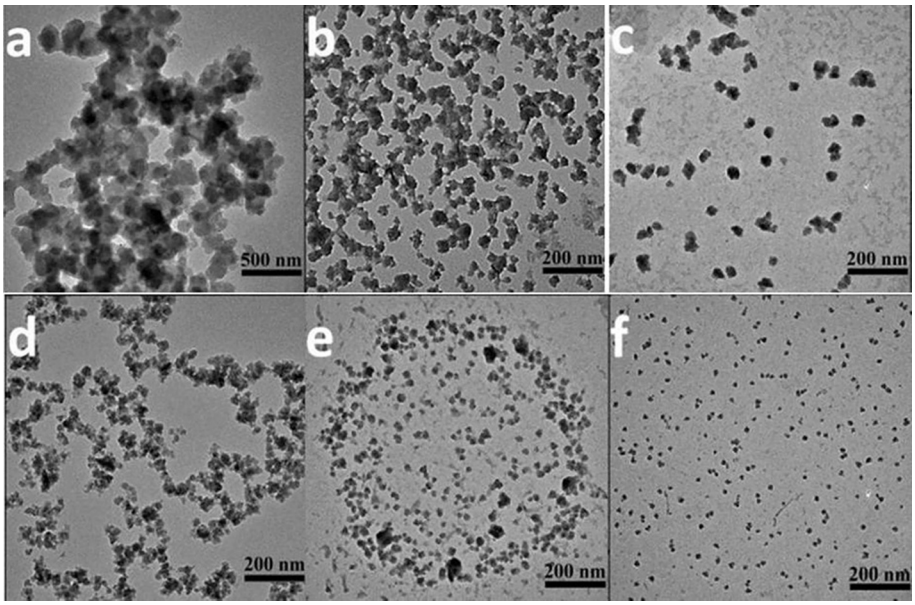

FIG. 2

TEM images of ZVI NPs samples (A) GT-Fe, (B) VC-Fe, (C) HG1-Fe, (D) HG2-Fe, (E) HG3-Fe, and (F) HG4-Fe.

Reproduced with permission from G. Kozma, A. Ronavari, Z. Konya, Á. Kukovecz, Environmentally benign synthesis methods of zero-valent iron nanoparticles, ACS Sustain. Chem. Eng. 4 (2016) 291–297, Copyright© 2016, ACS publication.

VC-Fe, C-Fe, and GT-Fe as the respective leaf extracts. Similarly, ZVI NPs made by semigreen synthesis methods using $Na_2S_2O_4$ and $NaBH_4$ as reducing agents were labeled HG1-Fe and HG2-Fe, respectively. The reference samples assigned as HG3-Fe and HG4-Fe were also prepared in this report by reducing $FeCl_3$ with $NaBH_4$ and by reducing $FeSO_4$ with $Na_2S_2O_4$, respectively.

The characteristics TEM images of synthesized ZVI NPs by green and semigreen synthesis methods are presented in Fig. 2. The average particle diameter of C-Fe and GT-Fe were found to be 124.2 ± 31.8 nm and 119.6 ± 25.8 nm, respectively. The particle diameters observed for VC-Fe, HG1-Fe, HG2-Fe, HG3-Fe, and HG4-Fe ZVI NPs are 47.5 ± 8.8, 70.9 ± 7.0, 23.5 ± 4.1, 25.2 ± 3.5, and 19.7 ± 2.2 nm, respectively. All these synthesized ZVI NPs showed isotropic morphology. The researchers have observed a triangular shape for HG3-Fe and HG4-Fe; otherwise, a spherical shape was obtained for the other five ZVI NPs.

Several forms of iron oxides exist in nature. The most common forms of iron oxide that exist in nature are hematite (α-Fe_2O_3), magnetite (Fe_3O_4), and maghemite (γ-Fe_2O_3). The n-type semiconductor (band gap of 2.2 eV) of α-Fe_2O_3 is a highly stable iron oxide under ambient circumstances. It has wide application in environmental remediation, organic catalysis reactions, pigments, and gas sensors because of its low cost and high corrosion resistivity. Fe_3O_4 is a very common and interesting iron oxide, which exists with a cubic inverse-spinel structure [60].

Iron oxide, magnetite (Fe_3O_4), and maghemite (γ-Fe_2O_3) have received amazing attention because of their exciting magnetic properties [52]. Both are most abundant and can be easily synthesized by

adopting different synthetic routes, which are also modified by incorporating different metal NPs such as Co, Ni, Cu, and Zn, among others (of the type MFe_2O_4, where M is defined as metal) [61]. Magnetite has a higher magnetization ability than maghemite, and in an aqueous solution, the point of zero charges for magnetite is close to 7 [62]. Because of these enormous properties, such a high magnetization and chemical activity, magnetite is widely engaged in further applications compared to maghemite.

Magnetic iron oxide NPs easily undergo agglomeration and form clusters because they possess high surface energies, resulting in an increase in particle size. Furthermore, iron NPs are chemically unstable, and they oxidize in air, resulting in the loss of magnetism and dispensability. The agglomeration of magnetic NPs was prevented by the surface modification by polymers, organic molecules, inorganic molecules, or biomolecules. Various carbonaceous materials, such as activated carbon and graphene, among others, and polymers, such as polymethylmethacrylate, poly(vinyl alcohol), poly(ethylene glycol), poly(lactide-*co*-glycolide), have been utilized for synthesizing magnetic iron oxide–based nanocomposite. Among others, inorganic materials, such as silica, and precious metals, such as gold, silver, platinum, zinc, copper, and so on, are commonly used [63, 64].

During the last few decades, two-dimensional (2D) sheets decorated with iron oxide NPs have been developed as magnetic nanomaterials. The graphene is widely utilized as 2D support materials for the synthesis of magnetic nanocomposites, which inhibited the aggregation of the NPs. Graphene, possessing a unique 2D honeycomb layer structure of sp^2-hybridized carbon atoms with a carbon-carbon distance of 0.142, has attracted a lot of attention because of its outstanding electrical, mechanical, optical, and thermal properties. In particular, graphene exhibits an extremely high theoretical specific surface area (2600 m^2/g) and offers excellent electron mobility at room temperature (200,000 $cm^2/V/s$) [65–67]. In this regard, different iron-based magnetic metal oxide NPs, such as Fe_3O_4, $CoFe_2O_4$, $ZnFe_2O_4$, $CoFe_2O_4$/CdS, $NiFe_2O_4$, Pd@Fe_3O_4, Al_2O_3- and SiO_2-coated Fe_3O_4, Fe_2O_3, and Fe_3O_4@TiO_2, among others, have been developed with graphene support [39, 40, 68–71].

The chemical co-precipitation method is the simplest chemical pathway for the synthesis of iron oxide NPs. In the chemical co-precipitation method, Fe_3O_4 and γ-Fe_2O_3 can be synthesized by using Fe(II) and Fe(III) salts stoichiometric mixture in a basic aqueous medium. An NaOH or NH_4OH solution is generally used to maintain the reaction medium at basic pH levels. A diameter of about 5–50 nm was obtained for the NPs by this synthesis method. The diameter of the NPs varied with the types of salt, salt concentration, Fe^{2+}/Fe^{3+} concentration ratio, pH of an aqueous medium, reaction temperature and the ionic force of the medium [63, 72]. The reaction involved during the synthesis of Fe_3O_4 may be written as provided in the following equation

$$Fe^{2+} + 2Fe^{3+} + 8OH^- \rightarrow Fe_3O_4 + 4H_2O$$

From the thermodynamic point of view, complete precipitation of Fe_3O_4 is anticipated at a pH range of 8–14 in the absence of oxygen environment, with 2:1 (Fe^{3+}/Fe^{2+}) stoichiometric ratio [64]. Fe_3O_4 is not highly stable, which is transformed into γ-Fe_2O_3 in an oxygen atmosphere.

$$Fe_3O_4 + 2H^+ \rightarrow \gamma - Fe_2O_3 + Fe^{2+} + H_2O$$

Oxidation of Fe_3O_4 in the air is not the only way to synthesize γ-Fe_2O_3. Numerous ion or electron transfer, depending on the pH of the suspension, is also responsible for the formation of γ-Fe_2O_3. The surface Fe^{2+} ions are adsorbed as hexa-aqua complexes in a solution under acidic conditions and in the absence of free oxygen. Ferrous ion oxidation is always correlated with the migration of cations over the lattice

framework, maintaining the charge balance, which creates the cationic vacancies. γ-Fe_2O_3 differs from Fe_3O_4 by the presence of cationic vacancies in the octahedral site; in γ-Fe_2O_3, iron ions are distributed in the tetrahedral (Td) and octahedral (Oh) sites of the spinel structure [73]. Hu et al. synthesized γ-Fe_2O_3 NPs in an inert atmosphere by heating Fe_3O_4 NPs at 250°C for 2 h [74].

Peik-See et al. synthesized magnetic Fe_3O_4 NPs on reduced graphene oxide (rGO) supported by a simple in situ chemical co-precipitation synthesis method [39]. In this approach, the $FeSO_4$ solution was taken in a GO suspension and the pH was maintained at 11–12 using ammonia solution and stirred at room temperature for overnight. This synthesized nanocomposite was designated as Fe_3O_4/rGO. Similarly, Li et al. also synthesized magnetic Fe_3O_4/GO by the in situ chemical co-precipitation method [75], where $FeCl_3{\cdot}6H_2O$ and $FeSO_4{\cdot}7H_2O$ were used metal oxide precursors. The co-precipitation reaction has been carried out under an N_2 atmosphere at 80°C, and the ammonia solution was added to this solution quickly to precipitate Fe^{2+}/Fe^{3+} ions. SEM, TEM, XRD, XPS, and VSM analysis (Fig. 3) results optimized the formation of GO/Fe_3O_4. A TEM image (Fig. 3B) shows that the Fe_3O_4 NPs are well distributed on the GO surface. Fe_3O_4 NPs with average particle size, around 10–15 nm, were obtained from TEM image. A TEM image (Fig. 3B) clearly show the well-dispersed Fe_3O_4 NPs on the surface of the GO. The XRD pattern of the GO/Fe_3O_4 nanocomposite shows the characteristics peaks at 2θ values of 30.15, 36.27, 43.32, 53.89, 57.13, and 62.29 degrees corresponds to the (220), (311), (400), (422), (511), and (440) planes, respectively, which indicate the formation of Fe_3O_4 NPs on the GO films. The XPS spectrum also shows that the binding energy peaks at 285, 530, and 711 eV corresponds to C1s, O1s, and Fe2p, respectively. From the VSM analysis, the saturation magnetization of a GO/Fe_3O_4 nanocomposite is found to be 31 emu/g (Fig. 3F), which indicates the magnetic properties of the synthesized GO/Fe_3O_4 nanocomposite.

Recently, an ammonia-modified graphene/Fe_3O_4 (AG/Fe_3O_4) nanocomposite was synthesized by using the chemical co-precipitation method [76]. In this report, graphene oxide was first factionalized by amide functional group using a concentrated liquid ammonia solution. Functionalized GO works as an oxidizing agent, and it is reduced to functionalized graphene sheets, and simultaneously Fe(II) is oxidized to Fe(II)(III), wherein $Fe_2Cl_2{\cdot}4H_2O$ is used as a precursor for the formation of Fe_3O_4 NPs at the basic medium. Synthesized magnetic Fe_3O_4 NPs are spherical in shape, with average particle sizes of 41 nm, and are well dispersed on the ammonia-modified graphene surface, which can be observed from TEM images and the particle size distribution curve. TEM and HRTEM images of AG/Fe_3O_4 nanocomposite are shown in Fig. 4.

The sol-gel process is one of the suitable processes for synthesizing iron oxide NPs. It is a chemical solution process; a sol is a colloidal suspension of solid particles in a solvent, a gel is a solvent from the sol that begins to evaporate, and the particles or ions begin to join by chemical reaction. Generally, a water solvent is used in the sol-gel synthesis method and either acid or base can be used to the hydrolyzed precursor. Parameters such as nature of precursors, pH, reaction rates, and temperature can affect the structures and size of iron oxide NPs in the sol-gel synthesis method [77]. For example, γ-Fe_2O_3 with an average particle diameter of 6–15 nm was synthesized by adopting sol-gel synthesis method [77]. Thermal decomposition is one of the efficient techniques utilized for synthesizing high-quality metal oxides NPs. Well-dispersed magnetic NPs are obtained through this method by thermal decomposition of organometallic compounds in organic solvents in the presence of surfactant used as a stabilizing agent. Oleic acid and hexadecylamine have generally used a surfactant [78, 79]. In this synthesis method, morphology and the controlled size of the NPs were dependent on parameters such as reaction temperature, aging time, and reaction time. In this approach, Tong et al. synthesized

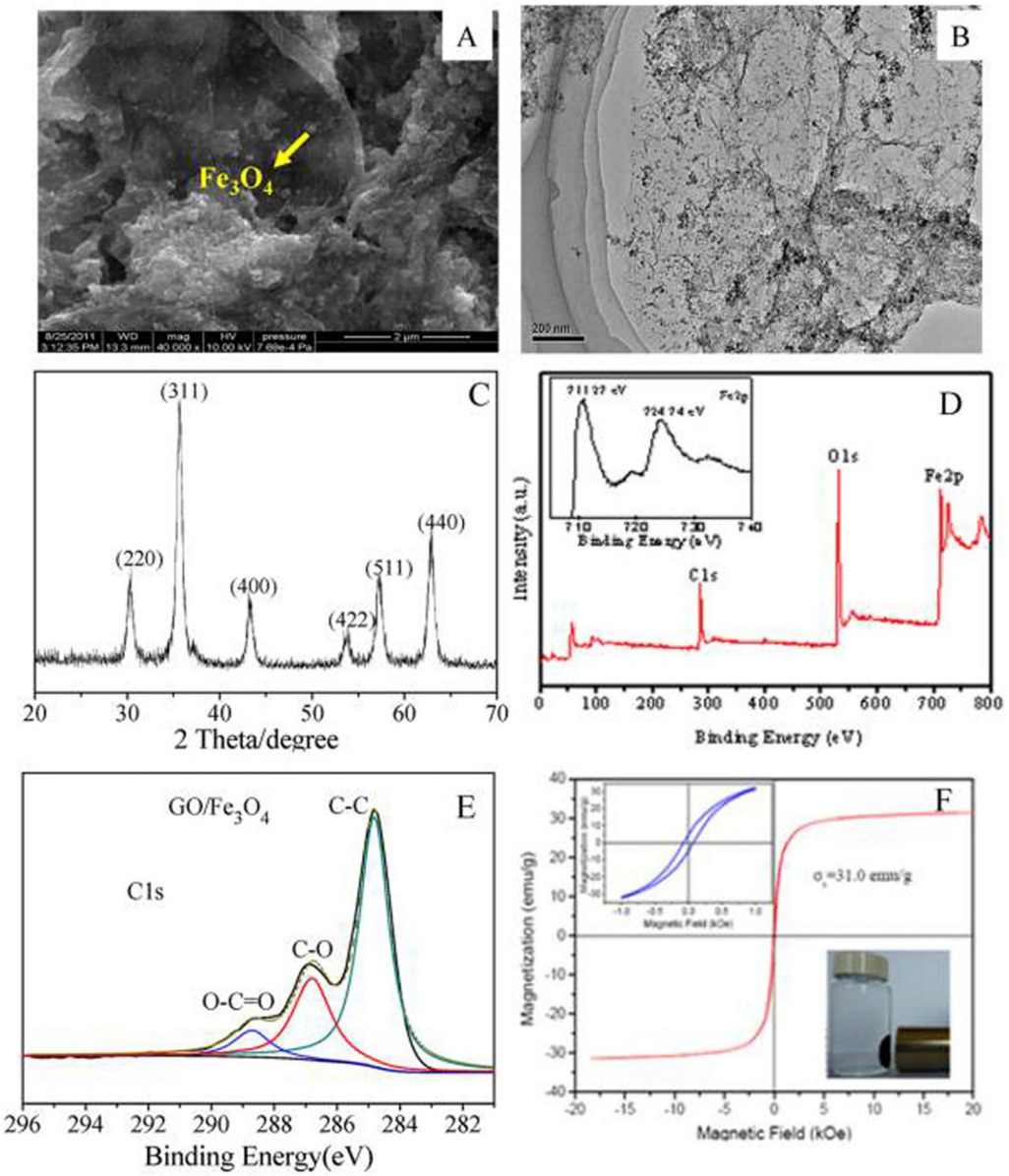

FIG. 3

(A) SEM, (B) TEM, (C) XRD pattern, (D) wide-scan XPS spectrum of GO/ Fe_3O_4 (the inset illustrates the high-resolution spectrum of Fe2p peak of GO/Fe_3O_4), (E) high resolution spectrum C 1s peak of GO/Fe_3O_4, and (F) magnetization curve of GO/Fe_3O_4 (below inset being separation of particles of GO/Fe_3O_4 by a magnet).

Reproduced with permission from J. Li, S. Zhang, C. Chen, G. Zhao, X. Yang, J. Li, X. Wang, Removal of Cu(II) and fulvic acid by graphene oxide nanosheets decorated with Fe_3O_4 nanoparticles, ACS Appl. Mater. Interfaces 4 (2012) 4991–5000, Copyright© 2012, ACS publication.

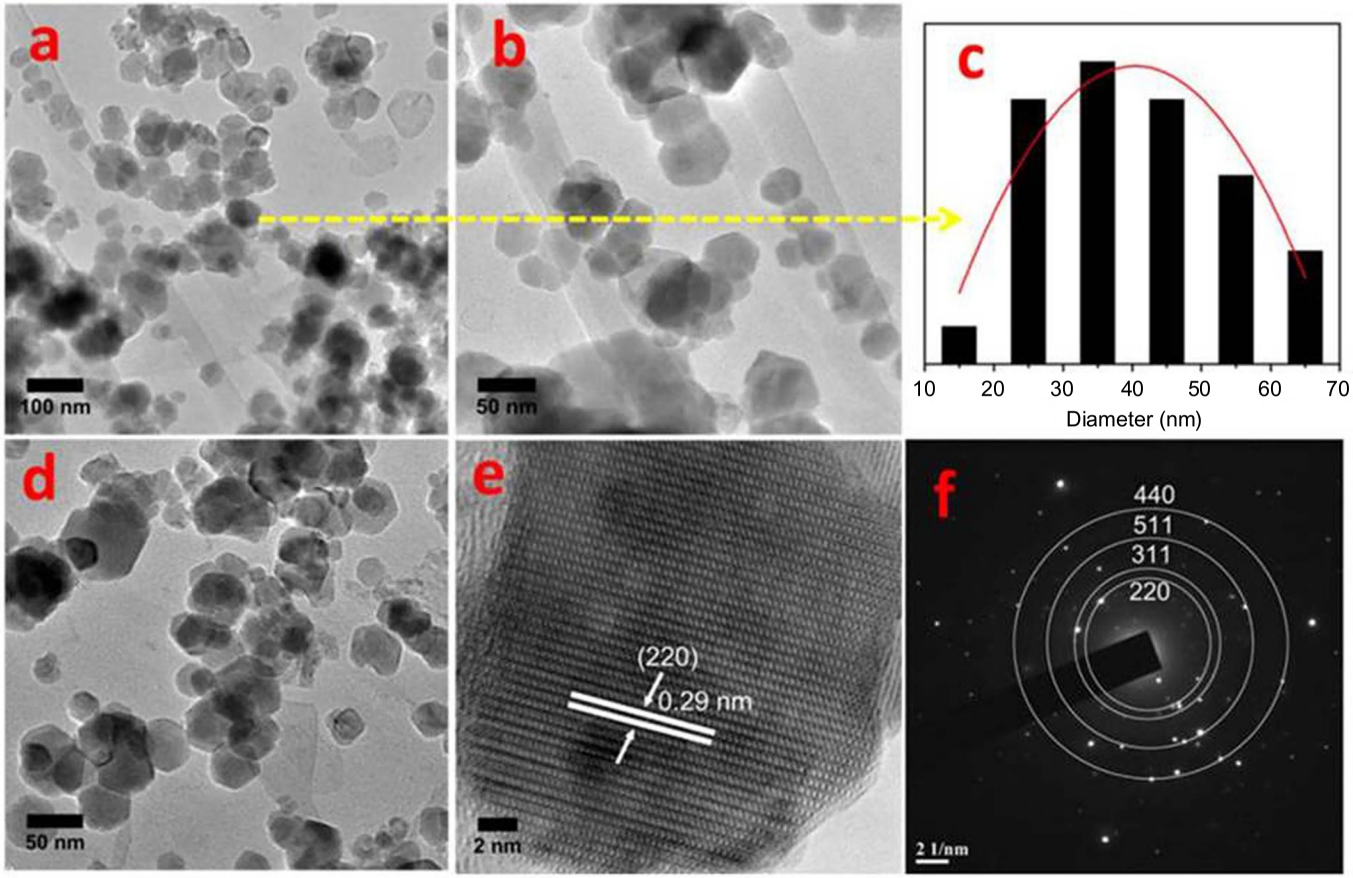

FIG. 4

The TEM (A,B,D) particle size distribution curves (C), HRTEM (E) and SAED pattern images of AG/Fe_3O_4 (F).

Reproduced with permission from P.K. Boruah, B. Sharma, I. Karbhal, M.V. Shelke, M.R. Das, Ammonia-modified graphene sheets decorated with magnetic Fe_3O_4 nanoparticles for the photocatalytic and photo-Fenton degradation of phenolic compounds under sunlight irradiation, J. Hazard. Mater. 325 (2017) 90–100, Copyright© 2017, Elsevier publication.

different-sized controlled Fe_3O_4 NPs by the thermodecomposition of iron acetylacetonate. TEM images of synthesized NPs are presented in Fig. 5. In this study, they have utilized two synthetic routes for controlling the size of the NPs. Nanocrystals with sizes of 6, 8, 11, and 15 nm were synthesized using seed-mediated growth. Otherwise, nanocrystals with sizes of 19, 25, 33, and 40 nm were synthesized by changing the ratio of oleic acid and oleylamine [80].

The hydrothermal and solvothermal methods are considered as another effective, versatile, and eco-friendly methods for the iron oxide NPs synthesis [81]. The hydrothermal synthesis strategy is based on heat-treating an aqueous reaction mixture under stirring conditions, which is executed by a separation mechanism and a general phase transfer at the interface of the solid, liquid, and solution phases. In this synthesis approach, the kinetics rate is slower at any given temperature compared to the other synthesis method, which is the main drawback of this method [30]. Various hydrothermal methods have been established for synthesizing iron oxide NPs and their composite materials. Among the reported nanomaterials, in most of the hydrothermal treatment reaction, graphene-based magnetic nanocomposites were obtained from the solution of graphene oxide and metal salt as a precursor. For example, Fu and Wang synthesized a magnetic $ZnFe_2O_4$–graphene nanocomposite photocatalyst with varying graphene contents in an ethanol-aqueous solution by a one-step hydrothermal method. In this report, $Zn(NO_3)_26H_2O$ and $Fe(NO_3)_39H_2O$ metal salts were used as precursors of $ZnFe_2O_4$, and GO was used as a source for graphene sheets. This hydrothermal treatment reaction was carried out in stainless steel autoclave at 180°C [40] The solvothermal synthesis technique is similar to the hydrothermal synthesis method, but in this technique, another organic solvent is used, rather than a water solvent, as a reaction medium. Xin et al. synthesized a $Fe_3O_4@TiO_2$ nanocomposite by adopting solvothermal technique, where an ethanol/acetonitrile (3/1, V/V) solvent system was used for the heat treatment of the reaction mixture [82].

3.2 NICKEL-BASED MAGNETIC NANOMATERIALS

Magnetic Ni and NiO NPs and their composite materials have wide-ranging applications in the field of magnetic fluid, magnetic recording media, solar energy adsorption, fuel cell electrodes, catalysis, permanent magnet, water contaminant adsorption, and photocatalysis, among others, because of their excellent magnetic properties. In this regard, the synthesis of nickel-based nanomaterials has attracted extensive attention. Nickel NPs are generally synthesized by using a strong reducing agent, such as $NaBH_4$, hydrazine, and so on, where metal salt used as a precursor. However, residual impurities are present when $NaBH_4$ is used, and hydrazine is a toxic chemical [83–89]. $Ni(CO)_4$ is an eminent carbonyl complex, which is thermally unstable, but it has been widely used as an Ni precursor for synthesizing Ni NPs because of its toxicity-preventive nature. The size of Ni NPs can be controlled by using a proper surfactant. Park and his coworkers synthesized size-controlled monodispersed Ni NPs by thermal decomposition of metal-surfactant (Ni-oleylamine) complexes at 215°C [90]. Fig. 6A–D shows TEM images of monodispersed Ni NPs with sizes 2, 5, and 7 nm. Bulky trioctylphosphine was used to control the growth of 2-nm-size NPs. The less bulky tributylphosphine and triphenylphosphine were used to control the 5 and 7 nm NPs size, respectively. The XRD pattern of synthesized 5-nm NPs is shown in Fig. 6D. The diffraction pattern showed two diffraction peaks corresponds to the Ni (111) and (220) crystallographic plane. XRD analysis has been carried for 5-nm NPs after exposing them in the air, as presented in Fig. 6E, which showed an NiO nanostructure. It was clearly observed from this XRD pattern that (Fig. 6E), the synthesized metallic Ni NPs were readily oxidized to NiO after exposing the NPs to air.

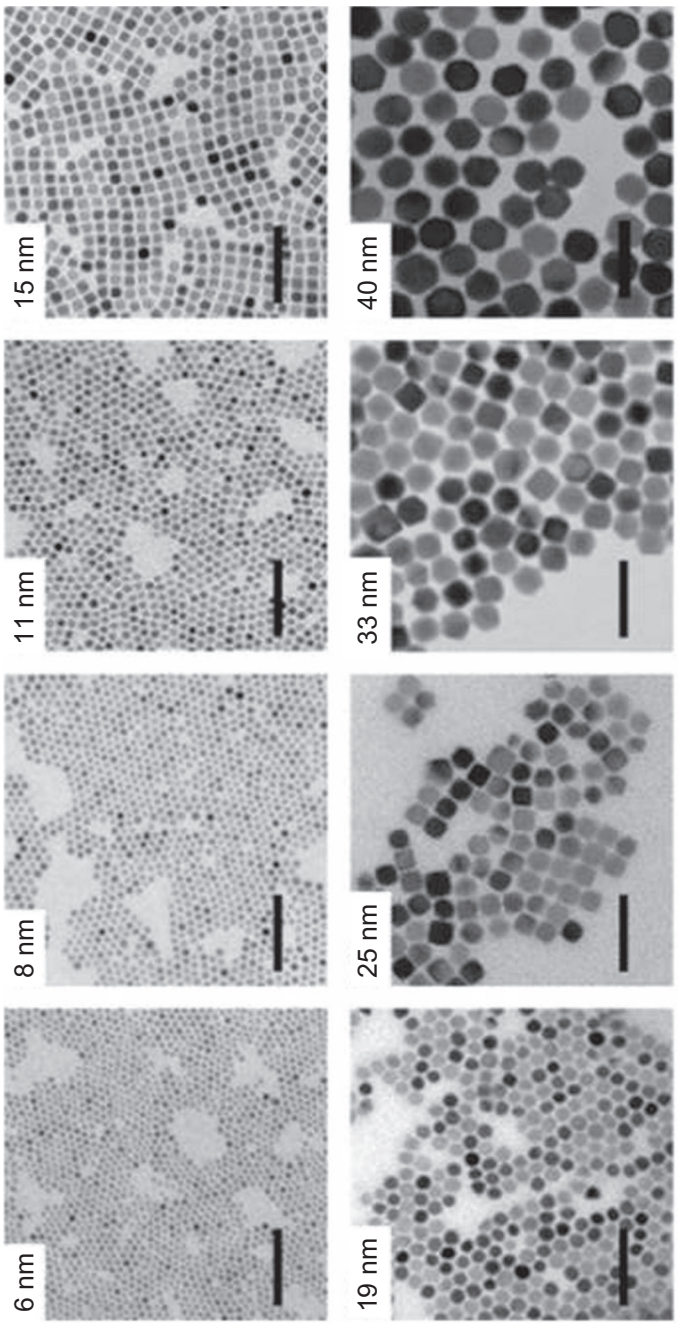

FIG. 5

TEM images of magnetic Fe_3O_4 NPs (scale bars are equal to 100 nm).

Reproduced with permission from S. Tong, C.A. Quinto, L. Zhang, P. Mohindra, G. Bao, Size dependent heating of magnetic iron oxide nanoparticles, ACS Nano 11 (2017) 6808–6816, Copyright© 2017, ACS publication.

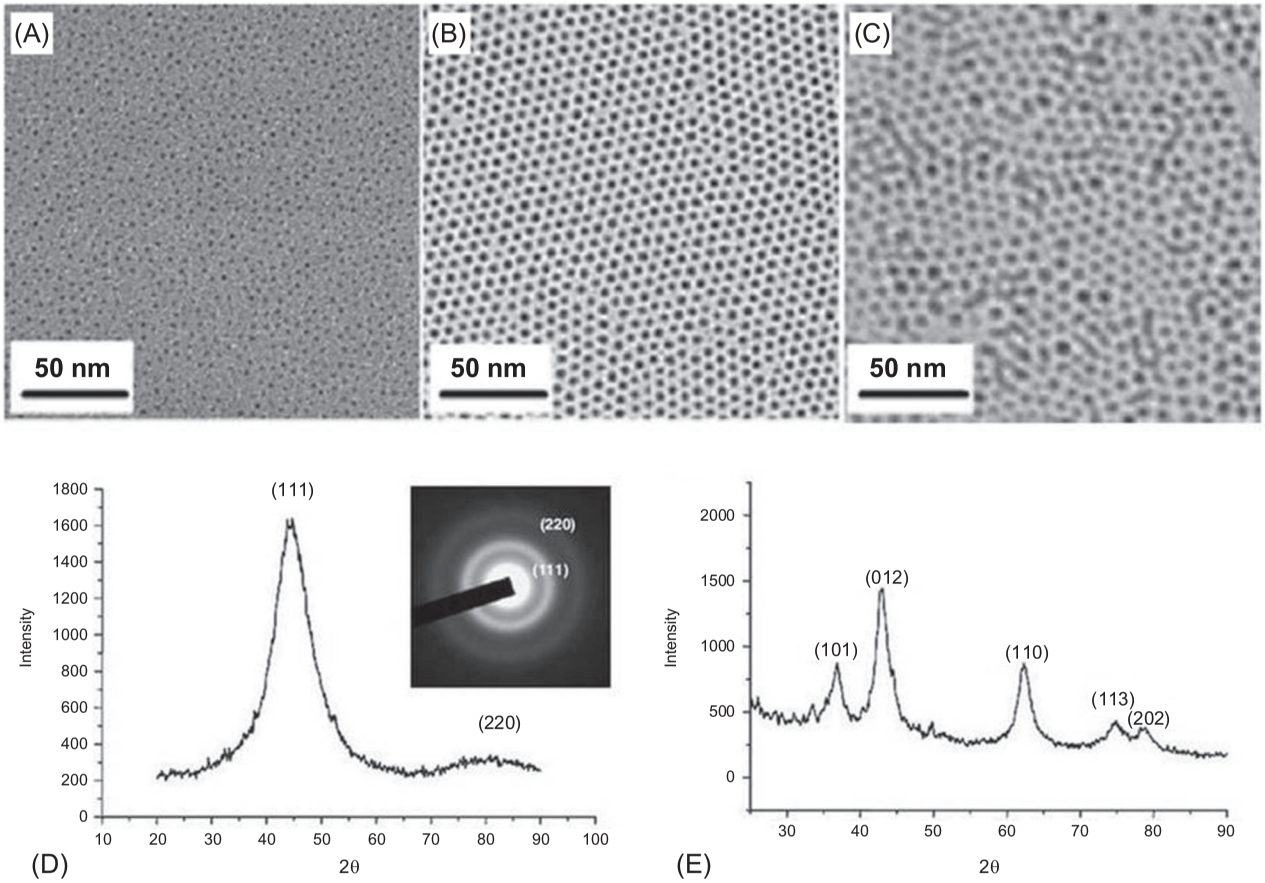

FIG. 6

TEM images of Ni NPs (A) 2 nm, (B) 5 nm, and (C) 7 nm and the XRD pattern of (D) 5 nm size Ni NPs (inset is the electron diffraction pattern) and (E) 5-nm NPs after air exposure.

Reproduced with permission from J. Park, E. Kang, S.U. Son, H.M. Park, M.K. Lee, J. Kim, K.W. Kim, H.J. Noh, J.H. Park, C.J. Bae, et al. Monodisperse nanoparticles of Ni and NiO: synthesis, characterization, self-assembled superlattices, and catalytic applications in the Suzuki coupling reaction, Adv. Mater. 17 (2005) 429–434, Copyright© 2005, Wiley publication.

Soofivand and Salavati-Niasari synthesized an NiO/graphene nanocomposite through the pregraphenization method and utilized a photocatalyst for organic pollutant degradation under UV and visible light irradiation. At first, they synthesized the NiO NPs by thermal decomposition method, which is doped onto the graphene sheet through pregraphenization. This method delivers a lot of sites for the decoration of NiO NPs on graphene sheets. Using TEM and SEM analysis, they observed NiO NPs with average sizes around 20 nm to 30 nm. Room-temperature VSM analysis has been carried out for NiO/graphene nanocomposite, which showed superparamagnetic behavior and the magnetization hysteresis loop are shown in Fig. 7. The saturation magnetization (Ms) of 4 emu/g is reached at an AMF of 600 Oe [91].

3.3 COBALT-BASED MAGNETIC NANOMATERIALS

One of the most significant ferromagnetic materials, cobalt exhibits three metastable phases with different crystallographic structures: the fcc phase, the hexagonal closed packed (hcp), and the epsilon phase [30, 92]. The bulk Co usually assumes either an hcp or an fcc lattice structure [93]. The fcc structure is preferred in high temperature, otherwise, the hcp structure is preferred at low temperature. However, at room temperature, both phases can coexist. Co NPs with fcc structures were synthesized by thermal decomposition of $Co_2(CO)_8$ in diphenyl ether. In this synthesis method, oleic acid and tributylphosphine (TBP) were used as surfactants, where TBP was used for Co nucleation and growth control and oleic acid was used for stabilization of Co NPs [93]. Similarly, Murray et al. synthesized Co NPs by replacing TBP with dioctylamine. In this study, a weaker surfactant was used to stimulate the decomposition of $Co_2(CO)_8$, which also facilitated the coating of an iron oxide layer on the Co NPs [94]. In this approach, the sizes of the Co NPs were controlled around 8–12 nm by varying the amount

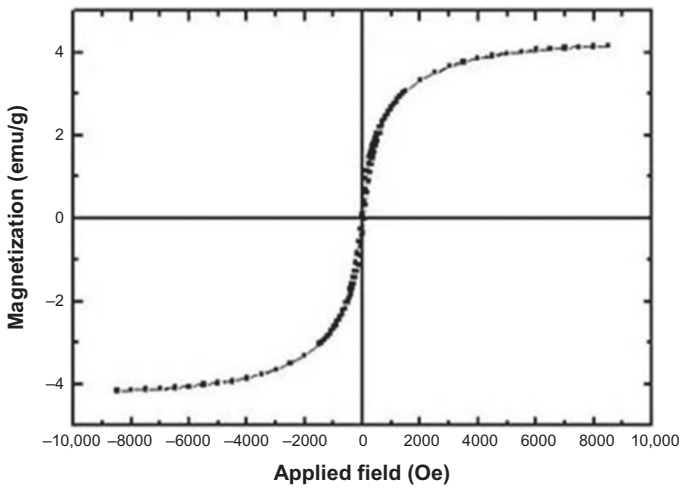

FIG. 7

Room-temperature magnetization vs AMF hysteresis loop for a NiO/graphene nanocomposite.

Reproduced with permission from F. Soofivand, M. Salavati-Niasari, Step synthesis and photocatalytic activity of NiO/graphene nanocomposite under UV and visible light as an effective photocatalyst, J. Photochem. Photobiol. A 337 (2017) 44–53, Copyright© 2017, Elsevier publication.

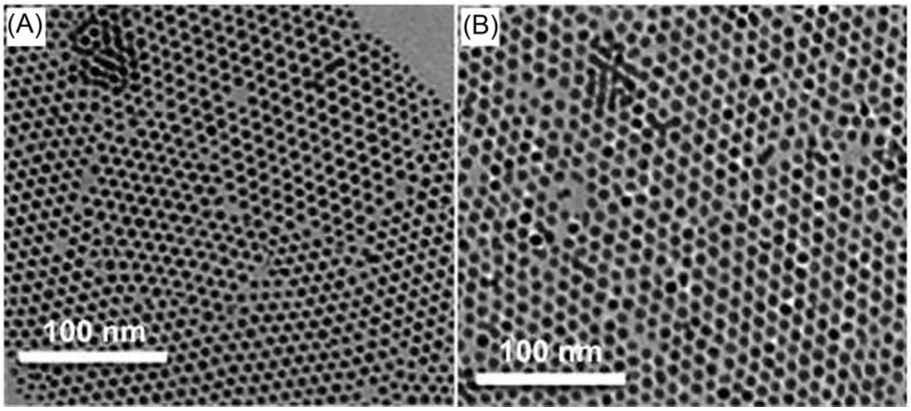

FIG. 8

TEM images of (A) polycrystalline Co NPs (7 nm) and (B) hcp-Co NPs (7 nm).

Reproduced with permission from Z.J. Yang, M. Cavalier, M. Walls, P. Bonville, I. Lisiecki, M.P. Pileni, A phase-solution annealing strategy to control the cobalt nanocrystal anisotropy: structural and magnetic investigations, J. Phys. Chem. C 116 (2012) 15723–15730, Copyright© 2012, ACS publication.

of oleic acid in the reaction system. Petit et al. synthesized polycrystalline Co NPs by alternative pathway, where Co NPs was produced in a reverse micelle by reducing cobalt(II) bis(2-ethylhexyl) sulfosuccinate [Co-$(AOT)_2$] through $NaBH_4$ [95]. These synthesized polycrystalline Co NPs were solution-phase annealed in dactylether; then they were converted to hcp-Co NPs [96, 97]. TEM images of polycrystalline Co NPs and hcp-Co NPs are shown in Fig. 8. The simple heating-up process was utilized for synthesizing monodisperse Co NPs. In this process, all the reagents were dissolved in the solvent under rapid heating conditions of the reaction mixture to an anticipated temperature [98].

Magnetic Co_3O_4 NPs are efficient magnetic materials that in recent years have been considered promising materials because of their applications in diverse fields; these include lithium-ion batteries, heterogeneous catalysis, energy storage, solid-state sensors, electrochemistry, environmental remediation, and pigments, among others [98]. Moro et al. synthesized magnetic Co_3O_4 NPs by adopting the hydrothermal method. In this approach, cobalt (II) acetate tetrahydrate (0.05 M $Co(C_2H_3O_2)_2{\cdot}4H_2O$) used as a cobalt precursor, where hydrogen peroxide was used to drive the oxidation of the cobalt precursor [99]. HRTEM images and the XRD pattern of the Co_3O_4 NPs are shown in Fig. 9A and B. Particle sizes averaging about 7 nm were observed for cubiclike Co_3O_4 NPs. The diffraction peaks correspond to the (111), (220), (311), (222), (400), (422) and (511) crystallographic plane are of Co_3O_4 NPs matched with JCPDS card No. ICCD PDF-948 of Co_3O_4. Average crystalline sizes of 12.3 nm were observed from the XRD pattern.

4 MAGNETIC SORBENTS

The essential characteristic of an adsorbent is that the adsorbent should be porous in structure with high surface area and smaller in size, which results in the high surface-to-volume ratio, as well as highly active sites for adsorption; also, the time necessary for attaining adsorption equilibrium should be short

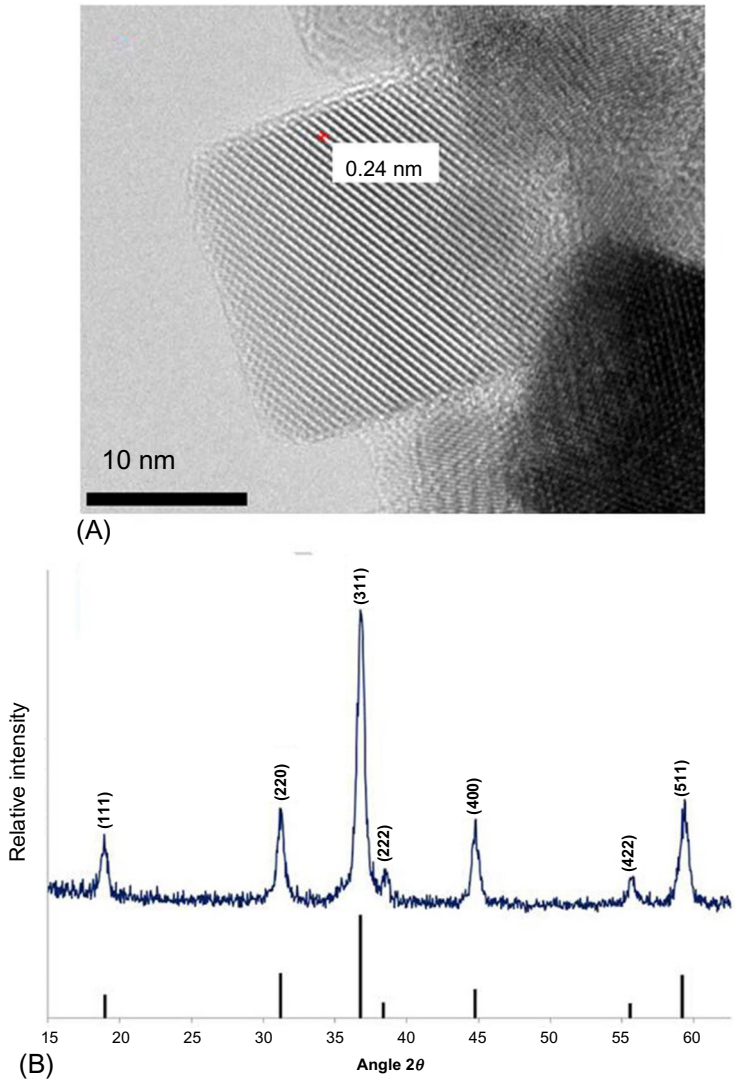

FIG. 9

(A) HRTEM and (B) XRD pattern of Co_3O_4 NPs.

Reproduced with permission from F. Moro, S. Tang, Y. Vi, F. Tuna, E. Lester, Magnetic properties of cobalt oxide nano-particles synthesised by a continuous hydro-thermal method, J. Magn. Magn. Mater. 348 (2013) 1–7, Copyright© 2013, Elsevier publication.

so that it can be used to remove pollutant molecules in a short period. Thus, the adsorption of pollutant molecules on the smaller-sized adsorbents leads to great advantages because of their surface areas lead to the highest adsorption capacity. But after achieving the saturation point of adsorption, the separation of the adsorbent from the water system becomes so hard. This drawback of utilizing the smaller-sized

adsorbent molecules swept over by the magnetic separation of adsorbents leads to promising techniques for wastewater treatment because of the decreasing chance of producing flocculants and of the large quantity of effluent that can be treated within a tiny period [100, 101]. The potential application of the adsorbents possessing magnetic properties leads to a considerable attraction in practical fields because of their simple recovery after completion of the adsorption process by using an external MF. In the case of NPs adsorbents, their unique magnetic properties are associated with their high surface-to-volume ratio and are beneficial for application in water purification [102, 103].

4.1 MAGNETIC SORBENTS FOR ORGANIC POLLUTANTS

Organic pollutants are the organic compounds that have the high resistivity toward chemical biological degradation process and thus they accumulate in the environment with potential adverse influences on the environment and the living beings. Using different magnetic adsorbent materials for removing pollutant molecules provides the most effective way to treat organic pollutants contained in industrial wastewater.

Zhang et al. reported that the magnetic hollow Fe_3O_4 nanospheres exhibited excellent adsorption efficiency for removing Congo red (CR) dye molecules with the maximum adsorption efficiency 59.1 mg/g. They also reported that the hollow Fe_3O_4 possesses higher adsorption ability because of its larger BET surface area, and its quick magnetic separation provides excellent performance in the wastewater treatment [104]. The kinetics parameters of the adsorption process can be calculated by using the following equation:

$$Q_e = (C_i - C_e)V/M_s$$

where Q_e (mg/g) is consigned as equilibrium adsorption capacity of adsorbent; C_i (mg/L) and C_e (mg/L) are the initial concentration and the equilibrium concentration, respectively; V (mL) is the volume of the solution; and M_s (g) is the mass of the adsorbent.

Recently, magnetic Fe_3O_4/rGO nanocomposite also employed as an adsorbent for removing five harmful pesticides—atrazine, simetone, simazine, prometryn, and ametryn—in an aqueous medium [105]. The adsorption efficiencies for atrazine, simetone, simazine, prometryn, and ametryn were found to be 75.24, 81.22, 88.55, 91.34, and 93.61, respectively, after 70 min at pH 5 and a temperature of 25°C. In this report, the Fe_3O_4/rGO nanocomposite was repeatedly used for the ametryn adsorption. For up to seven cycles, the Fe_3O_4/rGO nanocomposite achieved more than 80% ametryn adsorption efficiency, which indicates that Fe_3O_4/rGO nanocomposite is a sustainable adsorbent for the adsorption of different organic pollutants.

Bharath et al. developed magnetic (Fe_3O_4)/porous graphene nanocomposites by adopting a facile, cost-effective hydrothermal process for separating crystal violet (CV) dye molecules. They found that the synthesized nanocomposite possessed excellent adsorption efficiency due to its high specific surface area and easy recoverability from the reaction mixture in the presence of an external MF [106]. Cationic dyes such as CV can produce molecular cation (C^+) and reduced ions (CH^+). At normal pH, OH^- ions of the solution remains on the surface of the adsorbent. Thus, the cationic dye molecules adsorption favors a normal pH of the medium (Fig. 10A and B). The pseudo-second-order kinetic model followed the adsorption kinetic study of CV on the magnetic nanocomposites. The distribution of the dye molecules between liquid and Fe_3O_4/porous graphene nanocomposites was investigated through an isotherm study using Langmuir and Freundlich isotherm models. The researchers found

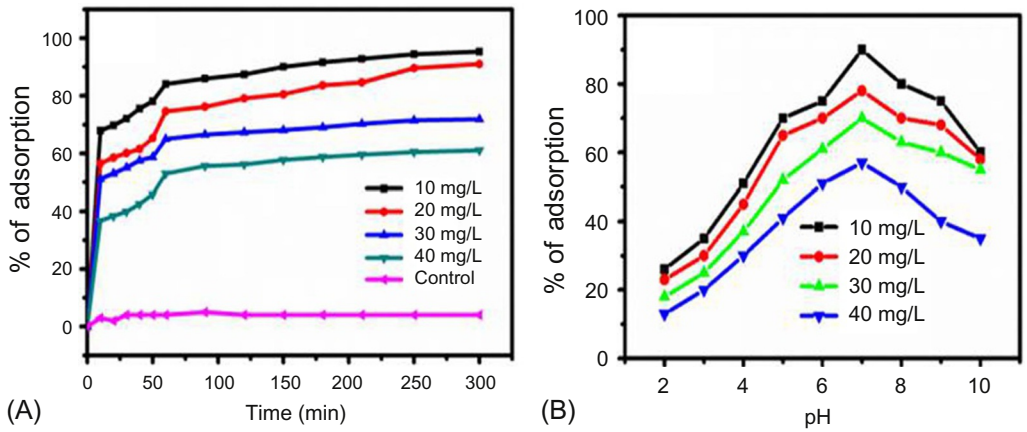

FIG. 10

(A) Effects of stirring time and (B) effect of pH on the adsorption of CV with a different initial concentration on Fe_3O_4/porous graphene nanocomposites.

Reproduced with permission from G. Bharath, E. Alhseinat, N. Ponpandian, M.A. Khan, M.R. Siddiqui, F. Ahmed, E.H. Alsharaeh, Development of adsorption and electrosorption techniques for removal of organic and inorganic pollutants from wastewater using novel magnetite/porous graphene-based nanocomposites, Sep. Purif. Technol. 188 (2017) 206–218, Copyright© 2017, Elsevier publication.

that the adsorption of CV followed monolayer adsorption, with maximum adsorption efficiency of 460 mg/g based on Langmuir isotherm model.

Similarly, Ni-based materials are also used for the adsorption of organic dye molecules present in the wastewater system. Mambrini et al. investigated the separation of organic dyes MB and indigo carmine (IC) using magnetic Ni/C and Ni/Mo_2C materials as adsorbents obtained by CVD at different temperatures. The adsorption of IC dye on the Ni/C composites was found to be 32%, 22%, and 22% at 700°C, 800°C, and 900°C, respectively, whereas for MB, the adsorption was found to be less than 10% (Fig. 11A). In the case of Ni/Mo_2C composites, adsorption of IC dye was found to be 43% and 31% at 700°C and 800°C, respectively. On the contrary, the adsorption of MB was reached about 100% after 20 min. At 900°C, the adsorption capacity was found to be 34% for MB and 99% for IC. These results indicate that both the hydrophobic interaction and the electronic interaction between the dye molecule, and the adsorbent surface plays an important role during the adsorption process. The negatively charged adsorbent surface can effectively bind with the positively charged molecules. In case of Ni/Mo_2C composite, the surface of the composite was negatively charged at the natural pH of the medium at 700°C and 800°C, and hence, adsorption of negatively charged MB was predominate, whereas at a higher temperature, 900°C, the surface of the composite was positively charged at the natural pH of the medium material; therefore, the absorption of anionic dye IC was more favorable [45].

Recently, the adsorption of both *Staphylococcus aureus* (*S. aureus*) and *Escherichia coli* (*E. coli*) was studied using Fe_3O_4 NPs synthesized by both top-down (Fe_3O_4A) and bottom-up (Fe_3O_4B) approaches as adsorbents [107]. The maximum adsorption capacity of Gram-negative bacterium *E. coli* and Gram-positive bacterium *S. aureus* onto a Fe_3O_4B surface was observed at about 592.32 and 559.44 mg/g, respectively. Because of the presence of different functional groups on

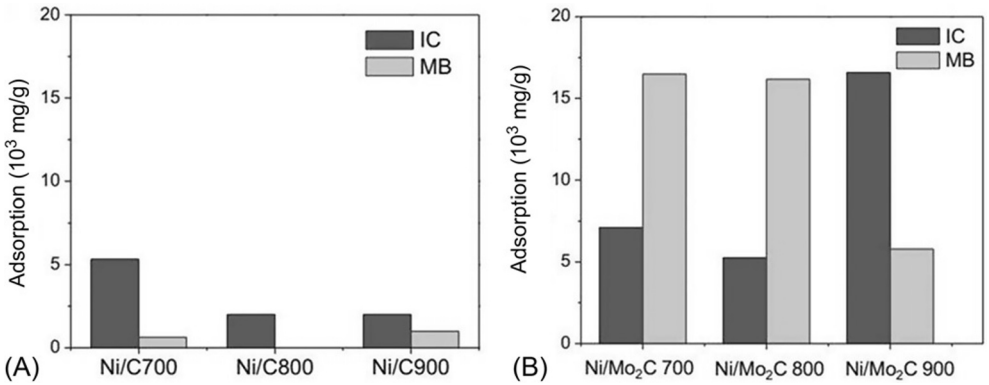

FIG. 11

Adsorption of IC and methylene blue on the (A) Ni/C and (B) Ni/Mo_2C materials, obtained after the ethanol/CVD process at different temperatures (pH = 4, natural pH of the dye solution).

Reproduced with permission from R.V. Mambrini, T.L. Fonseca, A. Dias, L.C.A. Oliveira, M.H. Araujo, F.C.C. Moura, Magnetic composites based on metallic nickel and molybdenum carbide: a potential material for pollutants removal, J. Hazard. Mater. 2012 (2012) 73–81, Copyright© 2012, Elsevier publication.

the bacteria cells; the cell may cause long-range electrostatic interactions as well as short-range electrostatic interactions, such as (1) π-π interactions, (2) van der Waal's interactions, (3) chemical (covalent, ionic, hydrogen), and (4) hydrophobic interactions. Steric effects were another factor that controls the adsorption of microorganism.

4.2 MAGNETIC SORBENTS FOR INORGANIC POLLUTANTS

A large number of heavy metal contaminants are discharged into the environmental water system, including rivers, lakes, seas, and so on, because of global industrialization. Adsorption of heavy metal ions using magnetic adsorbent materials opens an easy and simple path for removal processes. Lin et al. studied the adsorption of Cu^{2+}, Zn^{2+}, Cd^{2+}, Pb^{2+}, and Ni^{2+} ions on amine-functionalized magnetic iron oxide NPs (MIONPs-NH_2) [108]. Because of the presence of a hydratable hydroxyls (—OH) group on the MIONPs' surface, it possesses remarkable adsorption properties for removing heavy metal contaminants. In the case of cationic heavy metal ions adsorption, animation of MIONPs provides an excellent adsorption capacity of the adsorbent. They achieved about 80% adsorption of the heavy metal ions within 10 min at pH 6 (Fig. 12A). From the kinetic analysis, they found that the adsorption results followed the pseudo-second-order kinetic model. This result proves that the adsorption capacity of the adsorbent depends on the adsorption sites at which electron transfer between the adsorbent and the adsorbate takes place. Thus, the adsorption of various heavy metal cations occurs by forming a charge-transfer complex on the MIONPs-NH_2 surface. The adsorption isotherm study described that the adsorption processes obeyed the Langmuir model, with the saturated adsorption capacities for Cu^{2+}, Zn^{2+}, Cd^{2+}, Pb^{2+}, and Ni^{2+} being 0.67, 0.49, 0.30, 0.93, and 0.32 mmol/g, respectively (Fig. 12B).

Markeb and his coworkers studied the adsorption of fluoride (F^-) ions using magnetic core-shell Ce-Ti@Fe_3O_4 NPs. They explained that removal of fluoride ions occured through a surface

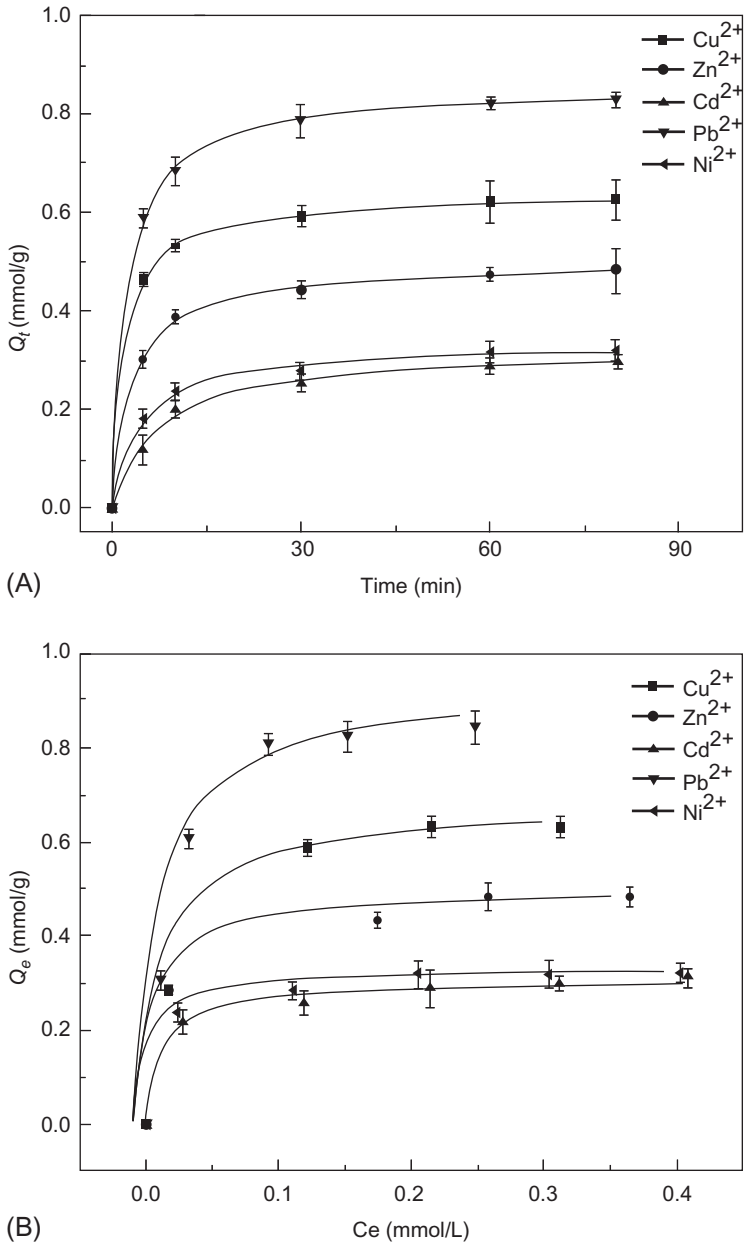

FIG. 12

(A) Kinetics of adsorption and (B) Langmuir adsorption isotherm for the adsorption heavy metals onto the MIONPs-NH_2 at 30°C.

Reproduced with permission from S. Lin, L. Liu, Y. Yang, K. Lin, Study on preferential adsorption of cationic-style heavy metals using amine-functionalized magnetic iron oxide nanoparticles (MIONPs-NH_2) as efficient adsorbents, Appl. Surf. Sci. 407 (2017) 29–35, Copyright© 2017, Elsevier publication.

ion-exchange process as physisorption based on the exchange of the hydroxyl ions (OH^-) from the surface of the adsorbent with F^- [109]. The mechanism of adsorption of F^- ions on the adsorbent surface consisting of OH^- ions was described by the following equation [110]:

$$M^{n+} + nH_2O \rightarrow M(OH)_n$$

$$M(OH)_n + xF^- \rightarrow M(OH)_{n-x}F_x + xOH^-$$

The presence of Mn(II) ions in the underground water affects the human health and ecosystem. Hence, in recent years, removal of Mn(II) ions has attracted more attention. Liu et al. analyzed the adsorption of Mn(II) ions in an aqueous media using magnetic Fe_3O_4 NPs in the presence AMF and in the absence of AMF. They found the adsorption capacity for Fe_3O_4 NPs in the presence of AMF and absence of AMF were 36.81 and 28.36 mg/g, respectively [111]. Zhang et al. utilized polyacrylic acid (PAA)–modified graphene oxide/Fe_3O_4 (PAA/GO/Fe_3O_4) composites for the adsorption of Cu^{2+}, Cd^{2+}, and Pb^{2+} ions. They found that the removal efficacy for the heavy metal ions increased with the increase in pH of the medium. This was because at a higher pH value, ionization of surface —COOH and —OH groups formed —COO^-— and —O—, and thus, the surface charge of the adsorbent became more negative. This was favorable for the Pb^{2+} or Cu^{2+} ions. In the case of PAA/GO/Fe_3O_4, the negatively charged sites were decreased at a higher pH. Moreover, Pb^{2+} and Cu^{2+} ions underwent hydrolysis, and the predominant species were hydrolysed Pb^{2+} and Cu^{2+} ions. Therefore, at a higher pH, the adsorption is reduced because of the coulombic repulsion. The higher adsorption efficiency of Cu^{2+} and Pb^{2+} ions on the PAA/GO/Fe_3O_4 was found to be 55% and 45%, respectively, at pH 3, whereas in the case of Cd^{2+} ions, the adsorption efficiency was about 85% at pH 8. This was because in the alkaline medium, the predominant species was free Cd^{2+} ions, and with the interaction between Cd^{2+} and H^+ ions with the surface active sites, the adsorbents were increased with increasing pH, leading to an increased removal efficiency of the adsorbent [112].

4.3 MAGNETIC SORBENTS FOR RADIOACTIVE POLLUTANTS

Accumulation of long-lived radioactive pollutant molecules in the environment occurs because of the leakage of radionuclides from geological disturbances, such as volcanic eruptions, earthquakes, and so on, as well as other activities, such as testing of nuclear devices. To clear out this contaminated ecosystem, magnetic adsorbents are used for the removal of the pollutant molecules. Papynov et al. studied the mechanism of uranium (VI) sorption from water media in the presence of materials based on iron oxides, having a different composition of crystal phases, for example, Fe^0/Fe_3O_4, Fe^0/γ-Fe_2O_3, Fe^0/α-Fe_2O_3. In weakly acidic solutions, the sorbent was more stable, and therefore, the sorption kinetics of uranium was high. But in alkaline media, the absence of reductive precipitation of uranium and its complexation in the presence of carbonate ions may cause minimal sorption effect. This effect is related to the formation of stable negatively charged uranium complexes with carbonate anions, forming on the sorbents surface, block its active centers, and consequently limit the sorption process. They suggested that adsorption of uranium in such systems occured through the following series of chemical processes [113]:

Electrochemical corrosion:

$$2Fe^0(s) + 4H^+(aq) + O_2 \rightarrow 2Fe^{2+} + 2H_2O$$

$$2Fe^0(s) + 2H_2O \rightarrow 2Fe^{2+} + H_2(g) + OH^-(aq)$$

1. *Reductive precipitation*:

$$UO_2^{2+}(aq) + Fe^0 \leftrightarrow UO_2(s) + Fe^{2+}$$

$$UO_2^{2+}(s\,or\,aq) + 2Fe^{2+}(s) \leftrightarrow UO_2(s) + 2Fe^{3+}(s)$$

$$UO_2^{2+} + H_2(g) \leftrightarrow UO_2(s) + 2H$$

$$UO_2(s) + 2Fe^{3+}(aq) \leftrightarrow UO_2^{2+}(s\,or\,aq) + 2Fe^{2+}(aq)$$

$$Fe(OH)_3 \leftrightarrow \alpha -, \beta - FeOOH, Fe_3O_4, Fe_2O_3$$

2. *Sorption*:

$$Fe(OH)_3 + UO_2^{2+} \leftrightarrow Fe(OH)_2OUO^+ + H^+$$

Similarly, Gadly and his coworkers evaluated the adsorption of actinide ions, such as Am^{3+}, UO_2^{2+}, Th^{4+} and Pu^{4+}, from mildly aqueous acidic solutions using superparamagnetic Fe_3O_4/GO nanocomposites. The mechanism of ion adsorption followed the ion exchange process, in which the hydrogen ion was replaced by the metal ion at a pH value close to the dissociation constants of the respective acidic protons present in graphene oxide:

$$S - H + M^+ = S - M + H^+$$

where S-H is the sorbent (magnetic GO) and M is a representative metal ion [114].

5 MAGNETICALLY SEPARABLE PHOTOCATALYST FOR WATER PURIFICATION

Photocatalytic splitting of water on TiO_2 electrodes has been reported for the first time as a semiconductor photocatalyst by Fujishima and Honda in 1972 [115]. In case of the semiconductor-based photocatalyst, the photocatalytic degradation process is initiated by the absorption of a photon by the photocatalyst under light irradiation, resulting in the excitation of an electron from the valence band (VB) to the conduction band (CB). The hole generated in the VB can come into contact with a water molecule in an aqueous medium, which results in the formation of hydroxyl radicals ($^{\bullet}OH$). An electron in the CB can contact with dissolved molecular oxygen, resulting in the formation of the super oxide radical anion ($^{\bullet}O_2^-$), which reacts with a water molecule and forms $^{\bullet}OH$. The $^{\bullet}OH$ is a strong oxidizing agent that oxidizes organic contaminants to the respective inorganic harmless anions and molecules (like NO_3^-, SO_4^{2-}, Cl^-, CO_2, H_2O, etc.) [24]. During the last decades, significant progress has been made in the area of photocatalysts because of their high applicability in energy and environmental field. In this regard, several semiconductor metal oxide NPs, such as ZnO, WO_3, CdS, Bi_2WO_4 and BiOCl, Fe_2O_3, Fe_3O_4, and so on, have been developed for the photocatalytic application under light irradiation [116]. Recently, magnetic Fe-, Co-, and Ni-based nanocomposites have been extensively used in photocatalysis because these nanomaterials are easily separable and repeatedly usable during the elimination of water contaminants. A schematic representation of the photocatalytic degradation using semiconductors metal oxide is presented in Fig. 13.

Bare iron oxide NPs are not normally used as photocatalysts because of their weak reactivity, but iron oxide-based composite materials are useful with the addition of moieties, such as TiO_2, SiO_2, GO,

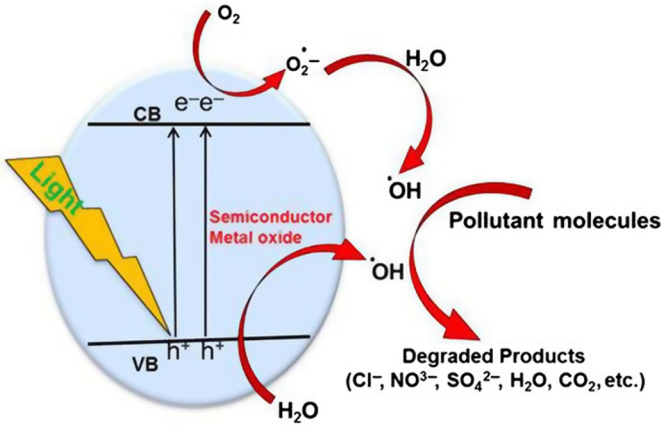

FIG. 13

Schematic representation of the photocatalytic degradation.

silver, gold, BiOBr, and other modifications [30, 39, 117–119]. Xin and his coworkers utilized core-shell Fe_3O_4@TiO_2 nanocomposite for degrading RhB dye molecules. More than 80% photodegradation efficiency was observed within 2 h of treatment under visible light irradiation. Moreover, the Fe_3O_4@TiO_2 nanocomposite is repeatedly used for the degradation of RhB; for up to six cycles, the nanocomposites showed superb photocatalytic activity.

The photogenerated holes and electrons are unstable for iron oxide NPs. Band-gap energy for Fe_3O_4 NPs is 1.4 eV, and for Fe_2O_3 NPs, 2.2 eV; because of smaller band-gap energies, photogenerated electrons are easily recombined without modification of the iron oxide NPs. Graphene plays an important role when semiconductor NPs are anchored with the graphene sheets. The excited electrons from the CB can trap the graphene to its surface, thereby suppressing the recombination rate of the electron hole pair of the semiconductor materials and enhancing its photocatalytic activity. In this regard, Fe_3O_4/rGO nanocomposite was utilized as an efficient photocatalyst for degrading different dye molecules, such as RhB, methyl blue (MBl), methyl green (MG), and others, under visible light and sunlight irradiation. Because the materials have band-gap energies below 3 eV, they are visible light responsive. About 44%–48% of visible light and 4%–6% of UV light are occupied by sunlight irradiation. The photocatalytic degradation efficiency is generally calculated by using the following equation:

$$\text{Dye removal efficiency } (\%) = [1 - C_t/C_o] \times 100$$

where C_o is the initial pollutant concentration and C_t is the concentration of pollutant molecules at time t, respectively. The Fe_3O_4/rGO nanocomposite showed superb photocatalytic activity; more than 90% degradation efficiency was observed for MG, MB, and RhB dye molecules in the presence of sunlight.

The mechanism of photocatalytic degradation was studied using a Fe_3O_4/rGO nanocomposite as a photocatalyst [39, 120]. The photocatalytic process was initiated by the initial adsorption of a photon by the using a Fe_3O_4/rGO nanocomposite photocatalyst. The promotion of an electron from the VB to the CB created an electron deficiency, or hole, in the VB. An electron in the CB could directly combine with dissolved molecular oxygen and the form $O_2^{\bullet -}$, which directly came into contact with a water

molecule in an aqueous medium, resulting in the formation of $^{\bullet}OH$. The hole generated in the VB also directly reacted with a water molecule and formed the $^{\bullet}OH$. $^{\bullet}OH$ is a strong oxidizing agent, which oxidized dye molecules to the nontoxic ions and molecules (Cl^-, $NO_3{}^-$, $SO_4{}^{2-}$, $CO_2{}^-$, and H_2O):

$$Fe_2O_4 + h\nu \rightarrow Fe_3O_4(e^- + h^+)$$

$$Fe_3O_4/rGO + h\nu \rightarrow Fe_3O_4(h^+) + rGO(e^-)$$

$$rGO(e^-) + O_2 \rightarrow rGO + O_2{}^{\bullet -}$$

$$rGO(e^-) + O_2{}^{\bullet} + H_2O \rightarrow HO_2{}^{\bullet} + OH^- + rGO$$

$$H_2O^{\bullet} + H^+ \rightarrow H_2O_2$$

$$rGO(e^-) + H_2O_2 + H^+ \rightarrow OH^{\bullet} + H_2O$$

$$Fe_3O_4(h^+) + OH^- \rightarrow Fe_3O_4 + OH^{\bullet}$$

$$\text{Dye molecules} + OH^{\bullet} \rightarrow \text{Degraded products}\left(Cl^-, NO_3{}^-, SO_4{}^{2-}, CO_2{}^-, \text{ and } H_2O\right)$$

A Fe_3O_4/rGO nanocomposite was also successfully employed for the photocatalytic reduction of toxic Cr(VI) to nontoxic Cr(III) under sunlight irradiation [120]. Excellent Cr(VI) reduction efficiency (more than 96%) was shown by a Fe_3O_4/rGO nanocomposite within a shorter time (25 min). A photogenerated electron in the CB is responsible for the reduction of Cr(VI) to nontoxic Cr(III). The following chemical reaction involves the photocatalytic reduction of Cr(VI):

$$Fe_3O_4/rGO + h\nu \rightarrow Fe_3O_4\,(h^+) + rGO\,(e^-)$$

$$Cr(VI)_{ads}Fe_3O_4/rGO + 3e^- \rightarrow Cr(III)_{ads}Fe_3O_4/rGO$$

$$Cr(III)_{ads}Fe_3O_4/rGO \rightarrow Cr(III) + Fe_3O_4/rGO$$

Tian and his coworkers exploited a core-shell magnetic γ-Fe_2O_3@SiO_2@AgBr:Ag nanocomposite, which was utilized as an efficient photocatalyst and showed excellent photocatalytic activity for degrading acid orange 7 (AO7) dye molecules under visible light irradiation. The synthesized photocatalyst achieved 93.1% degradation efficiency for AO7 dye in 20 min at an optimum condition, which is comparatively much higher than that of N-TiO_2 (17.3%) [117].

Magnetic NiO NPs and their composite materials are extensively used in the area of photocatalysis; they have wide band-gap energies (3.6–4 eV) and act as p-type semiconductors. For example, Fazlali and his coworkers exploited NiO NPs for degrading MO dye molecules. Under optimum condition, an 86% MO degradation efficiency was observed in presence of UV light [121]. Similarly, NiO-impregnated CeO_2 nanocomposite was utilized for the photocatalytic degradation of brilliant green (BG) dye molecule [122]. The band gap of this magnetic NiO/CeO_2 nanocomposite was found to be 3.24 eV, which established it as a potential photocatalyst for the degradation of pollutant molecules. An 82% BG degradation was achieved using this photocatalyst under UV light irradiation. Akhtar and his coworkers have been developed a core-shell structured epoxide functional NiO/SiO_2 nanocomposite (NiO/SiO_2/PGMA) for the photocatalytic degradation of CR dye molecules in an aqueous medium [123]. This nanocomposite exhibited excellent photocatalytic activity, 100% CR degradation was achieved within 10 min under sunlight irradiation because of the synergistic effects of NiO and SiO_2. They have thoroughly analyzed the mechanism of CR degradation. This synthesized nanocomposite particle is highly porous; as a result, NiO NPs absorb UV light, resulting in the

Table 1 Comparison of the Photodegradation Efficiency of Different Reported Magnetic Nanomaterials for the Degradation of Organic Contaminants

Nanomaterials	Pollutant	Photoreduction Efficiency (%)	Light Source	Irradiation Time (min)	References
Fe_2O_3/g_3N_4	Rhodamine B	100%	Visible light	105	[125]
NiO/g_3N_4	Rhodamine B	100%	Visible light	105	[125]
Co_3O_4/g_3N_4	Rhodamine B	100%	Visible light	105	[125]
NiO/graphene	Methyl orange	90.3%	UV-light	75	[91]
NiO-TiO_2 NTAs	Methylene blue	100%	Visible light	10	[126]
NiO/TiO_2/C	Methylene blue	98%	Visible light	25	[127]
AG/Fe_3O_4	Phenol	92.43%	Sunlight	120	[74]
AG/Fe_3O_4	2-Nitrophenol	98%	Sunlight	70	[74]
AG/Fe_3O_4	2-Chlorophenol	97.15%	Sunlight	70	[74]

excitation of an electron from the VB to the CB. Furthermore, the details mechanism is similar with the Fe_3O_4/rGO nanocomposite.

Cobalt-based magnetic nanomaterials have also been used as photocatalysts for removing water contaminants. Soofivand and Salavati-Niasari utilized a magnetic Co_3O_4/graphene nanocomposite for MO dye degradation. Bulk Co_3O_4 is an n-type semiconductor with optical band-gap values of 1.48 and 2.19 eV. The band gap of the synthesized Co_3O_4/graphene nanocomposite was found to be 2 and 3.2 eV, which is higher than that of bulk Co_3O_4. The band-gap value 2 eV corresponds to the $O^{2-} \rightarrow Co^{2+}$ charge transfer phenomena, while the band-gap value 3.2 eV attributed to the $O^{2-} \rightarrow Co^{2+}$ charge transfer phenomena. The MO degradation was observed at 54.9% using this nanocomposite in 75 min under UV light irradiation [124]. Until now, there have been several magnetic nanomaterials developed for the photocatalytic degradation of organic contaminants. Some of these are presented in Table 1 [74, 91, 125–127].

6 CONCLUSION AND FUTURE PROSPECTS

The work presented in this chapter focused on the synthesis, properties, and efficient uses of magnetic nanomaterials in water purification process. Magnetic nanomaterials have exhibited great efficacy for removing trace pollutants in an aqueous medium. The synthesis method summarized here for different iron-, cobalt-, and nickel-based magnetic nanomaterials will guide the future development of even better magnetic nanomaterials. In future, magnetic nanomaterials will provide new technologies for the

adsorption and degradation of pollutants in the environment. However, a few numbers of magnetic nanomaterials, such as Fe_2O_3, Fe_3O_4, zerovalent iron NPs, Co_3O_4, and NiO NPs, are available on the market. These are not sufficient for utilization in the water-contaminate removal process. Therefore, several existing problems need to be solved in the future for the practical use of the nanomaterials in water purification. First, the magnetic nanomaterials production cost should be minimized. The cost effect should be evaluated when the magnetic nanomaterials are introduced to the practical application in the environment field. Otherwise, it will not be viable to commonly use magnetic nanomaterials for water purification purposes. Second, the reasonable modification of the magnetic nanomaterials is required to avoid aggregation. Otherwise, it would easily undergo agglomeration. The aggregation of the magnetic NPs and composite materials will hamper the recycling uses of the nanomaterials in the practical environmental remediation field. If the magnetic nanomaterials cannot be used repeatedly, the cost of the water purification process will increase for technological purposes. Furthermore, minimizing the environmental risks resulting from introducing magnetic nanomaterials to the environmental remediation will be beneficial for developing technology for water purification using these magnetic nanomaterials. Improving magnetic nanomaterials will help confront the complex environmental changes that have arisen from global population growth and industrialization.

Iron oxides NPs have low toxicity to the human health and that of other organisms because low dosages of iron being released into the water bodies are safe and somewhat necessary. However, further dosages of iron released into the water bodies from iron-based nanomaterials are harmful to living organisms. Research on the toxicity assessment of magnetic nanomaterials is just at the beginning stage. Further assessments about the toxicity of the magnetic nanomaterials are required in the future to develop technology based on the magnetic nanomaterials for water purification. The technology based on the magnetic nanomaterials is required to facilitating green and sustainable economic growth. For water purification purposes, more low cost and efficient functional magnetic nanomaterials need to be developed because of their precious advantages over conventional approaches. Finally, the magnetic nanomaterials used in environmental remediation applications open an auspicious prospect in economic growth. But improving the technology and the processes is essential and should be transferred from the laboratory to the market, which will be beneficial for practical applications.

ACKNOWLEDGMENT

The authors thank the CSIR, New Delhi for financial support (Project No. OLP-2003) and also the Director, CSIR-North East Institute of Science and Technology, Jorhat, India for the interest in this work and facilities. P.K.B. acknowledges CSIR, New Delhi, India for Senior Research Fellowship grant. P.B. acknowledges DST, New Delhi, India for DST-INSPIRE Fellowship grant.

REFERENCES

[1] L. Chen, T. Ji, L. Mu, Y. Shi, L. Brisbin, Z. Guo, M.A. Khan, D.P. Youngd, J. Zhu, Facile synthesis of mesoporous carbon nanocomposites from natural biomass for efficient dye adsorption and selective heavy metal removal, RSC Adv. 6 (2016) 2259–2269.

[2] M.Y. Chen, D.J. Lee, N.Q. Ren, Degradation of phenol by acinetobacter strain isolated from aerobic granules, Chemosphere 67 (2007) 1566–1572.

[3] Y. Gong, X. Liu, L. Huang, W. Chen, Stabilization of chromium: an alternative to make safe leathers, J. Hazard. Mater. 179 (2010) 540–544.
[4] M. Gheju, A. Iovi, I. Balcu, Hexavalent chromium reduction with scrap iron in continous flow system Part 1: effect of feed solution pH, J. Hazard. Mater. 153 (2008) 655–662.
[5] D. Lewis, D. Gattie, Pathogen risks from applying sewage sludge to land, Environ. Sci. Technol. 36 (2002) 286–293.
[6] K. Agdi, A. Bouaid, A.M. Esteban, P.F. Hernando, A. Azmania, C. Camara, Removal of atrazine and four organophosphorus pesticides from environmental waters by diatomaceous earth–remediation method, J. Environ. Monit. 2 (2000) 420–423.
[7] M.A. Al-Ghouti, M.A.M. Khraisheh, S.J. Allen, M.N. Ahmad, The removal of dyes from textile wastewater: a study of the physical characteristics and adsorption mechanisms of diatomaceous earth, J. Environ. Manag. 69 (2003) 229–238.
[8] S. Zhu, S. Jiao, Z. Liu, G. Pang, S. Feng, High adsorption capacity for dye removal by CuZn hydroxyl double salts, Environ. Sci. Nano 1 (2014) 172–180.
[9] Y. Qin, M. Long, B. Tan, B. Zhou, RhB adsorption performance of magnetic adsorbent Fe_3O_4/RGO composite and its regeneration through a Fenton-like reaction, Nano-Micro Lett. 6 (2014) 125–135.
[10] A.C. Gomes, I.C. Gonçalves, M.N. De Pinho, The role of adsorption on nanofiltration of azo dyes, J. Membr. Sci. 255 (2005) 157–165.
[11] C. Das, P. Patel, S. De, S. DasGupta, Treatment of tanning effluent using nanofiltration followed by reverse osmosis, Sep. Purif. Technol. 50 (2006) 291–299.
[12] Q. Xiang, J. Yu, M. Jaroniec, Graphene-based semiconductor photocatalysts, Chem. Soc. Rev. 41 (2012) 782–796.
[13] P.T. Anastas, J.C. Warner, Green Chemistry Theory and Practice, Oxford University Press, Oxford, 1998.
[14] A.S. Matlack, Introduction to Green Chemistry, Marcel Dekker, New York, 2001.
[15] J.H. Clark, D.J. Macquarrie, Handbook of Green Chemistry and Technology, Blackwell Publishing, Abingdon, 2002.
[16] M. Lancaster, Green Chemistry: An Introductory Text, RSC, Cambridge, 2002.
[17] M. Poliakoff, J.M. Fitzpatrick, T.R. Farren, P.T. Anastas, Green chemistry: science and politics of change, Science 297 (2002) 807–810.
[18] R.A. Sheldon, Fundamentals of green chemistry: efficiency in reaction design, Chem. Soc. Rev. 41 (2012) 1437–1457.
[19] R.A. Sheldon, E factors, green chemistry and catalysis: an odyssey, Chem. Commun. 7 (2008) 3352–3365.
[20] P.T. Walsh, H. Li, C.A.A. de Parrodi, Green chemistry approach to asymmetric catalysis: solvent-free and highly concentrated reactions, Chem. Rev. 107 (2007) 2503–2545.
[21] R.B. Nasir Baig, R.S. Varma, Stereo- and regio-selective one-pot synthesis of triazole-based unnatural amino acids and b-amino triazoles, Chem. Commun. 48 (2012) 5853–5855.
[22] B. Nasir Baig, R.S. Varma, Alternative energy input: mechanochemical, microwave and ultrasound-assisted organic synthesis, Chem. Soc. Rev. 41 (2012) 1559–1584.
[23] S.B. Gawande, P.S. Brancoa, R.S. Varma, Nanocatalysis and prospects of green chemistry, ChemSusChem 5 (2012) 65–68.
[24] M.R. Hoffmann, S.T. Martin, W. Choi, D.W. Bahnemann, Environmental applications of semiconductor photocatalysis, Chem. Rev. 95 (1995) 69–96.
[25] Y. Ren, C. Sun, K. Li, L. Wang, M. song, Preparation of TiO_2–reduced graphene oxide-Pd nanocomposites for phenol photocatalytic degradation, Ceram. Int. 42 (2016) 1339–1344.
[26] S. Thangavel, K. Krishnamoorthy, V. Krishnaswamy, N. Raju, S.J. Kim, G. Venugopal, Graphdiyne–ZnO nanohybrids as an advanced photocatalytic material, J. Phys. Chem. C 119 (2015) 22057–22065.
[27] G.K. Pradhan, D.K. Padhi, K.M. Parida, Fabrication of Fe_2O_3 nanorod/RGO composite: A novel hybrid photocatalyst for phenol degradation, ACS Appl. Mater. Interfaces 5 (2013) 9101–9110.

[28] R. Narain, M. Gonzales, A.S. Hoffman, P.S. Stayton, K.M. Krishnan, Synthesis of monodisperse biotinylated p(NIPAAm)-coated iron oxide magnetic nanoparticles and their bioconjugation to streptavidin, Langmuir 23 (2007) 6299–6304.
[29] Q. Zhang, D.Q. Lima, I. Lee, F. Zaera, M. Chi, Y. Yin, A highly active titanium dioxide based visible-light photocatalyst with nonmetal doping and plasmonic metal decoration, Angew. Chem. Int. Ed. 50 (2011) 7088–7092.
[30] A.-H. Lu, E.L. Salabas, F. Schüth, Magnetic nanoparticles: synthesis, protection, functionalization, and application, Angew. Chem. Int. Ed. 46 (2007) 1222–1244.
[31] S. Shylesh, V. Schünemann, W.R. Thiel, Magnetically separable nanocatalysts: bridges between homogeneous and heterogeneous catalysis, Angew. Chem. Int. Ed. 49 (2010) 3428–3459.
[32] Y. Zhu, L.P. Stubbs, F. Ho, R. Liu, C.P. Ship, J.A. Maguire, N.S. Hosmane, Magnetic nanocomposites: a new perspective in catalysis, ChemCatChem 2 (2010) 365–374.
[33] V. Polshettiwar, R. Luque, A. Fihri, H. Zhu, M. Bouhrara, J.-M. Basset, Magnetically recoverable nanocatalysts, Chem. Rev. 111 (2011) 3036–3075.
[34] L.M. Rossi, M.A.S. Garcia, L.L.R. Vono, Recent advances in the development of magnetically recoverable metal nanoparticle catalysts, J. Braz. Chem. Soc. 23 (2012) 1959–1971.
[35] R.B.N. Baig, R.S. Varma, Magnetically retrievable catalysts for organic synthesis, Chem. Commun. 49 (2013) 752–770.
[36] J.F. Lutz, S. Stiller, A. Hoth, L. Kaufner, U. Pison, R. Cartier, One-pot synthesis of PEGylated ultrasmall iron-oxide nanoparticles and their in vivo evaluation as magnetic resonance imaging contrast agents, Biomacromolecules 7 (2006) 3132–3138.
[37] H.E. Ghandoor, H.M. Zidan, M.M.H. Khalil, M.I.M. Ismail, Synthesis and some physical properties of magnetite (Fe_3O_4), J. Electrochem. Sci. 7 (2012) 5734–5745.
[38] A.-F. Ngomsik, A. Bee, M. Draye, G. Cote, V. Cabuil, Magnetic nano- and microparticles for metal removal and environmental applications: a review, C. R. Chim. 8 (2005) 963–970.
[39] T. Peik-See, A. Pandikumar, L.H. Ngee, H.N. Ming, C.C. Hua, Magnetically separable reduced graphene oxide/iron oxide nanocomposite materials for environmental remediation, Catal. Sci. Technol. 4 (2014) 4396–4405.
[40] Y.S. Fu, X. Wang, Magnetically separable $ZnFe_2O_4$–Graphene catalyst and its high photocatalytic performance under visible light irradiation, Ind. Eng. Chem. Res. 50 (2011) 7210–7218.
[41] M. Baikousi, A.B. Bourlinos, A. Douvalis, T. Bakas, D.F. Anagnostopoulos, J. Tuček, K. Šafářova, R. Zboril, M.A. Karakassides, Synthesis and characterization of γ-Fe_2O_3/carbon hybrids and their application in removal of hexavalent chromium ions from aqueous solutions, Langmuir 38 (2012) 3918–3930.
[42] M. Kokate, K. Garadkar, A. Gole, One pot synthesis of magnetite–silica nanocomposites: applications as tags, entrapment matrix and in water purification, J. Mater. Chem. A 1 (2013) 2022–2029.
[43] Z. Ma, D. Zhao, Y. Chang, S. Xing, Y. Wua, Y. Gao, Synthesis of $MnFe_2O_4$@Mn–Co oxide core–shell nanoparticles and their excellent performance for heavy metal removal, Dalton Trans. 42 (2013) 14261–14267.
[44] K.K. Kefeni, B.B. Mamba, T.A.M. Msagati, Magnetite and cobalt ferrite nanoparticles used as seeds for acid mine drainage treatment, J. Hazard. Mater. 333 (2017) 308–318.
[45] R.V. Mambrini, T.L. Fonsec, A. Dias, L.C.A. Oliveira, M.H. Araujo, F.C. Moura, Magnetic composites based on metallic nickel and molybdenum carbide: a potential material for pollutants removal, J. Hazard. Mater. 241 (2012) 73–81.
[46] H. Zhao, Y. Dong, G. Wang, P. Jiang, J. Zhang, L. Wu, K. Li, Novel magnetically separable nanomaterials for heterogeneous catalytic ozonation of phenol pollutant: $NiFe_2O_4$ and their performances, Chem. Eng. J. 219 (2013) 295–302.
[47] R. Aitken, K. Creely, C. Tran, Nanoparticles: An Occupational Hygiene Review, England HSE Books, London, 2004.

[48] A. Ito, M. Shinkai, H. Honda, T. Kobayashi, Medical application of functionalized magnetic nanoparticles, J. Biosci. Bioeng. 100 (2005) 1–11.
[49] Y.K. Gun'ko, D.F. Brougham, Magnetic nanomaterials as MRI contrast agents, in: S.R. Kumar (Ed.), Magnetic Nanomaterials, John Wiley & Sons, Inc., United States, 2009
[50] A.G. Kolhatka, A.C. Jamison, D. Litvinov, R.C. Willson, T.R. Lee, Tuning the magnetic properties of nanoparticles, Int. J. Mol. Sci. 14 (2013) 15977–16009.
[51] S. Sun, Recent advances in chemical synthesis, self-assembly, and applications of FePt nanoparticles, Adv. Mater. 18 (2006) 393–403.
[52] J.H. Jang, H.B. Lim, Characterization and analytical application of surface modified magnetic nanoparticles, Microchem. J. 94 (2010) 148–158.
[53] S. Thurm, S. Odenbach, Magnetic separation of ferrofluids, J. Magn. Magn. Mater. 252 (2002) 247–249.
[54] S.M. Ponder, J.G. Darab, J. Bucher, D. Caulder, I. Craig, L. Davis, N. Edelstein, W. Lukens, H. Nitsche, L. Rao, Surface chemistry and electrochemistry of supported zerovalent iron nanoparticles in the remediation of aqueous metal contaminants, Chem. Mater. 13 (2001) 479–486.
[55] K. Kohara, S. Yamamoto, L. Seinberg, T. Murakami, M. Tsujimoto, T. Ogawa, H. Kurata, H. Kageyama, M. Takano, Carboxylated SiO_2-coated a-Fe nanoparticles: toward a versatile platform for biomedical applications, Chem. Commun. 49 (2013) 2563–2565.
[56] Q. Huang, X. Shi, R.A. Pinto, E.J. Petersen, W.J. Weber, Tunable synthesis and immobilization of zerovalent iron nanoparticles for environmental applications, Environ. Sci. Technol. 42 (2008) 8884–8889.
[57] Y. Liu, S.A. Majetich, R.D. Tilton, D.S. Sholl, G.V. Lowry, TCE dechlorination rates, pathways, and efficiency of nanoscale iron particles with different properties, Environ. Sci. Technol. 39 (2005) 1338–1345.
[58] D.W. Elliott, W.-X. Zhang, Field assessment of nanoscale bimetallic particles for groundwater treatment, Environ. Sci. Technol. 35 (2001) 4922–4926.
[59] G. Kozma, A. Ronavari, Z. Ko nya, Á. Kukovecz, Environmentally benign synthesis methods of zero-valent iron nanoparticles, ACS Sustain. Chem. Eng. 4 (2016) 291–297.
[60] R.M. Cornell, U. Schwertmann, The Iron Oxides: Structure, Properties, Reactions, Occurrences and Uses, John Wiley & Sons Inc., United States, 2003
[61] J. Li, Y. Ren, F. Ji, B. Lai, Heterogeneous catalytic oxidation for the degradation of *p*-nitrophenol in aqueous solution by persulfate activated with $CuFe_2O_4$ magnetic nano-particles, Chem. Eng. J. 324 (2017) 63–73.
[62] J.M. Monteagudo, A. Durán, R. González, A.J. Expósito, In situ chemical oxidation of carbamazepine solutions using persulfate simultaneously activated by heat energy, UV light, Fe^{2+} ions, and H_2O_2, Appl. Catal. B Environ. 176–177 (2015) 120–129.
[63] W. Wu, Q. He, V. Jiang, Magnetic iron oxide nanoparticles: synthesis and surface functionalization strategies, Nanoscale Res. Lett. 3 (11) (2008) 397–415.
[64] A.K. Gupta, M. Gupta, Synthesis and surface engineering of iron oxide nanoparticles for biomedical applications, Biomaterials 26 (18) (2005) 3995–4021.
[65] A.K. Geim, K.S. Novoselov, The rise of graphene, Nat. Mater. 6 (2007) 183–191.
[66] M.J. Allen, V.C. Tung, R.B. Kaner, Honeycomb carbon: a review of graphene, Chem. Rev. 110 (2010) 132–145.
[67] K.S. Novoselov, A.K. Geim, S.V. Morozov, D. Jiang, Y. Zhang, S.V. Dubonos, I.V. Grigorieva, A.A. Firsov, Electric field effect in atomically thin carbon films, Science 306 (2004) 666–669.
[68] X. Yang, W. Chen, J. Huang, Y. Zhou, Y. Zhu, C. Li, Rapid degradation of methylene blue in a novel heterogeneous Fe_3O_4@rGO@TiO_2-catalyzed photo-Fenton system, Sci. Rep. 5 (2015) 10632–10642.
[69] Y. Yao, Z. Yang, D. Zhang, W. Peng, H. Sun, S. Wang, Magnetic $CoFe_2O_4$-graphene hybrids: facile synthesis, characterization, and catalytic properties, Ind. Eng. Chem. Res. 51 (2012) 6044–6051.
[70] D. Zhang, Q. Ding, X. Pu, C. Su, X. Shao, G. Ding, Z.G. Zhang, Q. Fang, One-step combustion synthesis of $NiFe_2O_4$-reduced graphene oxide hybrid materials for photodegradation of methylene blue, Funct. Mater. Lett. 7 (2014) 1350065–1350068.

[71] M. Luo, S. Yuan, M. Tong, P. Liao, W. Xie, X. Xu, An integrated catalyst of Pd supported on magnetic Fe_3O_4 nanoparticles: simultaneous production of H_2O_2 and Fe^{2+} for efficient electro-Fenton degradation of organic contaminants, Water Res. 48 (2014) 190–199.
[72] J.P. Jolivet, C. Chaneac, E. Tronc, Iron oxide chemistry. From molecular clusters to extended solid networks, Chem. Commun. 5 (2004) 481–487.
[73] S. Laurent, D. Forge, M. Port, A. Roch, C. Robic, L.V. Elst, R.N. Muller, Magnetic iron oxide nanoparticles: synthesis, stabilization, vectorization, physicochemical characterizations, and biological applications, Chem. Rev. 108 (2008) 2064–2110.
[74] J. Hu, G. Chen, I. Lo, Selective removal of heavy metals from industrial wastewater using maghemite nanoparticle: performance and mechanisms, J. Environ. Eng. 132 (2006) 709–715.
[75] J. Li, S. Zhang, C. Chen, G. Zhao, X. Yang, J. Li, X. Wang, Removal of Cu(II) and fulvic acid by graphene oxide nanosheets decorated with Fe_3O_4 nanoparticles, ACS Appl. Mater. Interfaces 4 (2012) 4991–5000.
[76] P.K. Boruah, B. Sharma, I. Karbhal, M.V. Shelke, M.R. Das, Ammonia-modified graphene sheets decorated with magnetic Fe_3O_4 nanoparticles for the photocatalytic and photo-Fenton degradation of phenolic compounds under sunlight irradiation, J. Hazard. Mater. 325 (2017) 90–100.
[77] S.A. Teja, P.Y. Koh, Synthesis, properties, and applications of magnetic iron oxide nanoparticles, Prog. Cryst. Growth Charact. Mater. 55 (2009) 22–45.
[78] N.R. Jana, Y. Chen, X. Peng, Size-and shape-controlled magnetic (Cr, Mn, Fe, Co, Ni) oxide nanocrystals via a simple and general approach, Chem. Mater. 16 (2004) 3931–3935.
[79] S.A. Samia, K.K. Hyzer, J.H.J. Schlueter, C.J.C. Qin, J.S.J. Jiang, S.D.S. Bader, X.M.X. Lin, Ligand effect on the growth and the digestion of Co nanocrystals, J. Am. Chem. Soc. 127 (2005) 4126–4127.
[80] S. Tong, C.A. Quinto, L. Zhang, P. Mohindra, G. Bao, Size dependent heating of magnetic iron oxide nanoparticles, ACS Nano 11 (2017) 6808–6816.
[81] X. Wang, J. Zhuang, Q. Peng, Y. Li, A general strategies for nanocrystal synthesis, Nature 437 (2005) 121–124.
[82] T. Xin, M. Ma, H. Zhang, J. Gu, S. Wang, M. Liu, Q. Zhang, A facile approach for the synthesis of magnetic separable Fe_3O_4@TiO_2, core shell nanocomposites as highly recyclable photocatalysts, Appl. Surf. Sci. 288 (2014) 51–59.
[83] M. Green, P. O'Brien, The preparation of organically functionalized chromium and nickel nanoparticles, Chem. Commun. (19) (2001) 1912–1913.
[84] Y. Hou, S. Gao, Monodisperse nickel nanoparticles prepared from a monosurfactant system and their magnetic properties, J. Mater. Chem. 13 (2003) 1510–1512.
[85] D.-H. Chen, C.-H. Hsieh, Synthesis of nickel nanoparticles in aqueous cationic surfactant solutions, J. Mater. Chem. 12 (2002) 2412–2415.
[86] Y. Jeon, G.H. Lee, J. Park, B. Kim, Y. Chang, Magnetic properties of monodisperse NiHx nanoparticles and comparison to those of monodisperse Ni nanoparticles, J. Phys. Chem. B 209 (2005) 12257–12260.
[87] Y.T. Jeon, J.Y. Moon, G.H. Lee, J. Park, Y. Chang, Comparison of the magnetic properties of metastable hexagonal close-packed Ni nanoparticles with those of the stable face-centered cubic Ni nanoparticles, J. Phys. Chem. B 110 (2006) 1187–1191.
[88] L. Chen, J. Chen, H. Zhou, D. Zhang, H. Wan, Synthesis of dodecanethiol monolayer-stabilized nickel nanoparticles, Mater. Sci. Eng. A 452 (2007) 262–266.
[89] Z.G. Wu, M. Munoz, O. Montero, The synthesis of nickel nanoparticles by hydrazine reduction, Adv. Powder Technol. 21 (2010) 165–168.
[90] J. Park, E. Kang, S.U. Son, H.M. Park, M.K. Lee, J. Kim, K.W. Kim, H.J. Noh, J.H. Park, C.J. Bae, et al., Monodisperse nanoparticles of Ni and NiO: synthesis, characterization, self-assembled superlattices, and catalytic applications in the suzuki coupling reaction, Adv. Mater. 17 (2005) 429–434.
[91] F. Soofivand, M. Salavati-Niasari, Step synthesis and photocatalytic activity of NiO/graphene nanocomposite under UV and visible light as an effective photocatalyst, J. Photochem. Photobiol. A 337 (2017) 44–53.

[92] B.K. Pandey, A.K. Shahi, R.K. Swarnkar, R. Gopal, Magnetic property of novel cobalt sulfate nanoparticles synthesized by pulsed laser ablation, Sci. Adv. Mater. 4 (2012) 537–543.
[93] T. Nishizawa, K. Ishida, The Co (Cobalt) system, Bull. Alloy Phase Diagr. 4 (1983) 387–390.
[94] C.B. Murray, S.H. Sun, W. Gaschler, H. Doyle, T.A. Betley, C.R. Kagan, Colloidal Synthesis of nanocrystals and nanocrystal superlattices, J. Res. Dev. 45 (2001) 47–56.
[95] C. Petit, A. Taleb, M.P. Pileni, Cobalt Nanosized particles organized in a 2D superlattice: synthesis, characterization, and magnetic properties, J. Phys. Chem. B 103 (1999) 1805–1810.
[96] M. Cavalier, M. Walls, I. Lisiecki, M.P. Pileni, How can the Nanocrystallinity of 7 nm spherical co nanoparticles dispersed in solution be improved? Langmuir 27 (2011) 5014–5020.
[97] Z.J. Yang, M. Cavalier, M. Walls, P. Bonville, I. Lisiecki, M.P. Pileni, A phase-solution annealing strategy to control the cobalt nanocrystal anisotropy: structural and magnetic investigations, J. Phys. Chem. C 116 (2012) 15723–15730.
[98] J.V.I. Timonen, E.T. Seppala, O. Ikkala, R.H.A. Ras, From hot-injection synthesis to heating-up synthesis of cobalt nanoparticles: observation of kinetically controllable nucleation, Angew. Chem. Int. Ed. 50 (2011) 2080–2084.
[99] F. Moro, S. Tang, Y. Vi, F. Tuna, E. Lester, Magnetic properties of cobalt oxide nano-particles synthesised by a continuous hydro-thermal method, J. Magn. Magn. Mater. 348 (2013) 1–7.
[100] V. Rocher, Removal of organic dyes by magnetic alginate beads, Water Res. 42 (2008) 1290–1298.
[101] X. Luo, L. Zhang, High effective adsorption of organic dyes on magnetic cellulose beads entrapping activated carbon, J. Hazard. Mater. 171 (2009) 340–347.
[102] N.A. Frey, S. Peng, K. Cheng, S. Sun, Magnetic nanoparticles: synthesis, functionalization, and applications in bioimaging and magnetic energy storage, Chem. Soc. Rev. 38 (2009) 2532–2542.
[103] S. Singamaneni, V.N. Bliznyuk, C. Binek, E.Y. Tsymbal, Magnetic nanoparticles: recent advances in synthesis, self-assembly and applications, J. Mater. Chem. 21 (2011) 16819–16845.
[104] D. Zhang, D. Xu, Y. Ni, C. Lu, Z. Xu, A facile one-pot synthesis of monodisperse ring-shaped hollow Fe_3O_4 nanospheres for waste water treatment, Mater. Lett. 123 (2014) 116–119.
[105] P.K. Boruah, B. Sharma, N. Hussain, M.R. Das, Magnetically recoverable Fe_3O_4/graphene nanocomposite towards efficient removal of triazine pesticides from aqueous solution: investigation of the adsorption phenomenon and specific ion effect, Chemosphere 168 (2017) 1058–1067.
[106] G. Bharath, E. Alhseinat, N. Ponpandian, M.A. Khan, M.R. Siddiqui, F. Ahmed, E.H. Alsharaeh, Development of adsorption and electrosorption techniques for removal of organic and inorganic pollutants from wastewater using novel magnetite/porous graphene-based nanocomposites, Sep. Purif. Technol. 188 (2017) 206–218.
[107] G. Darabdharaa, P.K. Boruaha, N. Hussaina, P. Borthakura, B. Sharmaa, P. Senguptaa, M.R. Das, Magnetic nanoparticles towards efficient adsorption of gram positiveand gram negative bacteria: an investigation of adsorption parameters and interaction mechanism, Colloids Surf. A 516 (2017) 161–170.
[108] S. Lin, L. Liu, Y. yang, K. Lin, Study on preferential adsorption of cationic-style heavy metals using amine-functionalized magnetic iron oxide nanoparticles (MIONPs-NH_2) as efficient adsorbents, Appl. Surf. Sci. 407 (2017) 29–35.
[109] A.A. Markeb, L. Ordosgoitia, A. Alonso, A. Sanchez, X. Font, Novel magnetic core-shell Ce–Ti@Fe_3O_4 nanoparticles as an adsorbent for water contaminants removal, RSC Adv. 6 (2016) 56913–56917.
[110] K. Zhang, S. Wu, X. Wang, J. He, B. Sun, Y. Jia, et al., Wide pH range for fluoride removal from water by MHS-MgO/$MgCO_3$ adsorbent: kinetic, thermodynamic and mechanism studies, J. Colloid Interface Sci. 446 (2015) 194–202.
[111] Y. Liu, J. Bai, H. Duan, X. Yin, Static magnetic field-assisted synthesis of Fe_3O_4 nanoparticles and their adsorption of Mn(II) in aqueous solution, Chem. Eng. J. 25 (2017) 32–36.
[112] W. Zhang, X. Shi, Y. Zhang, W. Gu, B. Li, Y. Xian, Synthesis of water-soluble magnetic graphene nanocomposites for recyclable removal of heavy metal ions, J. Mater. Chem. A 1 (2013) 1745–1753.

[113] E.K. Papynov, A.S. Portnyagin, A.I. Cherednichenko, I.A. Tkachenko, E.B. Modin, A.N. Dran'kov, A. A. Kvach, I.V. Zemchenko, I.G. Tananaev, V.A. Avramenko, in: Sol-gel synthesis of magnetic sorbents based on porous iron oxides for the removal of U(VI) from aqueous solution, AIP Conference Proceedings, vol. 1809, 2017, p. 020044.
[114] T. Gadly, P.K. Mohapatra, D.K. Patre, R.B. Gujar, A. Gupta, A. Ballal, S.K. Ghosh, Superparamagnetic graphene oxide–magnetite nanoparticle composites for uptake of actinide ions from mildly acidic feeds, J. Chromatogr. A 1513 (2017) 18–26.
[115] A. Fujishima, K. Honda, Electrochemical photolysis of water at a semiconductor electrode, Nature 238 (1972) 37–38.
[116] Y. Xia, L. Yin, Core–shell structured a-Fe_2O_3@TiO_2 nanocomposites with improved photocatalytic activity in the visible light region, Phys. Chem. Chem. Phys. 15 (2013) 18627–18634.
[117] B. Tian, T. Wang, R. Dong, S. Bao, F. Yang, J. Zhang, Core–shell structured g Fe_2O_3@SiO_2@AgBr:Ag composite with high magnetic separation efficiency and excellent visible light activity for acid orange 7 degradation, Appl. Catal. B 147 (2014) 22–28.
[118] Y. Leng, W. Guo, X. Shi, Y. Li, A. Wang, F. Hao, L. Xing, Degradation of Rhodamine B by persulfate activated with Fe_3O_4: effect of polyhydroquinone serving as an electron shuttle, Chem. Eng. J. 240 (2014) 338–343.
[119] L. Zhang, W. Wang, S. Sun, Y. Sun, E. Gao, Z. Zhang, Elimination of BPA endocrine disruptor by magnetic BiOBr@SiO_2@Fe_3O_4 photocatalyst, Appl. Catal. B 148–149 (2014) 164–169.
[120] P.K. Boruah, P. Borthakur, G. Darabdhara, C.K. Kamaja, I. Karbhal, M.V. Shelke, P. Phukan, D. Saikiad, M.R. Das, Sunlight assisted degradation of dye molecules and reduction of toxic Cr(VI) in aqueous medium using magnetically recoverable Fe_3O_4/reduced graphene oxide nanocomposite, RSC Adv. 6 (2016) 11049–11063.
[121] F. Fazlali, A.R. Mahjoub, R. Abazari, A new route for synthesis of spherical NiO nanoparticles via emulsion nano-reactors with enhanced photocatalytic activity, Solid State Sci. 48 (2015) 263–269.
[122] S.V. Sancheti, C. Saini, R. Ambati, P.R. Gogate, Synthesis of ultrasound assisted nanostuctured photocatalyst (NiO supported over CeO_2) and its application for photocatalytic as well as sonocatalytic dye degradation, Catal. Today 1 (2017) 50–57.
[123] M.S. Akhtar, M.A. Alam, K. Tauer, M.S. Hossan, M.K. Sharafat, M.M. Rahman, H. Minami, H. Ahmad, Core-shell structured epoxide functional NiO/SiO_2 nanocomposite particles and photocatalytic decolorization of Congo red aqueous solution, Colloid Surf. A 529 (2017) 783–792.
[124] F. Soofivand, M. Salavati-Niasari, Co_3O_4/graphene nanocomposite: pre graphenization synthesis and photocatalytic investigation of various magnetic nanostructures, RSC Adv. 5 (2012) 64346–64353.
[125] K. Sridharana, T. Kuriakoseb, R. Philip, T.J. Parka, Transition metal (Fe, Co and Ni) oxide nanoparticles grafted graphitic carbon nitrides as efficient optical limiters and recyclable photocatalysts, Appl. Surf. Sci. 308 (2014) 139–147.
[126] Z. Wu, Y. Wang, L. Sun, Y. Mao, M. Wang, C. Lin, An ultrasound-assisted deposition of NiO nanoparticles on TiO_2 nanotube arrays for enhanced photocatalytic activity, J. Mater. Chem. A 2 (2014) 8223–8229.
[127] M. Wang, J. Han, Y. Hu, R. Guo, Y. Yin, Carbon-incorporated NiO/TiO_2 mesoporous shells with p – n heterojunctions for efficient visible light photocatalysis, ACS Appl. Mater. Interfaces 8 (2016) 29511–29521.

FURTHER READING

[128] N. Calace, E. Nardi, B.M. Petronio, M. Pietroletti, Adsorption of phenols by papermill sludges, Environ. Pollut. 118 (2002) 315–518.

CHAPTER

19 SURFACE MODIFICATIONS OF MAGNETIC NANOPARTICLES FOR WATER PURIFICATION

Luís Carlos de Morais

Chemistry Department, Federal University of Triangulo Mineiro-UFTM, ICENE Institute, Uberaba, Brazil

1 INTRODUCTION

This chapter discusses water pollution and strategies to overcome it using magnetic nanoparticles (MNPs). Surface water pollution consists of six types of severe pollutants: oil pollution, chemical pollution, ground water pollution, thermal pollution, and agricultural pollution. Because these pollutants are intrinsically linked to our way of life, we are indirectly responsible for what is happening in the environment. Water is the basis of almost everything we do in life, so when it is contaminated, then we and the environment are contaminated too. Because the great number of environmental issues to discuss is beyond the scope of this chapter, we will present only those strategies designed to overcome contamination by lead (II) and organic pollutants (pesticides and dyes).

The following discussion aims not to focus on work developed through research, but to shed light on the properties of magnetic nanoparticles and the chemical structures of substances used to cover them. Research results will be used herein to lead us through the strategies used for MNP surface modification. We will simultaneously analyze the purposes behind the research and use them to explore different pathways to increase the potential for using MNPs to remove pollutants from water and search for ways to improve system performance.

1.1 SYNTHESIS OF MNPs

Toward understanding surface modification, it can be useful to discuss synthesis and leaching of substances from MNPs.

Before applying MNPs to purification of water, generally, they must first choose an adequate synthesis method from the multiple methods available [1–4]. The most common method used is by coprecipitation in alkaline conditions with the use of iron salts, Fe (II) and Fe (III), with ammonium or hydroxide solution. The illustrative reaction of MNP synthesis is given by Eq. (1) [5]:

$$2\,FeCl_{3(aq)} + FeCl_{2(aq)} + 8\,NH_{3(aq)} + 4\,H_2O_{(l)} \rightarrow Fe_3O_{4(s)} + 8\,NH_4Cl_{(aq)} \quad (1)$$

Notice that the proportion between Fe (III) and Fe (II) is 2:1 (mol/mol), and the salts used can be based on chlorides, sulfates, nitrates, etc. This is not the only proportion used, and several researchers

Nanoscale Materials in Water Purification. https://doi.org/10.1016/B978-0-12-813926-4.00025-2

considered it in the formation of high-magnetization nanoparticles. It is one thing to theoretically estimate this proportion, but it is another thing altogether to evaluate the real proportion between Fe (III) and Fe (II) in MNPs. However, Powder X-ray diffraction (XRD) is able to assess which type of ferrite is present, and thus, discover the proportions of the elements in the crystal lattice.

If the bivalent metal Fe^{2+} is changed to M^{2+} ("M" is a metal = cobalt, zinc, copper, manganese, etc.), it is possible to synthesize different ferrites and apply them in different situations.

This synthesis method is low in cost, allows rapid removal of contaminants, and permits several cycles of reuse and recovery of substances. These are good qualities to consider in projecting scale-up of this synthesis method, when it will be applied to meet the considerable real demand for water treatment.

As reported by Lowery [6], the strength of the generated magnetic fields in MNPs decreases as distance from the particle increases.

This report is very interesting and useful to our discussion as it reveals the importance in developing a good strategy for synthesis of MNPs according to the desired application, because in certain situations, the strength of the generated magnetic field is a variable affecting the system. For now, we can imagine magnetic nanoparticles being applied to remove pollutants or chemical substances in high-viscosity media. But if the MNPs need to be separated from the media by application of a magnetic field, then magnetic MNPs' strength will make a difference and affect the synthesis conditions.

Generally, MNPs synthesis may generate great disparity in size that can impair the effectiveness of an external magnetic field. This can sometimes be a problem if part of the MNPs are removed by the magnet and the others remain dispersed in the aqueous medium.

Depending on the conditions of the synthesis, different morphologies and sizes can probably be obtained, that is, pH, solvent, temperature, pressure, stirring speed, presence of other substances, nature of solvents, etc.

After defining this first step, other aspects should be taken into account when we work with MNPs.

1.2 SOME ASPECTS TO BE CONSIDERED IN SURFACE MODIFICATION

During the application of MNPs, it is common to observe leaching of elements like iron, cobalt, manganese from the nanoparticles, and this cannot be allowed to happen. To overcome this, coverage of the magnetic surface is required [7]. Potential MNP applications increase substantially depending on the substances used to cover their surfaces. As we will see, this coverage has been used as strategy to produce modified MNPs in water purification. After surface modification, MNPs show good recyclability, maintaining their adsorption-desorption properties. Stability and selectivity of MNPs can be achieved, depending of the kind of substances covering the MNPs' surfaces.

The main point that contributes to MNP stabilization in liquid phase is a charge density formed at the surface. Positive (or negative) charges in each nanoparticle will contribute to repulsion, stabilization, and avoidance of agglomeration. This can be achieved by controlling the charges in the double layer or through steric effects, as reported by Sellmyer and Skomisk [8].

The nature of the charges (positive or negative) must be defined on the MNPs' surfaces. These charges are defined by using Zeta Potential (ζ) (which has been used as part of the characterization of colloid systems). When two phases such as liquid-solid are in contact, generally, a difference in potential is developed. In addition, if the phase liquid is polar, the dipole molecules tend to orient in a direction at the interface. The double layer effects phenomena are known as "electrokinetic effects"

and are divided into four distinct types: electrophoresis, electroosmosis, streaming potential, and sedimentation potential [9].

In magnetic nanoparticles, the electrical nature of solid-liquid interface changes with the pH, and thus, the surface of the nanoparticles can be positively or negatively charged [10]. Due to this, MNPs' surfaces are enriched in some chemical groups (or sites); at low pH, the prevailing group is $—OH_2^+$, at moderate pH, the prevailing group —OH, and at high pH, the prevailing group generated is $—O^-$ [11]. These acid-base properties will be responsible for governing some surface reactions used to change the MNPs' surfaces. This is one more point that should be remembered when one seeks to modify magnetic nanoparticle surfaces.

Despite these surfaces having charges that change at different pH, the application of ζ should always be performed, if possible. The surface zero charge (known as zero point of charge [ZPC]) gives us information about zero potential difference of the charges in the solid-liquid phases when they are in balance. In this condition, no significant change in potential occurs when the bulk activity of an ion is altered.

In another situation, when the ζ of MNPs is a function of the pH at various concentrations of an ion in the liquid phase (KNO_3, for example), the point at which $\zeta = 0$ is called the isoelectric point (IEP).

From these two observations, we see that in certain conditions, ZPC and IEP have the same ζ.

From this information about variation in charge as a function of pH, one can choose conditions that are adequate for inducing reactions on an MNP's surface. This will contribute to choosing better conditions and the right substances to cover MNPs' surfaces, allowing targeting to maximize the process of removing any substance.

After these considerations, we will understand better the purpose of this chapter by using some scientific works that show different strategies for removing pollutants from water, as illustrated by Fig. 1.

1.3 SOME STRATEGIES USED TO REMOVE PB^{2+} FROM WATER

The contamination of water by metallic ions is significant, and these ions differ according to adsorption process. In this section, we will focus on analyzing lead (II) removal from water using modified MNPs.

Human activities cause substantial water pollution through industry, fertilizers, automobile emissions, petroleum, etc. Most agricultural pollutants like pesticides, fungicides, etc., penetrate into the soil through leaching and contaminate ground water. The World Health Organization (WHO) recommends a maximum amount of lead in drinking water of $5\,\mu g\,L^{-1}$ [12]; the United States and the EU have already adopted this lead (II) contamination limit and they expend great effort to control it.

When we focus on removing metallic ions from water, one consideration is extremely important: the ions' capacity for precipitation depending on the pH. For example, lead (II) hydroxide, $Pb(OH)_2$, has a solubility product constant (K_{sp}) of 1.43×10^{-20} [13]. This means that, depending on the concentration of Pb^{2+}, even at a low pH, the amount of hydroxide ions (OH^-) will be enough to cause precipitation, and this will interfere severely with the quantification of Pb^{2+} removed. Sometimes tests performed in the Pb^{2+} solution (like adding an alkaline solution until a turbid solution forms) are adequate for estimating the start of precipitation, so the refract index of the media will alter severely at this point.

Some strategies for MNP surface modification are simple, but others can require several steps to complete synthesis.

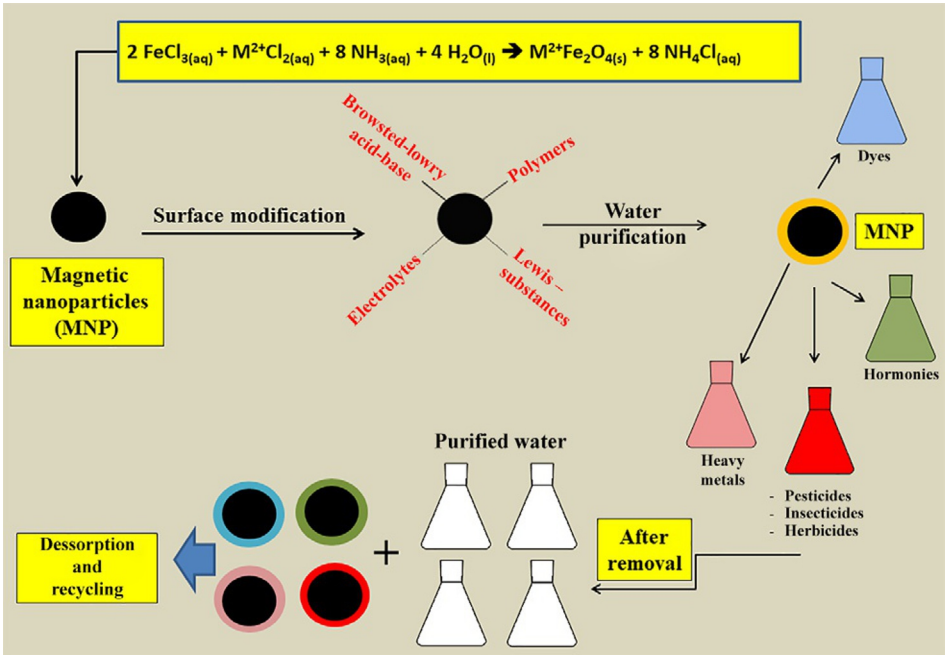

FIG. 1

Synthesis, surface modification, and some uses of MNP in removal processes.

There are infinite numbers of substances that have specific groups which interact well with Pb^{2+}, such as carboxylate (—COO—), hydroxide (—OH), ammine ($—NH_2$), and other groups that have great potential to coat the MNPs' surfaces. There are different mechanisms involved in Pb^{2+} removal; to illustrate one of them, adsorption of this cation from cellulose attached on an MNP surface is shown in Fig. 2.

As can be seen in Fig. 2, different interactions can occur during adsorption of Pb^{2+}, but the main mechanism is minimizing the free energy of adsorption ($\triangle G_{\text{adsorption}}$).

For now, we focus on analyzing the details of some scientific work regarding strategies to remove Pb^{2+} from water.

Liu et al. [14] coated Fe_3O_4 magnetic nanoparticles with humic acid (HA) to achieve highly efficient removal of Pb^{2+} and other metallic ions from water. In the MNPs' synthesis, chloride salts of Fe (II) and Fe (III) were solubilized in water and heated at 90°C. Then, a solution of ammonium hydroxide was added rapidly during stirring; after 30 min, a solution of sodium HA was added quickly and stirred at the same time. After this, the MNPs were already for application. Characterizations revealed that particle sizes of Fe_3O_4/HA were $\sim$10 nm in Fe_3O_4 cores, the aggregates in aqueous suspensions had an average hydrodynamic size of $\sim$140 nm, and the magnetization saturates were 79.6 emu g^{-1}. Applying the Langmuir adsorption model, the maximum adsorption capacities were from 46.3 to 97.7 mg g^{-1}. A great advantage of this composite was that variation in pH, whether basic or acid, did not influence the removal process. It was observed that it took only 15 min to reach equilibrium, and the presence of HA covering the surface prevented drastic leaching of iron elements. It was observed at pH 6.0 that almost 100% of Pb^{2+} was removed.

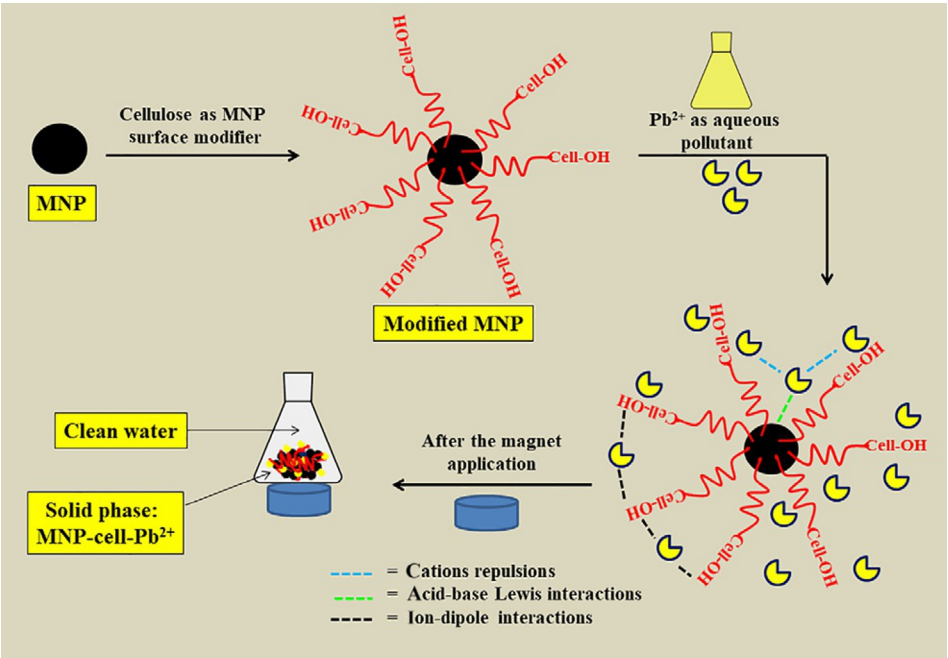

FIG. 2

Cellulose as MNP surface modifier used to remove Pb^{2+} from aqueous solution.

It is important to note that in this work, the studied Pb^{2+} concentration was 0.1 ppm, but the mass of HA that covered the MNP surface was not measured.

As mentioned by Duan and Gregory [15], HA was reported to have a wide range of molecular weights and could be regarded as natural anionic polyelectrolytes, having functional groups including carboxylic and phenolic, and a framework of randomly condensed aromatic rings.

These observations are important when considering the best conditions for surface modification. If we consider that (i) sodium HA produces an anionic polyelectrolyte, (ii) and during MNP synthesis, the use of HA sodium was done in alkaline medium, we can conclude that a poor interaction between HA and MNP will occur preferentially, rather than the adsorptive interactions. Therefore, as reported by Lobato et al. [16], magnetite and maghemite nanoparticles show positive charges on surfaces at $pH < 6.0$. Despite these considerations, a considerable amount of Pb^{2+} was removed from the water.

Some authors produce MNPs using a solvothermal method. In the work of Liu et al. [17] the MNPs are synthesized using $FeCl_3$, 1,6-hexanediamine and anhydrous sodium acetate added to ethylene glycol under via vigorous stirring in an autoclave at 200°C for 6 h.

Continuing our discussion, next we present data from two different works that used different strategies to remove Pb^{2+} with the same coverage substance, alginate.

Bée et al. [18] used magnetic alginate beads for removing Pb^{2+} ions from wastewater. They produced magnetite (Fe_3O_4) nanoparticles and converted them to maghemite (γ-Fe_2O_3) using nitric acid at first step and oxidation at 90°C as in second step. For this effort at surface modification of MNPs, the pH was kept strategically low, then, the maghemite MNPs were washed with acetone and ether to

maintain their acid form. In this condition, the MNPs were not stable during the dispersion in water, making it necessary to functionalize with citrate. Only after this was calcium-alginate used to encapsulate the MNPs to form beads. As a result, the maghemite-MNPs beads showed a distribution in average size of 1.39 mm ± 0.26 mm, and the saturation of magnetization occurred around 32.0 emu g^{-1} at high field yield. Despite the enormous size of the MNPs, they responded well in the presence of a magnet. The maximum capacity of Pb^{2+} removal was approximately 100 mg g^{-1}, as estimated by Langmuir isotherm using a dosage of 7.5 mg adsorbent per milliliter of solution, and the equilibrium time was 90 min; the best range of pH was between 2.3 and 6.0 from a 1500-ppm solution (7.25 mmol L^{-1}). Five cycles were tested in the adsorption/desorption mechanism and as result, almost 100% was obtained in each step.

In another work, Verma et al. [19] prepared MNPs by a coprecipitation method using hydrothermal conditions from salt solutions of Fe(II) and Fe(III) ions and adding ammonia solution to precipitate at pH 10. In the final step, the MNPs were dried in an oven at 250°C for 2 h. In the first step of surface modification, the MNPs were treated with 0.5 mol L^{-1} glycine solution at pH 6.0. In the second step, modified Fe_3O_4-glycine was added to a viscous solution of sodium alginate, then the mixture was added to calcium chloride solution to form stable gel beads. The resulting MNPs showed sizes ranging from micrometers to millimeters. Morphology indicated irregular structures with large surface areas. The saturations in magnetization were 2.352 and 1.732 emu g^{-1} for nonfunctionalized and functionalized MNPs, respectively. The capacity of Pb^{2+} removal from a 10-ppm solution was approximately 100% at pH 6.0, using a dose of 10 mg mL^{-1} (mass of MNPs per milliliter of solution) at 313 K (40°C). The maximum adsorption capacity was around 474 mg g^{-1} at 40°C using an 80-ppm solution of Pb^{2+}. In addition, 90% of the removal capacity was retained after four cycles.

Both of these two works used MNPs made of magnetite (Fe_3O_4). The different strategies used to prepare MNPs with modified surfaces to remove Pb^{2+} made the difference in the adsorption processes. Bée et al. [18] obtained magnetization that was much higher, which is very significant, because on an industrial scale, the MNPs would be recovered for reuse several times; if their magnetization was higher, it would be easier to extract MNPs using an external magnetic field.

A greater capacity to remove Pb^{2+} was observed from the Verma results; however, the assays of the concentration of Pb^{2+} should be taken into account [20].

There is one more important consideration about these chemical substances used to cover MNPs. Citrate has a carboxylate and hydroxyl groups in its framework, and the anionic form which will be present at pH 7.6 was employed. Glycine, an amino acid, has both amine and carboxylate groups in its chemical framework, and the zwitterion effect can happen, depending on the pH, due to the presence of alkaline and acidic groups in its chemical structure.

As reported by Huang and Chen [21], the carboxylate group has a preference for binding on MNPs' surfaces, rather than to amino groups; therefore, this group will be free for additional reactions.

As reported by Bée et al. [18] a surface complexation involving one or two carboxylate functions is considered, it means that two in each three carboxylates will be free for additional reactions. In this work, hydroxyl and carboxylate groups were free for adsorption of Pb^{2+}.

Both works used alginate as final coverage, and it was considered the major component in the adsorption process that has free carboxylate groups for adsorption. Because of this, we can treat these two works as similar. The main difference is that in Verma et al. [19] two groups contributed to the Pb^{2+} removal, which are the amino and carboxylate.

To better understand how these coverage substances help in Pb^{2+} removal, it is important to quantify each one of them. Sometimes thermogravimetric analysis is enough; sometimes others techniques are necessary. This way, it is possible to estimate accurately the number of chemical groups that were attached in the MNPs' surfaces and correlate them to the amount of removed pollutant.

Next, two works employed different strategies using ethylenediaminetetraacetic acid (EDTA) to coat MNPs surfaces and applied the MNPs to Pb^{2+} removal.

Huang and Keller [22] coated the MNPs' surfaces using the following steps: purchased maghemite nanoparticles with an average size of 30 nm were dispersed in toluene, then, 3-aminopropyltriethoxysilane (APTES) was added as a target to attach an amino group and allowed to reflux for 2 h at 90°C. After cooling, both EDTA and pyridine were added, and the same conditions were kept. The step was finished with several water washes, then the products were dried at room temperature for 24 h and stored.

The results evidenced that the maghemite was defined as a macroporous composite and the mass of substances coating was around 65% in mass, of which 12.5% was EDTA. The size of particles varied from 1 to 10 μm in range and show a very high porosity in the nanoscale. Maghemite (nonfunctionalized and functionalized) has magnetization saturation values of 59.0 and 52.8 emu g^{-1}, respectively. Zeta Potential showed that in a pH range from 4.0 to 10.0, the MNPs displayed negative surface charges. The composite showed fast removal capacity for Pb^{2+} with a time lower than 15 min with relatively high sorption capacity of 100.2 mg g^{-1} fitted by a Freundlich isotherm model. The removal occurred in a wide pH range from 3.0 to 10.0, as well in the presence of competitive metal ions. Recycling was very easy; recovery was accomplished by washing with 1% HCl, and the coated MNPs were reused for several cycles with high sorption capacity.

Ren et al. [23] modified magnetic Fe_3O_4 nanoparticles with SiO_2, chitosan, and EDTA. Fe_3O_4 microspheres were synthesized by solvothermal reduction and then were coated with silica layers via sol-gel method, forming SiO_2/Fe_3O_4 microspheres. These MNPs were added in a previous solution of chitosan (2% wt) dissolved in acetic acid and allowed under ultrasonication for 20 min followed by the addition of glutaraldehyde solution and allowed for 4 h. The composites were ground and sieved in a 150 meshes sieve. Then, the composites were added in a Na_2EDTA solution overnight by mechanical stirring and finalized with water-soluble 3-ethyl-1-(3-dimethylaminopropyl) carbodiimide hydrochloride (EDAC) as the cross-linker.

The results evidenced that the size varied from few to tens of micrometers. The saturation magnetization was 69.0, 56.3, 20.7, and 18.2 emu g^{-1} for Fe_3O_4, SiO_2/Fe_3O_4, SiO_2/Fe_3O_4/Chitosan, and Fe_3O_4/SiO_2/Chitosan/EDTA, respectively. The sample with EDTA showed about 25% losses in the adsorption capacity of heavy metal ions after 12 times in reuse. The maximum Pb^{2+} removal was 0.596 mmol g^{-1} (~123.5 mg g^{-1}). The equilibrium data were fitted with the Langmuir isothermal model. Around 100% of Pb^{2+} was removed using a dose of 1.0 mg mL^{-1}, pH range of 2.0 to 5.5, and a solution of 0.44 mmol mL^{-1} Pb^{2+} (~91.2 ppm). Equilibrium was reached after 100 min. Approximately 6.3% of EDTA was detected by thermogravimetric analysis.

Both works used different strategies to bind EDTA in a complexing agent in the outermost part of the MNPs' surfaces. Despite the fact that the amounts of EDTA in both cases were different (in one it was 6.3%, and in the other it was twice that), the capacities in removal were similar, with one extracting around 123.5 mg g^{-1} and the other around 100.2 mg g^{-1}. However, the magnetization saturation values were very different; one showed 52.8 emu g^{-1}, while the other was shown to be three times lower.

As mentioned previously, MNPs are not only made of magnetite or maghemite compositions; moreover, ferrites of cobalt and manganese are used to remove pollutants in water. As such, we can cite works with manganese ferrites in water treatment [24–26] and with cobalt ferrites [27, 28].

When thinking about large-scale magnetic applications to remove pollutants from water, we must account for the cost of all processes, that is, all energy involved in MNP production, quantity of water consumed, amounts of reactants spent, yield of MNPs after synthesis and purification steps, and so on.

There are thousands of articles published demonstrating the use of different substances and strategies for removal of water pollutants; because of this, it is impossible to include all of them in this section.

It is worth remembering that our main goal was to show some strategies used to extract Pb^{2+} from water under mimetic conditions in the lab or using water from a lake or river.

The next part of our discussion is about organic pollutants, especially dyes and pesticides as water contaminants.

1.4 REMOVAL OF ORGANIC POLLUTANTS FROM WATER

According to the EU Directive on water quality (98/83/EC) [29], the maximum concentration limit for pesticides in drinking water is $0.10\,\mu g\,L^{-1}$ for any individual pesticide and $0.5\,\mu g\,L^{-1}$ for pesticides in total.

Organic pollutants comprise a great class containing thousands of substances with different organic structures, from the simple to the complex, and complicated chemical structures. The chemical structures of organic pollutants control their solubility in water, and this correlates with the degree to which they each pollute. Dyes and pesticides cause several problems for both the environmental cycle and human health.

Some substances are considered persistent organic pollutants (POP), which means they remain intact for long periods after contaminating the environment, accumulating in the fatty tissue of living organisms, with several toxicity effects on both humans and wildlife. They are toxic, resistant to degradation, and bioaccumulative. Some POP examples include polychlorinated biphenyls (PCBs), hexabromocyclododecane (HBCD), perfluorinated chemicals (PFCs), and polybrominated diphenyl ethers (PBDEs) [30].

Effluents in a wide range of industrial applications, such as in the textile industry, contain large amounts of organic dyes which may cause severe water pollution. These dyes have chemical structures which confer solubility in water, allowing them to form anionic, cationic, and nonionic dyes [31].

It is worth remembering that the focus here is discussion of additional strategies for using MNPs to remove organic pollutants in the treatment of water; to this purpose, an illustration of how organic pollutants can be removed is shown in Fig. 3.

Fig. 3 illustrates how important it is to choose well the kind of dye, MNP, and surface modifier used. The nature of the MNP surfaces and the chemical structures of the surface-modifying agents will govern the kind of the adsorption mechanism used in the dye-removal process.

After previously discussing some points about modification of MNP surfaces, we now turn to some cases using MNPs to verify the strategies used by the authors with the respective results obtained, with comments whenever possible.

Graphene and its derivatives have been widely used in several research projects to remove water pollutants. Boruah et al. [32] used magnetic Fe_3O_4/graphene nanocomposite to remove five harmful

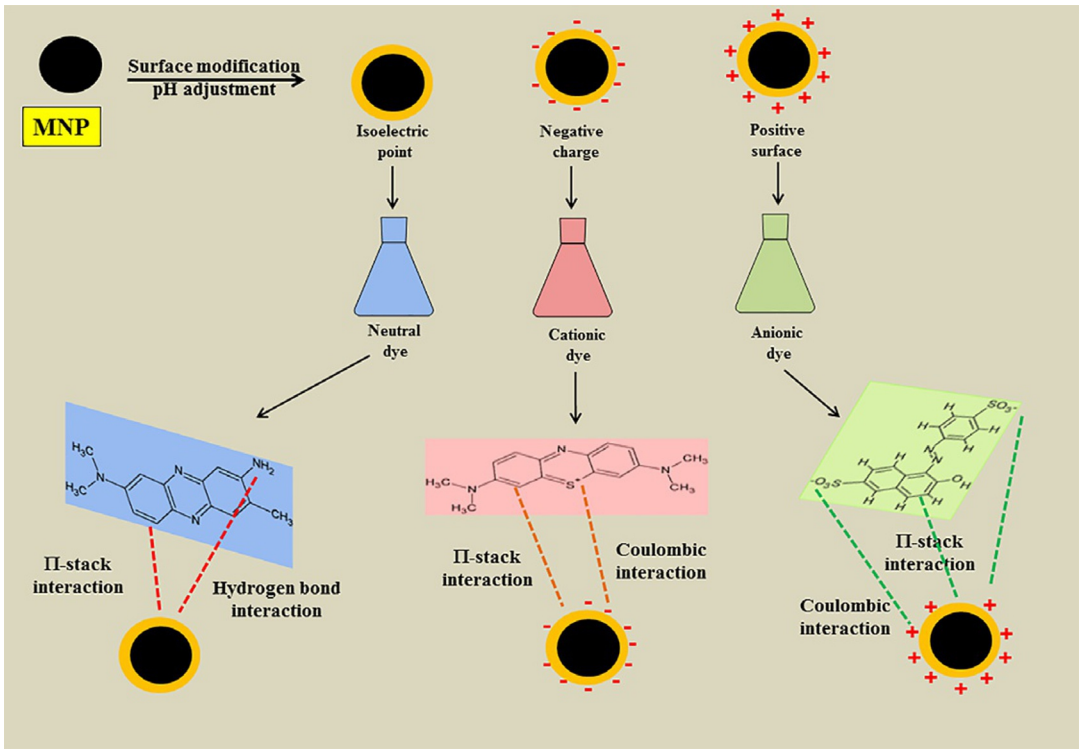

FIG. 3

Schematic illustration of organic removal pollutants from aqueous systems.

pesticides (ametryn, prometryn, simazine, simeton, and atrazine) from the aqueous medium. The strategy used to prepare the composite consisted of dispersing oxidized graphene (GO) nanosheets in deionized water by ultrasonication for 3 h. The pH was adjusted to 11.0 with ammonium solution, and after that, only chlorine salt ($FeCl_2$) was added very slowly while stirring. After 3 h of stirring, a black suspension of the rGO/Fe_3O_4 nanocomposite was separated using a magnet. One important difference in this strategy is GO oxidizing an amount of iron (II) to iron (III), allowing the formation of Fe_3O_4 and consequently reducing GO.

The Zeta Potential showed that below pH 5.5, a positive surface charge is formed in the composite, and over this pH, a negative surface charge prevails. Adsorption equilibrium of ametryn, prometryn simazine, simeton, and atrazine, respectively, at pH 5 and 25°C was achieved at 70 min, and adsorption efficiencies were found to be 93.61%, 91.34%, 88.55%, 81.22%, and 75.24%. Initial concentrations of pesticides were $10\,mg\,L^{-1}$. The efficiency removal was improved using an adsorbent dose of $0.5\,mg\,mL^{-1}$. The adsorption isotherm studies show that the maximum adsorption capacity was $54.8\,mg\,g^{-1}$ at pH 5.0, and it was enhanced in the presence of different ions (Mg^{2+}, Ca^{2+}, Na^{+}, and SO_4^{2-}). A maximum ametryn adsorption of $63.7\,mg\,g^{-1}$ was found in seawater medium. Thermodynamic parameters evidenced that the adsorption occurred spontaneously via physisorption. Generally,

the literature has only discussed the contributions of positive or negative charges from the adsorbates. However, in this work, the authors mentioned the additional contribution to adsorption of hydrophobic and π-π interactions between the aromatic rings of Fe_3O_4/rGO nanocomposite and the pesticide's molecules.

The authors optimized the adsorption of the Fe_3O_4/rGO nanocomposite at different pH levels (3, 5, 7, 9, 11) and at four different temperatures (20°C, 25°C, 30°C, and 35°C).

The balance in positive or negative charges is altered as a function of the pH, and this alteration will contribute to either improving or decreasing the adsorption process. Because of this effect, it is necessary to deeply analyze the chemical structures of each pesticide to understand how the charge-density distribution could favorably affect and contribute to the removal process. As an example, ametryn has three nitrogen atoms in its cycle structure, two more nitrogen atoms in side groups, and a sulfur atom linked to the cycle and in the methyl group. The ametryn structure and that of the other five pesticides is very similar, almost the same. Because of the different groups that are present in the chemical structures, the protonation changes in these groups will be severely dependent on the pH.

When some works explore the effects of extraction and recovery of the pollutants from water, the work is enriched, because currently, there is is a great necessity for work regarding recycling processes. First, chemical reagents, water, energy, and other substances are very expensive. Second, the possibility for reuse of the composites makes the removal process cheaper.

Related to these comments, Meseguer-Lloret et al. [33] worked with extraction and preconcentration of organophosphorus pesticides: phosmet (PHO), pirimiphos-methyl (PIR), and chlorpyrifos (CLO) in water by using a composite made of modified MNPs with polymethacrylate as sorbent. Synthesis was performed by a coprecipitation method using chlorine salts of Fe(II) and Fe(III) with a ratio of 2:1 in the presence of aqueous ammonia. Functionalization of MNPs was achieved with silanized glycidyl methacrylate (GMA). First, GMA-base material was prepared, and then, 3-aminopropyl trimethoxysilane (APTMS) was added to react with it. Finally, MNPs enriched with —OH groups were reacted with materials to produce a magnetic composite. The results showed that particle sizes were between 125 and 200 μm having a saturation magnetization of $24.52\,emu\,g^{-1}$. The recovery process was very sensitive to pH; however, at pH 5.0, high values were reached at close to 90%, for PHO and PIR and near 70% for CLO. The reusability endured up to fifty times without losses in the recovery. It is worth commenting that the conditions used were concentrations of $100\,ng\,mL^{-1}$ for PHO, $250\,ng\,mL^{-1}$ for PIR and CLO, sample volume of 5 mL; eluent volume of 4 mL; flow rate of $1\,mL\,min^{-1}$.

One detail that makes this research more interesting regards the extraction of pesticides in a flow. Despite the contact time being very short, removal by adsorption happens.

Another important point has to do with the superior efficiency of this magnetic composite in comparison to conventional methods, that is, short extraction time, no column blocking, good selectivity, and high reusability.

Dyes' cationic or anionic structures improve high solubility in aqueous media, which contributes to increasing their polluting effects. They represent a huge problem for both environmental and human health. Among the different techniques used to remove these water contaminants, MNP use has demonstrated a high potential for application in this area.

Rajabi et al. [34] synthesized Fe_3O_4 and modified it using aminopropyltriethoxysilane (APTES) by a chemical precipitation method. The MNPs were ground and placed with toluene in a sonic bath for 30 min. Then, the APTES was added at a 1:1 ratio, under nitrogen atmosphere and stirring. The system

was heated to 60°C for 12 h, and afterward, it was washed with dry toluene and finished with water/acetone (20:80 *v*/v). Finally, MNPs were put in a vacuum for 1 day at room temperature.

The modified MNPs were applied to remove sunset yellow (SY), an anionic dye. From measurements of transmission electron microscopy (TEM) and X-ray diffraction, the average size of the magnetic composite Fe_3O_4/APTES was estimated at 12 nm. The saturation magnetization was 54.3 emu g^{-1}. The equilibrium in removal was reached after 30 min. The adsorbed amount of SY decreased as SY concentration increased. The Langmuir model was the best to explain the adsorption process with an amount of 91.74 mg of SY per 1.0 mg of adsorbent from the following conditions: 50 mL of SY solution with initial concentrations varying from 7.5 to 30 mg L^{-1}, 10 mg of magnetic composite shaking during 45 min at pH 3.1. The MNPs' composite can be used for four times maintaining their removal properties.

What can we analyze to learn from this?

At pH 3.1, positive charges prevail on the MNPs' surfaces; if the chemical structure of the APTES was considered, it has a silicon central atom (hysterically prevented from adsorbing), three ethoxy groups (apolar), and one amino group (polar). This amino group is responsible for the positive charges in acidic media. The chemical structure of the sunset yellow, an azo compound, (as demonstrated by the authors) consists of two sodium sulfonate groups that confers anionic nature after the dye solubilizing. Sulfonic groups are conjugated bases of sulfonic acids; these are stronger acids (they generally have negative pKa). This means that sodium sulfonate groups will be a weak base, and in acidic medium, they will not be easily protonated. The other group in the chemical structure is the phenolic group (pH-OH); this one in alkaline conditions confers negative charges when it becomes a phenolate group.

From this, ionic interactions can be considered the major contribution to the adsorption of sunset yellow onto the MNP-APTES magnetic composite; however, the electron density distribution still needs to be well evaluated in this process. Considering the presence of three ethoxy groups and the aromatic rings (π-π) with their molecule conformations in the space, van der Waals forces contribute to the adsorption process. From a theoretical study, angles and energy values can be acquired.

Methylene blue (MB) is another dye that is much studied as a cationic model in the removal and degradation processes. Shao et al. [35] studied methylene blue removal using magnetic carbon nanospheres at the same time that they evaluated the catalytic degradation of MB in the presence of H_2O_2. The synthesis of Fe_3O_4 was performed by a one-pot hydrothermal method that basically uses trisodium citrate dihydrate dissolved in ethylene glycol under vigorous stirring for 1 h. Then, sodium acetate was added with stirring for 30 min. The mixture was sealed in a Teflon-lined stainless-steel autoclave and heated at 200°C for 10 h. A resulting black (Fe_3O_4 nanospheres) product was formed, and it was washed with deionized water and ethanol several times and finally dried under vacuum at 40°C.

One-pot magnetic composite was prepared with Fe_3O_4 nanospheres dispersed in ammonia aqueous in ethanol/water mixture solution (2:1 v/v) with stirring for 30 min under sonication. Then tetraethyl orthosilicate (TEOS) was added under vigorous stirring, after 10 min resorcinol was added and after again 10 min formaldehyde solution was added. The mixture was stirred for 24 h at 30°C, after this, the resulting mixture was transferred and sealed into a Teflon-lined stainless-steel autoclave. It was heated at 100°C for 24 h. The solid product was collected using a magnet, and it was purified and dried. The final step was to thermally treat the composite; for this, it was heated at 5°C min^{-1} from room temperature to 150°C and maintained in isothermal mode for 1 h under a nitrogen atmosphere. The temperature was increased at 5°C min^{-1} to 500°C and kept for 2 h. Next, the annealed sample was added into 10% wt NaOH solution, stirred for 3 h at 51°C to remove the SiO_2 shell. The resulting

sample was washed with distilled water until the pH was neutral, and then, it was dried under vacuum at 40°C.

The resulting magnetic composite showed a high specific surface area around $250\,m^2\,g^{-1}$. After encapsulation with SiO_2 and resorcinol-formaldehyde (RF), the size changed from 360 nm to approximately 460 nm, the SiO_2 and RF shell thickness being 78 ± 9 and 23 ± 4 nm, respectively. The saturation magnetization was $36.4\,emu\,g^{-1}$. The equilibrium of sorption was reached around 25 min from concentrations of 40 mg, 60 mg, and $80\,mg\,L^{-1}$, and the maximum adsorption capacity was $45.15\,mg\,g^{-1}$. The reusability was 89% of adsorption capacity after five cycles, with the total organic carbon (TOC) being measured.

Three planar rings form the chemical structure of the MB, with two terminal dimethyl amino groups and sulfur (positive charge with chlorine as counter-ion) and nitrogen atoms as heteroatoms in the middle ring. After removal of SiO_2 with NaOH and thermal treatment, the enriched carbon composite encapsulated by resorcinol reacted with formaldehyde. This latter reaction conferred thermal stability to the coverage, as indicated by thermal analysis. Therefore, it was not only the ionic groups that contributed to the adsorption. Because the resorcionol-formaldehyde reaction formed aromatic rings with —OH group in the *ortho* and *para* positions, these positions are involved in the crosslinking of the aromatic structures. As reported in the work, it was concluded that π-π stacking interactions first occur onto the magnetic composite, and after this, diffusion of the molecules into porous carbon will occur.

The control of some variables of a composite, such as pH, makes extractions of both cationic and anionic dyes possible, that is, the same material to extract two oppositely charged substances. Generally, authors sometimes prefer to study cationic or anionic dyes, but is difficult to find works that they study both at same time.

To understand this, Peng et al. [36] showed how to control the charges on the surface of the same composite to maximize the adsorption process. In certain pH levels, a cationic dye is preferably extracted, and at another level, an anionic dye is.

The strategy used to modify MNPs was to synthesize SBA-15 silica as a hard template and impregnate it with anthracene, which is the carbon source used to prepare ordered mesoporous carbon. Then, the mixture was heated at 160°C for 8 h to initiate carbonization, and it was repeated under the same conditions until the entire anthracene precursor solution was consumed. The composite was placed in a quartz glass tube and heated at 400°C for 4 h, carbonized under nitrogen at 800°C for another 4 h, used a rate of $5°C\,min^{-1}$. Finally, the mesoporous sample was filtered and washed with 1 M NaOH solution for 1 h at 100°C to remove the silica template. The end step consisted of the dispersal of $FeCl_3$ in ethanol, allowed under stirring for 6 h at room temperature. The sample was evaporated at 50°C, polymerized and carbonized at 900°C for 4 h under nitrogen atmosphere.

The results showed that a BET surface area was $731\,m^2$, average volumes of micropores of $0.24\,cm^3\,g^{-1}$, and mesopores of $0.67\,cm^3\,g^{-1}$. The saturation magnetization strength was $4.77\,emu\,g^{-1}$. The point zero charge (PZC) was estimated to be in pH 7.8, which means that over this pH, negative charges prevail on the magnetic surface of the composite. However, in a $pH < 7.8$, positive charges will prevail. Langmuir was the best model to explain the adsorption process, and the maximum adsorption capacities for anionic Orange II (O II) and cationic methylene blue (MB) dyes were 269 and $316\,mg\,g^{-1}$, respectively, from 50 mL of dye solution at pH 7.0. Despite the equilibrium time for both dyes being long, the adsorption mechanism was dominated by diffusion.

Again, analyzing the data, it is possible to see that the PZC was estimated at pH 7.8 and isotherms were performed at pH 7.0, which allows us conclude that a small amount of positive charges will prevail on the magnetic composite. This tends to favor more extraction of O II than MB, although the real

values obtained proved completely different. Therefore, this allow us to think that the chemical structures of these dyes could contribute to better explain the observed results. The O II has a central azo group that is linked in one side by a sulfonate benzene group, and the other side is linked by a 2-naftol (two aromatic rings linked with a hydroxyl group). Because the MB structure is more rigid than the O II, the latter has two sigma bounds linked to an azo group, which confers a greater degree of freedom to the molecule to accommodate onto a surface. Already, MB preferentially adsorbed in stacks due to the three connected planar rings and more rigid structure. Theoretical studies with molecular modeling involving adsorption sites and chemical structures of the dyes could contribute considerably to explain the process of adsorption in different density of surface charges. From theoretical studies, it is possible to optimize geometrical structures during the adsorption process and estimate how groups, angles, and molecule positions will better contribute to the process.

Jin et al. [37] combined experimental and theoretical studies with adsorption of 4-*n*-Nonylphenol (4-*n*-NP) and Bisphenol-A (BPA) on magnetic reduced graphene oxides. The interaction mechanisms between adsorbates and adsorvent were demonstrated by using B3LYP hybrid functional of DFT calculations with the 6-31G basis set method.

The preparation of oxide graphite (GO) was by a modification of the Hummers method, and the reduced graphite (rGO) was obtained by hydrazine hydrate. The magnetic composite of GO-magnetite was synthesized by a chemical coprecipitation method by using ferric chlorine salt and sulfate ferrous. The solutions of the iron salts were added dropwise in an aqueous dispersion of rGO previously treated in an ultrasonic bath. Ammonium solution was added under vigorous stirring until pH 10. After this, the mixture was heated at 90°C and hydrazine was added a dispersion and kept for 4 h, then a black dispersion was obtained.

The characterization evidenced that the saturation magnetization was $19.16\,\text{emu}\,\text{g}^{-1}$. The size of iron particles was 50 nm per 50 nm measured by TEM. Zeta Potentials of magnetic rGO were studied in pH range of 4.0–7.5 to avoid deprotonation of BPA and 4-*n*-NP that occurs at $\text{pH} > 8.0$. From Zeta Potential, the ZPC stays in a range of pH 5.0–7.0, at $\text{pH} < 5.0$ positive charges will occur onto magnetic rGO surface, and in a $\text{pH} > 7.0$ negative charges will prevail. Surface area of magnetic rGO was $112.15\,\text{m}^2\,\text{g}^{-1}$. The Freundlich model was the best to fit the results and showed a maximum removal of $63.96\,\text{mg}\,\text{g}^{-1}$ to 4-*n*-NP and $48.74\,\text{mg}\,\text{g}^{-1}$ to BPA, at 293 K and pH 6.5. Removal in a $\text{pH} > 8.0$ a little decrease was observed due to the negative charges formed in adsorbate and adsorbent, which repulsions tend to increase. However, even with negative charges on both adsorbent and adsorbate, adsorption occurred. This always strengthens the idea of taking into account the density of charge distribution in the chemical structures.

The theoretical calculations allowed to verify that adsorption energy of magnetic rGOs and 4-*n*-NP was $9.77\,\text{kcal}\,\text{mol}^{-1}$ mainly due to π-π stacking and flexible long alkyl chain of 4-*n*-NP. For rGOs and BPA was $6.71\,\text{kcal}\,\text{mol}^{-1}$ and molecules positions were almost similar in adsorption of 4-*n*-NP.

Finally, the authors report that, "DFT calculations indicate that the hydrogen bonding, hydrophobic interaction, and π-π stacking dominate the adsorption," which show us that adsorption is a phenomenon controlled not by one variable, but by several.

1.5 FINAL CONSIDERATIONS

There is a lot of research involved in this chapter that has not been presented. The main goal was to illustrate some strategies used by some researchers without worrying about what they did. Only one look was taken to involve the reader in the act of thinking about which variables control the adsorption

process. This will awaken one to the idea of reflection before thinking of producing magnetic nanoparticles, to afterward chemically modify their surfaces, and finally, apply them toward the purification of water.

Some characterization data from the articles, such as magnetization, zeta potential, surface area, pH variation, maximum removal capacity, chemical groups, etc., was put forth for the reader to quickly compare how different strategies for preparation of modified MNPs affect the adsorption process and consequently, the removal of pollutant from water.

Finally, it was seen that in most cases, theoretical calculations could contribute very much to understanding how the molecules adsorbed onto a surface with lower adsorption energy.

REFERENCES

[1] E. Mendelovici, R. Villalba, A. Sagarzazu, Thermochim. Acta 318 (1–2) (1998) 51–56.
[2] Y.I. Kim, D. Kim, C.S. Lee, B. Physica, Condens. Matter 337 (1–4) (2003) 42–51.
[3] F. Bensebaa, F. Zavaliche, P. L'Ecuyer, R.W. Cochrane, T. Veres, J. Colloid Interface Sci. 277 (1) (2004) 104–110.
[4] E. Tirosh, G. Shemer, G. Markovich, Chem. Mater. 18 (2) (2006) 465–470.
[5] P. Berger, N.B. Adelman, K.J. Beckman, D.J. Campbell, A.B. Ellis, G.C.J. Lisensky, Chem. Ed. 76 (7) (1999) 943–948.
[6] C.S.S.R. Kumar (Ed.), Nanomaterials for the life sciences, in: Magnetic Nanomaterials, Tom Lowery, Biosensing and Diagnosis in Nanomaterials-Based Magnetic Relaxation Switch Biosensors, Vol. 4, WILEY-VCH Verlag GmbH & Co. KGaA, Weinheim, ISBN: 978-3-527-32154-4, 2009.
[7] A.-H. Lu, E.L. Salabas, F. Schuth, Angew. Chem. Int. 46 (2007) 1222–1244.
[8] S. Sun, Self-assembled nanomagnets, Printed in the United States of America (Chapter 9), in: D. Sellmyer, R. Skomski (Eds.), Advanced Magnetic Nanostructures, Springer Science + Business Media, Inc., New York, 2006.
[9] R.J. Hunter, Zeta Potential in Colloid Science: Principles and Applications, Academic Press Limited, Oxford, 1981, p. 391p.
[10] F.A. Tourinho, A.F.C. Campos, R. Aquino, M.C.F.L. Lara, G.J. da Silva, J. Depey-rot, Braz. J. Phys. 32 (2002) 501–508.
[11] N.C. Feitoza, T.D. Gonçalves, J.J. Mesquita, J.S. Menegucci, M.-K.M.S. Santos, J.A. Chaker, R.B. Cunha, A.M.M. Medeiros, J.C. Rubim, M.H. Sousa, J. Hazard. Mater. 264 (2014) 153–160.
[12] A.A. Estelle, Mater. Sci. Technol. 32 (17) (2016) 1763–1770.
[13] W.M. Haynes, D.R. Lide, CRC Handbook of Chemistry and Physics, CRC Press/Taylor & Francis Group, New York, 2010.
[14] J.F. Liu, Z.S. Zhao, G.B. Jiang, Environ. Sci. Technol. 42 (2008) 6949–6954.
[15] J. Duan, J. Gregory, Adv. Colloid Interf. Sci. 100–102 (2003) 475–502.
[16] N.C.C. Lobato, M.B. Mansur, A.M. Ferreira, Mater. Res. 20 (3) (2017) 736–746.
[17] X. Liu, Q. Hu, Z. Fang, X. Zhang, B. Zhang, Langmuir 25 (2009) 3–8.
[18] A. Bée, D. Talbot, S. Abramson, V. Dupuis, J. Colloid Interface Sci. 362 (2011) 486–492.
[19] R. Verma, A. Asthana, A.K. Singh, S. Prasad, A.B.H. Susan, Microchem. J. 130 (2017) 168–178.
[20] Roque-Malherbe, M.A. Rolando, Adsorption and diffusion in nanoporous materials, Taylor & Francis Group, LLC, CRC Press is an imprint of Taylor & Francis Group, New York, 2007. 270p.
[21] S.-H. Huang, D.-H. Chen, J. Hazard. Mater. 163 (2009) 174–179.
[22] Y. Huang, A.A. Keller, Water Res. 80 (2015) 159–168.
[23] Y. Ren, H.A. Abbood, F. He, H. Peng, K. Huang, Chem. Eng. J. 226 (2013) 300–311.

[24] S.G. Wang, W.X. Gong, X.W. Liu, Y.W. Yao, B.Y. Gao, Q.Y. Yue, Sep. Purif. Technol. 58 (2007) 17–23.
[25] H.J. Cui, J.W. Shi, B. Yuan, M.L.J. Fu, Mater. Chem. A 1 (2013) 5902–5907.
[26] S. Kumar, R.R. Nair, P.B. Pillai, S.N. Gupta, M.A.R. Iyengar, A.K. Sood, ACS Appl. Mater. Interfaces 6 (2014) 17426–17436.
[27] Y. Zhang, L. Yan, W. Xua, X. Guo, L. Cui, L. Gao, Q. Wei, B. Du, J. Mol. Liq. 191 (2014) 177–182.
[28] S. Ma, S. Zhan, Y. Jia, Q. Zhou, ACS Appl. Mater. Interfaces 7 (2015) 10576–10586.
[29] EC, 1998. Council Directive 98/83/EC of 3 November 1998 on the quality of water intended for human consumption.
[30] S. Harrad, Persistent Organic Pollutants, John Wiley & Sons Ltd, Chichester, 2010.
[31] S.K. Sharma, Green Chemistry for Dyes Removal from Wastewater, John Wiley & Sons, Inc/Scrivener Publishing LLC, Hoboken, NJ/Salem, MA, 2015.
[32] P.K. Boruah, B. Sharma, N. Hussain, M.R. Das, Chemosphere 168 (2017) 1058–1067.
[33] S. Meseguer-Lloret, S. Torres-Cartas, M. Catalá-Icardo, E.F. Simó-Alfonso, J.M. Herrero-Martínez, Anal. Bioanal. Chem. 409 (2017) 3561–3571.
[34] H.R. Rajabi, H. Arjmand, S.J. Hoseini, H. Nasrabadi, J. Magn. Magn. Mater. 394 (2015) 7–13.
[35] Y. Shao, L. Zhou, C. Bao, J. Ma. Carbon 89 (2015) 378–391.
[36] X. Peng, D. Huang, T. Odoom-Wubah, D. Fu, J. Huang, Q. Qin, J. Colloid Interface Sci. 430 (2014) 272–282.
[37] Z. Jin, X. Wang, Y. Sun, Y. Ai, X. Wang, Environ. Sci. Technol. 49 (2015) 9168–9175.

CHAPTER

MAGNETIC NANOPARTICLES FOR WATER PURIFICATION

20

Carlos Martinez-Boubeta*, Konstantinos Simeonidis†

Freelancer in Bilbao, Bilbao, Spain Department of Chemical Engineering, Aristotle University of Thessaloniki, Thessaloniki, Greece†*

1 INTRODUCTION

The current and potential uses of nanomaterials refer to a wide range of applications in several sectors including manufactures, electronics, energy generation and storage, sensors, biomedicine, and environment processes. Whenever nanomaterials represent a primary or secondary constituent of a structure or device, their presence is essential throughout the expected lifetime of operation. However, very frequently, nanomaterials are considered an unpleasant byproduct after fulfilling their role in a process. The need to separate or recover nanomaterials usually relies on the high value of the used nanomaterial itself, the demand for high purity in the process outcome, or the potential adverse effects on human health and the natural environment. In the same regard, enabling the complete recovery of nanoparticles (a class of nanomaterials characterized as isolated crystalline units with dimensions in the nanoscale) by a posttreatment process is a major requirement for their successful implementation in water purification technology.

Water purification by nanoparticles is a rather challenging field of technology which is determined by a number of restrictions related to (i) the low concentrations of pollutants to be treated, (ii) the extremely low regulation limits that should be accomplished after treatment, and (iii) the need to ensure the absence of nanoparticles in purified water and waste streams. In general, a high uptake efficiency against inorganic (heavy metals) and organic (pesticides, microorganisms, pharmaceuticals) pollutants can be realized by case-specific inorganic nanoparticles which either work as the direct active phase (dispersed in water or attached on a solid matrix) or as a carrier onto which another active phase or molecule is loaded. However, beyond the attempt to develop optimized nanoparticles with high affinity to water pollutants, the separation of used nanoparticles from the purified water stream should be considered an equally important task of the process design. Suggestively, with respect to the large quantities of nanoparticles that should be removed in full-scale systems using particles dispersion, the cost for particles separation may be the dominant consideration if a typical nanofiltration step is applied. Other solid separation methods, such as coagulation, are in a position to diminish the cost of nanoparticles removal. Nevertheless, the main disadvantage is the addition of chemical agents, which destabilize the dispersion but may have severe impact on other water quality parameters, or even the chance for nanoparticles recycle.

Nanoscale Materials in Water Purification. https://doi.org/10.1016/B978-0-12-813926-4.00026-4

To overcome the issue of nanoparticles recovery after application in water purification, magnetic separation processes (i.e., magnetophoresis) present a more sophisticated way promising minimum chemical or physical interaction with treated water, very low cost, total recovery of nanoparticles, and multiple options for the design of the process. Magnetophoresis is also favorable due to the fact that many of the accessible nanoadsorbents consist of phases with high magnetic response (iron oxides, zero-valent iron) whereas magnetic nanoparticles can be easily used as substrates for other active phases. This chapter focuses on the current progress in the development of magnetic nanoparticles for the treatment of drinking water from emerging pollutants and the consecutive effort to provide integrated continuous-flow systems succeeding their sufficient dispersion and the complete recovery by means of magnetophoresis techniques. Considering the numerous studies presenting engineered magnetic nanoparticles as potential water treatment agents for various heavy metals and organic pollutants, discussion will emphasize only those research studies which succeed in competitive removal capacities under conditions similar to those met during the purification of natural water (pollutant concentrations, acidity, compliance with regulation limits). Another important part of the chapter will be devoted to the review of magnetic separation processes for the recovery of dispersed nanoparticles and the establishment of a direct correlation between the magnetic features of nanomaterials and the appropriate design of a magnetic separation unit.

2 MAGNETIC PROPERTIES OF NANOPARTICLES

In everyday life, magnetic fields are most often encountered as a force exerted on a magnet. Such is the case of alignment of the compass needle. So-called magnets have a permanent magnetization as a result of their structure at the atomic level, usually described as due to the spinning of electrons around certain orbits, though there is still some confusion and uncertainty about a general theory of magnetic phenomena, which requires a quantum-mechanical description [1]. Nonetheless, electricity and magnetism are fundamentally interlinked, in that a magnetic field is also established whenever electric charges are in motion. For instance, as discussed in Section 4, electromagnets create such fields from electric current moving through coils.

And because any material is composed of electrons, shows one or another type of magnetic response to a field. For a more detailed insight, the reader may refer to [2]. Fortunately, all one needs to know for the present discussion is that the magnetization vector field M represents how strongly a region of material is magnetized. Magnetization is defined as the net magnetic dipole moment per unit volume of that region. In terms of their magnetic behavior, materials respond to an applied field H by producing their own magnetization and, therefore, total magnetic field in the material comes as

$$B = \mu_0 (H + M) \tag{1}$$

which may also propagate outside the magnet as a stray field.

Materials called *diamagnetic* are those that laymen generally think of as nonmagnetic, and include water, most organic compounds, and many heavy metals such as copper and mercury. These substances are composed of atoms which have no unpaired electrons (i.e., all the orbital shells are filled) and thus, cannot accommodate a magnetic flux. And so, they are usually represented as materials with the magnetic permeability less than μ_0, the permeability of vacuum. This means that diamagnetic materials are weakly repelled by strong magnetic fields. Typically, any modelization of the response involves making a series of approximations, in which for such a small perturbation, the linear response theory

provides an appropriate relation as $M \sim \chi H$, being χ the magnetic susceptibility. So, Eq. 1 can be rewritten $B = \mu_0(H + \chi H) = \mu H$ because the magnetic susceptibility and the permeability are related as $\mu = \mu_0(1 + \chi)$, which means $\chi < 0$ in diamagnets.

On the other hand, $\chi > 0$ includes materials that are attracted to the regions of maximum observed field. In a *paramagnetic* material, there are unpaired electrons (i.e., partially filled orbitals). Examples include aluminum, magnesium, and oxygen molecules. While paired electrons are required by the Pauli exclusion principle to have their intrinsic "spin" magnetic moments pointing in opposite directions, causing their magnetic fields to cancel out, unpaired electrons are free to align themselves in the same direction as the applied field, thus reinforcing it. The susceptibility of paramagnetic materials is inversely proportional to their temperature, that is, magnetism is enhanced at lower temperatures (what is known as Curie's law). But they lack strong interactions, and so, in the absence of an applied field, the magnetic moments in a paramagnetic material do not spontaneously line up parallel to one another.

Another class of magnetic materials includes strongly electron-correlated materials with incomplete d- or f-electron shells. Obviously then, the relationship between field strength H and magnetization M is not linear but describes a loop named hysteresis (Fig. 1). For a large enough magnetic field

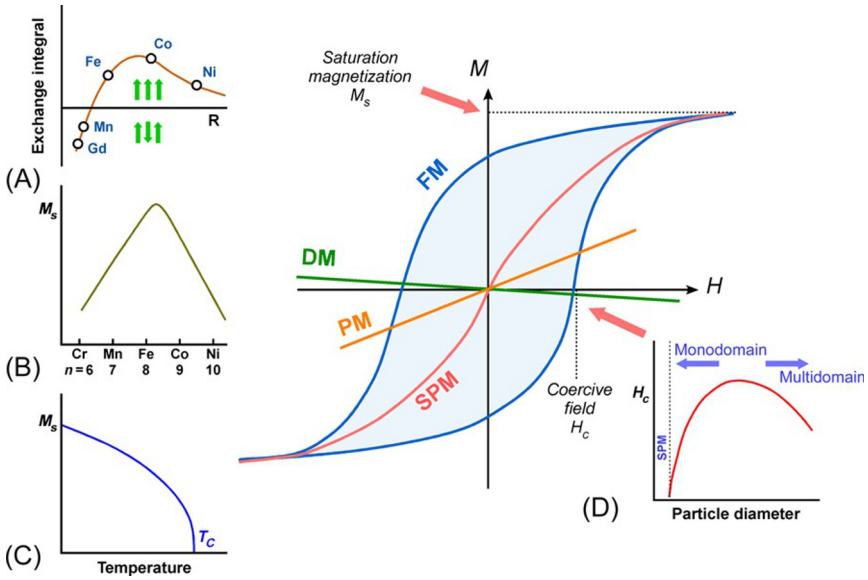

FIG. 1

Prototypical magnetic hysteresis curve (magnetization versus field) for a collection of ferromagnetic (FM) single-domain particles. The dia- (DM), para- (PM), and superpara- (SPM) magnetic dependencies are also illustrated. Schematics of the Bethe-Slater curve for the exchange energy, which is associated with the entanglement of electrons among orbits, as a function of the ratio of interatomic distance to diameter of 3d-orbit. (A). Slater-Pauling curve showing dependence of magnetization on the number of valence electrons per atom. (B). Magnetization dependence as a function of temperature. (C). Magnetization becomes null at the so-called Curie temperature T_C. Dependence of coercivity on particle size. (D). Coercivity is null for SPM particles, and maximizes in the mono-multidomain transition whereas only rotational processes are important, whilst in large volumes the reversal field is reduced owing to the nucleation and magnetic domain-wall movement.

that overcomes all sources of magnetic anisotropy (quantified by the corresponding constant K_{eff} which somehow reflects the interaction energy between spins on neighboring atoms) and aligns all of the atomic dipole moments, the magnet is said to be saturated. The saturation magnetization (M_S) is thus an intrinsic magnetic property of each material. Upon cycling of the field, it is not until a value called coercivity (H_c) that the magnetization reduces back to zero. And despite the fact that an upper bond for coercivity can be described in terms of M_S and the K_{eff}, the coercivity is usually considered an extrinsic property. The composition, size, and shape (which are considered the three main characteristics determining the magnetic response of a nanoparticle) are further analyzed hereafter.

2.1 COMPOSITION

The internal field in *ferromagnetism* may be a thousand times greater ($\chi \gg 1$) than that of diamagnetic and paramagnetic materials. Unfortunately, it is a relatively rare property among the elements, occurring only in the transition metals iron, nickel, and cobalt, and in the lanthanides. The simplest model to account for this many-body phenomenon roots in Heisenberg exchange nearest-neighbor interactions as a function of interatomic distance, graphically illustrated in Fig. 1A (known as the Bethe-Slater curve). A positive value of the exchange integral is therefore a necessary condition for ferromagnetism to occur; otherwise, the lowest energy state results from antiparallel spins (i.e., *antiferromagnetic* order).

Fig. 1B shows that magnetization scales with the number of valence electrons. It shows that the largest moments are to be expected in the case of bcc FeCo alloys. Interestingly, if by some means, the Mn-Mn distance is made large enough for the exchange interaction in Fig. 1A to become positive, as happens in many of the so-called Heusler alloys and perovskites (Cu_2MnSn, Mn_2VGa, $La_{1-x}Sr_xMnO_3$, etc.), ferromagnetic order will promote. The same issue applies to CrO_2.

The saturation moment of pure Fe, Ni and Co at room temperature amounts 210, 50, and 160 emu/g, respectively [3]. But particles made of these elements would inevitably need a rust-resistant protective coating, which comes at the cost of some loss in magnetization. In this regard, one of the goals has been to determine to what extent the magnetization could be increased as a result of the control of core-shell ratios in engineered nanoparticles [4, 5].

Therefore, and with the aim of reaching high magnetic signals and satisfactory chemical stability, iron oxides have been historically favored. Derivatives of Fe(III) oxides, called ferrites, exhibit a substantial spontaneous magnetization at room temperature. They are named *ferrimagnetic* substances. Many are spinels (e.g., $CoO{\cdot}Fe_2O_3$), although some ferrites have hexagonal crystal structure (e.g., $BaO{\cdot}6Fe_2O_3$). Just like ferromagnets, they exhibit hysteresis and their spontaneous magnetization disappears above a certain critical temperature, the Curie temperature (Fig. 1C). In fact, subtle differences in the approach to the critical point would permit to discern a ferro- from a ferrimagnet, the saturation magnetization of most ferrimagnetics decreases more rapidly than that of a ferromagnetic. Conclusively, the mentioned superior ferro- and ferrimagnetic properties are a significant advantage for the rapid sequestration of particles by means of magnetophoresis.

2.2 SIZE

For what matters to us, the magnetism in nanomaterials shows the effects of reduced dimensions. On the one hand, strong variations of coercivity with respect to particle size are well-known to arise from

thermal fluctuations that induce random flipping of the magnetic moment. The competing effects of anisotropy energy ($K_{\text{eff}}V$) and temperature (k_BT, being k_B the Boltzmann constant) produces a coercivity maximum that corresponds to the limiting size for the so-called monodomain region (Fig. 1D). Thus, above a so-called blocking temperature, the hysteresis loop collapses showing zero coercivity, as depicted in Fig. 1. The range of particle sizes over which iron oxides show single domain behavior and hysteresis at room temperature are about 20–100 nm, with bigger sizes leading to hysteresis but nonuniform magnetization states. When it comes to zero-valent iron, particles exhibit single-domain ferromagnetic behavior for dimensions about 15–30 nm with a transition to a nonuniform state beyond that point [6].

Another issue is that surface effects become increasingly important the smaller the size, when the number of spins located close to the particle surface is of the order of net magnetic dipoles. Therefore, not only does size make nanoparticles more chemically reactive, which could be advantageous for the adsorption of pollutants from the aqueous phase, but it also seems hardly possible to separate surface and volume magnetic degrees of freedom. For instance, the dominant phase in typical iron oxide nanocrystals around 5 nm in size is γ-Fe_2O_3, whereas, the proportion of the Fe_3O_4 component gradually increases on increasing the particle volume [7]. And the magnetization will change, as well, upon increasing the size because the number of Fe^{2+} ions in the octahedral sites to Fe^{3+} changes. Thus, assuming the average oxide density of about 5 g/cm^3, one would expect the saturation magnetization (bulk) about 80 emu/g, while values of only 40 emu/g are most normally reported. This probably stems from the presence of a certain amount of a nonstoichiometric (paramagnetic) Fe_xO wüstite.

2.3 SHAPE

Many of the aforementioned effects are enhanced when the geometrical shape factors of the particles are different, for example, rods, spheres, or cubes. In a very simple approximation, the anisotropy energy of a spherical particle with diameter D may be described by one contribution from the bulk (i.e., crystalline) and another from the surface: $K_{\text{eff}} = K_V + \frac{6}{D}K_S$, where K_V and K_S are the bulk and surface anisotropy energy constants, respectively. So, by decreasing the diameter, K_{eff} will normally increase. But the surface anisotropic terms would certainly also differ in spherical and cubic nanoparticles of similar dimensions, leading to differences in effective anisotropy energy and hence, in their magnetic behavior [8, 9], which does have strong implications for the optimization of a wide family of nanoadsorbent materials. An example of the latter refers to the microbial harvesting step in water treatment; it was found that rod-like particles are a superior candidate for enhancing the magnetophoretic separation compared to spherical ones, due to their stable magnetic moment originating from shape anisotropy and the tendency to form large chaining aggregates [10]. The presence of dipole-dipole interactions is responsible for the aggregation of magnetic particles, which can be used to facilitate the separation process [11].

3 MAGNETIC NANOPARTICLES IN WATER PURIFICATION

In recent research, nanoparticles consisting of materials with magnetic characteristics have been commonly tested as adsorbents for the removal of pathogenic and polluting compounds from water. Nevertheless, magnetism is not usually considered the major advantage for their use. The broad

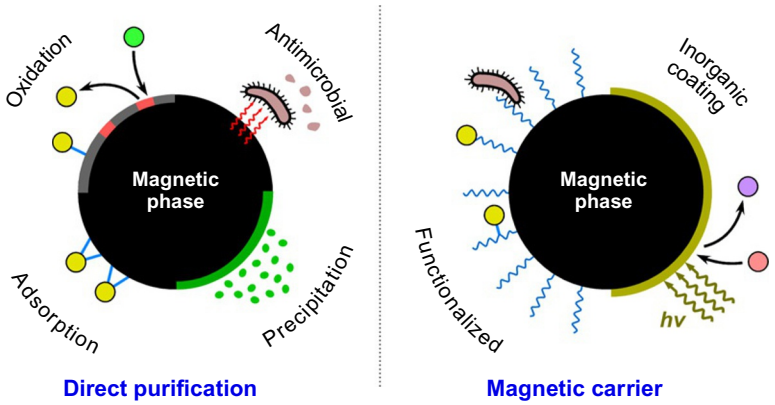

FIG. 2

Summary of possible water treatment mechanisms in engineered magnetic nanoparticles applied as direct purification agents or as magnetic carriers of other phases.

possibilities for tuning surface charge and redox activity or their good affinity to the soluble forms of many pollutants are typical reasons for their qualification among other nanomaterials. Therefore, an overview of relevant studies will be carried out on the basis of whether magnetic nanoparticles are applied as single-phase nanoadsorbents for their ability to uptake pollutants on their surface or as magnetically driven carriers of other active phases (Fig. 2).

3.1 DIRECT PURIFICATION AGENTS

Iron-based materials, including oxy-hydroxides (FeOOH), oxides (Fe_3O_4, α-Fe_2O_3, γ-Fe_2O_3), zero-valent iron (ZVI) and some alloys, are the most widely applied class of granulated adsorbents in water treatment technology. Their efficiency is the result of a variety of possible mechanisms occurring on their surface and their selectivity for nonreversible adsorption of pollutants through Fe-O bridges. Ideally, their performance should be multiplied when delivered in the form of nanoparticles because decrease of dimensions implies the increase of available binding surfaces for pollutants. Among them, Fe_3O_4, γ-Fe_2O_3 and ZVI combine these capabilities with considerable magnetic properties.

3.1.1 Zero-valent iron

Metallic iron nanoparticles illustrate the highest magnetization value, and therefore, their presence is expected to facilitate the magnetic recovery step. In addition, when stabilized, nanoscale ZVI shows extremely high surface activity and reducing potential. For this reason, ZVI nanoparticles are widely applied for the reduction of toxic heavy metals that appear in a high oxidation state in water. For instance, the highly mobile and toxic form of hexavalent chromium is reduced to the insoluble trivalent form during contact with the ZVI surface. Numerous studies examine such reduction of Cr(VI) followed by the precipitation of Cr(III) using ZVI nanoparticles whether dispersed or embedded on inert substrates. Few of them provide an estimation of their efficiency under realistic conditions of drinking water treatment. In a representative case, ZVI nanoparticles prepared by a physical vapor deposition technique, exhibited a Cr(VI) removal capacity of 3 mg/g for residual concentration equal to the current

regulation limit (50 μg/L) [12]. Unfortunately, in most cases, presented results are of limited practical interest due to the extremely high Cr(VI) concentrations and the low pH values studied. The ability of ZVI nanoparticles to capture Cr(VI) was sufficiently demonstrated at relatively high concentrations at pH 3 [13]. The proposed mechanism verifies the initial reduction of Cr(VI) and the gradual formation of a passivation layer of hydroxyl-chromites.

In order to improve Cr(VI) uptake efficiency, the limitation of particles aggregation or the inhibition of surface passivation are usually attempted. A good control over ZVI nanoparticles aggregation can be obtained by their immobilization on supporting structures. ZVI nanoparticles indicated a significant ability to remove Cr(VI) during experiments performed in a pH range 5–6.5 when mesoporous carbon [14], carbon nanotubes [15], graphene [16], or humus [17] were used as supporting structures. Bentonite-supported nano-ZVI indicates an improvement in Cr(VI) removal efficiency compared to unsupported particles [18]. Another approach introduces 80 nm ZVI nanoparticles immobilized on a mesoporous silica matrix as a way to achieve a higher contact surface with Cr(VI)-polluted water [19, 20]. In spite of the rapid kinetic of Cr(VI) removal at relatively high concentrations, the mentioned presence of surface oxidation on ZVI is an important drawback for further investigation.

Therefore, modification of routes for nanoscale ZVI preparation and application was also tested; their preparation in the presence of anionic dispersants [21], leaf extracts [22], or cation resins [23] appears to have a positive effect in the stabilization against passivation, enabling a higher reducing potential for Cr(VI) removal. Coupling with ultrasonics was also suggested as a way to activate ZVI nanoparticles by assisting better dispersion and chemical reactivity [24].

Apart from Cr(VI), redox-activated ZVI nanoparticles have been tested for the uptake of other high valent forms of heavy metals such as selenium, uranium, and antimony. In particular, the removal of Se was reported to take place through the initial reduction of Se(VI) in the presence of nano-ZVI or direct adsorption of Se(IV), though the experimental conditions were not representative of natural waters [25, 26]. A similar approach was followed to reduce U(VI) in the less mobile form of U(IV). A significant removal efficiency was observed under anoxic conditions [27]. The possibility to trigger the reducing-precipitation of U(VI) by ZVI nanoparticles under acidic conditions is also described in other relevant studies [28, 29]. However, the release of iron corrosion products into treated water and the easy leaching of U(IV) in the presence of dissolved oxygen are the main disadvantages of the process. Finally, the evaluation of their performance against Sb(V) indicated a very poor efficiency [30].

The spontaneous surface oxidation of ZVI nanoparticles may turn into an advantage when dealing with the removal of aqueous arsenic species. Formed iron oxides and oxy-hydroxides show a high affinity to both As(III) and As(V) oxy-ions providing a competitive adsorption capacity to nano-ZVI. A maximum capacity of 5 mg/g for residual concentration of As(V) equal to 10 μg/L has been reported for 15 nm ZVI nanoparticles [31], whereas lower values below 2 mg/g for As(III) and As(V) were found by other researchers [32–34]. The performance of nanoscale ZVI for the adsorption of bivalent heavy metals Pb^{2+}, Ni^{2+}, Cd^{2+}, and Hg^{2+} has been also demonstrated [35–38].

Similar to the biocidal activity of other zero-valent metals, such as silver, ZVI nanoparticles may also participate in antimicrobial processes and, thus, contribute in drinking water disinfection. The toxic effect has been demonstrated for a series of bacterial cells and fungi including *Escherichia coli* [39], *Bacillus subtilis* [40], *Pseudomonas fluorescens*, and *Aspergillus versicolor* [41]. The antimicrobial mechanism is based on the activation of a Fenton reaction between released Fe^{2+} ions and intercellular oxygen and hydrogen peroxide. In addition, due to their small dimensions, ZVI nanoparticles can penetrate easier to the cells of pathogens. The role of particles aging, the presence of

polyelectrolytes or natural organic matter and local pH variation are also determinant parameters of the observed antimicrobial properties [42, 43].

The category of organic pollutants includes chlorinated aliphatic and aromatic molecules, pharmaceuticals, pesticides, detergents, volatile organic compounds, and natural organic matter. The dechlorination of trichloroethylene is a widely studied example of nanoscale ZVI application in this field [44–47]. Zero-valent iron nanoparticles also appeared efficient in treating a variety of other chlorinated compounds such as alachlor [48], atrazine [49], lindane [50], perchlorate [51] and chlorophenols [52]. The removal of ibuprofen [53], dyes [54] and herbicides [55] are some other indicative uses of ZVI nanoparticles.

3.1.2 Magnetite (Fe_3O_4)

Iron oxide nanoparticles is another important class of magnetic nanoadsorbents frequently applied for water treatment, with magnetite (Fe_3O_4) being the dominant one. In comparison to nanoscale ZVI, magnetite nanoparticles appear much more stable against structural and chemical transformation though their magnetization values are less than the half of ZVI. Magnetite nanoparticles show a relative good affinity to a variety of heavy metals enabling direct adsorption of their oxy-ionic forms whereas they preserve some reducing potential due to the presence of a Fe^{2+} atom in their crystal structure.

For instance, magnetite nanoparticles show good performance in the reduction and precipitation of Cr(VI) from water. Experiments carried out under conditions similar to natural water treatment revealed that uptake capacity reaches 4.5 mg/g at a residual Cr(VI) concentration equal to 50 μg/L for 30 nm Fe_3O_4 nanoparticles [56]. Further research indicated that the effect of particles size and contact configuration are critical in the determination of the efficiency. Increasing the particles size is responsible for significant loss in Cr(VI) removal [12], whereas extending the contact period between particles and polluted water by placing nanoparticles in a column bed instead of the short term dispersion in a contact tank almost doubles the uptake capacity [57]. The capture mechanism of Cr(VI) by Fe_3O_4 nanoparticles initiates with the reduction of Cr(VI) by the Fe^{2+} sites located on the tetrahedral sites of its structure and proceeds with the diffusion, adsorption and complexation of Cr(III) on particles surface [58, 59]. This procedure causes the gradual passivation of particles surface and the formation of a γ-Fe_2O_3 layer. Batch experiments suggest that the uptake of Cr(VI) on Fe_3O_4 nanoparticles is an endothermic process with very fast kinetic [60–62].

The performance of Fe_3O_4 nanoparticles has been studied for the case of selenium as well. Importantly, when embedded on graphene oxide, Fe_3O_4 nanoparticles indicated an uptake capacity of around 1.9 mg/g at a Se(IV) residual concentration of 10 μg/L [63]. However, other relevant research suggests a much lower capacity for Se(VI) [64–67]. The reducing potential of Fe_3O_4 nanoparticles was also examined for the removal of Hg^{2+} [68, 69] and U(VI) [70].

It is worth mentioning that adsorption of arsenic species is the most discussed field for application of Fe_3O_4 nanoparticles in water treatment. However, only few works are focused on pH values and initial and residual concentrations similar to those met in drinking water. The best results were reported for oleic acid coated nanoparticles with a size 12 nm [71]. The estimated adsorption capacity for As(III) and As(V) is around 2 mg/g for residual concentration of 10 μg/L and follows a decreasing trend as the diameter of nanoparticles increases. Considering the interfering role of fatty acids on the surface activity [72], further optimization might be accesible if particles isolation could be handled with a different approach than surfactants. Plenty of other studies support the potential of Fe_3O_4 nanoparticles against arsenic oxy-ionic forms though providing much lower efficiency [73–75]. The high

concentration of cation vacancies in hollow nanoparticles adds to the increased specific surface area, hence indicating enhanced adsorption capacity for both As(III) and As(V) [76]. In this regard, adsorption of As(III) and As(V) by Fe_3O_4 nanoparticles follows a first-order rate equation requiring a minimum of 3 h to reach equilibrium [77].

The removal of bivalent ions such as Pb^{2+}, Cd^{2+}, and Ni^{2+} using Fe_3O_4 nanoparticles is also evidenced at high concentrations. In particular, electrochemically synthesized Fe_3O_4 nanorods indicate some potential to uptake these pollutants but the estimated capacity at low concentrations (5 μg/L) is very close to zero [78].

Last, magnetite nanoparticles attracted limited interest as antimicrobial agents as a consequence of their limited toxicity in cells. Consequently, the reported inactivation of *Staphylococcus aureus* [79] can be attributed to adsorption rather than any toxic interaction. More research has been carried out for the adsorption of organic pollutants such as pesticides and dyes by Fe_3O_4 nanoparticles. For instance, the efficient removal of organochlorine or organophosphorus pesticides [80–82], triazine herbicide [83], and bromelain [84] have been recently reported. It should be pointed that in many cases, the selective uptake of organic pollutants by Fe_3O_4 nanoparticles is oriented to analytical purposes rather than water purification.

3.1.3 Maghemite (γ-Fe_2O_3)

From the structural point of view, maghemite (γ-Fe_2O_3) has very similar crystal arrangement to magnetite. However, the substitution of the Fe^{2+} atoms by a void is responsible for the slight loss in magnetic properties. The exclusive presence of Fe^{3+} in γ-Fe_2O_3 nanoparticles implies to a high chemical stability but also to the absence of any reducing activity. For this reason, their efficiency mainly refers to the chemisorption of pollutants with high affinity to Fe^{3+}.

Maghemite nanoparticles are considered better adsorbents for As(V) than magnetite [85]. Their ability to bind with As(V) oxy-ions is attributed both to the adsorption on the γ-Fe_2O_3 structure or on the hydrolyzed surface formed after contact with water. In addition, γ-Fe_2O_3 nanoparticles may reach smaller sizes and, therefore, achieve a higher specific surface area or secondary porosity. In fact, the formation of a thin γ-Fe_2O_3 layer on Fe_3O_4 or ZVI nanoparticles most probably explicates the performance of these other phases against arsenic [7]. The evaluation of maghemite nanoparticles (23 nm) prepared by an electrochemical route in As(V) removal demonstrated the potential use of these systems in drinking water treatment [86]. Adsorption is characterized as an irreversible endothermic process which follows a pseudo-first order kinetic model limited by the mass transfer of As(V) oxy-ions. Further research signifies that decrease of particles dimensions improves capacity, while the oxidation of As(III) becomes favorable [87].

As explained earlier, γ-Fe_2O_3 nanoparticles are not considered redox-active systems, implying their weakness in contributing to the uptake high-valent heavy metal forms. Consequently, few works deal with the removal of Cr(VI), Se(IV), and Mo(VI) from water. The adsorption of Cr(VI) on γ-Fe_2O_3 nanoparticles, studied at relative high concentrations, shows fast kinetic following a two stage mechanism: surface diffusion sequenced by intraparticle diffusion [88, 89]. The possibility of applying maghemite nanoparticles as selenium or molybdenum adsorbents was also evaluated without significant results [90–92].

Not much effort has been expended concerning the efficiency of γ-Fe_2O_3 nanoparticles as direct organic pollutants adsorbent. Their potential was illustrated only for the uptake of organic dyes [93].

3.1.4 Ferrites

Nanoparticles consisting of ferrite structures is another class of magnetic materials tested in water treatment. In fact, ferrites are formed after the substitution of the Fe^{2+} atom in the crystal of magnetite by another bivalent metal, having a general formula of MFe_2O_4, M = Co, Mn, Ni, Cu, Zn, Mg, etc. These systems have shown some limited potential for the uptake of heavy metal forms from water. Suggestively, $MnFe_2O_4$ nanoparticles have been tested for the removal of Cr(VI) [94, 95], while $CuFe_2O_4$ [96] and $ZnFe_2O_4$ [97] ones indicated some efficiency for capturing Mo(VI), but experiments were carried out under unrealistic conditions for drinking water purifications. Hollow $CoFe_2O_4$ nanoparticles were also reported as potential U(VI) adsorbents [98]. In contrast to the case of high-valent heavy metals, ferrite nanoparticles showed better performance in the treatment of water polluted with arsenic. More specifically, small $MgFe_2O_4$ nanoparticles succeeded at achieving a significant capacity of around 10 mg/g for both As(III) and As(V) using polluted tap water [99]. Other studies also examined $CoFe_2O_4$, $NiFe_2O_4$, and $MnFe_2O_4$ nanoparticles for arsenic removal [100–102]. Magnetically recoverable graphene-supported $MnFe_2O_4$ nanoparticles displayed significant efficiency as photocatalysts for the degradation, mineralization and inactivation of antibiotics [103]. However, the leaching of metal ions which are also toxic pollutants (Mn, Co, Ni, Cu) or present high solubility (Mg, Zn) are important disadvantages for the adoption of ferrite nanomaterials in water purification.

3.1.5 Bimetallic phases

The implementation of bimetallic magnetic nanoparticles is intended to combine two or more contributions of zero-valent metals in the profit of water treatment. Most of the relevant cases refer to the presence of zero-valent iron as the major and magnetic phase. From another point of view, alloying or coupling of ZVI with another metal also enhances the uptake performance of pure ZVI against water pollutants as a consequence of passivation inhibition. For example, the doping of ZVI nanoparticles with Pd results in the improvement of trichloroethylene degradation and the removal of chlorinated aliphatic hydrocarbons [44, 104, 105]. In such process, palladium is considered as a dehalogenation catalyst while it lowers the activation energy increasing the reaction rate of ZVI [106, 107]. Bimetallic Ni/Fe nanoparticles appear also efficient to degrade DDT [108]. Particularly, the dehydrochlorination is favored by the coupling of Ni and Fe and the formation of galvanic cells. An improvement of up to nine times in degradation rate has been reported for bimetallic nanoparticles compared to pure ZVI ones [109, 110]. In another representative example, addition of Ag in ZVI nanoparticles promotes antimicrobial activity while preserving the efficiency of nanoscale iron as a drinking water nanoadsorbent [111]. Finally, a variety of bimetallic particles based on ZVI with Ag, Pd, Ni, Al, Cu, Co, or Zn were evaluated in Cr(VI) removal considering the reduction enhancement due to galvanic coupling [112]. In spite of the described advantages for bimetallic nanoparticles in water purification, especially facing organic pollutants, important issues related to the significant cost elevation and the added environmental risks should be also taken into consideration [113].

3.2 MAGNETIC CARRIERS

In many cases, the excellent behavior of nanoparticles consisting of magnetic phases as direct water pollutant adsorbents disorients research effort for the exploitation of their magnetic properties. More attention is brought to this aspect when magnetic nanoparticles are introduced only as a vehicle to deposit and carry another active phase during water treatment. The magnetic phase is usually considered

as an inert part of the nanocomposite which is only added to feature a sufficient magnetic response with respect to the easy separation at the end of the process. Still, the mass percentage of the magnetic nanoparticles is an important part of total quantity and, therefore, a significant decrease of observed specific efficiency should be expected. Nevertheless, unless magnetic nanoparticles are fully covered by the active phase, it is not always clear if the magnetic phase can interact with the pollutant and also contribute in the observed removal efficiency. Depending on the inorganic or organic nature of the attached active phase, there are two different approaches for the development of water treatment nanoadsorbents using magnetic nanoparticles as carriers: inorganic phases are deposited on the surface of magnetic nanoparticles forming a thin coating layer whereas active organic molecules are usually attached on the magnetic nanoparticles by adsorption.

3.2.1 Inorganic coatings

A variety of metals and oxides have been tested as coatings on magnetic nanoparticles in order to evaluate their efficiency to operate as heavy metals adsorbents and magnetic separable agents at the same time. Hematite-coated Fe_3O_4 nanospheres is a well-established case of this category showing significant efficiency for the uptake of As(III), As(V) and Sb(III) at concentrations close to the regulation limits [72, 96]. Furthermore, the cooperative action of MnO_2 with Fe_3O_4 nanoparticles supported on graphene oxide was introduced as a way to facilitate oxidation of As(III) and provide equal removal efficiency to that for As(V) together with high specific surface area and good magnetic response [114]. The adsorption of Cr(VI) through an outer-sphere complexation was reported to take place on δ-FeOOH coated maghemite nanoparticles [115] while deposition of hydroxyapatite improves efficiency for Cd^{2+} [116]. Many researchers also examined the combination of TiO_2 with magnetic nanoparticles to capture arsenic forms from water. In particular, the direct adsorption of arsenic species [117] and the photo-oxidation assisted removal of As(III) [118] were reported by (Fe_3O_4 or γ-Fe_2O_3)/TiO_2 nanoparticles. The potential of titania-coated Fe_3O_4 nanoparticles for water purification is also indicated by their good performance in analytical applications. Suggestively, Fe_3O_4 nanoparticles covered by SiO_2/TiO_2 were applied for the solid extraction of Cd^{2+}, Cr(III), Mn^{2+} and Cu^{2+} traces from water samples [119]. Furthermore, TiO_2-coated Fe_3O_4 nanoparticles were used as pesticides sensing agents [120] while Au-decorated TiO_2/Fe_3O_4 nanospheres indicated enhanced photocatalytic and antimicrobial activity with high efficiency for organic molecules degradation [121].

As explained, the formation of an oxide layer on metallic iron nanoparticles is a common side effect related to the spontaneous surface passivation. However, there are cases where the coating of ZVI by another inorganic phase is desirable in order to enhance their potential for the selective uptake of common water pollutants. In an example, covering of ZVI nanoparticles by Ag or Cu was suggested as a different approach to combine high Cr(VI) reduction efficiency with good resistivity against corrosion and strong magnetic properties [122, 123]. Similarly, the stabilization of Fe_3O_4 or iron sulfides (FeS_x) on ZVI nanoparticles was found to improve the Cr(VI) reduction or Cd^{2+} removal potential, respectively, compared to the pure ZVI nanoparticles [124, 125]. Elsewhere, the decoration of nanoscale ZVI by Au was proved very effective in the simultaneous removal of nitrates and Cd^{2+} [126].

3.2.2 Attached molecules

The functionalization of magnetic nanoparticles by organic compounds active in the uptake of water pollutants is another possibility. The main motivation in this approach is the high selectivity of attached molecules to capture specific pollutants since their operating lifetime, as implied by the low mass

percentage in the system, is limited. Considering the facile magnetic recovery of these nanoparticles, an essential requirement for qualification is the development of a regeneration step. Zero-valent iron and iron oxides nanoparticles are the common substrates for the attachment of active organic molecules. Functionalization of ZVI nanoparticles mostly refers to the improvement of Cr(VI) removal either by the stabilization of metal's surface and the positive contribution of the attached molecules. Coating by chitosan [127], carboxymethyl cellulose [128], polyphenols [129], starch [130], orange peel pith [131], and xanthan gum [132] were tested in this direction.

Corresponding attachment of organic molecules on Fe_3O_4 nanoparticles was examined to capture various heavy metals, organic pollutants and bacteria from water. For instance, chitosan- and humic-acid-coated Fe_3O_4 nanoparticles were tested for the removal of Cr(VI) in highly polluted water [133, 134]. Furthermore, arsenic adsorption was attempted with Fe_3O_4 nanoparticles modified by cetyltrimethylammonium bromide (CTAB) [135], starch [136] and ascorbic acid [137]. Many other heavy metal species (Cu^{2+}, Cd^{2+}, Pb^{2+}, Ni^{2+}, Hg^{2+}, Pb^{2+}, Cd^{2+}) were adsorbed on amines [138], polypyrrole [139], humic acid [140], cyclodextrin [141], polymers [142], and polyacrylic acid [143] bound on magnetite nanoparticles. Radioactive contaminants such as U(VI) and Cs might be also captured by chitosan, Prussian blue or amidoxime coated magnetite nanoparticles [144–146]. Even the significant removal of mercury by silica-coated Fe_3O_4 nanoparticles should be categorized as a case of organic coating since Hg adsorption is correlated to the functionalization of nanoparticles by thiol groups [147]. The potential of using Au/Fe_3O_4 nanoparticles functionalized by thiol ligands and able to magnetically extract diphenols and polycyclic aromatic hydrocarbons was also reported [148]. Several studies point out the potential removal of sulfathiazole and numerous anionic, cationic, and azo-dyes from aqueous solutions using carboxymethyl-β-cyclodextrin [149], CTAB [150], humic acid [151], polymers [152], or chitosan [153] coatings. The functionalization by carboxyl, amine, and thiol groups was also proven to introduce a better efficiency in the removal of bacteria [123].

A number of research works also evaluate functionalized γ-Fe_2O_3 nanoparticles for the removal of heavy metals and organic dyes. Glycine, polyrhodanine, and polydopamine coatings were applied for the removal of Cu^{2+}, Hg^{2+} and Cr(VI) from water [154–156], while sodium dodecyl sulfate modified maghemite nanoparticles were discussed for the removal of cationic dyes [157].

4 MAGNETIC SEPARATION IN WATER TREATMENT

4.1 FUNDAMENTALS

In order to move a magnetic bead, one should apply a magnetic force over it and overcome the drag force generated by the viscosity of the buffer. The first usual misunderstanding is the assumption that the force would be proportional to the magnetic field. But a uniform magnetic field will only make the beads rotate, not move from their position. The ultimate and detailed specification of the forces and motions to which the particles would be subjected depends on their complex magnetization behavior, so, we can frame our discussions in the most general case of a particle being replaced by an "equivalent" point dipole confined to a volume V. The magnetic force (F_m) may be calculated from the variation of its free energy [158], and is given by

$$F_m \sim \mathrm{V}(B\nabla)B \tag{2}$$

It is possible to simplify Eq. 2 considerably if the specimen is fully saturated, the magnetization is independent of field and the force scales with $M_S \cdot \nabla H$.

Conversely, the viscous drag force exerted by the medium and that opposses to the magnetic force goes with the radius of the particle (R) and the viscosity (η) of the solvent. Using the Navier-Stokes equations and balancing the magnetic force and the viscous drag gives the velocity as $v \sim \frac{1}{\eta}.M_S.R^2.\nabla H$ [159]. Thus, particles with different magnetization and projected cross-sectional area are distinguished by their unique trajectories, which facilitate their separation and sorting at various flow rates.

4.2 SEPARATION UNITS

In a typical case of using magnetic nanoparticles to capture pollutants with concentrations below 100 μg/L, the magnetic separation unit is placed close to the end of a water treatment line implying that nanoparticles are the only suspended solid in water flow. A higher quantity of solids is expected when nanoparticles are applied for their antimicrobial activity but most probably the organic mass will be found loaded on the surface of nanoparticles. As previously described, the main advantage of magnetic nanoparticles in water purification is the possibility of obtaining their maximum efficiency when dispersed in water due to their mobility and good contact with pollutants. Another option would be the implementation of nanoparticles aggregates in packed-bed filters considering the long-time technical experience of their design and operation together with the compatibility of their adoption in the water treatment lines and point-of-use or portable devices [160]. In order to become competitive, a system which enables sufficient dispersion and contact of nanoparticles with polluted water followed by a magnetic separation unit should be carefully designed. First, to deliver the improved efficiency and lower energy consumption of particles dispersions, the demand for extended contact time and larger volume of the facility compared to the packed-filters should be counterbalanced. Then, a significant issue comes from the small dimensions of nanoparticles which may turn into a serious drawback for their successful separation [161]. Typical solid separation methods such as nanofiltration or centrifugation are not as cheap, efficient or rapid as using a magnetic field to collect nanosized magnetic particles even in fast flows [162]. However, the magnetic force acting on a particle is proportional to the particle volume. So, reducing the size results in decreased amounts of heave, which may not be large enough to overcome Brownian motion in liquid, and limited separation will occur [163]. Next, we discuss the three approaches in the creation of the magnetic field: permanent magnet-based, electromagnet-based, and superconducting magnet-based (Fig. 3).

4.2.1 Easiness of permanent magnets

In recent years new magnetic materials based on rare-earth alloys became commonly available at a relatively low price. For instance, neodymium-iron-boron magnets ($Nd_2Fe_{14}B$) were introduced in 1984, and have attained maximum energy products exceeding 300 kJ/m^3. To put that into more familiar terms, it is twice the saturation magnetization of magnetite and coercivities easily exceeding 10^6 A/m (1.2 T); the magnetic moment is dominantly due to iron, while the lanthanide in effect provides the hardness.

If we consider a single long rod of radius 1 cm made of a permanent magnet material of polarization 1 T, the field at a distance of 3 cm from the magnet has magnitude 44 kA/m (55 mT), although at the surface could reach 500 mT [164]. And an appropriate geometrical arrangement (static or even varying

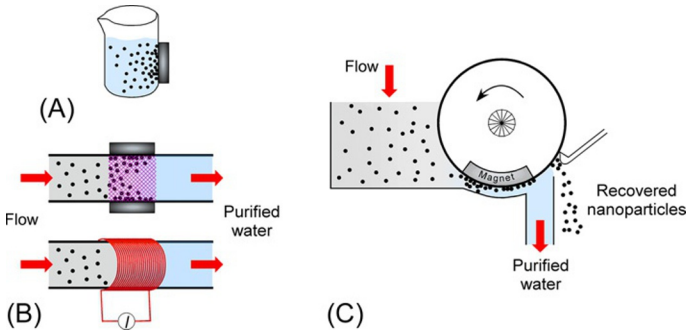

FIG. 3

Different types of magnetic separation units applied for magnetic nanoparticles separation. Batch separation (A), inline continuous flow separation in a flowing tube with permanent magnets enhanced by packed stainless steel ferromagnetic filaments or an electromagnet (B), and a rotating drum system capturing nanoparticles for the outflow of the contact tank (C).

continuously) of several magnets can provide magnetic fields from about ± 2 T in the working space, their contributions add vectorially.

For that reason most of the permanent magnet devices employ a sequence of magnets arranged so that the water passes alternately through magnetized and nonmagnetized regions, with a steep gradient among them [165]. A different example is based on sink-float separators, which utilize the levitation force of magnetic fluid [166]. Such a magnetic flocculation and separation has emerged as an ideal solution to treat industry wastewater, and it has offered great time, space, and cost savings; for instance, reduction in suspended solids contents of waters in the iron and coal mining industries often exceeds 99% [163].

Unfortunately, their performance deteriorates as temperature increases. Though, provided the device is used at temperatures less than around 80°C, conditions will remain constant for decades. So, permanent magnets provide a solution that gives long endurance with no need for cooling systems, no electrical power, and no maintenance fees.

4.2.2 Electromagnets for high-flow water processing

The main advantage of an electromagnet over a permanent magnet is that the magnetic field can be quickly changed by controlling the amount of electric current in the winding. Normal solenoids are usually made with insulated copper wire wound on a tube. The field strength can be calculated from the current, number of turns, and length of the winding, since these quantities can all be determined with good accuracy. At the midpoint is given by $H = \frac{4\pi ni}{10L}$ (in Oe units, where ni is the number of Ampere-turns and L the length of the winding in centimeters). Note that the field is independent of the solenoid radius as long as the radius is small compared to the length. Unfortunately, if you need to scale up a magnetic separation process, you also need to increase the electrical power. To achieve a higher field, it is preferable to increase n/L by winding the wire in two or more layers rather than to increase the current. Although H is proportional to i, the heat developed in the winding is proportional to i^2R, where R is its resistance. Thus, doubling the number of layers and keeping the current constant will double the field and the amount of heat, whereas doubling the current will double H, but quadruple

the heat, at significant expense. Besides, the additional cost of the refrigeration infrastructure able to control the temperature, and maintenance of coils, electronics, etc., must be considered.

An alternative configuration is the so-called "Helmholtz coils" that produce an almost uniform field over a much larger volume than a solenoid. Though, for the same energy consumption, Helmholtz coils produce a field which is only a few percent of that produced by a solenoid, thus they are restricted mainly to low-field applications. For a water-flow capacity of 100 m^3/h requiring a maximum of 0.1 T, a solution can be found at power consumption of a few tens of watts per m^3/h [167]. Different alternatives for large scale processes exist, such as High Gradient Magnetic Separation (HGMS) columns. HGMS systems have an excellent track record, being applied for the separation of magnetic solids under flow conditions in several industrial applications for more than 40 years [159]. These systems use an electromagnet to generate external fields of variable strength around a column packed with stainless steel ferromagnetic filaments about ~50 μm diameters and gaps of 10–100 μm between them. When ferromagnetic filaments are inserted, the distribution of flux lines is changed and resulting high gradient field yields. Exact measures of the field gradients in such a system are challenging to obtain, but gradients of 10^4 T/m are possible [168]. This would set the critical size for separation around 50 nm for the case of an iron-oxide particle.

4.2.3 High intensity fields with superconductors

Field intensities of order 100 mT demand bulky coils carrying large currents, which in turn, require substantial power supplies and water cooling. Therefore, the need for fields larger than those obtainable from conventional solenoids is met with superconductors. In principle, the technology has shown great energy saving potential because superconductors are dissipation-less [169]. If a current is started in a circuit formed of a superconductor maintained below its critical temperature, it will persist indefinitely without any power input or heat generation. However, one will need to cryogenically cool the coils, making this technology far too expensive. If this complex cooling were no longer necessary, it would mean a breakthrough for magnetic separation. And there is some hope for the future: in the beginning, superconductivity was known only in a few metals at temperatures just above absolute zero at minus 273°C, reachable with the aid of liquid helium. During the 1980s, it was discovered that some ceramic materials can reach this state at significantly higher temperatures, using liquid nitrogen. One such material, called yttrium barium copper oxide (YBCO), has since cornered the market. Search for room-temperature superconductors is a challenging study in materials science, and pressurization and hydrogenation have been considered as a way to push up the superconducting critical temperature. Right now, the highest temperature known superconducting material is pressurized hydrogen sulfide, whose working temperature reaches 203 K (−70°C) [170].

Meanwhile, high gradient magnetic field of more than 10 T can be formed using conventional superconducting coils [148, 171–174]. But although it was frequently observed that the removal efficiency of pollutants improved when the magnetic field intensity increased up to 1 T [175, 176], the effects of increasing the magnetic field to greater than 1 T, beyond saturation of most magnetic seeds (see Eq. 2), are controversial [177].

Various kinds of the superconducting magnetic have been constructed in order to develop the practical and industrial applications [178]. But while the magnetic field is strong, the cost is high, and maintaining the temperature conditions is difficult. For instance, [179] analyzed a face-to-face type superconducting magnet system, which consists of a pair of Sm-Ba-Cu-O bulk samples mounted on the respective cold stages in vacuum vessels. The bulk samples were cooled to 30 K and then magnetized

by feeding currents using the magnetizing pulse coils. On comparison of the experimental magnetic separation setup, the performances of HGMS and superconducting devices approximately equal to each other. Still, medium-sized electromagnets capital costs tend to dominate cryogenic costs and hence for small systems permanent magnets are best, while for applications requiring fields greater than 2 T, superconducting magnets would be preferred. It appears that the range of applicability of conventional electromagnets is being severely squeezed.

4.3 IMPLEMENTING MAGNETIC NANOPARTICLES IN WATER PURIFICATION SYSTEMS

The implementation of magnetic nanoparticles in integrated systems succeeding the removal of a pollutant and the complete magnetic recovery of solids has been mostly tested in laboratory experiments and simulations. Some typical examples are illustrated hereafter. Fig. 4 shows a laboratory-scale experiment for the separation of adsorbents oriented to meet the drinking water specifications. In general, the system consists of an agitating tank with high enough retention time to allow adequate contact between the polluted water (100 μg/L Cr(VI)) and the nanostructured solid (40 nm Fe_3O_4 nanoparticles), followed by a magnetic separator installed in the overflow tube. One or more electromagnets or permanent magnets supplying adjustable magnetic field are adapted parallel to the water flow.

In obtaining a separation rate of 100% and other technologically desirable parameters, the setup can be optimized by means of simulation. In this field, great progress has been made with the development

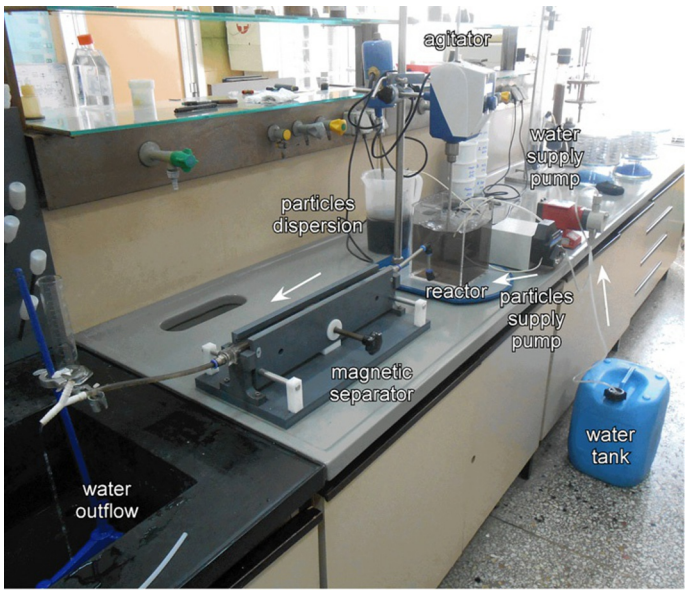

FIG. 4

Laboratory setup for the continuous-flow water purification by dispersed magnetite nanoparticles followed by their magnetic separation using permanent magnets.

of modeling, especially the finite element method and computational fluid analysis (CFD) software [180]. An example of modeling a setup similar to that in Fig. 4 is given by assuming a 0.5 m long horizontal separator tube (square cross-section 15×15 mm) and six pairs of NdFeB permanent magnets ($50 \times 30 \times 3$ mm) located at its sides. The flowrate of the water dispersion through the tube (10–140 mL/min) is determined by the retention time (10–120 min) in the water purification tank. Fig. 5A demonstrates, for the various combinations of magnets polarity, that those with high field gradients at the path of particles flow bring much better magnetic separation yields compared to the arrangements with high field homogeneity. Field intensity could be varied by changing the distance between the magnets. The role of field intensity as represented by the gap size is given for the opposite pole configuration (N against S in all pairs), where field intensity is almost completely homogenous between the magnets, in Fig. 5C. The separation efficiency drops from around 90% at the closest

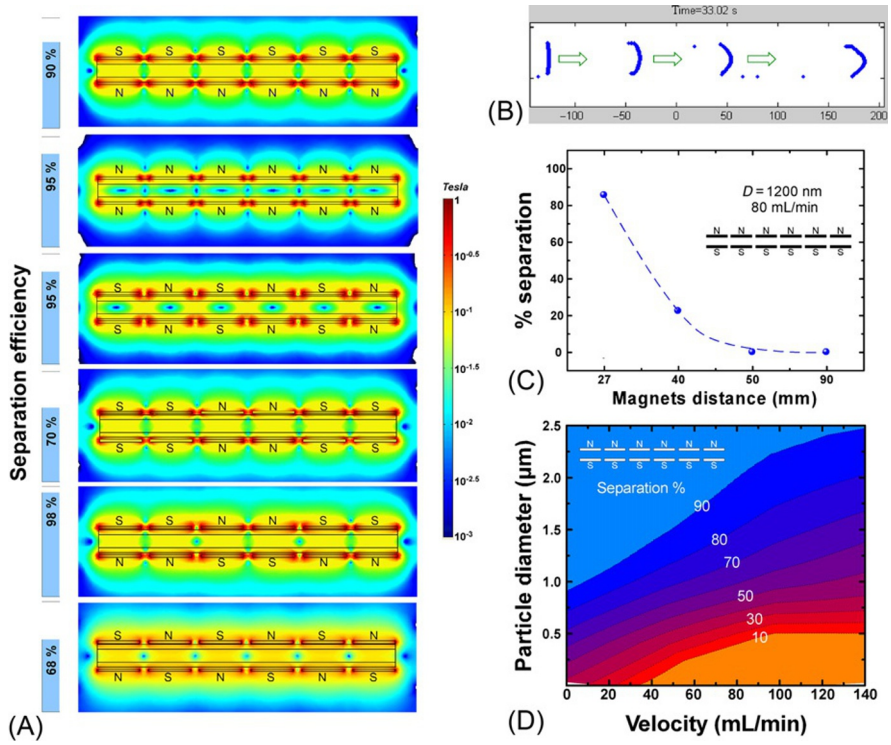

FIG. 5

Magnetic field intensity distribution obtained using CFD analysis in the flowing separation tube by placing pairs of permanent magnets with a gap distance of 2.7 cm and various S/N pole configurations (A). Separation efficiency is indicated at the left side of each diagram. Snapshots of particles movement simulation in the flowing separation tube (B). Removal efficiency as a function of magnets distance for the opposite pole configuration (N-S), particle diameter 1200 nm, magnetization value equal to that of magnetite (85 emu/g) and flowrate about 80 mL/min (C). Removal efficiency isobars for various particle diameters and flow rates with an opposite pole configuration (N-S) and magnets distance at 2.7 cm (D).

distance to almost zero when the magnets' distance is tripled, proportionally to the decrease of field intensity by four orders of magnitude. Also illustrated is the removal efficiency isobars for various particles diameters and flowrates for the same pole configuration (Fig. 5D). One can see that in order to reach complete magnetic separation, the particle size should be at least 1200 nm and the flow rate less than 40 mL/min.

Therefore, as the particle size became smaller, we would conclude that very large applied fields are required to ensure their complete separation. Save for the fact the force is not proportional to the magnetic field, but to the presence of steep gradient. Still, taking into account that a maximum field gradient of about 15 T/m is reasonable whenever permanent handheld magnets are used for a simple batch recovery arrangement, a nanoadsorbent with a magnetization value about 60 emu/g should have a diameter above 200 nm for efficient removal from the solution [71], which provides too harsh, constrained conditions, for a real point-of-use system.

The models described above might provide a realistic estimate of the forces acting on the particles for cases when dilute suspensions are employed (i.e., fluid-particle and particle-particle interactions can be neglected). Obviously, many considerations in the stability of particles exist, and several theories propose different forms for the drag force on particles in a fluid [181]. For instance, not only the surfactant adhered to particles influences the kinetics of field induced chain like aggregates, but particle volume fraction (i.e., concentration) and size have a strong impact on the dipolar interactions, that can affect the magnetophoresis process significantly [182, 183]. In this regard, several papers have calculated that dipole-dipole interactions become rather significant for separations below three particle diameters [184–186]. In fact, it is the lucky presence of dipole-dipole interactions that facilitates the aggregation-separation process and overcomes size limitations [11]. For instance, 30-nm magnetite particles used as arsenic adsorbents could be recovered completely under low-gradient magnetophoresis and at reasonable times [72]. In another example, the real-time magnetophoretic collection of *Chlorella* sp. is shown [10]. Therein, authors claimed rapid separation cannot be understood in terms of the simple model of noninteracting particles, but observations are most likely due to the formation of microsized magnetic aggregates.

Overall, despite the successful development in the laboratory, few magnetic technologies have been translated into commercial applications. There is little ability to predict how the many parameters will affect pollutant sequestration efficiency. This has forced magnetic separation design choices to be made based on intuition, empirical data and simple engineering estimates, and these rough tools are proving insufficient. Still, magnetic separation offers an alternative treatment process because of the high processing rates, the compactness of the filtering machinery and the simplicity of backwashing of the magnetic filter [187].

5 PERSPECTIVES AND CHALLENGES

A critical overview of the research related to magnetic nanoparticles as potential agents for efficient water purification indicates the main fields that should be improved before their successful implementation in large-scale units. In summary, the development of nanoparticles with the proper characteristics together with the design and adoption of a magnetic separator in a water treatment line should be separately handled to optimize an integrated solution for the removal of one or more pollutants from water oriented for drinking purposes.

It is clear that a large number of studies using nanoparticles, and more specifically magnetic ones, is already available, and the publication trend is exponential. Unfortunately, the vast majority of the cases originate from the field of materials science with minimum background in the water treatment demands. The usual message is, "We prepared some nice nanoparticles, and trying to find an application for them, we are presenting the adsorption isotherms for a heavy metal." For this reason, a number of experimental inconsistencies do not allow the evaluation of results with respect to drinking water purification. The use of toxic or high-cost nanoparticles, high pollutants concentrations, or acidic conditions are some typical examples frequently met. Even worse, extrapolation of given results to realistic conditions of water treatment operation suggests that the supposed high removal efficiency against specific pollutants disappears when trying to achieve the maximum drinking water regulation limit.

On the other side, a limited number of research studies provides sufficient data to support the potential of examined nanoparticles to meet the regulation limits. In this category of investigation, the question that arises is, "Can nanoparticles become competitive with existing granulated adsorbents or other technologies?" This is the second and probably the most difficult step for success. For instance, the application of magnetic nanoparticles as direct arsenic adsorbents should be able to deliver removal capacities at least equal to the commercial iron oxy-hydroxides, that is, higher than 10 mg/g for a residual concentration 10 μg/L. So, the prospect for nanoparticles' implementation in water purification is higher in the treatment of pollutants where competition is smaller due to the difficulty of developing an efficient and selective adsorbent or due to the early stage of research on it. A number of emerging heavy metals, including hexavalent chromium, antimony, and selenium may be referred as challenging fields for the adoption of nanoparticles toward efficient removal.

But using magnetic nanoparticles as direct adsorbents is only one of the options for their incorporation in water purification. Their magnetic response makes them advantageous substrates to load with any other kind of agent known for its high removal efficiency. This is probably the most promising application of magnetic nanoparticles for water purification. Numerous examples of testing them as magnetic carriers with attached organic molecules or inorganic phases were described in Section 3.2. Considering the low cost and the chemical stability of Fe_3O_4, such nanoparticles may work as an excellent carrier for a wide range of other active agents. Importantly, magnetite is well-known for its binding affinity with organic chains and its structural compatibility with metal oxy-hydroxides, which are usually applied in water purification. In the same direction, magnetic nanoparticles can be used in auxiliary procedures of water treatment such as pretreatment or adsorbents regeneration under conditions much different from drinking water [188].

Beyond laboratory studies and preliminary evaluation of applicability, developed magnetic nanoparticles should offer a number of economic and technological advantages for overcoming the "valley of death" for commercialization. First, the synthesis of nanoparticles should be a low-cost procedure, according to many points of view. Particularly, the cost involves the reagents, the consumed energy, the conditions of preparation, the environmental impact, and the required facilities. In addition, the selected method should be able to produce large quantities of the nanomaterials as defined by the needs of water treatment compared to other applications for nanoparticles. For this reason, iron oxides are preferable to any other magnetic phase because they can be synthesized in water solutions by cheap iron salts using conventional continuous-flow reactors.

Then, the implementation of developed nanoparticles is another field of optimization. Dispersion of nanoparticles in the water to be treated (Fig. 4) maximizes their efficiency whether they are applied as direct removal adsorbents or as carriers of other phases. This configuration requires a simple but

relatively large agitating tank and a magnetic separator to recover nanoparticles. The overall cost of this setup in comparison to a typical adsorption bed or a chemical precipitation reactor may determine the qualification of magnetic nanoparticles in large-scale facilities. Fortunately, the simplicity of the described setup enables numerous possibilities for enhancing operating efficiency and decreasing size by engineering the flowing geometry and the type of magnetic separator. Suggestively, a plug-flow contact reactor is expected to bring a faster reaction rate together with easier adoption in a linear magnetic separator.

Special attention should be given to the design of the magnetic separator in combination with the obtained magnetic properties of nanoparticles. Effective ways to enhance the magnetic force on a particle, and its separation from solution, include the increasing of magnetization, the tuning of particles' size, and the operational management of high-intensity nonuniform fields. Computational analysis is recommended as a way to design more complicated geometries for the positioning of permanents magnets, the flowing tube's path or the filling mesh able to bring the absolute 100% separation of magnetic nanoparticles from drinking water. The importance of this step is also valuable to enable a recycling procedure of the nanoparticles implying to a significant cost reduction and ensure the absence of released nanomaterials to the environment.

On the last point, more research is required to understand the ultimate fate of the nanoparticles and estimate the potential risks related to human and ecological health. In particular, apart for the establishment of a very efficient magnetic recovery step, it should be also examined whether magnetic nanoparticles loaded with high quantities of toxic pollutants can be handled as an inert or hazardous solid waste considering the possibility of secondary leaching procedures in nature [189].

6 CONCLUSIONS

In light of recent advances in nanomaterials and the increasing sensitivity of consumers regarding drinking water quality, a great challenge for the near future will be to develop and implement innovative processes to supply safe drinking water, at acceptable cost, and with a minimum of waste and byproducts. And it is when magnetic, nanoparticle-based technologies offer a world of possibilities. Magnetic nanoparticles can be used as low-cost consumables, whether as direct purifiers or just carriers, implemented into simple constructions operating at minimum energy consumption. Their magnetic properties are actually the key to overcoming the issues related to the low-dimensions of nanomaterials in a large-scale application which directly deals with humans' nutrition and sustainability. In spite of the important advantages, there is still much distance to cover before any technology based on magnetic nanoparticles will be adopted in water purification installations. Nevertheless, indications are sufficient to predict the pilot operation of integrated units in the very near future.

ACKNOWLEDGMENT

This scientific work was implemented within the frame of the action "Supporting Postdoctoral Researchers" of the Operational Program "Development of Human Resources, Education and Lifelong Learning 2014–2020" of IKY State Scholarships Foundation and is co-financed by the European Social Fund and the Greek State.

REFERENCES

[1] G.H. Livens, The thermodynamics of magnetization, Math. Proc. Camb. Philos. Soc. 44 (4) (1948) 534, https://doi.org/10.1017/S0305004100024543.

[2] A.H. Morrish, The Physical Principles of Magnetism, Wiley-IEEE Press, 1965. https://doi.org/10.1002/9780470546581.

[3] J. Crangle, G.M. Goodman, The magnetization of pure iron and nickel, Proc. Royal Soc. A Math. Phys. Eng. Sci. 321 (1547) (1971) 477–491, https://doi.org/10.1098/rspa.1971.0044.

[4] C. Martinez-Boubeta, L. Balcells, C. Monty, B. Martínez, The effects of exchange bias on Fe-Co/MgO magnetic nanoparticles with core/shell morphology, J. Physics. Condens. Matter 22 (2010) 26004, https://doi.org/10.1088/0953-8984/22/2/026004.

[5] M.E. McHenry, S.A. Majetich, J.O. Artman, M. Degraef, S.W. Staley, Superparamagnetism in carbon-coated Co particles produced by the Kratschmer carbon arc process, Phys. Rev. B 49 (16) (1994) 11358–11363, https://doi.org/10.1103/PhysRevB.49.11358.

[6] C. Gatel, F.J. Bonilla, A. Meffre, E. Snoeck, B. Warot-Fonrose, B. Chaudret, L.M. Lacroix, T. Blon, Size-specific spin configurations in single iron nanomagnet: from flower to exotic vortices, Nano Lett. 15 (10) (2015) 6952–6957, https://doi.org/10.1021/acs.nanolett.5b02892.

[7] C. Martínez-Boubeta, K. Simeonidis, M. Angelakeris, N. Pazos-Pérez, M. Giersig, A. Delimitis, L. Nalbandian, V. Alexandrakis, D. Niarchos, Critical radius for exchange bias in naturally oxidized Fe nanoparticles, Phys. Rev. B Condens. Matter Mater. Phys. 74 (5) (2006). https://doi.org/10.1103/PhysRevB.74.054430.

[8] R. Chalasani, S. Vasudevan, Form, content, and magnetism in iron oxide nanocrystals, J. Phys. Chem. C 115 (37) (2011) 18088–18093, https://doi.org/10.1021/jp204697f.

[9] C. Martinez-Boubeta, K. Simeonidis, A. Makridis, M. Angelakeris, O. Iglesias, P. Guardia, A. Cabot, L. Yedra, S. Estradé, F. Peiró, Z. Saghi, P.A. Midgley, I. Conde-Leborán, D. Serantes, D. Baldomir, Learning from nature to improve the heat generation of iron-oxide nanoparticles for magnetic hyperthermia applications, Sci. Rep. 3 (1) (2013) 1652, https://doi.org/10.1038/srep01652.

[10] J.K. Lim, D.C.J. Chieh, S.A. Jalak, P.Y. Toh, N.H.M. Yasin, B.W. Ng, A.L. Ahmad, Rapid magnetophoretic separation of microalgae, Small 8 (11) (2012) 1683–1692, https://doi.org/10.1002/smll.201102400.

[11] G. De Las Cuevas, J. Faraudo, J. Camacho, Low-gradient magnetophoresis through field-induced reversible aggregation, J. Phys. Chem. C 112 (4) (2008) 945–950, https://doi.org/10.1021/jp0755286.

[12] K. Simeonidis, M. Tziomaki, M. Angelakeris, C. Martinez-Boubeta, L. Balcells, C. Monty, M. Mitrakas, G. Vourlias, N. Andritsos, in: Development of iron-based nanoparticles for Cr(VI) removal from drinking water, EPJ Web of Conferences, vol. 40, 2013, p. 8007, https://doi.org/10.1051/epjconf/20134008007.

[13] V. Nahuel Montesinos, N. Quici, E. Beatriz Halac, A.G. Leyva, G. Custo, S. Bengio, G. Zampieri, M.I. Litter, Highly efficient removal of Cr(VI) from water with nanoparticulated zerovalent iron: understanding the Fe(III)–Cr(III) passive outer layer structure, Chem. Eng. J. 244 (2014) 569–575, https://doi.org/10.1016/j.cej.2014.01.093.

[14] Y. Dai, Y. Hu, B. Jiang, J. Zou, G. Tian, H. Fu, Carbothermal synthesis of ordered mesoporous carbon-supported nano zero-valent iron with enhanced stability and activity for hexavalent chromium reduction, J. Hazard. Mater. 309 (2016) 249–258, https://doi.org/10.1016/j.jhazmat.2015.04.013.

[15] X. Lv, J. Xu, G. Jiang, X. Xu, Removal of chromium(VI) from wastewater by nanoscale zero-valent iron particles supported on multiwalled carbon nanotubes, Chemosphere 85 (7) (2011) 1204–1209, https://doi.org/10.1016/j.chemosphere.2011.09.005.

[16] H. Jabeen, V. Chandra, S. Jung, J.W. Lee, K.S. Kim, S.B. Kim, Enhanced Cr(vi) removal using iron nanoparticle decorated graphene, Nanoscale 3 (9) (2011) 3583–3585, https://doi.org/10.1039/c1nr10549c.

[17] R. Fu, X. Zhang, Z. Xu, X. Guo, D. Bi, W. Zhang, Fast and highly efficient removal of chromium (VI) using humus-supported nanoscale zero-valent iron: influencing factors, kinetics and mechanism, Sep. Purif. Technol. 174 (2017) 362–371, https://doi.org/10.1016/j.seppur.2016.10.058.

[18] L. Shi, X. Zhang, Z. Chen, Removal of Chromium (VI) from wastewater using bentonite-supported nanoscale zero-valent iron, Water Res. 45 (2) (2011) 886–892, https://doi.org/10.1016/j.watres.2010.09.025.
[19] E. Petala, K. Dimos, A. Douvalis, T. Bakas, J. Tucek, R. Zbořil, M.A. Karakassides, Nanoscale zero-valent iron supported on mesoporous silica: characterization and reactivity for Cr(VI) removal from aqueous solution, J. Hazard. Mater. 261 (2013) 295–306, https://doi.org/10.1016/j.jhazmat.2013.07.046.
[20] X. Sun, Y. Yan, J. Li, W. Han, L. Wang, SBA-15-incorporated nanoscale zero-valent iron particles for chromium(VI) removal from groundwater: mechanism, effect of pH, humic acid and sustained reactivity, J. Hazard. Mater. 266 (2014) 26–33, https://doi.org/10.1016/j.jhazmat.2013.12.001.
[21] X. Wang, L. Le, A. Wang, H. Liu, J. Ma, M. Li, Comparative study on properties, mechanisms of anionic dispersant modified nano zero-valent iron for removal of Cr(VI), J. Taiwan Inst. Chem. Eng. 66 (2016) 115–125, https://doi.org/10.1016/j.jtice.2016.05.049.
[22] S.S. Poguberović, D.M. Krčmar, S.P. Maletić, Z. Kónya, D.D.T. Pilipović, D.V. Kerkez, S.D. Rončević, Removal of As(III) and Cr(VI) from aqueous solutions using "green" zero-valent iron nanoparticles produced by oak, mulberry and cherry leaf extracts, Ecol. Eng. 90 (2016) 42–49, https://doi.org/10.1016/j.ecoleng.
2016.01.083.
[23] A. Toli, K. Chalastara, C. Mystrioti, A. Xenidis, N. Papassiopi, Incorporation of zero valent iron nanoparticles in the matrix of cationic resin beads for the remediation of Cr(VI) contaminated waters, Environ. Pollut. 214 (2016) 419–429, https://doi.org/10.1016/j.envpol.2016.04.034.
[24] X. Zhou, B. Lv, Z. Zhou, W. Li, G. Jing, Evaluation of highly active nanoscale zero-valent iron coupled with ultrasound for chromium(VI) removal, Chem. Eng. J. 281 (2015) 155–163, https://doi.org/10.1016/j.cej.2015.06.089.
[25] L. Ling, B. Pan, W. Zhang, Removal of selenium from water with nanoscale zero-valent iron: mechanisms of intraparticle reduction of Se(IV), Water Res. 71 (2015) 274–281, https://doi.org/10.1016/j.watres.2015.01.002.
[26] J.T. Olegario, N. Yee, M. Miller, J. Sczepaniak, B. Manning, Reduction of Se(VI) to Se(-II) by zerovalent iron nanoparticle suspensions, J. Nanopart. Res. 12 (6) (2010) 2057–2068. Springer Netherlands. https://doi.org/10.1007/s11051-009-9764-1.
[27] Z.-J. Li, L. Wang, L.-Y. Yuan, C.-L. Xiao, L. Mei, L.-R. Zheng, J. Zhang, J.-H. Yang, Y.-L. Zhao, Z.-T. Zhu, Z.-F. Chai, W.-Q. Shi, Efficient removal of uranium from aqueous solution by zero-valent iron nanoparticle and its graphene composite, J. Hazard. Mater. 290 (2015) 26–33, https://doi.org/10.1016/j.jhazmat.2015.02.028.
[28] R.A. Crane, T.B. Scott, The removal of uranium onto nanoscale zero-valent iron particles in anoxic batch systems, J. Nanomater. 2014 (2014) 1–9, https://doi.org/10.1155/2014/956360.
[29] G. Sheng, X. Shao, Y. Li, J. Li, H. Dong, W. Cheng, X. Gao, Y. Huang, Enhanced removal of uranium(VI) by nanoscale zerovalent iron supported on Na–bentonite and an investigation of mechanism, J Phys. Chem. A 118 (16) (2014) 2952–2958. American Chemical Society. https://doi.org/10.1021/jp412404w.
[30] S. Saeidnia, G. Asadollahfardi, A. Khodadadi Darban, Simulation of adsorption of antimony on zero-valent iron nanoparticles coated on the industrial minerals (kaolinite, bentonite and perlite) in mineral effluent, Desalin. Water Treat. 57 (47) (2016) 22321–22328, https://doi.org/10.1080/19443994.2015.1130656.
[31] S.R. Kanel, J.M. Greneche, H. Choi, Arsenic(V) removal from groundwater using nano scale zero-valent iron as a colloidal reactive barrier material, Environ. Sci. Technol. 40 (6) (2006) 2045–2050, https://doi.org/10.1021/es0520924.
[32] A. Gupta, M. Yunus, N. Sankararamakrishnan, Zerovalent iron encapsulated chitosan nanospheres—a novel adsorbent for the removal of total inorganic arsenic from aqueous systems, Chemosphere 86 (2) (2012) 150–155, https://doi.org/10.1016/j.chemosphere.2011.10.003.
[33] S.R. Kanel, B. Manning, L. Charlet, H. Choi, Removal of arsenic(III) from groundwater by nanoscale zero-valent iron, Environ. Sci. Technol. 39 (5) (2005) 1291–1298, https://doi.org/10.1021/es048991u.

[34] H. Zhu, Y. Jia, X. Wu, H. Wang, Removal of arsenic from water by supported nano zero-valent iron on activated carbon, J. Hazard. Mater. 172 (2–3) (2009) 1591–1596, https://doi.org/10.1016/j.jhazmat.2009.08.031.
[35] P. Huang, Z. Ye, W. Xie, Q. Chen, J. Li, Z. Xu, M. Yao, Rapid magnetic removal of aqueous heavy metals and their relevant mechanisms using nanoscale zero valent iron (nZVI) particles, Water Res. 47 (12) (2013) 4050–4058, https://doi.org/10.1016/j.watres.2013.01.054.
[36] S.A. Kim, S. Kamala-Kannan, K.J. Lee, Y.J. Park, P.J. Shea, W.H. Lee, H.M. Kim, B.T. Oh, Removal of Pb(II) from aqueous solution by a zeolite-nanoscale zero-valent iron composite, Chem. Eng. J. 217 (2013) 54–60, https://doi.org/10.1016/j.cej.2012.11.097.
[37] T. Liu, Z.-L. Wang, X. Yan, B. Zhang, Removal of mercury (II) and chromium (VI) from wastewater using a new and effective composite: pumice-supported nanoscale zero-valent iron, Chem. Eng. J. 245 (0) (2014) 34–40, https://doi.org/10.1016/j.cej.2014.02.011.
[38] X. Zhang, S. Lin, X.Q. Lu, Z.L. Chen, Removal of Pb(II) from water using synthesized kaolin supported nanoscale zero-valent iron, Chem. Eng. J. 163 (3) (2010) 243–248, https://doi.org/10.1016/j.cej.2010.07.056.
[39] M. Auffan, W. Achouak, J. Rose, M.-A. Roncato, C. Chanéac, D.T. Waite, A. Masion, J.C. Woicik, M.R. Wiesner, J.-Y. Bottero, Relation between the redox state of iron-based nanoparticles and their cytotoxicity toward escherichia coli, Environ. Sci. Technol. 42 (17) (2008) 6730–6735, https://doi.org/10.1021/es800086f.
[40] J. Chen, Z. Xiu, G.V. Lowry, P.J.J. Alvarez, Effect of natural organic matter on toxicity and reactivity of nano-scale zero-valent iron, Water Res. 45 (5) (2011) 1995–2001, https://doi.org/10.1016/j.watres.2010.11.036.
[41] M. Diao, M. Yao, Use of zero-valent iron nanoparticles in inactivating microbes, Water Res. 43 (20) (2009) 5243–5251, https://doi.org/10.1016/j.watres.2009.08.051.
[42] R.J. Barnes, C.J. van der Gast, O. Riba, L.E. Lehtovirta, J.I. Prosser, P.J. Dobson, I.P. Thompson, The impact of zero-valent iron nanoparticles on a river water bacterial community, J. Hazard. Mater. 184 (1–3) (2010) 73–80, https://doi.org/10.1016/j.jhazmat.2010.08.006.
[43] Z. Li, K. Greden, P.J.J. Alvarez, K.B. Gregory, G.V. Lowry, Adsorbed polymer and NOM limits adhesion and toxicity of nano scale zerovalent iron to E. coli, Environ. Sci. Technol. 44 (9) (2010) 3462–3467, https://doi.org/10.1021/es9031198.
[44] H. Kim, H.J. Hong, J. Jung, S.H. Kim, J.W. Yang, Degradation of trichloroethylene (TCE) by nanoscale zero-valent iron (nZVI) immobilized in alginate bead, J. Hazard. Mater. 176 (1–3) (2010) 1038–1043, https://doi.org/10.1016/j.jhazmat.2009.11.145.
[45] C.B. Wang, W.X. Zhang, Synthesizing nanoscale iron particles for rapid and complete dechlorination of TCE and PCBs, Environ. Sci. Technol. 31 (7) (1997) 2154–2156, https://doi.org/10.1021/es970039c.
[46] L. Wu, M. Shamsuzzoha, S.M.C. Ritchie, Preparation of cellulose acetate supported zero-valent iron nanoparticles for the dechlorination of trichloroethylene in water, J. Nanopart. Res. (2005) 469–476, https://doi.org/10.1007/s11051-005-4271-5.
[47] Z. Xiu, Z. Jin, T. Li, S. Mahendra, G.V. Lowry, P.J.J. Alvarez, Effects of nano-scale zero-valent iron particles on a mixed culture dechlorinating trichloroethylene, Bioresour. Technol. 101 (4) (2010) 1141–1146, https://doi.org/10.1016/j.biortech.2009.09.057.
[48] A.N. Bezbaruah, J.M. Thompson, B.J. Chisholm, Remediation of alachlor and atrazine contaminated water with zero-valent iron nanoparticles, J. Environ. Sci. Health B Pestic. Food Contam. Agric. Wastes 44 (6) (2009) 518–524, https://doi.org/10.1080/03601230902997501.
[49] S.H. Joo, D. Zhao, Destruction of lindane and atrazine using stabilized iron nanoparticles under aerobic and anaerobic conditions: effects of catalyst and stabilizer, Chemosphere 70 (3) (2008) 418–425, https://doi.org/10.1016/j.chemosphere.2007.06.070.
[50] D.W. Elliott, H.-L. Lien, W.-X. Zhang, Degradation of lindane by zero-valent iron nanoparticles, J. Environ. Eng. (2009) 317–324, https://doi.org/10.1061/(ASCE)0733-9372(2009)135:5(317).

[51] Z. Xiong, D. Zhao, G. Pan, Rapid and complete destruction of perchlorate in water and ion-exchange brine using stabilized zero-valent iron nanoparticles, Water Res. 41 (15) (2007) 3497–3505, https://doi.org/10.1016/j.watres.2007.05.049.
[52] R. Cheng, J. Wang, W. Zhang, Degradation of chlorinated phenols by nanoscale zero-valent iron, Front. Environ. Sci. Eng. China 2 (1) (2008) 103–108, https://doi.org/10.1007/s11783-008-0009-9.
[53] S. Machado, W. Stawiński, P. Slonina, A.R. Pinto, J.P. Grosso, H.P.A. Nouws, J.T. Albergaria, C. Delerue-Matos, Application of green zero-valent iron nanoparticles to the remediation of soils contaminated with ibuprofen, Sci. Total Environ. 461–462 (2013) 323–329, https://doi.org/10.1016/j.scitotenv.2013.05.016.
[54] Y.T. Lin, C.H. Weng, F.Y. Chen, Effective removal of AB24 dye by nano/micro-size zero-valent iron, Sep. Purif. Technol. 64 (1) (2008) 26–30, https://doi.org/10.1016/j.seppur.2008.08.012.
[55] S.H. Joo, A.J. Feitz, T.D. Waite, Oxidative degradation of the carbothioate herbicide, molinate, using nano-scale zero-valent iron, Environ. Sci. Technol. 38 (7) (2004) 2242–2247, https://doi.org/10.1021/es035157g.
[56] K. Simeonidis, E. Kaprara, T. Samaras, M. Angelakeris, N. Pliatsikas, G. Vourlias, M. Mitrakas, N. Andritsos, Optimizing magnetic nanoparticles for drinking water technology: the case of Cr(VI), Sci. Total Environ. 535 (2015) 61–68, https://doi.org/10.1016/j.scitotenv.2015.04.033.
[57] E. Kaprara, K. Simeonidis, A. Zouboulis, M. Mitrakas, Rapid small-scale column tests for Cr(VI) removal by granular magnetite, Water Sci. Technol. Water Supply 16 (2) (2016) 525–532, https://doi.org/10.2166/ws.2015.164.
[58] C.A. Gorski, R.M. Handler, B.L. Beard, T. Pasakarnis, C.M. Johnson, M.M. Scherer, Fe atom exchange between aqueous Fe^{2+} and magnetite, Environ. Sci. Technol. 46 (22) (2012) 12399–12407, https://doi.org/10.1021/es204649a.
[59] F. Pinakidou, M. Katsikini, K. Simeonidis, E. Kaprara, E.C. Paloura, M. Mitrakas, On the passivation mechanism of Fe_3O_4 nanoparticles during Cr(VI) removal from water: a XAFS study, Appl. Surf. Sci. 360 (2016) 1080–1086, https://doi.org/10.1016/j.apsusc.2015.11.063.
[60] S.R. Chowdhury, E.K. Yanful, A.R. Pratt, Chemical states in XPS and Raman analysis during removal of Cr(VI) from contaminated water by mixed maghemite-magnetite nanoparticles, J. Hazard. Mater. 235–236 (2012) 246–256, https://doi.org/10.1016/j.jhazmat.2012.07.054.
[61] J. Hu, I.M.C. Lo, G. Chen, Removal of Cr(VI) by magnetite nanoparticle, Water Sci. Technol. 50 (12) (2004) 139–146.
[62] M.R. Lasheen, I.Y. El-Sherif, D.Y. Sabry, S.T. El-Wakeel, M.F. El-Shahat, Removal and recovery of Cr (VI) by magnetite nanoparticles, Desalin. Water Treat. 52 (34–36) (2013) 6464–6473, https://doi.org/10.1080/19443994.2013.822158.
[63] Y. Fu, J. Wang, Q. Liu, H. Zeng, Water-dispersible magnetic nanoparticle–graphene oxide composites for selenium removal, Carbon 77 (2014) 710–721, https://doi.org/10.1016/j.carbon.2014.05.076.
[64] C.M. Gonzalez, J. Hernandez, J.R. Peralta-Videa, C.E. Botez, J.G. Parsons, J.L. Gardea-Torresdey, Sorption kinetic study of selenite and selenate onto a high and low pressure aged iron oxide nanomaterial, J. Hazard. Mater. 211 (2012) 138–145, https://doi.org/10.1016/j.jhazmat.2011.08.023.
[65] J.H. Kwon, L.D. Wilson, R. Sammynaiken, Sorptive uptake of selenium with magnetite and its supported materials onto activated carbon, J. Colloid Interface Sci. 457 (2015) 388–397, https://doi.org/10.1016/j.jcis.2015.07.013.
[66] R.L.D.A. Loyo, S.I. Nikitenko, A.C. Scheinost, M. Simonoff, Immobilization of selenite on Fe_3O_4 and Fe/Fe_3C ultrasmall particles, Environ. Sci. Technol. 42 (7) (2008) 2451–2456, https://doi.org/10.1021/es702579w.
[67] X. Wei, S. Bhojappa, L.-S. Lin, R.C. Viadero, Performance of nano-magnetite for removal of selenium from aqueous solutions, Environ. Eng. Sci. 29 (6) (2012) 526–532, https://doi.org/10.1089/ees.2011.0383.
[68] T.S. Pasakarnis, M.I. Boyanov, K.M. Kemner, B. Mishra, E.J. O'Loughlin, G. Parkin, M.M. Scherer, Influence of chloride and Fe(II) content on the reduction of Hg(II) by magnetite, Environ. Sci. Technol. 47 (13) (2013) 6987–6994, https://doi.org/10.1021/es304761u.

[69] H.A. Wiatrowski, S. Das, R. Kukkadapu, E.S. Ilton, T. Barkay, N. Yee, Reduction of Hg(II) to Hg(0) by magnetite, Environ. Sci. Technol. 43 (14) (2009) 5307–5313, https://doi.org/10.1021/es9003608.
[70] D.M. Singer, S.M. Chatman, E.S. Ilton, K.M. Rosso, J.F. Banfield, G.A. Waychunas, U(VI) sorption and reduction kinetics on the magnetite (111) surface, Environ. Sci. Technol. 46 (7) (2012) 3821–3830, https://doi.org/10.1021/es203878c.
[71] C.T. Yavuz, J.T. Mayo, W.W. Yu, A. Prakash, J.C. Falkner, S. Yean, L. Cong, H.J. Shipley, A. Kan, M. Tomson, D. Natelson, V.L. Colvin, Low-field magnetic separation of monodisperse Fe_3O_4 nanocrystals, Science 314 (5801) (2006) 964–967. New York, N.Y. https://doi.org/10.1126/science.1131475.
[72] K. Simeonidis, T. Gkinis, S. Tresintsi, C. Martinez-Boubeta, G. Vourlias, I. Tsiaoussis, G. Stavropoulos, M. Mitrakas, M. Angelakeris, Magnetic separation of hematite-coated Fe_3O_4 particles used as arsenic adsorbents, Chem. Eng. J. 168 (3) (2011) 1008–1015, https://doi.org/10.1016/j.cej.2011.01.074.
[73] I. Akin, G. Arslan, A. Tor, M. Ersoz, Y. Cengeloglu, Arsenic(V) removal from underground water by magnetic nanoparticles synthesized from waste red mud, J. Hazard. Mater. 235 (2012) 62–68, https://doi.org/10.1016/j.jhazmat.2012.06.024.
[74] H.J. Shipley, K.E. Engates, A.M. Guettner, Study of iron oxide nanoparticles in soil for remediation of arsenic, J. Nanopart. Res. 13 (6) (2010) 2387–2397, https://doi.org/10.1007/s11051-010-9999-x.
[75] T. Türk, I. Alp, Arsenic removal from aqueous solutions with Fe-hydrotalcite supported magnetite nanoparticle, J. Ind. Eng. Chem. 20 (2) (2014) 732–738, https://doi.org/10.1016/j.jiec.2013.06.002.
[76] L. Balcells, C. Martínez-Boubeta, J. Cisneros-Fernández, K. Simeonidis, B. Bozzo, J. Oró-Sole, N. Bagués, J. Arbiol, N. Mestres, B. Martínez, One-step route to iron oxide hollow nanocuboids by cluster condensation: Implementation in water remediation technology, ACS Appl. Mater. Interfaces 8 (42) (2016) 28599–28606, https://doi.org/10.1021/acsami.6b08709.
[77] S.R. Chowdhury, E.K. Yanful, A.R. Pratt, Arsenic removal from aqueous solutions by mixed magnetite-maghemite nanoparticles, Environ. Earth Sci. 64 (2) (2011) 411–423, https://doi.org/10.1007/s12665-010-0865-z.
[78] H. Karami, Heavy metal removal from water by magnetite nanorods, Chem. Eng. J. 219 (2013) 209–216, https://doi.org/10.1016/j.cej.2013.01.022.
[79] N. Tran, A. Mir, D. Mallik, A. Sinha, S. Nayar, T.J. Webster, Bactericidal effect of iron oxide nanoparticles on Staphylococcus aureus, Int. J. Nanomed. 5 (1) (2010) 277–283.
[80] G. Guan, L. Yang, Q. Mei, K. Zhang, Z. Zhang, M.Y. Han, Chemiluminescence switching on peroxidase-like Fe_3O_4 nanoparticles for selective detection and simultaneous determination of various pesticides, Anal. Chem. 84 (21) (2012) 9492–9497, https://doi.org/10.1021/ac302341b.
[81] S. Ozcan, A. Tor, M.E. Aydin, Application of magnetic nanoparticles to residue analysis of organochlorine pesticides in water samples by GC/MS, J. AOAC Int. (2012) 1343–1349, https://doi.org/10.5740/jaoacint.SGE-Ozcan.
[82] X. Zheng, L. He, Y. Duan, X. Jiang, G. Xiang, W. Zhao, S. Zhang, Poly(ionic liquid) immobilized magnetic nanoparticles as new adsorbent for extraction and enrichment of organophosphorus pesticides from tea drinks, J. Chromatogr. A 1358 (2014) 39–45, https://doi.org/10.1016/j.chroma.2014.06.078.
[83] Z. He, P. Wang, D. Liu, Z. Zhou, Hydrophilic-lipophilic balanced magnetic nanoparticles: preparation and application in magnetic solid-phase extraction of organochlorine pesticides and triazine herbicides in environmental water samples, Talanta 127 (2014) 1–8, https://doi.org/10.1016/j.talanta.2014.03.074.
[84] D.H. Chen, S.H. Huang, Fast separation of bromelain by polyacrylic acid-bound iron oxide magnetic nanoparticles, Process Biochem. 39 (12) (2004) 2207–2211, https://doi.org/10.1016/j.procbio.2003.11.014.
[85] T. Tuutijärvi, J. Lu, M. Sillanpää, G. Chen, As(V) adsorption on maghemite nanoparticles, J. Hazard. Mater. 166 (2–3) (2009) 1415–1420, https://doi.org/10.1016/j.jhazmat.2008.12.069.
[86] H. Park, N.V. Myung, H. Jung, H. Choi, As(V) remediation using electrochemically synthesized maghemite nanoparticles, J. Nanopart. Res. 11 (8) (2009) 1981–1989, https://doi.org/10.1007/s11051-008-9558-x.

[87] M. Auffan, J. Rose, O. Proux, D. Borschneck, A. Masion, P. Chaurand, J.L. Hazemann, C. Chaneac, J.P. Jolivet, M.R. Wiesner, A. Van Geen, J.Y. Bottero, Enhanced adsorption of arsenic onto maghemites nanoparticles: As(III) as a probe of the surface structure and heterogeneity, Langmuir 24 (7) (2008) 3215–3222, https://doi.org/10.1021/la702998x.

[88] J. Hu, G. Chen, I.M.C. Lo, Removal and recovery of Cr(VI) from wastewater by maghemite nanoparticles, Water Res. 39 (18) (2005) 4528–4536, https://doi.org/10.1016/j.watres.2005.05.051.

[89] W. Jiang, M. Pelaez, D.D. Dionysiou, M.H. Entezari, D. Tsoutsou, K. O'Shea, Chromium(VI) removal by maghemite nanoparticles, Chem. Eng. J. 222 (2013) 527–533, https://doi.org/10.1016/j.cej.2013.02.049.

[90] A. Afkhami, R. Norooz-Asl, Removal, preconcentration and determination of Mo(VI) from water and wastewater samples using maghemite nanoparticles, Colloids Surf. A Physicochem. Eng. Asp. 346 (1–3) (2009) 52–57, https://doi.org/10.1016/j.colsurfa.2009.05.024.

[91] N. Jordan, A. Ritter, A.C. Scheinost, S. Weiss, D. Schild, R. Hübner, Selenium(IV) uptake by maghemite (γ-Fe_2O_3), Environ. Sci. Technol. 48 (3) (2014) 1665–1674, https://doi.org/10.1021/es4045852.

[92] A.W. Lounsbury, J.S. Yamani, C.P. Johnston, P. Larese-Casanova, J.B. Zimmerman, The role of counter ions in nano-hematite synthesis: implications for surface area and selenium adsorption capacity, J. Hazard. Mater. 310 (2016) 117–124, https://doi.org/10.1016/j.jhazmat.2016.01.078.

[93] S. Qu, F. Huang, S. Yu, G. Chen, J. Kong, Magnetic removal of dyes from aqueous solution using multi-walled carbon nanotubes filled with Fe_2O_3 particles, J. Hazard. Mater. 160 (2–3) (2008) 643–647, https://doi.org/10.1016/j.jhazmat.2008.03.037.

[94] K. Ahalya, N. Suriyanarayanan, V. Ranjithkumar, Effect of cobalt substitution on structural and magnetic properties and chromium adsorption of manganese ferrite nanoparticles, J. Magn. Magn. Mater. 372 (2014) 208–213, https://doi.org/10.1016/j.jmmm.2014.07.030.

[95] J. Hu, I.M.C. Lo, G. Chen, Fast removal and recovery of Cr(VI) using surface-modified jacobsite ($MnFe_2O_4$) nanoparticles, Langmuir 21 (24) (2005) 11173–11179, https://doi.org/10.1021/la051076h.

[96] Y.-J. Tu, C.-F. You, C.-K. Chang, T.-S. Chan, S.-H. Li, XANES evidence of molybdenum adsorption onto novel fabricated nano-magnetic $CuFe_2O_4$, Chem. Eng. J. 244 (2014) 343–349, https://doi.org/10.1016/j.cej.2014.01.084.

[97] Y.-J. Tu, T.-S. Chan, H.-W. Tu, S.-L. Wang, C.-F. You, C.-K. Chang, Rapid and efficient removal/recovery of molybdenum onto $ZnFe_2O_4$ nanoparticles, Chemosphere 148 (2016) 452–458, https://doi.org/10.1016/j.chemosphere.2016.01.054.

[98] J. Wei, X. Zhang, Q. Liu, Z. Li, L. Liu, J. Wang, Magnetic separation of uranium by $CoFe_2O_4$ hollow spheres, Chem. Eng. J. 241 (2014) 228–234, https://doi.org/10.1016/j.cej.2013.12.035.

[99] W. Tang, Y. Su, Q. Li, S. Gao, J.K. Shang, Superparamagnetic magnesium ferrite nanoadsorbent for effective arsenic (III, V) removal and easy magnetic separation, Water Res. 47 (11) (2013) 3624–3634, https://doi.org/10.1016/j.watres.2013.04.023.

[100] A. Dey, R. Singh, M.K. Purkait, Cobalt ferrite nanoparticles aggregated schwertmannite: a novel adsorbent for the efficient removal of arsenic, J. Water Process Eng. 3 (2014) 1–9, https://doi.org/10.1016/j.jwpe.2014.07.002.

[101] Garcia, S., Sardar, S., Maldonado, S., Garcia, V., Tamez, C. and Parsons, J. G. (2014) 'Study of As(III) and As(V) oxoanion adsorption onto single and mixed ferrite and hausmannite nanomaterials', Microchem. J., 117(0), pp. 52–60. https://doi.org/10.1016/j.microc.2014.06.008.

[102] N.D. Phu, P.C. Phong, N. Chau, N.H. Luong, L.H. Hoang, N.H. Hai, Arsenic removal from water by magnetic $Fe_{1-x}Co_xFe_2O_4$ and $Fe_{1-y}Ni_yFe_2O_4$ nanoparticles, J. Exp. Nanosci. 4 (3) (2009) 253–258, https://doi.org/10.1080/17458080802590474.

[103] S. Gautam, P. Shandilya, B. Priya, V.P. Singh, P. Raizada, R. Rai, M.A. Valente, P. Singh, Superparamagnetic $MnFe_2O_4$ dispersed over graphitic carbon sand composite and bentonite as magnetically recoverable photocatalyst for antibiotic mineralization, Sep. Purif. Technol. 172 (2017) 498–511, https://doi.org/10.1016/j.seppur.2016.09.006.

[104] D.W. Elliott, W.X. Zhang, Field assessment of nanoscale bimetallic particles for groundwater treatment, Environ. Sci. Technol. 35 (24) (2001) 4922–4926, https://doi.org/10.1021/es0108584.
[105] M. Zhang, F. He, D. Zhao, X. Hao, Degradation of soil-sorbed trichloroethylene by stabilized zero valent iron nanoparticles: effects of sorption, surfactants, and natural organic matter, Water Res. 45 (7) (2011) 2401–2414, https://doi.org/10.1016/j.watres.2011.01.028.
[106] F. He, D. Zhao, Preparation and characterization of a new class of starch-stabilized bimetallic nanoparticles for degradation of chlorinated hydrocarbons in water, Environ. Sci. Technol. 39 (9) (2005) 3314–3320, https://doi.org/10.1021/es048743y.
[107] B.W. Zhu, T.T. Lim, Catalytic reduction of chlorobenzenes with Pd/Fe nanoparticles: reactive sites, catalyst stability, particle aging, and regeneration, Environ. Sci. Technol. 41 (21) (2007) 7523–7529, https://doi.org/10.1021/es0712625.
[108] H. Tian, J. Li, Z. Mu, L. Li, Z. Hao, Effect of pH on DDT degradation in aqueous solution using bimetallic Ni/Fe nanoparticles, Sep. Purif. Technol. 66 (1) (2009) 84–89, https://doi.org/10.1016/j.seppur.2008.11.018.
[109] B. Schrick, J.L. Blough, A.D. Jones, T.E. Mallouk, Hydrodechlorination of trichloroethylene to hydrocarbons using bimetallic nickel-iron nanoparticles, Chem. Mater. 14 (12) (2002) 5140–5147, https://doi.org/10.1021/cm020737i.
[110] Y.H. Tee, E. Grulke, D. Bhattacharyya, Role of Ni/Fe nanoparticle composition on the degradation of trichloroethylene from water, Ind. Eng. Chem. Res. 44 (18) (2005) 7062–7070, https://doi.org/10.1021/ie050086a.
[111] Z. Marková, K.M. Šišková, J. Filip, J. Čuda, M. Kolář, K. Šafářová, I. Medřík, R. Zbořil, Air stable magnetic bimetallic Fe-Ag nanoparticles for advanced antimicrobial treatment and phosphorus removal, Environ. Sci. Technol. 47 (10) (2013) 5285–5293, https://doi.org/10.1021/es304693g.
[112] M. Rivero-Huguet, W.D. Marshall, Reduction of hexavalent chromium mediated by micro- and nano-sized mixed metallic particles, J. Hazard. Mater. 169 (1–3) (2009) 1081–1087, https://doi.org/10.1016/j.jhazmat.2009.04.062.
[113] D. O'Carroll, B. Sleep, M. Krol, H. Boparai, C. Kocur, Nanoscale zero valent iron and bimetallic particles for contaminated site remediation, Adv. Water Res. 51 (2013) 104–122, https://doi.org/10.1016/j.advwatres.2012.02.005.
[114] X. Luo, C. Wang, S. Luo, R. Dong, X. Tu, G. Zeng, Adsorption of As (III) and As (V) from water using magnetite Fe_3O_4-reduced graphite oxide–MnO_2 nanocomposites, Chemical Engineering Journal 187 (0) (2012) 45–52, https://doi.org/10.1016/j.cej.2012.01.073.
[115] J. Hu, I.M.C. Lo, G. Chen, Performance and mechanism of chromate (VI) adsorption by δ-FeOOH-coated maghemite (γ-Fe_2O_3) nanoparticles, Sep. Purif. Technol. 58 (1) (2007) 76–82, https://doi.org/10.1016/j.seppur.2007.07.023.
[116] Y. Feng, J.-L. Gong, G.-M. Zeng, Q.-Y. Niu, H.-Y. Zhang, C.-G. Niu, J.-H. Deng, M. Yan, Adsorption of Cd (II) and Zn (II) from aqueous solutions using magnetic hydroxyapatite nanoparticles as adsorbents, Chem. Eng. J. (2010) 487–494, https://doi.org/10.1016/j.cej.2010.05.049.
[117] J. Lan, Removal of arsenic from aqueous systems by use of magnetic Fe_3O_4@TiO_2 nanoparticles, Res. Chem. Intermed. 41 (6) (2015) 3531–3541, https://doi.org/10.1007/s11164-013-1469-5.
[118] L. Yu, X. Peng, F. Ni, J. Li, D. Wang, Z. Luan, Arsenite removal from aqueous solutions by α-Fe_2O_3-TiO_2 magnetic nanoparticles through simultaneous photocatalytic oxidation and adsorption, J. Hazard. Mater. 246–247 (2013) 10–17, https://doi.org/10.1016/j.jhazmat.2012.12.007.
[119] N. Zhang, H. Peng, B. Hu, Light-induced pH change and its application to solid phase extraction of trace heavy metals by high-magnetization Fe_3O_4@SiO_2@TiO_2 nanoparticles followed by inductively coupled plasma mass spectrometry detection, Talanta 94 (2012) 278–283, https://doi.org/10.1016/j.talanta.2012.03.040.
[120] X. Ge, W. Zhang, Y. Lin, D. Du, Magnetic Fe_3O_4@TiO_2 nanoparticles-based test strip immunosensing device for rapid detection of phosphorylated butyrylcholinesterase, Biosens. Bioelectron. 50 (2013) 486–491, https://doi.org/10.1016/j.bios.2013.07.017.

[121] C. Li, R. Younesi, Y. Cai, Y. Zhu, M. Ma, J. Zhu, Photocatalytic and antibacterial properties of Au-decorated Fe_3O_4@mTiO_2 core-shell microspheres, App. Catal. B Environ 156–157 (2014) 314–322, https://doi.org/10.1016/j.apcatb.2014.03.031.
[122] C.Y. Hu, S.L. Lo, Y.H. Liou, Y.W. Hsu, K. Shih, C.J. Lin, Hexavalent chromium removal from near natural water by copper-iron bimetallic particles, Water Res. 44 (10) (2010) 3101–3108, https://doi.org/10.1016/j.watres.2010.02.037.
[123] S. Singh, K.C. Barick, D. Bahadur, Surface engineered magnetic nanoparticles for removal of toxic metal ions and bacterial pathogens, J. Hazard. Mater. 192 (3) (2011) 1539–1547, https://doi.org/10.1016/j.jhazmat.2011.06.074.
[124] Y. Su, A.S. Adeleye, A.A. Keller, Y. Huang, C. Dai, X. Zhou, Y. Zhang, Magnetic sulfide-modified nanoscale zerovalent iron (S-nZVI) for dissolved metal ion removal, Water Res. 74 (2015) 47–57, https://doi.org/10.1016/j.watres.2015.02.004.
[125] Y. Wu, J. Zhang, Y. Tong, X. Xu, Chromium (VI) reduction in aqueous solutions by Fe_3O_4-stabilized Fe^0 nanoparticles, J. Hazard. Mater. 172 (2–3) (2009) 1640–1645, https://doi.org/10.1016/j.jhazmat.2009.08.045.
[126] Y. Su, A.S. Adeleye, Y. Huang, X. Sun, C. Dai, X. Zhou, Y. Zhang, A.A. Keller, Simultaneous removal of cadmium and nitrate in aqueous media by nanoscale zerovalent iron (nZVI) and Au doped nZVI particles, Water Res. 63 (2014) 102–111, https://doi.org/10.1016/j.watres.2014.06.008.
[127] B. Geng, Z. Jin, T. Li, X. Qi, Kinetics of hexavalent chromium removal from water by chitosan-Fe^0 nanoparticles, Chemosphere 75 (6) (2009) 825–830, https://doi.org/10.1016/j.chemosphere.2009.01.009.
[128] Q. Wang, H. Qian, Y. Yang, Z. Zhang, C. Naman, X. Xu, Reduction of hexavalent chromium by carboxymethyl cellulose-stabilized zero-valent iron nanoparticles, J. Contam. Hydrol. 114 (1–4) (2010) 35–42, https://doi.org/10.1016/j.jconhyd.2010.02.006.
[129] C. Mystrioti, N. Papassiopi, A. Xenidis, D. Dermatas, M. Chrysochoou, Column study for the evaluation of the transport properties of polyphenol-coated nanoiron, J. Hazard. Mater. 281 (2015) 64–69, https://doi.org/10.1016/j.jhazmat.2014.05.050.
[130] L. Alidokht, A.R. Khataee, A. Reyhanitabar, S. Oustan, Reductive removal of Cr(VI) by starch-stabilized Fe^0 nanoparticles in aqueous solution, Desalination 270 (1–3) (2011) 105–110, https://doi.org/10.1016/j.desal.2010.11.028.
[131] G. López-Téllez, C.E. Barrera-Díaz, P. Balderas-Hernández, G. Roa-Morales, B. Bilyeu, Removal of hexavalent chromium in aquatic solutions by iron nanoparticles embedded in orange peel pith, Chem. Eng. J. 173 (2) (2011) 480–485, https://doi.org/10.1016/j.cej.2011.08.018.
[132] S. Comba, R. Sethi, Stabilization of highly concentrated suspensions of iron nanoparticles using shear-thinning gels of xanthan gum, Water Res. 43 (15) (2009) 3717–3726, https://doi.org/10.1016/j.watres.2009.05.046.
[133] X. Liu, Q. Hu, Z. Fang, X. Zhang, B. Zhang, Magnetic chitosan nanocomposites: a useful recyclable tool for heavy metal ion removal, Langmuir 25 (1) (2009) 3–8, https://doi.org/10.1021/la802754t.
[134] N.N. Thinh, P.T.B. Hanh, L.T.T. Ha, L.N. Anh, T.V. Hoang, V.D. Hoang, L.H. Dang, N. Van Khoi, T.D. Lam, Magnetic chitosan nanoparticles for removal of Cr(VI) from aqueous solution, Mater. Sci. Eng. C 33 (3) (2013) 1214–1218, https://doi.org/10.1016/j.msec.2012.12.013.
[135] Y. Jin, F. Liu, M. Tong, Y. Hou, Removal of arsenate by cetyltrimethylammonium bromide modified magnetic nanoparticles, J. Hazard. Mater. 227–228 (2012) 46–468, https://doi.org/10.1016/j.jhazmat.2012.05.004.
[136] B. An, Q. Liang, D. Zhao, Removal of arsenic(V) from spent ion exchange brine using a new class of starch-bridged magnetite nanoparticles, Water Res. 45 (5) (2011) 1961–1972, https://doi.org/10.1016/j.watres.2011.01.004.
[137] L. Feng, M. Cao, X. Ma, Y. Zhu, C. Hu, Superparamagnetic high-surface-area Fe_3O_4 nanoparticles as adsorbents for arsenic removal, J. Hazard. Mater. 217–218 (2012) 439–446, https://doi.org/10.1016/j.jhazmat.2012.03.073.

[138] S.H. Huang, D.H. Chen, Rapid removal of heavy metal cations and anions from aqueous solutions by an amino-functionalized magnetic nano-adsorbent, J. Hazard. Mater. 163 (1) (2009) 174–179, https://doi.org/10.1016/j.jhazmat.2008.06.075.

[139] M. Bhaumik, A. Maity, V.V. Srinivasu, M.S. Onyango, Enhanced removal of Cr(VI) from aqueous solution using polypyrrole/Fe_3O_4 magnetic nanocomposite, J. Hazard. Mater. 190 (1–3) (2011) 381–390, https://doi.org/10.1016/j.jhazmat.2011.03.062.

[140] J. Liu, Z. Zhao, G. Jiang, Coating Fe_3O_4 magnetic nanoparticles with humic acid for high efficient removal of heavy metals in water, Environ. Sci. Technol. 42 (18) (2008) 6949–6954, https://doi.org/10.1021/es800924c.

[141] A.Z.M. Badruddoza, A.S.H. Tay, P.Y. Tan, K. Hidajat, M.S. Uddin, Carboxymethyl-β-cyclodextrin conjugated magnetic nanoparticles as nano-adsorbents for removal of copper ions: synthesis and adsorption studies, J. Hazard. Mater. 185 (2–3) (2011) 1177–1186, https://doi.org/10.1016/j.jhazmat.2010.10.029.

[142] F. Ge, M.-M. Li, H. Ye, B.-X. Zhao, Effective removal of heavy metal ions Cd^{2+}, Zn^{2+}, Pb^{2+}, Cu^{2+} from aqueous solution by polymer-modified magnetic nanoparticles, J. Hazard. Mater. (2012) 366–372, https://doi.org/10.1016/j.jhazmat.2011.12.013.

[143] A.R. Mahdavian, M.A.S. Mirrahimi, Efficient separation of heavy metal cations by anchoring polyacrylic acid on superparamagnetic magnetite nanoparticles through surface modification, Chem. Eng. J. 159 (1–3) (2010) 264–271, https://doi.org/10.1016/j.cej.2010.02.041.

[144] S.-C. Jang, S.-B. Hong, H.-M. Yang, K.-W. Lee, J.-K. Moon, B.-K. Seo, Y. Huh, C. Roh, Removal of radioactive cesium using prussian blue magnetic nanoparticles, Nanomaterials 4 (4) (2014) 894–901, https://doi.org/10.3390/nano4040894.

[145] L.C.B. Stopa, M. Yamaura, Uranium removal by chitosan impregnated with magnetite nanoparticles: adsorption and desorption, Int. J. Nucl. Energy Sci. Technol. 5 (4) (2010) 283, https://doi.org/10.1504/IJNEST.2010.035538.

[146] Y. Zhao, J. Li, L. Zhao, S. Zhang, Y. Huang, X. Wu, X. Wang, Synthesis of amidoxime-functionalized Fe_3O_4@SiO_2 core-shell magnetic microspheres for highly efficient sorption of U(VI), Chem. Eng. J. 235 (2014) 275–283, https://doi.org/10.1016/j.cej.2013.09.034.

[147] O. Hakami, Y. Zhang, C.J. Banks, Thiol-functionalised mesoporous silica-coated magnetite nanoparticles for high efficiency removal and recovery of Hg from water, Water Res. 46 (12) (2012) 3913–3922, https://doi.org/10.1016/j.watres.2012.04.032.

[148] Y. Li, L. Qi, Y. Shen, H. Ma, Facile preparation of surface-exchangeable core@shell iron oxide@gold nanoparticles for magnetic solid-phase extraction: use of gold shell as the intermediate platform for versatile adsorbents with varying self-assembled monolayers, Anal. Chim. Acta 811 (2014) 36–42, https://doi.org/10.1016/j.aca.2013.12.020.

[149] A.Z.M. Badruddoza, G.S.S. Hazel, K. Hidajat, M.S. Uddin, Synthesis of carboxymethyl-β-cyclodextrin conjugated magnetic nano-adsorbent for removal of methylene blue, Colloids Surf. A Physicochem. Eng. Asp. 367 (1–3) (2010) 85–95, https://doi.org/10.1016/j.colsurfa.2010.06.018.

[150] G.R. Chaudhary, P. Saharan, A. Kumar, S.K. Mehta, S. Mor, A. Umar, Adsorption studies of cationic, anionic and azo-dyes via monodispersed Fe_3O_4 nanoparticles, J. Nanosci .Nanotechnol. (2013). https://doi.org/10.1166/jnn.2013.7152.

[151] H. Niu, D. Zhang, S. Zhang, X. Zhang, Z. Meng, Y. Cai, Humic acid coated Fe_3O_4 magnetic nanoparticles as highly efficient Fenton-like catalyst for complete mineralization of sulfathiazole, J. Hazard. Mater. 190 (1–3) (2011) 559–565, https://doi.org/10.1016/j.jhazmat.2011.03.086.

[152] F. Ge, H. Ye, M.-M. Li, B.-X. Zhao, Efficient removal of cationic dyes from aqueous solution by polymer-modified magnetic nanoparticles, Chem. Eng. J. (2012) 11–17, https://doi.org/10.1016/j.cej.2012.05.074.

[153] Z. Zhou, S. Lin, T. Yue, T.C. Lee, Adsorption of food dyes from aqueous solution by glutaraldehyde cross-linked magnetic chitosan nanoparticles, J. Food Eng. 126 (2014) 133–141, https://doi.org/10.1016/j.jfoodeng.2013.11.014.

[154] N.C. Feitoza, T.D. Gonçalves, J.J. Mesquita, J.S. Menegucci, M.K.M.S. Santos, J.A. Chaker, R.B. Cunha, A.M.M. Medeiros, J.C. Rubim, M.H. Sousa, Fabrication of glycine-functionalized maghemite nanoparticles for magnetic removal of copper from wastewater, J. Hazard. Mater. 264 (2014) 153–160, https://doi.org/10.1016/j.jhazmat.2013.11.022.

[155] A. Nematollahzadeh, S. Seraj, B. Mirzayi, Catecholamine coated maghemite nanoparticles for the environmental remediation: hexavalent chromium ions removal, Chem. Eng. J. 277 (2015) 21–29, https://doi.org/10.1016/j.cej.2015.04.135.

[156] J. Song, H. Kong, J. Jang, Adsorption of heavy metal ions from aqueous solution by polyrhodanine-encapsulated magnetic nanoparticles, J. Colloid Interface Sci. 359 (2) (2011) 505–511, https://doi.org/10.1016/j.jcis.2011.04.034.

[157] A. Afkhami, M. Saber-Tehrani, H. Bagheri, Modified maghemite nanoparticles as an efficient adsorbent for removing some cationic dyes from aqueous solution, Desalination 263 (1–3) (2010) 240–248, https://doi.org/10.1016/j.desal.2010.06.065.

[158] E.C. Stoner, LXXXIV. Magnetic energy and the thermodynamics of magnetization, Lond. Edinb. Dublin Philos. Magaz. J. Sci. 23 (157) (1937) 833–857. Taylor & Francis Group. https://doi.org/10.1080/14786443708561859.

[159] J. Gómez-Pastora, S. Dominguez, E. Bringas, M.J. Rivero, I. Ortiz, Review and perspectives on the use of magnetic nanophotocatalysts (MNPCs) in water treatment, Chem. Eng. J. 310 (2017) 407–427, https://doi.org/10.1016/j.cej.2016.04.140.

[160] M.U. Sankar, S. Aigal, S.M. Maliyekkal, A. Chaudhary, K.A.A. Anshup, K. Chaudhari, T. Pradeep, Biopolymer-reinforced synthetic granular nanocomposites for affordable point-of-use water purification, Proc. Natl. Acad. Sci. U. S. A. 110 (21) (2013) 8459–8464, https://doi.org/10.1073/pnas.1220222110.

[161] P. Westerhoff, P. Alvarez, Q. Li, J. Gardea-Torresdey, J. Zimmerman, Overcoming implementation barriers for nanotechnology in drinking water treatment, Environ. Sci. Nano. 3 (6) (2016) 1241–1253. The Royal Society of Chemistry. https://doi.org/10.1039/C6EN00183A.

[162] R.D. Ambashta, M. Sillanpää, Water purification using magnetic assistance: A review, J. Hazard. Mater. (2010) 38–49, https://doi.org/10.1016/j.jhazmat.2010.04.105.

[163] L. Luo, A.V. Nguyen, A review of principles and applications of magnetic flocculation to separate ultrafine magnetic particles, Sep. Purif. Technol. 172 (2017) 85–99, https://doi.org/10.1016/j.seppur.2016.07.021.

[164] O. Cugat, P. Hansson, J.M.D. Coey, Permanent magnet variable flux sources, IEEE Trans. Magn. 30 (6) (1994) 4602–4604, https://doi.org/10.1109/20.334162.

[165] J.D. Navratil, M.T. Shing Tsair, Magnetic separation of iron and heavy metals from water, Water Sci. Technol. 47 (1) (2003) 29–32. Available at: http://www.ncbi.nlm.nih.gov/pubmed/12578170.

[166] J. Shimoiizaka, K. Nakatsuka, T. Fujita, A. Kounosu, Sink-float separators using permanent magnets and water based magnetic fluid, IEEE Trans. Magn. 16 (2) (1980) 368–371, https://doi.org/10.1109/TMAG.1980.1060588.

[167] L.C. Lipus, B. Ačko, A. Hamler, Electromagnets for high-flow water processing, Chem. Eng. Process. Process Intensif. 50 (9) (2011) 952–958, https://doi.org/10.1016/j.cep.2011.07.004.

[168] S.K. Baik, D.W. Ha, J.M. Kwon, Y.J. Lee, R.K. Ko, Magnetic force on a magnetic particle within a high gradient magnetic separator, Phys. C Supercond. 484 (2013) 333–337, https://doi.org/10.1016/j.physc.2012.03.033.

[169] A. Cieśla, Practical aspects of high gradient magnetic separation using superconducting magnets, Physicochem. Probl. Miner. Process. 37 (2003) 169–181.

[170] A.P. Drozdov, M.I. Eremets, I.A. Troyan, V. Ksenofontov, S.I. Shylin, Conventional superconductivity at 203 kelvin at high pressures in the sulfur hydride system, Nature 525 (7567) (2015) 73–76, https://doi.org/10.1038/nature14964.

[171] S.Q. Li, M.F. Wang, Z.A. Zhu, Q. Wang, X. Zhang, H.Q. Song, D.Q. Cang, Application of superconducting HGMS technology on turbid wastewater treatment from converter, Sep. Purif. Technol. (2012) 56–62, https://doi.org/10.1016/j.seppur.2011.09.034.
[172] J.-B. Song, K.L. Kim, D. Yang, Y.-G. Kim, J. Lee, M.C. Ahn, H. Lee, High-T_c superconducting high gradient magnetic separator using solid nitrogen cooling system for purification of CMP wastewater, IEEE Trans. Appl. Supercond. 23 (3) (2013) 3700505, https://doi.org/10.1109/TASC.2013.2255950.
[173] Y. Zhao, B. Xi, Y. Li, M. Wang, Z. Zhu, X. Xia, L.Y. Zhang, L. Wang, Z. Luan, Removal of phosphate from wastewater by using open gradient superconducting magnetic separation as pretreatment for high gradient superconducting magnetic separation, Sep. Purif. Technol. 86 (2012) 255–261, https://doi.org/10.1016/j.seppur.2011.11.014.
[174] W. Wei, S.Q. Li, Y. Liu, W.B. Wang, H.T. Wen, Application and development of superconducting high gradient magnetic separation on environmental protection, Adv. Mater. Res. 955–959 (2014) 2128–2132, https://doi.org/10.4028/www.scientific.net/AMR.955-959.2128.
[175] T. Oka, K. Tanaka, T. Kimura, D. Mimura, S. Fukui, J. Ogawa, T. Sato, M. Ooizumi, K. Yokoyama, M. Yamaguchi, Magnetic separation technique for environmental water purification by strong magnetic field generator loading HTS bulk magnets, Phys. C Supercond. Appl. (2010) 1799–1803, https://doi.org/10.1016/j.physc.2010.05.210.
[176] T. Okamoto, S. Tachibana, O. Miura, M. Takeuchi, Mercury removal from solution by superconducting magnetic separation with nanostructured magnetic adsorbents, Phys. C Supercond. Appl. (2011) 1516–1519, https://doi.org/10.1016/j.physc.2011.05.228.
[177] Y. Li, B. Zhou, F. Xu, H. Jiang, W. Zhang, The advantages of a superconducting magnetic intensity greater than 1 T for phosphate-ferric flocs separation in HGMS, Sep. Purif. Technol. 141 (2015) 331–338, https://doi.org/10.1016/j.seppur.2014.12.022.
[178] J. Kopp, Superconducting magnetic separators, Phys. Sep. Sci. Eng. 3 (1) (1991) 17–32.
[179] T. Oka, K. Yokoyama, Y. Itoh, H. Ikuta, U. Mizutani, H. Okada, K. Katagiri, K. Noto, Construction of a strong magnetic field generator with use of melt-processed bulk superconductors, IEEE Trans. Appl. Supercond. (2003) 1584–1587, https://doi.org/10.1109/TASC.2003.812796.
[180] T. Morisue, Magnetic vector potential and electric scalar potential in three-dimensional eddy current problem, IEEE Trans. Magn. 18 (2) (1982) 531–535, https://doi.org/10.1109/TMAG.1982.1061856.
[181] D. Fletcher, Fine particle high gradient magnetic entrapment, IEEE Trans. Magn. 27 (4) (1991) 3655–3677, https://doi.org/10.1109/20.102936.
[182] F.M. Pedrero, M.T. Miranda, A. Schmitt, J.C. Fernández, Forming chainlike filaments of magnetic colloids: the role of the relative strength of isotropic and anisotropic particle interactions, J. Chem. Phys. 125 (8) (2006) https://doi.org/10.1063/1.2220561.
[183] R. Regmi, C. Black, C. Sudakar, P.H. Keyes, R. Naik, G. Lawes, P. Vaishnava, C. Rablau, D. Kahn, M. Lavoie, V.K. Garg, A.C. Oliveira, Effects of fatty acid surfactants on the magnetic and magnetohydrodynamic properties of ferrofluids, J. Appl. Phys. 106 (11) (2009), https://doi.org/10.1063/1.3259382.
[184] Y. Chalopin, J.-C. Bacri, F. Gazeau, M. Devaud, Nanoscale brownian heating by interacting magnetic dipolar particles, Sci. Rep. 7 (2017) 1–9, https://doi.org/10.1038/s41598-017-01760-x.
[185] I. Conde-Leboran, D. Baldomir, C. Martinez-Boubeta, O. Chubykalo-Fesenko, M. Del Puerto Morales, G. Salas, D. Cabrera, J. Camarero, F.J. Teran, D. Serantes, A single picture explains diversity of hyperthermia response of magnetic nanoparticles, J. Phys. Chem. C 119 (27) (2015) 15698–15706, https://doi.org/10.1021/acs.jpcc.5b02555.
[186] M. Woińska, J. Szczytko, A. Majhofer, J. Gosk, K. Dziatkowski, A. Twardowski, Magnetic interactions in an ensemble of cubic nanoparticles: a Monte Carlo study, Phys. Rev. B Condens. Matter Mater. Phys. 88 (14) (2013), https://doi.org/10.1103/PhysRevB.88.144421.

[187] C. De Latour, Magnetic separation in water pollution control, IEEE Trans. Magn. 9 (3) (1973) 314–316, https://doi.org/10.1109/TMAG.1973.1067685.

[188] K. Simeonidis, C. Martinez-Boubeta, P. Rivera-Gil, S. Ashraf, T. Samaras, M. Angelakeris, S. Tresintsi, M. Mitrakas, W.J. Parak, C. Monty, L. Balcells, Regeneration of arsenic spent adsorbents by Fe/MgO nanoparticles, J. Chem. Technol. Biotechnol. (2017) John Wiley & Sons, Ltd. https://doi.org/10.1002/jctb.5187

[189] T.E. Abbott Chalew, G.S. Ajmani, H. Huang, K.J. Schwab, Evaluating nanoparticle breakthrough during drinking water treatment, Environ. Health Perspect. 121 (10) (2013) 1161–1166, https://doi.org/10.1289/ehp.1306574.

FURTHER READING

[190] Y. Li, J. Wang, Y. Zhao, Z. Luan, Research on magnetic seeding flocculation for arsenic removal by superconducting magnetic separation, Sep. Purif. Technol. 73 (2) (2010) 264–270, https://doi.org/10.1016/j.seppur.2010.04.011.

CHAPTER

NOBLE METAL NANOPARTICLES FOR WATER PURIFICATION 21

Ewa Kowalska[*,†], **Maya Endo**[*], **Zhishun Wei**[*,‡], **Kunlei Wang**[*,†], **Marcin Janczarek**[*,§]

Institute for Catalysis, Hokkaido University, Sapporo, Japan[*] Graduate School of Environmental Science, Hokkaido University, Sapporo, Japan[†] School of Materials and Chemical Engineering, Hubei University of Technology, Wuhan, China[‡] Department of Chemical Technology, Gdansk University of Technology, Gdansk, Poland[§]

1 INTRODUCTION

An enormous number and various kinds of indoor and outdoor pollutants are released during people's everyday lives affecting their health and surrounding flora and fauna. Both chemical and microbiological pollutants are very dangerous, for example, traffic-related air pollution was associated with prevalence of childhood asthma [1], the acute effect on respiratory symptoms and peak expiratory flow rate of fungus spores was found for *Cladosporium* sp. and *Epicoccum* sp. [2], everyday exposure to multiple chemicals was associated with asthma, allergy, autism, medically unexplained symptoms [3, 4], poisoning, neurobehavioral disorder [5], chronic cough [6], risk of cancer, and death [7]. Although environmental contaminations by chemical pollutants is usually well-monitored and controlled, especially in developed countries (due to strict environmental regulations [8–10]), microbiological pollution is often accidental and results in the out-of-control spreading of microorganisms. In addition, microorganisms (unlike chemical compounds) can grow very fast, for example, some bacteria and fungi can rapidly reproduce on the surface of building materials, such as wood, paper, gypsum, ceramic, mineral, paints, and plastics [11]. Moreover, positive, negative or neutral interactions between various bacteria and fungi via infochemicals produced by them [12, 13], as well as between microorganisms and chemical pollutants, may have crucial impact on an environment. For example, pathogenic bacteria *Pseudomonas aeruginosa* and chemical compounds with 12-carbon chain length (dodecanol, C12-acyl homoserine lactone) inhibited transition of fungal cells (*Candida albicans*) from nonvirulent to virulent [14]; whereas significant improvement of degradation of polycyclic aromatic hydrocarbons was observed by fungal-bacterial co-cultures in comparison with poor activities of sole cultures of fungi (*Penicillium janthinellum*) and bacteria (*Stenotrophomonas maltophilia*) [15]. The cooperation of bacteria and fungi was also found for degradation of alkylphenols, where the former assimilated the aromatic ring and the latter attacked the aliphatic chain [16]. Whereas, inconsistent effect of biosorption of heavy metals by microorganisms (*Micrococcus* sp. and *Aspergillus* sp. [17]) on an environment was reported, that is, (i) positive by removal of heavy metals from environment, and (2) negative by their subsequent (out-of-control) release into environment. Based on these studies, it is clear that interactions between microorganisms, chemical compounds, and the environment are highly complex and unpredictable,

Nanoscale Materials in Water Purification. https://doi.org/10.1016/B978-0-12-813926-4.00027-6

thus, development of environmentally-friendly techniques, which are simultaneously efficient in degradation of pollutants, is highly important and urgent.

Photocatalysis is considered as one of the best methods for environmental purification because additional chemical compounds, such as strong oxidants (ozone, hydrogen peroxide, chlorine) [18–25], are not introduced into an environment [26, 27]. The energy consumption is also much lower than in the case of other Advanced Oxidation Processes/Technologies (AOPs/AOTs), for example, wet air oxidation [28], supercritical water oxidation [29], H_2O_2/UV-C [30], because UV-A lamps or even solar radiation could be used for photocatalyst activation [31].

Titanium(IV) oxide (titania, TiO_2) is one of the most broadly used semiconductor photocatalyst, due to its many advantages, such as good stability, strong redox ability, nontoxicity (except usual toxicity of nanomaterials), cheapness, and high availability [32–35]. However, recombination of charge carriers (typical for all semiconducting materials) and inability of visible light absorption, due to its wide band-gap (ca. 3.0 eV for rutile and 3.2 eV for anatase), result in limitation of its common application to world regions of high intensity of solar radiation. Therefore, plenty of studies have been performed to improve titania performance by its surface modification, doping and preparation of coupled nanostructures [36–45]. Modification with metals (metallic nanoparticles (NPs) and clusters [46–50], and metal complexes [51–53]) has been one of the most often used methods for both enhancement of activity under UV light and titania activation toward visible light irradiation. It is well known that under UV irradiation, metallic deposits work as an electron pool inhibiting the recombination of charge carriers. Whereas, under visible light irradiation, either narrowing of band-gap [54–56] or energy/electron transfer from modifier to titania [57–59] causes the visible response. Recently, modification of titania with noble metals NPs (with visible light absorption, due to localized surface plasmon resonance [LSPR]) has been very extensively studied, and such obtained materials are called plasmonic photocatalysts. Although, contrary reports have been published concerning the mechanism of their action, that is, transfer of energy [60], transfer of charge carriers [61, 62] and plasmonic heating [63], their photocatalytic activities at very broad ranges of irradiation make them very promising materials for environmental purification and energy conversion. In addition, antibacterial properties of silver and copper extend the possible application to dark conditions.

This chapter will introduce noble metal-based nanomaterials for decomposition of both chemical and microbiological pollutants during water purification.

2 FORMS OF NOBLE METALS USED FOR WATER PURIFICATION

Noble metals could be applied for water purification in various forms, for example, ionic forms (metal cations), nanostructures (mainly NPs) and NPs supported on inert or active materials, as exemplary shown in Fig. 1. This chapter focuses on NPs of noble metals in the form of free NPs as well as supported ones. Although, the use of noble metals in the form of dissolved salts will not be discussed in this chapter, the role of cationic forms of noble metals cannot be omitted because this form is often the most active, especially against microorganisms.

There are few examples of the application of noble metals in unsupported forms (free NPs suspended in water). For example, Ag NPs were used for Cr(II) and Pb(II) ions adsorption [64]. Cu NPs and Fe-Cu bimetallic NPs were tested for antibacterial, antibiofouling and antioxidant applications

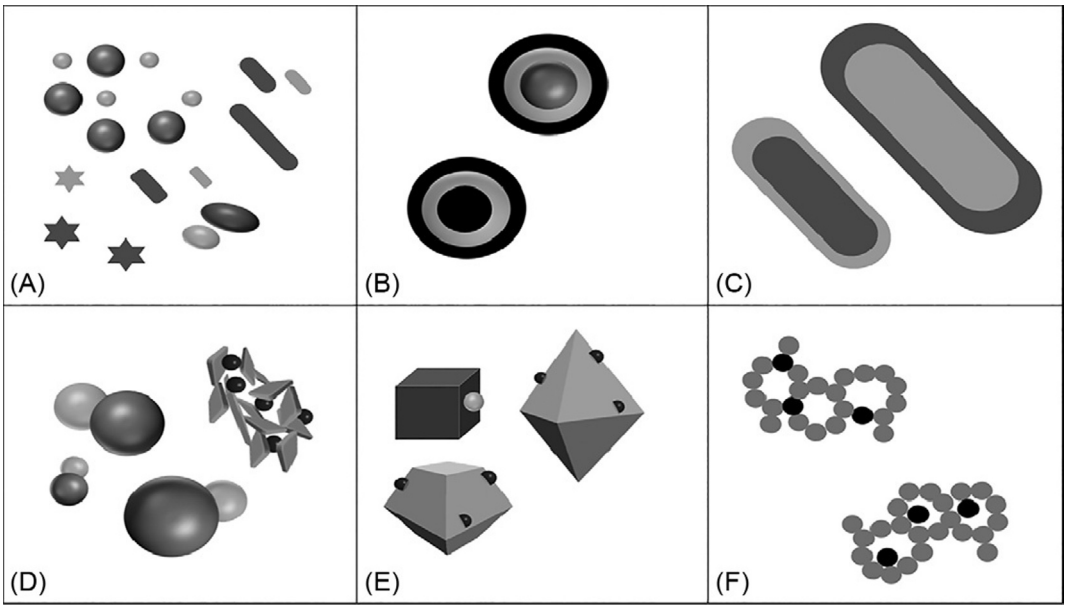

FIG. 1

Exemplary morphology of noble metals (NMs) composites for water purification; (A) unsupported NM nanostructures (nanocluster, nanorods, nanostars, nanorice); (B) tertiary nanoparticles (NPs); (C) core-shell nanorods; (D) supported NMNPs (Janus, NMNPs on nanoplates); (E) NMNPs on faceted support; (F) NMNPs incorporated in porosity or inside aerogel network.

in water purification systems [65]. It was found that those NPs had efficient antibacterial properties and could work as scavengers of free radicals and efficient inhibitors for biofilm formation and lipid oxidation. Moreover, the intrinsic magnetic properties of iron-based NPs could provide long-term benefits for antibacterial, antibiofouling treatment in water purification systems. Another applications were proposed for: (i) citrate-stabilized Ag NPs for degradation of organophosphorothioate pesticide (chlorpyrifos, CP) [66], and (ii) octahedral Pd NPs for reduction of bromate, a regulated carcinogenic oxyanion produced during drinking water disinfection [67].

There are various reasons for using supports of noble metals NPs for water treatment, for example, to avoid aggregation of NPs and to enable their reuse [66, 67]. However, the main reason relates to self-toxicity of noble metals, and thus noble metals must be removed from treated water. Therefore, for better separation of noble metals from water, various supports are used.

Many types of chemical compounds were used for synthesis and stabilization of noble metals NPs (NMNPs), and for their deposition on the support. For example, polyethylene glycol and chitosan were used in synthesis of porous chitosan-silver nanocomposite films due to their reductive abilities as well as stabilization of formed Ag NPs [68]. Interesting technique was proposed for preparation of fibrous membrane modified with Ag NPs, where silver was deposited on the membrane surface by inkjet printing of silver ink [69].

Recently, the use of microorganisms for synthesis of NM NPs has been very popular as a "Green Chemistry" approach. For example, Ag-Alginate biohydrogel was prepared by reduction of silver cations by actinobacteria (*Rhodococcus* NCIM 2891) [70].

In general, either first NMNPs are synthesized and then deposited on the support [62] or (i) the "support" is synthesized on NMNPs (e.g., titania synthesized on gold [71]), (ii) metal cations are directly reduced on the support by chemical [72–74], photochemical [75–77], radiolytic [49, 78], thermal [79], and sonochemical [80] methods, (iii) NMNPs are deposited on the support by other methods (electrophoresis and sintering [81], dc-magnetron sputtering [82], inkjet printing [69]), (iv) NMNPs and support are simultaneously synthesized during hydrothermal process [83], anodization (e.g., $Ag/Ag_2O/TiO_2$ obtained from one-step anodic oxidation of Ti—Ag alloys [84]), laser pyrolysis [85], and hydrolysis of metal alcoholates (support precursors, e.g., titanium isopropoxide/tetrabutoxide) in the presence of NM salts followed by calcination (support crystallization with simultaneous formation of NMNPs) [86].

Besides simple NMNPs deposited on the support, other complex nanostructures are also synthesized such as three-dimensional (3D) network of aerogels of titania with incorporated NMNPs (Fig. 1F) [87], titania mesocrystals with NMNPs deposited on basal and/or lateral surfaces [88], core-shell (Fig. 1C) and Janus nanostructures (Fig. 1D) [71]. The kind and the structure of the support, as well as the method of NM deposition, highly influence the properties of the resultant NM deposits. For example, (i) larger gold NPs were formed on larger titania NPs [61, 89] and on pure anatase, then on an anatase-rutile mixture [82], (ii) pores in titania film limited the size of deposited NMNPs, (iii) smaller gold NPs were formed by deposition-precipitation than sol-immobilization and photodeposition methods [62], (iv) larger gold and copper NPs were formed on premodified titania due to either repulsion or attraction between two modifiers (e.g., repulsion between Ru complex and gold precursor [90], and attraction between negatively charged Ag NPs (electron transfer from titania to Ag during Cu photodeposition) and copper cations [91]), (v) a decrease in gold NP size was observed when Ru complex was adsorbed on Au/TiO_2 due to gold reshaping [90]. Thermal posttreatment is often used for various purposes, such as (1) support crystallization, (2) NM reduction, (3) removal of adsorbed impurities like Cl^- (from NM precursor), capping [92] and stabilizing [81] agents of NM colloids, (4) enhancement of interface NMNP-support [81, 93], and (5) aggregation of NMNPs [81, 94].

It should be pointed that supports could be active (resulting in enhancement of water treatment) and inert. Shortly, these two kinds of systems would be presented below.

2.1 CHEMICALLY-INERT SUPPORT

An "inert" support means here a support which does not react with pollutants and/or does not actively participate in the primary mechanism of water purification. For example, (i) NPs of Ag and Au were supported on alumina to avoid NPs' aggregation and to enable their reuse during water purification [66], (ii) alumina, carbon, and silica were tested as supports for NPs of various noble metals (Pd, Pt, Ru, Ir, Rh, Ag, and Cu) for removal of nitrate and nitrite from drinking water by catalytic reduction with hydrogen on the surface of a noble metal [95], (iii) silica with dual function (as support and cover) was proposed for palladium NPs encapsulation in core-shell silica ($SiO_2@Pd@SiO_2$ (Fig. 1B), where well-defined mesoporous silica shell (2.3-nm mesopores) provides a physical barrier to prevent Pd NPs (ca. 6 nm) movement, aggregation and detachment from the support into water [67], (iv) Ag NPs were co-supported with Fe_3O_4 on fly ash for Pb(II) ions adsorption and bacteria removal (Although, Pb(II)

ions could also directly adsorb on fly ash, Ag NPs significantly enhanced this adsorption, and were responsible for bacteria inactivation. The fly ash was used for an increase of specific surface area by formation of fine NPs of Ag and Fe_3O_4, and Fe_3O_4 for easy separation of this composite by an external magnet after water treatment.) [96]; (v) Ag NPs were synthesized on diatomite for possible application in water purification, where diatomite could be used as a filtration material and Ag NPs as bacteriocyte [97]. It was found that possible release of silver (detachment) during filtration should not exceed the limit for silver level in drinking water, that is, 100 ppb by WHO standard. Similar application, that is a silver-embedded ceramic tablet, was tested as point-of-use water treatment (PoUWT) in Limpopo Province, S. Africa [98]. Silver with antimicrobial properties efficiently removed bacteria from water and the ceramic table functioned only as its support. The final concentration of released silver in water (< 20 ppb) did not exceed the drinking water standard. It was found that silver tablets could be used as stand-alone or more efficiently as a secondary PoUWT method (when placed in the lower reservoir of the ceramic water filter system). Another water purification PoUWT device was proposed for cork matrixes with enzymatically grafted chitosan-silver NPs [99].

Noble metal NPs were also used for modification of membranes to improve their performance, for example, biofouling resistance was observed for polysulfone ultrafiltration membranes impregnated with Ag NPs (Although, membranes actively participate in main mechanism of action (filtration), we have included them into "inert supports" because they are microbiologically inactive, and observed biocidal effect is caused only by adsorbed noble metals.) [100]. It was reported that membrane modification with silver (besides antibacterial and antiviral properties) resulted in an increase in hydrophilicity reducing the potential for different types of membrane fouling [100]. It was also shown that Ag NPs adsorbed on carbon nanotubes (a carbon nanotubes-silver NPs nanofilter) [101] and cork matrices (a cork filter with chitosan-silver NPs) [99] prevented bacterial clogging of the filter, due to antibacterial properties of silver. Bimetallic NPs were also proposed for improvement of membrane performance, for example, modification of polyetheresulfone (PES) membranes (for removal of Cr(VI) from water) with multiwalled carbon nanotubes (MWCNT) premodified with Ag–Fe NPs resulted in an increase in surface roughness, higher hydrophilicity, thermal stability and crystallinity, and enhanced surface charge density [102]. Moreover, modification of PES membranes with Ag-Fe/MWCNT caused an increase in water flux from 26.5 to 36.9 L/m^2 and higher rejection of Cr^{+6} ions from 9.3% to 94%. Similarly, an increase in water flux (for different feed solutions: water, urea and wastewater) and higher solute rejection were observed for nanocellulose composites after their modification with NPs of Ag and Pt [103].

An interesting application for water purification was proposed for blotting papers, used as supports for either Ag [104] or Cu NPs [105]. It was proposed that such filters could be efficiently used for point-of-use water filtration at very low costs, especially for Cu NPs (material cost of only a few cents per filter).

2.2 CHEMICALLY ACTIVE SUPPORT

Noble metal NPs may be deposited on an active support, which co-participate in overall mechanism. For example, similarly to Ag-Fe_3O_4-fly ash composite [96], Ag NPs was co-deposited with ZnO on fly ash [106]. In this system pollutants were decomposed by irradiated ZnO (photocatalyst), and Ag NPs enhanced photocatalytic activity. Similarly, Ag NPs improved photocatalytic decomposition of methyl orange (MO, from 80% to 92%) on mesoporous carbon blended with Nafion polymer under 254-nm

UV irradiation [107]. It is well known that noble metals work as an electron pool [75, 108–111] resulting in retardation of charge carriers recombination.

2.2.1 Photocatalysis

The mechanism of semiconductor photocatalysis consists in (i) excitation of semiconductor with light energy equal or larger than its band-gap energy ($E \geq E_g$), resulting in formation of pairs of charge carriers: electrons and holes (e^-/h^+; Fig. 2A), (ii) charge carriers migration to the semiconductor surface (or their recombination, "bulk recombination"; Fig. 2B), and (c) reaction of charge carriers with adsorbed species (or their recombination, "surface recombination"; Fig. 2C, right). In the presence of water and oxygen in the system, reactive oxygen species (ROS), such as superoxide ($^{\bullet}O_2^-$), hydrogen peroxide (H_2O_2), hydroxyl radicals ($^{\bullet}OH$), are formed and may easily react with all organic and inorganic compounds. Hydroxyl radicals are known as the strongest oxidant, which could be safety used in water, and the processes/technologies, which use $^{\bullet}OH$ are known as Advanced Oxidation Processes/Technologies (AOPs/AOTs). It should be pointed that ROS are generated by both oxidation and reduction pathways when oxygen is present in the system, that is, formation of $^{\bullet}O_2^-$ by scavenging of electrons by oxygen (as shown in Fig. 2C).

Titania is the most widely studied and applied photocatalyst, due to high activity, stability, nontoxicity (except of nanomaterial toxicity [33]) and availability [26, 112, 113]. There are only two limitations of its common use, such as (1) recombination of charge carriers (typical for all semiconducting materials) and (2) inactivity under visible light irradiation due to wide bandgap. Therefore, plenty of studies have been performed to improve performance of titania photocatalysts by morphology arrangements [114, 115], doping (with anions or cations [37, 38, 42, 116–118]), surface modification [119–122], and coupling with other semiconductors [123]. Noble metals in the form of adsorbed complexes [124, 125] and metallic deposits [46, 111, 126–128] have been extensively investigated for improvement of photocatalytic activity of titania under UV irradiation [109, 129]. Enhancement of photocatalytic activity mainly originates from prolongation of lifetime of charge carriers (photogenerated electrons and holes) [46], because noble metals serve as an electron sink (Fig. 3B), and thus accelerate the transfer of electrons from titania to substrates (for example, protons to evolve hydrogen [130, 131]), as confirmed in various studies. For example, decrease in photoluminescence (electron de-excitation across band gap to recombine with holes) [132–136], cathodic shift of flatband potential

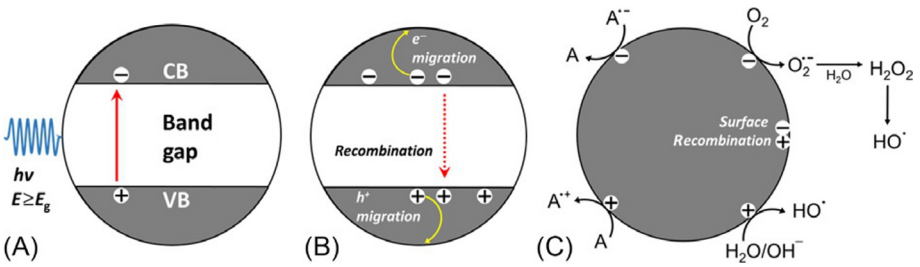

FIG. 2

Mechanisms of semiconductor photocatalysis: (A) semiconductor excitation; (B) charge carriers transfer to the surface and/or recombination (red dashed arrow); (C) reactions on photocatalyst surface; *CB*, conduction band; *VB*, valence band; *A*, adsorbate.

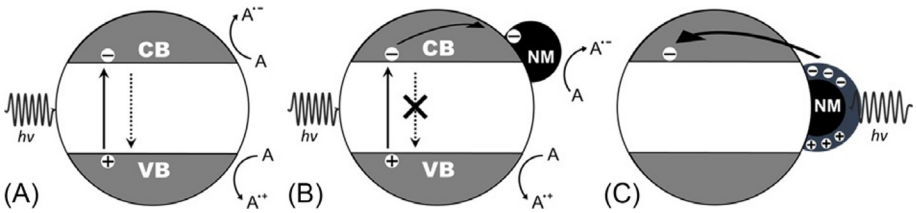

FIG. 3

Mechanisms of: (A) semiconductor activation with energy equal or larger than its band gap; (B) transfer of electron from semiconductor to NM (semiconductor excitation); (C) electron transfer from NM to semiconductor (plasmonic photocatalysis).

position and increase of photocurrent quantum yield [137], reduced lifetime of mobile electrons (by time resolved microwave conductivity (TRMC) measurements) [138], generation of various ROS (measured by electron paramagnetic resonance [EPR]) [62, 139] confirmed that noble metals are an electron pool. Moreover, there are plenty of examples indirectly proving an electron transfer from semiconductor to NM by enhancement of photocatalytic activity after semiconductor modification in both oxidation and reduction pathways, for example, gold NPs deposition on titanate-loaded silica (SBA-15) resulted in enhanced photocatalytic activities in both reduction (hydrogen evolution from methanol) and oxidation (hydroxylation of terephthalic acid) reactions [140, 141].

2.2.2 Plasmonic photocatalysis

Over the last decade another property of NM, that is, absorption of visible light due to plasmon resonance, has been used for activation of titania [58, 76, 142] and other wide bandgap semiconductors (CeO_2 [143, 144], ZnO [145]) toward visible light. Although plasmonic properties of noble metals were observed 100 years ago, explained >30 years ago and commercially used in many fields, for example, for biosensors [146], chemical sensors [147, 148], nano-lithography, nano-photonics [149, 150], surface enhanced Raman spectroscopy (SERS) [146, 148], medicine (drug delivery, cancer therapy) [148], and optical data storage [151], the examination of their usage for photocatalysis was started a decade ago. Despite the novelty of plasmonic photocatalysis, large number of studies has already been performed to improve photoactivity and stability as well as to clarify the mechanism under irradiation with visible light, and even a few reviews [152–156] and book chapter [157] were published on plasmonic photocatalysis.

The history of applications of localized surface plasmon resonance (LSPR) for photocatalysis research started at the beginning of this century when plasmonic properties were used for characterization of gold NPs deposited on titania, that is, their formation, properties (size and shape), and stability (under UV irradiation) [158]. The first reports, proving that plasmon resonance was responsible for the activity under visible light irradiation, were presented by action spectrum analyses for photocurrent generation [58] and for photooxidation of 2-propanol [76], in which action spectra resembled respective absorption spectra, as shown in Fig. 4.

Three main mechanisms are proposed for plasmonic photocatalysis (under visible light irradiation): (1) energy transfer, (2) charge transfer (mainly electron transfer [Fig. 3C]), and (3) plasmonic heating (thermal activation). The first two could be classified as "plasmon-assisted photocatalysis" because

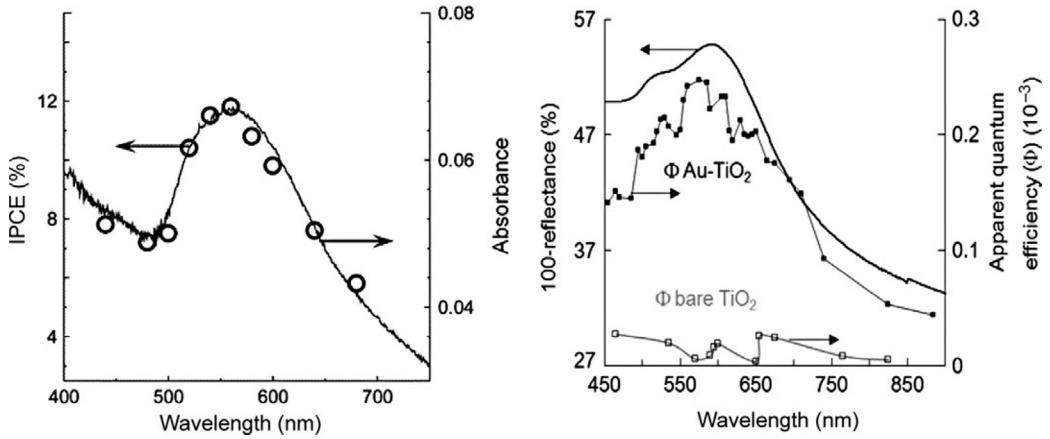

FIG. 4

Comparison of absorption spectra of Au/TiO_2 with action spectra of (left) short-circuit photocurrent for $Au\text{-}TiO_2$ photoanode and (right) 2-propanol oxidation on bare (□) and gold (■) modified rutile titania.

Reproduced with permission from Y. Tian, T. Tatsuma, J. Am. Chem. Soc. 127 (2005) 7632–7637, Copyright (2005) American Chemical Society; E. Kowalska, R. Abe, B. Ohtani, Chem. Commun. (2009) 241–243.

energy/charge transfer happens only under irradiation, whereas the last (3) can be classified as "plasmon-assisted catalysis" because LSPR only activates catalytic (thermal) reaction.

Energy transfer

Energy transfer between two semiconductors can take place when they have closely matched energy levels, for example, Ag/TiO_2 [142] (LSPR of Ag NPs: ca. 2.9–3 eV and band-gap of titania: ca. 3–3.2 eV). Therefore, in the case of Au/TiO_2, an energy transfer should not be expected because gold NPs plasmon energy (LSPR of ca. 2.2 eV) is much lower than the band-gap of titania (ca. 3 eV). In this regard, first reports suggesting energy transfer from gold NPs to titania were performed for premodified titania (with vis response). One of the first studies of the energy transfer (also called plasmon resonance energy transfer (PRET)) reported photocurrent generation on 5-nm gold NPs deposited on titania co-modified with nitrogen and fluorine [159]. Other premodified titania photocatalysts, for example, with nitrogen [85], narrow band-gap semiconductors (with vis activity) like $CuWO_4$ (2–2.5 eV) [160], titania with crystalline defects [161], and amorphous titania [71] with localized states inside band-gap (i.e., electron traps, ETs) are also possible materials for energy transfer due to the fact that their energy matches the LSPR of gold.

Charge transfer

In the case of plasmonic photocatalysis, charge transfer means an electron transfer (i.e., transfer of "hot" electrons from NMNP to conduction band (CB) of semiconductor), which was first proposed for Au/TiO_2 by Tian and Tatsuma in 2005 [58]. In general, the mechanism of decomposition of organic compounds on plasmonic photocatalysts is similar to activation by sensitizers, such as metal complexes or dyes, and thus, NM is also called "plasmonic photosensitizer." At first, incident photons are absorbed by NMNPs through their LSPR excitation, then "hot" electrons are transferred from NMNPs

into CB of semiconductor (Fig. 3C). Then, electrons reduce molecular oxygen adsorbed on the surface of the semiconductor, and the resultant electron-deficient NMNPs can oxidize organic compounds to recover their original metallic state. There are many proofs for electron transfer mechanism in the literature, for example, by femtosecond transient absorption spectroscopy with an IR probe [162], shift of electrode potential (negative or positive) and generation of anodic or cathodic photocurrent depending on electrode configuration: ITO/TiO_2/Au or ITO/Au/TiO_2, respectively [163], EPR experiments resulting in detection of different oxidation species under irradiation with UV and visible light [62].

Plasmonic heating

The first report showing plasmon-assisted catalysis was published by Chen et al. in 2008, in which heated gold NPs (by visible light excitation of LSPR) could activate organic compounds (OCs) to induce their oxidation [63]. Plasmonic heating was proposed as the main mechanism for catalytic reduction of CO_2 on Au/ZnO [145] and CO oxidation on gold NPs deposited on titania incorporated in mesoporous silica [164]. On the contrary, there are plenty of reports rejecting the mechanism of plasmonic heating, due to inactivity of gold-modified insulators or unsupported gold NPs in comparison to highly active gold-modified semiconductors [60, 61, 161, 165]. Studies on water spitting [159], photocurrent generation [166], hydrogen dissociation [167], activation energies for decomposition of OCs [144], and photocurrent generation [168], also exclude plasmonic heating as the main mechanism of plasmonic photocatalysis.

Various structures of plasmonic photocatalysts have been proposed, which significantly differ by physicochemical properties and thus photocatalytic activities. Therefore, it is not surprising that different photocatalytic mechanisms have been proposed for different structures, and the co-existence of several mechanisms during the (photo)catalytic reaction is also possible (for example, an electron or/and energy transfers were proposed for Ag@TiO_2, whereas only an electron transfer for Au@TiO_2, an energy transfer for Ag@SiO_2@TiO_2 and lack of plasmonic excitation for Au@SiO_2@TiO_2 [169]).

Various reports have shown the dependence of the plasmonic mechanism on the properties of photocatalysts, that is, properties of NMNPs, properties of supports, and the NM-support interaction/interface (as discussed in detail elsewhere [157]). Here, we will not discuss the mechanism in detail, but will mainly focus on possible applications of these photocatalysts for water purification (as shown in the next section).

Although, plasmonic photocatalysts are active for both oxidation and reduction of organic pollutants and microorganism inactivation, the activity is still low and should be improve for possible commercial application. Therefore, research on the improvement of the performance of plasmonic photocatalysts (activity, stability and reusability) is under extensive study nowadays. For example, different hybrid photocatalysts have been tested and proposed as novel plasmonic photocatalysts, for example, for (i) enhancement of light harvesting by ruthenium complexes (homogeneous photocatalyst) adsorbed on plasmonic photocatalysts [53, 90, 170], (ii) inhibition of charge carriers' recombination for Au/TiO_2 deposited on protonated zeolite, CuO, and Cu/SnO_2, (iii) enhancement of photocatalytic activity by: additional heterojunction between plasmonic photocatalyst and another semiconductor ($Zn_2Ti_3O_8$ and $ZnTiO_3$), efficient electron transfer from NM via titania to another support (CuO, Cu/SnO_2), and better dispersion of NMNPs on support (Au/TiO_2 on CuO), (iv) an increase in specific surface area for efficient pollutant adsorption (Au/TiO_2 on zeolite, Al_2O_3 and CuO), (v) improvement of the photocatalyst recovery (Au/TiO_2 on Fe_2O_3) [133, 171–175]. An interesting example has been recently reported for a $BiO(OH)_{0.06}Br_{0.94}$ photocatalyst with abundant oxygen vacancies supported

on AgBr semiconductor modified with Ag NPs [176]. It was proposed that vis-response was caused by both excitation of AgBr and plasmonic excitation of Ag NPs with subsequent "hot" electron transfer to CB of AgBr followed by one-electron reduction of adsorbed oxygen to $O_2^{\bullet -}$. Interestingly, it was proposed that the high stability of this photocatalyst (lack of silver [Ag^+] release) was caused by possible excitation of wide-band-gap $BiO(OH)_{0.06}Br_{0.94}$ by visible light due to electrons trapping in the oxygen vacancies, and their subsequent transfer to Ag NPs (to keep them in zero-valent state).

3 REMOVAL OF CHEMICAL POLLUTANTS

3.1 PHYSICAL METHODS FOR CONTAMINANTS REMOVAL

The simplest method to remove dangerous pollutants from water is based on their separation by various physicochemical processes, such as adsorption, filtration, flocculation, and coagulation. Although those methods do not result in decomposition of pollutants, they are often necessary for fast and efficient removal of some compounds, especially toxic and dangerous. For example, Ag and Fe NPs are efficient adsorbents for removal of heavy metals (Pb(II), Cr(II) and Cr(VI) ions) from aqueous solutions [64, 102]. It has been proposed that the mechanism of heavy metal removal involves the interaction between hydroxyl layer around the spherical metallic core of Ag/Fe NP in water and the metal ions [64]. The rejection behavior of Ag-Fe/MWCNT/PES membranes could be classified as Donnan exclusion mechanism, where both the membrane and the metal ($Cr_2O_7^{2-}$) are negatively charged [102].

In the case of virus removal, because of their extremely small size, nanofiltration or reverse osmosis must be used, which are expensive processes for water purification. Accordingly, it was found that modification of ultrafiltration membranes [100] and nanofilters [101] with Ag NPs resulted in antiviral properties.

3.2 DECOMPOSITION/DEGRADATION OF CHEMICAL POLLUTANTS

One of the first reports showing the application of NMNPs for water purification was proposed by S. Horod et al. for catalytic reduction of nitrate and nitride to nitrogen in the presence of hydrogen on the surface of supported noble metals (Pd, Pt, Ru, Ir, Rh, Ag, and Cu) [95]. It was shown that the formation of undesired ammonia (as a byproduct) could be limited by decrease in the amount of hydrogen and addition of palladium catalyst to the palladium-copper catalyst. Other catalytic reduction processes were also proposed for possible water purification, such as: (i) 4-nitrophenol reduction to 4-aminophenol in the presence of $NaBH_4$ on Ag NPs deposited in the polymer (Alginate biohydrogel) [70], (ii) bromate reduction to bromide using 1 atm H_2 at room temperature on unsupported and supported Pd NPs (Pd, SiO_2@Pd, SiO_2@Pd@SiO_2 (Encapsulation in the mesoporous silica shell enhanced catalytic activity of Pd by a factor of 10 due to BrO_3^- adsorption near the Pd active sites.) [67], (iii) organophosphorothioate pesticide (chlorpyrifos, CP) decomposition to 3,5,6-trichloro-2-pyridinol (TCP) and diethyl tiophosphate at room temperature on Ag and Au NPs (unsupported and supported on alumina). It was proposed that NMNPs could bind with sulfur and nitrogen atoms of CP to form a surface complex with P–O bond cleavage resulting in nucleophile attack of water at the electrophilic phosphorous site, as shown in Fig. 5 [66].

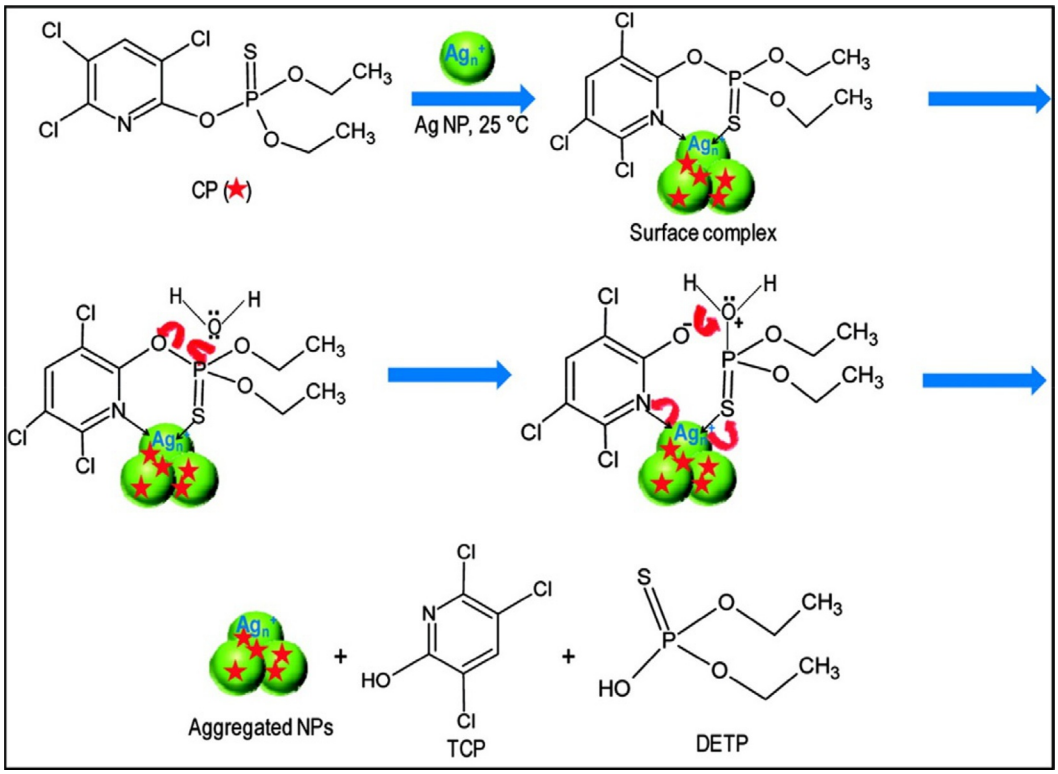

FIG. 5

Degradation of CP on Ag NPs. Adsorbed CP molecules were shown with *red stars*.

Reproduced with permission from M.S. Bootharaju, T. Pradeep, Langmuir 28 (2012) 2671–2679, Copyright (2013) American Chemical Society.

There are many reports showing decomposition of organic compounds by heterogeneous photocatalysis on NM-modified semiconductors. At first, noble metal-modified titania photocatalysts were used under UV irradiation for activity enhancement (inhibition of charge carriers' recombination as discussed above, Fig. 3B), for example, during oxidative decomposition of pollutants in liquid phase, such as oxalic acid [177], formic acid [85], stearic acid [178], salicylic acid [179], antibiotics (tetracycline hydrochloride [137], trimethoprim [180]) and dyes (Plasmocorinth B, Methylene Blue (MB) [135, 181], Congo Red [72], Rhodamine 6G (R6G) [182], and Methyl Orange (MO) [171]). The enhancement of activity was also observed during reductive decomposition of some pollutants, such as 2,2′-dipyridyl disulfide (RSSR), nitrobenzene and MB [183]. Usually, significant enhancement of activity was observed after NM deposition, that is, (i) two times higher activity for degradation of oxalic acid (Au NPs/P25) [177], congo red (Au NPs/TNTs [TiO_2 nanotubes]) [72], and MB (Au NPs/anatase) [135], (ii) four times higher: reduction of RSSR dye (Au NPs/TiO_2) [184], oxidation of MB dye (Au NPs/TiO_2-SiO_2 and Au NRs/TiO_2-SiO_2) [185], and oxidation of R6G dye (Au NPs/ZnO NRs) [182], (iii) 5 times faster decomposition of MB (Ag@SiO_2@TiO_2) [142], iv) >20 times faster oxidation of

benzene (Au NPs/TNTs) [186]. The influence of NM amount on photocatalytic activities was also studied, and existence of optimal amount suggested that NMNPs in excess could also be recombination centers, as confirmed by photoluminescence emission data [135]. It was proven that exceeding of the optimal amount of NM resulted in an enhancement of charge carriers' recombination, for example, 0.5 mol% of gold (among: 0.25, 0.5, 1.1, 2.2, and 3.1 mol%) was an optimal amount for MB degradation.

One of the first studies under natural solar radiation (India, 2006) showed that Au/TiO_2 had activity twice as high as that of bare titania [187]. Three reasons for activity enhancement were proposed: (i) the negative shift of the Fermi level (electron accumulation), (ii) improved efficiency of interface charge transfer, and (iii) shift in absorption wavelength to visible range of solar spectrum. The possibility of photocorrosion of Au/TiO_2 due to gold oxidation, either by photogenerated holes or hydroxyl radicals, was excluded after successful stability tests (recycling). Similarly, two times higher photocatalytic activity levels were obtained after modification with gold NPs of: (i) titania nanotubes (TNTs) premodified with 12-phosphotungstic acid (PTA) for degradation of Congo Red dye under simulated solar radiation [72], and (ii) titania/polyethene beads for degradation of Rhodamine-6-G dye under natural solar radiation (in Egypt) [188]. It must be pointed out that in the case of experiments under solar radiation, differentiation between titania activation (photocatalysis) and gold activation (plasmonic photocatalysis) is practically impossible. Therefore, those experiments are very important for application studies, but could not be used for mechanism explanation.

The first report under visible light irradiation did not show activity of gold/titania photocatalyst [83], possibly due to too small gold NPs (nanosized), the tested reaction (acetone oxidation), or too slow reaction (Usually reaction rate under visible light is even two orders of magnitude lower than that under UV [61]). Similarly, lack of visible activity of titania modified with nano-sized gold was observed for formic acid degradation [85]. The significant improvement of photocatalytic activity was shown for dye degradation, for example, Congo Red [72], MB [88], Rhodamine B (RhB) [88], MO [60, 171], Acid Orange 7 (AO7) [189]. However, it must be reminded that visible light activity of modified titania should not be tested for dyes, due to sensitization mechanism.

Finally, activity of plasmonic photocatalysts under visible light was proven for oxidative degradation of colorless compounds, such as: (i) methyl tert-butyl ether (MTBE) to carbon dioxide (mineralization) [172], (ii) 2-propanol to acetone [190–192] and carbon dioxide [191], (iii) cinnamyl alcohol to cinnamaldehyde [173], (iv) methyl parathion to 4-nitrophenolate [193], (v) phenol [189] to benzoquinone, hydroquinone, muconic acid, muconic aldehyde, and oxalic acid [194]. It was proposed that complete decomposition (mineralization) of some organic molecules did not proceed, due to stabilization of their degradation by-products by dipole effect formed in the gold plasmon [172].

Investigations on dependence of activity on the amount of gold resulted in contrary results, that is, (i) existence of an optimal amount of gold NPs, and (ii) increase in activity with gold amount increase. It was proposed that a decrease in activity after exceeding of an optimal gold amount (1 wt% for degradation of AO7 dye) was caused by enhanced recombination of charge carriers (gold as recombination center) [189], and the existence of the optimal amount of gold (1 wt%) resulted from the balance between gold particle size, morphology, substrate surface coverage, and population of residual hydroxyl groups (for degradation of rhodamine B dye and 2,4-dichlorphenol on Au/Bi_2O_3 [$\lambda \geq 420$ nm]) [195]. More detailed studies on the influence of gold amount on activity indicated that an optimal amount of gold also depended on the properties of titania support [192]. It was shown that for fine titania photocatalysts (crystalline size <15 nm), an increase in gold amount (>0.1 wt%) resulted in the formation of

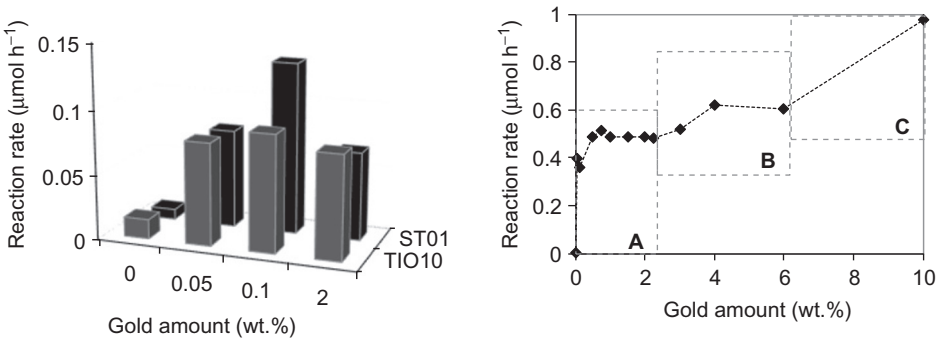

FIG. 6

Dependence of acetone generation rate on deposited amount of gold during irradiation with visible light (>450 nm) on Au/TiO_2 for different titania supports; (left) fine anatase: ST01 and TIO10, and (right) large rutile (Aldrich_R).

Data from E. Kowalska, S. Rau, B. Ohtani, J. Nanotechnol. (2012) 1–11.

dark photocatalysts of limited light penetration ("shielding effect"), and therefore, reduced photocatalytic activity (Fig. 6, left). Contrary, for larger rutile titania of ca. 550-nm crystallites, an increase in gold amount resulted in three successive growths of photocatalytic activity separated by two plateau regions for 0.5–2.25 wt% and 4–6 wt% of gold. It was proposed that the first increase in photocatalytic activity (from 0.05 to 0.5 wt%) was caused by an increase in absorbed photon flux by a larger number of gold deposits (similarly to the well-known dependence of photocatalytic activity on amount of photocatalyst in the reaction suspension reaching plateau at optimum light absorption) [196, 197], whereas the second (2.25–4 wt%) and third (6–10 wt%) increases in activities were caused by change in gold size and shape (due to gold aggregation).

Copper, with its high abundance and low cost, is a good candidate for a component of a plasmonic photocatalyst. Similarly to other noble metals (Au, Ag, Pt), copper is recognized as an efficient co-catalyst of titania. However, copper can be easily oxidized and loses its plasmonic properties under ambient conditions. Therefore, to apply Cu NPs-based photocatalysts in an oxidative environment, prevention of copper oxidation is required. De Sario et al. prepared titania aerogels supporting 5-nm Cu NPs (Fig. 1F) [198]. They found that plasmonic properties of Cu NPs were preserved by offering an extended interfacial contact with reduced TiO_2 support (characteristic design issue for aerogels). An arrangement of Cu NPs at high-surface area TiO_2 with multiple Cu to TiO_2 contacts per Cu nanoparticle allowed to obtain Cu/TiO_2 system with high Cu NPs content and high stability (almost the same plasmonic properties of Cu/TiO_2 before and after photoelectrochemical oxidation of methanol). Copper NPs can be also the part of cascade heterojunction systems, such as Cu/Cu_2O/TiO_2, with very intensive charge separation under UV/vis irradiation (tested for terephthalic acid degradation) [199]. It was proposed that lower Fermi energy level of Cu than that of p-type Cu_2O resulted in transfer of electrons from Cu_2O to Cu until the two Fermi levels were aligned. Whereas, holes in the VB of Cu_2O recombined with electrons in the CB of TiO_2. An increase in holes in the VB of TiO_2, due to efficient inhibition of their recombination with electrons, resulted in enhanced formation of hydroxyl radicals.

Recently, in addition to titania, other semiconductors have also been intensively examined as supports of NMNPs for decomposition of organic compounds, for example, 2-chlorophenol, 2,4-dichlorophenol, phenol, trichlorophenol, acid red B, reactive red K-2BP, cationic red X-GRL and methyl orange were efficiently decomposed on $BiO(OH)_{0.06}Br_{0.94}$-AgBr-Ag NPs photocatalyst under visible light irradiation [176]; rhodamine B (RB) and methylene blue (MB) on porous carbon modified with Ag/ZnO [200]; and methyl orange (MO) on three-dimensional cubic ordered mesoporous carbon (CMK-8) blended with nafion polymer and Ag NPs [107].

4 REMOVAL OF MICROBIOLOGICAL POLLUTANTS

In 2010, the UN General Assembly declared safe and clean drinking water and sanitation as the human right essential for the full enjoyment of life and all other human rights. Improving access to safe drinking-water should result in tangible benefits to health. Therefore, every effort should be made to achieve drinking-water that is as safe as practicable [201]. An adequate supply of microbial safe water is the highest priority, because pathogens can cause acute (e.g., diarrhea) and chronic (e.g., infectious hepatitis, cancer) health effects, with both relative symptoms (e.g., diarrhea), and serious ones (cholera, hemolytic-uremic syndrome by *E. coli* O157 and cancer). In general, the greatest microbial risks are associated with ingestion of water, that is contaminated with humans or animals feces [201, 202]. Feces can be a source of pathogenic bacteria, viruses, protozoa, and helminths. Therefore, prevention of fecal pollution and removing dangerous microorganisms from water are the most important issues to obtain safe and clean water.

Water disinfection is usually carried out by chlorine, and sometimes by more expensive methods, such as UV irradiation and ozonation. Although chlorine can inactivate some microorganisms completely, it may also negatively influence the aquatic organisms due to chlorine's ability to bind to nitrogen and organic compounds, resulting in highly toxic byproducts. In addition, the chlorine disinfection has low effect on some pathogenic protozoa (e.g., *Cryptosporidium* sp. responsible for a diarrhea and even death of immunocompromised patients) and viruses (e.g., norovirus). Whereas, UV disinfection is highly efficient against many microorganisms (even viruses), where nucleic acids absorb 253.7-nm UV light inducing the damage of genetic information and inactivation. However, chlorine disinfection is often complementarily used because some viruses have low sensitivity to UV irradiation (e.g., adenovirus), and UV does not possess residual disinfection ability (only during treatment/direct irradiation). Ozone disinfection is also efficient for degradation of microorganisms, either directly by ozone molecule or produced radicals. However, it should be reminded that ozone itself is harmful and can initiate generation of toxic compounds.

Therefore, inorganic antimicrobial agents have been extensively investigated because they are stable and safe for environment as compared with organic compounds. It has been found that some NMs have high antimicrobial activities. For example, silver is well known as one of the most active antimicrobial agents. Moreover, it is expected that the use of NM could prevent the production of drug-resistant pathogenic microorganisms, for example, methicillin-resistant *Staphylococcus aureus*, multidrug resistant *Pseudomonas aeruginosa*, and drug-resistant Human Immunodeficiency Virus. In this section, the antimicrobial activities of NMNPs will be shortly presented. At first, microbial activities due to the sole antimicrobial properties of NM (direct action) will be described (Section 4.1), and then antimicrobial activities due to photocatalysis, that is, generation of active species under irradiation (indirect action (Section 4.2)).

4.1 MICROBIAL INACTIVATION ON NOBLE METAL NANOPARTICLES—DIRECT ANTIMICROBIAL ACTION

4.1.1 Silver

Silver possesses excellent antimicrobial properties, and thus, it has been used in many antimicrobial applications, such as cosmetics, shoes, clothes, electric appliances, and even for treatment of teeth and cutlery, confirming that it is a safe material for humans and animals (LD50 > 5000 mg/kg [rats, oral]). The low levels of silver in drinking water (generally below 5 μg/L) are not relevant to human health with respect to argyria. Moreover, in natural environment the highly toxic ionic silver is not expected [203]. In contrast, special situations exist when silver salts are used to maintain the bacteriological quality of drinking water. Higher levels of silver (up to 0.1 mg/L) could be tolerated in such cases without risk to health [201]. Indeed, US-EPA guideline for drinking water defines silver-content limit to be <0.1 mg/L.

Silver is more effective for gram-negative bacteria than gram-positive ones, presumably due to the differences in their biological structures. Different mechanisms of bactericidal action of silver NPs have been proposed in the literature, as follows:

(1) adsorption of silver ions onto negatively charged bacterial cell wall, followed by disintegration of the cell wall and the plasma membrane, and thus release of substances outside the cell, leading to cell lysis and death [204, 205],
(2) interaction with thiol groups of transport and respiratory enzymes that are vital to the cell function, resulting in the uncoupling of respiration from synthesis of ATP [206],
(3) destabilization of the plasma membrane and reenergization of bacteria, inducing a massive leakage of protons and a collapse of membrane potential [207].

In order to obtain the sustainable release of silver ions from silver NPs (to keep long-term antimicrobial activities), silver NPs are often deposited on some supporting materials (as presented in point 4.2), for example, silica [208], clay (Fig. 7) [209], and zeolite [210].

Silver NPs also possess the antimicrobial activities against fungi, algae and viruses. The proposed mechanism of antivirus action is based on interaction between silver NPs and viral surface glycoproteins, which induces an inhibition of virus binding to target cells, as well as possible inhibition of virus replication when silver NPs penetrate virus cell [211, 212].

An interesting application has been shown for drinking water purification using a paper sheet containing silver NPs [213]. Silver NPs effectively killed filtrated bacteria through damage of cytoplasm membranes and cell walls. Although the amount of silver leaching from the filter papers was relatively high, this could be a cheap point-of-use water treatment (PoUWT) method in an emergency. Furthermore, silver NPs inside a polymer matrix were also proposed as efficient composite for inhibition of biofilm formation, and thus as a prospective material for antimicrobial coatings [205]. Similarly, silver NPs deposited on carbon nanotubes in a carbon nanotubes-silver NPs nanofilter, applied for virus removal (Polio-, Noro-, and Coxsackie viruses), prevented clogging of filter by bacteria present in water [101].

Another interesting application was shown for a stand-alone, silver-embedded ceramic tablet (tested as PoUWT in Limpopo Province, S. Africa) with efficiency reaching 75% reduction in *E. coli* after 2 months of use [98]. Moreover, application of silver tablet as secondary PoUWT improved existing PoUWT methods, for example, when placed in the lower reservoir of the ceramic water filter system to provide residual disinfection postfiltration, resulting in a 100% reduction in *E. coli* over 1 year.

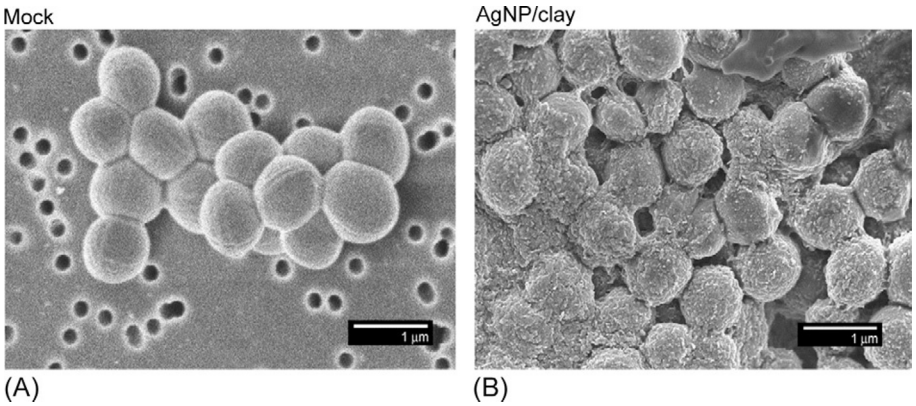

FIG. 7

FE-SEM images showing the untreated (A) and the Ag NP/Clay-encapsulated *S. aureus* (B).

Reproduced with permission from H.L. Su, C.C. Chou, D.J. Hung, S.H. Lin, I.C. Pao, J.H. Lin, F.L. Huang, R.X. Dong, J.J. Lin, Biomaterials 30 (2009) 5979–5987, Copyright (2009) Elsevier Ltd.

4.1.2 Copper

Since ancient times, it has been widely known that copper exhibits high antimicrobial activity, similar to silver. Copper is also considered as an environmental purifier due to its attractive cost and low toxicity (LD50 = 413 mg/kg [rats, oral] as a simple substance). The bactericidal mechanisms have been proposed, in which Cu ions adsorb on the surface of bacteria, and then: (i) the structure of surface proteins are denaturated [214], and/or (ii) adsorbed copper ions induce oxidative stress in bactericidal process [215]. The accumulation of copper ions inside bacteria has been reported as the main mechanism of inactivation of bacteria by Cu-modified blotting paper, that is, accumulating copper ions from direct contact with Cu NPs in the paper, and over time bacteria inactivation [105].

Furthermore, it has been proposed that Cu_2O has higher activity in inactivation of bacteria than CuO (Fig. 8) and silver [214]. On the other hand, copper NPs have lower toxicity than silver NPs against some species of fungi [216]. As an application for water purification, Deng et al. reported copper-graphene sponge for purification of drinking water with high efficiency of bacteria inactivation (in the case of $<10^3$ CFU/mL of bacteria as initial concentration) after filtration [215].

4.1.3 Gold

Gold is one of the most stable elements. However, gold ions are toxic for almost all organisms, due to its high oxidizability. For gold NPs, bactericidal activity is rarely observed for either gram-negative or gram-positive bacteria [217, 218]. It was found that gold NPs did not surround bacteria cells when gold NPs were dosed into water with bacteria, resulting in low activity [203]. On the other hand, gold NPs showed fungicidal activity [218, 219]. Ahmad et al. reported that the antifungal activity depended on the particle size of the gold NPs, that is, activity increased with a decrease in the particle size, due to an increase in the specific surface area of gold NPs, which enhanced the interaction between gold and the binding sites of the plasma membrane proteins, resulting in the inhibition of H^+-ATPase-mediated proton pumping [220]. Interestingly, gold NPs capped with some compounds exhibited an antiviral

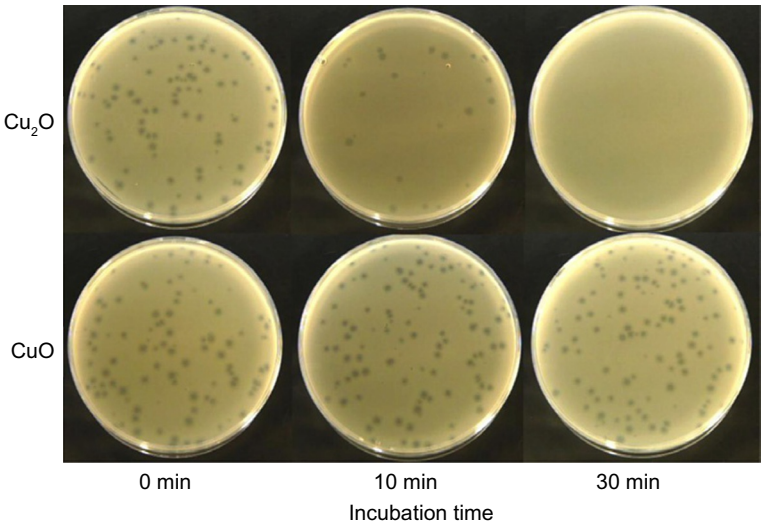

FIG. 8

Photograph of plaque assay data against bacteriophage Qβ after exposition to Cu_2O (upper) and CuO (lower) samples.

Reproduced with permission from K. Sunada, M. Minoshima, K. Hashimoto, J. Hazard. Mater. 235 (2012) 265–270, Copyright (2012) Elsevier B.V.

activity; for example, inhibition of viral attachment, entry, and cell-to-cell spread was reported for gold capped with mercaptoethanesulfonate (Au-MES NPs) [220]. In this case, gold did not kill the virus directly, but could be a candidate as a microbicidal agent.

4.1.4 Platinum

Cysplatin, a complex of platinum, is a famous medicine as an antitumor agent. Historically, platinum has been established for inhibition of bacterial-cell division. Based on this, the microbiological toxicity of platinum NPs in aqueous environment has been investigated [221]. It is thought that platinum NPs can damage cell walls and cause the release of substances (cytosolic proteins) for both bacteria and fungi [203, 222]. In addition, the platinum-based toxic effects based on the interaction with cellular components inside the cytoplasm and inside the nucleus have been reported [219]. It has been suggested that bactericidal properties (*Pseudomonas aeruginosa*) depend on the size of platinum NPs, that is, small platinum NPs (<3 nm) showed bacterio-toxic properties, whereas large NPs led to enhanced growth of bacteria [222].

4.1.5 Other noble metals

Antimicrobial effects of other noble metals NPs have been also reported, for example, for palladium and ruthenium. Palladium, which is widely used as a catalyst for many chemical reactions, has been also tested as an antimicrobial agent. Interestingly, palladium NPs are more effective for gram-positive bacteria than gram-negative bacteria, and exhibit size-dependent antimicrobial activity [223]. The mechanisms of antimicrobial activity (similar to silver) have been proposed, where metal ions

(i) interact with thiol groups of bacterial enzymes and denature them, (ii) inhibit bacterial respiratory mechanism, (iii) attack bacterial DNA and destroy it, (iv) disrupt the cellular transport system, (v) disrupt the bacterial cell membrane directly, and (vi) produce reactive oxygen species [224]. However, extensive accumulation of palladium NPs in vacuoles of *Tetrahymena thermophila* [225] could cause biological concentration of Pd in environment, and thus, unpredicted influence on other aquatic organisms. It has been reported that ruthenium NPs are used as an oxide and acetylcholine (Ach)-modified structures for antimicrobial agents [226, 227]. Ruthenium oxide NPs and Ach-modified ruthenium NPs under NIR light exhibit good bactericidal activity with the mechanisms similar to that of palladium NPs (described above).

4.2 MICROBIAL INACTIVATION ON NOBLE-METAL MODIFIED PHOTOCATALYSTS—INDIRECT ANTIMICROBIAL ACTION

Photocatalysts, which exhibit photocatalytic activity under irradiation, have been well investigated as antimicrobial materials. The antibacterial effect of titania photocatalyst was reported for the first time by Matsunaga et al. in 1985 [228]. It was found that bacteria in water were killed when platinum-modified TiO_2 was exposed to UV irradiation. Then, much research has occurred on modified-TiO_2 photocatalysts in order to obtain high antimicrobial activity, especially on modification with metal NPs [229–231]. A. Markowska-Szczupak et al. wrote comprehensive review on application of titania photocatalyst for inactivation of microorganisms [232]. They clearly presented various examples of antimicrobial properties of bare and modified titania photocatalysts, for example, for bacteria, viruses, prions, and fungi, with possible mechanisms of microorganisms' inactivation. In general, photogenerated reactive oxygen species (ROS) are proposed to be responsible for high antimicrobial properties of titania photocatalysts (as shown for bacteria in Fig. 9).

For example, it is proposed that high antimicrobial activity of silver-modified TiO_2 may be caused by the interaction between silver and TiO_2, that is, inhibition of electron-hole recombination, and thus improvement of photocatalytic efficiency (in this case, efficient generation of ROS) of titania, and antimicrobial activity of silver itself. The most important property of photocatalysis for inactivation of microorganisms is that microorganisms could be damaged directly by oxidative decomposition reaction, independently of the species of microorganisms and their structures, suggesting that there are no bacteria resistant to photocatalysis. Interestingly, silver-modified TiO_2 exhibits high antibacterial activity not only under UV, but also under visible-light irradiation, with simultaneous decomposition of bacterial cells (Fig. 10) [230]. It should be remembered that dark activity of silver contributes in overall activity. However, activity under irradiation is usually a few orders of magnitude higher than that in the dark [230, 233]. Interestingly, under UV irradiation, the antibacterial activity of Cu/TiO_2 was higher than that of Ag/TiO_2, Au/TiO_2, and Pt/TiO_2, probably due to formation of highly efficient heterojunctions: Cu_2O-TiO_2 and CuO-TiO_2 (similar to that for oxidative decomposition of organic compounds) [233]. It was also reported that the proper balance between Cu_2O and CuO content in Cu_xO/TiO_2 composite photocatalyst was important to achieve optimal antibacterial activity under visible light irradiation and under dark conditions. In the case of different copper-titania systems, Cu_2O/TiO_2 was reported to be more active than CuO/TiO_2 and Cu NPs/TiO_2 [121]. Antifungal properties of plasmonic photocatalysts were also reported, for example, silver-modified faceted anatase particles (octahedral anatase particles, OAP) showed activities twice as high (against *C. albicans*) under vis ($\lambda > 420$ nm) irradiation as those in the dark. Interestingly, inactive Pt/TiO_2(OAP) in the dark exhibited slight antifungal activities under vis irradiation. Antifungal properties of Au/TiO_2 were also reported [110].

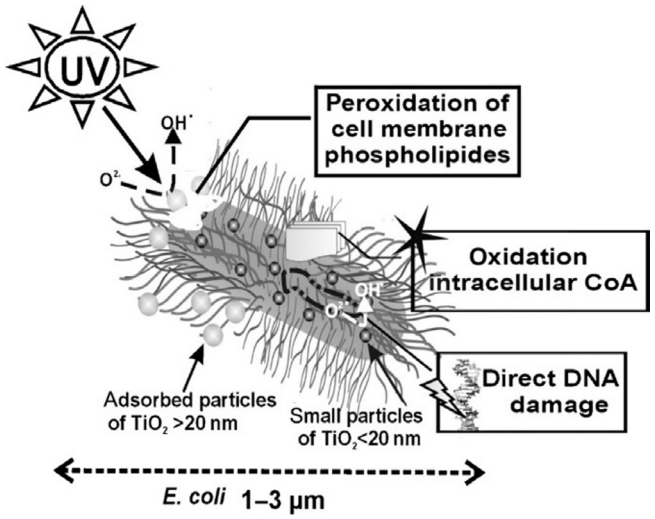

FIG. 9

The schematic mechanisms of photodegradation of bacterial cell.

Reproduced with permission from A. Markowska-Szczupak, K. Ulfig, W.A. Morawski, Catal. Today 161 (2011) 249–257. Copyright (2012) Elsevier B.V.

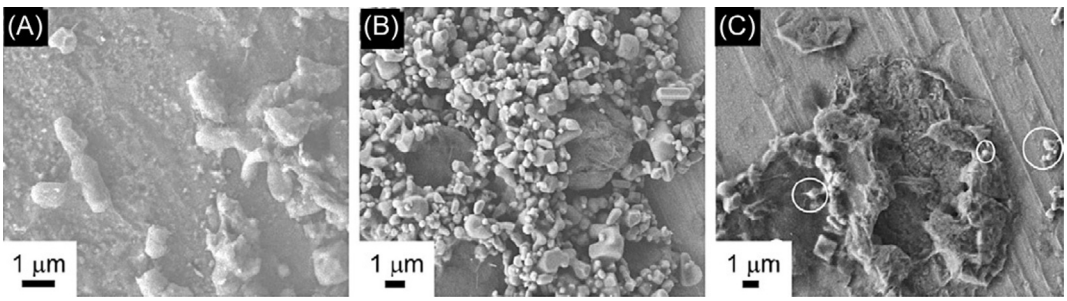

FIG. 10

SEM images showing bacterial cells: (A) before irradiation, (B) covered with photocatalyst, (C) destroyed after UV irradiation (circled NPs of photocatalyst).

Reproduced with permission from E. Kowalska, Z. Wei, B. Karabiyik, A. Herissan, M. Janczarek, M. Endo, A. Markowska-Szczupak, H. Remita, B. Ohtani, Catal. Today 252 (2015) 136–142, Copyright (2014) Elsevier B.V.

Although the inhibition of fungal growth on Au/TiO_2 under visible light irradiation was not high (ca. 30%–50% larger than that on bare titania, depending on properties of titania and gold NPs), the inhibition of sporulation and mycotoxins generation was significant, as shown in Fig. 11 (the lack of formed droplets containing mycotoxins in the presence of Au/TiO_2 in the support). Therefore, it is proposed that plasmonic photocatalysts with broad activities both for decomposition of chemical and microbiological pollutants under solar irradiation are perspective for future commercial applications for water purification.

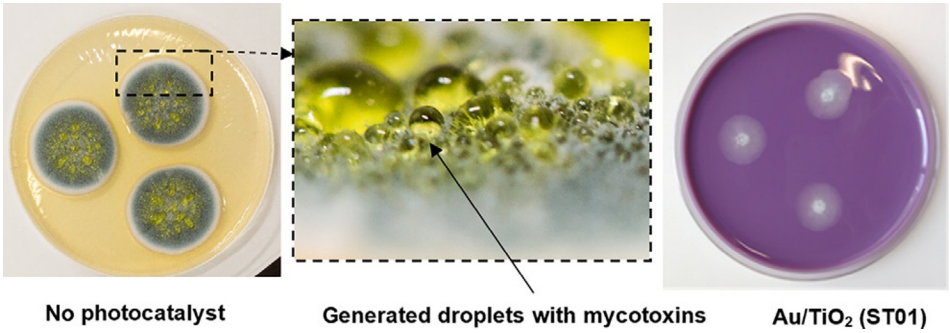

FIG. 11

Images of 8-day growth of *Penicillium chrysogenum* under fluorescent light irradiation in the absence (left) and presence (right) of Au/TiO_2(ST01) photocatalysts, (center) cross-section of mycelium with produced toxins.

From E. Kowalska, Z. Wei, B. Karabiyik, M. Janczarek, M. Endo, K. Wang, P. Rokicka, A. Markowska-Szczupak, B. Ohtani, Adv. Sci. Technol. 93 (2014) 174–183, Copyright Trans. Tech. Publications.

5 SUMMARY

The quality of water available for people and comprising the part of nature is still a critical problem across the world. Noble metal nanoparticles can be environmentally friendly, effective agents for water treatment, both for the degradation of toxic species and disinfection of microorganisms. However, each metal has both advantages and disadvantages. Therefore, to design efficient systems for water treatment based on noble metal nanoparticles, the proper analysis of metal properties in relation to the purpose and the application conditions is required. Furthermore, combinations of metals with other methods seem to be attractive as cost-effective, environmentally safe and highly-efficient treatment procedures. In many cases, the additional use of chemically inert or active supports for noble metals is also advantageous and often necessary (for recovery and safety). From this point of view, noble-metal-modified photocatalysts possess a high potential for application, due to their very high efficiency toward elimination of various pollutants.

However, it should be pointed out that for wide and common usage, it is necessary to investigate further evidence of antimicrobial effects, as well as the influence of NM on the environment and overall cost-benefit performance. N. Savage and S. Diallo pointed out some challenges facing nanomaterials for water purification in a comprehensive review [234]. Although their work focused on various nanomaterials, such as carbon nanotubes, metal and metal-oxides NPs, dendrimes, and zeolites, the challenges pointed by them are valid also for noble metal nanoparticles. Based on foregoing statement, one can formulate the following considerations for design water treatment techniques operating through noble metal nanoparticles:

(1) the availability of suppliers to provide large quantities of NMNPs,
(2) the integration of noble metal-based techniques into existing systems of water purification,
(3) the possible toxicity of novel noble metal-based nanomaterials (for example, the loss of Ag from Ag-polysulfone membrane [100] and from Ag-diatomite [97] observed during water filtration),

(4) possibility of noble metals inactivation by some components of water, for example, chloride, phosphates, sulfides, and compounds containing thiol groups [100],
(5) conditions of water environment (temperature, pH, salinity, etc.) influencing the efficiency of noble metal-based techniques,
(6) point-of-use water treatment (PoUWT) in the case of inaccessible access to municipal water treatment technologies or failure events in water purification systems.

REFERENCES

[1] R. McConnell, K. Berhane, L. Yao, M. Jerrett, F. Lurmann, F. Gilliland, N. Kunzli, J. Gauderman, E. Avol, D. Thomas, J. Peters, Environ. Health Perspect. 114 (2006) 766–772.
[2] L.M. Neas, D.W. Dockery, H. Burge, P. Koutrakis, F.E. Speizer, Am. J. Epidemiol. 143 (1996) 797–807.
[3] J.F. Zhang, K.R. Smith, Br. Med. Bull. 68 (2003) 209–225.
[4] H.M. Ammann, Mycotoxin Res. 21 (2005) 157–163.
[5] P.J. Landrigan, C.B. Schechter, J.M. Lipton, M.C. Fahs, J. Schwartz, Environ. Health Perspect. 110 (2002) 721–728.
[6] K.F. Chung, I.D. Pavord, Lancet 371 (2008) 1364–1374.
[7] A. Millman, D.L. Tang, F.P. Perera, Pediatrics 122 (2008) 620–628.
[8] V.G. Thomas, R. Guitart, Environ. Policy Gov. 20 (2010) 57–72.
[9] H.J.M. van Grinsven, H.F.M. ten Berge, T. Dalgaard, B. Fraters, P. Durand, A. Hart, G. Hofman, B.H. Jacobsen, S.T.J. Lalor, J.P. Lesschen, B. Osterburg, K.G. Richards, A.K. Techen, F. Vertes, J. Webb, W.J. Willems, Biogeosciences 9 (2012) 5143–5160.
[10] S. Beulke, W. van Beinum, L. Suddaby, Integr. Environ. Asses. 11 (2015) 276–286.
[11] A. Hyvarinen, T. Meklin, A. Vepsalainen, A. Nevalainen, Int. Biodeter. Biodegr. 49 (2002) 27–37.
[12] R.E. Wheatley, Anton Leeuw. Int. J. G. 81 (2002) 357–364.
[13] V. Artursson, R.D. Finlay, J.K. Jansson, Environ. Microbiol. 8 (2006) 1–10.
[14] D.A. Hogan, A. Vik, R. Kolter, Mol. Microbiol. 54 (2004) 1212–1223.
[15] S. Boonchan, M.L. Britz, G.A. Stanley, Appl. Environ. Microbiol. 66 (2000) 1007–1019.
[16] P.F.X. Corvini, A. Schaffer, D. Schlosser, Appl. Microbiol. Biotechnol. 72 (2006) 223–243.
[17] S. Congeevaram, S. Dhanarani, J. Park, M. Dexilin, K. Thamaraiselvi, J. Hazard. Mater. 146 (2007) 270–277.
[18] I. Arslan, I.A. Balcioglu, T. Tuhkanen, Environ. Technol. 20 (1999) 921–931.
[19] E. Kowalska, M. Janczarek, J. Hupka, M. Grynkiewicz, Water Sci. Technol. 49 (2004) 261–266.
[20] M. Barbeni, C. Minero, E. Pelizzetti, E. Borgarello, N. Serpone, Chemosphere 16 (1987) 2225–2237.
[21] E. Artuna, J. Hupka, Cent. Eur. J. Public Health 8 (2000) 88–89.
[22] S. Mozia, M. Tomaszewska, A.W. Morawski, Desalination 190 (2006) 308–314.
[23] C.H. King, E.B. Shotts Jr., R.E. Wooley, K.G. Porter, Appl. Environ. Microbiol. 54 (1988) 3023–3033.
[24] A. Mokrini, D. Ousse, E. Esplugas, Water Sci. Technol. 35 (1997) 95–102.
[25] D. Tomova, V. Iliev, S. Rakovsky, M. Anachkov, A. Eliyas, G.L. Puma, J. Photoch. Photobio. A 231 (2012) 1–8.
[26] M.R. Hoffmann, S.T. Martin, W.Y. Choi, D.W. Bahnemann, Chem. Rev. 95 (1995) 69–96.
[27] D. Bahnemann, J. Cunningham, M.A. Fox, E. Pelizzetti, P. Pichat, N. Serpone, Aquat. Surf. Photochem. (1994) 261–316.
[28] J.E. Duffy, M.A. Anderson, C.G. Hill Jr., W.A. Zeltner, Ind. Eng. Chem. Res. 39 (2000) 3698–3706.
[29] J. Sanchez-Oneto, F. Mancini, J.R. Portela, E. Nebot, F. Cansell, E.J.M. de la Ossa, Chem. Eng. J. 144 (2008) 361–367.
[30] O. Legrini, E. Oliveros, A.M. Braun, Chem. Rev. 93 (1993) 671–698.

[31] S. Malato, J. Blanco, C. Richter, D. Curco, J. Gimenez, Water Sci. Technol. 35 (1997) 157–164.
[32] K. Hashimoto, H. Irie, A. Fujishima, Jpn. J. Appl. Phys. 44 (2005) 8269–8285.
[33] P. Pichat, J. Adv. Oxid. Technol. 13 (2010) 238–246.
[34] A. Fujishima, T.N. Rao, D.A. Tryk, J. Photoch. Photobio. C 1 (2000) 1–21.
[35] P.A. Pekakis, N.P. Xekoukoulotakis, D. Mantzavinos, Water Res. 40 (2006) 1276–1286.
[36] M. Pelaez, N.T. Nolan, S.C. Pillai, M.K. Seery, P. Falaras, A.G. Kontos, P.S.M. Dunlop, J.W.J. Hamilton, J.A. Byrne, K. O'Shea, M.H. Entezari, D.D. Dionysiou, Appl. Catal. B Environ. 125 (2012) 331–349.
[37] A. Zaleska, Rec. Patent. Eng. 2 (2008) 157–164.
[38] R. Asahi, T. Morikawa, T. Ohwaki, K. Aoki, Y. Taga, Science 293 (2001) 269–271.
[39] D. Mitoraj, H. Kisch, Angew. Chem.-Int. Ed. 47 (2008) 9975–9978.
[40] S. Sakthivel, M. Janczarek, H. Kisch, J. Phys. Chem. B 108 (2004) 19384–19387.
[41] M. Bledowski, L.D. Wang, A. Ramakrishnan, O.V. Khavryuchenko, V.D. Khavryuchenko, P.C. Ricci, J. Strunk, T. Cremer, C. Kolbeck, R. Beranek, Phys. Chem. Chem. Phys. 13 (2011) 21511–21519.
[42] M.V. Dozzi, E. Selli, J. Photoch. Photobio. C 14 (2013) 13–28.
[43] J. Georgieva, S. Sotiropoulos, S. Armyanov, N. Philippidis, I. Poulios, J. Appl. Electrochem. 41 (2011) 173–181.
[44] G.Y. Li, X. Nie, Y.P. Gao, T.C. An, Appl. Catal. B Environ. 180 (2016) 726–732.
[45] N. Serpone, P. Maruthamuthu, P. Pichat, E. Pelizzetti, H. Hidaka, J. Photochem. Photobiol. A Chem. 85 (1995) 247–255.
[46] E. Kowalska, H. Remita, C. Colbeau-Justin, J. Hupka, J. Belloni, J. Phys. Chem. C 112 (2008) 1124–1131.
[47] J.M. Herrmann, J. Disdier, P. Pichat, Chem. Phys. Lett. 108 (1984) 618–622.
[48] A. Sclafani, M.N. Mozzanega, P. Pichat, J. Photochem. Photobiol. A Chem. 59 (1991) 181–189.
[49] Z.B. Hai, N. El Kolli, D.B. Uribe, P. Beaunier, M. Jose-Yacaman, J. Vigneron, A. Etcheberry, S. Sorgues, C. Colbeau-Justin, J.F. Chena, H. Remita, J. Mater. Chem. A 1 (2013) 10829–10835.
[50] B. Ohtani, H. Osaki, S. Nishimoto, T. Kagiya, J. Am. Chem. Soc. 108 (1986) 308–310.
[51] W. Macyk, G. Burgeth, H. Kisch, Photochem. Photobiol. Sci. 2 (2003) 322–328.
[52] R. Memming, F. Schroeppel, Chem. Phys. Lett. 62 (1979) 207–210.
[53] E. Kowalska, K. Yoshiiri, Z. Wei, S. Zheng, E. Kastl, H. Remita, S. Rau, B. Ohtani, Appl. Catal. Environ. 178 (2015) 133–143.
[54] J.A. Pedraza-Avella, R. Lopez, F. Martinez-Ortega, E.A. Paez-Mozo, R. Gomez, J. Nanopart. Res. 5 (2009) 95–104.
[55] M.V. Martin, P.I. Villabrille, J.A. Rosso, Environ. Sci. Pollut. R. 22 (2015) 14291–14298.
[56] M. Qamar, B. Merzougui, D. Anjum, A.S. Hakeem, Z.H. Yamani, D. Bahnemann, Catal. Today 230 (2014) 158–165.
[57] B. O'Regan, M. Grätzel, Nature 353 (1991) 737–740.
[58] Y. Tian, T. Tatsuma, J. Am. Chem. Soc. 127 (2005) 7632–7637.
[59] D.B. Ingram, S. Linic, J. Am. Chem. Soc. 133 (2011) 5202–5205.
[60] S.K. Cushing, J.T. Li, F.K. Meng, T.R. Senty, S. Suri, M.J. Zhi, M. Li, A.D. Bristow, N.Q. Wu, J. Am. Chem. Soc. 134 (2012) 15033–15041.
[61] E. Kowalska, O.O.P. Mahaney, R. Abe, B. Ohtani, Phys. Chem. Chem. Phys. 12 (2010) 2344–2355.
[62] J.B. Priebe, J. Radnik, A.J.J. Lennox, M.M. Pohl, M. Karnahl, D. Hollmann, K. Grabow, U. Bentrup, H. Junge, M. Beller, A. Bruckner, ACS Catal. 5 (2015) 2137–2148.
[63] X. Chen, H.-Y. Zhu, J.-C. Zhao, Z.-F. Zheng, X.-P. Gao, Angew. Chem. Int. Ed. 47 (2008) 5353–5356.
[64] A. Alqudami, N.A. Alhemiary, S. Munassar, Environ. Sci. Pollut. R. 19 (2012) 2832–2841.
[65] T. Chatzimitakos, A. Kallimanis, A. Avgeropoulos, C.D. Stalikas, Clean Soil Air Water 44 (2016) 794–802.
[66] M.S. Bootharaju, T. Pradeep, Langmuir 28 (2012) 2671–2679.
[67] Y. Wang, J.Y. Liu, P. Wang, C.J. Werth, T.J. Strathmann, ACS Catal. 4 (2014) 3551–3559.

[68] K. Vimala, Y.M. Mohan, K.S. Sivudu, K. Varaprasad, S. Ravindra, N.N. Reddy, Y. Padma, B. Sreedhar, K.M. Raju, Colloid Surf. B 76 (2010) 248–258.
[69] S.J. Lee, D.N. Heo, M. Heo, M.H. Noh, D. Lee, S.A. Park, J.H. Moon, I.K. Kwon, J. Ind. Eng. Chem. 46 (2017) 273–278.
[70] S.V. Otari, R.M. Patil, S.R. Waghmare, S.J. Ghosh, S.H. Pawar, Dalton Trans. 42 (2013) 9966–9975.
[71] Z.W. Seh, S.W. Liu, M. Low, S.-Y. Zhang, Z. Liu, A. Mlayah, M.-Y. Han, Adv. Mater. 24 (2012) 2310–2314.
[72] A. Pearson, H.D. Zheng, K. Kalantar-zadeh, S.K. Bhargava, V. Bansal, Langmuir 28 (2012) 14470–14475.
[73] M.G. Mendez-Medrano, E. Kowalska, A. Lehoux, A. Herissan, B. Ohtani, S. Rau, C. Colbeau-Justin, J.L. Rodriguez-Lopez, H. Remita, J. Phys. Chem. C 120 (2016) 25010–25022.
[74] A. Zielinska-Jureka, Z. Wei, I. Wysocka, P. Szweda, E. Kowalska, Appl. Surf. Sci. 353 (2015) 317–325.
[75] B. Ohtani, M. Kakimoto, S. Nishimoto, T. Kagiya, J. Phys. Chem. A Chem. 70 (1993) 265–272.
[76] E. Kowalska, R. Abe, B. Ohtani, Chem. Commun. (2009) 241–243.
[77] J.-M. Herrmann, J. Disdier, P. Pichat, J. Phys. Chem. 90 (1986) 6028–6034.
[78] M. Nischk, P. Mazierski, Z.S. Wei, K. Siuzdak, N.A. Kouame, E. Kowalska, H. Remita, A. Zaleska-Medynska, Appl. Surf. Sci. 387 (2016) 89–102.
[79] M.V. Dozzi, L. Prati, P. Canton, E. Selli, Phys. Chem. Chem. Phys. 11 (2009) 7171–7180.
[80] P.D. Cozzoli, M.L. Curri, C. Giannini, A. Agostiano, Small 2 (2006) 413–421.
[81] L.J. Brennan, F. Purcell-Milton, A.S. Salmeron, H. Zhang, A.O. Govorov, A.V. Fedorov, Y.K. Gun'ko, Nanoscale Res. Lett. 10 (2015) 1–12.
[82] B. Cojocaru, S. Neatu, E. Sacaliuc-Parvulescu, F. Levy, V.I. Parvulescu, H. Garcia, Appl. Catal. B Environ. 107 (2011) 140–149.
[83] S.V. Awate, A.A. Belhekar, S.V. Bhagwat, R. Kumar, N.M. Gupta, Int. J. Photoenergy (2008).
[84] P. Mazierski, A. Malankowska, M. Kobylanski, M. Diak, M. Kozak, M.J. Winiarski, T. Klimczuk, W. Lisowski, G. Nowaczyk, A. Zaleska-Medynska, ACS Catal. 7 (2017) 2753–2764.
[85] S. Bouhadoun, C. Guillard, F. Dapozze, S. Singh, D. Amans, J. Boucle, N. Herlin-Boime, Appl. Catal. B Environ. 174 (2015) 367–375.
[86] N.P. Tangale, A.A. Belhekar, K.B. Kale, S.V. Awate, Water Air Soil Pollut. 225 (2014).
[87] P.A. DeSario, J.J. Pietron, D.E. DeVantier, T.H. Brintlinger, R.M. Stroud, D.R. Rolison, Nanoscale 5 (2013) 8073–8083.
[88] Z.F. Bian, T. Tachikawa, P. Zhang, M. Fujitsuka, T. Majima, J. Am. Chem. Soc. 136 (2014) 458–465.
[89] X. Bokhimi, R. Zanella, A. Morales, J. Phys. Chem. C 111 (2007) 15210–15216.
[90] S. Zheng, Z. Wei, K. Yoshiiri, M. Braumuller, B. Ohtani, S. Rau, E. Kowalska, Photochem. Photobiol. Sci. 15 (2016) 69–79.
[91] M. Janczarek, Z. Wei, M. Endo, B. Ohtani, E. Kowalska, J. Photon. Energy 7 (2017) 1012008–1012001-1012016.
[92] M. Bowker, C. Morton, J. Kennedy, H. Bahruji, J. Greves, W. Jones, P.R. Davies, C. Brookes, P.P. Wells, N. Dimitratos, J. Catal. 310 (2014) 10–15.
[93] F. Menegazzo, M. Signoretto, D. Marchese, F. Pinna, M. Manzoli, J. Catal. 326 (2015) 1–8.
[94] M. Manzoli, F. Menegazzo, M. Signoretto, G. Cruciani, F. Pinna, J. Catal. 330 (2015) 465–473.
[95] S. Horold, K.D. Vorlop, T. Tacke, M. Sell, Catal. Today 17 (1993) 21–30.
[96] M.K. Joshi, H.R. Pant, N. Liao, J.H. Kim, H.J. Kim, C.H. Park, C.S. Kim, J. Colloid Interface Sci. 453 (2015) 159–168.
[97] Y.J. Xia, X.Y. Jiang, J. Zhang, M. Lin, X.S. Tang, J. Zhang, H.J. Liu, Appl. Surf. Sci. 396 (2017) 1760–1764.
[98] B. Ehdaie, C.T. Rento, V. Son, S.S. Turner, A. Samie, R.A. Dillingham, J.A. Smith, PLoS One 12 (2017).
[99] L.V.G. Pena, P. Petkova, R. Margalef-Marti, M. Vives, L. Aguilar, A. Gallegos, A. Francesko, I. Perelshtein, A. Gedanken, E. Mendoza, J.C. Casas-Zapata, J. Morato, T. Tzanov, Ind. Eng. Chem. Res. 56 (2017) 3599–3606.

[100] K. Zodrow, L. Brunet, S. Mahendra, D. Li, A. Zhang, Q.L. Li, P.J.J. Alvarez, Water Res. 43 (2009) 715–723.
[101] J.P. Kim, J.H. Kim, J. Kim, S.N. Lee, H.O. Park, J. Environ. Sci. China 42 (2016) 275–283.
[102] M.L. Masheane, L.N. Nthunya, S.P. Malinga, E.N. Nxumalo, B.B. Mamba, S.D. Mhlanga, Sep. Purif. Technol. 184 (2017) 79–87.
[103] P. Cruz-Tato, E.O. Ortiz-Quiles, K. Vega-Figueroa, L. Santiago-Martoral, M. Flynn, L.M. Diaz-Vazquez, E. Nicolau, Environ. Sci. Technol. 51 (2017) 4585–4595.
[104] T.A. Dankovich, Environ.-Sci. Nano 1 (2014) 367–378.
[105] T.A. Dankovich, J.A. Smith, Water Res. 63 (2014) 245–251.
[106] H.J. Kim, M.K. Joshi, H.R. Pant, J.H. Kim, E. Lee, C.S. Kim, Colloid Surf. A 469 (2015) 256–262.
[107] C.M. Tseng, H.L. Chen, S.N. Lai, M.S. Chen, C.J. Peng, C.J. Li, W.H. Hung, Nanoscale Res. Lett. (2017) 12.
[108] B. Kraeutler, A.J. Bard, J. Am. Chem. Soc. 100 (1978) 4317–4318.
[109] S. Nishimoto, B. Ohtani, H. Kajiwara, T. Kagiya, J. Chem. Soc. 79 (1983) 2685–2694.
[110] E. Kowalska, Z. Wei, B. Karabiyik, M. Janczarek, M. Endo, K. Wang, P. Rokicka, A. Markowska-Szczupak, B. Ohtani, Adv. Sci. Tech. 93 (2014) 174–183.
[111] A. Sclafani, M.-N. Mozzanega, J.M. Herrmann, J. Catal. 168 (1997) 117–120.
[112] K. Nakata, A. Fujishima, J. Photoch. Photobio. C 13 (2012) 169–189.
[113] D.F. Ollis, H. Al-Ekabi (Eds.), Photocatalytic Purification and Treatment of Water and Air, Elsevier, Amsterdam, 1993.
[114] Z. Wei, E. Kowalska, J. Verrett, C. Colbeau-Justin, H. Remita, B. Ohtani, Nanoscale 7 (2015) 12392–12404.
[115] M. Janczarek, E. Kowalska, B. Ohtani, Chem. Eng. J. 289 (2016) 502–512.
[116] J. Kuncewicz, P. Zabek, K. Kruczala, K. Szacilowski, W. Macyk, J. Phys. Chem. C 116 (2012) 21762–21770.
[117] J. Soria, J.C. Conesa, V. Augugliaro, L. Palmisano, M. Schiavello, A. Sclafani, J. Phys. Chem. 95 (1991) 274–282.
[118] T. Ohno, M. Akiyoshi, T. Umebayashi, K. Asai, T. Mitsui, M. Matsumura, Appl. Catal. A Gen. 265 (2004) 115–121.
[119] H. Kisch, S. Sakthivel, M. Janczarek, D. Mitoraj, J. Phys. Chem. C 111 (2007) 11445–11449.
[120] W. Macyk, K. Szacilowski, G. Stochel, M. Buchalska, J. Kuncewicz, P. Labuz, Coord. Chem. Rev. 254 (2010) 2687–2701.
[121] X.Q. Qiu, M. Miyauchi, K. Sunada, M. Minoshima, M. Liu, Y. Lu, D. Li, Y. Shimodaira, Y. Hosogi, Y. Kuroda, K. Hashimoto, ACS Nano 6 (2012) 1609–1618.
[122] M. Janus, B. Tryba, M. Inagaki, A.W. Morawski, Appl. Catal. B-Environ. 52 (2004) 61–67.
[123] K. Lalitha, G. Sadanandam, V.D. Kumari, M. Subrahmanyam, B. Sreedhar, N.Y. Hebalkar, J. Phys. Chem. C 114 (2010) 22181–22189.
[124] L. Zang, C. Lange, I. Abraham, S. Storck, W.F. Maier, H. Kisch, J. Phys. Chem. B 102 (1998) 10765–10771.
[125] B. Ohtani, S.-i. Nishimoto, J. Phys. Chem. B 97 (1993) 920–926.
[126] G.R. Banmwenda, S. Tsubota, T. Nakamura, M. Haruta, J. Photochem. Photobiol. A Chem. 89 (1995) 177–189.
[127] B. Ohtani, M. Kakimoto, H. Miyadzu, S. Nishimoto, T. Kagiya, J. Phys. Chem. 92 (1988) 5773–5777.
[128] G.A. Hope, A.J. Bard, J. Phys. Chem. 87 (1983) 1979–1984.
[129] N. Jaffrezic-Renault, P. Pichat, A. Foissy, R. Mercier, J. Phys. Chem. 90 (1986) 2733–2738.
[130] P. Pichat, J.M. Herrmann, J. Disdier, H. Courbon, M.N. Mozzanega, Nouv. J. Chim. 5 (1981) 627–636.
[131] B. Ohtani, Y. Ogawa, S.-i. Nishimoto, J. Phys. Chem. B 101 (1997) 3746–3752.
[132] W.T. Chen, A. Chan, Z.H.N. Al-Azri, A.G. Dosado, M.A. Nadeem, D. Sun-Waterhouse, H. Idriss, G.I.N. Waterhouse, J. Catal. 329 (2015) 499–513.
[133] A.G. Dosado, W.T. Chen, A. Chan, D. Sun-Waterhouse, G.I.N. Waterhouse, J. Catal. 330 (2015) 238–254.
[134] J.G. Yu, L. Yue, S.W. Liu, B.B. Huang, X.Y. Zhang, J. Colloid Interface Sci. 334 (2009) 58–64.

[135] F.B. Li, X.Z. Li, Appl. Catal. A. Gen. 228 (2002) 15–27.
[136] I.A. Mkhalid, J. Alloys Compd. 631 (2015) 298–302.
[137] N. Smirnova, V. Vorobets, O. Linnik, E. Manuilov, G. Kolbasov, A. Eremenko, Surf. Interface Anal. 42 (2010) 1205–1208.
[138] J.T. Carneiro, T.J. Savenije, G. Mul, Phys. Chem. Chem. Phys. 11 (2009) 2708–2714.
[139] I. Caretti, M. Keulemans, S.W. Verbruggen, S. Lenaerts, S. Van Doorslaer, Top. Catal. 58 (2015) 776–782.
[140] B. Mei, C. Wiktor, S. Turner, A. Pougin, G. van Tendeloo, R.A. Fischer, M. Muhler, J. Strunk, ACS Catal. 3 (2013) 3041–3049.
[141] E. Kowalska, L. Rosa, S. Rau, S. Juodkazis, B. Ohtani, *Chem. Commun.* (2018), in preparation.
[142] K. Awazu, M. Fujimaki, C. Rockstuhl, J. Tominaga, H. Murakami, Y. Ohki, N. Yoshida, T. Watanabe, J. Am. Chem. Soc. 130 (2008) 1676–1680.
[143] H. Kominami, A. Tanaka, K. Hashimoto, Chem. Commun. 46 (2010) 1287–1289.
[144] H. Kominami, A. Tanaka, K. Hashimoto, Appl. Catal. A. Gen. 397 (2011) 121–126.
[145] C.J. Wang, O. Ranasingha, S. Natesakhawat, P.R. Ohodnicki, M. Andio, J.P. Lewis, C. Matranga, Nanoscale 5 (2013) 6968–6974.
[146] A.J. Haes, C.L. Haynes, A.D. McFarland, G.C. Schatz, R.P. Van Duyne, S. Zou, MRS Bull. 30 (2005) 368–375.
[147] F. Stietz, F. Trager, Philos. Mag. 79 (1999) 1281–1298.
[148] N. Halas, MRS Bull. 30 (2005) 362–367.
[149] H.A. Atwater, S. Maier, A. Polman, J.A. Dionne, L. Sweatlock, MRS Bull. 30 (2005) 385–389.
[150] K. Okamoto, I. Niki, A. Shvarster, G. Maltezos, Y. Narukawa, T. Mukai, Y. Kawakami, A. Scherer, Phys. Status Solidi A 204 (2007) 2103–2107.
[151] P. Zijlstra, J.W.M. Chon, M. Gu, Nature 459 (2009) 410–413.
[152] K. Ueno, H. Misawa, J. Photoch. Photobio. C 15 (2013) 31–52.
[153] S.W. Verbruggen, J. Photoch. Photobio. C 24 (2015) 64–82.
[154] S. Sarina, E.R. Waclawik, H.Y. Zhu, Green Chem. 15 (2013) 1814–1833.
[155] Z.Z. Lou, Z.Y. Wang, B.B. Huang, Y. Dai, ChemCatChem 6 (2014) 2456–2476.
[156] W.B. Hou, S.B. Cronin, Adv. Funct. Mater. 23 (2013) 1612–1619.
[157] E. Kowalska, Plasmonic photocatalysis, in: C. Louis, O. Pluchery (Eds.), Gold Nanoparticles for Physics, Chemistry and Biology, World Scientific, Singapore, 2017, pp. 319–364.
[158] V. Subramanian, E. Wolf, P.V. Kamat, J. Phys. Chem. B 105 (2001) 11439–11446.
[159] Z. Liu, W. Hou, P. Pavaskar, M. Aykol, S.B. Cronin, Nano Lett. 11 (2011) 1111–1116.
[160] M. Valenti, D. Dolat, G. Biskos, A. Schmidt-Ott, W.A. Smith, J. Phys. Chem. C 119 (2015) 2096–2104.
[161] W. Hou, Z. Liu, P. Pavaskar, W. Hsuan Hung, S.B. Cronin, J. Catal. 277 (2011) 149–153.
[162] A. Furube, L. Du, K. Hara, R. Katoh, M. Tachiya, J. Am. Chem. Soc. 129 (2007) 14852–14853.
[163] N. Sakai, Y. Fujiwara, Y. Takahashi, T. Tatsuma, Chem. Phys. Chem. 10 (2009) 766–769.
[164] R.M. Mohamed, E.S. Aazam, Int. J. Photoenergy 2011 (2011) Article ID: 137328, https://www.hindawi.com/journals/ijp/2011/137328/.
[165] C.G. Silva, R. Juarez, T. Marino, R. Molinari, H. Garcia, J. Am. Chem. Soc. 133 (2011) 595–602.
[166] M.S. Son, J.E. Im, K.K. Wang, S.L. Oh, Y.R. Kim, K.H. Yoo, Appl. Phys. Lett. 96 (2010) 023115.
[167] S. Mukherjee, F. Libisch, N. Large, O. Neumann, L.V. Brown, J. Cheng, J.B. Lassiter, E.A. Carter, P. Nordlander, N.J. Halas, Nano Lett. 13 (2013) 240–247.
[168] Y. Nishijima, K. Ueno, Y. Yokata, K. Murakoshi, H. Misawa, J. Phys. Chem. Lett. 1 (2010) 2031–2036.
[169] S.K. Cushing, J.T. Li, J. Bright, B.T. Yost, P. Zheng, A.D. Bristow, N.Q. Wu, J. Phys. Chem. C 119 (2015) 16239–16244.
[170] S.Z. Zheng, K.L. Wang, Z.S. Wei, K. Yoshiiri, M. Braumuller, S. Rau, B. Ohtani, E. Kowalska, J. Adv. Oxid. Technol. 19 (2016) 208–217.

[171] J.W. Sun, N. Liu, S.R. Zhai, Z.Y. Xiao, Q.D. An, D.Z. Huang, Mater. Sci. Semicond. Process. 25 (2014) 286–293.
[172] V. Rodriguez-Gonzalez, R. Zanella, G. del Angel, R. Gomez, J. Mol. Catal. A Chem. 281 (2008) 93–98.
[173] S.-i. Naya, T. Kume, T. Okumura, H. Tada, Phys. Chem. Chem. Phys. 17 (2015) 18004–18010.
[174] B.L. Oliva, A. Pradhan, D. Caruntu, C.J. O'Connor, M.A. Tarr, J. Mater. Res. 21 (2006) 1312–1316.
[175] K. Yang, K. Huang, L.L. Lin, X. Chen, W.X. Dai, X.Z. Fu, J. Power Sources 284 (2015) 194–205.
[176] H.H. Ji, L. Lyu, L.L. Zhang, X.Q. An, C. Hu, Appl. Catal. B Environ. 199 (2016) 230–240.
[177] V. Iliev, D. Tomova, L. Bilyarska, G. Tyuliev, J. Mol. Catal. A Chem. 263 (2007) 32–38.
[178] A. Kafizas, S. Kellici, J.A. Darr, I.P. Parkin, J. Photoch. Photobio. A 204 (2009) 183–190.
[179] Z. Pap, A. Radu, I.J. Hidi, G. Melinte, L. Diamandescu, T. Popescu, L. Baia, V. Danciu, M. Baia, Chinese J. Catal. 34 (2013) 734–740.
[180] S. Oros-Ruiz, R. Zanella, B. Prado, J. Hazard. Mater. 263 (2013) 28–35.
[181] X.D. Wang, J. Choi, D.R.G. Mitchell, Y.B. Truong, I.L. Kyratzis, R.A. Caruso, ChemCatChem 5 (2013) 2646–2654.
[182] Z. Yi, Y. Chen, J. Luo, Y. Y, X. Kang, P. Ye, X. Gao, Y. Yi, Y. Tang, Plasmonics (2015) 1–8.
[183] R. Costi, A.E. Saunders, E. Elmalem, A. Salant, U. Banin, Nano Lett. 8 (2008) 637–641.
[184] T. Kiyonaga, M. Fujii, T. Akita, H. Kobayashi, H. Tada, Phys. Chem. Chem. Phys. 10 (2008) 6553–6561.
[185] T. Okuno, G. Kawamura, H. Muto, A. Matsuda, J. Sol Gel Sci. Techn. 74 (2015) 748–755.
[186] S.V. Awate, R.K. Sahu, M.D. Kadgaonkar, R. Kumar, N.M. Gupta, Catal. Today 141 (2009) 144–151.
[187] R.S. Sonawane, M.K. Dongare, J. Mol. Catal. A Chem. 243 (2006) 68–76.
[188] S.A. Elfeky, A.S.A. Al-Sherbini, J. Nanomater. 2011 (2011) Article ID: 570438, https://www.hindawi.com/journals/jnm/2011/570438/.
[189] G.N. Wang, X.F. Wang, J.F. Liu, X.M. Sun, Chem.-Eur. J. 18 (2012) 5361–5366.
[190] L.Q. Liu, T.D. Dao, R. Kodiyath, Q. Kang, H. Abe, T. Nagao, J.H. Ye, Adv. Funct. Mater. 24 (2014) 7754–7762.
[191] L.Q. Liu, S.X. Ouyang, J.H. Ye, Angew. Chem.-Ind. Edit. 52 (2013) 6689–6693.
[192] E. Kowalska, S. Rau, B. Ohtani, J. Nanotechnol. (2012) 1–11.
[193] S.A. Trammell, R. Nita, M. Moore, D. Zabetakis, E. Chang, D.A. Knight, Chem. Commun. 48 (2012) 4121–4123.
[194] A. Zielińska-Jurek, E. Kowalska, J.W. Sobczak, W. Lisowski, B. Ohtani, A. Zaleska, Appl. Catal. B-Environ. 101 (2011) 504–514.
[195] H.Y. Jiang, K. Cheng, J. Lin, Phys. Chem. Chem. Phys. 14 (2012) 12114–12121.
[196] J.M. Herrmann, Catal. Today 53 (1999) 115–129.
[197] H. Kisch, Angew. Chem. Int. Ed. 49 (2010) 9588–9589.
[198] P.A. DeSario, J.J. Pietron, T.H. Brintlinger, M. McEntee, J.F. Parker, O. Baturina, R.M. Stroud, D.R. Rolison, Nanoscale 9 (2017) 11720–11729.
[199] J. Xing, Z.P. Chen, F.Y. Xiao, X.Y. Ma, C.Z. Wen, Z. Li, H.G. Yang, Chem. Asian J. 8 (2013) 1265–1270.
[200] M.X. Liu, S.Z. Su, Y.M. Li, X.W. Song, F. Yu, X.W. Ding, H.B. Xing, X.L. Wang, ACS Sustain. Chem. Eng. 5 (2017) 5651–5656.
[201] WHO, Guidelines for Drinking-Water Quality, fourth ed., Gutenberg, Malta, 2011.
[202] A. Davison, G. Howard, M. Stevens, P. Callan, L. Fewtrell, D. Deere, J. Bartram, Water Safety Plans: Managing Drinking-Water Quality from Catchment to Consumer, World Health Organization, Geneva, 2005. http://www.who.int/water_sanitation_health/publications/wsp0506/en/.
[203] H.T. Ratte, Environ. Toxicol. Chem. 18 (1999) 89–108.
[204] A. Chwalibog, E. Sawosz, A. Hotowy, J. Szeliga, S. Mitura, K. Mitura, M. Grodzik, P. Orlowski, A. Sokolowska, Int. J. Nanomedicine 5 (2010) 1085–1094.
[205] V. Sambhy, M.M. MacBride, B.R. Peterson, A. Sen, J. Am. Chem. Soc. 128 (2006) 9798–9808.

[206] K.B. Holt, A.J. Bard, Biochemistry 44 (2005) 13214–13223.
[207] C.N. Lok, C.M. Ho, R. Chen, Q.Y. He, W.Y. Yu, H.Z. Sun, P.K.H. Tam, J.F. Chiu, C.M. Che, J. Proteome Res. 5 (2006) 916–924.
[208] Y. Tian, J.J. Qi, W. Zhang, Q. Cai, X.Y. Jiang, ACS Appl. Mater. Interfaces 6 (2014) 12038–12045.
[209] H.L. Su, C.C. Chou, D.J. Hung, S.H. Lin, I.C. Pao, J.H. Lin, F.L. Huang, R.X. Dong, J.J. Lin, Biomaterials 30 (2009) 5979–5987.
[210] M. Padervand, M.R. Elahifard, R.V. Meidanshahi, S. Ghasemi, S. Haghighi, M.R. Gholami, Mater. Sci. Semicond. Process. 15 (2012) 73–79.
[211] S. Galdiero, A. Falanga, M. Vitiello, M. Cantisani, V. Marra, M. Galdiero, Molecules 16 (2011) 8894–8918.
[212] J.L. Speshock, R.C. Murdock, L.K. Braydich, A.M. Schrand, S.M. Hussain, J. Nanobiotechnol. 8 (2010) 19–27.
[213] T.A. Dankovich, D.G. Gray, Environ. Sci. Technol. 45 (2011) 1992–1998.
[214] K. Sunada, M. Minoshima, K. Hashimoto, J. Hazard. Mater. 235 (2012) 265–270.
[215] C. Deng, J. Gong, G.M. Zeng, P. Zhang, B. Song, H. Zhang, H.J. Liu, S. Huan, Chemosphere 184 (2017) 347–357.
[216] A. Jafari, L. Pourakbar, K. Farhadi, L. Mohamadgolizad, Y. Goosta, Turk. J. Biol. 39 (2015) 556–561.
[217] R.M. Amin, M.B. Mohamed, M.A. Ramadan, T. Verwanger, B. Krammer, Nanomedicine 4 (2009) 637–643.
[218] N.U. Islam, K. Jalil, M. Shahid, A. Rauf, N. Muhammad, A. Khan, M.R. Shah, M.A. Khan, Arab. J. Chem. (2017), https://doi.org/10.1016/j.arabjc.2015.1002.1014 (in press).
[219] T. Ahmad, I.A. Wani, I.H. Lone, A. Ganguly, N. Manzoor, A. Ahmad, J. Ahmed, A.S. Al-Shihri, Mater. Res. Bull. 48 (2013) 12–20.
[220] D. Baram-Pinto, S. Shukla, A. Gedanken, R. Sarid, Small 6 (2010) 1044–1050.
[221] C.P. Davis, N. Wagle, M.D. Anderson, M.M. Warren, Antimicrob. Agents Ch. 35 (1991) 2131–2134.
[222] P.V. Asharani, N. Xinyi, M.P. Hande, S. Valiyaveettil, Nanomedicine 5 (2010) 51–64.
[223] C.P. Adams, K.A. Walker, S.O. Obare, K.M. Docherty, PLoS One 9 (2014) e85981.
[224] K. Tahir, S. Nazir, B.S. Li, A. Ahmad, T. Nasir, A.U. Khan, S.A.A. Shah, Z.U. Khan, G. Yasin, M. U. Hameed, J. Photochem. Photobiol. B 164 (2016) 164–173.
[225] V. Aruoja, S. Pokhrel, M. Sihtmae, M. Mortimer, L. Madler, A. Kahru, Environ. Sci. Nano 2 (2015) 630–644.
[226] S.K. Kannan, M. Sundrarajan, Adv. Powder Technol. 26 (2015) 1505–1511.
[227] X.Q. Huang, G.J. Chen, J.L. Pan, X. Chen, N. Huang, X. Wang, J. Liu, J. Mater. Chem. B 4 (2016) 6258–6270.
[228] T. Matsunaga, R. Tomoda, T. Nakajima, H. Wake, FEMS Microbiol. Lett. 29 (1985) 211–214.
[229] J.G. McEvoy, Z.S. Zhang, J. Photoch. Photobio. C 19 (2014) 62–75.
[230] E. Kowalska, Z. Wei, B. Karabiyik, A. Herissan, M. Janczarek, M. Endo, A. Markowska-Szczupak, H. Remita, B. Ohtani, Catal. Today 252 (2015) 136–142.
[231] M.P. Reddy, A. Venugopal, M. Subrahmanyam, Water Res. 41 (2007) 379–386.
[232] A. Markowska-Szczupak, K. Ulfig, W.A. Morawski, Catal. Today 161 (2011) 249–257.
[233] Z. Wei, M. Endo, K. Wang, E. Charbit, A. Markowska-Szczupak, B. Ohtani, E. Kowalska, Chem. Eng. J. 318 (2017) 121–134.
[234] N. Savage, M.S. Diallo, J. Nanopart. Res. 7 (2005) 331–342.

CHAPTER

22 SEMICONDUCTOR PHOTOCATALYSIS FOR WATER PURIFICATION

Carolina Belver, Jorge Bedia, Almudena Gómez-Avilés, Manuel Peñas-Garzón, Juan J. Rodriguez
Chemical Engineering Section, Universidad Autonoma de Madrid, Madrid, Spain

Photocatalysis appears to be an interesting approach for water purification, with the possibility of using sunlight as a sustainable and renewable source of energy. This technology is based on the use of a semiconductor that can be excited by light with an energy higher than its band gap, inducing the formation of energy-rich electron-hole pairs, which can be involved in redox reactions. Recent progress has explored the chemical nature of nanoscale semiconductors with the aim of improving their electronic and optical properties, enhancing their photoresponse to the visible light. Nanomaterials typically have high activity and a high degree of functionalization, large specific surface area, and size-dependent properties which make them suitable for application in water purification. In this chapter, the potential application of various nanomaterials such as metal nanoparticles, metal oxides, carbon compounds, zeolites, filtration membranes, etc., in the field of wastewater treatment by photocatalysis is discussed.

In recent years, most photocatalysts have been specifically devised for application under sunlight, but many researchers have focused their attention on UV-active systems. Thus, we will distinguish between UV and visible or sunlight-active nanoscale semiconductors. This chapter also includes a description of the most studied photocatalytic reactions related to water purification, the degradation of emerging pollutants, and potential applications in disinfection.

1 PHOTOCATALYSIS: STATE OF THE ART

For several decades, photocatalysis has been investigated as a potential way to address air and water purification, synthesis of chemical compounds, and energy-related developments. The term photocatalysis is commonly accepted to describe the activation of a chemical process by a solid (known as photocatalyst) irradiated by an UV-visible light source [1–4]. In this process, the incident light interacts with the photocatalyst, causing (in a femtosecond time scale) the generation of electron-hole (e^-/h^+) pairs if the energy is equal to or higher than the band gap (E_g) of the semiconductor material, as shown in Fig. 1. The band gap is an energy barrier between the valence band ("VB", highest energy band occupied with electrons) and the conduction band ("CB", lowest energy band empty of electrons) [3, 5]. Because of the light interaction, the electron (e^-_{CB}) is excited and promoted from the VB to the CB, while a hole (h^+_{VB}) is created in the VB (Fig. 1, Stages 1 and 2) [6, 7]. If these charges remain

Nanoscale Materials in Water Purification. https://doi.org/10.1016/B978-0-12-813926-4.00028-8

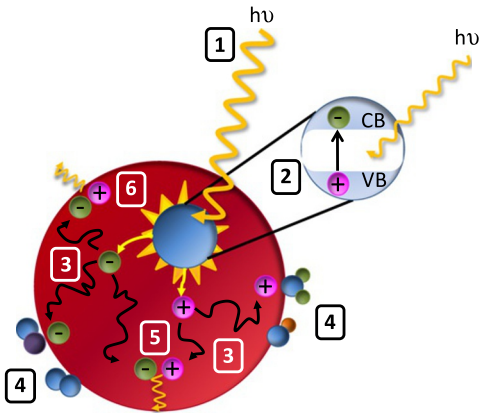

FIG. 1

Schematic illustration of an irradiated photocatalyst particle.

separated and migrate from the bulk to the semiconductor surface they can react there with adsorbed species (Fig. 1, Stages 3 and 4, respectively). In this sense, photoinduced electrons can be involved in reduction processes, while the holes can induce oxidation reactions. However, the e^-_{CB} and h^+_{VB} photogenerated charges also tend to recombine, both in the bulk and the surface of the semiconductor, dissipating energy as heat and returning to a non-excited state (Fig. 1, Stages 5 and 6, respectively) [8]. It is noteworthy that the relative occurrence of those steps (charge carriers' generation, migration, and recombination) depends on the inherent characteristics of the photocatalyst [9].

A wide diversity of potential photocatalytic materials (metal oxides such as ZnO, TiO_2, CeO_2, Nb_2O_5, Ta_2O_5, WO_3, and $SrTiO_3$; sulfides such as MOS_x, WS_x, BiS_x, CdS, and ZnS; or even nitrides, like TaN_x, SiN_x, or GeN_x) has been investigated in the literature [10, 11]. The works of Formenti et al. [12] and Fujishima and Honda [13] are commonly referred to as pioneering studies on photocatalysis. However, a number of earlier investigations were conducted in connection with this field, as summarized in Table 1.

Despite those interesting contributions, it was not until the publication of Fujishima and Honda in *Nature* in 1972 that scientists began to pay increasing attention to the potential applications of photocatalysis in different fields, including environmental engineering. Moreover, in the 1980s, the energy crisis and increasing environmental concerns boosted this technology. In subsequent decades, a growing number of publications on photocatalysis were registered, as can be seen in Fig. 2. Now, more than 8000 works relative to this field are published worldwide annually, with around 10% corresponding to water treatment. Hereafter, some of the most important applications of photocatalysis are briefly reviewed.

Photocatalytic production of hydrogen from water has received special attention. TiO_2 was the first photocatalyst used (and the preferred one so far, despite its limited efficiency) [32]. Other semiconductor materials have been tested, such as metal oxides, sulfides, nitrides, and oxynitrides [33, 34], which increase the quantum efficiency. Another important application of photocatalysis is the reduction of CO_2, addressed to both decreasing emissions and upgrading them to useful fuels [35]. Nano- and microstructures, such as microspheres of Bi_2S_3 [36] or TiO_2-graphene nanosheets [37], have been described to provide a high adsorption of CO_2 and a rapid charge separation and migration, some of the most critical factors that affect CO_2 photoconversion [34].

Table 1 Earlier Works Related to Photocatalysis

Reference	Event
Plotnikow [14]	"Photokatalyse" and "Photokatalytisch" terms appeared for first time
Eibner [15]	Study of the discoloration of Prussian blue on irradiated ZnO
Bruner and Kozak [16]	Oxalic acid oxidation in the presence of illuminated UO_2^+ salts
Landau [17]	Photocatalyst is active even if it is insoluble in the medium ("Heterogeneous photocatalysis," in a few words)
Renz [18]	TiO_2, CeO_2, Nb_2O_5, Ta_2O_5 reduction after irradiation with solar light in the presence of glycerol
Baur and Perret [19]	Photocatalytic deposition of dissolved silver salts over ZnO
Baur and Neuweiler [20]	Photocatalytic formation of hydroperoxide on ZnO
Renz [21]	Photocatalytic reduction of $AgNO_3$ to Ag^0 and $AuCl_3$ to Au^0 on TiO_2 and Nb_2O_5
Goodeve and Kitchener [22]	Dye photocatalytic decomposition on TiO_2
Jacobsen [23]	Reduction-oxidation mechanism of titania-based exterior paints chalking process
Markham and Laidler [24]; Rubin et al. [25]	Elaborated mechanism of hydroperoxide UV-light photoinduced formation on ZnO
Markham [26]	Organic compounds oxidation under UV-light
Kennedy et al. [26a]	O_2 and NO photoinduced adsorption on TiO_2 surface. Reduction of O_2 is included as a step of the process
Kuriacose and Markham [27]	Photopolymerization of methyl methacrylate in ZnO suspensions
Doerfler and Hauffe [28]	CO oxidation mechanism at ZnO surface
Filimonov [29]	Mechanism of isopropanol oxidation on ZnO and TiO_2
Markham and Upreti [30]	Study of photoelectric cells with ZnO and CdS electrodes
Fujishima et al. [31]	Photon energy is transformed in chemical energy almost without energy losses, giving high reactivity to photoinduced hole
Formenti et al. [12]	Isobutane oxidation using TiO_2 beads with UV-light
Fujishima and Honda [13]	H_2 and O_2 generation from H_2O splitting using UV-irradiated TiO_2 electrode

Regarding environmental applications, photocatalysis is one of the most investigated technologies among Advanced Oxidation Processes (AOPs). In the case of air purification, inorganic gases (mainly CO, NO_x, SO_x, and H_2S) and VOCs (Volatile Organic Compounds, like benzene, toluene, or formaldehyde) can be removed by photocatalytic oxidation [9]. For these processes, metal oxides (mostly TiO_2, WO_3, or ZnO) and ternary compounds (e.g., $MnFe_2O_4$ or $Zr_xTi_{1-x}O_2$) have been reported to yield good performances [38–40]. Photocatalysis has been mostly studied for water purification, with increasing interest in the potential use of solar radiation. Environmental and human health risks derived from toxic heavy metal ions and nitrate have promoted the investigation of different potential solutions, including photocatalysis [41]. Metal cations can be reduced, from a thermodynamic viewpoint, if the potential of the conduction band of the photocatalyst is more negative than the metal reduction potential [34, 42], which can be accomplished by a wide range of semiconductors. Otherwise, metal ions are

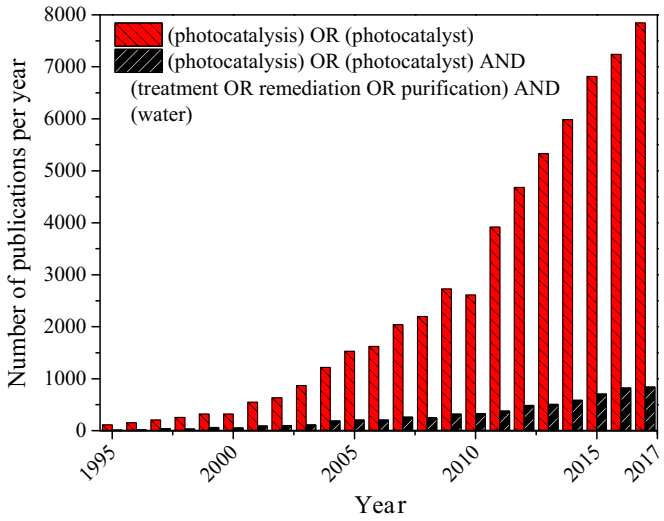

FIG. 2

Publications on photocatalysis within the last 2 decades (Scopus, https://www.scopus.com).

oxidized and form insoluble oxides, which then are deposited on the photocatalyst surface, allowing its extraction and separation. With respect to nitrate, it can be reduced to N_2. However, so far, photocatalysis has shown a significantly inconvenient high selectivity to NH_4^+ [43]. Most extensively studied applications of photocatalysis to the abatement of water pollutants deal with organic species such as pesticides, industrial additives, dyes, pharmaceuticals, and cyanotoxins, among others [44].

This chapter presents a review of the nanoscale semiconductors used in photocatalysis for water purification. First, we will briefly discuss the reactions and catalysts involved, with special attention to the challenges of this technology. Then, nanoscale semiconductors active under UV, visible light, and sunlight will be analyzed. Finally, the chapter includes an overview on the potential applications of higher current interest, addressed to emerging contaminants, disinfection, and cyanotoxins.

1.1 PHOTOCATALYSIS FOR WATER PURIFICATION

In the last two to three decades, there has been an increasing demand for the development of cost-effective technologies capable of dealing with recalcitrant (and commonly toxic) water pollutants. In this context, Advanced Oxidation Processes (AOPs) have been widely investigated. They are based on the creation of highly reactive radicals that can be generated in situ by different ways, including UV/H_2O_2, sonolysis, ozonation, Fenton-like oxidation, electrochemical oxidation, photocatalysis, and their combinations [45]. In particular, photocatalysis can be operated at mild conditions and can use only oxygen as its primary reagent. There is a current trend toward the use of visible and solar light as renewable and inexpensive energy sources [44, 46]. There has been a wide diversity of investigated pollutants (see Table 2), which can be classified in several main groups according to their origins and effects. These include contaminants of emerging concern (CECs), endocrine disrupting compounds (EDCs), pathogens, and cyanotoxins. CECs are characterized as substances which are

Table 2 Main Water Pollutants Treated via Photocatalysis

Type of Pollutant	Examples
Contaminants of Emerging Concern (CECs)	Additives (polybrominated diphenyl ethers) Antibiotics (amoxicillin, ampicillin, metronidazole) Disinfectants (haloacetic acids, trihalomethanes) Dyes (methylene blue, methyl orange, rhodamine B) Pharmaceuticals (carbamazepine, diclofenac, ibuprofen) Preservatives (dimethylphenols, parabens, salicylic acid)
Endocrine Disrupting Compounds (EDCs)	Alkylphenols (phenol, 4-methylphenol, 4-*n*-heptylphenol) Bisphenol A Heavy metals (Cr^{6+}, As^{5+}, Hg^{2+}, Cu^{2+}, Pb^{2+}) Organotins (monobutyltin, dibutylin, tributyltin) Pesticides (atrazine, chlorpyrifos, diazinon) Polycyclic aromatic hydrocarbon (phenanthrene, fluoranthene) Phthalates (dimethyl phthalate, di(2-ethylhexyl)phthalate) Steroid hormones (estrone, 17α-ethinylestradiol, 17β-estradiol)
Pathogenic germs (Disinfection)	*Bacillus subtilis*, *Escherichia coli*, *Micrococcus lylae*, *Salmonella typhi*, *Staphylococcus aureus*
Cyanotoxins	Microcystins, Cylindrospermopsin, Nodularins, and Anatoxin-a, as main cyanobacteria families studied

Adapted from R. Fagan, D.E. McCormack, D.D. Dionysiou, S.C. Pillai, A review of solar and visible light active TiO2 photocatalysis for treating bacteria, cyanotoxins and contaminants of emerging concern. Mater. Sci. Semicond. Process. 42 (2016) 2–14, V. Likodimos, D.D. Dionysiou, P. Falaras, CLEAN WATER: water detoxification using innovative photocatalysts. Rev. Environ. Sci. Biotechnol. 9 (2010) 87–94, and S. Merel, D. Walker, R. Chicana, S. Snyder, E. Baurès, O. Thomas, State of knowledge and concerns on cyanobacterial blooms and cyanotoxins. Environ. Int. 59 (2013) 303-327.

not usually monitored species in the environment, the adverse consequences of which are newly identified [47], while EDCs are those compounds which can have negative effects over the endocrine system of living beings [48]. It has also been reported that photocatalysis has bactericidal and, in general, germicidal potential, causing the breakdown of the microbial cells upon decomposition of the cell wall and subsequent destruction of the internal components [49]. In the case of cyanobacteria (photosynthetic bacteria present in surface water bodies), they represent a harmful threat to human health due to the dermatological, hepatic, and genotoxic effects of cyanotoxins, toxic metabolites synthesized by those microorganisms [50, 51].

As described in Section 1, a semiconductor can undergo a photoinduced process upon irradiation. This will consist of the promotion of one electron from the VB to the CB, leaving a hole in the valence band and thus creating the photogenerated e^-/h^+ pair. This process takes place when light with wavelength within the energy range of the semiconductor bandgap interacts with the solid. After that, charge carriers can migrate from the bulk to the surface of the material. When this occurs in an aqueous medium, dissolved oxygen can be adsorbed on the surface of the photocatalyst and reduced by electrons, giving rise to superoxide radical anions, $O_2^{\bullet-}$ (Eq. 1), while holes can oxidize water as well as hydroxyl anions, producing hydroxyl radicals, $HO^{\bullet}$ (Eqs. 2 and 3, respectively). Furthermore, $O_2^{\bullet-}$ can form hydroperoxyl radicals, $HOO^{\bullet}$, by protonation (Eq. 4). These oxidant radical species allow the mineralization of the pollutants (Eq. 5). Nevertheless, "scavenging" reactions can also

take place (Eqs. 6-8), including the recombination of charges (Eq. 9), which reduces the efficiency of the photocatalyst [52, 53].

$$(O_2)_{ads} + e^- \rightarrow O_2^{\bullet -} \quad (1)$$

$$H_2O + h^+ \rightarrow HO^\bullet + H^+ \quad (2)$$

$$OH^- + h^+ \rightarrow HO^\bullet \quad (3)$$

$$O_2^{\bullet -} + H^+ \rightarrow HOO^\bullet \quad (4)$$

$$HO^\bullet / HOO^\bullet / O_2^{\bullet -} + P \rightarrow \text{Oxidized Intermediates} \rightarrow CO_2 + H_2O \quad (5)$$

$$HO^\bullet + H^+ + e^- \rightarrow H_2O \quad (6)$$

$$HOO^\bullet + HOO^\bullet \rightarrow H_2O_2 + O_2 \quad (7)$$

$$HOO^\bullet + H^+ + e^- \rightarrow H_2O_2 \quad (8)$$

$$e^- + h^+ \rightarrow hv\,(\text{heat}) \quad (9)$$

Where P: Pollutant.

Thermodynamically, generation of the above oxidant radicals can take place when the potentials of the corresponding reactions fall within the band gap between the VB and the CB of the photocatalyst [34, 54]. TiO_2 (the most common photocatalyst) has different band gaps depending on its crystalline phase: 3.2 eV for anatase and brookite and 3.0 eV for rutile (being anatase and rutile the most photoactive phases). In the case of anatase, the CB potential ($E_{CB} = -0.51$ V, pH 7) allows the reduction of absorbed oxygen ($E^0_{(O_2/O_2^{\bullet -})} = -0.33$ V and $E^0_{(O_2/HO_2^\bullet)} = -0.45$ V, both vs. NHE—*Normal Hydrogen Electrode*) while the VB potential ($E_{VB} = +2.69$ V, pH 7) allows the oxidation of water and hydroxyl radicals ($E^0_{(H_2O/O_2)} = +0.82$ V and $E^0_{(OH^-/HO^\bullet)} = +2.29$ V). For rutile, its CB has a potential of -0.31 V (at pH 7), avoiding the above described reduction reactions [34, 55–57]. However, a balance is necessary in this respect, because wide band gaps have the main disadvantage of decreasing the efficiency of photocatalysis. Moreover, there are other factors that affect the photocatalytic activity of a semiconductor, such as the adsorption capacity, crystalline phases, size effect, or the presence of defects in the lattice, among others [58, 59].

In this sense, a wide variety of photocatalysts have been designed, investigated, and tested for water purification, including metal oxides, such as TiO_2, Fe_2O_3, or ZnO [60]; sulfides, as ZnS or CuS/ZnS [61]; ternary compounds, like titanates $BaTiO_3$ and $SrTiO_3$ [62, 63], tungstates, such as $ZnWO_4$ [64], and other metalates $A_xB_yO_z$ [46], or even multicomponent materials, as $BiVO_4/Bi_2O_2CO_3$ [65]. However, TiO_2 has been the preferred photocatalyst for water remediation mainly due to its high photocatalytic activity, chemical and photochemical stability, non-toxicity (this compound has been even used as an additive in food and medical treatments; [66]) and established industrial production at competitive cost [2, 3, 56, 67]. On the other hand, its difficult recovery when using TiO_2 powder and its relatively limited adsorption capacity and porosity are among its main drawbacks. Finally, because the current trend goes toward the use of solar light as energy source, the lower efficiency of TiO_2 under these conditions is noteworthy because the anatase band gap requires UV radiation ($\lambda \leq 387$ nm) for promoting the charge separation. Therefore, TiO_2 only uses 5% of the solar spectrum to yield the aforementioned photocatalytic reactions involved in water purification [68].

With the purpose of overcoming those drawbacks, electronic and morphological modifications of TiO_2 have been investigated. These modifications have been done by different approaches, which include doping, metal deposition, surface sensitizers, and heterojunctions. A detailed description of these approaches will be given throughout the chapter.

1.1.1 Operating conditions

The effects of various operating variables, such as catalyst dose, initial pollutant concentration, and UV light intensity have been investigated in the literature [69–71], although further research is needed to address practical application [72, 73].

Catalyst dose. The amount of catalyst is determined by the type and dimensions of the reactor and varies with the type of pollutant. In principle, higher concentrations of catalyst provide higher relative numbers of active sites and therefore, higher rates of reactive radicals generation. However, an excess of catalyst will produce negative effects due to particle aggregation and an increase of solution opacity, which will reduce the effective path-length of radiation. Guettaï et al. [74] analyzed the effect of the dose of a common commercial photocatalyst P25 on methyl orange (MO) ($15\,mg\,L^{-1}$) degradation in a static batch photoreactor. They reported that the optimal catalyst concentration was $0.8\,g\,L^{-1}$ and increasing the catalyst amount reduced the efficiency, which was attributed to light scattering due to the suspended catalyst.

Light intensity and wavelength. Electron-hole formation and initiation of the photochemical reaction strongly depend on the light intensity [75]. Increasing the intensity of radiation increases the rate of photons generation and electron-hole pairs formation. The effect of the wavelength and intensity of the light were studied in the oxidation of halide ions by Herrmann and Pichat [76]. They reported that only photons with wavelengths shorter than the absorption edge of TiO_2 promote the photochemical reaction. They also observed that there was a direct relationship between the incident flux and the conversion rate.

Dissolved oxygen. The effect of dissolved oxygen also affects to the photocatalytic reaction. Oxygen improves or hinders photodegradation depending on the mechanism/pathway of the reaction, but does not affect the adsorption of pollutants on the TiO_2 surface [77]. It enhances the generation of oxidant radicals following the reactions previously described in Eqs. (1)–(5). Shirayama et al. [78] reported the photodegradation of different chlorinated hydrocarbons in the absence and presence of dissolved oxygen in water. They concluded that dissolved oxygen could act as a "scavenger" or "inner filter" that decreases the light intensity in the reactor. Wang and Hong [79] reported the photomineralization of 2-chlorobiphenyl at different oxygen partial pressures. At 0.5 kPa, 75% of that compound was converted but with only 1% mineralized after 5 h of irradiation. They suggested that oxygen acts as an important reactant involved in successive reactions implying ring opening in the degradation of byproducts.

Effect of oxidants incorporation. To inhibit the electron-hole recombination in TiO_2 and improve the photodegradation of water pollutants, the addition of external oxidant/electron acceptors has been also studied. Because the formation of radicals has a decisive role in photodegradation, several authors have studied the effect of the incorporation of electron scavengers, such as H_2O_2, O_3, $(NH_4)_2S_2O_8$, and $KBrO_3$ in the degradation of dyes and phenolic compounds [72, 80–85]. Faisal et al. [86] evaluated the degradation rate of Acridine Orange (AO) and Ethidium Bromide (EB) in presence of different electron acceptors (H_2O_2, $KBrO_3$ and $(NH_4)_2S_2O_8$). In the case of AO, the presence of H_2O_2 and $KBrO_3$,

enhanced the breakdown rate, while $(NH_4)_2S_2O_8$ made the dye unstable in the suspension. With EB, all the acceptors caused a beneficial effect on the rate of degradation.

Stability. A photocatalyst must be resistant to photocorrosion, consistent under diverse reaction conditions, and able to perform efficiently upon repetitive or long term use. Okamoto et al. [87] studied the stability of anatase and ZnO, monitoring the presence of Ti^{4+} and Zn^{2+} cations in solution. There were no traces of titanium cations after complete degradation of phenol, indicating the good stability of the catalyst. However, a significant number of zinc cations were detected in solution, corresponding to the amount of phenol removed, thus indicating anodic photocorrosion.

2 UV-ACTIVE NANOSCALE SEMICONDUCTORS FOR WATER PURIFICATION

UV radiation has been extensively used to activate semiconductors for generating the charge carrier pair, emitting photons below 390 nm wavelength, which are able to induce the electronic transitions in several materials, such as TiO_2, ZnO, SnO_2, $SrTiO_3$, CeO_2, WO_3, Fe_2O_3, CdS, and ZnS. These materials gather the required features to be used as photocatalysts: (i) suitable band gap energies to absorb UV light; (ii) nontoxic nature; (iii) low cost; (iv) stability toward photocorrosion; and (v) chemical photostability. They also have the appropriate electronic structure to promote the charge separation, characterized by a high-energy occupied band (VB) and an unoccupied low energy band (CB). Some impurities or defects in the crystal lattice (e.g., presence of Ti^{3+} ions in TiO_2) are responsible for additional electronic levels (donor or acceptor) placed inside the forbidden gap of a semiconductor. Many researchers have reported that TiO_2, ZnO, and SnO_2 are the most active catalysts under UV light for the degradation of dyes, phenols, and pesticides [88–90], yielding high mineralization of a wide diversity of hazardous organic pollutants [5, 91]. Given the high number of publications reported in this field, this section is arranged according to the nature of the nanoscale semiconductor, with special attention to TiO_2, which has been extensively used for water treatment under UV radiation.

2.1 TiO_2

Titania has been the most thoroughly investigated semiconductor in the literature and it seems to be the most promising for photocatalytic breakdown of pollutants [92, 93]. As described before, the starting developments in photocatalysis were focused toward photoelectrochemical and microphotoelectrochemical systems for splitting water into hydrogen and oxygen, using TiO_2 as photoanode and Pt as cathode [13]. Ollis and his colleagues [94, 95] were pioneers in the application of photocatalysis for water purification, using TiO_2 for the mineralization of halogenated hydrocarbons under UV-illumination. Although the anatase phase of TiO_2 is the most used material in photocatalytic water detoxification [92, 93, 96], there are two other crystallographic phases, rutile and brookite. The mass density of anatase is slightly lower than that of rutile (5.16×10^{14} vs. 5.20×10^{14} sites cm^{-2}), and its band gap results somewhat wider (3.2 vs. 3.0 eV) [97, 98]. These structural differences lead to different electronic structures of the bands [99], related to the bond lengths of the unit cell. For example, in the anatase phase, the Ti-Ti distances are larger than in rutile, whereas the Ti-O ones are shorter [100]. Even though anatase has the highest photoactivity [96], the commercial product (Degussa P25) contains an anatase:rutile ratio of 80:20 and is one of the best TiO_2 photocatalysts under UV light,

frequently used as reference. Bickley et al. [101] formerly examined the photocatalytic activity of P25 and the structural relationship based on TEM images. Subsequently, Ohno et al. [102] provided the evidences on the synergistic effect of contacting anatase and rutile particles. They found that naphthalene was efficiently oxidized in a mixed suspension of both types of TiO_2 powders under UV irradiation and concluded that TiO_2 with both anatase and rutile structures showed higher activity in photocatalytic reactions.

During the last two decades, research has been addressed toward the use of nanosized materials [103]. TiO_2 nanoparticles (NPs) have shown excellent potential as water-remediation catalysts [104] and redox active agents because of their size, large surface areas, and their shape-dependent electronic, optical, and catalytic properties [105]. They can act both as oxidation and reduction catalysts for organic and inorganic contaminants. Chitose et al. [106] demonstrated TOC reduction from waters contaminated with organic species upon the addition of TiO_2 NPs under UV light. Kabra et al. [107] reported the efficient application of TiO_2 NPs to degrade organic compounds (e.g., PCBs, benzenes, furans, chlorinated alkanes, dioxins, etc.) and remove toxic metal ions (Pt^{2+}, Ag^{+}, Au^{3+}, Rh^{3+}, and Cr^{6+}) in aqueous solutions under UV light.

The application of TiO_2-based catalysts under UV light illumination has focused so far mainly on the removal of phenolic species and dyes [88]. Okamoto et al. [87] studied the photocatalytic decomposition of phenol in oxygenated aqueous suspensions of lightly reduced anatase at pH 3.5 and different wavelengths, being the quantum yield of the reaction almost constant below 370 nm. Photocatalytic degradation of polychlorinated dibenzo-*p*-dioxins (PCDDs) was carried out by Choi et al. [108] with TiO_2 films under UV light (>300 nm). The degradation rates increased with light intensity up to 2 mW cm^{-3} (300–400 nm). The influence of the intensity and wavelength of the UV light was also studied in the oxidation of halide ions by oxygen with TiO_2 suspensions. Herrmann and Pichat [76] concluded that only photons with wavelengths shorter than the absorption edge of TiO_2 ($\approx$400 nm) allowed photoinduced charge separation. Anionic and cationic dyes produced by textile industries have been also studied. Lachheb et al. [109] reported on the photocatalytic degradation of alizarin S, crocein orange G, methyl red, congo red, and methylene blue with TiO_2 under UV irradiation. Successful decolorization and mineralization were achieved. Degradation of the azo dye Reactive Orange 4 (RO4) using P25 (Degussa) was carried out by Muruganandham and Swaminathan [110]. They studied the effect of pH and some electron acceptors ($KBrO_3$, $(NH_4)S_2O_8$, and H_2O_2). Toxic inorganic anions can be also oxidized into harmless or less toxic species by using TiO_2 as photocatalyst under UV irradiation. Most studies are focused on the removal of Cr(VI) [111–113] and Ag^{+} [114].

Nevertheless, due to the difficulty of separating the TiO_2 NPs from the effluents and for the sake of improving the photocatalytic efficiency, other forms of nanosized TiO_2 have been studied, like nanotubes [115–117], nanospheres [118], nanorods or nanowires [119], and nanoflowers [120]. It has been claimed that those morphologies provide faster electron transfer, fewer inter-crystalline contacts, and a band gap shift toward 3.1 eV, thus favoring the photocatalytic efficiency [121, 122]. Kasuga et al. [123] and Zwilling et al. [124] were the first to describe the preparation of TiO_2 and titanate nanotubes (TNTs) via hydrothermal synthesis and electrochemical anodic oxidation, respectively. Compared with conventional TiO_2 NPs, TNTs present unique features for photocatalytic application, such as a large specific surface area and high pore volume, depending on the preparation procedure [125–136].

2.2 TiO_2 MODIFICATIONS

In the last two decades, several attempts have focused on the synthesis of modified TiO_2 to increase its photocatalytic efficiency under UV light. Different approaches have addressed this objective. One of them consisted of anatase doping to avoid the recombination of the photogenerated charges [137–141]. However, the activity of the doped TiO_2 greatly depends on the nature of the doping species and their relative amounts, in addition to the preparation method [142, 143]. Doping with different rare earths has been studied, with the resulting materials tested for phenol degradation under UV light [144, 145]. Xiuqin et al. [146] and Tinghong et al. [147] compared the photocatalytic activity of rare earths-doped and non-doped TiO_2. Li et al. [148] concluded that rare earth doping favored adsorption, electron-hole pairs separation and thermal stability. Doping with non-metal elements (nitrogen, carbon, sulfur, fluorine, or phosphorus) has been also studied, resulting in a reduction of the band gap and improved photocatalytic activity [149–153]. Different examples can be found in the literature focused on the removal of dyes by doped TiO_2, such as F-TiO_2 [154], Ce-TiO_2 [155], Fe-TiO_2 [156], or B- and N-TiO_2 [157].

Another approach described in the literature is the addition of noble metals, such as platinum (Pt), palladium (Pd), gold (Au), or silver (Ag), which act as electron traps. Au, for instance, has been used due to its stability, non-toxicity, and biocompatibility. Au-NPs/TiO_2 materials have received attention in the photocatalytic oxidation of azo dyes and phenols under UV light [158]. Ag-TiO_2 has also received special attention and many examples of its use in water treatment can be found in the literature. That system has been tested for the photodegradation of chloroform [159], chlorophenols [160], different dyes [161, 162], and phenol [163]. Lee et al. [164] have studied the enhanced photocatalytic activity of Ag/TiO_2 hybrid systems with controlled morphology of the Ag particles. Sakthivel et al. [165] reported on the application of Pt, Au, and Pd supported on TiO_2 for the photo-oxidation of acid green 16. Blazkova et al. [166] used Pt-TiO_2 immobilized on glass fibers to enhance UV phenol degradation.

Another approach for improving the photocatalytic activity of TiO_2 consists of its combination with other semiconductor oxides. One of the most used substances for increasing the lifetime of electrons on the surface of TiO_2 is WO_3 [167–171]. Georgieva et al. [172] reported on bi-layer WO_3-TiO_2 coatings for malachite green photo-oxidation under UV light. Gao et al. [173] carried out the photodegradation of the dyes Rhodamine B (RhB), methylene blue (MB), and methyl orange (MO) with WO_3/TiO_2 heterostructures and the photodegradation of bisphenol A using TiO_2-WO_3 composites has been described by Žerjav et al. [174]. SnO_2 is another promising oxide to combine with TiO_2 [175], which can accelerate the anatase-to-rutile phase transformation [90]. It has been reported that the efficiency of the TiO_2-SnO_2 heterojunction under UV light depends on the synthesis procedure. Huang et al. [176] compared different preparation methods of SnO_2-TiO_2 for the degradation of MB. Farhadi et al. [177] studied the application of TiO_2/SnO_2 core-shell NPs. Akurati et al. [178] synthesized TiO_2/SnO_2 NPs by flame pyrolysis. Yuan et al. [179] first used carbon spheres as templates to synthesize TiO_2/SnO_2 double-shelled hollow spheres, and Zhou et al. [180] used SnO_2/TiO_2 composite films on FTO glass, both tested for RhB degradation. Other less studied oxides for coupling with TiO_2 are ZrO_2, ZnO, and Ta_2O_5. Garcia-Benjume et al. [181] tested macroporous ZrO_2/TiO_2 composites in the degradation of MB under UV irradiation. In the same way, Li et al. [182] and Ou et al. [183] reported the synthesis of macro-mesoporous TiO_2/ZrO_2 materials and ZrO_2-incorporated TiO_2, respectively, for the UV-assisted breakdown of RhB. Wang et al. [184] reported the incorporation of Ta_2O_5. They obtained a three-dimensionally ordered macroporous (Zr or Ta)/TiO_2 used for the photodegradation of 4-nitrophenol and RhB. Cerium dioxide (CeO_2) has also received some attention due to its stability

under UV light and its wide absorption on the UV-visible spectrum [185, 186]. More recently, Taufik et al. [187] have reported the application of ternary $CuO/TiO_2/ZnO$ nanocomposites for improved photocatalytic degradation of MB under UV illumination, while Nadarajan et al. [188] used the ternary $TiO_2/SnO_2/WO_3$ with 1,2-dichlorobenzene. The strategy based on heterojunctions has also been transferred to combine doped TiO_2 with other semiconductor oxides. For instance, coupled N-doped TiO_2/WO_3 was evaluated for UV degradation of 2,4,6-trinitrotoluene [189] and a N-doped TiO_2/SnO_2 heterostructure has been recently used with 4-chlorophenol [190]. In these cases, the synergistic effect of coupling doped TiO_2 with other oxides enhanced the photocatalytic activity to an extent dependent upon the nature of the coupling oxide and the doping/anion.

Low surface area is a main limitation of TiO_2. Several investigations have focused on anchoring the TiO_2 on supports with high surface area and porosity [58]. Different mesoporous materials have been used as support, such as natural clays, carbon materials, or zeolites. Clays have been frequently selected because of their high adsorption capacity, non-toxic nature, and low cost. The most used have been kaolinite [191, 192], bentonite [193], montmorillonite [194, 195], and sepiolite [196–198]. Their applications have been extended toward the immobilization of heterojunctions and not only TiO_2. Hadjltaief et al. [199] used $ZnO\text{-}TiO_2$ supported on natural Tunisian clay for the photodegradation of methyl green (MG) under UV irradiation. Zhang et al. [200, 201] prepared $SnO_2\text{-}TiO_2$-palygorskite exhibiting promising results for the photodegradation of phenol and MO. On the other hand, two decades ago, Matos et al. [202] reported that activated carbon (AC) shows some favorable effects on the photocatalytic response of TiO_2. In the same way, Da Silva and Faria [203] and Tryba et al. [204] used different AC with TiO_2 for Solophenyl Green and phenol UV degradation, respectively. More recently, attempts are focused on the use of carbon nanotubes (CNT) [205] or multi-walled carbon nanotubes (MWCNT) [206] because of their conductive properties that can favor the separation of charges [207–209]. In this sense, Wang et al. [210] studied the ability of graphene-carbon nanotube-TiO_2 composites for MB and Cr(VI) removal under UV light irradiation. Finally, although zeolites are commonly used as supports in many catalytic reactions, there are few reports in the literature for water purification with zeolite-supported TiO_2 [211–213].

2.3 ZnO PHOTOCATALYSTS

ZnO has received much attention due to its low cost and its demonstrated activity in several photochemical and photoelectrochemical process [214–216]. It has a band gap similar to TiO_2 (3.2 eV) [217] and possesses greater quantum efficiency [218]. ZnO has three different phases: wurtzite, zinc blende, and rock salt. Generally, under ordinary conditions, the wurtzite phase (hexagonal crystal system) is the most stable [219]. Doménech and Muñoz [219a] studied the photocatalytic reduction of Cr(VI) in aqueous suspensions of ZnO and chromium-doped ZnO under UV light at different reaction times, initial concentrations, pH, and temperatures. Kamat et al. [220] established the reliability of using nanostructured ZnO films for the degradation of chlorinated phenols. Anandan et al. [221] studied the use of La-doped ZnO for the breakdown of thrichorophenol and they observed an improved efficiency respect to bare ZnO and TiO_2. Villaseñor et al. [222] reported the photo-degradation of pentachlorophenol on ZnO synthesized by different methods and Khodja et al. [223] studied the photodegradation of the 2-phenylphenol fungicide with TiO_2 and ZnO in aqueous suspensions. The degradation of 4-chlorocatechol using a TiO_2/ZnO photocatalyst was studied by Dhir et al. [224]. Other ZnO nanostructures used in water purification through UV photocatalysis include ZnO nanowires (NWs) and nanorods (NRs) [219]. Sugunan et al. [225] detailed the synthesis of ZnO-based hierarchical

nanostructures by growing radially-oriented ZnO wires on poly-L-lactide nanofibers for the photodecomposition of several organic contaminants, like diphenylamine, under UV irradiation.

Some publications have demonstrated a better photoresponse for ZnO compared to TiO_2 for the photocatalytic degradation of some dyes in water [226, 227]. However, two important drawbacks have to be considered regarding potential application of ZnO: (i) it suffers photocorrosion under UV light and (ii) it can be dissolved at high pH [133, 228]. The current trend in the search for novel photocatalysts active under visible light has led to numerous studies on the improvement and use of ZnO, which will be detailed in Section 4.

2.4 METAL SULFIDES

Metal sulfides, mainly CdS and ZnS, have been attempted as photocatalysts for water splitting and other applications, but only few works have been reported for the abatement of water pollutants. These semiconductors have been selected because their narrow band gaps and their valence bands location at relatively negative potentials. The works reported on water treatment under UV light are focused on the degradation of model dyes. Kansal et al. [229] investigated the photocatalytic degradation of MO and Rhodamine 6G under UV light with ZnS and CdS, while Neppolian et al. [230] studied CdS and other catalysts for the degradation of three commercial textile dyes (Reactive Yellow 17, Reactive Red 2, and Reactive Blue 4).

3 VISIBLE AND SUNLIGHT ACTIVE NANOSCALE SEMICONDUCTORS FOR WATER PURIFICATION

As mentioned before, a key challenge in the field of photocatalysis is the development of visible-light active semiconductor useful under sunlight as renewable energy source, avoiding the utilization of the current UV lamps and reducing the cost of the process. This has a particular interest regarding the abatement of water pollutants. The previous section described the most viable nanoscale semiconductors for photocatalysis, characterized by a band gap that can be activated only under UV light irradiation. Nevertheless, UV light represents a small fraction (5%) of the solar spectrum, so the photocatalytic efficiency of those semiconductors under sunlight is low. Therefore, several approaches have been followed by researchers for the development of nanoscale semiconductors with the appropriate characteristics of being active under visible and solar light for water purification.

Looking at the literature, the wide variety of contaminants under study is remarkable. In this sense, this chapter places special attention on the removal of contaminants of particular concern, including specific sections for emerging contaminants, cyanotoxins, and pathogens. The literature contains also many works focused on the degradation of organic dyes, used as target compounds to compare the activity of different semiconductors because they are easy to follow under reaction. Nevertheless, it is noteworthy that, when dyes are involved, the mechanisms can be different from other species, particularly for reactions performed under visible light, because the dye can act as a surface sensitizer of the semiconductor [55]. Due to the high number of publications in this research field, this section is organized according to the nature of the nanoscale semiconductors, starting with the TiO_2 modifications that cover a wide range of possibilities and following with alternatives to TiO_2 and novel combinations.

3.1 TiO_2 AND ITS MODIFICATIONS

The most studied semiconductor for photocatalysis is titanium dioxide in its anatase phase. TiO_2 has a large band gap of 3.2 eV that can be activated only under UV light irradiation of wavelength lower than 387 nm [13]. Increasing attention is being paid to shifting its optical response to the visible range (400–700 nm). An important option for enhancing the photoresponse of TiO_2 consists of favoring the creation of imperfections within the crystal structure, which significantly affects its phase stability and its electronic structure. This strategy has been recently named *self-structural modification*, a phrase which includes the nanoscale and the surface effects [230a]. Nanoscale semiconductors are characterized by the quantum size effect resulting in a band gap increase when the particle size is very low [10]. There are some discrepancies about the critical size of TiO_2 particles, but in practice, no quantum size effect and, then, no changes in the band gap occur in anatase nanoparticles of size >1.5 nm [231]. Nevertheless, size reduction also yields other modifications in the nanomaterial compared with the bulk, including shape and lattice parameter changes. Wider band gaps are described for poorly crystallized nanoparticles and thin films, reaching a band gap narrowing up to 0.2 eV for TiO_2 nanomaterials of 5–10 nm particle size [232].

The surface effects consist of defects located at the surface, which appear because the atoms lose the bulk stoichiometry and are not saturated with many dangling bonds, giving rise to reactive surfaces [230a]. In practice, the oxygen vacancies and Ti^{3+} sites are the most common surface defects that can enhance visible-light absorption [233]. It has been described that these defects introduce an electronic state in the band gap, about 2.0 eV above the valence band, which has been attributed to the formation of partially occupied Ti^{3+} states due to the presence of oxygen vacancies [234, 235]. Other authors found the energy state 1 eV below the Fermi level associated with empty Ti_{5c} 3d orbitals that accept two excess O electrons [236]. Therefore, some contradictory results exist in the literature about the proper position of Ti^{3+} associated levels, the discernment of which is a difficult task that would require theoretical methods [232]. Although these defects improve the absorption of visible light irradiation, the quantum efficiencies described by these photocatalysts are sometimes not as high as expected, because these defects increase the electron-hole recombination [237, 238]. Another kind of defect that can exist in TiO_2 refer to the interstitial oxygen (O_i) [230a]. This O_i bonds to lattice oxygen atoms and results in the formation of an O_2 dimer, causing a decrease in lattice parameters and narrowing the band gap because the O_i orbitals contribute to valence band shifting [239]. These interstitial oxygens can also act as electron traps, thus favoring photogenerated charges separation and photoefficiency. More recently, some have described a shift on the TiO_2 absorption to the visible region through hydrogenation of TiO_2, resulting in the so-called black TiO_2 [240]. The black TiO_2 nanoparticles are characterized by a disordered lattice that causes the formation of midgap states lying above the valence band maximum, thus narrowing the band gap. This photocatalyst depicted improved activity for the photodegradation of dyes and phenol associated with the separation of charges in the midgap states.

Although many works focused on the self-structural modification of TiO_2, major attention has been paid to anatase modification [38, 46, 241, 242]. The literature describes as the most feasible modifications doping (metal and non-metal), noble metal loading, and surface sensitization, which are described in the following.

3.1.1 Non-metal doping

In 2001, Asahi et al. [243] reported in *Science* the synthesis of N-doped TiO_2 materials photoactive for the degradation of several compounds (including methylene blue) in water under visible light. Since then, many efforts have been devoted to prepare visible light TiO_2 photocatalysts by doping with non-metal elements, such as N, C, S, and halides (F, Cl, Br, I). The initial purpose of this approach consists of the substitution of the oxygen lattice of TiO_2 by those species, altering both the electronic and structural properties of TiO_2, narrowing the band gap and creating oxygen-defect sites (Fig. 3). Comprehensive reviews have been reported summarizing representative results on this field [56, 67, 232, 244–246]. Most works are focused on the degradation of dyes (RhB, MB, etc.) and phenol as model pollutants, although in recent years, more attention has been paid to contaminants of emerging concern, pesticides, herbicides, and organic groundwater compounds [38, 247].

Nitrogen has been extensively studied because it can be easily introduced in the TiO_2 matrix thanks to its atomic size (comparable to oxygen), small ionization energy, and stability [67]. It was expected that the substitution of nitrogen would narrow the band gap by changing the valence band structure without modifying the position of the conduction band. Nevertheless, the literature reveals an open controversy regarding the cause of the absorption shift of TiO_2 to the visible region [232, 242]. One approach proposes that the narrowing of the band gap is due to changes on the valence band upon mixing the N 2p and O 2p states [243, 248], while Irie et al. [249] suggest that the N 2p levels are separated (not mixed) from the valence band (integrated by O 2p states), leading to an isolated narrow band responsible for the visible light sensitivity of the TiO_2 nanoparticles. Other authors claim that the band gap of TiO_2 is not modified, and the nitrogen doping generates defect sites. Serpone [250] argued that the formation of oxygen vacancies stabilized by the nitrogen substitution because of charge compensation, which act as color centers and are responsible for the absorption in the visible region. Ihara et al. [251] proposed the formation of oxygen-defect sites that act as charge-trapping centers, thus enhancing the activity of N-doped TiO_2. Other authors describe N-doping as interstitial lattice sites

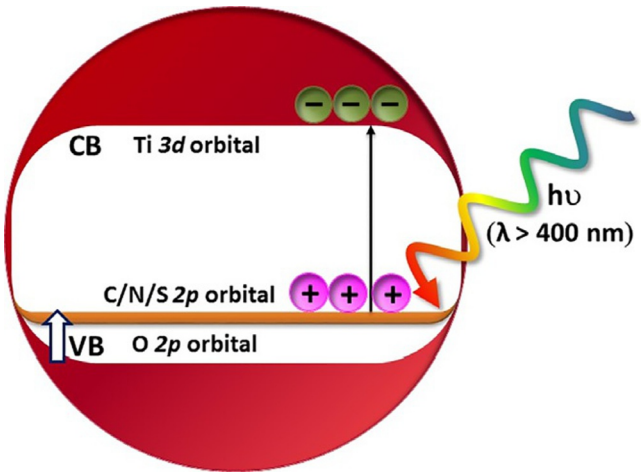

FIG. 3

Valence band displacement for non-metal doping of TiO_2.

instead of a substitutional element on the oxygen lattice of the TiO_2 matrix [38]. Sato et al. [252] state that nitrogen doping leads to NO or NO_2, and Ti-N bonding does not occur. It was found that there are no changes in the conduction or valence bands, but instead, there appear to be energy bonding states associated with the anti-bonding π^* N-O orbitals between the TiO_2 bands [253]. These states act as "stepping stones" for the excited electrons from the valence band, provoking a better separation of charges and improving the photoefficiency of the N-doped TiO_2. Livraghi et al. [254] studied N-doped TiO_2 by density functional theory (DFT) and EPR. They found single-atom impurities in the TiO_2 which constitute N bulk centers resulting in localized states in the band gap of the oxide. These centers can absorb the visible light because of the promotion of electrons from the localized states to the conduction band. It is noteworthy that the chemical structure and the location of the species responsible for the shift absorption of N-doped TiO_2 to the visible light is still a matter of debate. NO^{x-}, N^{x-}, and NO_x species have been mostly proposed over the years [38], although Chen and Burda [255] found NH_x species in interstitial sites due to nitrogen bonded to hydrogen.

It must be considered that the direct comparison of the photoefficiency of N-doped TiO_2 under visible light becomes extremely difficult because of the wide diversity of synthesis methods used in the literature [256–258]. Different physical procedures, like metal ion implantation or sputtering, as well as chemical methods have been used to prepare N-doped TiO_2 photocatalysts. The last ones include sol-gel method and hydrothermal synthesis, wet impregnation, chemical vapor deposition, and plasma technology [245, 247]. Sol-gel synthesis can be considered the most versatile because it does not require complex equipment and allows control of the nanostructure, porosity, and morphology of the N-doped TiO_2 by using different sources of nitrogen, like amines, nitrates, or urea [67]. Livraghi et al. [259] prepared N-doped TiO_2 comparing three different synthesis routes, sol-gel, mecanochemistry, and oxidation of TiN. All samples exhibited N bulk centers responsible for the absorption of the visible light but the one prepared by sol-gel showed the highest activity for organic compounds photodegradation, associated with a better anatase crystallization. Nevertheless, in a further work, Livraghi et al. [260] compared sol-gel synthesis with hydrothermal and pyrolytic methods. They found that the method of synthesis determines the nitrogen impurities formed within the TiO_2 nanoparticles. Sol-gel and hydrothermal procedures result in impurities weakly bonded at the surface, whereas by pyrolysis, the nitrogen impurities are more stable and lead to a higher activity for the photodegradation of cyanotoxin under visible light. Microwave technology has been also applied for the preparation of N-doped TiO_2 using urea as a nitrogen source [261]. By XPS, the authors concluded the creation of both substitutional and interstitial nitrogen sites on the TiO_2 surface, the interstitial lattice sites being responsible for a higher photocatalytic activity.

The preparation of N-TiO_2 films has been also studied in the literature [262]. Different preparation techniques have been used, including sputtering the TiO_2 in a N_2 or NH_3 atmosphere, pulse laser deposition on glass substrates, and chemical vapor deposition [245]. Most of these N-TiO_2 films have been tested for dyes photodegradation, showing higher photoactivities than the un-doped TiO_2 films, although the explanation on the effect of nitrogen is quite different depending of the synthetic route. Asahi et al. [243] assigned the activity to substitutional nitrogen atoms acting as active sites in the form of N states. Other authors found the occurrence of electron deficient nitrogen atoms that can trap the photogenerated electrons avoiding the recombination, thus increasing the quantum efficiency [263]. N-TiO_2 films with rutile structure have been also prepared by thermal oxidation of TiN films, whose activity under visible light for MB degradation was attributed to the generation of new electronic states above the valence band due to the formation of N^{3-} species in the TiO_2 lattice [264]. Despite the high

number of publications devoted to N-doped TiO_2 as photocatalysts, the efficiency under visible light is rather low compared with that displayed by TiO_2 under UV light [67, 245]. Barolo et al. [265] described that under visible light, the electrons are excited from NO^{x-} states located intra-band-gap to the conduction band of TiO_2. The limited number of these centers results in a moderate efficiency of N-TiO_2. But, the low mobility of the photogenerated holes and a high number of oxygen vacancies, formed upon nitrogen substitution, can also increase the recombination, thus lowering the efficiency [266, 267].

Carbon-containing TiO_2 is also a photocatalyst active under visible radiation, showing a band gap narrowing comparable to the value observed for nitrogen-doped titania [268]. During the preparation of C-doped TiO_2 nanoparticles and films, carbon replaces oxygen, leading to the formation of Ti^{3+} sites and oxygen vacancies upon charge neutralization [232, 269]. The formal oxidation state of carbon doping ranges from −4, forming Ti–C bonds, to +4, resulting in C–O bonds [270]. Characterization by DFT methods suggests that C atoms replace O sites, yielding mixed C 2p and O 2p states which give rise to a hybrid orbital above the valence band of TiO_2, narrowing the band gap [249, 271]. Further studies also demonstrated that C can exist as substitutional and interstitial lattice sites, depending on the synthetic route [270]. These species can act as trap centers enhancing the photocatalytic activity [67]. Nevertheless, ensuing photocatalytic activity depends on the band gap narrowing but also on the oxygen vacancies formed upon carbon doping, because those defects, in high concentrations, fill the in-gap impurity states and emit electrons, thereby inhibiting the photocatalytic reaction [272]. The synthesis procedure can also affect the TiO_2 band gap narrowing, making it possible to obtain systems with a narrow optical gap of 2.32 eV [273] and 2.0 eV [274] by thermal treatment in air. Other effective approaches for preparing C-TiO_2 nanoparticles include sol-gel modified with carbon precursors, treatment with gaseous carbon sources, flame pyrolysis of Ti metal, thermal oxidation of TiC, and carbonization of organic templates [244]. However, there is no a simple way to obtain C-TiO_2 with high photoefficiency, despite the great potential of carbon doping, because of its conductivity and high electron-storage capacity. Some drawbacks of carbon doping include aggregation of carbon species and the distortion of the TiO_2 lattice, both of which favor electron-hole recombination [275].

So far, other non-metal dopants have been studied to enhance the photocatalytic activity of TiO_2 under visible light, as sulfur, boride, and some halides [67, 232, 245]. Although S has a larger ionic radius than N or C, studies have reported the synthesis of titanium oxysulfide where S is bonded to Ti by substitution at O sites. Some band calculations indicate that the S 3p states mix with the O 2p ones of the valence band of TiO_2, increasing its width and decreasing the band gap energy [276, 277]. As for nitrogen doping, some controversy exists on the sulfur doping effect, because other studies state that the band gap narrowing is due to the creation of S 3p impurity levels above the valence band, but without mixing with the oxygen states [278, 279]. Sulfur can be inserted as cationic (S^{6+} and S^{4+}) or anionic (S^{2-}) species [245]. Both were identified by Han et al. [280] in S-doped TiO_2 films prepared by a modified sol-gel route using H_2SO_4 as sulfur source. S^{2-} is related to substitutional lattice sites while S^{6+}/S^{4+} cations are assigned to sulfate groups located on the TiO_2 surface. The anionic sulfur provides the energy states that narrow the band gap and provokes the generation of oxygen vacancies. These electronic properties together with a small crystal size and high porosity were responsible for a high photoefficiency for the degradation of microcystin contaminants. A promoting effect on the photocatalytic activity was also found in F-doped TiO_2. Fluorine doping enhances the surface acidity, favoring the adsorption of the reactant molecules on the catalyst surface, and causes the formation of oxygen vacancies and Ti^{3+} sites, due to the interaction between F^- and Ti^{4+} species [151, 281]. Therefore, F doping promotes charge separation and increases the photogenerated electron mobility,

leading to active photocatalysts under visible light [282]. At this point, it is relevant to mention a recent report which describes Se-doped TiO_2 as a novel visible-light photocatalyst. Selenium appears at substitutional and interstitial sites leading to Se^{4+} and Se^{2-} species responsible for absorption in the visible light range [283].

These studies demonstrate that doping can provoke an effective modification of the electronic structure of TiO_2 for visible light absorption. The literature also shows the incorporation of multiple dopants (codoping) as another strategy to extend the visible response of titania [67, 245, 247]. N–F co-doped TiO_2 showed optimum visible response attributed to a combination of the N-doping effect and the charge separation effect of F-doping [284, 285]. In addition, a synergistic effect of N/F codoping was described resulting in decreased formation of oxygen defects in the TiO_2 lattice, stabilizing the (F, N)-TiO_2 and reducing the electron-hole recombination [286]. This synergistic effect has been further found in N–F co-doped TiO_2 immobilized on glass by dip-coating. Several N paramagnetic centers were identified by EPR characterization, which are responsible for the creation of localized intra-gap states in TiO_2 and show catalytic activity under visible light [287]. Other examples of non-metal codoping can be found in the literature, including (B, N), (B, I), (B, F), (C, N), and (S, N)-codoped TiO_2 [232]. A complete review of non-metal codoping is reported by Devi and Kavitha [245]. The photocatalytic performance of these materials under visible light is usually associated with a synergistic effect between the individual anions. It can be seen how one dopant promotes the visible light absorption while the other neutralizes the charges, reducing the undesired lattice defects that can act as recombination centers. Likewise, C–N–S tri-doped TiO_2 has been also reported as an efficient photocatalyst for the degradation of an antibiotic in water under visible light [288]. Using a sol-gel route and urea as precursor, the authors found C substitution forming Ti–C bonds, N at substitutional and interstitial sites yielding Ti–N–O, Ti–O–N, and O–Ti–N bonds and S^{6+} in the Ti^{4+} lattice. The photocatalytic performance was associated with band gap narrowing, the presence of carbonaceous species that act as sensitizers and convenient structural and textural properties. Although doping can be used to enhance the overall efficiency of the photocatalysts under visible light, many factors need to be considered, such as the dopant concentration, type and number of dopants, and preparation method. The combined effects of such factors are likely to play a crucial role in the enhancement of the overall efficiency of photocatalysis.

3.1.2 Transition metal doping

Another way to improve the efficiency of TiO_2 under visible light consists of doping with transition metal ions. Ti substitution by metal ions introduces new energy states close to the conduction band or valence band edge, inducing visible light absorption at sub-band gap energies. The shift in band gap absorption to the visible region is attributed to charge transfer transition between the d electrons of the dopant and the TiO_2 bands. In addition to the absorption spectrum widening, some transition ions act as electron-hole trappers, increasing the charge carrier lifetimes and therefore avoiding recombination [289–292]. Many transition metal ions have been used as dopants, including Cu, Zr, Zn, Co, Ni, Cr, Mn, Mo, Nb, V, Fe, Ru, W, Sb, Sn, and even some lantanides, such as La, Ce, Er, Pr, Gd, Nd, or Sm [46, 142, 293–297]. However, the efficiency of metal doping depends on whether it serves as a charge trap or as a recombination center. While several authors have reported that transition metal doping enhances the photoefficiency of TiO_2 under visible light, some others state that these metal species promote structural instability of TiO_2 and decrease the lifetime of the charge carriers, limiting overall degradation efficiencies. In early works, visible light photoresponse was observed upon Mo, V,

Ru, Fe, Rh, and Os doping of TiO_2, while Al and Co caused the opposite effect [298]. Fe and Cu were recommended because they create energy levels in the band gap, allowing both electron and holes trapping, thus improving the photocatalytic performance [139]. Several metal-doped TiO_2 were further prepared by the metal ion implantation method, bombarding the TiO_2 with high-energy transition metal ions [68, 299]. The ability of metal ions to induce visible absorption followed the order: $V > Cr > Mn > Fe > Ni$. It was stated that this synthetic route is efficient because the metal ions must be incorporated on the TiO_2 surface, acting as charge trappers. If doping occurs at deeper positions of the TiO_2 lattice the photogenerated charges have lower mobility toward the surface and the dopant acts as a recombination center. Nagaveni et al. [300] reported the detrimental effect of W, V, Ce, Zr, Fe, and Cu as dopants in the photocatalytic degradation of 4-nitrophenol under visible light. Although these metal dopants introduce energy levels below the conduction and or above the valence band that can act as electron and hole trappers.

In more recent studies, V^{5+}, Mn^{2+}, Fe^{3+}, Ru^{3+}, Os^{3+}, Ni^{2+}, and Zn^{2+} were tested as TiO_2 dopants [301]. Mn-doped TiO_2 depicted the best activity under solar light due to the synergistic effects of adequate surface structure, band gap and oxygen vacancies which act as electron trappers. Meanwhile, Ni-doped TiO_2 was the less active because the energy states have not the optimal location in the band gap and the dopant acts as recombination center. Choi et al. [302] after TiO_2 doping with Ag^+, Rb^+, Ni^{2+}, Co^{2+}, Cu^{2+}, V^{3+}, Ru^{3+}, Fe^{3+}, Os^{3+}, Y^{3+}, La^{3+}, Pt^{4+}, Pt^{2+}, and Cr^{3+} found a positive effect for the degradation of several organic and inorganic pollutants under visible light. In particular, Pt and Cr-doped TiO_2 showed the best activity, although it was attributed to the crystallization of both rutile and anatase phases. Wang et al. [303] analyzed by ab initio calculations the electronic structures and band edge positions of anatase TiO_2 doped with 13 different transition metals. They stated that most of those metals enhanced the TiO_2 photoactivity and maintained its redox potential, although doping with Cr, Co, and Ni showed more energetically favorable.

Extending the research of element doping effects, two elements (a non-metal and a metal) have been introduced into the TiO_2 lattice to check their effects on the electronic structure, bandgap energy, and photocatalytic performance [232]. Zhu et al. [304] synthesized four anatase codoped TiO_2, (N, Cr^{3+}), (C, V^{5+}), (C, Cr^{3+}), and (N, V^{5+}). The metal substitutes Ti lattice sites while the non-metal substitutes neighboring O sites. This double substitution generates intermediate electronic states in the band gap of anatase that serve as "stepping stones" where the photogenerated electrons can transfer, thus enhancing visible absorption. Despite extensive research, it is difficult to establish unified criteria to correlate the semiconductor properties and photoactivity under visible light of metal-doped TiO_2. Based on the literature, the effect of metal doping depends on a complex combination among the dopant concentration, the energy level of dopants within the TiO_2, their d electronic configuration, the distribution of dopants within the particles, the electron donor concentration and the incident light intensity. Nevertheless, several recent reviews state that non-metal doping of TiO_2 is more promising than metal doping because the latter creates electron-hole recombination centers, thus lowering the quantum efficiency [67, 232, 245, 294].

3.1.3 Dye sensitizers

Another approach to improving efficiency under sunlight consists of dye photosensitization of TiO_2. In these systems, the dye absorbs visible light, and an electron is promoted from the highest occupied molecular orbital (HOMO) to the lowest unoccupied molecular orbital (LUMO) (Fig. 4). The excited dye allows injecting the electrons into the conduction band of the TiO_2. In this process,

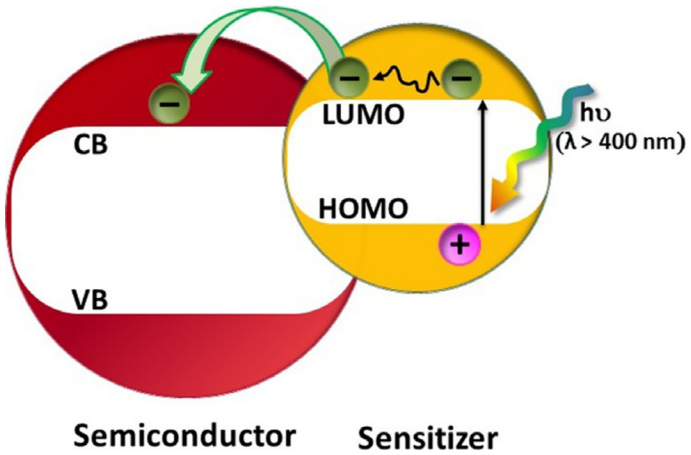

FIG. 4

Schematic illustration of the dye sensitizing mechanism.

the TiO_2 acts as mediator, receiving the photogenerated electrons from the dye. The LUMO of the dye needs to be located above the bottom of the semiconductor conduction band. A strong interaction between the dye and TiO_2 is also required for a fast and efficient electron injection. One of the advantages of the dye-sensitized TiO_2 is that the electron injection is very fast, occurring in femto to pico seconds, compared to the nanosecond scale of recombination [232, 305]. Consequently, sensitization enhances separation of the photogenerated charges and expands the light absorption to the visible region through the excitation of the dye. Most of the photosensitizing dyes reported in the literature are transition metal complexes of polypyridines (Ru), porphyrins, or phthalocyanines (Zn, Mg, Al) [306, 307]. For instance, ruthenium complexes, such as (*cis*-di(thiocyanato)-*N*,*N*-bis(2,2′-bipyridyl dicarboxylate) Ru(II) and the "black dye" based on trithiocyanato-ruthenium complex have been reported by Bauer et al. [308]. However, dye-sensitization needs to overcome some drawbacks. Sometimes the dye itself suffers degradation by irradiation, changing its structure, so that some regeneration procedure is needed for recovering its initial properties [309]. The synthesis of the dyes can be also an important issue involving organic reactions in several steps with low yields that increase their cost [310].

3.1.4 Metal deposition

Noble metal nanoparticles (NPs) have been deposited onto the TiO_2 surface as a way to develop highly efficient photocatalysts under visible and solar light [67, 232, 242, 244]. The mechanism consists of the migration of the photogenerated electron from the valence band of the TiO_2 to the metal nanoparticle via interfacial charge transfer, acting as an electron trap and avoiding the recombination of charges. Particularly important is the deposition of NPs (e.g., Au, Ag) capable to absorb visible light via surface plasmon resonance (SPR) [311, 312]. They can be excited by the light injecting electrons to the conduction band of TiO_2 and promoting charge separation (Fig. 5) [313–315]. SPR is an inherent property of nanoparticles allowing redistribution of the charge density when they are irradiated by light with a wavelength larger than their size. In this sense, Ag and Au NPs receive special attention because they can absorb in the visible region of the solar spectrum and thereby scatter photons due to the charge

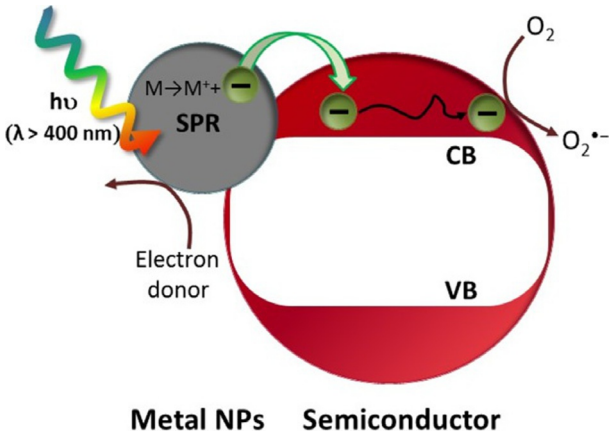

FIG. 5

Illustration of the behavior of metal NPs deposited on a semiconductor photocatalyst.

distribution [316]. The photocatalytic performance of these materials depends on the nature of the metal, but also on the procedure used to deposit the NPs and on their interaction with the TiO_2 surface. A number of synthesis approaches have been reported in the literature, including sol-gel and hydrothermal methods, deposition-precipitation, encapsulation, and photo deposition [232, 244, 312].

Most research works in this topic have been devoted to enhance the photocatalytic activity by decorating TiO_2 with Ag and Au [232, 244, 317]. Very recently, TiO_2 nano-flower films have been decorated with Ag NPs by a hydrothermal route, followed by a microwave-assisted reduction process [318]. The resulting composite showed a photodegradation rate 3.5 times higher than the unmodified TiO_2 film for the target dye under visible light. This improved performance was attributed to the synergistic effect between the charge separation and the SPR effect of the Ag NPs. An interesting study has reported on the deposition of mono- (Ag, Pd, and Pt) and bimetallic (Ag/Pd, Ag/Pt, and Pd/Pt) clusters onto commercial TiO_2 (P25) by radiolysis [319]. Depending on the way of metal precursors addition, simultaneous or successive, it was possible to control the size of the NPs incorporated. It ranges from 4 to 20 nm when the metals are added successively. Ag/Pd-TiO_2 depicted a photocatalytic activity four times higher than the unmodified P25 for phenol degradation under visible light. This behavior was associated with the direct electron transfer from the bimetallic NPs to the conduction band of TiO_2. More information about visible light photocatalysts based on the deposition of Ag and Au over TiO_2 for water treatment can be found in the reviews by Zhou et al. [312] and Ayati et al. [158].

Noble metal decoration of TiO_2 presents some benefits including: (i) separation of photogenerated electron-hole pair thanks to the metal NPs-TiO_2 interface; (ii) absorption of light in the visible region of the solar spectrum because the SPR feature, and (iii) modification of the TiO_2 surface reducing the number of defects that can act as recombination centers [317, 320, 321]. Unfortunately, the deposition of metal NPs on the TiO_2 surface also presents some important drawbacks. For instance, negatively charged NPs can be formed depending on the synthesis route, which can act as recombination centers lowering the photoefficiency. Moreover, high NPs concentration can block the surface of TiO_2 decreasing light absorption and thus the photocatalytic activity. Sung-Suh et al. [322] stablished an optimum

Ag content around 2% to achieve the highest photoefficiency. Likewise, other issues are related to the oxidation, corrosion, and leaching of the NPs in the reaction medium [323]. Research efforts are devoted to explore new metal-decorated photocatalysts with superior performance and stability [244].

3.2 ZnO AND OTHER OXIDES

Increasing research activity has been devoted to looking for photocatalytic materials that differ from TiO_2 for water purification, aimed to achieve more efficient use of solar light. ZnO and other oxides (WO_3, SnO_2, CeO_2, In_2O_3, Bi_2O_3) have been evaluated for aqueous contaminants degradation under visible light [38, 313, 324]. Although most photocatalytic activity tests have been focused on decolorization of organic dyes as target compounds, special attention is currently addresses toward persistent pollutants, species with emerging concerns and pathogens. ZnO is the most studied oxide after TiO_2 as photocatalyst. It has a band gap of 3.2–3.4 eV. Some authors have observed higher efficiencies with ZnO than with TiO_2 under solar light, due to the absorption of a large fraction of the solar spectrum [325–327]. However, ZnO also presents important disadvantages that hinder its potential application in water purification. It suffers photo corrosion in aqueous solution under UV irradiation, following a mechanism in which the holes photogenerated in its valence band react with the surface oxygen of ZnO, provoking its dissolution [328]. Likewise, ZnO is also soluble in strong acids and alkalis, which limits the working pH.

Different approaches are under study to improve the photocatalytic properties of ZnO. They are addressed to: (i) inhibit the electron-hole recombination by enhancing the charges separation; (ii) shift the absorption properties in the visible region of the solar light; (iii) improve the generation of radicals responsible for the redox reactions and (iv) enhance the photo-stability of ZnO [328]. The strategies to improve the visible light response of ZnO are analogous to those described for TiO_2, including doping with non-metal ions, metal ions and codoping, noble metal coating, and coupling with other semiconductors [246, 313, 324]. Unlike TiO_2, dye sensitization has been scarcely reported with ZnO. An interesting review on the most recent advances in ZnO modification has been presented by Lee et al. [328], including many examples from the literature. The improvement of photoefficiency upon doping usually involves the location of the dopant in substitutional and/or interstitial positions of the ZnO lattice, which can generate additional energy levels in the mid-gap of the ZnO and the creation of defect sites that can act as charge trappers reducing the recombination rate. Examples of doping with N, C, and S, and Fe, Co, Mg, Ce, Ce-Ag, and Zr-Ag have demonstrated photocatalytic activity for the degradation under visible light of organic dyes, phenolic compounds, and persistent organic pollutants. The Ce-Ag-ZnO system was tested under solar light, showing higher efficiencies than bare ZnO and the commercial reference P25. This was attributed to the trapping of the photogenerated electrons from the conduction band of ZnO and inhibition of the electron-hole recombination by Ag and Ce [329]. The results of doping depend on both the role of dopants incorporated into the ZnO semiconductor and the synthetic procedure. The literature also gathers results on Ag coating of ZnO due to the SPR property of Ag NPs previously seen. Its activity for microorganism deactivation has been demonstrated [330]. Due to the photo corrosion of ZnO in aqueous media, complementary modifications have been made to overcome this drawback. Some studies are focused on the surface modification of ZnO by anchoring different carbon types, including layers of polyaniline [331], fullerene [332], and reduced graphene oxide [333]. This approach aims to create a passive and less photo-active layer over the ZnO surface that suppresses photo corrosion.

WO_3 has been also evaluated as visible light-driven photocatalyst because it absorbs light around 480 nm, but it showed low activity for the degradation of organic contaminants under visible light. This low efficiency has been attributed to several causes, which include a high electron-hole recombination rate, photo corrosion in aqueous solutions and difficulty to transfer the photogenerated electrons to the O_2 adsorbed for producing superoxide radicals [38, 313]. Although some approaches have been studied to modify WO_3 in order to improve its photoefficiency, the degradation rates achieved were lower than with other nanoscale semiconductors. Examples of metal doping and Pt deposition can be found in the literature and it is noteworthy that the deposition of noble metals with SPR properties (Ag, Au) does not imply beneficial effects, unlike for TiO_2 and ZnO, because the SPR of metal NPs overlap with the band gap absorption of WO_3 [313]. However, WO_3 is currently used as additive to improve the photocatalytic activity of other semiconductors, giving rise to interesting novel heterojunctions of several semiconductors that will be described afterwards.

3.3 TERNARY OXIDES

More complex oxides than those previously cited have been also tested. The aim is looking for materials with a new balance band capable of absorbing visible irradiation while having the adequate redox potential for O_2 reduction. The literature reports a wide variety of nanostructured ternary oxides, so-called $A_xB_yO_z$, tested as visible photocatalysts and characterized by a combination of metals with s^2, d^0, or d^{10} configurations. They have been mostly tested for azo dye photodegradation [10, 38, 324]. The most active photocatalysts under visible light include vanadates ($BiVO_4$, Ag_3VO_4, $InVO_4$), wolframates (Bi_2WO_6), indanates (MIn_2O_4 (M = Ca, Sr, Ba)), bismutates ($CaBi_2O_4$) and niobates ($InNbO_4$). The working mechanisms of these materials depend on their electronic properties. For instance, the hybridization of the Bi 6s and O 2p orbitals widens the valence band of $CaBi_2O_4$ and increases the mobility of the photoholes, enhancing the photocatalytic performance [334]. DFT calculations with MIn_2O_4 showed that as the radius of the metal decreases the oxidizing power of the conduction band increases [335]. On the other hand, the structural properties also affect to the visible absorption of these materials. They usually have complex structures, such as perovskites, scheelites, spinels, or pyrochlores, which favor the creation of narrow conduction bands and the delocalization of the charge carriers. For example, the monoclinic structure of $BiVO_4$ yields efficient photocatalysts thanks to its low band gap, 2.34 eV, while its tetragonal phase shows a negligible activity because its larger band gap value, 3.11 eV [336]. Bi_2WO_6 described an orthorhombic Aurivillius-type structure with a band gap of 2.69 eV capable to absorb visible and solar light for azo dye degradation [337]. As occurred with other oxide photocatalysts, the photoresponse of ternary oxides can be also enhanced by doping with non-metal and metal ions. In this sense, an interesting review summarizes some examples of doped pyrochlores with structural defects applied in water treatment, including N-doped $K_2Ta_2O_6$, N and Sn-doped $KSbWO_6$, and Bi-doped $Na_2Ta_2O_6$, among other [338].

Nevertheless, these materials present some important drawbacks for their technological applications. They usually have low surface area, which reduces the amount of pollutant adsorbed. The stability of these materials in the reaction medium is also an important limitation. Characterization of $AgVO_3$ after reaction in aqueous solution under visible light demonstrated that the photocatalyst suffers important structural modifications upon reaction, being converted into a complex mixed $Ag^0/Ag_2O/Ag_4V_2O_7$ system [339]. Further efforts are being addressed to optimize the properties of these ternary oxides in order to improve their photoefficiency under visible light.

3.4 NON-OXIDES SEMICONDUCTORS AS PHOTOCATALYSTS

Transition metal sulphides have been also tested as visible photocatalysts because they have narrow band gap values, although they also present some drawbacks for water purification. Some examples have been summarized in recent reviews [38, 340]. CdS is, for instance, the most studied chalcogenide, mainly tested for decolorization of dyes. Although it has a low band gap, 2.42 eV, it is not suitable for water treatment because it suffers photocorrosion and releases toxic cadmium ions. Bi_2S_3 and NiS are also semiconductors with narrow band gap values (1.3 and 0.5 eV, respectively) but their preparation at nanoscale is usually accompanied of nanoparticles agglomeration forming clusters with low surface area, thereby showing low photoefficiency. In developing new nanostructured semiconductors, multinary chalcogenides have been more recently used for dyes degradation, including ternary I-III-VI_2 (e.g., $AgGaS_2$, $CuInS_2$ and $CuInSe_2$) and quaternary I_2-II-IV-VI_4 sulphides (e.g., Cu_2ZnGeS_4, Cu_2ZnSnS_4 and Ag_2ZnSnS_4). These compounds have band gaps suitable for visible absorption, and it is possible to control their size and shape for tuning the available active surface sites [340]. Nevertheless, special attention must be placed on the synthesis route because the formation of effective alloys is necessary, avoiding the creation of mixed phases.

Ag_3PO_4 has been also considered as a photocatalyst for water purification because of its narrow band gap, 2.43 eV, highly positive valence band position, and low toxicity. However, its photostability in aqueous solution is an important issue because it suffers photo corrosion, transferring Ag^0 particles to solution. Therefore, advanced research projects are focused on suppressing photo corrosion and creating photocatalysts that fulfill the requirements for potential application. Many attempts are focused on studying the morphological effects on the photocatalytic performance through the synthesis of nanostructured morphologies and porous structures with a controlled shape, aimed to improve the surface area and thereby, the transport and adsorption of the contaminants [341]. However, the photocatalytic activity of Ag_3PO_4 has been usually tested for dye decolorization, and the mineralization of organic contaminants is less frequently reported, mainly due to its instability. Therefore, the recent progress intends to create new photocatalysts by combining Ag_3PO_4 with other compounds yielding the heterojunctions that will be described later.

Bismuth oxyhalides represent another group of semiconductors used as photocatalysts. They have a layered structure and their band gap values are 1.76, 2.75 and 3.1 eV for BiOI, BiOBr and BiOCl, respectively [342]. Among them, BiOI has shown the best photoefficiency under solar light, due to its narrower band gap [343]. As occurred with the other semiconductors, the research tends to improve the photocatalytic performance of these bismuth oxyhalides by combining with other semiconductors, metals and other materials [344], creating different heterojunctions. The main challenges consist of the improvement of the visible absorption, charges separation, stability, reusability, and separation from the treated water.

Recently, graphitic carbon nitride (g-C_3N_4) has been used as nanoscale photocatalyst for water cleaning [345, 346]. It has attracted attention because of its intermediate band gap value, 2.65 eV, with good visible light response (up to 460 nm). This property, together with its low cost, easy preparation, chemical stability, and safe application, makes it a promising visible light-driven photocatalyst for water treatment. However, like other semiconductors previously described, g-C_3N_4 has some limitations for full-scale implementation. Its photocatalytic efficiency is limited due to insufficient solar light absorption, low surface area and fast recombination of photogenerated electron-hole pairs [345, 347]. Inspired by the modification strategies described for other semiconductors, different approaches have

been adopted to enhance the photocatalytic performance of g-C_3N_4, including modifications on shape and size, dye sensitization, doping and combination in different heterojunctions, as those that will be described afterwards. A comprehensive review on doping of g-C_3N_4 for photocatalysis has been recently reported, where the effects of non-metal doping, metal doping and codoping are described [348].

3.5 SEMICONDUCTOR HETEROJUNCTIONS

The synthesis of semiconductor heterojunction has attracted special attention as an interesting strategy to create novel nanoscale semiconductors with photocatalytic applications under visible and solar light. The literature reports a number of possibilities for semiconductors combination that were classified by Wang et al. [303] as follows: (i) semiconductor-semiconductor (S-S), (ii) semiconductor-metal (S-M), (iii) semiconductor-carbon materials (S-C), and (iv) multicomponent heterojunctions. When the semiconductors of a S-S heterojunction are irradiated, the photogenerated electrons and holes can be easily separated. The electrons can migrate from one semiconductor with a higher conduction band minimum to the other with a lower conduction band minimum. At the same time, the holes can transfer from a semiconductor with a lower valence band maximum to the other with a valence band maximum. This separation inhibits the electron-hole recombination and increases the number of charges in each semiconductor available for further generation of active radicals that can oxidize the organic compounds. Fig. 6 depicts an example where TiO_2 receives in its CB the electrons generated in other semiconductor with a narrower band gap (so that it can be activated with a larger wavelength radiation) and the CB with more negative oxidation potential. This synergistic system depends on the electronic properties of the semiconductor selected. In addition, the charge separation could be improved if the VB of TiO_2 presents a more positive oxidation potential than the other semiconductor, so that photoinduced holes would remain in the valence band of the latter, avoiding recombination [349, 350].

Many different S-S heterojunctions have been evaluated for water purification under visible and solar light, including combinations with TiO_2, ZnO and other semiconductors previously described.

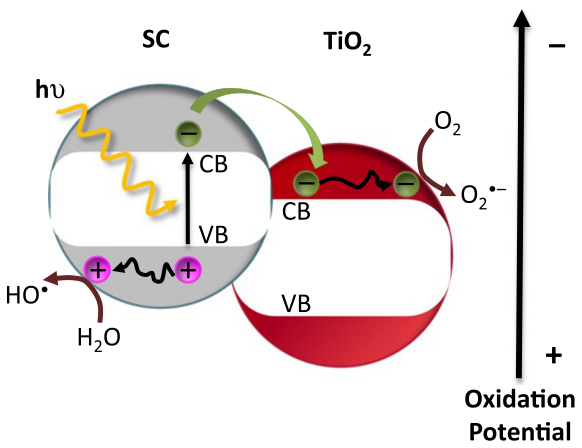

FIG. 6

S-S heterojunction between TiO_2 and other semiconductor (SC).

Table 3 Relevant Examples of S-S Heterojunctions, Their Synthesis Method and Application

Heterojunction	Synthesis	Pollutant/Light	Reference
$ZnO\text{-}TiO_2$ crystal	Pyrolysis	MO/solar	[351]
CdO-ZnO	Electrospinning	MB/solar	[352]
Nb_2O_5-ZnO	Hydrothermal-precipitation	Phenol/solar	[353]
Fe_2O_3-ZnO	Hydrothermal	Ciprofloxacin/visible	[354]
$NiO\text{-}SrBi_2O_4$	Co-precipitation	*Escherichia coli*/visible	[355]
BiOI-NiO	Solvothermal	Acid orange 7/visible	[356]
$Bi_2WO_6\text{-}BiVO_4$	Hydrothermal	RhB/visible	[357]
$g\text{-}C_3N_4\text{-}Bi_2WO_6$	Hydrothermal-calcination	Antibiotics/visible	[358]
$SrTiO_3$-BiOBr	Sol-gel-precipitation	Dyes/vis and solar	[359]
$Bi_2O_2CO_3\text{-}Bi_2O_4$	Hydrothermal	Phenol, BPA/visible	[360]
$AgI\text{-}Bi_2O_2CO_3$	Co-crystallization	2-Chlorophenol/visible	[361]
$AgI\text{-}Bi_5O_7I$	Deposition-precipitation	Antibiotics/visible	[362]
$CuInSe_2\text{-}TiO_2$	Solvothermal	MO/visible	[363]
$CdS\text{-}TiO_2$	Growing from SiO_2 templates	RhB/visible	[364]
$CdS\text{-}SnIn_4S_8$	Hydrothermal	Real wastewater/visible	[365]
$ZnIn_2S_4\text{-}g\text{-}C_3N_4$	Hydrothermal	Tetracycline	[366]

Some examples are collected in Table 3. It must be noted that the comparison of the photocatalytic activity of different types of S-S heterojunctions is very difficult, because that activity depends not only on the band gap, but on the morphology, particle size, porosity, and surface area. The optimum content of each semiconductor, the structural stability of the heterojunction, and the surface properties are also crucial for obtaining stable interfacial structures. Also, the nature of the target pollutant, the irradiation intensity, and the photoreactor design play important roles on the performance of a photocatalyst.

The S-M heterojunction is another approach for favoring charge separation and preventing recombination because the photogenerated electrons can flow through the semiconductor and the metal. The most common case of S-M heterojunction is the metal deposition described in previous sections for TiO_2 and ZnO. However, there are other promising photocatalysts that can be included in this group which have received special attention in the last years. Among them, the Ag-AgX and $Ag\text{-}Ag_3PO_4$ photocatalysts can be highlighted because of their strong absorption in the visible region due to the SPR properties of the Ag NPs. The photogenerated electrons are transported from Ag NPs to the conduction band of the semiconductor, yielding effective materials for the degradation of dyes. The main problem with these photocatalysts derives from the synthesis route, which usually involves complex procedures [303]. Their use for the degradation of more interesting pollutants has been barely investigated.

Several interesting reviews on heterojunctions based on semiconductor-carbon materials (S-C) can be found in the literature [38, 207, 303, 367]. These heterojunctions can be synthesized by different procedures, including thermal oxidation, sol-gel, hydrothermal, and solvothermal methods and deposition techniques, such as vapor (PVD), chemical vapor (CVD), and electrophoretic (EPD) deposition [207]. Different types of carbon nanomaterials have been used, including activated carbons, carbon nanotubes (CNTs), graphene, and fullerene, without a particularly different contribution to the

photocatalytic mechanism. Special attention has been paid to the toxicity of those nanomaterials, showing, for instance, that graphene has toxic effects on several biological systems, as opposed to the low cytotoxicity of graphene oxide [368].

Activated carbon (AC) is usually selected because it is quite stable, cheap, and easy to manufacture. Its contribution to photocatalytic performance is associated with its large surface area, which allows adsorption of the pollutants on the surface, favoring higher degradation rates. Nevertheless, AC is just used as support and does not directly affect the band gap of the semiconductor. Therefore, the research on visible-light-driven photocatalysts is focused on preparing modified TiO_2 loaded onto AC, following the investigations already made on TiO_2-AC. For example, CdS-TiO_2/AC shows photocatalytic activity under solar light [369].

CNTs provide also a high surface area, but in addition contribute with their conductivity. CNTs have an electronic structure which provides large electron-storage capacity, therefore they can act as trappers of photogenerated electrons, inhibiting the undesired recombination and enhancing the photocatalytic activity. Unlike AC, it has been reported that multiwalled CNTs can also act as photosensitizers. They can be excited by irradiation, transferring the electron to the conduction band of the semiconductor, enhancing the charges movement and thus favoring the efficiency of the heterojunction in the visible light region [370]. It is also interesting to remark upon the lower efficiency depicted by multiwalled carbon nanotubes (MWCNTs) compared with their single-walled counterparts (SWCNTs) in these heterojunctions. This has been attributed, in the case of TiO_2-CNTs, to a worse dispersion and interphase contact between the CNTs and the TiO_2 surface [205]. TiO_2-CNTs have been the most studied heterojunction for the degradation of different pollutants under visible and solar light. An interesting review by Leary and Westwood Leary and Westwood [207] summarizes representative examples, showing the relationship between the synthesis route and the photocatalytic performance.

Graphene and graphene-derived materials, like graphene oxide (GO) and reduced graphene oxide (rGO), possess a layered structure, high conductivity, great electron mobility, and large surface area. Their role in the S-C heterojunction consists of providing a wide surface for the adsorption of the target pollutants while promoting the charge separation. It has been described that this charge separation is favored by the flow of the photogenerated electrons from the conduction band of the semiconductor to the graphene layer [303]. More recently, Minella et al. [371] have found that the photocatalytic mechanism for TiO_2-rGO composites involves electron transfer from photoexcited states of rGO to the TiO_2, while the holes migrate from the TiO_2 to the rGO. The synergistic effects between the surface and conductivity properties are responsible for the improved photocatalytic performance of those nanoscale materials. The literature includes different examples of S-graphene heterojunctions using different semiconductors, such as TiO_2, modified TiO_2, CdS, and metallates. Some representative examples are collected in Table 4.

Other types of S-C heterojunctions can be also found in the literature. The core-shell structure TiO_2-carbon spheres have been recently reported as efficient photocatalysts for the degradation of different organic pollutants in aqueous solution under visible light [378]. It has been stated that the close-contacting interface between TiO_2 and the carbon spheres induces the creation of doping levels above the valence band of the TiO_2 (0.1–0.25 eV) upon the formation of C–O–Ti bonds (Fig. 7). These new energy levels in the interface make possible the electron transition by absorption of visible light, shifting the absorption edge to 400–420 nm. Thus, charge separation can be activated by visible light excitation, enhancing the photocatalytic activity.

Table 4 Representatives Examples of S-Graphene Heterojunctions, Their Synthesis and Application

Heterojunction	Synthesis	Pollutant/Light	Reference
TiO_2-graphene	Hydrothermal	Atenolol/visible	[372]
TiO_2-rGO	Reduction	Phenol, MB/visible	[371]
TiO_2-rGO	Hydrothermal	Risperidone/visible and solar	[373]
Co-TiO_2-GO	Sol-gel/hydrothermal	Phenol/visible and solar	[374]
Bi_2WO_6-graphene	Hydrothermal	RhB/visible	[375]
$BiVO_4$-graphene	Hydrothermal	Carbamazepine/solar	[376]
g-C3N4-GO	Sonochemical	2,4-Dichlorophenol	[377]

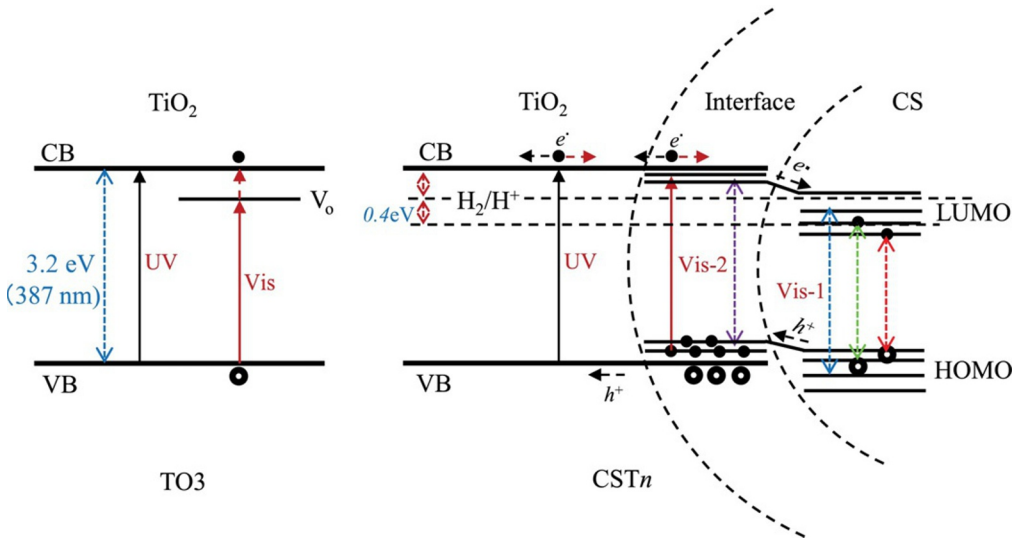

FIG. 7

Proposed mechanism for the photoinduced charge separation of carbon sphere-TiO_2 composite and titania.

Reprinted with permission of Elsevier from H. Wu, X.L. Wu, Z.M. Wang, H. Aoki, S. Kutsuna, K. Jimurac, S. Hayashi, Anchoring titanium dioxide on carbon spheres for high-performance visible light photocatalysis. Appl. Catal. B Environ. 207 (2017) 255–266.

The last case of heterojunction is the multicomponent type, which usually consists of an integrated system formed by two or more visible light-active components and an electron transfer system [303]. Some authors used the "hybrid" terminology to identify these multicomponent heterojunctions. The structure and mechanism are fairly diverse, depending on: (i) the band gap of the semiconductors involved, (ii) the electron and hole transfer between the components, (iii) the light absorption ability of those components different to the semiconductors (metals, graphene, etc.), and (iv) the recombination rate. Different examples can be found in the literature. For instance, Zhou et al. [312] reported several

hybrid photocatalysts based on silver and silver halides, intended to make use of the surface plasmon resonance (described in Section 3.1.4). Nanoflowers of Ag/AgBr/BiOBr were synthesized by combining ion-exchange between BiOBr and $AgNO_3$ and photoreduction with visible light [379]. This photocatalytic system has shown visible light response for the degradation of an azo dye, yielding higher conversion rates than commercial P25. The efficiency was attributed to the SPR excitation of the Ag NPs allowing electron injection from them to the conduction band of the AgBr and BiOBr. This charge movement leads to the formation of Ag^+ and O_2^- species, the latter through electron trapping by adsorbed O_2, that can oxidize the target pollutants. AgCl-Ag/rGO has been also described as an efficient visible photocatalyst for azo dye degradation [380]. The SPR characteristic of the Ag NPs generates electrons which are transferred to the rGO, its conductivity facilitating charge separation. The charges can then migrate to the surface and react with the target molecules adsorbed on the AgCl surface.

More recently, a globular flower-like $CuS/CdIn_2S_4/ZnIn_2S_4$ heterojunction was prepared by a microwave-assisted one-step method. Its photocatalytic activity under simulated sunlight and visible light for methyl orange degradation was higher than that of the single components and P25 [381]. This was attributed to its absorption in the visible region (670 nm), its high surface area due to its flower-like morphology and the microstructure of its crystals. There are many examples in the literature focused on multicomponent heterojunctions for dye degradation or decolorization, some of which are collected in Table 5. Their photocatalytic application for mineralization of other organic pollutants, removal of inorganic contaminants, and detoxification has not been extended so far, although novel results are currently reported.

In general, regarding the photocatalytic efficiency, comparison between heterojunctions is fairly difficult because their behavior depends on many factors. Some are related to the heterojunction itself, as the nature of the components, their relative amounts and the synthesis route. But others depend on the equipment and the application, such as the nature of the pollutant and the reaction conditions (concentration, light intensity, light source, reactor design, etc.). On the other hand, widespread application of

Table 5 Representative Examples of Multicomponent Heterojunctions, Their Synthesis, and Application

Heterojunction	Synthesis	Pollutant/Light	Reference
$Sb\text{-}SnO_2/TiO_2/SrTiO_3$	Hydrothermal	MB/solar	[382]
$rGO/SnS_2/ZnFe_2O_4$	Hydrothermal	2-Nitrophenol/visible	[383]
Carbon dots/g-C_3N_4/ZnO	Impregnation-thermal	Tetracycline/visible	[384]
TiO_2/carbon dots/rGO	Hydrothermal	*E. coli*/solar	[385]
$(C_{16}H_{33}(CH_3)_3N)_4W_{10}O_{32}$/g-$C_3N_4$/rGO	Surface bonding-reduction	MO, Phenol/visible	[386]
Ag/carbon dots/g-C_3N_4	Thermo-polymerization	Naproxen/visible	[387]
BiOI/BiOCl/g-C_3N_4	Precipitation	Acid orange 7/visible	[388]
$Bi_2O_3/Bi_2S_3/MoS_2$	Hydrothermal	MB/solar	[389]
$CuS/CdIn_2S_4/ZnIn_2S_4$	Microwave	MO/visible and solar	[381]
Ag/AgBr/BiOBr	Ion exchange	MO, *E. coli*/visible	[379]

nanoscale heterojunctions would require feasible synthesis routes, easy ways to recover the catalyst, and a detailed knowledge of the toxicity and environmental risks of the nanoscale components.

3.6 NOVEL NANOARCHITECTURES

The interest toward the development of visible and solar light photocatalytic materials has been growing in the last decade. Because fine particles suspended in water are difficult to separate from the solution increasing research efforts are being devoted to the synthesis of novel nanoarchitectures, composites or hybrid materials by anchoring nanostructured semiconductors on different supports. It is expected that synergistic effects in these nanoarchitectures, including photon absorption, improved electron-hole separation, and enhanced porosity, can help to overcome the limitations of nanoscale photocatalysts. The literature describes a wide variety of porous solids that can be used as supports [11], including zeolites, clays, layered double hydroxides, mesoporous silicas, and activated carbons. These last have been described in previous section as S-C heterojunctions.

Different approaches have been used for developing clay-based photocatalysts for water purification under visible light [390]. For instance, delaminated porous clay heterostructures were successfully prepared by sol-gel method, anchoring several M-doped TiO_2 NPs (M = Ce, Zr, W), ZnO-TiO_2 NPs, and Ag-ZnO-TiO_2 NPs on a delaminated montmorillonite. This method allowed preparing novel porous semiconductors easily recoverable from the aqueous suspension and showing high photocatalytic performance for the degradation of several emerging pollutants, including pharmaceuticals and herbicides, under simulated sunlight [391–396]. The photocatalytic activity was attributed to the light absorption by the nanostructured semiconductor and the adequate interface/surface for pollutants adsorption.

3.7 NANOSCALE PHOTOCATALYTS INMOBILIZATION

Typical photocatalytic reactors for water treatment are slurry type, where the powdered catalyst is suspended in liquid. The main advantages of that approach are simple configuration and high contact surface, while low efficiency of incident light and difficult photocatalyst separation are the main drawbacks [397, 398]. The immobilization of nanoscale photocatalysts can eliminate costly and impractical post-treatment recovery of spent photocatalysts for full-scale implementation. A wide variety of substrates have been used for immobilization. These include glass, ceramic membranes, polymers, biodegradable cellulosic materials, optical fibers, and metallic supports, among others. These coated materials are placed within the photocatalytic reactor, on the reactor walls, or even on the lamps, avoiding the separation and recovery stages. In addition, the photocatalyst can be integrated into novel membranes, improving its fouling resistance and permeability [399, 400]. In contrast, the photocatalytic efficiency of these systems can decrease as a result of the smaller contact area with the pollutants [401, 402]. The immobilized photocatalysts must fulfill some requirements that depend on both the nanoscale semiconductor and the substrate [403]: (i) strong interaction between the semiconductor and the substrate, (ii) high chemical and physical stability of both, (iii) high surface area for adsorption of the contaminant, and (iv) the semiconductor must hold its photocatalytic efficiency after immobilization. Different immobilization procedures have been reported in the literature, such as dip coating, cold plasma discharge, polymer-assisted hydrothermal decomposition, radio-frequency magnetron sputtering, photoetching, solvent casting, electrophoretic deposition, sol-gel, and spray pyrolysis.

Table 6 Representative Examples of Immobilized Photocatalysts Used for Water Purification Under Visible and Solar Light

Photocatalyst	Pollutant/Light	Reference
TiO_2-anodic films	RhB/visible	[404]
TiO_2-hollow fiber membranes	MB, Chlorhexidine Digluconate/solar	[405]
TiO_2-poly(vinyl alcohol) films	Triton X-100/solar	[406]
N-doped TiO_2-glass	MB, Eriochrome black/visible	[407]
S,N-doped TiO_2-glass	MO/visible and solar	[408]
TiO_2-SnS_2-glass	Diclofenac/solar	[409]
AgI-TiO_2-metal Ti substrate	Acid orange II/visible	[410]
Ag-TiO_2-ceramic tiles	Sugar refinery wastewater/solar	[411]
CdO/ZnO-polyurethane fibers	MB, Reactive black 5/visible	[412]
PAN/Ag-AgBr-$Bi_{20}TiO_{32}$ fibers	Isoproturon, Bacteria/visible	[413]
N,S-doped BiOBr-glass	RhB/visible	[414]
Polypropylene-$H_3PMo_{12}O_{40}$ membranes	Acid orange 7/visible	[415]

Selection depends on the nature of both the active semiconductor and the substrate. Comprehensive reviews have been reported on the topic [11]. Srikanth et al. [403] listed several examples of the most recent immobilized photocatalysts used for the degradation of dyes, pesticides and pharmaceuticals, although not exclusively focused on visible and solar light. Table 6 extends the revision including relevant and recent works under these light ranges. The results of all these works reveal that more efforts need to be addressed toward overcoming the current limitations of immobilized photocatalysts. They usually present mass transfer limitations, compared with powder photocatalysts. Reusability is also an important drawback, and many efforts are devoted to preparing immobilized photocatalysts with higher chemical and mechanical stability. Moreover, scale-up of the immobilization procedures will require additional research for industrial applications.

4 REMOVAL OF EMERGING CONTAMINANTS FROM WATER BY PHOTOCATALYSIS

Emerging contaminants (ECs) are defined as chemical compounds usually found in water which are only recently considered water pollutants despite their harmful effects on environment and human health [416, 417]. They have very different sources, natural or anthropogenic, including domestic wastewaters, discharges from manufacturing plants, hospital residues, and so on. They are usually found in low concentrations of parts per billion ($\mu g\,L^{-1}$) or even trillion ($ng\,L^{-1}$). The main problem with these compounds is that wastewater treatment plants (WWTPs) are not able to remove them, and it is reported that they can bioaccumulate in humans and animals. The number of chemical compounds included in the ECs category found in wastewaters is continuously growing due to production of new

chemicals and to the development of analytical techniques which allow detecting lower and lower concentrations. Some of the most representative of these newly concerning water pollutants include pharmaceuticals, pesticides, personal care products (PCPs), and hormones. Due to their negative effects on endocrine systems, they are included in the endocrine disrupting compounds (EDCs) group.

In recent years, much effort has been devoted to the removal of cyanotoxins which are present in numerous aquatic environments. Cyanobacteria (blue green algae) are photosynthetic bacteria naturally occurring in lakes, streams, ponds, and other nutrient-rich surface waters [418]. Cyanobacteria not only affect taste and odor, but also, under favorable conditions of light and nutrients, some species produce toxic secondary metabolites, known as cyanotoxins [419]. Among them, microcystins (MCs, see structure in Fig. 8) are the most widespread, microcystin-LR (MC-LR) being the most common and toxic variant. People can be exposed to MCs through the ingestion of contaminated drinking water. Absorption by the liver leads to subsequent cell necrosis, hemorrhage, and death [51]. As a consequence, in recent years, much research efforts have been addressed to analyze the problems derived from the presence of cyanotoxins in water bodies. MCs are released to water upon death and lysis of the cells, entering WTTPs both in intracellular and extracellular forms. Removal of toxin-containing cells must be performed avoiding further MCs release [420]. Most of the studies focused on the

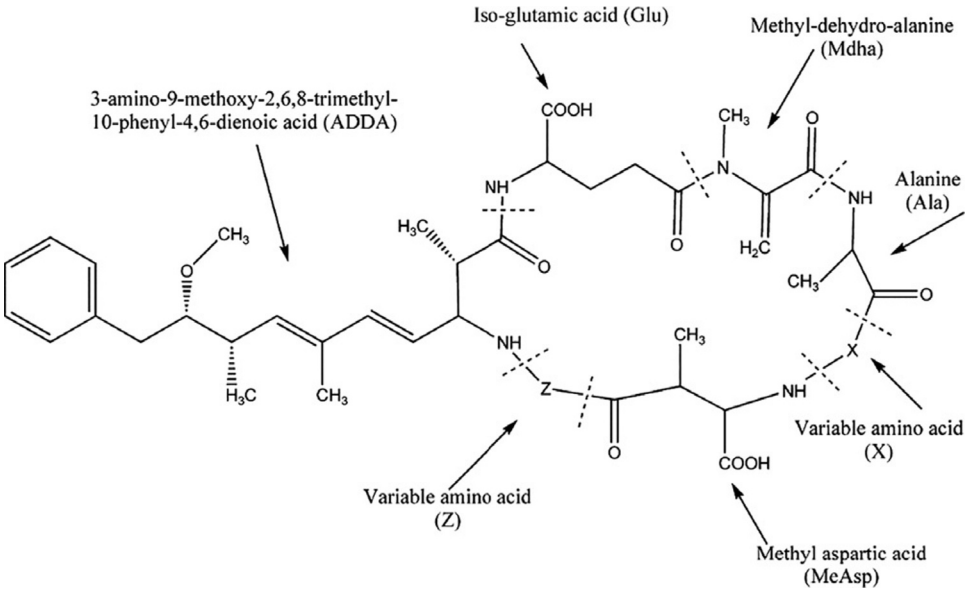

FIG. 8

Structure of the microcystins.

Reprinted with permission of Elsevier from V.K. Sharma, T.M. Triantis, M.G. Antoniou, X. He, M. Pelaez, C. Han, W. Song, K.E. O'Shea, A.A. de la Cruz, T. Kaloudis, A. Hiskia, D.D. Dionysiou, Destruction of microcystins by conventional and advanced oxidation processes: a review. Sep. Purif. Technol. 91 (2012) 3–17.

photocatalytic degradation of cyanotoxins use bare or non-metal-doped (C, N, F or S) TiO_2, with only a few papers dealing with graphene-based photocatalysts [44].

It is well-known that ECs are not efficiently removed from water in WWTPs, and consequently, non-conventional water treatment technologies have been developed in recent years for removing this type of pollutant from water and wastewater. These treatments can be broadly divided into non-destructive or phase-transfer technologies (adsorption on different porous solids and membrane separation) and destructive processes, including biological and chemical oxidation technologies. The literature contains extended reviews of the removal of ECs using these technologies and describing the advantages and inconveniences of their use [416, 418, 420, 421]. In recent years, an increasing interest on the removal of ECs by advanced oxidation processes (AOPs) has produced a growing number of publications on this topic [421]. AOPs are considered effective methods and environmentally-friendly treatments [422] based on their generation of strongly oxidizing species, such as hydroxyl (•OH) and other radicals, at ambient-like conditions, which are able to mineralize water pollutants. AOPs include ozonation, Fenton oxidation, ultrasound, electrooxidation, and photo-assisted oxidation. In the following, we will summarize the state of the art on heterogeneous photocatalysis under near-ultraviolet (UV) or solar visible light for the breakdown of emerging contaminants.

4.1 PHOTOCATALYTIC MATERIALS FOR THE DEGRADATION OF ECS FROM WATER

As with other pollutants, TiO_2 is by far the most-studied photocatalyst for the removal of ECs from water, due to its already-mentioned, convenient properties [93]. However, as indicated before, it also presents some drawbacks which have been faced through different approaches.

4.1.1 TiO_2-based photocatalysts

Metal doping

Ag-doped TiO_2 photocatalysts were analyzed for the degradation of the dexamethasone (DXM) corticosteroid in water. They showed a high activity under visible light [423]. The deposition of Au, Ag, Cu, and Ni nanoparticles on TiO_2-P25 for the photodegradation of trimethoprim, a commonly used antibiotic, has been also analyzed. The metallic particles on TiO_2-P25 provoked an increased activity with respect to the bare semiconductor. Under the same conditions, 80% vs. 50% mineralization was achieved upon deposition of Au or Ag metallic nanoparticles on TiO_2-P25 [320]. TiO_2 doped with Cu (Cu-TiO_2) by microwave sol-gel method and chemical reduction was tested in the degradation of bisphenol A under UV and visible light [424]. The Cu-TiO_2 composites increased the BPA degradation by inhibiting the e^-h^+ combination. Rate constant values up to 6.6 times higher than those with P25 were achieved under visible irradiation. [392–394]) synthesized novel hererostructures based on Ce-, W-, and Zr-doped TiO_2 nanoparticles immobilized on delaminated clays, which were used as solar light-active photocatalysts. In the case of the Zr-doped materials, it was proven that Zr was successfully incorporated into the anatase lattice, resulting in a decrease of the band gap value. These photocatalysts yielded higher degradation rates of antypirine, an analgesic drug, than the non-doped ones. W-TiO_2/clay photocatalysts were tested for atrazine degradation under solar irradiation, showing better performance that the non-doped TiO_2/clay system.

Non-metal doping

N-doped TiO_2 hollow spheres reduced the concentration (5 mg L^{-1}) of bisphenol-A (BPA) in water by 90% using visible-LED light (465 nm). This result was better than that achieved with bare TiO_2 and hollow spheres [425]. The introduction of N increased the surface area, resulting in a higher photoefficiency. N-TiO_2 was also prepared using diethanamine as the N source. It was tested for the degradation of dichlorodiphenyltrichloroethane (DDT) under UV and visible light irradiation. The doping with N enhanced very significantly the photoactivity under visible light, allowing complete conversion of DDT [426]. Atrazine and amitrole, two pesticides, have been also degraded by photocatalysis under solar light with the aid of persulfate and peroxymonosulfate as oxidants in the presence of co-doped N-F-TiO_2. When combined with the photocatalysts, both oxidants showed increased reactivity [427]. TiO_2 has been also co-doped with C and N, C-N-TiO_2, and used against BPA under visible light irradiation [428]. In this case, the mesoporosity of the material seems to favor the diffusion and adsorption of BPA, allowing 96% disappearance after 2 h and complete conversion after 5 h of irradiation. TiO_2 has been tri-doped with C, S, and N, leading to a very significant band gap reduction (2.67 eV). The resulting material was tested for the degradation of carbamazepine (CBZ) under visible-LED light, yielding 68% conversion after 120 min [429].

Regarding the removal of cyanotoxins, N-doped TiO_2 photocatalysts have been widely studied. Choi et al. [430] used N-TiO_2 for the removal of MC-LR under visible light with enhanced photoactivity. According to the authors, the reaction begins at four points of the MC-LR molecule, namely (i) the aromatic ring, (ii) the methoxy group, (iii) the conjugated double groups of the Adda group, and (iv) the cyclic structure of the Mdha amino acid. An improvement of the porosity and crystal size with a reduced band gap (2.85 eV) was obtained by co-doping TiO_2 with F and N. A detailed study on MC-LR degradation under visible light with NF-TiO_2 was reported in several works by Pelaez et al. [287, 430a,431]. Fotiou et al. [432] studied the photocatalytic degradation of different cyanotoxins, microcystin-LR (MC-LR) and cylindrospermopsin (CYN), using carbon-doped TiO_2 (C-TiO_2) under visible light. The main species in visible-driven photocatalysis is $O_2^{\bullet-}$, with the •OH radical playing a minor role. Carbon and nitrogen-doped TiO_2 films (C-N-TiO_2) were prepared by a sol-gel procedure and used for the visible-light photodegradation of MC-LR. The films showed an increased absorption in the visible region and a red shift in the band gap transition. The enhancement of the photocatalytic activity was assigned to the synergistic effects of carbon and nitrogen doping and the high surface roughness [433].

Dye sensitization

Atrazine (ATR) photocatalytic decomposition was analyzed using metalloporphyrin systems adsorbed on TiO_2 as sensitizers. Four different systems were analyzed, Cu^{2+}, Fe^{3+}, Zn^{2+}, and metal-free. The system with Cu^{2+}, TCPPCu(II), yielded the highest ATR removal (82% after 1 h), the •OH radicals being responsible for the oxidation [434]. A charge-transfer(CT) complex (Tiron-TiO_2) was prepared with the 1,2-dihydroxy-3,5-benzenedisulfonic acid disodium salt (Tiron) as chelate sensitizer (Fig. 9). UV–vis analysis showed that the formation of CT complex on the surface of TiO_2 significantly extends the photoresponse of Tiron-TiO_2 nanoparticles in the visible light range (400–600 nm). Compared with bare TiO_2, the modified approach showed excellent visible-light photocatalytic activity for the degradation of three kind of antibiotics, namely, chloramphenical (CAP), a widely used broad-spectrum

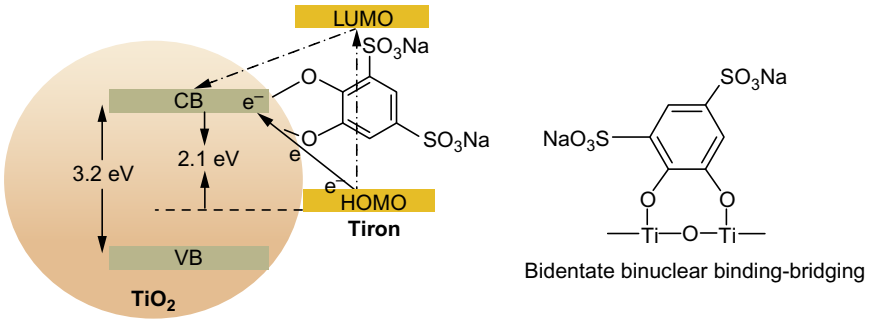

FIG. 9

Scheme of the charge-transfer(CT) complex (Tiron-TiO_2) using the 1,2-dihydroxy-3,5-benzenedisulfonic acid disodium salt (Tiron) as chelate sensitizer.

Reprinted with permission of Elsevier from B. Yao, C. Peng, P. Lu, Y. He, W. Zhang, Q. Zhang, Fabrication of iron-TiO2 charge-transfer complex with excellent visible-light photocatalytic performance. Mater. Chem. Phys. 184 (2016) 298–305.

synthetic antibiotic; sulfamethazine (SMT), a sulfonamide antibiotic used in human and veterinary medicines worldwide, and omefloxacin (LFC), probably the most major human-use fluoroquinolone antibiotic [435].

TiO_2-based composites

A sol-gel method was used for the synthesis of a photocatalytic composite of N-doped TiO_2 supported on AC (N-TiO_2/AC) used for the solar light photocatalytic decomposition of BPA [436]. This material showed greater BPA photodegradation efficiency than bare TiO_2 and P25, attributed to the presence of interstitial nitrogen doping. TiO_2/WO_3 composites were prepared in form of electrodes for the photodegradation of the 17-α-ethinylestradiol (EE2) hormone. It was stated that photogenerated e^- in TiO_2 should be transferred to the WO_3 conduction band, while h^+ displaced to the valence band of TiO_2, enhancing charge separation, and therefore, improving photoefficiency [437]. The solar photocatalytic degradation of acetaminophen (ACE) and antipyrine (ANT) was studied using TiO_2-ZnO/clay nanoarchitectures. ANT showed a higher degradation rate than ACE and in both cases the degradation was favored at low concentrations. Scavenger studies confirmed that degradation was controlled by holes, •OH and $O_2^{\bullet-}$ [396]. Several studies have analyzed the deposition of TiO_2 on activated carbons. As an example, Alalm et al. [438] described the photocatalytic activity of bare TiO_2 vs. TiO_2 immobilized on activated carbon (TiO_2/AC) for the degradation of four pharmaceuticals, namely amoxicillin, ampicillin, diclofenac, and paracetamol, under solar irradiation. The TiO_2/AC composite was more photoactive. An economic study was presented, resulting TiO_2/AC the cheapest option. Bi_2O_3/TiO_2 heterostructures were prepared by a straightforward hydrothermal method and used for the photocatalytic degradation of ofloxacin antibiotic under solar light. The photocatalyst exhibited a high activity, allowing complete conversion in 120 min, better than commercially available photocatalysts such as, TiO_2 P25 (Degussa), PC 50, and PC 500 [439].

4.1.2 Photocatalysts based on other semiconductors

Metal oxides

ZnO has been used for the photocatalytic oxidation of the antibiotic tetracycline (TC) under simulated solar light exhibiting a slightly higher oxidation rate than TiO_2. By means of scavengers, it was stated that photo-oxidation with ZnO is promoted by hydroxyl radicals [440]. Tri-doped ZnO with C, N, and S has been tested for the degradation of diazinon, an organophosphate insecticide, under UV-LED irradiation. The degradation rate constant with C-N-S-ZnO was two orders of magnitude higher than that obtained with bare ZnO [441]. Mixed ZnO-Fe_2O_3 was synthesized by a sol-gel method and used for the solar degradation of the commercial 3,6-dichloro-2-methoxybenzoic acid (Dicamba) and 2,4-dichlorophenoxyacetic acid (2,4-D) herbicides. Under the reaction conditions used in the study, complete degradation of both herbicides was achieved. Furthermore, complete and 70% dechlorinations were obtained for Dicamba and 2,4-D, respectively [442]. Bi_2O_3 nanoplates were synthesized by an ultrasound-assisted method yielding irregular ovoid and rectangular nanoplates, depending on the time under ultrasound. The photocatalytic activity was evaluated versus tetracycline hydrochloride (TC) in aqueous solution under Xe lamp irradiation. Mineralization reached 72% after 24 h [443]. β-Bi_2O_3 nanospheres were synthesized by a solvothermal-calcination process and used as photocatalyst for the visible light-induced degradation of acetaminophen. This material showed a narrow band gap (2.36 eV), resulting in a higher photoactivity than commercial Bi_2O_3, synthetic α-Bi_2O_3, nitrogen-doped TiO_2 (N-TiO_2), and Degussa P25. A hole-prevailing photodegradation pathway was proposed [444].

Metal sulfides

Cadmium sulphide (CdS) synthesized by a hydrothermal process, showing well-crystalline nanoparticles, was used as photocatalyst for the degradation of ofloxacion, a fluoroquinolone antibiotic, under visible light. Almost 80% conversion was achieved after 80 min, mainly by the action of •OH [445]. CdS nanoparticles synthesized under microwave irradiation and deposited by an electrophoretic process on aluminum plates were tested for the degradation of the tetracycline antibiotic under simulated sunlight irradiation. $O_2^{\bullet-}$ and •OH radicals were responsible for the degradation [446]. More complex heterostructures based on CdS have been also studied. Yang et al. [447] synthesized a CdS/MOF-derived porous carbon (MPC) composite as visible light photocatalyst through the pyrolysis of zeolitic imidazolate framework (ZIF-8) and subsequent growth of CdS. According to the authors, this structure reduces the bulk recombination and decreases the surface recombination, yielding a very good photocatalytic performance for the cephalexin antibiotic degradation, significantly better than the bare CdS [447]. Octahedral CdS/$SnIn_4S_8$ nano-heterojunctions were synthesized by a hydrothermal method at different CdS to $SnIn_4S_8$ molar ratios. The heterojunction with the optimal ratio (0.5:1) showed much higher visible-light photocatalytic activity than both CdS and $SnIn_4S_8$, probably due to the more efficient separation and transfer of photogenerated charges. This photocatalyst could effectively mineralize real pharmaceutical wastewater with excellent reusability [365].

Bismuth metallates

Tetracycline (TTHC) was photodegraded under visible light with bismuth oxybromide ($Bi_{24}O_{31}Br_{10}$) nanosheets. Decreasing the nanosheets' thickness seemed to enhance the separation and transportation efficiency of charge carriers so that the thinnest nanosheets yielded the highest photocatalytic TTCH

degradation [448]. Bismuth oxyhalide catalysts with photocatalytic activity to degrade 17 α-ethinyl estradiol (EE2) and estriol, both synthetic estrogens, at the ppm level in water were synthesized by Ahern et al. [449]. These BiOX photocatalysts were more photoactive than TiO_2. Bismuth oxybromide (BiOBr) from hydrothermal synthesis was used for the visible light-induced degradation of the ciprofloxacin antibiotic (CIP). The authors propose a degradation pathway in which hole oxidation plays a main role [450]. BiOBr was also tested for the photocatalytic degradation of acetochlor, a pesticide, under visible light irradiation. The reaction rate increased by increasing the catalyst dose in a significantly different way than the conventional photocatalytic patterns established for polar or water-soluble pollutants [451].

Graphene-based photocatalysts

Graphene oxide (GO) was used for the synthesis of a GO-TiO_2 composite showing improved activity in the degradation of MC-LR under solar light with respect to the reference TiO_2. The enhanced photoactivity was attributed to the inhibition of recombination [452]. GO-TiO_2 was also used for the photodegradation of atenolol (ATL) as model pharmaceutical pollutant under UV–vis and simulated solar light, showing much higher activity than the bare TiO_2 [372]. Reduced graphene oxide-TiO_2 composites (rGO-TiO_2) prepared by liquid-phase deposition followed by thermal reduction were evaluated for the degradation of diphenhydramine (DP) under both near-UV/Vis and visible light irradiation [453]. The best performance was observed for the composites treated at 200°C with 3.3–4.0 wt% GO, exceeding that of the benchmark P25 (Evonik). Photogenerated holes appeared the primary active species with bare TiO_2 and GO-TiO_2 under UV/Vis irradiation, while an enhanced contribution of radical-mediated oxidation was evidenced under visible light. These conclusions indicated that reduced GO acts as electron acceptor and electron donor (sensitizer) under UV and visible light, respectively. Reduced graphene oxide-tungsten oxide composites (rGO-WO_3) were synthesized and tested in the visible light-driven oxidation of sulfamethoxazole (SMX), a sulfonamide antibiotic. Almost complete SMX conversion was achieved in 3 h [454].

GO and carbon nanotubes (CNT) were used in the synthesis of GO-TiO_2 and CNT-TiO_2 for the photocatalytic degradation of a cyanobacterial toxin, microcystin-LA (MC-LA), in aqueous solution under both simulated solar and visible light. The highest photocatalytic activity (complete MC-LA conversion under solar light in 5 min) was obtained with a GO-TiO_2 with 4 wt% carbon content, higher than the corresponding to bare TiO_2. This high activity was attributed to effective inhibition of electron/hole recombination associated with the composite structure [455]. Fotiou et al. [452] tested GO-TiO_2 against MC-LR under UV-A and solar irradiation. It absorbs in the whole visible displaying in a photoactivity similar to that of Degussa P25 and much higher than that of the reference TiO_2. This was also attributed to the inhibition of electron-hole recombination. The authors concluded that •OH radicals played the main role.

Carbon nitride photocatalysts

The use of carbon nitride-based photocatalysts for the degradation of emerging contaminants from water using visible solar light is very recent. Mesoporous polymeric graphitic carbon nitrides (mpg-C_3N_4) were prepared and tested in the degradation of ibuprofen under sun light-equivalent UV and visible room light. The crystallinity of that material has a strong effect on the photocatalytic activity.

It was concluded that super oxide radical anions and hydroxyl radicals were the main reactive species with that photocatalyst [456]. Quantum-thick graphitic carbon nitride (g-C_3N_4) was deposited on the surface of anatase nanosheets to synthesize a novel TiO_2-g-C_3N_4 (TCN) heterojunction which was used for the degradation of tetracycline (TC). This heterojunction yielded higher TC degradation rate than that of TiO_2 or bulk g-C_3N_4. It was concluded that h^+ and $O_2^{\bullet-}$ were the main oxidant species [457]. Li et al. [458] presented an interesting work in which they analyzed the toxicity of the oxidation intermediates from the photodegradation of acyclovir, an antiviral, using a g-C_3N_4/TiO_2 hybrid photocatalyst under visible light irradiation. The results found that the toxicities of two of the intermediates were lower than that of acyclovir. However, the third intermediate, guanine, was more than double toxic. The literature also reports much more complex structures based on carbon nitrides. As example, graphitic carbon nitride/gadolinium and nitrogen co-doped titanium dioxide (g-C_3N_4/Gd-N-TiO_2) were prepared by a simple and reproducible in-situ synthetic method and used in the sunlight photocatalytic degradation of the antibiotic gatifloxacin. These heterostructures exhibited outstanding performance [459].

Metal organic frameworks

Metal organic frameworks (MOFs) have been recently rediscovered and they are defined as a class of crystalline materials resulting from coordination bonding of transition metal cations and multidentate organic linkers. Their outstanding properties, variety and multiplicity make MOFs ideal candidates for fuels (hydrogen and methane) storage, capture of carbon dioxide and catalytic applications, including photocatalysis [460–462]. The pioneer work using MOFs for the photocatalytic removal of ECs was presented by Liang et al. [463]. In that study, a Pd supported on MIL-100 (Fe) nanocomposite was synthesized and used under visible light for the photodegradation of three typical PPCPs, theophylline, ibuprofen, and bisphenol A. It was concluded that Pd NPs minimize the recombination of photogenerated electron-hole pairs, improving the photocatalytic performance. Mosleh and Rahimi [464] investigated the degradation of the abamectin pesticide under visible light with $Cu_2(OH)PO_4$-HKUST-1 MOF photocatalyst through sonophotocatalytic technique. The MOF showed a band gap value of 2.59 eV and almost complete conversion of the pesticide was achieved. The combined adsorption and visible-light photodegradation of aqueous clofibric acid (CA) and carbamazepine (CBZ) by a Fe-based metal-organic framework, MIL-53(Fe), was also investigated [465]. MIL-53(Fe) exhibited good adsorption capacity for both compounds, mainly due to electrostatic and π-π interactions. It showed also high activity and good stability under visible light and revealed excellent performance for the removal of both target pollutants from real municipal wastewater and river water. Its performance was improved by the addition of a small amount of H_2O_2.

Naturally-occuring photocatalysts

Ilmenite, $FeTiO_3$, is a mineral containing iron and titanium in its structure. It has been recently studied for the degradation of sulfonamide antibiotic by means of several advanced oxidation processes including photocatalysis under UV irradiation. This allowed complete conversion of the antibiotic within 30 min reaction time with 35% mineralization after 120 min [466].

5 PHOTOCATALYZED DISINFECTION

The access to safe water resources is still difficult in many parts of the world [467]. This lack of access to safe drinking water produces waterborne diseases transmitted through viruses, bacteria, and protozoa. In this context, there is a continuous need for the research and development of efficient, robust, low-cost, and easy-to-apply water sanitation techniques. Currently implemented water disinfection technologies can solve part of these problems, but their application entails some important drawbacks [468]. Chlorine-based procedures can lead to the formation of potentially mutagenic and carcinogenic disinfection byproducts (DBPs) [469]. Ozonation requires more complex systems [470] and can also produce DBPs, namely, aldehydes, carboxylic acids, ketones, and bromates [471]. The use of UV-irradiation for water disinfection suffers of microorganisms' regrowth after finishing the irradiation [472]. In addition to these problems, the technological and economical limitations hinder the application of current disinfection methods in many parts of the world. Consequently, further solutions are needed capable of facing these limitations. In this way, photocatalysis-based technologies have attracted great attention in the last few decades.

5.1 PHOTOCATALYTIC DISINFECTION MECHANISMS

Photocatalytic disinfection mechanisms have been reviewed in [473]. The process begins with the generation of the reactive oxidation species (ROS) which afterwards are able to provoke the inactivation of the pathogenic germs. It is generally assumed that •OH, $O_2^{\bullet -}$, h^+ and H_2O_2 are the ROS responsible for that inactivation. However, it is not still clear which of them play the major role. Furthermore, their role seems to be dependent upon their own photocatalyst. Identification of the most active ROS has been investigated by using partition systems with different scavengers [474].

Catalase (CAT) and superoxide dismutase (SOD) are intracellular enzymes that can be used as indicators of the oxidative stress of bacteria. High levels of these enzymes indicate that the bacterial are defending themselves against the ROS, converting them into less harmful species [475]. Typically, the disinfection process begins with an increase of the CAT and SOD levels, followed by a decrease once the defense capacity has been overwhelmed [476]. This leads to the destruction of the proteins, release of ions and formation of carbonyl derivates impeding the cell viability [477].

The inactivation of *E. Coli* under visible light with a $CdIn_2S_4$ photocatalyst was followed by Wang et al. [478] by transmission electronic microscopy (TEM) images at different stages of the process (Fig. 10). As can be seen, prior to disinfection, the *E. coli* cells show a well-defined wall (Fig. 10A). After 3 h of irradiation, the inner portion of the cell remains unaltered, but the integrity of part of the cell wall begins to be damaged (Fig. 10B). Further irradiation results in a clear destruction of the wall structure (Fig. 10C), followed by a continuous degradation of the inner cell, which is completely destroyed after 15 h irradiation, leaving only a small portion of cell debris (Fig. 10D).

5.2 PHOTOCATALYTIC MATERIALS FOR WATER DISINFECTION

As in most of the photocatalytic studies, in water disinfection TiO_2 has been the most widely used photocatalyst [431, 479, 480].

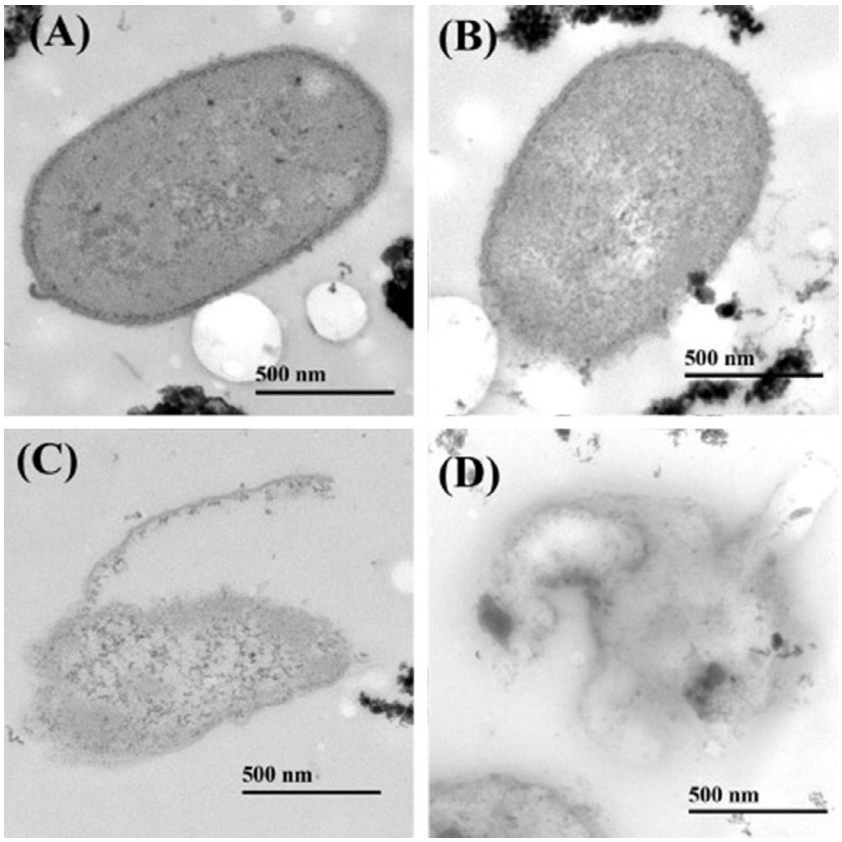

FIG. 10

TEM images of *E. coli* K-12 (2×10^7 cfu mL^{-1}, 50 mL) photocatalytically treated with $CdIn_2S_4$ microspheres (100 mg L^{-1}) under visible light (VL) irradiation. (A) 0 h, (B) 3 h, (C) 6 h, and (D) 15 h.

Reprinted with permission of Elsevier from W.J. Wang, T.W. Ng, W.K. Ho, J.H. Huang, S.J. Liang, T. An, G. Li, J.C. Yu, P.K. Wong, CdIn2S4 microsphere as an efficient visible-light-driven photocatalyst for bacterial inactivation: synthesis, characterizations and photocatalytic inactivation mechanisms. Appl. Catal. B Environ. 129 (2013) 482–490.

5.2.1 TiO_2-based photocatalysts

As indicated before, the main problem related to the use of TiO_2 is its low efficiency under visible or solar light. Therefore, as in the case of pollutant compounds breakdown, different modifications of TiO_2 have been also investigated for disinfection.

Metal deposition

Pt/TiO_2 showed a higher inactivation capacity of the *Bacilus thuringiensis* than bare TiO_2 due to a better charge carrier separation [481]. Photodeposition of Pt over P25 extends the optical absorption band to the visible light region allowing a highly efficient photocatalytic disinfection of *E. coli* under solar irradiation [482, 483]. Ag deposition combines the effect of the surface plasmon resonance of Ag to enhance

the efficiency of the photocatalyst under solar visible light and the well-known antimicrobial activity of Ag [484]. Ag/TiO_2 photocatalyst has shown higher bactericidal activity than UV, Ag/UV and UV/TiO_2 [485]. Other metals have been also tested (such as, Zn or Cu). Inclusion of Zn improved the photocatalytic activity for disinfection while the deposition of Cu provoked the opposite. The improvement derived from metal deposition on TiO_2 has been attributed to both the better adhesion of the bacterial cells to the photocatalyst and the photoactivity of the hole-derived radicals [486].

Doping

N-doped TiO_2 showed higher ability for *E. coli* inactivation than bare TiO_2 under solar irradiation [487]. S-doped TiO_2 exhibited a high inactivation toward *Micrococcus lylae* under visible light. The performance was improved by increasing the S amount due to the higher formation of hydroxyl radicals [488]. Bimetallic doping has been also analyzed in the literature with the aim of increasing the photo inhibition under visible/solar light. Almost complete inactivation of *E. coli* under visible light irradiation was achieved with a Fe-Cd/TiO_2 photocatalyst [489].

Dye sensitization

TiO_2 films immersed in copper(II) phthalocyanine chloride dye solution resulted in modified TiO_2 films with significant inactivation capacity toward *E. coli* under visible light [490]. Another study performed with TiO_2 film sensitized with a porphyrin dye exhibited inactivation efficiencies higher than 90% for different bacteria under visible irradiation [491].

TiO_2-based composites

CdS/TiO_2 composites prepared with uniform distribution of CdS nanocrystals dispersed on the TiO_2 surface showed excellent inactivation of *E. coli* ($\approx$ 99.9% after 10 min of visible irradiation). This is probably due to the widening of the absorption spectrum toward the visible light and the lower recombination rates of the electron-hole pairs [492]. TiO_2 has been also combined with other semiconductors for disinfection purposes. CeO_2/TiO_2 [493], SnO_2/TiO_2 [494] or ZnO/TiO_2 [495] are some examples.

5.2.2 Non-TiO_2-based photocatalysts

Metal oxides

ZnO has proved to be active for water disinfection under UV irradiation [496], with limitations similar to those of TiO_2 due to their similar band gap values (3.2 eV). ZnO has been also modified in order to enhance its photoactivity under visible light. Metal deposition of Cu^{2+} was tested and the inactivation of bacteria with Cu^{2+}-ZnO was several orders of magnitude higher than that of ZnO, commercial P25 or Cu^{2+}-TiO_2 [497]. Talebian et al. [498] synthesized SnO_2/ZnO composites by a sol-gel dip coating method at different molar ratios. The SnO_2/ZnO molar ratio of 0.5 yielded the best results in terms of bacterial inactivation. Fluorinated SnO_2 synthesized by hydrothermal method in presence of H_2O_2 has been also tested for disinfection. Highly porous hollow nanospheres with high inactivation photoactivity toward *E. coli* were obtained [499].

Metal sulfides

As indicated before, CdS has been widely investigated as photocatalyst because it shows a high absorption in the visible light range and has a low band gap value. However, it suffers from severe photo corrosion, resulting in acute lixiviation of Cd^{2+}, highly toxic. Due to this, its potential application

in water disinfection requires coupling with other materials capable of improving its photo-stability [500]. An alternative is using ternary sulfides, which are more stable in water, like $ZnIn_2S_4$. This sulfide was prepared in film and deposited over a Ti substrate, showing a higher absorption intensity in the visible light region and a good inactivation activity toward *E. coli* [501]. Combinations of sulfides, such as Ag_2S/Bi_2S_3, have shown also high bacterial inactivation under solar irradiation [502].

Bismuth metallates

Bismuth metallates, including $BiVO_4$, Bi_2WO_6, Bi_2MoO_6 and $CaBi_2O_4$, have been widely studied for water disinfection because they have shown high bacterial inactivation ability even under visible or solar irradiations. Bi_2WO_6 metallate exhibited a high inactivation toward *E. coli* under visible light [503]. Wang et al. [504] prepared $BiVO_4$ nanotubes using a solvothermal procedure and analyzed the role of ROS with the aid of different scavengers. They concluded that the major reactive species for bacterial inactivation were the photogenerated h^+. Ag deposition on different bismuth metallates has proved to increase the bacterial inactivation capacity under solar irradiation. $BiVO_4$ showed also a very high *E. coli* inactivation photoactivity under UV and/or visible light [505]. Interestingly, Bi_2MoO_6 was tested for water disinfection with blue light-emitting diode (LED) light. It showed a very high bacterial inactivation photoactivity toward *E. coli*, with the advantage of very low energy consumption compared with other light sources (although the goal should be to use solar light avoiding any electrical consumption) [506]. A composite of $Bi_2O_2CO_3/Bi_2MoO_6$, synthesized by a free solvothermal method in form of hollow nanospheres, also exhibited increased inactivation capacity toward *E. coli* under visible light irradiation [507].

Graphene-based photocatalysts

The use of graphene in photocatalytic applications, including those related with water disinfection, is spreading rapidly in the recent years. TiO_2 supported on graphene sheets showed a higher absorption in the visible light and higher *E. coli* inactivation than the bare TiO_2 [508]. A composite of 2D graphene oxide (GO) sheet, 1D TiO_2 nanorods and Ag nanoparticles was synthesized by Liu et al. [509]. This material (GO-TiO_2-Ag) exhibited significantly higher inactivation capacity toward *E. coli* than GO-TiO_2 and GO-Ag. Similarly, the combination of GO with ZnO and Ag nanoparticles (GO-ZnO-Ag) showed also enhanced efficiency under visible light [510]. GO has been combined with other semiconductors with the aim of obtaining highly active photocatalysts for water disinfection under visible/solar light, for instance, GO/Ag_3PO_4, GO/CdS or GO/Bi_2MoO_6.

Carbon nitride-based photocatalysts

Carbon nitrides (C_3N_4) have been tested as photocatalysts for water disinfection. Among them, graphitic carbon nitride (g-C_3N_4) is the most stable allotrope. Huang et al. [511] studied photocatalytic disinfection with mesoporous g-C_3N_4 prepared by condensation of cyanamide on a silica used as template. It was concluded that increase of the surface area resulted in an enhanced inactivation of *E. coli*. Further increase of the surface area was achieved by exfoliation to an atomic single layer (SL g.C_3N_4), which showed a higher bacterial inactivation than the bulk one under visible irradiation. This was attributed to the low charge transfer resistance and better charge separation [512].

Naturally-occurring photocatalysts

Natural spharelite (NS) has been used for water disinfection of different types of bacteria, namely *E. coli* and *Microbacterium barkeri*. It was shown that *M. barkeri* showed a higher resistance, probably due to its thicker cell wall [513]. Natural magnetic sphalerite (NMS) was also tested as photocatalysts in disinfection with the additional advantage of an easy separation from the water by an external magnetic field [514].

6 COMMERCIAL PHOTOCATALYSTS FOR WATER CLEANING

Despite the efforts made so far for the development of semiconductors for water treatment, most commercial photocatalysts are still based on TiO_2. Table 7 summarizes the commercial TiO_2 supplied by different companies with photocatalytic applications. Among them, P25 is commonly used as the model for comparing different photocatalytic processes. It was developed by Degussa (Evonik) with a small particle size (20-25 nm) and a mixed composition of anatase and rutile TiO_2 phases (ratio ca. 80:20). The main drawback of this commercial photocatalyst for water purification is its difficult separation and recovery from the aqueous medium. Its small particle size gives it rheological properties that allow it to form homogenous and stable aqueous suspensions.

Table 8 lists patented systems for photocatalytic water treatment. Most of them are based on TiO_2, although some other photocatalysts are also included. The type of reactor covers from slurry to tubes, planar surfaces or fibrous substrates where the photocatalyst is immobilized. The former requires a further step for catalyst separation and recovery. A particularly interesting system is the Photo-Cat, manufactured by Purifics Inc. It is a photocatalytic membrane system using TiO_2 and full-spectrum UV light, designed to remove chemical pollutants, biologicals, viruses, bromate, EDCs, PPCPs, and metals. Its main applications include drinking water, groundwater remediation, disinfection & sterilization, industrial process wastewater, high purity water, bilge and ballast water, and cleaning fluids.

Table 7 Commercial TiO_2 Photocatalysts

Commercial TiO_2 Photocatalyst	Supplier
P25 Degussa (Evonik), P90	Evonik Tego Chemie GmbH, Essen, Germany
Mikroanatas	Sachtleben Chemie GmbH, Duisburgo, Germany
Hombikat UV100, N100	Sachtleben Chemie GmbH, Duisburgo, Germany
Pretiox CG11, CG100, CG300, PK20A, CG100DSL	Precheza a.s., Czech Republic
Coteix KA-100	Coteix Co., South Korea
Millennium PC50, PC100, PC105, PC500	Millennium Inorganic Chemicals S.A.
Ishihara ST and STS series, MPT-623	Ishihara Sangyo Kaisha, LTD, Tokyo
CristalACTiVTM PC105	Cristal Global, Paris, France
Aeroxide P90/Evonik P90	Nippon Aerosil Co., LTD., Tokyo
VP Aeroperl P25/20	Nippon Aerosil Co., LTD., Tokyo

Table 8 Patented Photocatalytic Systems for Water Treatment

Name (Publication Number)	Description
Photo-Cat (US 5462674; US 5554300; US 5589078; US 6136203; US 6215126) Manufactured by Purifics Inc., Ontario. London	Slurry-type photocatalytic reactor. The incoming water stream is filtered and mixed with TiO_2 nanoparticles. Then, it passes through a 32 UV lamps reactor. TiO_2 is recovered using a ceramic membrane
System for treatment of polluted effluents (US 2017/297933 A1)	Slurry-type photocatalytic reactor. Influent water is mixed with the photocatalyst (TiO_2) and passed across a chamber holding a UV lamp. Before the stream exits the chamber, it is filtered through a membrane
Rotationally symmetric photocatalytic reactor for water purification (WO 2017/181125 A1)	Photoreactor in which the polluted water flows across a reaction tube. This tube presents a three dimensional support (silica) coated with a photocatalyst film (TiO_2). The system uses LED as UV radiation source
Adaptive catalytic technology water treatment system (US 2017/313611 A1)	This system consists of six modular stages: 1-Filtration of suspended solids; 2-Hardness reduction via electrochemical deposition and crystallization of $CaCO_3$; 3-Total Organic Carbon (TOC) removal via UVC-PhotoCatalystAlpha/Peroxide (using a UVC mercury lamp); 4-Ion-exchange for heavy metal removal; 5-Purification via UVA-PhotoCatalystBeta (using LED technology), and 6-Ultra-sound mix aeration
Photocatalytic purification of media (US 2014/0301897 A1)	Consists of a photoactive layer (TiO_2) disposed on a planar surface through which light energy is transferred. The water to be treated is kept in contact with the photocatalyst surface. The absorption of light does not take place by the side of the water but it occurs by the planar surface side
Disinfecting water device (US 2014/158641 A1)	Photocatalytic batch reactor. It consists of a first container for polluted water, a filter for removing particles and a second container for the treated stream. The photocatalyst is disposed over the filter and/or the internal faces of the container. The light source (UV) is placed in the first container
Ultraviolet photoreactor for the purification of fluids (US 2013/0323128 A1)	Photocatalytic reactor containing two different UV radiation sources. The first one (UVA, 370–385 nm) is used for activating the photocatalyst (TiO_2) and destroy organic pollutants, while the second (UVC, 265–285 nm) is for biological contaminants
Solar-activated photochemical fluid treatment (US 2013/180931 A1)	The treatment system consists of photocatalyst modules, with the possibility of being connected or not. Each module presents a fibrous substrate where the photocatalyst is coupled. Solar light illuminates the photocatalyst supported in contact with the liquid

7 CONCLUDING REMARKS AND OUTLOOK

Many opportunities related to the development of novel semiconductor photocatalysts with functional properties and the exploration of applications in water purification are still available. Current research in this area is mainly focused on the preparation of nanostructured semiconductors able to induce pollutant degradation under visible or solar light, but with low full-scale implementation, in general, so far.

TiO_2 modifications, ternary oxides, semiconductor heterojunctions, and novel nanoarchitectures offer a large number of opportunities for the preparation of functional and multifunctional semiconductors for water treatment. The photoefficiency of these semiconductors has been evaluated for the removal of different compounds, including dyes, phenolics, and other priority pollutants, but, in general, major efforts are currently focused on the degradation of emerging contaminants (pharmaceuticals, PCCPs, pesticides, industrial additives, and cyanotoxins, among others) as well as on the inactivation of pathogenic germs. To go further in this field, researchers have to find ways to implement the application of these semiconductor photocatalysts at industrial scale. In this way, the fundamental understanding of the semiconductors' behavior and the mechanism of the photocatalytic reactions will help in the exploration of process scale-up. The main issues are the separation and recovery of the photocatalyst, the design of optimal reactors, the operating conditions for using sunlight, and, of course, the nature of the pollutant.

ACKNOWLEDGMENTS

Financial support by project CTQ2016-78576-R (*Spanish National Program* $I+D+i$) is fully acknowledged. M. Peñas-Garzón thanks *Spanish* MECD for FPU16/00576 grant.

REFERENCES

[1] S.E. Braslavsky, Glossary of terms used in photochemistry, 3rd edition (IUPAC Recommendations 2006), Pure Appl. Chem. 79 (2007) 293–465.
[2] O. Carp, C.L. Huisman, A. Reller, Photoinduced reactivity of titanium dioxide, Prog. Solid State Chem. 32 (2004) 33–177.
[3] S.-Y. Lee, S.-J. Park, TiO_2 photocatalyst for water treatment applications, J. Ind. Eng. Chem. 19 (2013) 1761–1769.
[4] A. Mills, S. Le Hunte, An overview of semiconductor photocatalysis, J. Photochem. Photobiol. 108 (1997) 1–35.
[5] S. Ahmed, D.F. Ollis, Solar photoassisted catalytic decomposition of the chlorinated hydrocarbons trichloroethylene and trichloromethane, Sol. Energy 32 (1984) 597–601.
[6] M.R. Hoffmann, S.T. Martin, W. Choi, D.W. Bahnemann, Environmental applications of semiconductor photocatalysis, Chem. Rev. 95 (1995) 69–96.
[7] M. Schiavello, A. Sclafani, Thermodynamic and kinetic aspects in photocatalysis, in: N. Serpone, E. Pelizzetti (Eds.), Photocatalysis: Fundamentals and Applications, John Wiley and Sons, Inc, New York, 1989, pp. 159–173.
[8] A. Fujishima, X. Zhang, D.A. Trik, TiO_2 photocatalysis and related surface phenomena, Surf. Sci. Rep. 63 (2008) 515–582.
[9] Y. Boyjoo, H. Sun, J. Liu, V.K. Pareek, S. Wang, A review on photocatalysis for air treatment: from catalyst development to reactor design, Chem. Eng. J. 310 (2017) 537–559.
[10] G. Colón, C. Belver, M. Fernández-García, Nanostructured oxides in photo-catalysis, in: M. Fernández-García, J.A. Rodríguez (Eds.), Synthesis, Properties and Application of Oxide Nanoparticles, John Wiley & Sons, Inc, Hoboken, New Jersey, 2007, pp. 491–562.
[11] J.H. Pan, H. Dou, Z. Xiong, C. Xu, J. Ma, X.S. Zhao, Porous photocatalysts for advanced water purifications, J. Mater. Chem. 20 (2010) 4512–4528.

[12] M. Formenti, F. Juillet, S.J. Teichner, Controlled photooxidation of paraffins and olefins over anatase at room temperature, C. R. Seances Acad. Sci. Ser. C 270C (1970) 138–141.
[13] A. Fujishima, K. Honda, Electrochemical photolysis of water at a semiconductor electrode, Nature 238 (1972) 37–38.
[14] J. Plotnikow, Textbook of Photochemistry, Verlag von Willhelm Knapp, Berlin, 1910. 72 p.
[15] A. Eibner, Action of light on pigments I, Chem.-Ztg. 35 (1911) 753–755.
[16] L. Bruner, J. Kozak, Information on the photocatalysis: the light reaction in uranium salt plus oxalic acid mixtures, Z. Elktrochem. Angew. P. 17 (1911) 354–360.
[17] M. Landau, Le phénomène de la photocatalyse, Compt. Rend. 156 (1913) 1894–1896.
[18] C. Renz, Photo-reactions of the oxides of titanium, cerium, and the earth-acids, Helv. Chim. Acta 4 (1921) 961–968.
[19] E. Baur, A. Perret, On the action of light on dissolved silver salts in the presence of zinc oxide, Helv. Chim. Acta 7 (1924) 910–915.
[20] E. Baur, C. Neuweiler, On the photocatalytic formation of hydroperoxide, Helv. Chim. Acta 10 (1927) 901–907.
[21] C. Renz, Photoreduktionen von Metalloxyden, Helv. Chim. Acta 15 (1932) 1077–1084.
[22] C.F. Goodeve, J.A. Kitchener, Photosensitisation by titanium dioxide, Trans. Faraday Soc. 34 (1938) 570–579.
[23] A.E. Jacobsen, Titanium dioxide pigments: correlation between photochemical reactivity and chalking, Ind. Eng. Chem. 41 (1949) 523–526.
[24] M.C. Markham, K.J. Laidler, A kinetic study of photo-oxidations on the surface of zinc oxide in aqueous suspensions, J. Phys. Chem. 57 (1953) 363–369.
[25] T.R. Rubin, J.G. Calvert, G.T. Rankin, W. MacNevin, Photochemical synthesis of hydrogen peroxide at zinc oxide surfaces, J. Am. Chem. Soc. 75 (1953) 2850–2853.
[26] M.C. Markham, Photocatalyitic properties of oxides, J. Chem. Educ. 32 (1955) 540–543.
[26a] D.R. Kennedy, R. Mowbray, J. Mackenzie, The photosorption of oxygen and nitric oxide on titanium dioxide, Trans. Faraday Soc. 54 (1958) 119–129.
[27] J.C. Kuriacose, M.C. Markham, Mechanism of the photo-initiated polymerization of methyl methacrylate at zinc oxide surfaces, J. Phys. Chem. 65 (1961) 2232–2236.
[28] W. Doerfler, K. Hauffe, Heterogeneous photocatalysis II: the mechanism of the carbon monoxide oxidation at dark and illuminated zinc oxide surfaces, J. Catal. 3 (1964) 171–178.
[29] V.N. Filimonov, Photocatalytic oxidation of gaseous isopropanol on ZnO + TiO_2, Dokl. Akad. Nauk SSSR 154 (1964) 922–925.
[30] M.C. Markham, M.C. Upreti, Photoelectric effects at semiconductor electrodes, J. Catal. 4 (1965) 229–238.
[31] A. Fujishima, K. Honda, S.-I. Kikuchi, Photosensitized electrolytic oxidation on semiconducting n-type TiO_2 electrode, J. Chem. Soc. Japan 72 (1969) 108–113.
[32] B. Gupta, A.A. Melvin, T. Matthews, S. Dash, A.K. Tyagi, TiO2 modification by gold (Au) for photocatalytic hydrogen (H_2) production, Renew. Sust. Energ. Rev. 58 (2016) 1366–1375.
[33] A.A. Ismail, D.W. Bahnemann, Photochemical splitting of water for hydrogen production by photocatalysis: a review, Sol. Energy Mater. Sol. Cells 128 (2014) 85–101.
[34] X. Li, J. Yu, M. Jaroniec, Hierarchical photocatalysts, Chem. Soc. Rev. 45 (2016) 2603–2636.
[35] X. Zhang, L. Wang, Q. Du, Z. Wang, S. Ma, M. Yu, Photocatalytic CO_2 reduction over B_4C/C_3N_4 with internal electric field under visible light irradiation, J. Colloid Interface Sci. 464 (2016) 89–95.
[36] J. Chen, S. Qin, G. Song, T. Xiang, F. Xin, X. Yin, Shape-controlled solvothermal synthesis of Bi_2S_3 for photocatalytic reduction of CO_2 to methyl formate in methanol, Dalton Trans. 42 (2013) 15133–15138.
[37] W. Tu, Y. Zhou, Q. Liu, S. Yan, S. Bao, X. Wang, M. Xiao, Z. Zou, An in situ simultaneous reduction-hydrolysis technique for fabrication of TiO_2-graphene 2D sandwich-like hybrid nanosheets:

graphene-promoted selectivity of photocatalytic-driven hydrogenation and coupling of CO_2 into methane and ethane, Adv. Funct. Mater. 23 (2013) 1743–1749.
[38] A. Di Paola, E. García-López, G. Marci, L. Palmisano, A survey of photocatalytic materials for environmental remediation, J. Hazard. Mater. 211–212 (2012) 3–29.
[39] Q. Huang, W.J. Ma, X.K. Yan, Y.W. Chen, S.M. Zhu, S.B. Shen, Photocatalytic decomposition of gaseous HCHO by $Zr_xTi_{1-x}O_2$ catalysts under UV–vis light irradiation with an energy-saving lamp, J. Mol. Catal. A 366 (2013) 261–265.
[40] Y. Shen, L.F. Wang, Y.B. Wu, X.Y. Li, Q.D. Zhao, Y. Hou, W. Teng, Facile solvothermal synthesis of MnFe2O4 hollow nanospheres and their photocatalytic degradation of benzene investigated by in situ FTIR, Catal. Commun. 68 (2015) 11–14.
[41] D. Yue, X. Qian, Y. Zhao, Photocatalytic remediation of ionic pollutant, Sci. Bull. 60 (2015) 1791–1806.
[42] P. Pichat, M. Schiavello (Ed.), Photocatalysis and Environment: Trends and Applications, NATO Advanced Study Institute on New Trends and Applications, Kluwer Academic Publishers, Dordrecht, Boston, 1993, 399 p.
[43] M. Compagnoni, G. Ramis, F.S. Freyria, M. Armandi, B. Bonelli, I. Rossetti, Photocatalytic processes for the abatement of N-containing pollutants from waste water. Part 1: inorganic pollutants, J. Nanosci. Nanotechnol. 17 (2017) 1–22.
[44] R. Fagan, D.E. McCormack, D.D. Dionysiou, S.C. Pillai, A review of solar and visible light active TiO_2 photocatalysis for treating bacteria, cyanotoxins and contaminants of emerging concern, Mater. Sci. Semicond. Process. 42 (2016) 2–14.
[45] A.R. Ribeiro, O.C. Nunes, M.F.R. Pereira, A.M.T. Silva, An overview on the advanced oxidation processes applied for the treatment of water pollutants defined in the recently launched Directive 2013/39/EU, Environ. Int. 75 (2015) 33–51.
[46] A. Kubacka, M. Fernández-García, G. Colón, Advanced nanoarchitectures for solar photocatalytic applications, Chem. Rev. 112 (2012) 1555–1614.
[47] J. Rivera-Utrilla, M. Sánchez-Polo, M.A. Ferro-García, G. Prados-Joya, R. Ocampo-Pérez, Pharmaceuticals as emerging contaminants and their removal from water. A review, Chemosphere 93 (2013) 1268–1287.
[48] M. Boas, U. Feldt-Rasmussen, K.M. Main, Thyroid effects of endocrine disrupting chemicals, Mol. Cell. Endocrinol. 355 (2012) 240–248.
[49] P.K.J. Robertson, J.M.C. Robertson, D.W. Bahnemann, Removal of microorganisms and their chemical metabolites from water using semiconductor photocatalysis, J. Hazard. Mater. 211–212 (2012) 161–171.
[50] A.A. De la Cruz, A. Hiskia, T. Kaloudis, N. Chernoff, D. Hill, M.G. Antoniou, X. He, K. Loftin, K. O'Shea, C. Zhao, M. Pelaez, C. Han, T.J. Lynch, D.D. Dionysiou, A review on cylindrospermopsin: the global occurrence, detection, toxicity and degradation of a potent cyanotoxins, Environ. Sci. Process Impacts 15 (2013) 1979–2003.
[51] S. Merel, D. Walker, R. Chicana, S. Snyder, E. Baurès, O. Thomas, State of knowledge and concerns on cyanobacterial blooms and cyanotoxins, Environ. Int. 59 (2013) 303–327.
[52] M.N. Chong, B. Jin, C.W.K. Chow, C. Saint, Recent developments in photocatalytic water treatment technology: a review, Water Res. 44 (2010) 2997–3027.
[53] A. Hoffmann, E.R. Carraway, M. Hoffmann, Photocatalytic production of H_2O_2 and organic peroxides on quantum-sized semiconductor colloids, Environ. Sci. Technol. 28 (1994) 776–785.
[54] C. Chen, W. Ma, J. Zhao, Semiconductor-mediated photodegradation of pollutants under visible-light irradiation, Chem. Soc. Rev. 39 (2010) 4206–4219.
[55] B. Ohtani, Preparing articles on photocatalysis—beyond the illusions, misconceptions, and speculation, Chem. Lett. 37 (2008) 217–229.
[56] H. Park, Y. Park, W. Kim, W. Choi, Surface modification of TiO_2 photocatalyst for environmental applications, J. Photochem. Photobiol. C 15 (2013) 1–20.

[57] R. Salvador, On the nature of photogenerated radical species active in the oxidative degradation of dissolved pollutants with TiO_2 aqueous suspensions: a revision in the light of the electronic structure of adsorbed water, J. Phys. Chem. C 111 (2007) 17038–17043.
[58] G. Colón-Ibañez, C. Belver-Coldeira, M. Fernandez-Garcia, Nanostructured oxides in photo-catalysis, in: J. A. Rodríguez, M. Fernández-García (Eds.), Synthesis, Properties, and Applications of Oxide Nanomaterials, John Wiley & Sons, Inc, New Jersey, 2006, pp. 491–562. Chapter 17.
[59] H. Tada, Q. Jin, A. Iwaszuk, M. Nolan, Molecular-scale transition metal oxide nanocluster surface-modified titanium dioxide as solar-activated environmental catalysts, J. Phys. Chem. C 118 (2014) 12077–12086.
[60] J. Yu, X. Yu, Hydrothermal synthesis and photocatalytic activity of zinc oxide hollow spheres, Environ. Sci. Technol. 42 (2008) 4902–4907.
[61] J. Yu, J. Zhang, S. Liu, Ion-exchange synthesis and enhanced visible-light photoactivity of CuS/ZnS nanocomposite hollow spheres, J. Phys. Chem. C 114 (2010) 13642–13649.
[62] S. Ahuja, T.R.N. Kutty, Nanoparticles of $SrTiO_3$ prepared by gel to crystallite conversion and their photocatalytic activity in the mineralization of phenol, J. Photochem. Photobiol. A 97 (1996) 99–107.
[63] P. Wang, C. Fan, Y. Wang, G. Ding, P. Yuan, A dual chelating sol–gel synthesis of $BaTiO_3$ nanoparticles with effective photocatalytic activity for removing humic acid from water, Mater. Res. Bull. 48 (2013) 869–877.
[64] H. Fu, J. Lin, L. Zhang, Y. Zhu, Photocatalytic activities of a novel $ZnWO_4$ catalyst prepared by a hydrothermal process, Appl. Catal. A 306 (2006) 58–67.
[65] P. Madhusudan, J. Ran, J. Zhang, J. Yu, G. Liu, Novel urea assisted hydrothermal synthesis of hierarchical $BiVO_4/Bi_2O_2CO_3$ nanocomposites with enhanced visible-light photocatalytic activity, Appl. Catal. B 110 (2011) 286–295.
[66] Q. Wang, J.Y. Huang, H.Q. Li, Z. Chen, A.Z. Zhao, Y. Wang, K.Q. Zhang, H.T. Sun, S.S. Al-Deyab, Y.K. Lai, TiO_2 nanotube platforms for smart drug delivery: a review, Int. J. Nanomedicine 11 (2016) 4819–4834.
[67] M. Pelaez, N.T. Nolan, S.C. Pillai, M.K. Seery, P. Falaras, A.G. Kontos, P.S.M. Dunlop, J.W.J. Hamilton, J.A. Byrne, K. O'Shea, M.H. Entezari, D.D. Dionysiou, A review on the visible light active titanium dioxide photocatalysts for environmental applications, Appl. Catal. B 125 (2012) 331–349.
[68] M. Anpo, M. Takeuchi, The design and development of highly reactive titanium oxide photocatalysts operating under visible light irradiation, J. Catal. 216 (2003) 505–516.
[69] B. Bayarri, J. Gimenez, D. Curco, S. Esplugas, Photocatalytic degradation of 2,4-dichlorophenol by TiO2/UV: kinetics, actinometries and models, Catal. Today 101 (2005) 227–236.
[70] G.L. Puma, P.L. Yue, Effect of radiation wavelength on the rate of photocatalytic oxidation of organic pollutants, Ind. Eng. Chem. Res. 41 (2002) 5594–5600.
[71] H. Zangeneh, A.A.L. Zinatizadeh, M. Habibi, M. Akia, M. Hasnain Isa, Photocatalytic oxidation of organic dyes and pollutants in wastewater using different modified titanium dioxides: a comparative review, J. Ind. Eng. Chem. 26 (2015) 1–36.
[72] F.J. Beltran, F.J. Rivas, O. Gimeno, Comparison between photocatalytic ozonation and other oxidation processes for the removal of phenols from water, J. Chem. Technol. Biotechnol. 80 (2005) 973–984.
[73] K. Mogyorosi, A. Farkas, I. Dekany, TiO_2-based photocatalytic degradation of 2-chlorophenol adsorbed on hydrophobic clay, Environ. Sci. Technol. 36 (2002) 3618–3624.
[74] N. Guettaï, A. Amar, H. Amar, Photocatalytic oxidation of methyl orange in presence of titanium dioxide in aqueous suspension. Part I: parametric study, Desalination 185 (2005) 427–437.
[75] A.E. Cassano, O.M. Alfano, Reaction engineering of suspended solid heterogeneous photocatalytic reactors, Catal. Today 58 (2000) 167–197.
[76] J. Herrmann, P. Pichat, Heterogeneous photocatalysis oxidation of halide ions by oxygen in ultraviolet irradiated aqueous suspension of titanium dioxide, J. Chem. Soc. Faraday Trans. 1 (1980) 1138–1146.

[77] U.I. Gaya, A.H. Abdullah, Heterogeneous photocatalytic degradation of organic contaminants over titanium dioxide: a review of fundamentals, progress and problems, J Photochem Photobiol C: Photochem Rev 9 (2008) 1–12.
[78] H. Shirayama, Y. Tohezo, S. Taguchi, Photodegradation of chlorinated hydrocarbons in the presence and absence of dissolved oxygen in water, Water Res. 35 (2001) 1941–1950.
[79] Y. Wang, C. Hong, TiO_2 mediated photomineralization of 2-chlorobiphenyl: the role of oxygen, Water Res. 34 (2000) 2791–2797.
[80] M. Bertelli, E. Selli, Reaction paths and efficiency of photocatalysis on TiO_2 and of H_2O_2 photolysis in the degradation of 2-chlorophenol, J. Hazard. Mater. B 138 (2006) 46–52.
[81] C.-H. Chiou, C.-Y. Wu, R.-S. Juang, Influence of operating parameters on photocatalytic degradation of phenol in UV/TiO2 process, Chem. Eng. J. 139 (2008) 322–329.
[82] W. Chu, C.C. Wong, The photocatalytic degradation of dicamba in TiO2 suspension with the help of hydrogen peroxide by different near irradiation, Water Res. 38 (2003) 1037–1043.
[83] N. Daneshvar, M.A. Behnajady, Y.Z. Asghar, Photooxidative degradation of 4-nitrophenol in UV/H2O2 process: influence of operational parameters and reaction mechanism, J. Hazard. Mater. B 139 (2007) 275–279.
[84] E.J. Roenfeldt, K.G. Linden, S. Canonica, U. von Gunten, Comparison of the efficiency of OH radical formation during ozonation and the advanced oxidation processes O_3/H_2O_2 and UV/H_2O_2, Water Res. 40 (2006) 3695–3704.
[85] T. Yonar, K. Kestioglu, N. Azbar, Treatability studies on domestic wastewater using UV/H_2O_2 process, Appl. Catal. B Environ. 67 (2006) 223–228.
[86] M. Faisal, M. Abu Tariq, M. Muneer, Photocatalysed degradation of two selected dyes in UV-irradiated aqueous suspensions of titania, Dyes Pigments 72 (2007) 233–239.
[87] K. Okamoto, Y. Yamamoto, H. Tanaka, M. Tanaka, A. Itaya, Heterogeneous photocatalytic decomposition of phenol over TiO_2 powder, Bull. Chem. Soc. Jpn. 58 (1985) 2015–2022.
[88] S. Ahmed, G.M. Rasul, N.W. Martens, R. Brown, A.M. Hasib, Advances in heterogeneous photocatalytic degradation of phenols and dyes in wastewater: a review, Water Air Soil Pollut. 215 (2011) 3–29.
[89] V. Kruefu, H. Ninsonti, N. Wetchakun, B. Inceesungvorn, P. Pookmanee, S. Phanichpant, Photocatalytic degradation of phenol using Nb-doped ZnO nanoparticles, Eng. J. Can. 163 (2012) 90–99.
[90] W. Zhang, X.T. Chen, Y. Han, S.Y. Yao, Effect of SnO_2 addition on phase transformation of TiO_2 photocatalyst prepared by sol–gel method, Rare Metals 30 (2011) 229–232.
[91] R.W. Matthews, E. Pelizzetti, M. Schiavello (Eds.), Photochemical Conversion and Storage of Solar Energy, Kluwer Academic Publishers, Dordrecht, 1991, pp. 427–449.
[92] A. Fujishima, T.N. Rao, D.A. Tryk, Titanium dioxide photocatalysis, J. Photochem. Photobiol. C 1 (2000) 1–21.
[93] A.L. Linsebigler, G. Lu, J.T. Yates Jr., Photocatalysis on TiO_2 surfaces: principles, mechanisms, and selected results, Chem. Rev. 95 (1995) 735–758.
[94] C.-Y. Hsiao, C.-L. Lee, D.F. Ollis, Heterogeneous photocatalysis: degradation of dilute solutions of dichloromethane (CH_2Cl_2), chloroform ($CHCl_3$), and carbon tetrachloride (CCl_4) with illuminated TiO_2 photocatalyst, J. Catal. 82 (1983) 418–423.
[95] A.L. Pruden, D.F. Ollis, Photoassisted heterogeneous catalysis: the degradation of trichloroethylene in water, J. Catal. 82 (1983) 404–417.
[96] D.W. Bahnemann, D. Bockelmann, R. Goslich, M. Hilgendorff, D. Weichgrebe, Photocatalytic detoxification: novel catalysts mechanisms and solar applications, in: D.F. Ollis, H. Al-Ekabi (Eds.), Photocatalytic Purification and Treatment of Water and Air, Elsevier Science Publisher BV, Amsterdam, 1993, pp. 301–319.
[97] M. Plodinec, A. Gajović, G. Jakša, K. Žag, M. Čeh, High-temperature hydrogenation of pure and silver-decorated titanate nanotubes to increase their solar absorbance for photocatalytic applications, J. Alloys Compd. 591 (2014) 147–155.

[98] P. Roy, S. Berger, P. Schmuki, TiO2 nanotubes: synthesis and applications, Angew. Chem. Int. Ed. 50 (2011) 2904–2939.
[99] R. Asahi, Y. Taga, W. Mannstadt, A.J. Freeman, Electronic and optical properties of anatase TiO_2, Phys. Rev. B 61 (2000) 7459–7465.
[100] J.K. Burdett, T. Hughbands, J.M. Gordon, J.W. Richarson, J. Smith, Structural electronic relationships in inorganic solids—powder neutron-diffraction studies of the rutile and anatase polymorphs of titanium-dioxide at 15 and 295-K, J. Am. Chem. Soc. 109 (1987) 3639–3646.
[101] R.I. Bickley, T. Gonzalez-Carreno, J.S. Lees, L. Palmisano, R.J.D. Tilley, A structural investigation of titanium dioxide photocatalysts, J. Solid State Chem. 92 (1991) 178–190.
[102] T. Ohno, K. Sarukawa, K. Tokieda, M. Matsumura, Morphology or a TiO_2 photocatalyst (Degussa P-25) consisting of anatase and rutile crystalline phases, J. Catal. 203 (2001) 82–86.
[103] N. Savage, M.S. Diallo, Nanomaterials and water purification: opportunities and challenges, J. Nanopart. Res. 7 (2005) 331–342.
[104] A. Adesina, Industrial exploitation of photocatalysis progress, perspectives and prospects, Catal. Surv. Jpn. 8 (2004) 265–273.
[105] S.O. Obare, G.J. Meyer, Nanostructured materials for environmental remediation of organic contaminants in water, J. Environ. Sci. Health A 39 (2004) 2549–2582.
[106] N. Chitose, S. Ueta, T.A. Yamamoto, Radiolysis of aqueous phenol solutions with nanoparticles. 1. Phenol degradation and TOC removal in solutions containing TiO_2 induced by UV, gamma-ray and electron beams, Chemosphere 50 (2003) 1007–1013.
[107] K. Kabra, R. Chaudhary, R.L. Sawhney, Treatment of hazardous organic and inorganic compounds through aqueous-phase photocatalysis: a review, Ind. Eng. Chem. Res. 43 (2004) 7683–7696.
[108] W. Choi, S.J. Hong, Y. Chang, Y. Cho, Photocatalytic degradation of polychlorinated dibenzo-p-dioxins on TiO_2 film under UV or solar light irradiation, Environ. Sci. Technol. 34 (2000) 4810–4815.
[109] H. Lachheb, E. Puzenat, A. Houas, M. Ksibi, E. Elaloui, C. Guillard, J.-M. Herramann, Photocatalytic degradation of various types of dyes (Alizarin S, Crocein Orange G, Methyl Red, Congo Red, Methylene Blue) in water by UV-irradiated titania, Appl. Catal. B Environ. 39 (2002) 75–90.
[110] M. Muruganandham, M. Swaminathan, Photocatalytic decolourisation and degradation of Reactive Orange 4 by TiO_2-UV process, Dyes Pigments 68 (2006) 133–142.
[111] C.R. Chenthamarakshan, K. Rajeshwar, Heterogeneous photocatalytic reduction of Cr(VI) in UV-irradiated titania suspensions: effect of protons, ammonium ions, and other interfacial aspects, Langmuir 16 (2000) 2715–2721.
[112] Y. Ku, I.-L. Jung, Photocatalytic reduction of Cr(VI) in aqueous solutions by UV irradiation with the presence of titanium dioxide, Water Res. 35 (2001) 135–142.
[113] J.K. Yang, S.M. Lee, M. Farrokhi, O. Giahi, M. Shirzad Siboni, Photocatalytic removal of Cr(VI) with illuminated TiO2, Desalin. Water Treat. 46 (2012) 375–380.
[114] Y. Yonezawa, N. Kometani, T. Sakaue, A. Yano, Photoreduction of silver ions in a coloidal titanium dioxide suspension, J. Photochem. Photobiol. A Chem. 171 (2005) 1–8.
[115] S.-Y. Lee, K.Y. Rhee, S.-J. Park, Effect of hydrothermal temperature on photocatalytic properties of TiO_2 nanotubes, Curr. Appl. Phys. 14 (2014) 415–420.
[116] Y.L. Pang, S. Lim, H.C. Ong, W.T. Chong, A critical review on the recent progress of synthesizing techniques and fabrication of TiO_2-based nanotubes photocatalysts, Appl. Catal. A 481 (2014) 127–142.
[117] Y. Wang, Y. He, Q. Lai, M. Fan, Review of the progress in preparing nano TiO_2: an important environmental engineering material, J. Environ. Sci. 26 (2014) 2139–2177.
[118] A. Amarjargal, L.D. Tijing, M.T.G. Ruelo, D.H. Lee, C.S. Kim, Facile synthesis and immobilization of Ag-TiO_2 nanoparticles on electrospun PU nanofibers by polyol technique and simple immersion, Mater. Chem. Phys. 135 (2012) 277–281.

[119] Y. Xu, W. Wen, J.-M. Wu, Titania nanowires functionalized polyester fabrics with enhanced photocatalytic and antibacterial performances, J. Hazard. Mater. 343 (2018) 285–297.
[120] M. Li, Y. Jiang, R. Ding, D. Song, H. Yu, Z. Chen, Hydrothermal synthesis of anatase TiO_2 nanoflowers on a nanobelt framework for photocatalytic applications, J. Electron. Mater. 42 (2013) 1290–1296.
[121] D.V. Bavykin, J.M. Friedrich, F.C. Walsh, Protonated titanates and TiO_2 nanostructured materials: synthesis, properties and applications, Adv. Mater. 18 (2006) 2807–2824.
[122] K.-C. Huang, S.-H. Chien, Improved visible-light-driven photocatalytic activity of rutile/titania-nanotube composites prepared by microwave-assisted hydrothermal process, Appl. Catal. B 140/141 (2013) 283–288.
[123] T. Kasuga, M. Hiramatsu, A. Hoson, T. Sekino, K. Niihara, Formation of titanium oxide nanotube, Langmuir 14 (1998) 3160–3163.
[124] V. Zwilling, E. Darque-Ceretti, A. Boutry-Forveille, D. David, M.Y. Perrin, M. Aucouturier, Structure and physicochemistry of anodic oxide films on titanium and TA6V alloy, Surf. Interface Anal. 27 (1999) 629–637.
[125] W.L. Chin, S. Srimala, Incorporation of WO_3 species into TiO_2 nanotubes via wet impregnation and their water-splitting performance, Electrochim. Acta 87 (2013) 294–302.
[126] D.L. Jiang, S.Q. Zhang, H.J. Zhao, Photocatalytic degradation characteristics of different organic compounds at TiO_2 nanoporous film electrodes with mixed anatase/rutile phases, Environ. Sci. Technol. 41 (2007) 303–308.
[127] H. Jiang, Q. Wang, S. Zang, J. Li, Q. Wang, Enhanced photoactivity of Sm, N, P-tridoped anatase-TiO_2 nano-photocatalyst for 4-chlorophenol degradation under sunlight irradiation, J. Hazard. Mater. 261 (2013) 44–54.
[128] W.S. Lin, C.H. Huang, W.J. Yang, C.Y. Hsu, K.H. Hou, Photocatalytic TiO_2 films deposited by rf magnetron sputtering at different oxygen partial pressure, Curr. Appl. Phys. 10 (2010) 1461–1466.
[129] H. Liu, G. Liu, Q. Zhou, Preparation and characterization of Zr doped TiO_2 nanotube arrays on the titanium sheet and their enhanced photocatalytic activity, J. Solid State Chem. 182 (2009) 3238–3242.
[130] L.T. Mancic, B.A. Marinkovic, P.M. Jardim, O.B. Milosevic, F. Rizzo, Precursor particle size as the key parameter for isothermal tuning of morphology from nanofibers to nanotubes in the $Na_{2-x}H_xTi_nO_{2n+1}$ system through hydrothermal alkali treatment of rutile mineral sand, Cryst. Growth Des. 9 (2009) 2152–2158.
[131] A.N. Oket, O. Yilmaz, Characteristics of lanthanum loaded TiO_2-ZSM-5 photocatalysts: decolorization and degradation processes of methyl orange, Appl. Catal. A Gen. 354 (2009) 132–142.
[132] P. Pucher, M. Benmami, R. Azouani, G. Krammer, K. Chhor, J.F. Bocquet, A.V. Kanaev, Nano-TiO_2 sols immobilized on porous silica as new efficient photocatalyst, Appl. Catal. A Gen. 332 (2007) 297–303.
[133] M.V. Rao, K. Rajeshwar, V.R. Vernerker, J. Dubow, Photosynthetic production of hydrogen and hydrogen peroxide on semiconducting oxide grains in aqueous solutions, J. Phys. Chem. 84 (1980) 1987–1991.
[134] F.Y. Wei, H.L. Zeng, P. Cui, S.C. Peng, T.H. Cheng, Various TiO_2 microcrystals: controlled synthesis and enhanced photocatalytic activities, Chem. Eng. J. 144 (2008) 119–123.
[135] H. Wu, Z. Zhang, Photoelectrochemical water splitting and simultaneous photoelectrocatalytic degradation of organic pollutant on highly smooth and ordered TiO_2 nanotube arrays, J. Solid State Chem. 184 (2011) 3202–3207.
[136] F. Xianliang, H. Yingfei, Y. Yunguang, L. We, C. Shifu, Ball milled h-BN: an efficient holes transfer promoter to enhance the photocatalytic performance of TiO_2, J. Hazard. Mater. 244 (2013) 102–110.
[137] M.A. Barakat, H. Schaeffer, G. Hayes, S. Ismat Shah, Photocatalytic degradation of 2-chlorophenol by Co-doped TiO_2 nanoparticles, Appl. Catal. B Environ. 57 (2005) 23–30.
[138] V. Brezová, A. Blažková, L. Karpinský, J. Grošková, B. Havlínová, V. Jorík, M. Čeppan, Phenol decomposition using M^{n+}/TiO_2 photocatalysts supported by the sol-gel technique on glass fibres, J. Photochem. Photobiol. A Chem. 109 (1997) 177–183.
[139] M. Litter, Heterogeneous photocatalysis: transition metal ions in photocatalytic systems, Appl. Catal. B Environ. 23 (1999) 89–114.

[140] P. Vijayan, C. Mahendiran, C. Suresh, K. Shanthi, Photocatalytic activity of iron doped nanocrystalline titania for the oxidative degradation of 2,4,6-trichlorophenol, Catal. Today 141 (2009) 220–224.
[141] K. Wilke, H.D. Breuer, The influence of transition metal doping on the physical and photocatalytic properties of titania, J. Photochem. Photobiol. A Chem. 121 (1999) 49–53.
[142] D. Dvoranová, V. Brezová, M. Mazúr, M.A. Malati, Investigations of metal-doped titanium dioxide photocatalysts, Appl. Catal. B Environ. 37 (2002) 91–105.
[143] W. Lee, W.-M. Gao, K. Dwight, A. Wold, Preparation and characterization of titanium (IV) oxide photocatalysts, Mater. Res. Bull. 27 (1992) 685–692.
[144] C.-H. Chiou, R.-S. Juang, Photocatalytic degradation of phenol in aqueous solutions by Pr-doped TiO_2 nanoparticles, J. Hazard. Mater. 149 (2007) 1–7.
[145] D. De la Cruz Romero, G. Torres Torres, J.C. Arévalo, R. Gomez, A. Aguilar-Elguezabal, Synthesis and characterization of TiO_2 doping with rare earths by sol–gel method: photocatalytic activity for phenol degradation, J. Sol-Gel Sci. Technol. 56 (2010) 219–226.
[146] O. Xiuqin, M. Junping, W. Qimin, Y. Junmei, Enhanced photoactivity of layered nanocomposite materials containing rare earths, titanium dioxide and clay, J. Rare Earths 24 (2006) 251–254.
[147] H. Tinghong, M. Jian, Z. Xiaodong, T. Minding, STM and STS investigations of Ce-doped TiO_2 nanoparticles, Rare Metals 25 (2006) 331–336.
[148] F.B. Li, X.Z. Li, M.F. Hou, Photocatalytic degradation of 2-mercaptobenzothiazole in aqueous La^{3+}–TiO_2 suspension for odor control, Appl. Catal. B Environ. 48 (2004) 185–194.
[149] F. Dong, W. Zhao, Z. Wu, Characterization and photocatalytic activities of C, N and S co-doped TiO_2 with 1D nanostructure prepared by the nano-confinement effect, Nanotechnology 19 (2008) 365607–365616.
[150] M. Grandcolas, J. Ye, Preparation of fine, uniform nitrogen- and sulfur-modified TiO2 nanoparticles from titania nanotubes, Sci. Technol. Adv. Mater. 11 (2010) 1–6.
[151] J.C. Yu, J.G. Yu, W.K. Ho, Z.T. Jiang, L.Z. Zhang, Effects of F-doping on the photocatalytic activity and microstructures of nanocrystalline TiO_2 powders, Chem. Mater. 14 (2002) 3808–3816.
[152] J.C. Yu, L.Z. Zhang, Z. Zheng, J.C. Zhao, Synthesis and characterization of phosphated mesoporous titanium dioxide with high photocatalytic activity, Chem. Mater. 15 (2003) 2280–2286.
[153] B. Yu, W.M. Yu, J. Yang, Preparation and characterization of N–TiO_2 photocatalyst with high crystallinity and enhanced photocatalytic inactivation of bacteria, Nanotechnology 24 (2013) 335705–335709.
[154] A. Vijayabalan, K. Selvam, B. Krishnakumar, M. Swaminathan, Photocatalytic degradation of Reactive Orange 4 by surface fluorinated TiO_2 Wackherr under UV-A light, Sep. Purif. Technol. 108 (2013) 51–56.
[155] A. Touati, T. Hammedi, W. Najjar, Z. Ksibi, S. Sayadi, Photocatalytic degradation of textile wastewater in presence of hydrogen peroxide: effect of cerium doping titania, J. Ind. Eng. Chem. 35 (2016) 36–44.
[156] D.R. Reddy, G.K. Dinesh, S. Anandan, T. Sivasankar, Sonophotocatalytic treatment of Naphthol Blue Black dye and real textile wasterwater using synthesized Fe doped TiO_2, Chem. Eng. Process. 99 (2016) 10–18.
[157] A. Galenda, L. Crociani, N. El Habra, M. Favaro, M.M. Natile, G. Rossetto, Effect of reaction conditions on methyl red degradation mediated by boron and nitrogen doped TiO_2, Appl. Surf. Sci. 314 (2014) 919–930.
[158] A. Ayati, A. Ahmadpour, F.F. Bamoharram, B. Tanhaei, M. Mänttäri, M. Sillanpää, A review on catalytic applications of Au/TiO_2 nanoparticles in the removal of water pollutant, Chemosphere 107 (2014) 163–174.
[159] M.M. Kondo, W.F. Jardim, Photodegradation of chloroform and urea using Ag-loaded titanium dioxide as catalyst, Water Res. 25 (1991) 823–827.
[160] S. Rengaraj, X.Z. Li, Enhanced photocatalytic activity of TiO_2 by doping with Ag for degradation of 2,4,6-trichlorophenol in aqueous suspension, J. Mol. Catal. A Chem. 243 (2006) 60–67.
[161] M.A. Behnajady, N. Modirshahla, M. Shokri, B. Rad, Enhancement of photocatalytic activity of TiO_2 nanoparticles by silver doping: photodeposition versus liquid impregnation methods, Global Nest J. 10 (2008) 1–7.
[162] N. Sobana, K. Selvam, M. Swaminathan, Optimization of photocatalytic degradation conditions of Direct Red 23 using nano-Ag doped TiO_2, Sep. Purif. Technol. 62 (2008) 648–653.

[163] E. Pulido Melián, O. González Díaz, J.M. Doña Rodríguez, G. Colón, J.A. Navío, M. Macías, J. Pérez Peña, Effect of deposition of silver on structural characteristic and photoactivity of TiO_2-based photocatalysts, Appl. Catal. B Environ. 127 (2012) 112–120.
[164] T. Lee, B.-K. Chao, Y.-L. Kuo, C.-H. Hsueh, Improvement of photocatalytic activities of Ag/P25 hybrid systems by controlled morphology of Ag nanoprims, Mater. Chem. Phys. 192 (2017) 78–85.
[165] S. Sakthivel, M.V. Shankar, M. Palanichamy, B. Arabindoo, D.W. Bahnemann, V. Murugesan, Enhancement of photocatalytic activity by metal deposition: characterisation and photonic efficiency of Pt, Au and Pd deposited on TiO_2 catalyst, Water Res. 38 (2004) 3001–3008.
[166] A. Blazkova, I. Csolleova, V. Brezová, Effect of light source on phenol degradation using Pt/TiO_2 photocatalysts immobilized on glass fibers, J. Photochem. Photobiol. A Chem. 113 (1998) 251–256.
[167] T. He, Y. Ma, Y. Cao, X. Hu, H. Liu, G. Zhang, W. Yang, J. Yao, Photochromism of WO_3 colloids combined with TiO_2 nanoparticles, J. Phys. Chem. B 106 (2002) 12670–12676.
[168] Y. Liu, C. Xie, J. Li, T. Zou, D. Zeng, New insights into the relationship between photocatalytic activity and photocurrent of TiO_2/WO_3 nanocomposite, Appl. Catal. A Gen. 433–434 (2012) 81–87.
[169] J. Luo, M. Hepel, Photoelectrochemical degradation of naphthol blue black diazo dye on WO_3 film electrode, Electrochim. Acta 46 (2001) 2913–2922.
[170] A.K.L. Sajjad, S. Shamaila, B. Tian, F. Chen, J.L. Zhang, One step activation of WO_x/TiO_2 nanocomposites with enhanced photocatalytic activity, Appl. Catal. B Environ. 91 (2009) 397–405.
[171] T. Seyama, K. Adachi, S. Yamazaki, Kinetics of photocatalytic degradation of trichloroethylene in aqueous colloidal solutions of TiO_2 and WO_3 nanoparticles, J. Photochem. Photobiol. A Chem. 249 (2012) 15–20.
[172] J. Georgieva, S. Armyanov, E. Valova, I. Polulios, S. Sotiropoulos, Enhanced photocatalytic activity of electrosynthesised tungsten trioxide-titanium dioxide bi-layer coatings under ultraviolet and visible light illumination, Electrochem. Commun. 9 (2007) 365–370.
[173] L. Gao, W. Gan, Z. Qiu, X. Zhan, T. Qiang, J. Li, Preparation of heterostructured WO_3/TiO_2 catalysts from Wood fibers and its versatile photodegradation abilities, Sci. Rep. 7 (2017) 1–13.
[174] G. Žerjav, M.S. Arshad, P. Djinović, J. Zavašnik, A. Pintar, Electron trapping energy state of TiO_2-WO_3 composites and their influence on photocatalytic degradation of bisphenol A, Appl. Catal. B Environ. 209 (2017) 273–284.
[175] F. Fresno, M.D. Hernández-Alonso, D. Tudela, J.M. Coronado, J. Soria, Photocatalytic degradation of toluene over doped and coupled $(Ti,M)O_2$ (M = Sn or Zr) nanocrystalline oxides: influence of the heteroatom distribution on deactivation, Appl. Catal. B Environ. 84 (2008) 598–606.
[176] M. Huang, S. Yu, B. Li, L. Dong, F. Zhang, M. Fan, L. Wang, J. Yu, C. Deng, Influence of preparation methods on the structure and catalytic performance of SnO_2-doped TiO_2 photocatalysts, Ceram. Int. 40 (2014) 13305–13312.
[177] A. Farhadi, M.R. Mohammadi, M. Ghorbani, On the assessment of photocatalytic activity and charge carrier mechanism of $TiO_2@SnO_2$ core-shell nanoparticles for water decontamination, J. Photochem. Photobiol. A Chem. 338 (2017) 171–177.
[178] K.K. Akurati, A. Vital, R. Hany, B. Bommer, T. Graule, M. Winterer, One-step flame synthesis of SnO_2/TiO_2 composite nanoparticles for photocatalytic applications, Int. J. Photoenergy 7 (2005) 153–161.
[179] J. Yuan, X. Zhang, H. Li, K. Wang, S. Gao, Z. Yin, H. Yu, X. Zhu, Z. Xiong, Y. Xie, TiO_2/SnO_2 double-shelled hollow spheres-highly efficient photocatalyst for the degradation of rhodamine B, Catal. Commun. 60 (2015) 129–133.
[180] M. Zhou, J. Yu, S. Liu, P. Zhai, L. Jiang, Effects of calcination temperatures on photocatalytic activity of SnO_2/TiO_2 composite films prepared by an EPD method, J. Hazard. Mater. 154 (2008) 1141–1148.
[181] M.L. Garcia-Benjume, M.I. Espitia-Cabrera, M.E. Contreras-Garcia, Enhanced photocatalytic activity of hierarchical macro-mesoporous anatase by ZrO_2 incorporation, Int. J. Photoenergy 2012 (2012) 1–10.

[182] M. Li, X. Li, G. Jiang, G. He, Hierarchically macro-mesoporous ZrO_2-TiO_2 composites with enhanced photocatalytic activity, Ceram. Int. 41 (2015) 5749–5757.
[183] C.-C. Ou, C.-S. Yang, S.-H. Lin, Selective photo-degradation of Rhodamine B over zirconia incorporated titania nanoparticles: a quantitative approach, Catal. Sci. Technol. 1 (2011) 295–307.
[184] C. Wang, A. Geng, Y. Guo, S. Jiang, X. Qu, L. Li, A novel preparation of three-dimensionally ordered macroporous M/Ti (M = Zr or Ta) mixed oxide nanoparticles with enhanced photocatalytic activity, J. Colloid Interface Sci. 301 (2006) 236–247.
[185] H. Liu, M. Wang, Y. Wang, Y. Liang, W. Cao, Y. Su, Ionic liquid-templated synthesis of mesoporous CeO2-TiO2 nanoparticles and their enhanced photocatalytic activities under UV or visible light, J. Photochem. Photobiol. A Chem. 223 (2011) 157–164.
[186] B. Yuan, Y. Long, L. Wu, K. Liang, H. Wen, S. Luo, H. Huo, H. Yang, J. Ma, TiO_2@h-CeO_2: a composite yolk-shell microsphere with enhanced photodegradaton activity, Catal. Sci. Technol. 6 (2016) 6396–6405.
[187] A. Taufik, A. Albert, R. Saleh, Sol-gel synthesis of ternary CuO/TiO_2/ZnO nanocomposites for enhanced photocatalytic performance under UV and visible light irradiation, J. Photochem. Photobiol. A Chem. 344 (2017) 149–162.
[188] R. Nadarajan, W.A.W.A. Bakar, R. Ali, R. Ismali, Effect of structural defects towards the performance of TiO_2/SnO_2/WO_3 photocatalyst in the degradation of 1,2-dichlorobenzene, J. Taiwan Inst. Chem. Eng. 64 (2016) 106–115.
[189] M. Daous, V. Iliev, L. Petrov, Gold-modified N-doped TiO_2 and N-doped WO_3/TiO_2 semiconductors as photocatalysts for UV-visible light destruction of aqueous 2,4,6-trinitrotoluene solution, J. Mol. Catal. A Chem. 392 (2014) 194–201.
[190] H. Cao, S. Huang, Y. Yu, Y. Yan, Y. Lv, Y. Cao, Synthesis of TiO_2-N/SnO_2 heterostructure photocatalyst and its photocatalytic mechanism, J. Colloid Interface Sci. 486 (2017) 176–183.
[191] M.N. Chong, V. Vimonses, S. Lei, B. Jin, C. Chow, C. Saint, Synthesis and characterisation of novel titania impregnated kaolinite nano-photocatalyst, Microporous Mesoporous Mater. 117 (2009) 233–242.
[192] Y. Hai, X. Li, H. Wu, S. Zhao, W. Deligeer, S. Asuha, Modification of acid-activated kaolinite with TiO2 and its use for the removal of azo dyes, Appl. Clay Sci. 114 (2015) 558–567.
[193] Z. Sun, Y. Chen, Q. Ke, Y. Yang, J. Yuan, Photocatalytic degradation of a cationic azo dye by TiO_2/bentonite nanocomposite, J. Photochem. Photobiol. A Chem. 149 (2002) 169–174.
[194] R. Djellabi, M.F. Ghorab, G. Cerrato, S. Morandi, S. Gatto, V. Oldani, A. Di Michele, C.L. Bianchi, Photoactive TiO_2-montmorillonite composite for degradation of organic dyes in water, J. Photochem. Photobiol. A Chem. 295 (2014) 57–63.
[195] R. Kun, K. Mogyorósi, I. Dékány, Synthesis and structural and photocatalytic properties of TiO_2/montmorillonite nanocomposites, Appl. Clay Sci. 32 (2006) 99–110.
[196] F. Li, Y. Dai, M. Gong, T. Yu, X. Chen, Synthesis, characterization of magnetic-sepiolite supported with TiO_2 and the photocatalytic performance over Cr(VI) and 2,4-dichlorophenol co-existed wastewater, J. Alloys Compd. 638 (2015) 435–442.
[197] S. Suarez, J.M. Coronado, R. Portela, J.C. Martín, M. Yates, P. Avila, B. Sanchez, On the preparation of TiO_2-sepiolite hybrid materials for the photocatalytic degradation of TCE: influence of TiO_2 distribution in the mineralization, Environ. Sci. Technol. 42 (2008) 5892–5896.
[198] Y. Zhang, D. Wang, G. Zhang, Photocatalytic degradation of organic contaminants by TiO_2/sepiolite composites prepared at low temperature, Chem. Eng. J. 173 (2011) 1–10.
[199] H.B. Hadjltaief, M.B. Zina, M.E. Galvez, P. Da Costa, Photocatalytic degradation of methyl Green dye in aqueous solution over natural clay-supported ZnO-TiO2 catalyst, J. Photochem. Photobiol. A Chem. 315 (2016) 25–33.
[200] L. Zhang, L. Fujian, W. Zhang, R. Li, H. Zhong, Y. Zhao, Y. Zhang, X. Wang, Photodegradation of methyl orange by attapulgite–SnO_2–TiO_2 nanocomposites, J. Hazard. Mater. 171 (2009) 294–300.

[201] L. Zhang, J. Liu, C. Tang, J. Lv, H. Zhang, Y. Zhao, X. Wang, Palygorskite and SnO_2–TiO_2 for the photodegradation of phenol, Appl. Clay Sci. 1 (2011) 68–73.
[202] J. Matos, J. Laine, J.-M. Herramann, Synergy effect in the photocatalytic degradation of phenol on a suspended mixture of titania and activated carbon, Appl. Catal. B Environ. 18 (1998) 281–291.
[203] C.G. Da Silva, J.L. Faria, Photochemical and photocatalytic degradation of an azo dye in aqueous solution by UV irradiation, J. Photochem. Photobiol. A Chem. 155 (2003) 133–143.
[204] B. Tryba, A.W. Morawski, M. Inagaki, Application of TiO_2-mounted activated carbon to the removal of phenol from water, Appl. Catal. B Environ. 41 (2003) 427–433.
[205] Y. Yao, G. Li, S. Ciston, R.M. Lueptow, K.A. Gray, Photoreactive TiO_2/carbon nanotube composites: synthesis and reactivity, Environ. Sci. Technol. 42 (2008) 4952–4959.
[206] W. Wang, P. Serp, P. Kalck, J.L. Faria, Photocatalytic degradation of phenol on MWNT and titania composite catalysts prepared by a modified sol-gel method, Appl. Catal. B Environ. 56 (2005) 305–312.
[207] R. Leary, A. Westwood, Carbonaceous nanomaterials for the enhancement of TiO_2 photocatalysis, Carbon 49 (2011) 741–772.
[208] B.H. Nguyen, V.H. Nguyen, D.L. Vu, Photocatalytic composites based on titania nanoparticles and carbon nanomaterials, Adv. Nat. Sci. Nanosci. Nanotechnol. 6 (2015) 033001–033014.
[209] P. Serp, M. Corrias, P. Kalck, Carbon nanotubes and nanofibers in catalysis, Appl. Catal. A Gen. 253 (2003) 337–358.
[210] C. Wang, M. Cao, P. Wang, Y. Ao, J. Hou, J. Qian, Preparation of graphene-carbon nanotube-TiO_2 composites with enhanced photocatalytic activity for the removal of dye and Cr(VI), Appl. Catal. A Gen. 473 (2014) 83–89.
[211] C.-T. Chang, J.-J. Wang, T. Ouyang, Q. Zhang, Y.-H. Jing, Photocatalytic degradation of acetaminophen in aqueous solutions by TiO_2/ZSM-5 zeolite with low energy irradiation, Mater. Sci. Eng. B 196 (2015) 53–60.
[212] K.V. Subba Rao, M. Subrahmanyam, Synthesis of 2-methylpiperazine by photocatalytic reaction in a non-aqueous suspension of semiconductor–zeolite composite catalysts, Photochem. Photobiol. Sci. 1 (2002) 597–599.
[213] K. Zhou, X.-Y. Hu, B.-Y. Chen, C.-C. Hsueh, Q. Zhang, J. Wang, Y.-J. Lin, C.-T. Chang, Synthesized TiO_2/ZSM-5 composites used for the photocatalytic degradation of azo dye: intermediates, reaction pathway, mechanism and bio-toxicity, Appl. Surf. Sci. 383 (2016) 300–309.
[214] J. Doménech, A. Prieto, Photoelectrochemical reduction of Cu(II) ions in illuminated aqueous suspensions of ZnO, Electrochim. Acta 31 (1986) 1317–1320.
[215] J.R. Harbour, M.L. Hair, Radical intermediates in the photosynthetic generation of hydrogen peroxide with aqueous zinc oxide dispersions, J. Phys. Chem. 83 (1979) 652–656.
[216] J. Peral, J. Casado, J. Domenech, Light-induced oxidation of phenol over ZnO powder, J. Photochem. Photobiol. A Chem. 44 (1988) 209–217.
[217] A. Akyol, H.C. Yatmaz, M. Bayramoglu, Photocatalytic decolorization of Remazol Red RR in aqueous ZnO suspensions, Appl. Catal. B Environ. 54 (2004) 19–24.
[218] S. Sakthivel, B. Neppolian, B. Arabindoo, M. Palanichamy, V. Murugesan, ZnO/UV Mediated photocatalytic degradation of Acid Green 16, a commonly used leather dye, Indian J. Eng. Mat. Sci. 7 (2000) 87–93.
[219] I. Udom, M.K. Ram, E.K. Stefanakos, A.F. Hepp, D.Y. Goswami, One dimensional-ZnO nanostructures: synthesis, properties and environmental applications, Mater. Sci. Semicond. Process. 16 (2013) 2070–2083.
[219a] J. Doménech, J. Muñoz, Photocatalytical reduction of Cr(VI) over ZnO powder, Electrochim. Acta 32 (1987) 1383–1386.
[220] P.V. Kamat, R. Huehn, R. Nicolaescu, A "sense and shoot" approach for photocatalytic degradation of organic contaminants in water, J. Phys. Chem. B 106 (2002) 788–794.
[221] S. Anandan, A. Vinu, T. Mori, N. Gokulakrishnan, P. Srinivasu, V. Murugesan, K. Ariga, Photocatalytic degradation of 2,4,6-trichlorophenol using lanthanum doped ZnO in aqueous suspension, Catal. Commun. 8 (2007) 1377–1382.

[222] J. Villaseñor, P. Reyes, G. Pecchi, Photodegradation of pentachlorophenol on ZnO, J. Chem. Technol. Biotechnol. 72 (1998) 105–110.
[223] A.A. Khodja, T. Sehili, J.-F. Pilichowski, P. Boule, Photocatalytic degradation of 2-phenylphenol on TiO_2 and ZnO in aqueous suspensions, J. Photochem. Photobiol. A Chem. 141 (2001) 231–239.
[224] A. Dhir, N.T. Prakash, D. Sud, Comparative studies on TiO_2/ZnO photocatalyzed degradation of 4-chlorocatechol and bleach mill effluents, Desalin. Water Treat. 46 (2012) 196–204.
[225] A. Sugunan, K.G. Veerendra, A. Uheida, M.S. Toprak, M. Muhammed, Radially oriented ZnO nanowires on flexible poly-L-lactide nanofibers for continuous-flow photocatalytic water purification, J. Am. Ceram. Soc. 93 (2010) 3740–3744.
[226] N. Daneshvar, D. Salari, A.R. Khataee, Photocatalytic degradation of azo dye acid red 14 in water on ZnO as an alternative catalyst to TiO_2, J. Photochem. Photobiol. A Chem. 162 (2004) 317–322.
[227] K. Gouvea, F. Wypych, S.G. Moraes, N. Duran, N. Nagata, P. Peralta-Zamora, Semiconductor-assisted photocatalytic degradation of reactive dyes in aqueous solution, Chemosphere 40 (2000) 433–440.
[228] P. Spathis, I. Poulios, The corrosion and photocorrosion of zinc and zinc oxide coatings, Corros. Sci. 37 (1995) 673–680.
[229] S.K. Kansal, M. Singh, D. Sud, Studies on photodegradation of two commercial dyes in aqueous phase using different photocatalysts, J. Hazard. Mater. 141 (2007) 581–590.
[230] B. Neppolian, H.C. Choi, S. Sakthivel, B. Arabindoo, V. Murugesan, Solar/UV-induce photocatalytic degradation of three commercial textile dyes, J. Hazard. Mater. B89 (2002) 303–317.
[230a] L. Liu, X. Chen, Titanium dioxide nanomaterials: self-structural modifications, Chem. Rev. 114 (2014) 9890–9918.
[231] S. Monticone, R. Tufeu, A.V. Kanaev, E. Scolan, C. Sanchez, Quantum size effect in TiO_2 nanoparticles: does it exist? Appl. Surf. Sci. 162 (2000) 565–570.
[232] V. Etacheri, C. Di Valentin, J. Schneider, D. Bahnemann, S.C. Pillai, Visible-light activation of TiO2 photocatalysts: advances in theory and experiments, J Photochem Photobiol C: Photochem Rev 25 (2015) 1–29.
[233] M. Xing, W. Fang, M. Nasir, Y. Ma, J. Zhang, M. Anpo, Self-doped Ti^{3+} enhanced TiO_2 nanoparticles with a high-performance photocatalysis, J. Catal. 297 (2013) 236–243.
[234] X. Xin, T. Xu, J. Yin, L. Wang, C. Wang, Management on the location and concentration of Ti^{3+} in anatase TiO_2 for defects-induced visible-light photocatalysis, Appl. Catal. B 176–177 (2015) 354–362.
[235] Y. Zhang, Z. Zhao, J. Chen, L. Cheng, J. Chang, W. Sheng, C. Hu, S. Cao, C-doped hollow TiO_2 spheres: in situ synthesis, controlled shell thickness, and superior visible-light photocatalytic activity, Appl. Catal. B Environ. 165 (2015) 715–722.
[236] W.S. Epling, C.H.F. Peden, M.A. Henderson, U. Diebold, Evidence for oxygen adatoms on TiO_2(110) resulting from O_2 dissociation at vacancy sites, Surf. Sci. 412–413 (1998) 333–343.
[237] V. Etacheri, M.K. Seery, S.J. Hinder, S.C. Pillai, Highly visible light active $TiO_{2-x}N_x$ heterojunction photocatalysts, Chem. Mater. 22 (2010) 3843–3853.
[238] V. Etacheri, M.K. Seery, S.J. Hinder, S.C. Pillai, Oxygen rich titania: a dopant free, high temperature stable, and visible-light active anatase photocatalyst, Adv. Funct. Mater. 21 (2011) 3744–3752.
[239] S. Na-Phattalung, M.F. Smith, K. Kim, M.H. Du, S.H. Wei, S.B. Zhang, S. Limpi-jumnong, First-principles study of native defects in anatase TiO_2, Phys. Rev. B Condens. Matter 73 (2006) 125205.
[240] X. Chen, L. Liu, P.Y. Yu, S.S. Mao, Increasing solar absorption for photocatalysis with black hydrogenated titanium dioxide nanocrystals, Science 331 (2011) 746–750.
[241] G. Ghasemzadeh, M. Momenpour, F. Omidi, M.R. Hosseini, M. Ahani, A. Barzegari, Applications of nanomaterials in water treatment and environmental remediation, Front. Environ. Sci. Eng. 8 (2014) 471–482.
[242] N. Serpone, A.V. Emeline, Semiconductor photocatalysis: past, present, and future outlook, J. Phys. Chem. Lett. 3 (2012) 673–677.

[243] R. Asahi, T. Morikawa, T. Ohwaki, K. Aoki, Y. Taga, Visible-light photocatalysis in nitrogen-doped titanium oxides, Science 293 (2001) 269–271.
[244] J. Chen, F. Qiu, W. Xu, S. Cao, H. Zhu, Recent progress in enhancing photocatalytic efficiency of TiO_2-based materials, Appl. Catal. A 495 (2015) 131–140.
[245] L.G. Devi, R. Kavitha, A review on non metal ion doped titania for the photocatalytic degradation of organic pollutants under UV/solar light: role of photogenerated charge carrier dynamics in enhancing the activity, Appl. Catal. B Environ. 140–141 (2013) 559–587.
[246] S. Rehman, R. Ullah, A.M. Butt, N.D. Gohar, Strategies of making TiO_2 and ZnO visible light active, J. Hazard. Mater. 170 (2009) 560–569.
[247] P.A.K. Reddy, P.V.L. Reddy, E. Kwon, T. Akter, S. Kalagara, Recent advances in photocatalytic treatment of pollutants in aqueous media, Environ. Int. 91 (2016) 94–103.
[248] T. Morikawa, R. Asahi, T. Ohwaki, A. Aoki, Y. Taga, Band-gap narrowing of titanium dioxide by nitrogen doping, Jpn. J. Appl. Phys. 40 (2001) L561–L563.
[249] H. Irie, Y. Watanabe, K. Hashimoto, Nitrogen-concentration dependence on photocatalytic activity of $TiO_{2-x}N_x$ powders, J. Phys. Chem. B 107 (2003) 5483–5486.
[250] N. Serpone, Is the band gap of pristine TiO_2 narrowed by anion- and cationdoping of titanium dioxide in second-generation photocatalysts? J. Phys. Chem. B 110 (2006) 24287–24293.
[251] T. Ihara, M. Miyoshi, Y. Iriyama, O. Matsumoto, S. Sugihara, Visible-light-active titanium oxide photocatalyst realized by an oxygen-deficient structure and by nitrogen doping, Appl. Catal. B 42 (2003) 403–409.
[252] S. Sato, R. Nakamura, S. Abe, Visible-light sensitization of TiO_2 photocatalysts by wet-method N doping, Appl. Catal. A 284 (2005) 131–137.
[253] C. Di Valentin, E. Finazzi, G. Pacchioni, A. Selloni, S. Livraghi, M.C. Paganini, E. Giamello, N-doped TiO_2: Theory and experiment, Chem. Phys. 339 (2007) 44–56.
[254] S. Livraghi, M.C. Paganini, E. Giamello, A. Selloni, C.D. Valentin, G. Pacchioni, Origin of photoactivity of nitrogen-doped titanium dioxide under visible light, J. Am. Chem. Soc. 128 (2006) 15666–15671.
[255] X. Chen, C. Burda, Photoelectron spectroscopic investigation of nitrogen-doped titania nanoparticles, J. Phys. Chem. B 108 (2004) 15446–15449.
[256] C. Burda, Y. Lou, X. Chen, A.C.S. Samia, J. Stout, J.L. Gole, Enhanced nitrogen doping in TiO_2 nanoparticles, Nano Lett. 3 (2003) 1049–1051.
[257] Y. Kuroda, T. Mori, K. Yagi, N. Makihata, Y. Kawahara, M. Nagao, S. Kittaka, Preparation of visible-light-responsive $TiO_{2-x}N_x$ photocatalyst by a sol-gel method: analysis of the active center on TiO_2 that reacts with NH_3, Langmuir 21 (2005) 8026–8034.
[258] T. Sano, N. Negishi, K. Koike, K. Takeuchi, S. Matsuzawa, Preparation of a visible light-responsive photocatalyst from a complex of Ti^{4+} with a nitrogen-containing ligand, J. Mater. Chem. 14 (2004) 380–384.
[259] S. Livraghi, M.R. Chierotti, E. Giamello, G. Magnacca, M.C. Paganini, C.L. Bianchi, Nitrogen-doped titanium dioxide active in photocatalytic reactions with visible light: a multi-technique characterization of differently prepared materials, J. Phys. Chem. C 112 (2008) 17244–17252.
[260] S. Livraghi, M. Pelaez, J. Biedrzycki, I. Corazzar, E. Giamello, D.D. Dionysiou, Influence of the chemical synthesis on the physicochemical properties of N-TiO_2 nanoparticles, Catal. Today 209 (2012) 54–59.
[261] F. Peng, L. Cai, H. Yu, H. Wang, J. Yang, Synthesis and characterization of substitutional and interstitial nitrogen-doped titanium dioxides with visible light photocatalytic activity, J. Solid State Chem. 181 (2008) 130–136.
[262] H.M. Yates, M.G. Nolan, D.W. Sheel, M.E. Pemble, The role of nitrogen doping on the development of visible light-induced photocatalytic activity in thin TiO_2 films grown on glass by chemical vapour deposition, J. Photochem. Photobiol. A Chem. 179 (2006) 213–223.
[263] H. Li, Y. Hou, Highly active TiO_2N photocatalysts prepared by treating TiO_2 precursors in NH_3/ethanol fluid under supercritical conditions, J. Phys. Chem. B 110 (2006) 1559–1565.

[264] L. Wan, J.F. Li, J.Y. Feng, W. Sun, Z.Q. Mao, Improved optical response and photocatalysis for N-doped titanium oxide (TiO_2) films prepared by oxidation of TiN, Appl. Surf. Sci. 253 (2007) 4764–4767.
[265] G. Barolo, S. Livraghi, M. Chiesa, M.C. Paganini, E. Giamello, Mechanism of the photoactivity under visible light of N-doped titanium dioxide. Charge carriers migration in irradiated N-TiO_2 investigated by electron paramagnetic resonance, J. Phys. Chem. C 116 (2012) 20887–20894.
[266] K. Hashimoto, H. Irie, A. Fujishima, TiO_2 photocatalysis: a historical overview and future prospects, Jap. J. Appl. Phys. 44 (2005) 8269–8285.
[267] R. Katoh, A. Furube, K. Yamanaka, T. Morikawa, Charge separation and trapping in N-doped TiO2 photocatalysts: a time-resolved microwave conductivity study, J. Phys. Chem. Lett. 1 (2010) 3261–3265.
[268] S. Sakthivel, H. Kisch, Daylight photocatalysis by carbon-modified titanium dioxide, Angew. Chem. Int. Ed. 42 (2003) 4908–4911.
[269] Y. Choi, T. Umebayashi, M. Yoshikawa, Fabrication and characterization of C-doped anatase TiO_2 photocatalysts, J. Mater. Sci. 39 (2004) 1837–1839.
[270] D. Valentin, G. Pacchioni, A. Selloni, Theory of carbon doping of titanium dioxide, Chem. Mater. 17 (2005) 6656–6665.
[271] D. Zhang, M. Yang, S. Dong, Improving the photocatalytic activity of TiO_2 through reduction, RSC Adv. 5 (2015) 35661–35666.
[272] H. Kamisaka, T. Adachi, K. Yamashita, Density functional theory based first-principle calculation of Nb-doped anatase TiO_2 and its interactions with oxygen vacancies and interstitial oxygen, J. Chem. Phys. 123 (2005) 1–10.
[273] S. Khan, M. Al-Shahry, W.B. Ingeler, Efficient photochemical water splitting by a chemically modified n-TiO2, Science 297 (2002) 2243–2245.
[274] E. Barborini, A.M. Conti, I. Kholmanov, P. Piseri, A. Podestà, P. Milani, C. Cepek, O. Sakho, R. Macovez, M. Sancrotti, Nanostructured TiO_2 films with 2 eV optical gap, Adv. Mater. 17 (2005) 1842–1846.
[275] J. Fang, L. Xu, Z. Zhang, Y. Yuan, S. Cao, Z. Wang, L. Yin, Y. Liao, C. Xue, Au@TiO_2–CdS ternary nanostructures for efficient visible-light-driven hydrogen generation, ACS Appl. Mater. Interfaces 5 (2013) 8088–8092.
[276] T. Umebayashi, T. Yamaki, H. Itoh, K. Asai, Band gap narrowing of titanium dioxide by sulfur doping, Appl. Phys. Lett. 81 (2002) 454–456.
[277] T. Umebayashi, T. Yamaki, S. Yamamoto, A. Miyashita, S. Tanaka, T. Sumita, K. Asai, Sulfur-doping of rutile-titanium dioxide by ion implantation: photocurrent spectroscopy and first-principles band calculation studies, J. Appl. Phys. 93 (2003) 5156–5160.
[278] Y. Cui, H. Du, L. Wen, Origin of visible-light-induced photocatalytic properties of S-doped anatase TiO_2 by first-principles investigation, Solid State Commun. 149 (2009) 634–637.
[279] F. Tian, C. Liu, W. Zhao, X. Wang, Z. Wang, J.C. Yu, Cationic S-doped anatase TiO_2: a DFT study, J. Comput. Sci. Eng. 1 (2011) 32–40.
[280] C. Han, M. Pelaez, V. Likodimos, A.G. Kontos, P. Falaras, K. O'Shea, D.D. Dionysiou, Innovative visible light-activated sulfur doped TiO_2 films for water treatment, Appl. Catal. B Environ. 107 (2011) 77–87.
[281] D. Li, H. Haneda, S. Hishita, N. Ohashi, N.K. Labhsetwar, Fluorine-doped TiO_2 powders prepared by spray pyrolysis and their improved photocatalytic activity for decomposition of gas-phase acetaldehyde, J. Fluor. Chem. 126 (2005) 69–77.
[282] A.M. Czoska, S. Livraghi, M. Chiesa, E. Giamello, S. Agnoli, G. Granozzi, E. Finazzi, C. Di Valentin, G. Pacchioni, The nature of defects in fluorine-doped TiO_2, J. Phys. Chem. C 112 (2008) 8951–8956.
[283] M. Harb, New insights into the origin of visible-light photocatalytic activity in Se-modified anatase TiO_2 from screened coulomb hybrid DFT calculations, J. Phys. Chem. C 117 (2013) 25229–25235.
[284] S. Liu, J. Yu, W. Wang, Effects of annealing on the microstructures and photoactivity of fluorinated N-doped TiO_2, Phys. Chem. Chem. Phys. 12 (2010) 12308–12315.

[285] Y. Xie, Y. Li, X. Zhao, Low-temperature preparation and visible-light-induced catalytic activity of anatase F–N-codoped TiO_2, J. Mol. Catal. A Chem. 277 (2007) 119–126.
[286] C. Di Valentin, E. Finazzi, G. Pacchioni, A. Selloni, S. Livraghi, A.M. Czoska, M.C. Paganini, E. Giamello, Density functional theory and electron paramagnetic resonance study on the effect of $N-F$ codoping of TiO_2, Chem. Mater. 20 (2008) 3706–3714.
[287] M. Pelaez, P. Falaras, V. Likodimos, A.G. Kontos, A.A. de la Cruz, K. O'Shea, D.D. Dionysiou, Synthesis, structural characterization and evaluation of sol–gel-based NF-TiO_2 films with visible light-photoactivation for the removal of microcystin-LR, Appl. Catal. B Environ. 99 (2010) 378–387.
[288] P. Wang, P.S. Yap, T.T. Lim, C–N–S tridoped TiO_2 for photocatalytic degradation of tetracycline under visible-light irradiation, Appl. Catal. A Gen. 399 (2011) 252–261.
[289] P. Bouras, E. Stathatos, P. Lianos, Pure versus metal-ion-doped nanocrystalline titania for photocatalysis, Appl. Catal. B Environ. 73 (2007) 51–59.
[290] L.G. Devi, N. Kottam, S.G. Kumar, Preparation and characterization of Mn-doped titanates with a bicrystalline framework: correlation of the crystallite size with the synergistic effect on the photocatalytic activity, J. Phys. Chem. C 113 (2009) 15593–15601.
[291] M. Matsuoka, M. Kitano, M. Takeuchi, K. Tsujimaru, M. Anpo, J.M. Thomas, Photocatalysis for new energy production: recent advances in photocatalytic water splitting reactions for hydrogen production, Catal. Today 122 (2007) 51–61.
[292] J. Yu, Q. Xiang, M. Zhou, Preparation, characterization and visible-light-driven photocatalytic activity of Fe-doped titania nanorods and first-principles study for electronic structures, Appl. Catal. B Environ. 90 (2009) 595–602.
[293] M. Anpo, Second-generation titanium dioxide photocatalysts prepared by the application of an advanced metal ion-implantation method, Pure Appl. Chem. 72 (2000) 1787–1792.
[294] A.N. Banerjee, The design, fabrication, and photocatalytic utility of nanostructured semiconductors: focus on TiO_2-based nanostructures, Nanotechnol. Sci. Appl. 4 (2011) 35–65.
[295] A. Fuerte, M.D. Hernández-Alonso, A.J. Maira, A. Martínez-Arias, M. Fernández-García, J.C. Conesa, J. Soria, Visible light-activated nanosized doped-TiO_2 photocatalysts, Chem. Commun. (24) (2001) 2718–2719.
[296] T. Umebayashi, T. Yamaki, H. Itoh, K. Asak, Analysis of electronic structures of 3d transition metal-doped TiO2 based on band calculations, J. Phys. Chem. Solids 63 (2002) 1909–1920.
[297] J. Vargas Hernández, S. Coste, A. García Murillo, F. Carrillo Romo, A. Kassiba, Effects of metal doping (Cu, Ag, Eu) on the electronic and optical behavior of nanostructured TiO_2, J. Alloys Compd. 710 (2017) 355–363.
[298] W. Choi, A. Termin, M.R. Hoffmann, The role of metal ion dopants in quantum-sized TiO_2: correlation between photoreactivity and charge carrier recombination dynamics, J. Phys. Chem. 98 (1994) 13669–13679.
[299] H. Yamashita, M. Harada, J. Misaka, M.I.K. Takeuchi, M. Anpo, Degradation of propanol diluted in water under visible light irradiation using metal ion-implanted titanium dioxide photocatalysts, J. Photochem. Photobiol. A 148 (2002) 257–261.
[300] K. Nagaveni, M.S. Hegde, G. Madras, Structure and photocatalytic activity of Ti1-xMxO2 $\pm\delta$ (M = W, V, Ce, Zr, Fe, and Cu) synthesized by solution combustion method, J. Phys. Chem. B 108 (2004) 20204–20212.
[301] L.G. Devi, S.G. Kumar, Influence of physicochemical–electronic properties of transition metal ion doped polycrystalline titania on the photocatalytic degradation of Indigo Carmine and 4-nitrophenol under UV/solar light, Appl. Surf. Sci. 257 (2011) 2779–2790.
[302] J. Choi, H. Park, M.R. Hoffmann, Effects of single metal-Ion doping on the visible-light photoreactivity of TiO_2, J. Phys. Chem. C 114 (2010) 783–792.

[303] Y. Wang, R. Zhang, J. Li, L. Li, S. Lin, First-principles study on transition metal-doped anatase TiO_2, Nanoscale Res. Lett. 9 (2014) 46–53.
[304] W. Zhu, X. Qiu, V. Iancu, X.Q. Chen, H. Pan, W. Wang, N.M. Dimitrijevic, T. Rajh, H.M. Meyer, M.P. Paranthaman, G.M. Stocks, H.H. Weitering, B. Gu, G. Eres, Z. Zhang, Band gap narrowing of titanium oxide semiconductors by noncompensated anion-cation codoping for enhanced visible-light photoactivity, Phys. Rev. Lett. 103 (2009) 226401.
[305] J.B. Asbury, E. Hao, Y. Wang, H.N. Ghosh, T. Lian, Ultrafast electron transfer dynamics from molecular adsorbates to semiconductor nanocrystalline thin films, J. Phys. Chem. B 105 (2001) 4545–4557.
[306] Y.M. Choi, W.Y. Choi, C.H. Lee, T. Hyeon, H.I. Lee, Visible light-induced degradation of carbon tetrachloride on dye-sensitized TiO_2, Environ. Sci. Technol. 35 (2001) 966–970.
[307] A. Fung, B. Chiu, M. Lam, Surface modification of TiO_2 by a ruthenium(II) polypyridyl complex via silyl-linkage for the sensitized photocatalytic degradation of carbon tetrachloride by visible irradiation, Water Res. 37 (2003) 1939–1947.
[308] C. Bauer, G. Boschloo, E. Mukhtar, A. Hagfeldt, Electron injection and recombination in $Ru(dcbpy)_2(NCS)_2$ sensitized nanostructured ZnO, J. Phys. Chem. B 105 (2001) 5585–5588.
[309] R. Abe, K. Sayama, H. Arakawa, Efficient hydrogen evolution from aqueous mixture of I^- and acetonitrile using a merocyanine dye-sensitized Pt/TiO_2 photocatalyst under visible light irradiation, Chem. Phys. Lett. 362 (2002) 441–444.
[310] M. Anpo, Preparation, characterization, and reactivities of highly functional titanium oxide-based photocatalysts able to operate under UV-visible light irradiation: approaches in realizing high efficiency in the use of visible light, Bull. Chem. Soc. Jpn. 77 (2004) 1427–1442.
[311] S. Neatu, J.A. Maciá-Agulló, P. Concepción, H. Garcia, Gold-copper nanoalloys supported on TiO_2 as photocatalysts for CO_2 reduction by water, J. Am. Chem. Soc. 136 (2014) 15969–15976.
[312] X. Zhou, G. Liu, J. Yu, W. Fan, Surface plasmon resonance-mediated photocatalysis by noble metal-based composites under visible light, J. Mater. Chem. 22 (2012) 21337–21354.
[313] S.G. Kumar, K.S.R. Rao, Comparison of modification strategies towards enhanced chargecarrier separation and photocatalytic degradation activity of metaloxide semiconductors (TiO_2, WO_3 and ZnO), Appl. Surf. Sci. 391 (2017) 124–148.
[314] J.Y. Lan, X.M. Zhou, G. Liu, J.G. Yu, J.C. Zhang, L.J. Zhi, G.J. Nie, Enhancing photocatalytic activity of one-dimensional $KNbO_3$ nanowires by Au nanoparticles under ultraviolet and visible-light, Nanoscale 3 (2011) 5161–5167.
[315] N.T. Nolan, M.K. Seery, S.J. Hinder, L.F. Healy, S.C. Pillai, A systematic study of the effect of silver on the chelation of formic acid to a titanium precursor and the resulting effect on the anatase to rutile transformation of TiO_2, J. Phys. Chem. C 114 (2010) 13026–13034.
[316] M.A. Garcia, Surface plasmons in metallic nanoparticles: fundamentals and applications, J. Phys. D. Appl. Phys. 44 (2011) 1–20.
[317] L.G. Devi, R. Kavitha, A review on plasmonic metal-TiO_2 composite for generation, trapping, storing and dynamic vectorial transfer of photogenerated electrons across the Schottky junction in a photocatalytic system, Appl. Surf. Sci. 360 (2016) 601–622.
[318] Y. Hu, J. Fan, E. Liu, H. Li, X. Hu, Fabrication and enhanced photoactivities of plasmonic Ag/TiO_2 nanoflower films, J. Nanosci. Nanotechnol. 17 (2017) 1156–1162.
[319] M. Klein, J. Nadolna, A. Gołabiewska, P. Mazierski, T. Klimczuk, H. Remita, A. Zaleska-Medynska, The effect of metal cluster deposition route on structure and photocatalytic activity of mono- and bimetallic nanoparticles supported on TiO_2 by radiolytic method, Appl. Surf. Sci. 378 (2016) 37–48.
[320] S. Oros-Ruiz, R. Zanella, B. Prado, Photocatalytic degradation of trimethoprim by metallic nanoparticles supported on TiO_2-P25, J. Hazard. Mater. 263 (2013) 28–35.

[321] X. Zhang, Y. Zhu, X. Yang, S. Wang, J. Shen, B. Lin, C. Li, Enhanced visible light photocatalytic activity of interlayer-isolated triplex $Ag@SiO_2@TiO_2$ core–shell nanoparticles, Nanoscale 5 (2013) 3359–3366.
[322] H.M. Sung-Suh, J.R. Choi, H.J. Hah, S.M. Koo, Y.C. Bae, Comparison of Ag deposition effects on the photocatalytic activity of nanoparticulate TiO_2 under visible and UV light irradiation, J. Photochem. Photobiol. A 163 (2004) 37–44.
[323] C. Liu, Z. Lei, Y. Yang, H. Wang, Z. Zhang, Improvement in settleability and dewaterability of waste activated sludge by solar photocatalytic treatment in Ag/TiO_2-coated glass tubular reactor, Bioresour. Technol. 137 (2013) 57–62.
[324] M.D. Hernandez-Alonso, F. Fresno, S. Suarez, J.M. Coronado, Development of alternative photocatalysts to TiO_2: challenges and opportunities, Energy Environ. Sci. 2 (2009) 1231–1257.
[325] B. Dindar, S. Içli, Unusual photoreactivity of zinc oxide irradiated by concentrated sunlight, J. Photochem. Photobiol. A Chem. 140 (2001) 263–268.
[326] S.K. Pardeshi, A.B. Patil, A simple route for photocatalytic degradation of phenol in aqueous zinc oxide suspension using solar energy, Sol. Energy 82 (2008) 700–705.
[327] S. Sakthivel, B. Neppolian, M.V. Shankar, B. Arabindoo, M. Palanichamy, V. Murugesan, Solar photocatalytic degradation of azo dye: comparison of photocatalytic efficiency of ZnO and TiO_2, Sol. Energy Mater. Sol. Cells 77 (2003) 65–82.
[328] K.M. Lee, C.W. Lai, K.S. Ngai, J.C. Juan, Recent developments of zinc oxide based photocatalyst in water treatment technology: a review, Water Res. 88 (2016) 428–448.
[329] B. Subash, B. Krishnakumar, M. Swaminathan, M. Shanthi, Synthesis and characterization of cerium–silver co-doped zinc oxide as a novel sunlight-driven photocatalyst for effective degradation of Reactive Red 120 dye, Mater. Sci. Semicond. Process. 16 (2013) 1070–1078.
[330] S. Das, S. Sinha, M. Suar, S.I. Yun, A. Mishra, S.K. Tripathy, Solar-photocatalytic disinfection of Vibrio cholerae by using Ag@ZnO core–shell structure nanocomposites, J. Photochem. Photobiol. B Biol. 142 (2015) 68–76.
[331] S. Ameen, M.S. Akhtar, Y.S. Kim, O.B. Yang, H.S. Shin, An effective nanocomposite of polyaniline and ZnO: preparation, characterizations, and its photocatalytic activity, Colloid Polym. Sci. 289 (2011) 415–421.
[332] H.B. Fu, T.G. Xu, S.B. Zhu, Y.F. Zhu, Photocorrosion inhibition and enhancement of photocatalytic activity for ZnO via hybridization with C60, Environ. Sci. Technol. 42 (2008) 8064–8069.
[333] Y. Zhang, Z. Chen, S. Liu, Y.J. Xu, Size effect induced activity enhancement and anti-photocorrosion of reduced graphene oxide-ZnO composites for degradation of organic dyes and reduction of Cr(VI) in water, Appl. Catal. B Environ. 140–141 (2013) 598–607.
[334] J. Tang, Z. Zou, J. Ye, Efficient photocatalytic decomposition of organic contaminants over $CaBi_2O_4$ under visible-light irradiation, Angew. Chem. Int. Ed. 43 (2004) 4463–4466.
[335] J. Tang, Z. Zou, J. Ye, A novel series of photocatalysts $M_{2.5}VMoO_8$ (M = Mg, Zn) for O_2 evolution under visible light irradiation, Catal. Today 93–95 (2004) 891–894.
[336] X. Zhang, Z.H. Ai, F.L. Jia, L.Z. Zhang, X.X. Fan, Z.G. Zou, Selective synthesis and visible-light photocatalytic activities of $BiVO_4$ with different crystalline phases, Mater. Chem. Phys. 103 (2007) 162–167.
[337] C. Belver, C. Adan, M. Fernández-García, Photocatalytic behaviour of Bi_2MO_6 polymetalates for rhodamine B degradation, Catal. Today 143 (2009) 274–281.
[338] R.R. Jitta, R. Gundeboina, N.K. Veldurthi, R. Guje, V. Muga, Defect pyrochlore oxides: as photocatalyst materials for environmental and energy applications—a review, J. Chem. Technol. Biotechnol. 90 (2015) 1937–1948.
[339] C. Belver, C. Adan, S. García-Rodríguez, M. Fernández-García, Microemulsion synthesis of silver and bismuth vanadates with photocatalytic properties, Chem. Eng. J. 224 (2013) 24–31.

[340] U. Shamraiz, R.A. Hussain, A. Badshah, B. Raza, S. Saba, Functional metal sulfides and selenides for the removal of hazardous dyes from water, J. Photochem. Photobiol. B Biol. 159 (2016) 33–41.
[341] D.J. Martin, G. Liu, S.J.A. Moniz, Y. Bi, A.M. Beale, J. Ye, J. Tang, Efficient visible driven photocatalyst, silver phosphate: performance, understanding and perspective, Chem. Soc. Rev. 44 (2015) 7808–7828.
[342] H. Feng, Y. Du, C. Wang, W. Hao, Efficient visible-light photocatalysts by constructing dispersive energy band with anisotropic p and s-p hybridization states, Curr. Opin. Green Sust. Chem. 6 (2017) 93–100.
[343] X. Chang, J. Huang, Q. Tan, M. Wang, G. Ji, S. Deng, G. Yu, Photocatalytic degradation of PCP–Na over BiOI nanosheets under simulated sunlight irradiation, Catal. Commun. 10 (2009) 1957–1961.
[344] H. Li, L. Zhang, Photocatalytic performance of different exposed crystal facets of BiOCl, Curr. Opin. Green Sust. Chem. 6 (2017) 48–56.
[345] G. Mamba, A.K. Mishra, Graphitic carbon nitride (g-C_3N_4) nanocomposites: a new and exciting generation of visible light driven photocatalysts for environmental pollution remediation, Appl. Catal. B Environ. 198 (2016) 347–377.
[346] W.J. Ong, L.L. Tan, Y.H. Ng, S.T. Yong, S.P. Chai, Graphitic carbon nitride (g-C_3N_4)-based photocatalysts for artificial photosynthesis and environmental remediation: are we a step closer to achieving sustainability? Chem. Rev. 116 (2016) 7159–7329.
[347] S. Cao, J. Low, J. Yu, M. Jaroniec, Polymeric photocatalysts based on graphitic carbon nitride, Adv. Mater. 27 (2015) 2150–2176.
[348] L. Jiang, X. Yuan, Y. Pan, J. Liang, G. Zeng, Z. Wu, H. Wang, Doping of graphitic carbon nitride for photocatalysis: a review, Appl. Catal. B Environ. 217 (2017) 388–406.
[349] A. Kongkanand, K. Tvrdy, K. Takechi, M. Kuno, P.V. Kamat, Quantum dot solar cells. Tuning photoresponse through size and shape control of CdSe–TiO_2 architecture, J. Am. Chem. Soc. 130 (2008) 4007–4015.
[350] D. Robert, Photosensitization of TiO_2 by M_xO_y and M_xS_y nanoparticles for heterogeneous photocatalysis applications, Catal. Today 122 (2007) 20–26.
[351] X. Zheng, D. Li, X. Li, J. Chen, C. Cao, J. Fang, J. Wang, Y. He, Y. Zheng, Construction of ZnO/TiO_2 photonic crystal heterostructures for enhanced photocatalytic properties, Appl. Catal. B Environ. 168–169 (2015) 408–415.
[352] M. Samadi, A. Pourjavadi, A.Z. Moshfegh, Role of CdO addition on the growth and photocatalytic activity of electrospun ZnO nanofibers—UV vs. visible light, Appl. Surf. Sci. 298 (2014) 147–154.
[353] S.-M. Lam, J.-C. Sin, I. Satoshi, A.Z. Abdullah, A.R. Mohamed, Enhanced sunlight photocatalytic performance over Nb_2O_5/ZnO nanorod composites and the mechanism study, Appl. Catal. A General 471 (2014) 126–135.
[354] N. Li, J. Zhang, Y. Tian, J. Zhao, J. Zhang, W. Zuo, Precisely controlled fabrication of magnetic 3D γ-Fe_2O_3@ZnO core-shell photocatalyst with enhanced activity: ciprofloxacin degradation and mechanism insight, Chem. Eng. J. 308 (2017) 377–385.
[355] X. Hu, C. Hu, J. Qu, Photocatalytic decomposition of acetaldehyde and *Escherichia coli* using NiO/$SrBi_2O_4$ under visible light irradiation, Appl. Catal. B Environ. 69 (2006) 17–23.
[356] L. Yosefi, M. Haghighi, Fabrication of nanostructured flowerlike p-BiOI/p-NiO heterostructure and its efficient photocatalytic performance in water treatment under visible-light irradiation, Appl. Catal. B Environ. 220 (2018) 367–378.
[357] P. Ju, P. Wang, B. Li, H. Fan, S. Ai, D. Zhang, Y. Wang, A novel calcined Bi_2WO_6/$BiVO_4$ heterojunction photocatalyst with highly enhanced photocatalytic activity, Chem. Eng. J. 236 (2014) 430–437.
[358] F. Chen, D. Li, B. Luo, M. Chen, W. Shi, Two-dimensional heterojunction photocatalysts constructed by graphite-like C_3N_4 and Bi_2WO_6 nanosheets: enhanced photocatalytic activities for water purification, J. Alloys Compd. 694 (2017) 193–200.

[359] T. Kanagaraj, S. Thiripuranthagan, Photocatalytic activities of novel $SrTiO_3$–BiOBr heterojunction catalysts towards the degradation of reactive dyes, Appl. Catal. B Environ. 207 (2017) 218–232.
[360] M. Sun, S. Li, T. Yan, P. Ji, X. Zhao, K. Yuan, D. Wei, B. Du, Fabrication of heterostructured $Bi_2O_2CO_3$/Bi_2O_4 photocatalyst and efficient photodegradation of organic contaminants under visible-light, J. Hazard. Mater. 333 (2017) 169–178.
[361] L. Zhang, C. Hu, H. Ji, p-AgI anchored on {001} facets of n-$Bi_2O_2CO_3$ sheets with enhanced photocatalytic activity and stability, Appl. Catal. B Environ. 205 (2017) 34–41.
[362] F. Chen, Q. Yang, F. Yao, S. Wang, J. Sun, H. An, K. Yi, Y. Wang, Y. Zhou, L. Wang, X. Li, D. Wang, G. Zeng, Visible-light photocatalytic degradation of multiple antibiotics by AgI nanoparticle-sensitized Bi_5O_7I microspheres: enhanced interfacial charge transfer based on Z-scheme heterojunctions, J. Catal. 352 (2017) 160–170.
[363] Y. Liao, H. Zhang, Z. Zhong, L. Jia, F. Bai, J. Li, P. Zhong, H. Chen, J. Zhang, Enhanced visible-photocatalytic activity of anodic TiO_2 nanotubes film via decoration with $CuInSe_2$ nanocrystals, ACS Appl. Mater. Interfaces 5 (2013) 11022–11028.
[364] H.L. Meng, C. Cui, H.L. Shen, D.Y. Liang, Y.Z. Xue, P.G. Li, W.H. Tang, Synthesis and photocatalytic activity of TiO_2@CdS and CdS@TiO_2 double-shelled hollow spheres, J. Alloys Compd. 527 (2012) 30–35.
[365] F. Deng, X. Lu, X. Pei, X. Luo, S. Luo, D.D. Dionysiou, Fabrication of ternary reduced graphene oxide/SnS_2/$ZnFe_2O_4$ composite for high visible-light photocatalytic activity and stability, J. Hazard. Mater. 332 (2017) 149–161.
[366] F. Guo, Y. Cai, W. Guan, H. huang, Y. Liu, Graphite carbon nitride/ZnIn2S4 heterojunction photocatalyst with enhanced photocatalytic performance for degradation of tetracycline under visible light irradiation, J. Phys. Chem. Solids 110 (2017) 370–378.
[367] K. Woan, G. Pyrgiotakis, W. Sigmund, Photocatalytic carbon nanotube-TiO_2 composites, Adv. Mater. 21 (2009) 2233–2239.
[368] M. Minella, D. Fabbri, P. Calza, C. Minero, Selected hybrid photocatalytic materials for the removal of drugs from water, Curr. Opin. Green. Sust. Chem. 6 (2017) 11–17.
[369] W. Zhao, Z. Bai, A. Ren, B. Guo, C. Wu, Sunlight photocatalytic activity of CdS modified TiO_2 loaded on activated carbon fibers, Appl. Surf. Sci. 256 (2010) 3493–3591.
[370] W. Wang, P. Serp, P. Kalck, J.L. Faria, Visible light photodegradation of phenol on MWNT-TiO_2 composite catalysts prepared by a modified sol–gel method, J. Mol. Catal. A Chem. 235 (2005) 194–199.
[371] M. Minella, F. Sordello, C. Minero, Photocatalytic process in TiO_2/graphene hybrid materials. Evidence of charge separation by electron transfer from reduced graphene oxide to TiO_2, Catal. Today 281 (2017) 29–37.
[372] V. Bhatia, G. Malekshoar, A. Dhir, A.K. Ray, Enhanced photocatalytic degradation of atenolol using graphene TiO_2 composite, J. Photochem. Photobiol. A 332 (2017) 182–187.
[373] P. Calza, C. Hadjicostas, V.A. Sakkas, M. Saro, C. Minero, C. Medana, T.A. Albanis, Photocatalytic transformation of the antipsychotic drug risperidone in aqueous media on reduced graphene oxide-TiO_2 composites, Appl. Catal. B 183 (2016) 96–106.
[374] W.-K. Jo, S. Kumar, M.A. Isaacs, A.F. Lee, S. Karthikeyan, Cobalt promoted TiO_2/GO for the photocatalytic degradation of oxytetracycline and Congo Red, Appl. Catal. B Environ. 201 (2017) 159–168.
[375] E. Gao, W. Wang, M. Shang, J. Xu, Synthesis and enhanced photocatalytic performance of graphene-Bi_2WO_6 composite, Phys. Chem. Chem. Phys. 13 (2011) 2887–2893.
[376] L. Tang, J.J. Wang, C.T. Jia, G.X. Lv, G. Xu, W.T. Li, L. Wang, J. Zhang, M.H. Wu, Simulated solar driven catalytic degradation of psychiatric drug carbamazepine with binary $BiVO_4$ heterostructures sensitized by graphene quantum dots, Appl. Catal. B Environ. 205 (2017) 587–596.
[377] G. Liao, S. Chen, X. Quan, H. Yu, H. Zhao, Graphene oxide modified g-C_3N_4 hybrid with enhanced photocatalytic capability under visible light irradiation, J. Mater. Chem. 22 (2012) 2721–2726.

[378] H. Wu, X.L. Wu, Z.M. Wang, H. Aoki, S. Kutsuna, K. Jimurac, S. Hayashi, Anchoring titanium dioxide on carbon spheres for high-performance visible light photocatalysis, Appl. Catal. B Environ. 207 (2017) 255–266.
[379] H.F. Cheng, B.B. Huang, P. Wang, Z.Y. Wang, Z.Z. Lou, J.P. Wang, X.Y. Qin, X.Y. Zhang, Y. Dai, In situ ion exchange synthesis of the novel Ag/AgBr/BiOBr hybrid with highly efficient decontamination of pollutants, Chem. Commun. 47 (2011) 7054–7056.
[380] H. Zhang, X.F. Fan, X. Quan, S. Chen, H.T. Yu, Graphene sheets grafted Ag@AgCl hybrid with enhanced plasmonic photocatalytic activity under visible light, Environ. Sci. Technol. 45 (2011) 5731–5736.
[381] X. Chen, L. Li, W. Zhang, Y. Li, Q. Song, L. Dong, Fabricate globular flower-like CuS/$CdIn_2S_4$/$ZnIn_2S_4$ with high visible light response via microwave-assisted one-step method and its multipathway photoelectron migration properties for hydrogen evolution and pollutant degradation, ACS Sustain. Chem. Eng. 4 (2016) 6680–6688.
[382] S. Park, S. Kim, H.J. Kim, C.W. Lee, H.J. Song, S.W. Seo, H.K. Park, D.-W. Kim, K.S. Hong, Hierarchical assembly of TiO_2-$SrTiO_3$ heterostructures on conductive SnO_2 backbone nanobelts for enhanced photoelectrochemical and photocatalytic performance, J. Hazard. Mater. 275 (2014) 10–18.
[383] F. Deng, F. Zhong, L. Zhao, X. Luo, S. Luo, D.D. Dionysiou, One-step in situ hydrothermal fabrication of octahedral CdS/SnIn4S8 nano-heterojunction for highly efficient photocatalytic treatment of nitrophenol and real pharmaceutical wastewater, J. Hazard. Mater. 340 (2017) 85–95.
[384] F. Guo, W. Shi, W. Guan, H. Huang, Y. Liu, Carbon dots/g-C_3N_4/ZnO nanocomposite as efficient visible-light driven photocatalyst for tetracycline total degradation, Sep. Purif. Technol. 173 (2017) 295–303.
[385] X. Zeng, Z. Wang, N. Meng, D.T. McCarthy, A. Deletic, J.-H. Pan, X. Zhang, Highly dispersed TiO_2 nanocrystals and carbon dots on reduced graphene oxide: ternary nanocomposites for accelerated photocatalytic water disinfection, Appl. Catal. B Environ. 202 (2017) 33–41.
[386] X. Yang, F. Qian, Y. Wang, M. Li, J. Lu, Y. Li, M. Bao, Constructing a novel ternary composite $(C_{16}H_{33}(CH_3)_3N)_4W_{10}O_{32}$/g-$C_3N_4$/rGO with enhanced visible-light-driven photocatalytic activity for degradation of dyes and phenol, Appl. Catal. B Environ. 200 (2017) 283–296.
[387] F. Wang, Y. Wang, Y. Feng, Y. Zeng, Z. Xie, Q. Zhang, Y. Su, P. Chen, Y. Liu, K. Yao, W. Lv, G. Liu, Novel ternary photocatalyst of single atom-dispersed silver and carbon quantum dots co-loaded with ultrathin g-C_3N_4 for broad spectrum photocatalytic degradation of naproxen, Appl. Catal. B Environ. 221 (2018) 510–520.
[388] S.M. Aghdam, M. Haghighi, S. Allahyari, L. Yosefi, Precipitation dispersion of various ratios of BiOI/BiOCl nanocomposite over g-C_3N_4 for promoted visible light nanophotocatalyst used in removal of acid orange 7 from water, J. Photochem. Photobiol. A Chem. 338 (2017) 201–212.
[389] J. Ke, J. Liu, H. Sun, H. Zhang, X. Duan, P. Liang, X. Li, M.O. Tade, S. Liu, S. Wang, Facile assembly of Bi_2O_3/Bi_2S_3/MoS_2 n-p heterojunction with layered n-Bi_2O_3 and p-MoS_2 for enhanced photocatalytic water oxidation and pollutant degradation, Appl. Catal. B Environ. 200 (2017) 47–55.
[390] J. Liu, G. Zhang, Recent advances in synthesis and applications of clay-based photocatalysts: a review, Phys. Chem. Chem. Phys. 16 (2014) 8178–8192.
[391] C. Belver, J. Bedia, J.J. Rodriguez, Titania-clay heterostructures with solar photocatalytic applications, Appl. Catal. B Environ. 176–177 (2015) 278–287.
[392] C. Belver, J. Bedia, M.A. Alvarez-Montero, J.J. Rodriguez, Solar photocatalytic purification of water with Ce-doped TiO_2/clay heterostructures, Catal. Today 266 (2016) 36–45.
[393] C. Belver, J. Bedia, J.J. Rodriguez, Zr-doped TiO_2 supported on delaminated clay materials for solar photocatalytic treatment of emerging pollutants, J. Hazard. Mater. 322 (2017) 233–242.
[394] C. Belver, C. Han, J.J. Rodriguez, D.D. Dionysiou, Innovative W-doped titanium dioxide anchored on clay for photocatalytic removal of atrazine, Catal. Today 280 (2017) 21–28.

[395] C. Belver, M. Hinojosa, J. Bedia, M. Tobajas, M.A. Alvarez-Montero, V. Rodríguez-González, J.J. Rodriguez, Ag-coated heterostructures of ZnO-TiO_2/delaminated montmorillonite as solar photocatalysts. Materials (2017)https://doi.org/10.3390/ma10080960.
[396] M. Tobajas, C. Belver, J.J. Rodriguez, Degradation of emerging pollutants in water under solar irradiation using novel TiO_2-ZnO/clay nanoarchitectures, Chem. Eng. J. 309 (2017) 596–606.
[397] P. Du, J.T. Cameiro, J.A. Moulijn, G. Mul, A novel photocatalytic monolith reactor for multiphase heterogeneous photocatalysis, Appl. Catal. A 334 (2008) 119–128.
[398] D. Li, Q. Zhu, C. Han, Y. Yang, W. Jiang, Z. Zhang, Photocatalytic degradation of recalcitrant organic pollutants in water using a novel cylindrical multi-column photoreactor packed with TiO_2-coated silica gel beads, J. Hazard. Mater. 285 (2015) 398–408.
[399] Y. Gao, M. Hu, B. Mi, Membrane surface modification with TiO_2–graphene oxide for enhanced photocatalytic performance, J. Membr. Sci. 455 (2014) 349–356.
[400] J. Grzechulska-Damszel, M.A. Tomaszewska, W. Morawski, Integration of photocatalysis with membrane processes for purification of water contaminated with organic dyes, Desalination 241 (2009) 118–126.
[401] X.D. Wang, F. Shi, W. Huang, C.M. Fan, Synthesis of high quality TiO_2 membranes on alumina supports and their photocatalytic activity, Thin Solid Films 520 (2012) 2488–2492.
[402] C. Zhao, Y. Zhou, D.J. de Ridder, J. Zhai, Y.M. Wei, H.P. Deng, Advantages of TiO_2/5A composite catalyst for photocatalytic degradation of antibiotic oxytetracycline in aqueous solution: comparison between TiO_2 and TiO_2/5A composite system, Chem. Eng. J. 248 (2014) 280–289.
[403] B. Srikanth, R. Goutham, R. Badri Narayan, A. Ramprasath, K.P. Gopinath, A.R. Sankaranarayanan, Recent advancements in supporting materials for immobilised photocatalytic applications in waste water treatment, J. Environ. Manag. 200 (2017) 60–78.
[404] M.V. Diamanti, M. Ormellese, E. Marin, A. Lanzutti, A. Mele, M.P. Pedeferri, Anodic titanium oxide as immobilized photocatalyst in UV or visible light devices, J. Hazard. Mater. 186 (2012) 2103–2109.
[405] S. Chakraborty, S. Loutatidou, G. Palmisano, J. Kujawa, M.O. Mavukkandy, S. Al-Gharabli, E. Curcio, H.A. Arafat, Photocatalytic hollow fiber membranes for the degradation of pharmaceutical compounds in wastewater, J. Environ. Chem. Eng. 5 (2017) 5014–5024.
[406] P. Hegedüs, E. Szabó-Bárdos, O. Horváth, P. Szabó, K. Horváth, Investigation of a TiO_2 photocatalyst immobilized with poly(vinyl alcohol), Catal. Today 284 (2017) 179–186.
[407] V. Vaiano, O. Sacco, D. Sannino, P. Ciambelli, Nanostructured N-doped TiO_2 coated on glass spheres for the photocatalytic removal of organic dyes under UV or visible light irradiation, Appl. Catal. B Environ. 170–171 (2015) 153–161.
[408] H. Khalilian, M. Behpour, V. Atouf, S.N. Hosseini, Immobilization of S, N-codoped TiO_2 nanoparticles on glass beads for photocatalytic degradation of methyl orange by fixed bed photoreactor under visible and sunlight irradiation, Sol. Energy 112 (2015) 239–245.
[409] M. Kovacic, H. Kusic, M. Fanetti, U.L. Stangar, M. Valant, D.D. Dionysiou, A.L. Bozic, TiO_2-SnS_2 nanocomposites: solar-active photocatalytic materials for water treatment, Environ. Sci. Pollut. Res. 24 (2017) 19965–19979.
[410] J. Yi, L. Huang, H. Wang, H. Yu, F. Peng, AgI/TiO_2 nanobelts monolithic catalyst with enhanced visible light photocatalytic activity, J. Hazard. Mater. 284 (2015) 207–214.
[411] S. Saran, G. Kamalraj, P. Arunkumar, S.P. Devipriya, Pilot scale thin film plate reactors for the photocatalytic treatment of sugar refinery wastewater, Environ. Sci. Pollut. Res. 23 (2016) 17730–17741.
[412] A. Yousef, N.A.M. Barakat, S.S. Al-Deyab, R. Nirmala, B. Pant, H.Y. Kim, Encapsulation of CdO/ZnO NPs in PU electrospun nanofibers as novel strategy for effective immobilization of the photocatalysts, Colloids Surf. A Physicochem. Eng. Asp. 401 (2012) 8–16.
[413] Z. Mao, R. Xie, D. Fu, L. Zhang, H. Xu, Y. Zhong, X. Sui, PAN supported Ag-AgBr@$Bi_{20}TiO_{32}$ electrospun fiber mats with efficient visible light photocatalytic activity and antibacterial capability, Sep. Purif. Technol. 176 (2017) 277–286.

[414] G. Jiang, X. Li, Z. Wei, X. Wang, T. Jiang, X. Du, W. Chen, Immobilization of N, S-codoped BiOBr on glass fibers for photocatalytic degradation of rhodamine B, Powder Technol. 261 (2014) 170–175.
[415] S. Ma, J. Meng, J. Li, Y. Zhang, L. Ni, Synthesis of catalytic polypropylene membranes enabling visible-light-driven photocatalytic degradation of dyes in wáter, J. Membr. Sci. 453 (2014) 221–229.
[416] O.M. Rodriguez-Narvaez, J.M. Peralta-Hernandez, A. Goonetilleke, E.R. Bandala, Treatment technologies for emerging contaminants in water: a review, Chem. Eng. J. 323 (2017) 361–380.
[417] Y. Yang, Y.S. Ok, K.-H. Kim, E.E. Kwon, Y.F. Tsang, Occurrences and removal of pharmaceuticals and personal care products (PPCPs) in drinking water and water/sewage treatment plants: a review, Sci. Total Environ. 596–597 (2017) 303–320.
[418] M. Pelaez, M.G. Antoniou, X. He, D.D. Dionysiou, A.A. Cruz, K. Tsimeli, T. Triantis, A. Hiskia, T. Kaloudis, C. Williams, M. Aubel, A. Chapman, A. Foss, U. Khan, K.E. O'Shea, J. Westrick, Sources and occurrence of cyanotoxins worldwide, in: D. Fatta-Kassinos, K. Bester, K. Kümmerer (Eds.), Xenobiotics in the Urban Water Cycle, Springer, Netherlands, 2010, pp. 101–127.
[419] W.W. Carmichael, The toxins of cyanobacteria, Sci. Am. 270 (1994) 78–86.
[420] V.K. Sharma, T.M. Triantis, M.G. Antoniou, X. He, M. Pelaez, C. Han, W. Song, K.E. O'Shea, A.A. de la Cruz, T. Kaloudis, A. Hiskia, D.D. Dionysiou, Destruction of microcystins by conventional and advanced oxidation processes: a review, Sep. Purif. Technol. 91 (2012) 3–17.
[421] D.J. Lapworth, N. Baran, M.E. Stuart, R.S. Ward, Emerging organic contaminants in groundwater: a review of sources, fate and occurrence, Environ. Pollut. 163 (2012) 287–303.
[422] M. Klavarioti, D. Mantzavinos, D. Kassinos, Removal of residual pharmaceuticals from aqueous systems by advanced oxidation processes, Environ. Int. 35 (2009) 402–417.
[423] M. Pazoki, M. Parsa, R. Farhadpou, Removal of the hormones dexamethasone (DXM) by Ag doped on TiO_2 photocatalysis, J. Environ. Chem. Eng. 4 (2016) 4426–4434.
[424] L.-F. Chiang, R. Doong, Cu-TiO_2 nanorods with enhanced ultraviolet- and visible-light photoactivity for bisphenol A degradation, J. Hazard. Mater. 277 (2014) 84–92.
[425] D.P. Subagio, M. Srinivasan, M. Lim, T.T. Lim, Photocatalytic degradation of bisphenol-A by nitrogen-doped TiO_2 hollow sphere in a vis-LED photoreactor, Appl. Catal. B Environ. 95 (2010) 414–422.
[426] J. Ananpattarachai, P. Kajitvichyanukul, Photocatalytic degradation of p,p'-DDT under UV and visible light using interstitial N-doped TiO_2, J. Environ. Sci. Health B 50 (2015) 247–260.
[427] J. Andersen, M. Pelaez, L. Guay, Z. Zhang, K. O'Shea, D.D. Dionysiou, NF-TiO_2 photocatalysis of aminotrole and atrazine with addition of oxidants under simulated solar light: emerging synergies, degradation intermediates, and reusable attributes, J. Hazard. Mater. 260 (2013) 569–575.
[428] X. Wang, T.T. Lim, Solvothermal synthesis of C–N codoped TiO_2 and photocatalytic evaluation for bisphenol A degradation using a visible-light irradiated LED photoreactor, Appl. Catal. B Environ. 100 (2010) 355–364.
[429] P. Wang, A.G. Fane, T.T. Lim, Evaluation of a submerged membrane vis-LED photoreactor (sMPR) for carbamazepine degradation and TiO_2 separation, Chem. Eng. J. 215–216 (2013) 240–251.
[430] H. Choi, M.G. Antoniou, M. Pelaez, A.A. de la Cruz, J.A. Shoemaker, D.D. Dionysiou, Mesoporous nitrogen-doped TiO_2 for the photocatalytic destruction of the cyanobacterial toxin microcystin-LR under visible light irradiation, Environ. Sci. Technol. 41 (2007) 7530–7535.
[430a] M. Pelaez, A.A. de la Cruz, K. O'Shea, P. Falaras, D.D. Dionysiou, Effects of water parameters on the degradation of microcystin-LR under visible light-activated TiO_2 photocatalyst, Water Res. 45 (2011) 3787–3796.
[431] M. Pelaez, P. Falaras, A.G. Kontos, A.A. de la Cruz, K. O'Shea, P.S.M. Dunlop, J.A. Byrne, D.D. Dionysiou, A comparative study on the removal of cylindrospermopsin and microcystins from water with NF-TiO_2-P25 composite films with visible and UV–vis light photocatalytic activity, Appl. Catal. B Environ. 121–122 (2012) 30–39.

[432] T. Fotiou, T.M. Triantis, T. Kaloudis, K.E. O'Shea, D.D. Dionysiou, A. Hiskia, Assessment of the roles of reactive oxygen species in the UV and visible light photocatalytic degradation of cyanotoxins and water taste and odor compounds using C–TiO_2, Water Res. 90 (2016) 52–61.
[433] G. Liu, G. Han, M. Pelaez, D. Zhu, S. Liao, V. Likodimos, A.G. Kontos, P. Falaras, D.D. Dionysiou, Enhanced visible light photocatalytic activity of C-N-codoped TiO_2 films for the degradation of microcystin-LR, J. Mol. Catal. A Chem. 372 (2013) 58–65.
[434] G. Granados-Oliveros, E.A. Páez-Mozo, F.M. Ortega, C. Ferronato, J.M. Chovelon, Degradation of atrazine using metalloporphyrins supported on TiO_2 under visible light irratiation, Appl. Catal. B Environ. 89 (2009) 448–454.
[435] B. Yao, C. Peng, P. Lu, Y. He, W. Zhang, Q. Zhang, Fabrication of iron-TiO_2 charge-transfer complex with excellent visible-light photocatalytic performance, Mater. Chem. Phys. 184 (2016) 298–305.
[436] P.S. Yap, T.T. Lim, M. Lim, M. Srinivasan, Synthesis and characterization of nitrogen-doped TiO_2/AC composite for the degradation of aqueous bisphenol-A using solar light, Catal. Today 151 (2010) 8–13.
[437] H.G. Oliveira, L.H. Ferreira, R. Bertazzoli, C. Longo, Remediation of 17-α-ethinylestradiol aqueos solution by photocatalysis and electrochemically-assited photocatalysis using TiO_2 and TiO_2/WO_3 electrodes irradiated by a solar simulator, Water Res. 72 (2014) 305–314.
[438] M.G. Alalm, A. Tawfik, S. Ookawara, Enhancement of photocatalytic activity of TiO2 by immobilization on activated carbon for degradation of pharmaceuticals, J. Environ. Chem. Eng. 4 (2016) 1929–1937.
[439] S. Sood, S.K. Mehta, A.S.K. Sinha, S.K. Kansal, Bi_2O_3/TiO_2 heterostructures: synthesis, characterization and their application in solar light mediated photocatalyzed degradation of an antibiotic, ofloxacin, Chem. Eng. J. 290 (2016) 45–52.
[440] R.A. Palominos, M.A. Mondaca, A. Giraldo, G. Peñuela, M. Pérez-Moya, H.D. Mansilla, Photocatalytic oxidation of the antibiotic tetracycline on TiO_2 and ZnO suspensions, Catal. Today 144 (2009) 100–105.
[441] H. Hossaini, G. Moussavi, M. Farrokh, Oxidation of diazinon in CNS-ZnO/LED photocatalytic process: catalyst preparation, photocatalytic examination, and toxicity bioassay of oxidation by-products, Sep. Purif. Technol. 174 (2017) 320–330.
[442] M.L. Maya-Treviño, J.L. Guzmán-Mar, L. Hinojosa-Reyes, N.A. Ramos-Delgado, M.I. Maldonado, A. Hernández-Ramírez, Activity of the ZnO–Fe_2O_3 catalyst on the degradation of Dicamba and 2,4-D herbicides using simulated solar light, Ceram. Int. 40 (2014) 8701–8708.
[443] D. Sanchez-Martinez, I. Juárez-Ramírez, L.M. Torres-Martínez, I. de León-Abarte, Photocatalytic properties of Bi_2O_3 powders obtained by an ultrasound-assisted precipitation method, Ceram. Int. 42 (2016) 2013–2020.
[444] X. Xiao, R. Hu, C. Liu, C. Xing, C. Qian, X. Zuo, J. Nan, L. Wang, Facile large-scale synthesis of β-Bi_2O_3 nanospheres as a highly efficient photocatalyst for the degradation of acetaminophen under visible light irradiation, Appl. Catal. B Environ. 140–141 (2013) 433–443.
[445] M. Kaur, S.K. Mehta, S.K. Kansal, Visible light driven photocatalytic degradation of ofloxacin and malachite green dye using cadmium sulphide nanoparticles. J. Environ. Chem. Eng. (2017)https://doi.org/10.1016/j.jece.2017.04.006.
[446] A. Vazquez, D.B. Hernández-Uresti, S. Obregón, Electrophoretic deposition of CdS coatings and their photocatalytic activities in the degradation of tetracycline antibiotic, Appl. Surf. Sci. 386 (2016) 412–417.
[447] C. Yang, J. Cheng, Y. Chen, Y. Hu, CdS nanoparticles immobilized on porous carbon polyhedrons derived from a metal-organic framework with enhanced visible light photocatalytic activity for antibiotic degradation, Appl. Surf. Sci. 420 (2017) 252–259.
[448] C.-Y. Wang, X. Zhang, H.-B. Qiu, G.-X. Huang, H.-Q. Yu, $Bi_{24}O_{31}Br_{10}$ nanosheets with controllable thickness for visible–light–driven catalytic degradation of tetracycline hydrochloride, Appl. Catal. B Environ. 205 (2017) 615–623.
[449] J.C. Ahern, R. Fairchild, J.S. Thomas, J. Carr, H.H. Patterson, Characterization of BiOX compounds as photocatalysts for the degradation of pharmaceuticals in water, Appl. Catal. B Environ. 179 (2015) 229–238.

[450] X.X. Zhang, R. Li, M. Jia, S. Wang, Y. Huang, C. Chen, Degradation of ciprofloxacin in aqueous bismuth oxybromide (BiOBr) suspensions under visible light irradiation: a direct hole oxidation pathway, Chem. Eng. J. 274 (2015) 290–297.
[451] P. Yi-Zhu, M. Wan-Hong, J. Man-Ke, Z. Xiao-Rong, D.M. Johnson, H. Ying-Ping, Comparing the degradation of acetochlor to RhB using BiOBr under visible light: a significantly different rate-catalyst dose relationship, Appl. Catal. B Environ. 181 (2016) 517–523.
[452] T. Fotiou, T.M. Triantis, T. Kaloudis, L.M. Pastrana-Martinez, V. Likodimos, P. Falaras, M.T. Silva, A. Hiskia, Photocatalytic degradation of microcystin-LR and off-odor compounds in water under UV-A and solar light with a nanostructured photocatalyst based on reduced graphene oxide-TiO_2 composite. Identification of intermediate products, Ind. Eng. Chem. Res. 52 (2013) 13991–14000.
[453] L.M. Pastrana-Martínez, S. Morales-Torres, V. Likodimos, J.L. Figueiredo, J.L. Faria, P. Falaras, A.M.T. Silva, Advanced nanostructured photocatalysts based on reduced graphene oxide–TiO_2 composites for degradation of diphenhydramine pharmaceutical and methyl orange dye, Appl. Catal. B Environ. 123–124 (2012) 241–256.
[454] W. Zhu, F. Sun, R. Goei, Y. Zhou, Facile fabrication of rGO-WO_3 composites for effective visible light photocatalytic degradation of sulfamethoxazole, Appl. Catal. B Environ. 207 (2017) 93–102.
[455] M.J. Sampaio, C.G. Silva, A.M.T. Silva, L.M. Pastrana-Martínez, C. Han, S. Morales-Torres, J.L. Figueiredo, D.D. Dionysiou, J.L. Faria, Carbon-based TiO_2 materials for the degradation of Microcystin-LA, Appl. Catal. B Environ. 170–171 (2015) 74–82.
[456] M.F. Ibad, H. Kosslick, J.W. Tomm, M. Frank, A. Schulz, Impact of the crystallinity of mesoporous polymeric graphitic carbon nitride on the photocatalytic performance under UV and visible light, Microporous Mesoporous Mater. 254 (2017) 136–145.
[457] W. Wang, J. Fang, S. Shao, M. Lai, C. Lu, Compact and uniform TiO_2@g-C_3N_4 core-shell quantum heterojunction for photocatalytic degradation of tetracycline antibiotics, Appl. Catal. B Environ. 217 (2017) 57–64.
[458] G. Li, X. Nie, Y. Gao, T. An, Can environmental pharmaceuticals be photocatalytically degraded and completely mineralized in water using g-C_3N_4/TiO_2 under visible light irradiation?—implications of persistent toxic intermediates, Appl. Catal. B Environ. 180 (2016) 726–732.
[459] Y. Yu, J. Geng, H. Li, R. Bao, H. Chen, W. Wang, J. Xia, W.-Y. Wong, Exceedingly high photocatalytic activity of g-C_3N_4/Gd-N-TiO_2 composite with nanoscale heterojunctions, Sol. Energy Mater. Sol. Cells 168 (2017) 91–99.
[460] M. Alvaro, E. Carbonell, B. Ferrer, I. Llabrés, F.X. Xamena, H. Garcia, Semiconductor behavior of a metal-organic framework (MOF), Chem. Eur. J. 13 (2007) 5106–5112.
[461] J. Lee, O.K. Farha, J. Roberts, K.A. Scheidt, S.T. Nguyen, J.T. Hupp, Metal-organic framework materials as catalysts, Chem. Soc. Rev. 38 (2009) 1450–1459.
[462] J.-L. Wang, C. Wang, W. Lin, Metal-organic frameworks for light harvesting and photocatalysis, ACS Catal. 2 (2012) 2630–2640.
[463] R. Liang, S. Luo, F. Jing, L. Shen, N. Qin, L. Wu, A simple strategy for fabrication of Pd@MIL-100(Fe) nanocomposite as a visible-light-driven photocatalyst for the treatment of pharmaceuticals and personal care products (PPCPs), Appl. Catal. B Environ. 176–177 (2015) 240–248.
[464] S. Mosleh, M.R. Rahimi, Intensification of abamectin pesticide degradation using the combination of ultrasonic cavitation and visible-light driven photocatalytic process: synergistic effect and optimization study, Ultrason. Sonochem. 35 (2017) 449–457.
[465] Y. Gao, G. Yu, K. Liu, S. Deng, B. Wang, J. Huang, Y. Wang, Integrated adsorption and visible-light photodegradation of aqueous clofibric acid and carbamazepine by a Fe-based metal-organic framework, Chem. Eng. J. 330 (2017) 157–165.
[466] P. García-Muñoz, G. Pliego, J.A. Zazo, A. Bahamonde, J.A. Casas, Sulfonamides photoassisted oxidation treatments catalyzed by ilmenite, Chemosphere 180 (2017) 523–530.

[467] M.A. Montgomery, M. Elimelech, Water and sanitation in developing countries: including health in the equation, Environ. Sci. Technol. 41 (2007) 17–24.
[468] S. Malato, P. Fernandez-Ibañez, M.I. Maldonado, J. Blanco, W. Gernjak, Decontamination and disinfection of water by solar photocatalysis: recent overview and trends, Catal. Today 147 (2009) 1–59.
[469] M.J. Nieuwenhuijsen, M.B. Toledano, N.E. Eaton, J. Fawell, P. Elliott, Chlorination disinfection byproducts in water and their association with adverse reproductive outcomes: a review, Occup. Environ. Med. 57 (2000) 73–85.
[470] C. Sichel, J. Blanco, S. Malato, P. Fernandez-Ibanez, Effects of experimental conditions on E. coli survival during solar photocatalytic water disinfection, J. Photochem. Photobiol. A 189 (2007) 239–246.
[471] W.J. Huang, G.C. Fang, C.C. Wang, The determination and fate of disinfection by-products from ozonation of polluted raw water, Sci. Total Environ. 345 (2005) 261–272.
[472] D. Haaken, V. Schmalz, T. Dittmar, E. Worch, Limits of UV disinfection: UV/electrolysis hybrid technology as a promising alternative for direct reuse of biologically treated wastewater, J. Water Supply Res Technol. 62 (2013) 442–451.
[473] W. Wang, G. Li, D. Xia, T. An, H. Zhao, P.K. Wong, Photocatalytic nanomaterials for solar-driven bacterial inactivation: recent progress and challenges. Environ. Sci. Nano (2017)https://doi.org/10.1039/C7EN00063D.
[474] W.J. Wang, L.Z. Zhang, T.C. An, G.Y. Li, H.Y. Yip, P.K. Wong, Comparative study of visible-light-driven photocatalytic mechanisms of dye decolorization and bacterial disinfection by B–Ni-codoped TiO_2 microspheres: the role of different reactive species, Appl. Catal. B Environ. 108 (2011) 108–116.
[475] T.Y. Leung, C.Y. Chan, C. Hu, J.C. Yu, P.K. Wong, Photocatalytic disinfection of marine bacteria using fluorescent light, Water Res. 42 (2008) 4827–4837.
[476] Y.M. Chen, A.H. Lu, Y. Li, L.S. Zhang, H.Y. Yip, H.J. Zhao, T. An, P.K. Wong, Naturally occurring sphalerite as a novel cost-effective photocatalyst for bacterial disinfection under visible light, Environ. Sci. Technol. 45 (2011) 5689–5695.
[477] F. Bosshard, K. Riedel, T. Schneider, C. Geiser, M. Bucheli, T. Egli, Protein oxidation and aggregation in UVA-irradiated Escherichia coli cells as signs of accelerated cellular senescence, Environ. Microbiol. 12 (2010) 2931–2945.
[478] W.J. Wang, T.W. Ng, W.K. Ho, J.H. Huang, S.J. Liang, T. An, G. Li, J.C. Yu, P.K. Wong, $CdIn_2S_4$ microsphere as an efficient visible-light-driven photocatalyst for bacterial inactivation: synthesis, characterizations and photocatalytic inactivation mechanisms, Appl. Catal. B Environ. 129 (2013) 482–490.
[479] H.A. Foster, I.B. Ditta, S. Varghese, A. Steele, Photocatalytic disinfection using titanium dioxide: spectrum and mechanism of antimicrobial activity, Appl. Microbiol. Biotechnol. 90 (2011) 1847–1868.
[480] S. Helali, M.I. Polo-Lopez, P. Fernandez-Ibanez, B. Ohtani, F. Amano, S. Malato, C. Guillard, Solar photocatalysis: a green technology for *E. coli* contaminated water disinfection. Effect of concentration and different types of, suspended catalyst, J. Photochem. Photobiol. A Chem. 276 (2014) 31–40.
[481] E.A. Kozlova, A.S. Safatov, S.A. Kiselev, V.Y. Marchenko, A.A. Sergeev, M.O. Skarnovich, E.K. Emelyanova, M.A. Smetannikova, G.A. Buryak, A.V. Vorontsov, Inactivation and mineralization of aerosol deposited model pathogenic microorganisms over TiO_2 and Pt/TiO_2, Environ. Sci. Technol. 44 (13) (2010) 5121–5126.
[482] S.P. Devipriya, S. Yesodharan, E.P. Yesodharan, Solar photocatalytic removal of chemical and bacterial pollutants from water using Pt/TiO_2-coated ceramic tiles, Int. J. Photoenergy 2012 (2012) 970474–970480.
[483] Q. Zhang, C. Sun, Y. Zhao, S. Zhou, X. Hu, P. Chen, Low Ag-doped titanium dioxide nanosheet films with outstanding antimicrobial property, Environ. Sci. Technol. 44 (2010) 8270–8275.
[484] M. Bosetti, A. Masse, E. Tobin, M. Cannas, Silver coated materials for external fixation devices: in vitro biocompatibility and genotoxicity, Biomaterials 23 (2002) 887–892.

[485] M.H. Li, M.E. Noriega-Trevino, N. Nino-Martinez, C. Marambio- Jones, J.W. Wang, R. Damoiseaux, F. Ruiz, E.M.V. Hoek, Synergistic bactericidal activity of Ag–TiO_2 nanoparticles in both light and dark conditions, Environ. Sci. Technol. 45 (2011) 8989–8995.
[486] A. Kubacka, M.J. Munoz-Batista, M. Ferrer, M. Fernandez-Garcia, UV and visible light optimization of anatase TiO_2 antimicrobial properties: surface deposition of metal and oxide (Cu, Zn, Ag) species, Appl. Catal. B Environ. 140 (2013) 680–690.
[487] L. Rizzo, D. Sannino, V. Vaiano, O. Sacco, A. Scarpa, D. Pietrogiacomi, Effect of solar simulated N-doped TiO_2 photocatalysis on the inactivation and antibiotic resistance of an E. coli strain in biologically treated urban wastewater, Appl. Catal. B Environ. 144 (2014) 369–378.
[488] J.C. Yu, W.K. Ho, J.G. Yu, H. Yip, P.K. Wong, J.C. Zhao, Efficient visible-light-induced photocatalytic disinfection on sulfur-doped nanocrystalline titania, Environ. Sci. Technol. 39 (2005) 1175–1179.
[489] M. Feilizadeh, G. Mul, M. Vossoughi, E. coli inactivation by visible light irradiation using a Fe-Cd/TiO_2 photocatalyst: statistical analysis and optimization of operating parameters, Appl. Catal. B Environ. 168 (2015) 441–447.
[490] J.C. Yu, Y.D. Xie, H.Y. Tang, L.Z. Zhang, H.C. Chan, J.C. Zhao, Visible light-assisted bactericidal effect of metalphthalocyanine-sensitized titanium dioxide films, J. Photochem. Photobiol. A Chem. 156 (2003) 235–241.
[491] K.S. Yao, D.Y. Wang, C.Y. Chang, K.W. Weng, L.Y. Yang, S.J. Lee, T.C. Cheng, C.C. Hwuang, Photocatalytic disinfection of phytopathogenic bacteria by dye-sensitized TiO_2 thin film activated by visible light, Surf. Coat. Technol. 202 (2007) 1329–1332.
[492] P. Gao, J.C. Liu, T. Zhang, D.D. Sun, W. Ng, Hierarchical TiO_2/CdS "spindle-like" composite with high photodegradation and antibacterial capability under visible light irradiation, J. Hazard. Mater. 229 (2012) 209–216.
[493] M.J. Muñoz-Batista, M. Ferrer, M. Fernandez-Garcia, A. Kubacka, Abatement of organics and Escherichia coli using CeO_2–TiO_2 composite oxides: ultraviolet and visible light performances, Appl. Catal. B Environ. 154 (2014) 350–359.
[494] P. Kongsong, L. Sikong, S. Niyomwas, V. Rachpech, Photocatalytic antibacterial performance of glass fibers thin film coated with N-doped SnO_2/TiO_2, Sci. World J. 869706 (2014) 1–9.
[495] R. Dhanalakshmi, A. Pandikumar, K. Sujatha, P. Gunasekaran, Photocatalytic and antimicrobial activities of functionalized silicate sol–gel embedded ZnO–TiO_2 nanocomposite materials, Mater. Express 3 (2013) 291–300.
[496] H.L. Liu, T.C.K. Yang, Photocatalytic inactivation of Escherichia coli and Lactobacillus helveticus by ZnO and TiO_2 activated with ultraviolet light, Process Biochem. 39 (2003) 475–481.
[497] R. Kumar, S. Anandan, K. Hembram, T.N. Rao, Efficient ZnO-based visible-light-driven photocatalyst for antibacterial applications, ACS Appl. Mater. Interfaces 6 (2014) 13138–13148.
[498] N. Talebian, M.R. Nilforoushan, E.B. Zargar, Enhanced antibacterial performance of hybrid semiconductor nanomaterials: ZnO/SnO_2 nanocomposite thin films, Appl. Surf. Sci. 258 (2011) 547–555.
[499] S.W. Liu, G.C. Huang, J.G. Yu, T.W. Ng, H.Y. Yip, P.K. Wong, Porous fluorinated SnO_2 hollow nanospheres: transformative self-assembly and photocatalytic inactivation of bacteria, ACS Appl. Mater. Interfaces 6 (2014) 2407–2414.
[500] P. Gao, J.C. Liu, D.D. Sun, W. Ng, Graphene oxide-CdS composite with high photocatalytic degradation and disinfection activities under visible light irradiation, J. Hazard. Mater. 250 (2013) 412–420.
[501] H.T. Yu, X. Quan, Y.N. Zhang, N. Ma, S. Chen, H.M. Zhao, Electrochemically assisted photocatalytic inactivation of Escherichia coli under visible light using a $ZnIn_2S_4$ film electrode, Langmuir 24 (2008) 7599–7604.
[502] B. Sun, Z. Qiao, K. Shang, H. Fan, S.Y. Ai, Facile synthesis of silver sulfide/bismuth sulfide nanocomposites for photocatalytic inactivation of Escherichia coli under solar light irradiation, Mater. Lett. 91 (2013) 142–145.

[503] J. Ren, W.Z. Wang, L. Zhang, J. Chang, S. Hu, Photocatalytic inactivation of bacteria by photocatalyst Bi_2WO_6 under visible light, Catal. Commun. 10 (2009) 1940–1943.
[504] W.J. Wang, Y. Yu, T.C. An, G.Y. Li, H.Y. Yip, J.C. Yu, P.K. Wong, Visible-light-driven photocatalytic inactivation of E. coli K-12 by bismuth vanadate nanotubes: bactericidal performance and mechanism, Environ. Sci. Technol. 46 (2012) 4599–4606.
[505] C. Adan, J. Marugan, S. Obregon, G. Colon, Photocatalytic activity of bismuth vanadates under UV-A and visible light irradiation: inactivation of Escherichia coli vs oxidation of methanol, Catal. Today 240 (2015) 93–99.
[506] Z.J. Zhang, W.Z. Wang, J. Ren, J.H. Xu, Highly efficient photocatalyst Bi_2MoO_6 induced by blue light-emitting diode, Appl. Catal. B Environ. 123 (2012) 89–93.
[507] Y.S. Xu, Y.X. Yu, W.D. Zhang, Wide bandgap $Bi_2O_2CO_3$-coupled Bi_2MoO_6 heterostructured hollow microspheres: one-pot synthesis and enhanced visible-light photocatalytic activity, J. Nanosci. Nanotechnol. 14 (2014) 6800–6808.
[508] B.C. Cao, S. Cao, P.Y. Dong, J. Gao, J. Wang, High antibacterial activity of ultrafine TiO_2/graphene sheets nanocomposites under visible light irradiation, Mater. Lett. 93 (2013) 349–352.
[509] L. Liu, H.W. Bai, J.C. Liu, D.D. Sun, Multifunctional graphene oxide-TiO_2–Ag nanocomposites for high performance water disinfection and decontamination under solar irradiation, J. Hazard. Mater. 261 (2013) 214–223.
[510] P. Gao, K. Ng, D.D. Sun, Sulfonated graphene oxide-ZnO–Ag photocatalyst for fast photodegradation and disinfection under visible light, J. Hazard. Mater. 262 (2013) 826–835.
[511] J.H. Huang, W.K. Ho, X.C. Wang, Metal-free disinfection effects induced by graphitic carbon nitride polymers under visible light illumination, Chem. Commun. 50 (2014) 4338–4340.
[512] H. Zhao, H. Yu, X. Quan, S. Chen, Y. Zhang, H. Zhao, H. Wang, Fabrication of atomic single layer graphitic-C_3N_4 and its high performance of photocatalytic disinfection under visible light irradiation, Appl. Catal. B Environ. 152 (2014) 46–50.
[513] Y.M. Chen, T.W. Ng, A.H. Lu, Y. Li, H.Y. Yip, T. An, G. Li, H. Zhao, M. Gao, P.K. Wong, Comparative study of visible-light-driven photocatalytic inactivation of two different wastewater bacteria by natural sphalerite, Chem. Eng. J. 234 (2013) 43–48.
[514] D.H. Xia, T.W. Ng, T. An, G.Y. Li, Y. Li, H.Y. Yip, H. Zhao, A. Lu, P.K. Wong, A recyclable mineral catalyst for visible-light-driven photocatalytic inactivation of bacteria: natural magnetic sphalerite, Environ. Sci. Technol. 47 (2013) 11166–11173.

FURTHER READING

[515] E. Bae, W. Choi, J.W. Park, H.S. Shin, S.B. Kim, J.S. Lee, Effects of surface anchoring groups (carboxylate vs phosphonate) in ruthenium-complex-sensitized TiO_2 on visible light reactivity in aqueous suspensions, J. Phys. Chem. B 108 (2004) 14093–14101.
[516] D.W. Chen, A.K. Ray, Photocatalytic kinetics of phenol and its derivatives over UV irradiated TiO_2, Appl. Catal. B Environ. 23 (1999) 143–157.
[517] M. Huang, J. Yu, B. Li, C. Deng, L. Wang, W. Wu, L. Dong, F. Zhang, M. Fan, Intergrowth and coexistence effects of TiO_2-SnO_2 nanocomposite with excellent photocatalytic activity, J. Alloys Compd. 629 (2015) 55–61.
[518] V. Likodimos, D.D. Dionysiou, P. Falaras, CLEAN WATER: water detoxification using innovative photocatalysts, Rev. Environ. Sci. Biotechnol. 9 (2010) 87–94.
[519] K.H. Wang, Y.H. Hsieh, M. Yeuan, C.Y. Chang, Photocatalytic degradation of 2-chloro and 2-nitrophenol by titanium dioxide suspensions in aqueous solution, Appl. Catal. B Environ. 21 (1999) 1–8.

[520] H.C. Wang, P. Liu, S.M. Wang, W. Han, X.X. Wang, X.Z. Fu, Nanocrystalline zinc oxide in perfluorinated ionomer membranes: preparation, characterization, and photocatalytic properties, J. Mol. Catal. A Chem. 273 (2007) 21–25.
[521] WWAP (United Nations World Water Assessment Programme), The United Nations World Water Development Report 2017. Wastewater: The Untapped Resource, UNESCO, Paris, 2017. 2 p.
[522] Y. Zhang, J.C. Crittenden, D.W. Hand, D.L. Perram, Fixed-bed photocatalysts for solar decontamination of water, Environ. Sci. Technol. 28 (1994) 435–442.
[523] F. Zhang, J. Zhao, L. Zang, T. Shen, H. Hidaka, E. Pelizzetti, N. Serpone, TiO_2-assisted photodegradation of dye pollutants II. Adsorption and degradation kinetics of eosin in TiO_2 dispersions under visible light irradiation, Appl. Catal. B Environ. 15 (1998) 147–156.

CHAPTER

RECENT ADVANCES IN PHOTOCATALYTIC DETOXIFICATION OF WATER

23

Priyanka Ganguly[*,†], **Suyana Panneri**[‡,§], **U.S. Hareesh**[‡,§], **Ailish Breen**[*,†], **Suresh C. Pillai**[*,†]

*Nanotechnology and Bio-Engineering Research Group, Department of Environmental Science, School of Science, Institute of Technology Sligo, Sligo, Ireland** *Centre for Precision Engineering, Materials and Manufacturing Research (PEM), Institute of Technology Sligo, Sligo, Ireland*† *Materials Science and Technology Division, National Institute for Interdisciplinary Science and Technology (CSIR-NIIST), Thiruvananthapuram, India*‡ *Academy of Scientific and Innovative Research (AcSIR), New Delhi, India*§

1 INTRODUCTION

Access to clean and safe drinking water is one of the pressing global problems of the 21st century [1–4]. The predicted rise in world population (from 7 billion to 9 billion by 2050) will certainly increase the demand for water exponentially [5]. At the same time, the growing concern about pollution of drinking water sources in the developing and industrialized countries poses a critical concern [6–8]. A study by the World Health Organization (WHO) estimates the death of about 3.4 million people, annually, from water-related diseases [9, 10]. About 884 million people lack access to even basic drinking water. Moreover, it is estimated that by 2025, half of the world's population will be living in water-stressed areas [11, 12]. Therefore, in 2010, the UN general assembly recognized that access to safe drinking water and sanitation is a basic human right and not a privilege.

The water detoxification process deals with important pathways for alleviating disinfection and decontamination of water sources [13–15]. Strategies involve the removal, inactivation, and complete termination of the growth and reproduction of microorganisms. On the other hand, water decontamination implies strategies for removal of hazardous substances such as chemicals, radioactive materials, etc., from water sources [16, 17]. The existing traditional detoxification processes employed in wastewater treatment plants are archaic and do not account for present-day threats [18–20]. Therefore, there is a desperate need for alternative low-cost and energy-efficient detoxification processes. In the past few decades, photocatalysis has emerged as a credible substitute for archaic detoxification methods [21]. As the energy source for this process, light has emerged to be a clean and green alternative [22].

The present chapter provides a brief overview of the photocatalytic mechanism and discusses recent advances in the detoxification process. It seeks to refine recent studies on photocatalytic disinfection and decontamination by new-generation, nonconventional photocatalysts. It discusses factors affecting the disinfection process and defines the disinfection mechanism of several microbial strains. The chapter also discusses the state of the art degradation pathways and profiles of several emerging

Nanoscale Materials in Water Purification. https://doi.org/10.1016/B978-0-12-813926-4.00029-X

contaminants like endocrine disrupting agents and pesticides. The rise in antibiotic-resistant microbial strains and pharmaceutical effluents has prompted a discussion of recent studies on degradation techniques which have evolved in the past few years for dealing with these pollutants.

2 PHOTOCATALYTIC MECHANISM

Photocatalysis is defined as "acceleration of a photo-generated electron in the presence of a catalyst," in which the catalyst neither undergoes any changes nor is consumed in the reaction [23, 24]. While the chemical reaction occurs in more than one medium, it is generally referred to as heterogeneous photocatalysis [24–26]. A semiconductor surface, on irradiation with light, generates an electron-hole pair (Eq. 1) [23, 26–29]. The impinging photon should have an energy greater than or equal to the band gap of the semiconductor material. The electron from the valence band excites to the conduction band, leaving a hole behind in the valence band. (Fig. 1) The electron in the conduction band reacts with the molecular oxygen dissolved inside water to form Reactive Oxygen Species (ROS) like superoxide radicals ($^{\bullet}O_2^-$), or hydroperoxide radicals ($^{\bullet}HO_2$) (Eq. 2). Similarly, the holes generated in the valence band react with water to generate hydroxyl radicals ($^{\bullet}OH$) and hydrogen ions (H^+) (Eq. 3) [25, 30–32].

$$\text{Photocatalyst} + h\nu \rightarrow h_{VB}^+ + e_{CB}^- \tag{1}$$

$$e_{CB}^- + O_2 \rightarrow O_2^- \tag{2}$$

$$h_{VB}^+ + H_2O \rightarrow {}^*OH + H^+ \tag{3}$$

The toxic molecule (microorganisms, organic effluents, pesticides, etc.) interacts on the catalyst surface to undergo fragmentation [33, 34]. The ROS generated on the surface participates in this

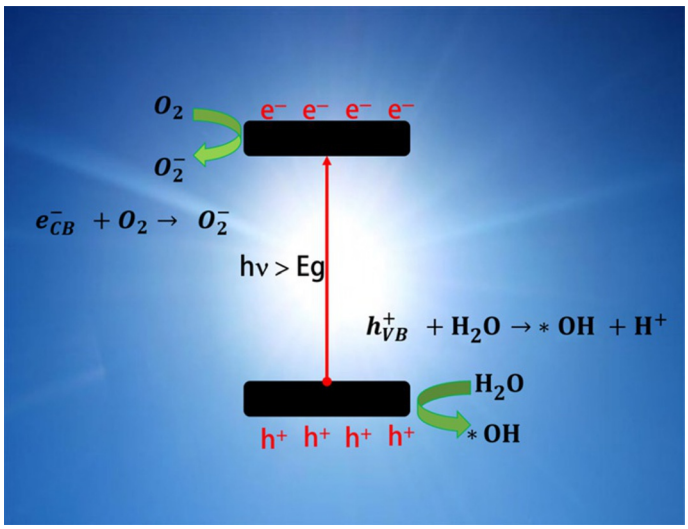

FIG. 1

Photocatalytic mechanism.

disintegration process and converts the harmful effluents into simpler products like carbon dioxide, water, etc. [30, 35–38].

However, with photogenerated charge carriers, there is a high probability they will undergo recombination, which results in low quantum efficiency. Therefore, vast effort is exerted to prevent the recombination process [38, 39].

3 PHOTOCATALYTIC DISINFECTION

Photocatalytic disinfection of water was first reported by Matsunaga et al. in 1985. The authors reported the photo-electrochemical inactivation of *Lactobacillus acidophilus*, *Saccharomyces cerevisiae*, and *Escherichia coli* by Pt-loaded TiO_2. Thereafter, a wide range of research has been carried out, exploiting the beneficial effect of photocatalysis.

3.1 DISINFECTION MECHANISM

Understanding the disinfection mechanism is essential in order to improve the prevailing treatment processes [40, 41]. It was Matsunaga and colleagues who demonstrated the inactivation of bacterial strains and attributed the degradation of Coenzyme A by potential ROS as the reason behind the disinfection process [42]. Following studies by Saito et al. asserted that the cell inactivation occurred due to the destruction of the cell membrane. The Transmission Electron Microscopy (TEM) images of this study illustrated the complete destruction of the cells [43]. In later studies, Jacoby et al. furnished evidence on complete mineralization of the inactivated cells. The Scanning Electron Microscopy (SEM) images displayed the disappearing colonies of bacteria and the ^{14}C radioisotope labeling indicated the change in the carbon content [44]. Similarly, Sokmen and colleagues quantified the lipid peroxidation by quantifying the Malondialdehyde formed in the process. The gas chromatography mass spectrometry (GC/MS) measurements calculated and monitored the by-products formed in the due process [45]. In a noteworthy contribution, Remy et al. investigated the bacterial targets and studied the inactivation process in dark and visible light irradiation. The titania nanoparticles exhibited toxic behavior against the bacterial cells and necessarily contributed to the inactivation process. The increase in the nanoparticle concentration introduced cellular wall damage and effectively increased the bactericidal nature. However, the cell wall integrity remained unaffected in the presence of silica nanoparticles. The difference in the surface charge of the cell wall and the nanoparticle was observed to be the fundamental cause. In further analysis, the genetic content (RNA and DNA) of the bacterial cells were observed to be the bacterial targets of the oxidative damage by the ROS generated [46]. In a fresher effort to understand the complete inactivation mechanisms, Matai et al. defined plausible routes of inactivation caused by Ag-ZnO composite (Fig. 2). The dissolution of Ag and Zn ions contributes to the surface oxidation of the cell wall. This direct interaction of the bacterial cell with the composite constitutes the first route of inactivation. The ROS generated in the disinfection process is considered as the second possible method of inactivation. The authors postulate the interaction of the ROS with the sugar-phosphate group contributes to the gene alteration. This tampering with the genetic data causes changes in the protein expression responsible for cellular metabolism. Lastly, the breakdown of cell membrane and the release of the cytosolic components is depicted as the final route of inactivation [47].

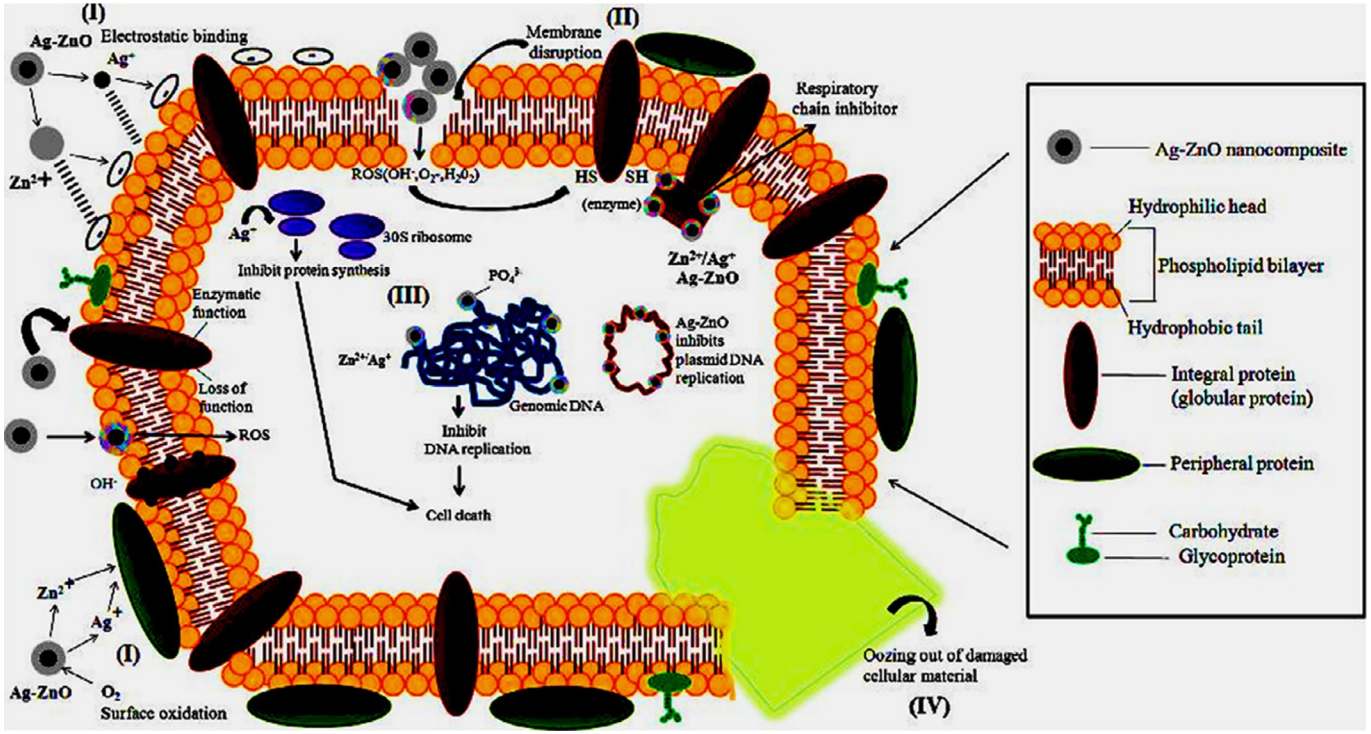

FIG. 2

Schematic representation of antibacterial mechanism of Ag–ZnO nanocomposite.

Reprinted with permission of I. Matai, A. Sachdev, P. Dubey, S.U. Kumar, B. Bhushan, P. Gopinath, Antibacterial activity and mechanism of Ag–ZnO nanocomposite on S. aureus and GFP-expressing antibiotic resistant E. coli, Colloids Surf. B: Biointerfaces 115 (2014) 359–367. Full details are given in the respective publication.

3.2 DISINFECTION KINETIC MODELS

The kinetic modeling of any chemical reaction aids in understanding the key elements responsible for the reaction [48–50]. The photocatalytic disinfection process is a very complex phenomenon. It involves multiple factors, for example, pH of the sample, different catalyst loading, irradiation intensity, turbidity, the temperature of the reaction mixture, and most importantly, the complex structure of the microorganism [51, 52]. The presence of different strains of microorganisms, various target organs inside their body, and the mineralization of the target component are among the few key factors governing the kinetic process. The model helps to simplify the complicated reaction phases into simpler mathematical expression [53, 54]. The kinetic models portray survival curves, a graphical illustration signifying the semilog plot of inactivation on contact time. The variation in the shape of the survival curves plays a crucial factor in the assessment of the mechanism of microbial inactivation [55]. Fig. 3 shows the different survival curves observed in general. Curve (A) in Fig. 3 exhibits a first order kinetics of inactivation, which illustrates the exponential death of microbes with time. Curve (B) in Fig. 3 displays an exponential disinfection but shows a shoulder initially, which implies the delay in diffusion of the disinfectant molecules to the sites of action. Curve (C) in Fig. 3 shows a curve of a shoulder and a tailing off, while Curve (D) is only limited by having a tailing off sequence at the end of the curve. The presence of several families of microbes in the sample with varying degrees of resistance causes a decrease in the rate of inactivation, which results in the tailing-off nature [51, 55–58].

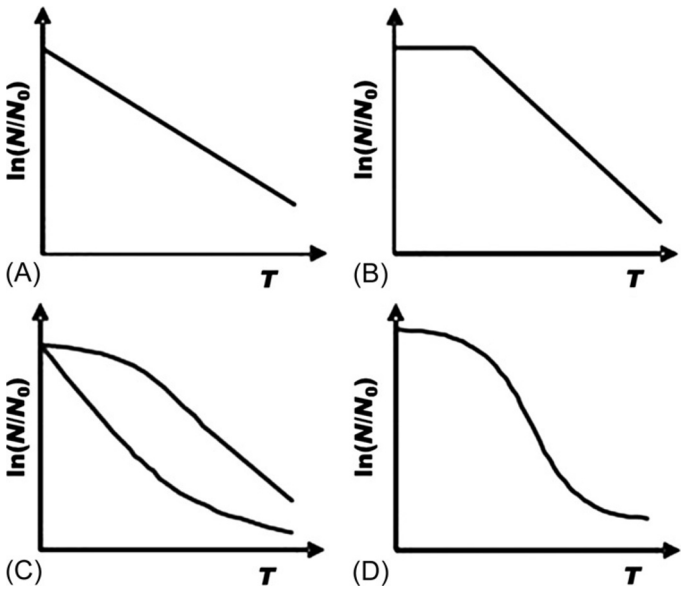

FIG. 3

Survival curves observed for different kinetic models used in the photocatalytic disinfection. Curve (A) first-order kinetics of inactivation,exhibits the exponential death of microbes with time, Curve (B) exponential disinfection but with an initial shoulder, Curve (C) curve with a shoulder and a tailing off, and Curve (D) curve with a tailing off sequence at the end.

Reprinted with permission of J. Marugán, R. van Grieken, C. Sordo, C. Cruz, Kinetics of the photocatalytic disinfection of Escherichia coli suspensions, Appl. Catal. B Environ., 82 (2008) 27–36. Full details are given in the respective publication.

The kinetic inactivation models are derived based on the following assumptions: (a) uniform distribution of microorganisms and the disinfectant molecules, (b) constant pH, temperature, and the concentration of the catalyst (disinfectant), and (c) adequate mixing to evade liquid diffusion as a potential limiting agent in the chemical reaction [51]. There exist four common kinetic models; (1) Chick's model, (2) Chick-Watson model, (3) Delayed Chick-Watson model, and (4) Hom's model. The general expression of the differential rate law used by these kinetic models is as (Eq. 20); [51, 55–58]

$$\frac{dN}{dt} = -KmN^x C^n t^{m-1} \tag{4}$$

Where:

$\frac{dN}{dt}$=Rate of inactivation.
N=Number of survivors at contact time t.
K=Reaction rate constant.
C=Concentration of the disinfectant.
m, n, x=Empirical constants.

3.2.1 Chick's model

Chick's 1908 paper on "The laws of disinfection" compared the bacterial inactivation to a chemical reaction, where individual bacteria was considered as molecules [59].

$$xN + nC \xrightarrow{K_1} S\,(\text{dead microorganisms}) \tag{5}$$

The rate of reaction for the following reaction is given as: [60]

$$\frac{dN}{dt} = -K_1 N^x C^n (d\text{ead microorganisms})^S \tag{6}$$

Here x and $n=1$ and considering the reaction is irreversible, thus $S=0$. Hence, Eq. (6) results in

$$\frac{dN}{dt} = -K^* N \tag{7}$$

Where K^* is considered as the pseudo first order rate constant where $K^*=K_1C$. Thus, Eq. (7) is the generalized rate law expression of Chick's law. It states that the rate of inactivation is proportional to the number of surviving microbes at a constant disinfectant concentration (Fig. 3A).

Integration of Eq. (7) results in:

$$\ln\frac{N}{N_0} = -K^* T \tag{8}$$

Where N_0=Initial microbial population.

In a more recent study, Danae and Dionissios explain the importance of the true order of this kinetic model [50]. The authors found that the reaction parameters such as temperature, catalyst concentration, etc., are accounted for as a constant called a pseudo-first-order constant. Hence, at different N_0 values, a constant experimental setup should render constant K^* value. If the value remains constant, then indeed it could be termed a first-order constant. The authors also explained the importance of ROS concentration in the reaction mixture. The ROS in the reaction mixture is a predominant factor governing the rate of disinfection; hence, the "N" value cannot alone be considered an exclusive factor. The excess

of ROS will potentially cause quicker disinfection and display a first order kinetics, meanwhile, a low ROS concentration will become a potential limiting agent in the disinfection process. Therefore, ROS is certainly a principal factor governing the kinetics of the disinfection process. Hence, the ROS produced in the reaction depends on the constant experimental factors. Thus, the experimental parameters are the true controllers of the disinfection kinetics [51, 61, 62].

3.2.2 Chick-watson model

The Chick's law assumes first-order kinetics and in most instances, the microbial inactivation does not follow this assumption. Watson (in the same year, 1908) modified Chick's law by incorporating the concentration-time product which considers the effect of varying concentration of disinfectant (Eq. 9) [59]

$$K = C^n T \tag{9}$$

Where *"K"* is a constant for a microbe and a set of conditions, "*N*" is a constant, and "*T*" is the time required to attain a certain activation point. An n value less than 1 signifies the increased importance of the contact time, more than the disinfectant concentration. The addition of Watson's function in Chick's law results in a Chick-Watson pseudo-first-order rate law as: [59, 63]

$$\frac{dN}{dt} = -KNC^n \tag{10}$$

Where K is the first-order rate constant. Integration of the above expression results in (Fig. 3A) [59, 63]

$$ln\frac{N}{N_0} = -KC^n T \tag{11}$$

$$\frac{N}{N_0} = e^{-KC^n T} \tag{12}$$

3.2.3 Delayed chick-watson model

The simplified nature of the Chick-Watson model makes it equitable in most studies. However, the Chick-Watson model has its own pitfalls; it assumes that the microbes are of a single strain, and the inactivation occurs on a single hit and at a single spot. It shows neither the initial shoulder (lag phase) nor the tailing-off nature. The delayed Chick-Watson model introduces a time lag parameter to overcome the shoulder observed in the disinfection process (Fig. 3B) [64–67].

$$\frac{N}{N_0} = \begin{cases} 1, & T \le T_{lag} \\ e^{-KC^n T}, & T > T_{lag} \end{cases} \tag{13}$$

3.2.4 Hom's and modified hom's model

The delayed Chick-Watson model can represent the shoulder or the tailing off at a time but the concurrent presence of both cannot be expressed using this model. The Hom's disinfection model proposed in 1972 provides a generalized expression for the time-concentration product. It is very similar to the Chick-Watson model; an addition of a power factor m for time is observed. When $m = 1$, the equation reduces to the Chick-Watson model, $m > 1$ results in the appearance of the initial shoulder in the curves,

while $m<1$ leads to the appearance of the tailing off (Fig. 3C). Hence, the Hom's model also does not allow the occurrence of both the initial lag and the tailing off in the curve at the same time [60, 68, 69].

$$ln\frac{N}{N_0} = -KC^nT^m \tag{14}$$

Thereafter, a modification is introduced in the Hom's model which allows the presence of the initial lag, the log-linear phase, and the tailing off at the end of the curve. The modified Hom's model is as (Fig. 3D); [60, 68, 69]

$$ln\frac{N}{N_0} = -K_1[1 - \exp(-K_2T)]^{K_3} \tag{15}$$

Where K_1, K_2, K_3 are the empirical constants in this model.

In a more recent study by Marugan et al., the authors evaluate the photocatalytic disinfection of *E. coli* using a simplified kinetic model having three parameters; kinetic constant (k), pseudo-adsorption constant (K) and inhibition coefficient (n). This model takes into account the three different phases (the initial lag phase, log-linear phase, and the tailing-off nature) in the survival curve [70].

Thus, the bacterial cell reduction is expressed as a function of the log of the relative cell population and the function of time. The reduction parameter defines the decrease of the levels of microbes in the samples by factors of 10, which is easily converted into a percentage (%) expression. Hence a 1-log reduction signifies a death of 90%, 2-log reduction indicates a death of 99%, and 3-log reduction implies a death of 99.9% of the microbes [71].

3.3 FACTORS INFLUENCING THE DISINFECTION MECHANISM

There are multiple factors affecting the disinfection mechanism [72–76]. pH is a crucial factor of concern among them [77]. The surface charge of the catalyst and its microbial cell wall is dependent on the overall pH of the system. Watts et al. found that the bactericidal property remained unaltered between the pH of 5 and 8 [71]. Conversely, Herrera et al. observed that the rate of disinfection process was improved in TiO_2-based system at pH 5 [78]. Improved activity was observed in the presence of TiO_2 and not just by acidification of the cells. There are several reports illustrating the non-dependence of pH in the disinfection process [66]. Catalyst loading is another important operational factor of concern. It has been witnessed in numerous studies that the disinfection method advances with the increase in the catalyst concentration. Nevertheless, it rapidly reaches a saturation limit, at which the rate of the reaction remains constant even with increase in the catalyst concentration. Increase in the catalyst concentration eventually leads to turbidity and obstructs the absorption of the incoming radiation [15, 79–82]. Similarly, irradiation length plays vital part in the disinfection mechanism [83–85]. Studies by Rincon et al. showed that continuous irradiation (in absence of catalyst) causes complete disinfection, but ceasing the illumination could lead to increase in the number of viable bacterial cells to its initial value [74]. The bacterial cell produces superoxide dismutase (SOD) enzyme as a protective mechanism to survive against the disparate amount of ROS generated inside the cell (in the presence of a catalyst) and lessens the oxidative stress. Nevertheless, the ROS created in the presence of the catalyst on due irradiation of light is significantly high, which eventually leads to total bacterial annihilation. The results acquired from this study are quite inconsistent with other previously reported literature. It was observed that the discontinuous illumination amplified the bacterial inactivation. Hence,

the effect of continuous and intermittent irradiation is governed by the type of microorganism [86]. Likewise, Li et al. also observed no bactericidal activity in the *E. coli* samples in absence of any disinfectant, and the rate of photocatalytic inactivation reduced as the samples with catalyst loaded were in the shade [87]. On the other hand, irradiation intensity is another key parameter determining the bactericidal course [88]. Increasing the illumination intensity certainly increases the ROS production. Apart from the enhanced ROS levels, the surface area of the catalyst is a key factor [17]. The enhanced surface area, renders enough site for ROS production, which eventually contributes to the complete bacterial inactivation [88]. In contrast, operating temperature is not considered to be an important factor in the disinfection mechanism [89]. The heat energy supplied to the reaction mixture is not enough to overcome the ban gap barrier of the catalyst. However, this energy is utilized to activate the reactant on the catalyst surface. Nevertheless, there are some studies contradicting this analysis and overrules the less importance of temperature. It was observed that increasing the temperature decreased the time for complete annihilation as the enhanced temperature amplified the collision frequency of the molecules and resulted in a better rate of reaction. [66, 90] Generally, in photocatalytic disinfection the use of sunlight could be justified as the potential source of light and heat, this makes the practice an effective substitute to the conventional water treatment approaches, which consumes a fair share of energy in the heating process. [17, 89, 91] Turbidity is one more vital factor which marks the decontamination process. The existence of small insoluble subparticles (e.g., clay, planktons, and microorganisms) is the cause of this turbidity. The turbid water causes attenuation of incoming light, and the absorption level differs considerably. It was detected that improved altitudes of turbidity in the water sample cut the photocatalytic inactivation rate. The increased particulate level diminishes the ability of the incoming irradiation to breach through the turbid water. Moreover, the catalyst addition leads to aggregation, which lessens the disinfection action, and the heat captivated in the system raises bacterial growth [72, 92, 93].

3.4 PHOTOCATALYTIC TREATMENT OF PATHOGENIC MICROORGANISMS

There are several photocatalysts like titania, zinc oxide, zinc sulfide, and several other conventional metal oxides, for which researchers are exploring photocatalytic disinfection ability. The present section will discuss the new generation catalysts and the state of the art improvement involved in the disinfection process.

3.4.1 Bacteria

In recent years, layered materials like graphene and its anomalies have certainly spawned interest among researchers to characteristically understand and exploit their interesting properties. The use of 2D carbon materials for multifunctional applications has been widely studied in years, including photocatalytic disinfection. Graphene, the favorite among the 2D class of materials, has been explored to its utmost [94]. It has zero potential band gaps, and hence, incorporation of this material has craftily led to the formation of composites with improved photocatalytic activities. Liu et al. and Deng et al. reported the synthesis of a novel composite of graphene oxide (GO) enwrapped Ag_3PO_4 and evaluated the visible light disinfection of the bacterial strains. Complete disinfection was reported both by the composite and bare Ag_3PO_4, while GO sheets alone did not possess any antibacterial property. The release of Ag ions contributed to the non-viability of the bacterial cells [95, 96]. Akhavan and Ghaderilt fabricated nanocomposites of TiO_2 and reduced graphene oxide that displayed improved bactericidal

efficiency under solar light. The enhanced activity was attributed to the electron sink or the electron acceptor ability of the reduced graphene oxide which effectively introduced charge separation and delayed the recombination rate [97]. Later, Liu et al. reported the formation of graphene oxide-TiO_2 nanorod composites, which illustrated enhanced *E. coli* inactivation compared to that of the titania nanorods. The improved efficiency was attributed to the cooperative effect of the two-dimensional graphene sheets deposited on the high surface area of titania nanorods [98]. In a similar attempt, Gao et al. also illustrated the bacterial inactivation of the strains of *E. coli* using the titania-graphene composite under visible light illumination [99]. Ibanez et al. studied the inactivation of the same composite using two different strains of bacteria (*E. coli* and *F. solani*) and compared the results with P25 (TiO_2 nanoparticles with mixed anatase and rutile phase). The composites illustrated rapid disinfection compared to the inactivation results of P25, and their improved efficacy was attributed to the formation of singlet oxygen in the reaction mixture [100]. In a very recent study, the same group elaborated the plausible disinfection mechanism by altering the irradiation parameter and usage of several ROS scavengers. The hydroxyl radical, singlet oxygen, and hydrogen peroxide were the major ROS generated, under visible light irradiation, but the singlet oxygen was found to be the dominant ROS [101]. Xia et al. studied the bacterial inactivation mechanisms by graphene sheets grafted with plasmonic Ag/AgX (X=Cl, Br, I) composite under visible light irradiation. The graphene sheets delayed the recombination rate by providing necessary charge separation, and the Ag ions effectively enhanced the levels of ROS produced [102]. A ternary composite of titania nanocrystals, carbon dots, and reduced graphene oxide was fabricated and evaluated for its photocatalytic disinfection ability. The addition of carbon dots improved the charge separation and contributed to the delayed recombination ability, which consequently resulted in improved bactericidal efficiency (Fig. 4) [103].

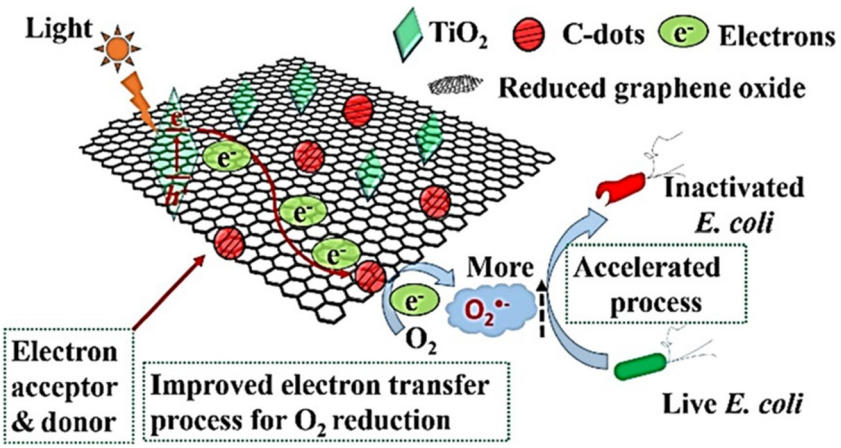

FIG. 4

Schematic illustration of the plausible disinfection mechanism using the ternary composite of TiO_2, carbon dots on reduced graphene oxide.

Reprinted with permission of X. Zeng, Z. Wang, N. Meng, D.T. McCarthy, A. Deletic, J.-H. Pan, X. Zhang, Highly dispersed TiO_2 nanocrystals and carbon dots on reduced graphene oxide: ternary nanocomposites for accelerated photocatalytic water disinfection, Appl. Catal. B Environ. 202 (2017) 33–41. Full details are given in the respective publication.

Khadgi et al. recently reported the formation of $ZnFe_2O_4$ co-modified with Ag and rGO. The composite showed more than 7-log inactivation efficiency within 60 min of irradiation. The SEM micrographs of the destructed bacterial remains are showed in Fig. 5 [104].

Among metal free photocatalysts, layered graphitic carbon nitride (g-C_3N_4) attracted enormous interest in recent years owing to positive attributes like ease of synthesis from inexpensive precursors, band compatibility with other semiconductors for heterostructure formation, and its high thermal stability even in air atmosphere (up to 650°C) [105]. The framework topology of g-C_3N_4 is identified as defect-rich, N-bridged, aromatic poly-tri-s-triazine units forming a sheet like π conjugated structure, as in graphite, with strong C-N covalent bond and layers held together by van der Waals forces [106]. The thermal evaporation condensation of low-cost nitrogen rich precursors like melamine, cyanamide, dicyandiamide, urea, thiourea, or their mixtures yields g-C_3N_4 [107, 108]. The microbial disinfection utilizing g-C_3N_4 was first studied by Wang et al. They evaluated the bacterial inactivation of *E. coli* K12, using a heterojunction photocatalyst of α-sulfur co-modified with graphene and graphitic carbon nitrides. Two altered structures were synthesized by varying the distribution of sheets of carbon nitride ($CNRGOS_8$) or the reduced graphene ($RGOCNS_8$) across the α-sulfur. The $CNRGOS_8$ showed

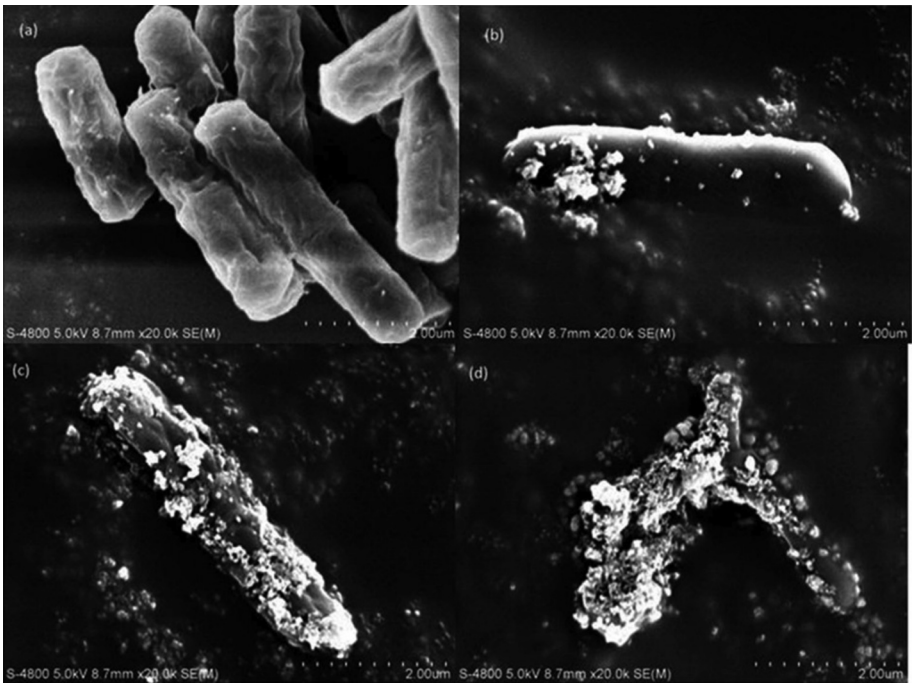

FIG. 5

SEM images of *E. coli* (A) before the addition of the nanocomposite, at the time (B) 0 min, (C) 30 min, and (D) 60 min.

Reprinted with permission of N. Khadgi, A.R. Upreti, Y. Li, Simultaneous bacterial inactivation and degradation of an emerging pollutant under visible light by $ZnFe_2O_4$ co-modified with Ag and rGO, RSC Adv. 7 (2017) 27007–27016. Full details are given in the respective publication.

improved photocatalytic inactivation efficiency compared to $RGOCNS_8$. Moreover, the core-shell composite particles displayed reduced photocatalytic disinfection in anaerobic condition. The disinfection process of the composite structures in the aerobic and anaerobic condition is illustrated in Fig. 6 [109]. However Huang et al. studied the photocatalytic disinfection of *E. coli* by *g*-C_3N_4 for the first time [110]. The light induced bacterial inactivation of the strains of *E. coli* was completed within 4 h of irradiation on the mesoporous surface of carbon nitride (surface area value of 230 m^2/g). Instead, the bare C_3N_4 showed only 90% of kill rate after being irradiated for 6 prolonged hours. Thus, the study portrayed the significance of the surface area for the antibacterial effects on the catalyst surface. The practical applications of *g*-C_3N_4 are still challenging due to their low specific surface area, a vital parameter in catalysis- and adsorption-based applications [111]. Also the relatively large bandgap of 2.7 eV enables the absorption of only a small portion of visible spectrum [112]. Hence several strategies like elemental doping, exfoliation techniques, mesoporous generation, and heterostructure formation with other compatible semiconductors are reported [15]. In such an attempt, Zhao et al. prepared single-layer *g*-C_3N_4 sheets and later studied the photocatalytic disinfection of *E. coli*. The single layer sheets of *g*-C_3N_4 exhibited complete inactivation within 4 h of irradiation, while the bulk *g*-C_3N_4 showed only 3-log of inactivation for the same irradiation length. The improved efficiency of the single layer *g*-C_3N_4 sheets was attributed to the low charge transfer resistance and efficient charge separation [113].

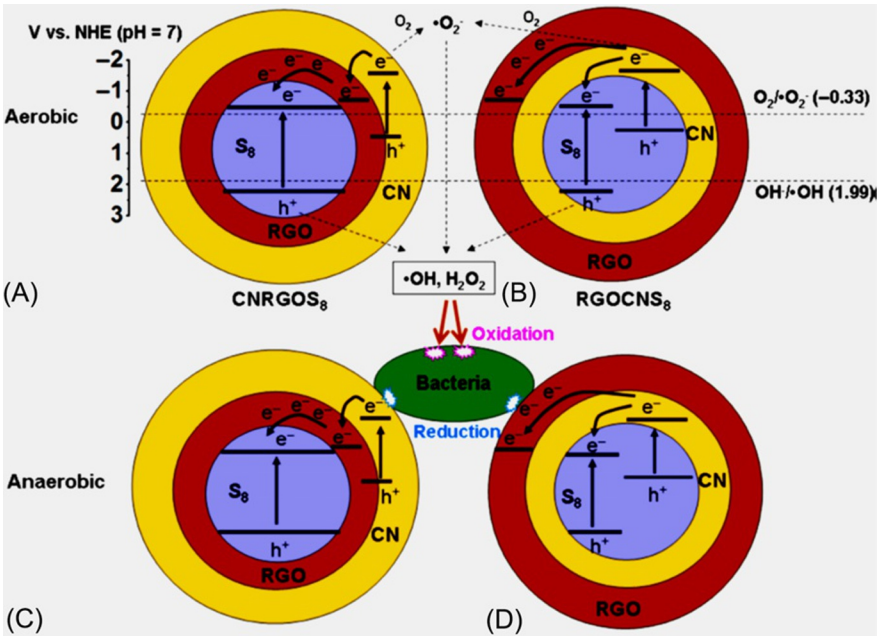

FIG. 6

The disinfection mechanism of the composite structures in the aerobic and anaerobic condition. (A) $CNRGOS_8$ and (B) $RGOCNS_8$ in aerobic condition, and (C) $CNRGOS_8$ and (D) $RGOCNS_8$ in anaerobic condition.

Reprinted with permission of W. Wang, J.C. Yu, D. Xia, P.K. Wong, Y. Li, Graphene and g-C_3N_4 nanosheets cowrapped elemental -sulfur as a novel metal-free heterojunction photocatalyst for bacterial inactivation under visible-light, Environ. Sci. Technol. 47 (2013) 8724–8732 American Chemical Society.

In a similar effort at alteration, there are a few studies on Ag-doped C_3N_4 composites demonstrating their photocatalytic disinfection ability. Bing et al. were the first to elucidate the possible biofilm elimination and bactericidal activity under visible light irradiation using the as-prepared composites (Fig. 7) [114]. The addition of silver atoms in the matrix led to an increase in the ROS production, which effectively aided the bacterial disinfection. In recent studies, the authors were interested in understanding the disinfection kinetics of bacterial strains of *E. coli*. The incorporation of Ag improved the visible light absorption and effectively reduced the rate of recombination. Unlike metal doping, there are few other studies of C_3N_4-based composites of titania, fullerene, and binary metal oxides exploring their photocatalytic bacterial disinfection [115]. Incorporation of a secondary constituent in the C_3N_4 matrix resulted in narrowing the band gap and resulted in the effective transfer of the photo-induced electrons.

More recently, Liu et al. demonstrated the use of vertically aligned 2D MoS_2 thin film for photocatalytic disinfection process. The band gap of the layered MoS_2 sheets was increased, but it necessarily helped in the formation of potential ROS. The bacterial inactivation was enhanced exponentially compared to bulk MoS_2. The authors claimed to improve the disinfection rate again by incorporating Cu film, which increased the charge separation within the layered structure and enhanced the rate of ROS production [116].

Bai et al. reported the fabrication of transparent nano-titania coatings with enhanced antimicrobial potential (*A. niger*). The coating utilized polyhydroxy fullerene (PHF) as an enhancer for nano-TiO_2 photocatalysis [117]. Similarly, Wang et al. lately reported the formation of 2D titania thin films with memory of photocatalytic activities. Upon irradiation, photogenerated electrons were produced and stored in the thin film matrix, which further participated in the bacterial inactivation process in the dark (Fig. 8) [118]. Apart from titania thin films, antimicrobial activity of titania nanotubes has also been reported. Carroll et al. investigated the bactericidal nature of the nanotubes against the strains of *E. coli*, *S. aureus*. The tubes showed improved inactivation (Log-2) compared to P25 under 24 hrs of UV irradiation. The surface hydroxyl radicals were observed to be the key participant in the inactivation process, which subsequently embarked the importance of the high aspect ratio of the nanotube [119].

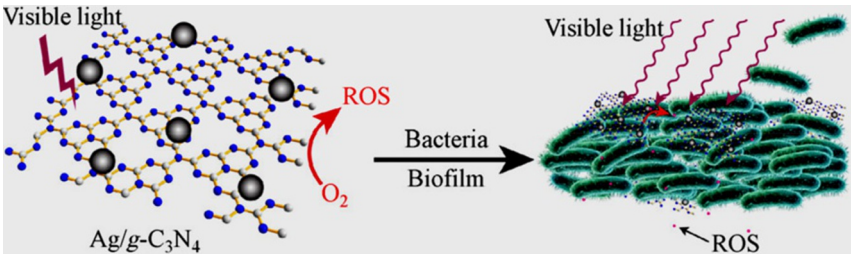

FIG. 7

Schematic illustrating the biofilm elimination and antibacterial activity of Ag/*g*-C_3N_4 under visible light irradiation.

Reprinted with permission of W. Bing, Z. Chen, H. Sun, P. Shi, N. Gao, J. Ren, X. Qu, Visible-light-driven enhanced antibacterial and biofilm elimination activity of graphitic carbon nitride by embedded Ag nanoparticles, Nano Res. 8 (2015) 1648. Full details are given in the respective publication.

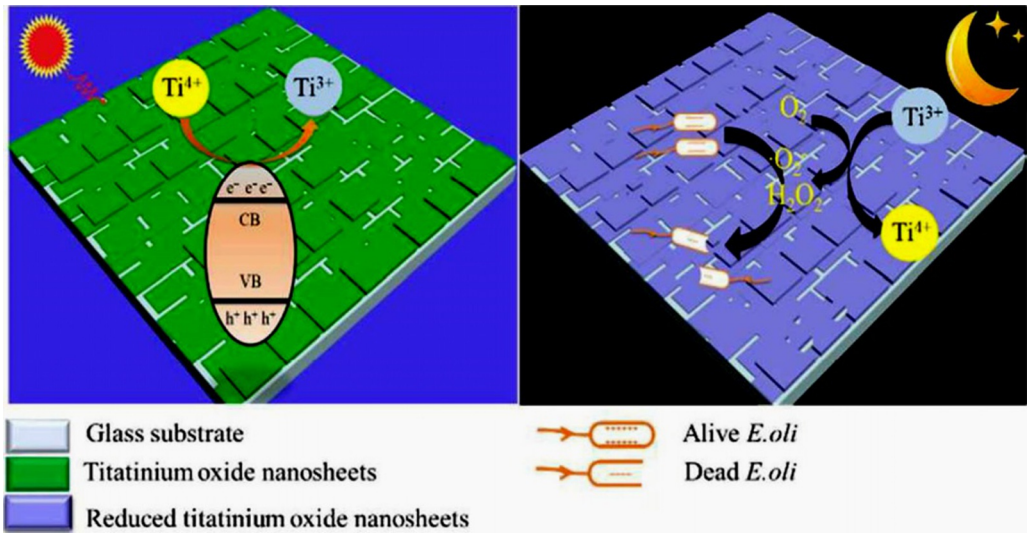

FIG. 8

Schematic illustration of the antibacterial mechanism on the titania nanosheets.

Reprinted with the permission of G. Wang, Z. Xing, X. Zeng, C. Feng, D.T. McCarthy, A. Deletic, X. Zhang, Ultrathin titanium oxide nanosheets film with memory bactericidal activity, Nanoscale 8 (2016) 18050–18056. Full details are given in the respective publication.

3.4.2 Algae

There are only a few reports detailing the photocatalytic disinfection efficiency of algae. Linkous et al. utilized TiO_2 and WO_3 coating with noble co-catalysts Pt and Ir to study the disinfection strategy of the filamentous Oedogonium algae in the presence and absence of the coating [120]. The results revealed that a cement surface coated with TiO_2 was highly effective in the disinfection process compared to an uncoated surface when irradiated with a combination of black and fluorescent light. In a more notable contribution, Alfaro and colleagues have studied the algal disinfection effect using different metal oxides. Binary oxides like Bi_2MoO_6, Bi_2WO_6, and $Bi_2W_2O_9$ were evaluated for their photocatalytic efficiency. The combined effect of the UV radiation and the photocatalysts showed the disinfection of alga *A. carterae* within 30 min and *T. suecica* in 60 min [121]. The same group also looked at Ag-TiO_2 composites; in these studies, the authors again validated the complete annihilation of the algal cells, hence, proving the effective disinfection property of the photocatalysts. They utilized these composites as potential coatings on foamed waste-glass and studied the photocatalytic disinfection of microalgae. A plausible mechanism of the disinfection activity was elaborated in the study (Fig. 9) [122]. Lee et al. also reported the formation of the Ag/titania composite and studied the algal disinfection of *T. suecica* and *A. carterae*. The composite produced a substantial amount of ROS, which resulted in oxidative damage to the algal cells, and suffered a high degree of fragmentation [123].

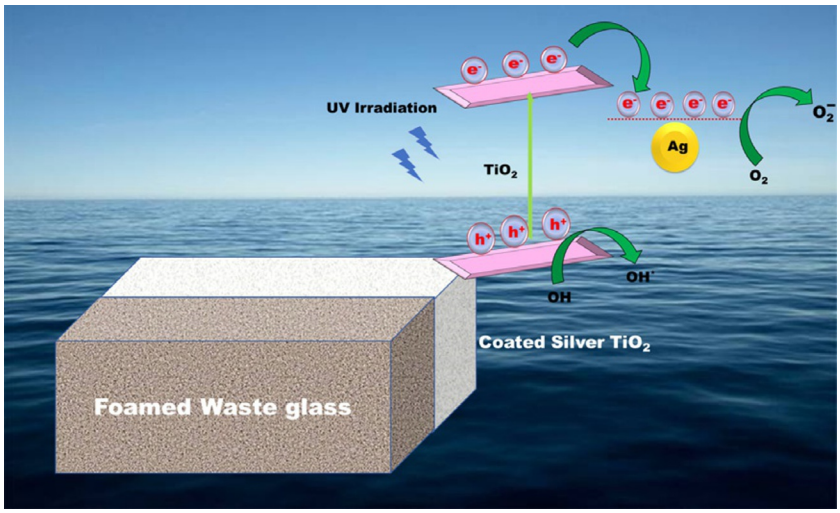

FIG. 9

Photocatalytic coatings of silver-TiO_2 nanocomposites on foamed waste glass.

3.4.3 Virus

Apart from bacterial disinfection, Li et al. studied the visible-light inactivation of strains of viruses (MS2) using bare C_3N_4 and compared the results with other conventional photocatalysts such as N-TiO_2, Bi_2WO_6, and Ag@AgCl. The bare C_3N_4 showed 7-log of virus inactivation; conversely, the TiO_2 and Bi_2WO_6 catalyst revealed decreased inactivation. The reduced disinfection efficacy is ascribed to the quick recombination of the electron-hole pairs. The improved inactivation showed by Ag@AgCl is attributed to the Ag atoms acting as an electron sink to facilitate the charge separation, and additionally, the Ag ions in the disinfection mixture embodied biocidal nature. The ROS species generated caused disruption of the viral membrane and, on 6 h of irradiation, led to the complete dismantling of the shape of the virus particles (Fig. 10) [124].

4 PHOTOCATALYTIC DECONTAMINATION

4.1 PHOTOCATALYTIC KINETICS

Chemical kinetics is essential to understanding the rate and the factors influencing the chemical process to attain equilibrium at any given amount of time [125]. A rise of interest in heterogeneous photocatalysis has ensued to several reports on different kinetic models [126].

4.1.1 Langmuir-hinshelwood (L-H Model)

Photocatalysis as a heterogeneous catalysis was always explained using the classical L-H model [127–129]. It is based on the assumptions that the adsorption of the reactants occurs on the catalyst surface [127, 130]. The reaction proceeds between the adsorbed species and later the products desorb from the surface [127]. In a significant contribution, Herman et al. have tried to explain several myths

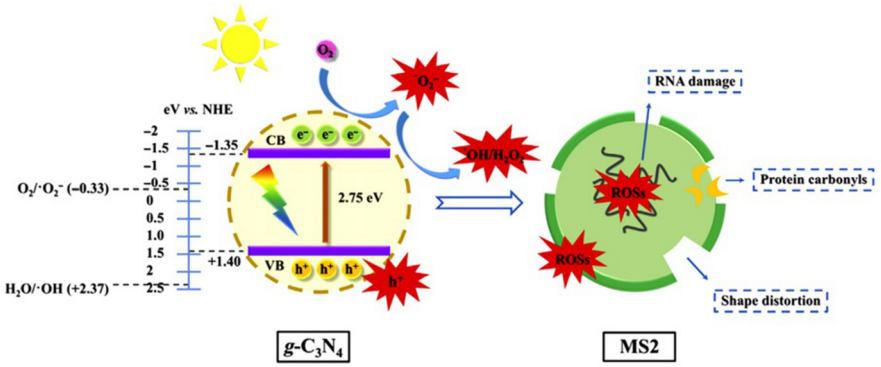

FIG. 10

Schematic illustration of the plausible mechanism of viral inactivation by *g*-C_3N_4 under visible light irradiation.

Reprinted with permission of Y. Li, C. Zhang, D. Shuai, S. Naraginti, D. Wang, W. Zhang, Visible-light-driven photocatalytic inactivation of MS2 by metal-free gC_3N_4: Virucidal performance and mechanism, Water Res. 106 (2016) 249–258. Full details are given in the respective publication.

related to photocatalysis, and among all, he explained this model in a more generalized approach, taking into the account to the several changes made to this model to result into a modified L-H model [125, 131, 132]. In a bimolecular reaction:

$$A + B \rightarrow C + D \tag{16}$$

The rate of the chemical process is proportional to the surface coverage of the reactant

$$r = k\Theta_A\Theta_B \tag{17}$$

Where the coverage Θ_i varies as:

$$\Theta_i = \frac{K_i X_i}{1 + K_i X_i} \tag{18}$$

Where

$K_i \rightarrow$ Adsorption constant (in dark)
$X_i \rightarrow$ Concentration in liquid phase or partial pressure P_i in gas phase.

Hence, Eq. (17) becomes:

$$r = \frac{k K_A K_B X_A X_B}{(1 + K_A X_A)(1 + K_B X_B)} \tag{19}$$

$k \rightarrow$ True rate constant.

Generally, one of the two reactants for Example A would have high concentration and the other reactant B would have low concentration. Therefore, the change in concentration of A remains constant, because its small consumption makes a negligible change in concentration [125, 132].

Therefore, Eq. (17) reduces to Eq. (20) (Fig. 11)

$$r = k'\Theta_B \,[\text{where}, k' = k\Theta_A] \tag{20}$$

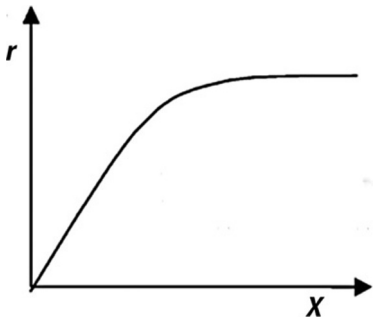

FIG. 11

Langmuir-Hinshelwood model. Variation of photocatalytic kinetics (r) in due influence of the catalyst concentration (X).

$k' \rightarrow$Pseudo true rate constant.

$$\Longrightarrow r = \frac{k' K_B X_B}{(1 + K_B X_B)} \text{ (Fig.11)} \tag{21}$$

Hence,

If $X = X_{max} \Longrightarrow \Theta_B = 1$

Therefore, Eq. (21) reduces to $r = k'$

Or if; $X << X_{max} \Longrightarrow \Theta_B = \frac{K_B X_B}{(1 + K_B X_B)} \approx K_B X_B$

Therefore, Eq. (21) reduces to

$$r = k' K_B X_B = k_{App} X_B \tag{22}$$

$k_{App} \rightarrow$ Apparent first-order constant.

4.1.2 Direct-indirect model (D-I Model)

Satoca et al. introduced an alternative kinetic approach, the "Direct-Indirect" (D-I) model [133]. The model proposes several major concepts on direct, indirect, adiabatic, and inelastic interfacial transfer of charge, which further establishes a physical meaning for the kinetic parameters involved. The L-H model discusses the kinetics of the reaction in an equilibrated adsorption/desorption of reactants on the surface of the semiconductor material under a constant illumination. Moreover, it also fails to establish a meaningful relationship between the incoming radiant flux (Φ) and the reactant concentration (X). However, the present model furnishes a functional dependence of the photo-oxidation rate (r) on the experimental parameters (photon flux and pollutant concentration).

The rate of photooxidation depends on all the interfacial charge transfer and the reaction between the conduction band electrons and the dissolved O_2 to form potential reactive species, which is certainly the rate determining step amongst all of them [134]. However, the discussion stumbles upon the debate on the participation of photogenerated valence band holes (h_f^+) in a direct reaction (DT) with organic substrate or transfer via an indirect transfer (IT) mechanism by utilizing hydroxyl radicals (surface trapped holes h_s^+). The brief number of possible routes of direct and indirect transfer are:

$$1. h_f^+ + [X]_{aq} \rightarrow [X]_{aq}^* + H_{aq}^+ \tag{23}$$

Photogenerated holes reacting with reactants in the aqueous solution (not absorbed on the catalyst surface).

$$2.h_f^+ + [X]_s \rightarrow [X]_s^* + H_{aq}^+ \tag{24}$$

Photogenerated holes reacting with reactants absorbed on the catalyst surface.

$$3.h_s^+ + [X]_{aq} \rightarrow [X]_{aq}^* + H_{aq}^+ \tag{25}$$

Surface trapped holes reacting with reactants in the aqueous solution (not absorbed on the catalyst surface).

$$4.h_s^+ + [X]_s \rightarrow [X]_s^* + H_{aq}^+ \tag{26}$$

Surface trapped holes reacting with reactants absorbed on the catalyst surface.

When the organic molecules are not adsorbed on the catalyst surface, the hole transfer between the reactants in the aqueous solution occurs adiabatically. Marcus developed a Fluctuating Energy Level Model which defines this transfer mechanism, and later, Gerischer interpreted it on the semiconductor electrolyte interface [135–137]. This model helps in predicting a hole transfer rate constant (k_{ox}^{adb})

$$k_{ox}^{adb} \propto exp\left[\frac{-(E_{red} - E_s)^2}{4\lambda kT}\right] \tag{27}$$

Where

$E_s \rightarrow$ Energy of the surface trapped holes.
$E_{red} \rightarrow$ The most probable energy of the occupied energy levels of reactants in the aqueous solution.
$\lambda \rightarrow$ The reorganization energy (between 0.5 and 1.0 eV).

However, under strong interaction that increases the competitive adsorption between the reactant molecules and the water molecules. In such a case, the hole transfer mechanism is not adiabatic but inelastic, and is not governed by this model anymore. Thus, the modified rate constant (k_{ox}^{ins}) is:

$$k_{ox}^{ins} \propto \sigma \hat{c} \tag{28}$$

Where

$\sigma \rightarrow$ Hole capture cross-section of filled surface states.
$\hat{c} \rightarrow$ Thermal velocity of free hole.

The direct transfer mechanism of holes is more largely predominant than indirect mechanism, but on the other hand, indirect mechanism is the only transfer process available in the absence of specific adsorption.

The L-H model is based on the equilibrated adsorption of the reactants; hence, in a Langmuir type adsorption isotherm, the relationship between the concentration of dissolved and adsorbed species is given as:

$$[X]_s = \frac{ab[X]_{aq}}{1 + a[X]_{aq}} \tag{29}$$

Where

$a \rightarrow$ Adsorption constant.
$b \rightarrow$ Desorption constant.

However, in this model the author's utilizes Ollis et al.'s idea of non-equilibrated adsorption of the reactants. Ollis proposes a pseudo-steady-state analysis for reaction in the event of tampered adsorption-desorption equilibrium under illumination conditions. In this case, the adsorbed species are attacked by the photogenerated valence band free holes through an inelastic direct transfer process [125]. So, according to the pseudo-steady-state approach proposed by Ollis, the surface coverage (Θ_A) of a reactant A, assuming that $\frac{d\Theta_A}{dt} = 0$, then:

$$\frac{d\Theta_A}{dt} = [X]_{aq} k_1 (1 - \Theta_A) - k_{-1}\Theta_A - k_{ox}^d \left[h_f^+\right]\Theta_A = 0 \tag{30}$$

Where k_1 and k_{-1} are the adsorption and the desorption constant, thus Eq. (29) reduces to

$$[X]_s = \frac{ab[X]_{aq}}{1 + a\left\{[X]_{aq} + \left(\frac{k_{ox}^d}{k_{-1}}\right)\left(\frac{k_0'}{k_1\left[O_s^{2-}\right]} + k_{ox}^d [X]_s\right)\right\}} \tag{31}$$

Thus, Eq. (31) defines that the concentration of the reactant adsorbed on the catalyst surface decreases with the increasing radiant flux [138]. Apart from this D-T model, there were several other improvements suggested, but none turned out to be influential as both these models [139–143].

4.2 PHOTOCATALYTIC DECONTAMINATION OF POTENTIAL POLLUTANTS

4.2.1 Endocrine disrupting compounds

Endocrine disrupting compounds (EDC) are the xenobiotic materials that effect the normal functioning of the endocrine system [144]. This eventually induces adverse effects in humans and animals even at low exposure levels [145]. Mineralization and degradation of these compounds are studied extensively using multiple methods [146]. However, the low cost, low toxicity, and easy operation of heterogeneous photocatalysis makes it an effective substitute. There exist numerous compounds enlisted as potential EDC's. In this section, we shall discuss the degradation activity of two class of materials, polycyclic hydrocarbon (Bisphenol-A) and pesticides by several new generation photocatalysts.

Bisphenol-A, used readily in polycarbonate manufacturing and epoxy resins, is easily bioaccumulated in nearby water body sources [147]. It is categorically classified as an endocrine disrupting compound and is resistant to conventional water treatment processes [148]. Fresh studies on photocatalytic degradation of Bisphenol-A are abundant, elucidating the intermediates and exhibiting complete mineralization within a shorter illumination period. In such a similar event, Xu et al. reported the formation of nanosheets of C_3N_4 by a two-step fabrication process (hydrothermal treatment and thermal etching). The high surface area sheets exhibited almost double the degradation efficiency compared to the bulk material [149]. Similarly, mesoporous C_3N_4 sheets with Ag atoms were prepared by co-condensation technique. The samples showed excellent degradation activity; the addition of metal atoms acted as an electron sink, which effectively contributed to charge separation [150]. In another study, authors studied a sonochemical assisted visible light degradation of Bisphenol-A using C_3N_4, the intermediates of the degradation were identified using GC/MS [151]. Lin et al. also proposed a degradation pathway of the Bisphenol-A utilizing sulfur-doped C_3N_4 (Fig. 12) [152].

Mu et al. recently reported the formation of graphene hydrogel composite with silver phosphate. The as-prepared composite exhibited excellent adsorption cum photocatalytic degradation of 100% Bisphenol-A within 12 min of exposure. The graphene nanosheets contributed to the nonporous adsorption, and the Ag_3PO_4 anchored within these sheets caused effective degradation [153]. The same group

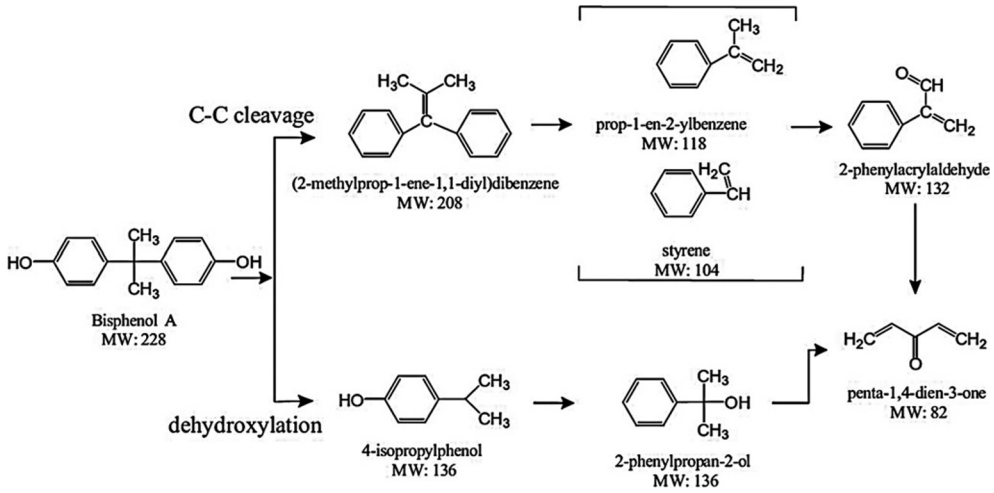

FIG. 12

Degradation pathway of Bisphenol-A by sulfur-doped C_3N_4.

Reprinted with permission of K.-Y.A. Lin, Z.-Y. Zhang, Degradation of Bisphenol A using peroxymonosulfate activated by one-step prepared sulfur-doped carbon nitride as a metal-free heterogeneous catalyst, Chem. Eng. J. 313 (2017) 1320–1327. Full details are given in the respective publication.

also evaluated degradation using a 3D hydrogel composite of graphene/AgBr with reduced graphene oxide [154]. This superior photocatalytic activity in a synergistic approach paved the way toward future exploration for several other potential effluents. However, Ag_3PO_4 as a visible light active catalyst had earlier been subjected for Bisphenol-A degradation and mineralization, and showed improved degradation activity compared to conventional catalysts like titania and its composites [155].

In recent years, bismuth-based composites have attracted reasonable attention as an efficient visible light active photocatalyst [156–158]. Degradation of Bisphenol-A by several such composites has been evaluated. Bi_2WO_6 exhibited complete degradation and mineralization within 30 min of irradiation. The complete removal of the total organic carbon (TOC) was only observed after an irradiation period of 120 min [159]. Xiao et al. reported the formation of $Bi_7O_9I_3$ microsheets (using a rapid microwave treatment) that showed excellent visible light absorption and 99% degradation of the compound within 60 min of irradiation [160]. Xiao et al. also reported the formation of 3D BiOI/BiOCl composite which showed effective degradation in 60 min [161]. In a similar account, Chang et al. reported the synthesis of a novel 3D Bi/BiOI composite using a solvothermal technique, which reportedly showed complete degradation within 90 min of exposure [162]. In a more recent account, Kanigaridou et al. fabricated a $CuO/BiVO_4$ p-n heterojunction which showed excellent degradation activity in the presence of bicarbonate ions [163].

Pesticides are also another class of compounds categorized as a potential EDC. There are several synthetic compounds tampering the metabolic functioning of humans and animals [164]. Jiang et al. reported the formation of visible light active Ag@AgBr composite and studied the efficiency of the composite by degradation of pentachlorophenol. The pollutants were degraded rapidly under artificial

daylight simulation [165]. Imidacloprid degradation was studied by g-C_3N_4, the authors reported complete mineralization within 5 h of illumination and identified 2 major byproducts [166]. Atrazine and amitrole degradation was evaluated using $AgCl@C_3N_4$. The catalyst fabricated showed an impressive degradation profile for both the pesticides and showed above 95% degradation within 60 min of irradiation [167]. Similarly, norfloxacin degradation was reported recently by another bismuth composite (Bi_2WO_6) using visible light irradiation. The authors predicted 3 possible photodegradation pathways (Fig. 13) [168].

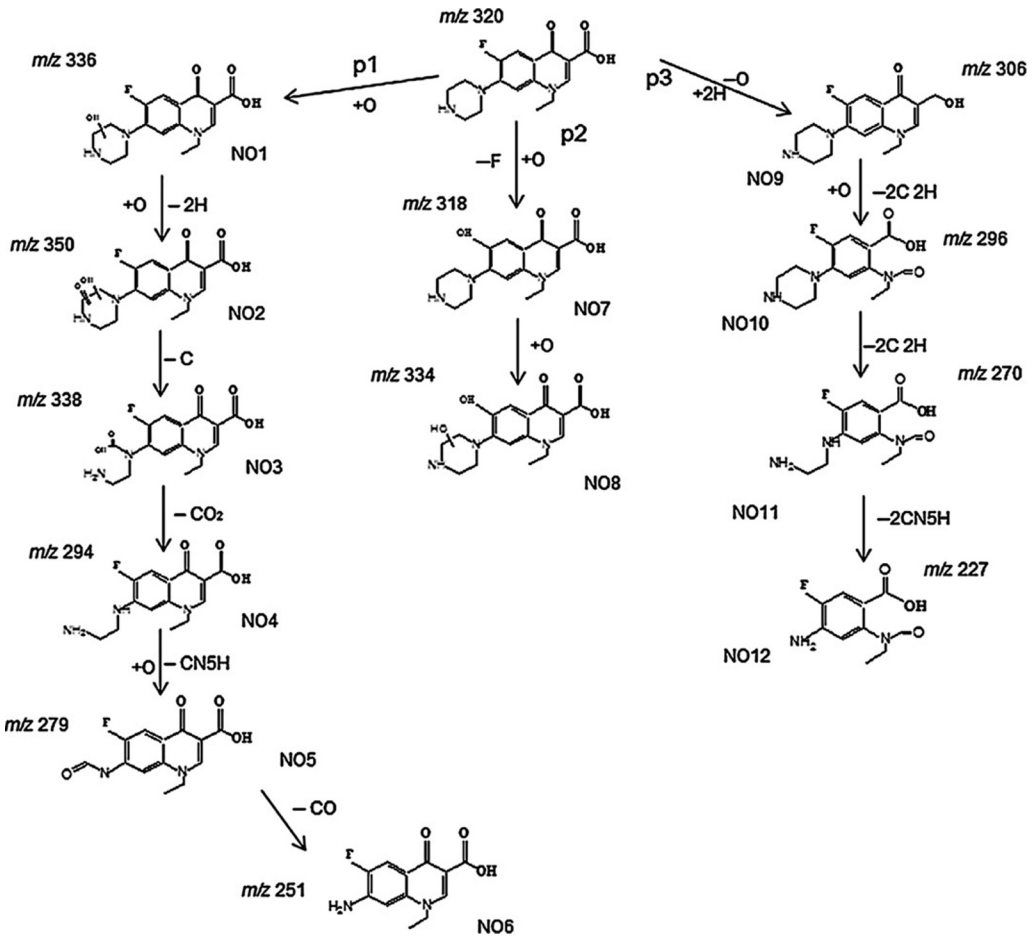

FIG. 13

Degradation pathway of Norfloxacin by Bi_2WO_6.

Reprinted with permission of L. Tang, J. Wang, G. Zeng, Y. Liu, Y. Deng, Y. Zhou, J. Tang, J. Wang, Z. Guo, Enhanced photocatalytic degradation of norfloxacin in aqueous Bi_2WO_6 dispersions containing nonionic surfactant under visible light irradiation, J. Hazard. Mater. 306 (2016) 295–304. Full details are given in the respective publication.

In a more recent approach, a ternary structure of biochar/Fe_3O_4/$BiVO_4$ composite was reported for methyl paraben degradation within 2 h of irradiation [169]. Similarly, reports of a novel ternary structure of Ru/WO_3/ZrO_2 for carbofuran degradation within 240 min [170].

4.2.2 Pharmaceutical effluents

The surge in cases of antibiotic resistance, pharmaceutically active compounds (PhACs), and their relative impact across the aisle has grown in the past few years. The use of Photo-Fenton and conventional photocatalysts like titania are readily studied for photocatalytic detoxification of pharmaceutical waste effluents [171]. There are several recent reports exploiting new generation catalysts and studying the mineralization kinetics and degradation pathways of these toxic pharmaceutical effluents [172, 173]. The present section details several such studies illustrating the recent advances in the detoxification process. Acetaminophen (ACTP) and hydroxyphenylacetic acid (p-HPA), adsorption cum degradation was studied by $BiOCl_xI_y$ nanospheres. 100% removal of p-HPA and 80% of ACTP were removed within 3 h of irradiation. Superoxide radical and dissolved oxygen were the major reactive agents in the degradation process [174]. Gao et al. reported the photocatalytic degradation of carbamazepine using hierarchical BiOCl microspheres. The authors studied the effect of key operational parameters in the degradation pathway. The presence of inorganic anions did not affect the degradation, while the cations reduced its efficiency. Prolonged illumination resulted in complete degradation of carbamazepine [175]. Recently, Tang et al. reported the formation of a $BiVO_4$ and graphene quantum dot heterostructure. The as-prepared heterojunction exhibited almost complete degradation within 180 min [176]. Another group studied the degradation of carbamazepine by g-C_3N_4 functionalized by isonicotinic acid (INA) and coordinated with $FePcCl_{16}$ to make a distinctive catalyst g-C_3N_4-INA-$FePcCl_{16}$. Under visible light irradiation, the following catalyst activates peroxymonosulfate (PMS)-based advanced oxidation processes (AOPs). The sulphate ions and the hydroxyl radical necessarily neutralizes the carbamazepine molecules [177]. Lei et al. reported the formation of visible-light responsive graphene quantum dot/$AgVO_3$ heterostructure. The photocatalyst formed showed impressive degradation of ibuprofen within 180 min of illumination. Increased loading of graphene quantum dot content reduced the degradation efficiency. The $AgVO_3$ nanoribbons and the graphene quantum dots improved the charge separation and effectively contributed to the degradation mechanism [178]. Similarly, another group reported the degradation of ibuprofen and clofibric acid utilizing Au@Ag@AgCl core-double shells nanoparticles. The nanoparticles synthesized using a green route showed 98% and 97% photocatalytic degradation of ibuprofen and clofibric acid, respectively. The plasmonic effect of the Au core is effective at definite shell size of Ag and AgCl. The possible intermediates and the degradation pathway are illustrated in Fig. 14 [179].

Photocatalytic antibiotic degradation of several antibiotics effluent is also an emerging concern. Sturini et al. reported the photodegradation of ofloxacin under simulated solar light using g-C_3N_4 suspension. The photocatalyst illustrated complete degradation and showed impressive degradation rate compared to P25 [180]. The same catalyst has been recently explored widely for tetracycline degradation. Xue et al. reported a ternary heterostructure of Au/Pt/g-C_3N_4, the fabricated composite showed a 3.4 times higher degradation rate compared to bare g-C_3N_4. The incorporation of Au and Pt nanoparticles contributed plasmonic nature and resulted in improved visible light absorption [181]. g-C_3N_4 prepared from 4 different precursors were evaluated for their degradation efficiency [105]. Panneri et al. demonstrated that urea-derived carbon nitride samples with large surface area contributed in quick degradation. The same group also studied the degradation profiles using different composite heterostructures of C_3N_4. Porous structures of C_3N_4 were fabricated by spray drying the urea-thiourea mixture to form microspheres using polyvinyl alcohol binder (Fig. 15). The post-thermal treatment

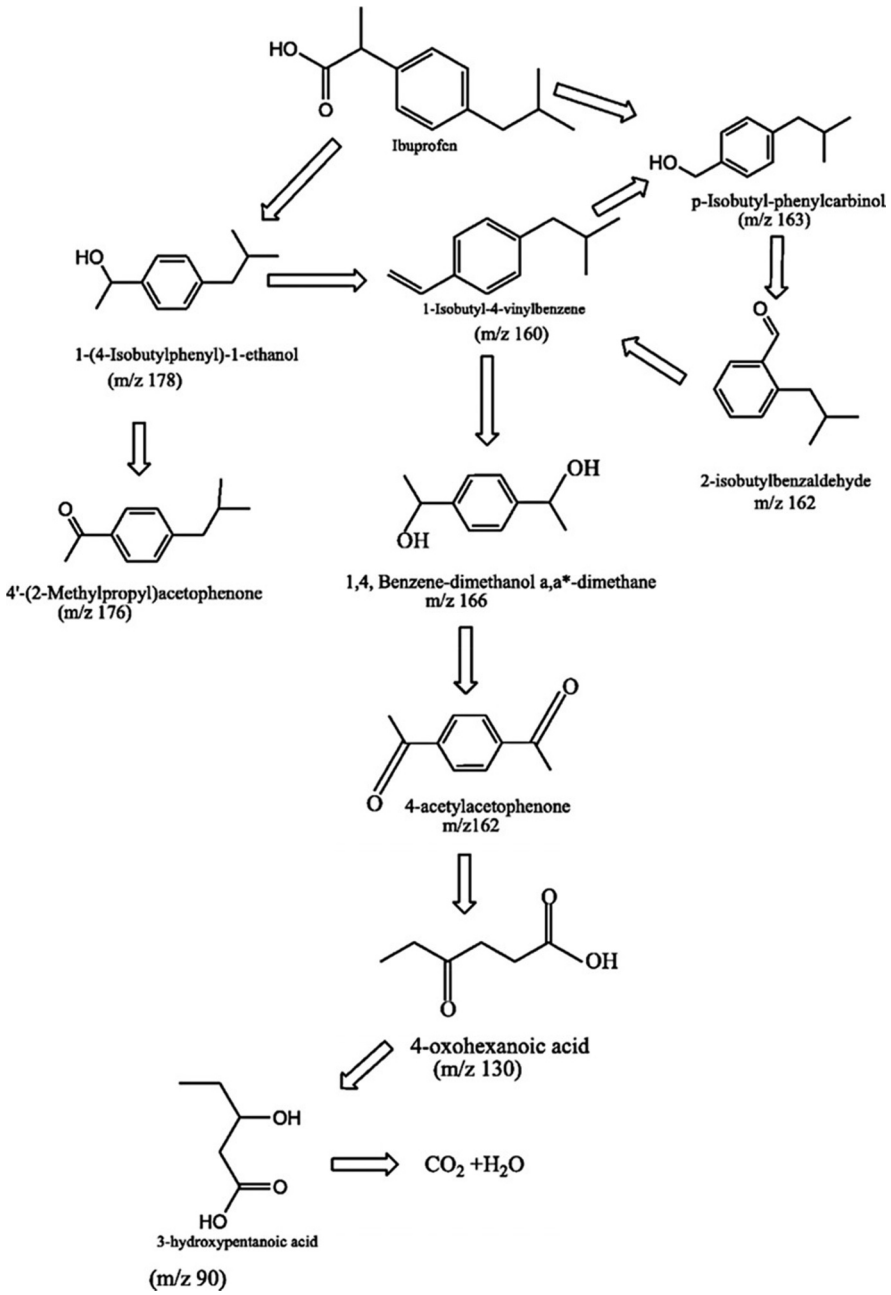

FIG. 14

Degradation pathway of ibuprofen utilizing Au@Ag@AgCl.

Reprinted with permission of T.B. Devi, M. Ahmaruzzaman, Bio-inspired facile and green fabrication of Au@ Ag@ AgCl core–double shells nanoparticles and their potential applications for elimination of toxic emerging pollutants: a green and efficient approach for wastewater treatment, Chem. Eng. J. 317 (2017) 726–741. Full details are given in the respective publication.

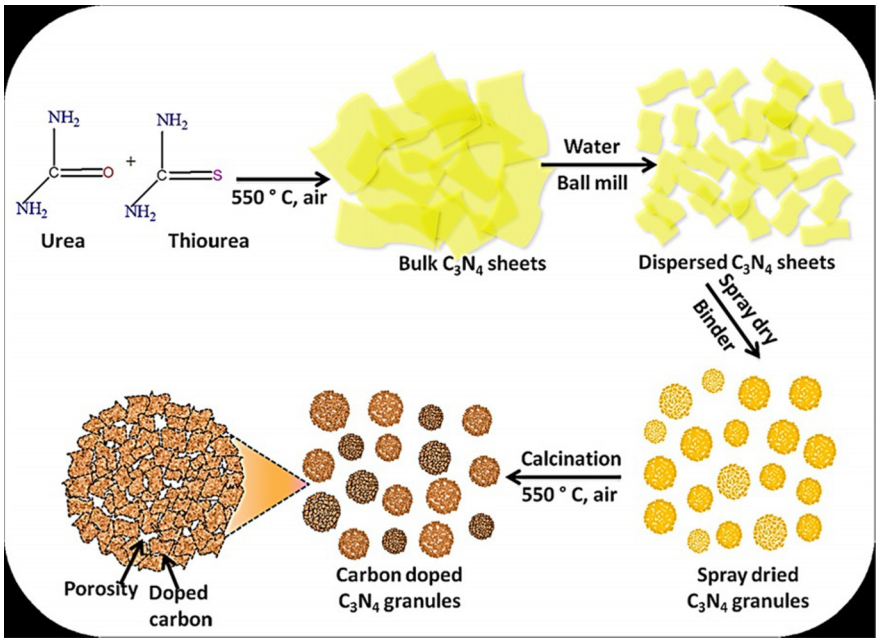

FIG. 15

Schematic representation of the formation of spray-dried porous C_3N_4 granules with carbon doping.

Reprinted with permission of S. Panneri, P. Ganguly, M. Mohan, B.N. Nair, A.A.P. Mohamed, K.G. Warrier, U. Hareesh, Photoregenerable, bifunctional granules of carbon-doped g-C_3N_4 as adsorptive photocatalyst for the efficient removal of tetracycline antibiotic, ACS Sustain. Chem. Eng. 5 (2017) 1610–1618. Full details are given in the respective publication.

resulted in carbon doping, which improved the visible light absorption and contributed to effective absorption cum photocatalytic degradation of tetracycline [182]. Similar absorptive catalysts were formed by incorporating MOF like ZIF-8, which resulted in impressive degradation profile within 90 min of sunlight irradiation [183].

Similarly, $NiFe_2O_4/Bi_2O_3$ magnetic heterostructure composite was synthesized and studied for tetracycline degradation. A Type-II heterostructure resulted in efficient charge separation that decisively contributed to the effective degradation profile. The catalyst samples after degradation were able to be easily recovered and studied afterward for three runs of recyclability [184]. Manganese-doped $SrTiO_3$ nanocubes synthesized showed improved visible light absorption. The Mn^{4+} replaced in the $SrTiO_3$ lattice and shifted towards the visible light region. The following composite showed excellent tetracycline degradation within 60 min of illumination [185].

5 EMERGENCE OF VISIBLE LIGHT ACTIVE PHOTOCATALYST

Enormous progress in visible light active photocatalysts has been observed in recent years for multiple applications including the water detoxification process [186]. However, these semiconductor surfaces suffer from multiple limitations which necessarily increase the quest for improvement [187].

Exploiting the surface of these semiconductor materials with metal/non-metal dopants and making hybrid heterostructures are a few of the processes for alleviating these shortcomings [25]. Recent reports on band gap engineering and morphological alterations have shown enhanced degradation outcomes [188]. Sang et al. reported the formation of WS_2 nanosheets with extremely small band gap (1.38 eV). The nanosheet showed absorption from UV to near infrared range, the extreme broad absorption spectrum contributed to impressive degradation of methyl orange under all the illumination [189]. Recently, Yang et al. reported the formation of a ternary heterostructure of $Ag/AgCl/SrTiO_3$, the addition of Ag ions enhanced the visible light absorption capability of the composite. The composite showed complete mineralization of phenol within 30 min of irradiation. The scavenger study helped to determine superoxide radical as the dominant species [190]. A Cu_2O-rGO composites were fabricated with tunable Cu_2O crystal facets ({1 1 1}, {1 1 0}, and {1 0 0} facets. The as-prepared composites exhibited similar surface area and surface properties. The Cu_2O{1 1 1}-rGO composite showed best degradation profile of methylene blue compared to the other composites. The electronic arrangements of this composite helped the presence of oxygen defects and Cu ions [191]. Xia and colleagues reported the formation of hybrid nanosheets of carbon quantum dots (CQDs)/BiOX (X = Br, Cl) heterostructure. This composite showed excellent visible light absorption and significant degradation of ciprofloxacin and Bisphenol-A within 4 and 170 min of visible light irradiation [192]. In a more recent study, a novel adsorption cum photocatalyst polyacrylic acid-grafted-carboxylic graphene/titanium nanotube composite was reported. The composite exhibited complete mineralization of enrofloxacin within 90 min of illumination. It had a band gap of 2.6 eV and showed a maximum adsorption capacity of 13.4 mg/g [193]. Similarly, Liu et al. reported a core shell hybrid structure of silver phosphate and polyaniline (PANI) (Fig. 16). The composite showed complete mineralization of phenol and 2,4-dichlorophenol. The compatible bandgap of Ag_3PO_4 and PANI contributed to effective charge separation. Moreover, the higher charge mobility due to the conjugated structure of PANI and the hybridization effect arising from Ag_3PO_4 and PANI contributed equally to the impressive degradation profile [194].

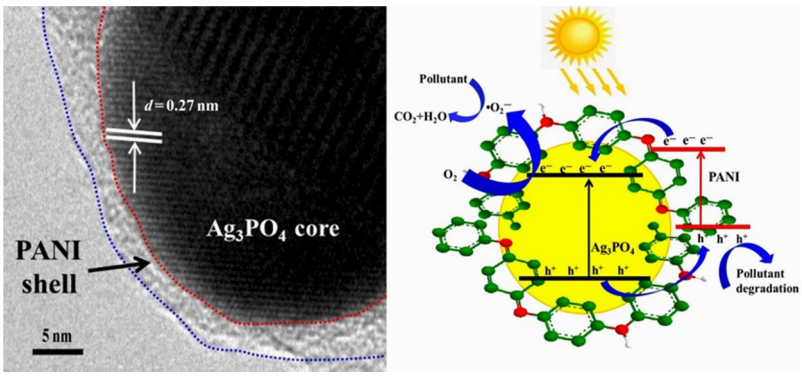

FIG. 16

TEM image of Ag_3PO_4@PANI core-shell structure and photocatalytic degradation mechanism.

Reprinted with permission of L. Liu, L. Ding, Y. Liu, W. An, S. Lin, Y. Liang, W. Cui, A stable Ag3PO4@PANI core-shell hybrid: enrichment photocatalytic degradation with π-π conjugation, Appl. Catal. B Environ. 201 (2017) 92–104. Full details are given in the respective publication.

6 CONCLUSIONS

This chapter discussed the state of the art studies in disinfection and decontamination and underscored the importance of visible-light-induced detoxification process. It also summarized the photocatalytic mechanism and disinfection pathways affecting the various microbial strains. The chapter also provided a detailed understanding of a range of factors affecting the disinfection process. It discussed the degradation pathways and profiles of several pharmaceutical effluents and endocrine disrupting compounds, utilizing non-conventional photocatalysts. However, these new generation catalysts have their own pitfalls of concern. Low visible light utilization, poor surface area, and cumbersome synthetic protocols are a few of these major concerns. Amid all these limitations, these materials have opened the doors for discussion and understanding for improvement in all the realms of the photocatalytic detoxification process. With the surge of interest in green and eco-friendly energy routes, photocatalysis is certainly a process worth exploring for wastewater remediation.

ACKNOWLEDGMENTS

Author PG would like to thank the IT Sligo President's bursary and SP to CSIR for providing financial support.

REFERENCES

[1] P.H. Gleick, The world's Water Volume 8: The Biennial Report on Freshwater Resources, Island Press, 2014.
[2] W.J. Cosgrove, F.R. Rijsberman, World Water Vision: Making Water Everybody's Business, Routledge, 2014.
[3] P.H. Gleick, The human right to water, Water Policy 1 (1998) 487–503.
[4] M.A. Shannon, P.W. Bohn, M. Elimelech, J.G. Georgiadis, B.J. Mariñas, A.M. Mayes, Science and technology for water purification in the coming decades, Nature 452 (2008) 301–310.
[5] World Health Organization, The Burden of Health Care-Associated Infection Worldwide, www. wholint/gpsc/country_work/burden/hcai/en, (2013).
[6] E.J. Septimus, M.L. Schweizer, Decolonization in prevention of health care-associated infections, Clin. Microbiol. Rev. 29 (2016) 201–222.
[7] A.I. Hidron, J.R. Edwards, J. Patel, T.C. Horan, D.M. Sievert, D.A. Pollock, S.K. Fridkin, Antimicrobial-resistant pathogens associated with healthcare-associated infections: annual summary of data reported to the National Healthcare Safety Network at the Centers for Disease Control and Prevention, 2006–2007, Infect. Control Hosp. Epidemiol. 29 (2008) 996–1011.
[8] T.C. Horan, M. Andrus, M.A. Dudeck, CDC/NHSN surveillance definition of health care-associated infection and criteria for specific types of infections in the acute care setting, Am. J. Infect. Control 36 (2008) 309–332.
[9] E. Mintz, J. Bartram, P. Lochery, M. Wegelin, Not just a drop in the bucket: expanding access to point-of-use water treatment systems, Am. J. Public Health 91 (2001) 1565–1570.
[10] M. Elimelech, The global challenge for adequate and safe water, J. Water Supply Res. Technol. AQUA 55 (2006) 3–10.
[11] R.M. Klevens, J.R. Edwards, C.L. Richards Jr., T.C. Horan, R.P. Gaynes, D.A. Pollock, D.M. Cardo, Estimating health care-associated infections and deaths in US hospitals, 2002, Public Health Rep. 122 (2007) 160–166.

[12] D.M. Sievert, P. Ricks, J.R. Edwards, A. Schneider, J. Patel, A. Srinivasan, A. Kallen, B. Limbago, S. Fridkin, Antimicrobial-resistant pathogens associated with healthcare-associated infections summary of data reported to the National Healthcare Safety Network at the Centers for Disease Control and Prevention, 2009–2010, Infect. Control Hosp. Epidemiol. 34 (2013) 1–14.
[13] D. Robert, S. Malato, Solar photocatalysis: a clean process for water detoxification, Sci. Total Environ. 291 (2002) 85–97.
[14] D. Bahnemann, D. Bockelmann, R. Goslich, Mechanistic studies of water detoxification in illuminated TiO2 suspensions, Solar Energy Mater. 24 (1991) 564–583.
[15] S. Malato, M.I. Maldonado, P. Fernandez-Ibanez, I. Oller, I. Polo, R. Sanchez-Moreno, Decontamination and disinfection of water by solar photocatalysis: the pilot plants of the Plataforma Solar de Almeria, Mater. Sci. Semicond. Process. 42 (2016) 15–23.
[16] R.L. Pozzo, M.A. Baltanas, A.E. Cassano, Supported titanium oxide as photocatalyst in water decontamination: state of the art, Catal. Today 39 (1997) 219–231.
[17] S. Malato, P. Fernández-Ibáñez, M.I. Maldonado, J. Blanco, W. Gernjak, Decontamination and disinfection of water by solar photocatalysis: recent overview and trends, Catal. Today 147 (2009) 1–59.
[18] K. Pirkanniemi, M. Sillanpää, Heterogeneous water phase catalysis as an environmental application: a review, Chemosphere 48 (2002) 1047–1060.
[19] M.A. Oturan, J.-J. Aaron, Advanced oxidation processes in water/wastewater treatment: principles and applications. A review, Crit. Rev. Environ. Sci. Technol. 44 (2014) 2577–2641.
[20] S.-Y. Lee, S.-J. Park, TiO2 photocatalyst for water treatment applications, J. Ind. Eng. Chem. 19 (2013) 1761–1769.
[21] R. Das, C.D. Vecitis, A. Schulze, B. Cao, A.F. Ismail, X. Lu, J. Chen, S. Ramakrishna, Recent advances in nanomaterials for water protection and monitoring, Chem. Soc. Rev. (2017).
[22] M. Nasalevich, M. Van der Veen, F. Kapteijn, J. Gascon, Metal–organic frameworks as heterogeneous photocatalysts: advantages and challenges, CrystEngComm 16 (2014) 4919–4926.
[23] T. Lammel, P. Boisseaux, M.L. Fernandez-Cruz, J.M. Navas, Internalization and cytotoxicity of graphene oxide and carboxyl graphene nanoplatelets in the human hepatocellular carcinoma cell line Hep G2, Part. Fibre Toxicol. 10 (2013) 27.
[24] L.A.V. de Luna, A.C.M. de Moraes, S.R. Consonni, C.D. Pereira, S. Cadore, S. Giorgio, O.L. Alves, Comparative in vitro toxicity of a graphene oxide-silver nanocomposite and the pristine counterparts toward macrophages, J. Nanobiotechnol. 14 (2016) 12.
[25] M. Pelaez, N.T. Nolan, S.C. Pillai, M.K. Seery, P. Falaras, A.G. Kontos, P.S. Dunlop, J.W. Hamilton, J. A. Byrne, K. O'shea, A review on the visible light active titanium dioxide photocatalysts for environmental applications, Appl. Catal. B Environ. 125 (2012) 331–349.
[26] M. Teta, M.M. Rankin, S.Y. Long, G.M. Stein, J.A. Kushner, Growth and regeneration of adult β cells does not involve specialized progenitors, Dev. Cell 12 (2007) 817–826.
[27] H. Dumortier, S. Lacotte, G. Pastorin, R. Marega, W. Wu, D. Bonifazi, J.-P. Briand, M. Prato, S. Muller, A. Bianco, Functionalized carbon nanotubes are non-cytotoxic and preserve the functionality of primary immune cells, Nano Lett. 6 (2006) 1522–1528.
[28] A. Faria, A. Moraes, P. Marcato, D. Martinez, N. Durán, A. Filho, Eco-friendly decoration of graphene oxide with biogenic silver nanoparticles: antibacterial and antibiofilm activity, J. Nanopart. Res. 16 (2014).
[29] J. Li, Y. Zhu, W. Li, X. Zhang, Y. Peng, Q. Huang, Nanodiamonds as intracellular transporters of chemotherapeutic drug, Biomaterials 31 (2010) 8410–8418.
[30] H. Yue, W. Wei, Z.G. Yue, B. Wang, N.N. Luo, Y.J. Gao, The role of the lateral dimension of graphene oxide in the regulation of cellular responses, Biomaterials 33 (2012).
[31] G. Kroemer, L. Galluzzi, P. Vandenabeele, J. Abrams, E. Alnemri, E. Baehrecke, M. Blagosklonny, W. El-Deiry, P. Golstein, D. Green, Classification of cell death: recommendations of the Nomenclature Committee on Cell Death 2009, Cell Death Differ. 16 (2009) 3–11.

[32] E.H. Baehrecke, How death shapes life during development, Nat. Rev. Mol. Cell Biol. 3 (2002) 779–787.
[33] C. Garrido, G. Kroemer, Life's smile, death's grin: vital functions of apoptosis-executing proteins, Curr. Opin. Cell Biol. 16 (2004) 639–646.
[34] L. Galluzzi, N. Joza, E. Tasdemir, M. Maiuri, M. Hengartner, J. Abrams, N. Tavernarakis, J. Penninger, F. Madeo, G. Kroemer, No death without life: vital functions of apoptotic effectors, Cell Death Differ. 15 (2008) 1113–1123.
[35] J. Schneider, M. Matsuoka, M. Takeuchi, J. Zhang, Y. Horiuchi, M. Anpo, D.W. Bahnemann, Understanding TiO2 photocatalysis: mechanisms and materials, Chem. Rev. 114 (2014) 9919–9986.
[36] R. Abe, Recent progress on photocatalytic and photoelectrochemical water splitting under visible light irradiation, J Photochem Photobiol C: Photochem Rev 11 (2010) 179–209.
[37] K. Maeda, K. Domen, Photocatalytic water splitting: recent progress and future challenges, J. Phys. Chem. Lett. 1 (2010) 2655–2661.
[38] A. Fujishima, X. Zhang, D.A. Tryk, TiO2 photocatalysis and related surface phenomena, Surf. Sci. Rep. 63 (2008) 515–582.
[39] T. Yoshihara, R. Katoh, A. Furube, Y. Tamaki, M. Murai, K. Hara, S. Murata, H. Arakawa, M. Tachiya, Identification of reactive species in photoexcited nanocrystalline TiO2 films by wide-wavelength-range (400 – 2500 nm) transient absorption spectroscopy, J. Phys. Chem. B 108 (2004) 3817–3823.
[40] J.A. Ibáñez, M.I. Litter, R.A. Pizarro, Photocatalytic bactericidal effect of TiO2 on Enterobacter cloacae: comparative study with other Gram (−) bacteria, J. Photochem. Photobiol. A Chem. 157 (2003) 81–85.
[41] Y. Li, W. Zhang, J. Niu, Y. Chen, Mechanism of photogenerated reactive oxygen species and correlation with the antibacterial properties of engineered metal-oxide nanoparticles, ACS Nano 6 (2012) 5164–5173.
[42] T. Matsunaga, R. Tomoda, T. Nakajima, H. Wake, Photoelectrochemical sterilization of microbial cells by semiconductor powders, FEMS Microbiol. Lett. 29 (1985) 211–214.
[43] T. Saito, T. Iwase, J. Horie, T. Morioka, Mode of photocatalytic bactericidal action of powdered semiconductor TiO2 on mutans streptococci, J. Photochem. Photobiol. B Biol. 14 (1992) 369–379.
[44] W.A. Jacoby, P.C. Maness, E.J. Wolfrum, D.M. Blake, J.A. Fennell, Mineralization of bacterial cell mass on a photocatalytic surface in air, Environ. Sci. Technol. 32 (1998) 2650–2653.
[45] M. Sökmen, F. Candan, Z. Sümer, Disinfection of E. coli by the Ag-TiO2/UV system: lipidperoxidation, J. Photochem. Photobiol. A Chem. 143 (2001) 241–244.
[46] S. Pigeot-Rémy, F. Simonet, E. Errazuriz-Cerda, J. Lazzaroni, D. Atlan, C. Guillard, Photocatalysis and disinfection of water: identification of potential bacterial targets, Appl. Catal. B Environ. 104 (2011) 390–398.
[47] I. Matai, A. Sachdev, P. Dubey, S.U. Kumar, B. Bhushan, P. Gopinath, Antibacterial activity and mechanism of Ag–ZnO nanocomposite on S. aureus and GFP-expressing antibiotic resistant E. coli, Colloids Surf. B: Biointerfaces 115 (2014) 359–367.
[48] B.F. Severin, M.T. Suidan, R.S. Engelbrecht, Kinetic modeling of UV disinfection of water, Water Res. 17 (1983) 1669–1678.
[49] J. Moreno-Andrés, L. Romero-Martínez, A. Acevedo-Merino, E. Nebot, UV-based technologies for marine water disinfection and the application to ballast water: does salinity interfere with disinfection processes? Sci. Total Environ. 581 (2017) 144–152.
[50] D. Venieri, D. Mantzavinos, Disinfection of waters/wastewaters by solar photocatalysis, in: Advances in Photocatalytic Disinfection, Springer, 2017, pp. 177–198.
[51] L.L. Gyürék, G.R. Finch, Modeling water treatment chemical disinfection kinetics, J. Environ. Eng. 124 (1998) 783–793.
[52] J. Marugán, R. Van Grieken, C. Pablos, M.L. Satuf, A.E. Cassano, O.M. Alfano, Rigorous kinetic modelling with explicit radiation absorption effects of the photocatalytic inactivation of bacteria in water using suspended titanium dioxide, Appl. Catal. B Environ. 102 (2011) 404–416.

[53] M. Cho, H. Chung, J. Yoon, Disinfection of water containing natural organic matter by using ozone-initiated radical reactions, Appl. Environ. Microbiol. 69 (2003) 2284–2291.
[54] R. Sadiq, M.J. Rodriguez, Disinfection by-products (DBPs) in drinking water and predictive models for their occurrence: a review, Sci. Total Environ. 321 (2004) 21–46.
[55] O.K. Dalrymple, E. Stefanakos, M.A. Trotz, D.Y. Goswami, A review of the mechanisms and modeling of photocatalytic disinfection, Appl. Catal. B Environ. 98 (2010) 27–38.
[56] J.C. Hoff, Inactivation of Microbial Agents by Chemical Disinfectants, Water Engineering Research Laboratory, 1986.
[57] M.Y. Lim, J.-M. Kim, G. Ko, Disinfection kinetics of murine norovirus using chlorine and chlorine dioxide, Water Res. 44 (2010) 3243–3251.
[58] X. Ma, K. Bibby, Free chlorine and monochloramine inactivation kinetics of Aspergillus and Penicillium in drinking water, Water Res. (2017).
[59] H.E. Watson, A note on the variation of the rate of disinfection with change in the concentration of the disinfectant, J. Hyg. 8 (1908) 536–542.
[60] J. Marugán, R. van Grieken, C. Sordo, C. Cruz, Kinetics of the photocatalytic disinfection of Escherichia coli suspensions, Appl. Catal. B Environ. 82 (2008) 27–36.
[61] M.A. Benarde, W.B. Snow, V.P. Olivieri, B. Davidson, Kinetics and mechanism of bacterial disinfection by chlorine dioxide, Appl. Microbiol. 15 (1967) 257–265.
[62] C.N. Haas, A mechanistic kinetic model for chlorine disinfection, Environ. Sci. Technol. 14 (1980) 339–340.
[63] C.N. Haas, S.B. Karra, Kinetics of microbial inactivation by chlorine—I. Review of results in demand-free systems, Water Res. 18 (1984) 1443–1449.
[64] L.L. del Carmen Huesca-Espitia, V. Aurioles-López, I. Ramírez, J.L. Sánchez-Salas, E.R. Bandala, Photocatalytic inactivation of highly resistant microorganisms in water: a kinetic approach, J. Photochem. Photobiol. A Chem. 337 (2017) 132–139.
[65] J.L. Rennecker, B.J. Mariñas, J.H. Owens, E.W. Rice, Inactivation of Cryptosporidium parvum oocysts with ozone, Water Res. 33 (1999) 2481–2488.
[66] M. Cho, H. Chung, W. Choi, J. Yoon, Linear correlation between inactivation of E. coli and OH radical concentration in TiO2 photocatalytic disinfection, Water Res. 38 (2004) 1069–1077.
[67] M. Cho, Y. Lee, W. Choi, H. Chung, J. Yoon, Study on Fe (VI) species as a disinfectant: quantitative evaluation and modeling for inactivating Escherichia coli, Water Res. 40 (2006) 3580–3586.
[68] C.N. Haas, J. Joffe, Disinfection under dynamic conditions: modification of Hom's model for decay, Environ. Sci. Technol. 28 (1994) 1367–1369.
[69] M.N. Chong, B. Jin, C.P. Saint, Bacterial inactivation kinetics of a photo-disinfection system using novel titania-impregnated kaolinite photocatalyst, Chem. Eng. J. 171 (2011) 16–23.
[70] M. Castro-Alférez, M.I. Polo-López, J. Marugán, P. Fernández-Ibáñez, Mechanistic model of the Escherichia coli inactivation by solar disinfection based on the photo-generation of internal ROS and the photo-inactivation of enzymes: CAT and SOD, Chem. Eng. J. 318 (2017) 214–223.
[71] R.J. Watts, S. Kong, M.P. Orr, G.C. Miller, B.E. Henry, Photocatalytic inactivation of coliform bacteria and viruses in secondary wastewater effluent, Water Res. 29 (1995) 95–100.
[72] A.-G. Rincon, C. Pulgarin, Effect of pH, inorganic ions, organic matter and H2O2 on E. coli K12 photocatalytic inactivation by TiO2: implications in solar water disinfection, Appl. Catal. B Environ. 51 (2004) 283–302.
[73] A. Rincón, C. Pulgarin, Photocatalytical inactivation of E. coli: effect of (continuous–intermittent) light intensity and of (suspended–fixed) TiO2 concentration, Appl. Catal. B Environ. 44 (2003) 263–284.
[74] A.-G. Rincón, C. Pulgarin, Bactericidal action of illuminated TiO2 on pure Escherichia coli and natural bacterial consortia: post-irradiation events in the dark and assessment of the effective disinfection time, Appl. Catal. B Environ. 49 (2004) 99–112.

[75] D. Gumy, A. Rincon, R. Hajdu, C. Pulgarin, Solar photocatalysis for detoxification and disinfection of water: different types of suspended and fixed TiO2 catalysts study, Sol. Energy 80 (2006) 1376–1381.
[76] A.-G. Rincón, C. Pulgarin, Field solar E. coli inactivation in the absence and presence of TiO2: is UV solar dose an appropriate parameter for standardization of water solar disinfection? Sol. Energy 77 (2004) 635–648.
[77] N. Daneshvar, D. Salari, A. Khataee, Photocatalytic degradation of azo dye acid red 14 in water on ZnO as an alternative catalyst to TiO2, J. Photochem. Photobiol. A Chem. 162 (2004) 317–322.
[78] J.H. Melián, J.D. Rodrıguez, A.V. Suárez, E.T. Rendón, C.V. Do Campo, J. Arana, J.P. Peña, The photocatalytic disinfection of urban waste waters, Chemosphere 41 (2000) 323–327.
[79] M. Murdoch, G. Waterhouse, M. Nadeem, J. Metson, M. Keane, R. Howe, J. Llorca, H. Idriss, The effect of gold loading and particle size on photocatalytic hydrogen production from ethanol over Au/TiO2 nanoparticles, Nat. Chem. 3 (2011) 489.
[80] A. Akyol, H. Yatmaz, M. Bayramoglu, Photocatalytic decolorization of Remazol Red RR in aqueous ZnO suspensions, Appl. Catal. B Environ. 54 (2004) 19–24.
[81] H.C. Yatmaz, N. Dizge, M.S. Kurt, Combination of photocatalytic and membrane distillation hybrid processes for reactive dyes treatment, Environ. Technol. (2016) 1–25.
[82] D. Bahnemann, Solar photocatalytic disinfection of water, Photocatal. Appl. 15 (2016) 72.
[83] A. Benabbou, Z. Derriche, C. Felix, P. Lejeune, C. Guillard, Photocatalytic inactivation of Escherischia coli: effect of concentration of TiO2 and microorganism, nature, and intensity of UV irradiation, Appl. Catal. B Environ. 76 (2007) 257–263.
[84] L. Caballero, K. Whitehead, N. Allen, J. Verran, Inactivation of Escherichia coli on immobilized TiO2 using fluorescent light, J. Photochem. Photobiol. A Chem. 202 (2009) 92–98.
[85] H. Bodaghi, Y. Mostofi, A. Oromiehie, Z. Zamani, B. Ghanbarzadeh, C. Costa, A. Conte, M.A. Del Nobile, Evaluation of the photocatalytic antimicrobial effects of a TiO2 nanocomposite food packaging film by in vitro and in vivo tests, LWT-Food Sci. Technol. 50 (2013) 702–706.
[86] H.N. Pham, T. McDowell, E. Wilkins, Photocatalytically-mediated disinfection of water using tio2 as a catalyst and spore-forming Bacillus pumilus as a model, J. Environ. Sci. Health A 30 (1995) 627–636.
[87] Q. Li, Y.W. Li, P. Wu, R. Xie, J.K. Shang, Palladium oxide nanoparticles on nitrogen-doped titanium oxide: accelerated photocatalytic disinfection and post-illumination catalytic "memory" Adv. Mater. 20 (2008) 3717–3723.
[88] J. Murcia, E. Ávila-Martínez, H. Rojas, J. Navío, M. Hidalgo, Study of the E. coli elimination from urban wastewater over photocatalysts based on metallized TiO2, Appl. Catal. B Environ. 200 (2017) 469–476.
[89] U.I. Gaya, A.H. Abdullah, Heterogeneous photocatalytic degradation of organic contaminants over titanium dioxide: a review of fundamentals, progress and problems, J Photochem Photobiol C: Photochem Rev 9 (2008) 1–12.
[90] E. Evgenidou, K. Fytianos, I. Poulios, Semiconductor-sensitized photodegradation of dichlorvos in water using TiO2 and ZnO as catalysts, Appl. Catal. B Environ. 59 (2005) 81–89.
[91] M.N. Chong, B. Jin, C.W. Chow, C. Saint, Recent developments in photocatalytic water treatment technology: a review, Water Res. 44 (2010) 2997–3027.
[92] C.M. Ling, A.R. Mohamed, S. Bhatia, Performance of photocatalytic reactors using immobilized TiO2 film for the degradation of phenol and methylene blue dye present in water stream, Chemosphere 57 (2004) 547–554.
[93] C. Tang, V. Chen, The photocatalytic degradation of reactive black 5 using TiO2/UV in an annular photoreactor, Water Res. 38 (2004) 2775–2781.
[94] S. Dervin, D.D. Dionysiou, S.C. Pillai, 2D nanostructures for water purification: graphene and beyond, Nanoscale 8 (2016) 15115–15131.
[95] L. Liu, J. Liu, D.D. Sun, Graphene oxide enwrapped Ag3PO4 composite: towards a highly efficient and stable visible-light-induced photocatalyst for water purification, Catal. Sci. Technol. 2 (2012) 2525–2532.

[96] C.-H. Deng, J.-L. Gong, L.-L. Ma, G.-M. Zeng, B. Song, P. Zhang, S.-Y. Huan, Synthesis, characterization and antibacterial performance of visible light-responsive Ag3PO4 particles deposited on graphene nanosheets, Process Saf. Environ. Prot. 106 (2017) 246–255.
[97] O. Akhavan, E. Ghaderi, Photocatalytic reduction of graphene oxide nanosheets on TiO2 thin film for photoinactivation of bacteria in solar light irradiation, J. Phys. Chem. C 113 (2009) 20214–20220.
[98] J. Liu, L. Liu, H. Bai, Y. Wang, D.D. Sun, Gram-scale production of graphene oxide–TiO2 nanorod composites: towards high-activity photocatalytic materials, Appl. Catal. B Environ. 106 (2011) 76–82.
[99] B. Cao, S. Cao, P. Dong, J. Gao, J. Wang, High antibacterial activity of ultrafine TiO2/graphene sheets nanocomposites under visible light irradiation, Mater. Lett. 93 (2013) 349–352.
[100] P. Fernández-Ibáñez, M. Polo-López, S. Malato, S. Wadhwa, J. Hamilton, P. Dunlop, R. D'sa, E. Magee, K. O'shea, D. Dionysiou, Solar photocatalytic disinfection of water using titanium dioxide graphene composites, Chem. Eng. J. 261 (2015) 36–44.
[101] B.R. Cruz-Ortiz, J.W. Hamilton, C. Pablos, L. Díaz-Jiménez, D.A. Cortés-Hernández, P.K. Sharma, M. Castro-Alférez, P. Fernández-Ibañez, P.S. Dunlop, J.A. Byrne, Mechanism of photocatalytic disinfection using titania-graphene composites under UV and visible irradiation, Chem. Eng. J. 316 (2017) 179–186.
[102] D. Xia, T. An, G. Li, W. Wang, H. Zhao, P.K. Wong, Synergistic photocatalytic inactivation mechanisms of bacteria by graphene sheets grafted plasmonic Ag AgX (X = Cl, Br, I) composite photocatalyst under visible light irradiation, Water Res. 99 (2016) 149–161.
[103] X. Zeng, Z. Wang, N. Meng, D.T. McCarthy, A. Deletic, J.-H. Pan, X. Zhang, Highly dispersed TiO2 nanocrystals and carbon dots on reduced graphene oxide: ternary nanocomposites for accelerated photocatalytic water disinfection, Appl. Catal. B Environ. 202 (2017) 33–41.
[104] N. Khadgi, A.R. Upreti, Y. Li, Simultaneous bacterial inactivation and degradation of an emerging pollutant under visible light by ZnFe2O4 co-modified with Ag and rGO, RSC Adv. 7 (2017) 27007–27016.
[105] S. Panneri, P. Ganguly, B.N. Nair, A.A.P. Mohamed, K.G.K. Warrier, U.N.S. Hareesh, Role of precursors on the photophysical properties of carbon nitride and its application for antibiotic degradation, Environ. Sci. Pollut. Res. 24 (2017) 8609–8618.
[106] S. Cao, J. Low, J. Yu, M. Jaroniec, Polymeric photocatalysts based on graphitic carbon nitride, Adv. Mater. 27 (2015) 2150–2176.
[107] R. Kuriki, K. Sekizawa, O. Ishitani, K. Maeda, Visible-light-driven CO2 reduction with carbon nitride: enhancing the activity of ruthenium catalysts, Angew. Chem. Int. Ed. 54 (2015) 2406–2409.
[108] S. Yan, Z. Li, Z. Zou, Photodegradation of rhodamine B and methyl orange over boron-doped g-C3N4 under visible light irradiation, Langmuir 26 (2010) 3894–3901.
[109] W. Wang, J.C. Yu, D. Xia, P.K. Wong, Y. Li, Graphene and g-C3N4 nanosheets cowrapped elemental α-sulfur as a novel metal-free heterojunction photocatalyst for bacterial inactivation under visible-light, Environ. Sci. Technol. 47 (2013) 8724–8732.
[110] J. Huang, W. Ho, X. Wang, Metal-free disinfection effects induced by graphitic carbon nitride polymers under visible light illumination, Chem. Commun. 50 (2014) 4338–4340.
[111] C. Ye, J.-X. Li, Z.-J. Li, X.-B. Li, X.-B. Fan, L.-P. Zhang, B. Chen, C.-H. Tung, L.-Z. Wu, Enhanced driving force and charge separation efficiency of protonated g-C3N4 for photocatalytic O2 evolution, ACS Catal. 5 (2015) 6973–6979.
[112] X. Wang, K. Maeda, A. Thomas, K. Takanabe, G. Xin, J.M. Carlsson, K. Domen, M. Antonietti, A metal-free polymeric photocatalyst for hydrogen production from water under visible light, Nat. Mater. 8 (2009) 76–80.
[113] H. Zhao, H. Yu, X. Quan, S. Chen, Y. Zhang, H. Zhao, H. Wang, Fabrication of atomic single layer graphitic-C3N4 and its high performance of photocatalytic disinfection under visible light irradiation, Appl. Catal. B Environ. 152 (2014) 46–50.
[114] W. Bing, Z. Chen, H. Sun, P. Shi, N. Gao, J. Ren, X. Qu, Visible-light-driven enhanced antibacterial and biofilm elimination activity of graphitic carbon nitride by embedded Ag nanoparticles, Nano Res. 8 (2015) 1648.

[115] G. Li, X. Nie, J. Chen, Q. Jiang, T. An, P.K. Wong, H. Zhang, H. Zhao, H. Yamashita, Enhanced visible-light-driven photocatalytic inactivation of Escherichia coli using gC3N4/TiO2 hybrid photocatalyst synthesized using a hydrothermal-calcination approach, Water Res. 86 (2015) 17–24.
[116] C. Liu, D. Kong, P.-C. Hsu, H. Yuan, H.-W. Lee, Y. Liu, H. Wang, S. Wang, K. Yan, D. Lin, Rapid water disinfection using vertically aligned MoS2 nanofilms and visible light, Nat. Nanotechnol. (2016).
[117] W. Bai, V. Krishna, J. Wang, B. Moudgil, B. Koopman, Enhancement of nano titanium dioxide photocatalysis in transparent coatings by polyhydroxy fullerene, Appl. Catal. B Environ. 125 (2012) 128–135.
[118] G. Wang, Z. Xing, X. Zeng, C. Feng, D.T. McCarthy, A. Deletic, X. Zhang, Ultrathin titanium oxide nanosheets film with memory bactericidal activity, Nanoscale 8 (2016) 18050–18056.
[119] J. Podporska-Carroll, E. Panaitescu, B. Quilty, L. Wang, L. Menon, S.C. Pillai, Antimicrobial properties of highly efficient photocatalytic TiO2 nanotubes, Appl. Catal. B Environ. 176 (2015) 70–75.
[120] C.A. Linkous, G.J. Carter, D.B. Locuson, A.J. Ouellette, D.K. Slattery, L.A. Smitha, Photocatalytic inhibition of algae growth using TiO2, WO3, and cocatalyst modifications, Environ. Sci. Technol. 34 (2000) 4754–4758.
[121] S.O. Alfaro, A. Martínez-de la Cruz, L.M. Torres-Martínez, S. Lee, Remove of marine plankton by photocatalysts with Aurivillius-type structure, Catal. Commun. 11 (2010) 326–330.
[122] S.W. Lee, S. Obregón-Alfaro, V. Rodríguez-González, Photocatalytic coatings of silver–TiO2 nanocomposites on foamed waste-glass prepared by sonochemical process, J. Photochem. Photobiol. A Chem. 221 (2011) 71–76.
[123] S.-W. Lee, S. Obregón, V. Rodríguez-González, The role of silver nanoparticles functionalized on TiO2 for photocatalytic disinfection of harmful algae, RSC Adv. 5 (2015) 44470–44475.
[124] Y. Li, C. Zhang, D. Shuai, S. Naraginti, D. Wang, W. Zhang, Visible-light-driven photocatalytic inactivation of MS2 by metal-free gC3N4: Virucidal performance and mechanism, Water Res. 106 (2016) 249–258.
[125] D.F. Ollis, Kinetics of liquid phase photocatalyzed reactions: an illuminating approach, J. Phys. Chem. B 109 (2005) 2439–2444.
[126] M.L. Satuf, M.J. Pierrestegui, L. Rossini, R.J. Brandi, O.M. Alfano, Kinetic modeling of azo dyes photocatalytic degradation in aqueous TiO2 suspensions. Toxicity and biodegradability evaluation, Catal. Today 161 (2011) 121–126.
[127] A. Emeline, V. Ryabchuk, N. Serpone, Dogmas and misconceptions in heterogeneous photocatalysis. Some enlightened reflections, J. Phys. Chem. B 109 (2005) 18515–18521.
[128] C. Passalía, M.E. Martínez Retamar, O.M. Alfano, R.J. Brandi, Photocatalytic degradation of formaldehyde in gas phase on TiO2 films: a kinetic study, Int. J. Chem. React. Eng. 8 (2010).
[129] C. Minero, F. Catozzo, E. Pelizzetti, Role of adsorption in photocatalyzed reactions of organic molecules in aqueous titania suspensions, Langmuir 8 (1992) 481–486.
[130] M.R. Hoffmann, S.T. Martin, W. Choi, D.W. Bahnemann, Environmental applications of semiconductor photocatalysis, Chem. Rev. 95 (1995) 69–96.
[131] S.J. Thomson, G.C. Webb, Heterogeneous Catalysis, Wiley, 1968.
[132] J.-M. Herrmann, Photocatalysis fundamentals revisited to avoid several misconceptions, Appl. Catal. B Environ. 99 (2010) 461–468.
[133] D. Monllor-Satoca, R. Gómez, M. González-Hidalgo, P. Salvador, The "Direct–Indirect" model: an alternative kinetic approach in heterogeneous photocatalysis based on the degree of interaction of dissolved pollutant species with the semiconductor surface, Catal. Today 129 (2007) 247–255.
[134] H. Gerischer, Photocatalysis in aqueous solution with small TiO2 particles and the dependence of the quantum yield on particle size and light intensity, Electrochim. Acta 40 (1995) 1277–1281.
[135] R.A. Marcus, On the theory of oxidation-reduction reactions involving electron transfer. I, J. Chem. Phys. 24 (1956) 966–978.

[136] H. Gerischer, Charge transfer processes at semiconductor-electrolyte interfaces in connection with problems of catalysis, Surf. Sci. 18 (1969) 97–122.
[137] H. Gerischer, W. Mindt, The mechanisms of the decomposition of semiconductors by electrochemical oxidation and reduction, Electrochim. Acta 13 (1968) 1329–1341.
[138] C. Minero, Kinetic analysis of photoinduced reactions at the water semiconductor interface, Catal. Today 54 (1999) 205–216.
[139] J. Montoya, J. Velasquez, P. Salvador, The direct–indirect kinetic model in photocatalysis: a reanalysis of phenol and formic acid degradation rate dependence on photon flow and concentration in TiO2 aqueous dispersions, Appl. Catal. B Environ. 88 (2009) 50–58.
[140] S. Valencia, F. Catano, L. Rios, G. Restrepo, J. Marín, A new kinetic model for heterogeneous photocatalysis with titanium dioxide: case of non-specific adsorption considering back reaction, Appl. Catal. B Environ. 104 (2011) 300–304.
[141] A. Mills, C. O'Rourke, K. Moore, Powder semiconductor photocatalysis in aqueous solution: an overview of kinetics-based reaction mechanisms, J. Photochem. Photobiol. A Chem. 310 (2015) 66–105.
[142] J. Montoya, J. Peral, P. Salvador, Commentary on the article:"A new kinetic model for heterogeneous photocatalysis with titanium dioxide: case of non-specific adsorption considering back reaction, by S. Valencia, F. Catano, L. Rios, G. Restrepo and J. Marin, published in Applied Catalysis B: Environmental, 104 (2011) 300–304" Appl. Catal. B Environ. 111 (2012) 649–650.
[143] J.F. Montoya, J. Peral, P. Salvador, Comprehensive kinetic and mechanistic analysis of TiO2 photocatalytic reactions according to the direct–indirect model:(I) theoretical approach, J. Phys. Chem. C 118 (2014) 14266–14275.
[144] J. Muncke, Exposure to endocrine disrupting compounds via the food chain: is packaging a relevant source? Sci. Total Environ. 407 (2009) 4549–4559.
[145] M.J. Benotti, R.A. Trenholm, B.J. Vanderford, J.C. Holady, B.D. Stanford, S.A. Snyder, Pharmaceuticals and endocrine disrupting compounds in US drinking water, Environ. Sci. Technol. 43 (2008) 597–603.
[146] R. Fagan, D.E. McCormack, D.D. Dionysiou, S.C. Pillai, A review of solar and visible light active TiO2 photocatalysis for treating bacteria, cyanotoxins and contaminants of emerging concern, Mater. Sci. Semicond. Process. 42 (2016) 2–14.
[147] C.A. Staples, P.B. Dome, G.M. Klecka, S.T. Oblock, L.R. Harris, A review of the environmental fate, effects, and exposures of bisphenol A, Chemosphere 36 (1998) 2149–2173.
[148] K.L. Howdeshell, A.K. Hotchkiss, K.A. Thayer, J.G. Vandenbergh, F.S. Vom Saal, Environmental toxins: exposure to bisphenol A advances puberty, Nature 401 (1999) 763.
[149] J. Xu, Z. Wang, Y. Zhu, Enhanced visible-light-driven photocatalytic disinfection performance and organic pollutants degradation activity of porous g-C3N4 nanosheets, ACS Appl. Mater. Interfaces 9 (2017) 27727–27735.
[150] Y. Wang, X. Zhao, D. Cao, Y. Wang, Y. Zhu, Peroxymonosulfate enhanced visible light photocatalytic degradation bisphenol A by single-atom dispersed Ag mesoporous gC3N4 hybrid, Appl. Catal. B Environ. 211 (2017) 79–88.
[151] S. Sunasee, K.H. Leong, K.T. Wong, G. Lee, S. Pichiah, I. Nah, B.-H. Jeon, Y. Yoon, M. Jang, Sonophotocatalytic degradation of bisphenol A and its intermediates with graphitic carbon nitride, Environ. Sci. Pollut. Res. (2017) 1–12.
[152] K.-Y.A. Lin, Z.-Y. Zhang, Degradation of Bisphenol A using peroxymonosulfate activated by one-step prepared sulfur-doped carbon nitride as a metal-free heterogeneous catalyst, Chem. Eng. J. 313 (2017) 1320–1327.
[153] C. Mu, Y. Zhang, W. Cui, Y. Liang, Y. Zhu, Removal of bisphenol A over a separation free 3D Ag3PO4-graphene hydrogel via an adsorption-photocatalysis synergy, Appl. Catal. B Environ. 212 (2017) 41–49.

[154] F. Chen, W. An, L. Liu, Y. Liang, W. Cui, Highly efficient removal of bisphenol A by a three-dimensional graphene hydrogel-AgBr@ rGO exhibiting adsorption/photocatalysis synergy, Appl. Catal. B Environ. (2017).
[155] H. Katsumata, M. Taniguchi, S. Kaneco, T. Suzuki, Photocatalytic degradation of bisphenol A by Ag3PO4 under visible light, Catal. Commun. 34 (2013) 30–34.
[156] Y. Liu, G. Zhu, J. Gao, M. Hojamberdiev, R. Zhu, X. Wei, Q. Guo, P. Liu, Enhanced photocatalytic activity of Bi4Ti3O12 nanosheets by Fe3+-doping and the addition of Au nanoparticles: photodegradation of phenol and bisphenol A, Appl. Catal. B Environ. 200 (2017) 72–82.
[157] C.-Y. Wang, X. Zhang, H.-B. Qiu, W.-K. Wang, G.-X. Huang, J. Jiang, H.-Q. Yu, Photocatalytic degradation of bisphenol A by oxygen-rich and highly visible-light responsive Bi12O17Cl2 nanobelts, Appl. Catal. B Environ. 200 (2017) 659–665.
[158] S. Gao, C. Guo, J. Lv, Q. Wang, Y. Zhang, S. Hou, J. Gao, J. Xu, A novel 3D hollow magnetic Fe3O4/BiOI heterojunction with enhanced photocatalytic performance for bisphenol A degradation, Chem. Eng. J. 307 (2017) 1055–1065.
[159] C. Wang, H. Zhang, F. Li, L. Zhu, Degradation and mineralization of bisphenol A by mesoporous Bi2WO6 under simulated solar light irradiation, Environ. Sci. Technol. 44 (2010) 6843–6848.
[160] X. Xiao, R. Hao, X. Zuo, J. Nan, L. Li, W. Zhang, Microwave-assisted synthesis of hierarchical Bi7O9I3 microsheets for efficient photocatalytic degradation of bisphenol-A under visible light irradiation, Chem. Eng. J. 209 (2012) 293–300.
[161] X. Xiao, R. Hao, M. Liang, X. Zuo, J. Nan, L. Li, W. Zhang, One-pot solvothermal synthesis of three-dimensional (3D) BiOI/BiOCl composites with enhanced visible-light photocatalytic activities for the degradation of bisphenol-A, J. Hazard. Mater. 233 (2012) 122–130.
[162] C. Chang, L. Zhu, Y. Fu, X. Chu, Highly active Bi/BiOI composite synthesized by one-step reaction and its capacity to degrade bisphenol A under simulated solar light irradiation, Chem. Eng. J. 233 (2013) 305–314.
[163] Y. Kanigaridou, A. Petala, Z. Frontistis, M. Antonopoulou, M. Solakidou, I. Konstantinou, Y. Deligiannakis, D. Mantzavinos, D.I. Kondarides, Solar photocatalytic degradation of bisphenol A with CuOx/BiVO4: Insights into the unexpectedly favorable effect of bicarbonates, Chem. Eng. J. 318 (2017) 39–49.
[164] T. Colborn, F.S. vom Saal, A.M. Soto, Developmental effects of endocrine-disrupting chemicals in wildlife and humans, Environ. Health Perspect. 101 (1993) 378.
[165] J. Jiang, H. Li, L. Zhang, New insight into daylight photocatalysis of AgBr@ Ag: synergistic effect between semiconductor photocatalysis and plasmonic photocatalysis, Chem Eur J 18 (2012) 6360–6369.
[166] X. Liu, X. Wu, Z. Long, C. Zhang, Y. Ma, X. Hao, H. Zhang, C. Pan, Photodegradation of imidacloprid in aqueous solution by the metal-free catalyst graphitic carbon nitride using an energy-saving lamp, J. Agric. Food Chem. 63 (2015) 4754–4760.
[167] R. Mohamed, Synthesis and characterization of AgCl@ graphitic carbon nitride hybrid materials for the photocatalytic degradation of atrazine, Ceram. Int. 41 ((2015) 1197–1204.
[168] L. Tang, J. Wang, G. Zeng, Y. Liu, Y. Deng, Y. Zhou, J. Tang, J. Wang, Z. Guo, Enhanced photocatalytic degradation of norfloxacin in aqueous Bi2WO6 dispersions containing nonionic surfactant under visible light irradiation, J. Hazard. Mater. 306 (2016) 295–304.
[169] A. Kumar, G. Sharma, M. Naushad, A. Kumar, S. Kalia, C. Guo, G.T. Mola, Facile hetero-assembly of superparamagnetic Fe3O4/BiVO4 stacked on biochar for solar photo-degradation of methyl paraben and pesticide removal from soil, J. Photochem. Photobiol. A Chem. 337 (2017) 118–131.
[170] M.G. Alalm, S. Ookawara, D. Fukushi, A. Sato, A. Tawfik, Improved WO3 photocatalytic efficiency using ZrO2 and Ru for the degradation of carbofuran and ampicillin, J. Hazard. Mater. 302 (2016) 225–231.
[171] M. Taheran, S.K. Brar, M. Verma, R.Y. Surampalli, T.C. Zhang, J.R. Valéro, Membrane processes for removal of pharmaceutically active compounds (PhACs) from water and wastewaters, Sci. Total Environ. 547 (2016) 60–77.

[172] M. Badia-Fabregat, I. Oller, S. Malato, Overview on Pilot-Scale Treatments and New and Innovative Technologies for Hospital Effluent, Springer, 2017.
[173] J. Li, S. Sun, R. Chen, T. Zhang, B. Ren, D.D. Dionysiou, Z. Wu, X. Liu, M. Ye, Adsorption behavior and mechanism of ibuprofen onto BiOCl microspheres with exposed {001} facets, Environ. Sci. Pollut. Res. 24 (2017) 9556–9565.
[174] X. Wang, W. Bi, P. Zhai, X. Wang, H. Li, G. Mailhot, W. Dong, Adsorption and photocatalytic degradation of pharmaceuticals by BiOCl x I y nanospheres in aqueous solution, Appl. Surf. Sci. 360 (2016) 240–251.
[175] X. Gao, X. Zhang, Y. Wang, S. Peng, B. Yue, C. Fan, Photocatalytic degradation of carbamazepine using hierarchical BiOCl microspheres: some key operating parameters, degradation intermediates and reaction pathway, Chem. Eng. J. 273 (2015) 156–165.
[176] L. Tang, J.-j. Wang, C.-t. Jia, G.-x. Lv, G. Xu, W.-t. Li, L. Wang, J.-y. Zhang, M.-h. Wu, Simulated solar driven catalytic degradation of psychiatric drug carbamazepine with binary BiVO4 heterostructures sensitized by graphene quantum dots, Appl. Catal. B Environ. 205 (2017) 587–596.
[177] F. Wu, H. Huang, T. Xu, W. Lu, N. Li, W. Chen, Visible-light-assisted peroxymonosulfate activation and mechanism for the degradation of pharmaceuticals over pyridyl-functionalized graphitic carbon nitride coordinated with iron phthalocyanine, Appl. Catal. B Environ. 218 (2017) 230–239.
[178] Z.-d. Lei, J.-j. Wang, L. Wang, X.-y. Yang, G. Xu, L. Tang, Efficient photocatalytic degradation of ibuprofen in aqueous solution using novel visible-light responsive graphene quantum dot/AgVO3 nanoribbons, J. Hazard. Mater. 312 (2016) 298–306.
[179] T.B. Devi, M. Ahmaruzzaman, Bio-inspired facile and green fabrication of Au@ Ag@ AgCl core–double shells nanoparticles and their potential applications for elimination of toxic emerging pollutants: a green and efficient approach for wastewater treatment, Chem. Eng. J. 317 (2017) 726–741.
[180] M. Sturini, A. Speltini, F. Maraschi, G. Vinci, A. Profumo, L. Pretali, A. Albini, L. Malavasi, g-C3N4-promoted degradation of ofloxacin antibiotic in natural waters under simulated sunlight, Environ. Sci. Pollut. Res. 24 (2017) 4153–4161.
[181] J. Xue, S. Ma, Y. Zhou, Z. Zhang, M. He, Facile photochemical synthesis of Au/Pt/g-C3N4 with plasmon-enhanced photocatalytic activity for antibiotic degradation, ACS Appl. Mater. Interfaces 7 (2015) 9630–9637.
[182] S. Panneri, P. Ganguly, M. Mohan, B.N. Nair, A.A.P. Mohamed, K.G. Warrier, U. Hareesh, Photoregenerable, bifunctional granules of carbon-doped g-C3N4 as adsorptive photocatalyst for the efficient removal of tetracycline antibiotic, ACS Sustain. Chem. Eng. 5 (2017) 1610–1618.
[183] S. Panneri, M. Thomas, P. Ganguly, B.N. Nair, A.P. Mohamed, K. Warrier, U. Hareesh, C3 N4 anchored ZIF8 composites: photo-regenerable, high capacity sorbents as adsorptive photocatalysts for the effective removal of tetracycline from water, Catal. Sci. Technol. (2017).
[184] A. Ren, C. Liu, Y. Hong, W. Shi, S. Lin, P. Li, Enhanced visible-light-driven photocatalytic activity for antibiotic degradation using magnetic NiFe2 O4/Bi2O3 heterostructures, Chem. Eng. J. 258 (2014) 301–308.
[185] G. Wu, P. Li, D. Xu, B. Luo, Y. Hong, W. Shi, C. Liu, Hydrothermal synthesis and visible-light-driven photocatalytic degradation for tetracycline of Mn-doped SrTiO3 nanocubes, Appl. Surf. Sci. 333 (2015) 39–47.
[186] T.P. Yoon, M.A. Ischay, J. Du, Visible light photocatalysis as a greener approach to photochemical synthesis, Nat. Chem. 2 (2010) 527–532.
[187] D.M. Schultz, T.P. Yoon, Solar synthesis: prospects in visible light photocatalysis, Science 343 (2014) 1239176.
[188] Y. Wang, Q. Wang, X. Zhan, F. Wang, M. Safdar, J. He, Visible light driven type II heterostructures and their enhanced photocatalysis properties: a review, Nanoscale 5 (2013) 8326–8339.
[189] Y. Sang, Z. Zhao, M. Zhao, P. Hao, Y. Leng, H. Liu, From UV to near-infrared, WS2 nanosheet: a novel photocatalyst for full solar light spectrum photodegradation, Adv. Mater. 27 (2015) 363–369.

[190] S.-F. Yang, C.-G. Niu, D.-W. Huang, H. Zhang, C. Liang, G.-M. Zeng, SrTiO3 nanocubes decorated with Ag/AgCl nanoparticles as photocatalysts with enhanced visible-light photocatalytic activity towards the degradation of dyes, phenol and bisphenol A, Environ. Sci. Nano 4 (2017) 585–595.
[191] W. Zou, L. Zhang, L. Liu, X. Wang, J. Sun, S. Wu, Y. Deng, C. Tang, F. Gao, L. Dong, Engineering the Cu2O–reduced graphene oxide interface to enhance photocatalytic degradation of organic pollutants under visible light, Appl. Catal. B Environ. 181 (2016) 495–503.
[192] J. Xia, J. Di, H. Li, H. Xu, H. Li, S. Guo, Ionic liquid-induced strategy for carbon quantum dots/BiOX (X= Br, Cl) hybrid nanosheets with superior visible light-driven photocatalysis, Appl. Catal. B Environ. 181 (2016) 260–269.
[193] T.S. Anirudhan, F. Shainy, J. Christa, Synthesis and characterization of polyacrylic acid-grafted-carboxylic graphene/titanium nanotube composite for the effective removal of enrofloxacin from aqueous solutions: adsorption and photocatalytic degradation studies, J. Hazard. Mater. 324 (2017) 117–130.
[194] L. Liu, L. Ding, Y. Liu, W. An, S. Lin, Y. Liang, W. Cui, A stable Ag3PO4@ PANI core@ shell hybrid: enrichment photocatalytic degradation with π-π conjugation, Appl. Catal. B Environ. 201 (2017) 92–104.

CHAPTER

SEMICONDUCTOR PHOTOCATALYSIS FOR WATER PURIFICATION

24

Youji Li*, Feitai Chen*, Rongan He†, Yingchun Wang*, Ningmei Tang*

National Demonstration Center for Experimental Chemistry Education, Jishou University, Jishou, China Hunan Province Key Laboratory of Applied Environmental Photocatalysis, Changsha University, Changsha, China†*

1 INTRODUCTION

The rapid developments of industry and social economy have produced hazardous wastes, most of which were released to air, rivers, lakes, and seas, causing serious environmental contamination. Consequently, clean water sources became more and more inadequate, and worse, the demand for water increased quickly. The sustainable supply of good quality water has become a serious problem for the development of human beings. The recycling and reuse of wastewater effluents are important to increase the insufficient supply of clean water [1]. Previously, there have been some water-treatment approaches that had to be carried out to obtain reliable fresh water, such as adsorption [2], biological treatment [3], membrane-based separations [4], and chemical treatment [5]. However, the traditional treatments were developed to effectively remove various types of contaminants from water eventually resulted in the production of secondary pollutants, such as soluble refractory organic compounds, chlorine as well as health-threatening bacteria which are difficult to remove [6]. Therefore, the development of a green, sustainable, and nondestructive technology for wastewater treatment is of great importance.

2 IMPORTANCE OF SEMICONDUCTOR PHOTOCATALYSIS IN WATER PURIFICATION

Today, the rapid progress in urbanization and industrialization, and huge increases in population have resulted in environmental problems such as contaminated air and groundwater as well as hazardous wastes. The urgent demand for clean water sources has attracted great consideration all over the world. The recycling of wastewater (conversion of wastewater to harmless and readily disposable water) is considered a key to solving the problem of water shortage, and thus raises an increasing concern for the decontamination of waste water [1–4]. Because the organic compounds discharged in water are multiple and complex, including organic dyes, phenols, surfactants, pesticides, antibiotics, and personal care pharmaceuticals, it has become difficult to find a unique treatment procedure that can entirely eliminate all types of organic pollutants [1, 3]. To meet the demand for organic waste remediation

Nanoscale Materials in Water Purification. https://doi.org/10.1016/B978-0-12-813926-4.00030-6

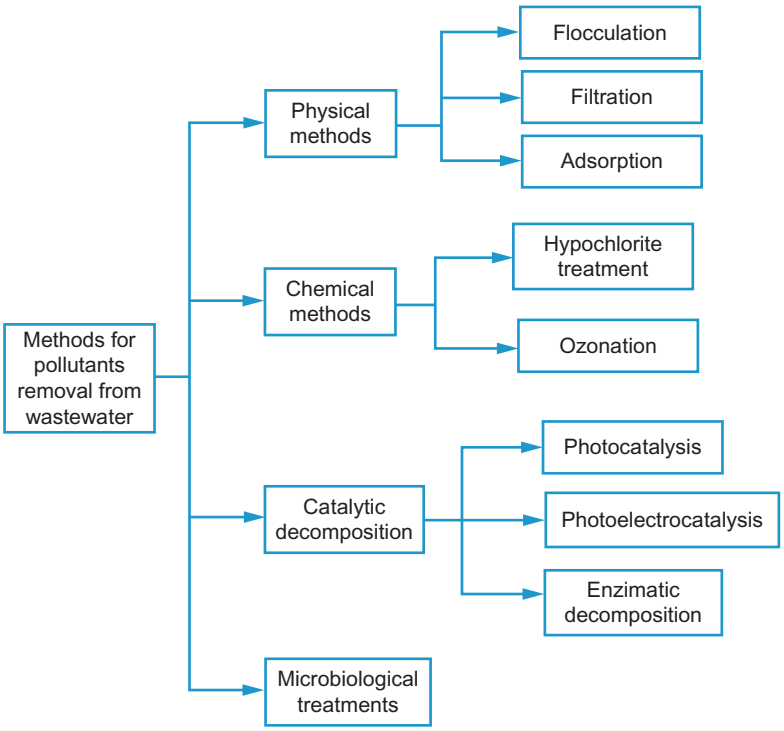

FIG. 1

Main methods applied to the removal of organic dyes from wastewaters.

in water, various practical strategies and solutions have been adopted to yield more viable water resources [2, 5, 6]. These methods and technologies could be roughly classified as physical methods, biological methods, chemical methods and combined approaches [5]. They could also be classified in more detail as physicochemical, chemical, advanced oxidation processes (AOPs), biological, and electrochemical, as shown in Fig. 1 [6].

Physical methods such as coagulation, flocculation, membrane separation, and adsorption on activated charcoal are non-destructive and only transfer the pollutants to other media, thus giving rise to secondary pollution [3]. For example, in coagulation, though soluble pollutant molecules are removed by their electrostatic attraction to the polymer molecules with oppositely charged, large amounts of sludge and high amounts of dissolved solids were left in the effluent and needed to be treated further [6]. Adsorption and membranes separation could remove pollutant molecules in the effluent without generating sludge, but the removed pollutant still exists and needs post-treatment, not to mention the expensive regeneration of adsorbent and the high cost of renewing the fouled membrane involves the loss of adsorbent [7]. Commonly used biological methods are environmentally friendly, effective, generate less sludge, and are relatively inexpensive. Unfortunately, biological approaches are time-consuming and need large land, and they are some sensitive to the toxicity of pollutants, some

pollutants are originally insecticide, insecticide or antibiotics [7, 8]. Moreover, some pollutants are difficult to biodegrade [6, 8].

For the above reason, more powerful and environmental oxidation methods, such as ozonation, Fenton oxidation, photocatalytic oxidation, supercritical water oxidation, and the electrochemical method were widely used in the remediation of wastewater [1, 6]. Among these, photocatalytic oxidation has been found to be a safe, highly efficient, cost effective technique, and is regarded as the most realistic solution to aqueous pollutants [3, 9, 10].

The main problems are how to oxidize those non-biodegradable organic pollutants which are resistant to conventional treatment methods, and how to kill waterborne pathogens without the formation of harmful toxic disinfection byproducts which might result from the disinfection process [5]. Photocatalysis can not only solve these problems, but is also capable of destroying pollutants with less energy consumption and less chemical utilization. Therefore, it attracts increasing attention and has become a well-known advanced oxidation process.

In a photocatalysis procedure, electrons and holes are generated from semiconductors under light irradiation, organic molecules are oxidized by photo-generated holes, and reactive radical species (such as $\cdot O_2^-$, $\cdot OH$) are formed from the reduction of O_2. Because all these radical species are strong oxidizing agents, all organic molecules in water could be non-selectively destroyed. Hence, photocatalysis has been widely used for photocatalytic degradation of all kinds of organic pollutants in water, such as dye, and current and emerging microbial pathogens. Because visible light energy is the main constituent of solar energy, visible-light-responsive photocatalysts are more preferable in the field of photocatalysis.

3 TYPES OF SEMICONDUCTOR

3.1 PURE SEMICONDUCTOR

Compared with doped semiconductors and semiconductor compounds, the electronic structure and basic property of pure semiconductors are relatively simple. Additionally, the morphology, crystal structure, and surface state of pure semiconductors are easy to control. These characteristics make it convenient to study the photocatalytic mechanism of semiconductor catalysts [11]. In fact, considerable efforts regarding photocatalysis began from the research on pure semiconductors. Therefore, it is very important to understand the intrinsic properties of pure semiconductors.

A semiconductor is a material with conductivity between insulator and conductor. Its photoelectronic property is usually characterized by its energy band structure. As shown in Fig. 2, it mainly consists of a valance band (VB) and a conduction band (CB). In a semiconductor, the valance band is fully filled with electrons, while the conduction band is empty of electron orbitals at low temperature. The energy region between VB and CB has no electron states, and is known as the band gap. When a semiconductor is illuminated by photons with energy equal to or greater than its band gap, electrons that acquire the energy will be excited to the CB. Meanwhile, holes are left in the VB; thus, photogenerated electron-hole pairs are produced. Generally, the excited electrons possess strong reduction capacity, while holes have strong oxidation capacity. When photogenerated electrons and holes transfer to the surface of a semiconductor, they can act as reductant and oxidant, respectively.

It should be noted that the redox capacity of photogenerated carriers is closely related with the positions of their VB and CB. Under a certain pH condition, the photogenerated hole has a stronger

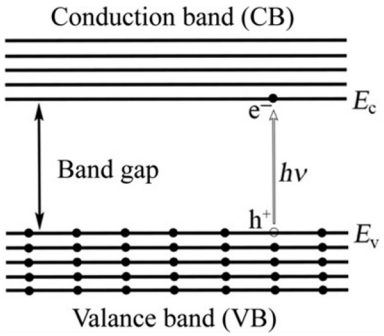

FIG. 2

Energy band structure of pure semiconductor and the formation of photogenerated electron and hole pairs.

oxidation capacity when the VB potential is more positive, while photogenerated electron exhibits more powerful reduction capacity when the CB potential is more negative [12]. Therefore, a semiconductor photocatalyst should have a suitable energy band structure in order to remove organic pollutants effectively. It is generally accepted that the VB should have a potential of +1.0 to +3.5 V versus the normal hydrogen electrode (NHE) and the CB should have a potential of +0.5 to −1.5 V versus the NHE [13–15]. TiO_2, a typical semiconductor photocatalyst, is considered to be one of the best candidates for photocatalytic application. The photocatalytic mechanism of the semiconductor is illuminated through the example of TiO_2. Some key steps during photocatalysis are given as follows.

$$TiO_2 + h\nu(UV) \rightarrow TiO_2(e^-) + TiO_2(h^+) \quad (1)$$

$$h^+ + H_2O \rightarrow OH^\bullet + H^+ \quad (2)$$

$$e^- + O_2 \rightarrow O_2^{\bullet -} \quad (3)$$

$$H_2O + O_2^{\bullet -} \rightarrow HO_2^\bullet + OH^\bullet \quad (4)$$

$$2HO_2^\bullet \rightarrow H_2O_2 + O_2 \quad (5)$$

$$H_2O_2 + O_2^{\bullet -} \rightarrow 2OH^\bullet + OH^- + O_2 \quad (6)$$

$$\text{Organic} + OH^\bullet \rightarrow H_2O + CO_2 \quad (7)$$

Briefly, a photocatalytic reaction includes three key processes: (a) the semiconductor absorbs photons to produce electron-hole pairs; (b) photogenerated carriers migrate to the semiconductor's surface to form reactive oxygen species such as $O_2^{\bullet -}$, H_2O_2, and $OH^\bullet$; (c) organic pollutant reacts with holes and reactive oxygen species.

Since Fujishima and Honda discovered that a TiO_2 electrode can split water into hydrogen and oxygen under UV irradiation in 1972, researchers in the fields of physics, chemistry, and material science began to study the photocatalytic performance of semiconductors. After decades of development, a series of pure semiconductor materials such as ZnO [16], CdS [17], and WO_3 [18] were found to be excellent candidates for photocatalytic application. In order to obtain an improved photo-absorption efficiency for pure semiconductors, various morphological micro/nanostructures with large specific

surface áreas, such as hollow microsphere [19], nanoflower [20], nanosheet [21], and nanotube [22], have been synthesized.

3.2 ELEMENT-DOPED SEMICONDUCTOR

Pure semiconductors have been widely used as catalysts for photocatalytic degradation. However, the rapid recombination of photogenerated electron-hole pairs usually results in a low photo quantum yield. Additionally, some pure semiconductors can only utilize UV light because of their wide band gap. For example, TiO_2 is the most widely studied for its high activity, nontoxicity, stability, and low-cost. Nevertheless, the application of TiO_2 is limited for its wide band gap (3.2 eV), only responsive to UV light. Similarly, many other wide band gap photocataysts, such as TiO_2, ZnO, ZnS, $SrTiO_3$, and BiOCl, also face the same problem [23–25]. It is well known that UV light on Earth's surface only accounts for ca. 5% of solar spectrum energy. Obviously, the utilization efficiency of solar light is not high for this kind of pure semiconductors. These drawbacks greatly restrict their practical application in the field of photocatalysis. In order to suppress the recombination of photogenerated carriers and extend the spectral response to the visible-light region, considerable effort has been devoted over the past decades. Element doping was considered to be a potential method for improving the spectral absorption and photoelectric efficiency. Through element doping, a donor level closer to the CB could form in the semiconductors, and consequently, the band gap could be reduced and the light adsorption range could be expanded to the visible region, as shown in Fig. 2; this would take effect if such states possessed very low probability for back electronic decay and had negligible activity as carrier recombination centers [10, 26]. Furthermore, doping might also improve the transmission properties of semiconductors, resulting in higher efficiency of carriers [27].

Asahi et al. found that the optical absorption and photocatalytic activity of TiO_2 under visible light irradiation can be improved through the substitutional doping of nonmetal elements such as N, C, and P [28]. Su et al. reported that multivalency iodine-doped TiO_2 had visible-light response, exhibiting high photocatalytic activity for the degradation of gaseous acetone under irradiation of visible light with a wavelength greater than 420 nm [29]. Rare-earth doping and metal doping were widely used to improve the photocatalytic activity of semiconductor in recent years [30].

Gao et al. [31] prepared Fe-doped BiOCl by a simple combustion method. The Fe^{3+} doping leads to a red-shift of absorption edge and an expanded visible light absorption, and consequently, brings about an obvious increase in the visible-light photocatalytic activity of BiOCl on the degradation of rhodamine (Fig. 3).

In addition, co-doping of different elements onto pure semiconductors was also adopted to improve the photocatalytic activities of semiconductor photocatalysts [32, 33]. Comparing strategies such as depositing with noble metals and coupling with narrow band-gap semiconductors, doping with foreign elements has an advantage: low concentration doping can markedly improve the photocatalytic property of pure semiconductors. Though doping could obviously increase the visible light absorption of wide band gap photocatalysts, the doping shortage is also obvious. The reason is that the formed doping levels are usually discrete; the newly formed doping level might also act as the recombination center for carriers, resulting in increased recombination of electrons and holes [26, 34]. To overcome the shortage of doping, preparing solid solution can be an alternative, providing another effective way to adjust the band structure of photocatalysts. In a solid solution, two or more crystalline phases hybridized at the atomic scale; therefore, the energy levels in it are uniform, so the formation of additional discrete

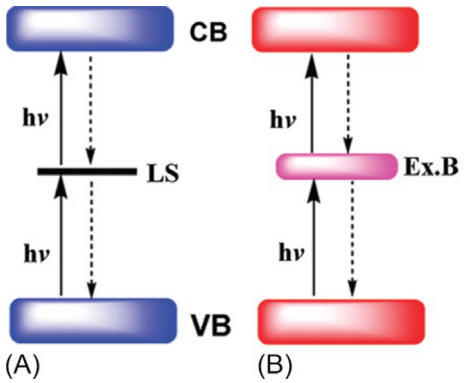

FIG. 3

Mechanism of energy level for doped photocatalysts.

doping level could be prevented. By now, many solid solutions, such as $Cd_xZn_{1-x}S$ [35], $Mn_xCd_{1-x}S$ [36], $BiOCl_xBr_{1-x}$ [37], $Zn_{1-x}Cd_xS$ [38], and $NiFe_{2-x}Mn_xO_4$ [39], have been prepared and exhibited improved photocatalytic activities on degradation of pollutants and H_2 evolution.

3.3 POROUS MATERIAL-SUPPORTED SEMICONDUCTOR

Nanosized semiconductor powder usually exhibits excellent photocataltyic activity for the degradation of organic pollutant in aqueous systems. This is because of its larger specific surface area, compared with bulk materials, which can provide a lot of adsorption sites and reaction-active sites. Besides, small particle size is beneficial to the separation of photogenerated electron-hole pairs. In addition, nanoparticles have good dispersion capability in aqueous solutions. A typical semiconductor powder is commercial TiO_2 of Deggusa P25, which has been widely used to treat all kinds of organic pollutants via photocatalytic degradation due to the advantages mentioned above. However, researchers found that some organic pollutant molecules or their intermediate products can cause nanosemiconductor powder to coagulate during the photocatalytic reaction, thereby reducing the reaction-active surface and reducing photocatalytic activity. Furthermore, it is very difficult to separate semiconductor nanoparticles from aqueous solution [40]. Obviously, recovering and reusing semiconductor nanoparticles is extremely important. These drawbacks seriously restrict their practical application in the field of water purification. In order to overcome these issues, porous material-supported semiconductors have been developed.

The advantages of loading semiconductor nanoparticles onto a porous support mainly lie in the following aspects. First, this method can fully exploit the advantages of nanoparticles. Furthermore, the light reflection and scattering resulting from the porous structure are beneficial to light harvesting. In addition, the use of support material makes it easy to recover and reuse the semiconductor photocatalyst after each cycle of photocatalytic degradation. After several decades of development, various substrates such as microporous zeolites [41], mesoporous silicas [42], alumina clays, and activated carbon have been employed as semiconductor nanoparticle supports [43, 44].

Using a simple synthesis method, Guesh et al. successfully loaded TiO_2 on different zeolite frameworks [45]. The synthesized samples exhibited markedly higher photocatalytic activity than pure TiO_2 for the degradation of real wastewater from the textile industry. More importantly, the obtained hybrid exhibited excellent recoverability and reusability in the cycle photocatalytic test. Some researchers (including our group) found that zeolite-supported photocatalysts possessed enhanced phtocatalytic activity due to the improved adsorption capacity of the composites and high dispersion of the semiconductor on the support surface [46, 47]. In fact, nanoparticles as well as other morphological semiconductor photocatalysts are usually used to load onto porous supports. For instance, Liu et al. [48] synthesized honeycomb-like ZnO nanowalls on zeolite in order to maximum the specific surface area, which exhibited huge potential application in wastewater treatment. In our previous work [49], ordered mesoporous titania/activated carbon was synthesized by a template technique, and it displayed much higher photocatalytic activity than pure mesoporous titania and commercial P25, resulting from the pore-pore synergistic amplification effect of the photocatalyst. At present, porous-materials-supported semiconductors have been widely used to treat all kinds of organic pollutants in water and air [50–52].

4 DESIGN OF PHOTOCATALYTIC REACTOR FOR WATER PURIFICATION

In order to make full use of the photocatalytic property of a semiconductor photocatalyst, it is extremely important to fabricate a photocatalytic reactor with a reasonable design. Considerable research reveals that the photocatalytic efficiency of a photocatalytic reaction is closely related to the following factors: spectral response range of photocatalyst under irradiation [53], photon-capturing efficiency of the photocatalyst [54], and utilization of produced reactive oxygen species on the photocatalyst's surface [55].

Therefore, a suitable light source which can provide spectra with enough width is necessary so as to ensure the effective excitation of photogenerated carriers. If the utilized photocatalyst possesses a wide band gap, the UV-light source needs to be configured in a photocatalytic reactor. Besides, it is necessary to configure an artificial visible-light source if the photocatalyst used possesses visible-light response, because direct utilization of solar energy to remove organic pollutants through photocatalytic degradation has been demonstrated to be of limited success. In addition, the location of the light source in the reactor is also a major factor because it affects the efficiency of light reaching the surface of the photocatalyst. In brief, the choice and arrangement of light source are extremely important to a photocatalytic reactor. On the other hand, the distribution state of the semicondutor photocatalyst in the photocatalytic reaction process is another important aspect which must be considered, as it directly affects the light-capturing efficiency and the contact chance of produced active oxygen species with organic molecules. Of course, other factors such as the pH, temperature in a reactor and the recyclability of photocatalyst are also worth considering when designing a photocatalytic reactor.

Over 2 decades of development, various photocatalytic reactors have been designed and utilized for water purification [46, 56–59]. These reactors can be broadly classified to two categories: slurry and immobilized photocatalytic reactors. Fig. 4 shows the schematic diagram of a slurry photocatalytic reactor. It can be seen that the photocatalyst was dispersed into the reaction liquid uniformly through air sparging. Some slurry reactors may use electric or magnetic stirring to achieve dispersion of the photocatalyst. The advantage of this kind of design is that it decreases the agglomeration and

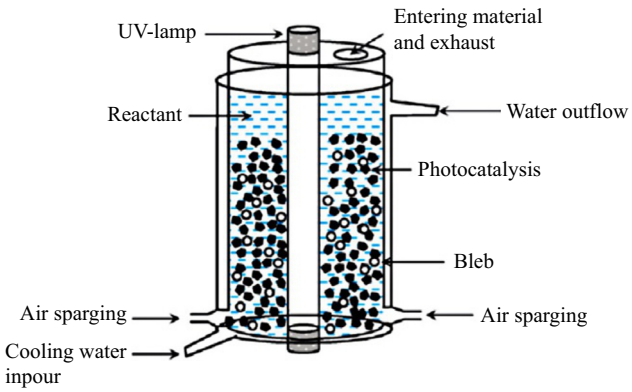

FIG. 4

Schematic diagram of slurry photocatalytic reactor.

accumulation of the photocatalyst so as to capture many more photons and react with organic molecules efficiently. The light resource is located in the center of the reactor in this sample, which can be placed outside of the reactor. The pH value of the solution can be adjusted through adding NaOH or HNO_3. In addition, the temperature of system is maintained at a low level by water circulation. The main drawback of this kind of reactor is that photocatalysts (especially those possessing small particle size) are difficult to recycle.

Fig. 5 shows a schematic diagram of an immobilized photocatalytic reactor. It can be observed that the photocatalyst in this reactor was immobilized on the wall of quartz tubes. In other cases, photocatalysts may be immobilized on the surface of supported materials or on the surface of the light resource [60, 61]. This can avoid the problem of photocatalyst recycle existing in the slurry reactor. However,

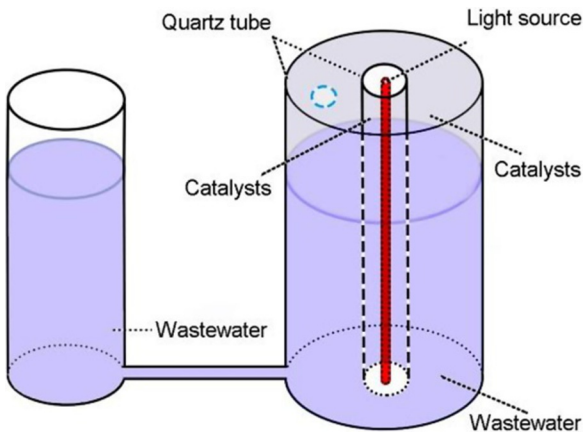

FIG. 5

Schematic diagram of immobilized photocatalytic reactor.

the available surface area of the photocatalytic reaction is sacrificed. In order to immobilize much more photocatalyst in a reactor with fixed volume, the quartz tubes are designed to curve. Some researchers loaded photocatalysts onto porous support materials to realize the same purpose. It should be noted that an LED light resource was used in photocatalytic reactors in recent years, and these LEDs displayed numerous advantages such as long life, little heat production, and good linearity of emitted light intensity.

5 PHOTOELECTROCATALYSIS

Over the last few years, the photoelectrocatalytic oxidation technique combining both electrochemical and photocatalytic technologies was found to be one of the most powerful techniques for removing recalcitrant organic pollutants [62]. In the photoelectrocatalytic process, applying an external potential prevents charge recombination, increases the lifetime of the active holes, and consequently increases the degradation efficiency of the organic compounds [63–65]. The whole reaction process as viewed at both macroscopic and microscopic scales iss shown in Fig. 6 [66].

This photoelectrocatalytic method consists of the application of a constant bias anodic potential (E_{anod}) to a TiO_2-based thin-film anode subjected to UV illumination. Meanwhile, the photogenerated holes could oxidize the organic compounds at the anode surface (Fig. 6A), while the photoinduced electrons were continuously extracted from the anode by an external electrical circuit (Fig. 6B). This would cause the inhibition of reactions (8) and favor the production of a higher number of holes H^+ and heterogeneous $^{\bullet}OH$, largely enhancing organic oxidation (9).

$$e_{CB}^{-} + h_{VB} \rightarrow TiO_2 + \text{heat} \tag{8}$$

$$\text{Organic} + OH^{\bullet} + H^{+} \rightarrow H_2O + CO_2 \tag{9}$$

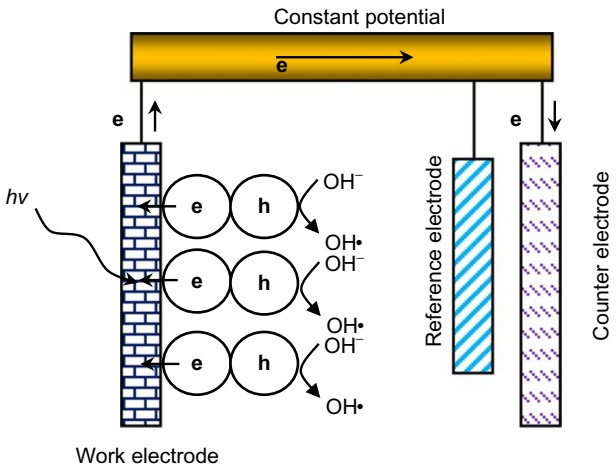

FIG. 6

Schematic representation of whole photoelectrocatalytic reaction process.

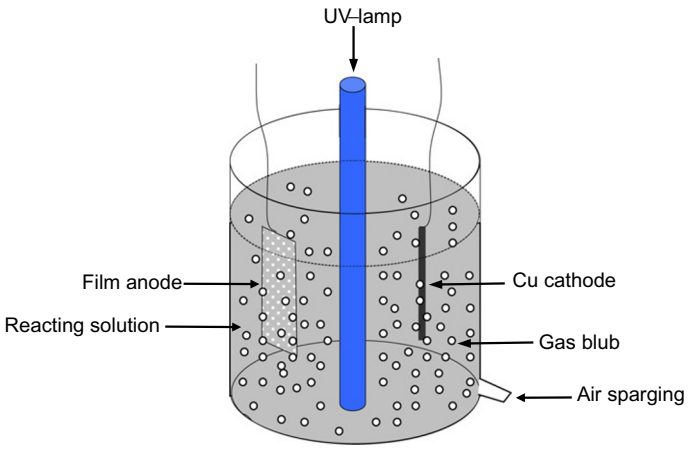

FIG. 7

Schematic diagram of the electrochemical cell employed to carry out photocatalytic degradation of 4-chlorophenol.

The electrochemical cells used in photoelectrocatalysis are usually tank or flow reactors that permit the passage of UV light through a quartz glass to reach the exposed surface of the TiO_2-based anode with minimum loss of incident irradiation. Examples of systems and cells for treating synthetic organic compounds can be seen in Fig. 7 [67].

Additionally, a setup for the photoelectrocatlytic reaction in aqueous solution is similar to a photoelectrochemical cell, consisting of a counter electrode, a working electrode coated with catalyst film, and a reference electrode in an electrolyte solution [68]. But, this mode is obviously unsuitable for the removal of volatile organic compounds and other gaseous pollutants [69]. Herein, we presented an electrically enhanced photocatalysis (EEP) suitable for gas-phase application in photoelectrocatlytic type. An EEP reactor is shown in Fig. 8. A copper disc was used as the counter electrode, with an inter-electrode gap of 1 cm. The power of the light irradiated on the surface of photocatalytic sample was varied by changing the distance between the lamp and anode [70].

6 PARAMETER AFFECTING PHOTOCATALYSIS INVESTIGATION

The actual photocatalytic degradation effectiveness of a pollutant may be affected by many factors, such as photocatalysts' activity, light wavelength, irradiation intensity, aqueous media, and reaction circumstance. Among these factors, photocatalyst activity usually plays the key role; therefore, the main attention of researchers studying photocatalytic wastewater remediation is focused on improving the activity of photocatalysts. It well-known that photocatalysts' activity is related to morphology, efficiency of charge transfer, and so on; hence, various strategies have been developed to improve the activities of photocatalysts.

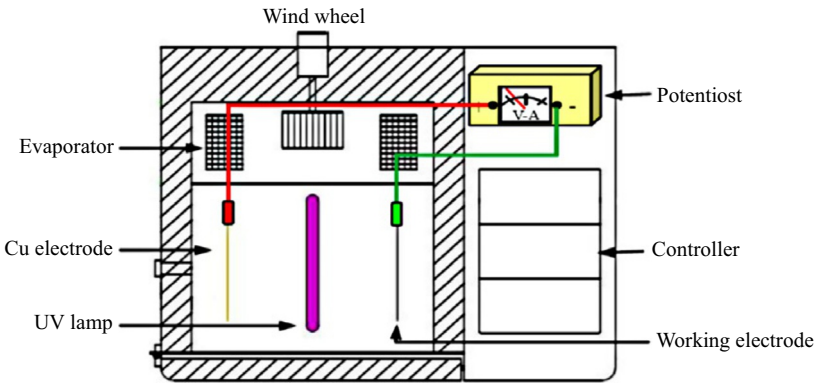

FIG. 8

Schematic of the electrically enchanced photocatalytic apparatus [70].

6.1 MORPHOLOGY

The visible light responsible semiconductors (e.g., ≤ 3 eV), like Ag_2O, $InTaO_4$, $BiVO_4$, Cu_2O, Ag_3VO_4, CdS, CdSe, Bi_2S_3, SiC, g-C_3N_4, and Si, can be excited by visible light and are more favorable to solar utilization [11–13, 71]. However, the performances of these semiconductors in bulk are not as high as expected because of their poor utilization of photo-generated carriers and their good visible light responsibilities. In order to fully exploit these photocatalysts, morphology control has been widely and extensively studied, because the photocatalytic properties of semiconductors are highly dependent on their morphologies and sizes. High surface area, low thickness, and hierarchical and hollow structure could increase the light absorption and accessibility of photocatalysts, enabling the carriers migrate to the surface more quickly and reducing the dosage of photocatalysts. Accordingly, the performance of photocatalysts could be enhanced through morphology control, such as facet exposure, reducing thickness, and building hierarchical structures [72–75].

Since Yang et al. [74] reported their work on hierarchically ordered oxides, research on hierarchical-structured photocatalysts has attracted increasing attention. The photocatalysts with hierarchical structures usually exhibit better performance than bulk photocatalysts, because of the former's high specific surface areas, efficient light harvesting, ready accessibility, and transportation for reactants. Hierarchically structured TiO_2 [76], ZnO [77], $BiVO_4$ [78], etc., exhibited enhanced photocatalytic performance in either oxidation or reduction reactions, for the above reasons.

6.2 CARRIER TRANSFER AND SEPARATION EFFICIENCY

In addition to band structures and morphology, the carrier transfer and separation efficiency of photocatalysts also affect their activities. For most photocatalysts, the fast recombination of photo-generated electrons and holes is one of the main obstacles to activity enhancement of photocatalysts; therefore, effectively suppressing the recombination of carriers is very important in the design and preparation of high activity photocatalysts. For this reason, heterojunction construction and surface modification have been widely adopted to improve the generation, separation, and utilization of electrons and holes [9, 79–82].

A heterojunction could form when the position of the conduction band and valance band of the coupled semiconductors are different. In this situation, the photo-generated electrons and holes could migrate to the conduction band or valance band of the coupled semiconductor, thus hindering the recombination of carriers [13, 83]. Among those reported, the p-n heterojunction is the most familiar type, in which electrons and holes migrate in different directions and recombination is suppressed.

The p-n junction is the most common type of heterostructure, in which photo-excited holes move from the VB of the n-type semiconductor to the VB of the p-type semiconductor, while photo-excited electrons move from the CB of the p-type semiconductor to the n-type. Thus, the electrons and holes are effectively separated, and the photocatalytic activity of photocatalysts is enhanced [79].

Though p-n heterojunction can effectively separate holes and electrons, it still has an undesirable shortage. That is, this kind of charge carrier migration could reduce both the oxidizing power of holes and the reducing power of electrons because they migrate to the less negative conduction band and less positive valance band, respectively. Recently, a kind of Z-scheme heterojunction was found to be able to prevent this shortage, and it has attracted increasing attention [84]. In a Z-scheme heterojunction, the migration of electrons occurs from the less negative CB of one coupled part to the less positive VB of another. Compared to p-n junction, Z-scheme migration of carriers prefers to maintain holes and electrons with the higher redox capacity for reaction, at the cost of losing some carriers with lower redox capacity, as shown in Fig. 9 [71]. Hence, the designation of Z-scheme heterojunction is a more promising method for improving the performance of photocatalysts [84, 85].

Coupling photocatalysts with conductive materials is another effective way to improve their photocatalytic performance. The conductive materials usually act as electron acceptors to improve the migration of photo-generated electrons, and consequently facilitate the separation of carriers. Novel metal, carbon-based materials and conductive polymers can be adopted as electron trapping agents to enhance the carrier separation of photocatalysts [81, 86, 87].

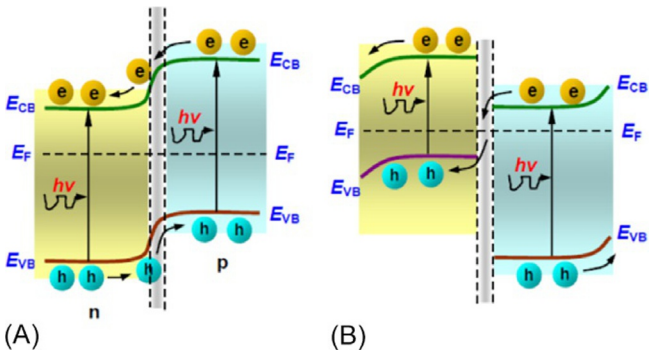

FIG. 9

Schematic illustration of the migration of electrons and holes in a common p-n heterostructure (A) and a Z-scheme heterostructure (B) [71].

7 CHALLENGES

Semiconductor photocatalysis is undoubtedly a desirable tool in dealing with wastewater treatment for environmental protection. Many of the most recent advances in photocatalysis have been realized by selective control of the morphology of nanomaterials, element doping, design of photocatalytic reactors, and porous material support. However, there are extensive challenges to the fabrication of high-quality, prepared nanosemiconductor materials. On the one hand, it is urgent to seek new modification methods in order to improve the transfer efficiency of photocarriers and suppress the recombination of electrons and holes. A survey of efforts exploring suitable materials and attempting to optimize their energy band configurations for the design and fabrication of advanced photocatalysts in the framework of nanotechnology will be introduced. Additionally, other features such as morphological architecture, the choice of semiconductor materials, and surface properties affecting photocatalysis will be considered when designing a stable and efficient photocatalyst material. The current theoretical understanding of key aspects of photocatalytic materials will be discussed.

8 CONCLUSION

In this chapter, first, semiconductor-based photocatalysts were introduced as one of the most successful approaches for water/wastewater treatment. The most suitable nanosemiconductor materials have been established in most photocatalytic techniques for different reactors. Photocatalytic methods with hole generation and heterogeneous $^{\bullet}OH$ as oxidants at the surface of nanosemiconductor-based materials have demonstrated themselves to be effective and economical technologies for the degradation of pollutants in wastewater. In the sections that follow, focus is placed on types of semiconductors, design of the photocatalytic reactor, and photo-electrocatalysis for the environmental remediation process. Much emphasis has been placed upon the emerging approaches and the fundamental mechanisms of photocatalytic enhancement for doping, morphology control, design of photocatalytic reactors, and porous-material-supported photocatalyst materials. This review provides in-depth knowledge of the fundamental mechanism and understanding of the photocatalysis process that is useful for designing and fabricating novel catalysts in order to expand nanoscale materials' applicability in water purification.

REFERENCES

[1] M.M. Khin, A.S. Nair, V.J. Babu, R. Murugan, S. Ramakrishna, A review on nanomaterials for environmental remediation, Energy Environ. Sci. 5 (2012) 819–875.

[2] W. Wang, M.O. Tadé, Z. Shao, Research progress of perovskite materials in photocatalysis- and photovoltaics-related energy conversion and environmental treatment, Chem. Soc. Rev. 44 (2015) 5371–5548.

[3] R. Ameta, S. Benjamin, A. Ameta, S.C. Ameta, Photocatalytic degradation of organic pollutants: a review, Mater. Sci. Forum 734 (2012) 247–272.

[4] J. Wang, S. Wang, Removal of pharmaceuticals and personal care products (PPCPs) from wastewater: a review, J. Environ. Manag. 182 (2016) 620–640.

[5] R.K. Ibrahim, M. Hayyan, M.A. AlSaadi, A. Hayyan, S. Ibrahim, Environmental application of nanotechnology: air, soil, and water, Environ. Sci. Pollut. R. 23 (2016) 13754–13788.
[6] E. Brillas, C.A. Martínez-Huitle, Decontamination of wastewaters containing synthetic organic dyes by electrochemical methods. An updated review, Appl. Catal. B Environ. 166–167 (2015) 603–643.
[7] E. Forgacs, T. Cserháti, G. Oros, Removal of synthetic dyes from wastewaters: a review, Environ. Int. 30 (2004) 953–971.
[8] O.J. Hao, H. Kim, P. Chiang, Decolorization of wastewater, Crit. Rev. Environ. Sci. Technol. 30 (2000) 449–505.
[9] P.A.K. Reddy, P.V.L. Reddy, E. Kwon, K. Kim, T. Akter, S. Kalagara, Recent advances in photocatalytic treatment of pollutants in aqueous media, Environ. Int. 91 (2016) 94–103.
[10] N. Serpone, A.V. Emeline, Semiconductor photocatalysis—past, present, and future outlook, J. Phys. Chem. Lett. 3 (2012) 673–677.
[11] S. Bai, J. Jiang, Q. Zhang, Y. Xiong, Steering charge kinetics in photocatalysis: intersection of materials syntheses, characterization techniques and theoretical simulations, Chem. Soc. Rev. 44 (2015) 2893–2939.
[12] F. Han, T. Gao, Y. Zhu, K.J. Gaskell, C. Wang, A battery made from a single material, Adv. Mater. 27 (2015) 3473–3483.
[13] H. Wang, L. Zhang, Z. Chen, J. Hu, S. Li, Z. Wang, J. Liu, X. Wang, Semiconductor heterojunction photocatalysts: design, construction, and photocatalytic performances, Chem. Soc. Rev. 43 (2014) 5234–5244.
[14] H.T. Chung, J.H. Won, P. Zelenay, Active and stable carbon nanotube/nanoparticle composite electrocatalyst for oxygen reduction, Nat. Commun. 4 (2013) 1922.
[15] S. Zhang, J. Li, M. Zeng, J. Xu, X. Wang, Bandgap engineering and mechanism study of nonmetal and metal ion codoped carbon nitride: C + Fe as an example, Chem. Eur. J. 20 (2014) 9805–9812.
[16] W. Yu, D. Xu, T. Peng, Enhanced photocatalytic activity of g-C_3N_4 for selective CO_2 reduction to CH_3OH via facile coupling of ZnO: a direct Z-scheme mechanism, J. Mater. Chem. A 3 (2015) 19936–19947.
[17] J. Chen, X.-J. Wu, L. Yin, B. Li, X. Hong, Z. Fan, B. Chen, C. Xue, H. Zhang, One-pot synthesis of CdS nanocrystals hybridized with single-layer transition-metal dichalcogenide nanosheets for efficient photocatalytic hydrogen evolution, Angew. Chem. Int. Ed. 54 (2015) 1210–1214.
[18] D. Chen, J. Ye, Hierarchical WO_3 hollow shells: dendrite, sphere, dumbbell, and their photocatalytic properties, Adv. Funct. Mater. 18 (2008) 1922–1928.
[19] C. Tang, L. Liu, Y. Li, Z. Bian, Aerosol spray assisted assembly of TiO_2 mesocrystals into hierarchical hollow microspheres with enhanced photocatalytic performance, Appl. Catal. B 201 (2017) 41–47.
[20] Z. Liu, F. Chen, Y. Gao, Y. Liu, P. Fang, S. Wang, A novel synthetic route for magnetically retrievable Bi_2WO_6 hierarchical microspheres with enhanced visible photocatalytic performance, J. Mater. Chem. A 1 (2013) 7027–7030.
[21] F. Chen, K. Zhu, G. Li, D. Lu, P. Fang, Y. Li, A novel synthesis of ultrathin TiO_2-based nanosheets with excellent photocatalytic performance, Mater. Lett. 164 (2016) 516–519.
[22] M. Nischk, P. Mazierski, M. Gazda, A. Zaleska, Ordered TiO_2 nanotubes: the effect of preparation parameters on the photocatalytic activity in air purification process, Appl. Catal. B 144 (2014) 674–685.
[23] Y. Xu, M.A.A. Schoonen, The absolute energy positions of conduction and valence bands of selected semiconducting minerals, Am. Mineral. 85 (2000) 543–556.
[24] X. Li, J. Yu, J. Low, Y. Fang, J. Xiao, X. Chen, Engineering heterogeneous semiconductors for solar water splitting, J. Mater. Chem. A 3 (2015) 2485–2534.
[25] A. Kudo, Y. Miseki, Heterogeneous photocatalyst materials for water splitting, Chem. Soc. Rev. 38 (2009) 253–278.
[26] I. Tsuji, H. Kato, H. Kobayashi, A. Kudo, Photocatalytic H_2 evolution reaction from aqueous solutions over band structure-controlled $(AgIn)_xZn_{2(1-x)}S_2$ solid solution photocatalysts with visible-light response and their surface nanostructures, J. Am. Chem. Soc. 126 (2004) 13406–13413.

[27] L. Shan, Y. Liu, Er^{3+}, Yb^{3+} doping induced core-shell structured $BiVO_4$ and near-infrared photocatalytic properties, J. Mol. Catal. A Chem. 416 (2016) 1–9.
[28] R. Asahi, T. Morikawa, T. Ohwaki, K. Aoki, Y. Taga, Visible-light photocatalysis in nitrogen-doped titanium oxides, Science 293 (2001) 269–271.
[29] W. Su, Y. Zhang, Z. Li, L. Wu, X. Wang, J. Li, X. Fu, Multivalency iodine doped TiO: preparation, characterization, theoretical studies, and visible-light photocatalysis, Langmuir 24 (2008) 3422–3428.
[30] A.W. Xu, Y. Gao, H.Q. Liu, The preparation, characterization, and their photocatalytic activities of rare-earth-doped TiO_2 nanoparticles, J. Catal. 207 (2002) 151–157.
[31] M. Gao, D. Zhang, X. Pu, H. Li, W. Li, X. Shao, D. Lv, B. Zhang, J. Dou, Combustion synthesis of Fe-doped BiOCl with high visible-light photocatalytic activities, Sep. Purif. Technol. 162 (2016) 114–119.
[32] J. Zhang, C. Pan, P. Fang, J. Wei, R. Xiong, Mo + C codoped TiO_2 using thermal oxidation for enhancing photocatalytic activity, ACS Appl. Mater. Interfaces 2 (2010) 1173–1176.
[33] Y.L. Pang, A.Z. Abdullah, Effect of carbon and nitrogen co-doping on characteristics and sonocatalytic activity of TiO_2 nanotubes catalyst for degradation of rhodamine B in water, Chem. Eng. J. 214 (2013) 129–138.
[34] T. Jing, Y. Dai, Development of solid solution photocatalytic materials, Acta Phys. -Chim. Sin. 33 (2017) 295–304.
[35] F. Xue, W. Fu, M. Liu, X. Wang, B. Wang, L. Guo, Insight into Cd0.9Zn0.1S solid-solution nanotetrapods: growth mechanism and their application for photocatalytic hydrogen production, Int. J. Hydrogen Energy 41 (2016) 20455–20464.
[36] J. Lai, Y. Qin, L. Yu, C. Zhang, GSH-assisted hydrothermal synthesis of MnxCd1-xS solid solution hollow spheres and their application in photocatalytic degradation, Mater. Sci. Semicond. Process. 52 (2016) 82–90.
[37] T. Wu, X. Li, D. Zhang, F. Dong, S. Chen, Efficient visible light photocatalytic oxidation of NO with hierarchical nanostructured 3D flower-like BiOClxBr1-x solid solutions, J. Alloys Compd. 671 (2016) 318–327.
[38] Y. Hsu, N. Suen, C. Chang, S. Hung, C. Chen, T. Chan, C. Dong, C. Chan, S. Chen, H.M. Chen, Heterojunction of zinc Blende/Wurtzite in Zn1-xCdxS solid solution for efficient solar hydrogen generation: X-ray absorption/diffraction approaches, ACS Appl. Mater. Interfaces 7 (2015) 22558–22569.
[39] G. Rekhila, Y. Bessekhouad, M. Trari, Hydrogen evolution under visible light over the solid solution NiFe2-xMnxO4 prepared by sol gel, Int. J. Hydrogen Energy 40 (2015) 12611–12618.
[40] W. Wu, C. Jiang, V.A. Roy, Recent progress in magnetic iron oxide-semiconductor composite nanomaterials as promising photocatalysts, Nanoscale 7 (2015) 38–58.
[41] A. Bhattacharyya, S. Kawi, M.B. Ray, Photocatalytic degradation of orange II by TiO_2 catalysts supported on adsorbents, Catal. Today 98 (2004) 431–439.
[42] M.-J. López-Muñoz, R. Grieken, J. Aguado, J. Marugán, Role of the support on the activity of silica-supported TiO_2 photocatalysts: structure of the TiO_2/SBA-15 photocatalysts, Catal. Today 101 (2005) 307–314.
[43] G. Li Puma, A. Bono, D. Krishnaiah, J.G. Collin, Preparation of titanium dioxide photocatalyst loaded onto activated carbon support using chemical vapor deposition: a review paper, J. Hazard. Mater. 157 (2008) 209–219.
[44] Z. Ding, X. Hu, P.L. Yue, G.Q. Lu, P.F. Greenfield, Synthesis of anatase TiO_2 supported on porous solids by chemical vapor deposition, Catal. Today 68 (2001) 173–182.
[45] K. Guesh, Á. Mayoral, C. Márquez-Álvarez, Y. Chebude, I. Díaz, Enhanced photocatalytic activity of TiO_2 supported on zeolites tested in real wastewaters from the textile industry of Ethiopia, Microporous Mesoporous Mater. 225 (2016) 88–97.
[46] Y. Li, W. Chen, Photocatalytic degradation of rhodamine B using nanocrystalline TiO_2–zeolite surface composite catalysts: effects of photocatalytic condition on degradation efficiency, Catal. Sci. Technol. 1 (2011) 802–809.

[47] J.D. Pilar-Albaladejo, P.K. Dutta, Topotactic transformation of zeolite supported cobalt (II) hydroxide to oxide and comparison of photocatalytic oxygen evolution, ACS Catal. 4 (2013) 9–15.
[48] Z. Liu, Z. Liu, T. Cui, J. Li, J. Zhang, T. Chen, X. Wang, X. Liang, Photocatalysis of two-dimensional honeycomb-like ZnO nanowalls on zeolite, Chem. Eng. J. 235 (2014) 257–263.
[49] C. Liu, Y. Li, P. Xu, M. Li, M. Zeng, Controlled synthesis of ordered mesoporous TiO_2-supported on activated carbon and pore-pore synergistic photocatalytic performance, Mater. Chem. Phys. 149-150 (2015) 69–76.
[50] M.H. Sun, S.Z. Huang, L.H. Chen, Y. Li, X.Y. Yang, Z.Y. Yuan, B.L. Su, Applications of hierarchically structured porous materials from energy storage and conversion, catalysis, photocatalysis, adsorption, separation, and sensing to biomedicine, Chem. Soc. Rev. 45 (2016) 3479–3563.
[51] C.M. Parlett, K. Wilson, A.F. Lee, Hierarchical porous materials: catalytic applications, Chem. Soc. Rev. 42 (2013) 3876–3893.
[52] T. Kamegawa, Y. Ishiguro, H. Seto, H. Yamashita, Enhanced photocatalytic properties of TiO_2-loaded porous silica with hierarchical macroporous and mesoporous architectures in water purification, J. Mater. Chem. A 3 (2015) 2323–2330.
[53] Y. Jia, S. Zhan, S. Ma, Q. Zhou, Fabrication of TiO_2-Bi_2WO_6 binanosheet for enhanced solar photocatalytic disinfection of E. coli: insights on the mechanism, ACS Appl. Mater. Interfaces 8 (2016) 6841–6851.
[54] M. Sohail, H. Xue, Q. Jiao, H. Li, K. Khan, S. Wang, Y. Zhao, Synthesis of well-dispersed TiO_2@reduced graphene oxide (rGO) nanocomposites and their photocatalytic properties, Mater. Res. Bull. 90 (2017) 125–130.
[55] F. Shahrezaei, Y. Mansouri, A.A.L. Zinatizadeh, A. Akhbari, Process modeling and kinetic evaluation of petroleum refinery wastewater treatment in a photocatalytic reactor using TiO_2 nanoparticles, Powder Technol. 221 (2012) 203–212.
[56] M.J. Benotti, B.D. Stanford, E.C. Wert, S.A. Snyder, Evaluation of a photocatalytic reactor membrane pilot system for the removal of pharmaceuticals and endocrine disrupting compounds from water, Water Res. 43 (2009) 1513–1522.
[57] Y. Li, S. Sun, M. Ma, Y. Ouyang, W. Yan, Kinetic study and model of the photocatalytic degradation of rhodamine B (RhB) by a TiO_2-coated activated carbon catalyst: effects of initial RhB content, light intensity and TiO_2 content in the catalyst, Chem. Eng. J. 142 (2008) 147–155.
[58] P.S. Mukherjee, A.K. Ray, Major challenges in the design of a large-scale photocatalytic reactor for water treatment, Chem. Eng. Technol. 22 (1999) 253–260.
[59] K. Natarajan, T.S. Natarajan, H.C. Bajaj, R.J. Tayade, Photocatalytic reactor based on UV-LED/TiO_2 coated quartz tube for degradation of dyes, Chem. Eng. J. 178 (2011) 40–49.
[60] A. Alexiadis, I. Mazzarino, Design guidelines for fixed-bed photocatalytic reactors, Chem. Eng. Process. 44 (2005) 453–459.
[61] J. Saien, M. Asgari, A.R. Soleymani, N. Taghavinia, Photocatalytic decomposition of direct red 16 and kinetics analysis in a conic body packed bed reactor with nanostructure titania coated Raschig rings, Chem. Eng. J. 151 (2009) 295–301.
[62] M.A. Oturan, J.J. Aaron, Advanced oxidation processes in water/wastewatertreatment: principles and applications. A review, Crit. Rev. Environ. Sci. Technol. 44 (2014) 2577–2641.
[63] G.S. Sergi, B. Enric, Applied photoelectrocatalysis on the degradation of organicpollutants in wastewaters, J. Photochem. Photobiol. C Photochem. Rev. 31 (2017) 1–35.
[64] B.P. Chaplin, Critical review of electrochemical advanced oxidation processes for water treatment applications, Environ. Sci. Proc. Impacts 16 (2014) 1182–1203.
[65] H.J. Lewerenz, C. Heine, K. Skorupska, N. Szabo, T. Hannappel, T. Vo-Dinh, S.A. Campbell, H.W. Klemm, A.G. Munoz, Photoelectrocatalysis: principles,nanoemitter applications and routes to bio-inspired system, Energy Environ. Sci. 3 (2010) 748–760.

[66] E. Zarei, R. Ojani, Fundamentals and some applications of photoelectrocatalysis and effective factors on its efficiency: a review, J. Solid State Electrochem. 21 (2017) 305–336.
[67] K. Vinodgopa, S. Hotchandani, P.V. Kama, Electrochemically assisted photocatalysis. Ti O_2 particulate film electrodes for photocatalytic degradation of 4-chlorophenol, J. Phys. Chem. 97 (1993) 9040–9044.
[68] N. Liu, I. Paramasivam, P. Schmuki, M. Yang, Some critical factors for photocatalysis on self-organized TiO_2 nanotubes, J. Solid State Electrochem. 16 (2012) 3499–3504.
[69] T. Ochiai, A. Fujishima, Photoelectrochemical properties of TiO2photocatalyst and its applications for environmental purification, J. Photochem. Photobio. C Photochem. Rev. 13 (2012) 247–262.
[70] M. Li, Y.J. Li, F.T. Chen, X. Lin, Q.J. Feng, Electrically enhanced photocatalysis for gas-phase benzaldehyde degradation by ordered mesoporous titania/conductive carbon felts, Electrochim. Acta 216 (2016) 517–527.
[71] R. He, S. Cao, P. Zhou, J. Yu, Recent advances in visible light Bi-based photocatalysts, Chin. J. Catal. 35 (2014) 989–1007.
[72] J.L. Vivero-Escoto, Y. Chiang, K.C. Wu, Y. Yamauchi, Recent progress in mesoporous titania materials: adjusting morphology for innovative applications, Sci. Technol. Adv. Mater. (2012) 13.
[73] X. Li, J. Yu, M. Jaroniec, Hierarchical photocatalysts, Chem. Soc. Rev. 45 (2016) 2603–2636.
[74] P. Yang, T. Deng, D. Zhao, P. Feng, D. Pine, B.F. Chmelka, G.M. Whitesides, G.D. Stucky, Hierarchically ordered oxides, Science 282 (1998) 2244–2246.
[75] T. Xiong, F. Dong, Z. Wu, Enhanced extrinsic absorption promotes the visible light photocatalytic activity of wide band-gap (BiO)2 CO3 hierarchical structure, RSC Adv. 4 (2014) 56307–56312.
[76] Z. He, Y. Su, S. Yang, L. Wu, S. Liu, C. Ling, H. Yang, Hierarchical structure engineering of brookite TiO2 crystals for enhanced photocatalytic and external antitumor property, Sci. Bull. 61 (2016) 1818–1825.
[77] J. Sin, S. Lam, Hydrothermal synthesis of europium-doped flower-like ZnO hierarchical structures with enhanced sunlight photocatalytic degradation of phenol, Mater. Lett. 182 (2016) 223–226.
[78] L. Chen, D. Meng, X. Wu, J. Wang, Y. Wang, Y. Liang, Shape-controlled synthesis of novel self-assembled BiVO4 hierarchical structures with enhanced visible light photocatalytic performances, Mater. Lett. 176 (2016) 143–146.
[79] S. Wang, J. Yun, B. Luo, T. Butburee, P. Peerakiatkhajohn, S. Thaweesak, M. Xiao, L. Wang, Recent progress on visible light responsive heterojunctions for photocatalytic applications, J. Mater. Sci. Technol. 33 (2017) 1–22.
[80] L. Chen, J. He, Y. Liu, P. Chen, C. Au, S. Yin, Recent advances in bismuth-containing photocatalysts with heterojunctions, Chin. J. Catal. 37 (2016) 780–791.
[81] R. He, S. Cao, J. Yu, Recent advances in morphology control and surface modification of Bi-based photocatalysts, Acta Phys. -Chim. Sin. 32 (2016) 2841–2870.
[82] X. An, T. Li, B. Wen, J. Tang, Z. Hu, L. Liu, J. Qu, C.P. Huang, H. Liu, New Insights into Defect-Mediated Heterostructures for Photoelectrochemical Water Splitting, Adv. Energy Mater. 6 (2016) 1502268.
[83] R. Marschall, Semiconductor composites: strategies for enhancing charge carrier separation to improve photocatalytic activity, Adv. Funct. Mater. 24 (2014) 2421–2440.
[84] P. Zhou, J.G. Yu, M. Jaroniec, All-solid-state Z-scheme photocatalytic systems, Adv. Mater. 26 (2014) 4920–4935.
[85] J. Low, C. Jiang, B. Cheng, S. Wageh, A.A. Al-Ghamdi, J. Yu, A review of direct Z-scheme photocatalysts, Small Methods (2017) 10–1002.
[86] N. Liu, X. Chen, J. Zhang, J.W. Schwank, A review on TiO_2-based nanotubes synthesized via hydrothermal method: formation mechanism, structure modification, and photocatalytic applications, Catal. Today 225 (2014) 34–51.
[87] H. Park, Y. Park, W. Kim, W. Choi, Surface modification of TiO_2 photocatalyst for environmental applications, J. Photochem. Photobiol. C 15 (2013) 1–20.

CHAPTER

NANOSCALE MATERIALS FOR ARSENIC REMOVAL FROM WATER

25

Abhijit Maiti, Saurabh Mishra, Mohit Chaudhary

Department of Polymer and Process Engineering, Indian Institute of Technology Roorkee, Roorkee, India

1 INTRODUCTION

Arsenic is the 20th most abundant and ubiquitous natural element found in the earth's crust. It was first discovered in 1250 AD by Albertus Magnus. Naturally, in pure elemental form, it exists as a solid crystalline metalloid structure which is gray in color and exhibits features of both metals and nonmetals [1]. It has the ability to alter its oxidation state and can exist in four different forms, that is, As^{-3} (arsine), As^{0} (arsenic), As^{+3} (arsenite), and As^{+5} (arsenate) [2]. This element, on reaction with other elements in the geochemical cycle, is converted into a white or colorless, tasteless, and odorless element compound which is difficult to identify. Generally, arsenic in water can exist either in the form of trivalent arsenite (As(III)) as a nonionic species or in the form of pentavalent arsenate (As(V)), depending on pH and redox potential. In an aquifer with near-neutral pH, As(III) as H_3AsO_3 species becomes dominant. On the other hand, under an oxidizing environment with pH above 7, the most stable negatively charged arsenate becomes the dominant arsenic species [3]. Moreover, arsenic is also found in various organic forms in the environment, such as dimethyl arsenic acid, arsenosugar, and arsenolipids which are less toxic than inorganic ones [4]. Since its discovery, this element has been controversial in its use and consumption. It has been used for the production of medicine in the pharmaceutical industry, as a component of fertilizer in agriculture, and for other uses in the electronics and metallurgy industries [5]. In contrast, the additional excessive input of arsenic into the environment by natural and anthropogenic activities (such as mining, fossil fuel combustion, and the agricultural use of arsenic-containing fertilizers) has severely affected biotic organisms [6]. According to Mondal et al. [7], globally, more than 150 million humans in 105 countries (especially India, Bangladesh, Mexico, Mongolia, Argentina, Taiwan, and Thailand) face serious health risks due to excess intake of arsenic via drinking water. Drinking water is mostly obtained from groundwater, into which arsenic enters either by leaching from sources in the earth's crust, such as rocks and sediment, or by biological action and geochemical reactions [8]. After intake, arsenic is readily absorbed by the mammalian gastrointestinal tract, and upon long-term exposure to its toxicity, arsenic causes various health problems in humans such as skin lesions (like keratosis, hyperkeratosis, melanosis, and leucomelanosis), circulatory disorders, diabetes, and cancer of the skin, lung, bladder, and kidney [9]. Due to the widespread human health risk created by arsenic-contaminated drinking water, various serious preventive strategies have been formulated and

Nanoscale Materials in Water Purification. https://doi.org/10.1016/B978-0-12-813926-4.00032-X

implemented to resolve this problem at both national and international levels. Various treatment techniques (oxidation and subsequent adsorption, coagulation-flocculation, adsorption, ion exchange, and electrocoagulation, membrane separation processes, biosorption, phytoremediation) have been investigated to remove arsenic from real contaminated water [10]. But these remediation technologies are not favored due to their own limitations such as the production of toxic or carcinogenic byproducts (in the coagulation process), the requirement of an additional oxidation step to remove neutral arsenite ions more efficiently (oxidative process), interference from other ions (adsorption), low efficiency, very high operational and capital costs, prerequisite pretreatment (membrane processes), and long duration (phytoremediation) [11]. However, the excellent properties of nanoparticles (such as large specific surface area, high selectivity, high reactivity due to availability of a large quantity of active hydroxyl functionality, and catalytic and oxidative potential) play a significant role in overcoming various drawbacks associated with conventional arsenic removal technologies and enhance the removal of As(III). In the current scenario, adsorption using nanomaterials is considered a better option for the treatment of large amounts of arsenic-contaminated water. Olyaie et al. [12] investigated arsenic decontamination from water using calcium peroxide nanoparticles which acted as an oxidant medium for As(III) and which subsequently acted an adsorbent. These nanoparticles exhibited about 88% removal efficiency for an initial level of 0.4 mg/L arsenic with adsorbent dosages of 40 mg/L at pH 7.5 within 30 min of contact time. Xu et al. [13] investigated the removal of arsenic from contaminated water using CeO_2-ZrO_2 nanospheres. They found that 0.2 mg/L of adsorbent dose for the initial arsenic solution of 0.5–60 mg/L at pH range of 6–10 exhibited maximum sorption capacity of 27.1 and 9.2 mg/g for As(V) and As(III), respectively. The materials were tested on a large-scale wastewater treatment system and proved to be promising for real drinking water treatment plants. Pirila et al. [14] studied hydrous titanium dioxide's potential capacity to remove both As(III) and As(V) ions at pH 4–6 with varying adsorbent dosages of 25–100 mg/L in the initial arsenic concentration range of 0.2 to 8.5 mg/L. The maximum removal efficiency of nanomaterials was found to 31.8 mg/g for As(III) and 33.4 mg/g for As(V) at pH 4, and the adsorption process was better described by the power-law kinetic model. Vunain et al. [15] fabricated, characterized, and investigated polymer nanocomposites [ethylene-vinyl acetate (EVA) (70%), polycaprolactone (15%), and Fe_3O_4 (15%)] for removal of arsenic (III) from water. They found that polymer nanocomposite had maximum adsorption capacity of 2.83 mg/g and exhibited 95.3% removal of As(III) at pH 8.6 and at 26°C.

Including nanotechnology in pollution abetment reduces the use of resources and raw materials and eliminates the requirement of frequent regeneration steps, further minimizing the production of secondary pollutants [16]. Undoubtedly, the adsorption process is well accepted by rural people in arsenic-affected areas in various parts of the world, particularly Bangladesh and India, due to its simple operation, low recurring cost, lower space requirement, and its potential for producing lower volumes of sludge. Though using nanomaterials for arsenic removal from water has various advantages over conventional technologies, adverse environmental effects may arise when nanoparticles are released into the environment [17, 18]. More research is required to develop environmentally sustainable nanoparticles for eco-friendly water treatment systems. In this chapter, we discuss the merits and demerits of the application of various forms of nanoparticles (such as single metallic nanoparticles, magnetic nanoparticles, composite nanoparticles, mixed metal oxide/hydroxide-based nanoparticles, photocatalytic nanoparticles, and nanoparticles in composite membranes) to remove arsenic ions from water. We also explore future trends and practices for large-scale application of nanoparticles as adsorbents to remove arsenic from contaminated groundwater and wastewater.

2 SINGLE METALLIC NANOPARTICLES AS ADSORBENT

Nanomaterials based on inorganic oxide/hydroxide are being widely used to mitigate arsenic in water. Recently, researchers have investigated a wide range of metal oxide/hydroxide based on iron [19], cerium [13], and others with regard to their arsenic removal efficiency and suitability for use in large-scale applications. The arsenic removal efficiency of various single metallic nanoparticles reported in literature has been illustrated in Table 1.

Arcibar-Orozco et al. [20] investigated the forced hydrolysis of $FeCl_3$ in activated carbon by adding phosphate as a capping agent and revealed that the surface area of new material was about 900 m^2/g for molar ratio of 0.1 (PO_4/Fe). The smallest iron nanoparticles (sizes ranging from 2 to 300 nm) were obtained at higher phosphate concentrations. Authors found that the newly modified nanoparticles showed a 40% increase for As(V) adsorption capacity at PO_4/Fe molar ratio of 1.5. Iron-based arsenic adsorbents are also discussed in the chapter sections on magnetic nanoparticles, mixed oxide

Table 1 Adsorption of Arsenic From Contaminated Water Using Single Metallic Nanoparticles

Nanoparticles	Experimental Conditions	Amount of Adsorbent	Amount of Adsorbate	Maximum Removal Efficiency	Remarks	Ref.
Ultrafine δ-FeOOH	At pH 7	10 mg/40 mL arsenic solution	2.5, 5, 10, or 20 mg/L As(V)	37.3 mg/g at pH 7 97%, 84%, 50%, and 28% removal, respectively within 60 min	δ-FeOOH can be characterized as a low cost and easily available adsorbent	[19]
Hydrous cerium oxide (HCO)	At pH range of 3–11	0.01 g/L	1 to 100 mg/L	170 mg/g for As(III) and 107 mg/g for As(V) at pH 7	The amount of As(III) and As(V) adsorbed by HCO nanoparticles, at very low equilibrium arsenic concentrations, was over 13 mg/g at 10 μg/L and over 40 mg/g at 50 μg/L, which were higher than the arsenic adsorption capacity of commercial adsorbents available	[21]

Continued

Table 1 Adsorption of Arsenic From Contaminated Water Using Single Metallic Nanoparticles—cont'd

Nanoparticles	Experimental Conditions	Amount of Adsorbent	Amount of Adsorbate	Maximum Removal Efficiency	Remarks	Ref.
Amorphous zirconium oxide (am-ZrO_2)	Temperature ~25°C, pH 7 and mixtures were shaken at 500 rpm	For As(III), amounts of am-ZrO_2 nanoparticles ranged from 0.01 to 0.15 g/L For As(V), amounts of am-ZrO_2 nanoparticles ranged from 0.01 to 0.04 g/L	~1 and 0.1 mg/L	Over 83 mg/g for As(III) and over 32.4 mg/g for As(V)	The adsorption process was effective at neutral pH and required no pretreatment like oxidation/pH adjustment The adsorption mechanism followed the inner-sphere complexation mechanism	[23]
Copper (II) oxide	Temperature effect was studied at 25° C, 40°C, and 50°C At pH 3.6–11.6 Stirring speed: 150, 200, and 250 rpm	1 g/L	100, 200, 500, and 1000 μg/L of As	~100% arsenic was adsorbed for up to 200 μg/L of initial arsenic concentration, for contact time of 300 min	The arsenic adsorption process by CuO nanoparticles was kinetically faster and followed the pseudo-second-order rate kinetics The regenerated CuO nanoparticles were shown effective in reuse	[24, 25]
Cobalt ferrite	Temperature 25°C, 40°C and 60°C, Initial pH 3–11	0.25–2 g/L	200–600 μg/L of As	Maximum adsorption capacity: 1.01 mg/g	Regenerated adsorbents showed good adsorption efficiencies	[26]
Anatase nanosorbent	At pH range of 3.0–9.0 at 25°C	0.015 g/30 mL	10 mg/L of As(III) solution	Maximum arsenic adsorption uptakes 16.98 mg/g	As(III) uptake percentages were identical in the wide range of pH	[27]
Mesoporous ɣ-Al_2O_3	Mixture stirred vigorously for 1 h	0.1 g/L	100 μg/L of As(III)	52.6% removal	Mesoporous ɣ-Al_2O_3 can be utilized as adsorbent for the removal of arsenic from polluted water	[28]

Table 1 Adsorption of Arsenic From Contaminated Water Using Single Metallic Nanoparticles—cont'd

Nanoparticles	Experimental Conditions	Amount of Adsorbent	Amount of Adsorbate	Maximum Removal Efficiency	Remarks	Ref.
Calcium peroxide	At pH range from 6.5 to 8.5	Nanoparticles dosage (0.4, 0.8, 2, 4 and 40 mg/L)	0.2, 0.4, 0.6, 0.8, 1, and 2 mg/L	Up to 91% for As(III) at pH 6.5	CaO_2 nanoparticles efficiency decreased by increasing pH and initial arsenic concentration in solution Removal efficiency showed direct relation to contact time and dosage of CaO_2 nanoparticles	[29]
Maghemite (sol-gel method)	At pH 3–9	100 mg/L	1000–11,000 μg/L	Adsorption capacity 25.0 mg/g	The maximum adsorption capacity found at pH 3	[30]
Zeolitic imidazolate framework-8	Temperature 25°C, pH 7.0, and agitation 170 rpm	0.2 g/L	20 mg/L	The maximal adsorption capacities of As(III) and As(V) were of 49.49 and 60.03 mg/g, respectively	Co-existing anions PO_4^{3-} and CO_3^{2-} have negative impact on adsorption of arsenic	[31]

nanoparticles, and nanocomposites. Prucek et al. [18] investigated the removal of arsenite and arsenate from water using nanocrystalline iron(III) oxide. Authors claimed that it was the first reported example of trapping arsenic into the γ-Fe_2O_3 nanoparticles' crystal structure, which was formed in situ from ferrate (VI) during treatment of arsenic-contaminated water. Potassium ferrate (VI) decomposition in water yielded nanoparticles having core-shell nanoarchitectures with a γ-FeOOH as shell and γ-Fe_2O_3 as core. Faria et al. [19] examined ultrafine δ-FeOOH adsorbents (particle size 20 nm) to remove arsenic from drinking water. They observed that higher values of zero point of the charge of δ-FeOOH (pH_{ZPC}: 8.4) favor negative arsenate ions' adsorption onto the δ-FeOOH surface, even at neutral pH 7. In that study, the maximum As(V) adsorption capacity of nano-δ-FeOOH was reported as 37.3 mg/g at pH 7. They suggested that the high adsorption capacity of the nanoparticle was due to its smaller size and the high specific surface area of the δ-FeOOH nanoparticle. Li et al. [21] investigated the arsenic adsorption behavior of hydrous cerium oxide nanoparticles (HCO). They observed that the excellent arsenic adsorption behavior of HCO (specifically, higher adsorption capacity and faster

kinetics) was due to its high specific surface area (198 m^2/g) and the strong affinity of its surface hydroxyl groups towards arsenic ions. The adsorption capacity of HCO at pH 7 was found to be 170 mg/g and 107 mg/g for As(III) and As(V), respectively. Moreover, the adsorption of As(III) and As(V) by nanoparticles at low equilibrium concentration was around 13 mg/g and 40 mg/g, respectively. The arsenic removal efficiency of hydrous nano-zirconium oxide natural water was investigated by Hang et al. [22]. The adsorption capacities for As(III) and As(V) at pH 7 were ~0.6 mg/g for As(III) and ~3.6 mg/g for As(V) ions, respectively, against an initial concentration of 0.01 mg/L, while adsorption capacities at the high equilibrium As(V) and As(III) concentrations were more than 47 mg/g and 29 mg/g, respectively. Cui et al. [23] synthesized amorphous zirconium oxide (am-ZrO_2) nanoparticles by hydrothermal process and investigated its arsenic adsorption capacity from water. These nanoparticles had shown high specific surface area (327.1 m^2/g) and large mesopore volume (0.68 cm^3/g) which supported the adsorption capacity of 0.92 mg/g for As(III) and over 5.2 mg/g for As(V), respectively. The adsorption mechanism of arsenic species onto am-ZrO_2 was followed mainly by inner sphere complex mechanism. Reddy et al. [24] designed a reactor using CuO nanoparticles to conduct continuous flow-through adsorption system for arsenic removal from groundwater samples. During their batch adsorption studies, they found the higher pseudo-second-order adsorption kinetic rate of 36.18 g/mg-min for initial arsenic concentration of 100 µg/L and the adsorbent dosage 4.0 mg/L. Although nanoparticles have shown good arsenic removal potential as adsorbents for a water medium, they have shown a natural tendency toward agglomeration due to their high surface energy, and it is difficult to separate spent nano-adsorbents from aqueous medium [5, 12]. Agglomeration greatly reduces the specific surface area and arsenic sorption capacity. Surface modification of nanoparticles reduces the tendency of agglomeration. Starch and carboxymethyl cellulose are effective stabilizers used for stabilization of various metal and metal oxide-based nanoparticles [12, 13]. Stabilizers can also lead to better dispersion of nanoparticles in water [13]. Solid nanoparticles in a water medium exhibit significant leaching in a strongly acidic environment [14].

2.1 MIXED METAL-BASED NANOPARTICLES

Recently, mixed metal-based nanoparticles have been studied as potential arsenic adsorbents, and they have shown better performance removing contaminants from water. Nanoparticles such as Fe-Ce oxide [25], Fe-Zr binary oxide [32], and Zn-Fe oxide [33] have reportedly exhibited enhanced arsenic removal efficiency due to their higher specific surface areas, higher density of surface hydroxyl reactive groups, and the easy accessibility of their pores' surfaces. Table 2 summarizes the arsenic removal efficiency of various mixed metal-based nanoparticles.

Dey et al. [26] synthesized cobalt ferrite nanoparticles along with iron oxide/hydroxide and studied the arsenic adsorption behavior of the aggregated adsorbent. Authors claimed the improvement of magnetic properties of iron oxyhydroxide in the presence of cobalt ferrite nanoparticles. More than 95% arsenic was adsorbed for up to 200 µg/L initial arsenic concentration using 1 g/L adsorbent dose within 240 min. Basu and Ghosh et al. [34] investigated the arsenic removal capability of iron(III)-cerium(IV) mixed oxide from contaminated water. The authors reported that the maximum sorption capacity was found to be 2.42 mg/g for As(III) and 2.11 mg/g for As(V) when the adsorption study was carried out with adsorbent dose of 2 g/L with initial arsenic concentration of 5.0–250.0 mg/L and in the pH range of 3–7. The reaction kinetics followed a pseudo-second-order kinetics model. Chowdhury and Yanful et al. [35] studied the chromium and arsenic removal efficiency of mixed magnetite-maghemite

Table 2 Adsorption of Arsenic From Contaminated Water Using Mixed Metal Based Nanoparticles

Nanoparticles	Experimental Conditions	Amount of Adsorbent	Amount of Adsorbate	Maximum Removal Efficiency	Remarks	Ref.
Mixed magnetite-maghemite nanoparticles	At pH 2	0.4 g/L	1.5 mg/L for both arsenic species	96%–99% arsenic uptake under controlled pH conditions The maximum arsenic adsorption occurred at pH 2 with values of 3.69 mg/g for As(III) and 3.71 mg/g for As(V)	In natural groundwater containing more than 5 mg/L phosphate and 1.13 mg/L of arsenic, less than 60% arsenic uptake was achieved, which demonstrated as high arsenic uptake in field applications	[33]
Fe-hydrotalcite-supported magnetite nanoparticles (M-FeHT)	Maximum adsorption of arsenic on M-FeHT was observed around pH 9.0	0.5 g	Initial arsenic concentration of 100–1000 µg/L	95% removal of As(V) and As(III) The adsorption capacities of As(V) and As(III) on M-FeHT were 1.28 and 0.12 mg/g, respectively, at pH 9	At a magnetic field intensity of 2 T, separation efficiency of M-FeHT was 91% Adsorption using by M-FeHT, Residual arsenic concentration was obtained >10 µg/L	[37]
Iron-zirconium binary oxide adsorbent	Agitated at 140 rpm for 36 h at 25 ± 1°C	10 mg	5 to 40 mg/L	As(V) and As(III) removal; the maximum adsorption capacities were 46.1 and 120.0 mg/g, respectively, at pH 7.0	The Fe-Zr binary oxide is able to absorb arsenic in the presence of competing anions and across a wide range of pH	[36]
CeO_2-ZrO_2 nanospheres	At pH 6.9 ± 0.2, shaking mixture at 140 rpm for 24 h	0.2 g/L	0.5–60 mg/L	Adsorption capacity of 27.1 and 9.2 mg/g for As(V) and As(III), respectively, at equilibrium arsenic concentration 0.01 mg/L CeO_2-ZrO_2 nanospheres were able to remove over 97% arsenic in real under groundwater with initial arsenic concentration 0.376 mg/L	Promising for practical drinking water treatment	[13]
Iron(III)-cerium (IV) mixed oxide	pH (7.0 ±0.1), Temperature (30 ± 1.0)°C	2 g/L	4.5–6.5 mg As(V)/L 4.8 mg As(III)/L	Adsorption capacity 2.42 mg/g for As(III) and 2.11 mg/g for As(V).	Groundwater-occurring other ions exhibit a notable decrease of As(V)-sorption capacity (no other ion > chloride ~ silicate > sulfate > bicarbonate > phosphate), but insignificant influence shown on As(III)-sorption capacity	[32]
Magnetite and maghemite	Samples were shaken for 24 h at 25.0 ± 0.2°C in a temperature-controlled shaker at 150 rpm	1 g/L	1 to 7 mg/L	As(III) and As(V) were 2.90 and 3.05 mg/g (0.25 and 0.27 mg/m^2), respectively	The surface area-normalized adsorption capacities for As(III) and As(V) were shown to be comparatively higher than other nanoparticles	[38]
Hematite nanorods (Fe_3O_4) and magnetite (α-Fe_2O_3)	Fe_3O_4 and α-Fe_2O_3 were equilibrated in 50 mL of 0.1 M NaCl solution for 2 h at pH 3 and mixtures were shaken at 140 rpm under 25° C	0.4 g/L	60 mg/L of As(V)	For Fe_3O_4 was 80.5 mg/g and α-Fe_2O_3 calcined at 350°C, 550°C, and 750°C were 94.9 mg/g, 74.1 mg/g, and 70.5 mg/g, respectively	Calcination atmosphere and temperatures were affected the pore sizes and types of the obtained materials, and influenced the removal of As(V) The α-Fe_2O_3 and Fe_3O_4 materials had relatively high BET surface area (92.8 and 150.9 m^2/g) and showed good performance for As(V) adsorption	[39]
Nano hydrous Fe (III)-Al(III) mixed oxide (NHIAO)	Temperature 30°C and optimized pH 7.0 (±0.2)	2.0 g/L	5.5 mg As(III)/L	Langmuir capacity (58.30 ± 3.15 mg/g) in the absence of other ion About 90% removals	About 12%–16% loss of As(III) removal efficiency of NHIAO (250°C) examined in the presence of SO_4^{2-}, PO_4^{3-} and HCO_3^-	[40]

nanoparticles, and the effect of phosphate on removal. The authors reported that magnetite-maghemite nanoparticles have good potential for removing arsenic and chromium from contaminated water. The arsenic adsorption capacity was found to be 3.69 mg/g for As(III) and 3.71 mg/g for As(V), while 2.4 mg/g for Cr (VI) at pH 2, when initial concentration of both metal solutions were 1.5 mg/L and adsorbent dose 0.4 g/L. The experimental data was well-suited to the Freundlich isotherm. The result revealed that the magnetite-maghemite nanoparticles were more efficient than chromium in removing arsenic from groundwater at pH 6.5–8.5. However, the magnetite-maghemite particles' efficiency at removing arsenic from groundwater was reduced by 60% when the phosphate concentration was $\geq$5 mg/L. This indicates the negative effect of phosphate ions on the adsorption of arsenic ions. Ren et al. [36] studied iron-zirconium binary oxide nanoparticles as arsenic adsorbent, and the maximum adsorption capacities obtained at pH 7.0 were 46.1 mg/g for As(V) and 120.0 mg/g for As(III) in the presence of coexisting ions (PO_3^{-4}, SiO_2^{-3}, CO_2^{-3}, and SO_4^{-2}). The authors reported that the sorption process follows a pseudo-first-order model, and among the coexisting anions, only phosphate had a negative impact on the nanoparticles' sorption of arsenic.

2.2 MAGNETIC NANOPARTICLES

Magnetic nanoparticles have been found to exhibit good adsorption capacity for pollutants with the tendency to generate fewer secondary effluents. However, the problems associated with magnetic nanoparticles are demagnetization and a higher tendency to agglomerate during the adsorption process. The arsenic removal efficiency of various magnetic nanoparticles reported in the literature has been illustrated in Table 3.

Song et al. [41] examined the arsenic adsorption capacity of magnetic iron oxide nanoparticles (magnetite ($Fe(II)Fe(III)_2O_4$) and maghemite (Υ-$Fe(III)_2O_3$) mixture) prepared by electrical wire explosion. The authors reported that the maximum adsorption capacities of nanoparticles for As(III) and As(V) were 2.90 and 3.05 mg/g (0.25 and 0.27 mg/m^2 of specific surface area), respectively. The average particle size and the saturation magnetization were reported as 34 nm and 91.9 emu/g, respectively. Tuutijarvi et al. [42] studied As(V) adsorption on maghemite-nanoparticles (particle size: 3.8 to 18.4 nm) and used three types of nanoparticles which were commercially available, lab-made through the mechano-chemical method, and lab-made through the sol-gel process. Results revealed that mechano-chemical maghemite-nanoparticles displayed a maximum As(V) adsorption capacity of 50 mg/g at optimum pH 3. Adsorption of As(III) on maghemite-nanoparticless was not considered in this study, which was later completed by Lin et al. [43] Authors examined As removal efficiency of magnetic Υ-Fe_2O_3 nanoparticles and concluded that nanoparticles had higher removal efficiency for As(V) (88.4–105.2 mg/g) compared to As(III) (59.2–74.8 mg/g). Adsorption capacity of magnetic Υ-Fe_2O_3 nanoparticles for As(III) was observed to increase with an increase in temperature. Magnetic Υ-Fe_2O_3 nanoparticles were synthesized by the coprecipitation method and studied both As(V) and As(III) adsorption in aqueous media. The As(V) and As(III) maximum adsorption capacities of studied adsorbent were 95.37 mg/g and 67.02 mg/g at 30°C, respectively. Magnetic Υ-Fe_2O_3 nanoparticles retained over 40% of their initial adsorption capacity for arsenic after 6 cycles of operation. Feng et al. [29] investigated the As(V) and As(III) species removal capacity of super paramagnetic Fe_3O_4 nanoparticles from water having high specific surface area. Authors found that super paramagnetic ascorbic acid-coated Fe_3O_4 had maximum adsorption capacity for As(III) (46.06 mg/g) compared to arsenic (V) ions (16.56 mg/g). The synthesized ascorbic acid-coated Fe_3O_4 nanoparticles had shown

Table 3 Adsorption of Arsenic From Contaminated Water Using Magnetic Nanoparticles

Nanoparticles	Experimental Conditions	Amount of Adsorbent	Amount of Adsorbate	Maximum Removal Efficiency	Remarks	Ref.
Magnetic nanoparticles modified with Fe-Mn binary oxide (Mag-Fe-Mn)	At pH 4–11 Mixtures were shaken at 25°C and with 200 rpm	0.1 g/L	Initial As(III) concentrations from 1 to 15 mg/L	Adsorption and desorption efficiencies were 98% and 87%, respectively	The adsorption efficiencies of As(III) maintained above 98% throughout adsorption/desorption cycles, indicating Mag-Fe-Mn particles could be employed as an effective, convenient, and cost effective adsorbent for the trace As(III) removal from water	[49]
Magnetic nanoparticles activated microfibrillated cellulose (FeNP/MFC)	At pH 2 and 5	0.100 g	As(V) at concentration ranging from 0.14 to 10.68 mmol/L	2.46 mmol/g	FeNP/MFC showed greatly improved As(V) uptake properties compared to original Fe nanoparticles Maximum adsorption capacity was found at pH ~2	[50]
Cetyltrimethyl ammonium bromide-modified magnetic nanoparticles	At pH range from 3 to 9	0.1 g/L	100 µg/L of As(V)	95% of As(V)	High removal of As(V) onto Fe_3O_4 with CTAB can be obtained even in presence of strong competing anions such as phosphate	[47]
Magnetic nanoparticles modified with arginine and lysine	At pH range from 3 to 9	0.1 g/L	100 µg/L	As(V) adsorption capacities of Arg-MNPs and Lys-MNPs were 29.14 and 23.86 mg/g, respectively Over 90% of As(V)	The removal of As(V) observed >83% even in presence of extremely high concentration of phosphate (50 mg/L) Both Arg-MNPs and Lys-MNPs could effectively remove arsenic from water in the presence of coexisting anions including sulfate, silicate and bicarbonate (up to 10 mg/L) The As(V) adsorption capacities of both regenerated adsorbents had shown 10 mg/g even in the fifth cycle of adsorption/desorption operation	[48]
Superparamagnetic ascorbic acid-coated Fe_3O_4	Mixture shaken for 24 h with 60 rpm at room temperature, pH 7	Ascorbic acid-coated Fe_3O_4 5.67 to 157.68 mg/L Concentrations of Fe ions less than 0.1 mg/L	As(III) solution (0.10 mg/L)	Maximum adsorption capacity of 16.56 mg/g for As(V), and 46.06 mg/g for As(III)	The use of the ascorbic acid improves the dispersability of Fe_3O_4 nanoparticles in aqueous suspensions, and also effectively inhibits the leaching of Fe into the solution	[29]

Continued

Table 3 Adsorption of Arsenic From Contaminated Water Using Magnetic Nanoparticles—cont'd

Nanoparticles	Experimental Conditions	Amount of Adsorbent	Amount of Adsorbate	Maximum Removal Efficiency	Remarks	Ref.
Magnetic ɣ-Fe_2O_3 nanoparticles	At pH range from 3 to 11, presence of coexisting Cl^- ions SO_4^{2-}, and NO_3^-, PO_4^- and temperature 10°C, 30°C, and 50°C	0.08 to 0.16 g	As(III) and As(V), 10 to 150 mg/L and from 10 to 200 mg/L, respectively	As(III) and As(V) were 59.2–74.8 mg/g and 88.4–105.2 mg/g, respectively	The As(III) and As(V) adsorption was stable in the pH of 3 to 11 and not affected by Cl^- ions SO_4^{2-}, and NO_3^-, while PO_4^- led to reduction in the adsorption capacity The adsorption capacities for As(III) reached 59.25, 67.02, and 74.83 mg/g at 10°C, 30°C, and 50°C, respectively	[43]
Ultrafine superparamagnetic iron(III) oxide	At pH 7	2.15 g/L	100 mg/L of As(V)	100% removal	Optimal pH range was found 5 to 7.6 to obtain higher removal of As(V) ions from the aqueous environment Nanoparticles showed the highest Freundlich adsorption coefficient and equilibrium sorption capacity	[51]
Magnetic nanoparticles impregnated chitosan beads (MICB)	At pH 6.8 ± 0.2, shaking at 140 rpm	1 g/L	1 mg/L of As(V) and As(III)	35.7 mg/g for As(V) and 35.3 mg/g for As(III) at pH 6.8, respectively MICB retain 88.2% and 76.02% adsorption capacity for As(V) and As(III) after 5 cycles of reuse	Spent adsorbent could easily be separated from solutions by applying an external magnetic field	[45]
Magnetic nanoscale Fe-Mn binary oxides loaded zeolite	Agitation speed of 200 rpm in the dark and at temperature of 298 K for 3 h, pH 7.0	2 mg/L	0.5 g/L	99.0% at pH 7.0	The kinetic rates and maximum adsorption capacities of MFM for As(III) were obtained higher than As(V)	[44]
Magnetic multi walled carbon nanotube/iron oxide composites	At pH range 2–10, mixture shaken at 150 rpm and 298 K for 24 h	10 mg	1 to 15 mg/L	47.41 and 24.05 mg/g for As(V) and As(III), respectively	High specific surface area, desirable magnetic properties, and good dispersibility properties of these composite adsorbents were found promising	[52]

an average diameter 10 nm and specific surface area 179 m^2/g. The ascorbic acid imparted high dispersibility and stability of nanoparticles in aqueous solutions. Kong et al. [44] studied the removal of arsenic from synthetic groundwater using magnetic nanoscale Fe-Mn binary oxides-loaded zeolite having a surface area of 340 m^2/g. The adsorption kinetics was well-suited to both pseudo-second-order kinetic and Weber-Morris models. The authors reported the removal efficiency of nanoparticles for arsenic was $\geq$99% at pH 7 with initial arsenic concentration of 2 mg/L, and at adsorbent dose of 0.5 g/L. In this case, the kinetic rates and maximum adsorption capacities for As(III) were examined to be higher than As(V). Wang et al. [45] studied the efficiency of arsenic removal from water by magnetic nanoparticle-impregnated chitosan beads,. The nanoparticles had shown BET surface area and pore volume 50.20 m^2/g and 0.052 cm^3/g, respectively. The adsorption was performed in the pH range of 5–9 with an adsorbent dose of 1.0 g/L for the initial arsenic concentration 1 mg/L. Authors reported that the adsorption follows the both pseudo-first-order and pseudo-second-order kinetic models with a maximum uptake of 35.7 mg/g for As(V) and 35.3 mg/g for As(III). Moreover, nanoparticles were found to have the ability to retain about 88.2% and 76.02% of the original adsorption capacity after five adsorption cycles for As(V) and As(III) ions, respectively. The major advantage of these nanoparticles is that they can be easily separated from solution by applying an external magnetic field. Turk and Alp et al. [46] studied the arsenic removal efficiency of Fe-hydrotalcite-supported magnetite nanoparticles at pH 3, 5, 7, 9, and 12, with initial arsenic concentrations of 100–1000 μg/L. Authors reported that the kinetics of the process followed the pseudo-second-order model, and the nanoparticles could remove ~95% of both forms of arsenic (As(III) and As(V), that is, they reduced the arsenic concentration to less than 10 μg/L, the WHO's maximum permissible limit of arsenic in drinking water. In numerous other studies, magnetic nanoparticles have been investigated to show high arsenic adsorption efficiency in the presence of other ions such as cetyltrimethyl ammonium bromide. Modified magnetic nanoparticles showed high removal rates for As(V) even in the presence of strong competing anions such as phosphate. Jin et al. [47] reported that magnetic nanoparticles modified with arginine and lysine removed more than 83% of arsenic, even with an extremely high concentration of phosphate (50 mg/L) in water. Latter, Zhang et al. [48] investigated separately modified Fe_3O_4 nanoparticles with arginine and lysine as As(V) adsorbents and found that As(V) adsorption capacities of arginine (Arg-MNPs) and lysine (Lys-MNPs) modified Fe_3O_4 nanoparticles were 29.1 and 23.9 mg/g, respectively, which were twice larger than that of bare magnetic Fe_3O_4 nanoparticles. Both adsorbents (0.1 g/L) were shown capable of removing over 90% of As(V) (initial concentration: 100 μg/L) from water over a wide range of pH, from 3 to 9. Both Arg-MNPs and Lys-MNPs could effectively remove arsenic from water in the presence of coexisting anions including sulfate, silicate, and bicarbonate (up to 10 mg/L) [43].

2.3 NANOCOMPOSITE

Nanocomposite materials are advantageous for providing good dispersion of nanoparticles into a suitable porous medium, which reduces the agglomeration among nanoparticles. Furthermore, their separation from a water medium after use is quite easy compared to bare nanoparticles. Moreover, various porous media have been examined, such as mineral support, polymer supports, surface of agriculture waste materials, graphene, graphene oxide, and carbon. Among all, chitosan was the most common polymeric material investigated as a porous medium in various composite nanoparticles studies [53]. Nanocomposite adsorbents can be categorized into three different types on the basis of their corresponding porous support medium: nanocomposites using an inorganic framework, nanocomposites

using a porous polymeric matrix, and a carbon/graphene-based porous medium. The arsenic removal efficiency of various nanocomposites has been illustrated in Tables 4 and 5.

2.3.1 Nanocomposites using inorganic frameworks

Zeolite and other different types of clay minerals have been examined as porous media for dispersing nanomaterials and have been subsequently used to remove arsenic from water. Jian et al. [31] studied arsenic adsorption using a novel zeolitic imidazolate framework-8 (ZIF-8) nanocomposite. The maximum adsorption capacities of As(III) and As(V) were found to be 49.49 and 60.03 mg/g, respectively, at 25°C and pH ~ 7.0. The ZIF-8 was found to be stable at both neutral and basic conditions. However, a large amount of Zn^{2+} was released into water from the adsorbent under acidic conditions. Moreover, the authors reported that ZiF-8 nanoparticles exhibited a significantly large specific surface area of 1063.5 m^2/g. Tandon et al. [54] synthesized clay-supported zero-valent iron nanoparticles (average size of 59.08 ± 7.81 nm) with the help of tea liquor, and demonstrated As(III) adsorption from water. Zero-valent iron nanoparticles were supported on montmorillonite K10 stirred for 30 min, and exhibited 99% removal of As(III) from contaminated water at both high and low pH. However, montmorillonite K10 alone had shown only less than 10% removal efficiency. In another study, Tian et al. [55] developed well-dispersed magnetic iron oxide nanocrystals (particle size of ~9 nm) on a sepiolite nanofiber matrix for arsenic removal and found that adsorption capacity of composite for As(III) was 50.35 mg/g. Authors also found that composite exhibited 96.4% removal efficiency for 456.5 μg/L arsenic concentration without any pretreatment step in real groundwater. Excellent arsenic adsorption capacity of composite was due to high specific surface area, higher density of surface active groups, no agglomeration among nanoparticles even at higher loading of Fe_2O_3 nanocrystals, good dispersion, and superior magnetic properties. Later, Fan et al. [56] studied the removal of arsenic using nano-iron(NI)/oyster shell (OS) composites from simulated wastewater in the wide pH range of 2–11 and temperature ranges of 0–50°C, with initial adsorbent dose of 0.3 g and initial arsenic concentration of 1.8 mg/L. The specific surface area of the OS, NI, and NI-OS composites were found to be 3.5 m^2/g, 3.8 m^2/g, and 4.4 m^2/g, respectively. Authors have reported 100% As(III) removal efficiency using this nanomaterial.

2.3.2 Nanocomposites using a porous polymeric matrix

The dispersion of inorganic nanomaterials inside of polymers which exhibit attractive porous media could be an attractive choice for preparation of nanocomposites. The polymeric matrices have their advantages. Porous networks inside polymeric matrices can be easily controlled; and the presence of various functional groups like —NH_2, and —COOH in polymers enhances adsorption capacity. Malana et al. [57] studied the adsorption of arsenic on nano-aluminium-doped manganese copper ferrite (average size 13 nm) polymer methacrylate (MA), vinyl acetate (VA), and acrylic acid (AA) composite and revealed that nano-aluminium-doped manganese copper ferrite had an adsorption capacity 0.053 mg/g at pH 6 and followed a pseudo-second-order kinetic model. In another study, Sharma et al. [58] investigated the efficiency at which iron-doped phenolic resin-based activated carbon removed arsenic from contaminated water. The researchers found that the adsorption isotherm followed the Langmuir isotherm model when the adsorbent dose of 0.1 g/L was applied to an arsenic solution of 0.5 to 20 mg/L at wider pH range of 2–8. The maximum sorption capacity of these adsorbents was found to be 15 and 5 mg/g for As(III) and As(V), respectively. Wen et al. [59] reported the maximum adsorption capacities of As(III) and As(V) by magnetic thin-film MnO2 nanosheet-coated flowerlike Fe_3O_4 nanocomposites were 76.73 mg/g and 120.50 mg/g, respectively. Latter, Sadeghi et al. [60]

Table 4 Adsorption of Arsenic From Contaminated Water Using Nanocomposite Nanoparticles

Nanoparticles	Experimental Conditions	Amount of Adsorbent	Amount of Adsorbate	Maximum Removal Efficiency	Remarks	Ref.
Fe_3O_4-graphene macroscopic composites	At neutral (pH 7.0), adsorption time of 24 h, and temperature of 20°C, 30°C, and 40°C	2.0 g/L	100, 300, 500, 800, and 1000 μg/L	–	The modification of polydopamine strengthened the 3D graphene-based macroscopic architecture and enhanced the loadage and binding ability of Fe_3O_4	[69]
Nano-iron/oyster shell composites	A pH value of 6.8, a temperature of 20°C	0.3 g	Initial concentration of As(III) of 1.8 mg/L	100%	Composite had good acid/alkali resistance and thermal endurance for the removal of As(III)	[56]
Chitosan/Cu $(OH)_2$and chitosan/CuO composite sorbents	At pH range 4–6	For sorption isotherms, 50 mg of sorbent (m) were mixed with 20 mL (V) of As(V) solutions For uptake kinetics, 300 mg of sorbent were mixed with 120 mL of As(V) solutions	10 and 100 mg As/L	39.0 and 28.1 mg As/g for chitosan/Cu $(OH)_2$ and chitosan/CuO, respectively	The decrease in sorption and desorption performances did not exceed 5%: from 97.8% to 93.1% for sorption and from 97.0% to 95.0% for desorption in the case of chitosan/Cu $(OH)_2$ sorbent	[53]
Nanocomposites of graphene oxide-hydrated zirconium oxide	At 25.5 ± 0.2°C and pH 7.0 ± 0.2	10 mg/20 mL As	2 to 80 mg/L	Adsorption capacity 95.15 and 84.89 mg/g for As(III) and As(V), respectively Over 95% removal in 10 min	When the As(III) to As(V) concentration ratio is 1:3 and 3:1, the total adsorption capacity is 59.53 and 71.79 mg/g, respectively	[64]
Polymer Nanocomposites	At pH range 2.0 to 12.0	1.7 g/L	5–100 mg/L	95.3% removal at 26 ± 2°C, at pH 8.6 Adsorption capacity 2.83 mg/g	The kinetics showed that adsorption of As(III) ions onto polymer nanocomposites was very fast initially until equilibrium was reached	[15]

Continued

Table 4 Adsorption of Arsenic From Contaminated Water Using Nanocomposite Nanoparticles—cont'd

Nanoparticles	Experimental Conditions	Amount of Adsorbent	Amount of Adsorbate	Maximum Removal Efficiency	Remarks	Ref.
Nano-aluminium-doped manganese copper ferrite polymer (MA, VA, AA) composite	At pH 6.0	0.05 g	20–200 ppb	Adsorption capacity 0.053 mg/g	Adsorption of arsenic on the nanocomposite followed pseudo-second-order kinetics	[57]
Magnetite Fe_3O_4 reduced graphite oxide MnO_2 nanocomposites	At pH range 2–10	0.5 mg/mL	0.01–10 mg/L	At pH 7.0 Adsorption capacity 14.04 mg/g and 12.22 mg/g for As(III) and As(V), respectively	Arsenic adsorption remained stable in a wide pH range 2–10, which is the limitation in most adsorbents	[63]
Nano-alumina dispersed in chitosan-grafted polyacrylamide	At pH 7.2 and the equilibrium time was 6 h. Temperature (250°C)	2.0 g	25 to 80 mg/L	Adsorption capacity 6.56 mg/g	The regeneration of the adsorbent had retention of 94% capacity in the fifth cycle Though phosphate and sulfate had negative impact on adsorption of arsenic, while the presence of nitrate and chloride showed no impact	[61]
Zero-valent iron-impregnated chitosan-caboxymethyl-bcyclodextrin composite beads	pH was 6.0, shaking mixture with 120 rpm for 12 h	0.1 to 1 g/30 mL	1–20 mg/L of As(III) and As(V)	Adsorption capacity 18.51 mg/g and 13.51 mg/g for As(III) and As(V), respectively	It is capable of chemisorption in a wide range of pH The adsorption rates of As(III) and As(V) were similar from cycle 1 to cycle 3	[62]
Activated alumina by impregnation with alum	At pH range of 2.8–11.5	0.5–16 g/L	As(V) (1–25 mg/L)	As(V) lower up to 40 ppb	PO_4^{3-} retards the adsorption of As(V) onto alum-impregnated activated alumina	[60]

Table 5 Adsorption of Arsenic From Contaminated Water Using Carbon/Graphene Based Nano-Adsorbent

Nanoparticles	Experimental Conditions	Amount of Adsorbent	Amount of Adsorbate	Maximum Removal Efficiency	Remarks	Ref.
Carbonized yeast cells containing silver nanoparticles	At pH range 3–11 Mixing at 150 rpm, at room temperature	100 mg/50 mL	0.5–2.0 mg/L	Adsorption capacity 0.975 mg/g Removal efficiency 99.52%	The maximum desorption of arsenic was found to be 49.2% at pH 11 As(V) adsorption efficiency of CCY, and CSY was investigated in batch mode by varying parameters like contact time, initial concentration, and pH	[70]
Iron hydro (oxide) nanoparticles onto activated carbon	At pH 7	The iron content of ACZ-Fe carbons ranged 0.92%–4.63%, ACP-Fe samples 2.18%–5.27% and for F400-Fe activated carbons 0.73%–2.2%	1–1.5 mg/L	Adsorption capacity of 4.56 mg As/g at 1.5 mg/L As at equilibrium and pH 7	The arsenic adsorption capacity at pH 7, 25°C, and 1 mg/L of arsenic concentration at equilibrium is 3.25, 1.45 and 1.65 mg As/g for bituminous coal under physical activation (F400), bagasse-based chemically activated carbon using $ZnCl_2$ (ACZ) and H_3PO_4 (ACP) as chemical agents	[71]
Carbon with iron nanoparticles and iron carbide	At room temperature	30 mg of both nanoparticles/30 mL As solution.	20 μg/L	Maximum As(V) uptake was 1.8 mg/g for Carbon with iron and 1.4 mg/g for iron carbide	The As(V) adsorption was satisfactory	[66]
Iron doped phenolic resin based activated carbon micro and nanoparticles	At pH levels ranging from 2.0 to 8.0	0.1 g adsorbent dose	Arsenic solutions of 0.5 to 20 mg/L	The equilibrium loading (∼3–15 mg/g)	Maximum adsorption obtained in the pH range 5.5–6.5	[58]

Continued

Table 5 Adsorption of Arsenic From Contaminated Water Using Carbon/Graphene Based Nano-Adsorbent—cont'd

Nanoparticles	Experimental Conditions	Amount of Adsorbent	Amount of Adsorbate	Maximum Removal Efficiency	Remarks	Ref.
Granular activated carbon media impregnated with zirconium dioxide	pH 7.5 ± 0.2 and Temperature 25 ± 0.1°C	0.03 to 0.65 g dry media/L	120 µg/L	Lignite Zr-GAC removed ~1.5 mg As/g Zr, while bituminous Zr-GAC removed ~3.0 mg As/g of Zr	A favorable adsorption energies and higher or similar adsorption capacities than commercially available or experimental adsorbents when compared on the basis of metal content	[72]
Iron-impregnated granular activated carbon (Fe-GAC)	At pH range 2–12, mixture shaken for 48 h at 30 rpm and 25°C	100 mg of Fe-GAC	3 mg/L arsenate	The maximum adsorption capacity ranged from 0.6 to 1.95 mg/g for Fe-GACs with iron contents from 1.48% to 12.13%	High affinity (1.3–4.7 L/mg) for arsenate Removal rate maintained close to 100% with pH less than 6 while it declined quickly above pH 7	[68]
Activated carbon, calcium alginate, and their composite beads	At pH of 7.5	0.1 g	75 mg/L of As	Maximum As(V) adsorption (66.7 mg/g at 30°C)	Activated carbon, calcium alginate composite beads had higher adsorption capacity for arsenic compared to calcium alginate beads and potassium hydroxide activated carbon-based apricot stone	[73]

studied the application of Fe_3O_4/TiO_2-SiO_2 magnetic nanocomposite modified with zinc as sorbent for the removal of As(III) from natural contaminated water. They found that equilibrium data were well-suited with the Langmuir model, rather than the Freundlich isotherm model, and the sorption reaction achieved equilibrium within 90–120 min. The maximum monolayer As(III) adsorption capacity of nanocomposite estimated by the Langmuir isotherm was 24.01 mg/g. Saha et al. [61] synthesized nano-alumina-chitosan-grafted polyacrylamide nanocomposite for arsenic removal from drinking water. The authors reported that the nanocomposite exhibited high adsorption capacity of 6.56 mg/g, at pH 7.2. Wang et al. [45] studied arsenic removal efficiency of magnetic nanoparticles-impregnated chitosan beads, from water. The nanoparticle had shown BET surface area and pore volume of 50.20 m^2/g and 0.052 cm^3/g, respectively. Authors reported that the adsorption kinetics followed pseudo-second-order kinetic models with maximum uptake of 35.7 mg/g for As(V) and 35.3 mg/g for As(III). Moreover, nanoparticles were found to have capability to retain about 88.2% and 76.02% of its original adsorption capacity even after 5 adsorption cycles. These nanoparticles can be easily be separated by applying an external magnetic field, which is the major advantage for this adsorbent. Sikder et al. [62] investigated zero-valent iron impregnated chitosan-caboxymethyl-β cyclodextrin composite beads for arsenic removal and found that the beads had good adsorption capacities for both As(III) and As(V) ions as 18.5 mg/g and 13.5 mg/g, respectively.

2.3.3 Carbon/graphene-based nanocomposites

Luo et al. [63] examined adsorption of As(III) and As(V) from water using magnetite (Fe_3O_4)-reduced graphite oxide-MnO_2 nanocomposite. Authors found that the maximum adsorption capacities for As(III) and As(V) were 14.04 mg/g and 12.22 mg/g, respectively, and that they remained stable in the pH range 2–10, which was the same limitation for most of the other adsorbents. Luo et al. [64] reported maximum adsorption capacities for As(III) and As(V) as 95.15 and 84.89 mg/g, respectively, using a composite adsorbent of (GO-$ZrO(OH)_2$) of graphene oxide-hydrated zirconium oxide (particle size below 5 nm). Zhu et al. [65] investigated adsorption behavior and the mechanism of arsenic removal from water of graphene modified by iron-manganese binary oxide ($FeMnO_x$/RGO). Authors found that graphene modified by iron-manganese binary oxide had adsorption capacities of 10.16 mg/g and 11.49 mg/g for As(III) and As(V), respectively, at an initial arsenic concentration of 1 mg/L. Later, Gutierrez-Muniz et al. [66] studied removal of As(V) from water using the carbon with iron nanoparticles (CFe) and iron carbide (CarFe). The researchers used adsorbent dose 20 μg/L in 1 mg/L of As(V) solution and reported that the maximum As(V) uptake was 1.8 mg/g for CFe and 1.4 mg/g for CarFe. The kinetic study has been reported to use the pseudo-first-order and pseudo-second-order models at pH 7 to describe the sorption of As(V) by CFe and CarFe at various time intervals. Jang et al. [67] incorporated hydrous ferric oxide (HFO) into granular activated carbon (GAC) for the purpose of arsenic removal and found that the arsenic sorption capacity of HFO-loaded GAC was 26 mg/g at 0.3 mg/L influent arsenic concentrations. Chang et al. [68] synthesized iron-impregnated granular activated carbon (Fe-GACs) for arsenic removal from drinking water. Fe-GACs showed high affinity (1.3–4.7 L/mg) for arsenate at acidic pH, while adsorption declined quickly with pH above 7. The adsorption efficiency based on iron alone was found to be 40–46 mg As/g Fe, when iron content was less than 4.22% in the nanocomposite. The authors reported that the iron-impregnated granular activated carbon (Fe-GAC) showed arsenate adsorption capacity (mg/g) increased when iron content increased up to 4.22%, while it declined when iron content was greater than 4.22%.

The probable reason for the decrease in the arsenic adsorption capacity beyond the 4.22% loading point was the enhanced agglomeration of iron nanoparticles.

Based on the literature available, it has been revealed that nanocomposites could prove to be effective in treating arsenic-contaminated water to bring it in line with drinking water standard limits. Moreover, composites also exhibited good anti-interference ability with respect to co-existing anions, and are excellent candidates for regeneration.

2.4 PHOTOCATALYTIC NANOPARTICLES/NANOCOMPOSITES (MAINLY TITANIUM-BASED NANOPARTICLES)

Titanium oxide (TiO_2) is the most-used photocatalyst in water treatment due to its low toxicity, chemically stable properties [67]. The arsenic removal efficiency of various photocatalytic nanomaterials like hydrous TiO_2, mixed oxide of Al_2O_3 and TiO_2-impregnated chitosan beads, TiO_2-pillared montmorillonite, cationic polymeric-TiO_2 composite, and Fe(III)-Ti(IV) mixed oxide have been examined by numerous researchers [14, 21, 74–78].

Bang et al. [76] studied the arsenic removal efficiency of granular titanium dioxide adsorbent from groundwater in the pH range 4–11 with the adsorbent dose of 1 g/L and an initial arsenic concentration of 0.3 mg/L. Authors reported the maximum uptake of arsenic onto the nanoparticle was 41.4 mg/g for As(V) and 32.4 mg/g As(III) with BET surface area of 250.7 m^2/g. Urbano et al. [77] worked on the removal of arsenic from contaminated water using a cationic polymer-TiO_2 nanocomposite and reported that the maximum sorption capacity of 150 mg As/g evaluated by Langmuir isotherm. Authors reported a strong decrease in sorption of arsenic onto the nanocomposite in the presence of sulfate ions. In the presence of UV irradiation, TiO_2 acts as photocatalytic oxidant for As(III) ions as well as an adsorbent, while it functions as an adsorbent in the absence of UV irradiation [79]. The photocatalytic activity of TiO_2 produces superoxide and hydroxyl radicals to degrade organic contaminants and inactivate pathogens during water treatment [80]. The photo-activity of nano-TiO_2 can be enhanced by optimizing particle size and shape, lowering volume electron/hole (e^-/h^+) recombination [74, 80]. Titanium oxide exhibits high adsorption capacity at acidic pH [81, 82]. However, there is a need to investigate the effects of a wider range of pH and the presence of coexisting ions on the removal efficiency of these nanoparticles for arsenic removal from water in both small and large-scale applications.

2.5 NANOCOMPOSITE MEMBRANES

Numerous recent studies have focused on the removal of arsenic using nanocomposite membranes to overcome the problem of post-treatment nanoparticle separation from water. Gohari et al. [83] fabricated a nanocomposite ultra-filtration membrane which consisted of polyether sulfone (PES) and titanate nanotubes (TNTs) and carried out adsorptive studies of arsenic. Authors also examined the effect of different weight ratios of TNT: PES (ranging from 0 to 1.5) on various properties like structural morphology, hydrophilicity, porosity, pure water permeability, and As(V) uptake capacity of a mixed matrix membrane. The study revealed that the membrane with the highest TNT concentration (TNT: PES ratio 1.5) had shown a maximum adsorption capacity of 125 mg/g and generated the permeation of arsenic concentration less than 10 μg/L, which meets the criteria set by WHO. Rezaee et al. [84] fabricated and characterized a polysulfone-graphene oxide nanocomposite membrane for arsenate

removal from water. The authors found that the mixed matrix composite membrane exhibited 83.65% arsenic rejection at a transmembrane pressure of 4 bars, and arsenate rejection increased with increasing pH. They also observed that addition of graphene oxide nanoparticles into polysulfone enhanced various properties of the membrane such as hydrophilicity, porosity, flux, and arsenate rejection. Min et al. [85] synthesized a chitosan-based electro-spun nanofiber membrane and used it to treat an aqueous solution, revealing that the highly porous and large specific surface area of the adsorbent led to high adsorption capacity (30.8 mg/g). The authors found that the highest adsorption capacity was obtained at lower pH, in contrast to SO_4^{-2}, PO_4^{-3} ions, and humid acid had shown negative effect on arsenic rejection.

3 ADSORPTION MECHANISM OF ARSENIC ON NANOPARTICLES AND NANOCOMPOSITES

As(V) adsorption is rapid and the substance is easy to remove from water by applying available treatment techniques. However, As(III) adsorption in the absence of an oxidation step is a slow process, and numerous researchers investigated simultaneous oxidation-adsorption of As(III) using a metal oxide oxidant or photocatalyst. The mechanisms of As(III) oxidation and subsequent adsorption have been addressed in this section. Wang et al. [86] demonstrated the possible mechanism of arsenic adsorption on mixed nanomaterials like Fe_2O_3:Cu particles. The mechanism of arsenic on Fe_2O_3:Cu surface is presented in Fig. 1 [86]. The mixture of Cu and Cu^{2+} doped in Fe_2O_3 nanoparticles constituted Fe_2O_3:Cu particles. Authors explained through XPS scans results of adsorbents before and after arsenic adsorption that Cu^{2+} was responsible for accelerating the redox reaction, such as when Cu^{2+} catalyzed the efficient oxidation of As(III) to As(V) species.

Studies also demonstrated that doped copper ions significantly facilitated the redox of As(III) by O_2. Finally, charged As(V) ions adsorb through active hydroxyl groups on the surfaces of nanocomposites. Zhu et al. [65] demonstrated the As(III) adsorption mechanism on MnO_2 nanoparticles loaded onto graphene in the presence of iron oxide nanoparticles. As the adsorbent was added into an As(III) solution, part of the As(III) was converted into As(V) by MnO_2. The adsorption mechanism is illustrated in Fig. 2 [65], and reactions are presented in Eqs. (1)–(3).

$$MnO_2 + H_3AsO_3 + 2H^+ = Mn^{2+} + H_3AsO_4 + H_2O \quad (1)$$

$$2MnO_2 + H_3AsO_3 = 2MnOOH^* + H_3AsO_4 \quad (2)$$

$$2MnOOH^* + H_3AsO_3 + 4H^+ = 2Mn^{2+} + H^3AsO^4 + 3H_2O \quad (3)$$

In the next step, As(V) would diffuse into the bulk solution because of its high concentration on the surface of MnO_2. Then, As(V), together with the small amount of As(III), was attracted toward iron(III) oxide attached tightly on graphene surfaces. As a result, hydroxyl groups on the iron oxide surfaces could be replaced by As(III)/As(V) via ligand exchange mechanism, ultimately forming inner sphere surface complexes [65]. Liu et al. [87] also demonstrated arsenic adsorption on a magnetite adsorbent through a surface complexation mechanism, and the schematic diagram of this mechanism is presented in Fig. 3 [87].

Yu et al. [88] described As(V) adsorption mechanism on hydrous cerium-oxide-modified graphene (GNP-HCO), and it is presented in Fig. 4. Fig. 4 shows that the M-OH group on the surface of the

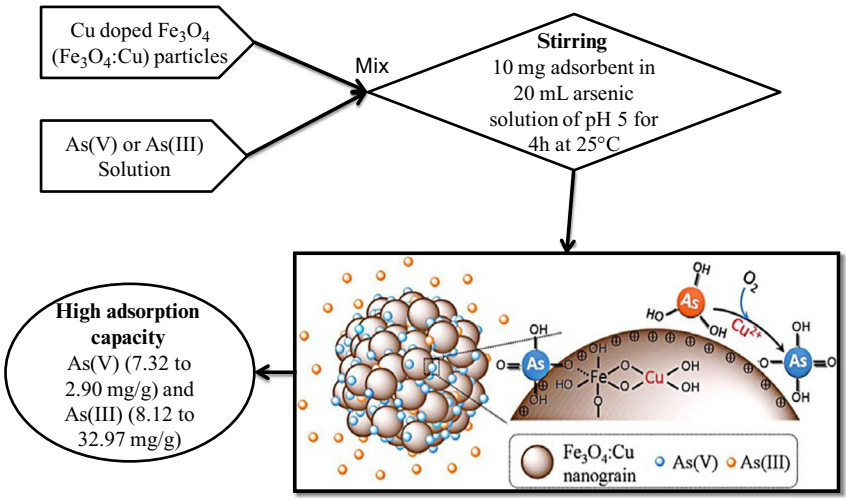

FIG. 1

The As(III) redox and adsorption on Fe_3O_4:Cu particle [86].

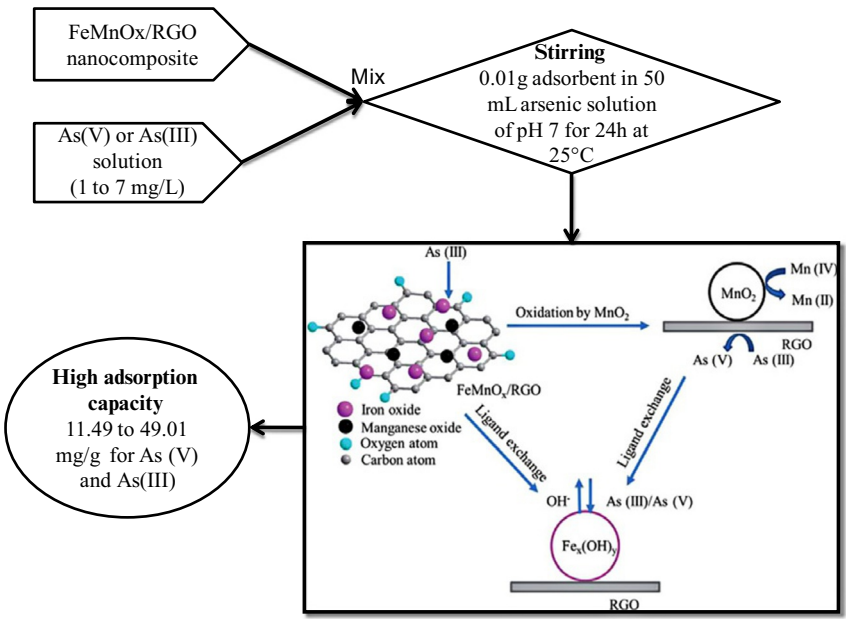

FIG. 2

Schematic removal mechanism of As(III) on FeMnOx/RGO [65].

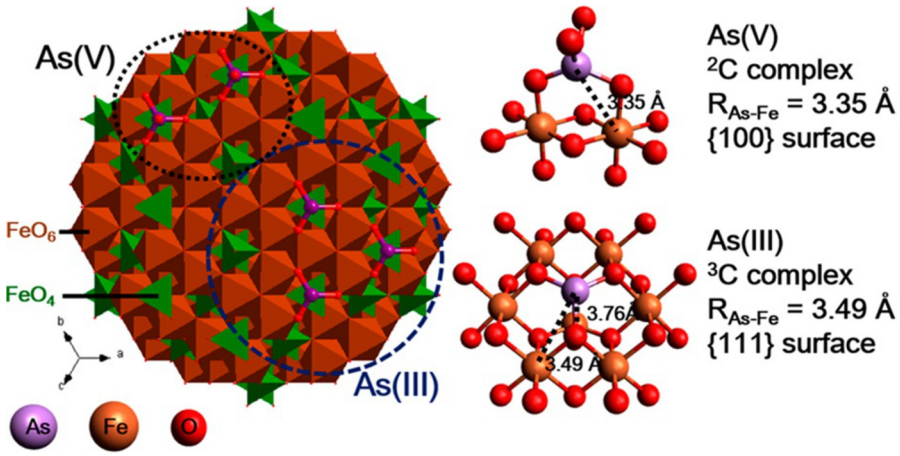

FIG. 3

Schematic of arsenic adsorption on magnetite with proposed surface complexes [87].

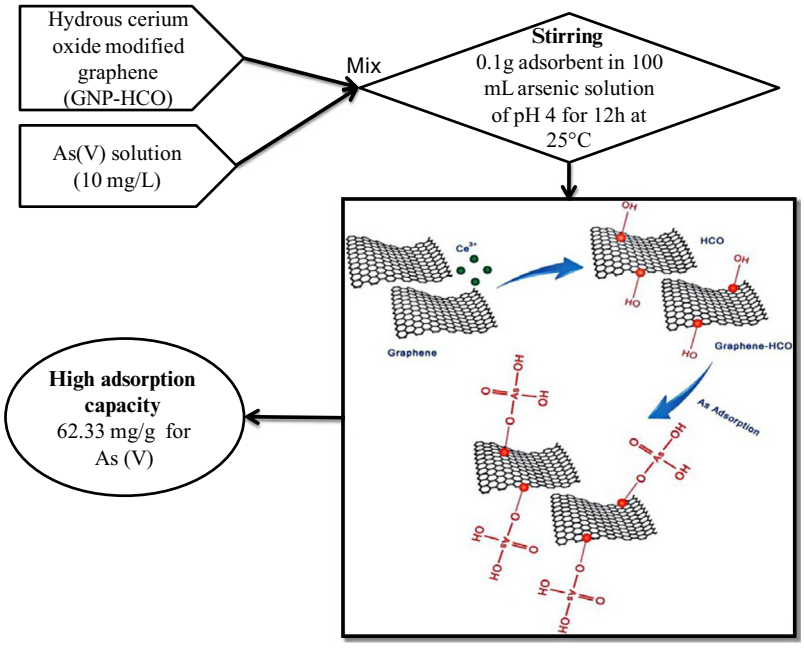

FIG. 4

Schematic diagram of adsorption mechanism of arsenate onto GNP-HCO [88].

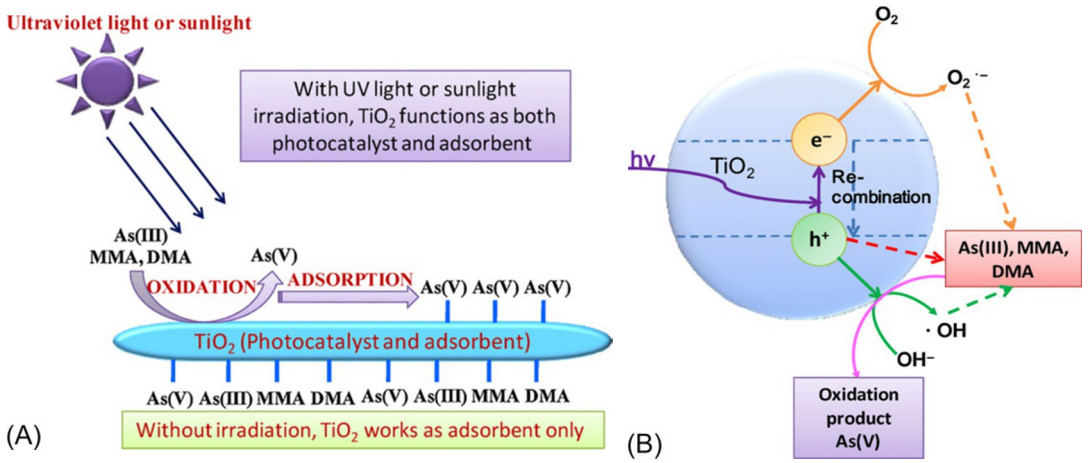

FIG. 5

(A) Schematic diagram for the photooxidation of As(III) on TiO_2 nanocomposite. (B) Schematic illustration of TiO2-catalyzed As(III)/organic arsenic photooxidation pathways [79].

adsorbent may be protonated at acidic pH, which causes an enhanced electrostatic attraction between negatively charged As(V) and active sites, and subsequently increases the arsenic adsorption.

The application of TiO_2 in arsenic removal can be divided into two aspects: TiO_2 functions as photocatalyst as well as adsorbent in the presence of sunlight and UV light irradiation, but it acts as only adsorbent in the absence of irradiation. Guan et al. [79] illustrated this mechanism, and this is presented in Fig. 5A. The oxidation of As(III) and organo-arsenic species into As(V) using a TiO_2 photocatalyst occur through the three different routes such as (i) superoxide/hydroxide radicals (O_2/HO_2), (ii) positive hole ($h^+_{\sqrt{B}}$), and (iii) hydroxyl radical ($^{\bullet}OH$) [79]. The schematic diagram of the detailed mechanism is presented in Fig. 5B [79]. Maiti et al. [89–91], investigated iron and aluminium oxyhydroxide nanoparticles-coated sand prepared from an abundant material, laterite. The studies explain the adsorption mechanism of arsenite and arsenate ions through surface active hydroxyl groups of modified adsorbent [89–91]. Authors concluded that adsorption of arsenic species increased significantly due to an increase in hydroxyl surface active groups per unit specific surface area after chemical treatment of natural adsorbents [89–91].

4 CONCLUDING REMARKS AND FUTURE TRENDS

Extensive arsenic contamination of groundwater and surface water has been reported worldwide. High levels of arsenic in groundwater not only cause significant problems in the availability of safe drinking water, but they have raised concern regarding arsenic contamination through the food chain. A large number of studies have been implemented to remove arsenic at the laboratory scale using either synthetic arsenic solution or contaminated groundwater. Furthermore, nanomaterials have been found

to be the most attractive technology for mitigating the arsenic problem due to their special properties including high specific surface area, higher density of hydroxyl surface active sites per unit specific surface area, larger pore volume, and easily accessible pores. Nanomaterials based on inorganic oxides and hydroxides have been investigated to assess their performance. The wide range of metal oxides/hydroxides based on iron, aluminium, titanium, cerium, zirconium, copper, and calcium have been investigated to assess their arsenic removal efficiency as nanomaterials. Several challenges still need to be addressed to minimize agglomeration, cost minimization in production, better and dispersibility of nanomaterials into aqueous medium, to optimize the design of the adsorber based on nanomatrials for practical large-scale applications. To address the problem related to agglomeration and dispersibility of nanoparticles in water, researchers tried nanomaterials dispersed in porous matrices, such as inorganic frameworks, polymeric matrices, and carbon/graphene-based materials. It has been also found that mixed-oxide nanoparticles show favorable adsorption behavior compared to single metallic-based nanomaterials. The reason for this might be the oxidative power of one metal oxide (like MnO_2, TiO_2) in the presence or absence of UV/sunlight irradiation), where As(III) oxidized to charged As(V) species are easily absorbed through other metallic nanoparticles' surfaces.

Future trends in research based on arsenic removal using nanomaterials lies in the composite nano-adsorbent and nanocomposite membranes, but both have only been explored in the laboratory thus far. There are no large-scale water treatments available using nanomaterials due to the high cost associated with production of nanomaterials and their inferior recyclability. Extensive research demonstrated preparation of new and inexpensive bifunctional materials based on TiO_2, which displays a higher photocatalytic efficiency that can utilize wider solar spectra and has a high arsenic adsorption capacity due to oxidation of As(III) species. Numerous nanomaterials dispersed in polymers and carbon/graphene have shown better arsenic adsorption performance compared to bare nanoparticles.

REFERENCES

[1] B.K. Mandal, K.T. Suzuki, Arsenic round the world: a review, Talanta 58 (2002) 201–235.
[2] S.U. Rehman, M. Siddiq, H. Al-Lohedan, N. Aktas, M. Sahiner, S. Demirci, N. Sahiner, Fast removal of high quantities of toxic arsenate via cationic p(APTMACl) microgels, J. Environ. Manag. 166 (2016) 217–226.
[3] K.T. Lim, M.Y. Shukor, H. Wasoh, Physical, Chemical, and Biological Methods for the Removal of Arsenic Compounds. Hindawi Publishing Corporation BioMed Research International, 2014. https://doi.org/10.1155/2014/503784.
[4] B.V. Tangahu, S.R.S. Abdullah, A review on heavy metals (As, Pb, and Hg) uptake by plants through phytoremediation. Int. J. Chem. Eng. (2011). https://doi.org/10.1155/2011/939161.
[5] M. Habuda-Stanic, M. Nujic, Arsenic removal by nanoparticles: a review, Environ. Sci. Pollut. Res. 22 (2015) 8094–8123.
[6] R. Singh, S. Singh, P. Parihar, V.P. Singh, S.M. Prasad, Arsenic contamination, consequences and remediation techniques: a review, Ecotoxicol. Environ. Saf. 112 (2015) 247–270.
[7] P. Mondal, S. Bhowmick, D. Chatterjee, A. Figoli, B.V.D. Bruggen, Remediation of inorganic arsenic in groundwater for safe water supply: a critical assessment of technological solutions, Chemosphere 92 (2013) 157–170.
[8] X. Zhao, L. Lv, B. Pan, W. Zhang, S. Zhang, Q. Zhang, Polymer-supported nanocomposites for environmental application: a review, Chem. Eng. J. 170 (2011) 381–394.
[9] B. Zhang, H. Misak, P.S. Dhanasekaran, D. Kalla, R. Asmatulu, Environmental impacts of nanotechnology and its products, in: Proceedings of the 2011 Midwest Section Conference of the American Society for Engineering Education, 2011.

[10] S.P. Thomas, E.M. Al-Mutairi, S.K. De, Impact of nanomaterials on health and environment, Arab. J. Sci. Eng. 38 (2013) 457–477.
[11] A. Lopez-Serrano, R.M. Olivas, J.S. Landaluze, C. Camara, Nanoparticles: a global vision. Characterization, separation, and quantification methods: potential environmental and health impact, Anal. Methods 6 (2014) 38–56.
[12] E. Olyaie, H. Banejad, A. Afkhami, A. Rahmani, J. Khodaveisi, Development of a cost-effective technique to remove the arsenic contamination from aqueous solutions by calcium peroxide nanoparticles, Sep. Purif. Technol. 95 (2012) 10–15.
[13] W. Xu, J. Wang, L. Wang, G. Sheng, J. Liu, H. Yu, X.J. Huanga, Enhanced arsenic removal from water by hierarchically porous CeO_2–ZrO_2 nanospheres: role of surface- and structure-dependent properties, J. Hazard. Mater. 260 (2013) 498–507.
[14] M. Pirila, M. Martikainen, K. Ainassaari, T. Kuokkanen, R.L. Keiski, Removal of aqueous As(III) and As(V) by hydrous titanium dioxide, J. Colloid Interface Sci. 353 (2011) 257–262.
[15] E. Vunain, A.K. Mishra, R.W. Krause, Fabrication, characterization and application of polymer nanocomposites for Arsenic (III) removal from water, J. Inorg. Organomet. Polym. Mater. 23 (2013) 293–305.
[16] M.A.V. Ramos, W. Yan, X. Li, B.E. Koel, W. Zhang, Simultaneous oxidation and reduction of arsenic by zero-valent iron nanoparticles: understanding the significance of the core-shell structure, J. Phys. Chem. C 113 (2009) 14591–14594.
[17] W. Yang, A.T. Kan, W. Chen, M.B. Tomson, pH-dependent effect of zinc on arsenic adsorption to magnetite nanoparticles, Water Res. 44 (2010) 5693–5701.
[18] R. Prucek, J. Tucek, J. Kolarík, J. Filip, Z. Marusak, V.K. Sharma, R. Zboril, Ferrate(VI)-induced arsenite and arsenate removal by in situ structural incorporation into magnetic Iron(III) oxide nanoparticles, Environ. Sci. Technol. 47 (2013) 3283–3292.
[19] M.C.S. Faria, R.S. Rosemberg, C.A. Bomfeti, D.S. Monteiro, F. Barbosa, L.C.A. Oliveira, M. Rodriguez, M.C. Pereira, J.L. Rodrigues, Arsenic removal from contaminated water by ultrafine δ-FeOOH adsorbents, Chem. Eng. J. 237 (2014) 47–54.
[20] J.A. Arcibar-Orozco, M. Avalos-Borja, J.R. Rangel-Mendez, Effect of phosphate on the particle size of ferric oxyhydroxides anchored onto activated carbon: As(V) removal from water, Environ. Sci. Technol. 46 (2012) 9577–9583.
[21] R. Li, Q. Li, S. Gao, J.K. Shang, Exceptional arsenic adsorption performance of hydrous cerium oxide nanoparticles: part A. Adsorption capacity and mechanism, Chem. Eng. J. 185–186 (2012) 127–135.
[22] C. Hang, Q. Li, S. Gao, J.K. Shang, As(III) and As(V) Adsorption by hydrous zirconium oxide nanoparticles synthesized by a hydrothermal process followed with heat treatment, Ind. Eng. Chem. Res. 51 (2011) 353–361.
[23] H. Cui, Q. Li, S. Gao, J.K. Shang, Strong adsorption of arsenic species by amorphous zirconium oxide nanoparticles, J. Ind. Eng. Chem. 18 (2012) 1418–1427.
[24] K.J. Reddy, K.J. McDonald, H. King, A novel arsenic removal process for water using cupric oxide nanoparticles, J. Colloid Interface Sci. 397 (2013) 96–102.
[25] A. Goswami, P.K. Raul, M.K. Purkait, Arsenic adsorption using copper (II) oxide nanoparticles, Chem. Eng. Res. Des. 90 (2012) 1387–1396.
[26] A. Dey, R. Singh, M.K. Purkait, Cobalt ferrite nanoparticles aggregated schwertmannite: a novel adsorbent for the efficient removal of arsenic, J. Water Process Eng. 3 (2014) 1–9.
[27] Z.O. Kocabas-Atakli, Y. Yurum, Synthesis and characterization of anatase nanoadsorbent and application in removal of lead, copper and arsenic from water, Chem. Eng. J. 225 (2013) 625–635.
[28] A.K. Patra, A. Dutta, A. Bhaumik, Self-assembled mesoporous ϒ-Al_2O_3 spherical nanoparticles and their efficiency for the removal of arsenic from water, J. Hazard. Mater. 201– 202 (2012) 170–177.
[29] L. Feng, M. Cao, X. Ma, Y. Zhu, C. Hu, Superparamagnetic high-surface-area Fe_3O_4 nanoparticles as adsorbents for arsenic removal, J. Hazard. Mater. 217–218 (2012) 439–446.

[30] T. Tuutijarvi, J. Lu, M. Sillanpaa, G. Chen, As(V) adsorption on maghemite nanoparticles, J. Hazard. Mater. 166 (2009) 1415–1420.
[31] M. Jian, B. Liu, G. Zhang, R. Liu, X. Zhang, Adsorptive removal of arsenic from aqueous solution by zeoliticimidazolate framework-8 (ZIF-8) nanoparticles, Colloids Surf. A Physicochem. Eng. Asp. 465 (2015) 67–76.
[32] M.M. Khin, A.S. Nair, V.J. Babu, R. Murugan, S. Ramakrishna, A review on nanomaterials for environmental remediation, Energy Environ. Sci. 5 (2012) 8075–8109.
[33] G. Di, Z. Zhu, H. Zhang, J. Zhu, H. Lu, W. Zhang, Y. Qiu, L. Zhu, S. Küppers, Simultaneous removal of several pharmaceuticals and arsenic on Zn-Fe mixed metal oxides: combination of photocatalysis and adsorption, Chem. Eng. J. 328 (2017) 141–151.
[34] T. Basu, U.C. Ghosh, Nano-structured iron(III)–cerium(IV) mixed oxide: synthesis, characterization and arsenic sorption kinetics in the presence of co-existing ions aiming to apply for high arsenic ground water treatment, Appl. Surf. Sci. 283 (2013) 471–481.
[35] S.R. Chowdhury, E.K. Yanful, Arsenic and chromium removal by mixed magnetiteemaghemite nanoparticles and the effect of phosphate on removal, J. Environ. Manag. 91 (2010) 2238–2247.
[36] Z. Ren, G. Zhang, J.P. Chen, Adsorptive removal of arsenic from water by an iron–zirconium binary oxide adsorbent, J. Colloid Interface Sci. 358 (2011) 230–237.
[37] T. Turk, I. Alp, Arsenic removal from aqueous solutions with Fe-hydrotalcite supported magnetite nanoparticle, J. Ind. Eng. Chem. 20 (2014) 732–738.
[38] S.C.N. Tang, I.M.C. Lo, Magnetic nanoparticles: essential factors for sustainable environmental applications, Water Res. 47 (2013) 2613–2632.
[39] Z.M. Liu, S.H. Wu, S.Y. Jia, F.X. Qin, S.M. Zhou, H.T. Ren, P. Na, Y. Liu, Novel hematite nanorods and magnetite nanoparticles prepared from MIL-100(Fe) template for the removal of As(V), Mater. Lett. 132 (2014) 8–10.
[40] T. Basu, U.C. Ghosh, Arsenic (III) removal performances in the absence/presence of groundwater occurring ions of agglomerated Fe (III)–Al (III) mixed oxide nanoparticles, J. Ind. Eng. Chem. 17 (2011) 834–844.
[41] K. Song, W. Kim, C.Y. Suh, D. Shin, K.S. Ko, K. Ha, Magnetic iron oxide nanoparticles prepared by electrical wire explosion for arsenic removal, Powder Technol. 246 (2013) 572–574.
[42] T. Tuutijarvi, J. Lu, M. Sillanpaa, G. Chen, As(V) adsorption on maghemite nanoparticles, J. Hazard. Mater. 166 (2009) 1415–1420.
[43] S. Lin, D. Lu, Z. Liu, Removal of arsenic contaminants with magnetic Υ-Fe_2O_3 nanoparticles, Chem. Eng. J. 211–212 (2012) 46–52.
[44] S. Kong, Y. Wang, Q. Hu, A.K. Olusegun, Magnetic nanoscale Fe–Mn binary oxides loaded zeolite for arsenic removal from synthetic groundwater, Colloids Surf. A Physicochem. Eng. Asp. 457 (2014) 220–227.
[45] J. Wang, W. Xu, L. Chen, X. Huang, J. Liu, Preparation and evaluation of magnetic nanoparticles impregnated chitosan beads for arsenic removal from water, Chem. Eng. J. 251 (2014) 25–34.
[46] T. Turk, I. Alp, Arsenic removal from aqueous solutions with Fe-hydrotalcite supported magnetite nanoparticle, J. Ind. Eng. Chem. 20 (2014) 732–738.
[47] Y. Jin, F. Liu, M. Tong, Y. Hou, Removal of arsenate by cetyltrimethylammonium bromide modified magnetic nanoparticles, J. Hazard. Mater. 227– 228 (2012) 461–468.
[48] C. Zhang, C. Shan, Y. Jin, M. Tong, Enhanced removal of trace arsenate by magnetic nanoparticles modified with arginine and lysine, Chem. Eng. J. 254 (2014) 340–348.
[49] C. Shan, M. Tong, Efficient removal of trace arsenite through oxidation and adsorption by magnetic nanoparticles modified with Fe-Mn binary oxide, Water Res. 47 (2013) 3411–3421.
[50] S. Hokkanen, E. Repo, S. Lou, M. Sillanpaa, Removal of arsenic (V) by magnetic nanoparticle activated microfibrillated cellulose, Chem. Eng. J. 260 (2015) 886–894.

[51] M. Kilianova, R. Prucek, J. Filip, J. Kolarik, L. Kvitek, A. Panacek, J. Tucek, R. Zboril, Remarkable efficiency of ultrafine superparamagnetic iron (III) oxide nanoparticles toward arsenate removal from aqueous environment, Chemosphere 93 (2013) 2690–2697.
[52] B. Chen, Z. Zhu, J. Maa, M. Yang, J. Hong, X. Hu, Y. Qiu, J. Chen, One-pot, solid-phase synthesis of magnetic multiwalled carbon nanotube/iron oxide composites and their application in arsenic removal, J. Colloid Interface Sci. 434 (2014) 9–17.
[53] K.Z. Elwakeel, E. Guibal, Arsenic (V) sorption using chitosan/Cu $(OH)_2$ and chitosan/CuO composite sorbents, Carbohydr. Polym. 134 (2015) 190–204.
[54] P.K. Tandon, R.C. Shukla, S.B. Singh, Removal of arsenic(III) from water with clay-supported zerovalent iron nanoparticles synthesized with the help of tea liquor, Ind. Eng. Chem. Res. 52 (2013) 10052–10058.
[55] N. Tian, X. Tian, L. Ma, C. Yang, Y. Wang, Z. Wang, L. Zhang, Well-dispersed magnetic iron oxide nanocrystals on sepiolite nanofibers for arsenic removal, RSC Adv. 5 (2015) 25236–25243.
[56] L. Fan, S. Zhang, X. Zhang, H. Zhou, Z. Lu, S. Wang, Removal of arsenic from simulation wastewater using nano-iron/oyster shell composites, J. Environ. Manag. 156 (2015) 109–114.
[57] M.A. Malana, R.B. Qureshi, M.N. Ashiq, Adsorption studies of arsenic on nano aluminium doped manganese copper ferrite polymer (MA, VA, AA) composite: kinetics and mechanism, Chem. Eng. J. 172 (2011) 721–727.
[58] A. Sharma, N. Verma, A. Sharma, D. Deva, N. Sankararamakrishnan, Iron doped phenolic resin based activated carbon micro and nanoparticles by milling: synthesis, characterization and application in arsenic removal, Chem. Eng. Sci. 65 (2010) 3591–3601.
[59] Z. Wen, Y. Zhang, Y. Wang, L. Li, R. Chen, Redox transformation of arsenic by magnetic thin-film MnO2 nanosheet coated flowerlike Fe_3O_4 nanocomposites, Chem. Eng. J. 312 (2017) 39–49.
[60] M. Sadeghi, M. Irandoust, F. Khorshidi, M. Feyzi, F. Jafari, T. Shojaeimehr, M. Shamsipur, Removal of Arsenic (III) from natural contaminated water using magnetic nanocomposite: kinetics and isotherm studies, J. Iran. Chem. Soc. 13 (2016) 1175–1188.
[61] S. Saha, P. Sarkar, Arsenic remediation from drinking water by synthesized nano-alumina dispersed in chitosan-grafted polyacrylamide, J. Hazard. Mater. 227– 228 (2012) 68–78.
[62] M.T. Sikder, S. Tanaka, T. Saito, M. Kurasaki, Application of zerovalent iron impregnated chitosan-caboxymethyl-bcyclodextrin composite beads as arsenic sorbent, J. Environ. Chem. Eng. 2 (2014) 370–376.
[63] X. Luo, C. Wang, S. Luo, R. Dong, X. Tu, G. Zeng, Adsorption of As(III) and As(V) from water using magnetite Fe_3O_4-reduced graphite oxide–MnO_2 nanocomposites, Chem. Eng. J. 187 (2012) 45–52.
[64] X. Luo, C. Wang, L. Wang, F. Deng, S. Luo, X. Tu, C. Au, Nanocomposites of graphene oxide-hydrated zirconium oxide for simultaneous removal of As(III) and As(V) from water, Chem. Eng. J. 220 (2013) 98–106.
[65] J. Zhu, Z. Lou, Y. Liu, R. Fu, S.A. Baigab, X. Xu, Adsorption behavior and removal mechanism of arsenic on graphene modified by iron–manganese binary oxide ($FeMnO_x$/RGO) from aqueous solutions, RSC Adv. 5 (2015) 67951–67961.
[66] O.E. Gutierrez-Muniz, G. Garcia-Rosales, E. Ordonez-Regil, M.T. Olguin, A. Cabral-Prieto, Synthesis, characterization and adsorptive properties of carbon with iron nanoparticles and iron carbide for the removal of As(V) from water, J. Environ. Manag. 114 (2013) 1–7.
[67] M. Jang, W. Chen, F. Cannon, Preloading hydrous ferric oxide into granular activated carbon for arsenic removal, Environ. Sci. Technol. 42 (2008) 3369–3374.
[68] Q. Chang, W. Lina, W. Ying, Preparation of iron-impregnated granular activated carbon for arsenic removal from drinking water, J. Hazard. Mater. 184 (2010) 515–522.
[69] L. Guo, P. Ye, J. Wang, F. Fu, Z. Wu, Three-dimensional Fe_3O_4-graphene macroscopic composites for arsenic and arsenate removal, J. Hazard. Mater. 298 (2015) 28–35.
[70] R. Selvakumar, N.A. Jothi, V. Jayavignesh, K. Karthikaiselvi, G.I. Antony, P.R. Sharmila, S. Kavitha, K. Swaminathan, As(V) removal using carbonized yeast cells containing silver nanoparticles, Water Res. 45 (2011) 583–592.

[71] C. Nieto-Delgado, J.R. Rangel-Mendez, Anchorage of iron hydro (oxide) nanoparticles onto activated carbon to remove As(V) from water, Water Res. 46 (2012) 2973–2982.
[72] R. Sandoval, A.M. Cooper, K. Aymar, A. Jain, K. Hristovski, Removal of arsenic and methylene blue from water by granular activated carbon media impregnated with zirconium dioxide nanoparticles, J. Hazard. Mater. 193 (2011) 296–303.
[73] A.F. Hassana, A.M. Abdel-Mohsen, H. Elhadidy, Adsorption of arsenic by activated carbon, calcium alginate and their composite beads, Int. J. Biol. Macromol. 68 (2014) 125–130.
[74] X. Qu, P.J.J. Alvarez, Q. Li, Applications of nanotechnology in water and wastewater treatment, Water Res. 47 (2013) 3931–3946.
[75] J.S. Yamani, S.M. Miller, M.L. Spaulding, J.B. Zimmerman, Enhanced arsenic removal using mixed metal oxide impregnated chitosan beads, Water Res. 46 (2012) 4427–4434.
[76] S. Bang, M. Patel, L. Lippincott, X. Meng, Removal of arsenic from groundwater by granular titanium dioxide adsorbent, Chemosphere 60 (2005) 389–397.
[77] B.F. Urbano, I. Villenas, B.L. Rivas, C.H. Campos, Cationic polymer–TiO_2 nanocomposite sorbent for arsenate removal, Chem. Eng. J. 268 (2015) 362–370.
[78] K. Gupta, U.C. Ghosh, Arsenic removal using hydrous nanostructure iron(III)–titanium(IV) binary mixed oxide from aqueous solution, J. Hazard. Mater. 16 (2009) 1884–1892.
[79] X. Guan, J. Du, X. Meng, Y. Sun, B. Sun, Q. Hu, Application of titanium dioxide in arsenic removal from water: a review, J. Hazard. Mater. 215–216 (2012) 1–16.
[80] X. Qu, J. Brame, Q. Li, P.J.J. Alvarez, Nanotechnology for a safe and sustainable water supply: enabling integrated water treatment and reuse, Acc. Chem. Res. 46 (3) (2013) 834–843.
[81] H. Jezequel, K.H. Chu, Enhanced adsorption of arsenate on titanium dioxide using Ca and Mg ions, Environ. Chem. Lett. 3 (2005) 132–135.
[82] M.J. López-Munoz, A. Arencibia, Y. Segura, J.M. Raez, Removal of As(III) from aqueous solutions through simultaneous photocatalytic oxidation and adsorption by TiO_2 and zero-valent iron, Catal. Today 280 (2017) 149–154.
[83] R.J. Gohari, W.J. Lau, E. Halakoo, A.F. Ismail, F. Korminouri, T. Matsuura, M.S.J. Goharib, M.N. K. Chowdhurya, Arsenate removal from contaminated water by a highly adsorptive nanocomposite ultra filtration membrane. New J. Chem. (2015). https://doi.org/10.1039/C5NJ00690B.
[84] R. Rezaee, S. Nasseri, A.H. Mahvi, R. Nabizadeh, S.A. Mousavi, A.R.A. Jafari, S. Nazmara, Fabrication and characterization of a polysulfone-graphene oxide nanocomposite membrane for arsenate rejection from water, J. Environ. Health Sci. Eng. 13 (2015) 61.
[85] L. Min, Z. Yuan, L. Zhong, Q. Liu, R. Wua, Y. Zheng, Preparation of chitosan based electrospun nanofiber membrane and its adsorptive removal of arsenate from aqueous solution, Chem. Eng. J. 267 (2015) 132–141.
[86] T. Wang, W. Yang, T. Song, C. Li, L. Zhang, H. Wang, L. Chai, Cu doped Fe_3O_4 magnetic adsorbent for arsenic: synthesis, property, and sorption application, RSC Adv. 5 (2015) 50011–50018.
[87] C.-H. Liu, Y.-H. Chuang, T.-Y. Chen, Y. Tian, H. Li, M.-K. Wang, W. Zhangh, Mechanism of arsenic adsorption on magnetite nanoparticles from water: thermodynamic and spectroscopic studies, Environ. Sci. Technol. 49 (2015) 7726–7734.
[88] L. Yu, Y. Ma, C.N. Ong, J. Xie, Y. Liu, Rapid adsorption removal of arsenate by hydrous cerium oxide–graphene composite, RSC Adv. 5 (2015) 64983–64990.
[89] A. Maiti, J.K. Basu, S. De, Experimental and kinetic modeling of As(V) and As(III) adsorption on treated laterite using synthetic and contaminated groundwater: effects of phosphate, silicate and carbonate ions, Chem. Eng. J. 191 (2012) 1–12.
[90] A. Maiti, J.K. Basu, S. De, Development of a treated laterite for arsenic adsorption: effects of treatment parameters, Ind. Eng. Chem. Res. 49 (2010) 4873–4886.
[91] A. Maiti, J.K. Basu, S. De, Fe-Al nano-oxide prepared by sol-gel method using precursor of HCl digested liquid fraction of laterite: Arsenic adsorption performance, Int. J. Nanosci. 10 (2011) 1173–1177.

CHAPTER

26

CHALLENGES AND OPPORTUNITIES OF GRAPHENE-BASED MATERIALS IN CURRENT DESALINATION AND WATER PURIFICATION TECHNOLOGIES

M. Ahmed, A. Giwa, S.W. Hasan

Department of Chemical Engineering, Khalifa University of Science and Technology, Abu Dhabi, United Arab Emirates

1 INTRODUCTION

Carbon has been a pivotal building block as a construction unit in different carbon nanostructures that exhibit unique physical and chemical properties; it can form zero-dimensional (0D), one-dimensional (1D), two-dimensional (2D), and three dimensional (3D) elemental crystal nanostructures [1]. Graphene, in its pristine form, is a 2D single layer of carbon atoms arranged in a sp^2-bonded aromatic structure in a hexagonal honeycomb lattice with a carbon-carbon bond length of 0.142 nm [2]. Graphene has chemical features similar to carbon nanotubes (CNTs) but with a different structure, as CNTs are tubular, while graphene is planar. Graphene-based materials can be produced at a price that is negligible compared to CNTs. Moreover, the exfoliated 2D single-layer form of graphene results in a surface area much larger than that of single-walled nanotubes (SWNTs). This larger surface area allows a wide range of modifications, functionalization, and incorporation in nanocomposites with other nanomaterials [3,4]. Moreover, graphene can be identified as a basic building block for all other 0D, 1D, and 3D graphitic materials [5]. Compared to CNTs, using graphene-based materials can offer several advantages. For instance, single-layered graphene materials have two basal planes, and thus allow a larger surface area for adsorption to take place. The inner walls in CNTs, on the other hand, are not accessible by adsorbates. Moreover, graphene-based materials such as graphene oxide (GO) and reduced graphene oxide (rGO) can be synthesized by chemical exfoliation of graphite, a process that does not require using a complex apparatus or metallic catalysts [6].

GO is an oxidized form of graphene endowed with oxygen functional groups such as carbonyl, hydroxyl, carbnyl, and epoxy in the carbon lattice. GO can be produced at low cost through oxidation and exfoliation of graphene. Oxidation increases the interlayer distance from 0.34 to 0.65 nm, which

Nanoscale Materials in Water Purification. https://doi.org/10.1016/B978-0-12-813926-4.00033-1

decreases energy requirements to separate the layers. Interlayer disatance is further increased due to the hydrophilicity of GO, reaching 1.15 nm, which allows water to adsorb into the lamellar structure [7]. rGO can be obtained using reducing agents, thermal annealing, photoreduction, and microwave-assisted reduction [7].

2 GRAPHENE IN MEMBRANE AND DESALINATION APPLICATIONS

Despite the fact that pristine graphene exhibits impermeable characteristics, nanporous grahene sheets are considered to be a promosing, size-selective seperation membrane [8]. Initial efforts at utilizing graphene-based nanomaterials for desalination applications were attempted through molecular dynamics simulations and computational studies. These initial studies predicted that the large slip length of water molecules allows negligible friction with graphene surfaces, which makes water flow easily through planar graphene nanochannels [9,10]. Thus, water permeability can be siginificantly higher than when commercially available reverse osmosis (RO) membranes and nanofiltration membranes by several magnitudes [11]. Graphene-based materials can be involved in water desalination as (i) graphene-based membrane, (ii) nanocomposite membrane, and (iii) capacitive deionization (CDI) electrode materials. Furthermore, the antibacterial properties of GO helps in the development of biofouling resistant membranes [12].

2.1 GRAPHENE-BASED MEMBRANES

The design of nanoporous semipermeable membranes that contain continous channels allows a greater volume of water to pass at a pressure far lower than that required by conventionally used membranes. The channel pores must be carefully designed to obstruct the passage of ions; the precise control of pore size in a nanoporous graphene membrane remains one of the challenges in membrane design. The delocalized electron clouds of the π orbitals block the gap that would be found in the atomic rings of graphene, which restrains the passage of even the smallest molecular species [13]. Simulation also shows that graphene nanoporous membranes allow for fast convective water flow across well-defined channels, contrary to the slower solution-diffusion water transport mechanism in RO membranes. The fast flow rate of water is justified by the atomic thickness of graphene membrane; it has been concluded that a reduction of thickness to approximately 10 nm increases the level of performance by 100 times when compared to RO technologies [14]. Two strategies have been utilized for graphene-based materials applications in membrane processes: nanoporous graphene sheets and stacked GO barriers.

Cohen-Tanugi and Grossman found through molecular dynamic simulations that the membrane could perform more than 99% salt rejection and could provide water transport of up to 66 L/cm^2.d.MPa [15]. Intuitively, as pore diameter and applied pressure increase, the flow rate of water through nanopores increases as well. Salt rejection, on the other hand, decreases when applied pressure is high, in the range ~90–225 MPa, which is in contrast to the behavior of conventional diffusive RO membranes [15]. This result is caused by the large effective volume of salt ions in the solution, which leads their higher response to increase in pressure when compared to water molecules. However, in the case of RO membranes, osmotic pressure is the driving force, which leads to a higher flux of water molecules when compared to salt ions when pressure increases.

Expectedly, functionalizing nanopores with negatively charged functional groups showed excellent salt rejection [16]. Membranes that have pores functionalized with hydroxyl groups and hydrogen atoms were tested to study the impact of pores chemistry on desalination dynamics. Hydrogen terminated pores showed higher water selectivity, and hydroxyl groups functionalized pores enhanced the water transport rate. Moreover, another effect of hydroxyl groups' functionalization is lowering salt rejection due to the replacement of water molecules by hydroxyl groups, thus, allowing more salt ions to pass [15]. Crock et al. integrated metallic nanoparticles into the membrane matrix. Graphene nanoplatelets decorated with gold (Au) nanoparticles were used in the preparation of polysulfone (PSF) nanocomposite membrane. It was found that Au loading controlled membrane reactivity, while graphene loading controlled membrane structure. The flux was found to increase linearly with an increase in Au loading, but was found to be independent of graphene loading [17].

Several techniques, such as exposure to electron beam, ultraviolet-induced oxidative etching, diblock copolymer templating, and helium ion beam drilling [15,18–23], have been used to create nanopores in graphene layers that generally include high-energy impact to dislocate thousands of carbon atoms from the graphene lattice by using an energy above the carbon knockout potential (80 kV) [24]. Fine control of pore sizes in subnanometer range on a large surface area of graphene is challenging. Nanopores of controlled pore size can be created in graphene using focused electron beam irradiation as shown in Table 1. The limitation of this technique is that large areas of high pore densities cannot be formed by this technique; alternatively, chemical, or oxidative etching is used for larger surface areas [18,27]. The drawback of the later techniques is the heterogeneous nature of defects associated with using this technique, which makes controlling pore size distribution challenging [30]. Moreover, chemical techniques such as oxidative etching need careful control and might leave residues on the membrane. Using an electron beam that has a very high energy to form nanopores causes significant enlargement to pore sizes and damage to graphene around the nanopores; resulting in adverse effects on the mechanical properties of nanoporous graphene (NPG) [31]. O'Hern et al. utilized low energy ion beams and chemical oxidation etching to form nanopores in graphene having a size distribution of 0.2 nm; the membrane obtained by using this method showed either rejection of anions when oxidation time was short or rejection of organic dyes when oxidation time was long. This method was the best approach because it yielded well-defined pore size distribution in addition to scalability. However, the drawback of this technique is the damage and defects that could form in the graphene

Table 1 Several Methods for Nanopore Creation in Graphene Reported in Literature

Method	Pore Size (nm)	Reference
Focused electron beam	0.7 5–23	[25] [21]
Focused electron beam using TEM	2–5	[26]
Nitrogen-assisted electron beam irradiation	5.9 ± 0.4	[24]
Block copolymer lithography and plasma etching	$>5 \pm 2$	[27]
Oxygen plasma treatment	0.5–1	[28]
UV oxidative etching	0.4–10	[18]
Controlled dielectric breakdown	2	[29]
Low energy ion beam and chemical oxidation	0.4 ± 0.2	[19]

sheet [19]. As a result, producing a large-area, damage-free single layer graphene on a porous support is the next challenge to be addressed, taking into account both the economic and technical implications. Table 1 summarizes some methods for nanopores creation reported in the literature.

2.2 STACKED GO MEMBRANES

One other alternative to graphene-based water separation is based on stacked GO membranes, as GO sheets are cheaper and easier to produce on large scale than NPG. Water passes between GO layers via the narrow hydrophobic channels formed by the unoxidized regions on GO [32]. The primary rejection mechanism of ions and molecules is size exclusion. Other mechanisms of rejection are electrostatic interaction and adsorption of ionic species on GO sheets. When GO nanosheets are submerged in an ionic solution, hydration takes place, and the interspacing between the sheets increases from approximately 3 to 9 Å. Thus, water flux increases, but the selectivity of membrane decreases [33,34]. Moreover, another factor that determines the interspacing distance between the sheets is electrostatic the interactions between the charged oxygen-containing functional groups of GO. Increasing ionic strength and pH changes the surface charge of GO, thus, affecting the interspacing distance. In one study, water permeability for GO membranes was found to be 12.2, 71.0, and 18.9 L/m^2.h.bar at pH 3, 6 and 12, respectively [35]. The main challenge when GO membranes are used is the instability of the nanochannels formed by stacking GO sheets, which affects membrane selectivity. Two possible approaches to counter the interspacing distance expansion are by: (i) using rGO, which increases π-π interactions between the sheets, and thus enables the nanosheets to be in closer proximity to allow for the filtration of small hydration radius such as K^+ (0.53 nm), and (ii) using charged species such as charged polymers and nanowires between GO to stabilize the GO by electrostatic attraction, as well as creating covalent bonds between nanosheets by crosslinking using chemical groups; these covalent bonds can counter the unavoidable effect of hydration forces [34].

Many techniques have been followed to fabricate GO nanosheets such as vacuum filtration, layer-by-layer deposition, drop casting, and spin coating [34]. Membranes fabricated by vacuum filtration often have weak bonding between nanosheets; layer-by-layer deposition and drop-casting methods are often more cost effective and scalable. Moreover, membranes fabricated by the aforementioned methods normally have more stable covalent bonds between GO interlayers. Layer-by-layer deposition provides more control over the GO layer thickness and channel width [34].

Stacked GO membranes are an alternative to NPG due to the previously mentioned technical and economic challenges associated with the production of NPG, as opposed to scalability and the relatively inexpensive price of GO membranes. GO membranes, on the other hand, are more brittle than single-layer NPG. To overcome this problem, a highly porous support layer has been proposed in previous studies [16,35]. Hu and Mi prepared a water filtration membrane with layered GO nanosheets on polydopamine coated PSF support with 1,3,5-benzenetricarbonyl trichloride as crosslinkers [11]. Furthermore, ultra-stiff GO thin films can be formed by crosslinking GO with borate; it was reported that adding 0.94 wt% boron to the final composite of GO film enhances stiffness by over 25.5%. This can be justified by the formation of covalent bonds between borate ions and hydroxyl groups on GO nanosheets [36].

GO laminates can be stacked on top of each other to form a single membrane that has millions of nanocapillaries. Smaller ions can move very fast through the membrane, which is an effect called "ion sponging." Ion sponging allows smaller ions to move faster than their normal movement due to

diffusion mechanism because of the presence of nanocapillaries [37]. Ion sponging is independent of the charge of the ion, as it only depends on the hydrated radii of the species. Hydrated ions with a radius larger than 4.5 Å are retained by stacked GO membranes. This method is not suitable for seawater desalination because the GO mesh should be reduced from 9 to 6 Å to be able to retain the fine salts in seawater [37]. GO sieving is a proposed novel method that has not been applied yet due to the required improvements for sieve because the mesh size of the GO sieve is not small enough to filter out small seawater ions [37].

2.3 CAPACITIVE DEIONIZATION ELECTRODES

Capacitive deionization (CDI) based on electrosorption has been addressed as an environmentally friendly desalination technique when compared to other conventional technologies of membrane separation and thermal distillation. CDI is an electrochemically controlled method based on electric double-layer capacitors (EDLCs). The charged ions can be adsorbed onto the surface or the pores of porous electrodes to form EDLCs when an external voltage is applied; ions can be released from the electrodes when the charge is removed or reversed. Graphene is one of the most promising CDI electrode materials with good salt removal ability due to its high theoretical specific surface area, good electrical conductivity, and controllable morphology structure.

Graphene nanosheets were first employed by many researchers, among whom were Li and his colleagues' group. Graphene was fabricated by a modified Hummer's method and a hydrazine reduction process. The initial attempt resulted in relatively low Na^+ electrosorption capacity (1.85 mg/g) due to aggregation of graphene nanosheets, which resulted from the relatively low surface area (14.2 m^2/g). Aggregation and restacking of graphene is due to the strong π-π interactions and van der Waals forces between the planar basal planes of graphene sheets. Li et al. proposed that electrosrption of NaCl onto graphene electrodes is caused by a physisorption process, and they took into account the thermodynamic parameters [38]. Li et al. synthesized graphene-like nanoflakes that had a surface area of 222.01 m^2/g. Graphene-like materials had an interlayer structure that is more accessible for ions, while activated carbon had a large fraction of inaccessible micropores. Salt adsorption capacity for graphene-like nanoflakes was reported to be 1.35 mg/g for Na^+ in NaCl solution that had a conductivity of 55 μS/cm at 1.2 V. This reported adsorption capacity outweighs that reported for activated carbon under the same experimental conditions. It is true that activated carbon had a larger surface area due to the presence of micropores, and thus, should intuitively provide more adsorption sites; however, the presence of dead pores and the lack of interconnected network decrease the adsorption capacity on activated carbon [39].

From the discussion above, it is clear that the salt adsorption capacity of graphene nanosheets is not satisfactory for lack of pores in the graphene nanosheets. However, despite the lower surface area of graphene nanosheets electrodes when compared to activated carbon electrodes, graphene nanosheets demonstrated higher electrosorption capacity due to the interlayer structure of graphene that is more accessible to ions than the small micropores of activated carbon. These results suggested the potential of graphene for CDI applications, with the condition that the surface area of the graphene-based electrode should be increased to yield a higher salt adsorption.

Fabricating interconnected electrode materials with a high specific surface area and porous structure has been the focus of many recent studies. These graphene-based macrostructures with 3D porous networks include aerogels, hydrogels, foams, frameworks, and sponges. These 3D graphene materials,

consisting of micro-, meso-, and macroporous networks, can provide high surface area and fast ion/electron transport [38]. Pan et al. fabricated a novel graphene sponge that displays a porous structure with a surface area of 356 m^2/g and a pore volume of 1.51 cm^3/g. The resulting electrosorption capacity was 14.0 mg/g when initial NaCl concentration was ~500 ppm and voltage applied was 1.2 V; the high capacity is attributed to the unique 3D interconnected porous structure, large surface area, and low charge transfer resistance [40]. Lee et al. introduced ion exchange membranes positioned between a pair of electrodes, which allowed improvement of charge efficiency and salt storage capacity [41]. Many studies have targeted introducing modifications on the electrode materials including graphene, CNTs, and others, and introduced novel cell architectures. In a very recent study, Cho et al. created a novel 3D desalination system from a honeycomb-shaped porous substrate by coating an ion exchange membrane and a graphene layer within the channels. This new architecture provides many advantages over the conventional alternatives. The size of this cell is much smaller than the conventional CDI cells. Furthermore, all the components needed to construct the new desalination cell are cost-effective. Scaling up of such 3D cells is a much simpler process than for conventional CDI stacks. Moreover, this cell allows flexible tunability of the cell design, and no pressure increase in feed water is generated [42].

Graphene-based composites have also been employed for the development of CDI cell electrodes. Li et al. synthesized rGO and activated carbon composite for the capacitive removal of salt ions from brackish water. The electrosorption capacity of the composite electrode was 2.94 mg/g in a NaCl solution with an initial conductivity of 0.1 mS/cm at 1.2 V [43]. Composites of graphene-based materials and metal oxides have also been tested for CDI. Tang et al. fabricated 3D graphene aerogel/metal oxide (including TiO_2, CeO_2, Fe_2O_3, and Mn_3O_4 nanoparticle hybrids). The incorporation of metal oxide remarkably improved the capacitance of graphene-based materials, and a high specific capacitance of graphene aerogel/TiO_2 composite was obtained. The reported electro-adsorption capacity of graphene aerogel/TiO_2 reached to 15.1 mg/g in NaCl solution with an initial conductivity of 500 ppm at an applied voltage of 1.2 V [38]. Furthermore, nitrogen-doped graphene and functionalized graphene have also been investigated in the literature. Table 2 illustrates some graphene-based materials used in CDI.

Table 2 Examples of Some Graphene-Based Materials Used to Construct CDI Electrodes in Previous Studies

Materials	N_2 (%)	Surface Area (m^2/g)	Applied Voltage (V)	Initial NaCl Conc.	Salt Adsorption Capacity (mg/g)	Reference
Holey graphene hydrogel	–	1261.7	1.2	500 ppm	16.0	[44]
Three-dimensional graphene	–	2680	1.4	300 ppm	14.08	[45]
Graphene sponge	–	356.0	1.2	500 ppm	14.9	[40]
Microporous graphene	–	3513	2.0	160 μS/cm	11.86	[46]
rGO-activated carbon	–	779	1.2	100 μS/cm	2.94	[38]
rGO-Fe_3O_4	–	150.8	1.2	500 μS/cm	8.33	[47]
Graphene-chitosan-Mn_3O_4	–	240	1.6	300 μS/cm	12.7	[38]
Polypyrrole-MnO_2	–	331	2.0	600 μS/cm	12.5	[48]

Table 2 Examples of Some Graphene-Based Materials Used to Construct CDI Electrodes in Previous Studies—cont'd

Materials		N_2 (%)	Surface Area (m^2/g)	Applied Voltage (V)	Initial NaCl Conc.	Salt Adsorption Capacity (mg/g)	Reference
Graphene aerogel/TiO_2		–	187.60	1.2	600 ppm	24.2	[38]
N_2-doped materials							
Nitrogen-doped graphene	Doping by thermal treatment in ammonia atmosphere	10.8	352.0	2.0	1000 μS/cm	21.9	[49]
Nitrogen-doped rGO-carbon nanofiber composite	Doping by thermal treatment in ammonia atmosphere	8.3	864.1	1.2	100 μS/cm	3.9	[50]
Three-dimensional rGO-melamine formaldehyde composite	Doping by carbonization with melamine formaldehyde	10.8	352.0	2.0	1000 μS/cm	21.9	[38]

3 GRAPHENE FOR CONTAMINANTS ADSORPTION

3.1 ADSORPTION OF INORGANIC CONTAMINANTS

Graphene-based nanomaterials have been reported for the removal of inorganic pollutants such as heavy metals cations, radionuclide, and anionic pollutants. The removal mechansim of inorganic pollutants on graphene-based materials is attributed to physical adsorption, electrostatic interaction, precipitation, and chemical interaction between the ions and surface functional groups of these materials [3]. Haung et al. tested sorption of Pb(II) on pristine graphene nanosheets (GNSs) and thermally modified GNSs. It was found that the sorption of Pb(II) was enhanced by heat treatment when compared to prostine GNSs due to increasing Lewis basicity and elctrocstatic attraction of graphene [51]. However, graphene-based adsorbents possess hydrophobicity, which reduces the adsorption of metal cations; thus, Song et al. synthesized polyphenols functionalized GNSs to avoid the aforementioned drawback. Tea polyphenols functionalized GNSs have advantages that include water solubility, low toxicity, and biodegradability. It was reported that functionalized GNSs by tea polyphenols had Pb (II) sorption capacity of 1126 mg/g [52]. The use of graphene with magnetic nanoparticles composites is very common in the removal of metal cations. Despite the high adsorption capacity and magnetic property of iron oxide nanoparticles, their application in continuous flow systems is not practical due to their small size and potential to oxidation and dissolution [53].

The adsorption capacity of GO is influenced by many factors such as ionic strength, pH, and number of oxygen-cotaining groups [54]. Sitko et al. reported that the maximum adsorption capacities of Cu(II), Zn(II), Cd(II), and Pb(II) at pH 5 were 294, 345, 530, and 1119 mg/g, respectively [54]. Moreover, Zhao et al. studied the removal of Cd(II) and Co(II) from aquous solutions using GO; they found that adsorption efficiencies were 106.3 mg/g for Cd(II) and 68.2 mg/g for Co(II) [55]. The adsortion of metal ions by GO is highly dependent on pH. When the solution pH is higher than the point of zero charge pH (pH_{pzc}), GO surface is negatively charged due to the deprotonation of oxygen-containing functional groups. Thus, electrostatic interaction with positively charged metal ions become favorable, which enhances adsorption capacity. In contast, when the $pH < pH_{pzc}$, GO becomes positively charged and electrostatic interactions are weakedned due to repulsion [54]. Not only does electrostatic interaction between the oxygenated functional groups of GO and metal cations contribute to metal adsorption, but also, Huang et al. suggested another mechanim. It was suggested that the delocalized π-electrons in the sp^2 network of graphene can act as Lewis bases that donate electrons to the positively charged metal ions [51,56]. The adsorption of heavy metal ions on few-layered (FGO) was reported to be mainly domainated by strong inner-sphere surface complexation rather than outer surface complexation [56]. Moreover, it was reported by Sun et al. that Eu(III) was bound to six to seven oxygen atoms at a bond distance of ~2.44 Å in the first coordination shell indicating the formation of inner sphere complexation on FGO [57].

Graphene-based materials have also been reported to be efficient in removing anionic pollutants such as phosphate (PO_4^{3-}), fluoride (F^-), and perchlorate (ClO_4^-) [58–61]. The mechanism of adsorption of anions on graphene-based materials is mainly attributed to anion-π interactions, which take place due to the interaction between the anion with an electron-deficient aromtic ring on graphene layer [61]. Table 3 shows a summary of examples of inorganics adsorption.

Table 3 Graphene-Based Materials for Inorganics Adsorption

Graphene-Based Material	Adsorbate	Q_e (mg/g)	Reference
GNS	Pb(II)	22.42	[51]
Heat-treated at 500°C GNS	Pb(II)	35.21	[51]
Heat-treated at 700°C GNS	Pb(II)	35.46	[51]
GO	U(VI)	299	[62]
GO	Cu(II) Zn(II) Cd(II) Pb(II)	294 345 530 1119	[54]
GO	Cu(II)	117.5	[63]
Few-layered GO	Pb(II)	842	[56]
δ-MnO_2-graphene composite	Ni(II)	46.6	[64]
Magnetite rGO	As(III)	13.10	[65]
Graphene	F^-	17.65	[58]
Graphene	PO_4^{3-}	89.37	[59]

3.2 ADSORPTION OF ORGANIC CONTAMINANTS

Graphene-based materials have been used as adsorbents to remove organic contaminants such as dyes, antibiotics, hydrocarbons, and natural organic matter from water. The mechanisms of removal of organic pollutants are π-π interactions, anion-π interaction, cation-π interaction, electrostatic interactions, hydrogen bonds, anion-cation interactions, and interactions with functional groups. Graphene and GO have been found to be effective in anionic and cationic dye removal; the mechansim was described to be by electrostatic and van der Waals interactions depending on the case [66]. Electrostatic interaction is dominant when the adsorbate has charged functional groups, while the adsorbents maintain their charged surface. The adsorption of cationic dyes such as methylene blue and methyl violet by GO over a pH range 6–10 is attributed to electrostatic interactions between GO and the dye molecules. On the other hand, adsorption of anionic dyes such as orange G by GO was not favorable due to the repulsion between the negatively charged functional groups and the dye molecules [66]. Moreover, few studies suggested that the adsorption of cationic dyes is also attributed to π-π interactions [67]. 3D GO sponges were found to be effiecient in the removal of methylene blue and methyl violet; the predominant mechansim for this process was described to be π-π stacking and anion-cation interaction [67]. Furthermore, spongy graphene showed a higher efficiency in the removal of petroleum products than conventional adsorption methods in addition to its capacity for being regenerated (>10 times) by heat treatment, yielding almost complete release of adsorbates. It has been found that as the oxidation degree for graphene-based materials increases, the mechanism of adsorption is presumed to change from π-π stacking to electrostatic interactions [3].

The use of rGO-based materials did not increase the adsorption efficiency of cationic dyes, but increased the adsorption of anionic dyes. In addition to electrostatic interactions, the major mechanism of adsorption was found to be van der Waals interactions between aromatic rings and both adsorbate and adsorbent [66]. Li et al. synthesized $Mg(OH)_2$-rGO composite and tested its efficiency in adsorption of methylene blue. The composite exhibited excellent efficiency in methylene blue removal, and could be recycled without a significant decrease in adsorption efficiency [68]. As mentioned earlier, in addition to dye removal from water, graphene-based materials were used for the removal of other organic contaminants. The mechanism of tetracycline removal by GO was found to be via π-π interaction and cation-π bonding [69]. Xu et al. employed graphene for Bisphenol A removal, and the mechanism of removal was ascribed to be π-π intercations and hydrogen bonds formation [70]. Hydrogen bonding plays an important role when the species involved in adsorption have functional groups such as amine and hyroxyl groups. As a result, hydrogen bonding contributes to adsorption of polar hydrocarbons such as napthanol by GO-based materials. Hydrophobic interactions, on the other hand, contribute to the adsorption of non-polar hydrocarbons such as napthalene on rGO or pristine graphene sheets because their surfaces are more hydrohphobic than GO [7]. Table 4 shows examples of adsorption of organics by graphene-based materials.

4 GRAPHENE FOR DISINFECTION

The control of bacterial growth is a challenging task in many environmental applications. The formation of biofilm is a critical hurdle for efficient operation of, for example, membrane-based water

Table 4 Graphene-Based Materials for Organics Adsorption

Graphene-Based Material	Adsorbate	Q_e (mg/g)	Reference
GO-Fe_3O_4-SiO_2	Methylene blue	111.1	[71]
GO-FeO-Fe_2O_3	Napthalene	2.63	[72]
GO	Methylene blue	714	[7]
	Oxytretracycline	212.31	[69]
	PCB-52 (2,2′,5,5′-tetrachlorobiphenyl)	0.87 ± 0.83	[73]
	Tetracycline antibiotics	313	[69]
Graphene	Methylene blue	153.85	[74]
Sulfonated graphene	Naphthalene	297	[75]
	1-Naphthol	6.4	[76]
rGO	Bisphenol A	181.81	[70]
	Orange G	5.98	[66]
Magnetic chitosan-GO	Methyl blue	95.16	[77]
Magnetic graphene	Organic dye fuchsine	89.4	[78]

treatment and purification technologies, as well as heat exchangers in industrial applications. The antimicrobial effect of graphene-based materials is attributed to cell walls breaking by direct contact or photo-induced degradation. Bacterial inactivation by graphene-based nanomaterials may involve direct puncture of the cell membrane, production of reactive oxygen species (ROS), adhesion of graphene sheets on bacterial cell surfaces, and extraction of phospholipids from the lipid bilayer [7]. Graphene sheets can penetrate into the lipid bilayer; larger and more oxidized graphene sheets were found to penetrate more easily into the lipid bilayer due to lower energy state associated to an oxidized graphene sheet penetrating into the membrane [79]. Moreover, generation of ROS, or oxidative stress, is also a mechanism of antibacterial activity; oxidative stress is usually found to be higher in cells exposed to GO when compared to rGO due to the colloidal stability of GO. Moreover, the high density of defects on GO sheets also plays a factor in the generation of ROS. That is, generation of ROS was found to be mediated by the adsorption of O_2 on the defect sites and edges [7].

Graphene nanomaterials have been utilized for the synthesis of antimicrobial nanocomposites with enhanced antimicrobial activity. Phosphonium salts, polymers, metals, semiconductors, and metal nanoparticles are examples of materials that have been used in previous studies to be attached to graphene-based nanomaterials to enhance their antimicrobial activity. That is, graphene can also be used as a support to disperse and stabilize various nanomaterials leading to high antibacterial activity due to a synergistic effect. CdS/GNs composite showed excellent antimicrobial activity in the photocatalytic disinfection of water; *E. coli* and *B. subtilis* were removed by ~90%–100% after 10 min treatment [80]. Silver (Ag) is the most extensively studied material for graphene-based antimicrobial nanocomposites. The released Ag ions can destroy bacterial cell membranes and penetrate the cells to inactivate enzymes; however, Ag-NPs alone aggregate when in contact with bacteria, and hence, lose their active surface area. To overcome this challenge, nanocomposites consisting of Ag and graphene have been synthesized and investigated for antimicrobial activity. Similarly, copper (Cu) is also an efficient inexpensive antibacterial agent; however, Cu cannot be used alone due to agglomeration. Alternatively, rGO-Cu hybrid was prepared by anchoring AuNPs on poly-L-lysine-modified rGO. The novel nanocomposite exhibited efficient antimicrobial effect in addition to remarkable water solubility

[81]. Akhavan et al. studied the increased efficiency of graphene in the photo-inactivation of *E. coli* under solar irradiation using rGO-TiO_2 thin films. After 4 h of exposure to UV, rGO-TiO_2 showed the 7.5-fold higher antibacterial activity than pure TiO_2 films [82]. It has been found that, even in the absence of a light source, Ag on crumpled GO-TiO_2 and AgNP/GO showed excellent ability in the inactivation of *E. coli*, *B. subtilis*, and *S. aureus* in water with reduction percentage in the range of 87.6%–100% [83,84]. In addition to 2D graphene structures, 3D structured graphene hydrogels have also been used in disinfection. An Ag/rGO hydrogel-based bacterial filter has been developed for water disinfection analysis through the use of lake and creek water containing *E. coli*. The efficiency of *E. coli* inactivation of up to a range of 94%–98% was reported [85]. Furthermore, graphene-based composite materials have been utilized as antibacterial surface coating. Blending GO sheets in a polymer polyvinyl-*N*-carbazole (PVK) leads to high bacterial inactivation using only 3% of the amount of graphene needed for the same antimicrobial efficiency; thus, using this type of nanocomposite reduces costs and environmental impact associated with the use of graphene. PVK-graphene composite coating was found to inactivate bacterial cells and reduce biofouling [7]. Table 5 summarizes some cases of using graphene-based materials for disinfection.

The antibacterial mechanism of graphene has not been completely understood. For example, identification of the determinant factor in graphene's antibacterial activity is still under research; the questions of whether physical or chemical factors, the edges, or basal planes contribute the most have not been answered yet [81]. Moreover, more computational simulations should be introduced to investigate and analyze the interactions between graphene-based materials and biosystems. Future work should also address developing more innovative functionalized graphene and graphene-based hybrids with desirable properties to overcome the current shortcomings; for example, novel nanocomposites should be synthesized with better dispersibility in Biosystems, as the main limitation of graphene-based materials is their tendency to agglomerate due to their high surface energies, which can reduce their antimicrobial activities by altering their surface and edge properties. More factors such as experimental conditions (i.e., pH), and potential impurities should be considered. When studying the effect of one factor, such as the lateral size of graphene-based materials, other factors, such as the degree of oxidation, should be controlled.

5 GRAPHENE-BASED MATERIALS FOR CATALYTIC, PHOTOCATALYTIC, ELECTROCATALYTIC, AND ELECTROPHOTOCATALYTIC OXIDATIVE DEGRADATION OF CONTAMINANTS

5.1 GRAPHENE-BASED MATERIALS FOR CATALYTIC OXIDATIVE DEGRADATION OF ORGANIC CONTAMINANTS

Graphene-based materials are widely used as catalysts for organic compound removal. They act as adsorbent materials for organic contamination and activate the oxidizing agent (such as H_2O_2 and ozone). Xu et al. employed graphene-$CoFe_2O_4$ composite to activate peroxymonosulfate (PMS) to degrade dimethyl phthalate (DMP), and it was found that the composite yielded a higher efficiency than the stand-alone $CoFe_2O_4$ alloy [92]. The active sites on graphene-based materials can be attributed to oxygen-containing active sites, catalytic activity of periphery, carbon vacancies, and even the basal plane, or doping [93]. A study conducted on graphene-$CoFe_2O_4$ showed that the composite acts as

Table 5 A Summary of Some Examples of Graphene-Based Materials Used for Disinfection

Graphene-Based Materials and Composites	Conc.	Species	% Removal	Irradiation Type	Direct Contact Time	Mechanism	Reference
Graphene oxide nanowells (GONWs)	–	*E. coli* *S. aureus*	74 59	–	1 h	Direct puncture by cell membrane	[86]
Reduced graphene oxide nanowells (RGONWs)	–	*E. coli* *S. aureus*	84 95	–	1 h	Direct puncture by cell membrane	[86]
GO functionalized with ethylenediamine triacetic acid (GO-EDTA)	1000 μg/L	*C. metallidurans* *B. subtilis*	99.1 92.3	–	3 h	Induction of oxidative stress in the bacterial cells	[87]
TiO_2/graphene sheet nanocomposites	4.2 wt% graphene 1.4 wt% graphene 7 wt% graphene Pure TiO_2	*E. coli*	90.5 75.2 63.3 8.8	Visible light	12 h	Prolonged light absorption, which enhances charge separation, and involves hydroxyl and super oxide radicals	[88]

TiO_2/graphene sheet nanocomposites	4.2 wt% graphene	*E. coli*	No antibacterial activity	No light	12 h	–	[88]
Polyelectrolyte-stabilized reduced graphene oxide sheets on a quartz substrate thin film (PEL-rGO LBL)	–	*E. coli* *B. subtilis*	>90% >90%	Solar irradiation	12 min	Solar radiation in the near-infrared region generates rapid localized heating on the multilayer	[89]
GO-TiO_2-Ag	100 µg/L	*E. coli*	~100%	Visible light	–	Synergistic effect of cell membrane disrupting properties of graphene, which allows for the penetration of silver ions leached from the nanoparticles, in addition to TiO_2 disinfection mechanism	[90,91]

a supporting material to enhance adsorption of DMP rather than the catalyst. DMP is desorbed by PMS ions and DMP is degraded by $OH^{\bullet}$ and $SO_4^{\bullet}$ radicals [92]. Magnetic $MnFe_2O_4$-rGO composites have also been employed to activate PMS for the degradation of dye molecules; the nanocomposite showed a Fenton-like activity [94]. Manganese/magnetite/graphene oxide (Mn-MGO) was also reported to activate PMS to generate sulfide radicals for the removal of bisphenol A from water; GO functioned as a platform to immobilize the composite and provide better dispersibility in aqueous solutions. PMS activation is due to electron transfer from MnO_2 or Mn_2O_3 to PMS with the generation of sulfide radicals, protons, and MnO_2, in addition to reduction of MnO_2 by PMS simultaneously [95]. Zent el al. employed doped graphene to serve as a support for the advanced oxidation processes (AOPs) to activate PMS for the degradation of organic pollutants; the doped material fabricated was a heterogeneous sulfate radical-based advanced oxidation (SR-AOPs) catalyst with Co nanoparticles embedded in nitrogen-doped rGO matrix (NRGO-Co) [96]. Li et al. used rGO for the transformation of 1,4-hydroquinone to 1,4-benzoquinone. rGO was capable of oxidizing 76% of 1,4-hydroquinone without adding any oxidizing agents. The proposed mechanism suggests that dissolved oxygen reacts with rGO to generate molecular oxygen intermediates, which entrap hydrogen ions from 1,4-hydroquinone to produce semiquinone radicals. The latter radicals transfer an electron to oxygen intermediates to generate superoxide radicals (O^{2-}), which in turn react with 1,4-hydroquinone to generate O^{2-} and H_2O_2 [97].

5.2 GRAPHENE-BASED MATERIALS FOR PHOTOCATALYTIC OXIDATIVE DEGRADATION OF ORGANIC CONTAMINANTS

One of the characteristics that widens the applications of graphene-based materials is their electron acceptor and transport properties. That is, they are endowed with high photocatalytic properties due to their capability of generating electron-hole pair in the presence of a source of irradiation. TiO_2, in specific, is widely used in graphene-based photocatalytic nanocomposites due to its low cost and strong oxidizing activity. rGO decorated with TiO_2 nanotubes (rGO-TNT) were synthesized and employed by Perera et al. for the photodegradation of malachite green dye; the study found that the performance at the optimum rGO/TNT ratio was three times higher compared to using pure TiO_2 [98]. The mechanism by which graphene-TiO_2 composites yield high degradation efficiency is through a three-step process: (i) dye molecules are adsorbed on graphene by π-π stacking interactions, (ii) electrons on valence band are excited to the conduction band of TiO_2 nanoparticles upon irradiation with UV or visible light; these electrons can travel through the sp^2-hybridized network of graphene sheets, (iii) ROS are generated due to electron transfer to O_2; ROS trigger degradation of organic matter [98,99]. However, a study conducted by Xiong et al. resulted in different findings; the study found that excitation of rhodamine B dye molecules under visible light had led to photodegradation. That is, electrons transfer to GO surface and are conducted to the semiconductor nanoparticles [100]. Hierarchically ordered macro-mesoporous TiO_2-graphene composite films were tested in the removal of methylene blue, and it was found that the employment of 3D materials improved the photocatalytic performance when compared to 2D hexagonal TiO_2 mesoporous films because 3D materials provided open channels and improved surface area [7]. Graphene-based materials were also used for the reduction of heavy metals by photocatalysis. A nanocomposite of graphene sheets and ZnO nanoparticles was used to reduce Cr(VI); photocatalytic reduction was enhanced from 58% when ZnO was used solely to 98% when the nanocomposite was utilized. Cr(VI) was reduced under UV light by the

Table 6 Graphene-Based Materials for the Photocatalytic Degradation of Organic Contaminants

Graphene-Based Material	Organic Contaminant	% Removal	Irradiation	Remarks	Reference
TiO_2/MCM-41/graphene	2-Propanol	100%	UV light	–	[102]
GO/Bi_2MoO_6	Red X-3B dye Phenol	>90% >90%	Visible light	High loading of GO does not favor the photodegradation of Red X-3B dye	[103]
rGO/chitosan/Ag hydrogel	Methylene blue Rhodamine B	100% 90%	UV light	Efficient photocatalytic activity due to the presence of silver nanoparticles on rGO sheets, and chitosan functioned as a gelation medium	[104]
Graphene/CeO_2/TiO_2	Reactive Red 195 2,4-Dichlorophenoxyacetic	90% 67%	UV light	The composite exhibited higher removal than CNTs/CeO_2/TiO_2. The photocatalytic activity of the composite decreased as graphene content increased	[105]
Ag/rGO/TiO_2 nanotubes	2,4-Dichlorophenoxy acetic acid (herbicide)	97.3%	Solar light	–	[106]
Fe-doped TiO_2 nanowire/graphene	17β-estradiol (endocrine disrupting hormone)	95%	Solar irradiation	–	[107]

reduction of electron-hole pair recombination with the presence of graphene sheets in addition to the increased light adsorption intensity and range [101]. Table 6 shows a summary of some examples of photocatalytic degradation reported in the literature.

5.3 GRAPHENE-BASED MATERIALS FOR ELECTROCATALYTIC AND PHOTOELECTROCATALYTIC OXIDATIVE DEGRADATION OF ORGANIC CONTAMINANTS

Many graphene-based materials have been successfully utilized to function as an electrocatalysts for the oxidative degradation of organic contaminants. Electro-active oxidants are generated using

graphene-based materials modified electrodes for the degradation of various organic contaminants. The electrocatalytic oxidative degradation can be used as an alternative to photocatalytic degradation. As have been discussed, electron-hole pairs are generated when voltage is applied in electrocatalysis. Zhai el al. prepared rGO/TiO_2/carbon cloth (rGO/TiO_2/CC) electrodes for the degradation of methylene blue. The prepared electrode showed up to 15.6% degradation of methylene blue upon applying 0.9 V for 160 min. Under the same conditions, rGO/TiO_2/CC showed 26.2% photodegradation of methylene blue in visible light, and the combined photocatalytic and electrocatalytic showed 41.8% degradation of the organic dye. Thus, photoelectrocatalytic degradation method showed the highest removal among the three tested configurations [108]. Zhang et al. prepared anthraquinone and rGO nanocomposite cathodes (AQ/rGO) and used them for the degradation of rhodamine B in N_2 and O_2 saturated solution. AQ/rGO in saturated N_2 solution and AQ/rGO in O_2 saturated solution systems in 0.5 M Na_2SO_4 and $MgSO_4$ solutions showed 12% degradation of rhodamine B. AQ/rGO composite completely removed rhodamine B when FeOOH/γ-Al_2O_3 was used as a catalyst in electrolytic solutions with the same concentrations of Na_2SO_4 and $MgSO_4$. The significantly enhanced removal is attributed to the high activity of FeOOH nanoparticles and their ability to convert the electrogenerated H_2O_2 into oxidative radicals [7].

As has been discussed, electrophotocatalysis is an emerging promising technology for water treatment. Yang et al. prepared TiO_2/graphene/Cu_2O mesh for the photoelectrocatalytic degradation of bisphenol A under visible light irradiation. The composite exhibited 64% degradation of Bisphenol A under visible light. The synthesized material's high performance is due to the high conductive and interconnected 3D channels inside the nanocomposite mesh [109]. To improve the degradation, 50 mM H_2O_2 was poured into a reactor, and the reaction was conducted under similar conditions; degradation of Bisphenol increased to 92% in 250 min. Complete degradation took place under UV light [109]. Zhai et al. prepared rGO modified TiO_2 nanotube arrays (rGO-TNTs) for the electrophotocatalytic degradation of methyl orange in the presence of visible light; rGO/TNTs exhibited 30% removal of the dye with a bias potential of 1.0 V under visible light [7].

6 ECOTOXICOLOGICAL EFFECTS OF GRAPHENE-BASED MATERIALS

Because of the wide range applications of graphene-based materials, large-scale production is expected, which necessitates the study of their fate in the environment and their potential impact. The fate of these materials is, in certain cases, unknown, and they could eventually end up in water treatment systems, which has adverse effects on the microbial community. It was found that GO exposure in the range of 10–300 ppm on a wastewater microbial community significantly compromises its metabolic activity, and negatively affects the effluent quality and sludge dewaterability [110]. A study investigated the effect of different concentrations (0 to 1000 ppm) of GO on the viability and activity of *P. putida*, assuming that the species is a simplified model of an activated sludge biotreatment microbial community; the growth of *P. putida* was inhibited by the presence of GO concentrations higher than 50 ppm [111]. GO presence in wastewater adversely affects the microbial communities in wastewater systems due to the production of ROS, which in turn, increases toxicity and inhibits essential biological functions of bacteria including biodegradation, nitrogen removal, and phosphorus accumulation in activated sludge processes. Interestingly, despite the fact that GO inhibits ammonia oxidizing bacteria (AOB), it can enhance the activity of anammox bacteria for nitrogen

removal; thus, graphene-based materials' effect depends on the type of functional microorganisms present [112].

Almost all soil systems are very complex, and soil is an important sink for nanomaterials after their release into the environment. Graphene-based materials' release into soil causes interactions; however, graphene-based materials' fate and transport in soil systems needs to be investigated further to fill this knowledge gap [113]. Graphene-based materials studies on terrestrial ecosystems have led to conflicting results. A study investigated evaluating the antibacterial actions of monolayer graphene film on conductor Cu, semiconductor Ge, and insulator SiO_2. The study used *S. aureus* and *E. coli* to evaluate the antibacterial action. SiO_2-containing surfaces showed no antibacterial activity, in contrast to Cu- and Ge-containing surfaces which induced the disruption of both species cell membranes. The suggested explanation links the toxicity to the conductivity of the soil components. It was proposed that the membrane electrons were extracted by the graphene, which caused bacterial death [114]. This finding was refuted in a more recent study that explored the potential toxicity of chemical vapor deposited (CVD) graphene on conductive substrate of Au and Cu; the study resulted in no antibacterial activity for either of the two bacterial species [115]. Du el al. investigated the changes of bacterial communities in soil after aging for 90 days; the study found that the diversity of soil bacterial communities increased after the introduction of pristine GO. Interestingly, pristine GO was linked to the selective enriching of some nitrogen-fixing bacteria genera such as *Azospirillum*. Furthermore, some changes occurred in pristine GO properties in soil including surface morphology, chemical groups, and charges; however, a detailed explanation for the internal changes was not clear [116].

Another toxicity aspect that should be taken into consideration is in the raw materials used to fabricate graphene-based materials. For instance, the most common reducing agents used to produce graphene are highly toxic and explosive such as hydrate hydrazine, hydroquinone, and $NaBH_4$. Therefore, many attempts have been made to develop green reductants including urea, metal powders, sugar, vitamin C, and alcohol. Although great achievements have been made, the reduction efficiency and exfoliation degree may be compromised, in addition to the complexity of the reducing process. Hence, a more feasible and environmentally friendly chemical reduction approach should be the aim of future research [38]. Despite the fact that many studies have been conducted to evaluate the ecotoxicological effects of graphene-based materials, there is still a large knowledge gap that needs to be filled. There are still challenges and opportunities that must be addressed. For instance, the long-term effect of these materials needs to be investigated thoroughly, and the effect of the coexistence of graphene-based materials with other pollutants needs to be scrutinized. Bussy et al. indicated that the future direction should also encompass improving safety related to using these materials and developing materials with modified surface properties and dispersion characteristics [117].

7 COMMERCIAL CHALLENGES OF GRAPHENE-BASED MATERIALS

There has been significant progress in the development of graphene-based materials manufacturing methods, and they are starting to experience the need for quality, quantity, reliability, and price. Many factors can contribute to slowing down adoption of graphene-based materials. For instance, limited material availability can potentially slow down the commercial adoption of graphene. A production capacity of 1 kilotons per year of GO and graphene nanoplatelets and a million square meters per

year for graphene films should be sufficient to support short-term product development and commercialization. Another significant market barrier that could slow down the speed of adoption of graphene is the presence of cheaper alternatives in the market. For instance, for adsorption purposes, many low-cost adsorbents can be used instead for heavy metals and organics removal. Another factor that should be taken into consideration is ease of storage and transport for these products. The transport of graphene films is safe and relatively easy; however, for GO and graphene nanoplatelets, the decision of whether to handle graphene in wet (as a suspension in water) or dry form during manufacture and storage will affect costs and complexity of distribution. GO storage in the suspended form is safe; however, in case of very dilute dispersions, the efficiency and economics of transporting a product that is mainly water presents a challenge. This challenge can be overcome by supplying GO in dried form (in films for instance) or as intermediate products, where GOs are incorporated into a matrix material, such as polymer matrices. However, this is infeasible, as many manufacturers do not allow dry nanomaterial powders in their premises for health and safety concerns [118].

Moreover, some technical drawbacks might adversely affect the commercialization potential of graphene-based materials. For instance, as has been explained, applying an external cell voltage (typically 1.0–1.5 V) to a pair of electrodes in a CDI cell allows for the cations and anions in the saline feed water flowing through the spacer channel to be transported and adsorbed in the electrical double layers of the electrode pores. However, as time passes, the ion-storing capacity of the electrodes is saturated, and no more ions can be removed, creating the main hurdle for the CDI process. This drawback necessitates the presence of a discharging step. Many methods are used mainly by lowering the applied cell voltage or even applying reverse voltage. These methods are both time-intensive, costly, and laborious, which limits the mass production and scaling-up of CDI systems for commercial plants. Innovative technical solutions should be explored to overcome such disadvantages of conventional CDI systems by increasing the ion adsorption capacity, salt removal rate, and efficiency [42].

8 CONCLUSIONS

Significant progress has been made in the area of graphene research over the past decade. Graphene remains a unique material endowed with properties that allows for wide application, from atomically thin membranes to materials with ultra-high surface areas. However, future work should address finding novel methods for graphene-based materials to be easily and inexpensively produced in large scale, and a further understanding of the properties of graphene and mechanisms of contaminants removal should be explored. Moreover, the toxicity of those materials should be thoroughly analyzed. Graphene-based materials will emerge as a rising star in the area of water purification if the technical, economic, and environmental challenges addressed in this chapter are investigated.

ACKNOWLEDGMENT

The library database support provided by Khalifa University of Science and Technology, Masdar City Campus, Abu Dhabi, United Arab Emirates, is highly appreciated.

REFERENCES

[1] R. Lv, E. Cruz-Silva, M. Terrones, Building complex hybrid carbon architectures by covalent interconnections: graphene–nanotube hybrids and more, ACS Nano 8 (2014) 4061–4069.

[2] J.C. Slonczewski, P.R. Weiss, Band structure of graphite, Phys. Rev. 109 (1958) 272–279.

[3] H. Wang, X. Yuan, Y. Wu, H. Huang, X. Peng, G. Zeng, et al., Graphene-based materials: fabrication, characterization and application for the decontamination of wastewater and wastegas and hydrogen storage/generation, Adv. Colloid Interf. Sci. 195–196 (2013) 19–40.

[4] P.S. Goh, A.F. Ismail, Graphene-based nanomaterial: the state-of-the-art material for ccutting edge desalination technology, Desalination 356 (2015) 115–128.

[5] A.K. Geim, K.S. Novoselov, The rise of graphene, Nat. Mater. 6 (2007) 183–191.

[6] B. Zawisza, R. Sitko, E. Malicka, E. Talik, Graphene oxide as a solid sorbent for the preconcentration of cobalt, nickel, copper, zinc and lead prior to determination by energy-dispersive X-ray fluorescence spectrometry, Anal. Methods 5 (2013) 6425–6430.

[7] F. Perreault, A. Fonseca de Faria, M. Elimelech, Environmental applications of graphene-based nanomaterials, Chem. Soc. Rev. 44 (2015) 5861–5896.

[8] J.S. Bunch, S.S. Verbridge, J.S. Alden, A.M. van der Zande, J.M. Parpia, H.G. Craighead, et al., Impermeable atomic membranes from graphene sheets, Nano Lett. 8 (2008) 2458–2462.

[9] S.K. Kannam, B.D. Todd, J.S. Hansen, P.J. Daivis, Slip length of water on graphene: limitations of non-equilibrium molecular dynamics simulations, J. Chem. Phys. 136 (2012) 024705.

[10] M.C. Gordillo, J. Marti, Water on graphene surfaces, J. Phys. Condens. Matter 22 (2010) 284111.

[11] M. Hu, B. Mi, Enabling graphene oxide nanosheets as water separation membranes, Environ. Sci. Technol. 47 (2013) 3715–3723.

[12] S. Liu, T.H. Zeng, M. Hofmann, E. Burcombe, J. Wei, R. Jiang, et al., Antibacterial activity of graphite, graphite oxide, graphene oxide, and reduced graphene oxide: membrane and oxidative stress, ACS Nano 5 (2011) 6971–6980.

[13] V. Berry, Impermeability of graphene and its applications, Carbon 62 (2013) 1–10.

[14] A. Nicolai, B.G. Sumpter, V. Meunier, Tunable water desalination across graphene oxide framework membranes, Phys. Chem. Chem. Phys. 16 (2014) 8646–8654.

[15] D. Cohen-Tanugi, J.C. Grossman, Water desalination across nanoporous graphene, Nano Lett. 12 (2012) 3602.

[16] Y. Han, Z. Xu, C. Gao, Ultrathin graphene nanofiltration membrane for water purification, Adv. Funct. Mater. 23 (2013) 3693–3700.

[17] C.A. Crock, A.R. Rogensues, W. Shan, V.V. Tarabara, Polymer nanocomposites with graphene-based hierarchical fillers as materials for multifunctional water treatment membranes, Water Res. 47 (2013) 3984–3996.

[18] S.P. Koenig, L. Wang, J. Pellegrino, J.S. Bunch, Selective molecular sieving through porous graphene, Nat. Nanotechnol. 7 (2012) 728–732.

[19] S.C. O'Hern, M.S. Boutilier, J.C. Idrobo, Y. Song, J. Kong, T. Laoui, et al., Selective ionic transport through tunable subnanometer pores in single-layer graphene membranes, Nano Lett. 14 (2014) 1234–1241.

[20] K. Sint, B. Wang, P. Kral, Selective ion passage through functionalized graphene nanopores, J. Am. Chem. Soc. 130 (2008) 16448–16449.

[21] S. Garaj, W. Hubbard, A. Reina, J. Kong, D. Branton, J.A. Golovchenko, Graphene as a subnanometre trans-electrode membrane, Nature 467 (2010) 190–193.

[22] M. Bieri, M. Treier, J. Cai, K. Ait-Mansour, P. Ruffieux, O. Groning, et al., Porous graphenes: two-dimensional polymer synthesis with atomic precision, Chem. Commun. (2009) 6919–6921.

[23] S.S. Kim, J.Y. Choi, K. Kim, B.H. Sohn, Large area tunable arrays of graphene nanodots fabricated using diblock copolymer micelles, Nanotechnology 23 (2012)125301.

[24] H. Zhang, M. Boese, D. Zhou, J. Coleman, D. Fox, A. O'Neill, Nitrogen assisted etching of graphene layers in a scanning electron microscope, Appl. Phys. Lett. 98 (2011) 243117.
[25] B. Song, G.F. Schneider, Q. Xu, G. Pandraud, C. Dekker, H. Zandbergen, Atomic-scale electron-beam sculpting of near-defect-free graphene nanostructures, Nano Lett. 11 (2011) 2247–2250.
[26] B. Sommer, J. Sonntag, A. Ganczarczyk, D. Braam, G. Prinz, A. Lorke, et al., Electron-beam induced nano-etching of suspended graphene, Sci. Rep. 5 (2015) 7781.
[27] J. Bai, X. Zhong, S. Jiang, Y. Huang, X. Duan, Graphene nanomesh, Nat. Nanotechnol. 5 (2010) 190–194.
[28] S.P. Surwade, S.N. Smirnov, I.V. Vlassiouk, R.R. Unocic, G.M. Veith, S. Dai, et al., Water desalination using nanoporous single-layer graphene, Nat. Nanotechnol. 10 (2015) 459–464.
[29] H. Kwok, K. Briggs, V. Tabard-Cossa, Nanopore fabrication by controlled dielectric breakdown, PLoS One 9 (2014).
[30] S.C. O'Hern, C.A. Stewart, M.S. Boutilier, J.C. Idrobo, S. Bhaviripudi, S.K. Das, et al., Selective molecular transport through intrinsic defects in a single layer of CVD graphene, ACS Nano 6 (2012) 10130–10138.
[31] N. Lu, J. Wang, H.C. Floresca, M.J. Kim, In situ studies on the shrinkage and expansion of graphene nanopores under electron beam irradiation at temperatures in the range of 400–1200°C, Carbon 50 (2012) 2961–2965.
[32] R.R. Nair, H.A. Wu, P.N. Jayaram, I.V. Grigorieva, A.K. Geim, Unimpeded permeation of water through helium-leak-tight graphene-based membranes, Science 335 (2012) 442–444.
[33] P. Sun, F. Zheng, M. Zhu, Z. Song, K. Wang, M. Zhong, et al., Selective trans-membrane transport of alkali and alkaline earth cations through graphene oxide membranes based on cation-pi interactions, ACS Nano 8 (2014) 850–859.
[34] B. Mi, Graphene oxide membranes for ionic and molecular sieving, Science 343 (2014) 740.
[35] H. Huang, Y. Mao, Y. Ying, Y. Liu, L. Sun, X. Peng, Salt concentration, pH and pressure controlled separation of small molecules through lamellar graphene oxide membranes, Chem. Commun. (Camb.) 49 (2013) 5963–5965.
[36] Z. An, O.C. Compton, K.W. Putz, L.C. Brinson, S.T. Nguyen, Bio-inspired borate cross-linking in ultra-stiff graphene oxide thin films, Adv. Mater. 23 (2011) 3842–3846.
[37] A. Aghigh, V. Alizadeh, H.Y. Wong, M.S. Islam, N. Amin, M. Zaman, Recent advances in utilization of graphene for filtration and desalination of water: a review, Desalination 365 (2015) 389–397.
[38] P. Liu, T. Yan, L. Shi, H.S. Park, X. Chen, Z.-G. Zhao, et al., Graphene-based materials for capacitive deionization, J. Mater. Chem. A 5 (2017) 13907–13943.
[39] H. Li, L. Zou, L. Pan, Z. Sun, Novel graphene-like electrodes for capacitive deionization, Environ. Sci. Technol. 44 (2010) 8692.
[40] X. Xu, L. Pan, Y. Liu, T. Lu, Z. Sun, D.H.C. Chua, Facile synthesis of novel graphene sponge for high performance capacitive deionization, Sci. Rep. 5 (2015) 8458.
[41] M.E. Suss, S. Porada, X. Sun, P.M. Biesheuvel, J. Yoon, V. Presser, Water desalination via capacitive deionization: what is it and what can we expect from it? Energy Environ. Sci. 8 (2015) 2296–2319.
[42] Y. Cho, K.S. Lee, S. Yang, J. Choi, H.-r. Park, D.K. Kim, A novel three-dimensional desalination system utilizing honeycomb-shaped lattice structures for flow-electrode capacitive deionization, Energy Environ. Sci. 10 (2017) 1746–1750.
[43] H. Li, L. Pan, C. Nie, Y. Liu, Z. Sun, Reduced graphene oxide and activated carbon composites for capacitive deionization, J. Mater. Chem. 22 (2012) 15556–15561.
[44] W. Kong, X. Duan, Y. Ge, H. Liu, J. Hu, X. Duan, Holey graphene hydrogel with in-plane pores for high-performance capacitive desalination, Nano Res. 9 (2016) 2458–2466.
[45] A.G. El-Deen, R.M. Boom, H.Y. Kim, H. Duan, M.B. Chan-Park, J.H. Choi, Flexible 3D nanoporous graphene for desalination and bio-decontamination of Brackish water via asymmetric capacitive deionization, ACS Appl. Mater. Interfaces 8 (2016) 25313–25325.

[46] Z. Li, B. Song, Z. Wu, Z. Lin, Y. Yao, K.-S. Moon, et al., 3D porous graphene with ultrahigh surface area for microscale capacitive deionization, Nano Energy 11 (2015) 711–718.
[47] H. Li, Z.Y. Leong, W. Shi, J. Zhang, T. Chen, H.Y. Yang, Hydrothermally synthesized graphene and Fe3O4 nanocomposites for high performance capacitive deionization, RSC Adv. 6 (2016) 11967–11972.
[48] X. Gu, Y. Yang, Y. Hu, M. Hu, J. Huang, C. Wang, Facile fabrication of graphene-polypyrrole-Mn composites as high-performance electrodes for capacitive deionization, J. Mater. Chem. A 3 (2015) 5866–5874.
[49] X. Gu, Y. Yang, Y. Hu, M. Hu, J. Huang, C. Wang, Nitrogen-doped graphene composites as efficient electrodes with enhanced capacitive deionization performance, RSC Adv. 4 (2014) 63189–63199.
[50] Y. Liu, X. Xu, T. Lu, Z. Sun, D.H.C. Chua, L. Pan, Nitrogen-doped electrospun reduced graphene oxide-carbon nanofiber composite for capacitive deionization, RSC Adv. 5 (2015) 34117–34124.
[51] Z.H. Huang, X. Zheng, W. Lv, M. Wang, Q.H. Yang, F. Kang, Adsorption of lead(II) ions from aqueous solution on low-temperature exfoliated graphene nanosheets, Langmuir 27 (2011) 7558–7562.
[52] H. Song, L. Hao, Y. Tian, X. Wan, L. Zhang, Y. Lv, Stable and water-dispersible graphene nanosheets: sustainable preparation, functionalization, and high-performance adsorbents for Pb2+, ChemPlusChem 77 (2012) 379–386.
[53] J. Zhu, S. Wei, H. Gu, S.B. Rapole, Q. Wang, Z. Luo, et al., One-pot synthesis of magnetic graphene nanocomposites decorated with core@double-shell nanoparticles for fast chromium removal, Environ. Sci. Technol. 46 (2012) 977–985.
[54] R. Sitko, E. Turek, B. Zawisza, E. Malicka, E. Talik, J. Heimann, et al., Adsorption of divalent metal ions from aqueous solutions using graphene oxide, Dalton Trans. 42 (2013) 5682–5689.
[55] G. Zhao, J. Li, X. Ren, C. Chen, X. Wang, Few-layered graphene oxide nanosheets as superior sorbents for heavy metal ion pollution management, Environ. Sci. Technol. 45 (2011) 10454–10462.
[56] G. Zhao, X. Ren, X. Gao, X. Tan, J. Li, C. Chen, et al., Removal of Pb(ii) ions from aqueous solutions on few-layered graphene oxide nanosheets, Dalton Trans. 40 (2011) 10945–10952.
[57] Y. Sun, Q. Wang, C. Chen, X. Tan, X. Wang, Interaction between Eu(III) and graphene oxide nanosheets investigated by batch and extended X-ray absorption fine structure spectroscopy and by modeling techniques, Environ. Sci. Technol. 46 (2012) 6020–6027.
[58] Y. Li, P. Zhang, Q. Du, X. Peng, T. Liu, Z. Wang, et al., Adsorption of fluoride from aqueous solution by graphene, J. Colloid Interface Sci. 363 (2011) 348–354.
[59] S. Vasudevan, J. Lakshmi, The adsorption of phosphate by graphene from aqueous solution, RSC Adv. 2 (2012) 5234–5242.
[60] S. Zhang, Y. Shao, J. Liu, I.A. Aksay, Y. Lin, Graphene–polypyrrole nanocomposite as a highly efficient and low cost electrically switched ion exchanger for removing $ClO4^-$ from wastewater, ACS Appl. Mater. Interfaces 3 (2011) 3633–3637.
[61] G. Shi, Y. Ding, H. Fang, Unexpectedly strong anion–π interactions on the graphene flakes, J. Comput. Chem. 33 (2012) 1328–1337.
[62] Z. Li, F. Chen, L. Yuan, Y. Liu, Y. Zhao, Z. Chai, et al., Uranium(VI) adsorption on graphene oxide nanosheets from aqueous solutions, Chem. Eng. J. 210 (2012) 539–546.
[63] W. Wu, Y. Yang, H. Zhou, T. Ye, Z. Huang, R. Liu, et al., Highly efficient removal of Cu(II) from aqueous solution by using graphene oxide, Water Air Soil Pollut. 224 (2012) 1372.
[64] Y. Ren, N. Yan, Q. Wen, Z. Fan, T. Wei, M. Zhang, et al., Graphene/δ-MnO2 composite as adsorbent for the removal of nickel ions from wastewater, Chem. Eng. J. 175 (2010) 1–7.
[65] V. Chandra, J. Park, Y. Chun, J.W. Lee, I.-C. Hwang, K.S. Kim, Water-dispersible magnetite-reduced graphene oxide composites for arsenic removal, ACS Nano 4 (2010) 3979–3986.
[66] G.K. Ramesha, A.V. Kumara, H.B. Muralidhara, S. Sampath, Graphene and graphene oxide as effective adsorbents toward anionic and cationic dyes, J. Colloid Interface Sci. 361 (2011) 270–277.

[67] F. Liu, S. Chung, G. Oh, T.S. Seo, Three-dimensional graphene oxide nanostructure for fast and efficient water-soluble dye removal, ACS Appl. Mater. Interfaces 4 (2012) 922–927.
[68] B. Li, H. Cao, G. Yin, Mg(OH)2@reduced graphene oxide composite for removal of dyes from water, J. Mater. Chem. 21 (2011) 13765–13768.
[69] Y. Gao, Y. Li, L. Zhang, H. Huang, J. Hu, S.M. Shah, et al., Adsorption and removal of tetracycline antibiotics from aqueous solution by graphene oxide, J. Colloid Interface Sci. 368 (2012) 540–546.
[70] J. Xu, L. Wang, Y. Zhu, Decontamination of bisphenol A from aqueous solution by graphene adsorption, Langmuir 28 (2012) 8418–8425.
[71] Y. Yao, S. Miao, S. Yu, L. Ping Ma, H. Sun, S. Wang, Fabrication of Fe3O4/SiO2 core/shell nanoparticles attached to graphene oxide and its use as an adsorbent, J. Colloid Interface Sci. 379 (2012) 20–26.
[72] X. Yang, J. Li, T. Wen, X. Ren, Y. Huang, X. Wang, Adsorption of naphthalene and its derivatives on magnetic graphene composites and the mechanism investigation, Colloids Surf. A Physicochem. Eng. Asp. 422 (2013) 118–125.
[73] B. Beless, H.S. Rifai, D.F. Rodrigues, Efficacy of carbonaceous materials for sorbing polychlorinated biphenyls from aqueous solution, Environ. Sci. Technol. 48 (2014) 10372–10379.
[74] T. Liu, Y. Li, Q. Du, J. Sun, Y. Jiao, G. Yang, et al., Adsorption of methylene blue from aqueous solution by graphene, Colloids Surf. B: Biointerfaces 90 (2012) 197–203.
[75] G. Zhao, L. Jiang, Y. He, J. Li, H. Dong, X. Wang, et al., Sulfonated graphene for persistent aromatic pollutant management, Adv. Mater. 23 (2011) 3959–3963.
[76] G. Zhao, J. Li, X. Wang, Kinetic and thermodynamic study of 1-naphthol adsorption from aqueous solution to sulfonated graphene nanosheets, Chem. Eng. J. 173 (2011) 185–190.
[77] L. Fan, C. Luo, M. Sun, X. Li, F. Lu, H. Qiu, Preparation of novel magnetic chitosan/graphene oxide composite as effective adsorbents toward methylene blue, Bioresour. Technol. 114 (2012) 703–706.
[78] C. Wang, C. Feng, Y. Gao, X. Ma, Q. Wu, Z. Wang, Preparation of a graphene-based magnetic nanocomposite for the removal of an organic dye from aqueous solution, Chem. Eng. J. 173 (2011) 92–97.
[79] J. Mao, R. Guo, L.-T. Yan, Simulation and analysis of cellular internalization pathways and membrane perturbation for graphene nanosheets, Biomaterials 35 (2014) 6069–6077.
[80] P. Gao, J. Liu, D.D. Sun, W. Ng, Graphene oxide-CdS composite with high photocatalytic degradation and disinfection activities under visible light irradiation, J. Hazard. Mater. 250–251 (2013) 412–420.
[81] H. Ji, H. Sun, X. Qu, Antibacterial applications of graphene-based nanomaterials: recent achievements and challenges, Adv. Drug Deliv. Rev. 105 (2016) 176–189.
[82] O. Akhavan, E. Ghaderi, Photocatalytic reduction of graphene oxide nanosheets on TiO2 thin film for photoinactivation of bacteria in solar light irradiation, J. Phys. Chem. C 113 (2009) 20214–20220.
[83] Q. Bao, D. Zhang, P. Qi, Synthesis and characterization of silver nanoparticle and graphene oxide nanosheet composites as a bactericidal agent for water disinfection, J. Colloid Interface Sci. 360 (2011) 463–470.
[84] Y. Jiang, D. Liu, M. Cho, S.S. Lee, F. Zhang, P. Biswas, et al., In situ photocatalytic synthesis of Ag nanoparticles (nAg) by crumpled graphene oxide composite membranes for filtration and disinfection applications, Environ. Sci. Technol. 50 (2016) 2514.
[85] X. Zeng, D.T. McCarthy, A. Deletic, X. Zhang, Silver/reduced graphene oxide hydrogel as novel bactericidal filter for point-of-use water disinfection, Adv. Funct. Mater. 25 (2015) 4344–4351.
[86] O. Akhavan, E. Ghaderi, Toxicity of graphene and graphene oxide nanowalls against bacteria, ACS Nano 4 (2010) 5731–5736.
[87] I.E. Mejias Carpio, J.D. Mangadlao, H.N. Nguyen, R.C. Advincula, D.F. Rodrigues, Graphene oxide functionalized with ethylenediamine triacetic acid for heavy metal adsorption and anti-microbial applications, Carbon 77 (2014) 289–301.
[88] B. Cao, S. Cao, P. Dong, J. Gao, J. Wang, High antibacterial activity of ultrafine TiO2/graphene sheets nanocomposites under visible light irradiation, Mater. Lett. 93 (2013) 349–352.

[89] L. Hui, J.T. Auletta, Z. Huang, X. Chen, F. Xia, S. Yang, et al., Surface disinfection enabled by a layer-by-layer thin film of polyelectrolyte-stabilized reduced graphene oxide upon solar near-infrared irradiation, ACS Appl. Mater. Interfaces 7 (2015) 10511–10517.
[90] L. Liu, H. Bai, J. Liu, D.D. Sun, Multifunctional graphene oxide-TiO_2-Ag nanocomposites for high performance water disinfection and decontamination under solar irradiation, J. Hazard. Mater. 261 (2013) 214–223.
[91] X. Cai, M. Lin, S. Tan, W. Mai, Y. Zhang, Z. Liang, et al., The use of polyethyleneimine-modified reduced graphene oxide as a substrate for silver nanoparticles to produce a material with lower cytotoxicity and long-term antibacterial activity, Carbon 50 (2012) 3407–3415.
[92] L.J. Xu, W. Chu, L. Gan, Environmental application of graphene-based CoFe2O4 as an activator of peroxymonosulfate for the degradation of a plasticizer, Chem. Eng. J. 263 (2015) 435–443.
[93] S. Navalon, A. Dhakshinamoorthy, M. Alvaro, M. Antonietti, H. Garcia, Active sites on graphene-based materials as metal-free catalysts, Chem. Soc. Rev. 46 (2017) 4501–4529.
[94] Y. Yao, Y. Cai, F. Lu, F. Wei, X. Wang, S. Wang, Magnetic recoverable MnFe(2)O(4) and MnFe(2)O(4)-graphene hybrid as heterogeneous catalysts of peroxymonosulfate activation for efficient degradation of aqueous organic pollutants, J. Hazard. Mater. 270 (2014) 61–70.
[95] Y. Xu, J. Ai, H. Zhang, The mechanism of degradation of bisphenol A using the magnetically separable CuFe2O4/peroxymonosulfate heterogeneous oxidation process, J. Hazard. Mater. 309 (2016) 87–96.
[96] T. Zeng, H. Zhang, Z. He, J. Chen, S. Song, Mussel-inspired approach to constructing robust cobalt-embedded N-doped carbon nanosheet toward enhanced sulphate radical-based oxidation, Sci. Rep. 6 (2016) 33348.
[97] C. Li, L. Li, L. Sun, Z. Pei, J. Xie, S. Zhang, Transformation of hydroquinone to benzoquinone mediated by reduced graphene oxide in aqueous solution, Carbon 89 (2015) 74–81.
[98] S.D. Perera, R.G. Mariano, K. Vu, N. Nour, O. Seitz, Y. Chabal, et al., Hydrothermal synthesis of graphene-TiO2 nanotube composites with enhanced photocatalytic activity, ACS Catal. 2 (2012) 949–956.
[99] H. Zhang, X. Lv, Y. Li, Y. Wang, J. Li, P25-graphene composite as a high performance photocatalyst, ACS Nano 4 (2010) 380–386.
[100] Z. Xiong, L.L. Zhang, J. Ma, X.S. Zhao, Photocatalytic degradation of dyes over graphene-gold nanocomposites under visible light irradiation, Chem. Commun. 46 (2010) 6099–6101.
[101] X. Liu, L. Pan, T. Lv, T. Lu, G. Zhu, Z. Sun, et al., Microwave-assisted synthesis of ZnO-graphene composite for photocatalytic reduction of Cr(vi), Catal. Sci. Technol. 1 (2011) 1189–1193.
[102] T. Kamegawa, D. Yamahana, H. Yamashita, Graphene coating of TiO2 nanoparticles loaded on mesoporous silica for enhancement of photocatalytic activity, J. Phys. Chem. C 114 (2010) 15049–15053.
[103] P. Wang, Y. Ao, C. Wang, J. Hou, J. Qian, A one-pot method for the preparation of graphene–Bi2MoO6 hybrid photocatalysts that are responsive to visible-light and have excellent photocatalytic activity in the degradation of organic pollutants, Carbon 50 (2012) 5256–5264.
[104] T. Jiao, H. Zhao, J. Zhou, Q. Zhang, X. Luo, J. Hu, et al., Self-assembly reduced graphene oxide nanosheet hydrogel fabrication by anchorage of chitosan/silver and its potential efficient application toward dye degradation for wastewater treatments, ACS Sustain. Chem. Eng. 3 (2015) 3130–3139.
[105] S. Ghasemi, S.R. Setayesh, A. Habibi-Yangjeh, M.R. Hormozi-Nezhad, M.R. Gholami, Assembly of CeO2-TiO2 nanoparticles prepared in room temperature ionic liquid on graphene nanosheets for photocatalytic degradation of pollutants, J. Hazard. Mater. 199–200 (2012) 170–178.
[106] Y. Tang, S. Luo, Y. Teng, C. Liu, X. Xu, X. Zhang, et al., Efficient removal of herbicide 2,4-dichlorophenoxyacetic acid from water using Ag/reduced graphene oxide co-decorated TiO2 nanotube arrays, J. Hazard. Mater. 241 (2012) 323–330.
[107] N. Farhangi, R.R. Chowdhury, Y. Medina-Gonzalez, M.B. Ray, P.A. Charpentier, Visible light active Fe doped TiO2 nanowires grown on graphene using supercritical CO2, Appl. Catal. B Environ. 110 (2011) 25–32.

[108] C. Zhai, M. Zhu, F. Ren, Z. Yao, Y. Du, P. Yang, Enhanced photoelectrocatalytic performance of titanium dioxide/carbon cloth based photoelectrodes by graphene modification under visible-light irradiation, J. Hazard. Mater. 263 (2013) 291–298.
[109] L. Yang, Z. Li, H. Jiang, W. Jiang, R. Su, S. Luo, et al., Photoelectrocatalytic oxidation of bisphenol A over mesh of TiO2/graphene/Cu2O, Appl. Catal. B Environ. 183 (2016) 75–85.
[110] F. Ahmed, D.F. Rodrigues, Investigation of acute effects of graphene oxide on wastewater microbial community: a case study, J. Hazard. Mater. 256–257 (2013) 33–39.
[111] R.G. Combarros, S. Collado, M. Diaz, Toxicity of graphene oxide on growth and metabolism of Pseudomonas putida, J. Hazard. Mater. 310 (2016) 246–252.
[112] K. He, G. Chen, G. Zeng, M. Peng, Z. Huang, J. Shi, et al., Stability, transport and ecosystem effects of graphene in water and soil environments, Nanoscale 9 (2017) 5370–5388.
[113] A.M. Jastrzębska, A.R. Olszyna, The ecotoxicity of graphene family materials: current status, knowledge gaps and future needs, J. Nanopart. Res. 17 (2015) 1–21.
[114] J. Li, G. Wang, H. Zhu, M. Zhang, X. Zheng, Z. Di, et al., Antibacterial activity of large-area monolayer graphene film manipulated by charge transfer, Sci. Rep. 4 (2014) 4359.
[115] L. Dellieu, E. Lawarée, N. Reckinger, C. Didembourg, J.-J. Letesson, M. Sarrazin, et al., Do CVD grown graphene films have antibacterial activity on metallic substrates? Carbon 84 (2014) 310–316.
[116] J. Du, X. Hu, Q. Zhou, Graphene oxide regulates the bacterial community and exhibits property changes in soil, RSC Adv. 5 (2015) 27009–27017.
[117] C. Bussy, H. Ali-Boucetta, K. Kostarelos, Safety considerations for graphene: lessons learnt from carbon nanotubes, Acc. Chem. Res. 46 (2013) 692–701.
[118] A. Zurutuza, C. Marinelli, Challenges and opportunities in graphene commercialization, Nat. Nanotechnol. 9 (2014) 730–734.

CHAPTER

27

PHOTOCATALYSIS OF GRAPHENE AND CARBON NITRIDE-BASED FUNCTIONAL CARBON QUANTUM DOTS

Amit Mishra*, Soumen Basu*, Nagaraj P. Shetti†,a, Kakarla Raghava Reddy‡, Tejraj M. Aminabhavi§

*School of Chemistry and Biochemistry, Thapar Institute of Engineering and Technology, Patiala, India** *Electrochemistry and Materials Group, Department of Chemistry, K. L. E. Institute of Technology, Hubballi, India†* *School of Chemical and Biomolecular Engineering, The University of Sydney, Sydney, NSW, Australia‡* *Sonia College of Pharmacy, Dharwad, India§*

1 INTRODUCTION

Day by day, global energy demands increase due to the rapid consumption of depleting fossil fuels and environmental pollution. This has led to the search for materials capable of both energy conversion and elimination of environmental pollutants through the aid of renewable solar energy [1]. This is a promising approach for meeting future energy requirements and eliminating environmental pollutants. In this pursuit, semiconductor photocatalysts have immense potential for solving both energy and environmental issues [2]. To date, numerous semiconductor materials have been explored, including those of metal oxides [3], chalcogenides [4], borates [5], titanates [6], tungstates [7], vanadates [8], zirconates [9], oxyhalides [10], and metal-based interstitial compounds [11]. However, the majority of these suffer from limitations such as complex synthesis procedures, limited light absorption range due to their wide band gap, high cost, and toxicity-related issues. Over the past decade, carbon-based nanomaterials have gained attention in the field of photocatalysis. Many recent articles have placed emphasis upon metal-free carbon-based photocatalytic systems for degradation of organic pollutants and hydrogen production from water splitting. The prime merit of these nanomaterials is that they originate from naturally abundant constituent elements such as carbon, nitrogen, and oxygen, making them more economical than their metal-based counterparts. Most reported carbon-based photocatalysts have tunable band gap energies, enhancing their optical absorption range. Band gap energy can be tuned by varying synthesis conditions and precursors, resulting in the formation of nanomaterials with different morphologies. The preparation procedures for most carbon-based nanomaterials are less complex than those of metal-based materials.

Among the carbon-based materials, graphene is well known for its high thermal and mechanical stability, excellent charge carrier mobility, high surface area, excellent mechanical strength, and high

[a]Affiliated with Visvesvaraya Technological University, Hubballi, India

Nanoscale Materials in Water Purification. https://doi.org/10.1016/B978-0-12-813926-4.00035-5

flexibility [12]. Being a two-dimensional single atomic layer of carbon, it acts as a zero band gap semimetal whose conduction and valence bands (comprised of π and π*) meet at the Dirac point [13]. As the lateral dimensions of graphene approach the nanoscale (<10 nm), the conduction and valence bands separate, and this gives rise to a band gap in zero-dimensional graphene nanostructures such as graphene quantum dots (GQDs) due to quantum confinement and edge effects [13, 14]. Band gaps of GQDs are between 2 and 3 eV, which gives rise to their green or blue florescence [13]. GQDs have few layers or a single layer of graphene <100 nm and are highly promising candidates for a large number of applications related to energy conversion and the environment [15]. Moreover, low toxicity, low cost, stable photoluminescence and excellent solubility make GQDs more advantageous than conventional semiconductor quantum dots [15, 16]. GQDs have found application in several fields such as sensing, bio-imaging, energy storage, and photocatalysis [14]. There are a number of recent reports on GQD-based heterostructure photocatalysts for water splitting and wastewater treatment [17].

Carbon nitride is a semiconductor of polymeric nature having carbon and nitrogen as its prime constituents, and its molecular structure is similar to graphene [18]. g-C_3N_4 consists of layers of two-dimensional, π-conjugated, polymeric structures with *s*-triazine or tri-*s*-triazine(*s*-heptazine) units connected to each other through tertiary amines [18, 19]. There are weak van der Waals forces between layers giving it sheet-like graphitic features, and atoms in each layer are arranged in a honeycomb configuration with strong covalent bonds [20]. The graphite-like planar configuration with π-conjugated systems enables transport of charge carriers, and the band gap of around 2.7 eV makes it visible-light-responsive around 460 nm [18]. It is thermally and chemically stable under ambient conditions, biocompatible, ecofriendly, and resistant to acidic and alkaline conditions [21, 22]. It can be easily prepared from thermal polycondensation of cheap, nitrogen-rich,carbon-based precursors such as dicyanamide [23], cyanamide [24], melamine [23], urea [25], and thiourea [23].

Bulk g-C_3N_4 has several applications as an adsorbent [26], sensor [26], supercapacitor [27], electrocatalyst [28], and photocatalyst for water splitting and the degradation of organic pollutants [19]. However, bulk g-C_3N_4 has several limitations in the field of photocatalysis due to its low crystallinity, such as low conductivity [18, 29, 30] of photogenerated charge carriers and its high recombination rate [31, 32], which lowers its photocatalytic performance. Several approaches have been developed in order to increase its photoactivity, such as modification in nanostructure [33], ,elemental doping, noble metal loading [34–36], coupling with other photoactive materials [37, 38], and g-C_3N_4-based homojunction formation [39, 40]. Through nanostructure modification, one can increase the number of reactive sites, increase the optical absorption coefficient, and decrease the diffusion distance of photogenerated charge carriers to the reaction sites [41].

Several nanostructures of g-C_3N_4, like nanosheets [42], nanotubes [43], nanorods [44], and mesoporous g-C_3N_4[45] have been synthesized and used in photocatalytic applications. Over the past few years, g-C_3N_4 quantum dots (GCNQDs) have gained tremendous attention. Few recent reports are available on the synthesis of GCNQDs and their applications in photocatalytic degradation of organic pollutants and water splitting for H_2 generation. Just like graphene, as the lateral dimensions of g-C_3N_4 approach the nanoregime (<10 nm), it shows quantum confinement, which leads to bright fluorescence, better water solubility, and enhancement in visible light and NIR response [46–48]. Compared to bulk g-C_3N_4, GCNQDs are rich in catalytic active sites, such as pyridinic N, graphitic N, and amine groups [47].

2 GRAPHENE QUANTUM DOT (GQDs)-BASED HETEROSTRUCTURED PHOTOCATALYSTS: PREPARATION METHODS AND PHOTOCATALYTIC APPLICATIONS FOR WASTEWATER TREATMENT AND WATER SPLITTING

2.1 SYNTHESIS PROCEDURES FOR GQDs BASED HETEROSTRUCTURES

Numerous methods have been developed for synthesis of GQD-based heterostructured photocatalysts. Majumdar et al. [49] synthesized GQDs and nitrogen-doped GQDs (N-GQDs) by a hydrothermal process, which were then incorporated upon ZnO nanorods by simply immersing the ZnO nanorods in GQDs/N-GQDs solution for a duration ranging from 30 min to 17 h. The ZnO nanorods were prepared by two-step chemical processes that involved the preparation of ZnO nanoparticle seeds as nucleating agents by a sol-gel process and their subsequent hydrothermal treatment. The resulting material was used as a photoanode for solar energy conversion. An alkali-catalyzed, water phase, molecular fusion method was used by Pan et al. to prepare amine-functionalized GQDs [17] which were deposited on TiO_2 by a hydrothermal deposition method, and the resulting photocatalyst was used to degrade methyl orange dye.

GQDs have been synthesized by cyclic voltammetry using two graphite rods as working and counter electrodes and Ag/AgCl as a reference electrode using a PBS saline buffer as an electrolyte [50]. The Ag nanoparticles were then deposited upon the GQDs by photoreduction of $AgNO_3$ and Ag-loaded GQDs (Ag-GQDs) were further used for photodegradation of rhodamine dye. Pyrolysis of $C_6H_{17}N_3O_7$ resulted in the formation of N-GQDs, which were incorporated upon $BiVO_4$/g-C_3N_4 to form Z-scheme N-GQDs-$BiVO_4$/g-C_3N_4 photocatalysts for the degradation of antibiotics such as tetracycline, oxytetracycline, and ciprofloxacin [51]. Graphene oxide (GO) nanosheets were reduced to graphene at 200°C for 6 h and oxidized under ultrasonic conditions using concentrated HNO_3 and H_2SO_4, followed by hydrothermal treatment for 12 h to obtain GQDs [52]. The as-obtained GQDs were anchored on a TiO_2 surface by a photo-assisted approach which enhanced the H_2 generation from water splitting. Similarly, surface-intact,nitrogen-doped graphene oxide quantum dots (iNGO-QDs) were obtained by treating GO with a flow of NH_3 at 500°C, followed by its mild oxidation using concentrated HNO_3 under sonication at room temperature [53]. This led to the coexistence of both p and n type domains on the surface of iNGO-QDs, which resulted in high H_2 yield from water splitting.

Bu et al. [54] prepared nanocomposites of black TiO_2 and N-GQDs photocatalysts meant for photocatalytic sewage treatment. In this process, black TiO_2 was prepared by treating anatase TiO_2 powder with $NaBH_4$ and subsequently heating it to 400 °C overnight in a crucible. N-GQDs were synthesized by ultrasonicating GO in dimethylformamide followed by its hydrothermal treatment. The N-GQDs were decorated upon the black TiO_2 surface through the addition of black TiO_2 into N-GQDs aqueous solution, which was then dispersed and finally calcined at 200°C for 2 h under an N_2 atmosphere.

Zhang et al. [55] prepared GOQD-sensitized, porous TiO_2 microspheres (GOQDs/TiO_2) by adding TiO_2 microspheres into GOQDs solution under stirring at room temperature. For this purpose, GOQDs were prepared by refluxing Vulcan CX-72 carbon black with nitric acid. GQDs prepared by thermally treating citric acid were anchored upon phosphorus-doped tubular g-C_3N_4(P-TCN) (synthesized by hydrothermal treatment of melamine and H_3PO_3 mixture) by the lyophilization method where P-TCN was dispersed into a GQDs aqueous solution, and the mixture was freeze dried to form P-TCN/GQDs heterostructures [56].

2.2 GQD-BASED HETEROSTRUCTURED PHOTOCATALYSTS FOR WASTEWATER TREATMENT

The fundamental principle behind photocatalytic wastewater treatment process is the in-situ generation of charge carriers on the semiconductor's surface after its illumination by light of a frequency corresponding to an energy greater than or equal to its band gap (Fig. 1). The photo-generated electron-hole pairs initiate the formation of free radicals which react with pollutant molecules and finally decompose them to simple and less harmful products. Since the GQDs have a band gap <2.1 eV, which makes them active in visible solar light, they can be said to be highly promising materials for photocatalytic wastewater treatment.

There are many recent efforts regarding treatment of wastewater using GQD-based heterogeneous photocatalysts. Anchoring aminofunctionalized GQDs with an absorption edge at 490 nm on TiO_2 expands their optical absorption from UV to the visible region [17]. Another feature of aminofunctionalized GQDs is that they can absorb more oxygen than TiO_2, and this leads to the generation of a higher number of O_2 species for effective degradation of methyl orange dye (MO). The degradation of MO by GQDs/TiO_2 composite was 15 times higher than that of pristine TiO_2. The high photoactivity can be attributed to the effective charge carrier separation by GQD-based heterojunction. GQDs-Ag nanocomposites prepared by photoreduction of $AgNO_3$ upon the GQDs' surface possessed high efficiency for rhodamine B (RhB) degradation under sunlight [50]. The high efficiency of the as-prepared photocatalyst could be ascribed to the synthetic role played by AgNPs and GQDs, in which Ag absorbs visible light, and GQDs mediate the separation of electrons and RhB degradation (Fig. 2A).

Black TiO_2/N-GQDs nanocomposite photocatalysts show high photoactivity for RhB degradation at a rate constant of $0.86\,min^{-1}$ [54]. The high photocurrent density of $2.7\,mA\,cm^{-2}$ indicates excellent charge separation in the nanocomposite which can be attributed to the high energy barrier between NGQDs and black TiO_2. The photoactivity of the N-GQDs-$BiVO_4$/g-C_3N_4Z-scheme heterojunction photocatalyst was evaluated by the degradation of antibiotics (tetracycline, oxytetracycline, and ciprofloxacin) on its surface [51]. Upon investigation of the photoactivity, it was found that the N-GQD

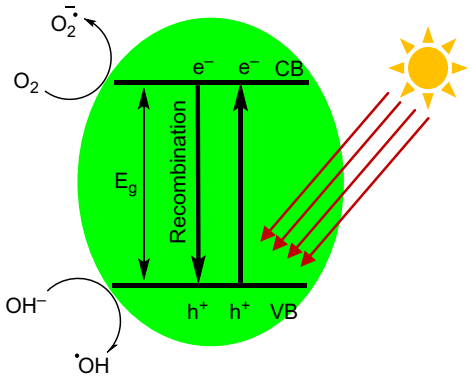

FIG. 1

Schematic representation of generation of electron hole pairs on semiconductor surface during heterogeneous photocatalysis.

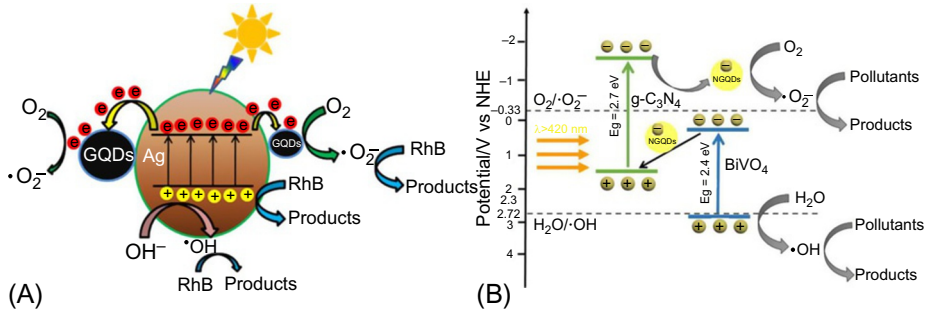

FIG. 2

(A) Mechanism of electron hole separation in GQDs/Ag photocatalyst. (B) Schematic representation of charge separation and transfer in Z-scheme N-GQDs-$BiVO_4$/g-C_3N_4 photocatalyst.

Reprinted with permission from (A) L. Wang, Y. Li, S. Li, Y. Wang, W. Kong, W. Xue, C. Li, Synthesis, characterization and photocatalytic activity of graphene quantum dots-ag solar driven photocatalyst, J. Mater. Sci. Mater. Electron. 28 (2017) 17570–17577, copyright (2017) Springer. (B) M. Yan, F. Zhu, W. Gu, L. Sun, W. Shi, Y. Hua, Construction of nitrogen-doped graphene quantum dots-BiVO 4/gC 3 N 4 Z-scheme photocatalyst and enhanced photocatalytic degradation of antibiotics under visible light, RSC Adv. 6 (2016) 61162–61174, copyright (2017) Royal Society of Chemistry.

amount and $BiVO_4$/g-C_3N_4 ratio (B/CN ratio) influenced its photocatalytic performance. The high photocatalytic activity of the nanocomposite was ascribed to the crucial role played by N-GQDs and Z-scheme photocatalytic systems, which resulted in effective charge separation and strong oxidation and reduction ability for degrading organic pollutants (Fig. 2B).

In the same manner, the photocatalytic activity of a N-GQDs-BiOI/$MnNb_2O_6$ p-n junction photocatalyst was evaluated by the degradation of antibiotics such as tetracycline (TC), oxytetracycline, ciprofloxacin, and doxycycline [57]. The N-GQDs-BiOI/$MnNb_2O_6$ could more effectively degrade the antibiotics than BiOI and $MnNb_2O_6$. The ratio of BiOI/$MnNb_2O_6$ (Bi/Mn) as well as the quantity of N-GQDs had significant impact on the photocatalytic performance of the nanocomposite. Studies based upon ESR and reactive species scavenging experiments reveal that the cooperative effects of the p-n junction formed between p-type BiOI and n-type $MnNb_2O_6$, together with the high charge carrier mobility of N-GQDs, resulted in an efficient charge separation (Fig. 2B). Table 1 shows the summary of photocatalytic performance of GQD-based heterostructures regarding water treatment.

2.3 GQD-BASED HETEROSTRUCTURES FOR WATER SPLITTING

Hydrogen generation from water splitting is energetically an uphill process with positive change in standard Gibb's free energy ($\Delta G = 237$ kJ/mol) [63, 64]. Hydrogen evolution from photocatalytic water splitting (Fig. 3) requires three steps: (i) formation of electrons and holes by optical photons having energy greater than or equal to the band gap (E_g) of the semiconductor, (ii) separation and transfer of charge carriers to the semiconductor surface, and (iii), the photogenerated electrons in the conduction band reduce H^+ to H_2 (hydrogen evolution reaction, or HER), and holes in the valence band oxidize H_2O to O_2 (oxygen evolution reaction, or OER) (Fig. 4) [18, 63, 65].

Table 1 Summary of Photocatalytic Performance of GQD-Based Heterostructures Regarding Water Treatment

Photocatalyst	Model Pollutant	Catalytic Amount (mg/mL)	Pollutant Concentration (ppm)	% Degradation	Rate Constant (min^{-1})	Ref.
GQDs/TiO_2	MO dye	0.4	10	>99	–	[17]
Ag-GQDs	RhB	–	4	–	0.3	[50]
BlackTiO_2/N-GQDs	RhB	0.3	10	100	0.86	[54]
N-GQDs-$BiVO_4$/g-C_3N_4	Tetracycline	0.5	10	91.5	0.0804	[51]
N-GQDs-BiOI/$MnNb_2O_6$	Tetracycline	0.5	10	87.2	0.0331	[57]
GQDs/Mn-N-TiO_2/g-C_3N_4	4-Nitrophenol	0.5	10	89	–	[58]
GQDs/mpg-C_3N_4	Tetracycline hydrochloride	1	20	97	–	[59]
S-Doped GQDs/TiO_2	MO	0.5	20	70	–	[60]
GQDs/Zinc porphyrin	MB	0.01	56	95	–	[61]
GQDs/ZnO NW	MB	0.3	10^{-5} M	–	0.0070	[62]

Two important parameters which are used to evaluate the photocatalytic water splitting performance of an evaluated material are solar to hydrogen (STH) conversion efficiency and apparent quantum efficiency (AQE), or apparent quantum yield (AQY). STH is defined as:

$$\mathrm{STH} = \frac{\text{Output energy as } H_2}{\text{Energy of incident solar light}},$$

And apparent quantum efficiency is defined as:

$$\mathrm{AQE\ or\ AQY} = \frac{nR}{I}$$

Here, n is the number of electrons required for the reaction (it is equal to 2 for photocatalytic hydrogen generation), R is the rate of hydrogen generation, and I is the rate of incident photons [18, 66, 67]. Water splitting is carried out in two ways, photocatalytic and photo-electrochemical (PEC). PEC systems require an electrochemical cell, photoanode, photocathode, and sacrificial agents. On the other hand, a particulate photocatalyst, sacrificial agents, and a light source are required for photocatalytic water splitting. Hence, photocatalytic water splitting using a particulate photocatalyst is much less costly than PEC water splitting systems [18]. In this chapter, photocatalytic water splitting using particulate photocatalyst has been discussed.

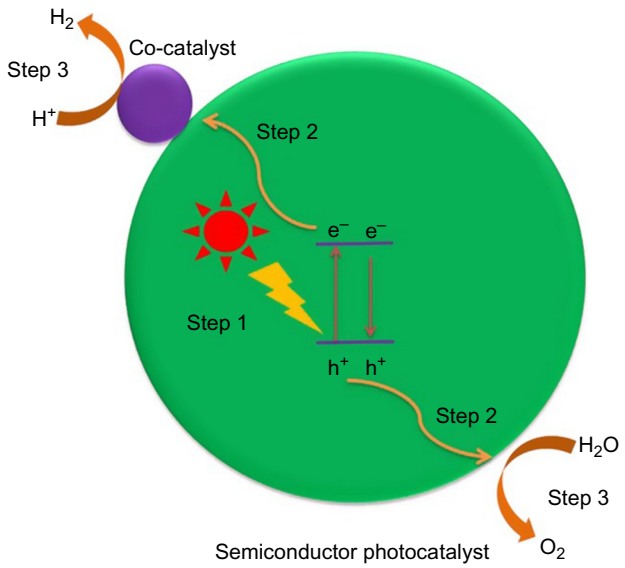

FIG. 3

Basic steps involved in photocatalytic water splitting.

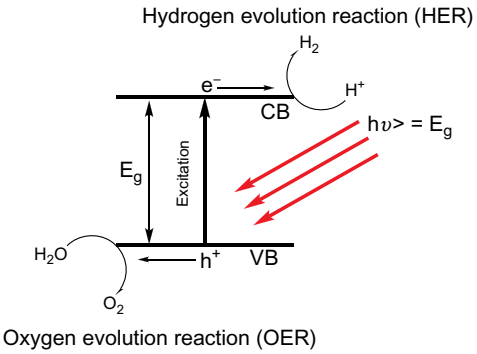

FIG. 4

Schematic representation of water splitting taking place as two half reactions.

Surface-intact nitrogen-doped GOQds (iNGO-QDs) containing abundant constituents such as carbon, nitrogen, oxygen, and nitrogen have been found to exhibit high H_2 generation yield from water splitting [53]. Nitrogen doping not only repairs vacancy type defects but also introduces n-type conductivity to compensate for unbalanced charges in p-type GO, and, in turn, suppresses the leakage of photogenerated charge carriers. Upon visible light illumination, there was steady generation of H_2 on the surface of iNGO-QDs from aqueous solution containing triethanoloamine (TEOA) as a sacrificial agent. After being deposited with a Pt cocatalyst, the H_2 evolution activity of iNGO-QDs was enhanced

with an AQE of 12.8% under monochromatic light ($\lambda > 420$ nm). The high H_2 evolution activity (2.2 millimole in 6 days) of iNGO-QDs can be ascribed to the coexistence of n and p-type domains on the iNGO-QDs surface to facilitate charge separation.

The GQDs have been found to act as effective sensitizers for many of the semiconductor photocatalysts such as TiO_2 [52], hexagonal tubular C_3N_4 [56], and nanocomposites such as $ZnNbO_6$/g-C_3N_4 [68] during water splitting. H_2 evolution catalyst consisting of N-GQDs-$ZnNbO_6$/g-C_3N_4 heterostructure was demonstrated by Yan et al. [68] The heterostructure favored the light harvesting and charge separation that resulted in high photocatalytic H_2 production (340.9 $\mu mol\, h^{-1}\, g^{-1}$) (Table 2) which was ascribed to the cooperative effects of NGQDs and heterojunction which generated more electron-hole pair and accelerated the charge separation across the interface (Fig. 5A). Cost effective hexagonal tubular C_3N_4 decorated with GQDs (P-TCN/GQDs) showed high H_2 production yield of 112.1 $\mu mol\, h^{-1}$(Table 2), which was almost 9 times greater than that of bulk C_3N_4 [56], which was attributed to photosensitization, electron acceptance by GQDs, and high light absorption (Fig. 5B). Similarly, GQDs act as solid-state electron transfer agents when anchored upon TiO_2 and tend to enhance the H_2 evolution activity [52]. The high H_2 evolution yield (41.26 $\mu mol\, h^{-1}$) was ascribed to the transfer of electrons from photo-excited GQDs to conduction band of TiO_2. Table 2 shows the summary of photocatalytic performance of GQD-based heterostructures for water splitting.

Table 2 Summary of Photocatalytic Performance of GQD-Based Heterostructures for Water Splitting

Photocatalyst	Photocatalyst Amount (mg/mL)	Sacrificial Agent	Cocatalyst	H_2 Evolution Yield ($\mu mol\, h^{-1}$)	STH (%)	AQE (%)	Ref.
iNGO-QDs	–	TEOA	Pt	15.2	–	12.8	[53]
GQDs-TiO_2	0.2	Methanol	–	41.26	–	–	[52]
P-TCN/GQDs	1.25	Methanol	Pt	112.1	–	–	[56]
N-GQDs-$ZnNbO_6$/g-C_3N_4	0.25	Methanol	Pt	17.04	–	–	[68]
S,N co-doped GQDs/TiO_2	0.2	Methanol	–	5.7	–	–	[69]
GQDs/Mn-N-TiO_2/g-C_3N_4	0.5	4 Nitrophenol	Pt	195.75	–	–	[58]
S doped GOQDs	2.5	Ethanol	–	76.29	–	–	[70]
g-C_3N_4/GQDs	0.25	TEOA	Pt	43.6	–	5.25	[24]
N doped GO-QDs	6	–	–	0.6	–	–	[71]
GQDs/BNPTL	1	TEOA	Pt	130	–	5.6	[13]

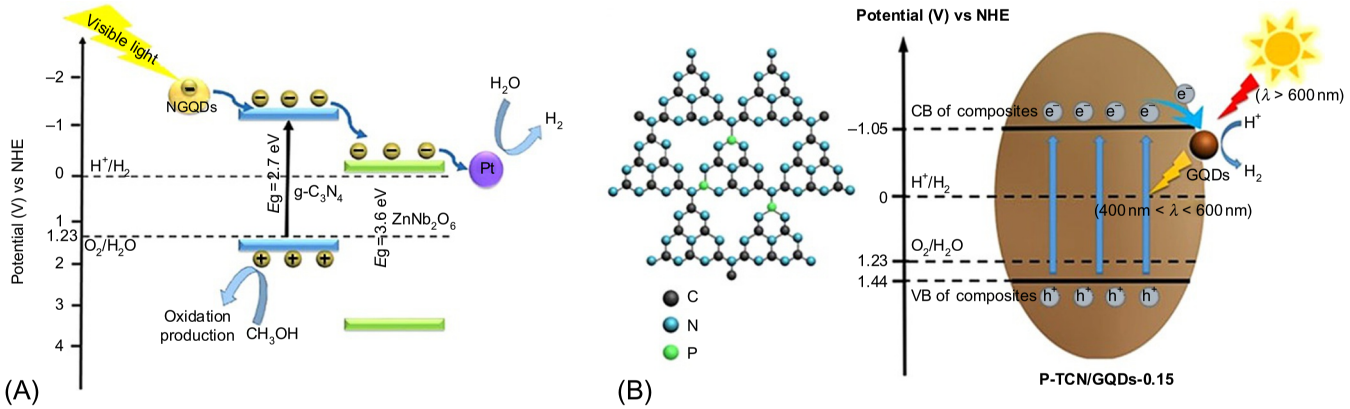

FIG. 5

Proposed mechanism of H_2 evolution over. (A) N-GQDs-$ZnNbO_6$/g-C_3N_4 and (B) PTCN/GQDs photocatalysts.

Reprinted with permission from (A) M. Yan, Y. Hua, F. Zhu, L. Sun, W. Gu, W. Shi, Constructing nitrogen doped graphene quantum dots-ZnNb2O6/g-C3N4 catalysts for hydrogen production under visible light, Appl. Catal. Environ. 206 (2017) 531–537, copyright (2017) Elsevier. (B) Y. Gao, F. Hou, S. Hu, B. Wu, Y. Wang, H. Zhang, B. Jiang, H. Fu, Graphene quantum-dot-modified hexagonal tubular carbon nitride for visible-light photocatalytic hydrogen evolution, ChemCatChem 10 (2018) 1330–1335, copyright (2018) Wiley.

3 C_3N_4 QUANTUM DOTS-BASED HETEROSTRUCTURED PHOTOCATALYSTS—PREPARATION METHODS AND PHOTOCATALYTIC APPLICATIONS FOR WASTEWATER TREATMENT AND WATER SPLITTING

3.1 SYNTHESIS PROCEDURES FOR GCNQDs BASED HETEROSTRUCTURES

Like GQD-based heterostructures, heterostructures based upon GCNQDs can be prepared by several procedures. GCNQDs were prepared from bulk g-C_3N_4 by a thermal chemical etching process [72] which involved the treatment of bulk g-C_3N_4 with concentrate HNO_3 and H_2SO_4 under mild ultrasonication, resulting in the formation of g-C_3N_4 nanorods which were hydrothermally treated to obtain GCNQDs. Hui et al. [73] have embedded GCNQDs upon Sb_2S_3/ultrathin g-C_3N_4 sheets. For this purpose, g-C_3N_4 sheets anchored with GCNQDs were synthesized by calcination of dicyanamide, followed by ultrasonication of g-C_3N_4 suspension, which was then centrifuged to remove large particles. $Na_2S.9H_2O$ was then added to the above suspension, which was further added to Sb_2Cl_3 solution in HCl and hydrothermally treated to obtain the resulting nanocomposite.

Xu et al. [74] carried out in situ growth of Ag and GCNQDs upon Bi_2MoO_6 nanosheets. The GCNQDs were prepared by a similar process as that described above, for which melamine was heated at 550 °C for 4 h to prepare bulk g-C_3N_4 which was treated with concentrated HNO_3 and H_2SO_4, and finally, hydrothermally treated for 24 h. Bi_2MoO_6 nanosheets were also hydrothermally prepared using $Bi(NO_3)_3$ and $(NH_4)_6Mo_7O_{24}$ as precursors. Recently, self-modified g-C_3N_4 with GCNQDs were synthesized by Zhou et al. [75], and for this purpose, GCNQDs were separately prepared from bulk g-C_3N_4 by treating it with concentrated HNO_3 and H_2SO_4 under ultrasonic conditions, followed by overnight hydrothermal treatment. The bulk g-C_3N_4 was dispersed in GCNQDs solution in ethanol and subjected to solvothermal treatment to obtain the final product.

3.2 GCNQD-BASED HETEROSTRUCTURED PHOTOCATALYSTS FOR WASTEWATER TREATMENT

Due to the presence of π-conjugated systems in GCNQDs, these also tend to have high charge carrier mobility apart from an optimum band gap (2.7 eV), making them highly promising for photocatalytic wastewater treatment and water splitting. There have been some recent efforts to investigate the photocatalytic activity of GCNQD-based materials for wastewater treatment. GCNQDs embedded on Sb_2S_3/ultrathin g-C_3N_4 sheets resulted in enhanced solar light absorption and fast electron transport of the resulting nanocomposite [73]. Also, the as-prepared nanocomposite possessed the photoelectric conversion property in near infrared (NIR) wavelength range. The photocatalytic performance was evaluated from degradation of methyl orange (MO) dye under NIR irradiation. The dye was degraded on the nanocomposite surface with a rate constant of 0.0103 min^{-1}, which was 2.6 times higher than pure Sb_2S_3. The improved photoactivity in NIR can be due to improved optical absorption in this region and upconversion PL property of GCNQDs. GCNQDs/Ag/Bi_2MoO_6 prepared by in situ growth of GCNQDs and Ag on Bi_2MoO_6 sheets showed significantly high photoactivity by degrading almost 100% RhB under visible light [74].

The extended optical absorption in the visible spectrum due to GCNQDs loading, interfacial separation of photo-induced charge carriers, and high surface area were the main factors which tended to enhance photocatalytic performance. GCNQD-decorated bulk g-C_3N_4 was employed for

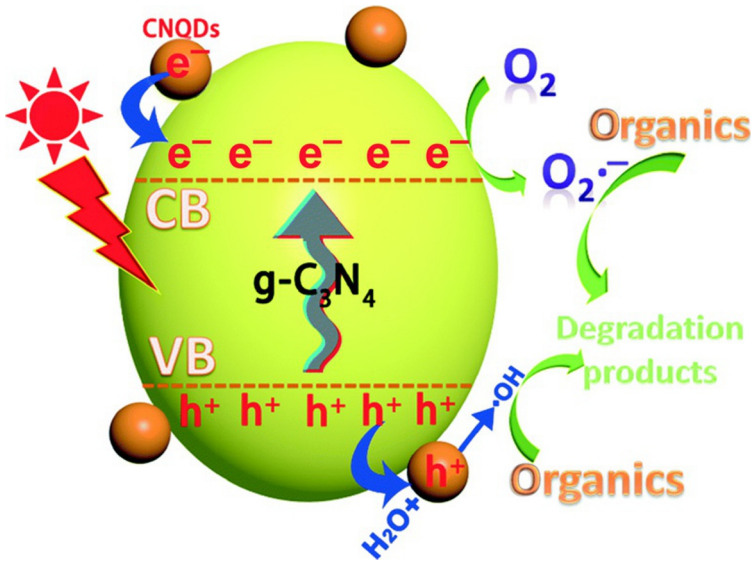

FIG. 6

Schematic illustration of electrohole separation in GCNQD-decorated bulk g-C_3N_4.

Reprinted with permission from L. Zhou, Y. Tian, J. Lei, L. Wang, Y. Liu, J. Zhang, Self-modification of gC 3 N 4 with its quantum dots for enhanced photocatalytic activity, Cat. Sci. Technol. (2018), copyright (2018) Royal Society of Chemistry.

photocatalytic degradation of RhB dye, and compared to bulk g-C_3N_4, the as-prepared nanocomposites were highly active in photocatalytic degradation of dye [75]. The key factors responsible for this high photoactivity are the efficient separation of electrons and holes (Fig. 6), fast electron transfer, longer charge carrier lifetime, and higher optical absorption. The stable interfaces between the GCNQDs and bulk g-C_3N_4 led to its high reusable efficiency. Table 3 briefly summarizes the photocatalytic performance of GCNQD-based heterostructures regarding water treatment.

3.3 GCNQD-BASED HETEROSTRUCTURES FOR WATER SPLITTING

In one of the earlier efforts made by Wang et al. [72] regarding water spitting from GCNQDs prepared by the abovementioned thermal chemical etching process, it was found that the GCNQDs showed strong blue emission and strong upconversion behavior that led to 2.27 times higher H_2 evolution rate compared to bulk g-C_3N_4 (Fig. 7A). Three-dimensional TiO_2 nanotube arrays combined with GCNQDs showed higher H_2 production yield than bulk g-C_3N_4 and TNA (Fig. 7B) [77]. The reduction in electron-hole recombination was the prime aspect that led to high performance by the photocatalyst. This can be attributed to the synergistic effect due to hetero-junction between GCNQDs and TNA. The well-ordered TNA nanostructure also contributed to the high photocatalytic performance. The average production of H_2 by the as-prepared photocatalysts was about 4.7 times higher ($243\,\mu mol\,h^{-1}\,g^{-1}$) compared to bulk g-$C_3N_4$. Table 4 summarizes the photocatalytic performance of GCNQD-based heterostructures for water splitting.

Table 3 Summary of Photocatalytic Performance of GCNQD-Based Heterostructures Regarding Water Treatment

Photocatalyst	Model Pollutant	Catalytic Amount (mg/mL)	Pollutant Concentration (ppm)	% Degradation	Rate Constant (min^{-1})	Ref.
GCNQDs-Sb_2S_3/ultrathin g-C_3N_4 sheets	MO	1	10	–	0.0103	[73]
GCNQDs/Ag/Bi_2MoO_6	RhB	0.2	0.01 mM	100	–	[74]
GCNQD-decorated bulk g-C_3N_4	RhB	1	20	–	0.08	[75]
GCNQDs/$InVO_4$/$BiVO_4$	RhB	0.5	0.01 mM	100	–	[76]

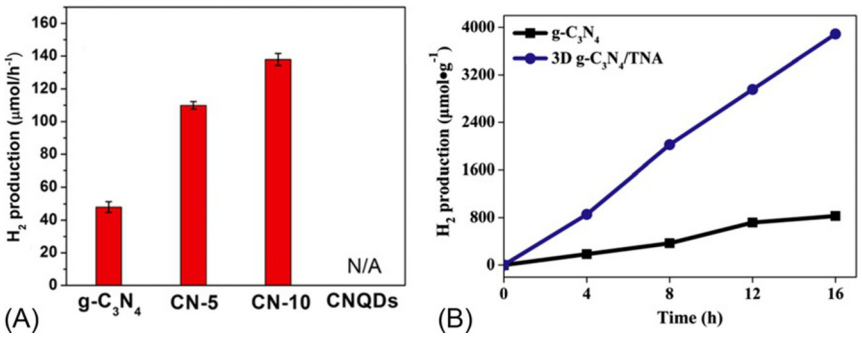

FIG. 7

(A) H_2 evolution for GCNQDs samples. (B) H_2 evolution for GCNQDs/TNA compared to bulk g-C_3N_4.

Reprinted with permission from (A) W. Wang, C.Y. Jimmy, Z. Shen, D.K. Chan, T. Gu, gC 3 N 4 quantum dots: direct synthesis, upconversion properties and photocatalytic application, Chem. Commun. 50 (2014) 10148–10150, copyright (2014) RSC. (B) Q. Zhang, H. Wang, S. Chen, Y. Su, X. Quan, Three-dimensional TiO_2 nanotube arrays combined with gC 3 N 4 quantum dots for visible light-driven photocatalytic hydrogen production, RSC Adv. 7 (2017) 13223–13227, copyright (2017) Royal Society of Chemistry.

4 CARBON QUANTUM DOTS-BASED HETEROSTRUCTURED PHOTOCATALYSTS: PREPARATION METHODS AND PHOTOCATALYTIC APPLICATIONS FOR WASTEWATER TREATMENT AND WATER SPLITTING

4.1 SYNTHESIS PROCEDURES FOR CQD-BASED HETEROSTRUCTURES

Carbon quantum dots (CQDs), carbon nanodots (CNDs), and carbon dots (CDs) are a class of carbon-based nanomaterials whose dimensions are all <10 nm; these can be called zero-dimensional carbon materials. GQDs discussed above also fall into this category. However, the major difference between the GQDs and the above carbon-based materials is that GQDs have sp^2 hybridized carbon, whereas

Table 4 Summary of Photocatalytic Performance of GCNQDs Based Heterostructures For Water Splitting

Photocatalyst	Photocatalyst Amount (mg/mL)	Sacrificial Agent	Cocatalyst	H_2 evolution Yield ($\mu mol\,h^{-1}$)	STH (%)	AQE (%)	Ref.
GCNQDs	0.5	TEOA	Pt	137.84	–	–	[72]
GCNQDs/TNA	1.11	Methanol	Pt	24.3	–	–	[77]

these consist of both sp^2- and sp^3-hybridized carbon atoms [78]. CQDs can be synthesized using both top-down and bottom-up approaches, in which the former technique includes laser ablation, electrochemical etching, arc discharge, etc., and the latter includes solvothermal/hydrothermal treatment, ultrasonic treatment in alkaline and acidic medium, pyrolysis, etc. [78, 79]

For preparation of CQD-based heterostructures, various approaches have been adopted. CQDs/TiO_2 heterostructures were prepared by simply adding as-prepared CQDs to the TiO_2 microsphere suspension. For this purpose, CQDs were synthesized by hydrothermal treatment of ascorbic acid (Fig. 8). Citric acid, along with diethyltriamine, was hydrothermally treated to prepare CNDs which were further hydrothermally coupled to WO_3 to obtain highly active CNDs/WO_3 heterojunctions whose photoactivity was examined by MB degradation [80]. CQDs/Bi_2MoO_6 nanocomposites were prepared by treating CQDs and Bi_2MoO_6 nanosheets under hydrothermal conditions. For this purpose, CQDs were prepared by a hydrothermal method using glucose as a precursor. Bi_2MoO_6 nanosheets were prepared by hydrothermal synthesis using $Bi(CH_3COOH)_3.5H_2O$ and $(NH_4)_6Mo_7O_{24}.4H_2O$ as starting materials [81].

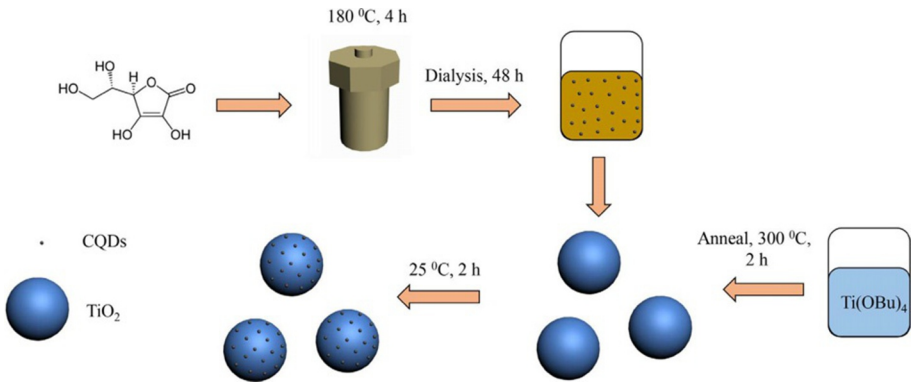

FIG. 8

Schematic diagram representing CQDs/TiO_2 synthesis.

Reprinted with permission from J. Ke, X. Li, Q. Zhao, B. Liu, S. Liu, S. Wang, Upconversion carbon quantum dots as visible light responsive component for efficient enhancement of photocatalytic performance, J. Colloid Interface Sci. 496 (2017) 425–433, copyright (2017) Elsevier.

4.2 CQD-BASED HETEROSTRUCTURED PHOTOCATALYSTS FOR WASTEWATER TREATMENT

Over the past few years, CQDs have appeared as an alternative to metal-oxide-based photocatalytic materials, as they mimic semiconductors' photophysical and electrochemical properties. Due to these promising features, these have found extensive application in photocatalytic wastewater treatment and water splitting. Like GQDs and GCQNDs, these have also been used as photosensitizers for semiconductors like TiO_2 [82–84]. CQDs have also been found to possess a photoluminescence (PL) upconversion property, by which a high energy photon is emitted by CQDs by absorbing two or more low energy photons. However, conventional semiconductor quantum dots emit long wavelength or low frequency photons after absorbing high frequency photons, and energy lost in the process is dissipated as heat, which tends to reduce the efficiency of semiconductor-based photocatalysts.

Ke [84] exploited this phenomenon by coupling CQDs with TiO_2 microspheres which led to notably high photocatalytic degradation of MB, as 90% of it was degraded by the resulting nanocomposite, which is about 3.6 times higher than pure TiO_2 (Figs. 9A–B). According to their proposed mechanism, when the nanocomposite was illuminated by visible light, then electrons photogenerated in the CQDs are transferred to the conduction band (CB) of TiO_2 (Fig. 9C). Higher frequency photons produced because of upconversion phenomena in CQDs tend to generate electron-hole pairs in TiO_2. Hence, these two processes contribute to high photoactivity of the nanocomposite. CNDs also play an important role in enhancing the photoactivity of CNDs/WO_3 nanocomposite photocatalysts by acting as electron trap, leading to the total degradation of MB dye [80]. Table 5 briefly summarizes the photocatalytic performance of CQD-/CD-/CND-based heterostructures regarding water treatment.

4.3 CQD-BASED HETEROSTRUCTURES FOR WATER SPLITTING

The development of CQD-based heterogeneous photocatalysts for H_2 production from water splitting has gained much importance in recent years. It has been found that carbon quantum dot-based heterostructures are capable of generating H_2 from water through some modifications. Some unique features of CQDs such as their high conductivity, high number of active sites, and tunable size and composition have made CQDs eligible candidates for water splitting application. As observed by Pan et al. [90] H_2 evolution activity of g-C_3N_4 TiO_2 increases upon the introduction of CQDs upon their surface, and further enhances by two orders of magnitude in CQDs/TiO_2/g-C_3N_4. It also provides an economical choice for photocatalytic water splitting without the aid of any sacrificial agent.

According to the proposed mechanism, the upconversion PL property of CQDs must have led to the emission of ultraviolet or near-ultraviolet light from visible light absorption in CQDs by two photon processes. The upconversion fluorescence (Fig. 10A) of CQDs under different excitation wavelengths ranging from 550 to 850 nm is excitation dependent and lies around 360 nm, which could excite TiO_2, leading to multiexciton generation (Fig. 10B) and high photocatalytic H_2 evolution. The CDs were also capable of obstructing the photocorrosion of CdS in CDs/CdS heterojunction photocatalysis by diminishing the interaction between holes and S^{2-} for stabilizing the catalyst [91]. Table 6 summarizes the photocatalytic performance of CQD-/CD-/CND-based heterostructures for water splitting.

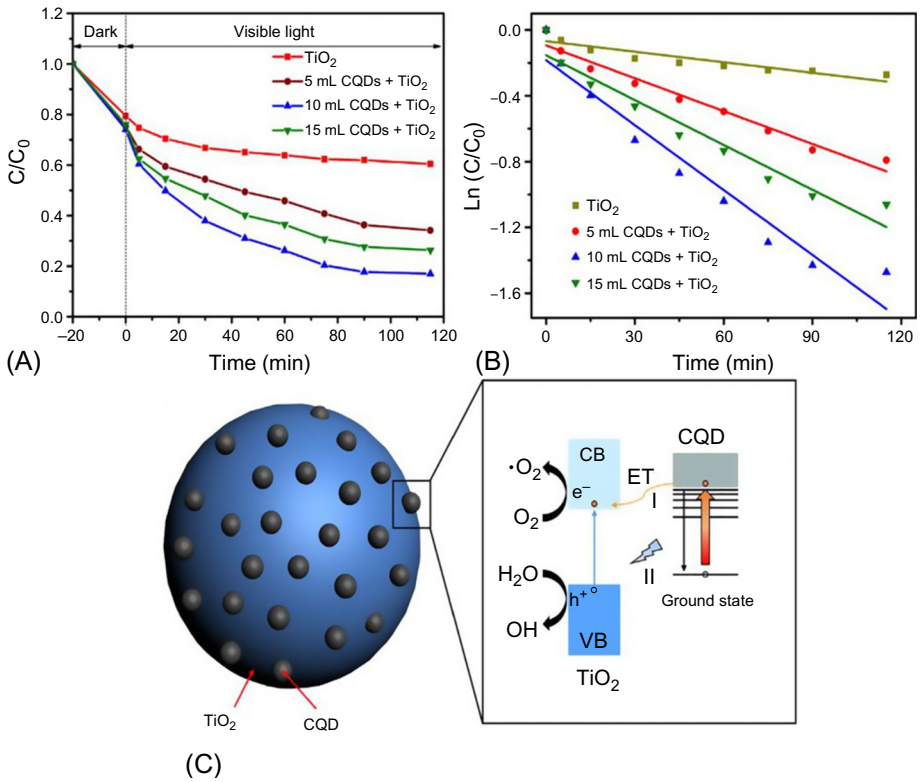

FIG. 9

(A) and (B) degradation efficiency of CQDs/TiO_2 photocatalyst for MB dye (C) proposed mechanism showing excitation of TiO_2 by PL upconversion phenomena in CQDs.

Reprinted with permission from J. Ke, X. Li, Q. Zhao, B. Liu, S. Liu, S. Wang, Upconversion carbon quantum dots as visible light responsive component for efficient enhancement of photocatalytic performance, J. Colloid Interface Sci. 496 (2017) 425–433, copyright (2017) Elsevier.

5 LIMITATIONS AND CHALLENGES

Even though GQDs and GCQDs have high potential in the field of photocatalysis, they suffer from some limitations which could hamper their practical use. Most GQDs and GCQDs are active in the blue/green region, which limits their light-harvesting capability. Low overall efficiency is still a major hurdle in GQD- and GCQD-based photocatalysts for water splitting. Modification of the electronic structure of GQDs and GCQDs can be a better strategy for countering this drawback [79].

The majority of GQD- and GCQD-based systems require noble metal cocatalysts for increasing the H_2 production yield, which, in turn, increases the cost for large-scale industrial application. Not all carbon-based quantum dots can generate H_2 by water splitting because the HOMO and LUMO of CQDs vary with their size, as observed from DFT calculations, and photosensitizers and sacrificial

Table 5 Summary of Photocatalytic Performance of CQD-/CD-/CND-Based Heterostructures Regarding Water Treatment

Photocatalyst	Model Pollutant	Catalytic Amount (mg/mL)	Pollutant Concentration (ppm)	% Degradation	Rate Constant (min^{-1})	Ref.
N-doped CQDs/P25	MB	0.5	10	91	0.044	[82]
TiO_2/CQDs	MB	0.5	20 μM	–	0.0136	[83]
Hydroxy-apatite-supported N-CQDs	MB	1	20	90	–	[85]
CQDs/TiO_2	MB	0.25	10	90	–	[84]
CNDs/WO_3	MB	0.6	10	100	–	[80]
AgBr/CDs/g-C_3N_4	RhB	0.5	10	96	0.07648	[86]
N-doped ZnO/CDs	Malachite Green	0.05	20	85	0.00912	[87]
Core-shell Cu@CQDs@ carbon hollow nanospheres	RhB	0.01	10	100	0.0796	[88]
CQDs/hydrogenated TiO_2 nanobelt	MO	1	20	50	–	[89]
CQDs/Bi_2MoO_6	RhB	1	10	100	0.029	[81]
	MB	1	10	100	0.048	

agents are required in most cases. Formation of an internal p-n junction can be a better strategy for increasing H_2 generation yield, but noble metal cocatalysts are still required to obtain high quantum efficiency. The PL upconversion phenomena in CQDs seems to be highly promising, but its efficiency is still needs improvement for better utilization in the photocatalysis field.

6 CONCLUSION

The carbon-based quantum dots such as GQDs, GCNQDs, and CQDs are promising candidates for application in the field of photocatalytic water purification and H_2 generation from water splitting. These can be readily obtained from carbon and nitrogen containing precursors by microwave and hydrothermal methods, and even by physical means such as ball milling, laser ablation, electrochemical etching, etc. These can act as excellent sensitizers for photocatalytic materials and enhance their performance not only for degradation of environmental effluents but also for H_2 generation from water splitting. Their excellent features such as low cost, low toxicity, band gap tunability, PL upconversion, and photostability make them distinguishable from and better than conventional metal-based quantum dots such as CdSe, CdS, CdTe, PbS, etc. Additionally, they also tend to inhibit the photo-instability of other semiconductors such as CdS by protecting them from being degraded by their own

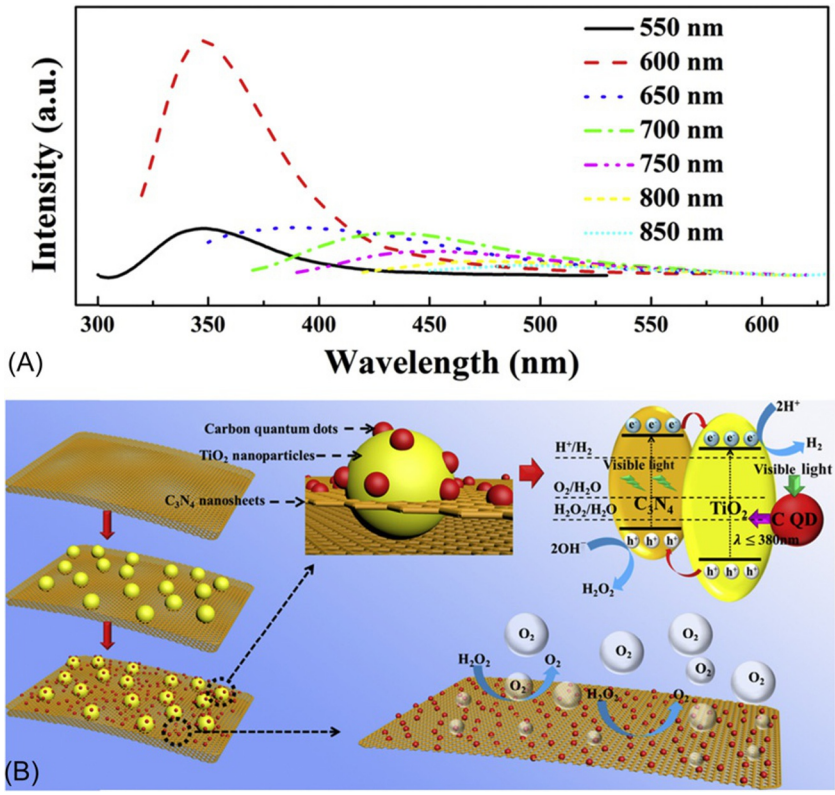

FIG. 10

(A) PL upconversion spectra of CQDs in the excitation wavelength range 550–850 nm. (B) Schematic representation of multiexciton generation by excitation of TiO_2 in visible light by PL upconversion in CQDs.

Reprinted with permission from J. Pan, M. You, C. Chi, Z. Dong, B. Wang, M. Zhu, W. Zhao, C. Song, Y. Zheng, C. Li, The two dimension carbon quantum dots modified porous g-C3N4/TiO2 nano-heterojunctions for visible light hydrogen production enhancement, Int. J. Hydrogen Energy 43 (2018) 6586–6593, copyright (2018) Elsevier.

Table 6 Summary of Photocatalytic Performance of CQD-/CD-/CND-Based Heterostructures Regarding Water Splitting

Photocatalyst	Photocatalyst Amount (mg/mL)	Sacrificial Agent	Cocatalyst	H_2 Evolution Yield ($\mu mol\,h^{-1}$)	STH (%)	AQE (%)	Ref.
CQDs/g-C_3N_4/TiO_2	0.5	–	–	0.3248	–	–	[90]
CQDs	0.068	EDTA	NiNPs	4.488	–	–	[92]
CDs/CdS	2	–	–	2.55	–	–	[91]
$BiVO_4$/CDs/CdS	0.8	–	–	1.24	–	–	[93]
Au@CQDs	1 mL	Methanol	–	56	1.89	–	[94]
CQDs/hydrogenated TiO_2 nanobelt	0.5	Ethanol	Pt	371	–	–	[89]

photogenerated holes. Moreover, the PL upconversion property leads to the excitation of wide band gap semiconductors such as TiO_2, making them a somewhat active participant in photocatalytic activity in visible light illumination. However, the dependence of these photoactive materials on noble metal cocatalysts like Au and Pt for obtaining high yield tends to increase their cost and makes them more efficient without the use of noble metal cocatalysts, which is, indeed, a crucial challenge that needs to be addressed.

REFERENCES

[1] X. Li, J. Low, J. Yu, Photocatalytic hydrogen generation, in: Photocatalysis, 2016, pp. 255–302.
[2] Z. Ma, R. Sa, Q. Li, K. Wu, Interfacial electronic structure and charge transfer of hybrid graphene quantum dot and graphitic carbon nitride nanocomposites: insights into high efficiency for photocatalytic solar water splitting, Phys. Chem. Chem. Phys. 18 (2016) 1050–1058.
[3] M. Batzill, Fundamental aspects of surface engineering of transition metal oxide photocatalysts, Energ. Environ. Sci. 4 (2011) 3275–3286.
[4] L. Nie, Q. Zhang, Recent progress in crystalline metal chalcogenides as efficient photocatalysts for organic pollutant degradation, Inorg. Chem. Front. 4 (2017) 1953–1962.
[5] H. Huang, Y. He, Z. Lin, L. Kang, Y. Zhang, Two novel Bi-based borate photocatalysts: crystal structure, electronic structure, photoelectrochemical properties, and photocatalytic activity under simulated solar light irradiation, J. Phys. Chem. C 117 (2013) 22986–22994.
[6] D. He, Q. Fu, Z. Ma, H. Zhao, Y. Tu, Y. Tian, D. Zhou, G. Zheng, H. Lu, Facile Synthesis and Photocatalytic Activity of ZnO/Zinc Titanate Core-Shell Nanorod Arrays, Materials Research Express, 2018.
[7] H. Huang, K. Liu, K. Chen, Y. Zhang, Y. Zhang, S. Wang, Ce and F comodification on the crystal structure and enhanced photocatalytic activity of Bi_2WO_6 photocatalyst under visible light irradiation, J. Phys. Chem. C 118 (2014) 14379–14387.
[8] C. Adán, J. Marugán, S. Obregón, G. Colón, Photocatalytic activity of bismuth vanadates under UV-A and visible light irradiation: inactivation of Escherichia coli vs oxidation of methanol, Catal. Today 240 (2015) 93–99.
[9] X. Chen, J. Wang, C. Huang, S. Zhang, H. Zhang, Z. Li, Z. Zou, Barium zirconate: a new photocatalyst for converting CO_2 into hydrocarbons under UV irradiation, Cat. Sci. Technol. 5 (2015) 1758–1763.
[10] F.-Q. Ma, J.-W. Yao, Y.-F. Zhang, Y. Wei, Unique band structure enhanced visible light photocatalytic activity of phosphorus-doped BiOI hierarchical microspheres, RSC Adv. 7 (2017) 36288–36296.
[11] W. Zhong, Y. Lou, S. Jin, W. Wang, L. Guo, A new Bi-based visible-light-sensitive photocatalyst BiLa 1.4 Ca 0.6 O 4.2: crystal structure, optical property and photocatalytic activity, Sci. Rep. 6 (2016) 23235.
[12] J. Lin, Z. Peng, C. Xiang, G. Ruan, Z. Yan, D. Natelson, J.M. Tour, Graphene nanoribbon and nanostructured SnO_2 composite anodes for lithium ion batteries, ACS Nano 7 (2013) 6001–6006.
[13] Y. Yan, J. Chen, N. Li, J. Tian, K. Li, J. Jiang, J. Liu, Q. Tian, P. Chen, Systematic bandgap engineering of graphene quantum dots and applications for photocatalytic water splitting and CO_2 reduction, ACS Nano 12 (2018) 3523–3532.
[14] X.T. Zheng, A. Ananthanarayanan, K.Q. Luo, P. Chen, Glowing graphene quantum dots and carbon dots: properties, syntheses, and biological applications, Small 11 (2015) 1620–1636.
[15] G. Rajender, J. Kumar, P. Giri, Interfacial charge transfer in oxygen deficient TiO_2-graphene quantum dot hybrid and its influence on the enhanced visible light photocatalysis, Appl. Catal. Environ. 224 (2018) 960–972.
[16] A. Bayat, E. Saievar-Iranizad, Graphene quantum dots decorated rutile TiO_2 nanoflowers for water splitting application, J. Energy Chem. 27 (2018) 306–310.

[17] D. Pan, J. Jiao, Z. Li, Y. Guo, C. Feng, Y. Liu, L. Wang, M. Wu, Efficient separation of electron–hole pairs in graphene quantum dots by TiO_2 heterojunctions for dye degradation, ACS Sustain. Chem. Eng. 3 (2015) 2405–2413.
[18] A. Naseri, M. Samadi, A. Pourjavadi, A.Z. Moshfegh, S. Ramakrishna, Graphitic carbon nitride (gC_3N_4)-based photocatalysts for solar hydrogen generation: recent advances and future development directions, J. Mater. Chem. A 5 (2017) 23406–23433.
[19] W.-J. Ong, L.-L. Tan, Y.H. Ng, S.-T. Yong, S.-P. Chai, Graphitic carbon nitride (gC_3N_4)-based photocatalysts for artificial photosynthesis and environmental remediation: are we a step closer to achieving sustainability? Chem. Rev. 116 (2016) 7159–7329.
[20] X. Wang, K. Maeda, A. Thomas, K. Takanabe, G. Xin, J.M. Carlsson, K. Domen, M. Antonietti, A metal-free polymeric photocatalyst for hydrogen production from water under visible light, Nat. Mater. 8 (2009) 76.
[21] Y. Zhang, Q. Pan, G. Chai, M. Liang, G. Dong, Q. Zhang, J. Qiu, Synthesis and luminescence mechanism of multicolor-emitting gC_3N_4 nanopowders by low temperature thermal condensation of melamine, Sci. Rep. 3 (2013). Article No. 1943. https://doi.org/10.1038/srep01943.
[22] Y. Sun, W. Ha, J. Chen, H. Qi, Y. Shi, Advances and applications of graphitic carbon nitride as sorbent inanalytical chemistry for sample pretreatment, TrAC Trends Anal. Chem. 84 (2016) 12–21.
[23] S. Panneri, P. Ganguly, B.N. Nair, A.A.P. Mohamed, K.G.K. Warrier, U.N.S. Hareesh, Role of precursors on the photophysical properties of carbon nitride and its application for antibiotic degradation, Environ. Sci. Pollut. Res. 24 (2017) 8609–8618.
[24] J.-P. Zou, L.-C. Wang, J. Luo, Y.-C. Nie, Q.-J. Xing, X.-B. Luo, H.-M. Du, S.-L. Luo, S.L. Suib, Synthesis and efficient visible light photocatalytic H 2 evolution of a metal-free gC_3N_4/graphene quantum dots hybrid photocatalyst, Appl. Catal. Environ. 193 (2016) 103–109.
[25] M. Zhou, Z. Hou, L. Zhang, Y. Liu, Q. Gao, X. Chen, N/n junctioned gC_3N_4 for enhanced photocatalytic H 2 generation, Sust. Energy Fuels 1 (2017) 317–323.
[26] S. Wang, Q. Lu, X. Yan, M. Yang, R. Ye, D. Du, Y. Lin, "On-off-on" fluorescence sensor based on gC_3N_4 nanosheets for selective and sequential detection of ag^+ and S2, Talanta 168 (2017) 168–173.
[27] X. Chang, X. Zhai, S. Sun, D. Gu, L. Dong, Y. Yin, Y. Zhu, MnO_2/gC_3N_4 nanocomposite with highly enhanced supercapacitor performance, Nanotechnology 28 (2017) 135705.
[28] Y. Zheng, Y. Jiao, Y. Zhu, Q. Cai, A. Vasileff, L.H. Li, Y. Han, Y. Chen, S.-Z. Qiao, Molecule-level gC_3N_4 coordinated transition metals as a new class of electrocatalysts for oxygen electrode reactions, J. Am. Chem. Soc. 139 (2017) 3336–3339.
[29] L. Lin, H. Ou, Y. Zhang, X. Wang, Tri-s-triazine-based crystalline graphitic carbon nitrides for highly efficient hydrogen evolution photocatalysis, ACS Catal. 6 (2016) 3921–3931.
[30] S. Cao, J. Yu, gC_3N_4-based photocatalysts for hydrogen generation, J. Phys. Chem. Lett. 5 (2014) 2101–2107.
[31] S. Ye, R. Wang, M.-Z. Wu, Y.-P. Yuan, A review on gC_3N_4 for photocatalytic water splitting and CO_2 reduction, Appl. Surf. Sci. 358 (2015) 15–27.
[32] S. Yang, Y. Gong, J. Zhang, L. Zhan, L. Ma, Z. Fang, R. Vajtai, X. Wang, P.M. Ajayan, Exfoliated graphitic carbon nitride nanosheets as efficient catalysts for hydrogen evolution under visible light, Adv. Mater. 25 (2013) 2452–2456.
[33] Y.-P. Zhu, T.-Z. Ren, Z.-Y. Yuan, Mesoporous phosphorus-doped gC_3N_4 nanostructured flowers with superior photocatalytic hydrogen evolution performance, ACS Appl. Mater. Interfaces 7 (2015) 16850–16856.
[34] S. Samanta, S. Martha, K. Parida, Facile synthesis of Au/g-C_3N_4 nanocomposites: an inorganic/organic hybrid Plasmonic Photocatalyst with enhanced hydrogen gas evolution under visible-light irradiation, ChemCatChem 6 (2014) 1453–1462.
[35] S. Liang, Y. Xia, S. Zhu, S. Zheng, Y. He, J. Bi, M. Liu, L. Wu, Au and Pt co-loaded gC_3N_4 nanosheets for enhanced photocatalytic hydrogen production under visible light irradiation, Appl. Surf. Sci. 358 (2015) 304–312.

[36] Y. Chen, W. Huang, D. He, Y. Situ, H. Huang, Construction of heterostructured $gC_3N_4/Ag/TiO_2$ microspheres with enhanced photocatalysis performance under visible-light irradiation, ACS Appl. Mater. Interfaces 6 (2014) 14405–14414.
[37] B. Wang, J. Zhang, F. Huang, Enhanced visible light photocatalytic H_2 evolution of metal-free gC_3N_4/SiC heterostructured photocatalysts, Appl. Surf. Sci. 391 (2017) 449–456.
[38] Y. Hong, Y. Meng, G. Zhang, B. Yin, Y. Zhao, W. Shi, C. Li, Facile fabrication of stable metal-free CQDs/gC_3N_4 heterojunctions with efficiently enhanced visible-light photocatalytic activity, Sep. Purif. Technol. 171 (2016) 229–237.
[39] Z. Tong, D. Yang, Y. Sun, Y. Nan, Z. Jiang, Tubular gC_3N_4 isotype heterojunction: enhanced visible-light photocatalytic activity through cooperative manipulation of oriented electron and hole transfer, Small 12 (2016) 4093–4101.
[40] G. Liu, G. Zhao, W. Zhou, Y. Liu, H. Pang, H. Zhang, D. Hao, X. Meng, P. Li, T. Kako, In situ bond modulation of graphitic carbon nitride to construct p–n homojunctions for enhanced photocatalytic hydrogen production, Adv. Funct. Mater. 26 (2016) 6822–6829.
[41] Y. Yang, S. Wang, Y. Li, J. Wang, L. Wang, Strategies for efficient solar water splitting using carbon nitride, Chem. Asian J. 12 (2017) 1421–1434.
[42] F. He, G. Chen, Y. Yu, Y. Zhou, Y. Zheng, S. Hao, The sulfur-bubble template-mediated synthesis of uniform porous gC_3N_4 with superior photocatalytic performance, Chem. Commun. 51 (2015) 425–427.
[43] L. Wang, Strategies for efficient solar water splitting using carbon nitride, Chem. Asian J. 12 (2017) 1421–1434.
[44] H.-J. Li, D.-J. Qian, M. Chen, Templateless infrared heating process for fabricating carbon nitride nanorods with efficient photocatalytic H_2 evolution, ACS Appl. Mater. Interfaces 7 (2015) 25162–25170.
[45] X. Wang, K. Maeda, X. Chen, K. Takanabe, K. Domen, Y. Hou, X. Fu, M. Antonietti, Polymer semiconductors for artificial photosynthesis: hydrogen evolution by mesoporous graphitic carbon nitride with visible light, J. Am. Chem. Soc. 131 (2009) 1680–1681.
[46] A. Wang, C. Wang, L. Fu, W. Wong-Ng, Y. Lan, Recent advances of graphitic carbon nitride-based structures and applications in catalyst, sensing, imaging, and LEDs, Nano Micro Lett. 9 (2017) 47.
[47] A. Bandyopadhyay, D. Ghosh, N.M. Kaley, S.K. Pati, Photocatalytic activity of gC_3N_4 quantum dots in visible light: effect of physicochemical modifications, J. Phys. Chem. C 121 (2017) 1982–1989.
[48] J. Wu, S. Yang, J. Li, Y. Yang, G. Wang, X. Bu, P. He, J. Sun, J. Yang, Y. Deng, Electron injection of phosphorus doped gC_3N_4 quantum dots: controllable photoluminescence emission wavelength in the whole visible light range with high quantum yield, Adv. Opt. Mater. 4 (2016) 2095–2101.
[49] T. Majumder, S.P. Mondal, Advantages of nitrogen-doped graphene quantum dots as a green sensitizer with ZnO nanorod based photoanodes for solar energy conversion, J. Electroanal. Chem. 769 (2016) 48–52.
[50] L. Wang, Y. Li, S. Li, Y. Wang, W. Kong, W. Xue, C. Li, Synthesis, characterization and photocatalytic activity of graphene quantum dots-ag solar driven photocatalyst, J. Mater. Sci. Mater. Electron. 28 (2017) 17570–17577.
[51] M. Yan, F. Zhu, W. Gu, L. Sun, W. Shi, Y. Hua, Construction of nitrogen-doped graphene quantum dots-$BiVO_4/gC_3N_4$ Z-scheme photocatalyst and enhanced photocatalytic degradation of antibiotics under visible light, RSC Adv. 6 (2016) 61162–61174.
[52] X. Hao, Z. Jin, J. Xu, S. Min, G. Lu, Functionalization of TiO_2 with graphene quantum dots for efficient photocatalytic hydrogen evolution, Superlattice. Microst. 94 (2016) 237–244.
[53] T.-F. Yeh, S.-J. Chen, H. Teng, Synergistic effect of oxygen and nitrogen functionalities for graphene-based quantum dots used in photocatalytic H_2 production from water decomposition, Nano Energy 12 (2015) 476–485.
[54] X. Bu, S. Yang, Y. Bu, P. He, Y. Yang, G. Wang, H. Li, P. Wang, X. Wang, G. Ding, Highly active black TiO_2/N-doped graphene quantum dots nanocomposites for sunlight driven photocatalytic sewage treatment, Chem. Select 3 (2018) 12260–12265.

[55] Y. Zhang, F. Qi, Y. Li, X. Zhou, H. Sun, W. Zhang, D. Liu, X.-M. Song, Graphene oxide quantum dot-sensitized porous titanium dioxide microsphere: visible-light-driven photocatalyst based on energy band engineering, J. Colloid Interface Sci. 498 (2017) 105–111.
[56] Y. Gao, F. Hou, S. Hu, B. Wu, Y. Wang, H. Zhang, B. Jiang, H. Fu, Graphene quantum-dot-modified hexagonal tubular carbon nitride for visible-light photocatalytic hydrogen evolution, ChemCatChem 10 (2018) 1330–1335.
[57] M. Yan, Y. Hua, F. Zhu, W. Gu, J. Jiang, H. Shen, W. Shi, Fabrication of nitrogen doped graphene quantum dots-BiOI/$MnNb_2O_6$ pn junction photocatalysts with enhanced visible light efficiency in photocatalytic degradation of antibiotics, Appl. Catal. Environ. 202 (2017) 518–527.
[58] Y.-C. Nie, F. Yu, L.-C. Wang, Q.-J. Xing, X. Liu, Y. Pei, J.-P. Zou, W.-L. Dai, Y. Li, S. L. Suib, Photocatalytic degradation of organic pollutants coupled with simultaneous photocatalytic H_2 evolution over graphene quantum dots/Mn-N-TiO_2/g-C_3N_4 composite catalysts: performance and mechanism, Appl. Catal. Environ. 227 (2018) 312–321.
[59] J. Liu, H. Xu, Y. Xu, Y. Song, J. Lian, Y. Zhao, L. Wang, L. Huang, H. Ji, H. Li, Graphene quantum dots modified mesoporous graphite carbon nitride with significant enhancement of photocatalytic activity, Appl. Catal. Environ. 207 (2017) 429–437.
[60] Y. Luo, M. Li, G. Hu, T. Tang, J. Wen, X. Li, L. Wang, Enhanced photocatalytic activity of sulfur-doped graphene quantum dots decorated with TiO_2 nanocomposites, Mater. Res. Bull. 97 (2018) 428–435.
[61] Q. Lu, Y. Zhang, S. Liu, Graphene quantum dots enhanced photocatalytic activity of zinc porphyrin toward the degradation of methylene blue under visible-light irradiation, J. Mater. Chem. A 3 (2015) 8552–8558.
[62] M. Ebrahimi, M. Samadi, S. Yousefzadeh, M. Soltani, A. Rahimi, T.-c. Chou, L.-C. Chen, K.-H. Chen, A. Z. Moshfegh, Improved solar-driven photocatalytic activity of hybrid graphene quantum dots/ZnO nanowires: a direct Z-scheme mechanism, ACS Sustain. Chem. Eng. 5 (2016) 367–375.
[63] K. Maeda, Photocatalytic water splitting using semiconductor particles: history and recent developments, J Photochem Photobiol C Photochem Rev 12 (2011) 237–268.
[64] R. Abe, Recent progress on photocatalytic and photoelectrochemical water splitting under visible light irradiation, J Photochem Photobiol C Photochem Rev 11 (2010) 179–209.
[65] R. Li, Latest progress in hydrogen production from solar water splitting via photocatalysis, photoelectrochemical, and photovoltaic-photoelectrochemical solutions, Chin. J. Catal. 38 (2017) 5–12.
[66] T. Hisatomi, J. Kubota, K. Domen, Recent advances in semiconductors for photocatalytic and photoelectrochemical water splitting, Chem. Soc. Rev. 43 (2014) 7520–7535.
[67] G. Ma, T. Hisatomi, K. Domen, Semiconductors for photocatalytic and photoelectrochemical solar water splitting, in: From Molecules to Materials, Springer, 2015, pp. 1–56.
[68] M. Yan, Y. Hua, F. Zhu, L. Sun, W. Gu, W. Shi, Constructing nitrogen doped graphene quantum dots-$ZnNb_2O_6$/g-C_3N_4 catalysts for hydrogen production under visible light, Appl. Catal. Environ. 206 (2017) 531–537.
[69] H. Xie, C. Hou, H. Wang, Q. Zhang, Y. Li, S, N co-doped graphene quantum dot/TiO_2 composites for efficient photocatalytic hydrogen generation, Nanoscale Res. Lett. 12 (2017) 400.
[70] T.-K. Wu, J. Gliniak, J.-H. Lin, Y.-T. Chen, C.-R. Li, E. Jokar, C.-H. Chang, C.-S. Peng, J.-N. Lin, W.-H. Lien, Sulfur-doped graphene oxide quantum dots as photocatalysts for hydrogen generation in the aqueous phase, ChemSusChem (2017).
[71] T.F. Yeh, C.Y. Teng, S.J. Chen, H. Teng, Nitrogen-doped graphene oxide quantum dots as photocatalysts for overall water-splitting under visible light illumination, Adv. Mater. 26 (2014) 3297–3303.
[72] W. Wang, C.Y. Jimmy, Z. Shen, D.K. Chan, T. Gu, gC_3N_4 quantum dots: direct synthesis, upconversion properties and photocatalytic application, Chem. Commun. 50 (2014) 10148–10150.
[73] H. Wang, X. Yuan, H. Wang, X. Chen, Z. Wu, L. Jiang, W. Xiong, G. Zeng, Facile synthesis of Sb_2S_3/ultrathin gC_3N_4 sheets heterostructures embedded with gC_3N_4 quantum dots with enhanced NIR-light photocatalytic performance, Appl. Catal. Environ. 193 (2016) 36–46.

[74] X. Lin, D. Xu, R. Zhao, Y. Xi, L. Zhao, M. Song, H. Zhai, G. Che, L. Chang, Highly efficient photocatalytic activity of gC_3N_4 quantum dots (CNQDs)/Ag/Bi_2MoO_6 nanoheterostructure under visible light, Sep. Purif. Technol. 178 (2017) 163–168.
[75] L. Zhou, Y. Tian, J. Lei, L. Wang, Y. Liu, J. Zhang, Self-modification of gC_3N_4 with its quantum dots for enhanced photocatalytic activity, Cat. Sci. Technol. 8 (2018) 2617–2623.
[76] X. Lin, D. Xu, J. Zheng, M. Song, G. Che, Y. Wang, Y. Yang, C. Liu, L. Zhao, L. Chang, Graphitic carbon nitride quantum dots loaded on leaf-like $InVO_4$/$BiVO_4$ nanoheterostructures with enhanced visible-light photocatalytic activity, J. Alloys Compd. 688 (2016) 891–898.
[77] Q. Zhang, H. Wang, S. Chen, Y. Su, X. Quan, Three-dimensional TiO_2 nanotube arrays combined with gC_3N_4 quantum dots for visible light-driven photocatalytic hydrogen production, RSC Adv. 7 (2017) 13223–13227.
[78] S. Zhu, Y. Song, X. Zhao, J. Shao, J. Zhang, B. Yang, The photoluminescence mechanism in carbon dots (graphene quantum dots, carbon nanodots, and polymer dots): current state and future perspective, Nano Res. 8 (2015) 355–381.
[79] H. Yu, R. Shi, Y. Zhao, G.I. Waterhouse, L.Z. Wu, C.H. Tung, T. Zhang, Smart utilization of carbon dots in semiconductor photocatalysis, Adv. Mater. 28 (2016) 9454–9477.
[80] F. Yan, D. Kong, Y. Fu, Q. Ye, Y. Wang, L. Chen, Construction of carbon nanodots/tungsten trioxide and their visible-light sensitive photocatalytic activity, J. Colloid Interface Sci. 466 (2016) 268–274.
[81] C. Sun, Q. Xu, Y. Xie, Y. Ling, J. Jiao, H. Zhu, J. Zhao, X. Liu, B. Hu, D. Zhou, High-efficient one-pot synthesis of carbon quantum dots decorating Bi_2MoO_6 nanosheets heterostructure with enhanced visible-light photocatalytic properties, J. Alloys Compd. 723 (2017) 333–344.
[82] N.C. Martins, J. Ângelo, A.V. Girão, T. Trindade, L. Andrade, A. Mendes, N-doped carbon quantum dots/TiO_2 composite with improved photocatalytic activity, Appl. Catal. Environ. 193 (2016) 67–74.
[83] A. Tyagi, K.M. Tripathi, N. Singh, S. Choudhary, R.K. Gupta, Green synthesis of carbon quantum dots from lemon peel waste: applications in sensing and photocatalysis, RSC Adv. 6 (2016) 72423–72432.
[84] J. Ke, X. Li, Q. Zhao, B. Liu, S. Liu, S. Wang, Upconversion carbon quantum dots as visible light responsive component for efficient enhancement of photocatalytic performance, J. Colloid Interface Sci. 496 (2017) 425–433.
[85] Q. Chang, K. Li, S. Hu, Y. Dong, J. Yang, Hydroxyapatite supported N-doped carbon quantum dots for visible-light photocatalysis, Mater. Lett. 175 (2016) 44–47.
[86] X. Miao, Z. Ji, J. Wu, X. Shen, J. Wang, L. Kong, M. Liu, C. Song, gC_3N_4/AgBr nanocomposite decorated with carbon dots as a highly efficient visible-light-driven photocatalyst, J. Colloid Interface Sci. 502 (2017) 24–32.
[87] S. Sharma, S. Mehta, S. Kansal, N doped ZnO/C-dots nanoflowers as visible light driven photocatalyst for the degradation of malachite green dye in aqueous phase, J. Alloys Compd. 699 (2017) 323–333.
[88] B. De, J. Balamurugan, N.H. Kim, J.H. Lee, Enhanced electrochemical and photocatalytic performance of core–shell CuS@ carbon quantum dots@ carbon hollow nanospheres, ACS Appl. Mater. Interfaces 9 (2017) 2459–2468.
[89] J. Tian, Y. Leng, Z. Zhao, Y. Xia, Y. Sang, P. Hao, J. Zhan, M. Li, H. Liu, Carbon quantum dots/hydrogenated TiO_2 nanobelt heterostructures and their broad spectrum photocatalytic properties under UV, visible, and near-infrared irradiation, Nano Energy 11 (2015) 419–427.
[90] J. Pan, M. You, C. Chi, Z. Dong, B. Wang, M. Zhu, W. Zhao, C. Song, Y. Zheng, C. Li, The two dimension carbon quantum dots modified porous gC_3N_4/TiO_2 nano-heterojunctions for visible light hydrogen production enhancement, Int. J. Hydrogen Energy 43 (2018) 6586–6593.
[91] C. Zhu, C. Liu, Y. Zhou, Y. Fu, S. Guo, H. Li, S. Zhao, H. Huang, Y. Liu, Z. Kang, Carbon dots enhance the stability of CdS for visible-light-driven overall water splitting, Appl. Catal. Environ. 216 (2017) 114–121.

[92] C.N. Virca, H. Winter, A.M. Goforth, M.R. Mackiewicz, T.M. McCormick, Photocatalytic water reduction using a polymer coated carbon quantum dot sensitizer and a nickel nanoparticle catalyst, Nanotechnology 28 (2017) 195402.

[93] X. Wu, J. Zhao, L. Wang, M. Han, M. Zhang, H. Wang, H. Huang, Y. Liu, Z. Kang, Carbon dots as solid-state electron mediator for $BiVO_4$/CDs/CdS Z-scheme photocatalyst working under visible light, Appl. Catal. Environ. 206 (2017) 501–509.

[94] A. Mehta, D. Pooja, A. Thakur, S. Basu, Enhanced photocatalytic water splitting by gold carbon dot core shell nanocatalyst under visible/sunlight, New J. Chem. 41 (2017) 4573–4581.

CHAPTER

NEW GENERATION NANO-BASED ADSORBENTS FOR WATER PURIFICATION

28

Ankita Dhillon*, Dinesh Kumar†

Department of Chemistry, Banasthali University, Rajasthan, India School of Chemical Sciences, Central University of Gujarat, Gandhinagar, India†*

1 INTRODUCTION

Despite being one of the most abundant resources, <1% of the available worldwide water supply is safe for human utilization [1]. It has been estimated that over 760 million people lacked sufficient drinking water in 2011, according to the World Health Organization (WHO) [2]. Rising energy costs, increasing populations, and other environmental issues have resulted in the increased cost of potable water [1, 3]. Additionally, there is an increasing risk of water contamination, particularly by pharmaceuticals and personal care products, due to the increasing number of drinking water sources [4, 5]. Such water challenges necessitate the utilization of novel water treatment procedures to harmonize [6] or substitute ongoing treatment technologies. Although engineered nanomaterials (ENMs) show potential application in full-scale water treatment and environmental remediation [7–9], their utilization in water treatment is still limited as effective adsorbents [10], filters [11], and disinfectants [12, 13].

Although nanoscale zerovalent iron has been utilized in water treatment methods in a few pilot and full-scale plants according to the literature [14–16], most other water purification studies utilizing ENMs remain at the laboratory-scale stage. Regulatory issues, methodological hurdles, lack of public awareness, environmental effect of nanomaterials, and the lack of comprehensive cost-benefit analyses with ongoing treatment technologies are barriers to innovative, proper utilization of these nanomaterials for water treatment purposes [17–19].

Although the latter drawback has been addressed by several publications involving the investigation of the utilization of ENMs for water purification [7, 19–21], not many evaluations have been done comparing ongoing water treatment technologies and nanotechnology. This chapter deals with the utilization of nanosized adsorbents for water and wastewater treatment. Finally, a discussion of the impact of toxic ENMs on public health and the environment is included.

Nanoscale Materials in Water Purification. https://doi.org/10.1016/B978-0-12-813926-4.00036-7

2 ADSORPTION

The process of adsorption involves the adhesion of pollutants on the surface of a solid substance (known as the adsorbent). Adsorption is mainly a surface phenomenon which involves physical forces, but, occasionally, it also involves some weak chemical bonding during the adsorption process [22]. The molecule or pollutant adsorbed on the solid surface is known as an adsorbate, and the surface on which the process of adsorption takes place is known as an adsorbent.

The phenomenon of adsorption is affected by different factors like temperature, adsorbate and adsorbent nature, and other existing pollutants, together with experimental parameters like pH, concentration, contact time, temperature, etc. First, the adsorption process was studied in batch method, and afterward, column studies were evaluated. Initially, a pilot-scale adsorption technology was developed which was later utilized at industrial scale in large columns.

3 WATER TREATMENT USING NANOPARTICLES

The utilization of nanoparticles (1–100 nm size) presents potential benefits in the field of wastewater treatment due to their unique properties. The small size, catalytic properties, excellent reactivity, high surface area, easy fabrication, and the presence of numerous active sites are important properties which made these particles the ultimate adsorbents in wastewater treatment. These characteristic properties increase the surface area, free active adsorption sites, and surface energies, which ultimately leads to their high adsorption capacities. Various commonly utilized nanoparticles in the field of wastewater treatment include alumina, anatase, akageneite, cadmium sulfide, cobalt ferrite, copper oxide, gold, iron oxide, nickel oxide, silica, stannous oxide, titanium oxide, zinc oxide, zirconia, and some alloys.

3.1 INORGANIC POLLUTANTS REMEDIATION

The process of adsorption is an efficient method utilized for the removal of inorganic pollutants from water. Oxides of aluminum, iron, and titanium are frequently utilized as nanoparticles for metal ion remediation. Iron oxide nanoparticles have been utilized for efficient water treatment because of their high surface areas and the ease of their fabrication methods [23–27]. Alternatively, zerovalent iron nanoparticles have also been utilized for the removal of various heavy metal ions from contaminated wastewater [28, 29]. Moreover, alumina nanoparticles have also gained attention in cadmium, copper, chromium, lead, and mercury metal ion remediation because of their cost-effective nature, high surface area, and excellent thermal stability [30–32]. Some metal ion contaminants and their removal efficiencies using various nanoparticles are discussed below.

3.1.1 Arsenic

Because of groundwater arsenic contamination in about 70 countries, people are drinking arsenic-contaminated water globally [33]. Therefore, it is imperative to remediate this hazardous metal ion from water.

In this regard, a nanocrystalline high surface area hybrid akaganeite has been developed for As(III) remediation [34]. Pena et al. carried out both As(III) and As(V) sorption on nanocrystalline titanium dioxide in 1 h [35]. The sorbent presented sorption capacity of 133.0 μM/g. A better adsorption of these

contaminants was achieved by Kanel et al. using nanoscale iron than that achieved using zerovalent iron [28]. The authors presented an inner-sphere surface complexation mechanism using laser light scattering analysis. Hristovski et al. studied 16 metal oxides nanoparticles for As(V) removal [36], out of which TiO_2, Fe_2O_3, ZrO_2, and NiO were most important. All the nanoparticles presented ~98% removal capacity except for ZrO_2. Zhu et al. developed nano-zerovalent, iron-loaded, activated carbon for arsenic adsorption [37]. Although the authors claimed it was an ideal adsorbent in arsenic-contaminated drinking water treatment, its low adsorption capacity further limited its large-scale application. Therefore, this group further developed a novel activated carbon-impregnated nano-zerovalent iron adsorbent for arsenate removal [38]. The adsorbent presented enhanced adsorption capacity compared to the previous one. Therefore, the authors claimed it was an appropriate adsorbent for drinking water treatment.

In a study, nanosized iron-oxide-coated quartz (IOCQ) utilized for the adsorption of As(V). The authors claimed 100% removal of arsenic within 5.0 min [39]. Chowdhury and Yanful developed magnetite-maghemite nanoparticles for the successful remediation of arsenic from aqueous solution [40]. The authors claimed 96%–99% arsenic uptake with maximum arsenic sorption of 3.69 mg/g and 3.71 mg/g for As(III) and As(V), respectively. Further, the presence of phosphate anions was found to negatively affect arsenic uptake. Jegadeesan et al. carried out sorption of As(III) and As(V) species on nanosized amorphous and crystalline TiO_2, with the former demonstrating good arsenic removal capacity in the 4–9 pH range [41]. The adsorption isotherms showed that the sorption capacities were a function of site density, surface area, and the crystalline nature of adsorbent. The adsorbent presented a binuclear, bidentate, inner-sphere complexation mechanism for As(III) and As(V) adsorption.

3.1.2 Cadmium

Adsorption technology has been employed for the removal of cadmium metal ions from water. In this regard, Deliyanni and Matis utilized akaganeite nanocrystals for the sorption of cadmium from aqueous solutions [42]. The adsorbent showed chemisorption of metal ions with the adsorption capacity of 17.1 mg/g. Adsorption capacity increased with temperature, demonstrating the endothermic nature of the adsorption process. In another study, alumina silica nanoparticles were developed for cadmium uptake from wastewater [43]. Almost 96.4% adsorption on Si-Al particles was reported. The presence of hydroxyl, alkoxy, and oxy groups on nanoparticles participated in cationic exchange process during the adsorption.

3.1.3 Chromium

The electroplating, leather tanning, dye, photography, and cement industries are common sources of chromium pollution. Lazaridis et al. employed rod-shaped nanocrystalline akaganeite adsorbent that carried out 80.0 mg/g removal of Cr(VI) ions at pH 5.5 [44]. In a study, the maghemite (γ-Fe_2O_3) nanoparticles carried out successful uptake of Cr(VI) from wastewater in the presence of Ni(II) and Cu(II) [45]. The nanoparticles were synthesized using the sol-gel method and showed 198 m^2/g BET surface area. The short duration equilibrium time (1.0 min) made it an excellent method for Cr(VI) removal. The adsorption capacities were in the order of Cu(II) > Ni(II) > Cr(VI). Different sized magnetic nanoparticles ($MnFe_2O_4$, $CoFe_2O_4$, $ZnFe_2O_4$, $CuFe_2O_4$, $NiFe_2O_4$, and $MgFe_2O_4$) were utilized by Hu et al. for the removal of chromium from aqueous systems [46]. Out of them, $MnFe_2O_4$ nanoparticles presented the highest adsorption efficiency (99.5%) at acidic pH because of the highest surface area of $MnFe_2O_4$ nanoparticles (180 m^2/g). The adsorption capacity order for Cr(VI) was

$MnFe_2O_4 > MgFe_2O_4 > ZnFe_2O_4 > CuFe_2O_4 > NiFe_2O_4 > CoFe_2O_4$. Guan et al. developed Fe_3O_4/*Sphaerotilus natans* for the adsorption of Cr(VI) metal ion [47]. The adsorbent presented a low adsorption capacity of 0.0217 mM/g at acidic pH. The —$CONH_2$— and —NH— groups of Fe_3O_4/*Sphaerotilus natans* adsorbent carried out trapping of Cr(VI) metal ions by electrostatic attraction.

3.1.4 Cobalt

The electroplating, alloy, metallurgical, petrochemical paints, and coal industries are the most common cobalt contamination sources. Due to the low toxicity of cobalt, less research has been done on its uptake from aqueous solutions by using nanoparticles. Chang et al. carried out quick 27.5 mg/g adsorption of cobalt using magnetic chitosan nanoparticles from aqueous solutions at pH 3.0–7.0 [48]. The exothermic nature of adsorption process might be because of the low electrostatic force of attraction at high temperature. In another study, Fe_3O_4 and γ-Fe_2O_3 nanoparticles were developed by Uheida et al. for cobalt removal [49]. The Fe_3O_4 and γ-Fe_2O_3 nanoparticles presented 5.8×10^{-5} and 3.7×10^{-5} mol/m^2 maximum adsorption capacities, correspondingly. The process displayed an endothermic nature.

3.1.5 Copper

Fertilizer waste waters, and the electrical, paint, electroplating, pigment, and wood manufacturing industries are some common copper pollution sources [50]. Monodisperse chitosan-bound Fe_3O_4 nanoparticles were developed by Chang and Chen for the efficient removal of Cu(II) ions [51]. The adsorbent presented maximum Langmuir adsorption capacity of 21.5 mg/g. The adsorption capacity increased with pH from pH 2–5, and an exothermic process occurred. Due to almost negligible internal diffusion resistance, fast removal (1 min) of Cu(II) ions occurred. A magnetic nanoadsorbent was prepared by Banerjee and Chen by treating Fe_3O_4 nanoparticles with gum arabic, and it was utilized for copper metal ion uptake from aqueous solution [52]. Attachment of gum arabic with Fe_3O_4 occurred by the interaction of the COO^- groups of gum arabic with the surface OH^- of Fe_3O_4. Due to almost negligible internal diffusion resistance, fast removal (2 min) of Cu(II) ions occurred with increasing pH. On comparing the adsorption of Cu(II) onto the magnetic and gum arabic-modified magnetic nanoparticles, it was found that the adsorption capacity of modified nanoparticles (38.5 mg/g) was superior to nonmodified (17.6 mg/g) nanoparticles. This was because modified nanoparticles have carboxylic groups of gum arabic, complexation of the amine group of gum arabic, and surface hydroxyl groups of iron oxide.

In a study, nanohydroxyapatite (n-HAp) was prepared with chitin and chitosan by Gandhi et al. for the removal of Cu(II) ions from the water [53]. The adsorbent showed adsorption capacity in the order n-HAp/chitosan (n-HApCs) composite > n-HAp/chitin (n-HApC) composite > n-Hap with a contact time of 30 min. Hao et al. prepared a magnetic nanoadsorbent (MNP-NH_2) via covalent binding of 1,6-Hexadiamine on the Fe_3O_4 surface and utilized it for copper ion uptake from aqueous solution [54]. The adsorption process was optimized in terms of contact time, temperature, pH, salinity, MNP-NH_2 concentration, and copper ion initial concentration. The adsorbent showed maximum Langmuir adsorption capacity of 25.77 mg/g at room temperature. Goethite and hematite (nanogoethite and nanohematite) nanoparticles were developed by Chen et al. [55] Both the nanohematite and nanogoethite presented good adsorption capacity of 149.25 mg/g and 84.46 mg/g for copper ions, correspondingly.

3.1.6 Selenium

Agricultural exercises, industrial processes like mining, the petrochemical industry, and so forth are the chief sources of selenium contamination. Titanium dioxide nanoparticles were developed by Zhang et al. for the selenium ion sorption [56]. Both boundary layer diffusion and intraparticle diffusion steps were found to affect the adsorption process. Dubinin-Radushkevich (D-R) adsorption isotherm presented 14.46 kJ/mol mean energy of adsorption at room temperature. Thermodynamic studies showed the exothermic nature of adsorption.

3.1.7 Miscellaneous metal ions

The above-discussed methods presented a specific metal ion uptake by a specific nanoparticle, but few researchers carried out more than one metal ion uptake using a single adsorbent which is presented herein. In a study, a polymeric hybrid nanoparticle sorbent (ZrPS-001) was developed by Zhang et al. for sorption of lead, cadmium, and zinc ions from wastewater [57]. A 2,4-dinitrophenylhydrazine (DNPH) immobilized on sodium dodecyl sulfate-coated nanoalumina sorbent was developed by Afkhami et al. for Pb(II), Cd(II), Cr(III), Co(II), Ni(II), and Mn(II) metal cations uptake from wastewater [58]. The maximum adsorption was found in the case of Pb(II), Cr(III), and Cd(II) ions from aqueous systems. Deliyanni et al. efficiently removed zinc ion using akaganeite nanoparticles [59]. Thermodynamic studies showed the exothermic nature of adsorption with 95% adsorption at almost neutral pH.

3.1.8 Anions

Elevated concentration of anions, like metal ions, beyond the permissible limit is not desirable in drinking water because of their ill effects on human health. Both domestic and agriculture activities are the chief sources of anions contamination in water. In addition, some industries are also known to augment anion concentration in water. Therefore, a lot of research is dedicated to the utilization of nanoparticles for anions uptake from contaminated water.

In continuous efforts for developing high-efficiency adsorbents, we have developed an Fe-Ce-Ni nanoporous adsorbent for fluoride removal [60]. The adsorbent showed excellent adsorption capacity in the most favorable pH range from 5.0 to 7.0. The chemical composition of the adsorbent was studied using energy-dispersive X-ray spectroscopy (EDS) analysis that confirmed the presence of Fe, Ce, Ni, and O elements. The elemental F peak in the EDS spectrum after fluoride adsorption confirmed fluoride adsorption. FTIR analysis demonstrated the adsorption mechanism. The reduction in FTIR band intensity at 1385.8 cm^{-1} suggested the ion exchange of nitrate with fluoride. Further, the decrease in intensity of FTIR bands at 3410 and 1634 cm^{-1} attributed to the fluoride interaction with the adsorbent hydroxyl groups, demonstrating an ion exchange mechanism of fluoride adsorption.

Further, we have developed another Fe-Ca-Ce nanoporous adsorbent having higher adsorption capacity than the previous one for fluoride removal [61]. The adsorbent showed excellent adsorption capacity of 384.6 mg/g. The chemical composition of the adsorbent was studied using EDS analysis that confirmed the presence of Fe, Ca, Ce, and O elements. The elemental F peak in the EDS spectrum after fluoride adsorption confirmed fluoride adsorption. The XRD peaks at 28.57, 47.60 and 59.13 degrees were demonstrated to be the characteristic CeO_2 peaks. The absences of FeO_2 and CaO_2 phase were due to the development of a Fe-Ca-Ce solid solution, wherein the Fe and Ca species had entered the lattice of CeO_2. FTIR analysis demonstrated the adsorption mechanism. The reduction in FTIR band intensity at 1648.7 cm^{-1} was attributed to fluoride interaction with the adsorbent hydroxyl groups,

demonstrating an ion exchange mechanism of fluoride adsorption. Furthermore, the appearance of two new adsorption peaks at 459.6 and 525.8 cm^{-1} were attributed to the Fe-F, and Ce-F bonds, respectively, that supported the electrostatic adsorption mechanism. A new characteristic XRD peak at 20 degrees further supported the adsorption of fluoride. In our continuous efforts in water purification, we have developed a promising hybrid metal oxide nanoadsorbent for the collective removal of fluoride and a disinfectant for *E. coli* [62]. A hydrous hybrid Fe-Ca-Zr oxide nanoadsorbent showed excellent fluoride adsorption capacity of 250 mg/g at pH 7.0 much greater than other commercially accessible adsorbents for both synthetic and real water samples. FTIR analysis demonstrated the ion exchange adsorption mechanism. The reduction in FTIR band intensity at 1113 cm^{-1} suggested the ion exchange of hydroxyl groups with fluoride. Additionally, the appearance of an adsorption peak at 459 cm^{-1} was attributed to the Fe-F.

Hydrated ferric oxide nanoparticles dispersed as polymeric anion exchanger beads were developed by Martin et al. for high phosphate uptake from water [63]. Xi et al. utilized nanoscale iron for the sulfide removal from water [64]. On increasing the iron dosage and decreasing initial concentration and pH, the efficiency of sulfide removal increased. Increasing and decreasing the temperature beyond 25°C decreased the adsorption capacity. The process of removal occurred via the development of surface complexes onto the iron nanoparticles by means of FeOSH and iron sulfides (FeS, FeS_2, FeS_n). A magnetic nanoadsorbent was developed by Huang and Chen by covalent binding of poly(acrylic acid) (PAA) onto the surface of Fe_3O_4 nanoparticles, followed by amino functionalization [65]. The whole process was carried out via diethylenetriamine (DETA) via carbodiimide activation. The developed nanoadsorbent showed efficient uptake of a few anions.

3.2 REMOVAL OF ORGANIC POLLUTANTS

Nanoparticles have been utilized in adsorption technology for organic pollutant remediation from water. Various metal nanoparticles demonstrated efficient normal and halogenated hydrocarbons removal. The removal of various organic pollutants is discussed below.

3.2.1 Dyes

The various textile, paper, rubber, plastics, paints, printing, and leather industries are the main sources of dye pollution. Various nanoadsorbents are discussed herein for dye removal. Belessi et al. reported the removal of reactive red 195 azo dye using TiO_2 nanoparticles [66]. The process optimization was carried out in terms of pH, the concentration of dye, and adsorbent dose. The adsorbent showed maximum adsorption capacity of 87.0 mg/g at pH 3.0 and 30°C temperature. The adsorption kinetic showed a rapid sorption of dye within 30 min, and equilibrium was achieved in 1 h. Moussavi and Mahmoudi developed high surface area MgO nanoparticles for azo and anthraquinone reactive dyes remediation from industrial wastewaters [67]. Both blue 19 and reactive red 198 dyes were 98% removed within 5 min with a 0.2 g adsorbent dose, pH 8.0.

Chen et al. developed templated cross-linked chitosan, ECH-RB5, and ECH-3R nanoparticles for azo dye uptake from water [68]. Thermodynamic studies demonstrated the spontaneous and exothermic nature of the adsorption process. The adsorption kinetics indicated the physicochemical nature of adsorption process, with predominant adsorption occurring via a chemisorption step. Removal of acid dyes, namely, orange G and acid green, was achieved by Chang and Chen using carboxymethylated chitosan conjugated Fe_3O_4 nanoparticles [69]. Increases in both pH and ionic strength reduced the

adsorption capacity. Similarly, adsorption of acid dye onto chitosan nanoparticles was achieved by Cheung and Szeto [70]. The adsorbent showed Langmuir adsorption capacities of 1.54, 2.66, 1.11, 1.25, and 1.03 mM/g for orange 10, acid orange 12, acid red 18, acid red 73, and acid green 25, respectively. Predominantly, the adsorbent followed an intraparticle diffusion-adsorption mechanism, but it was also found to be a function of pore size due to the diffusion of dyes through micropores, mesopores, and micropores, respectively.

A chain of biopolymer chitosan/montmorillonite (CTS/MMT) nanocomposites were synthesized by Wang and Wang for Congo red dye removal [71]. The developed CTS/MMT nanocomposites presented higher adsorption capacity than the individual CTS and MMT adsorbent. The silica nanosheets were derived from vermiculite via acid leaching by Zhao et al. for the adsorption of methylene blue [72]. The adsorption process was favored by a high concentration of dye, and low pH and temperature. Thermodynamic studies demonstrated an increase in the entropy of the system during the adsorption process. The effect of in situ ZrO_2 nanoparticle development on granulated activated carbon (GAC) properties was investigated by Sandoval et al. for methylene blue uptake from water [73]. Iram et al. developed hollow Fe_3O_4 nanospheres for dye decontamination from aqueous systems [74]. The hollow Fe_3O_4 nanospheres presented monolayer adsorption capacity of 105 mg/g. The spontaneous and endothermic nature of adsorption was confirmed by thermodynamic study.

3.2.2 Pesticides

Various industries, as well as agricultural, forestry, and domestic activities, are the chief pesticide pollution sources. Additionally, dust particles in air also adsorbed on the pesticide, which through rainwater finally contaminate water bodies, sediments, and soil. Still, not enough research has been carried out in the field of removal of pesticides by using nanoparticles. Only Li et al. synthesized nano-SiO_2 and nanokaolin particles for the adsorption of atrazine [75]. The optimization of adsorption parameter was done in terms of ionic strength, atrazine concentration, and pH. It has been found that increasing ionic strength decreased the adsorption of atrazine. Interestingly, an increase in pH decreased the adsorption process, possibly because of atrazine speciation change as the dominant factor during the adsorption mechanism.

3.2.3 Hydrocarbons

Dry cleaning practices, paint, spot remover, and some industries are the chief hydrocarbon pollutant sources, and the petrochemical industry plays a major role in elevating hydrocarbon concentration. Nano-TiO_2 and ZnO particles have been developed by Yang and Xing for the phenanthrene adsorption [76]. The process parameters were optimized by the authors to achieve maximum adsorption. The same authors carried out the coating of nanosized alumina using sequentially extracted humic acids for the sorption of phenanthrene [77].

3.3 REMOVAL OF BIOLOGICAL POLLUTANTS

Domestic activities are responsible for biological contamination, and some agricultural activities are responsible for biological water contamination. Not many papers are available in the literature for biological pollutant remediation by adsorption on nanoparticles.

3.3.1 Viruses and bacteria

Virus and bacteria are known to be responsible for various types of human diseases. These pathogens are toxic and a threat to human health. Researchers have developed nanoparticles for remediation of water contaminated by these pathogens. Four varieties of iron oxide nanoparticles were developed by Shen et al. for virus adsorption, and reportedly, they demonstrated 100% adsorption on α-Fe_2O_3 nanoparticles [78]. A decrease in initial virus concentration increased the adsorption percentage. High ionic strength of the background solution was found to reduce virus adsorption, demonstrating the electrostatic interaction between the adsorbent and viral agent. In another study, nanoscale zerovalent iron (NZVI) has been utilized as a bactericidal agent against *Escherichia coli* [79]. The developed nanoparticles were tested for their bactericidal properties against various molecules. Adsorption of polystyrene sulfonate (PSS), poly(aspartate) (PAP), or NOM on NZVI without any change in Fe(0) concentration considerably reduced its toxicity against the tested bacteria. However, the nanoparticles displayed minimum inhibitory concentration (MIC) of 5.0 mg/L after 24 h despite Fe(0) concentration. The PSS, PAP, and NOM-coated NZVI showed MIC of 500, 100, and 100 mg/L, respectively. The efficient antibacterial activity of the nanoparticles might be due to the adsorption phenomenon which inhibits the *E. coli* growth.

3.4 NANOTUBES APPLICATIONS

Carbon nanotubes are a special type of nanosized structure. Because of their high chemical constancy and surface area, they have gained popularity as adsorbents in wastewater purification. The successful uptake of various metal ions by these nanotubes has resulted in their being utilized for water purification more than any other nanoadsorbent. As a result, we have made a separate subsection to detail metal ion removal by nanotubes. Carbon nanotubes have been further subdivided into single-walled carbon nanotubes (SWCNT) and multiwalled carbon nanotubes (MWCNT). Some imperative studies on the utilization of CNT for heavy metal ion remediation from wastewater are discussed as follows.

Pb(II) adsorption kinetics and thermodynamics were studied by Li et al. on CNTs [80]. Similarly, MWCNTs were utilized by Kochkar et al. for Cd(II), Pb(II), and Cu(II) ion remediation from water [81]. The MWCNTs showed Langmuir adsorption capacities of 97.08, 24.49, and 10.86 mg/g for Pb(II), Cu(II), and Cd(II), respectively. Yang et al. utilized the Stone-Wales defect sites of zigzag and armchair single-walled carbon nanotubes for nickel adsorption [82]. The reactivity of Stone-Wales defects having carbon-carbon was more as compared to a perfect hexagon, thereby enhancing nickel uptake. A correlation with the orientation of the Stone-Wales defects relating to the tube axis was found for nickel adsorption. Lu and Chiu studied zinc ion adsorption on commercial single-walled and multiwalled CNTs from water [83]. The adsorption efficiency increased up to pH 8.0, and adsorption equilibrium was achieved within 60 min. MWCNTs showed higher adsorption capacity as compared to SWCNTs toward Zn(II) ions. An aligned carbon nanotube was developed by Di et al. for chromium removal from drinking water [84]. A 1.5 times higher adsorption capacity (30.2 mg/g) than activated carbon at neutral pH. Carbon nanotubes (CNT) and titanate nanotubes (TNT) were developed by Doong and Chiang for the removal of copper metal ions [85]. The optimized adsorbent presented Langmuir adsorption capacities for copper in the range of 83–124 mg/g and for lead in the range of 192–588 mg/g. Oxygeneous functional groups on acidified MWCNTs were involved in the adsorption mechanism.

Wu modified CNTs with HNO_3 and NaOCl for the removal of Cu(II) ions [86]. A change in the pH from acidic to basic range increased the adsorption capacities of Cu(II). Dissolved organic matter (DOM) in wastewater was remediated by Lou et al. using single-walled carbon nanotubes [87]. Various parameters like pH, ionic strength, and temperature were controlled for better adsorption, and it was found that increasing DOM concentration increased adsorption capacity, while enhancing ionic strength reduced the adsorption capacity of SWCNTs. SWCNTs showed maximum adsorption capacities of 26.1–20.8 mg/g at pH 4, and equilibrium was achieved only after 120 min. A reactive red M-2BE textile dye was removed by Machado and colleagues from aqueous solutions by using MWCNTs [88]. Parameter optimization showed that acidic pH was favorable for dye adsorption, and equilibrium was attained after 1 h. In a study, remediation of benzene, toluene, and m-xylene was described on thin multiwalled carbon nanotubes (t-MWCNTs). The van't Hoff equation was utilized for the calculation of isosteric heat of adsorption, and the results suggested good adsorption of these hydrocarbons from wastewater. Although CNTs have found wide application in the field of water purification practices, they still have certain limitations in the adsorption method of water treatment. At times, they become coagulated in water and lose their nano-characteristics, especially in the presence of organic matter and algae. Further, CNT doses are also known to affect their coagulation rate. For that reason, these aspects of CNTs should be kept in mind during water purification. An efficient water treatment can be achieved by taking a suitable dose of CNT devoid of organic matter and algae.

4 NANOTOXICOLOGY

Nanoparticles (<100 nm diameter) display toxicity which is a threat to both the environment and human health. Due to the small size of nanoparticles, they can easily penetrate living systems. Titanium dioxide, alumina, zinc oxide nanoparticles, carbon black, and carbon nanotubes have predominantly been studied for nanotoxicity.

Nanoparticles may cause inflammation (mostly of lung tissue) due to their larger surface area, surface charge, and aggregation. Moreover, the ability of some nanoparticles to translocate from one point to another may affect important human organs, for instance, blood, liver, skin, gut, and brain. These nanoparticles commonly enter the human body via skin [89], inhalation [90], ingestion [91], and so on, after which they can reach different body parts like the brain, heart, liver, kidneys, spleen, bone marrow, and nervous system via the bloodstream [92–95].

Due to their nanosize range and high surface-area-to-volume ratio, they show high chemical reactivity and biological activity, thereby resulting in the development of reactive oxygen species (ROS). These ROS and free radicals are mainly generated by carbon fullerenes, carbon nanotubes, and metal oxide nanoparticles, which are the chief mechanisms of nanotoxicity. The generation of ROS and free radicals can result in oxidative stress, soreness, and subsequent harm to proteins, cell membranes, and DNA [96]. Moreover, a few are known to activate stress reactions, thereby causing inflammation and damaging the body's immune system. Some studies have claimed adsorption of these nanoparticles can occur on the surface of macromolecules in our body, thereby harming enzymes' and other proteins' functional mechanisms. It has also been demonstrated that nanoparticles may cause DNA mutation, mitochondrial damage, and cell death in living systems [93, 97].

Environmental toxicity from nanoparticles is because of the agglomeration phenomenon. Several excellent reviews have been published on nanotoxicology [98–101], in which various aspects of

nanotoxicology (for instance, sources, cytotoxicities, public health concerns, regulatory perspectives, etc.) have been discussed. Interestingly, the mechanism of action of nanoparticles within the human body is still unclear and needs to be dealt with. The characterization of nanoscale contaminants is a major complication in determining nanotoxicology. Additionally, precise nanoscale-level knowledge of biological systems is still unclear. Because of these shortcomings, the exact determination of nanoparticles' toxicities in our earth's ecosystem must still be addressed [102]. Nanotoxicology is a rapidly emerging area that requires more attention from scientists all over the world toward investigating the entirety of nanoparticle toxicity.

Inhalation of and skin contact with nanoparticles are the basic means by which nanotoxicity affects us, and they can be minimized by the following safety measures:

1. *Stop*. A nanotechnology facility should prohibit the entry of outsiders like guests, visitors, and so on.
2. *Separate*. All work with nanomaterials should always be done in isolated systems.
3. *Aerate*. Always work with nanomaterials under a fume lid or an aerated area.
4. *Safety*. All the time, take respiratory safety precautionary measures and wear gloves while working with nanoparticles.
5. *Disposal*. Transport and discard nanowastes in closed systems according to the guidelines for disposing harmful chemical wastes.
6. *Supervision*. Always take care to not dispose of nanowastes in open places.

5 FUTURE PERSPECTIVES

Regardless of the excellent application of nanoparticles to water management, nanotechnology is associated with some safety-related issues, as discussed above. Utilization of nanoparticles for water treatment is a new area of research and may become a serious environmental issue in the future. Not all nanoparticles are ecofriendly, and some can penetrate living systems [103]. At present, no nanoparticles are ecofriendly and non-hazardous. Their discharge via synthesis, application, and disposal management steps can increase the chances of environmental contamination. As a result, there is an urgent requirement for the development of a safe and appropriate approach for their disposal. Further, considering environmental sustainability, environmentally friendly nanoparticles may be developed. Development of more competent, low-cost, and recyclable nanoparticles can lead to safer water treatment in the near future. Further, both genotoxicity and cytotoxicity tests should be performed via in vivo toxicity models prior to their introduction at a community level. Both the safety measures and the working potential of nanoparticles should be considered when determining their future utilization. Although many times, nanoparticles and low-cost adsorbents have been compared in determining their future outlooks, interestingly, no paper yet has reported the relationship between pilot and commercial-scale nanoparticle application. Because the development of exhausted nanoparticles management is still incomplete, it is not feasible to compare the practical usability of nanoparticles and low-cost adsorbents.

In brief, despite several problems, literature studies indicate nanoparticles are the future of water treatment systems. Therefore, to avoid environmental hazards, they should be eco-friendly, and they should be used carefully for future water treatment at community levels. At present, poor water quality requires the use of nanoparticles in water purification, and the future of these particles appears to be bright.

6 CONCLUSION

A thorough study of nanomaterial-based adsorbents in this present chapter indicates the potential for successful utilization of nanoparticles in the remediation of metal ions, anions, and organic and biological species from water. Nanoparticles can remediate these pollutants at the nanomolar level under specified reaction conditions. The requirement of a lower dose and shorter contact time makes them even more economical for field applications. Because of these properties, they are ideal candidates for fast, economical water treatment plants. Further, some researchers united other technologies with nanoparticles for overall water treatment. This requires advanced research into the development of novel nanomaterials with enhanced adsorption capacity, high selectivity, and large-scale column operations. For the application of nanoadsorption technology to improving human beings' welfare, adsorption conditions should be adapted to column operations.

Further, the nanotoxicology of recovered nanoparticles can be minimized by developing sustainable waste management systems. To the best of our knowledge, present poor water quality requires the use of nanoparticles in water purification, and therefore, the future of these particles appears to be bright, but the combined efforts of researchers and industrialists are required to realize the dream of rapid, inexpensive, and practical, water treatment worldwide.

ACKNOWLEDGMENTS

Dinesh Kumar is thankful to Prof. S. A. Bari, vice-chancellor of Central University of Gujarat for providing a research facility in SCS at Central University of Gujarat, Gandhinagar. We gratefully acknowledge support from the Ministry of Human Resource Development, Department of Higher Education, Government of India, under the scheme of Establishment of Centre of Excellence for Training and Research in Frontier Areas of Science and Technology (FAST), vide letter No. F. No. 5-5/201 4-TS. Vll.

REFERENCES

[1] D. Grey, D. Garrick, D. Blackmore, J. Kelman, M. Muller, C. Sadoff, Water security in one blue planet: twenty-first-century policy challenges for science, Philos. Trans. R. Soc. Math. Phys. Eng. Sci. 371 (2013) 20120406.
[2] WHO, Progress on Sanitation and Drinking-Water—2013 Update: 2013, p. 40.
[3] R. Levin, P. Epstein, T. Ford, W. Harrington, E. Olson, E. Reichard, US drinking water challenges in the twenty-first century, Environ. Health Perspect. 110 (2002) 43–52.
[4] C.J. Houtman, Emerging contaminants in surface waters and their relevance for the production of drinking water in Europe, J. Integr. Environ. Sci. 7 (2010) 271–295.
[5] WHO, Pharmaceuticals in Drinking-Water, World Health Organization, 2012.
[6] Y.L.F. Musico, C.M. Santos, M.L.P. Dalida, D.F. Rodrigues, Surface modification of membrane filters using graphene and graphene oxide-based nanomaterials for bacterial inactivation and removal, ACS Sustain. Chem. Eng. 2 (2014) 1559–1565.
[7] X. Qu, P.J. Alvarez, Q. Li, Applications of nanotechnology in water and wastewater treatment, Water Res. 47 (2013) 3931–3946.

[8] D. Ren, L.M. Colosi, J.A. Smith, Evaluating the sustainability of ceramic filters for point-of-use drinking water treatment, Environ. Sci. Technol. 47 (2013) 11206–11213.
[9] A. Dhillon, M. Nair, D. Kumar, Analytical methods for determination and sensing of fluoride in biotic and abiotic sources: a review, Anal. Methods 8 (2016) 5338–5352.
[10] M.A. Tofighy, T. Mohammadi, Adsorption of divalent heavy metal ions from water using carbon nanotube sheets, J. Hazard. Mater. 185 (2011) 140–147.
[11] A.S. Brady-Estévez, S. Kang, M. Elimelech, A single-walled-carbon-nanotube filter for removal of viral and bacterial pathogens, Small 4 (2008) 481–484.
[12] Q. Li, S. Mahendra, D.Y. Lyon, L. Brunet, M.V. Liga, D. Li, P.J.J. Alvarez, Antimicrobial nanomaterials for water disinfection and microbial control: potential applications and implications, Water Res. 42 (2008) 4591–4602.
[13] T.A. Dankovich, D.G. Gray, Bactericidal paper impregnated with silver nanoparticles for point-of-use water treatment, Environ. Sci. Technol. 45 (2001) 1992–1998.
[14] N. Mueller, J. Braun, J. Bruns, M. Cernik, P. Rissing, D. Rickerby, B. Nowack, Application of nanoscale zero valent iron (NZVI) for groundwater remediation in Europe, Environ. Sci. Pollut. Res. 19 (2012) 550–558.
[15] B. Karn, T. Kuiken, M. Otto, Nanotechnology and in situ remediation: a review of the benefits and potential risks, Environ. Health Perspect. 117 (2009) 1823–1831.
[16] T. Kuiken, Cleaning up contaminated waste sites: is nanotechnology the answer? Nano Today 5 (2010) 6–8.
[17] A.S. Adeleye, D. Huang, Z. Layton, S. Paladugu, J. Twining, CERNS: A Condensed EH&S Reference for Nanotechnology Startups, Bren School of Environmental Science & Management, University of California, Santa Barbara, 2011.
[18] T. Hillie, M. Hlophe, Nanotechnology and the challenge of clean water, Nat. Nanotechnol. 2 (2007) 663–664.
[19] N. Savage, M. Diallo, Nanomaterials and water purification: opportunities and challenges, J. Nanopart. Res. 7 (2005) 331–342.
[20] J. Theron, J. Walker, T. Cloete, Nanotechnology and water treatment: applications and emerging opportunities, Crit. Rev. Microbiol. 34 (2008) 43–69.
[21] J. Brame, Q. Li, P.J.J. Alvarez, Nanotechnology-enabled water treatment and reuse: emerging opportunities and challenges for developing countries, Trends Food Sci. Technol. 22 (2011) 618–624.
[22] S.D. Faust, O.M. Aly, Chemistry of Water Treatment, Butterworth, Stoneham, MA, 1983.
[23] A. Dhillon, S. Prasad, D. Kumar, Recent advances and spectroscopic perspectives in fluoride removal, Appl. Spectr. Rev. 52 (2017) 175–230.
[24] A. Dhillon, T.K. Sharma, S.K. Soni, D. Kumar, Fluoride adsorption on a cubical ceria nanoadsorbent: function of surface properties, RSC Adv. 6 (2016) 89198–89209.
[25] A. Dhillon, S.K. Soni, D. Kumar, Enhanced fluoride removal performance by Ce–Zn binary metal oxide: adsorption characteristics and mechanism, J. Fluor. Chem. 199 (2017) 67–76.
[26] A. Dhillon, D. Kumar, Dual adsorption behaviour of fluoride from drinking water on Ca-Zn$(OH)_2CO_3$ adsorbent, Surf. Interf. 6 (2017) 154–161.
[27] D. Pokhrel, T. Viraraghavan, Arsenic removal in an iron oxide-coated fungal biomass column: analysis of breakthrough curves, Bioresour. Technol. 99 (2008) 2067–2071.
[28] S.R. Kanel, B. Manning, L. Charlet, H. Choi, Removal of arsenic (III) from groundwater by nanoscale zero-valent iron, Environ. Sci. Technol. 39 (2005) 1291–1298.
[29] C. Zhu, Z. Luan, Y. Wang, X. Shan, Removal of cadmium from aqueous solutions by adsorption on granular red mud (GRM), Sep. Purif. Technol. 57 (2007) 161–169.
[30] E. Alvarez-Ayuso, A. Garcia-Sanchez, X. Querol, Adsorption of Cr(VI) from synthetic solutions and electroplating wastewaters on amorphous aluminium oxide, J. Hazard. Mater. 142 (2007) 191–198.
[31] J. Sanchez-Valente, X. Bokhimi, J.A. Toledo, Synthesis and catalytic properties of nanostructured aluminas obtained by sol–gel method, Appl. Catal. A 26 (2004) 175–181.

[32] S. Pacheco, R. Rodríguez, Adsorption properties of metal ions using alumina nano-particles in aqueous and alcoholic solutions, J. Sol-Gel Sci. Technol. 20 (2001) 263–273.
[33] H. Brammer, P. Ravenscroft, Arsenic in groundwater: a threat to sustainable agriculture in South and Southeast Asia, Environ. Int. 35 (2009) 647–654.
[34] E.A. Deliyanni, L. Nalbandian, K.A. Matis, Adsorptive removal of arsenites by a nanocrystalline hybrid surfactant–akaganeite sorbent, J. Colloid Interface Sci. 302 (2006) 458–466.
[35] M.E. Pena, G.P. Korfiatis, M. Patel, L. Lippincott, X. Meng, Adsorption of As(V) and As(III) by nanocrystalline titanium dioxide, Water Res. 39 (2005) 2327–2337.
[36] K. Hristovski, A. Baumgardner, P. Westerhoff, Selecting metal oxide nanomaterials for arsenic removal in fixed bed columns: from nanopowders to aggregated nanoparticle media, J. Hazard. Mater. 147 (2007) 265–274.
[37] H.J. Zhu, Y.F. Jia, X. Wu, H. Wang, Removal of arsenite from drinking water by activated carbon supported nano zero-valent iron, Huan Jing Ke Xue 30 (2009) 1644–1648.
[38] H.J. Zhu, Y.F. Jia, S.H. Yao, X. Wu, S.Y. Wang, Removal of arsenate from drinking water by activated carbon supported nano zero-valent iron, Huan Jing Ke Xue 30 (2009) 3562–3567.
[39] M.G. Mostafa, Y.H. Chen, J.S. Jean, C.C. Liu, H. Teng, Adsorption and desorption properties of arsenate onto nano-sized iron-oxide-coated quartz, Water Sci. Technol. 62 (2010) 378–386.
[40] S.R. Chowdhury, E.K. Yanful, Arsenic and chromium removal by mixed magnetite–maghemite nanoparticles and the effect of phosphate on removal, J. Environ. Manage. 91 (2010) 2238–2247.
[41] G. Jegadeesan, S.R. Al-Abed, V. Sundaram, H. Choi, K.G. Scheckel, D.D. Dionysiou, Arsenic sorption on TiO_2 nanoparticles: size and crystallinity effects, Water Res. 44 (2010) 965–973.
[42] E.A. Deliyanni, K.A. Matis, Sorption of Cd ions onto akaganeite-type nanocrystals, Sep. Purif. Technol. 45 (2005) 96–102.
[43] S. Pacheco, J. Tapia, M. Medina, R. Rodriguez, Cadmium ions adsorption in simulated wastewater using structured alumina–silica nanoparticles, J. Non Cryst. Solids 352 (2006) 5475–5481.
[44] N.K. Lazaridis, D.N. Bakoyannakis, E.A. Deliyanni, Chromium(VI) sorptive removal from aqueous solutions by nanocrystalline akaganeite, Chemosphere 58 (2005) 65–73.
[45] J. Hu, G. Chen, I.M. Lo, Selective removal of heavy metals from industrial wastewater using maghemite nanoparticle: performance and mechanisms, J. Environ. Eng. 132 (2006) 709–715.
[46] J. Hu, I.M. Lo, G. Chen, Comparative study of various magnetic nanoparticles for Cr (VI) removal, Sep. Purif. Technol. 56 (2007) 249–256.
[47] X.H. Guan, Y.C. Qin, Y.H. Qin, R. Yin, M.J. Sun, Removing Cr(VI) by composite biosorbent of nano FeO4/Sphaerotilus natans, Huan Jing Ke Xue 28 (2007) 2096–2100.
[48] Y.C. Chang, S.W. Chang, D.H. Chen, Magnetic chitosan nanoparticles: studies on chitosan binding and adsorption of Co (II) ions, React. Funct. Polym. 66 (2006) 335–341.
[49] A. Uheida, G. Salazar-Alvarez, E. Björkman, Z. Yu, M. Muhammed, Fe_3O_4 and γ-Fe_2O_3 nanoparticles for the adsorption of Co^{2+} from aqueous solution, J. Colloid Interface Sci. 298 (2006) 501–507.
[50] C. Sun, R. Qu, C. Ji, C. Wang, Y. Sun, Z. Yue, G. Cheng, Preparation and adsorption properties of crosslinked polystyrene-supported low-generation diethanolamine-typed dendrimer for metal ions, Talanta 70 (2006) 14–19.
[51] Y.C. Chang, D.H. Chen, Preparation and adsorption properties of monodisperse chitosan-bound Fe_3O_4 magnetic nanoparticles for removal of Cu (II) ions, J. Colloid Interface Sci. 283 (2005) 446–451.
[52] S.S. Banerjee, D.H. Chen, Fast removal of copper ions by gum arabic modified magnetic nano-adsorbent, J. Hazard. Mater. 147 (2007) 792–799.
[53] M.R. Gandhi, G.N. Kousalya, S. Meenakshi, Removal of copper (II) using chitin/chitosan nano-hydroxyapatite composite, Int. J. Biol. Macromol. 48 (2011) 119–124.

[54] Y.M. Hao, C. Man, Z.B. Hu, Effective removal of Cu (II) ions from aqueous solution by amino-functionalized magnetic nanoparticles, J. Hazard. Mater. 184 (2010) 392–399.
[55] Y.H. Chen, F.A. Li, Kinetic study on removal of copper (II) using goethite and hematite nano-photocatalysts, J. Colloid Interface Sci. 347 (2010) 277–281.
[56] L. Zhang, N. Liu, L. Yang, Q. Lin, Sorption behavior of nano-TiO_2 for the removal of selenium ions from aqueous solution, J. Hazard. Mater. 170 (2009) 1197–1203.
[57] Q. Zhang, B. Pan, B. Pan, W. Zhang, K. Jia, Q. Zhang, Selective sorption of lead, cadmium and zinc ions by a polymeric cation exchanger containing nano-Zr $(HPO_3S)_2$, Environ. Sci. Technol. 42 (2008) 4140–4145.
[58] A. Afkhami, M. Saber-Tehrani, H. Bagheri, Simultaneous removal of heavy-metal ions in wastewater samples using nano-alumina modified with 2, 4-dinitrophenylhydrazine, J. Hazard. Mater. 181 (2010) 836–844.
[59] E.A. Deliyanni, E.N. Peleka, K.A. Matis, Removal of zinc ion from water by sorption onto iron-based nanoadsorbent, J. Hazard. Mater. 141 (2007) 176–184.
[60] A. Dhillon, D. Kumar, Development of a nanoporous adsorbent for the removal of health-hazardous fluoride ions from aqueous systems, J. Mater. Chem. A 3 (2015) 4215–4228.
[61] A. Dhillon, D. Kumar, Nanocomposite for the detoxification of drinking water: effective and efficient removal of fluoride and bactericidal activity, New J. Chem. 39 (2015) 9143–9154.
[62] A. Dhillon, M. Nair, S.K. Bhargava, D. Kumar, Excellent fluoride decontamination and antibacterial efficacy of Fe–Ca–Zr hybrid metal oxide nanomaterial, J. Colloid Interface Sci. 457 (2015) 289–297.
[63] B.D. Martin, S.A. Parsons, B. Jefferson, Removal and recovery of phosphate from municipal wastewaters using a polymeric anion exchanger bound with hydrated ferric oxide nanoparticles, Water Sci. Technol. 60 (2009) 2637–2645.
[64] H.B. Xi, Q. Yang, H.T. Shang, C.B. Hao, Z.L. Li, Sulfide removal from wastewater by nanoscale iron, Huan Jing Ke Xue 29 (2008) 2529–2535.
[65] S.H. Huang, D.H. Chen, Rapid removal of heavy metal cations and anions from aqueous solutions by an amino-functionalized magnetic nano-adsorbent, J. Hazard. Mater. 163 (2009) 174–179.
[66] V. Belessi, G. Romanos, N. Boukos, D. Lambropoulou, C. Trapalis, Removal of reactive red 195 from aqueous solutions by adsorption on the surface of TiO_2 nanoparticles, J. Hazard. Mater. 170 (2009) 836–844.
[67] G. Moussavi, M. Mahmoudi, Removal of azo and anthraquinone reactive dyes from industrial wastewaters using MgO nanoparticles, J. Hazard. Mater. 168 (2009) 806–812.
[68] C.Y. Chen, J.C. Chang, A.H. Chen, Competitive biosorption of azo dyes from aqueous solution on the templated crosslinked-chitosan nanoparticles, J. Hazard. Mater. 185 (2011) 430–441.
[69] Y.C. Chang, D.H. Chen, Adsorption kinetics and thermodynamics of acid dyes on a carboxymethylated chitosan-conjugated magnetic nano-adsorbent, Macromol. Biosci. 5 (2005) 254–261.
[70] W.H. Cheung, Y.S. Szeto, G. McKay, Intraparticle diffusion processes during acid dye adsorption onto chitosan, Bioresour. Technol. 98 (2007) 2897–2904.
[71] L. Wang, A. Wang, Adsorption characteristics of Congo red onto the chitosan/montmorillonite nanocomposite, J. Hazard. Mater. 147 (2007) 979–985.
[72] M. Zhao, Z. Tang, P. Liu, Removal of methylene blue from aqueous solution with silica nano-sheets derived from vermiculite, J. Hazard. Mater. 158 (2008) 43–51.
[73] R. Sandoval, A.M. Cooper, K. Aymar, A. Jain, K. Hristovski, Removal of arsenic and methylene blue from water by granular activated carbon media impregnated with zirconium dioxide nanoparticles, J. Hazard. Mater. 193 (2011) 296–303.
[74] M. Iram, C. Guo, Y. Guan, A. Ishfaq, H. Liu, Adsorption and magnetic removal of neutral red dye from aqueous solution using Fe_3O_4 hollow nanospheres, J. Hazard. Mater. 181 (2010) 1039–1050.
[75] Y. Li, J.J. Lu, B.Y. Shi, Y.Y. Wu, Sorption of atrazine onto nano-SiO_2 and nano-kaolin particles, Huan Jing Ke Xue 29 (2008) 1687–1692.

[76] K. Yang, B. Xing, Sorption of phenanthrene by humic acid-coated nanosized TiO_2 and ZnO, Environ. Sci. Technol. 43 (2009) 1845–1851.
[77] K. Yang, L. Zhu, B. Xing, Sorption of phenanthrene by nanosized alumina coated with sequentially extracted humic acids, Environ. Sci. Pollut. Res. Int. 17 (2010) 410–419.
[78] L.L. Shen, B.Z. Zhao, J.B. Zhang, J. Chen, H. Zheng, Virus adsorption onto nano-sized iron oxides as affected by different background solutions, Huan Jing Ke Xue 31 (2010) 983–989.
[79] Z. Li, K. Greden, P.J. Alvarez, K.B. Gregory, G.V. Lowry, Adsorbed polymer and NOM limits adhesion and toxicity of nano scale zerovalent iron to *E. coli*, Environ. Sci. Technol. 44 (2010) 3462–3467.
[80] Y.H. Li, Z. Di, J. Ding, D. Wu, Z. Luan, Y. Zhu, Adsorption thermodynamic, kinetic and desorption studies of Pb^{2+} on carbon nanotubes, Water Res. 39 (2005) 605–609.
[81] H. Kochkar, A. Turki, L. Bergaoui, G. Berhault, A. Ghorbel, Study of Pd(II) adsorption over titanate nanotubes of different diameters, J. Colloid Interface Sci. 331 (2009) 27–31.
[82] S.H. Yang, W.H. Shin, J.K. Kang, Ni adsorption on stone-Wales defect sites in single-wall carbon nanotubes, J. Chem. Phys. 125 (2006). 084705.
[83] C. Lu, H. Chiu, Adsorption of zinc (II) from water with purified carbon nanotubes, Chem. Eng. Sci. 61 (2006) 1138–1145.
[84] Z.C. Di, J. Ding, X.J. Peng, Y.H. Li, Z.K. Luan, J. Liang, Chromium adsorption by aligned carbon nanotubes supported ceria nanoparticles, Chemosphere 62 (2006) 861–865.
[85] R.A. Doong, L.F. Chiang, Coupled removal of organic compounds and heavy metals by titanate/carbon nanotube composites, Water Sci. Technol. 58 (2008) 1985–1992.
[86] C.H. Wu, Studies of the equilibrium and thermodynamics of the adsorption of Cu^{2+} onto as-produced and modified carbon nanotubes, J. Colloid Interface Sci. 311 (2007) 338–346.
[87] J.C. Lou, M.J. Jung, H.W. Yang, J.Y. Han, W.H. Huang, Removal of dissolved organic matter (DOM) from raw water by single-walled carbon nanotubes (SWCNTs), J. Environ. Sci. Health 46 (2011) 1357–1365.
[88] F.M. Machado, C.P. Bergmann, T.H. Fernandes, E.C. Lima, B. Royer, T. Calvete, S.B. Fagan, Adsorption of reactive red M-2BE dye from water solutions by multi-walled carbon nanotubes and activated carbon, J. Hazard. Mater. 192 (2011) 1122–1131.
[89] J.P. Ryman-Rasmussen, J.E. Riviere, N.A. Monteiro-Riviere, Penetration of intact skin by quantum dots with diverse physicochemical properties, Toxicol. Sci. 91 (2006) 159–165.
[90] G. Oberdörster, A. Maynard, K. Donaldson, V. Castranova, J. Fitzpatrick, K. Ausman, J. Carter, B. Karn, W. Kreyling, D. Lai, S. Olin, Principles for characterizing the potential human health effects from exposure to nanomaterials: elements of a screening strategy, Part. Fibre Toxicol. 2 (2005) 8.
[91] O.V. Salata, Applications of nanoparticles in biology and medicine, J. Nanobiotechnol. 2 (2004) 3.
[92] G. Oberdörster, E. Oberdörster, J. Oberdörster, Nanotoxicology: an emerging discipline evolving from studies of ultrafine particles, Environ. Health Perspect. 1 (2005) 823–839.
[93] N. Li, C. Sioutas, A. Cho, D. Schmitz, C. Misra, J. Sempf, M. Wang, T. Oberley, J. Froines, A. Nel, Ultrafine particulate pollutants induce oxidative stress and mitochondrial damage, Environ. Health Perspect. 111 (2003) 455.
[94] A.E. Porter, M. Gass, K. Muller, J.N. Skepper, P. Midgley, M. Welland, Visualizing the uptake of C_{60} to the cytoplasm and nucleus of human monocyte-derived macrophage cells using energy-filtered transmission electron microscopy and electron tomography, Environ. Sci. Technol. 41 (2007) 3012–3017.
[95] M. Geiser, B. Rothen-Rutishauser, N. Kapp, S. Schürch, W. Kreyling, H. Schulz, M. Semmler, V. I. Hof, J. Heyder, P. Gehr, Ultrafine particles cross cellular membranes by nonphagocytic mechanisms in lungs and in cultured cells, Environ. Health Perspect. 1 (2005) 1555–1560.
[96] A. Nel, T. Xia, L. Mädler, N. Li, Toxic potential of materials at the nanolevel, Science 311 (2006) 622–627.
[97] R. Savić, L. Luo, A. Eisenberg, D. Maysinger, Micellar nanocontainers distribute to defined cytoplasmic organelles, Science 300 (2003) 615–618.

[98] J.M. Zook, R.I. MacCuspie, L.E. Locascio, M.D. Halter, J.T. Elliott, Stable nanoparticle aggregates/agglomerates of different sizes and the effect of their size on hemolytic cytotoxicity, Nanotoxicology 5 (2011) 517–530.
[99] D.R. Hristozov, S. Gottardo, A. Critto, A. Marcomini, Risk assessment of engineered nanomaterials: a review of available data and approaches from a regulatory perspective, Nanotoxicology 6 (2012) 880–898.
[100] S. Arora, J.M. Rajwade, K.M. Paknikar, Nanotoxicology and in vitro studies: the need of the hour, Toxicol. Appl. Pharmacol. 258 (2012) 151–165.
[101] E.J. Petersen, T.B. Henry, Methodological considerations for testing the ecotoxicity of carbon nanotubes and fullerenes: review, Environ. Toxicol. Chem. 31 (2012) 60–72.
[102] J. Fauré, G. Lachenal, M. Court, J. Hirrlinger, C. Chatellard-Causse, B. Blot, J. Grange, G. Schoehn, Y. Goldberg, V. Boyer, F. Kirchhoff, Exosomes are released by cultured cortical neurones, Mol. Cell. Neurosci. 31 (2006) 642–648.
[103] P.H. Hoet, I. Brüske-Hohlfeld, O.V. Salata, Nanoparticles–known and unknown health risks, J. Nanobiotechnol. 2 (2004) 12.

CHAPTER

29 CHITOSAN-BASED MEMBRANES FOR WASTEWATER DESALINATION AND HEAVY METAL DETOXIFICATION

Sapna*, Rekha Sharma*, Dinesh Kumar†

Department of Chemistry, Banasthali University, Rajasthan, India School of Chemical Sciences, Central University of Gujarat, Gandhinagar, India†*

1 INTRODUCTION

To control the contamination of drinking water, membrane technology has emerged as new and promising due to its inherent properties which are superior to those of several other technologies including adsorption, distillation, and extraction [1–3]. In the last few years, the availability of pure drinking water has become a major challenge worldwide. Due to rapid development in human society, demographic and industrial evolution resulted in diminished water resources [4–7]. Human activities have dirtied the water with huge amounts of pesticides, minerals, drugs, and different deposits [8–10]. As a result, new innovations and materials are being considered for water purification. Various membranes made of polymers and coated with biomaterials have huge potential for decontaminating and purifying water. A membrane is a selective barrier to a complex mixture of certain types of particles, molecules, and ions [11]. Membranes have the ability to remove fine as well as a large-sized particles. Exclusion of unwanted species and dirt particles depends upon the pore diameter of the membrane, which allows things above a certain size to pass [12]. Several kinds of membrane are commercially available for separating various sizes of particle molecules through microfiltration, conventional filtration, nanofiltration, ultrafiltration, and reverse osmosis. Conventional filtration membranes only block particles visible to the naked eye, while particle and microfiltration membranes separate particles whose sizes range from about 0.1–10 μm, such as microorganisms. An ultrafiltration membrane separates particles with dimensions between 10 and 1000 Å, such as macromolecules or colloids. Nanofiltration and reverse osmosis membranes are used mainly for separation of ions and salt, and both work using the principle of the pressure gradient [13–16]. Due to their selective separation ability, particles of specific dimensions have been widely used in food biomedicine and electronics, for sensors, and for industrial purposes. Using biopolymers such as chitosan and impregnation with other biomaterials enhances the membranes' versatility as well their efficacy [17]. Over the last few decades, researchers have paid attention to membrane adsorbents and have proven membrane-coated adsorbents to be powerful,

Nanoscale Materials in Water Purification. https://doi.org/10.1016/B978-0-12-813926-4.00037-9

attractive tools with which to separate hazardous components, such as heavy metal ions, dyes, and toxic organic compounds which are present in trace amounts, from wastewater. Among the numerous membrane adsorbents, chitosan prepared and modified adsorbents and their biopolymers have emerged as having high potential toward the removal of toxic heavy metals from many water resources. Chitosan biopolymers and their derivatives have attracted great interest because of their biodegradability, nontoxicity, reactivity, and favorable hydrophilicity, and the fact they are the cheapest biopolymer in nature and readily available in the market [18,19]. Due to the presence of hydroxyl and amine groups, they are widely used for the removal of heavy metal ions from aqueous solutions [20–24], although, it has some drawbacks, including low acid stability, inadequate mechanical properties, lower thermal stability, and lower surface area and porosity [25]. To overcome these drawbacks, some scientists have prepared chitosan composite adsorbents via physical or chemical methods because physical modification, or conversion of chitosan powder into gel beads, membranes, film, or nanoparticles enhances the porosity, surface area, and adsorption active sites, and increase its mechanical properties [26–29]. Through chemical modification, chitosan can become highly flexible and chemically stable and less susceptible to degradation in acid media. Recently, grafting, cross-linking, and impregnation have taken place on the functional groups of chitosan (mainly amino groups), all as a result of the chemical modification method [30–32]. This chapter is focused on providing a framework for better insight into the fabrication methods and applications of chitosan-based adsorptive membranes.

2 BLENDED AND SUPPORTED CHITOSAN MEMBRANE

Polymer blending and coating are promising strategies for synthesizing selective chitosan membranes that play an important role in detoxification as well as desalination. Blending polymers to fabricate chitosan membranes is simple and easy [33–36].

Boricha et al. observed chitosan coated onto a polyethersulfone substrate enhanced the separation rate of heavy metal ions. Here, acrylonitrile butadiene styrene was utilized as a modifier in a coated membrane to achieve better mechanical properties (rigidity, strength). The prepared membrane showed higher rejection of toxic heavy metal mercury with 5 ppm concentration and sodium ions at 96.25% and 89.74%. The blended membrane was characterized using the FTIR-ATR, XRD, SEM, EDXA, TGA techniques [37]. In another study, Boricha et al. further synthesized a blended membrane which showed higher rejection of chromium and copper ions. Here, their membrane was composed of a combination of two polymers, *N*, *O*-carboxymethyl and cellulose acetate. Acetone was used as the solvent to fabricate the nanofiltration membrane. The newly prepared blended membrane had a molecular weight cutoff observed at 710 Da, which confirmed it as being in the nanofiltration category. The *N*, *O*-carboxymethyl favored increasing the separation rate for metal ions, and cellulose acetate acted as a polymer matrix, providing mechanical strength for the membranes. The highest removal of Cr(VI) and Cu(II) ions from common effluent treatment plant wastewater was 83.40% and 72.60% at 1 MPa applied pressure and 16 L per minute feed flow rate, respectively. The thermal stability and the morphology of blended membrane were characterized through TGA and SEM [38].

Kanagaraj et al. utilized the phase inversion technique to develop a blended ultrafiltration membrane for the rejection of biomolecules and heavy metals. *N*-phthaloyl chitosan was used as the macromolecular additive and was blended onto polyetherimide. The blended membrane showed high

rejection of the heavy metal ions such as Cr(III), Zn(II), Cd(II), and Pb(II), and permeation of protein flux, like bovine serum albumin (BSA), egg albumin (EA), pepsin, and trypsin [39].

Han et al. developed a blended hollow fiber membrane which contained a high content of chitosan (CS) and cellulose acetate. The addition of surfactant sodium dodecyl sulfate (SDS) reduced the size of chitosan to around the nanoscale, ranging from 50 nm to 150 nm. A further adsorption study confirmed the copper ion removal and demonstrated the higher adsorption capacity of the blended hollow fibers up to 31 mg Cu(II)/g blend hollow fibers or 105.4 mg Cu(II) in terms of per-gram CS at pH 5. This has been attributed to the high CS content and, possibly, improved accessibility of CS in the blended hollow fiber membranes. Coating chitosan is not constrained to polymeric supports [40]. There are diverse cases for utilization of chitosan as an altering layer for inorganic supports.

Steenkamp et al. synthesized tubular ceramic membranes by the centrifugal casting method using different types of powders and powder mixtures. Here, with chitosan prepared by the phase inversion technique using water with low and high pH values as a solvent and nonsolvent system, a porous film of chitosan was coated onto the inner surface of the tubular ceramic membrane to increase the removal efficiency of copper ions from water. Almost complete removal of copper has been achieved using a chitosan-coated ceramic membrane [41].

Jana et al. prepared a chitosan-based ceramic ultrafiltration membrane by using local clay and kaolin with an average pore size of 1093 nm and porosity of 0.37 by a dip-coating technique. Here, glutaraldehyde was used as a crosslinker to increase the hydrophilicity and decrease the solubility in water and to provide stability to the membrane, as determined by TGA and DSC analysis. They found the lowest pore size to be 760–13 nm, meaning the membrane would be applicable for both microfiltration (MF) and ultrafiltration (UF). But the pore size 13 nm was responsible for the removal of Hg(II) and As(III) from wastewater [42].

3 CHITOSAN-BASED COMPOSITE MEMBRANES

Due to the versatility of synthesis methods, many composites have been prepared by various synthetic methods for the rejection of toxic ions from contaminated water.

Singh et al. prepared chitosan thiomer via the microwave irradiation method. This had the capability to remove both arsenic forms without any change in the medium's pH; it demonstrated good efficiency for the removal of both ionic forms found in groundwater, obtaining 85.4% removal for As(III) and 87% for As(V). The synthesized thiomer tended to reduce the arsenic concentration of 10–3.2 ppb, which is lower than the WHO recommended limit. The adsorption of both arsenic forms on the surface of the chitosan thiomer adsorbent was confirmed by many of the best analysis methods, including FTIR, Raman spectroscopy, XPS, and cyclic voltammetry. Isotherms studies, such as by Freundlich isotherm, revealed its adsorption on the surface and simultaneously confirmed that its adsorption was accomplished via the chemisorption process. The adsorption efficiency was calculated at 17.0 and 17.6 $mg\,g^{-1}$ at 50 ppb for As(III) and As(V), respectively [43].

Tang et al. fabricated a novel chitosan (CTS), polyvinylidene fluoride (PVDF) (CTS(Cd(II))/PVDF) composite through the one-step film-forming process. Here, PVDF and CTS were used as starting material. The prepared composite membrane exhibited excellent mechanical strength, good adsorption capacity, and better selectivity toward the Cd(II) over the Pb(II). The adsorption capacity achieved

was 64.35 mg g^{-1} for Cd(II) and 6.17 mg g^{-1} for Pb(II), which is four times higher than Pb(II). The prepared membranes were characterized using FTIR and SEM techniques, and SEM images confirmed the synthesis was accomplished by the proposed method [44].

Gedam et al. developed an iodate-doped chitosan (I-CS) composite for the adsorption of toxic metal ion lead from wastewater. The highest adsorption efficiency was obtained at 22.22 mg g^{-1} for Pb(II) ions by the adjusting pH to 6 and contact time to 4 h. The adsorption phenomenon was described by Langmuir and Freundlich models. The adsorption data fit well with the models used. The prepared composite was characterized by BET TGA, DSC, FTIR, XRD, and SEM analysis. The adsorption performance was checked with respect to different physiochemical parameters such as the effect of pH, contact time, adsorbent dose, and initial metal ion concentration. Here, the surface area of iodate chitosan was reduced after modification, although it showed a good adsorption capacity because the physisorption of I-CS sorbent for Pb(II) removal is limited, and the adsorptive mechanism will mainly be chemisorption. FTIR study revealed in the adsorption mechanism the involvement of complexation and ion exchange process in addition to purely electrostatic interaction. The functional groups —OH, C—N, C═O, iodate, and NH_2 were responsible for the adsorption of lead on the surface of the I-CS composite [45].

Lei et al. fabricated an apatite-based mineral on chitosan, hydroxyapatite, which was very stable and had low water solubility and retained higher removal capacity. The nano-hydroxyapatite chitosan possessed adsorption capacity of 208.0–548.9 mg g^{-1} by reducing pH values of metal ion solutions from 7.0 to 2.5. The formation of PbHAP and CS-Pb complex after adsorbing Pb(II) ions was confirmed by FTIR analysis. At pH 5.5, the adsorbent seemed to be more highly efficient, at 286.5 mg g^{-1} in this study, and the adsorption data of Pb(II) ions on HCPMs were best fitted with the Freundlich and Langmuir isotherms. The equilibrium this study revealed follows the pseudo-second-order kinetic. Hence, this bioinspired nanohydroxyapatite chitosan proved to an efficient adsorbent for the removal of Pb(II) from wastewater [46].

Wang et al. prepared a symmetric and porous chitosan membrane via an immersion precipitation method for the adsorption of Cu(II); here, silica was used as porogen which was responsible for generating porosity. The membrane possessed an interconnected pore structure with a pore size between 1.9 and 4.6 μm, with an average size of 3.3 μm. The experimental equilibrium adsorption data was well described by pseudo-second-order kinetics and three other isotherm models, namely Langmuir, Freundlich, and Toth. Of these three, the adsorption isotherm that fit the adsorption data best was the Toth isotherm model, possessing the highest R^2 value and lowest x^2 means. Overall, based on all three models, adsorption occurred on the heterogeneous surface. The membrane exhibited an adsorption capacity of 87.5 mg g^{-1} in a static condition [47].

Razzaz et al. developed chitosan/TiO_2 composite nanofibrous adsorbents using two different techniques, a coating method and an entrapped method. The composite nanofibers were analyzed by SEM, FTIR, and BET techniques. The nanofibers showed the maximum efficiency for both heavy metal ions Cu(II) and Pb(II). The chitosan/TiO_2 composite nanofibrous adsorbent had a higher potential for metal ion sorption than TiO_2-coated chitosan nanofibers. In a binary system, the adsorption selectivity for the Cu(II) ion is higher than the Pb(II) by the entrapped method. Both nanofibrous adsorbents obtained the maximum adsorption efficiency 710.3, 579.1 and 526.5, 475.5 mg g^{-1} correspondingly as determined by the Redlich-Peterson isotherm model. The kinetics and equilibrium data were best described by the pseudo-first-order kinetics for sorption Pb(II) and Cu(II) ions [48].

Habiba et al. fabricated a chitosan/polyvinyl alcohol (PVA)/zeolite nanofibrous composite membrane through the electrospinning method. Adsorption studies revealed its removal efficiency for several hazardous ions present in wastewater in ionic form, such as Cr(VI), Fe(III), and Ni(II). The adsorption mechanism was characterized using XRD, FESEM, FTIR, swelling test, and adsorption test. The composite membrane underwent regeneration and reusability studies up to a repeated four to five cycles, and no loss of adsorption capacity was observed. The investigation of kinetics and isotherm models indicated that the kinetic and equilibrium data of Cr(VI), Fe(III), and Ni(II) ions using chitosan/PVA/zeolite nanofibers adsorbents were best described by Langmuir isotherm and Lagergren first-order, pseudo-second-order, and intraparticle diffusion kinetic models [49].

Zavareh et al. synthesized a Cu-chitosan/Fe_3O_4 nanocomposite for the rejection of phosphate ions from an aqueous system, using the facile method. The composite exhibited higher adsorption capacity than neat chitosan, at 88 mg g^{-1}. The porous structure with the higher surface was investigated using BET. The FTIR study stated that the complex formation occurred after adsorption between Cu(II) and the amine group of Chitosan. XRD techniques described its crystallography structure and compared all three adsorbents' crystal structures. After incorporation of Cu(II) on the magnetic surface, the spectrum peak at $2\theta = 19.6$ degrees considerably decreased, possibly because of the interaction between amine groups of Chitosan and Cu(II) on the surface. The mechanism of adsorption of phosphate on the copper magnetic surface [50].

Zuo et al. prepared novel poly(vinyl alcohol)/citric acid/chitosan (PVA/CA/CHT, PCC) beads with different mass ratios (I, II, III, IV, V, and VI) as adsorbents for the removal of Cr(III) in aqueous solutions. Out of these, PCC beads II, with a mass ratio of 1/5/1 of PVA/CA/CHT retained its high potential toward the removal of Cr(III). The surface characterization of adsorbents was determined by SEM and FTIR spectroscopy. Sorption studies determined the capacity of the adsorbent at varying dose amounts, pH values, and stock solution concentrations. These parameters concluded the PCC beads II were highly dependent and showed higher adsorption, 41.5 mg g^{-1} at pH 6.0. The kinetics study was described by the pseudo-second-order equation with high regression coefficients and best fit the Langmuir isotherm model [51].

Mohseni-Bandp et al. synthesized a novel magnetite-chitosan composite for the removal of toxic ion fluoride. Here, by using a chemical coprecipitation method, chitosan was impregnated with magnetite nanoparticle. The adsorption performance of the adsorbent was optimized with several parameters, including contact time, pH, initial fluoride concentration, adsorbent dosage, and temperature. Adsorption was more favorable at pH 7 ± 0.2, with increased temperature. The adsorbent showed a maximum adsorption capacity 9.43 mg g^{-1}, as evaluated by the Langmuir adsorption isotherm. It proved to be easily reused, as confirmed by the adsorption-desorption study, up to five cycles without any significant loss in adsorption capacity [52]. Teimouri et al. developed a biocompatible nanocomposite with a series 1:1 M ratio of chitosan/montmorillonite/zirconium oxide for the uptake of fluoride. The nanocomposite showed more adsorption than pure chitosan due to its large surface area (62.448 m^2 g^{-1}) and pore diameter (0.923 nm), which was larger than the fluoride ion at 0.238 nm. Hence, the fluoride ion was easy to assess in the pores of nanocomposite, as confirmed by BET analysis. Further, surface morphology and the adsorption process were characterized using several techniques, such as SEM, FTIR, and XRD. They found that maximum adsorption was achieved at 23 mg g^{-1} at pH 4, temperature 30°C, contact time 60 min, solution volume 25.00 mL, the concentration of fluoride stock solution of 20 ppm, and 0.1 g of adsorbent dosage [53].

Dorraji et al. synthesized chitosan-based nanocomposite hollow fibers for the expulsion of Se(VI) from the industrial wastewater. Here, Fe_3O_4 nanoparticles impregnated on wet-spun chitosan hollow fibers were optimized by statistical design Response Surface Methodology (RSM) including pH, adsorbent dosage, and the initial concentration of the solution. The batch sorption experiments implied the involvement of second-order rate kinetics of the adsorption process. The adsorption capacity in optimum conditions obtained through the experiment was $1.34\,\mu g\,mg^{-1}$, which was higher than the predicted $1.28\,\mu g\,mg^{-1}$ [54].

El-Reash et al. utilized modified silver chitosan polyacrylamide membrane for removal and separation of Cu(II) from aqueous solutions. The adsorption study was carried out at different temperatures. The adsorption data fit well with the Lagergren model and followed the pseudo-second-order kinetics [55].

Sharma et al. prepared chitosan-based nanohydrogels (chitosan-crosslinked-poly [alginic acid]) by the copolymerization method for exclusion of Cr. The surface characterization of nanohydrogels was determined by SEM and TEM. The results obtained indicated the appearance of smooth surface with an average size of particles in the range of 30–80 nm. To optimize the adsorption involves various parameters, such as the effect of shaking time, temperature, adsorbent dosage, and initial metal ion concentration. The kinetics and equilibrium study was described by the pseudo-second-order equation. The thermodynamic study revealed its spontaneous and chemical nature. The FTIR study described the mechanism of adsorption of chromium onto the surface of CN-cl-PL(AA)NHG. The presence of three peaks at 1114, 1600, and $3390\,cm^{-1}$ showed the presence of C—O stretching, C═O stretching, and O—H stretching vibrations of the chitosan moiety. One absorption peak corresponding to the bending vibration of N—H was observed at $1520\,cm^{-1}$. The peak observed at about $2347\,cm^{-1}$ was assigned to the occurrence of a C—H bond [42]. The occurrence of the abovementioned peaks revealed the cross-linking of alginic acid and chitosan. But after the adsorption of Cr(VI), the intensities and position of some peaks (—OH, N—H and CO) changed, which indicated that —OH, —NH, and —CO groups were responsible for adsorption of Cr(VI) metal ions onto CN-cl-PL(AA)NHG [56].

Li et al. developed chitosan nanofibers with average diameter 75 nm were electrospun on polymer polyester via a versatile electrospinning technique. The membrane exhibited good adsorption capacity, depending on the pH, flow rate, and membrane packing. The maximum adsorption capacity obtained for $1\,mg\,L^{-1}$ Cr (VI) using the nanofiber membranes at 10% breakthrough was 16.5 mg Cr/g chitosan, exceeding the saturation capacity of static adsorption of 11.0 mg Cr/g chitosan using chitosan nanofiber mats, indicating the membranes' better potential for dynamic adsorption [57].

Fan et al. synthesized the magnetic chitosan beads via convenient embedding method and cross-linked with the glutaraldehyde for the removal of Cu(II) from the aqueous system. Adsorbent possesses excellent adsorption capacity ($167.22\,mg\,g^{-1}$). The thermodynamic study demonstrated the adsorption process was spontaneous and exothermic. Further, the adsorbent was analyzed by various analytical methods like TGA, FTIR, and XRD. Equilibrium isotherm data were well described by the Langmuir adsorption. It was stable at higher temperatures above 100°C and in different magnetic fields (≤ 0.3 T). Therefore, magnetic chitosan beads showed good stability without significant loss in adsorption capacity and in saturated magnetization after regeneration of five repeated cycles [58].

4 CHITOSAN MEMBRANES AND COMPOSITES FOR THE REMOVAL OF ORGANIC POLLUTANTS AND DYES

Dyes are widely utilized in various textile industries, raised from discharging dye-polluted wastes without degradation, and directly disposed of into rivers and water plants without an effective treatment, which leads to serious carcinogenic effects on the aquatic environment as well as on human health [59–62]. Usually, according to chemical structure, method, and domain of usage, and their chromogen, dyes are classified as anionic (directly, acid and reactive dyes), cationic (basic) dyes and nonionic (disperse) dyes are a classification proposed by Mishra and Tripathy. Azo and anthraquinone colorants are the main classes of synthetic dyes and pigments which represent about 90% of all organic colorants [63,64]. To diminish the visible color of polluted dye and reduce the carcinogenic effect, degradation, adsorption, and filtration methods have been widely used [65–67]. These mentioned polluted dyes and other heavy metal ions could be removed to a large extent by using chitosan membranes and their derivatives [68–74].

Li et al. investigated the Al-doped chitosan nonwoven was more efficient for the removal of dyes than chitosan nonwoven because of the presence of chelation interaction between the dyes and metal centers in the doped adsorbent. They demonstrated the maximum adsorption capacity, 260.03 $mg\,g^{-1}$. The reusability study, pH sensitivity, and the effect of the coexisting ions and the adsorption of other organic dyes indicated that the Al-doped chitosan nonwoven fixed in a cylindrical sleeve reactor was technically feasible and highly efficient [75].

Karim et al. developed fully biobased composite membranes for water purification that were fabricated with cellulose nanocrystals (CNCs) as functional entities in a chitosan matrix via a freeze drying process, followed by compacting. The average pore size of membrane calculated by BET analysis was 13–10 nm. Despite the low water flux (64 $Lm^{-2}h^{-1}$), the membranes successfully removed 98%, 84%, and 70%, respectively, of positively charged dyes like Victoria blue 2B, methyl violet 2B, and rhodamine 6G, after a contact time of 24 h [76]. To increase the catalytic activity of the bimetal complex, despite its high adsorption capacity for the expulsion of dyes from the aqueous system, Rashid et al. discovered a feasible, highly efficient, and cost-effective material in a chitosan-Cu-Fe bimetal complex/H_2O_2 system. The adsorbent displayed good adsorption efficiency and removed >90% of dyes within 10 min under a wide range of pH 4–12 with RB 5 removal; it also removed other anionic dyes such as, C. I. Acid Red 73 and C. I. Reactive Blue 19, and achieved 97.38% and 92.39% removal efficiency with no negative effect of coexisting ions. Further, the structure and the mechanism of the bimetal complex were determined by the various characterization methods, such as SEM, FTIR, EDX, and XPS [77].

Makaremi et al. functionalized a low-cost polyacrylonitrile nanofiber with zinc oxide nanoparticles (ZnO), further enhancing the mechanical strength, antibacterial, and water filtration performance of the membranes it coated with the functional group containing NH_2 and OH^- crosslinked chitosan. They found that the incorporation of zinc oxide NPs to polyacrylonitrile nanofiber improved the adsorption efficiency from 12.3 to 36.8 $mg\,g^{-1}$ attributed the interaction to negative sites on surface hydroxyl groups of ZnO. Similarly, high surface area, inter- and intrapores, as well as many of the chelating groups of chitosan, increase the adsorption efficiency to 72.7 $mg\,g^{-1}$ for removal of Cr(III) of electrospun functionalized polyacrylonitrile chitosan bilayer membranes [78].

Mahmoud et al. designed a novel nanocomposite by cross-linking of chitosan nanolayers onto surface of titanium oxide nanoparticles for the sorption of rare earth metal La(III). Here, glutaraldehyde was used as the cross-linking agent. The $NTiO_2$-Glu-NChit nanocomposite obtained via a facile and green chemical approach. The developed nanocomposite presented adsorption capacity 1200, 1050, and 1150 $\mu mol\, g^{-1}$ at pH 1.0, 3.0, and 6.0, correspondingly. The morphology of the adsorbent was confirmed by SEM and HR-TEM, and the particle was in the size range of 52–58 nm. The equilibrium isotherm studies were done using Langmuir and Freundlich adsorption isotherm models [79].

Ma et al. successfully synthesized Ethylenediaminetetraacetic acid (EDTA) cross-linked chitosan and *N*, *N*-methylene bisacrylamide (MBA) crosslinked polyacrylamide based double network hydrogel for uptake of heavy metal ions from contaminated aquatic systems. A batch study was performed to check the adsorption efficiency. They investigated the various effects, such as ionic strength, adsorbent dosage pH, and contact time. The CTS/PAM gel showed the uptake of various toxic metal ions Cd(II), Cu(II), and Pb(II). The adsorbent achieved the maximum adsorption capacity 86.00, 99.44, and 138.41 $mg\, g^{-1}$. It exhibited good recyclability and excellent mechanical strength [80].

Toxic metal ions in lower concentration are difficult to remove by the reverse osmosis process because of a few limitations on them. They possess low flux value, high cost, high water rejection, and so forth. The cerium-functionalized PVA-chitosan nanofiber adsorbent was formed for the rejection of highly toxic ion Hg(II), which presented in a lower concentration in the aqueous system. The resultant functionalized chitosan showed 31.44 $mg\, g^{-1}$ at pH 6, as calculated from the Langmuir isotherm model [81].

Ekambaram et al. utilized phase inversion method to modify the surface of PVDF nanofiltration membrane with the carboxymethyl chitosan-zinc oxide nanocomposite. Nanofiltration membranes can consist of least irreversible fouling ratio with excellent rejection of inorganic salts and humic acid. A modified membrane demonstrated higher rejection comparable to that of the pure membrane. The rejection order of inorganic salts was as follows: $Na_2SO_4 > MgSO_4 > NaCl > MgCl_2 > LiCl$. Because of fabrication of the nanocomposite in the PVDF matrix, fouling rates diminished, but it enhanced the tensile strength, thermal property, rejection performance of inorganic salts, and provides good durability up to repeated three cycles [82].

Sabourian et al. prepared chitosan/tetraethylorthosilicate/aminopropyl triethoxysilane composite nanofibrous adsorbent to utilize electrospinning method. They obtained very good absorbance toward the ternary system in following manner: Ni (II) > Cu (II) > Pb (II). The adsorption efficiency was 696.2, 640.5, and 575.5 $mg\, g^{-1}$, as calculated per the Langmuir isotherm model. The equilibrium data were followed by pseudo-first-order kinetic at optimum conditions, contact time 30 min, and temperature 45°C [83]. Various composites and some membranes had efficiencies sufficient to remove heavy metal as well as dyes from polluted wastewater, as listed below in Table 1.

5 SUMMARY

This chapter intended to describe the current progress associated with the desalination and heavy metal ion detoxification of water and wastewater using chitosan-based membranes over the previous 10–15 years. The adsorption capacities demonstrated in the various publications present the effectiveness of the sorbents for the specific types of metal species, which, in turn, depend on various experimental parameters. The utilization of chitosan-based membranes for water and wastewater

Table 1 The Adsorption Capacities of Various Adsorbents for the Hazardous Metal Ion and Dyes

Adsorbent	Target Metal Ion/Dyes	Removal Capacity ($mg\,g^{-1}$)	Reference
Chitosan magnetic nanoparticles	Methylene blue, Crystal violet, Malachite green	223.58, 248.42, 144.79	[84]
MCCG nano-adsorbent	Methylene blue	84.32	[85]
GDP-modified chitosan	Acid red 73	121.8	[86]
N,*O*-carboxymethyl-Chitosan/ montmorillonite	Congo red	74.24	[87]
Chitosan/montmorillonite nanocomposite	Congo red	54.52	[88]
Poly(vinylalcohol)/chitosan beads	Cu(II), Pb(II), Cd(II)	98.77, 98.61, 70.16	[89]
Chitosan-poly(vinyl alcohol) hydrogel	Cu(II), Pb(II), Cd(II)	78.68, 13.6, 32.12	[90]
Zr-based chitosan microcomposite	Orange II	962	[91]
Imidazolium-crosslinked chitosan aerogel	Yellow 27	2340	[92]
Chitosan-functionalized MWCNT	Eriochrome cyanine R dye, Pb(II)	2.021, 0.22	[93]
Ti^{4+} cross-linked chitosan	Orange II	1120	[94]
Chitosan/cellulose hydrogels	Congo red	166.10	[95]
Magnetic $ZnFe_2O_4$@chitosan	Organic dyes, basic fuchsin	335.57	[96]
Modified magnetic chitosan nano-adsorbent	Methylene blue	3.3	[97]
Magnetic chitosan beads	As(V), As(III)	35.7, 35.3	[98]
Chitosan/MWCNTs/Fe_3O_4 nanofibers	Cr(VI)	358	[99]
Chitosan-tripolyphosphate beads	Cu(II)	208.30	[100]
Fe_3O_4@hexadecyl trimethoxysilane@chitosan composites	Cu(II)	261.78	[101]
Chitosan-modified biochars	Cr(VI)	206	[102]
Chitosan membrane	Cu(II)	5.9	[103]
Chitosan transparent thin membrane	Cu(II)	8.41	[104]
Chitosan nanofiber	Pb(II), Cu(II)	56.54,5.75	[105]
CSTG adsorbent	Hg(II), Cu(II), Zn(II)	$98 \pm 2,76 \pm 1$ 52 ± 1	[106]
Chitosan/clinoptilolite composite	Cu(II), Co(II), Ni(II)	11.32, 7.94, 4.209	[107]

desalination and heavy metal detoxification presents excellent adsorption capacity toward metal ions, economic viability, nonhazardous nature, and biocompatibility. However, the swelling of chitosan is known as a serious drawback preventing its utilization at large scale. Still, there are some industries that utilize industrial-grade chitosan for water and wastewater desalination and heavy metal detoxification. Therefore, the potential of modified materials is still to be explored for the large-scale utilization of these membranes.

6 FUTURE SCENARIO

Although extensive studies in the literature on the utilization of chitosan membrane and composites for desalination and heavy metal ion detoxification of water and wastewater have been done, there are still many research gaps that require filling. Some of the vital characteristics that need to be addressed can be summarized as:

1. Most of the studies revealed the few drawbacks of the chitosan-based membranes and their composites in case stability, and lower adsorption efficiency, especially magnetic chitosan toward the dye removal.
2. To increase the adsorption efficiency toward various industrial dyes, organic pollutants, the optimization of various conditions leading to chitosan with high amino groups on its surface is required.
3. Modification of chitosan-based membrane by incorporation of many metal oxides as filler should be encouraged to obtain highly efficient membranes with low fabrication cost.
4. The capability of regeneration should be retained in chitosan derivatives and fabricated chitosan membrane to recover the metals with the adsorbent.
5. Utilization of chitosan membrane at large scale requires high adsorption rates and capacity for simultaneous removal of multicomponent contaminants like metal ions and dyes.
6. To reduce the effect of coexisting contaminants on efficiency, various other parameters should be checked for the presence of phenols and dyes on adsorption of metal ions.
7. In addition to lab-based batch studies, large-scale pilot-plant studies are needed to test chitosan derivatives' applications at the industrial level.
8. The adsorption capacity not only depends on the interaction of the adsorbent and adsorbate but also on different experimental conditions. Therefore, these variables need to be considered for studying the efficiency of chitosan composites.

Therefore, development of a chitosan-based membrane having all the above-stated properties may present more noteworthy benefits than the presently developed, commercially available, costly activated carbons.

ACKNOWLEDGMENT

We gratefully acknowledge support from the Ministry of Science and Technology and Department of Science and Technology, Government of India, under the Scheme of Establishment of Women Technology Park, for providing the necessary financial support to carry out this study vide letter No, F. No SEED/WTP/063/2014.

REFERENCES

[1] E.M. Eminoğlu, F. Beypınar, M.V. Kahraman, A. Durmuş, Fabrication of photo-cross-linked polyethyleneimine-based barriers for CO_2 capture, Polym. Adv. Technol. 26 (9) (2015) 1053–1058.

[2] A. Al-Amoudi, R.W. Lovitt, Fouling strategies and the cleaning system of NF membranes and factors affecting cleaning efficiency, J. Membr. Sci. 303 (1) (2007) 4–28.

[3] A.W. Mohammad, Y.H. Teow, W.L. Ang, Y.T. Chung, D.L. Oatley-Radcliffe, N. Hilal, Nanofiltration membranes review: Recent advances and future prospects, Desalination 356 (2015) 226–254.
[4] M.K. Thakur, R.K. Gupta, V.K. Thakur, Surface modification of cellulose using silane coupling agent, Carbohydr. Polym. 111 (2014) 849–855.
[5] S.R. Lim, J.M. Schoenung, Human health and ecological toxicity potentials due to heavy metal content in waste electronic devices with flat panel displays, J. Hazard. Mater. 177 (1) (2010) 251–259.
[6] K. Karlsson, M. Viklander, L. Scholes, M. Revitt, Heavy metal concentrations and toxicity in water and sediment from stormwater ponds and sedimentation tanks, J. Hazard. Mater. 178 (1) (2010) 612–618.
[7] P. Madoni, M.G. Romeo, Acute toxicity of heavy metals towards freshwater ciliated protists, Environ. Pollut. 141 (1) (2006) 1–7.
[8] M. Mondal, S. De, Preparation, characterization, and performance of a novel hollow fiber nanofiltration membrane, Polym. Adv. Technol. 26 (9) (2015) 1155–1167.
[9] L.B. Zhao, M. Liu, Z.L. Xu, Y.M. Wei, M.X. Xu, B.H. Jiang, Modification of polysulfone hollow fiber ultrafiltration membranes using hyperbranched polyesters with different molecular weights, Polym. Adv. Technol. 26 (4) (2015) 353–361.
[10] V.K. Thakur, D. Vennerberg, M.R. Kessler, Green aqueous surface modification of polypropylene for novel polymer nanocomposites, ACS Appl. Mater. Interfaces 6 (12) (2014) 9349–9356.
[11] M. Rahimnejad, G. Bakeri, M. Ghasemi, A. Zirepour, A review on the role of proton exchange membrane on the performance of microbial fuel cell, Polym. Adv. Technol. 25 (12) (2014) 1426–1432.
[12] J. Li, J. Gao, G. Sui, L. Jia, C. Zuo, Q. Deng, Influence of a glycerin additive on the structure and water vapor permeance of chitosan membranes, Mater. Express 4 (6) (2014) 491–498.
[13] Z.V.P. Murthy, L.B. Chaudhari, Application of nanofiltration for the rejection of nickel ions from aqueous solutions and estimation of membrane transport parameters, J. Hazard. Mater. 160 (1) (2008) 70–77.
[14] D. Nanda, K.L. Tung, C.C. Hsiung, C.J. Chuang, R.C. Ruaan, Y.C. Chiang, C.S. Chen, T.H. Wu, Effect of solution chemistry on water softening using charged nanofiltration membranes, Desalination 234 (1) (2008) 344–353.
[15] G.G. Kagramanov, E.N. Farnosova, G.I. Kandelaki, Heavy metal cationic wastewater treatment with membrane methods, in: Water Treatment Technologies for the Removal of High-Toxicity Pollutants, Springer, 2009, pp. 177–182.
[16] P.S. Sudilovskiy, G.G. Kagramanov, A.M. Trushin, V.A. Kolesnikov, Use of membranes for heavy metal cationic wastewater treatment: flotation and membrane filtration, Clean Technol. Environ. Policy 9 (3) (2007) 189–198.
[17] D.F. Stamatialis, B.J. Papenburg, M. Gironés, S. Saiful, S.N. Bettahalli, S. Schmitmeier, M. Wessling, Medical applications of membranes: drug delivery, artificial organs and tissue engineering, J. Membr. Sci. 308 (1) (2008) 1–34.
[18] H. Sashiwa, S.I. Aiba, Chemically modified chitin and chitosan as biomaterials, Prog. Polym. Sci. 29 (9) (2004) 887–908.
[19] M.N.R. Kumar, A review of chitin and chitosan applications, React. Funct. Polym. 46 (1) (2000) 1–27.
[20] M. Aliabadi, M. Irani, J. Ismaeili, H. Piri, M.J. Parnian, Electrospun nanofiber membrane of PEO/chitosan for the adsorption of nickel, cadmium, lead and copper ions from aqueous solution, Chem. Eng. J. 220 (2013) 237–243.
[21] M. Aliabadi, M. Irani, J. Ismaeili, S. Najafzadeh, Design and evaluation of chitosan/hydroxyapatite composite nanofiber membrane for the removal of heavy metal ions from aqueous solution, J. Taiwan Inst. Chem. Eng. 45 (2) (2014) 518–526.
[22] S. Haider, S.Y. Park, Preparation of the electrospun chitosan nanofibers and their applications to the adsorption of cu (II) and Pb (II) ions from an aqueous solution, J. Membr. Sci. 328 (1) (2009) 90–96.
[23] N. Gupta, A.K. Kushwaha, M.C. Chattopadhyaya, Adsorptive removal of Pb^{2+}, Co^{2+} and Ni^{2+} by hydroxyapatite/chitosan composite from aqueous solution, J. Taiwan Inst. Chem. Eng. 43 (1) (2012) 125–131.

[24] A.H. Chen, S.C. Liu, C.Y. Chen, C.Y. Chen, Comparative adsorption of cu (II), Zn (II), and Pb (II) ions in aqueous solution on the crosslinked chitosan with epichlorohydrin, J. Hazard. Mater. 154 (1) (2008) 184–191.
[25] M. Vakili, M. Rafatullah, B. Salamatinia, A.Z. Abdullah, M.H. Ibrahim, K.B. Tan, Z. Gholami, P. Amouzgar, Application of chitosan and its derivatives as adsorbents for dye removal from water and wastewater: a review, Carbohydr. Polym. 113 (2014) 115–130.
[26] M. Li, Y. Hong, Z. Wang, S. Chen, M. Gao, R.T. Kwok, W. Qin, J.W. Lam, Q. Zheng, B. Z. Tang, Fabrication of chitosan nanoparticles with aggregation-induced emission characteristics and their applications in long-term live cell imaging, Macromol. Rapid Commun. 34 (9) (2013) 767–771.
[27] W. Jiang, W. Wang, B. Pan, Q. Zhang, W. Zhang, L. Lv, Facile fabrication of magnetic chitosan beads of fast kinetics and high capacity for copper removal, ACS Appl. Mater. Interfaces 6 (5) (2014) 3421–3426.
[28] A. Jaiswal, S.S. Ghsoh, A. Chattopadhyay, Quantum dot impregnated-chitosan film for heavy metal ion sensing and removal, Langmuir 28 (44) (2012) 15687–15696.
[29] V. Nayak, M.S. Jyothi, R.G. Balakrishna, M. Padaki, A.F. Ismail, Preparation and characterization of chitosan thin films on mixed-matrix membranes for complete removal of chromium, Chem. Open 4 (3) (2015) 278–287.
[30] S. Zhang, M.H. Peh, Z. Thong, T.S. Chung, Thin film interfacial cross-linking approach to fabricate a chitosan rejecting layer over poly (ether sulfone) support for heavy metal removal, Ind. Eng. Chem. Res. 54 (1) (2014) 472–479.
[31] B. Hastuti, A. Masykur, S. Hadi, Modification of chitosan by swelling and crosslinking using epichlorohydrin as heavy metal Cr(VI) adsorbent in batik industry wastes, in: In IOP Conference Series: Materials Science and Engineering, 107, (1), IOP Publishing, 2016, p. 012020.
[32] İ. Sargin, G. Arslan, Effect of glutaraldehyde cross-linking degree of chitosan/sporopollenin microcapsules on removal of copper (II) from aqueous solution, Desalin. Water Treat. 57 (23) (2016) 10664–10676.
[33] S.K. Vaisnavi, S.C.G.K. Daniel, K. Ruckmani, M. Sivakumar, Fabrication of chitosan–magnetite nanocomposite strip for chromium removal, Appl. Nanosci. 6 (2) (2016) 277–285.
[34] W.R. Bowen, T.A. Doneva, H.B. Yin, Separation of humic acid from a model surface water with PSU/SPEEK blend UF/NF membranes, J. Membr. Sci. 206 (1) (2002) 417–429.
[35] Y.L. Ji, Q.F. An, F.Y. Zhao, C.J. Gao, Fabrication of chitosan/PDMCHEA blend positively charged membranes with improved mechanical properties and high nanofiltration performances, Desalination 357 (2015) 8–15.
[36] M. Li, Z. Lv, J. Zheng, J. Hu, C. Jiang, M. Ueda, X. Zhang, L. Wang, Positively charged nanofiltration membrane with dendritic surface for toxic element removal, ACS Sustain. Chem. Eng. 5 (1) (2016) 784–792.
[37] A.G. Boricha, Z.V.P. Murthy, Preparation of N, O-carboxymethyl chitosan/cellulose acetate blend nanofiltration membrane and testing its performance in treating industrial wastewater, Chem. Eng. J. 157 (2) (2010) 393–400.
[38] A.G. Boricha, Z.V.P. Murthy, Acrylonitrile butadiene styrene/chitosan blend membranes: preparation, characterization and performance for the separation of heavy metals, J. Membr. Sci. 339 (1) (2009) 239–249.
[39] P. Kanagaraj, A. Nagendran, D. Rana, T. Matsuura, S. Neelakandan, T. Karthikkumar, A. Muthumeenal, Influence of N-phthaloyl chitosan on poly (ether imide) ultrafiltration membranes and its application in biomolecules and toxic heavy metal ion separation and their antifouling properties, Appl. Surf. Sci. 329 (2015) 165–173.
[40] W. Han, C. Liu, R. Bai, A novel method to prepare high chitosan content blend hollow fiber membranes using a non-acidic dope solvent for highly enhanced adsorptive performance, J. Membr. Sci. 302 (1) (2007) 150–159.

[41] G.C. Steenkamp, H.W.J.P. Neomagus, H.M. Krieg, K. Keizer, Centrifugal casting of ceramic membrane tubes and the coating with chitosan, Sep. Purif. Technol. 25 (1) (2001) 407–413.
[42] S. Jana, A. Saikia, M.K. Purkait, K. Mohanty, Chitosan based ceramic ultrafiltration membrane: preparation, characterization and application to remove Hg (II) and As (III) using polymer enhanced ultrafiltration, Chem. Eng. J. 170 (1) (2011) 209–219.
[43] P. Singh, K. Chauhan, V. Priya, R.K. Singhal, A greener approach for impressive removal of As(III)/As (V) from an ultra-low concentration using a highly efficient chitosan thiomer as a new adsorbent, RSC Adv. 6 (69) (2016) 64946–64961.
[44] X. Tang, L. Gan, Y. Duan, Y. Sun, Y. Zhang, Z. Zhang, A novel Cd^{2+} imprinted chitosan-based composite membrane for Cd^{2+} removal from aqueous solution, Mater. Lett. 198 (2017) 121–123.
[45] A.H. Gedam, R.S. Dongre, Adsorption characterization of Pb (II) ions onto iodate doped chitosan composite: equilibrium and kinetic studies, RSC Adv. 5 (67) (2015) 54188–54201.
[46] Y. Lei, W. Chen, B. Lu, Q.F. Ke, Y.P. Guo, Bioinspired fabrication and lead adsorption property of nanohydroxyapatite/chitosan porous materials, RSC Adv. 5 (120) (2015) 98783–98795.
[47] X. Wang, Y. Li, H. Li, C. Yang, Chitosan membrane adsorber for low concentration copper ion removal, Carbohydr. Polym. 146 (2016) 274–281.
[48] A. Razzaz, S. Ghorban, L. Hosayni, M. Irani, M. Aliabadi, Chitosan nanofibers functionalized by TiO_2 nanoparticles for the removal of heavy metal ions, J. Taiwan Inst. Chem. Eng. 58 (2016) 333–343.
[49] U. Habiba, A.M. Afifi, A. Salleh, B.C. Ang, Chitosan/(polyvinyl alcohol)/zeolite electrospun composite nanofibrous membrane for adsorption of Cr^{6+}, Fe^{3+} and Ni^{2+}, J. Hazard. Mater. 322 (2017) 182–194.
[50] S. Zavareh, Z. Behrouzi, A. Avanes, Cu (II) binded chitosan/Fe_3O_4 nanocomomposite as a new biosorbent for efficient and selective removal of phosphate, Int. J. Biol. Macromol. 101 (2017) 40–50.
[51] X. Zuo, R. Balasubramanian, Evaluation of a novel chitosan polymer-based adsorbent for the removal of chromium(III) in aqueous solutions, Carbohydr. Polym. 92 (2) (2013) 2181–2186.
[52] A. Mohseni-Bandpi, B. Kakavandi, R.R. Kalantary, A. Azari, A. Keramati, Development of a novel magnetite–chitosan composite for the removal of fluoride from drinking water: adsorption modeling and optimization, RSC Adv. 5 (89) (2015) 73279–73289.
[53] A. Teimouri, S.G. Nasab, S. Habibollahi, M. Fazel-Najafabadi, A.N. Chermahini, Synthesis and characterization of a chitosan/montmorillonite/ZrO_2 nanocomposite and its application as an adsorbent for removal of fluoride, RSC Adv. 5 (9) (2015) 6771–6781.
[54] M.S. Dorraji, A.R. Amani-Ghadim, Y. Hanifehpour, S.W. Joo, A. Figoli, M. Carraro, F. Tasselli, Performance of chitosan based nanocomposite hollow fibers in the removal of selenium (IV) from water, Chem. Eng. Res. Des. 117 (2017) 309–317.
[55] Y.A. El-Reash, A.M. Abdelghany, A.A. Elrazak, Removal and separation of Cu(II) from aqueous solutions using nano-silver chitosan/polyacrylamide membranes, Int. J. Biol. Macromol. 86 (2016) 789–798.
[56] G. Sharma, M. Naushad, H. Ala'a, A. Kumar, M.R. Khan, S. Kalia, M. Bala, A. Sharma, Fabrication and characterization of chitosan-crosslinked-poly (alginic acid) nanohydrogel for adsorptive removal of Cr(VI) metal ion from aqueous medium, Int. J. Biol. Macromol. 95 (2017) 484–493.
[57] L. Li, Y. Li, C. Yang, Chemical filtration of Cr (VI) with electrospun chitosan nanofiber membranes, Carbohydr. Polym. 140 (2016) 299–307.
[58] C. Fan, K. Li, Y. Wang, X. Qian, J. Jia, The stability of magnetic chitosan beads in the adsorption of Cu^{2+}, RSC Adv. 6 (4) (2016) 2678–2686.
[59] G. Crini, Recent developments in polysaccharide-based materials used as adsorbents in wastewater treatment, Prog. Polym. Sci. 30 (1) (2005) 38–70.
[60] R.G. Saratale, S.S. Gandhi, M.V. Purankar, M.B. Kurade, S.P. Govindwar, S.E. Oh, G. D. Saratale, Decolorization and detoxification of sulfonated azo dye CI Remazol red and textile effluent by isolated Lysinibacillus sp. RGS, J. Biosci. Bioeng. 115 (6) (2013) 658–667.

[61] C. Shen, Y. Wen, Z. Shen, J. Wu, W. Liu, Facile, green encapsulation of cobalt tetrasulfophthalocyanine monomers in mesoporous silicas for the degradative hydrogen peroxide oxidation of azo dyes, J. Hazard. Mater. 193 (2011) 209–215.
[62] N. Ali, A. Hameed, S. Ahmed, Physicochemical characterization and bioremediation perspective of textile effluent, dyes and metals by indigenous bacteria, J. Hazard. Mater. 164 (1) (2009) 322–328.
[63] G. Crini, P.M. Badot, Application of chitosan, a natural aminopolysaccharide, for dye removal from aqueous solutions by adsorption processes using batch studies: a review of recent literature, Prog. Polym. Sci. 33 (4) (2008) 399–447.
[64] N.B. Devi, S. Mishra, Solvent extraction equilibrium study of manganese (II) with Cyanex 302 in kerosene, Hydrometallurgy 103 (1) (2010) 118–123.
[65] J. Cao, Y. Tan, Y. Che, H. Xin, Novel complex gel beads composed of hydrolyzed polyacrylamide and chitosan: an effective adsorbent for the removal of heavy metal from aqueous solution, Bioresour. Technol. 101 (7) (2010) 2558–2561.
[66] L. Huang, C. Xiao, B. Chen, A novel starch-based adsorbent for removing toxic Hg (II) and Pb (II) ions from aqueous solution, J. Hazard. Mater. 192 (2) (2011) 832–836.
[67] A. Masoumi, M. Ghaemy, Removal of metal ions from water using nanohydrogel tragacanth gum-g-polyamidoxime: Isotherm and kinetic study, Carbohydr. Polym. 108 (2014) 206–215.
[68] P. Daraei, S.S. Madaeni, E. Salehi, N. Ghaemi, H.S. Ghari, M.A. Khadivi, E. Rostami, Novel thin film composite membrane fabricated by mixed matrix nanoclay/chitosan on PVDF microfiltration support: preparation, characterization and performance in dye removal, J. Membr. Sci. 436 (2013) 97–108.
[69] S.S. Moghaddam, M.A. Moghaddam, M. Arami, Coagulation/flocculation process for dye removal using sludge from water treatment plant: optimization through response surface methodology, J. Hazard. Mater. 175 (1) (2010) 651–657.
[70] Y. Gao, X. Pu, D. Zhang, G. Ding, X. Shao, J. Ma, Combustion synthesis of graphene oxide–TiO_2 hybrid materials for photodegradation of methyl orange, Carbon 50 (11) (2012) 4093–4101.
[71] S. Zhang, Y. Zhang, J. Liu, Q. Xu, H. Xiao, X. Wang, H. Xu, J. Zhou, Thiol modified Fe_3O_4@ SiO_2 as a robust, high effective, and recycling magnetic sorbent for mercury removal, Chem. Eng. J. 226 (2013) 30–38.
[72] B. Shi, G. Li, D. Wang, C. Feng, H. Tang, Removal of direct dyes by coagulation: the performance of preformed polymeric aluminum species, J. Hazard. Mater. 143 (1) (2007) 567–574.
[73] D. Robati, B. Mirza, M. Rajabi, O. Moradi, I. Tyagi, S. Agarwal, V.K. Gupta, Removal of hazardous dyes-BR 12 and methyl orange using graphene oxide as an adsorbent from aqueous phase, Chem. Eng. J. 284 (2016) 687–697.
[74] W.W. Ngah, S. Fatinathan, Adsorption of cu(II) ions in aqueous solution using chitosan beads, chitosan–GLA beads and chitosan–alginate beads, Chem. Eng. J. 143 (1) (2008) 62–72.
[75] S. Li, J. Yang, S. Rashid, C. Shen, J. Liu, Al-doped chitosan nonwoven in a novel adsorption reactor with a cylindrical sleeve for dye removal: performance and mechanism of action, RSC Adv. 6 (112) (2016) 110935–110942.
[76] Z. Karim, A.P. Mathew, M. Grahn, J. Mouzon, K. Oksman, Nanoporous membranes with cellulose nanocrystals as functional entity in chitosan: removal of dyes from water, Carbohydr. Polym. 112 (2014) 668–676.
[77] S. Rashid, C. Shen, X. Chen, S. Li, Y. Chen, Y. Wen, J. Liu, Enhanced catalytic ability of chitosan–Cu–Fe bimetal complex for the removal of dyes in aqueous solution, RSC Adv. 5 (110) (2015) 90731–90741.
[78] M. Makaremi, C.X. Lim, P. Pasbakhsh, S.M. Lee, K.L. Goh, H. Chang, E.S. Chan, Electrospun functionalized polyacrylonitrile–chitosan bi-layer membranes for water filtration applications, RSC Adv. 6 (59) (2016) 53882–53893.
[79] M.E. Mahmoud, S.A.A. Ali, A.M. Nassar, S.M. Elweshahy, S.B. Ahmed, Immobilization of chitosan nanolayers on the surface of nano-titanium oxide as a novel nanocomposite for efficient removal of La(III) from water, Int. J. Biol. Macromol. 101 (2017) 230–240.

[80] J. Ma, G. Zhou, L. Chu, Y. Liu, C. Liu, S. Luo, Y. Wei, Efficient removal of heavy metal ions with an EDTA functionalized chitosan/polyacrylamide double network hydrogel, ACS Sustain. Chem. Eng. 5 (1) (2016) 843–851.
[81] R. Sharma, N. Singh, S. Tiwari, S.K. Tiwari, S.R. Dhakate, Cerium functionalized PVA–chitosan composite nanofibers for effective remediation of ultra-low concentrations of hg (II) in water, RSC Adv. 5 (22) (2015) 16622–16630.
[82] K. Ekambaram, M. Doraisamy, Surface modification of PVDF nanofiltration membrane using carboxymethylchitosan-zinc oxide bionanocomposite for the removal of inorganic salts and humic acid, Colloids Surf. A Physicochem. Eng. Asp. 525 (2017) 49–63.
[83] V. Sabourian, A. Ebrahimi, F. Naseri, M. Irani, A. Rahimi, Fabrication of chitosan/silica nanofibrous adsorbent functionalized with amine groups for the removal of Ni(II), Cu(II) and Pb(II) from aqueous solutions: batch and column studies, RSC Adv. 6 (46) (2016) 40354–40365.
[84] A. Debrassi, A.F. Corrêa, T. Baccarin, N. Nedelko, A. Ślawska-Waniewska, K. Sobczak, P. Dłużewski, J. M. Greneche, C.A. Rodrigues, Removal of cationic dyes from aqueous solutions using N-benzyl-O-carboxymethylchitosan magnetic nanoparticles, Chem. Eng. J. 183 (2012) 284–293.
[85] L. Fan, C. Luo, M. Sun, H. Qiu, X. Li, Synthesis of magnetic β-cyclodextrin–chitosan/graphene oxide as nanoadsorbent and its application in dye adsorption and removal, Colloids Surf. B Biointerfaces 103 (2013) 601–607.
[86] Y. Wen, C. Shen, Y. Ni, S. Tong, F. Yu, Glow discharge plasma in water: a green approach to enhancing ability of chitosan for dye removal, J. Hazard. Mater. 201 (2012) 162–169.
[87] L. Wang, A. Wang, Adsorption behaviors of Congo red on the N, O-carboxymethyl-chitosan/montmorillonite nanocomposite, Chem. Eng. J. 143 (1) (2008) 43–50.
[88] L. Wang, A. Wang, Adsorption characteristics of Congo red onto the chitosan/montmorillonite nanocomposite, J. Hazard. Mater. 147 (3) (2007) 979–985.
[89] X. Li, Y. Li, Z. Ye, Preparation of macroporous bead adsorbents based on poly (vinyl alcohol)/chitosan and their adsorption properties for heavy metals from aqueous solution, Chem. Eng. J. 178 (2011) 60–68.
[90] X. Wang, W. Deng, Y. Xie, C. Wang, Selective removal of mercury ions using a chitosan–poly (vinyl alcohol) hydrogel adsorbent with three-dimensional network structure, Chem. Eng. J. 228 (2013) 232–242.
[91] L. Zhang, L. Chen, X. Liu, W. Zhang, Effective removal of azo-dye orange II from aqueous solution by zirconium-based chitosan microcomposite adsorbent, RSC Adv. 5 (114) (2015) 93840–93849.
[92] J.A. Sirviö, M. Visanko, H. Liimatainen, Synthesis of imidazolium-crosslinked chitosan aerogel and its prospect as a dye removing adsorbent, RSC Adv. 6 (61) (2016) 56544–56548.
[93] S. Kheirandish, M. Ghaedi, K. Dashtian, F. Heidari, F. Pourebrahim, S. Wang, Chitosan extraction from lobster shells and its grafted with functionalized MWCNT for simultaneous removal of Pb^{2+} ions and eriochrome cyanine R dye after their complexation, Int. J. Biol. Macromol. 102 (2017) 181–191.
[94] J. Gao, L. Zhang, X. Liu, W. Zhang, Hierarchically structured, well-dispersed Ti^{4+} cross-linked chitosan as an efficient and recyclable sponge-like adsorbent for anionic azo-dye removal, RSC Adv. 6 (108) (2016) 106260–106267.
[95] H. Tu, Y. Yu, J. Chen, X. Shi, J. Zhou, H. Deng, Y. Du, Highly cost-effective and high-strength hydrogels as dye adsorbents from natural polymers: chitosan and cellulose, Polym. Chem. 8 (19) (2017) 2913–2921.
[96] X.L. Wu, P. Xiao, S. Zhong, K. Fang, H. Lin, J. Chen, Magnetic $ZnFe_2O_4$@ chitosan encapsulated in graphene oxide for adsorptive removal of organic dye, RSC Adv. 7 (45) (2017) 28145–28151.
[97] X. Zhu, Z. Zhang, G. Yan, Methylene blue adsorption by novel magnetic chitosan nanoadsorbent, J. Water Environ. Technol. 14 (2) (2016) 96–105.
[98] J. Wang, W. Xu, L. Chen, X. Huang, J. Liu, Preparation and evaluation of magnetic nanoparticles impregnated chitosan beads for arsenic removal from water, Chem. Eng. J. 251 (2014) 25–34.

[99] H. Beheshti, M. Irani, L. Hosseini, A. Rahimi, M. Aliabadi, Removal of Cr(VI) from aqueous solutions using chitosan/MWCNT/Fe_3O_4 composite nanofibers-batch and column studies, Chem. Eng. J. 284 (2016) 557–564.
[100] S.J. Wu, T.H. Liou, C.H. Yeh, F.L. Mi, T.K. Lin, Preparation and characterization of porous chitosan–tripolyphosphate beads for copper (II) ion adsorption, J. Appl. Polym. Sci. 127 (6) (2013) 4573–4580.
[101] Y. Liu, L. Chen, Y. Yang, M. Li, Y. Li, Y. Dong, The efficient removal of Cu(II) from aqueous solutions by Fe_3O_4@ hexadecyl trimethoxysilane@chitosan composites, J. Mol. Liq. 219 (2016) 341–349.
[102] X. Huang, Y. Liu, S. Liu, X. Tan, Y. Ding, G. Zeng, Y. Zhou, M. Zhang, S. Wang, B. Zheng, Effective removal of Cr(VI) using β-cyclodextrin–chitosan modified biochars with adsorption/reduction bifuctional roles, RSC Adv. 6 (1) (2016) 94–104.
[103] A. Ghaee, M. Shariaty-Niassar, J. Barzin, T. Matsuura, Effects of chitosan membrane morphology on copper ion adsorption, Chem. Eng. J. 165 (1) (2010) 46–55.
[104] Z. Cheng, X. Liu, M. Han, W. Ma, Adsorption kinetic character of copper ions onto a modified chitosan transparent thin membrane from aqueous solution, J. Hazard. Mater. 182 (1) (2010) 408–415.
[105] R.M. Nthumbi, J.C. Ngila, A. Kindness, B. Moodley, L. Petrik, Method development for flow adsorption and removal of lead and copper in contaminated water using electrospun nanofibers of chitosan blend, Anal. Lett. 44 (11) (2011) 1937–1955.
[106] M. Monier, Adsorption of Hg^{2+}, Cu^{2+} and Zn^{2+} ions from aqueous solution using formaldehyde cross-linked modified chitosan–thioglyceraldehyde Schiff's base, Int. J. Biol. Macromol. 50 (3) (2012) 773–781.
[107] M.V. Dinu, E.S. Dragan, Evaluation of Cu^{2+}, Co^{2+} and Ni^{2+} ions removal from aqueous solution using a novel chitosan/clinoptilolite composite: kinetics and isotherms, Chem. Eng. J. 160 (1) (2010) 157–163.

CHAPTER

30

RECENT PROGRESS IN TiO_2- AND ZnO-BASED NANOSTRUCTURED HYBRID PHOTOCATALYSTS FOR WATER PURIFICATION AND HYDROGEN GENERATION

Ch. Venkata Reddy*, Kakarla Raghava Reddy†, Nagaraj P. Shetti‡,a, Amit Mishra§, Soumen Basu§

School of Mechanical Engineering, Yeungnam University, Gyeongsan, South Korea School of Chemical and Biomolecular Engineering, The University of Sydney, Sydney, NSW, Australia† Electrochemistry and Materials Group, Department of Chemistry, K. L. E. Institute of Technology, Hubballi, India‡ School of Chemistry and Biochemistry, Thapar Institute of Engineering & Technology, Patiala, India§*

1 INTRODUCTION

Energy and clean environmental conditions are the two basic requirements for the survival and progress of human civilization. The Industrial Revolution was a prime factor in the rapid development of human society. However, the industrial malpractices of waste disposal and extensive use of fossil fuels have led human society to face a number of challenges such as global warming, and water and air pollution. Also, the extensive use of pesticides in agriculture has led to high toxicity in soil and ground water, which can pose a big threat to human and wildlife [1]. A recent WHO report shows that about 3.7 million people globally die each year in the 21st century from the hazards of water and air pollution, and 92% of the world's population still does not have access to pure water [2]. The fossil fuel resources are limited in their ability to cater to the energy demands of the growing world's population and are on the verge of exhaustion in the near future. This has led to the fear of energy crises, which can prove fatal for human society. Hence, the search for an ultimate and clean energy source, as well as the development of technologies for the remediation of hazardous materials from the environment have become topics of high international concern. There have been several attempts to harness alternative energy sources such as wind, water tides, biomass and solar energy, etc., as well as to design methods for the remediation of environmental pollutants. Hence, the development of cleaner, low carbon, and sustainable technologies is a bigger challenge for scientists and engineers worldwide [3]. Some technologies have been developed to harness alternative energy sources, but these have proven either inefficient or too expensive. Also,

[a]Affiliated with Visvesvaraya Technological University, Hubballi, India

Nanoscale Materials in Water Purification. https://doi.org/10.1016/B978-0-12-813926-4.00039-2

efforts toward the removal of harmful environmental pollutants are either inefficient or have their own side effects [4]. Among renewable energy sources, solar energy is available in abundance and has the potential for overcoming current environmental impacts. However, its unavailability at night, and during rainy and foggy seasons make it difficult to properly harness. Hence, transforming energy from sunlight to the chemical energy of hydrogen through photocatalytic water splitting could be a more promising approach [5]. Solar energy is also gaining attention for water treatment. There have been a number of metal oxide-based photocatalysts prepared for degrading organic pollutants such as dyes and pesticides. This chapter stresses H_2 generation through photocatalytic and photoelectrochemical water splitting and photocatalytic water treatment using two well-known photocatalysts, ZnO and TiO_2.

2 H_2 PRODUCTION FROM PHOTOCATALYTIC AND PHOTOELECTROCHEMICAL WATER SPLITTING

Over the past century, the rapid development of the global economy and related industrialization has brought about serious issues revolving around global warming and climate change, due to the rapid consumption of fossil fuel resources and carbon-based fossil fuel energy sources [6]. These issues have inspired an urgent need for unconventional, environment-friendly, renewable sources of clean and green energy technology. For future energy demands, photocatalytic hydrogen (H_2) production, either by directly splitting water into hydrogen and oxygen or by restructuring organic compounds (and especially metal oxide semiconductors), is said to be an ideal alternate energy source, compared to conventional fossil fuels. The photocatalysis procedure does not create any contaminants because it relies upon energy from light photons and water, and this will strongly influence clean energy and environmental health [7]. Photocatalytic water splitting is considered to be a great approach which is highly promising for hygienic and renewable solar-to-hydrogen energy transformation. In order to obtain effective photocatalytic activity, the photocatalyst must have a great transfer of charge carriers, appropriate bandgap, and much greater light absorbance [8]. Furthermore, for greater efficiency of light-driven photocatalytic H_2 generation, balance is required between light absorbance and reduced power in the investigated material [9]. It is also essential that the photocatalyst materials exhibit efficient charge separation and transfer capability of photo-excited electron-hole pairs. Furthermore, for higher photocatalytic activity, the system needs a low recombination rate to confirm the reduction and oxidation responses in the conduction band (CB) and valence band (VB) of a catalyst material.

Using titanium dioxide (TiO_2) for water splitting was first investigated in 1972 by Fujishima and Honda using photocatalytic activity. Later, many researchers were focused on TiO_2 nanoparticles due to their huge surface area and simple preparation, and they have demonstrated outstanding performance as photocatalysts [10]. However, titanium dioxide's quick recombination of charge carriers, slower electron transfer, hole pair, and extraordinary reprocessing cost limit its photocatalytic performance. Furthermore, TiO_2 has a low usage of the solar spectrum because of its higher bandgap.

According to a literature survey, various procedures have been developed in order to increase TiO_2 photocatalytic performance, such as elemental doping [11, 12], morphology change to reduce the diffusion length of minority carriers, and pairing with lesser bandgap photocatalysts to improve optical absorbance capacity [13]. In particular, a heterojunction photo-electrode having two or more distinct photocatalysts suggested favorable benefits in a PEC system, which not only can develop optical absorption capability due to narrow bandgap photocatalysts, but can also improve the electron-hole

separation efficiency due to suitable band alignments [14, 15]. Hence, in order to attain extraordinary hydrogen generation rates and great permanence, more attempts have been dedicated to enrich the photocatalytic surface of effective photocatalysts, creating heterostructures, and band structure engineering to reach desired, exact energy levels.

2.1 H_2 GENERATION BY TIO_2

For low-cost photoanode and maintainable photoelectrochemical (PEC) methods for potential solar water splitting, nanostructured titanium dioxide (TiO_2) is considered a suitable material. However, it has low water oxidation kinetics as it cannot be achieved maximum theoretical solar to hydrogen conversion efficiency (STH). Therefore, it is necessary to modify the TiO_2 surface with suitable co-catalysts. Through bandgap narrowing, the disorder of the crystal structure at the surface and light absorption capacity can be improved. In this regard, Xu et al. [16] reported an anatase TiO_2 nanotube array photoanode for PEC water splitting. In order to introduce lattice disorder, the prepared nanotube arrays were irradiated using a pulsed UV laser in a deionized water environment for 60 s. As a result, the photocurrent was enhanced by 1.6-fold compared to that of pure TiO_2 nanotube arrays under simulated sunlight at 1.23 VRHE. Moreover, at lower bias (0.5–0.7V_{RHE}), the water oxidation reaction kinetics are restrictive for the solar-to-current conversion; at 1.23 VRHE modified nanotube arrays show 78% water oxidation selectivity compared to pristine TiO_2 nanotubes (65%). This enhancement can be attributed to the laser irradiation, which enhanced the number of shallow donors, decreasing the deep trap density of states. The vertically aligned 1D crystalline nanostructures with small bandgap materials exhibited efficient solar energy conversion due to its short diffusion length and the lengthy axial direction. Jang et al. [17] fabricated vertically associated $PbTiO_3$@TiO_2core/shell heterostructure nanotube arrays on an FTO glass substrate using a single three-step procedure for PEC and photocatalytic applications under visible light irradiation.

Fig. 1A shows a pure TiO_2 nanotubes SEM image with a tube diameter around 54 nm, tube wall width about 13 nm, with 1 μm of length. Fig. 1B shows an SEM image of top-surface of core-shell $PbTiO_3$@TiO_2heterojunction nanotube arrays. The SEM images indicate that the nanotube wall and interior width become thicker and smaller, respectively. The change identified on the tube surfaces specifies that formation of $PbTiO_3$ took place inside of the TiO_2 nanotubes. Fig. 1C shows a TEM image of $PbTiO_3$@TiO_2 heterojunction nanotube arrays. As a result, in order to make a heterostructure of $PbTiO_3$- with TiO_2 for effective charge separation, $PbTiO_3$ acts as a photosensitizer because it has a narrow bandgap. Upon visible light illumination, the $PbTiO_3$@TiO_2 nanotube array shows enhanced photoactivity activity compared to pure TiO_2 nanotubes for PEC water splitting and photocatalytic dye degradation. Fig. 1D shows a graphic representation of a $PbTiO_3$@TiO_2 heterojunction nanotube for water splitting. When the PEC cell is irradiated under visible light, photogenerated electrons of $PbTiO_3$ are moved to the conduction band of TiO_2 due to its potential difference. For charge gathering by FTO substrate, the electrons of the nanotube create a directional passage over the axial path. The electron movement in the 1D is much quicker than the electron movement in particles. To oxidize water, the $PbTiO_3$ valence band holes are gathered to diffuse the interface of the anode/electrolyte. Moreover, the hole transmission length is small radially through the tube wall. Hence, there can be an effective separation of light-induced charge carriers. This decreases the recombination rate of electrons and holes. In order to decrease H^+ ions to H_2 gas, the gathered photoelectrons transfer over the outer circuit to the cathode (Pt). Furthermore, linking of $PbTiO_3$ and TiO_2 heterojunction charge important for improving the PEC efficiency.

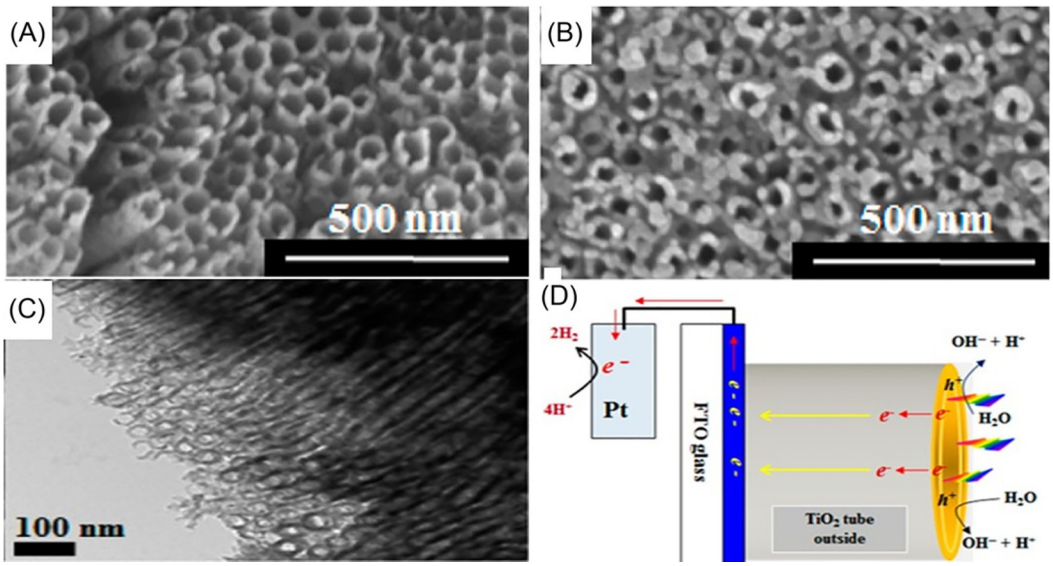

FIG. 1

(A) SEM image of the pure TiO_2 nanotube, (B, C) SEM and TEM images of $PbTiO_3$@TiO_2, and (D) schematic representation of $PbTiO_3$@TiO_2 electrode for PEC water splitting [17].

Coupling TiO_2 with other visible light photoactive elements (dyes, quantum dots, lesser bandgap semiconductors, and metal nanoparticles) has been extensively studied [18] for improving the efficiency of solar water splitting of TiO_2-based PEC electrodes. Several coupling strategies have been established. Among these, decoration with noble metals (Au nanoparticles) displays specific benefits for effective water splitting through the surface plasmon resonance (SPR) effect. This methodology suggested outstanding photostability and tunable contacts with the solar spectrum. SPR can be defined as the photo-induced collective oscillation of free electrons on a metal surface in resonance with the frequency of the incident light. The intensity and frequency of the plasmonic oscillation depend upon the size and shape of the metal nanoparticle, as well as the dielectric constant of the nearby environment. Li et al. [19] reported that decorated Au NPs on 3D TiO_2 nanorods have been fabricated using a sputtering method for improved PEC performance. Fig. 2A illustrates the process of 3D TiO_2 NR architecture with decoration of AuNPs. Fig. 2B and C show SEM and higher-resolution SEM images of Au NPs 3D TiO_2 NR arrays. Fig. 2D and E show TEM and HRTEM images of fabricated arrays. The Au NPs' size and magnitude could be influenced in a precise way by a one-step sputtering procedure. The resulting fabricated electrode exhibited extraordinary improvement of photocurrent densities upon simulated sunlight (42%) and visible light (267%) when compared to pure TiO_2. Moreover, PEC activity was further improved by 87.8% when amorphous Al_2O_3 films were applied to the photoelectrodes. This enhancement is attributed to the inherent SPR effect from Au nanoparticles and the Au-TiO_2 nanorod 3D design. Furthermore, finite-difference time-domain simulations proposed that the improved activity is due to the Au NPs decoration and SPR effect.

There have been many attempts to enhance the PEC performance of TiO_2 nanotubes (TNTs) by increasing absorption of the solar spectrum. Many researchers have concentrated on incorporating

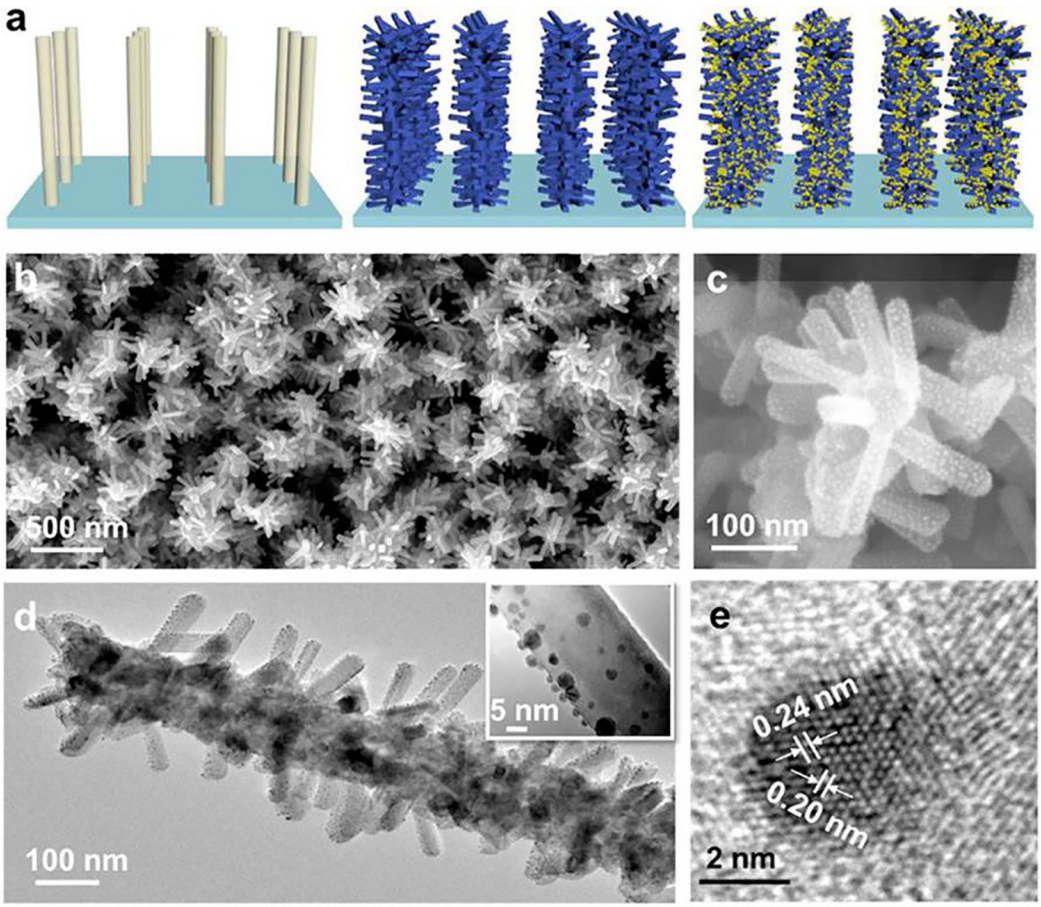

FIG. 2

(A) Schematic depiction of Au-NP-decorated 3D branched TiO_2 NR architectures, (B, C) top-viewed SEM and HR-SEM images of AuNPs-3D TiO_2 NR nanostructure arrays, (D) TEM image of separate TiO_2 NR. Inset: decorated TiO_2 NR with Au NPs and (E) HR-TEM Au-TiO_2 NR nanostructures [19].

nonmetals or metals into TNTs crystal lattices [20, 21]. Different doping elements can prompt new energy levels, positioned near the band edges or mid-gap states, therefore, reducing the bandgap. However, doping of foreign elements can encourage photocatalytic activity under visible light. Moreover, it certainly creates more structural defects, which lead to improved recombination centers. In the case of homo-element doping technique, Ti^{3+} self-doping has recently gained much consideration and has been considered a particularly capable strategy for improving the PEC activity of TiO_2 [22]. Ti^{3+}-self-doped TiO_2 nanotube arrays (TNTs) have been prepared using a simple electrochemical reduction process for improved PEC water splitting performance by Song et al. [23] Under optimal reduction conditions, the Ti^{3+}-self-doped TNTs show extremely greater photocurrent density and photoconversion efficiency, which were approximately 3.1 and 1.75 times higher, respectively, compared to pure TNTs. Improvement of the PEC activity is due to the better electrical conductivity, faster charge transfer rate at the

TNTs/electrolyte interface, increased charge density, and the enriched visible light absorbance response. Furthermore, when compared with pure TNTs, the flat band potential of Ti^{3+}-self-doped TNTs showed a negative shift, which could successfully allow the charge transfer.

Nanostructure modification is an effective method for improving TiO_2 photoresponse, and it has numerous benefits. Numerous works have concentrated on TiO_2 surface functionalization with a variety of metal oxide nanomaterials (ZnO, SnO_2, Cu_2O, and Fe_2O_3) [24, 25]. Among these, Fe_2O_3 (Eg$\sim$2.2 eV) is a capable material for TiO_2 photoanode for PEC solar energy conversion because of its better photostability, easy availability, nontoxicity, and low cost. When Fe_2O_3 combines with TiO_2, the light absorption capacity has been extended to the visible region [26]. The heterostructure developed using Fe_2O_3 and TiO_2 composites can also encourage the separation and transport of photo-generated charge carriers. Yao et al. reported a Fe_2O_3 nanothorns/TiO_2 nanosheets hybrid composite photoanode created using a template-free hydrothermal technique and chemical bath deposition for solar energy conversion [27].

The surface morphology of prepared pure TiO_2 nanosheets and Fe_2O_3/TiO_2 nanosheets are shown in Fig. 3. Fig. 3A and B displays FE-SEM images of the TiO_2 nanosheets array film. The TiO_2 nanosheets were grown vertically and evenly, with a thickness of about 1.29 mm. From the figure, it is observed that the anatase TiO_2 nanosheets interlock with each other. The FE-SEM images of Fe_2O_3/TiO_2 heterostructure films are shown in Fig. 3C and D. From these images, it is observed that the film surface is rough. The prepared heterostructure is mostly composed of TiO_2 nanosheets and branch-like Fe_2O_3 nanothorns with a typical length of around 200 nm, as shown in the inset of Fig. 3C. The 2D TiO_2 nanosheets offer an exceptionally permeable matrix and high activity area for deposition of Fe_2O_3. In the prepared nanostructure, Fe_2O_3 acts as a sensitizer. As a result, Fe_2O_3/TiO_2 heterostructure achieved optimum photocurrent density of 2.50 mA/cm^2 and the photoconversion competence is 1.25%, which is six times greater than the TiO_2 film (0.2%). The outcomes specify the easy separation of photo-excited charge carriers and their transfer to Fe_2O_3/TiO_2 heterostructure because of the Type-II band configuration.

Due to the following reasons, the enhanced PEC properties can be explained. For the growth of Fe_2O_3 nanothorns acting as a sensitizer, 2D TiO_2 nanosheets provide huge photo-activity area and encourage the redox reaction between the photoanode and electrolyte. The heterostructure with extraordinary absorbance favors the diffusion of the electrolyte. Due to the narrow bandgap of Fe_2O_3, the absorption is prolonged into the visible solar spectrum. Magnetic Fe_2O_3 tend to agglomerate in the submicrometer diameter that is comparable to the wavelengths of incident light, resulting in the traveling distance of light is significantly extended by several times, leading to an increase in the catalytic efficiency of the photoanode. Fe_2O_3 construct a Type II heterojunction with TiO_2 nanosheets as shown in Fig. 3E. When the junction formed, the electrons moved from Fe_2O_3 to TiO_2 until their Fermi levels align at symmetry. When the Fe_2O_3 nanothorns are absorbed by incident photons, the photo-generated electrons in the conduction band of Fe_2O_3 will quickly introduce into TiO_2 to reduce its energy level. Then, this type of band arrangement effectively prevents the recombination of the photo-excited electrons and holes and leads to enhanced energy conversion ability.

Exploration of the heterostructured photo-electrode with nanostructures can motivate band engineering through the interface for effective charge separation. Particularly, ferroelectric-based heterojunctions can lead to band structures of interfacial and charge transmission properties through switchable ferroelectric polarization that is driven by an internal electric field, leading to an improved PEC activity. Moreover, due to the screening of the depolarization field, surface band bending can be

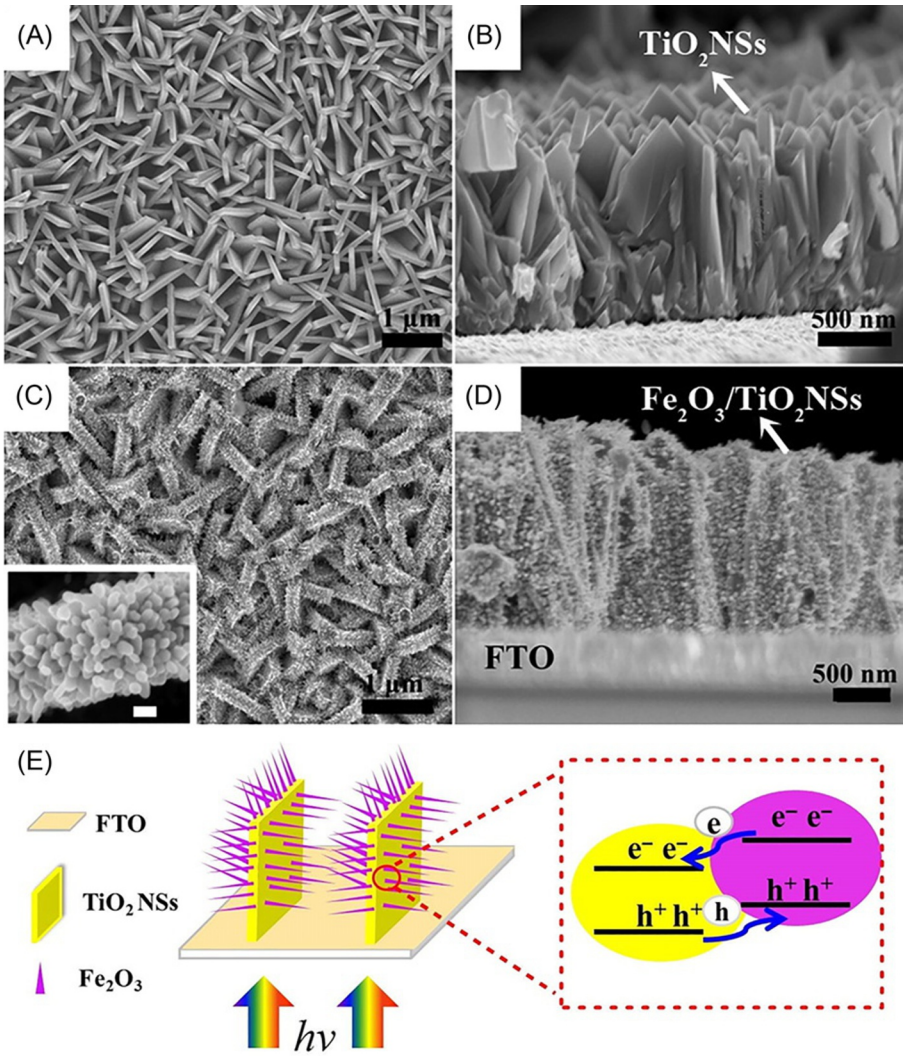

FIG. 3

(A, B) FESEM images of TiO_2NSs, (C, D) Fe_2O_3NTs/TiO_2NSs heterostructure films, and (E) energy band of Fe_2O_3/TiO_2 heterostructure [27].

encouraged by ferroelectric polarization. Some electrochemical surface responses can be altered, specifically, that the ferroelectric-based heterostructure can possibly link with an advanced nanostructure system for other active solar water splitting. Lee et al. [28] prepared highly ordered ferroelectric $BiFeO_3/TiO_2$ nanotube (TNT) heterostructures developed using a pulsed laser deposition technique. Under visible light irradiation, the developed $BiFeO_3$/TNT photoelectrode is photoactive, displaying higher photocurrent for better water oxidation when compared to that of the pristine TNT

photoelectrode. The $BiFeO_3$ coating thickness substantially affects the PEC properties. The improved PEC activity can be credited to the active separation of charge carriers and the favorable band structures for water oxidation, initiating from the ferroelectric polarization-associated internal field.

2.2 H_2 GENERATION BY ZnO

Zinc oxide (ZnO) is a capable material for the photocatalytic applications due to its unique properties [29]. Moreover, ZnO nanostructures are very favorable for various applications because of their unique electronic and photophysical properties [30]. The improved optical and electrical properties of the ZnO materials could be credited to the increase in the specific surface area and the generation rate of electron hole and absorption capacity in the visible range. Among the different nanostructures, 1D metal oxide semiconductor nanostructures are suitable with improvement potential [31] for energy conversion applications [32]. The improved optical and electrical characteristics of ZnO materials could be credited to its enhanced specific surface area and the high generation rate of electron-hole pairs. However, due to its larger bandgap energy, ZnO is incapable of absorbing the solar spectrum [33], reducing its photocatalytic performance.

The development of 1D nanostructures can improve the light absorption capacity, increasing the electrochemical reactions within the active area and allowing the movement of electrons and holes with better effectiveness [34]. In the core/shell of nanowire/nanorod devices, higher photocurrent can be produced by the incident photons through a greater active absorption length. Hence, coating ZnO NRs with lower bandgap material core/shell nanostructures enables them to absorb the solar spectrum region. Therefore, ZnO-based core/shell nanostructures support improving the absorption capacities and increase the PEC activity. The core material (ZnO) role is to serve as an effective electrical pathway for movement of gathering charge carriers and to provide a huge active surface area for the generation of hydrogen. However, the nanorods' surface defects lead to surface trap states and produce over the potential of the surface at the photoanode, both of which ultimately reduce the PEC performance. Both of these issues can be solved through the use of 1D nanostructured materials consisting of single crystals free of defects. Furthermore, the selected area electron in TEM-SAED pattern and surface engineering of 1D crystalline catalysts has been studied by crystal facet engineering [35].

Kumar et al. [36] reported ZnO/PbS core/shell self-assembled nanostructures created using a two-step, chemical bath, deposition technique for PEC cell performance. In the ZnO/PbS core/shell, the optimal shell thickness (20 nm) exhibited greater photocurrent density of $\sim$13.6 mA/cm^2 and photoconversion efficiency of 1.7% vs. RHE under visible light illumination. This enhancement is due to the presence of reduced defects interface, larger surface to volume ratio, photon transmission or absorption in the core/shell, lower diffusion length, and rapid free charge carrier movement with diminished recombination rate. Furthermore, the obtained photocurrent at +1.0 V vs. Ag/AgCl is enormously significant for improved PEC water splitting ability for hydrogen production. A single-component ZnO system was extensively used as a stable material under UV light only. Hence, suitable co-catalysts such as noble metals [37], metal sulfides [38], and metal oxides [39] can be used for increasing light-gathering range and enhancing electron utilization efficiency. In a similar way, materials with comparatively lower bandgap energy ($>$3.0 eV) namely PbS, CdS [40], or ternary sulfide compound ($ZnIn_2S_4$) [41] has also been used to absorb the visible light energy, which covers the 40% of nature sunlight energy [42]. Among those thin bandgap catalysts, CdS is extensively used for hydrogen generation due to its low bandgap energy (2.44 eV) and suitable conduction band position [43]. However, due

to its drawbacks of easy recombination and photocorrosion, heterostructures are more suitable for solving these issues. Bak et al. reported [44] a pseudo-microspherical ZnO/CdS core-shell photocatalyst with uniform shape and size prepared using a facile precipitation technique for solar water splitting with different CdS wt% content. The prepared photocatalyst exhibited an improved rate of hydrogen generation (146 μmol/g/h) by a sample containing 63 wt% CdS in visible light irradiation. Moreover, after thermal treatment, the hydrogen generation rate was further enhanced to 241.2 μmol/g/h at the same CdS composition as that of the pure sample. This enhancement may be because of amplified crystalline nature and effective charge flow with the assistance of an extra CdO component.

Because of its appropriate band edge position and bandgap energy (2.2–2.6 eV), gathering capability of wide range spectrum, and exceptional catalytic activity, a GaN/ZnO composite photocatalyst has been recommended for higher PEC water splitting performance [45]. However, the GaN/ZnO electrode created a problem due to its charge separation and surface reaction, which reduced its PEC water splitting efficiency. Hence, the particulate electrode is essential for improving the catalyst semiconductor interfaces to increase the high PEC water splitting. Wang et al. [46] reported the promotion of charge separation and transfer at the surface of the photoanode (GaN/ZnO) to obtain extraordinarily efficient solar conversion with the help of moisture-assisted nitridation and HCl acid treatment. After this treatment, the electron-hole separation could be significantly enhanced due to the photoanode boundaries in GaN/ZnO and enhancing the recombination centers that are present at the interfaces of GaN/ZnO photoanode. Additionally, when loading NiCoFeP on photoelectrode, the addition of surface charge significantly stimulates the photocurrent (3.9 mA/cm^2) and 1% solar conversion efficiency was attained.

Ma et al. [47] reported the rational development of 0D CdS quantum dots (QDs)/2D ZnO nanosheets (NSs) heterojunction for photocatalytic hydrogen evolution. Using the ultrasonic-assisted hydrothermal technique in the presence of NaOH, the 2D ZnO NSs and ZnO microflowers (MFs) were prepared. Furthermore, CdS QDs were placed on both sides of ZnO NSs via this reaction technique. Moreover, ultrasonication was responsible for the preparation of ZnO NSs, whereas the NaOH was responsible for microflowers. Surface morphological images of ZnO are shown in Fig. 4.

Fig. 4A shows the flower-like morphology of ZnO MFs, having an average diameter of about 2.5 μm. The formation of ZnO MFs is due to the self-assembly of 2D ZnO NSs. ZnO MFs as seen from low and high magnification SEM images are shown in Fig. 4B. From the figure, it can be seen that a smooth surface has been observed on both sides of ZnO NSs, as shown in inset Fig. 4B. Furthermore, the tiny CdS QDs were settled on every side of the ZnO NSs surface (Fig. 4C), and due to this, the ZnO NSs' surface appearance was very uneven. As a result, the CdS/ZnO heterostructure exhibited improved hydrogen generation (22.12 mmol/g/h) when compared to single CdS (1.68 mmol/g/h) and ZnO (0.16 mmol/g/h), respectively. The improved photocatalytic hydrogen generation is due to the Z-scheme catalytic system, QDs' and NSs' influence, and the close interaction between CdS and ZnO. Furthermore, the Z-scheme system extraordinarily encouraged the charge separation and movement of photogenerated electrons and holes carriers, and the effect of small size could efficiently reduce the recombination possibility of charge carriers. Fig. 4D shows the mechanism proposed for the improved catalytic activity. Upon visible light illumination, CdS QDs and ZnO NSs absorbed the photons and generated photo-excited charge carriers. Per the direct Z-scheme mechanism, the photo-generated electrons moved to the VB of CdS from the CB of ZnO. Furthermore, the photoexcited electrons in the CB of CdS can be captured via the Schottky barrier between Pt and CdS. Hence, this Schottky barrier behaves as an electron trap, and further reduces the recombination rate, strongly

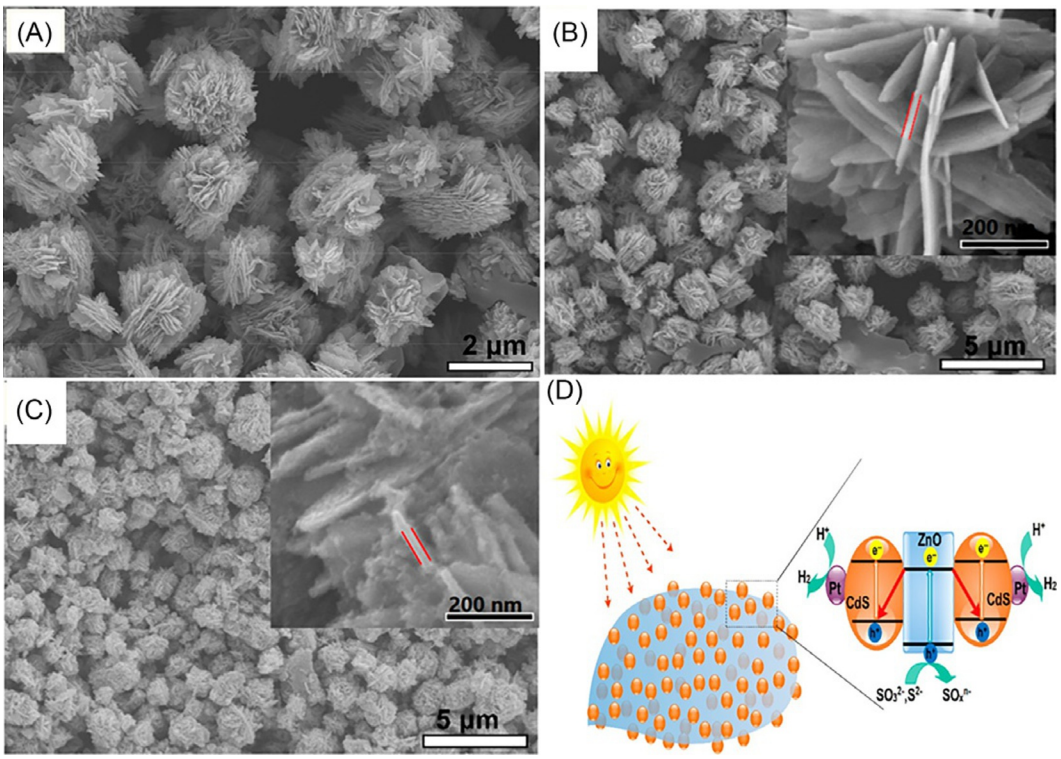

FIG. 4

(A, B) SEM image of as-synthesized ZnO MFS, (inset shows ZnO NS thickness), (C) SEM image of CdS/ZnO, and (D) schematic representation of CdS/ZnO for the hydrogen generation [47].

increasing the hydrogen generation. In ZnO, the photogenerated holes of VB can be trapped by the sacrificial agent. Hence, the Z-scheme system encourages the effective separation of photo-excited charge carriers and maintains the strong redox ability of the photo-excited electrons and holes, which leads to extraordinarily improved catalytic activity. Furthermore, the movement of the charge carrier's distance could be decreased by both QDs and NSs from the inside to the surface, which could also considerably reduce the possibility of recombination rate. Moreover, CdS QDs are thickly dispersed on ZnO NSs, resulting in the fast movement of photo-excited electrons and holes, which results in the Z-scheme mechanism. Furthermore, the passage resistance of the photo-generated charge carrier can be efficiently decreased due to the close interaction of CdS and ZnO. The abovementioned key issues successfully improve the hydrogen generation of the CdS QDs/ZnO NSs heterojunction.

Increasing the light absorption capacity in the solar spectrum and photocatalytic activity of ZnO could be achieved from the creation of oxygen vacancies through hydrogenation [48]. For example, Lv et al. reported the surface oxygen vacancy induced visible activity of ZnO [49]. As a result, upon light irradiation, it was observed that ZnO containing oxygen vacancies showed 7 and 12 times greater photocurrent and quicker photodegradation than the pure sample. However, it was also confirmed that

the created vacancies of oxygen in the hydrogenated ZnO sample do not absorb the visible spectra, but demonstrate better utilization of UV light than other ZnO samples. In this regard, the defects' role in hydrogenation ZnO nanorods for visible light-mediated PEC water splitting was investigated by Gurylev et al. [48] The PEC response in visible light can be achieved by simultaneous generation of oxygen (V_O) and zinc (V_{Zn}) vacancies in the hydrogenated ZnO. Due to the creation of zinc and oxygen vacancies, the hydrogenated ZnO sample exhibited extra absorption of light and four times greater PEC activity upon light illumination. The utilization of photons having inferior energies can be effectively increased through the defects, and can generate transition states between the conduction and valence bands, because electrons can move to conduction band from the valence band by leaping through these transitional states. Moreover, defect levels and vacancy can also advantageous for charge capture and absorbed light scattering, which contributes to the improved photoefficiency after hydrogenation.

Karmakar et al. [50] have developed a novel p-n $CuFeO_2$ nanolayers/ZnO nanorods heterojunction photoanode using simple and inexpensive techniques by combining electrodeposition and chemical synthesis for better H_2 generation. In order to obtain better PEC properties of the photoelectrode, p-type $CuFeO_2$ outer layer thickness (10 min electrodeposition of p-$CuFeO_2$) plays a significant role. Upon visible light irradiation, the photoconversion effectiveness of p-$CuFeO_2$/n-ZnO photoanode exhibited 450% greater performance than that of a pure ZnO nanorod electrode. Because of its suitable interface band alignment, the nanoengineering of a p-n $CuFeO_2$/ZnO heterojunction photoanode significantly increases the light absorption capacity, rapid movement of the charge carrier, and separation of the charge carrier. Furthermore, this photoanode displays extraordinarily enhanced photostability. Moreover, the creation of a p-n heterojunction photoanode can also improve the holes' journey to the interface (electrode/electrolyte), whereas, the electrons journey to the counter electrode (Pt).

Liu et al. [51] reported hierarchical structures of a ZnO/CdS/$Ni(OH)_2$ photoanode for PEC water splitting with the mixed nanorod/nanosheets of ZnO.

The SEM image of ZnO nanorod-nanosheets is shown in Fig. 5A. The long and tiny nanorods of ZnO and the intervals of nanosheets filled with the ZnO nanorods can be observed in the SEM image. The uniform growth of ZnO nanorods on both sides of the nanosheets is shown in the inset of Fig. 5A. The TEM and HR-TEM images of ZnO/CdS/$Ni(OH)_2$ are displayed in Fig. 5B. After the subsequent integration of $Ni(OH)_2$, there is no considerable surface morphology change observed, as shown in the inset image of Fig. 5B. Furthermore, $Ni(OH)_2$ shows the amorphous phase on the surface of CdS. From the result and analyses, the ZnO/CdS/$Ni(OH)_2$ photoanode exhibited 4.12% photocurrent efficiency, which is 20.6 times higher than the pure ZnO nanosheets photoanode. More significantly, due to the effective hole depletion of $Ni(OH)_2$ catalyst, the PEC photo-stability can be significantly improved. The proposed mechanism of H-ZnO/CdS/$Ni(OH)_2$ is shown in Fig. 5C. The effective utilization of light can be achieved by the mixture of 2D/1D hierarchical structures, resulting in an exposed, huge, interface active area of the photoanode. Upon light irradiation, the photo-generated charge carriers between ZnO and CdS were successfully separated because of bandgap differences. Moreover, the high electron movement of electrons and their collection on ZnO nanosheets and the nanorods were advantageous for hydrogen generation reaction. Meanwhile, for Ni^{2+} to oxidize to higher Ni^{3+}/Ni^{4+}, the photo-generated holes moved to Ni species and were trapped. Then the Ni^{3+}/Ni^{4+} ions of oxidative nature successively contributed in the oxygen generation process, where reduction of oxidative ions back to Ni^{2+} took place. The addition of Ni^{2+}/Ni^{3+}/Ni^{4+} redox processes mainly enhanced the holes' depletion and resulted in efficient photoconversion and photostability.

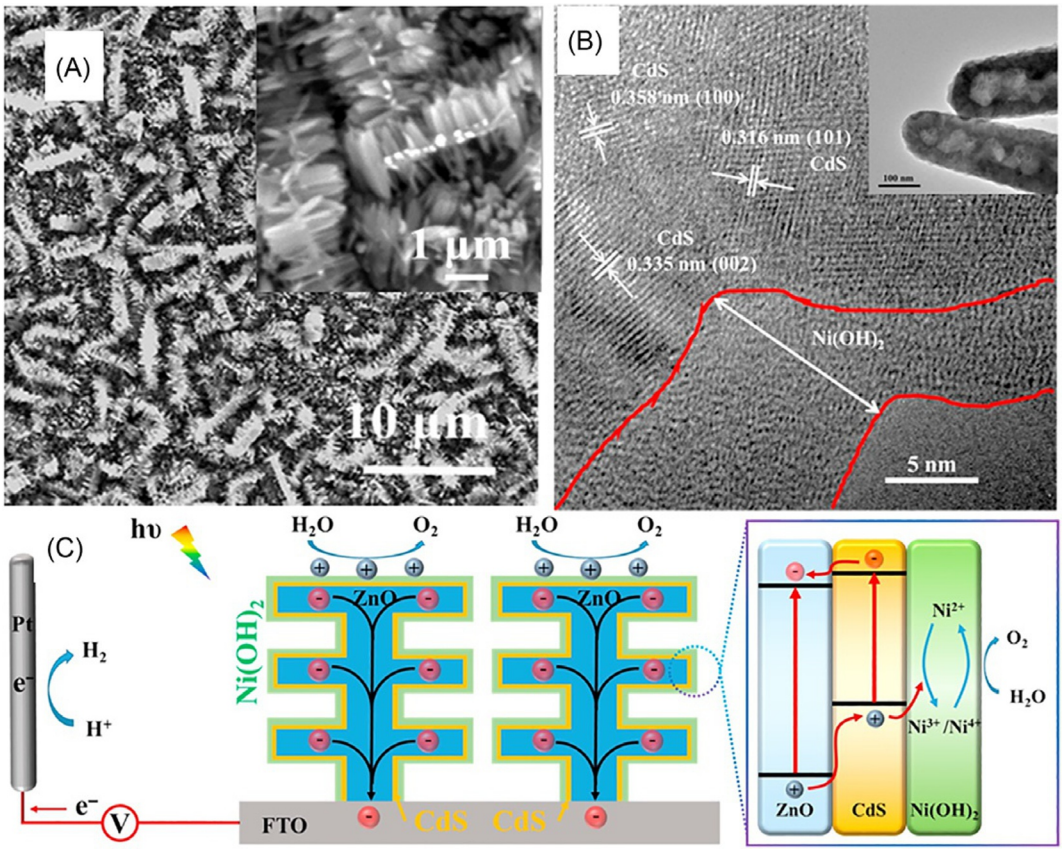

FIG. 5

(A) ZnO nanorod-nanosheets SEM image, (B) TEM image of ZnO/CdS/$Ni(OH)_2$, and (C) proposed water-splitting mechanism of H-ZnO/CdS/$Ni(OH)_2$ [51].

Yang et al. [52] developed the visible-light-driven composite electrode having carbon nitride quantum dots (CNQDs)/ZnO nanowire arrays for water splitting. Typical SEM images of nanowire arrays of ZnO are shown in Fig. 6A and B. From the figures, it can be observed that the ZnO nanowire arrays are evenly grown, with an average diameter of 200 nm and vertical lengths of about 2 μm. A TEM image of ZnO@CNQDs is shown in Fig. 6C. From the image, it can be observed that the carbon nitride quantum dots (diameter 20 nm) were nicely settled on the surface of the ZnO nanowire arrays. As a result, the PEC activity of the composite electrode was greatly improved due to the decoration of CNQDs onto the ZnO surface. Moreover, due to the small size of CNQDs, the quantum confinement effect was achieved. Due to the typical structure (Herpes-Rods) of CNQDs/ZnO composite, greatly separated the photo-excited electron and hole, and hence, improved photoelectric current. The composite electrode displayed improved PEC activity and hydrogen evolution rates in contrast to that of ZnO nanowire arrays. The composite electrode exhibited hydrogen generation about five times greater than that

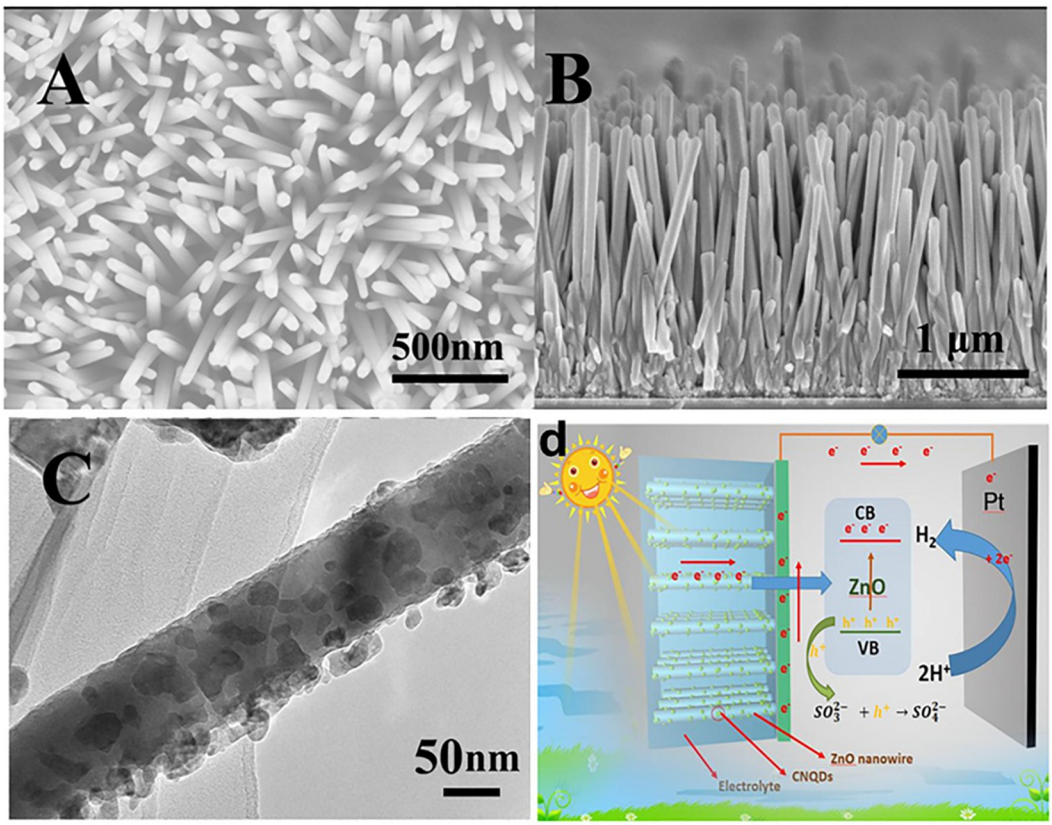

FIG. 6

(A, B) SEM image of ZnO nanowire arrays and cross-section, (C) TEM image of ZnO@CNQDs, and (D) schematic of PEC hydrogen generation of CNQDs/ZnO composite electrode [52].

of the pure ZnO, confirming that the CNQDs encourage the PEC performance of ZnO. Furthermore, the association of CNQDs encouraged the charge transmission procedure. Moreover, the photocurrent properties of ZnO were further improved due to the introduction of CNQDs because the ZnO nanowire had greater electron movement and a lesser onset potential.

The proposed mechanism for hydrogen generation of the CNQDs/ZnO composite electrode is shown in Fig. 6D. Upon light illumination, the photo-generated photons were moved to the CB of CNQDs from the VB of ZnO and left an equal number of holes on the VB. The CNQDs captured the photogenerated electrons, and hence, the photoexcited electrons on ZnO efficiently moved by the support of CNQDs and its recombination with the hole was suppressed. Then, the captured electron with CNQDs rapidly moved to the Pt surface. Hence, for the evolution of hydrogen, the hole that comes from the electrolyte could be joined with the electrons on the Pt surface. Meanwhile, the hole can be responded to with sulfite to make sulfate. Hence, the proposed electrode exhibited improved hydrogen generation.

According to a literature survey, it was confirmed that nanostructured metal oxide photocatalysts exhibited enhanced photocatalytic activity due to their decreased diffusion length of photo-generated charge carriers, enhanced surface reactions, and enriched surface development kinetics [53]. In particular, metal oxide photocatalysts with hierarchical nanostructures have shown better efficiency for water splitting as well as for increasing the surface area and light absorption capacity, decreasing recombination, and improving charge collection efficiency [54]. Dong et al. [55] reported the simple, extensive production of a 3D (n-ZnO/p-CuO nanoparticles/dandelion) heterostructure composite synthesized using a low temperature and facile chemical technique for visible-light PEC water splitting. The prepared n-ZnO/p-CuO photoelectrodes show substantial enhancement in PEC water splitting due to the incorporation of nanoparticles of n-type ZnO. The n-ZnO/p-CuO nanoparticles/dandelion heterostructures exhibited higher photocathodic current with the optimal loading of 4.6 wt% ZnO nanoparticles. The improved photoanode current is mainly due to the highly effective separation of the photoexcited charge carriers motivated by the p-n junction between CuO/ZnO interface.

3 APPLICATION OF PHOTOCATALYSIS IN WATER PURIFICATION

Degradation of water pollutants by heterogeneous photocatalysis is mediated by the in-situ formation of reactive oxygen species or radicals on the catalyst surface. When a light photon of energy greater than or equal to the bandgap falls on the photocatalyst surface, this results in the formation of electrons and holes (Fig. 7) [56, 57]. The electrons in the conduction band (CB) take part in the formation of superoxide radicals ($O_2^{\cdot-}$), while in the valence band (VB), holes give rise to hydroxyl radicals ($OH^{\cdot}$). These radicals oxidize harmful organic pollutants to H_2O and CO_2 [57]. Hence, it can be said

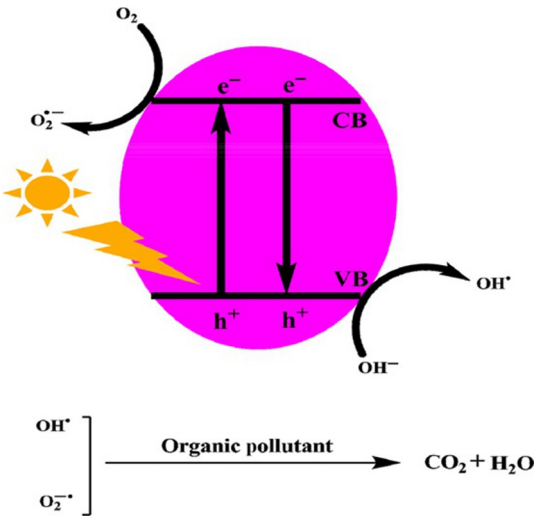

FIG. 7

Generation of reactive organic species during photocatalytic process and subsequent degradation of organic pollutants (self-drawn).

to be an ecofriendly process for water treatment. There have been a number of photocatalysts mainly metal oxides such as Cu_2O, CdS, CdSe, TiO_2, ZnO, V_2O_5, etc. Among these TiO_2 and ZnO are highly investigated due to their extraordinary properties which have been discussed in subsequent subsections.

3.1 PHOTOCATALYTIC WATER PURIFICATION BY TIO_2

TiO_2 is the most preferred semiconductor photocatalyst in the area of wastewater treatment because it has a high mobility of charge carrier and high stability [58]. Its visible light inactivity can be overcome by doping [59], heterojunction formation, and loading of noble metal or coinage metal nanoparticles [60]. Loading of coinage metal nanoparticles is one of the highly preferred strategies for activating TiO_2 in visible light due to the localized surface plasmon effect (LSPR), which mediates electron transfer from excited metal nanoparticles to the conduction band (CB) of TiO_2 during visible light illumination [61, 62]. However, this depends upon the work function of loaded metal nanoparticles and upon their size and dimensions [61–63].

Recent trends have focused more toward sensitizing TiO_2 using carbon-based materials such as carbon quantum dots [64] and g-C_3N_4 [58, 65] due to their easy preparation methods and low bandgap. Hence, these can act as effective sensitizers for TiO_2 [66]. A solid-phase calcination process was carried out to prepare a sequence of composite materials based upon g-C_3N_4 and TiO_2 doped with nitrogen (N-TiO_2). Nitrogen was found to be successfully doped on the TiO_2 lattice by simultaneous calcination of melamine and titanium nitride (TiN) in the process which not only resulted in the formation of Ti-N bonds but also g-C_3N_4. The nanocomposites which were examined by methylene blue degradation possessed excellent photocatalytic activity [58]. The high photoactivity of the as-synthesized photocatalyst was attributed to the enhancement in light absorption and charge carrier transfer. In an another investigation by Mohini et al. [67], the results revealed that the deposition of TiO_2 nanoparticles over g-C_3N_4 provided the high surface area required for adsorption of pollutant molecules and suppressed charge carrier recombination. Hydrogenated TiO_2 (H-TiO_2) has also gained tremendous attention. Hydrogenation is a simple procedure for extending the activity of TiO_2 to the visible region and even to the near infra-red (NIR) region of the solar spectrum [68]. The improved UV-Visible photocatalytic activity of the as-prepared photocatalyst was due to increased optical absorbance, trapping of charge carriers, and hindrance of the photo-generated charge carrier recombination. The hindrance of charge carrier recombination was attributed to vacant sites of oxygen and Ti^{3+} cations present in TiO_2 which are created as a result of hydrogenation.

Some of the other limitations of TiO_2 hampering its practical application in the field of water purification are its low porosity, surface area, and low reusability efficiency because it makes a milky suspension with the reaction mixture [69]. For overcoming these drawbacks, materials such as mesoporous silica [70], clays [71–73], zeolites [74], activated carbon [75], and graphene [76] have been used as catalytic supports for TiO_2. The support materials play an important role in imparting surface area, porosity, and catalytic active sites to TiO_2 to improve its efficiency [71]. TiO_2 nanoparticles supported upon SBA-15 (mesoporous silica) were prepared by Mehta et al. [70] using a microwave-assisted method. Morphological analysis revealed that TiO_2 nanoparticles with sizes around 4–10 nm were found to possess homogeneous distribution throughout the SBA-15 surface. The mesoporous nature of SBA-15 was undisturbed upon TiO_2 incorporation, and the resulting nanocomposites still possessed Type IV adsorption-desorption isotherm (Fig. 8A). However, loading TiO_2 nanoparticles led to a decrease in pore volume (0.93-0.50 cm^3/g) as seen from their pore distribution (Fig. 8B). The evaluation

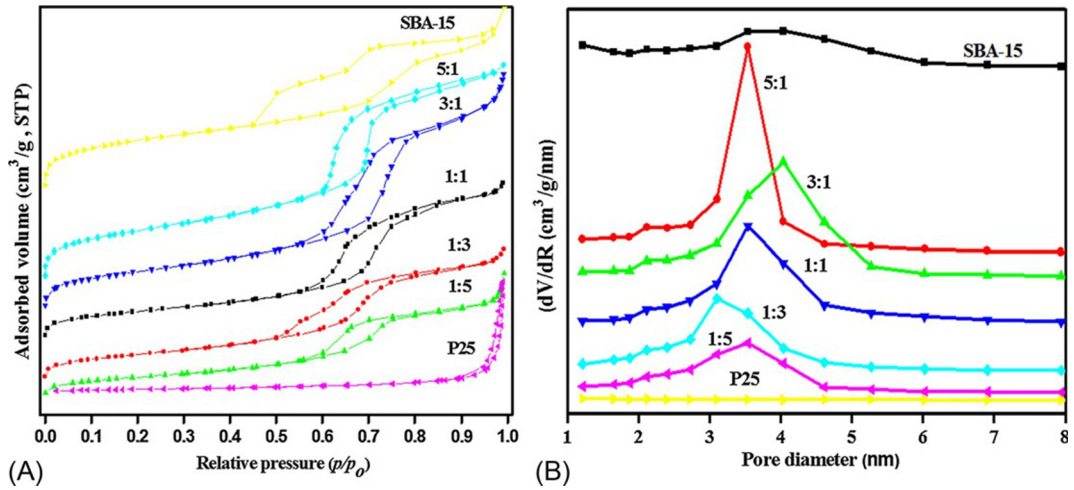

FIG.8

(A) N_2 adsorption/desorption hysteresis loops of SBA-15/TiO_2 composites and (B) their pore distributions [70].

of photocatalytic activity of the as-prepared nanocomposites was carried by alizarin dye and pentachlorophenol degradation under UV light irradiation. The photocatalytic activity of SBA-15/TiO_2 nanocomposites was higher than pure TiO_2 (P25) due to their high surface area and uniform distribution of TiO_2 on SBA-15. The composite having SBA-15 and TiO_2 in the ratio 1:5 showed high photocatalytic activity due to higher TiO_2 content. TiO_2/clay nanocomposites were prepared using different clays having textural differences (1:1 and 2:1) by a simple, facile, time-saving, cost-effective, microwave-assisted method by Mishra et al. [71] Anatase TiO_2 nanoparticles were successfully formed on the surface of clays in 10 min at 180°C. The photocatalytic activity of the nanocomposites depended upon the clay's texture and its optical properties. The 2:1 clays (bentonite and kunipia) were found to be better supports than 1:1 clay (kaolin) for photocatalytic decomposition of methylene blue and chlorobenzene.

Graphene has gained tremendous interest from material scientists due to its high electron mobility of about 15,000 $cm^2/V/s$ [77]. Graphene promotes charge separation, hampering the recombination of electron and holes [76]. Continuous fibers of graphene/TiO_2 were prepared for the first time by Zhang et al. [78] by a novel route which consisted of a combination of force spinning and water vapor annealing. The weakening of the PL emission peak (Fig. 9A) upon introduction of graphene clearly depicts the diminishing recombination of electron-hole pairs and their transfer conduction band (CB) of TiO_2 to graphene (Fig. 8B). Also the π-π conjugation in graphene, C-Ti bond formation, the presence of Ti^{3+}, and vacant oxygen sites are said to be some of the other factors which promote the separation of charge carriers and suppress their recombination (Fig. 9B). The evaluation of photocatalytic activity was carried out by photodegradation of X-3B dye. It was found that adsorption of X-3B dye in the nanocomposite increased by increasing graphene content which was assigned to the high porosity of nanocomposites and their large surface area. The high adsorption facilitated effective degradation

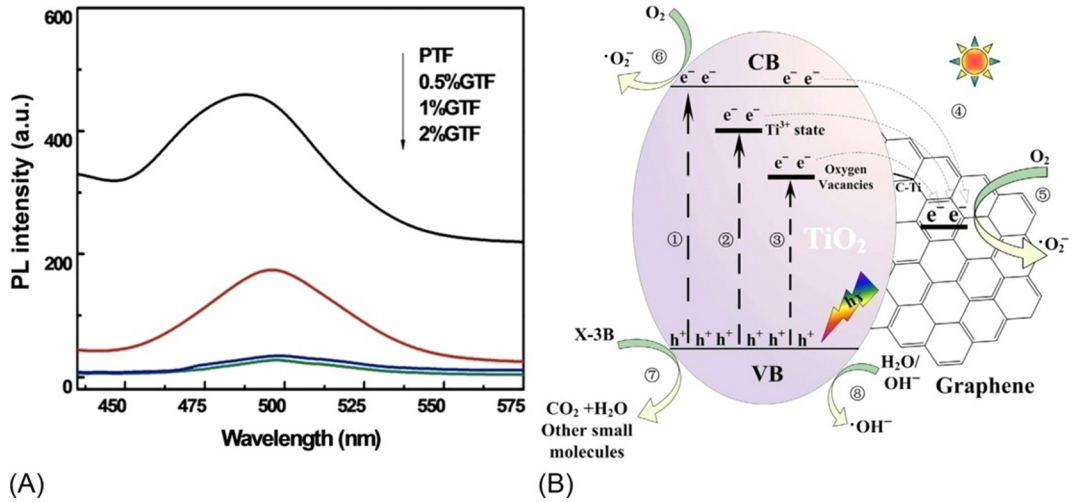

FIG. 9

(A) PL spectra of TiO_2/graphene showing a decrease in the PL emission peak and (B) electron transfer and trapping mechanism in TiO_2/graphene [78].

of X-3B dye. The composite containing 2% of graphene degraded 98% of dye in 120 min, showing it to be the optimal quantity of graphene for incorporation in TiO_2.

Apart from this, different morphologies of TiO_2 nanostructures have gained significant attention due to the uniqueness of their photophysical properties [79]. The morphology of TiO_2 nanostructures can be modified by specifically designing protocols with more precise control of hydrolysis of the precursor and crystal growth, as well as the organization of oligomer by itself. A variety of TiO_2 nanostructures have been synthesized such as nanocubes, nanobelts, nanohelix, nanorods, nanospheres, nanotubes, and many other hierarchical nanostructures [80]. The correlation between morphology and photocatalytic performance is considered to be the biggest challenge in the photocatalysis field. Zhang et al. [81] sought to discover a relation between photocatalytic activity and morphology of TiO_2 regarding the degradation of direct blue dye under ultraviolet light. Four different morphologies of anatase TiO_2 were synthesized, including slice, bipyramids, daisy, and sphere-like nanostructures using the hydrothermal procedure. TiO_2 having daisy-like morphology (TiO_2-D) was found to possess high degradation efficiency (Fig. 10). Upon investigating the dependence of photocatalytic performance over four different morphologies, it was found that catalytic activity depended upon the nanoparticles' shape. Different shapes of TiO_2 lead to different bandgap energies and different crystal facets. The bandgap energy could be considered a prime factor in the relationship of photocatalytic activity with the morphological structure of TiO_2.

At present, green synthesis methods of TiO_2 nanostructures have gained much attention because green chemistry relies upon processes and products that require less use of hazardous substances that are harmful to both humans and the environment. In this regard, Sundrishwary et al. [82] synthesized anatase mesoporous TiO_2 by the green chemistry approach using a solvent-free and simple precipitation process at low temperature, in which titanium tetraisopropoxide acted as a precursor and soluble

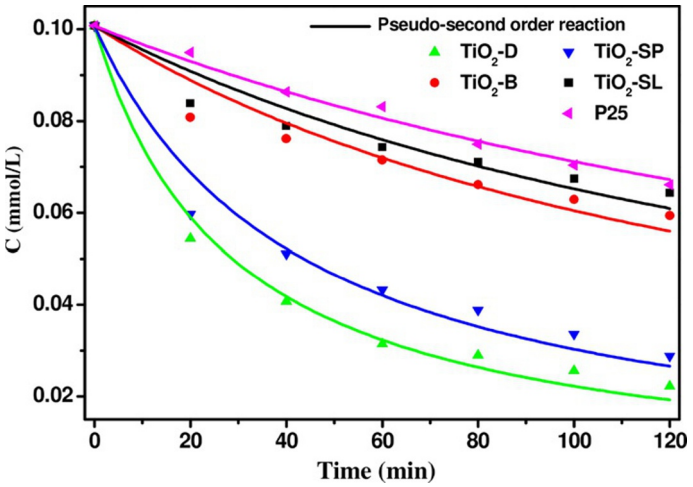

FIG. 10

Photocatalytic of different morphological samples of TiO_2 under UV light illumination [81].

starch acted as a template. Its photocatalytic activity was examined by methylene blue degradation. It was found that the as-prepared TiO_2 nanoparticles were more active near the visible region than UV, which can be attributed to the self-doping of TiO_2 by Ti^{3+} and carbon doping [83] from starch, as observed from XPS analysis (Fig. 11). It has been reported by Zhou et al. [84] that Ti^{3+} present as a surface defect in TiO_2 plays an important role in providing oxygen adsorption sites and electron traps to hamper electron-hole recombination. The photodegradation of methylene blue obeyed the Langmuir Hinshelwood first-order kinetics. The as-prepared TiO_2 nanoparticles were revealed to be highly stable against the photodegradation process of TiO_2, and could be reused up to 10 cycles (Fig. 12).

3.2 PHOTOCATALYTIC WATER PURIFICATION BY ZnO

Just as TiO_2, ZnO has been highly investigated as a photocatalyst for water purification because it is economical, has low toxicity, and has a high conductivity of charge carriers [85, 86]. Similar to TiO_2, it is a wide bandgap semiconductor and has a high optical bandgap of 3.3 eV which makes it active in UV light, and the photodegradation mechanism on the ZnO surface has close similarity with that of TiO_2 [85, 87]. There are some reports which highlighted the higher photocatalytic efficiency of ZnO (compared to TiO_2) in the degradation of some dyes in water which allows it to act as a suitable alternative to TiO_2 [87]. However, ZnO is less photo-stable, and it is more prone to photocorrosion, which results in a decrease in its photocatalytic activity [88, 89]. There have been a number of efforts made to overcome the above limitations of ZnO.

In order to make ZnO active in the visible region of solar spectra, researchers have experimented with efforts such as elemental doping [90, 91], plasmonic and coinage metal nanoparticles loading [92, 93], and integrating it with other visible active photocatalysts [94]. Like TiO_2, current trends stress coupling ZnO with carbon-based photoactive materials such as carbon quantum dots [95] and g-C_3N_4 [86, 96]. Chen et al. [97] prepared composite of ZnO on mesoporous g-C_3N_4 (mpg-C_3N_4) by a facile solvothermal approach. Pure ZnO nanoparticles with sizes around 10–30 nm having almost

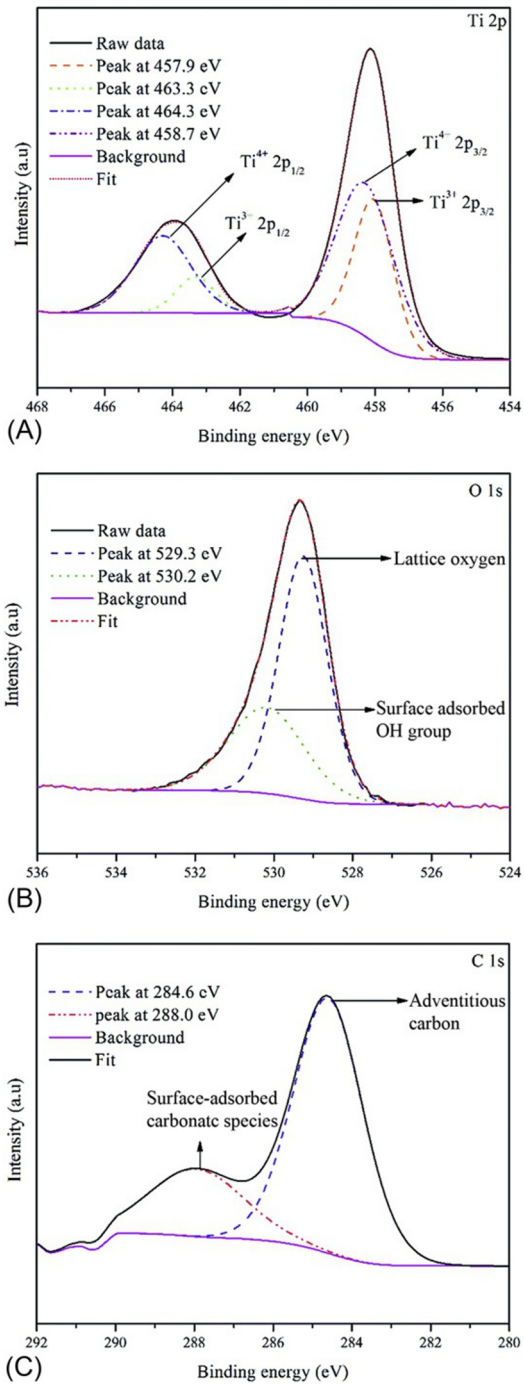

FIG. 11

High resolution XPS spectra of Ti2p, O1s and C1s of TiO_2 nanoparticles prepared by the green synthesis method [82].

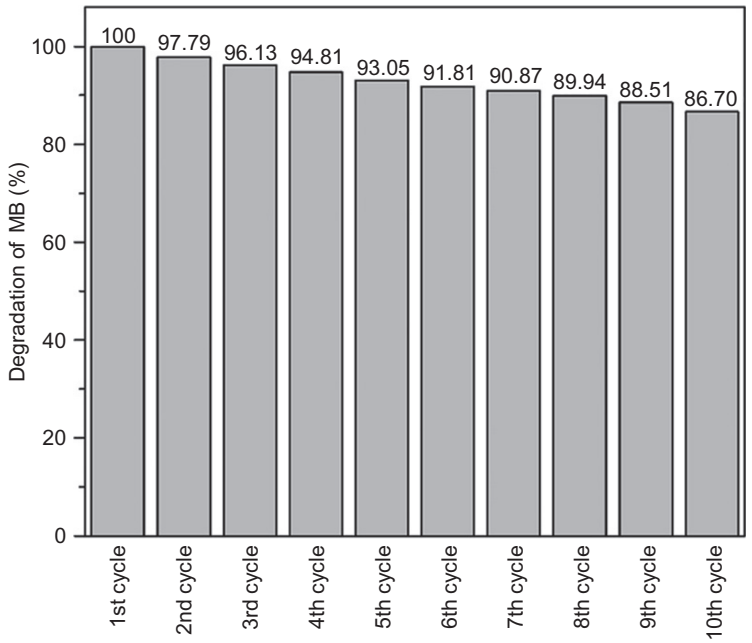

FIG. 12

Reusability of TiO_2 nanoparticles prepared by the green synthesis method [82].

spherical shape were formed. The HRTEM (Fig. 13) image depicted the presence of nanoparticles of ZnO on the planes and edges of mpg-C_3N_4. The lattice spacing of planes was found to be around 0.281 nm, corresponding to (100) crystal plane (Fig. 13D) of wurtzite ZnO, and it was consistent with the SAED pattern (Fig. 13 [inset]). The ZnO/mpg-C_3N_4 nanocomposite containing 24.9% ZnO showed the highest photocatalytic activity regarding methylene blue, which was almost 2.3 times more than pure mpg-C_3N_4 under visible light.

Also, impregnating ZnO upon support materials such as mesoporous silica [98], activated carbon [99], clays [100], zeolites [101], and graphene [102] not only enhances its catalytic activity but also hampers its photocorrosion. Muthirulan et al. [99] prepared ZnO supported on activated carbon (AC) by a simple and economical procedure in which a ZnO suspension in ethanol was infiltrated on activated carbon under vacuum conditions for 45 min in a rotary evaporator. The alizarin cyanin green (ACG) dye was degraded successfully by the as-prepared ZnO/AC composite. The rate of photocatalytic degradation of ACG dye by ZnO/AC composite was higher than that of ZnO and could be controlled by the reaction pH. The influence of pH can be explained on the basis of the zero-point charge, which for ZnO is 6.25. ZnO has a negative surface charge at pH higher than 8.8, and a positive charge below that. Because ACG dye is acidic in nature and possesses a negative charge in solution, this results in electrostatic attraction between ACG dye and the ZnO/AC surface, which results in better adsorption of the dye molecules. ZnO/graphene composite was synthesized via simple chemical corrosion phenomena and was found to have a porous structure. 8 mg of the nanocomposite was able to degrade 87% of methylene orange dye in 180 min. The presence of graphene promoted an effective charge separation, similar to the TiO_2/graphene composite discussed in the previous section, resulting

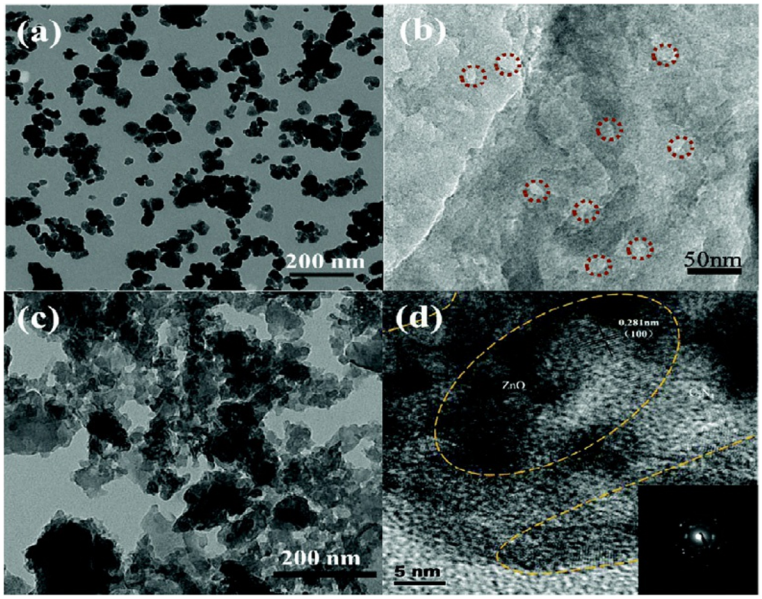

FIG. 13

(A) ZnO nanoparticles, (B) mpg-C_3N_4, (C) ZnO/mpg-C_3N_4 nanocomposite, (D) high-resolution image of ZnO/mpg-C_3N_4 nanocomposite and SAED pattern (inset) [97].

in an increased photocatalytic activity [102]. ZnO photoactivity is also affected by the morphological characteristics as discussed for TiO_2 in the previous section. Different nanostructures of ZnO have been synthesized, such as ZnO nanosheets, nanoflakes [103], nanorods [104], and dots [103], etc. Peter et al. [103] synthesized ZnO nanostructures (nanoflakes, nanorods, and nanodots) and investigated the morphological effect upon photocatalytic activity. The availability of surface active sites and uniformity in adsorption were found to depend upon nanostructure dimensions because the sharp corners of the nanomaterials acted as active adsorption sites. The 2D ZnO nanoflakes prepared in this work had blunt corners, and rods were observed to have hexagonal cross-sections of their respective SEM images (Fig. 14), which seemed to be less favorable for adsorption. On the other hand, ZnO quantum dots have a large surface area, and the extent of their sphericity results in homogeneity in adsorption of dye molecules (Fig. 15). The quantum dots were observed to possess a higher absorbance range compared to nanoflakes and nanorods. Hence, it can be said that active sites accessible for photocatalytic activity are considerably enhanced upon lowering the dimension of ZnO nanostructure, and therefore, nanodots had higher photocatalytic activity than nanoflakes and nanorods.

4 CONCLUSION

Both ZnO and TiO_2 have been extensively investigated as semiconductors for photocatalytic for H_2 production from water splitting and water purification. Both share similarities in properties because both of them are wide bandgap semiconductors with a bandgap of 3.3 eV for ZnO and 3.2 eV for TiO_2.

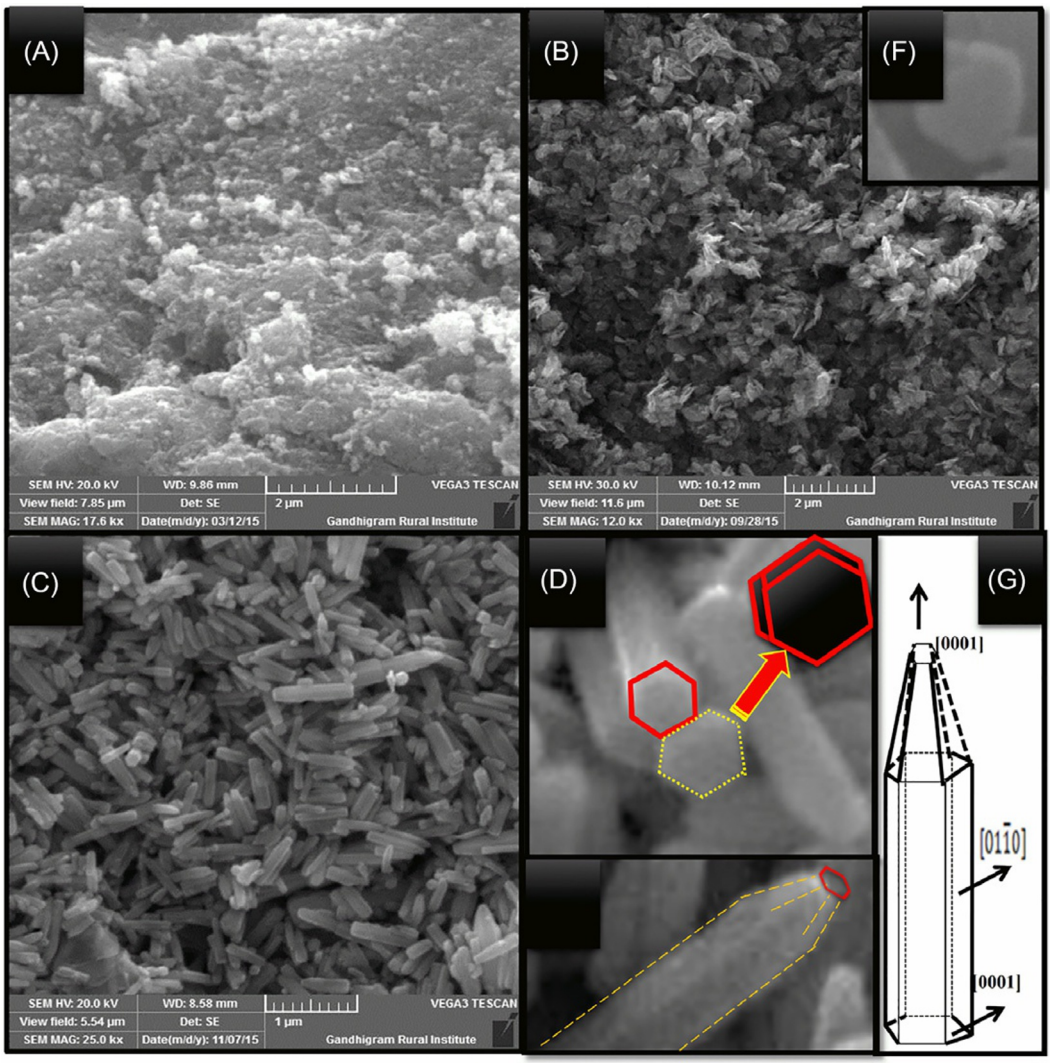

FIG. 14

SEM image of ZnO (A) nanodots, (B) nanoflakes, (C) nanorods, (D) nanorod cross-section, (E) single nanorods, (F) single flake, and (G) illustrative showing growth direction [103].

Both are nontoxic, have high charge carrier mobility, and are less costly and easy to synthesize. However, in terms of stability, ZnO is prone to photocorrosion. The conduction band potentials of ZnO and TiO_2 are near 0 V, which is the reduction potential of H^+ to H_2, which makes them highly promising for photocatalytic and photoelectrochemical water splitting. These semiconductors are also capable of degrading a number of water pollutants. However, their large bandgap energy makes leads to

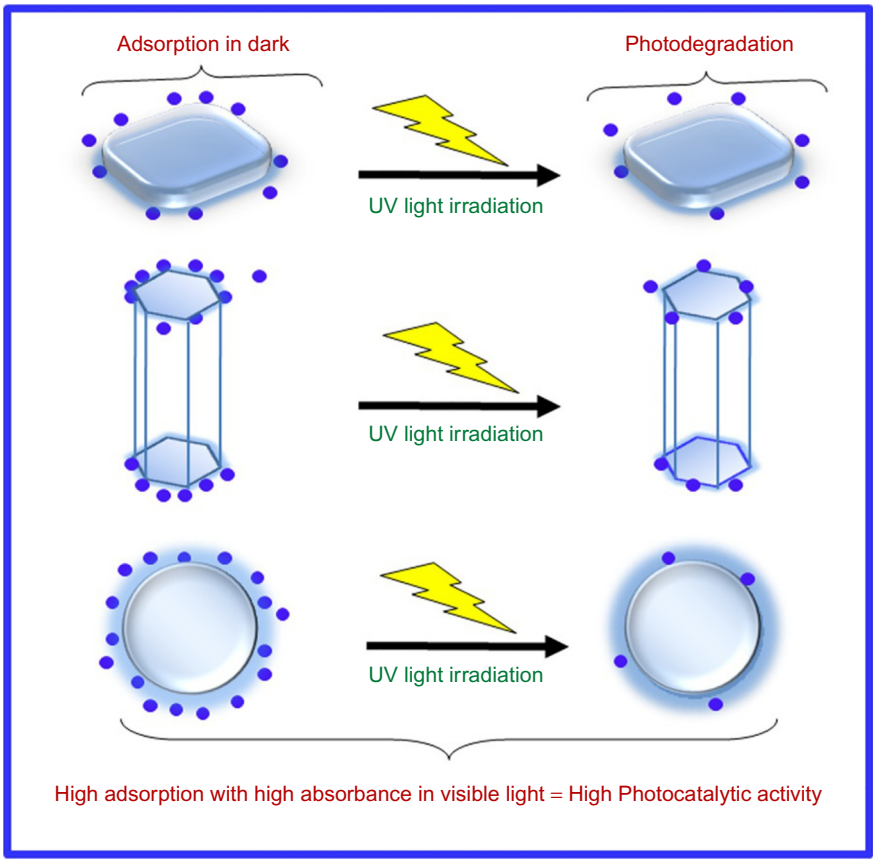

FIG. 15

Schematic demonstration showing structural effects on photocatalytic activity [103].

their inactivity in visible light, and this hampers their practical application in photocatalysis. To make them work in visible solar spectrum, numerous efforts have been made, both in the case of H_2 production and water purification, which include elemental doping, loading of noble metals, and heterojunction formation with other semiconductors. The current trend stresses heterojunction formation of ZnO and TiO_2 with carbon-based materials such as carbon quantum dots and g-C_3N_4 because these are cheap and easy to prepare. Apart from this, they are less porous and have a lower number of active sites. To overcome these limitations, there are materials used as supports which impart porosity and active sites to these photocatalysts. Nanostructure shape and morphology of the photocatalysts have a prime influence on their photoactivity, which is roughly assigned to different bandgap energies of nanostructures and availability of adsorption sites. Hence, with these improvements, ZnO- and TiO_2-based photocatalysts can still be said to have their hold in the photocatalysis field.

REFERENCES

[1] H. Ali, E. Khan, Environmental chemistry in the twenty-first century, Environ. Chem. Lett. 15 (2017) 329–346.

[2] A.C. Rai, P. Kumar, F. Pilla, A.N. Skouloudis, S. Di Sabatino, C. Ratti, A. Yasar, D. Rickerby, End-user perspective of low-cost sensors for outdoor air pollution monitoring, Sci. Total Environ. 607 (2017) 691–705.

[3] S. Bandyopadhyay, Evaluating Sustainable Economic Development, Springer, 2017.

[4] A. Babuponnusami, K. Muthukumar, A review on Fenton and improvements to the Fenton process for wastewater treatment, J. Environ. Chem. Eng. 2 (2014) 557–572.

[5] C.C. Nguyen, N.N. Vu, T.-O. Do, Recent advances in the development of sunlight-driven hollow structure photocatalysts and their applications, J. Mater. Chem. A 3 (2015) 18345–18359.

[6] Z. Han, F. Qiu, R. Eisenberg, P.L. Holland, T.D. Krauss, Robust photogeneration of H2 in water using semiconductor nanocrystals and a nickel catalyst, Science 338 (2012) 1321–1324.

[7] G. Chiarello, M. Dozzi, E. Selli, TiO_2-based materials for photocatalytic hydrogen production, J. Energy Chem. 26 (2017) 250–258.

[8] A. Reshak, Active photocatalytic water splitting solar-to-hydrogen energy conversion: chalcogenide photocatalyst Ba2ZnSe3 under visible irradiation, Appl. Catal. B Environ. 221 (2018) 17–26.

[9] X. Fan, L. Zang, M. Zhang, H. Qiu, Z. Wang, J. Yin, H. Jia, S. Pan, C. Wang, A bulk boron-based photocatalyst for efficient dechlorination: K3B6O10Br, Chem. Mater. 26 (2014) 3169–3174.

[10] M. Ge, J. Cai, J. Iocozzia, C. Cao, J. Huang, X. Zhang, J. Shen, S. Wang, S. Zhang, K.-Q. Zhang, A review of TiO_2 nanostructured catalysts for sustainable H_2 generation, Int. J. Hydrog. Energy 42 (2017) 8418–8449.

[11] W.Q. Fang, X.L. Wang, H. Zhang, Y. Jia, Z. Huo, Z. Li, H. Zhao, H.G. Yang, X. Yao, Manipulating solar absorption and electron transport properties of rutile TiO_2 photocatalysts via highly n-type F-doping, J. Mater. Chem. A 2 (2014) 3513–3520.

[12] Y. Lin, Z. Jiang, C. Zhu, X. Hu, X. Zhang, H. Zhu, J. Fan, S.H. Lin, C/B codoping effect on band gap narrowing and optical performance of TiO_2 photocatalyst: a spin-polarized DFT study, J. Mater. Chem. A 1 (2013) 4516–4524.

[13] Q. Liu, J. He, T. Yao, Z. Sun, W. Cheng, S. He, Y. Xie, Y. Peng, H. Cheng, Y. Sun, Aligned Fe_2 TiO5-containing nanotube arrays with low onset potential for visible-light water oxidation, Nat. Commun. 5 (2014) 5122.

[14] D. Liu, W. Zi, S.D. Sajjad, C. Hsu, Y. Shen, M. Wei, F. Liu, Reversible electron storage in an all-vanadium photoelectrochemical storage cell: synergy between vanadium redox and hybrid photocatalyst, ACS Catal. 5 (2015) 2632–2639.

[15] H. Wang, L. Zhang, Z. Chen, J. Hu, S. Li, Z. Wang, J. Liu, X. Wang, Semiconductor heterojunction photocatalysts: design, construction, and photocatalytic performances, Chem. Soc. Rev. 43 (2014) 5234–5244.

[16] Y. Xu, M.A. Melia, L.-K. Tsui, J.M. Fitz-Gerald, G. Zangari, Laser-induced surface modification at anatase TiO_2 nanotube array photoanodes for photoelectrochemical water oxidation, J. Phys. Chem. C 121 (2017) 17121–17128.

[17] J.S. Jang, C.W. Ahn, S.S. Won, J.H. Kim, W. Choi, B.-S. Lee, J.-H. Yoon, H.G. Kim, J.S. Lee, Vertically aligned core–shell $PbTiO_3$@ TiO_2 heterojunction nanotube array for photoelectrochemical and photocatalytic applications, J. Phys. Chem. C 121 (2017) 15063–15070.

[18] I.S. Cho, C.H. Lee, Y. Feng, M. Logar, P.M. Rao, L. Cai, D.R. Kim, R. Sinclair, X. Zheng, Codoping titanium dioxide nanowires with tungsten and carbon for enhanced photoelectrochemical performance, Nat. Commun. 4 (2013) 1723.

[19] H. Li, Z. Li, Y. Yu, Y. Ma, W. Yang, F. Wang, X. Yin, X. Wang, Surface-plasmon-resonance-enhanced photoelectrochemical water splitting from au-nanoparticle-decorated 3D TiO_2 nanorod architectures, J. Phys. Chem. C 121 (2017) 12071–12079.

[20] J. Jiao, J. Tang, W. Gao, D. Kuang, Y. Tong, L. Chen, Plasmonic silver nanoparticles matched with vertically aligned nitrogen-doped titanium dioxide nanotube arrays for enhanced photoelectrochemical activity, J. Power Sources 274 (2015) 464–470.
[21] J. Li, C. Liu, Y. Ye, J. Zhu, S. Wang, J. Guo, T.-K. Sham, Tracking the local effect of fluorine self-doping in anodic TiO_2 nanotubes, J. Phys. Chem. C 120 (2016) 4623–4628.
[22] X. Cui, G. Jiang, Z. Zhao, C. Xu, W. Bai, Y. Wang, A. Duan, J. Liu, Y. Wei, Facile regulation of crystalline phases and exposed facets on Ti3+ self-doped TiO_2 for efficient photocatalytic hydrogen evolution, J. Mater. Sci. 51 (2016) 10819–10832.
[23] J. Song, M. Zheng, X. Yuan, Q. Li, F. Wang, L. Ma, Y. You, S. Liu, P. Liu, D. Jiang, Electrochemically induced Ti 3+ self-doping of TiO_2 nanotube arrays for improved photoelectrochemical water splitting, J. Mater. Sci. 52 (2017) 6976–6986.
[24] H. Jun, M. Careem, A. Arof, Quantum dot-sensitized solar cells—perspective and recent developments: a review of Cd chalcogenide quantum dots as sensitizers, Renew. Sust. Energ. Rev. 22 (2013) 148–167.
[25] N.S. McCool, J.R. Swierk, C.T. Nemes, C.A. Schmuttenmaer, T.E. Mallouk, Dynamics of electron injection in SnO_2/TiO_2 core/shell electrodes for water-splitting dye-sensitized photoelectrochemical cells, J. Phys. Chem. Lett. 7 (2016) 2930–2934.
[26] W. Yuan, J. Yuan, J. Xie, C.M. Li, Polymer-mediated self-assembly of TiO_2@ Cu_2O core–shell nanowire array for highly efficient photoelectrochemical water oxidation, ACS Appl. Mater. Interfaces 8 (2016) 6082–6092.
[27] H. Yao, L. Liu, W. Fu, H. Yang, Y. Shi, Fe_2O_3 nanothorns sensitized two-dimensional TiO_2 nanosheets for highly efficient solar energy conversion, FlatChem 3 (2017) 1–7.
[28] H. Lee, H.-Y. Joo, C. Yoon, J. Lee, H. Lee, J. Choi, B. Park, T. Choi, Ferroelectric $BiFeO_3/TiO_2$ nanotube heterostructures for enhanced photoelectrochemical performance, Curr. Appl. Phys. 17 (2017) 679–683.
[29] D. Yolaçan, N.D. Sankir, Enhanced photoelectrochemical and photocatalytic properties of 3D-hierarchical ZnO nanostructures, J. Alloys Compd. 726 (2017) 474–483.
[30] K. Shingange, Z. Tshabalala, B. Dhonge, O. Ntwaeaborwa, D. Motaung, G. Mhlongo, 0D to 3D ZnO nanostructures and their luminescence, magnetic and sensing properties: influence of pH and annealing, Mater. Res. Bull. 85 (2017) 52–63.
[31] C.-H.M. Chuang, P.R. Brown, V. Bulović, M.G. Bawendi, Improved performance and stability in quantum dot solar cells through band alignment engineering, Nat. Mater. 13 (2014) 796.
[32] R.C. Pawar, C.S. Lee, Single-step sensitization of reduced graphene oxide sheets and CdS nanoparticles on ZnO nanorods as visible-light photocatalysts, Appl. Catal. B Environ. 144 (2014) 57–65.
[33] X. Li, J. Li, C. Cui, Z. Liu, Y. Niu, PbS nanoparticle sensitized ZnO nanowire arrays to enhance photocurrent for water splitting, J. Phys. Chem. C 120 (2016) 4183–4188.
[34] Z. Zhang, C. Gao, Z. Wu, W. Han, Y. Wang, W. Fu, X. Li, E. Xie, Toward efficient photoelectrochemical water-splitting by using screw-like SnO_2 nanostructures as photoanode after being decorated with CdS quantum dots, Nano Energy 19 (2016) 318–327.
[35] G. Liu, C.Y. Jimmy, G.Q.M. Lu, H.-M. Cheng, Crystal facet engineering of semiconductor photocatalysts: motivations, advances and unique properties, Chem. Commun. 47 (2011) 6763–6783.
[36] D. Kumar, R. Bai, S. Chaudhary, D.K. Pandya, Enhanced photoelectrochemical response for hydrogen generation in self-assembled aligned ZnO/PbS core/shell nanorod arrays grown by chemical bath deposition, Mater. Today Energy 6 (2017) 105–114.
[37] Y. Wang, J. Yu, W. Xiao, Q. Li, Microwave-assisted hydrothermal synthesis of graphene based Au–TiO_2 photocatalysts for efficient visible-light hydrogen production, J. Mater. Chem. A 2 (2014) 3847–3855.
[38] E. Hong, D. Kim, J.H. Kim, Heterostructured metal sulfide (ZnS–CuS–CdS) photocatalyst for high electron utilization in hydrogen production from solar water splitting, J. Ind. Eng. Chem. 20 (2014) 3869–3874.

[39] T. Hisatomi, C. Katayama, Y. Moriya, T. Minegishi, M. Katayama, H. Nishiyama, T. Yamada, K. Domen, Photocatalytic oxygen evolution using $BaNbO_2N$ modified with cobalt oxide under photoexcitation up to 740 nm, Energy Environ. Sci. 6 (2013) 3595–3599.
[40] W. Cui, Y. Qi, L. Liu, D. Rana, J. Hu, Y. Liang, Synthesis of PbS–K2La2Ti3O10 composite and its photocatalytic activity for hydrogen production, Progr. Nat. Sci.: Mater. Int. 22 (2012) 120–125.
[41] W. Cui, D. Guo, L. Liu, J. Hu, D. Rana, Y. Liang, Preparation of $ZnIn_2S_4/K_2La_2Ti_3O_{10}$ composites and their photocatalytic H2 evolution from aqueous Na_2S/Na_2SO_3 under visible light irradiation, Catal. Commun. 48 (2014) 55–59.
[42] A.A. Ismail, D.W. Bahnemann, Photochemical splitting of water for hydrogen production by photocatalysis: a review, Sol. Energy Mater. Sol. Cells 128 (2014) 85–101.
[43] H. Zhao, Y. Dong, P. Jiang, G. Wang, H. Miao, R. Wu, L. Kong, J. Zhang, C. Zhang, Light-assisted preparation of a ZnO/CdS nanocomposite for enhanced photocatalytic H2 evolution: an insight into importance of in situ generated ZnS, ACS Sustain. Chem. Eng. 3 (2015) 969–977.
[44] D. Bak, J.H. Kim, Facile fabrication of pseudo-microspherical ZnO/CdS core-shell photocatalysts for solar hydrogen production by water splitting, Ceram. Int. 43 (2017) 13493–13499.
[45] K. Lee, Y.-G. Lu, C.-H. Chuang, J. Ciston, G. Dukovic, Synthesis and characterization of (Ga1 − x Znx) (N1 − x Ox) nanocrystals with a wide range of compositions, J. Mater. Chem. A 4 (2016) 2927–2935.
[46] Z. Wang, X. Zong, Y. Gao, J. Han, Z. Xu, Z. Li, C. Ding, S. Wang, C. Li, Promoting charge separation and injection by optimizing the interfaces of GaN: ZnO photoanode for efficient solar water oxidation, ACS Appl. Mater. Interfaces 9 (2017) 30696–30702.
[47] D. Ma, J.-W. Shi, Y. Zou, Z. Fan, X. Ji, C. Niu, Highly efficient photocatalyst based on a CdS quantum dots/ZnO nanosheets 0D/2D heterojunction for hydrogen evolution from water splitting, ACS Appl. Mater. Interfaces 9 (2017) 25377–25386.
[48] V. Gurylev, C.-Y. Su, T.-P. Perng, Hydrogenated ZnO nanorods with defect-induced visible light-responsive photoelectrochemical performance, Appl. Surf. Sci. 411 (2017) 279–284.
[49] Y. Lv, W. Yao, X. Ma, C. Pan, R. Zong, Y. Zhu, The surface oxygen vacancy induced visible activity and enhanced UV activity of a ZnO1 − x photocatalyst, Catal. Sci. Technol. 3 (2013) 3136–3146.
[50] K. Karmakar, A. Sarkar, K. Mandal, G.G. Khan, Nano-engineering of p–n $CuFeO_2$-ZnO heterojunction photoanode with improved light absorption and charge collection for photoelectrochemical water oxidation, Nanotechnology 28 (2017) 325401.
[51] Y. Liu, Z. Kang, H. Si, P. Li, S. Cao, S. Liu, Y. Li, S. Zhang, Z. Zhang, Q. Liao, Cactus-like hierarchical nanorod-nanosheet mixed dimensional photoanode for efficient and stable water splitting, Nano Energy 35 (2017) 189–198.
[52] H. Yang, Z. Jin, H. Hu, G. Lu, Y. Bi, Fivefold enhanced photoelectrochemical properties of ZnO nanowire arrays modified with C3N4 quantum dots, Catalysts 7 (2017) 99.
[53] K. Sun, Y. Jing, C. Li, X. Zhang, R. Aguinaldo, A. Kargar, K. Madsen, K. Banu, Y. Zhou, Y. Bando, 3D branched nanowire heterojunction photoelectrodes for high-efficiency solar water splitting and H2 generation, Nanoscale 4 (2012) 1515–1521.
[54] M. Ji, J. Cai, Y. Ma, L. Qi, Controlled growth of ferrihydrite branched nanosheet arrays and their transformation to hematite nanosheet arrays for photoelectrochemical water splitting, ACS Appl. Mater. Interfaces 8 (2015) 3651–3660.
[55] G. Dong, B. Du, L. Liu, W. Zhang, Y. Liang, H. Shi, W. Wang, Synthesis and their enhanced photoelectrochemical performance of ZnO nanoparticle-loaded CuO dandelion heterostructures under solar light, Appl. Surf. Sci. 399 (2017) 86–94.
[56] I.K. Konstantinou, T.A. Albanis, Photocatalytic transformation of pesticides in aqueous titanium dioxide suspensions using artificial and solar light: intermediates and degradation pathways, Appl. Catal. B Environ. 42 (2003) 319–335.
[57] A. Mills, S. Le Hunte, An overview of semiconductor photocatalysis, J. Photochem. Photobiol. A Chem. 108 (1997) 1–35.

[58] S. Sun, M. Sun, Y. Fang, Y. Wang, H. Wang, One-step in situ calcination synthesis of gC3N4/N-TiO2 hybrids with enhanced photoactivity, RSC Adv. 6 (2016) 13063–13071.
[59] Z. Li, F. Wang, A. Kvit, X. Wang, Nitrogen doped 3D titanium dioxide nanorods architecture with significantly enhanced visible light photoactivity, J. Phys. Chem. C 119 (2015) 4397–4405.
[60] X. Zhou, G. Liu, J. Yu, W. Fan, Surface plasmon resonance-mediated photocatalysis by noble metal-based composites under visible light, J. Mater. Chem. 22 (2012) 21337–21354.
[61] S.T. Kochuveedu, Y.H. Jang, D.H. Kim, A study on the mechanism for the interaction of light with noble metal-metal oxide semiconductor nanostructures for various photophysical applications, Chem. Soc. Rev. 42 (2013) 8467–8493.
[62] S. Sarina, E.R. Waclawik, H. Zhu, Photocatalysis on supported gold and silver nanoparticles under ultraviolet and visible light irradiation, Green Chem. 15 (2013) 1814–1833.
[63] R. Kaur, B. Pal, Plasmonic coinage metal–TiO_2 hybrid nanocatalysts for highly efficient photocatalytic oxidation under sunlight irradiation, New J. Chem. 39 (2015) 5966–5976.
[64] J. Chen, J. Shu, Z. Anqi, H. Juyuan, Z. Yan, J. Chen, Synthesis of carbon quantum dots/TiO_2 nanocomposite for photo-degradation of Rhodamine B and cefradine, Diam. Relat. Mater. 70 (2016) 137–144.
[65] F. Raziq, C. Li, M. Humayun, Y. Qu, A. Zada, H. Yu, L. Jing, Synthesis of TiO_2/g-C_3N_4 nanocomposites as efficient photocatalysts dependent on the enhanced photogenerated charge separation, Mater. Res. Bull. 70 (2015) 494–499.
[66] X.-j. Wang, W.-y. Yang, F.-t. Li, Y.-b. Xue, R.-h. Liu, Y.-j. Hao, In situ microwave-assisted synthesis of porous N-TiO_2/g-C_3N_4 heterojunctions with enhanced visible-light photocatalytic properties, Ind. Eng. Chem. Res. 52 (2013) 17140–17150.
[67] R. Mohini, N. Lakshminarasimhan, Coupled semiconductor nanocomposite g-C_3N_4/TiO_2 with enhanced visible light photocatalytic activity, Mater. Res. Bull. 76 (2016) 370–375.
[68] J. Tian, Y. Leng, Z. Zhao, Y. Xia, Y. Sang, P. Hao, J. Zhan, M. Li, H. Liu, Carbon quantum dots/hydrogenated TiO_2 nanobelt heterostructures and their broad spectrum photocatalytic properties under UV, visible, and near-infrared irradiation, Nano Energy 11 (2015) 419–427.
[69] H. Dong, G. Zeng, L. Tang, C. Fan, C. Zhang, X. He, Y. He, An overview on limitations of TiO_2-based particles for photocatalytic degradation of organic pollutants and the corresponding countermeasures, Water Res. 79 (2015) 128–146.
[70] A. Mehta, A. Mishra, M. Sharma, S. Singh, S. Basu, Effect of silica/titania ratio on enhanced photooxidation of industrial hazardous materials by microwave treated mesoporous SBA-15/TiO_2 nanocomposites, J. Nanopart. Res. 18 (2016) 209.
[71] A. Mishra, A. Mehta, M. Sharma, S. Basu, Enhanced heterogeneous photodegradation of VOC and dye using microwave synthesized TiO_2/Clay nanocomposites: a comparison study of different type of clays, J. Alloys Compd. 694 (2017) 574–580.
[72] A. Mishra, A. Mehta, S. Kainth, S. Basu, Effect of different plasmonic metals on photocatalytic degradation of volatile organic compounds (VOCs) by bentonite/M-TiO2 nanocomposites under UV/visible light, Appl. Clay Sci. 153 (2018) 144–153.
[73] A. Mishra, A. Mehta, S. Kainth, S. Basu, A comparative study on the effect of different precursors for synthesis and efficient photocatalytic activity of gC_3N_4/TiO_2/bentonite nanocomposites, J. Mater. Sci. 53 (2018) 1–17.
[74] M.N. Chong, Z.Y. Tneu, P.E. Poh, B. Jin, R. Aryal, Synthesis, characterisation and application of TiO_2–zeolite nanocomposites for the advanced treatment of industrial dye wastewater, J. Taiwan Inst. Chem. Eng. 50 (2015) 288–296.
[75] P. Singh, M. Vishnu, K.K. Sharma, R. Singh, S. Madhav, D. Tiwary, P.K. Mishra, Comparative study of dye degradation using TiO_2-activated carbon nanocomposites as catalysts in photocatalytic, sonocatalytic, and photosonocatalytic reactor, Desalin. Water Treat. 57 (2016) 20552–20564.
[76] Y. Yang, L. Xu, H. Wang, W. Wang, L. Zhang, TiO_2/graphene porous composite and its photocatalytic degradation of methylene blue, Mater. Des. 108 (2016) 632–639.

[77] S.P. Lonkar, Y.S. Deshmukh, A.A. Abdala, Recent advances in chemical modifications of graphene, Nano Res. 8 (2015) 1039–1074.
[78] Q. Zhang, N. Bao, X. Wang, X. Hu, X. Miao, M. Chaker, D. Ma, Advanced fabrication of chemically bonded graphene/TiO_2 continuous fibers with enhanced broadband photocatalytic properties and involved mechanisms exploration, Sci. Rep. 6 (2016) 38066.
[79] S.B. Khan, M. Hou, S. Shuang, Z. Zhang, Morphological influence of TiO_2 nanostructures (nanozigzag, nanohelics and nanorod) on photocatalytic degradation of organic dyes, Appl. Surf. Sci. 400 (2017) 184–193.
[80] Z. Sun, T. Liao, L. Sheng, L. Kou, J.H. Kim, S.X. Dou, Deliberate design of TiO_2 nanostructures towards superior photovoltaic cells, Chem Eur J 22 (2016) 11357–11364.
[81] H. Zhang, H. Zhang, P. Zhu, F. Huang, Morphological effect in photocatalytic degradation of direct blue over mesoporous TiO_2 catalysts, ChemistrySelect 2 (2017) 3282–3288.
[82] S.S. Muniandy, N.H.M. Kaus, Z.-T. Jiang, M. Altarawneh, H.L. Lee, Green synthesis of mesoporous anatase TiO_2 nanoparticles and their photocatalytic activities, RSC Adv. 7 (2017) 48083–48094.
[83] W. Mai, F. Wen, D. Xie, Y. Leng, Z. Mu, Structure and composition study of carbon-doped titanium oxide film combined with first principles, J. Adv. Ceram. 3 (2014) 49–55.
[84] Y. Zhou, C. Chen, N. Wang, Y. Li, H. Ding, Stable Ti3+ self-doped anatase-rutile mixed TiO_2 with enhanced visible light utilization and durability, J. Phys. Chem. C 120 (2016) 6116–6124.
[85] M. Wang, F. Ren, J. Zhou, G. Cai, L. Cai, Y. Hu, D. Wang, Y. Liu, L. Guo, S. Shen, N doping to ZnO nanorods for photoelectrochemical water splitting under visible light: engineered impurity distribution and terraced band structure, Sci. Rep. 5 (2015) 12925.
[86] F. Guo, W. Shi, W. Guan, H. Huang, Y. Liu, Carbon dots/g-C3N4/ZnO nanocomposite as efficient visible-light driven photocatalyst for tetracycline total degradation, Sep. Purif. Technol. 173 (2017) 295–303.
[87] Y. Wang, R. Shi, J. Lin, Y. Zhu, Enhancement of photocurrent and photocatalytic activity of ZnO hybridized with graphite-like C3N4, Energy Environ. Sci. 4 (2011) 2922–2929.
[88] R. Sapkal, S. Shinde, T. Waghmode, S. Govindwar, K. Rajpure, C. Bhosale, Photo-corrosion inhibition and photoactivity enhancement with tailored zinc oxide thin films, J. Photochem. Photobiol. B Biol. 110 (2012) 15–21.
[89] J. Ishioka, K. Kogure, K. Ofuji, K. Kawaguchi, M. Jeem, T. Kato, T. Shibayama, S. Watanabe, In situ direct observation of photocorrosion in ZnO crystals in ionic liquid using a laser-equipped high-voltage electron microscope, AIP Adv. 7 (2017) 035220.
[90] H. Sudrajat, S. Babel, A novel visible light active N-doped ZnO for photocatalytic degradation of dyes, J. Water Process Eng. 16 (2017) 309–318.
[91] W. Bousslama, H. Elhouichet, M. Férid, Enhanced photocatalytic activity of Fe doped ZnO nanocrystals under sunlight irradiation, Optik 134 (2017) 88–98.
[92] A. Senthilraja, B. Krishnakumar, B. Subash, A.J. Sobral, M. Swaminathan, M. Shanthi, Sn loaded Au–ZnO photocatalyst for the degradation of AR 18 dye under UV-A light, J. Ind. Eng. Chem. 33 (2016) 51–58.
[93] M.J. Sampaio, M.J. Lima, D.L. Baptista, A.M. Silva, C.G. Silva, J.L. Faria, Ag-loaded ZnO materials for photocatalytic water treatment, Chem. Eng. J. 318 (2017) 95–102.
[94] T. Chang, Z. Li, G. Yun, Y. Jia, H. Yang, Enhanced photocatalytic activity of ZnO/CuO nanocomposites synthesized by hydrothermal method, Nano-Micro Lett. 5 (2013) 163–168.
[95] H. Bozetine, Q. Wang, A. Barras, M. Li, T. Hadjersi, S. Szunerits, R. Boukherroub, Green chemistry approach for the synthesis of ZnO–carbon dots nanocomposites with good photocatalytic properties under visible light, J. Colloid Interface Sci. 465 (2016) 286–294.
[96] W. Liu, M. Wang, C. Xu, S. Chen, Facile synthesis of g-C3N4/ZnO composite with enhanced visible light photooxidation and photoreduction properties, Chem. Eng. J. 209 (2012) 386–393.
[97] D. Chen, K. Wang, T. Ren, H. Ding, Y. Zhu, Synthesis and characterization of the ZnO/mpg-C3N4 heterojunction photocatalyst with enhanced visible light photoactivity, Dalton Trans. 43 (2014) 13105–13114.

[98] V. Vo, T.P.T. Thi, H.-Y. Kim, S.J. Kim, Facile post-synthesis and photocatalytic activity of N-doped ZnO–SBA-15, J. Phys. Chem. Solids 75 (2014) 403–409.
[99] P. Muthirulan, M. Meenakshisundararam, N. Kannan, Beneficial role of ZnO photocatalyst supported with porous activated carbon for the mineralization of alizarin cyanin green dye in aqueous solution, J. Adv. Res. 4 (2013) 479–484.
[100] H. Peng, X. Liu, W. Tang, R. Ma, Facile synthesis and characterization of ZnO nanoparticles grown on halloysite nanotubes for enhanced photocatalytic properties, Sci. Rep. 7 (2017) 2250.
[101] V.R. Batistela, L.Z. Fogaça, S.L. Fávaro, W. Caetano, N.R.C. Fernandes-Machado, N. Hioka, ZnO supported on zeolites: photocatalyst design, microporosity and properties, Colloids Surf. A Physicochem. Eng. Asp. 513 (2017) 20–27.
[102] J. Xu, Y. Cui, Y. Han, M. Hao, X. Zhang, ZnO–graphene composites with high photocatalytic activities under visible light, RSC Adv. 6 (2016) 96778–96784.
[103] I.J. Peter, E. Praveen, G. Vignesh, P. Nithiananthi, ZnO nanostructures with different morphology for enhanced photocatalytic activity, Mater. Res. Express 4 (2017) 124003.
[104] M.T. Man, J.-H. Kim, M.S. Jeong, A.-T.T. Do, H.S. Lee, Oriented ZnO nanostructures and their application in photocatalysis, J. Lumin. 185 (2017) 17–22.

Index

Note: Page numbers followed by *f* indicate figures and *t* indicate tables.

B

C

D

E

F

G

H

I

J

K

L

M

N

O

P

Q

R

S

T

X

Y

Z